

Lecture Notes on Multidisciplinary Industrial Engineering  
*Series Editor: J. Paulo Davim*

M. S. Shunmugam  
M. Kanthababu *Editors*


# Advances in Unconventional Machining and Composites

Proceedings of AIMTDR 2018

 Springer

# Lecture Notes on Multidisciplinary Industrial Engineering

## Series Editor

J. Paulo Davim , Department of Mechanical Engineering, University of Aveiro, Aveiro, Portugal

“Lecture Notes on Multidisciplinary Industrial Engineering” publishes special volumes of conferences, workshops and symposia in interdisciplinary topics of interest. Disciplines such as materials science, nanosciences, sustainability science, management sciences, computational sciences, mechanical engineering, industrial engineering, manufacturing, mechatronics, electrical engineering, environmental and civil engineering, chemical engineering, systems engineering and biomedical engineering are covered. Selected and peer-reviewed papers from events in these fields can be considered for publication in this series.

More information about this series at <http://www.springer.com/series/15734>

M. S. Shunmugam · M. Kanthababu  
Editors

# Advances in Unconventional Machining and Composites

Proceedings of AIMTDR 2018

 Springer

*Editors*

M. S. Shunmugam  
Manufacturing Engineering Section  
Department of Mechanical Engineering  
Indian Institute of Technology Madras  
Chennai, Tamil Nadu, India

M. Kanthababu  
Department of Manufacturing Engineering  
College of Engineering, Guindy  
Anna University  
Chennai, Tamil Nadu, India

ISSN 2522-5022

ISSN 2522-5030 (electronic)

Lecture Notes on Multidisciplinary Industrial Engineering

ISBN 978-981-32-9470-7

ISBN 978-981-32-9471-4 (eBook)

<https://doi.org/10.1007/978-981-32-9471-4>

© Springer Nature Singapore Pte Ltd. 2020

This work is subject to copyright. All rights are reserved by the Publisher, whether the whole or part of the material is concerned, specifically the rights of translation, reprinting, reuse of illustrations, recitation, broadcasting, reproduction on microfilms or in any other physical way, and transmission or information storage and retrieval, electronic adaptation, computer software, or by similar or dissimilar methodology now known or hereafter developed.

The use of general descriptive names, registered names, trademarks, service marks, etc. in this publication does not imply, even in the absence of a specific statement, that such names are exempt from the relevant protective laws and regulations and therefore free for general use.

The publisher, the authors and the editors are safe to assume that the advice and information in this book are believed to be true and accurate at the date of publication. Neither the publisher nor the authors or the editors give a warranty, expressed or implied, with respect to the material contained herein or for any errors or omissions that may have been made. The publisher remains neutral with regard to jurisdictional claims in published maps and institutional affiliations.

This Springer imprint is published by the registered company Springer Nature Singapore Pte Ltd. The registered company address is: 152 Beach Road, #21-01/04 Gateway East, Singapore 189721, Singapore

# **AIMTDR 2018 Conference's Core Organizing Committee**

## **Patrons**

Dr. M. K. Surappa, Vice Chancellor, Anna University  
Dr. J. Kumar, Registrar, Anna University

## **President (NAC-AIMTDR)**

Mr. P. Kaniappan, Managing Director, WABCO India Ltd.

## **Vice-President (NAC-AIMTDR)**

Dr. Uday Shanker Dixit, Professor, IIT Guwahati, India

## **Co-patrons**

Dr. A. Rajadurai, Dean, MIT Campus, Anna University  
Dr. T. V. Geetha, Dean, CEG Campus, Anna University  
Dr. L. Karunamoorthy, Chairman, Faculty of Mechanical Engineering,  
Anna University  
Dr. S. Rajendra Boopathy, Head, Department of Mechanical Engineering,  
Anna University

## **Chairman**

Dr. S. Gowri, Honorary Professor, Department of Manufacturing Engineering, Anna University

## **Co-chairman**

Dr. P. Hariharan, Professor, Department of Manufacturing Engineering, Anna University

## **Organizing Secretary**

Dr. M. Kanthababu, Professor and Head, Department of Manufacturing Engineering, Anna University

## **Joint Organizing Secretaries**

Dr. M. Pradeep Kumar, Professor, Department of Mechanical Engineering, Anna University

Dr. A. Siddharthan, Associate Professor, Department of Production Technology, Anna University

## **International Scientific Committee**

Prof. Abhijit Chandra, Iowa State University, USA  
Prof. Ajay P. Malshe, University of Arkansas, USA  
Prof. Andrew Y. C. Nee, NUS, Singapore  
Prof. Chandrasekar S., Purdue University, USA  
Prof. Dean T. A., University of Birmingham, UK  
Prof. Hong Hocheng, National Tsing Hua University, Taiwan  
Prof. John Sutherland, Purdue University, USA  
Prof. Kamlakar P. Rajurkar, University of Nebraska, USA  
Prof. Kornel Ehmann, Northwestern University, USA  
Prof. Liao Y. S., National Taiwan University, Taiwan  
Prof. McGeough J. A., University of Edinburgh, UK  
Prof. Mustafizur Rahman, NUS, Singapore

Prof. Philip Koshy, McMaster University, Canada  
 Prof. Rakesh Nagi, University of Buffalo, USA  
 Prof. Shiv Gopal Kapoor, University of Illinois, USA  
 Prof. Srihari Krishnasami, Binghamton University, USA  
 Prof. Tae Jo Ko, Yeungnam University, South Korea  
 Prof. Tugrul Ozel, State University of New Jersey, USA

## **National Advisory Committee**

Prof. Ahuja B. B., Government College of Engineering Pune  
 Prof. Amitabha Ghosh, BESU  
 Prof. Bijoy Bhattacharyya, Jadavpur University, Kolkata  
 Prof. Biswanath Doloi, Jadavpur University, Kolkata  
 Prof. Chattopadhyay A. K., IIT Kharagpur  
 Prof. Deshmukh S. G., IIT Gwalior  
 Shri. Dhand N. K., MD, Ace Micromatic, Bangalore  
 Prof. Dixit U. S., IIT Guwahati, Guwahati  
 Prof. Jain P. K., IIT Roorkee, Roorkee  
 Prof. Jain V. K., IIT Kanpur  
 Prof. Jose Mathew, NIT Calicut  
 Shri. Lakshminarayan M., WABCO India Ltd.  
 Prof. Lal G. K., IIT Kanpur  
 Prof. Mehta N. K., IIT Roorkee  
 Prof. Mohanram P. V., PSG Institute of Technology and Applied Research  
 Shri. Mohanram P., IMTMA, Bangalore  
 Dr. Mukherjee T., Tata Steel Ltd., Jamshedpur  
 Shri. Muralidharan P., Lucas TVS Ltd., Vellore  
 Prof. Narayanan S., VIT University, Vellore  
 Mr. Niraj Sinha, Scientist 'G', PSA, GOI  
 Prof. Pande S. S., IIT Bombay, Mumbai  
 Dr. Prasad Raju D. R., MVGREC  
 Prof. Radhakrishnan P., PSG Institute of Advanced Studies, Coimbatore  
 Prof. Radhakrishnan V., IIST, Trivandrum  
 Prof. Ramaswamy N., IIT Bombay (Former)  
 Prof. Ramesh Babu N., IIT Madras  
 Shri. Rangachar C. P., Yuken India Ltd., Bangalore  
 Prof. Rao P. V., IIT Delhi  
 Dr. Santhosh Kumar, IIT BHU  
 Dr. Sathyan B. R., CMTI, Bangalore  
 Prof. Satyanarayan B., Andhra University (Former)  
 Prof. Selvaraj T., NIT Trichy  
 Prof. Shan H. S., IIT Roorkee (Former)  
 Prof. Shunmugam M. S., IIT Madras



Shri. Shirgurkar S. G., Ace Designers Ltd., Bangalore

Dr. Sumantran V., Celeris Technologies

Dr. Suri V. K., BARC, Mumbai

Shri. Venu Gopalan P., DRDL Hyderabad

Prof. Vinod Yadav, Motilal Nehru National Institute of Technology, Allahabad

# Foreword

It gives us immense pleasure to present the Advances in Manufacturing Technology and Design—Proceedings of All India Manufacturing Technology, Design and Research (AIMTDR) Conference 2018.

We would like to express our deep gratitude to all the members of Organizing Committee of AIMTDR 2018 Conference and also to authors, reviewers, sponsors, volunteers, etc., for their wholehearted support and active participation. Our special thanks to Mr. P. Kaniappan, Managing Director, WABCO India Ltd., Chennai, who kindly agreed to act as President of National Advisory Committee (NAC) of the AIMTDR 2018 Conference. We also express our sincere thanks to Chairman Dr. S. Gowri, Honorary Professor, and Co-chairman Dr. P. Hariharan, Professor, Department of Manufacturing Engineering, Anna University, Chennai, for their wholehearted support. We would like to express our sincere thanks to research scholars Mr. K. R. Sunilkumar, Mr. U. Goutham, Mr. V. Mohankumar, Mr. R. Prabhu and also UG/PG students of the Department of Manufacturing Engineering, Anna University, for their contributions in the preparation of this volume.

High-quality papers have been selected after peer review by technical experts. We hope you find the papers included in the Proceedings of AIMTDR 2018 Conference are interesting and thought-provoking.

We also like to express our gratitude for the support provided by Wabco India Ltd., Chennai, Kistler Instruments India Pvt. Ltd., Chennai, Ametek Instruments India Pvt. Ltd., Bengaluru, Central Manufacturing Technology Institute, Govt. of India, Bengaluru, Defence Research and Development Organisation, Government of India, New Delhi, and Ceeyes Engineering Industries Pvt. Ltd., Trichy.

Finally, we would like to express our gratitude to National Advisory Committee (NAC) members of AIMTDR 2018 for providing the necessary guidance and support.

Guwahati, India

Uday Shanker Dixit  
Vice-President  
National Advisory Committee  
AIMTDR

# Preface

All India Manufacturing Technology, Design and Research (AIMTDR) Conference is considered globally as one of the most prestigious conferences held once in two years. It was started in 1967 at national level at Jadavpur University, Kolkata, India, and achieved the international status in the year 2006. It was organized by various prestigious institutions such as Jadavpur University, IIT Bombay, IIT Madras, CMTI Bangalore, PSG Tech, IIT Kanpur, CMERI, IIT Delhi, NIT Warangal, IIT Kharagpur, BITS Ranchi, VIT Vellore, IIT Roorkee, Andhra University, IIT Guwahati and College of Engineering Pune.

The recent edition of the AIMTDR Conference, 7th International and 28th All India Manufacturing Technology, Design and Research (AIMTDR) Conference 2018, was jointly organized by the Departments of Manufacturing Engineering, Mechanical Engineering and Production Technology during 13–15 December 2018, at College of Engineering, Guindy, Anna University, Chennai, India, with the theme ‘Make in India – Global Vision’. A major focus was given on recent developments and innovations in the field of manufacturing technology and design through keynote lectures. About 550 participants registered for the conference. During the conference, researchers from academia and industries presented their findings and exchanged ideas related to manufacturing technology and design.

Of the 750 papers received initially, 330 papers were finally selected after rigorous review process for publication in the Springer Proceedings. Selected papers from the conference are being published by Springer in the series Lecture Notes on Multidisciplinary Industrial Engineering in five volumes, namely **Volume 1**—Additive Manufacturing and Joining, **Volume 2**—Forming, Machining and Automation, **Volume 3**—Unconventional Machining and Composites, **Volume 4**—Micro and Nano Manufacturing and Surface Engineering and **Volume 5**—Simulation and Product Design and Development.

Chennai, India  
May 2018

M. S. Shunmugam  
M. Kanthababu

# Contents

## Part I Unconventional Machining

<b>1</b>	<b>Powder Mixed Near Dry Electric Discharge Machining Parameter Optimization for Tool Wear Rate</b> .....	<b>3</b>
	Sanjay Sundriyal, Ravinder Singh Walia and Vipin	
<b>2</b>	<b>Comparative Study of Dielectric and Debris Flow in Micro-Electrical Discharge Milling Process Using Cylindrical and Slotted Tools</b> .....	<b>17</b>
	S. A. Mullya and G. Karthikeyan	
<b>3</b>	<b>Parametric Investigation into Electrochemical Micromachining for Generation of Different Micro-surface Textures</b> .....	<b>27</b>
	S. Kunar, S. Mahata and B. Bhattacharyya	
<b>4</b>	<b>Investigations into Wire Electrochemical Machining of Stainless Steel 304</b> .....	<b>41</b>
	Vyom Sharma, V. K. Jain and J. Ramkumar	
<b>5</b>	<b>Nanofinishing of External Cylindrical Surface of C60 Steel Using Rotating Core-Based Magnetorheological Finishing Process</b> .....	<b>53</b>
	Manpreet Singh, Ashpreet Singh and Anant Kumar Singh	
<b>6</b>	<b>Effect of Laser Parameters on Laser-Induced Plasma-Assisted Ablation (LIPAA) of Glass</b> .....	<b>67</b>
	Upasana Sarma and Shrikrishna N. Joshi	
<b>7</b>	<b>An Experimental Study of Electrochemical Spark Drilling (ECSD)</b> .....	<b>77</b>
	Arvind Kumar Yadav and S. K. S. Yadav	
<b>8</b>	<b>Development and Experimental Study of Ultrasonic Assisted Electrical Discharge Machining Process</b> .....	<b>89</b>
	Shubham Srivastava, Pravendra Kumar and S. K. S. Yadav	

<b>9</b>	<b>Effect of Finishing Time on Surface Finish of Spur Gears by Abrasive Flow Finishing (AFF) Process</b> . . . . .	101
	Anand C. Petare, Neelesh Kumar Jain and I. A. Palani	
<b>10</b>	<b>Experimental Study on Improving Material Removal Rate and Surface Roughness in Wire-Cut EDM of Low Conductive Material</b> . . . . .	113
	Dhiraj Kumar, Sadananda Chakraborty, Anand Ranjan and Dipankar Bose	
<b>11</b>	<b>Machining Performance Evaluation of Al 6061 T6 Using Abrasive Water Jet Process</b> . . . . .	127
	Pankaj Kr. Shahu and S. R. Maity	
<b>12</b>	<b>Formulating Empirical Model of MRR in Near-Dry EDM</b> . . . . .	141
	Gurinder Singh Brar, Nimo Singh Khundrakpam and Dharpal Deepak	
<b>13</b>	<b>A Model for Average Surface Roughness for Abrasive Waterjet Cut Metal Matrix Composites</b> . . . . .	149
	N. R. Prabhu Swamy and S. Srinivas	
<b>14</b>	<b>Abrasive Jet Machining of Soda Lime Glass and Laminated Glass Using Silica Sand</b> . . . . .	163
	A. Karmakar, D. Ghosh, Deb Kumar Adak, Bijoy Mandal, Santanu Das, Ahmed Mohammed and Barun Haldar	
<b>15</b>	<b>A Novel Magnetorheological Grinding Process for Finishing the Internal Cylindrical Surfaces</b> . . . . .	179
	Ankit Aggarwal and Anant Kumar Singh	
<b>16</b>	<b>A Study on Micro-tool and Micro-feature Fabrication in Micro-EDM</b> . . . . .	191
	Biswesh Ranjan Acharya, Abhijeet Sethi, Akhil Dindigala, Partha Saha and Dilip Kumar Pratihar	
<b>17</b>	<b>Influence of Graphite Nanopowder-Mixed Dielectric Fluid on Machining Characteristics of Micro Electric Discharge Milling</b> . . . . .	203
	K. V. Arunpillai and P. Hariharan	
<b>18</b>	<b>Realization of Green Manufacturing Using Citric Acid Electrolyte for WC-Co Alloy Micro-tool Fabrication in Micro-WECDM</b> . . . . .	211
	Abhijeet Sethi, Biswesh Ranjan Acharya, Pranai Kumar, Rajib Chakraborty and Partha Saha	

<b>19</b>	<b>Effect of Powder Mix and Ultrasonic Assistance on Pulse Train-Based Specific Energy in EDM of D3 Steel</b> .....	<b>225</b>
	R. Rajeswari and M. S. Shunmugam	
<b>20</b>	<b>Performance Evaluation of Si–Cu-Hybrid Dust as a Powder Additive of EDM Dielectrics to Machine Ti6Al4V with Copper Electrode</b> .....	<b>239</b>
	Shirsendu Das, Swarup Paul, Biswanath Doloi and Kumar Rahul Dey	
<b>21</b>	<b>Experimental Study on Material Removal Rate and Over-Cut in Electrochemical Machining of Monel 400 Alloys with Coated Tools</b> .....	<b>255</b>
	S. Ayyappan and N. Vengatajalapathi	
<b>22</b>	<b>Experimental Investigations into Ultrasonic-Assisted Magnetic Abrasive Finishing of Freeform Surface</b> .....	<b>269</b>
	Akshay Kumar Singh, Girish Chandra Verma, Vipin Chandra Shukla and Pulak Mohan Pandey	
<b>23</b>	<b>Fiber Laser Cutting of Nimonic C263 Alloy and Investigation of Surface Integrity</b> .....	<b>287</b>
	Mukul Anand, Niladri Mandal, Vikas Kumar, Shakti Kumar, A. K. Sharma and Alok Kumar Das	
<b>24</b>	<b>Generation of Three-Dimensional Features on Ti6Al4V by EC Milling</b> .....	<b>299</b>
	K. Mishra, S. Sinha, B. R. Sarkar and B. Bhattacharyya	
<b>25</b>	<b>Enhancement in Machining Efficiency and Accuracy of ECDM Process Using Hollow Tool Electrode</b> .....	<b>313</b>
	Rajendra Kumar Arya and Akshay Dvivedi	
<b>26</b>	<b>Evaluation of Cutting Force and Surface Roughness of Inconel 718 Using a Hybrid Ultrasonic Vibration-Assisted Turning and Minimum Quantity Lubrication (MQL)</b> .....	<b>325</b>
	Habtamu Alemayehu, Sudarsan Ghosh and P. V. Rao	
<b>27</b>	<b>On Performance Evaluation of Helical Grooved Tool During Rotary Tool Micro-ultrasonic Machining</b> .....	<b>335</b>
	Sandeep Kumar and Akshay Dvivedi	
<b>28</b>	<b>Experimental Investigation on Surface Topography of the Natural Ceramics in Abrasive Water Jet Cutting and Its Optimization Validation by Formulated Model</b> .....	<b>347</b>
	Vijay Mandal, Amandeep Singh, Ganesh Singh Yadav, J. Ramkumar and S. Agrawal	

<b>29 Prediction and Comparison of Vision Parameter of Surface Roughness in WEDM of Al-6%Si<sub>3</sub>N<sub>4</sub> and Al-10%Si<sub>3</sub>N<sub>4</sub> Using ANN</b> .....	361
H. R. Gurupavan, H. V. Ravindra and T. M. Devegowda	
<b>30 Performance Study of Electrical Discharge Drilling of Metal Matrix Composite</b> .....	373
Anjani Kumar Singh and Vinod Yadava	
<b>31 Multi-objective Optimisation of Electro Jet Drilling Process Parameters for Machining of Crater in High-Speed Steel Using Grey Relational Analysis</b> .....	385
Kalinga Simant Bal, Amal Madhavan Nair, Dipanjan Dey, Anitesh Kumar Singh and Asimava Roy Choudhury	
<b>32 Machining of Bio-Implant Materials Using WEDM and Optimization of Process Parameters</b> .....	397
P. Hema, J. Mallikarjuna Rao and C. Eswara Reddy	
<b>33 Experimental Investigations of Abrasive Waterjet Machining Parameters on Titanium Alloy Ti-6Al-4V Using RSM and Evolutionary Computational Techniques</b> .....	413
A. Gnanavelbabu and P. Saravanan	
<b>34 Design of Fixture for Trimming of a Composite Material Shim by Abrasive Water Jet Machining</b> .....	427
Kushal Singh, Ch. Venkateswarlu, B. Hari Prasad and A. P. Dash	
<b>35 Fabrication and Characterization of Helical Grooved Cylindrical Electrodes Generated by WED Turning Process</b> .....	437
Jacob Serah Krupa and G. L. Samuel	
<b>36 A Study of Wire Electrical Discharge Machining of Carbon Fibre Reinforced Plastic</b> .....	451
Hrishikesh Dutta, Kishore Debnath and Deba Kumar Sarma	
<b>37 Development of a Bore Using Jet Electrochemical Machining (JECM) in SS316 Alloy</b> .....	461
J. Deepak, N. Vivek, B. MouliPrasanth and P. Hariharan	
<b>38 Machining and Characterization of Channels on Quartz Glass using Hybrid Non-conventional Machining Process <math>\mu</math>-ECDM</b> .....	473
J. Bindu Madhavi and Somashekhar S. Hiremath	
<b>39 Parametric Study of a Newly Developed Magnetorheological Honing Process</b> .....	483
Talwinder Singh Bedi and Anant Kumar Singh	

<b>40</b>	<b>Investigation on Surface Roughness During Finishing of Al-6061 Hybrid Composites Tube with Traces of Rare Earth Metals Using Magnetic Abrasive Flow Machining</b> .....	<b>493</b>
	V. K. Sharma, V. Kumar and R. S. Joshi	
<b>41</b>	<b>Part Program-Based Process Control of Ball-End Magnetorheological Finishing</b> .....	<b>503</b>
	F. Iqbal, Z. Alam, D. A. Khan and S. Jha	
<b>42</b>	<b>Modelling and Analysis of Change in Shape of sintered Cu-TiC tool tip during Electrical Discharge Machining process</b> .....	<b>515</b>
	Arminder Singh Walia, Vineet Srivastava, Vivek Jain and Mayank Garg	
<b>43</b>	<b>Experimental Investigations on C-263 Alloy by Electrochemical Milling</b> .....	<b>527</b>
	K. Mishra, S. Sinha, B. R. Sarkar and B. Bhattacharyya	
<b>44</b>	<b>Influence of Discharge Energy on Electrical Discharge Machining of Ti-Foam Material</b> .....	<b>537</b>
	S. Avinash, Karthick Chetti, M. Haribaskar, S. Jeyanthi, Abimannan Giridharan and R. Krishnamurthy	
<b>45</b>	<b>Gang Drilling of Square Micro-Holes on Glass Using USM</b> .....	<b>549</b>
	T. Debnath, K. K. Patra and P. K. Patowari	
<b>46</b>	<b>Parametric Optimization of Micro Ultrasonic Drilling of Quartz Based on RSM</b> .....	<b>559</b>
	S. Kumar, B. Doloi and B. Bhattacharyya	
<b>47</b>	<b>Investigations into the Effect of Varying Electrode Diameter on Cutting Rate and Kerf Width in WEDM of Varying Thickness Inconel718</b> .....	<b>571</b>
	Susheel Ramchandra Dhale and Bhagyesh B. Deshmukh	
<b>48</b>	<b>Comparative Evaluation of Drilling on GFRP Made by Different Fabrication Techniques</b> .....	<b>583</b>
	R. Raja and Sabitha Jannet	
<b>49</b>	<b>An Experimental Analysis of Square Stepped Hole Fabrication on Zirconia Bio-Ceramics</b> .....	<b>599</b>
	S. Das, S. Kumar, B. Doloi and B. Bhattacharyya	
<b>50</b>	<b>Pulse and Work Revolution Parameters of Wire Electrical Discharge Turning on Ti-6Al-4V Alloy</b> .....	<b>611</b>
	S. Ram Prakash, K. Rajkumar and G. Selvakumar	



<b>51</b>	<b>Modeling of Areal Surface Roughness Using Soft-Computing-Based ANN and GA to Estimate Optimal Process Parameters During Wire Electrical Discharge Turning of Inconel 825</b> . . . . .	<b>621</b>
	Jees George, G. Ravi Chandan, R. Manu and Jose Mathew	
<b>52</b>	<b>Investigation on the Influence of Process Parameters on Surface Roughness and Kerf Properties in Abrasive Water Jet Machining of Carbon Fibre Vinyl Ester Composite</b> . . . . .	<b>631</b>
	Bhavik Tank and Shailendra Kumar	
<b>53</b>	<b>Fluidized Bed Hot Abrasive Jet Machining (FB-HAJM) of K-60 Alumina Ceramic</b> . . . . .	<b>641</b>
	B. K. Nanda, A. Mishra, Sudhansu Ranjan Das and D. Dhupal	
<b>54</b>	<b>Performance Evaluation of Abrasive Water Jet Machining on AA6061-B<sub>4</sub>C-HBN Hybrid Composites Using Taguchi Methodology</b> . . . . .	<b>651</b>
	A. Gnanavelbabu, K. T. Sunu Surendran and K. Rajkumar	
<b>55</b>	<b>Empirical Modelling and Optimisation of Bio-Micromachining on Antimicrobial Copper to Fabricate Micromixing System</b> . . . . .	<b>661</b>
	Abhishek Singh, Arul Manikandan, M. Ravi Sankar, K. Pakshirajan and L. Roy	
<b>56</b>	<b>Investigation on Magnetic Field-assisted Near-dry Electrical Discharge Machining of Inconel 600</b> . . . . .	<b>671</b>
	G. Manno Rajkumar, Abimannan Giridharan, R. Oyyaravelu and A. S. S. Balan	

## **Part II Composites**

<b>57</b>	<b>Selection of Aluminum Hybrid Metal Matrix Composite Material Using Additive Ratio Assessment Approach and Comparing with the Experimental Results Varying Different Weight Percentage of the Reinforcements</b> . . . . .	<b>687</b>
	Soutrik Bose and Titas Nandi	
<b>58</b>	<b>The Role of HBN Solid Lubricant Reducing Cutting Forces of Dry Machined Al-B<sub>4</sub>C Composite</b> . . . . .	<b>697</b>
	M. Rajesh, K. Rajkumar, A. Gnanavelbabu and K. M. Nambiraj	
<b>59</b>	<b>Experimental Investigation on Influence of Process Parameters of Abrasive Water Jet Machining on Kerf Taper of Glass Fiber-Reinforced Polymer Composites</b> . . . . .	<b>707</b>
	H. J. Prajapati, Puneet Kumar, Shailendra Kumar and Ravi Kant	
<b>60</b>	<b>WEDM Studies on TiB<sub>2</sub>-15% SiC Ceramic Composite Processed Through SPS Process</b> . . . . .	<b>715</b>
	K. Jayakumar	

<b>61 Study of Mechanical Properties and Thermal Conductivity of Carbon and Basalt Fibre-Reinforced Hybrid Polymer Composites</b> .....	725
V. Durga Prasada Rao, N. V. N. Sarabhayya and A. Balakrishna	
<b>62 Design and Fabrication of Aluminium/Alumina Ultra-fine Composite and Functionally Graded Material Using Powder Metallurgy Route</b> .....	739
Aravind Tripathy, Rajat Gupta, Saroj Kumar Sarangi and Anil Kumar Chaubey	
<b>63 Mechanical and Crystallization Behaviour of Sisal Fiber and Talc Reinforced Polylactic Acid Composites</b> .....	749
A. Suresh Babu, M. Jaivignesh and D. Poovarasana	
<b>64 Assessment on Hole Quality During Drilling of Al/CFRP Stack</b> .....	757
Tarakeswar Barik, Swagatika Sarangi and Kamal Pal	
<b>65 Experimental and Analytical Outcomes of Carbon Fiber Orientation in Epoxy Resin Composite Laminate Under Tensile Loading</b> .....	771
A. Rajesh, S. Deva Prasad, B. Singaravel, T. Niranjan and T. Shravan Kumar	

## About the Editors

**M. S. Shunmugam** is a Professor (Emeritus) in the Manufacturing Engineering Section in the Department of Mechanical Engineering, Indian Institute of Technology (IIT) Madras. After receiving his PhD in Mechanical Engineering from IIT Madras in 1976, he has worked in IIT Bombay (from 1977 to 1980) and in IIT Madras from 1980 onwards. He was a visiting faculty member at Michigan Technological University during 1989-1991 and was a member in the board of governors of IIT Madras during 2012-2013. Dr. Shanmugam's research interests include metrology, machine tools, manufacturing, gears, micro-machining and computer applications in manufacturing. He has published about 130 peer-reviewed international journal papers, 15 peer-reviewed national journal papers, 75 international conferences and about 80 national conferences.

**M. Kanthababu** is a Professor in the Department of Manufacturing Engineering in Anna University, Chennai, India and the Director of the Centre for Intellectual Property Right and Trade Marks in Anna University. He has completed his MS in Mechanical engineering and PhD in Advanced Manufacturing Technology from IIT Madras. Prof Kanthababu's research interests include manufacturing technology, composite materials and machining, and automation in manufacturing. He has published more than 30 peer reviewed international journal papers and 2 books, and holds one patent.

**Part I**  
**Unconventional Machining**

# Chapter 1

## Powder Mixed Near Dry Electric Discharge Machining Parameter Optimization for Tool Wear Rate



Sanjay Sundriyal, Ravinder Singh Walia and Vipin

**Abstract** The powder mixed near dry electric discharge machining (PMND-EDM) is an advanced process for machining very hard and complex geometries. PMND-EDM is an eco-friendly process, which uses minute amount of metalworking fluids (MWF) with metallic powders for machining purposes. In this study, an approach has been made to reduce tool wear rate (TWR) by optimizing process parameters using Taguchi optimization technique. Taguchi ( $L_9$ ) array has been used for four parameters and three levels. Parameters selected for the study were tool diameter, flow rate, metallic powder concentration, and pressure of dielectric mist. It has been validated by the experiments and analysis that PMND-EDM has led to considerable reduction in TWR. The effect of influencing input parameters was analyzed and it was revealed that tool dimensions played a major role in effecting TWR. Second, powder concentration was effective in reducing TWR followed by flow rate while pressure of mist was least significant parameter.

**Keywords** Powder mixed near dry EDM · Tool wear rate · Taguchi · ANOVA · Residual stress

### 1.1 Introduction

Near dry machining (NDM) is done with a very small quantity of liquid droplets or in a form of mist, which is almost equal to dry situation of machining. It was beneficial in terms of reducing cost of machining. Metalworking fluids (MWFs) or lubricants needed were very minute amount of quantity, therefore, it led to reduction in cost of production. Near dry machining was first explored in 1989 [1]. NDM can be performed in electric discharge machining, which eventually led to new method

---

S. Sundriyal · R. S. Walia (✉) · Vipin  
Production Engineering, Department of Mechanical Engineering, Delhi Technological University,  
Delhi 110042, India  
e-mail: [waliaravinder@yahoo.com](mailto:waliaravinder@yahoo.com)

S. Sundriyal  
e-mail: [ss95576@yahoo.in](mailto:ss95576@yahoo.in)

© Springer Nature Singapore Pte Ltd. 2020  
M. S. Shunmugam and M. Kanthababu (eds.), *Advances in Unconventional Machining and Composites*, Lecture Notes on Multidisciplinary Industrial Engineering, [https://doi.org/10.1007/978-981-32-9471-4\\_1](https://doi.org/10.1007/978-981-32-9471-4_1)

of machining known as near dry EDM. This method of machining eliminated problems like improper flushing and debris attachment. At the same time, this technology also led to the reduction of harmful gases that are evolved while machining which made it an eco-friendly process. There are several advantages of NDM such as easy control of liquid concentration with air and other gases, which could be tailored to give required quality of dielectric medium in EDM process according to the user need in order to achieve required output in machining such as low tool wear rate (TWR) and production-related benefits [2]. NDM led to increase in tool life as compared to shorter tool life in dry machining or machining with dielectric in complete gaseous form without liquid aerosols [3]. New trending method of machining known as powder mixed near dry EDM (PMND-EDM) came into existence after further research in ND-EDM [4]. Near dry machining was proved advantageous in terms of good characteristics of product developed such as high quality of machined product, which was quite economically produced. At the same time, it led to reduction in harmful fumes evolved while machining.

## 1.2 Indigenous Developed Setup for Powder Mixed Near Dry EDM

The setup was built indigenously in Delhi Technological University, Delhi at precision manufacturing lab. The setup comprises of control panel for control of mist flow rate and its pressure. A separate dielectric tank was made where liquid dielectric is fed along with metallic powder and other stabilizing agents such as glycerol in appropriate proportion. This mixture of dielectric is converted into a form of high-pressure mist with the help of pressurized compressed air generated from air compressor. Figure 1.1 represents the complete setup along with EDM machine (Sparkonix India limited). Specially designed tools of copper material were fabricated and designed in precision engineering lab, DTU. Figure 1.2a shows internal design features of tool while Fig. 1.2b shows external features of different tools developed for experimentation. Table 1.1 shows the different dimensions of tools.

## 1.3 Working Principle of PMND-EDM

The working principle of machining in PMND-EDM is quite similar to EDM. In PMND-EDM the machining takes due to high electrothermal energy of sparking at the interelectrode gap (IEG) tool. This sparking is responsible for erosion of material from the workpiece as well as the wear of the electrode. In PMND-EDM, the dielectric kerosene oil has been replaced by the mist of kerosene oil along with metallic powder to enhance the machining rate and reduce the tool wear. The dielectric mist is fed through the hollow copper electrode under high pressure. The erosion process starts

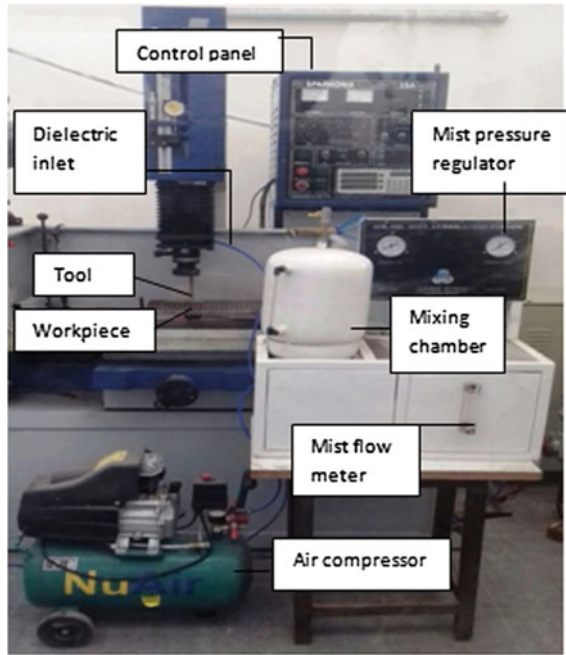


**Fig. 1.1** Developed experimental setup for PMND-EDM

as the mist comes out from the sparking end. The presence of metallic powder forms a bridge of chain of conductive metallic powder particles, which increases the thermal conductivity and thus also reduces the insulation effect which eventually results in more energized plasma of arc at the IEG as shown in Fig. 1.3. This reduced electrical density enhances the gap size or the IEG, which results in larger and more uniformly distributed plasma for machining.

## 1.4 Process Parameters Selection and Experimentation

### 1.4.1 Selection of Workpiece and Tool

En-31 material was used as the workpiece due to its favorable properties like good thermal conductivity, hardness, tensile strength, and melting point with excellent machinability properties. Copper electrode was chosen as tool for the machining purpose.

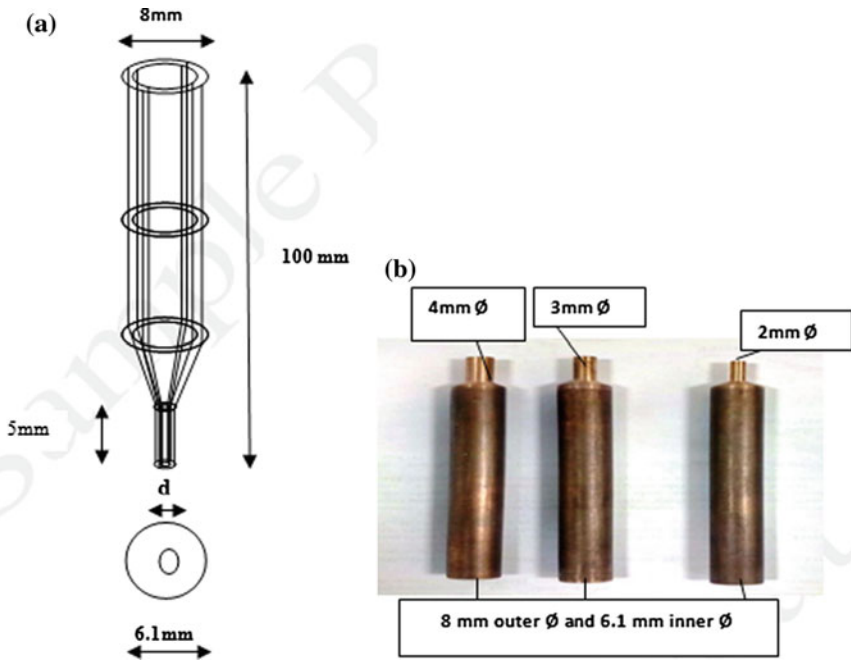


**Fig. 1.2** a Design and top view of tool developed for powder mixed NDED. b Hollow copper electrode of different dimensions

**Table 1.1** Dimensions of tools developed for experimentation

Tool type	Dimensions of tool	
	Inner dia (Ø) mm	Outer dia (Ø) mm
Tool 1	2	3
Tool 2	3	4
Tool 3	4	5

### 1.4.2 Response Characteristic (Tool Wear Rate)

Tool wear rate signifies the amount of material removed from the tool during machining.

Tool wear rate was calculated from the formula:

$$TWR = (T_i - T_f) / T_m$$

where

T<sub>i</sub> Weight of tool before machining

T<sub>f</sub> Weight of tool after machining

T<sub>m</sub> Time taken for machining

TWR mg/min.



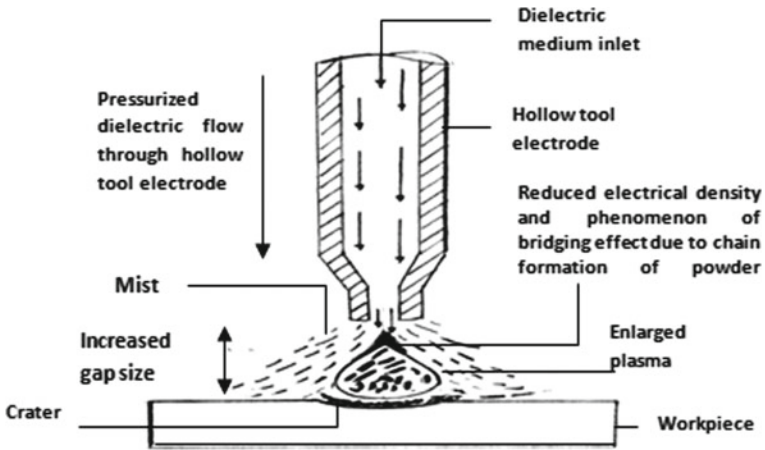


Fig. 1.3 Working principle and erosion process in PMND-EDM

Table 1.2 Operating conditions in PMND-EDM [5, 6, 12]

Process parameters	Values
Powder concentration (g/l)	2, 5, 8
Dielectric pressure (MPa)	0.4, 0.5, 0.6
Mist flow rate (ml/min)	5, 10, 15
Electrode polarity	Positive
Duty factor	0.86
Dielectric fluid	Kerosene (LL21)
Stabilizing agent	Glycerol
Grain size of metallic powder ( $\mu\text{m}$ )	2.5

Electronic balance of least count 0.001 g was used to measure weight of the tool (Asia Techno weigh India).

The process parameters were constant in nature. The values of the constant parameters for experimentation are shown in Table 1.2.

### 1.4.3 Scheme of Experiments

Design of experiments was performed to study the effect of input parameters on out response such as tool wear rate (TWR). Taguchi orthogonal array of  $L_9$  was used with three levels and four parameters as per the data shown in Table 1.3.

**Table 1.3** Process parameters and their values at different levels [5, 6]

Symbol	Process parameters	Unit	Level 1	Level 2	Level 3
A	Tool dia	mm	2	3	4
B	Flow rate	ml/min	5	10	15
C	Powder conc	g/l	2	5	8
D	Pressure	MPa	0.4	0.5	0.6

Values of other constant parameters: Machining time 10 min;  $T_{on}$  500  $\mu$ s;  $T_{off}$  75  $\mu$ s; Discharge current 12 A; Tool electrode Copper; Workpiece EN-31

**Table 1.4** Experimental results for TWR as per  $L_9$  orthogonal array

Exp. No	Parameter trial condition				TWR			S/N (db)
	A	B	C	D	R1	R2	R3	
1	2	5	2	4	1.65	1.45	1.81	-4.31
2	2	10	5	5	1.70	1.42	1.39	-3.57
3	2	15	8	6	1.50	1.78	1.60	-4.24
4	3	5	5	6	1.37	1.23	1.11	-1.87
5	3	10	8	4	0.41	0.55	0.78	4.44
6	3	15	2	5	0.91	0.85	0.90	1.04
7	4	5	8	5	0.77	0.65	0.98	1.81
8	4	10	2	6	0.55	0.75	0.61	3.84
9	4	15	5	4	1.4	1.55	1.58	-3.59
Total					10.26	10.23	10.76	
					Overall mean TWR ( $\bar{T}$ ) = 1.15 mg/min			

As per design of experiments, the experiments were conducted successfully for three runs. The results of TWR at different levels are shown in Table 1.4. The experiments were performed in three runs under the same condition of parameter trial condition.

## 1.5 Results and Discussion

### 1.5.1 Effect of Machining Parameters on TWR

Powder concentration is a significant factor affecting TWR [5]. At low concentration, the heat dissipation is not proper due to small discharge gap and leads to increase in tool wear but with increasing of powder concentration, discharge gap is enlarged. This resulted in improvement of cooling in discharge gap, as a result, TWR is decreased as shown in Fig. 1.4c.

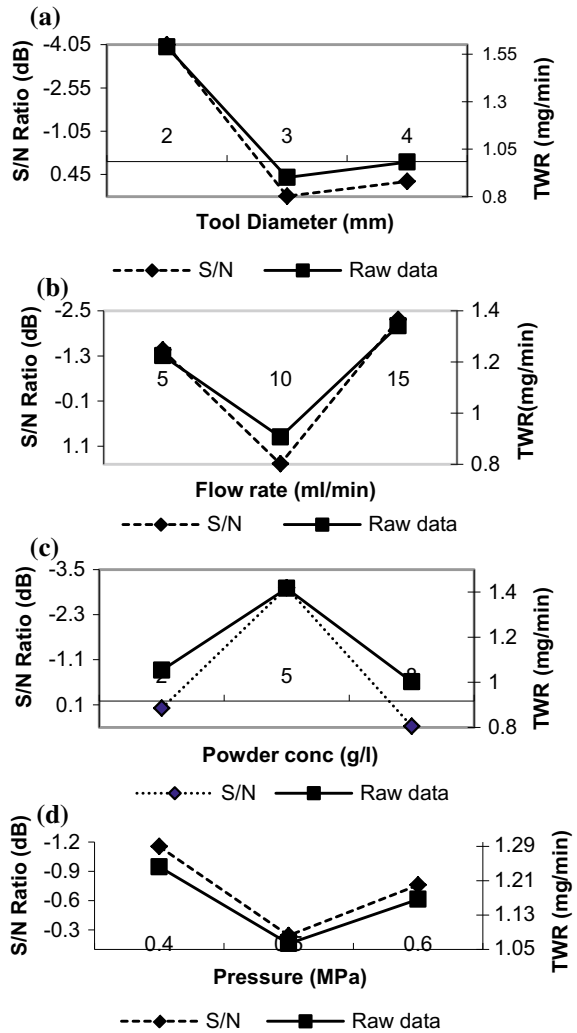
**Fig. 1.4** Effect of different dimension of tools, flow rate, powder concentration, and pressure on TWR



The TWR decreases with increase in dimensions of tool diameter because the flushing takes place more efficiently which provides better cooling condition at the tooltip, which brings down the temperature at the sparking ends of the hollow tool electrodes. However with further increase in tool diameters, there is no significant effect on TWR as seen in Fig. 1.4a. TWR first decreases at low flow rate due to poor heat dissipation [6] and this resulted in some part of molten eroded material forming a solidified layer at the tooltip, which reduces the wear at the tool end but further increases in flow rate facilitates material removal of the tool electrode because simultaneously more material is also gets eroded from the workpiece which consumes the tooltips rapidly due to better machining efficiency as shown in Fig. 1.4b. The powder concentration effects the TWR in a certain manner. Initially with increase of powder concentration, the TWR increases but afterward with further increase in powder concentration the TWR starts decreasing as shown in Fig. 1.4c. The reason is that powder concentration influences the heat received by the tool and adhesion of molten material on the face of the tool [6]. Due to this phenomenon, molten materials solidification takes place in discharge gap. As a result, materials that can adhere onto the surface of tool electrode are reduced, and therefore TWR is increased. On the other hand with further increase of metallic powder concentration, heat at discharge gap gets increased which forms adhesive layer over the tool end which reduces TWR. Powder concentration was significant factor affecting TWR. TWR increases with lower range of powder concentration but then decreases [5]. Parametric optimization of TWR was studied with different combinations of tool electrode composition such as half of the chemical composition of tool was made up of conductive material such as copper and another half of the tool composition is made up of conductive abrasive [7]. It was revealed with the study that the with abrasives the TWR tends to decrease as compared to simple conductive tool without any conductive abrasive particles embedded in the tool. By addition of graphite powder the discharge gap was increased and stable machining was initiated with reduced gap voltage which reduced the TWR [7]. The wear of sparking end of the tool electrode tip after machining can be seen in Fig. 1.5.

TWR shows the decreasing trend when the air pressure changes from 0.4 to 0.5 Mpa as shown in Fig. 1.4d. With increase of air pressure, there were more molecules at the IEG which enhances discharging. The discharge gap got enlarged due to this phenomenon which led to improved deionization effect. Effects of abnormal short circuit and arc discharge were reduced, which eventually led to better

**Fig. 1.5** Wear of tool electrodes tip after PMND-EDM process



heat dissipation and reduced heat transfer at the tool. All these factors contributed to reduction in TWR till 0.5 Mpa. But with further increase of pressure, the gap voltage increases due to which the plasma generated is not uniformly distributed and improper erosion takes place which led to increase in TWR [8].

### 1.5.2 Taguchi Analysis

There were two types of data available as per analysis such as raw data and S/N data at three levels L1, L2, and L3. The average % value was calculated for TWR for different parameters. After that main effects % of TWR were calculated by expression (L2–L1) and (L3–L2). Finally, the difference between L2, L1 and L3, L2 was calculated as shown in Table 1.5. Analysis of variance was done for TWR S/N ratio on the results obtained at 95% confidence level. Table 1.6 shows the pooled ANOVA raw data for TWR analysis at 95% confidence level and critical F-ratio of 3.55. Pooled ANOVA raw data (S/N) ratio for TWR at 95% confidence level and critical F-ratio of 19 is shown in Table 1.7. The predicted values of TWR and experimental values at confidence of intervals of confirmation of experiment and confidence of population at 95% confidence level is shown in Table 1.8. The most optimum level of different input process parameter were A<sub>2</sub>, B<sub>2</sub>, C<sub>3</sub>, and D<sub>2</sub>. Among the process parameters, nonlinear behavior can be studied only if there are more than two levels of the parameters. Therefore, each parameter was analyzed at three levels [9–12].

### 1.5.3 Estimation of Optimum Performance Characteristics (TWR)

The optimum value of TWR was predicted at the selected levels of significant parameters A<sub>2</sub>, B<sub>2</sub>, C<sub>3</sub>, and D<sub>2</sub> as per Table 1.7. The estimated mean of the response characteristic (TWR) can be determined [13, 14] as

$$\text{TWR} = \bar{A}_2 + \bar{B}_2 + \bar{C}_3 + \bar{D}_2 - 3\bar{T} \quad (1.1)$$

where  $\bar{T}$  (overall mean of TWR) = 1.15 mg/min (Table 1.4), A<sub>2</sub> (Average TWR at the second level of tool diameter) = 0.90 mg/min, B<sub>2</sub> (Average TWR at the second level of flow rate) = 0.90 mg/min, C<sub>3</sub> (Average TWR at the third level of powder concentration) = 1.00 mg/min, and D<sub>2</sub> (Average TWR at the second level of pressure) = 1.06 mg/min.

Upon substituting the above values in Eq. (1.1),

$$\text{TWR} = 0.90 + 0.90 + 1.00 + 1.06 - 3 \times 1.15 = 0.41 \text{ mg/min.}$$

The 95% confidence interval of conformation experiments (CICE) and confidence interval of population (CIPOP) was calculated by using the following equations:

$$\text{CI}_{\text{CE}} = \sqrt{F_{\alpha}(1, f_c) V_e \left[ \frac{1}{n_{\text{eff}}} + \frac{1}{R} \right]} = \pm 0.21, \quad (1.2)$$

**Table 1.5** Raw data and signal to noise ratio for different parameters

Process parameter	Level	Tool dia (A)		Flow rate (B)		Powder conc (C)		Pressure (D)	
		S/N Ratio	Raw data	S/N Ratio	Raw data	S/N Ratio	Raw data	S/N Ratio	Raw data
Avg values (% TWR)	L1	-4.04	1.58	-1.45	1.22	0.19	1.05	-1.15	1.24
	L2	1.20	0.90	1.56	0.90	-3.01	1.41	-0.24	1.06
	L3	0.68	0.98	-2.26	1.34	0.66	1.00	-0.75	1.16
Main effects (%TWR)	L2-L1	5.24	-0.68	3.01	-0.32	-4.23	0.36	0.91	-0.18
	L3-L2	-0.52	0.08	-3.82	0.44	3.67	-0.41	-0.51	0.10
Differences (L3-L2) - (L2-L1)		-5.76	0.76	-6.83	0.76	7.9	-0.77	-1.42	0.28

L1, L2, L3 represent levels 1, 2 and 3 respectively of parameters. (L2-L1) is the average main effect when the corresponding parameter changes from Level 1 to Level 2. (L3-L2) is the main effect when the corresponding parameter changes from Level 2 to Level 3

**Table 1.6** Pooled ANOVA raw data for TWR

Source	SS	DOF	V	F-ratio	SS'	P%
Tool Dia	2.54	2	1.27	49.84	2.50	541.25
Flow rate	0.91	2	0.45	17.83	0.86	17.80
Powder conc	0.91	2	0.45	17.99	0.87	17.99
Pressure	*	*	*	–	*	*
Error	0.51	20	0.02	–	0.63	12.94
Total	4.88	26	–	–	4.88	100

\*Significant at 95% confidence level, F critical = 3.55 (Tabular value), SS-Sum of squares, DOF-Degree of freedom, V-variance, SS' Pure sum of squares

**Table 1.7** Pooled ANOVA raw data (S/N) for TWR

Source	SS	DOF	V	F-ratio	SS'	P%
Tool Dia	50.24	2	25.12	39.88	48.98	48.92
Flow rate	24.54	2	12.27	19.48	23.28	23.25
Powder conc	24.08	2	12.04	19.12	22.82	22.79
Pressure	*	*	*	–	*	*
Error	1.25	2	0.62	–	5.03	5.03
Total	100.13	8	–	–	100.13	100

\*Significant at 95% confidence level, F critical = 19 (Tabular value), SS-Sum of squares, DOF-Degree of freedom, V-variance, SS' Pure sum of squares

**Table 1.8** Predicted optimal values, confidence intervals, and results of confirmation experiments

Response characteristic	Optimal process parameters	Predicted optimal value	Confidence intervals 95%	Actual value (Avg of confirmation Exp)
TWR	A <sub>2</sub> B <sub>2</sub> C <sub>3</sub> D <sub>2</sub>	0.41 mg/min	CI <sub>CE</sub> 0.20 < TWR < 0.62 CI <sub>POP</sub> 0.26 < TWR < 0.56	0.43 mg/min

$$CI_{POP} = \sqrt{\frac{F_{\alpha}(1, f_e)V_e}{n_{eff}}} = \pm 0.15 \tag{1.3}$$

where,  $F_{\alpha}(1, f_e)$  = the F-ratio at the confidence level of  $(1 - \alpha)$  against DOF 1.

$$n_{eff} = \frac{N}{1 + [\text{DOF associated in the estimate of mean response}]} = 3$$

N (total number of experiments) = 27;

Treatment = 9, repetition = 3;  
 R = sample size for confirmation experiments = 3.  
 $V_e$  (error variance) = 0.02 (Table 1.7),  $f_e$  (error DOF) = 18 (Table 1.7).  
 $F = 3.5546$  (tabulated F value).

So,  $CI_{CE} = \pm 0.21$ ,  $CI_{POP} = \pm 0.15$ .

The predicted optimal range of confidence interval of conformation experiments ( $CI_{CE}$ ) is:

Mean TWR -  $CI_{CE} < TWR$  (mg/min)  $< \text{mean TWR} + CI_{CE}$   
 i.e.,  $0.20 \text{ mg/min} < TWR$  (mg/min)  $< 0.62$ .

The predicted optimal range of confidence interval of population ( $CI_{POP}$ ) is:

Mean TWR -  $CI_{POP} < MR$  (mg/min)  $< \text{mean TWR} + CI_{POP}$   
 i.e.,  $0.26 \text{ mg/min} < TWR$  (mg/min)  $< 0.56 \text{ mg/min}$ .

Thus, it is proven by the range that the predicted value of TWR lies in the optimum range.

### 1.5.4 Confirmation of Tests

Confirmation tests were performed in three runs in order to bring out the validation between predicted and experimental results. The experiments were performed at most optimum levels of different input process parameters. It was revealed by experiments that the predicted values were within  $\pm 5\%$  error range as shown in Table 1.9. The residual stress analysis was done on  $\mu X-360$  pulsetec machine under experimental conditions. Residual stress analysis of the most optimum tool was done and the variation of the residual stresses was analyzed as shown in Fig. 1.6. Tensile residual stress of 293 MPa was found at the sparking end of the 3 mm dimensional diameter tool. The residual stresses generated in the tool in PMND-EDM were found to be considerably lower as compared to high residual stresses (425.43 MPa) generated in the tool by conventional EDM. The residual stress induced in the products machined

**Table 1.9** Confirmation experiments at optimum levels

Test for response (TWR)	Optimal process parameters	Values of parameters	Avg value of TWR in three runs (mg/min)		
			1	2	3
			0.40	0.42	0.47
A		3			
B		10			
C		8	Overall TWR		
D		0.5	0.43		



**Fig. 1.6** Residual stress analysis of the tool

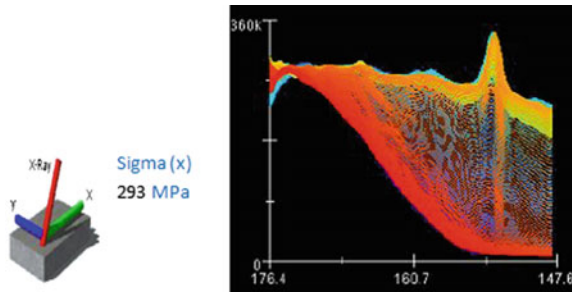
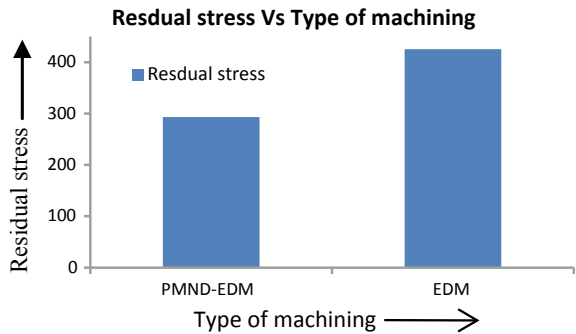


**Fig. 1.7** Comparison of residual stress between EDM and PMND-EDM



by PMND-EDM decreased by 45.20% as compared to NDEDM process as shown in Fig. 1.7. The reason attributed to this fact is that better flushing condition resulted in an increase in heat dissipation at the discharge machining gap due to which lower compressive residual stresses were generated.

The experiments conducted at optimum levels of four parameters gave TWR of 0.43 mg/min. The three sets of experiments were conducted under optimized conditions as shown in Table 1.9.

### 1.6 Conclusions

The optimization of TWR was successfully conducted by experimentation and analysis using Taguchi methodology and ANOVA technique. The PMND-EDM improved the efficiency of electrical discharging machining. It was concluded from the results that the TWR can be significantly reduced by optimizing the parameters in PMND-EDM and also thereby reducing the cost of machining thus making PMND-EDM an efficient and environmentally friendly method of machining. It was concluded

by ANOVA analysis that tool diameter played the most important role in reducing TWR. Second, powder concentration was significant parameter followed by flow rate in effecting TWR. Pressure of mist was found to be insignificant or least effecting parameter in reducing TWR.

## References

1. Tanimura, T., Isuzugawa, K., Fujita, I., Iwamoto, A., Kamitani, T.: Development of EDM in the mist. In: Proceedings of Ninth International Symposium of Electro Machining, vol. 9, pp. 313–316 (1989)
2. Kao, C.C., Tao, J., Shih, A.J.: Near dry electrical discharge machining. *Int. J. Mach. Tools Manuf.* **47**(15), 2273–2281 (2007)
3. Astakhov, V.P.: *Tribology of Metal Cutting*. Elsevier (2006)
4. Gao, Q., Zhang, Q.H., Zhang, J.H.: Experimental study of powder-mixed near dry electrical discharge machining. *Chin. J. Mech. Eng.* **45**(1), 169–175 (2009)
5. Ojha, K., Garg, R.K., Singh, K.K.: Experimental investigation and modeling of PMEDM process with chromium powder suspended dielectric. *Int. J. Appl. Sci. Eng.* **9**(2), 65–81 (2011)
6. Bai, X., Zhang, Q., Yang, T., Zhang, J., Tan, J.: Research on tool wear rate of powder mixed near dry electrical discharge machining. *Adv. Mater. Res.* **652–654**, 2222–2227 (2013)
7. Jeswani, M.L.: Effects of the addition of graphite powder to kerosene used as the dielectric fluid in electrical discharge machining. *Wear* **70**, 133–139 (1981)
8. Mane, S.G., Hargude, N.V.: Parametric optimization of near dry electrical discharge machining process for AISI SAE D-2 tool steel. *Int. J. Adv. Res. Eng. Technol.* **6**(1), 99–114 (2015)
9. Singh, J., Satsangi, P.S., Walia, R.S., Singh, V.P.: Micro-hardness and machined surface damage study for continuous and discontinuous ultrasonic vibration assisted electrical discharge machining. *Mater. Manuf. Process.* (2011)
10. Walia, R.S., Shan, H.S., Kumar, P.: Parametric optimization of centrifugal force-assisted abrasive flow machining (CFAAFM) by the Taguchi method. *Mater. Manuf. Process.* **21**, 375–382 (2007)
11. Goyal, T., Walia, R.S., Sidhu, T.S.: Multi-response optimization of low-pressure cold-sprayed coatings through Taguchi method and utility concept. *Int. J. Adv. Manuf. Technol.* **64**, 903–914 (2013)
12. Bai, X., Zhang, Q., Zhang, J., Kong, D., Yang, T.: Machining efficiency of powder mixed near dry electrical discharge machining based on different material combinations of tool electrode and workpiece electrode. *J. Manuf. Process.* **15**, 474–482 (2013)
13. Kumar, P., Barua, P.B., Gainder, J.L.: Quality of V-process method through the Taguchi technique. *Qual. Reliab. Eng. Int.* **12**, 421–427 (1996)
14. Jain, R.K., Jain, V.K.: Optimum selection of machining conditions in abrasive flow machining using neural network. *J. Mater. Process. Technol.* **108**, 62–67 (2000)

# Chapter 2

## Comparative Study of Dielectric and Debris Flow in Micro-Electrical Discharge Milling Process Using Cylindrical and Slotted Tools



S. A. Mullya  and G. Karthikeyan 

**Abstract** Micro-Electrical Discharge Milling ( $\mu$ ED-milling) is a commonly used process to machine intricate micro-channels ( $\mu$ channels) with high aspect ratio. It can cut blind slots with a simple cylindrical tool, which is difficult using wire EDM. The flushing of machining by-products is the major concern in the process as the interelectrode gap (IEG) is of few microns. Different techniques have been explored by the researchers to enhance debris flushing from the gap. The rotation of the tool electrode is the major driving force for the removal of debris from the gap. In this paper, the flow simulation of dielectric and debris in the IEG are studied using computational fluid dynamics (CFD). Comparative study of the cylindrical and slotted tool is presented with contour plots. The slotted tool is found better as compared to the cylindrical tool as the accretion of particles is very less in case of the slotted tool.

**Keywords** Micro-electrical discharge milling · Interelectrode gap · Dielectric · Debris · Computational fluid dynamics

### 2.1 Introduction

The electrical discharge machining (EDM) is a popular technique for machining intricate and precise geometry. It can cut high aspect ratio slot and a hole in the micro-domain. The probability of the occurrence of spark is more where the interelectrode gap (IEG) is minimum. However, this small IEG creates a problem in the machining performance. The by-products of the EDM process pollute the IEG and must be effectively removed from the IEG. The effective flushing of debris from the IEG avoids secondary discharge and improves the machining efficiency. The high-velocity dielectric fluid is injected through a nozzle for flushing the debris from the gap. Many researchers have proposed different flushing methods to improve flushing efficiency.

---

S. A. Mullya (✉) · G. Karthikeyan

Department of Mechanical Engineering, BITS Pilani K K Birla Goa Campus, Goa 403726, India  
e-mail: [mullyasatish@gmail.com](mailto:mullyasatish@gmail.com)

© Springer Nature Singapore Pte Ltd. 2020

M. S. Shunmugam and M. Kanthababu (eds.), *Advances in Unconventional Machining and Composites*, Lecture Notes on Multidisciplinary Industrial Engineering, [https://doi.org/10.1007/978-981-32-9471-4\\_2](https://doi.org/10.1007/978-981-32-9471-4_2)

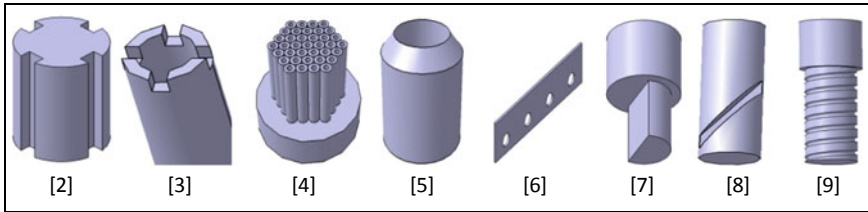


**Fig. 2.1** Various shapes of tools [2–9]

The rotation of the tool and high electrode jump are an effective method of debris flushing from the gap. The simple cylindrical tool is modified by the slotted tool to enhance flushing and improve Material Removal Rate (MRR).

The various shapes of tools used by the different researcher for various machining process are given in Fig. 2.1. Kunieda et al. (1988) proposed horizontal EDM and rotary horizontal EDM. The buoyancy of bubbles is responsible for flushing of debris from the gap. Rotation of the tool and workpiece improves machining accuracy and performance [1]. Nastasi et al. (2014) utilized slotted tools for electrical discharge drilling (EDD) of high aspect ratio holes and observed a 300% increase in MRR as compared to cylindrical tools [2]. Puthumana et al. (2011) used electrodes with peripheral slots to improve MRR, reduce tool wear rate (TWR) and radius over-cut (ROC) by dry EDM in gas [3]. Li et al. (2012) proposed a new tool containing bunched hollow electrode to improve flushing efficiency. The dielectric fluid velocity increased tenfold reducing the debris in the gap and also observed uniform distribution of debris particles [4]. Pei et al. (2017) used tubular tools in ED-milling and observed that the machining error is controlled within 2% and surface fluctuation is less than 4  $\mu\text{m}$ , improving the accuracy and the efficiency of the process [5]. Flaño et al. (2018) studied the effect of size and position of the holes on the lateral surfaces of the electrode to machine high aspect ratio slots using EDM. It reduced the machining time considerably and improved machining stability [6]. Yang et al. (2009) investigated the machining characteristics of micro-holes using a semicylindrical tool with and without ultrasonic vibrations in micro-electrochemical machining (ECM). The semicylindrical tool provided more flow space for the electrolyte which resulted in 76  $\mu\text{m}$  hole at a depth of 300  $\mu\text{m}$  on stainless steel. With ultrasonic vibrations, machining is more effective with a reduction in machining time [7]. Kumar et al. (2018) studied response characteristics of micro-EDD of holes by using slotted tools with inclined micro slots. The need for flushing is eliminated and the slotted tool acts as a self-flushing electrode which further eliminates the occurrence of arcing and shortcircuiting. The slotted electrode improved MRR, TWR, taper angle, corner radius and aspect ratio at tool speed of 1000 rpm [8]. Hsue et al. (2016) proposed a hybrid synchronized process for precision drilling and polishing using micro-EDM grinding process (micro-EDMG). The helical micro-tool improved penetration and surface quality of the machined micro-hole. The Ra value achieved is 0.107  $\mu\text{m}$  and the difference between the entrance and exit diameters of the through micro-hole is 5  $\mu\text{m}$  with a depth of 300  $\mu\text{m}$  [9].

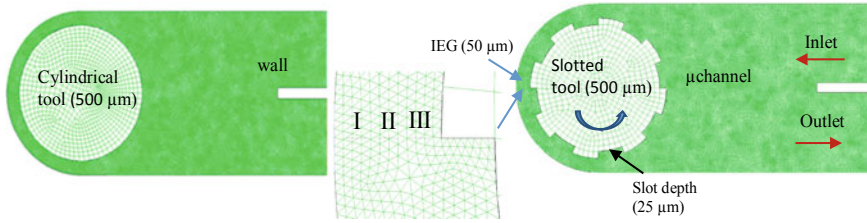


**Fig. 2.2** 2D CFD model showing cylindrical and slotted tool with discrete meshing

The objective of this paper is to study the effect of slotted tools and compare it with the cylindrical tool used in the  $\mu$ ED-milling process. The Computational Fluid Dynamics (CFD) technique is used to study the flow simulation of dielectric fluid and debris in the gap. The effect of IEG, inlet nozzle velocity, the dimension of  $\mu$ channel and tool speed on the velocity of the dielectric fluid in the gap is studied and presented. The accretion rate of the debris on the work surface is calculated. The results are compared with the cylindrical tools and the contour plots are plotted.

## 2.2 CFD Model

In the  $\mu$ ED-milling process, the rotating tool electrode travels in a longitudinal direction to cut the  $\mu$ channel along a predefined path. The width of the  $\mu$ channel cut depends on tool diameter and gap length. The 2D simulation model representing the  $\mu$ channel, the cylindrical and slotted tool is as shown in Fig. 2.2. The tool ( $\phi$  500  $\mu$ m) rotates and travels in a straight path from right to left while cutting a  $\mu$ channel. The IEG of 50  $\mu$ m is kept constant between the tool and the workpiece. The  $\mu$ channel width (600  $\mu$ m) is kept constant and different shapes of the tool are studied. Eight slots of depth 25  $\mu$ m are equally spaced along the periphery of the slotted tool. The dielectric for flushing the debris enters through the inlet and the used dielectric flows through the outlet. The wall which is not present in the actual EDM process is used to distinguish between inlet and outlet flow in simulation. The IEG is divided equally into three parts I, II, and III for injecting the particles. The position I represent near to workpiece, position II at the center and position III represent near to tool as shown in Fig. 2.2.

## 2.3 Boundary Conditions

In the  $\mu$ ED-milling process, tool and workpiece are submerged under dielectric fluid and the additional dielectric fluid is supplied through the nozzle for flushing the by-products of machining. The fluid domain represents  $\mu$ channel cut and is

finely meshed to study the flow behavior. The solid domain represents the slotted tool electrode which is coarsely meshed to reduce the element count and also, no behavioral changes occur in the solid domain. The angular rotational speed of the tool is provided using moving reference frame. The dielectric fluid used is kerosene. The velocity inlet and pressure outlet conditions are given for dielectric fluid flow. The Discrete Phase Modeling (DPM) is used to study the trajectory of a particle in the gap. The commercial ANSYS Fluent software is used to perform CFD simulations. In ANSYS Fluent, DPM follows the Euler–Lagrange model. The primary phase is the fluid phase which is treated as a continuum by solving the Navier–Stokes equations, while the carrier phase is the secondary phase which is solved by tracking a large number of particles through the calculated flow field. In the present study, the primary phase is kerosene and the carrier phase are the spherical steel particles of diameter 4, 8, and 12  $\mu\text{m}$ . The spherical steel particles represent debris in the actual EDM process. The carrier (dispersed) phase can exchange momentum, mass, and energy with the fluid phase. The DPM is used when the volume of the dispersed phase is less than 12% of the primary phase. The particles are injected from three positions (I, II and III) as given in Fig. 2.2 and the trajectory of the particles are studied.

## 2.4 Results and Discussion

### 2.4.1 Dielectric Fluid Flow

#### 2.4.1.1 Effect of Interelectrode Gap (IEG)

In the  $\mu\text{ED}$ -milling process, the size of the IEG formed depends on the input machining parameters. Due to this, the IEG of less than 50  $\mu\text{m}$  is formed between the two electrodes. The kerosene as a dielectric is supplied with a velocity of 0.01 cm/s through the inlet cross section. The effect of IEG size on the velocity of dielectric in the gap is studied for various tool speed. The tool speeds of 100, 500, and 800 rpm are considered for simulation. The gap size considered for simulation are 30, 40, and 50  $\mu\text{m}$ . Figure 2.3 shows the average velocity of dielectric fluid using cylindrical and slotted tool for different tool speed and IEG size. It is observed that, the increase in gap size decreases the dielectric velocity in the gap for cylindrical as well as a slotted tool. The average dielectric velocity is maximum near the tool surface and it reduces toward the work surface where it is minimum. This implies if the gap is small and the debris is near the tool, the flushing is effective. As compared to the cylindrical tool, the average velocity of dielectric using slotted tool is less for different tool speeds. This is due to the local turbulence created in the gap due to slots on the tool. The average velocity of dielectric increases with tool speed as expected.

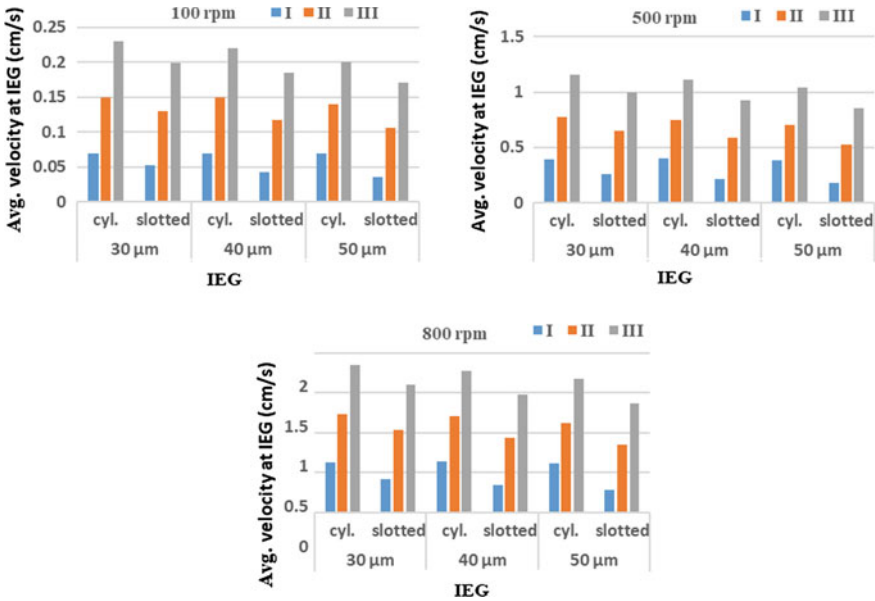


Fig. 2.3 Effect of gap size on the average dielectric velocity at IEG for tool speed of 100, 500 and 800 rpm using the cylindrical and slotted tool

2.4.1.2 Effect of Inlet Nozzle Velocity

The high-velocity dielectric supplied through nozzle refers to the inlet nozzle velocity. This is required to maintain the dielectric level in the tank, recirculation of fresh dielectric and for debris flushing. In the simulation, nozzle velocity is applied at the inlet cross section and its value is varied from 0.001 to 50 cm/s. It is observed that for lower inlet velocities between 0.001 and 10 cm/s, the average dielectric velocity in the IEG is constant. But at higher inlet velocity of 50 cm/s, there is a drop in the average dielectric velocity at IEG as shown in Fig. 2.4. This is due to the variation in flow pattern due to slots on the tool. In case of a cylindrical tool, initially the average velocity is constant but there is an increase in the average dielectric velocity at 50 cm/s due to the nozzling effect. Figure 2.5 shows the velocity vector in the μchannel. The dielectric flow direction and the vortex formed at the back of the tool is clearly observed. With the rise in inlet nozzle velocity, the vortex with smaller size is observed. The large variation of pressure is observed at the gap inlet and gap outlet in case of the cylindrical tool. The pressure difference is observed on the two edges of the slot in case of slotted tool as shown in Fig. 2.6.

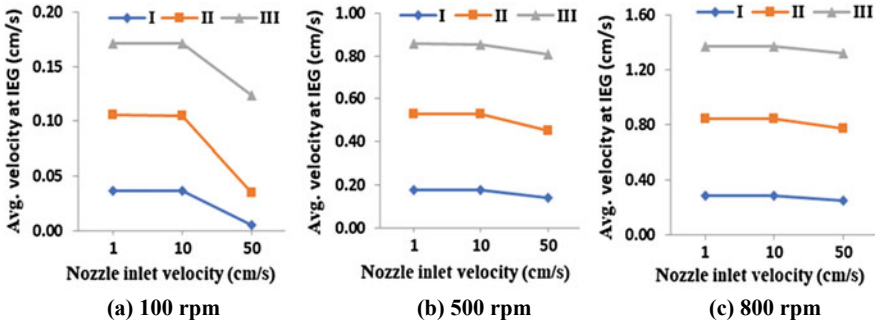


Fig. 2.4 Effect of inlet nozzle velocity on the average dielectric velocity at IEG for different tool speed using the slotted tool

Fig. 2.5 Velocity vector (cm/s) contour plots

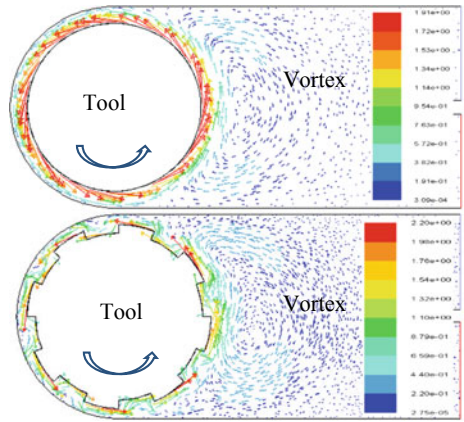
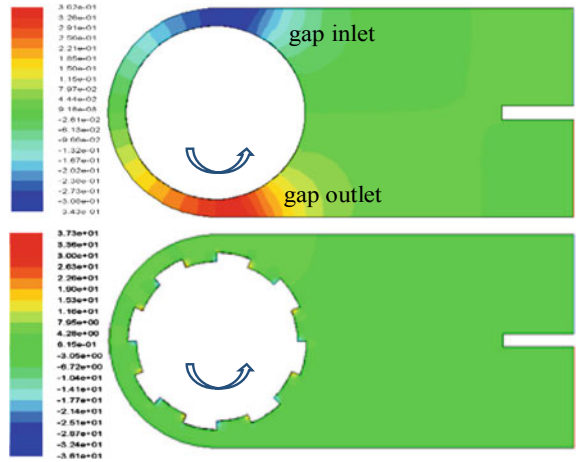


Fig. 2.6 Pressure (Pa) contour plots





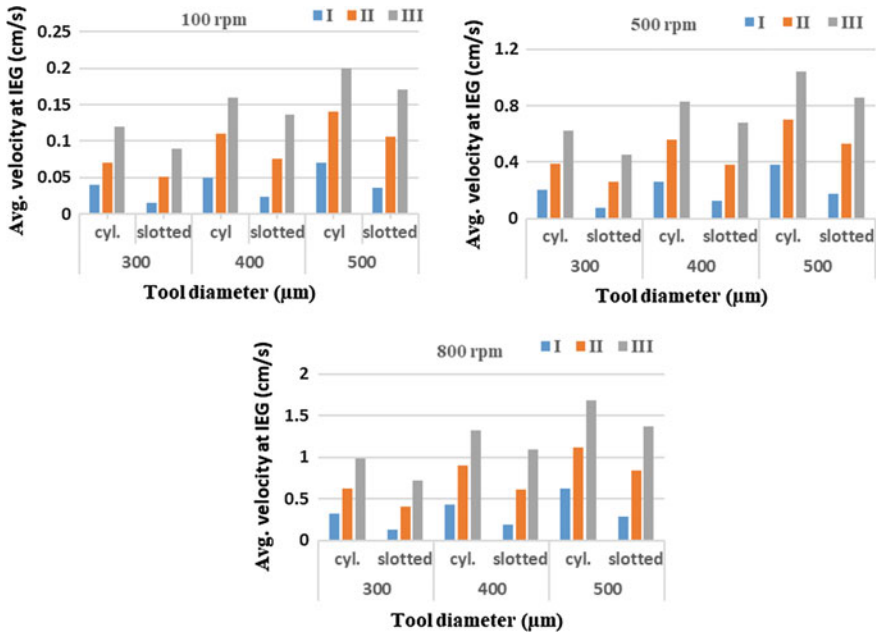


Fig. 2.7 Average dielectric velocity at IEG using cylindrical and slotted tools for different tool diameter and speed

### 2.4.1.3 Effect of Tool and μchannel Size

The effect of tool size and μchannel width on the dielectric velocity is studied. The IEG is kept constant with 50 μm. The diameter of tool considered are 300, 400, and 500 μm with the corresponding μchannel width of 400, 500, and 600 μm with constant IEG of 50 μm. This condition can prevail while machining various slot size with the same energy conditions. The comparative study of average dielectric velocity using cylindrical and slotted tools for various size are shown in Fig. 2.7. It is observed that the average dielectric velocity increases with tool diameter due to the higher centrifugal force exerted by the tool. With the higher tool speed, average dielectric velocity increases as expected. In this case also, the average dielectric velocity for slotted tools is less as compared to cylindrical tools for different tool rotation speed.

### 2.4.2 Debris Particle

The spherical particles are injected from the position I, II and III as discussed earlier. The particles get dragged from this position due to rotating dielectric around the tool. The velocity contours of the dielectric in the slot is shown in Fig. 2.8. The trajectory

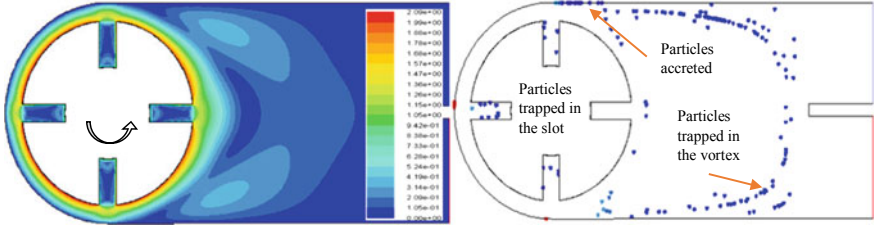


**Fig. 2.8** Velocity contours of dielectric in the slot and particles trapped in the slot and the vortex

shows multiple rotations of the particles around the tool and finally accretion on the work surface. The accretion is the accumulation of the particles on the work surface and it is calculated at the wall surface. The accretion rate is calculated as material addition per unit time and area. The accretion rate is given by

$$R_{accretion} = \sum_{p=1}^{N_{particles}} \frac{\dot{m}}{A_{face}} \tag{2.1}$$

where  $A_{face}$  is the cell face area at the wall ( $mm^2$ ) and  $\dot{m}$  is the mass flow rate of debris particles ( $gm/s$ ) [10].

The debris particles trapped in the slot and the vortex is clearly observed in Fig. 2.8. The tool rotation is in a counterclockwise direction and hence the accretion of particles is observed at the gap inlet on one side of the  $\mu$ channel. It is observed that there is a drop-in accretion of particles with the higher tool speed. Also, the accretion is minimum when the particle is initially near to tool. The accretion of particles using slotted tools for different tool speeds is shown in Fig. 2.9 and the comparative study with the cylindrical tool is shown in Fig. 2.10. It is observed that the accretion values using slotted tools are very less as compared to cylindrical tools. The slotted tools are effective in flushing the debris particles as it captures the particles in the slot.

**Fig. 2.9** Accretion of particles on the work surface using slotted tools

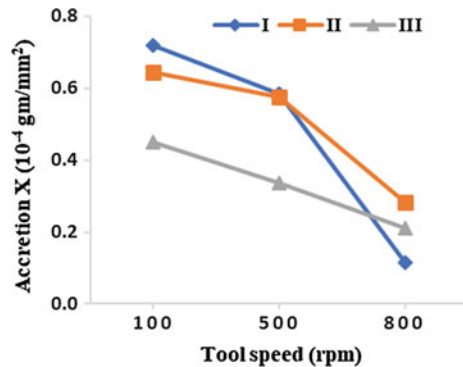
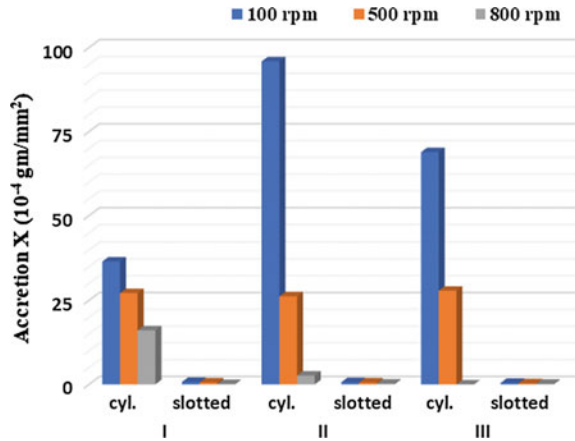


**Fig. 2.10** Comparative study of accretion of particles on the work surface using the cylindrical and slotted tool



## 2.5 Conclusions

The CFD is a useful technique to study the dielectric and debris flow at the IEG of few microns. It is rather complicated to develop experimental setup to study flow simulation due to the small size of the gap and short duration discharge. In the present study, the average dielectric velocity in the IEG is found for different input variables such as tool speed, inlet nozzle velocity, gap size, and dimension of  $\mu$ channel using cylindrical and slotted tools. It is found that the average dielectric velocity in the IEG is maximum for cylindrical tools as compared to slotted tools for all the cases. The velocity of the dielectric is the major force to drag the debris from the gap. However, in the case of slotted tools, the accretion of debris particles on the workpiece is found to be very less as compared to cylindrical tools. This may be due to stirring action of slotted tools in the gap which creates local turbulence and is responsible for the exclusion of debris particles from the IEG. The slots on the tool collect the debris and remove it from the IEG.

## References

1. Kunieda, M., Masuzawa, T.: A fundamental study on a horizontal EDM. *Ann. CIRP* **37**(1) (1988)
2. Nastasi, R., Koshy, P.: Analysis and performance of slotted tools in electrical discharge drilling. *CIRP Ann.—Manuf. Technol.* **63**, 205–208 (2014)
3. Puthumana, G., Joshi, S.: Investigations into performance of dry EDM using slotted electrodes. *Int. J. Precis. Eng. Manuf.* **12**, 957–963 (2012)
4. Li, L., Gu, L., Xi, X., Zhao, W.: Influence of flushing on performance of EDM with bunched electrode. *Int. J. Adv. Manuf. Technol.* **58**, 187–194 (2012)
5. Pei, J., Zhuang, X., Zhang, L., Zhu, Y., Liu, Y.: An improved fix-length compensation method for electrical discharge milling using tubular tools. *Int. J. Mach. Tools Manuf.* (2017). <https://doi.org/10.1016/j.ijmactools.2017.09.005>

6. Flaño, O., Ayesta, I., Izquierdo, B., Sánchez, J., Zhao, Y., Kunieda, M.: Improvement of EDM performance in high-aspect-ratio slot machining using multi-holed electrodes. *Precis. Eng.* **51**, 223–231 (2018)
7. Yang, I., Park, M., Chu, C.: Micro ECM with ultrasonic vibrations using a semi-cylindrical tool. *Int. J. Precis. Eng. Manuf.* **10**, 5–10 (2009)
8. Kumar, R., Singh, I.: Productivity improvement of micro EDM process by improvised tool. *Precis. Eng.* **51**, 529–535 (2018)
9. Hsue, A., Chang, Y.: Toward synchronous hybrid micro-EDM grinding of micro-holes using helical taper tools formed by Ni-Co/diamond Co-deposition. *J. Mater. Process. Technol.* **234**, 368–382 (2016)
10. Mullya, S.A., Karthikeyan, G.: Dielectric flow observation at inter-electrode gap in micro-electrodischarge milling process. *Proc IMechE Part B: J Eng. Manuf.* **232**(6), 1079–1089 (2018)

# Chapter 3

## Parametric Investigation into Electrochemical Micromachining for Generation of Different Micro-surface Textures



S. Kunar , S. Mahata  and B. Bhattacharyya

**Abstract** To fabricate various micro-surface textures at short time and low cost for modern industrial applications, a novel and substitute method of maskless electrochemical micromachining (EMM) is exploited due to its multiple advantages such as higher machining rate, better surface quality, reusability of a single patterned tool, irrespective to material hardness, no thermal effect, and burr-free surface. One textured tool containing different masked micro-patterns of SU-8 2150 and PMMA masks can fabricate many different textured surfaces with higher machining efficiency. The indigenously developed EMM setup having maskless electrode fixtures, EMM cell, electrolyte guiding scheme, and power supply connections can produce high-quality micro-patterned workpieces. The research study investigates the influence of process variables including electrolyte flow rate and interelectrode gap (IEG) on depth and overcut of different textured surfaces produced by this technique. Various types of textured patterns containing different sizes of micro-circular patterns and varactor micro-patterns are successfully fabricated using NaCl+NaNO<sub>3</sub> electrolyte. An analysis has been carried out to acquire the appropriate process variables with good machined characteristics of various micro-patterns using different micrographs.

**Keywords** Maskless EMM · Array of circular impressions · Varactor micro-pattern · Reusable textured tool · Overcut

### 3.1 Introduction

Textured surfaces play a significant role for performing various functions to different product surfaces. Micro-surface texturing method is used to modify the surface morphologies for achieving identical distributed depressions or asperities with controlled shape and size. Micro-surface textures perform the significant functions in the

---

S. Kunar (✉) · S. Mahata · B. Bhattacharyya  
Department of Production Engineering, Jadavpur University, Kolkata 700032, India  
e-mail: [sandip.sandip.kunar@gmail.com](mailto:sandip.sandip.kunar@gmail.com)

advancement of many engineering fields such as aviation, optics, information technology, electronics, and biomimetics [1]. For the enhancement of different micromachining technologies in the area of surface texture, the textured micro-patterns have played many vital functions economically in many micro-engineering applications such as sensors, electronics, micro-reactors, computer, biomedical, chemical micro-electromechanical systems. Many advanced micro-fabrication techniques carry out different machining activities such as fabrication of array of micro-dimples, grooves, micro-squares for extraordinary applications of electronic and computer industries.

To fabricate an array of micro-circular impressions, through-mask electrochemical micromachining (TMEMM) method is used and the influence of pulsed parameters on dimple characteristics is explored [2]. Micro-dimple arrays are fabricated by TMEMM method using low aspect ratio masks and the effect of process parameters on undercut, depth, etch factor, and surface roughness is studied during generation of array of circular impressions [3]. TMEMM process shows the machinability and applicability of the process for producing micro-dimples with controlled geometry on the planar and nonplanar surfaces. The effect of mask thickness, clamp force, and duty ratio is investigated on dimple diameter and dimple depth during fabrication of micro-dimple arrays [4]. Through-mask EMM is time consuming and expensive process for generation of dimple arrays due to individual masking of each workpiece before machining. Sandwich-like EMM is applied to generate deeper micro-dimples with proper geometrical shape using smaller porous metal cathode in enclosed electrochemical reaction unit [5]. Sometimes, accumulated sludges in the micromachining zone may deteriorate the shape and size of machined samples in enclosed electrochemical reaction unit. Varactor micro-patterns are generated by maskless EMM method, which is used in radio frequency communication including voltage-controlled oscillators and filters, microwave applications, etc. [6]. Electrochemical etching method is utilized to fabricate linear and square profiles using 0.1M  $\text{CuSO}_4$  solution. The linear profiles have feature width of 76  $\mu\text{m}$  and depth of 1.5  $\mu\text{m}$ . The square profiles have side length of 120  $\mu\text{m}$  and etch depth of 1.5  $\mu\text{m}$  [7]. The depth of etched pattern is very low. To generate array of circular impressions maskless EMM is employed using different types of electrolytes and the influence of flow rate, IEG, electrolyte concentration and machining time on depth and overcut is examined [8].

Many micro-fabrication techniques are applied to fabricate various micro-surface textures namely, lithography technology, LBM, mechanical machining, chemical etching, EDM, through-mask EMM, etc. However, most of the methods are not suitable to accomplish the requirements of modern industries for fabrication of economical micro-surface textures. These processes are expansive due to post-machined cleaning cost and lower productivity. So, maskless EMM is an important substitute technique for generating different microstructures due to its several advantages including higher machining efficiency, bright surface finish, reusability of a single patterned tool, no heat affected zone, burr free surface and no tool wear.

A novel and alternative concept of maskless EMM has been used to generate different types of micro-patterns, i.e., various sizes micro-circular patterns and varactor micro-patterns with good surface quality. One textured tool using different masks

can produce more than 24 textured samples with controlled geometry. The developed setup consisting of EMM cell and other accessories can generate good textured samples using constricted electrolyte guiding scheme. This process is applied to explore the effect of EMM variables such as flow rate and IEG on depth and overcut during the generation of different textured samples. An attempt has been made to acquire the suitable parameter setting for better textured characteristics of different textured micro-patterns.

### 3.2 Experimental Procedure

The indigenously developed maskless EMM system is used to fabricate different micro-surface textured patterns on SS-304 as shown in Fig. 3.1. The well planned experimental setup consists of different subsystems such as maskless electrochemical micromachining cell, job and tool fixtures, power supply connections, and electrolyte supply system for carrying out the experiments to generate different textured samples. Perspex material is used to fabricate EMM cell with electrode fixtures to avoid corrosion from environment. The outlet and inlet ports of the developed cell are fabricated by SS-304 material to protect from oxidation. Corrosion-free stainless steel gear pump is used to deliver the electrolyte uniformly in the micromachining zone at desired pressure. The important feature of electrolyte system is constricted vertical cross-flow electrolyte system, in which the flowing electrolyte passes parallel to two electrodes perpendicularly from downward to upward directions. Vertical cross-flow

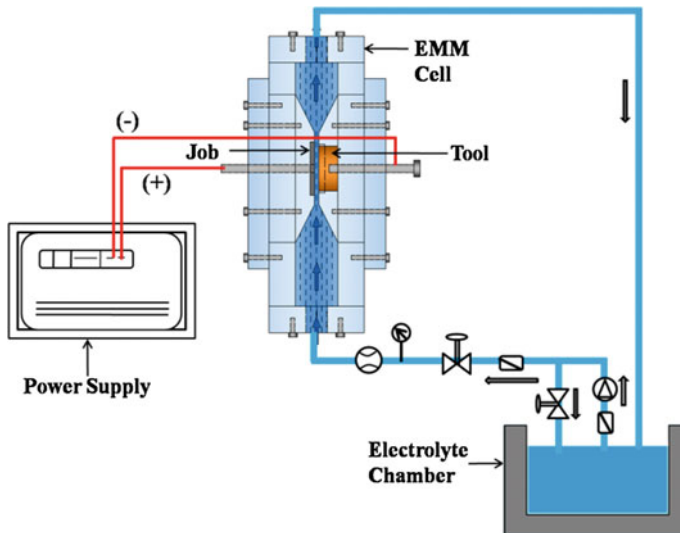


Fig. 3.1 Maskless EMM setup

electrolyte system always generates additional back pressure during machining time, which is more appropriate for circulation of clean electrolyte in the micromachining zone. This flow maintains the better surface quality of the textured surfaces than other flow modes. The pulsed DC power supply is used to provide the pulse current to the electrodes at constant voltage mode using square waveform.

The textured patterned tools having diameters of 200, 400, and 600  $\mu\text{m}$  are fabricated by UV lithography process on stainless steel wafer bonding with reusable SU-8 2150 mask having thickness 230  $\mu\text{m}$ . The micro-fabricated varactor patterned tool is fabricated by deep X-ray lithography process on brass wafer using reusable PMMA (Polymethyl methacrylate) mask having thickness 250  $\mu\text{m}$ . After preparing these samples, a small copper rod is attached with wafers using adhesive silver paste and then precision micrometer is connected with copper rod for interelectrode gap settings. Extra area of tool is insulated with enamel to protect from current density distribution.

The major EMM process variables are selected on the basis of extensive trial experiments to evaluate the outcomes of EMM parameters on the desired machined characteristics. Final experiments are conducted by changing one factor at a time with other fixed parameter setting based on good experimental results. Influences of flow rate and IEG are investigated on mean machining depth and mean machining accuracy of different micro-patterned samples. The ranges of IEG and electrolyte flow rate are 50–200  $\mu\text{m}$  and 3.35–6.35  $\text{m}^3/\text{h}$ , respectively. Other constant parameter settings are current cut off of 2A, duty ratio of 30%, voltage of 10 V, electrolyte concentration of  $\text{NaNO}_3$  (0.26M)+ $\text{NaCl}$  (0.18M), pulse frequency of 25 kHz, texturing time of 3 min, and flow pressure of 0.1  $\text{kg}/\text{cm}^2$ . Combined electrolyte of  $\text{NaNO}_3$ + $\text{NaCl}$  is preferred for controlled machining because  $\text{NaCl}$  has higher machining rate for higher metallic ions and  $\text{NaNO}_3$  has lower overcut for lower metallic ions. The repetition of each experiment is five and mean result of each machined response is calculated. The standard deviations of machining performances are computed to decide the superiority of different textured surfaces. The machined responses of different micro-patterns are deliberated with 3D Non-Contact Profilometer and Optical Microscope (Leica EZ4D, Germany).

### 3.3 Results and Discussion

Effects of significant process variables such as IEG and flow rate on performance criteria including overcut and depth of different micro-patterns are investigated in the form of graphs.



### 3.3.1 Influences of EMM Parameters

Effect of IEG is investigated on overcut and machining depth of different textured patterns with constant flow rate of  $6.35 \text{ m}^3/\text{h}$ . Figure 3.2 shows that the machining accuracy of circular and varactor micro-patterns deteriorates with the increase in IEG. The fabricated circular and varactor micro-patterns are almost uniform in geometrical shape and size in lower IEG because the distribution of machining current is more uniform for controlled current flux distribution in lower IEG. The overcut of different micro-textured patterns is higher because of non-uniform stray current distribution across the periphery of micro-patterns in higher IEG. The electrolysis products and gas bubbles accumulate below interelectrode gap of  $50 \mu\text{m}$  results in micro-sparking. Lower standard deviations in overcut of different micro-patterns are observed at lower interelectrode gap due to controlled etching. For better machining accuracy and lower standard deviation, lower IEG is recommended. The micro-patterns do not generate properly for electrolyte boiling and accumulation of sludges below IEG of  $50 \mu\text{m}$  and the generated micro-patterns are irregular in shape and size for uncontrolled stray current distribution beyond the limit of IEG of  $200 \mu\text{m}$ .

Experimentation is performed to examine the effect of IEG on textured depth as shown in Fig. 3.3. In higher IEG, the textured depth of micro-patterns decreases

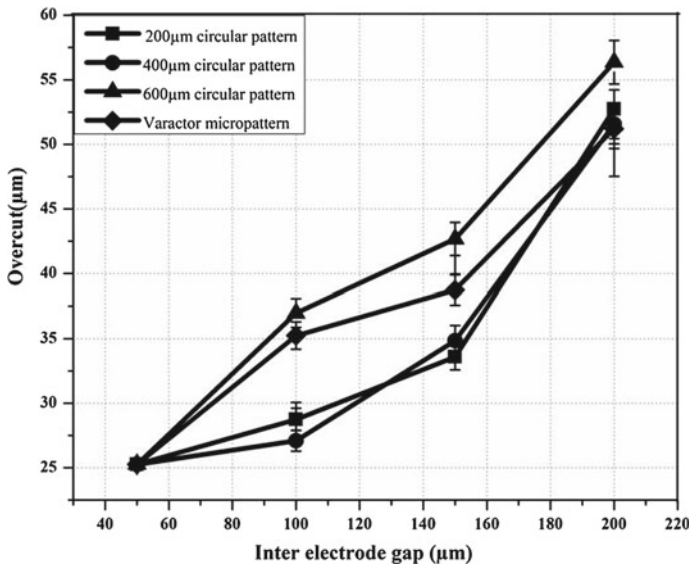
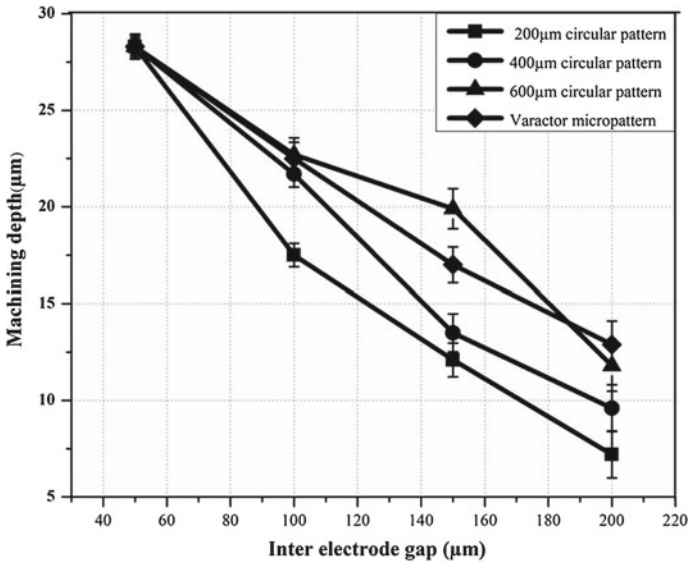


Fig. 3.2 Influence of IEG on overcut



**Fig. 3.3** Influence of IEG on machining depth

because uncontrolled machining occurs throughout the machining zone for non-uniform current flux distribution. In lower IEG, the machining depth of micro-patterns is almost controlled because higher anodic dissolution takes place for homogeneous current distribution. Lower standard deviations in machining depth of different micro-patterns are observed at lower interelectrode gap due to higher machining localization. Machining with lower IEG is recommended for controlled depth and lower standard deviations to acquire precise micro-patterns. The micro-patterns are not generated properly due to the accrual of reactive products below interelectrode gap of  $50\ \mu\text{m}$ . The generated micro-patterns are improper and distribution of depth is non-uniform for higher stray current effect above IEG of  $200\ \mu\text{m}$ .

The textured patterns are generated to study the influence of flow rate on overcut and depth keeping constant IEG of  $50\ \mu\text{m}$ . Figure 3.4 represents that the overcut of different circular and varactor micro-patterns decreases with increasing flow rate because the controlled machining takes place due to lower stray current effect at higher electrolyte flow rate for faster eradication of sludges from the micromachining zone. The overcut is uncontrolled throughout the micro-patterns at lower flow rate because lower flow rate performs uncontrolled machining localization all over the machining zone for improper removal of electrolysis products. The standard deviations in overcut of different micro-patterns are lower at higher electrolyte flow rate due to controlled etching. Higher flow rate is suggested for higher machining accuracy and lower standard deviations. The textured patterns of different micro-patterns are not formed appropriately due to the storage of sludges below flow rate of  $3.35\ \text{m}^3/\text{h}$ . Above flow rate of  $6.35\ \text{m}^3/\text{h}$ , the textured patterns are fabricated with irregular geometrical shape for higher stray current effect.

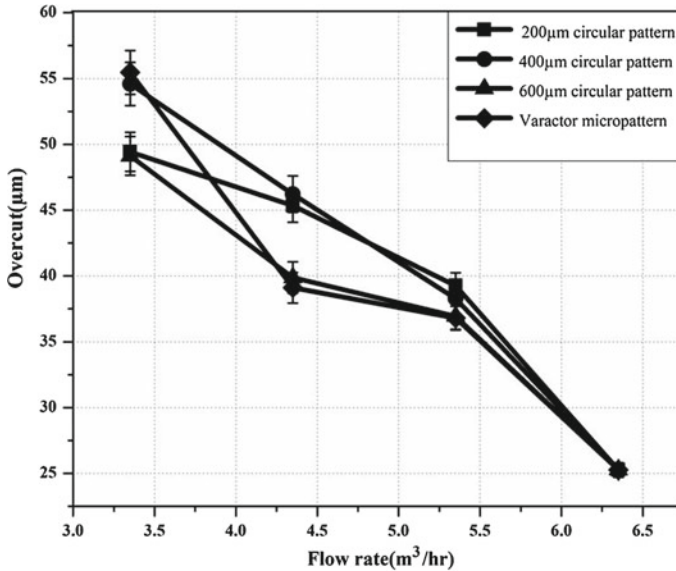


Fig. 3.4 Effect of flow rate on overcut

Influences of flow rate on textured depth of different micro-patterns are shown in Fig. 3.5. The textured depth of different micro-patterns increases with increasing flow rate because controlled anodic dissolution occurs at higher flow rate for faster removal of sludges. In lower flow rate, the depth is lower for all textured patterns because uncontrolled anodic dissolution occurs for storage of electrolysis products. Lower standard deviations in machining depth are observed at lower electrolyte flow rate due to uniform etching. For better shape of micro-patterns, machining with higher flow rate is suggested for lower standard deviations and controlled depth. Below electrolyte flow rate of 3.35 m<sup>3</sup>/h, the micro-patterns are not formed accurately due to lower machining localization. Above electrolyte flow rate of 6.35 m<sup>3</sup>/h, the micro-patterns deteriorate the proper geometrical shape for uncontrolled machining.

### 3.3.2 Analysis of Micrographs

All texturing experiments have been conducted by different micro-circular patterned tools using SU-8 2150 mask and varactor micro-patterned tool using PMMA mask by maskless EMM method. All masked patterned tools do not distort during texturing operation and these are used for fabrication of textured samples more than 24 times. These textured patterned tools are reused many times due to higher strength, faster drying capacity, higher adhesiveness, etc. During experimentation, all masked patterned tools are observed very carefully that very little distortion takes place in the masked tools after generation of many samples. This type of deformation has

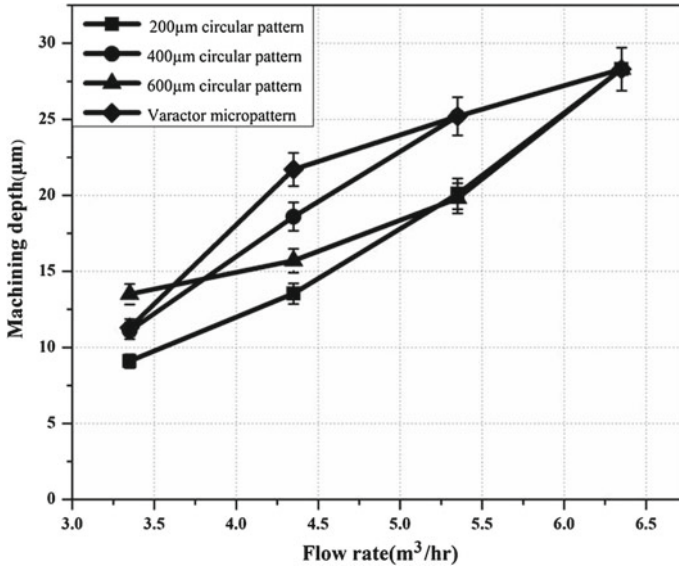
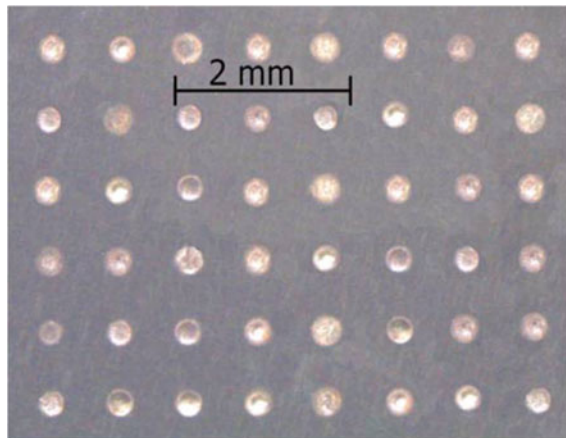


Fig. 3.5 Effect of flow rate on machining depth

been ignored during fabrication of textured samples and does not affect the textured samples during fabrication. All masked patterned tools have more effectiveness for the production of different textured samples with higher machining accuracy. These results recommend that these masks can generate multiple good micro-circular patterns and varactor micro-patterns without deformation of photoresist.

The optical image of fabricated array of micro-circular impressions is shown in Fig. 3.6 and machined by SU-8 2150 masked patterned tool having average diameter of 200 µm at a particular machining conditions such as electrolyte flow rate of

Fig. 3.6 Regular micro-circular pattern generated by 200 µm tool diameter



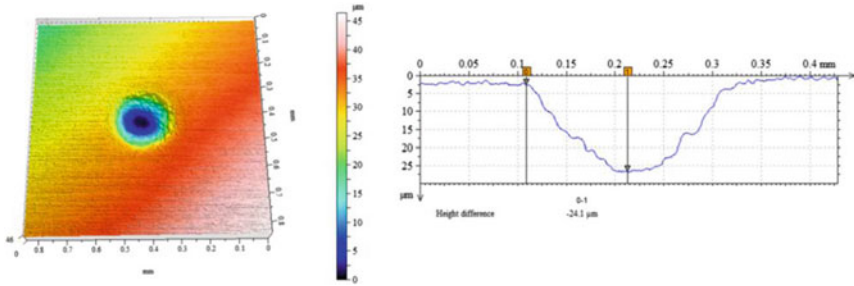


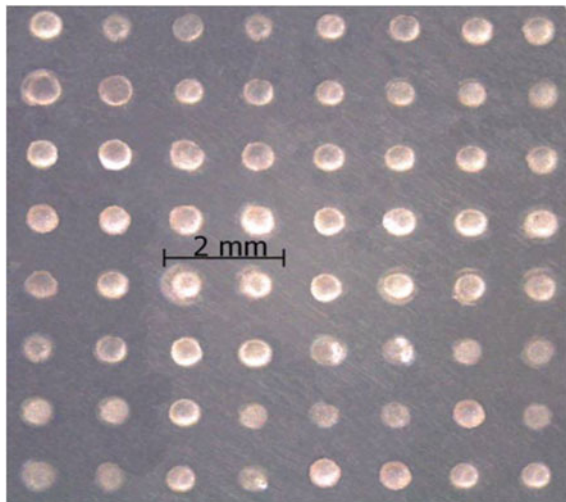
**Fig. 3.7** 3D view and depth profile of a micro-circular impression generated by 200  $\mu\text{m}$  tool diameter

6.35  $\text{m}^3/\text{h}$ , pulse frequency of 25 kHz, voltage of 10 V, duty ratio of 30%, machining time of 3 min, IEG of 50  $\mu\text{m}$ , and electrolyte of  $\text{NaNO}_3$  (0.26M)+ $\text{NaCl}$  (0.18M). The generated array of micro-circular impressions has good geometrical shape due to uniform etching throughout the machining area for regular current distribution. The material removal is quite uniform from the margin of array of circular impressions. The distribution of machining depth is almost uniform across the machining zone due to controlled machining. The average radial overcut and average depth of micro-circular pattern are 23.26  $\mu\text{m}$  and 21.5  $\mu\text{m}$ , respectively.

3D view of a micro-circular impression with the height difference of 24.1  $\mu\text{m}$  is shown in Fig. 3.7 and it is fabricated by SU-8 2150 masked tool having a diameter of 200  $\mu\text{m}$ .

The fabricated array of micro-circular impressions is shown in Fig. 3.8 and it is machined by SU-8 2150 masked patterned tool having average diameter of 400  $\mu\text{m}$  at a parametric combination, i.e., electrolyte of  $\text{NaNO}_3$  (0.26M)+ $\text{NaCl}$  (0.18M), duty ratio of 30%, texturing time of 3 min, IEG of 50  $\mu\text{m}$ , flow rate of 6.35  $\text{m}^3/\text{h}$ ,

**Fig. 3.8** Regular micro-circular pattern machined by 400  $\mu\text{m}$  tool diameter



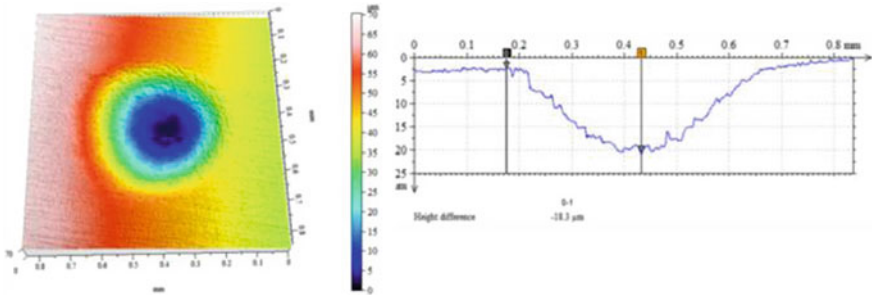


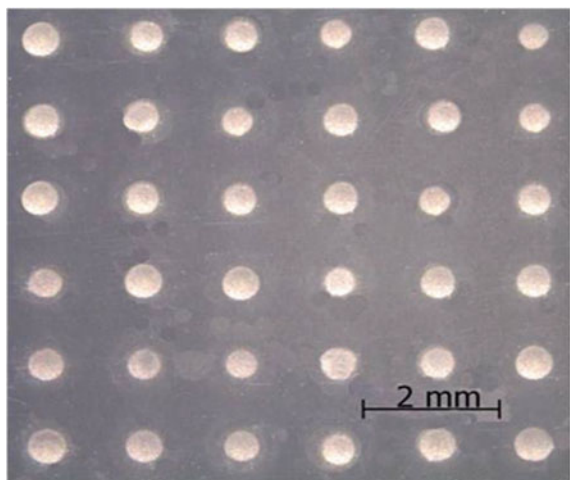
**Fig. 3.9** 3D view and depth profile of a micro-circular impression machined by 400  $\mu\text{m}$  tool diameter

pulse frequency of 25 kHz, and voltage of 10 V. The geometrical shape of array of micro-circular impressions is almost regular all over the machining area due to controlled dissolution. The distribution of patterned depth is also uniform due to controlled anodic dissolution. Very little distortion of patterned tool may not affect the shape of generated textured patterns. The average radial overcut and average depth of micro-circular pattern are 19.26  $\mu\text{m}$  and 23.3  $\mu\text{m}$ , respectively.

Figure 3.9 shows 3D view of a circular impression with depth profile having a depth of 18.3  $\mu\text{m}$ , which is machined by SU-8 2150 masked tool having diameter of 400  $\mu\text{m}$ .

The optical microscopic image of array of micro-circular impressions is shown in Fig. 3.10 and produced by SU-8 2150 masked patterned tool having average diameter of 600  $\mu\text{m}$  at a specified parametric setting, namely, pulse frequency of 25 kHz, voltage of 10 V, duty ratio of 30%, texturing time of 3 min, IEG of 50  $\mu\text{m}$ , electrolyte of  $\text{NaNO}_3$  (0.26M)+ $\text{NaCl}$  (0.18M), and flow rate of 6.35  $\text{m}^3/\text{h}$ . The fabricated

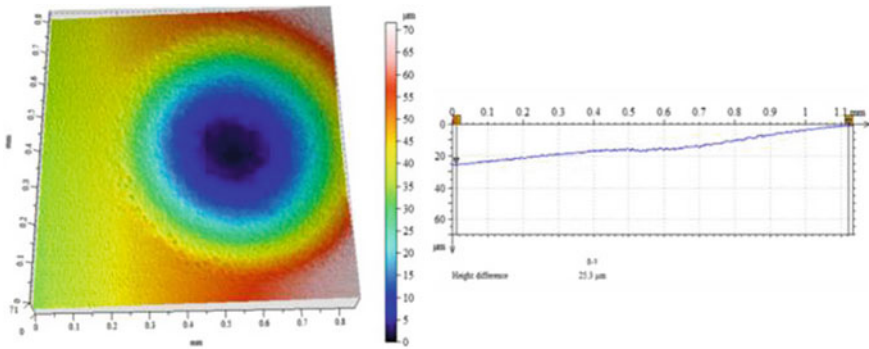
**Fig. 3.10** Regular array of micro-circular impressions fabricated by 600  $\mu\text{m}$  tool diameter



micro-circular pattern has proper geometrical shape due to controlled machining. The machining depth is also more or less identical owing to controlled machining throughout the texturing area. The average radial overcut and average depth of micro-circular pattern are  $22.26\ \mu\text{m}$  and  $27.3\ \mu\text{m}$ , respectively.

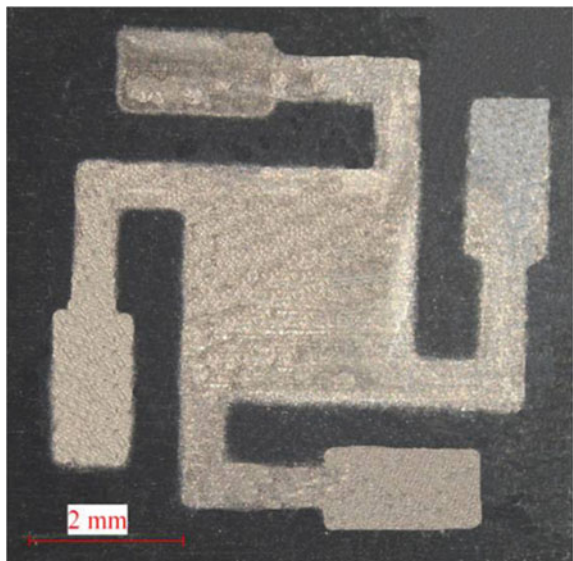
Figure 3.11 shows a 3D view of a circular impression with depth profile having a depth of  $25.3\ \mu\text{m}$ . It is generated by SU-8 2150 masked tool having diameter of  $600\ \mu\text{m}$ .

The optical image of varactor micro-pattern is shown in Fig. 3.12 and produced at a particular machining combination namely, electrolyte of  $\text{NaNO}_3$  ( $0.26\text{M}$ )+ $\text{NaCl}$  ( $0.18\text{M}$ ), texturing time of 3 min, pulse frequency of 25 kHz, IEG of  $50\ \mu\text{m}$ , duty ratio of 30%, flow rate of  $6.35\ \text{m}^3/\text{h}$  and voltage of 10 V using PMMA mask. The



**Fig. 3.11** 3D view and details of depth of a micro-circular impression fabricated by  $600\ \mu\text{m}$  tool diameter

**Fig. 3.12** Regular varactor micro-pattern



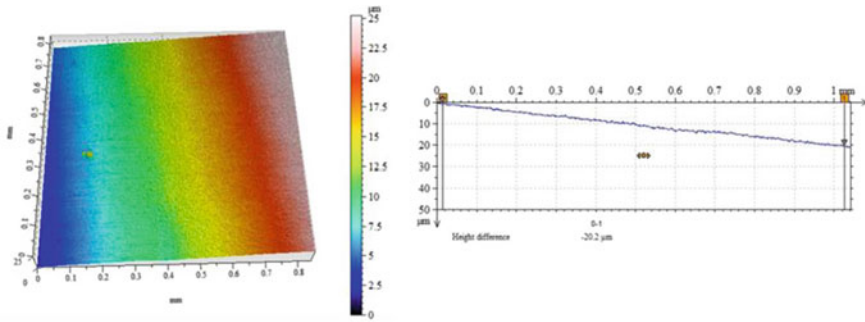


**Fig. 3.13** 3D view and details of depth of a segment of varactor micro-pattern

fabricated complex micro-pattern, i.e., varactor micro-pattern has proper geometrical shape due to controlled machining. The distribution of machining depth is almost homogeneous due to higher machining localization for controlled current density distribution. The average radial overcut and average depth of varactor micro-pattern are  $31.26 \mu\text{m}$  and  $26.3 \mu\text{m}$ , respectively.

Figure 3.13 shows a 3D view of the segment of varactor micro-pattern with depth profile having a depth of  $36.1 \mu\text{m}$ . It is produced by PMMA masked patterned tool having varactor shape.

### 3.4 Conclusions

Generation of micro-surface texture by maskless EMM method is one of the key micro-features in micro-products for various applications. The quality of various textured patterns influence product functionalization and service life of micro-products. The following conclusions can be drawn as follows:

- (i) Various micro-surface textures are produced by a novel and alternative texturing method of maskless EMM economically. The developed maskless EMM cell with other precisioned accessories is utilized for generation of better texturing samples with regular shape and size using constricted vertical cross flow electrolyte system.
- (ii) One single-masked patterned tool can produce more than 24 textured samples using SU-8 2150 and PMMA masks for various micro-circular patterns and varactor micro-patterns respectively.
- (iii) For controlled depth, higher machining accuracy and lower standard deviations, lower IEG and higher flow rate are suggested.
- (iv) From the investigation of various micro-patterns, it can be concluded that the parametric setting, i.e., electrolyte of NaCl (0.18M)+NaNO<sub>3</sub> (0.26M), voltage



of 10 V, duty ratio of 30%, machining time of 3 min, IEG of 50  $\mu\text{m}$ , electrolyte flow rate of 6.35  $\text{m}^3/\text{h}$ , and pulse frequency of 25 kHz generates many high-quality textured micro-patterns.

Maskless EMM is very needful for choosing the significant EMM process parameters for fabricating different micro-textured patterns of various shapes and sizes for advanced applications. For better micro-texturing patterns, the design of proper textured tools and machining on curved surfaces need to be improved further.

## References

1. Bruzzon, A.A.G., Costa, H.L., Lonardo, P.M., Lucca, D.A.: Advances in engineered surfaces for functional performance. *CIRP Ann.* **57**, 750–769 (2008). <https://doi.org/10.1016/j.cirp.2008.09.003>
2. Chen, X., Qu, N., Li, H., Xu, Z.: Pulsed electrochemical micro machining for generating micro-dimple arrays on a cylindrical surface with a flexible mask. *Appl. Surf. Sci.* **343**, 141–147 (2015). <https://doi.org/10.1016/j.apsusc.2015.03.087>
3. Mahata, S., Kunar, S., Bhattacharyya, B.: Micro dimple array fabrication by through mask electrochemical micro machining utilizing low-aspect ratio mask. *J. Electrochem. Soc.* **165**, E129–E137 (2018). <https://doi.org/10.1149/2.0521803jes>
4. Ming, P., Zhang, X., Zhou, W., Zhao, C., Zhou, H., Ge, Q.: Development of a modified through-mask electrochemical micro machining for micro patterning nonplanar surface. *Int. J. Adv. Manuf. Technol.* **93**, 2613–2623 (2017). <https://doi.org/10.1007/s00170-017-0541-5>
5. Zhang, X., Qu, N., Fang, X.: Sandwich-like electrochemical micro machining of micro-dimples using a porous metal cathode. *Surf. Coat. Technol.* **311**, 357–364. <https://doi.org/10.1016/j.surfcoat.2017.01.035>
6. Kunar, S., Mahata, S., Bhattacharyya, B.: Influence of electrochemical micro machining process parameters during fabrication of varactor micro pattern. *Int. J. Adv. Manuf. Technol.* **96**, 411–427 (2018). <https://doi.org/10.1007/s00170-017-1563-8>
7. Schönenberger, I., Roy, S.: Micro scale pattern transfer without photolithography of substrates. *Electrochimica Acta* **51**, 809–819 (2005). <https://doi.org/10.1016/j.electacta.2005.04.053>
8. Kunar, S., Mahata, S., Bhattacharyya, B.: Influence of electrolytes on surface texture characteristics generated by electrochemical micro machining. *J. Micro Manuf.* **1**, 124–133 (2018). <https://doi.org/10.1177/2516598418765355>

# Chapter 4

## Investigations into Wire Electrochemical Machining of Stainless Steel 304



Vyom Sharma , V. K. Jain  and J. Ramkumar 

**Abstract** Wire Electrochemical Micromachining (Wire-ECMM) is now under investigation by researchers around the globe due to the agility it offers to manufacturers over other advanced machining processes. A key application of this process is in cutting different shapes out of parent workpiece material of variable or uniform thickness by moving the tool along a predetermined path. The key features associated of a cut cavity (kerf) in Wire-ECMM are the fillet radius (FR) along the thickness of workpiece material, corner radius (CR) at curves and width of the kerf (S). In the present work, the dependency of these characteristic features is examined on different process parameters like applied potential (V), electrolyte concentration (C) and tool feed rate (f). Based on the results, optimum values of these parameters are identified and features like circle, triangle and square spiral are machined on Stainless steel 304.

**Keywords** Fillet radius · Corner radius · Side gap · Kerf width

### 4.1 Introduction

Wire electrochemical machining (Wire-ECMM) has gained significant attention from the researchers around the world in the recent past. One of the primary reasons for the growing popularity of this machining process is its cost-effectiveness. When compared to its counterpart in thermal-based machining process which is wire electric discharge machining (Wire-EDM), the setup cost and running cost are significantly low and material removal rate is relatively very high. In the domain of micromachining, Wire-ECMM has a clear advantage as there is a limitation to the minimum

---

V. Sharma · J. Ramkumar (✉)

Department of Mechanical Engineering, Indian Institute of Technology Kanpur, Kanpur  
208016, India  
e-mail: [jrkumar@iitk.ac.in](mailto:jrkumar@iitk.ac.in)

V. K. Jain

Department of Mechanical Engineering, Maulana Azad National Institute of Technology, Bhopal  
462003, India

© Springer Nature Singapore Pte Ltd. 2020

M. S. Shunmugam and M. Kanthababu (eds.), *Advances in Unconventional Machining and Composites*, Lecture Notes on Multidisciplinary Industrial Engineering, [https://doi.org/10.1007/978-981-32-9471-4\\_4](https://doi.org/10.1007/978-981-32-9471-4_4)

diameter of tool (wire) that can be used in Wire-EDM because in the latter case, the wire is constantly worn out as machining progresses while in the earlier case theoretically wire life is infinite. However, when the parameter of evaluation is machining precision, these two processes are not at par. Wire-ECMM has a clear superiority over Wire-EDM in terms of material removal rate but machining precision in former case has a big scope for improvement. In case of electrochemical dissolution, various inherent phenomena occurring at anode and cathode make the process of predicting final anode profile very complex. There is generation of gas bubbles as a product of electrolysis along with the sludge in the electrolyte which fills the gap between the two electrodes. It is primarily due to this reason that the electrolyte can no longer be modelled as a single-phase medium. At high values of circuit current, the temperature rises of electrolyte predominantly due to Joule's heating which alters its conductivity along the electrolyte flow direction in the interelectrode gap (IEG). Quick and effective replenishment of electrolyte in the gap has become a key area of research in the Wire-ECMM. Different researchers have adopted their unique ways to overcome this problem. Zeng et al. [1] presented the expression for the distribution of electrolyte flow velocity in the IEG. The electrolyte flow velocity was observed to increase with increasing wire travelling velocity. By employing a unidirectional travelling wire, the slit width was reported to increase with increasing travel velocity of wire along the thickness of workpiece. This is explained based on the fact that the electrolysis fraction decreases with increasing travelling velocity and the conductivity of electrolyte in IEG increases resulting in increased material removal rate (MRR). He et al. [2] simulated electrolyte flow velocity in the IEG in (Wire-ECMM) when the tool is imparted axial vibrations. Highest electrolyte velocity was shown to exist in the region near the tool and minimum velocity in the region near workpiece. As the amplitude of vibration increased, the slit width reduced up to a certain level. However, the electrolyte conductivity was assumed to depend upon the temperature and hydrogen bubbles only. It added for the inaccuracy because electrolyte is 3-phase mixture rather than only 2-phase mixture. Jain and Chouksey [3] developed a mathematical model for calculating the electrolyte electrical conductivity, considering it a three-phase mixture and also validated the model by carrying out extensive experimental investigations. The primary reason for the occurrence of fillet along the thickness of workpiece material in Wire-ECMM is the higher current density at sharp corners leading to an increase in material dissolution rate at sharp edges and also due to the effect of stray current attack. Both these factors result in the formation of the fillets at the corners. This also causes the top surface of workpiece material to dissolve at higher rate leading to a variation in the kerf width at the top and bottom workpiece surfaces.

Figure 4.1 shows a schematic diagram of Wire-ECMM with fillet radius along the thickness of workpiece. This fillet is a characteristic feature of a kerf machined using Wire-ECMM and one of the ways to control it is by reducing the effect of stray current. In order to put a check on this effect either wire can be insulated leaving open only a small part of it for machining or by carefully controlling different process parameters namely, potential, electrolyte concentration and tool feed rate so

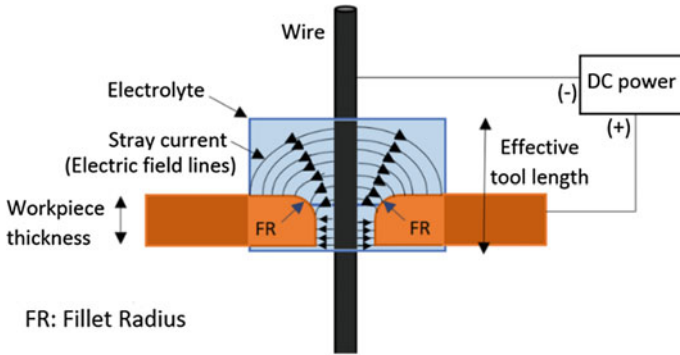


**Fig. 4.1** Schematic diagram showing fillet radius formation at the top surface of the workpiece and the presence of stray current

as to localize dissolution in the close vicinity of wire. Figure 4.2 shows a schematic diagram of a slit machined using Wire-ECMM along with corner radius and width of a kerf. Frontal and side IEGs are also indicated in the figure.

For applications in micromachining, kerf width should be very close to the diameter of the tool and hence the side IEG should be minimum. Different researchers around the globe have adopted different methods to minimize the side IEG in order to keep the kerf width to its minimum. He et al. [4] attempted to improve accuracy in Wire-ECMM of titanium alloy by keeping the wire stationary and flushing the electrolyte axially to the tool. Axial electrolyte flushing aided with the force of gravity helps in effective removal of electrolysis products from the machining gap and improves current efficiency. Besides imparting motion to the wire, researchers have also investigated the effectiveness of shaped tools in quick replenishment of fresh electrolyte in the IEG. Fang et al. [5] demonstrated the use of helical electrode

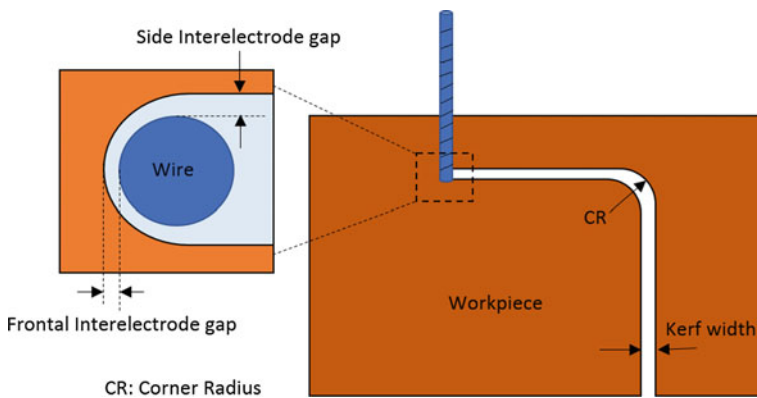


**Fig. 4.2** Diagram of a slit machined using Wire-ECMM along with corner radius

rotating about its axis in place of wire for achieving higher MRR and slit width uniformity in the depth direction. Helical electrodes when rotated impart axial velocity to electrolyte which drags it upwards. Zou et al. [6] demonstrated that pulsed current can be generated in the IEG by using a constant DC power supply with a ribbed wire tool. Particle tracing simulations carried out in the investigation suggests that a ribbed wire removes sludge generated during electrolysis more efficiently. Both the pulsating effect of current and effective sludge removal contribute to higher degree of dissolution localization in Wire-ECMM. Xu et al. [7] used etched wire to enhance mass transport in the IEG. It was claimed that a high surface hydrophilia (hydrophilic in nature) creates thicker boundary layer and makes electrolyte more viscous in this region. This assists in better mass transport in interelectrode gap. Fang et al. [8] presented a study on the use of a ribbed wire in place of a conventional smooth tool and high amplitude vibrations. As explained in their work, the fraction of by-products is very small to affect the electrolyte conductivity and hence, the focus is on removal of hydrogen bubbles from the IEG. Vibrating the ribbed wire at large amplitudes intensifies the bubble removal process in upwards and downwards direction. In the present work, the dependency of kerf width, fillet radius and corner radius on process parameters namely applied potential, electrolyte concentration and tool feed rate are experimentally examined on stainless steel 304 workpiece. No literature could be found which studies the effect of above process parameters on the fillet radius and corner radius in Wire-ECMM.

## 4.2 Experimental Setup

The workpiece holder and electrolyte basin are mounted on X-Y drive of the stage, which is interfaced with computer using a microcontroller. Regulated DC power supply with voltage rating from 0 to 32 V and minimum resolution for current as 0.01 A is used. Electrolyte is delivered from the flexible delivery tube connected to a pressurized electrolyte tank with pressure controller. Wire is held tight in a C-clamp and is locked to X-axis of the stage. Workpiece is imparted a tilt with the help of a servo motor of rating 12 V and 0.6 A. Shaft made of brass is attached with the motor shaft with the help of a flexible coupling and it is supported by two bearings to restrict its lateral movement. This is to ensure proper centering of the shaft. The schematic diagram of the setup is shown in Fig. 4.3.

## 4.3 Design of Experiments

Experiments are designed to investigate the effect of each of the process parameter namely, applied potential (V), electrolyte concentration (C), and tool feed rate (f) on different responses namely, fillet radius (FR), corner radius (CR) and kerf width (S)

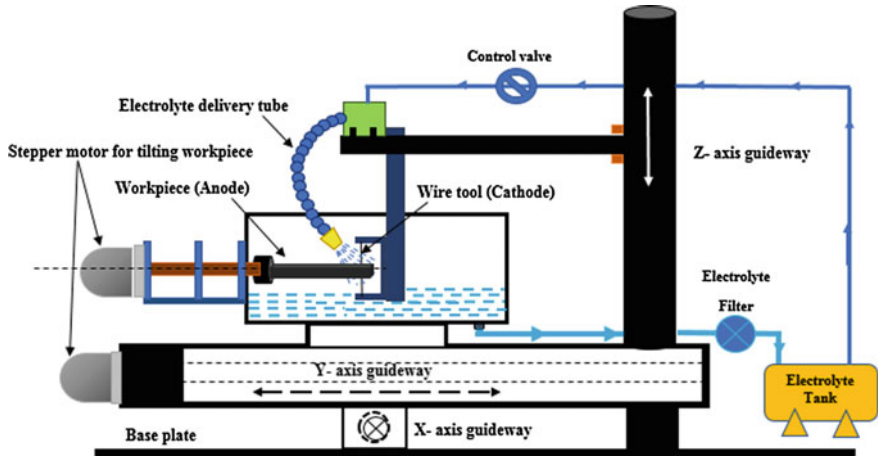


Fig. 4.3 Schematic diagram of experimental setup

Table 4.1 Range of input process parameters

S. No.	Input parameter	Unit	Range
1.	Potential	V	5–9.5
2.	Electrolyte concentration (NaNO <sub>3</sub> )	mol/L	0.2–0.5
3.	Tool feed rate	μm/s	2–5

by keeping other factors constant and varying one parameter at a time. Copper wire of diameter 30 μm is used in all experiments. The range of different input parameters is listed in Table 4.1 and they are obtained by conducting pilot experiments.

## 4.4 Results and Discussions

Effect of different input parameters on various responses is evaluated by varying only one of the factors at a time and keeping other parameters constant. Fillet radius, corner radius and kerf width are measured using Nikon Eclipse LV100 Industrial Optical Microscope.

### 4.4.1 Effect of Process Parameters on Fillet Radius (FR)

Figure 4.4a shows the optical images of fillet radii obtained at variable potentials and fixed values of tool feed rate and electrolyte concentration. Figure 4.4b shows the dependency of fillet radius on tool feed rate. As the tool feed rate is increased

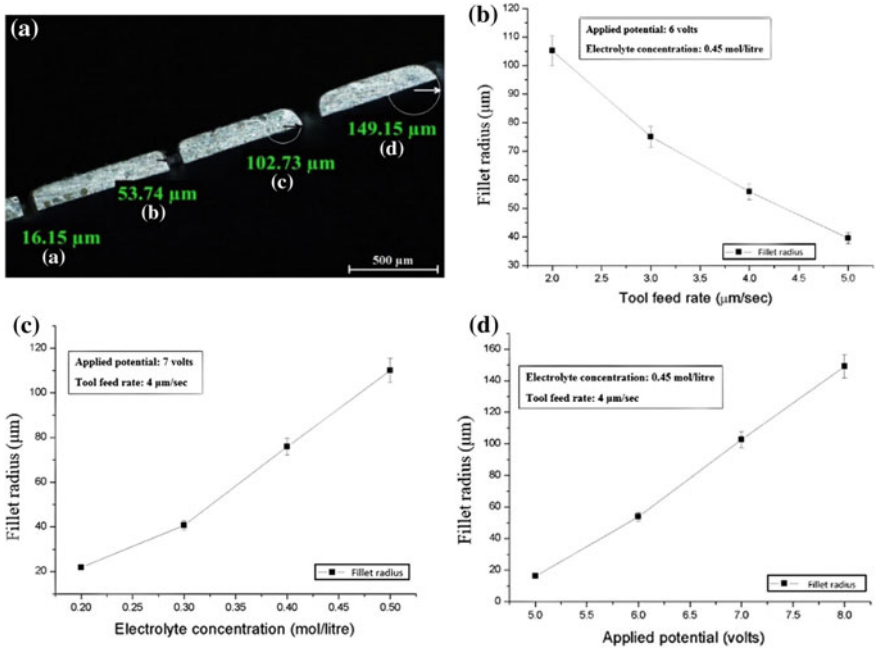


**Fig. 4.4** a Variation of fillet radius with applied potential (A) 5 V (B) 6 V (C) 7 V (D) 8 V **4. b** Variation of fillet radius with tool feed rate. **c** Variation of fillet radius with electrolyte concentration. **d** Variation of fillet radius with applied potential

from 2 to 5  $\mu\text{m}/\text{s}$ , the fillet radius is observed to decrease. This is primarily due to the fact that less time is available for dissolution at any point on sharp edges of kerf and hence less material is dissolved when the tool feed rate is increased. Figure 4.4c shows the dependency of fillet radius on electrolyte concentration. As the electrolyte concentration increases from 0.2 to 0.5 mol/L, the number of charge carriers in the solution increases and it decreases the resistance of IEG. This results in an increase in MRR. Thus, with an increase in electrolyte concentration, fillet radius also tends to increase. Figure 4.4d shows the variation of fillet radius with applied potential. Fillet radius is observed to increase significantly with increasing potential. As the applied potential increases from 5 to 8 V, fillet radius increases from 16.15 to 149.15  $\mu\text{m}$ . This trend is primarily due to increase in current flowing in the circuit with increase in applied potential and leading to increase in rate of material dissolution. Although not much significant, but with the increase in applied potential, the temperature of electrolyte also rises due to Joule heating leading to increase in electrolyte conductivity which further aids in increase in rate of material dissolution and leading to rapid dissolution of sharp edges.

### 4.4.2 Effect of Process Parameters on Corner Radius (CR)

Figure 4.5a shows variation of corner radius with tool feed rate. The primary reason for the occurrence of this radius is the increase in current density at sharp vertex. As the tool feed rate increases from 2 to 5  $\mu\text{m/s}$ , the corner radius decreases from 149.18 to 104.74  $\mu\text{m}$ . Even though the rate of material removal is locally increased due to increase in current density, the amount of material dissolved at slower feed rates is higher than that at higher feed rates. This leads to decrease in corner radius with increase in tool feed rate. Figure 4.5b shows the variation of corner radius with electrolyte concentration. As the electrolyte concentration increases from 0.2 to 0.5 mol/L, the corner radius increases almost linearly from 98.29 to 164.95  $\mu\text{m}$ . Increased concentration increases overall current flowing in the circuit hence leading to increase in current density at all points on workpiece. Higher current density corresponds to higher MRR and hence, corner radius also increases. Figure 4.5c shows the variation of corner radius with applied potential. As the applied potential increases from 6.5 to 9.5 V in steps of 1 V, the corner radius increases from 77.09 to 159.44  $\mu\text{m}$ . Experiments are conducted at tool feed rate of 4  $\mu\text{m/s}$  and electrolyte concentration of 0.32 mol/L. Similar to increase in electrolyte concentration, increase in applied potential also increases the amount of current flowing in the circuit leading to an increase in material dissolution rate. This causes the corner radius to increase with increase in applied potential. The trend is non-linear with piecewise linearity between two consecutive points of observation. Figure 4.5d shows an optical image of corner radius measured for different values of applied potentials.

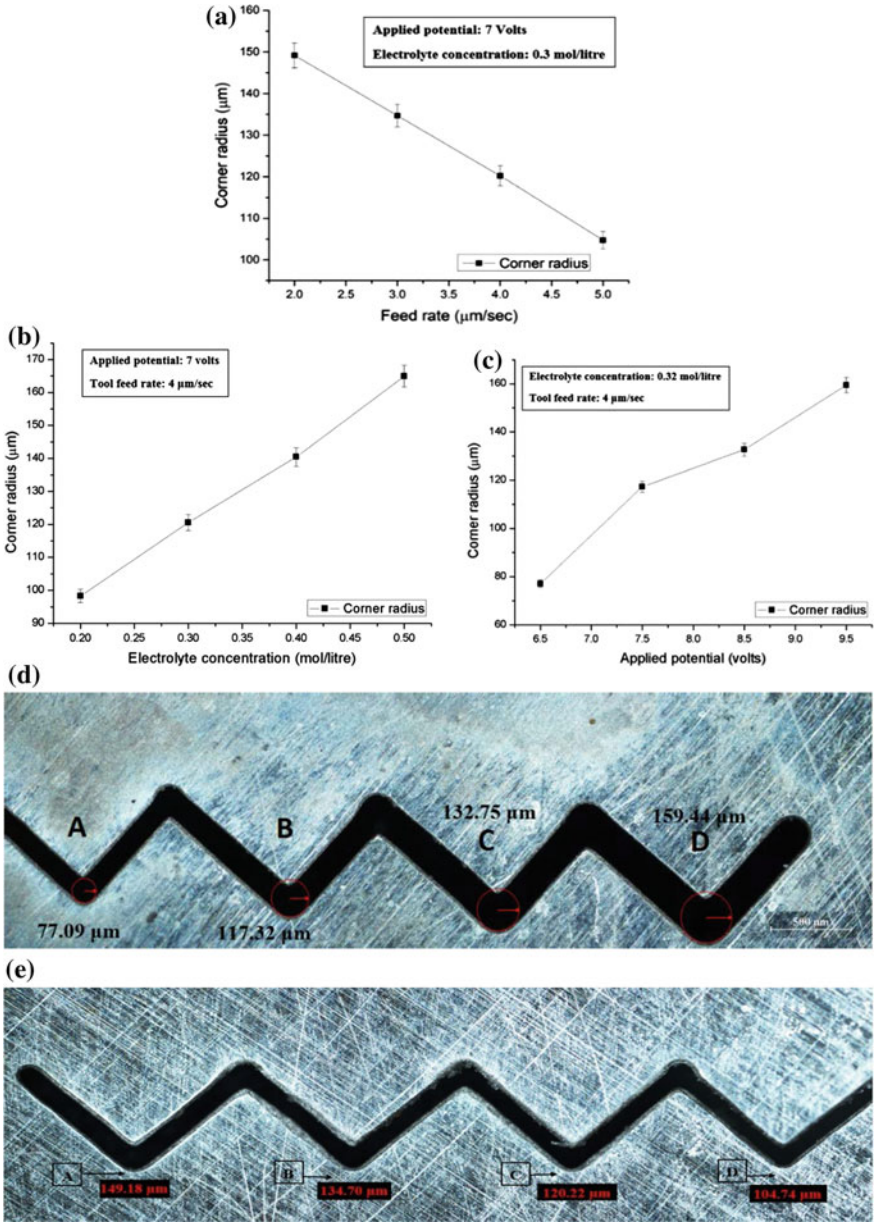
### 4.4.3 Effect of Process Parameters on Kerf Width (S)

Figure 4.6a shows the variation of kerf width with tool feed rate. As the kerf width is equal to wire diameter added with twice the side IEG ( $y$ ), the increase in ( $y$ ) will lead to increase in overall kerf width. For equilibrium machining conditions when the current flowing in the circuit is constant, the expression for interelectrode gap ( $y$ ) can be written as [9]

$$y = y_o + \left( \frac{\eta(E - \Delta E)J}{F\rho_a} - f \right) \Delta t \quad (1)$$

where,  $y_o$  is the initial interelectrode gap,  $f$  is the tool feed rate,  $E$  is the applied potential in volts,  $\Delta E$  is overpotential of the circuit,  $J$  is the current density on anode surface,  $\Delta t$  is the small time interval over which current density  $J$  is assumed to remain constant,  $\rho_a$  is density of anode (workpiece) material,  $\eta$  is current efficiency of the system and  $F$  is faradays constant and its value is 96,500 coulombs. From Eq. (1), it can be seen that with increase in tool feed rate ( $f$ ), side interelectrode gap and hence the overall kerf width decreases. Figure 4.6b shows the variation





**Fig. 4.5** a Variation of corner radius with tool feed rate. b Variation of corner radius with electrolyte concentration. c Variation of corner radius with applied potential. d Variation of corner radius with applied potential. e Variation of corner radius with tool feed rate (A) 2  $\mu\text{m}/\text{s}$  (B) 3  $\mu\text{m}/\text{s}$  (C) 4  $\mu\text{m}/\text{s}$  (D) 5  $\mu\text{m}/\text{s}$

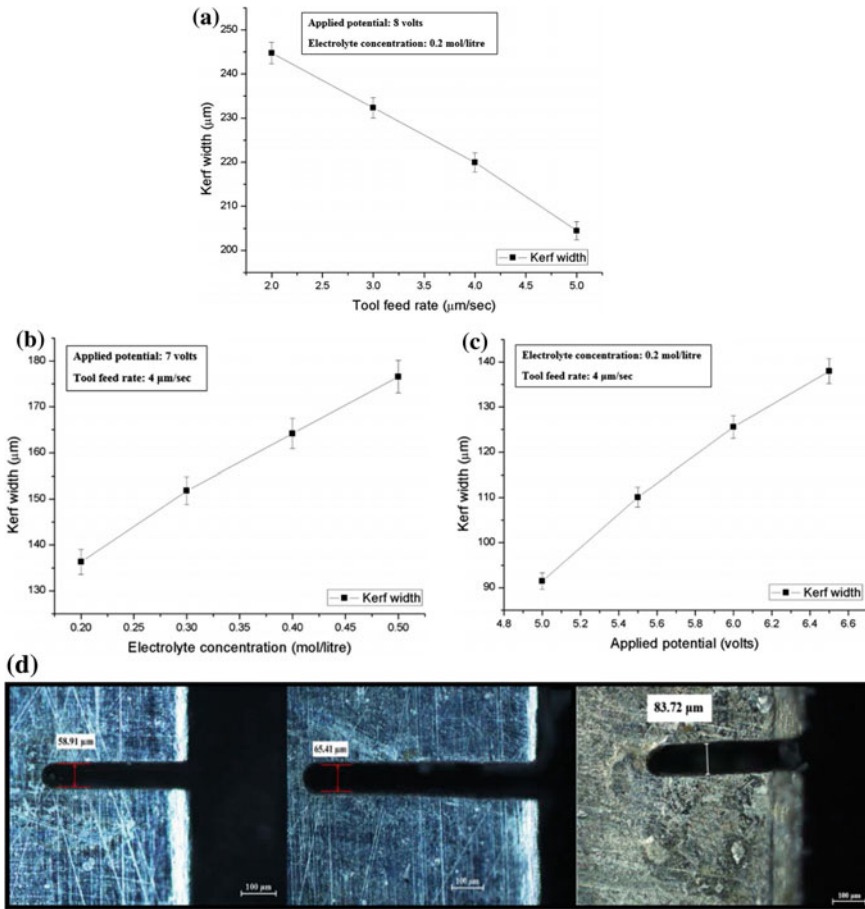


**Fig. 4.6** a Variation of kerf width with tool feed rate. b Variation of kerf width with electrolyte concentration. c Variation of kerf width with applied potential. d Optical image of slits machined at (A) 4 V (B) 4.5 V (C) 5 V

of kerf width with electrolyte concentration. As the concentration increases, the conductivity ( $k$ ) of electrolyte also increases due to increase in number of charge carriers in the solution and interelectrode gap also increases. This is because of increase in volumetric material dissolution rate due to increase in current flowing in the electrochemical cell at a fixed value of applied potential. Figure 4.6c shows the variation of kerf width with applied potential. Increasing the value of applied potential increases the value of side interelectrode gap, as can be seen from Eq. (1). This is mainly caused due to increase in the value of current flowing in the circuit when the electrolyte resistance is kept constant and potential difference between the two electrodes is increased. This, in turn, leads to increment in material dissolution rate and increase in kerf width is observed.

Figure 4.6d shows optical images of slits machined at electrolyte concentration of 0.2 mol/L, tool feed rate of 5  $\mu\text{m/s}$  and applied potential of (A) 4 V with a kerf width of 58.91  $\mu\text{m}$  (B) 4.5 V with a kerf width of 65.41  $\mu\text{m}$  and (C) 5 V with a kerf width of 83.72  $\mu\text{m}$  on stainless steel 304 workpiece of uniform thickness 100  $\mu\text{m}$ .

## 4.5 Generation of Different Features on Stainless Steel 304

Based on the results obtained in Sect. 4.4, it is evident that small fillet radius can be achieved by keeping the values of applied potential and electrolyte concentration at a lower level and the value of tool feed rate at a higher level, although there is a limit to maximum feed rate that can be achieved (for stable machining condition) at a given value of applied potential and electrolyte concentration. For achieving lower value of corner radius, values of applied potential and electrolyte concentration must be kept at a lower level and value of tool feed rate at a higher level. The same stands true for obtaining lower value of kerf width. For stable machining, optimum values of process parameters are selected to generate different features on stainless steel 304 workpiece of uniform thickness 100  $\mu\text{m}$ . Figure 4.7a shows an optical image of a circle with diameter 2 mm machined at applied potential of 6 V, electrolyte concentration of 0.3 mol/L and tool feed rate of 4  $\mu\text{m/s}$ . Radius of positive part is 915.96  $\mu\text{m}$  and that of negative part is 1059.63  $\mu\text{m}$ . The value of constant current was 0.02 A. Figure 4.7b, c shows an optical image of a right triangle with hypotenuse of 4 mm and a square spiral machined at similar values of process parameters as used for feature shown in Fig. 4.7a.

## 4.6 Conclusions

Based on experimental findings reported in Sect. 4.4, the following conclusions can be drawn: Minimum fillet radius of 16.15  $\mu\text{m}$  was achieved at applied potential of 5 V, tool feed rate of 4  $\mu\text{m/s}$  and electrolyte concentration of 0.45 mol/L. Minimum corner radius of 77.09  $\mu\text{m}$  was achieved at applied potential of 6.5 V, tool feed rate of 4  $\mu\text{m/s}$  and electrolyte concentration of 0.32 mol/L. Minimum kerf width of 91.47  $\mu\text{m}$  was achieved at tool feed rate of 2  $\mu\text{m/s}$  and electrolyte concentration of 0.2 mol/L non-passivating electrolyte of  $\text{NaNO}_3$  was used for all the experiments. Different features were machined on stainless steel 304 workpiece of uniform thickness 100  $\mu\text{m}$  in order to demonstrate the capabilities of this process in various operations like generation of micro-channels for micro mixtures, micro-cantilever sensing instruments and trepanning of large size cores out of parent workpiece material.

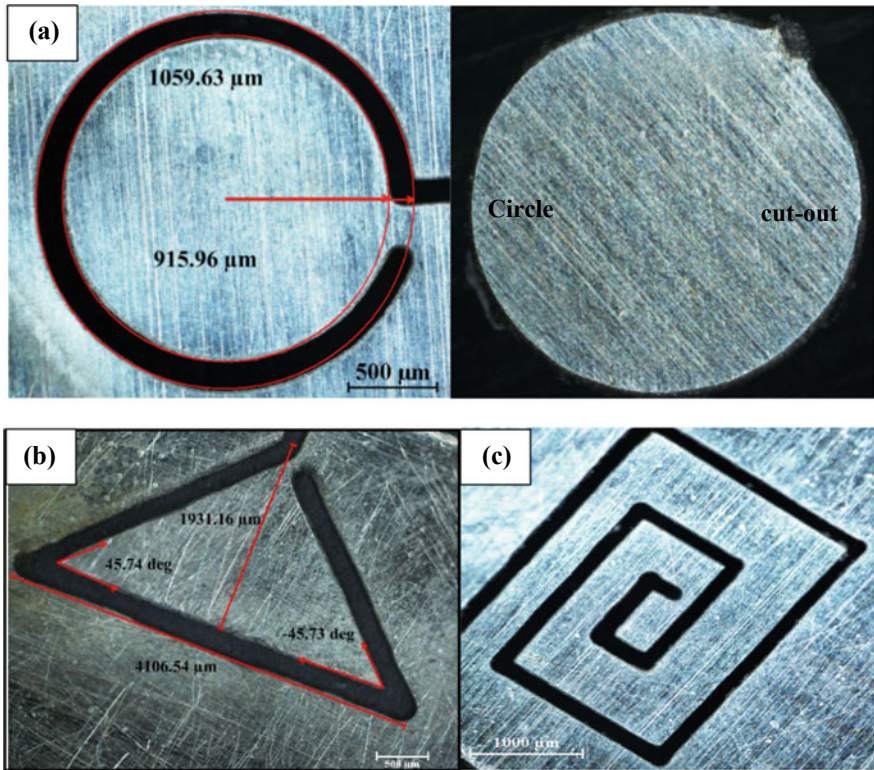


**Fig. 4.7** **a** Optical image of circle machined at applied potential of 6 V, tool feed rate of 4  $\mu\text{m/s}$  and electrolyte concentration of 0.3 mol/L. **b** Optical image of a right-angled triangle and. **c** Square helix machined at 6 V

## References

1. Zeng, Y., Qia, Yu., Fang, X., Kun, X., Li, H., Ningsong, Q.: Wire electrochemical machining with monidirectional traveling wire. *Int. J. Adv. Manuf. Technol.* **78**(5–8), 1251–1257 (2015)
2. He, H., Zeng, Y., Yao, Y., Ningsong, Q.: Improving machining efficiency in wire electrochemical micromachining of array microstructures using axial vibration-assisted multi-wire electrodes. *J. Manuf. Process.* **25**, 452–460 (2017)
3. Jain, V.K., Chouksey, A.K.: A comprehensive analysis of three-phase electrolyte conductivity during electrochemical macromachining/micromachining. *Proc. Inst. Mech. Eng. Part B: J. Eng. Manuf.* 0954405417690558 (2017)
4. He, H., Ningsong, Q., Zeng, Y., Fang, X., Yao, Y.: Machining accuracy in pulsed wire electrochemical machining of  $\gamma$ -TiAl alloy. *Int. J. Adv. Manuf. Technol.* **86**(5–8), 2353–2359 (2016)
5. Fang, X., Zhang, P., Zeng, Y., Qu, N., Zhu, D.: Enhancement of performance of wire electrochemical micromachining using a rotary helical electrode. *J. Mater. Process. Technol.* **227**, 129–137 (2016)
6. Zou, X., Fang, X., Chen, M., Zhu, D.: Investigation on mass transfer and dissolution localization of wire electrochemical machining using vibratory ribbed wire tools. *Precis. Eng.* **51**, 597–603 (2018)

7. Xu, K., Zeng, Y., Li, P., Fang, X., Zhu, D.: Effect of wire cathode surface hydrophilia when using a travelling wire in wire electrochemical micro machining. *J. Mater. Process. Technol.* **235**, 68–74 (2016)
8. Fang, X.L., Zou, X.H., Chen, M., Zhu, D.: Study on wire electrochemical machining assisted with large amplitude vibrations of ribbed wire electrodes. *CIRP Ann.* **66**(1), 205–208 (2017)
9. Jain, V.K.: *Advanced Machining Processes*. Allied Publishers (2009)

# Chapter 5

## Nanofinishing of External Cylindrical Surface of C60 Steel Using Rotating Core-Based Magnetorheological Finishing Process



Manpreet Singh , Ashpreet Singh  and Anant Kumar Singh 

**Abstract** A rotating core-based magnetorheological finishing process has been developed for nanofinishing of external cylindrical surfaces. Shaft made of steel grade C60 is taken as workpiece, which finds its application in manufacturing of various automotive products such as crankshafts, rocker arm shafts, and steering tie rods. The present work involved the parametric studying the developed magnetorheological finishing process. To plan and examine the effect of process parameters, namely, current, tool core's rotation, workpiece rotation and abrasives concentration on the percentage change in surface roughness, the response surface methodology has been employed. Examination of the experimental data depicted that the large contribution to response variable is made by the current and tool speed, which is followed by the rotational speed of cylindrical workpiece and abrasives concentration. The initial surface roughness value of 320 nm reduced to a final value of 52 nm in finishing time of 90 min with optimized parameters.

**Keywords** Cylindrical external surfaces · Magnetorheological finishing · Response surface methodology · Surface roughness

### 5.1 Introduction

Surface finish is one of the vital characteristics in research areas and requirement in industries especially medical, aerospace and automobile sectors [1]. High-strength applications such as in automobile sector, the improved quality of the product is desired to enhance the wear characteristics and service life of the product [2]. The higher quality of the surface is essential to attain the desired performance of functions such as fatigue life. Higher fatigue life is required for the various power transmitting shafts such as crankshaft. [3]. Traditional methods of finishing result in the involvement of large magnitude of cutting forces which is a cause for not attaining better

---

M. Singh · A. Singh (✉) · A. K. Singh  
Department of Mechanical Engineering, Thapar Institute of Engineering and Technology, Patiala  
147001, Punjab, India  
e-mail: [anantsingh@thapar.edu](mailto:anantsingh@thapar.edu)

© Springer Nature Singapore Pte Ltd. 2020  
M. S. Shunmugam and M. Kanthababu (eds.), *Advances in Unconventional Machining and Composites*, Lecture Notes on Multidisciplinary Industrial Engineering, [https://doi.org/10.1007/978-981-32-9471-4\\_5](https://doi.org/10.1007/978-981-32-9471-4_5)

surface finish. To get over these restrictions, several advanced fine finishing methods have been developed [4]. Out of the available fine finishing processes, magnetorheological polishing (MRP) fluid utilized in magnetic field-assisted processes. These processes not only provide low magnitude cutting forces but also permit to regulate them. Moreover, the MRP fluid has got rheological properties, which is attracting the various field of finishing applications including complex intricate surfaces [5–7]. Singh et al. developed an improved ball end magnetorheological finishing (BEMRF) process with a central rotating core and a cooling jacket in which stationary electromagnetic coil wrapped with copper coils is provided which is supplied with cooling medium from a low-temperature bath [8]. In the present modified finishing process, both workpiece and the electromagnetic core tool with flat tool tip are made to rotate with their axis of rotation perpendicular to each other as shown in Fig. 5.1. The electromagnetic tool comprises of a central rotating solid core which rotate with respect to the stationary electromagnet with copper coil windings.

The d.c. current is supplied to the stationary the electromagnet coil to generate the magnetic field at the tip of tool core. The MR polishing (MRP) fluid consists of non-magnetic abrasives and magnetic carbonyl iron particles (CIPs) in base fluid. Carrier fluid is a combination of heavy paraffin oil, various surfactants and additives. The top view of the experimental setup is depicted in Fig. 5.1 As observed from Fig. 5.1, the cylindrical workpiece is supported in between shaft bearing seats fitted with ball bearing to provide the relative rotation. A rotating core-based electromagnetic tool with flat tip is lied on horizontal z-slide. Three different programmable servo motors are used in the complete setup. Two motors provide rotating motion to the cylindrical workpiece and the tool, and the third one provides reciprocating motion to the tool for the feeding proposes. A belt pulley drive system transmits rotational motion to the workpiece from servo motor. The whole set up is placed on the non-magnetic

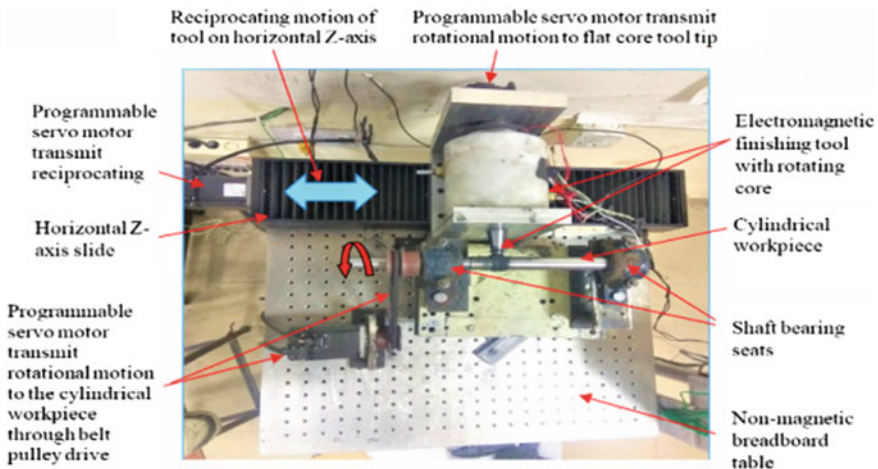


**Fig. 5.1** Top view of the rotating solid core-based magnetorheological nanofinishing experimental setup for finishing of external cylindrical surfaces

breadboard. The mechanism of the material removal is shown in Fig. 5.2a–c. The stiffened fluid sticks on the rotating tip and approach, the roughness peaks of the cylindrical rotating workpiece surface as shown in Fig. 5.2a. In Fig. 5.2b the active abrasives shear off the roughness peaks from the initial workpiece surface in the first finishing cycle. After the first finishing cycle, the sharp ended peaks of surface get shear off by the active abrasives as shown Fig. 5.2b.

To further remove the roughness peaks, cutting edge of the active abrasives erodes out and get the fine finished surface of C60 steel cylindrical workpiece. In the last finishing cycle as shown in Fig. 5.2c, the surface gets smoothed by removing out the very small-sized chips. The spectroscopy tests revealed the resemblance of the given shaft's material with a steel of grade C60 and its corresponding chemical composition is given in Table 5.1. So, shafts of grade C60 material with external diameter of 22 mm have been taken as workpiece as shown in Fig. 5.2. Since there are various applications of the C60 steel grade such as in hydraulic cylinders, crankshafts, steering rack bar, rocker arm shaft, rack pinion power steering tie rods and various die punches, so C60 steel material has been chosen for experimentation. The purpose of this paper is to examine the individual effect and interaction effect of process parameters with the surface roughness and optimize the process parameters to get the significant finishing result.

## 5.2 Design of Experiment

The cylindrical shafts workpiece made of steel with grade C60 and having an external diameter of 22 mm as shown in Fig. 5.3. Table 5.2 represents the absolute values of the controllable independent process variables and their selected levels for experimentation. Table 5.3 represents the experimental conditions.

Experiments were performed on the setup based on the magnetorheological finishing process utilizing solid rotating tool core as depicted in Fig. 5.1. The initial surface roughness  $R_a$  lied in the range of 320–410 nm which was obtained after plain cylindrical grinding. A constant feed rate of 30 cm/min is provided.

Response surface methodology (RSM) is a mathematical tool, which is used for modelling and optimizing the engineering problems. Design of experiments (DOE) is an important aspect of RSM. To know the interaction between the different independent controllable variables, a second-order model is employed which can be best constructed by the central composite design (CCD) methodology. To know the individual and the combined impact of the independent controllable parameters on the response, 'F' test from the analysis of variance (ANOVA) has been performed. In the present work, the MR polishing fluid constitutes 60% of the carrier fluid (paraffin oil 80% and AP3 grease 20% by weight), 20% of the abrasive particles of 600 mesh size and 20% of the carbonyl iron particles (CIPs) of 400 mesh size by volume.



**Fig. 5.2** Mechanism of the material removal during rotating core-based magnetorheological nanofinishing process for finishing of external cylindrical surfaces

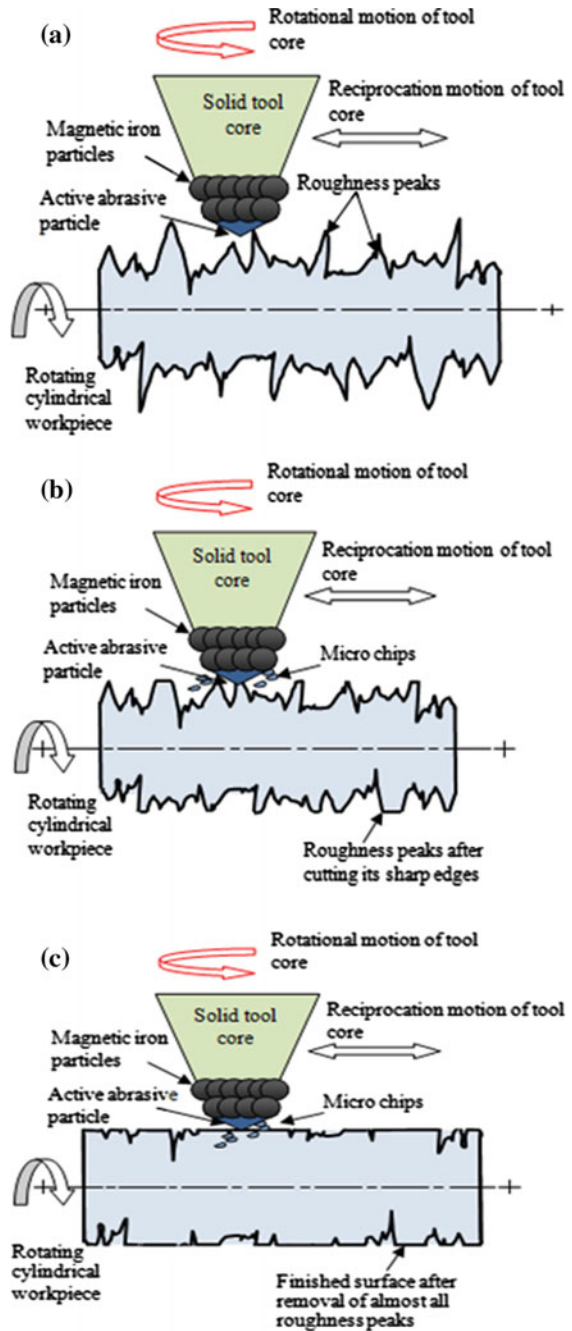


**Table 5.1** Chemical composition of C60 steel

Elements	C	Si	Mn	P	S	Cr	Mo	Ni	Fe
mass%	0.5	0.3	0.8	0.02	0.03	0.1	0.01	0.03	Balance

**Fig. 5.3** Cylindrical grounded shafts of C60 steel having external diameter of 22 mm

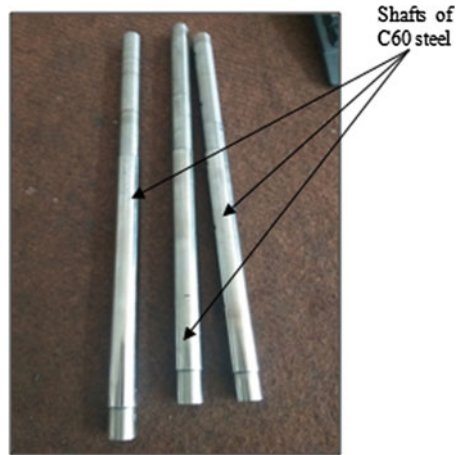


**Table 5.2** Independent controllable variables and their corresponding coded levels

S. No.	Parameter	Unit	Levels				
			-2	-1	0	1	2
1	Current (I)	A	1.5	2	2.5	3	3.5
2	Tool rotation (T)	rpm	1200	1450	1700	1950	2200
3	Workpiece rotation (W)	rpm	60	80	100	120	140
4	Abrasive concentration (Z)	%	10	15	20	25	30

**Table 5.3** Experimental conditions

Parameters	Conditions
Finishing cycle time	30 min
Abrasives silicon carbide (SiC) powder	600 mesh
Constant feed rate to workpiece for to and fro motion	30 mm/min
Workpiece material	C60 (ferromagnetic)
CIP powder	400 Mesh

### 5.2.1 Response Surface Regression Analysis

The initial ( $R_{ai}$ ) and after finishing surface roughness ( $R_{af}$ ) values and the percentage reduction in roughness value ( $\% \Delta R_a$ ) as a response parameter. The percentage reduction in  $R_a$  values acting as response can be calculated by using Eq. (5.1).

$$\Delta R_a(\%) = [(R_{ai} - R_{af})/R_{ai}] \times 100 \quad (5.1)$$

Highest order polynomial was selected till the model was not aliased from the calculation of sequential model sum of square. The highest F-value and the least  $p$ -value signify the addition of quadratic terms to two-factor interaction which suggests its suitability. Table 5.4 reported the ANOVA analysis for the model containing all the terms and their interactions such as I, T, W, Z, IT, IW, IZ, TW, TZ, WZ,  $I^2$ ,  $T^2$ ,  $W^2$  and  $Z^2$ . The F-value of model lies at 55.04 which indicate the significance of the model. Values of 'Prob > F' or  $p$ -value greater than 0.05 shows that the model terms are insignificant and the rest are significant terms. Terms such as I, T, W, Z, IW, IZ, TZ,  $I^2$  and  $Z^2$  have  $p$ -value less than 0.05 which acknowledges these terms as significant. Insignificant terms are neglected to make the model more efficient. There are five insignificant terms which are T2, W2, IT, TW and WZ. Table 5.4 showed the ANOVA analysis after eliminating the insignificant terms. The other ANOVA parameter R-squared is a measure of the amount of reduction in the variability of the response variable from the fitted regression line. Thus, it is preferred to observe other parameters like adjusted R-squared, predicted R-squared values which are 0.94 and 0.90. According to the regression analysis performed, the final equation in coded

**Table 5.4** ANOVA for percentage change in  $R_a$  after dropping the insignificant terms

Source	SS	DF	MS	F-value	$p$ -value	% contribution
Model	2659	9	295	55.0	<0.0001	
I	988.1	1	988	184.0	<0.0001	38.67
T	580.1	1	580	108.0	<0.0001	22.70
W	240.6	1	240	44.8	<0.0001	9.42
Z	50.0	1	50	9.3	0.0063	1.96
$I^2$	110.1	1	110	20.5	0.0002	4.31
$Z^2$	307.0	1	307	57.1	<0.0001	12.01
IW	182.2	1	182	33.9	<0.0001	7.13
IZ	64.0	1	64.0	11.9	0.0025	2.50
TZ	25.0	1	25.0	4.6	0.0433	0.97
Residual	107.3	20	5.3			
Lack of Fit	99.3	15	6.6	4.1	0.0623	
Pure Error	8.00	5	1.6			
Cor Total	2766	29				

factors is given as in Eq. (5.2).

$$\begin{aligned} \% \Delta R_a = & 76.5 + 6.42A + 4.92B - 3.17C - 1.63D + 3.3AC \\ & + 2.0AD - 1.25BD - 1.96A^2 - 4.33D^2 \end{aligned} \quad (5.2)$$

The final equation in terms of actual factors is given as

$$\begin{aligned} \% \Delta R_a = & 48.1 + 3.76I + 0.015T - 0.29W + 1.49Z + 0.08IW \\ & + 0.2IA - 0.0002TZ - 1.95I^2 - 0.04Z^2 \end{aligned} \quad (5.3)$$

Table 5.4 reported the contributions in percentage made by the significant process parameters on the response variable. Current was making largest contribution to the process performance which was followed by tool rotational speed, workpiece rotational speed and abrasives concentration. This confirmed the dominance of normal force acted due to the supplied current over the tangential force due to the tool rotation. Also, the significant contribution made by the tool rotation acknowledged its importance which is being used in the present process.

## 5.3 Results and Discussion

Based on the regression analysis as obtained from Eq. (5.3), the response with respect to the effect of current, tool rotation, workpiece rotation and abrasives concentration on the response variable have been examined. The effects of current are found to be maximum speed which is followed by tool rotational speed, workpiece rotational speed and abrasives concentration. The independent controllable variable effects and their various interactions are found to be significant in ANOVA analysis and therefore discussed below.

### 5.3.1 Effect of Current

The effect of current on percentage reduction in Ra value at different tool core rotational speeds with workpiece rotation at 100 rpm and abrasives concentration at 20% is shown in Fig. 5.4. Increase in the value of current result in the increasing value of the response variable (% $\Delta R_a$ ). As the value of supplied d.c. current is increased, the strength of the magnetic flux density also increased. This result in firmly holding of the active abrasives by the carbonyl iron particle (CIPs) chains and thereby results in an enhanced finishing performance.

**Fig. 5.4** Effect of current on percentage reduction in surface roughness value

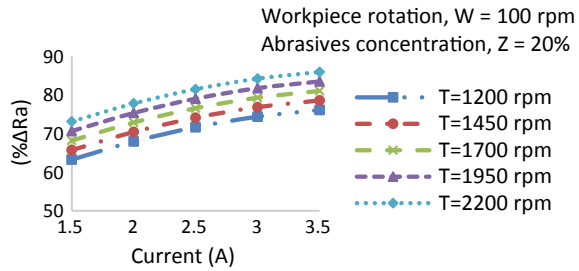
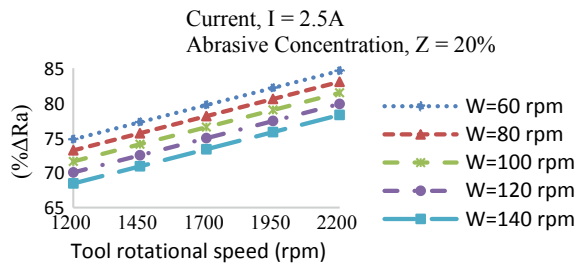


**Fig. 5.5** Effect of tool rotation on percentage reduction in surface roughness value



### 5.3.2 Effect of Rotational Speed of Tool Core

The effect of rotational speed of tool core on percentage decrement in surface roughness at different workpiece rotational speeds with current of 2.5 A and abrasives concentration at 20% is shown in Fig. 5.5. It can be easily depicted from Fig. 5.4 that at higher tool core rotational speed, higher percentage decrease in surface roughness was observed. Due to the magnetic flux density present at the tool core tip, the carbonyl iron particles (CIPs) chains stick to it, resulting in the rotation of chains along with the tool core. Hence, increase in rotational speed increases the speed of the abrasives. It can be easily depicted from Fig. 5.5 that at higher tool core rotational speed, higher percentage change in roughness was observed. High tool core rotation results in higher relative movement of the active abrasives on the surface of the workpiece which results in drastic increase of the material removal rate. Also, because of the tool rotation tangential force into action which contributes to the resultant force responsible for the overall finishing action.

### 5.3.3 Effect of Workpiece Rotational Speed

The effect of cylindrical workpiece rotational speed on percentage decrement in surface roughness at different abrasives concentrations with current at 2.5 A and tool core's rotational speed at 1700 rpm is shown in Fig. 5.6. There is decreased trend of percentage reduction in surface roughness with increasing workpiece rotation. This

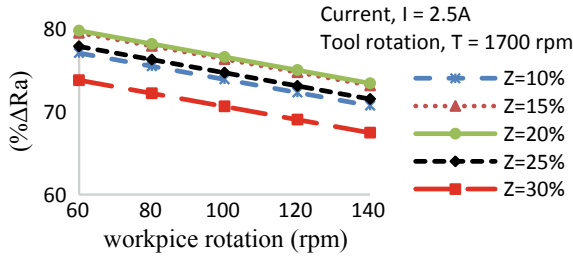


Fig. 5.6 Effect of workpiece rotation on percentage reduction in surface roughness value

trend can be understood by realizing the force representation as shown in Fig. 5.7a, b. As shown in Fig. 5.7a, two vertical forces are involved in the process namely  $F_1$  and  $F_2$  neglecting other horizontal forces.  $F_1$  is the tangential force acted on the cylindrical workpiece by the abrasive particle due to tool rotation whereas  $F_2$  is the tangential force acted on the abrasive particle by the cylindrical workpiece due to its rotation. Since the tool is rotating at a constant speed of 1700 rpm, therefore the magnitude of tangential force  $F_1$  remains constant. Suppose, the workpiece is rotating at slow speed, i.e. at 60 rpm, the magnitude of  $F_2$  becomes lesser than  $F_1$ . Thus,  $F_1$  dominates  $F_2$  resulting in the removal of roughness peaks in the form of micro-chips. Now as the workpiece rotational speed starts increasing and so the magnitude of  $F_2$  increases. After some time, a workpiece rotational value can be reached where the magnitude of  $F_2$  completely dominates magnitude of  $F_1$ . Thus, abrasive particle does not possess enough force to shear off the roughness peaks and it is dispersed away from the CIPs chains as shown in Fig. 5.7b. Therefore, at higher workpiece rotational speeds, the reduction in surface roughness value  $R_a$  is lesser as compared to lower workpiece rotational speeds.

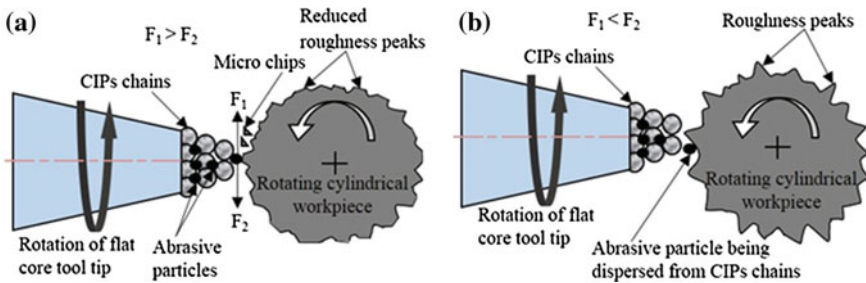
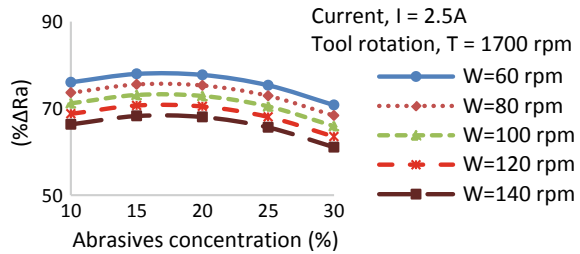


Fig. 5.7 Force representation; a at low workpiece rotational speed ( $F_1 > F_2$ ) and b at high workpiece rotational speed ( $F_1 < F_2$ )

**Fig. 5.8** Effect of abrasives concentration on percentage reduction in surface roughness value



### 5.3.4 Effect of Abrasives Concentration

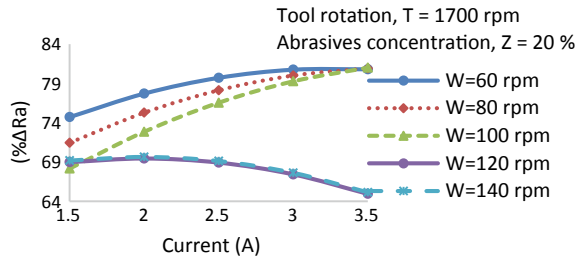
The effect of abrasives concentration on percentage decrement in surface roughness at different rotational speeds of cylindrical workpiece with current at 2.5 A and tool rotation at 1700 rpm is shown in Fig. 5.8. Abrasives concentration is of high importance as the abrasives are the sole medium of chipping off the material from the surface of the workpiece. As depicted in the graph, the value of response parameter, i.e. percentage decrement in surface roughness increases up to an abrasive's concentration of 20%. However, the value of the response variable decreases with further rises in abrasive particles concentration. The material removal rate depends on the forces involved. Furthermore, the magnitude of these forces depends on the bonding strength of CIPs. At high concentration, these particles begin to break the chain structure which ultimately results in decrease in stiffness of MR polishing fluid under shearing action.

This results in decreasing the magnitude of the forces involved and so the material removal rate. However, at low concentration, there is less number of particles available to get trapped in the same CIPs chain structure. This results in increasing the magnitude of the forces involved and so the material removal rate. It is seen that the optimum concentration of abrasive particles is in between 18% to 20% for 20% CIPs concentration.

### 5.3.5 Effect of Interaction of Current and Workpiece Rotation

The effect of interaction of current and workpiece rotation on percentage change in Ra value at tool rotational speed of 1700 rpm and 20% abrasives concentration is shown in Fig. 5.9. In this graph, it can be clearly observed that there are two groups of distinct curves one is increasing and others are decreasing. Increasing curves comprised of three workpiece rotational speeds namely 60, 80 and 100 rpm indicate that percentage decrement in surface roughness Ra value increased on increasing current. Although these three curves meet at the highest value of percentage decrement in Ra value at 3.5 A current but overall curve corresponding to workpiece rotational speed of 60 rpm, i.e. lowest value show high values of percentage reduction in surface

**Fig. 5.9** Effect of interaction of current and workpiece rotation on percentage reduction in surface roughness value

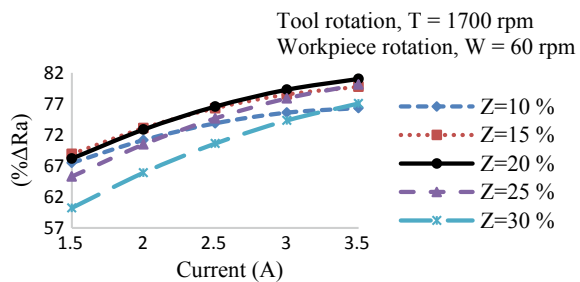


roughness in comparison with other increasing curves. Decreasing curves comprised of high workpiece rotational speeds of 120 and 140 rpm indicate that with increase in current value, the response parameter ( $\% \Delta Ra$ ) decreases. Moreover, with comparison to increasing curves, these curves are showing much less value of response parameter. Therefore, in the end, it is concluded that the workpiece with low rotational speed shows high value of percentage decrement in surface roughness value Ra with increase in magnitude of current.

### 5.3.6 Effect of Interaction of Current and Abrasives Concentration

The effect of interaction of current and abrasives concentration on percentage change in Ra value at tool core rotational speed of 1700 rpm and workpiece rotation of 100 rpm is shown in Fig. 5.10. In this graph, it can be clearly observed that on an individual curve high current value results in higher percentage reduction in Ra value. Moreover, on comparing these curves, the curve corresponding to 20% abrasives concentration show the highest value of response parameter ( $\% \Delta Ra$ ) followed by the curves corresponding to 15% abrasives concentration and 25% abrasives concentration. The difference of the response variable value on 20% abrasives concentration curve at 3.5 A current is small as compared to its neighbour curves corresponding to abrasives concentrations of 15 and 25%. Moreover, the curves corresponding to the abrasives concentrations of 10 and 30% show a large difference with abrasives

**Fig. 5.10** Effect of interaction of current and abrasives concentration on percentage reduction in surface roughness value





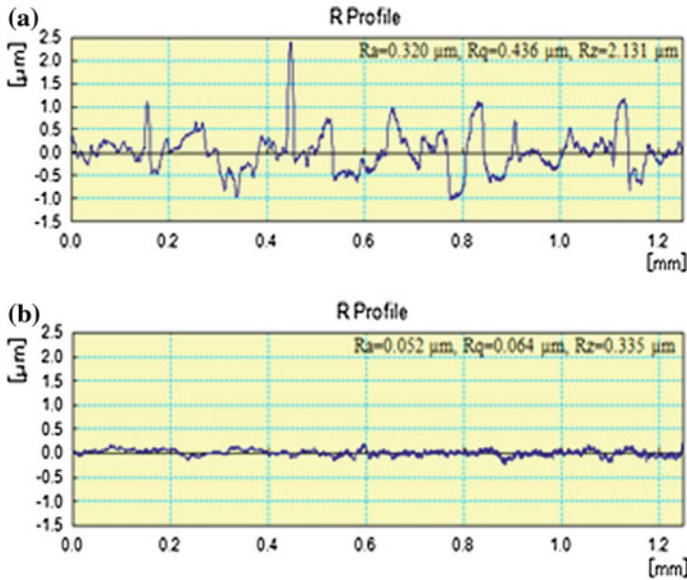


**Fig. 5.11** Surface roughness profile from Mitutoyo surf test SJ-400 **a** before finishing and **b** after 90 min of finishing at optimum parameters

concentration curve of 20%. Therefore, in the end, it is concluded that abrasives concentration in the range of 15–25% result in the high value of response variable parameter ( $\% \Delta R_a$ ). The surface roughness profiles of initial and final after finishing with the optimized parameters are shown in Fig. 5.11. The scanning electron microscope (SEM) photographs at  $250\times$  optical zoom of the initial surface and the final surface done with optimized parameters are shown in Fig. 5.12. This clearly indicates the better features of the MR finished surface in comparison with the initial surface of the workpiece. The initial ground surface show scratch marks on the external surface because of external cylindrical grinding which are removed later on using the present magnetorheological finishing process, which is helpful for industrial applications.

### 5.3.7 Confirmation Experiments for Validation of the Model

Using the optimizing tool of the Software Design expert 6.0, it was found that the best process parameters are current of 3.5 A, 2200 rpm of tool rotation, 60 rpm of workpiece rotation and 20% of abrasives concentration. The final surface roughness value  $R_a$  obtained after performing the finishing at these values of the parameters was 52 nm in 90 min finishing time while the initial value of  $R_a$  was 320 nm. Thus, the percentage decrement in surface roughness was found as 83.75%. The predicted value of percentage decrement in surface roughness ( $\% \Delta R_a$ ) can be calculated by

**Fig. 5.12** SEM images of the external cylindrical workpiece at 250× magnification **a** initial ground surface and **b** after finishing for 90 min with optimized parameters

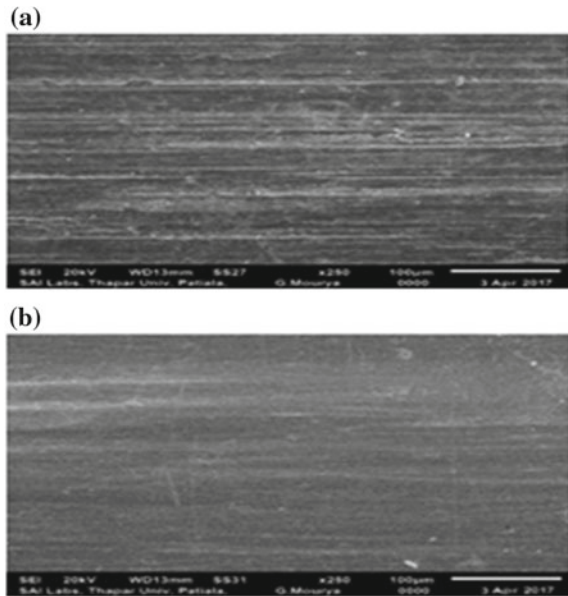


**Table 5.5** Comparison between the experimental and theoretical  $\% \Delta R_a$  with the optimized parameters for finishing

S.No	Optimized process parameters				Experimental $\% \Delta R_a$	Predicted $\% \Delta R_a$	Error (%)
	I	T	W	Z			
1	3.5	2200	60	20	83.75	88.91	6.16

putting the value of optimized parameters in Eq. (5.3). The theoretical value of  $\% \Delta R_a$  was found as 88.91% using Eq. (5.3). The comparison between the experimentally obtained  $R_a$  value and theoretical  $R_a$  value is reported in Table 5.5, which showed that the error between the experimental and theoretical values are in a good agreement, i.e. within 6.16%.

### 5.4 Conclusions

An experimental evaluation through statistical design has been carried out to determine at the effect of various parameters for nanofinishing of the C60 grade shaft by present MR finishing process. It was found that the percentage decrement in surface roughness value ( $\% \Delta R_a$ ) increased with increase in current (I) and tool rotational speed (T). However, it decreased with increase in workpiece rotational speed (W). The  $\% \Delta R_a$  increase with rise in abrasives concentration (Z) up to a limit of 20%

but after that, it starts decreasing with further rise in abrasives concentration. The largest contribution was observed by the current (38.67%) and the tool rotational speed (22.7%) which was followed by workpiece rotational speed (9.42%) and abrasives concentration (1.96%). Hence, the percentage reduction in surface roughness mainly dependent on the current and tool rotational speed for nanofinishing of C60 grade steel in the present MR finishing process. The least surface finish Ra value was obtained as 52 nm from the initial Ra value of 350 nm in 90 min of finishing time at the optimized finishing conditions of  $I = 3.5$  A,  $T = 2200$  rpm,  $W = 60$  rpm and  $Z = 20\%$ .

## References

1. Jain, V.K., Jayswal, S.C., Dixit, P.M.: Modeling and simulation of surface roughness in magnetic abrasive finishing using non-uniform surface profiles. *Mater. Manuf. Process.* **22**(2), 256–270 (2007)
2. Barman, A., Das, M.: Design and fabrication of a novel polishing tool for finishing freeform surfaces in magnetic field assisted finishing (MFAF) process. *Precis. Eng.* **49**, 61–68 (2017)
3. Hashimoto, F., Yamaguchi, H., Krajnik, P., Wegener, K.: Abrasive fine-finishing technology. *CIRP Ann.-Manuf. Technol.* **65**(2), 597–620 (2016)
4. Bedi, T.S., Singh, A.K.: Magnetorheological methods for nanofinishing—a review. *Part. Sci. Technol.* **34**(4), 412–422 (2016)
5. Jain, V.K.: Magnetic field assisted abrasive based micro-nano-finishing. *J. Mater. Process. Technol.* **209**(20), 6022–6038 (2009)
6. Singh, A.K., Jha, S., Pandey, P.M.: Parametric analysis of an improved ball end magnetorheological finishing process. Part B: *J. Eng. Manuf.* **226**(9), 1550–1563 (2012)
7. Singh, G., Singh, A.K., Garg, P.: Development of magnetorheological finishing process for external cylindrical surfaces. *Mater. Manuf. Process.* **32**(5), 581–588 (2017)
8. Maan, S., Singh, G., Singh, A.K.: Nano-surface-finishing of permanent mold punch using magnetorheological fluid-based finishing processes. *Mater. Manuf. Process.* **32**(9), 1004–1010 (2016)

# Chapter 6

## Effect of Laser Parameters on Laser-Induced Plasma-Assisted Ablation (LIPAA) of Glass



Upasana Sarma and Shrikrishna N. Joshi

**Abstract** Laser-Induced Plasma-Assisted Ablation (LIPAA) is an advanced machining process, in which, the laser beam passes through the substrate and irradiates the target metal placed behind the transparent material. The laser fluence is set above the ablation threshold of the target metal and below the ablation threshold of the transparent material. As the laser beam reaches the target metal, plasma-generated flies towards the substrate at a high speed of approximately  $10^4$  m/s resulting in both target and glass substrate removal. In the present work, a systematic experimental study has been carried out to study of the effects of laser parameters (scanning speed, laser peak power and pulse duration) on crater width of glass. Glass material was successfully processed using Nd:YAG laser. Microscopic studies have been carried out to understand the mechanism of ablation. Results provide useful guidelines to create features on transparent material.

**Keywords** LIPAA · Ablation threshold · Crater width · Transparent materials · Glass

### 6.1 Introduction

The glass is one of the most trending materials in scientific and industrial applications such as optics, photonics, microelectronics, display industries due to its high transparency over a wide range of wavelength. Also, glass has a very good resistance to chemical reactions, high thermal stability, and high hardness. Due to these qualities, it has become one of the most widely used materials today. In spite of its excellent properties, its brittleness and hardness make it difficult to machine. Precision and crack free machining of glass is a challenging task. Lasers are widely used in machining of brittle and hard materials. However, lasers are not suitable for processing of transparent materials such as glass, as no laser beam is absorbed for

---

U. Sarma · S. N. Joshi (✉)

Department of Mechanical Engineering, Indian Institute of Technology Guwahati, Guwahati 781039, India  
e-mail: [snj@iitg.ac.in](mailto:snj@iitg.ac.in)

© Springer Nature Singapore Pte Ltd. 2020

M. S. Shunmugam and M. Kanthababu (eds.), *Advances in Unconventional Machining and Composites*, Lecture Notes on Multidisciplinary Industrial Engineering, [https://doi.org/10.1007/978-981-32-9471-4\\_6](https://doi.org/10.1007/978-981-32-9471-4_6)

any thermal action to take place. Literature reports various processing techniques to fabricate different structures in transparent materials viz. photolithography [1], chemical etching [2], abrasive jet machining [3]. They are capable of processing the glass material, however, they have limited applicability as the photolithography requires high vacuum condition. Chemical etching may cause hazardous problem as etching material contains atoms of lead or sodium and thus results in production of non-volatile halogen compounds. Abrasive jet machining [3] results in rough surface and limited to larger components. Ultrasonic machining requires complex setup. However, laser has been found as a promising tool if it is applied with proper setting of laser parameters such as wavelength, laser power. It is known that laser beam must be highly absorbed to achieve ablation. For high absorption, short wavelength in the visible ultra-violet (VUV) region (high energy photons) and short pulse width in the sub-picosecond range were first attempted, but such laser faced difficulties due to its high capital cost, small beam diameter which results in low material removal rate and slow scanning process [4]. For research and other applications, the development of a new fabrication technique of glass was desired and hence, in 1998 a group of Japanese scientists invented laser-induced plasma-assisted mechanism, which can be used to process transparent materials.

Laser-Induced Plasma-Assisted Ablation (LIPAA) [5] is a high potential ablation scheme for transparent, hard and brittle material. In this process, the glass and metal sheet are placed one above the other and the plasma is formed with assistance from the metal ablation when the laser transmitted through the glass irradiates the metal. It is used to get colour printing characters, surface metallization of electrodes and even images on the glass substrate. However, the mechanism varies slightly depending upon the distance between the target metal and the glass substrate. Further improvement of the process can be witnessed using confined ablation conditions. This plasma ablates the transparent material on its rear side. It is characterized by high etching rate and no incubation effects are found. In this work, an experimental study has been carried out to apply LIPAA methodology to ablate the glass substrate. Moreover, a systematic parametric study has also been carried out. These are presented in the next sections.

## 6.2 Experimental

### 6.2.1 Experimental Setup

In the present study, a conventional Nd: YAG pulsed millisecond laser (Model: 500 W pulsed Nd: YAG CNC Laser, Make: Suresh Indu Lasers Pvt. Ltd) having a wavelength of 1064 nm is used. The frequency was set at a fixed value of 20 Hz with varying laser peak power, scanning speed and pulse duration. The laser workstation consists of the beam bending, expanding, collimating and focusing optical units and

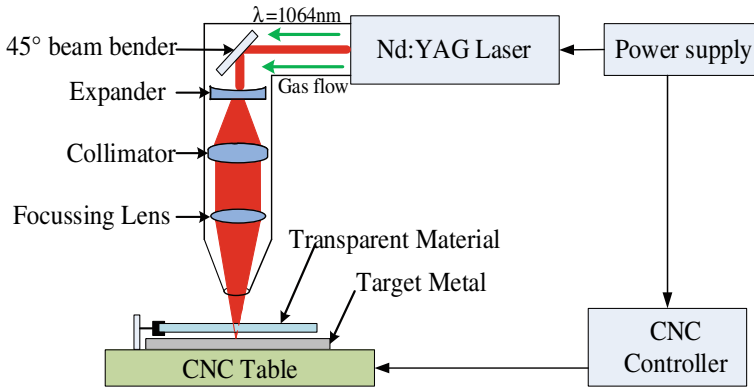


**Fig. 6.1** Schematic diagram of the experimental setup

a computer-controlled x-y position stage. Figure 6.1 shows the schematic diagram of the experimental setup used for the study of LIPAA process.

In this technique, the transparent material and the metal target sheet are arranged one above the other with the glass slide above the metal sheet on a CNC table connected to a CNC controller. The profile to be cut or scanned, its dimensions and the direction of motion is given through the RD-Works software and controlled by the CNC controller. The transparent material is chosen such that it is transparent to wavelength of the homogenized laser beam. The laser beam passes through the substrate and irradiates the target metal placed behind the glass substrate. The laser fluence for this method is set above the ablation threshold of the target metal and below the ablation threshold of the transparent material. When the peak power density exceeds the ionization threshold potential of the metal surface, the generation of free electrons at the focal spot through ionization takes place in the focal region, leading to the formation of dense and optically opaque plasma. The plasma generated flies towards the substrate at a high speed (of the order of  $10^4 \text{ m/s}$ ) [6]. The plasma generated further absorbs the energy of the incoming laser pulses through the laser–plasma interaction process [7]. Thus, there is a strong interaction among the laser beam, plasma and the transparent material, which results in increased fluence. This causes heating, melting, vaporization of the transparent material. The heating of the surface and eventually conduction into the material results in the generation of temperature distribution. Also when the incident fluence is very high, it results in phase transformation (melting and vaporization), which serves as the material removal mechanisms.

## 6.2.2 Materials

In the present a transparent material, glass slide of dimension  $75 \times 26 \times 1.4 \text{ mm}$  has been used. Microscopic glass slides are generally of soda–lime glass or borosilicate

glass. In this work soda–lime glass was used as work material. Its chemical composition is 73 wt%  $\text{SiO}_2$ +16 wt%  $\text{Na}_2\text{O}$ +9 wt%  $\text{CaO}$  with certain additives like  $\text{MgO}$  and  $\text{Al}_2\text{O}_3$  and its maximum transmission is in the range of wavelength 500–2500 nm approximately.

The target metal chosen was a sheet of aluminium of thickness 1 mm. An important property of aluminium is that it is a good reflector of both visible light and radiated heat. Taking into consideration this property, aluminium was chosen as the metal target for well-defined ablation to take place at the rear side of the transparent material.

### 6.3 Results and Discussion

Using the conventional millisecond Nd: YAG laser system, ablation on the rear side of glass has been carried out by the LIPAA technique. The experiments were carried out at fixed repetition rate of 20 Hz and with no gap between the glass and the aluminium sheet. Vertical lines were traced on both the glass and the aluminium sheet by varying the current in the range of 50–80 A, speed in the range of 2–20 mm/s and pulse duration from 0.5 to 4 ms.

Ablation on both the aluminium sheet and the glass substrate were achieved by this technique. Figure 6.2 shows the ablated aluminium sheet and glass substrate.

Ablation takes place due to the phase change of the material. Phase change of the glass material takes place due to thermal effects of the plasma. The molten glass material is removed by the plasma-induced shock wave whereas some molten metals redeposits on the crater resulting in a recast layer. Figure 6.3 shows the optical microscope image of the crater with the recast layer formed on the surface of the crater giving it a glassy appearance.

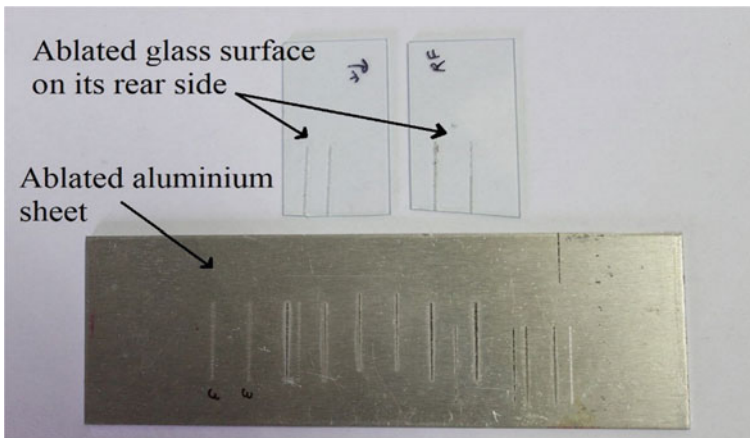


**Fig. 6.2** Ablated glass substrate and aluminium sheet

**Fig. 6.3** Optical microscope image of a crater with recast layer (Current: 80 A, Scanning speed: 20 mm/s, Pulse Duration: 2 ms)

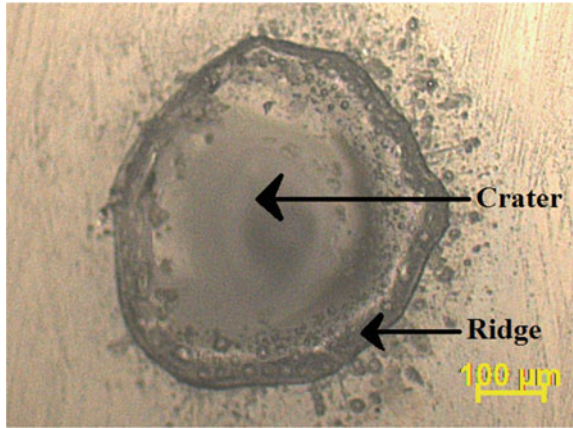
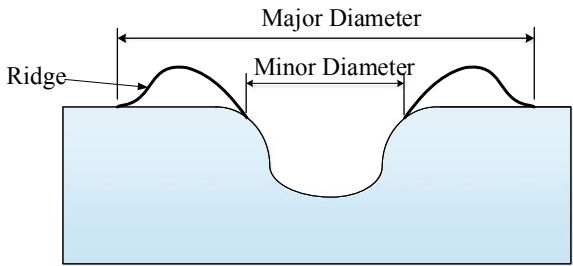


**Fig. 6.4** Ridge formation on the ablated crater



It is the recast layer that results in a doughnut-shaped ridge formation around the crater. A schematic of the ridge formation is shown in Fig. 6.4. As observed in optical microscope, the major and the minor diameters are measured and for further analysis of the crater width, the average of the major and minor diameters is considered.

Mathematically,

$$Crater\ Width, D_{avg} = \frac{Major\ Diameter + Minor\ Diameter}{2} \tag{6.1}$$

### 6.3.1 Effect of Laser Parameters on Ablated Crater Width by LIPAA

**Laser Scanning Speed.** As depicted in Fig. 6.5, it can be observed that the crater width decreases with the increase in scanning speed and also decreases with the decrease in current. However, at 15 mm/s instead of decrease in crater width with the



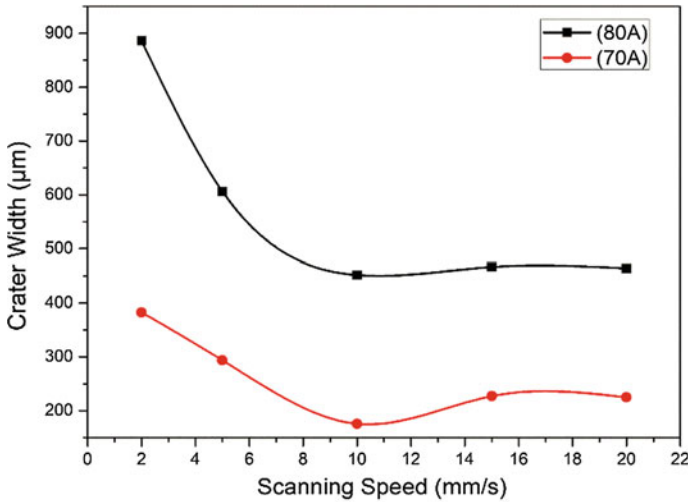


**Fig. 6.5** Effect of scanning speed on average crater width

increase in scanning speed, an increase in the width is seen and further increasing the scanning speed, crater width again decreases.

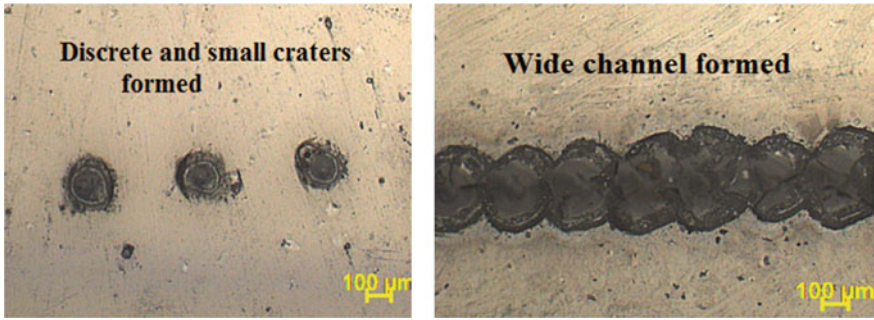
The reason for such variation may be stated as, with the slowing down of the scanning speed the laser irradiation per unit area increases and hence, more energy per unit area by the laser-induced plasma. It can also be stated that with the slowing down of the scanning speed, the laser-induced plasma interacts with the glass for longer duration which results in more material removal and greater Heat-Affected Zone (HAZ). Further, at a high speed, the successive laser pulse moves far away from the former laser pulse and hence, there is no interaction between the HAZ of the two consecutive laser pulses. Therefore, increase in scanning speed results in reduced crater width. However, the reason for increase in crater width at 15 mm/s scanning speed may be stated that the deposition of the metal particles on the rear side of the glass by the former laser pulses plasma get accumulated which acts as the site for higher absorption of the plasma.

Figure 6.6 shows the optical microscope images of the rear surface of the LIPAA processed glass material taking aluminium as the metal target at two different scanning speeds 10 and 5 mm/s.

**Laser Peak Power.** It has been observed in Fig. 6.7 that with the increase in current corresponding to a laser peak power there is an increase in the average ablation depth. The reason for such variation may be that as the pump current increases it induces higher population inversion, which gives greater stimulated emission and hence increase in output power.

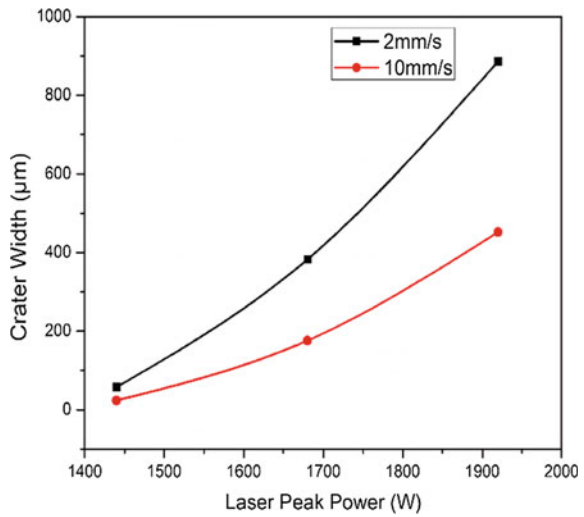
The relation between current change and power change is linear and is given by

$$P = \eta VI \quad (6.2)$$



**Fig. 6.6** Optical microscope images of the rear surface of the LIPAA-processed glass material with 0 μm distance between the glass and the aluminium sheet, 70 A current and (a) 10 mm/s (b) 5 mm/s scanning speed

**Fig. 6.7** Effect of laser peak power on average crater width



where

- $P$  Pulse power
- $n$  Radiation efficiency
- $I$  Current input.

Hence with the increase in current, laser peak power is increased and more plasma is generated as the laser irradiates with the metal behind the glass. The generated plasma has a greater thermal effect on the glass material and more material removal resulting in wider crater width. However, the ablation geometry not only depends on the current but also on the metal used. Figure 6.8 shows the optical microscope images of the rear surface of the LIPAA processed glass material taking aluminium as the metal target at various laser peak power levels.

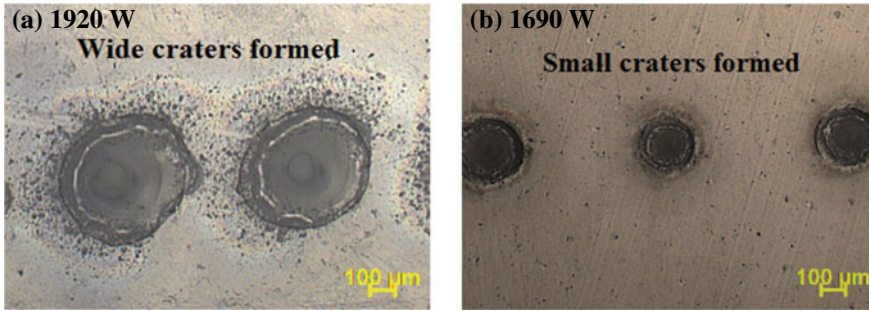
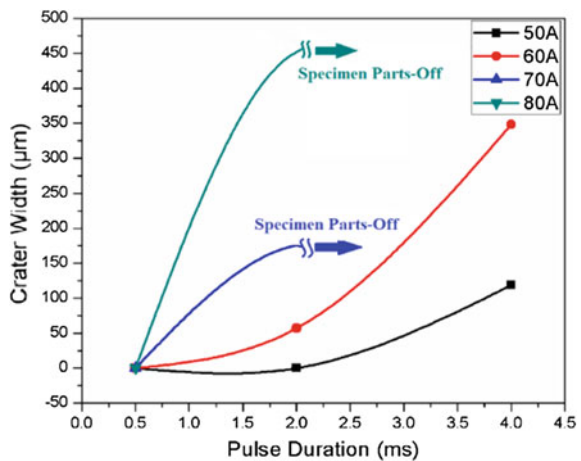


**Fig. 6.8** Optical microscope images of the rear surface of the LIPAA-processed glass material with  $0\ \mu\text{m}$  distance between the glass and the aluminium sheet,  $15\ \text{mm/s}$  scanning speed and laser power of (a)  $1920\ \text{W}$  (b)  $1690\ \text{W}$

**Pulse Duration.** As observed in Fig. 6.9, the average crater width increases with the increase in pulse duration. Also with the increase in current an increase in the width is seen. But at a higher value of current, i.e. 70 and 80 A, the glass parts-off into two pieces on reaching a pulse duration value greater than 2 ms. When low pulse duration is used deeper holes are produced whereas for high pulse duration wider holes are ablated.

The reason may be such that, when the laser irradiates the metal sheet, it absorbs the heat energy, melts, gets vaporized and plasma is generated. Longer pulse duration interacts with the metal for a longer period of time and hence expanded plasma is generated with high initial velocity. Thus, it has a greater and longer thermal effect on the glass material which, in turn, gets melted and vaporized resulting in a wider ablation. Also, higher the pulse duration, higher is the pulse energy. This is also a reason for increase in width with the increase in pulse duration. It is given by the relation

**Fig. 6.9** Effect of pulse duration on average crater width



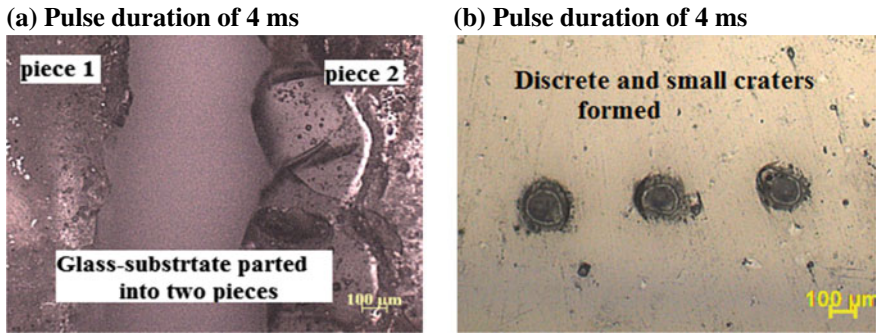


**Fig. 6.10** Optical microscope images of the rear surface of the LIPAA-processed glass material with  $0 \mu\text{m}$  distance between the glass and the aluminium sheet, at 70 A current and pulse duration of (a) 4 ms (b) 2 ms

$$\tau = 0.88 \frac{E}{P} \quad (6.3)$$

where

$\tau$  pulse duration

$E$  pulse energy

$P$  peak pulse power.

Figure 6.10 shows the optical microscope images of the rear surface of the LIPAA-processed glass material taking aluminium as the metal target at different pulse duration.

## 6.4 Conclusions

In this study, laser-induced plasma-assisted ablation (LIPAA) on glass material with aluminium as the metal target was performed using a conventional millisecond Nd:YAG laser having a wavelength of 1064 nm. In the scope of present process conditions, from the experimental investigations and microscopic studies, the following conclusions can be drawn.

- When the scanning speed of the laser increases, the average crater width decreases. The average crater width at the same scanning speed was higher for a higher value of current. At higher scanning speed, LIPAA does not produce continuous channel. Therefore, higher scanning speed are usually not recommended for the fabrication of channels in practice.
- The increase in the current value results in increase in the crater width. Also, at a constant current value, when the scanning speed decreases the width reduces.
- With the increase in the pulse duration, it has been observed that the crater width increases. Also, at a constant pulse duration, higher the current applied higher is

the crater width. However, at the current values of 70 and 80 A, the glass parts-off into two pieces at pulse duration greater than 2 ms. It is due to the longer interaction of the laser pulse with the metal which results in the generation of expanded plasma with high initial velocity. Also higher the pulse duration, higher is the pulse energy. This is also one of the reasons for increase in width with the increase in pulse duration.

## References

1. Das, S., Srivastava, V.C.: Microfluidic-based photocatalytic microreactor for environmental application: a review of fabrication substrates and techniques, and operating parameters. *Photochem. Photobiol. Sci.* **15**, 714–730 (2016). <https://doi.org/10.1039/c5pp00469a>
2. Zhang, L., Wang, W., Ju, X., Xie, R., Liu, Z., Chu, L.Y.: Fabrication of glass-based microfluidic devices with dry film photoresists as pattern transfer masks for wet etching. *RSC Adv.* **5**, 5638–5646 (2015). <https://doi.org/10.1039/C4RA15907A>
3. Azmir, M.A., Ahsan, A.K.: A study of abrasive water jet machining process on glass/epoxy composite laminate. *J. Mater. Process. Technol.* **209**, 6168–6173 (2009). <https://doi.org/10.1016/j.jmatprotec.2009.08.011>
4. Kopitkovas, G., Lippert, T., Ventirini, J., David, C., Wokaun, A.: Laser Induced backside wet etching: mechanisms and fabrication of micro-optical elements. In: 8th International Conference on Laser Ablation, pp. 526–532. IOP Publishing, Canada (2005). <https://doi.org/10.1088/1742-6596/59/1/113>
5. Zhang, J., Sugioka, K., Midorikawa, K.: Micromachining of glass materials by laser-induced plasma-assisted ablation (LIPAA) using a conventional nanosecond laser. In: SPIE Conference on Laser Applications in Microelectronic and Optoelectronic Manufacturing IV, pp. 363–370. California (1999). <https://doi.org/10.1117/12.352699>
6. Hong, M., Sugioka, K., Wu, D.J., Lu, Y., Midorikawa, K., Chong, T.C.: Laser-induced-plasma-assisted ablation for glass microfabrication. In: SPIE Conference on Photonic Systems and Applications, pp. 138–147. Singapore (2001). <https://doi.org/10.1117/12.446603>
7. Kumar, P., Ehmann, K.F.: Feasibility of Laser Induced Plasma Micro-machining (LIP-MM). In: International Precision Assembly Seminar, pp. 73–80. Heidelberg (2010). [https://doi.org/10.1007/978-3-642-11598-1\\_8](https://doi.org/10.1007/978-3-642-11598-1_8)

# Chapter 7

## An Experimental Study of Electrochemical Spark Drilling (ECSD)



Arvind Kumar Yadav and S. K. S. Yadav

**Abstract** Electrochemical spark machining (ECSM) is an emerging hybrid machining process, which is used in the current scenario to machine non-conductive advanced engineering materials which is difficult to machine by conventional machining processes as well as by advanced machining processes due to restriction on electrical conductivity. Electrochemical Spark drilling has combined effect of electric discharge machining (EDM) and electrochemical machining (ECM). Basically electrochemical spark drilling is an appropriate machining process for making holes in non-conductive materials with significant improvement in final machining and productivity as compared to the electro discharge machining and electrochemical machining processes. In ECSM process, individual limitations of both machining processes are restricted while improving their individual advantages. The present work focuses experimental study of Electrochemical spark drilling process. This paper also depicts mechanism of ECSM process during machining of small holes.

**Keywords** Electrochemical spark drilling · Electrochemical machining · Electro discharge machining

### 7.1 Introduction

In modern era, the non-conductive materials like glass, quartz, ceramics materials have been rapidly used in wide application in mechanical system, medical, semiconductor industry and optical. The electrochemical discharge machining is hybrid machining process used to machine electrically conductive and non-conductive materials. It comprises of thermal energy-based two advance machining processes, that is EDM and ECM. In Electrochemical discharge drilling the material removal involves

---

A. K. Yadav (✉) · S. K. S. Yadav  
Department of Mechanical Engineering, Harcourt Butler Technical University, Kanpur 208002,  
India  
e-mail: [arvind.21000@gmail.com](mailto:arvind.21000@gmail.com)

S. K. S. Yadav  
e-mail: [sanjeevyadav276@gmail.com](mailto:sanjevyadav276@gmail.com)

© Springer Nature Singapore Pte Ltd. 2020  
M. S. Shunmugam and M. Kanthababu (eds.), *Advances in Unconventional  
Machining and Composites*, Lecture Notes on Multidisciplinary  
Industrial Engineering, [https://doi.org/10.1007/978-981-32-9471-4\\_7](https://doi.org/10.1007/978-981-32-9471-4_7)

melting, vaporization and chemical etching simultaneously. Due to the combined effect of both machining ECM and EDM, the Electrochemical spark drilling successfully overcomes the drawback of the constituting processes (EDM AND ECM) as essential need of the electrically conductive materials for machining. In ECSM the material removal is much higher (approx 5–50 times) as compared to ECM AND EDM, respectively, at same machining conditions. Skrabalak and Stwora [1] used in their experiment, a batch electrode consist of nine square working tips of size  $2 \times 2$  mm. These electrodes are capable of flowing electrolyte through the inside of tooltip. The experiments were conducted on ECM, EDM and ECDM machining. Coteata et al. [2] used in their experiments a rotating tool and passivating electrolyte in electrochemical discharge drilling process. The drilling tool and passivating electrolyte has significant results on machining. Peng and Liao [3] used a travelling wire in their Electrochemical discharge machining. Jiang et al. [4] has experimented on glass in electrochemical machining. In experimental study, glass used as working material and micro-drilling has done in electrochemical machining. Kulkarni et al. [5] have machined on copper workpiece with graphite anode and copper wire as cathode. In their experiment transient and synchronised measurements were performed successfully. It concluded from experiments that discharge temperature increases due to attaching of electrons, generated during the electrochemical discharge machining process. Zhong et al. [6] experimented on nickel-based single crystal superalloys with tube electrode. The process called as Tube electrode high-speed electrochemical discharge drilling (TSECDD). In their experiments, they compare the machining with electro discharge machining and concluded that surface quality is better and eliminates the recast layer as compared to EDM. Bindu Madhavi et al. [7] had experimented on Borosilicate and Soda–lime glass. The response parameters were taken a material removal rate, tool wear rate and radial over cut. The tungsten carbide alloy of dia 0.3 mm is taken as tool and tungsten copper alloy as counter tool material. The Design of Experiments used to conduct the experiments. Paul and Koral [8] conduct experiment and made a thermal model for determining the material removal rate (MRR) with direct current DC and pulse in ECDM process. They concluded that pulse DC is better than DC at higher Hajian et al. [9] present a thermal model on the finite element method (FEM) to predict the machining depth in ECD milling. In the model, the input parameters of FEM calculated on voltage, electrolyte concentrations. The mathematical model validated after conducting same experiments conditions. The final results concluded that good agreement finds between FEM models and Experiment in between range of 600–850 °C. Paul and Kurian [10] had experimented and concluded that temperature of electrolyte has major role in MRR and heat-affected zone (HAZ). In their experiment, they used NaOH as a electrolyte and heated it at different temperature. It was found that at higher temperature, spark reduces but causes an increase in HAZ. The experimental result shows that machining rate improves with gradual increase in temperature. Kang and Tang [11] have investigated those current waveforms for the machining of both coating and the machining of superalloys. It showed that only the electrochemical discharge exists during the machining of coating. Mehrabi et al. [12] concluded that in deep holes electrolyte circulation has important role. In this work they had used hollow electrodes with high

pressure. An injection system provided for flow of electrolyte. Results showed that at different level of pressure and different dia electrode which used in machining, improved material removal rate (MRR) and drilling speed. This research work concluded the electrochemical discharge microscale drilling had improved with using electrode with hole inside it.

## 7.2 Working Principle of ECDM

The Electrochemical discharge machining is a combination of Electric discharge machining (EDM) and Electrochemical machining (ECM). It is Hybrid machining process for mainly conducting and non-conducting materials both. In ECDM process the material removal takes place through melting or vaporization by electric sparks and chemical etching action. First, a DC current is applied between both electrodes (i.e. tool electrode and counter electrode). The tool electrode is smaller in size as compare to counter electrode. Tool electrode is dipped into some millimetres depth into electrolyte solution. These two electrodes are separated few centimetres distance into electrolyte solution. After applying DC current, electrolysis starts and formation of hydrogen bubbles consequently seen near the tool electrode and near the counter tool electrode oxygen gas bubbles evolve. On increasing the voltage the gas bubbles near the tool electrode start increasing. Gas film shield is created near the tool electrode which acts like dielectric medium. When a potential difference becomes high beyond certain limit, a spark is produced between the tool electrode and workpiece. Due to this spark machining takes place in the form of melting the workpiece, vaporization takes place. Further some chemical etching action also involves in the machining of workpiece. The schematic diagram of ECDM is shown in Fig. 7.1.

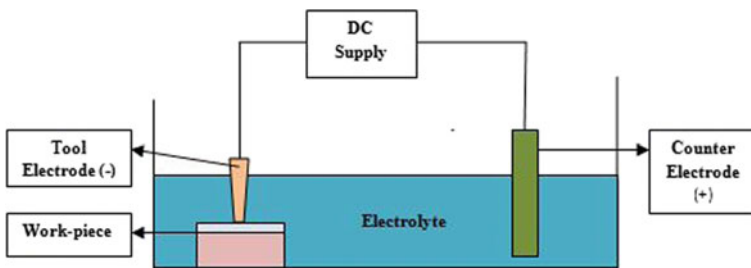


Fig. 7.1 Schematic diagram of working of ECDM process



### 7.3 Experimental Setup

An ECSM drilling facility is composed of following main elements

- i. Positioning system XY axis as per the requirement of machining shape.
- ii. For drilling action, the motion of Z-axis is given by Stepper motor Nema 23.
- iii. Power supply of DC voltage is given to tool electrode. The primary tool is given as negative and counter tool electrode has given positive terminal.
- iv. Electrodes used for machining. The primary tool electrode used for machining is HSS tool and copper as counter electrode. The workpiece used for experiment is soda–lime glass which has 25 mm × 25 mm with 6 mm thickness. The chemical composition of soda–lime glass is given below in Table 7.1.
- v. Electrolyte used for machining is NaOH. The ECS cell is filled with electrolyte. The electrolyte level is maintained at 1 mm above the flat surface of the workpiece.
- vi. An exhaust system is used to remove fumes after generating electrolysis.

At the cathode, sparking occurs at supply voltage of 50 V and above. During Experiment, it is observed that workpiece sample started cracking above 70 V applied voltage. Hence, the Experimental range decided for supply is 50–70 V. The workpiece immersed in electrolyte solution and tool electrode dipped into this solution at few mm. Experiments are conducted with Voltage, Duty cycle and rpm as the control variables. High-speed steel electrode of  $\Phi 2$  mm is used as tool and copper electrode of  $\phi 9$  mm is used as auxiliary electrode. Figure 7.2, shows the photograph of the experimental setup. The depth of anode (auxiliary electrode) inside the electrolyte is also maintained at fixed position. Figures 7.3 and 7.4 shows the machined workpiece (Fig. 7.5 and Tables 7.2, 7.3).

The experiment resulted in total of 27 experiments, which are performed at 50–70 V supply voltage, 0.5–0.7 duty cycle and 500–800 rpm of rotational speed of cathode tool as the values for the control variables. The machining time 20 min and DC current 1.5 A has kept constant throughout the experiments. The one response measured is material removal rate (MRR) (Table 7.4).

### 7.4 Results and Discussion

The experiments have been done on Soda–lime glass using ECDM machine to investigate the influence of the most influential process parameters such as voltage, Duty cycle and tool Rpm on the material removal rate (MRR). The DC current 1.5 A has

**Table 7.1** Chemical composition of workpiece (Soda–Lime Glass)

Element	SiO <sub>2</sub>	Na <sub>2</sub> O	CaO	Al <sub>2</sub> O <sub>3</sub>	K <sub>2</sub> O	Fe <sub>2</sub> O <sub>3</sub>	SO <sub>3</sub>
wt%	74	13	10.5	1.3	0.3	0.04	0.2



**Fig. 7.2** Photograph of experimental setup

**Fig. 7.3** Machined glass workpieces



**Fig. 7.4** Single machined workpiece



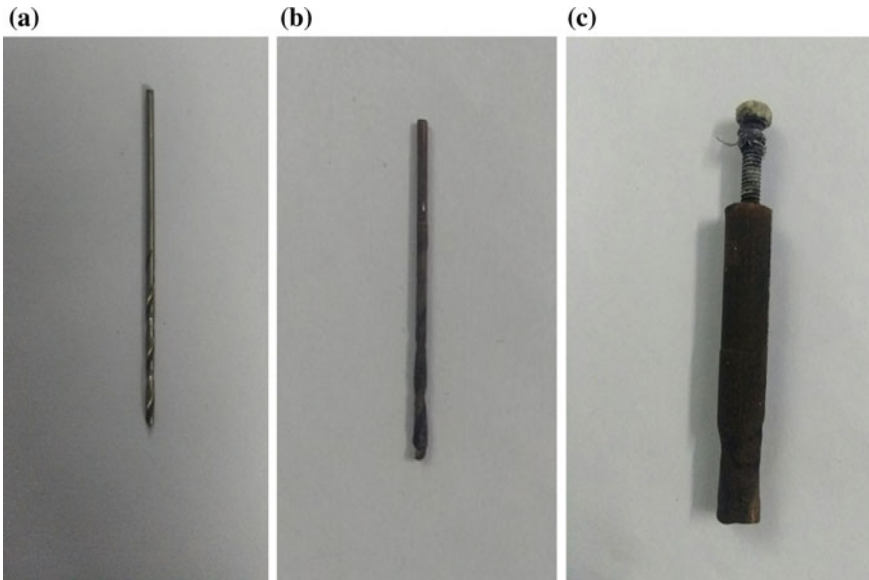


**Fig. 7.5** a HSS tool before machining, b tool after machining of hole, c auxiliary copper tool electrode

**Table 7.2** Machining conditions for analysis

Machining condition	Specification
Tool electrode material	HSS
Auxiliary electrode materials	Copper
Level of electrolyte	1 mm above the workpiece
Workpiece material	Soda–lime glass
Machining time	20 min
Applied voltage	50–70 V
Duty cycle	0.5–0.7
RPM	500–1100 rpm

**Table 7.3** Process parameter and their levels

Sr. No	Machining parameters	Level 1	Level 2	Level 3
1	Applied voltage (V)	50	60	70
2	Duty cycle	0.5	0.6	0.7
3	RPM	500	800	1100

**Table 7.4** Experimental data

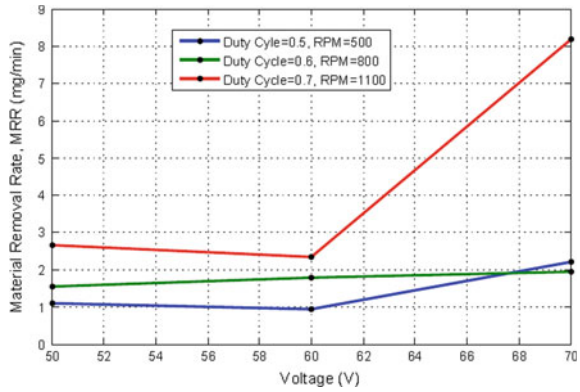
Sr. No.	Voltage (V)	Duty cycle	RPM	MRR (mg/min)
1	70	0.7	800	5.00
2	50	0.5	1100	3.60
3	70	0.5	1100	5.60
4	50	0.6	500	1.35
5	60	0.6	500	1.25
6	70	0.5	500	2.20
7	60	0.5	800	1.25
8	60	0.7	500	4.50
9	70	0.7	500	7.50
10	70	0.7	1100	8.20
11	50	0.7	500	0.40
12	70	0.6	500	2.10
13	60	0.6	800	0.80
14	70	0.6	800	1.95
15	50	0.6	800	4.55
16	50	0.5	800	0.75
17	60	0.7	1100	2.35
18	50	0.6	1100	7.50
19	70	0.6	1100	2.50
20.	50	0.7	800	0.60
21.	70	0.5	800	0.80
22.	60	0.5	1100	0.45
23.	60	0.5	500	0.95
24.	60	0.7	800	1.80
25.	50	0.5	500	1.10
26.	50	0.7	1100	2.65
27.	60	0.6	1100	1.50

been kept constant throughout the experiment. The following given graph has shown the effect of input parameters on MRR.

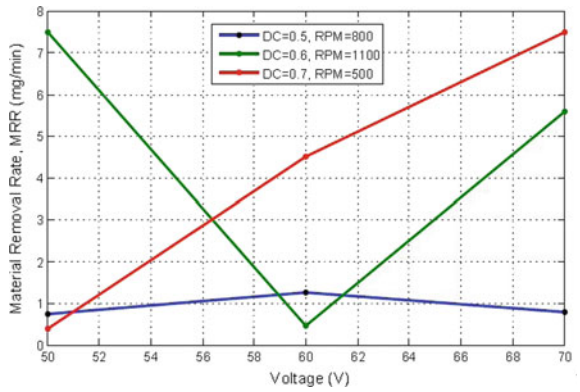
#### **7.4.1 Effect of Voltage on MRR**

This is due to at higher voltage, stronger spark is generated so melting starts earlier, Hence, as the voltage increases the material removal rate is increased due to increasing spark energy. When the voltage increases, the potential difference increases, causing

**Fig. 7.6** a Effect of voltage on MRR. b Effect of voltage on MRR



(a). Effect of voltage on MRR



(b). Effect of voltage on MRR

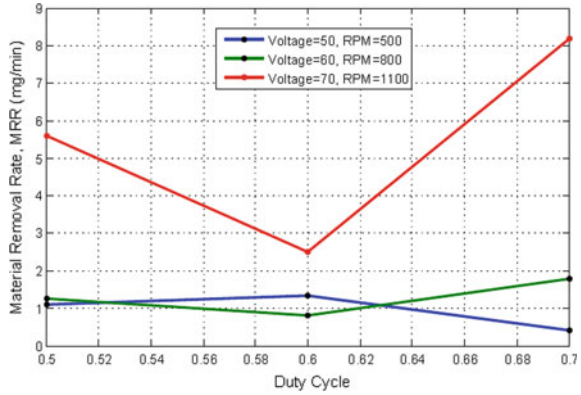
a passivation effect on the surface of the workpiece, thereby more material removal takes place leading to weak surface finish.

From Fig. 7.6a, b, it is observed that on increasing voltage from 50 to 70 V the MRR increases from 2.65 to 8.20 mg/min at constant 0.7 duty cycle and 1100 rpm. At the second stage when duty cycle 0.5 and 500 rpm constant, the MRR increases from 1.10 to 5.60 mg/min.

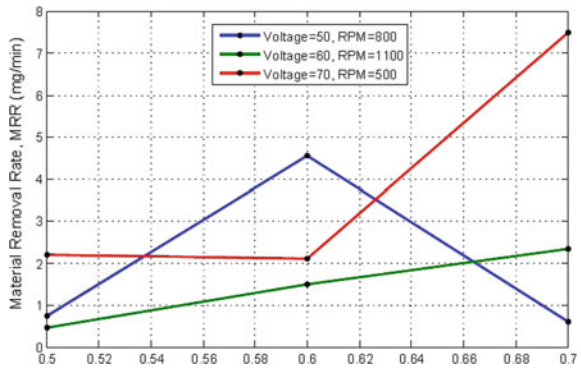
### 7.4.2 Effect of Duty Cycle on MRR

The duty cycle affected the material removal rate. On higher voltage and tool rpm the MRR increases. It is observed that from Fig. 7.7a, b, Duty cycle increases from 0.5 to 0.7 the MRR increases from 2.20 to 7.50 mg/min at constant 70 V and 500 rpm.

**Fig. 7.7** **a** Effect of duty cycle on MRR. **b** Effect of duty cycle on MRR



(a). Effect of Duty Cycle on MRR



(b). Effect of Duty Cycle on MRR

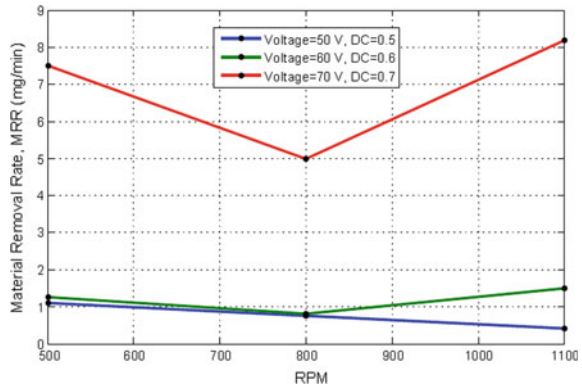
### 7.4.3 Effect of Tool Rpm on MRR

From Fig. 7.8a, b, it is observed that on increasing the tool Rpm the Material removal rate increases. The above graph shows the effect of tool Rpm on MRR On max voltage 70 and 1100 Rpm the max MRR we get. On the DC 0.6 and 1100 tool rpm the max MRR is 7.50 mg/min. Above graph show interrelation of trends like MRR, voltage, Duty cycle, tool rpm gap. There is an increased trend in MRR observe at a voltage of 70 V and 1100 rpm while above the 70 V the glass has a breakdown.

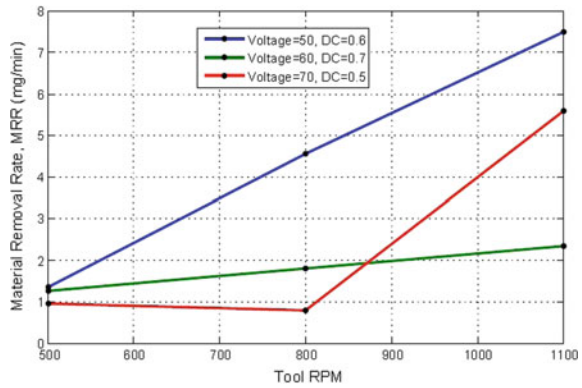
## 7.5 Conclusions

Experimental work is performed for material removal in drilled holes by ECSD process. The preliminary experiments were performed on Soda–lime glass as work

**Fig. 7.8** a Effect of RPM on MRR. b Effect of RPM on MRR



(a). Effect of RPM on MRR



(b). Effect of RPM on MRR

material using NaOH as electrolyte, for only one response variables such as MRR. Three process parameters were selected such as applied voltage, Duty cycle, and tool Rpm from the Final experiments, it is concluded that:

- i. Applied voltage is found to be the most influential parameter for MRR. The MRR value increases from 50 to 70 V from 2.65 to 8.20 mg/min at constant 0.7 duty cycle and 1100 rpm.
- ii. Tool Rpm is a secondary fact of concern affecting the material removal rate. At higher Rpm 1100 the material removal rate is increased from 1.35 to 7.50 mg/min.
- iii. Duty cycle also affected the material removal rate. As increasing the duty cycle, the MRR also increases. On Duty cycle increases from 0.5 to 0.7, the MRR increases from 2.20 to 7.50 mg/min at constant 70 V and 500 rpm.

**Acknowledgements** The authors gratefully acknowledge the Council of Science and Technology, U.P. for providing financial assistance for this work.

## References

1. Skrabalak, G., Stwora, A.: Electrochemical, electrodischarge and electrochemical-discharge hole drilling and surface structuring using batch electrodes. In: 18th CIRP Conference on Electro Physical and Chemical Machining, vol. 42, pp. 766–771 (2016)
2. Coteata, M., Pop, N., Schilze, H.P., Slătineanu, L., Dodun, O. Investigation on Hybrid electrochemical discharge drilling process using passivating electrolyte. In: 18th CRP Conference on Electro Physical and Chemical Machining, vol. 42, pp. 778–782 (2016)
3. Peng, W.Y., Liao, Y.S.: Study of electrochemical discharge machining technology for slicing non conductive brittle materials. *J. Mater. Proc. Technol.* **149**, 363–369 (2004)
4. Jiang, B., Lan, S., Ni, J. Investigation of micro-drilling assisted electrochemical discharge machining. In: 9th International Workshop on Micro factories, pp. 5–8 (2014)
5. Kulkari, A.V.: Electrochemical discharge machining process. *Def. Sci. J.* **57**, 700–765 (2007)
6. Zhong, Y., Xu, Z., Zhu, Y., Zhu, D.: Machining of a film-cooling hole in a single crystal super alloy by high-speed electrochemical discharge drilling. *Chin. J. Aeronaut.* **29**, 560–570 (2016)
7. Bindu Madhavi, J.: Somashekhans Hiremath, Investigation on machining of holes and channels on borosilicate and sodalime glass using  $\mu$ -ECDM setup, global colloquium in recent advancement and effectual researches in engineering. *Sci. Technol. (RAEREST)* **25**, 1257–1264 (2016)
8. Paul, L., Koral, L.V.: Effect of power source in ECDM with FEM modelling. In: Global Colloquium Recent Advancement and Effectual Researches in Engineering, Science and Technology (RAEREST 2016), vol. 25, pp. 1175–1181 (2016)
9. Hajian, M., Razfar, M.R., Movahed, S.: Experimental and numerical investigation of machining depth for glass material in Electrochemical discharge milling. *Precis. Eng.* **51**, 521–528 (2018)
10. Paul, L., Kurian, D.G.: Effect of preheating electrolyte in micro ECDM process. *Mater. Today Process.* **5**, 11882–11887 (2018)
11. Kang, X., Tang, W.: Micro drilling in ceramic-coated Ni-superalloy by electrochemical discharge machining. *J. Mater. Process. Tech.* **255**, 656–664 (2018)
12. Mehrabi, F., Farahnakian, H., Elhami, S., Razljar, M.R.: Application of Electrolyte injection to the electro chemical discharge machining (ECDM) on the optical glass. *J. Mater. Process. Tech.* **255**, 665–672 (2018)



# Chapter 8

## Development and Experimental Study of Ultrasonic Assisted Electrical Discharge Machining Process



Shubham Srivastava , Pravendra Kumar  and S. K. S. Yadav 

**Abstract** In the modern era, the prime focus of researchers and industries is to develop new machining technologies and to improve the performance of existing machining processes. Ultrasonic-assisted Electrical Discharge Machining (UAEDM) is a hybrid machining process in which ultrasonic vibrations imparted either to tool electrode or workpiece improve the material removal mechanism by effective flushing of debris particles from machining area. In this paper, an attempt has been made to combine the Electrical Discharge Machining (EDM) with ultrasonic machining. In order to do so, a setup for imparting ultrasonic vibration to workpiece is developed and experiments have been performed to study the effect of EDM input parameters and ultrasonic vibrations on process performance of EDM. Copper is selected as tool material and Titanium grade 5 alloy ( $Ti_6Al_4V$ ) is selected as workpiece material. From experimental analysis, it has been observed that low-frequency ultrasonic vibrations supplied to workpiece material improve the material removal rate (MRR) of Electrical Discharge Machining (EDM) process in considerable amount.

**Keywords** HMPs · UAEDM · Transducer · MRR

### 8.1 Introduction

Titanium is an exceptionally important advanced engineering material in modern manufacturing industries. It is utilized by worldwide industries due to its high strength, durability, lightweight and several other distinct properties. Machining of titanium and its alloys is very difficult due to their advanced mechanical and thermal properties such as hardness, toughness, high melting point. Electrical Discharge Machining (EDM) is one of the most successful advanced machining processes for machining engineering materials having extremely enhanced properties regardless of their hardness and toughness. The only limitation of EDM process is that it can

---

S. Srivastava · P. Kumar · S. K. S. Yadav (✉)  
Department of Mechanical Engineering, Harcourt Butler Technical University, Kanpur 208002,  
India  
e-mail: [sanjeevyadav276@gmail.com](mailto:sanjeevyadav276@gmail.com)

© Springer Nature Singapore Pte Ltd. 2020  
M. S. Shunmugam and M. Kanthababu (eds.), *Advances in Unconventional Machining and Composites*, Lecture Notes on Multidisciplinary Industrial Engineering, [https://doi.org/10.1007/978-981-32-9471-4\\_8](https://doi.org/10.1007/978-981-32-9471-4_8)

machine electrically conductive materials only. Both the tool electrode and workpiece should be electrically conductive. In EDM process, the material is removed by recurring electrical sparks occurring between tool electrode and workpiece immersed in a dielectric. A very narrow gap (less than 0.5 mm) is maintained between tool electrode and workpiece by means of servomechanism. When a series of voltage pulses 20–12 V DC is applied to tool and workpiece it causes electrical breakdown of dielectric in a channel of about 10  $\mu\text{m}$  radius. The breakdown of dielectric causes flow of electrons, emitted from cathode and electrons present in the gap, towards anode. These electrons strike with neutral atoms of dielectric, resulting in generation of positive ions and more stray electrons. The positive ions travel towards the cathode and the electrons move towards anode. As soon as the electrons and the positive ions reach the anode and cathode respectively, their kinetic energy is liberated in the form of heat. Extremely high temperature (around 10,000  $^{\circ}\text{C}$ ) is attained by spark for a very short time period generally a fraction of a second (0.1–2000  $\mu\text{s}$ ). Such high temperature of spark is more than sufficient for melting of workpiece as well as tool material. The spark also causes evaporation of the dielectric, as a result of which the pressure of plasma channel increases rapidly of the order of about 200 atm. Such a huge pressure discontinues the evaporation of the superheated metal. As soon as the pulse ends, sudden pressure drop takes place and the superheated molten metal evaporates explosively. This is phenomenon behind removal of material from workpiece as well as tool electrode. Due to pressure difference, fresh dielectric fluid flows in, carries away the debris and act as a cooling medium for workpiece and tool both. The un-flushed molten metal re-solidifies on workpiece and tool surface and referred to as recast layer. The flushed molten metal solidifies into minute spheres distributed in the dielectric liquid along with tool material debris [1].

## 8.2 Ultrasonic-Assisted Electrical Discharge Machining (UAEDM) Process

Ultrasonic-assisted Electrical Discharge Machining (UAEDM) process is a hybrid machining process developed by combining ultrasonic vibrations to EDM process. Hybrid Machining Processes (HMPs) are defined as enhanced material removal processes in which two or more machining processes are successfully combined together to improve machining effect. When all the constituent processes directly take part in material removal then it is termed as cooperative hybrid machining processes. On the other end, when one of the machining processes is directly involved in material removal and the others assist in main process by improving the machining conditions, it is referred to as collaborative hybrid machining process [2]. Ultrasonic-assisted electrical discharge machining process comes under the category of collaborative HMPs as the ultrasonic vibrations help in effective flushing of debris particles from machining area. Thoe et al. have studied ultrasonic-assisted electrical discharge machining of ceramic coated nickel alloy using tungsten wire, silver steel, stainless

steel, mild steel and copper rod. They have observed that UAEDM resulted in an increased MRR, a more stable discharge and a lower incidence of arcing. The use of appropriate tool material was critical for effective UAEDM operation [3]. Ghorishi et al. have done comparative experimental study of machining characteristics in vibratory, rotary and vibro-rotary electro discharge machining. They found that the effect of high-frequency vibration on MRR is more worthy especially in the finishing regime as compared to low-frequency vibrations. The vibro-rotary EDM resulted in increased MRR, TWR and Ra. Thus for optimum parameter setting, a compromise should be made between Ra and MRR or TWR. They have also observed that in semi-finishing regime, Vibro-rotary EDM increases MRR by up to 35% as compared to vibratory EDM and up to 100% as compared to rotary EDM [4]. Zhenglong et al. have performed ultrasonic-assisted micro-electric discharge machining to deep and small hole on titanium alloy. From experimental study, they have observed that ultrasonic vibrations-assisted EDM can easily make holes of less than 0.2 mm diameter and an aspect ratio of more than 15. By using a rotating single notch microelectrode to EDM a small and deep hole enlarged the space through which the debris flows and therefore increased machining efficiency with minimized taper [5]. Shabgard et al. have studied the effect of ultrasonic vibration of workpiece in electrical discharge machining of AISI H13 tool steel. They found that the MRR of UAEDM was three times higher than the EDM for small pulse durations and low currents. The surface roughness (Ra) value of UAEDM was found slightly higher than EDM [6]. Andreas Schubert et al. made an investigation on enhancing micro-EDM using ultrasonic vibration and approaches for machining of non-conducting ceramics. In their study they applied ultrasonic vibrations directly to workpiece and indirectly to dielectric and the effects were observed in the process. They found that using ultrasonically-assisted micro-EDM, the machining process speed was raised by up to 40%. This hybrid process was able to bore less than 90  $\mu\text{m}$  diameter holes with aspect ratio  $>40$  in metallic materials and an aspect ratio  $>5$  for nonconductive ceramic materials which make it possible to manufacture complex shapes in micro parts with high accuracy [7]. Lin et al. investigated machining characteristics of hybrid EDM with ultrasonic vibration and assisted magnetic force. In their study they integrated the EDM process with ultrasonic vibration and magnetic force. They have observed that the process resulted in improved MRR with a finer surface integrity. MRR increased as the pulse current was increased but after a peak value there was a reduction in MRR. Greater TWR was observed with increased peak current and pulse duration. Also positive polarity machining, i.e. tool being positive, resulted in an increased TWR as compared to negative polarity machining. Initially Ra was increased with peak current as pulse duration increased but after a peak value of pulse duration Ra decreased afterwards. Higher Ra was observed with positive polarity machining as compared to negative polarity machining [8]. Lin et al. [8] studied ultrasonic vibration-assisted electro discharge machining of Nitinol using Tungsten tool. The ultrasonic vibration-assisted micro-EDM (UV-MEDM) performance was compared with the micro-EDM (MEDM) without ultrasonic vibrations. They found that a greater ultrasonic vibration amplitude results in a higher efficiency and smaller electrode wear. A higher applied

voltage leads to higher efficiency as well as larger electrode wear. There are two possible configurations of ultrasonic-assisted EDM process on the basis of ultrasonic vibrations supplied. In UAEDM, ultrasonic vibrations can be applied either to tool electrode or to workpiece material. The present work deals with ultrasonic vibrations imparted to workpiece material.

### 8.3 Development of Experimental Setup for UAEDM

The major requirement of ultrasonic-assisted EDM is the selection of appropriate ultrasonic transducer. As in present work, ultrasonic vibrations are given to workpiece therefore during the selection of suitable ultrasonic transducer, it is taken into consideration that it can transmit ultrasonic vibrations while being submerged inside the dielectric of EDM. For this purpose, a sandwich-type piezoelectric ultrasonic transducer having 22 kHz resonant frequency is selected, as shown in Fig. 8.1. We know that the range of human hearing is 20–20,000 Hz. Sound waves having frequency greater than 20 kHz are referred to as ultrasonic waves which are beyond human hearing. In order to obtain maximum amplification and good efficiency, the transducer must be designed to operate at resonance frequency.

The ultrasonic transducer is mounted on EDM worktable with the help of an iron clamp in such a way that the transducer remains in vertical position and produce longitudinal vibrations perpendicular to the worktable of EDM. The iron clamp is

**Fig. 8.1** Piezoelectric ultrasonic transducer



**Fig. 8.2** Photograph of UADEM setup



rigidly fixed to T-slots of EDM worktable by means of two M8 T-bolts so that there is no transverse vibration during operation of ultrasonic transducer. At the top of the ultrasonic transducer, an acrylic sheet of  $100 \times 100 \times 6$  mm is mounted on which workpiece is placed with the help of small hand vice. The acrylic sheet is selected so that the electric supply of EDM and ultrasonic transducer remain neutral to each other. The photograph of ultrasonic-assisted EDM setup is shown in Fig. 8.2.

## 8.4 Experimental Details

The experiments were carried out on SPARKONIX make Z-axis numerically controlled Electrical Discharge Machine available at Advance Manufacturing Lab in Mechanical Engineering Department of HBTU Kanpur, as shown in Fig. 8.3.

### 8.4.1 Selection of Workpiece and Tool Material

The uses for titanium in industry are growing faster than ever before as more and more engineers are discovering it can reduce lifecycle costs across a broad range of equipment and processes. Titanium has an exceptionally high strength to weight

**Fig. 8.3** Z-axis numerical control EDM (SPARKONIX)



ratio. About half as much titanium is required to do the same job, based on strength. Titanium forms a very tenacious surface oxide layer, which is an outstanding corrosion inhibitor. In present work, Titanium grade 5 alloy ( $Ti_6Al_4V$ ) is selected for conducting experiments. Titanium grade 5 is lightweight, stronger than pure titanium, heat treatable, corrosion-resistant, easily welded and fabricated. Titanium alloys are very hard and their melting temperature is too high therefore it is very difficult to machine titanium alloys with conventional machines. Moreover Titanium alloys are very much chemically reactive at high machining temperature as a result of which welding action at tool work interface takes place which results in increased tool wear. Copper electrode of 6 mm diameter is used to conduct experiments on Titanium grade 5 workpieces of  $30 \times 30 \times 5$  mm dimension (Figs. 8.4, 8.5).

**Fig. 8.4** Machined workpiece of Ti alloy



**Fig. 8.5** Copper electrode

### 8.4.2 Selection of Machining Process Parameters

In order to obtain a comparative analysis of EDM and ultrasonic-assisted EDM, experiments were carried out varying one parameter at a time approach. Four independent process parameters namely pulse current ( $I_p$ ), pulse-on-time ( $T_{ON}$ ), pulse-off-time ( $T_{OFF}$ ) and ultrasonic power (%) are selected as input parameters for experimental study. During all experiments, voltage is in the range of 200–230 V and it does not vary due to the machine limitation. The stand-off distance, i.e. distance between tool and workpiece is maintained constant by servo mechanism and it is generally less than half a mm ( $<0.5$  mm). Material Removal Rate (MRR) is selected as output parameter. MRR is calculated by weight loss method. The experiments are conducted varying one parameter at a time approach. Range of input parameters is given in Table 8.1 and experimental data observed is shown in Table 8.2.

## 8.5 Results and Discussion

The effect of input process parameters on material removal rate are discussed below:

**Table 8.1** Range of input parameters

S. No.	Parameter	Unit	Range
1	Pulse current ( $I_p$ )	A	6, 9, 12, 15, 21
2	Pulse-on-time ( $T_{ON}$ )	$\mu$ s	30, 60, 90, 120, 150
3	Pulse-off-time ( $T_{OFF}$ )	$\mu$ s	15, 45, 90, 200, 450
4	Ultrasonic power	%	20, 40, 60, 80, 100

**Table 8.2** Experimental data

S. No.	Pulse current $I_p$ (A)	Pulse-on-time $T_{ON}$ ( $\mu$ s)	Pulse-off-time $T_{OFF}$ ( $\mu$ s)	Ultrasonic power (%)	MRR (mg/min)
1	6	90	90	60	0.3871
2	9	90	90	60	1.1333
3	12	90	90	60	1.3333
4	15	90	90	60	1.7333
5	21	90	90	60	3.0000
6	12	30	90	60	0.6000
7	12	60	90	60	0.8000
8	12	90	90	60	1.2000
9	12	120	90	60	1.7333
10	12	150	90	60	1.8000
11	12	90	15	60	4.6667
12	12	90	45	60	2.0000
13	12	90	90	60	1.2667
14	12	90	200	60	0.6667
15	12	90	450	60	0.5333
16	12	90	90	20	1.6000
17	12	90	90	40	1.2667
18	12	90	90	60	1.2667
19	12	90	90	80	1.2667
20	12	90	90	100	1.2000

### 8.5.1 Effect of Pulse Current on MRR

The effect of pulse current on MRR is shown in Fig. 8.6. It is observed that MRR increases with increase in pulse current. This is due to the reason that with increase in pulse current more energy is available per unit time for melting and evaporation of work material thus increasing MRR.

### 8.5.2 Effect of Pulse-on-Time on MRR

Pulse-on-time ( $T_{ON}$ ) is the time duration during which spark is generated between tool and workpiece. The effect of pulse-on-time on MRR is shown in Fig. 8.7. It is observed that MRR increases with increase in pulse-on-time. This is due to the fact that with increase in pulse-on-time, duration of spark increases which in turn melts more amount of material and hence results in increased MRR.



**Fig. 8.6** Effect of pulse current on MRR

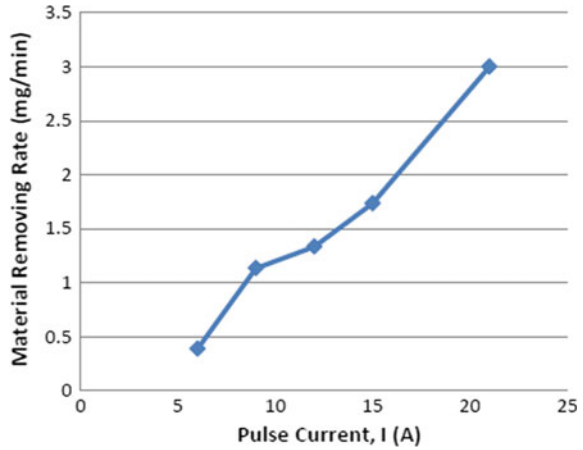
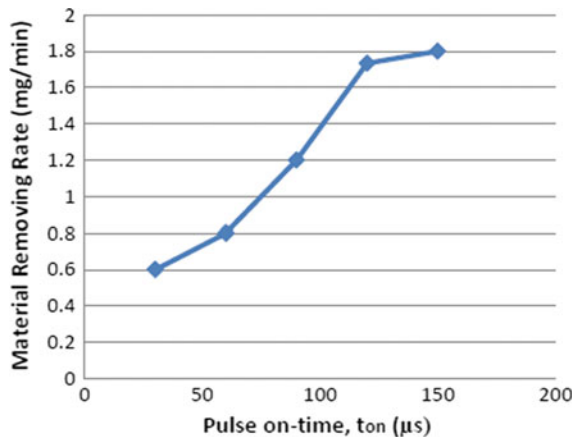


**Fig. 8.7** Effect of pulse-on-time on MRR

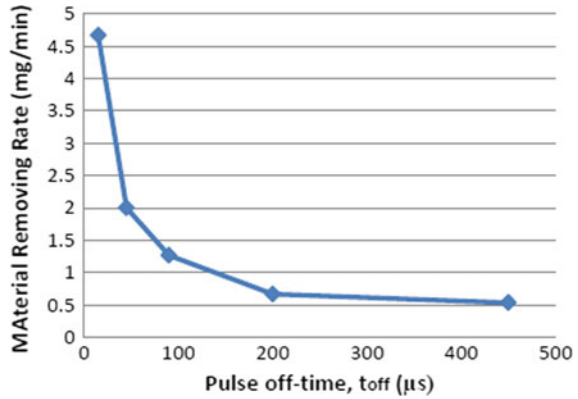


### 8.5.3 Effect of Pulse-off-Time on MRR

Pulse-off-time ( $T_{OFF}$ ) is the time duration between two successive sparks. Pulse-off-time is a critical factor in EDM. The removed material is flushed away in the form of debris during this period. But excessive pulse-off-time has adverse effect on machining performance. The effect of pulse-off-time on MRR is shown in Fig. 8.8.

It is observed that MRR decreases with increase in pulse-off-time and after 200  $\mu s$  it became almost constant. This is due to reason that with increase in pulse-off-time, melted material has sufficient time for re-solidification and form a recast layer and therefore results in decreased MRR.

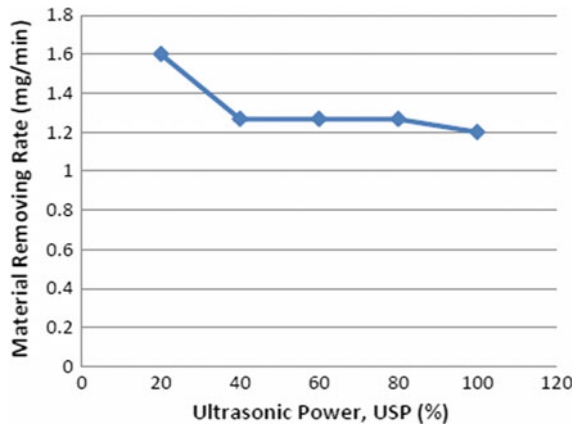
**Fig. 8.8** Effect of pulse-off-time on MRR



### 8.5.4 Effect of Ultrasonic Power on MRR

In the present work, ultrasonic power is varied from 20 to 100%. The effect of ultrasonic power on MRR is shown in Fig. 8.9. It is observed that highest MRR is obtained at low range of ultrasonic power. Further increase in ultrasonic power leads to almost constant MRR. This is due to the fact that low range of ultrasonic power is capable of effective flushing of debris from machining area. With increase in ultrasonic power, high frequency of ultrasonic vibration may not lead effective flushing and thereby resulted in less MRR compared with low ultrasonic power.

**Fig. 8.9** Effect of ultrasonic power on MRR



## 8.6 Conclusions

From the experimental study of ultrasonic-assisted electrical discharge machining (UAEDM) process following conclusions may be drawn:

- Low-frequency ultrasonic vibrations applied to workpiece have a positive effect on machining process performance.
- It has been observed that about 33% more MRR is obtained at 20% ultrasonic power as compared to 100% ultrasonic power. This is due to the fact that at 20% ultrasonic power, the transducer provides vibration at resonance frequency. At resonance frequency, maximum amplification is obtained at good efficiency.
- It is observed that MRR increases with an increase in pulse current and pulse-on-time whereas MRR decreases with increase in pulse-off-time.

## References

1. El-Hofy, H.A.G.: *Advanced Machining Processes, Non-Traditional and Hybrid Machining Processes*. Tata McGraw-Hill
2. Rajurkar, K.P., Gu, L.: Recent research and developments in hybrid machining processes. In: *Proceedings of the 3rd International and 23rd AIMTDR Conference, Visakhapatnam, vol. 1, pp. 39–44 (2010)*
3. Thoe, T.B., Aspinwall, D.K., Killely, N.: Combined ultrasonic and electrical discharge machining of ceramic coated nickel alloy. *J. Mater. Process. Technol.* **92–93**, 323–328 (1999)
4. Ghoreishi, M., Atkinson, J.: A comparative experimental study of machining characteristics in vibratory, rotary and vibro-rotary electrodischarge machining. *J. Mater. Process. Technol.* **120**, 374–384 (2002)
5. Wansheng, Z., Zhenlong, W., Shichun, D., Guanxin, C., Hongyu, W.: Ultrasonic and electrical discharge machining to deep and small hole on titanium alloy. *J. Mater. Process. Technol.* **120**, 101–106 (2002)
6. Shabgard, M.R., Sadizadeh, B., Kakoulvand, H.: The effect of ultrasonic vibration of workpiece in electrical discharge machining of AISI H13 tool steel. *World Acad. Sci. Eng. Tech.* **3(4)**, 323–327 (2009)
7. Schubert, A., Zeidler, H., Hackert, M.O., Schneider, J., Hahn, M.: Enhancing micro-EDM using ultrasonic vibrations and approaches for machining of non-conducting materials. *Strojnicki Vestnik J. Mech. Eng.* **59(3)**, 156–164 (2013)
8. Lin, Y.C., Hung, J.C., Chow, H.M., Wang, A.C., Chen, J.T.: Machining characteristics of a hybrid process of EDM in gas combined with ultrasonic vibration and AJM. *Procedia CIRP*, **42**, 167–172 (2016)

# Chapter 9

## Effect of Finishing Time on Surface Finish of Spur Gears by Abrasive Flow Finishing (AFF) Process



Anand C. Petare , Neelesh Kumar Jain  and I. A. Palani 

**Abstract** Abrasive flow finishing (AFF) is an advanced finishing process for deburring, polishing and radiusing of difficult to reach surfaces and object having complex geometrical shape. Surface finish and material removal in AFF process are significantly affected by the finishing time. This paper reports the effect of finishing time on surface quality and material removal rate of spur gear made of 20MnCr<sub>5</sub>. An experimental setup has been designed and developed for AFF of spur gears using hydraulic power pack unit, medium cylinder and a specially designed fixture for finishing of gear teeth. The fixture ensures proper holding of workpiece gear and direct abrasive medium to flow over entire face width of the workpiece gear uniformly. The results obtained show the highest improvement in surface roughness and material removal rate at 25 min of finishing time. The scanning electron microscope (SEM) images and bearing area curve (BAC) shown improvement in the flank surface quality of gear without any undesirable effect and improved noise and vibration characteristics. All these results have proven AFF as a viable and productive alternative gear finishing process.

**Keywords** Abrasive · AFF · Gear · Gear finishing · Material removal · Surface roughness

### 9.1 Introduction

Spur gear is frequently used to transmit motion and power or to change the direction of motion between two parallel shafts. The major applications of spur gear are in automobiles, aerospace, machine tools, wind turbines, marine and defence applications, construction machinery, toys, office automation equipment and micro and nanodevices. Annually, billions of gears consumed by industries for various applications and this demand are continuously growing. Gears are expected to transmit

---

A. C. Petare (✉) · N. K. Jain · I. A. Palani  
Discipline of Mechanical Engineering, Indian Institute of Technology Indore, Simrol 453552,  
MP, India  
e-mail: [phd1401103001@iiti.ac.in](mailto:phd1401103001@iiti.ac.in)

© Springer Nature Singapore Pte Ltd. 2020  
M. S. Shunmugam and M. Kanthababu (eds.), *Advances in Unconventional Machining and Composites*, Lecture Notes on Multidisciplinary Industrial Engineering, [https://doi.org/10.1007/978-981-32-9471-4\\_9](https://doi.org/10.1007/978-981-32-9471-4_9)

high power and torque, low maintenance, long service life, high wear resistance, smooth meshing with noise and vibration, resist overload and high mechanical efficiency from gears. To meet above expectations required, high-quality surface finish on flank surface of gear teeth. Various traditional gear finishing processes such as gear grinding, gear shaving, gear grinding is a well-established finishing process for finishing case hardened gear having hardness above 40 HRC. It gives burn marks due to heat generation in between grinding wheel and gear flank surface. It also generates grinding lays on gear flank surface which deteriorates surface quality and causes noise and vibration in gear; Gear lapping is used for correcting minor deviations of tooth profile after heat treatment. It takes long time to finish gears and increasing lapping cycle may cause decrease in form accuracy. Mating gears are only lapped and they cannot be interchanged; Gear shaving is applicable for finishing unhardened gear having hardness up to 40 HRC. It is a costly process in terms of high cost of shaving cutter. It affects gear transmission efficiency if more material is removed from pitch surface of gear; Gear honing is used for finishing hardened gear. It is a slow process having very high wear rate and high cost of honing tools; Gear burnishing is applicable for finishing unhardened gears by using burnishing dies. It is used to improve gear quality at cold stage. It causes generation of localized stresses and non-uniformity on gear flank surface [1].

Traditional gear finishing processes are alone not capable to finish gears completely. Therefore, to overcome their limitations, a requirement of hybrid or advanced gear finishing process which is economical, easy to operate, sustainable and generalized arisen. Recently, some advanced, hybrid gear finishing process such as electrochemical honing (ECH), pulse electrochemical honing (PECH) and abrasive flow finishing (AFF) are reported for different types of gear. The following is the summary of the past work:

- Shaikh et al. [2] used ECH process for finishing of straight bevel gears by using the concept of twin complementary cathode gears. They reported 58.54% improvement in average surface roughness ' $R_a$ ' 44.44% improvement in maximum surface roughness ' $R_{max}$ ' and improvement in percentage material in bearing area curve (BAC) after ECH.
- Pathak et al. [3] used the concept of pulse power supply in ECH to vary current and voltage in the interelectrode gap and named it PECH process. They reported reduction in average surface roughness ' $R_a$ ' value from 2.84 to 1.03  $\mu\text{m}$ , maximum surface roughness ' $R_{max}$ ' value from 24.59 to 6.06  $\mu\text{m}$ , depth of roughness ' $R_z$ ' value from 13.51 to 5.42  $\mu\text{m}$ .
- Kenda et al. [5] applied AFF for finishing wire spark erosion machining (WSEM) manufactured injection moulding die of AISI H11 grade tool steel for the production of spur gear. They reported average surface roughness ' $R_a$ ' value reduced from 0.68 to 0.07  $\mu\text{m}$  within a finishing time of 2 min with completely removed cutter marks and improved profile and achieved required fatigue strength.
- Xu et al. [4] finished helical gears by AFF and reduced average surface roughness ' $R_a$ ' 84% in left flank, 80% right flank and 35% in root surface, respectively.

- Venkatesh et al. [6, 7] finished straight bevel gear using AFF and ultrasonic-assisted AFF (UA-AFF). They reported a reduction of 55% in average surface roughness ' $R_a$ ' by using AFF and 73% reduction by using UA-AFF, respectively.

On conclusion of above literature, survey AFF finds a more suitable process for gear finishing because it uses an abrasive-laden viscoelastic medium, which extruded back and forth in the gear teeth gaps with high pressure and acts as a flexible grinding stone which improves finishing of surface. AFF is nano-finishing process used for deburring, radiusing, polishing, to finish complicated geometry with difficult to reach areas and to improve fatigue strength. Application area of AFF are aerospace components, mould and dies, biomedical implants, automobile, turbines blades, pump casing, gears and additive manufacturing [8]. Past research work on gear finishing by AFF is focused on improving the surface finish of helical and straight bevel gear only. No work was reported on improving surface finish of spur gear by AFF. Therefore, the present work is focused to (i) explore AFF process for finishing of spur gears with focus on reduction in surface roughness; (ii) investigate effect of variation of finishing time on surface roughness and material removal rate in AFF; and (iii) to optimize value of finishing time which will maximize reduction in surface roughness and material removal rate.

## 9.2 Details of Experimentation

### 9.2.1 *Experimental Setup and Fixture*

An AFF experimental setup developed for finishing of the spur gear is depicted in Fig. 9.1. It consists of oppositely positioned two hydraulic cylinders operated by hydraulic power pack unit. Both hydraulic cylinders are connected with two medium cylinders, respectively. AFF medium is extruded back and forth in between the restrictions created at workpiece gear and fixture.

A special fixture of metalon for finishing of spur gear was designed (schematics is shown in Fig. 9.2). It consists of two cylindrical discs having a concentric pivot to hold gear and circumferential holes drill at radial location according to pitch circle diameter of workpiece gear. AFF medium is extruded back and forth through the drilled holes over the flank surface which causes abrasion and imparts fine finishing.

### 9.2.2 *Gear Materials and Specification*

20MnCr5 alloy steel is commercially used as a gear material and is selected for experimentation having chemical composition (by % Wt.) as 0.8–1.1% Cr; 1–1.3% Mn; 0.14–0.19% C; 0.035% P and S; 0.15–0.40% and balance Fe. Spur gear teeth were cut on hobbing machine. The specifications are module: 3 mm; outside diameter:

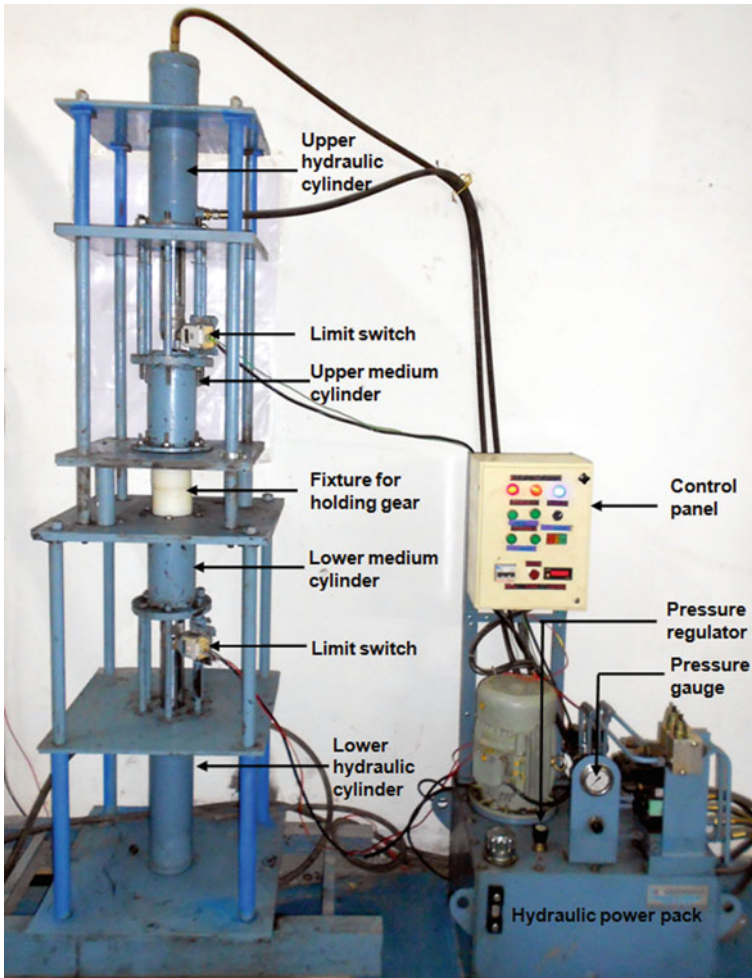


**Fig. 9.1** Photograph of the developed experimental apparatus for finishing the gears by abrasive flow finishing (AFF) process (Source From [9] Elsevier © 2018, reproduced with permission)

54 mm; pitch circle diameter: 48 mm. number of teeth: 16; pressure angle: 20°; face width: 10 mm.

### 9.2.3 Medium Preparation

To prepare medium moulding clay (named as silly putty), abrasive particle (Silicon carbide, mesh size 100) and silicon oil as a blending agent mixed. A volumetric concentration of 60%, modelling clay 30%, abrasive particle and 10% silicon oil

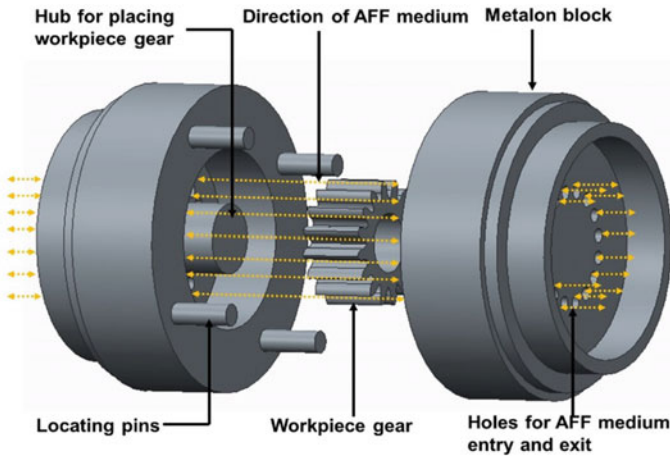


**Fig. 9.2** Schematics of the workpiece fixture used for holding a spur gear for its finishing by the AFF process

prepared based on the medium cylinder volume i.e. 1146 cm<sup>3</sup>. Viscosity of prepared medium was checked by the rheometer (MCR-301 from Anton Paar, Germany).

### 9.2.4 Details of Process Parameters and Responses

AFF process parameters are extrusion pressure, finishing type, abrasive particle concentration type and size, type and concentration of blending oil, the viscosity of finishing medium, workpiece geometry, type and hardness. Finishing time ‘*t*’ is selected as variable parameters and extrusion pressure ‘*P*’, abrasive mesh size ‘*M<sub>a</sub>*’, viscosity of AFF medium ‘*η*’ and concentration of abrasive ‘*C<sub>av</sub>*’ were used as fixed parameters. Change in average surface roughness ‘ $\Delta R_a$ ’ and change in maximum surface roughness ‘ $\Delta R_{max}$ ’ and material removal rate ‘MRR’ were selected as response parameters. Values of fixed parameters and levels of variable parameters are presented in Table 9.1.

**Table 9.1** Selected process parameters and values

Input process parameters	Levels						
Variable parameters	1	2	3	4	5	6	7
Finishing time ‘ <i>t</i> ’ (min)	10	15	20	25	30	35	40

Fixed parameters: AFF medium viscosity ‘*η*’ = 135 kPa.s; Concentration of abrasive particles in the AFF medium ‘*C<sub>av</sub>*’ = 30 vol%; Extrusion pressure ‘*P*’ = 5 MPa; abrasive mesh size ‘*M<sub>a</sub>*’ = 100 mesh and temperature ‘*T*’ = 27 °C



### 9.2.5 Measurement of Responses

Average surface roughness ' $R_a$ ' and maximum surface roughness ' $R_{max}$ ' before finishing and after finishing of spur gear were measured by using surface roughness measuring station LD-130 (MarSurf from Mahr Metrology, Germany). Surface roughness measured at two places of randomly selected tooth of unfinished spur gear and best-finished spur gear by AFF. An arithmetic average of measured values was taken to calculate average value of the change in average surface roughness ' $\Delta R_a$ ' using the following equation.

$$\Delta R_a = \text{Initial } R_a \text{ value} - \text{Final } R_a \text{ value} \quad (\text{in } \mu\text{m}) \quad (1)$$

Similarly, change in maximum surface roughness ' $\Delta R_{max}$ ' calculated. Material removed was measured by using weighing balance DS-852 from Essae Teraoka Ltd., (India) having accuracy 0.01 gm and material removal rate 'MRR' were measured by using the following equation:

$$MRR = \frac{\text{Initial weight} - \text{Final weight}}{\text{Finishing time}} \quad (\text{in mg/min}) \quad (2)$$

Scanning electron microscopic (SEM) images of flank surface unfinished spur gear and best-finished spur gear tooth were taken by using field emission SEM (Supra 55 from Carl Zeiss NTS GmbH, Germany) to see microstructure improvement.

## 9.3 Results and Discussions

Table 9.2 present values of process parameter and responses obtained for all experiments. It can be seen from these results that at 25 min of finishing time (experiment no. 4) gives maximum change in average surface roughness ' $\Delta R_a$ ' (i.e. 0.215  $\mu\text{m}$ ),

**Table 9.2** Values of process parameters and responses

Exp. No.	Process parameters	Responses		
	Finishing time ' $t$ ' (min)	$\Delta R_a$ ( $\mu\text{m}$ )	$\Delta R_{max}$ ( $\mu\text{m}$ )	MRR (mg/min)
1	10	0.036	0.041	0.00067
2	15	0.101	0.281	0.00099
3	20	0.122	0.397	0.00120
4	<b>25</b>	<b>0.215</b>	<b>0.868</b>	<b>0.00207</b>
5	30	0.211	0.848	0.00234
6	35	0.176	0.745	0.00193
7	40	0.154	0.722	0.00113

in maximum surface roughness ' $\Delta R_{max}$ ' (i.e. 0.868  $\mu\text{m}$ ) and in material removal rate ' $MRR$ ' (i.e. 0.00207  $\text{mg}/\text{min}$ ).

At finishing time of 10 min rate of change of average surface roughness, maximum surface roughness and material removal rate is less because of the presence of high surface roughness peaks due to gear cutter marks (see Figs. 9.3, 9.4 and 9.5). At initial stage, abrasive particle tries to reduce height of higher surface peaks and attained approximately equal height for next experiment. From 15 to 25 min, change in average surface roughness, maximum surface roughness and material removal rate increases rapidly due to the availability of approximately equally heighted surface roughness peaks. Further, increase of finishing time from 30 to 40 min rate of change of average surface roughness, maximum surface roughness and material removal rate decreases because of bluntness of cutting edges of abrasive particles. The continuous movement of abrasive particle over the flank surface causes blunting of cutting edges

**Fig. 9.3** Variation of change in average surface roughness ' $\Delta R_a$ ' with finishing time

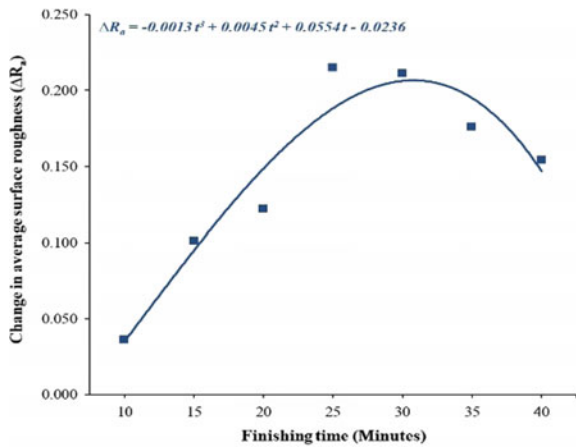


**Fig. 9.4** Variation of change in maximum surface roughness ' $\Delta R_{max}$ ' with finishing time

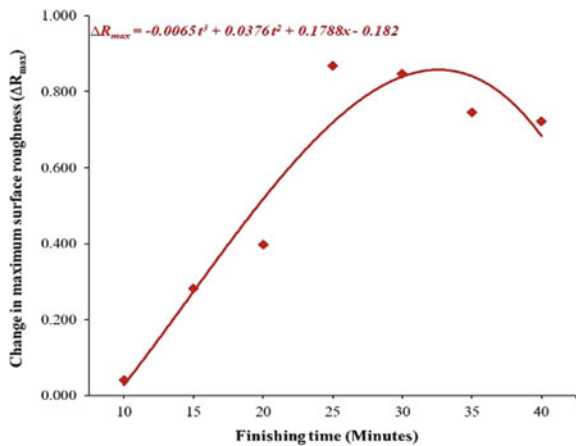
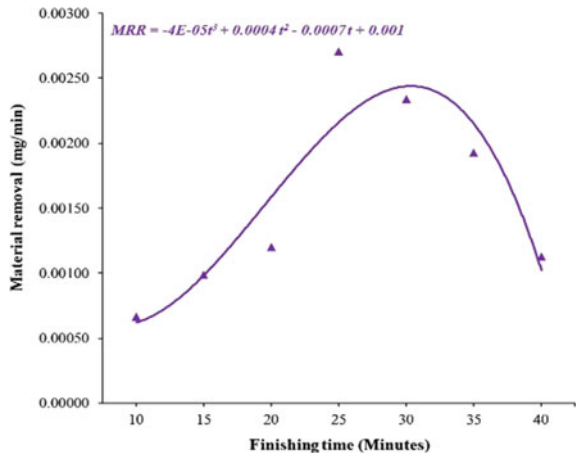


**Fig. 9.5** Variation of change in material removal rate 'MRR' with finishing time



and also mixing of microchips in AFF medium is due to previously finished gears. Therefore, abrasive particle starts rotating over the flank surface rather than abrasion and reduces rate of change of average surface roughness, maximum surface roughness and material removal rate. The above result and discussion shows that finishing time of 25 min yield maximum improvement in average surface roughness, maximum surface roughness and material removal rate. Microstructure of flank surface of gear tooth obtained by SEM at unfinished stage and at 25 min of finishing time shown in Fig. 9.6. In Fig. 9.6, gear cutter marks, cracks, roughness valleys and peaks were present on gear flank surface. Figure 9.7 shows flank surface finished at 25 min finishing time, which is completely free from cutter marks, cracks and having smooth surface. Marks of abrasive particles in the direction of extrusion shows material removal is due to abrading action with micro-cutting and micro-ploughing.

**Fig. 9.6** SEM micrographs displaying microstructure of flank surface at unfinished stage



**Fig. 9.7** SEM micrographs displaying microstructure of gear flank surface at 25 min finishing time by AFF

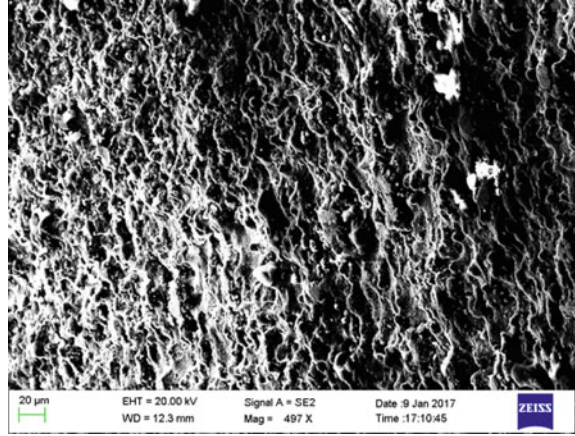


**Fig. 9.8** Bearing area curve of gear flank surface in unfinished stage

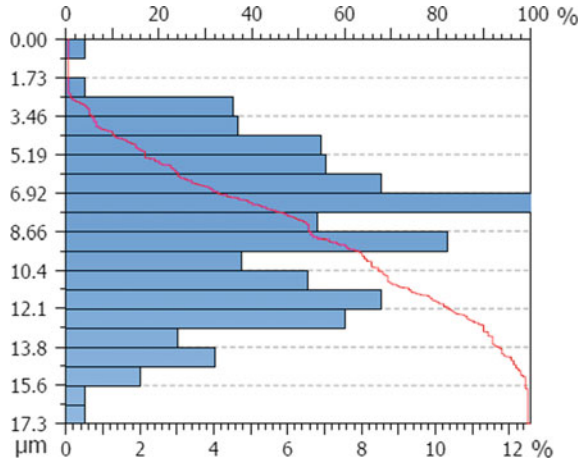
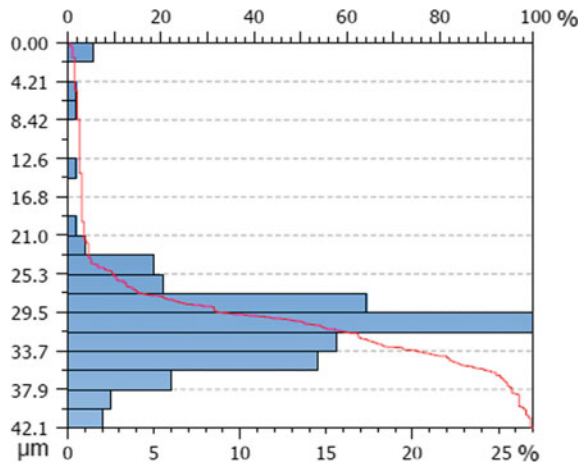


**Fig. 9.9** Bearing area curve of best-finished gear flank surface by AFF



Figures 9.8 and 9.9 show bearing area curve (BAC) of gear flank surface before finishing and best-finished gear flank surface by AFF. The material ratio ' $R_{mr}$ ' improved from 3.37 to 4.73%, and it results in more contact area and less wear and noise and vibration in gear.

## 9.4 Conclusions

This paper reports on the effect of finishing time on improvement of surface quality of spur gear in AFF. The following inferences conclusions have been drawn based on result and discussion:

- Finishing time in AFF is very influential parameters it affects surface quality and material removal rate.
- The changes in average surface roughness, maximum surface roughness and material removal rate increases with increase in finishing and it obtained the maximum value at 25 min. Increasing finishing time beyond 25 min rate of change in average surface roughness, maximum surface roughness and material removal rate start decreasing due to wear of abrasive particle.
- SEM micrograph shows that AFF is capable to remove gear cutter marks, microcracks, burrs and to improve the surface quality of gear flank surface which improves operating performance and service life of gear.
- Improvement in bearing area curves ensure availability of more smooth surface which will reduce noise and vibration of gear.
- Surface produced by AFF is free from any stress and undesirable effect like grinding burn in gear grinding, localized stress in gear burnishing, more material removal from pitch circle in case of gear shaving and lapping.
- Design of fixture play a very important role in AFF to achieve the desired improvement in surface finish. Reduction in surface roughness can be increased by modifying design of fixture.
- Above work shows that AFF as cost-effective, easy operational and alternative gear finishing solution.

## References

1. Jain, N.K., Petare, A.C.: (2017) 1.4 review of gear finishing processes A2—Hashmi, MSJ. In: *Comprehensive Materials Finishing*. Elsevier, Oxford, pp. 93–120. <https://doi.org/10.1016/b978-0-12-803581-8.09150-5>
2. Shaikh, J.H., Jain, N.K., Venkatesh, V.C.: Precision finishing of bevel gears by electrochemical honing. *Mater. Manuf. Process.* **28**(10), 1117–1123 (2013). <https://doi.org/10.1080/10426914.2013.811737>
3. Pathak, S., Jain, N.K., Palani, I.A.: Investigations on surface quality, surface integrity and specific energy consumption in finishing of straight bevel gears by PECH process. *Int. J. Adv. Manuf. Technol.* **85**, 2207–2222 (2016) <https://doi.org/10.1007/s00170-016-8876-x>
4. Xu, Y.C., Zhang, K.H., Lu, S., Liu, Z.Q.: Experimental investigations into abrasive flow machining of helical gear. *Key Eng. Mater.* **546**, 65–69 (2013). [www.scientific.net/KEM.546.65](http://www.scientific.net/KEM.546.65)
5. Kenda, J., Duhovnik, J., Tavčar, J., Kopač, J.: Abrasive flow machining applied to plastic gear matrix polishing. *Int. J. Adv. Manuf. Technol.* **71**, 141–151 (2014). <https://doi.org/10.1007/s00170-013-5461-4>
6. Venkatesh, G., Sharma, A.K., Kumar, P.: On ultrasonic assisted abrasive flow finishing of bevel gears. *Int. J. Mach. Tools Manuf.* **89**, 29–38 (2015) <https://doi.org/10.1016/j.ijmactools.2014.https://doi.org/10.014>
7. Venkatesh, G., Sharma, A.K., Singh, N., Kumar, P.: Finishing of bevel gears using abrasive flow machining. *Procedia Eng.* **97**, 320–328 (2014). <https://doi.org/10.1016/j.proeng.2014.12.255>
8. Petare, A.C., Jain, N.K.: A critical review of past research and advances in abrasive flow finishing process. *Int. J. Adv. Manuf. Technol.* **97**(1), 741–782 (2018). <https://doi.org/10.1007/s00170-018-1928-7>
9. Petare, A.C., Jain, N.K.: On simultaneous improvement of wear characteristics, surface finish and microgeometry of straight bevel gears by abrasive flow finishing process. *Wear* **404–405**, 38–49 (2018)

## Chapter 10

# Experimental Study on Improving Material Removal Rate and Surface Roughness in Wire-Cut EDM of Low Conductive Material



Dhiraj Kumar , Sadananda Chakraborty , Anand Ranjan   
and Dipankar Bose 

**Abstract** Wire electric discharge machining (WEDM) has become a widely accepted electrothermal process for electrically conductive materials. Still, it puts a certain restriction that the limiting criteria of electrical conductivity should be 0.01 S/cm. To overcome this limiting criterion, a copper foil is applied over the workpiece surface. Due to application of copper foil, voltage drop and energy loss in workpiece material are reduced. Kerosene is used as dielectric fluid because it is a combustible hydrocarbon liquid, thereby, formation of continuous cracked carbon from working oil maintains the required electrical conductivity during machining. It is experimented that peak current and pulse on time are the most dominant factors that impact the machining characteristics. The optimum parameter setting obtained for best MRR and SR in WEDM is  $V_G = 30$ ,  $T_{ON} = 80$ ,  $T_{OFF} = 5$ , and  $I_P = 2.84$ . The surface texture of the machined sample is studied to estimate the responses.

**Keywords** WEDM · Chromium carbide · Conductivity · RSM · ANOVA

## 10.1 Introduction

Wire electrical discharge machining is a nontraditional machining process used for machining of very hard materials, superalloys and the composite matrix for manufacturing very complex shapes of through cutting profile whose machining is not possible by the conventional machining process and also other nontraditional processes. It is a well-ordered metal removal process and material removal takes place by mean of an electric spark. One of the requirements of wire electrical discharge machining process is that the material of workpiece should be electrically conductive. Moreover, there are some of the low conductive materials such as silicon and chromium carbide which are hard and brittle in nature, though, it can be machined

---

D. Kumar · S. Chakraborty (✉) · A. Ranjan · D. Bose  
Manufacturing Technology, Department of Mechanical Engineering, National Institute of  
Technical Teachers' Training and Research, Kolkata 700106, India  
e-mail: [sadananda116@gmail.com](mailto:sadananda116@gmail.com)

© Springer Nature Singapore Pte Ltd. 2020  
M. S. Shunmugam and M. Kanthababu (eds.), *Advances in Unconventional  
Machining and Composites*, Lecture Notes on Multidisciplinary  
Industrial Engineering, [https://doi.org/10.1007/978-981-32-9471-4\\_10](https://doi.org/10.1007/978-981-32-9471-4_10)

by abrasive wire saw method and plasma arc etching method, but, there are certain drawbacks as this process takes very time and expensive because of its extreme hardness. The prior research has shown that EDM can be used to machine low conductive materials if the electrical resistivity is less than  $100 \Omega \text{ cm}$ . WEDM works on the principle of the erosive effect of the electrical discharges between two electrodes, therefore, it does not depend on the mechanical properties of workpiece material but rather by thermal characteristics such as thermal conductivity, melting point, and density [1].

Generally, WEDM is used when cutting technologies such as grinding or turning fail due to their technological and geometrical restriction. Manish Gangil et al. introduced the different advanced optimization technique to improve the material removal rate and surface roughness [2]. Most of the ceramics are nonconductive material except silicon carbide, boron carbide, titanium carbide which are low conductive in nature. The compositions of the material greatly influence on mechanical properties and EDM process. An attempt has been made on developing tailored ED machinable ZTA ceramics and machining through EDM processes for high MRR and low surface roughness [3].

Ayan Pramanick et al. optimized the process parameters for machining of conductive boron carbide ( $B_4C$ ) [4] and established a mathematical model between input and out parameter by considering pulse on time, peak current, pulse off time, servo feed rate, water pressure as machining parameters. There are a different number of techniques to improve the sparking efficiency including some experimental steps in WEDM [5].

Jerzy Kozak et al. reported that the machining of low conductive materials is possible by applying the conductive silver coating over the workpiece surface by WEDM process. It is also monitored that the variation in resistance can be minimized by applying the conductive silver coating and the productivity of the process also increases [6]. The researchers investigated that the machining of insulating ceramics is possible by arranging a metal plate or metal mesh on the surface of the ceramic insulator as an assisting electrode [7]. It is seen that the existence of nickel metal is very important for initiating discharges. Younghua Zhao et al. compared the effect of input parameters on machining characteristics of SiC and cold tool steel [8], it is found that discharge current of cold tool steel is a little larger than that of SiC due to its lower electrical resistivity. The higher cutting speed is achieved using the dielectric fluid as deionized water in comparison to EDM oil [9]. Negative polarity with high ignition voltage and low pulse duration give the best erosion effect on sic material [10]. In this investigation, a new principal of increasing conductivity of ceramics has been found due to copper solidification of the machined surface.

Tanveer Saleh et al. studied that the conductivity of silicon is increased by temporarily coating Si with a high conductive material such as gold. Here, it is important to note that if the thickness of the conductive coating is increased, the resistivity of the composite will decrease to converge towards that of the conductive coating [11]. Kamlesh Joshi et al. narrated the impact of main process parameters on machining of Si wafer by wire electrical discharge machining process while minimizing the kerf loss and maximizing the Slicing rate [12]. K. Muralova et al. have studied



the surface morphology and topography by using SEM and surface topography for evaluating the best quality surface finish with very small kerf width in precision manufacturing [13].

It can be seen from the literature survey that some experimental investigation has been done to machine the low conductive materials using a different technique. But there is a lag in the comparative investigation on improving both material removal rate and surface roughness simultaneously in low conductive materials by WEDM. Some researcher has tried to machine the low conductive material by applying the coating and developed material for successive machining with better dimensional accuracy. But, it is found out that coating thickness over the workpiece material is a major problem. Several researchers optimized the performance parameter but there is gap in optimization of low conductive material. Material removal rate and surface roughness are taken into consideration in the present investigation so that performance of machining will get improve. Copper is a highly electrically and thermal conductivity material that is why it is used for triggering discharges. The quantitative relationship between input and output parameters can be established by applying the response surface methodology (RSM).

## 10.2 Experimental Details

The experimental work is carried out to find the machining capabilities of low conductive materials by Wire Electrical Discharge machining process. A series of experiments are conducted in chromium carbide plate (2 mm thick) by using EZEECUT PLUS CNC WEDM. A hard type brass wire (0.25 mm in diameter) is used as tool electrode and kerosene is used as a dielectric fluid during the experimentation. The experimental setup of the WEDM machine tool is shown in Fig. 10.1. It comprises (a) WEDM CNC type machine tool, (b) machine control panel, (c) work-path profile, (d) wire (tool) and workpiece, (e) main work table and wire drive mechanisms.

Chromium carbide is used as work material because of its growing range of application in the field of automotive uses such as high-performance ceramic brake discs and an electronic application such as LED and detectors. It is a corrosion-resistant material, thereby it is used as anti-wear plates. The chemical composition and basic properties of the chromium carbide are shown in Tables 10.1, 10.2.

The material removal rate has been estimated in  $\text{mm}^3/\text{min}$ . and surface roughness is measured in micrometer with the help of Marsurf PS1 surface roughness tester. The material removal rate is calculated by the following formula:

$$\text{MRR} = \frac{(W_1 - W_2) * 1000}{\rho * t} \text{ mm}^3/\text{min}. \quad (10.1)$$

where  $W_1$  and  $W_2$  are the mass of workpiece before and after machining in grams,  $\rho$  is the density of material in  $\text{g/cc}$  and  $t$  is the time in a minute.

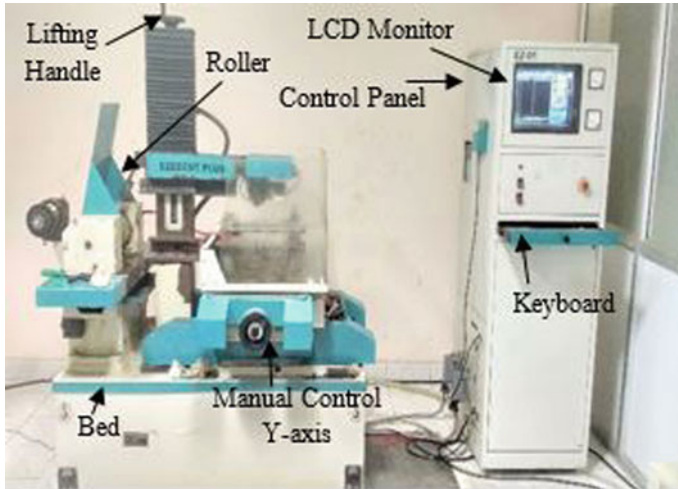


**Fig. 10.1** Ezeecut plus CNC WEDM

**Table 10.1** Chemical composition of chromium carbide

Elements	C	Mn	Si	Cr	W
Contribution (%)	5	0.5	1	28	2.5

**Table 10.2** The properties of chromium carbide

Density	Melting point	Thermal conductivity	Thermal expansion	Hardness
6.68 g/cc	1800 °C	189.77 W/mk	10.4 μm/mk	62 HRC

### 10.2.1 Machining Performance Evaluation

Material removal rate (MRR) and surface roughness (SR) are considered to examine the machine surface quality in the present study. The SR is measured using ‘MarSurf PS1 Surface Roughness tester’. The SR of each machining sample is measured at five different locations and the average of them is considered for analysis. The traversing length of 1.75 mm is chosen due to limitation of specimen size and used to measure the SR at stylus speed of 0.25 mm/s. Cut off length determines the wavelength at which a filter becomes effective. The cut off length of 0.25 mm has been selected corresponding to traversing length to measure the surface roughness value along a line. The unit of SR is measured in μm.

**Table 10.3** Control factors with their level

Process parameters	Symbol	Units	Level		
			-1	0	1
Gap voltage	$V_g$	V	30	50	70
Pulse on time	$T_{on}$	$\mu s$	40	60	80
Pulse off time	$T_{off}$	$\mu s$	5	7	9
Peak current	$I_p$	A	2	3	4

### 10.2.2 Data Collection

Box–Behnken technique has been used to design the experiment in the present experimental study. It is used to perform the nonsequential experiments. There is no axial point in this design, thus, all design point falls within the safe operating zone. The control factors and their level are given in Table 10.3.

### 10.2.3 Methodology

In the present work, Response Surface Methodology has been used for modeling and optimization of response variables which are affected by several input variables. Moreover, many other methodologies are available but RSM explores the best desirable relationship between several explanatory variables and one or more response variables. The main characteristics of RSM are to use a sequence of a designed experiment to achieve an optimal response. It examines the importance of parameters by establishing the relationship between several input and output parameters. The criteria for optimal design experiments are mostly associated with the mathematical model of the process [14]. These mathematical models are second-order polynomial in nature as given below:

$$y = f(x_1, x_2, x_3, \dots x_n) \pm \epsilon \tag{10.2}$$

where  $\epsilon$  is the response error, a second-order polynomial is given by [12],

$$f = a_0 + \sum_{i=1}^n a_i x_i + \sum_{i=1}^n a_{ii} x_i^2 + \sum_{i < j}^n a_{ij} x_i x_j + \epsilon \tag{10.3}$$

where  $a_{ii}$  shows the quadratic effect of  $x_i$ ,  $a_i$  shows the linear effect of  $x_i$ ,  $a_{ij}$  denotes line to line interaction between  $x_i$  and  $x_j$ , and  $x_i$  and  $x_j$  are the design variables.

### 10.3 Results and Discussion

The results obtained through the experiment is tabulated as given in Table 10.4.

The measurement of surface roughness of each machining sample at five different locations and the average of them has been considered for analysis. For example, the SR values at five different locations in first experiment are 3.214, 3.452, 3.982, 4.190, and 3.567  $\mu\text{m}$ , respectively. Therefore, average of them is calculated as

$$SR = \frac{3.214 + 3.452 + 3.982 + 4.190 + 3.567}{5} = 3.681$$

**Table 10.4** Experimental results

S. No.	V <sub>G</sub> (V)	T <sub>ON</sub> ( $\mu\text{s}$ )	T <sub>OFF</sub> ( $\mu\text{s}$ )	I <sub>P</sub> (A)	MRR ( $\text{mm}^3/\text{min}$ )	SR ( $\mu\text{m}$ )
1	50	40	7	2	1.009	3.681
2	70	60	5	3	1.088	4.033
3	30	60	7	4	2.920	4.053
4	30	60	9	3	1.112	4.126
5	50	40	5	3	2.560	3.873
6	50	80	7	4	2.220	3.134
7	50	80	5	3	2.630	3.208
8	30	60	5	3	3.015	3.270
9	70	40	7	3	1.873	4.084
10	50	60	7	3	1.579	3.884
11	50	60	7	3	1.269	3.894
12	50	80	9	3	1.212	3.858
13	30	40	7	3	1.944	3.656
14	50	80	7	2	1.049	3.846
15	50	60	5	2	1.485	3.390
16	70	60	7	2	1.017	4.355
17	70	60	7	4	1.488	2.923
18	70	80	7	3	1.369	3.254
19	50	60	5	4	2.717	3.551
20	70	60	9	3	1.402	3.295
21	50	60	7	3	1.886	3.854
22	50	60	9	2	0.778	4.096
23	30	80	7	3	1.727	3.818
24	50	60	9	4	1.869	3.004
25	50	40	7	4	3.640	3.347
26	50	40	9	3	2.051	3.452
27	30	60	7	2	1.319	3.152

### 10.3.1 Analysis of MRR

ANOVA has been applied to find the effect of individual parameters on MRR, Minitab 17 statistical software is used to tabulate the above experimental results and the following results have been obtained with a confidence level of 95%. ANOVA for MRR has been given in Table 10.5.

The linear terms, interaction terms, and the squared terms have been summarized in the ANOVA table. The small  $p$ -values for the interactions ( $p = 0.017$ ) and the squared terms ( $p = 0.166$ ) show that there is curvature in the response surface. It can be concluded that small  $p$ -values for  $V_g$ ,  $T_{on}$ ,  $T_{off}$ ,  $I_p$ , the interaction of  $T_{on}$  with itself, the interaction of  $V_g$  by  $T_{off}$ , and the interaction of  $T_{on}$  by  $I_p$  indicates that these effects are statistically significant. The correlation co-efficient R-square for MRR has a value of 91.95% which reveals that the modeled equation is accurate. The surface plot has been plotted to see the effect of  $T_{on}$  and  $I_p$  on material removal rate as shown in Fig. 10.2.

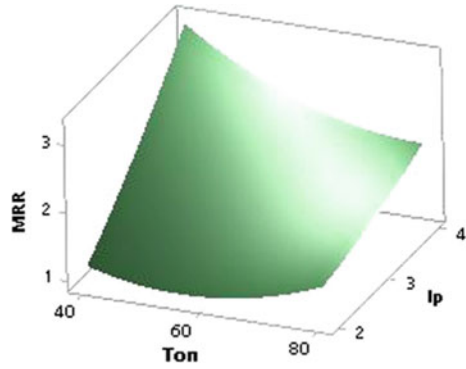
The equation generated for MRR is given as in Eq. (10.4)

$$MRR = 3.52 - 0.0429 V_g - 0.012 T_{on} - 0.996 T_{off} + 2.08 I_p - 0.000167 V_g * V_g + 0.000773 T_{on} * T_{on} + 0.0347 T_{off} * T_{off} + 0.088 I_p * I_p - 0.000179 V_g * T_{on} * T_{on} + 0.000179 V_g * T_{off} * T_{off} + 0.000179 V_g * I_p * I_p$$

**Table 10.5** ANOVA for MRR

Source	DF	Adj. SS	Adj. MS	F-value	$p$ -value
Model	14	12.66	0.90	9.79	0.000
Linear	4	9.63	2.40	26.05	0.000
$V_g$	1	1.20	1.20	13.02	0.004
$T_{on}$	1	0.68	0.68	7.43	0.018
$T_{off}$	1	2.14	2.14	23.18	0.000
$I_p$	1	5.59	5.59	60.58	0.000
Square	4	0.72	0.18	1.96	0.166
$V_g * V_g$	1	0.02	0.02	0.26	0.620
$T_{on} * T_{on}$	1	0.51	0.51	5.52	0.037
$T_{off} * T_{off}$	1	0.10	0.10	1.11	0.313
$I_p * I_p$	1	0.04	0.04	0.44	0.518
2-way interaction	6	2.31	0.38	4.17	0.017
$V_g * T_{on}$	1	0.02	0.02	0.22	0.645
$V_g * T_{off}$	1	1.22	1.22	13.29	0.003
$V_g * I_p$	1	0.31	0.31	3.45	0.088
$T_{on} * T_{off}$	1	0.20	0.20	2.23	0.161
$T_{on} * I_p$	1	0.53	0.53	5.57	0.033
$T_{off} * I_p$	1	0.00	0.01	0.05	0.821

**Fig. 10.2** Surface plot of MRR vs  $T_{on}$  and  $I_p$



$$T_{on} + 0.01386 V_g * T_{off} - 0.01413 V_g * I_p - 0.00568 T_{on} * T_{off} - 0.01825 T_{on} * I_p - 0.0176 T_{off} * I_p \quad (10.4)$$

### 10.3.2 Analysis of SR

ANOVA has been applied to find the effect of individual parameters on SR, Minitab 17 statistical software is used to tabulate the above experimental results and the following results have been obtained with a confidence level of 95%. ANOVA for SR has been given in Table 10.6.

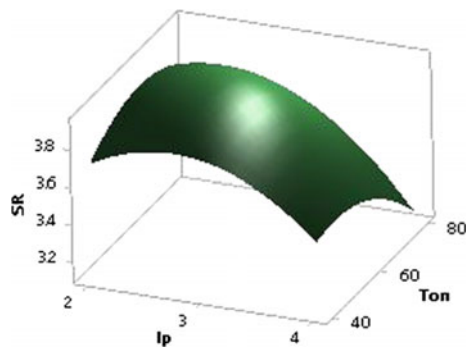
The linear terms, interaction terms, and the squared terms have been summarized in the ANOVA table. The small  $p$ -values for the interactions ( $p = 0.001$ ) show that there is curvature in the response surface [14]. It can be concluded that the small  $p$ -values for  $T_{on}$ ,  $I_p$ , the interaction of  $T_{on}$ ,  $T_{off}$ , and  $I_p$  with itself are statistically significant. The correlation co-efficient R-square for SR has a value of 97.62%, which reveals that the modeled equation is accurate. The surface plot has been plotted to see the effect of  $T_{on}$  and  $I_p$  on SR as shown in Fig. 10.3. The equation generated for SR is given in Eq. (10.5).

$$\begin{aligned} SR = & -11.74 + 0.2036 V_g + 0.0361 T_{on} + 1.101 T_{off} + 3.976 I_p - \\ & 0.000097 V_g * V_g - 0.000349 T_{on} * T_{on} - 0.03664 T_{off} * T_{off} - 0.2245 I_p * I_p - \\ & 0.00620 V_g * T_{on} - 0.00997 V_g * T_{off} - 0.02916 V_g * I_p + 0.00669 T_{on} * T_{off} - \\ & 0.00472 T_{on} * I_p - 0.1567 T_{off} * I_p \end{aligned} \quad (10.5)$$

**Table 10.6** ANOVA for SR

Source	DF	Adj. SS	Adj. MS	F-value	P-value
Model	14	3.92	0.28	35.09	0.000
Linear	4	0.62	0.15	19.61	0.000
$V_g$	1	0.01	0.001	0.18	0.678
$T_{on}$	1	0.07	0.07	9.89	0.008
$T_{off}$	1	0.02	0.02	2.66	0.129
$I_p$	1	0.52	0.52	65.71	0.000
Square	4	0.34	0.08	10.66	0.001
$V_g * V_g$	1	0.04	0.02	1.00	0.337
$T_{on} * T_{on}$	1	0.10	0.10	13.02	0.037
$T_{off} * T_{off}$	1	0.11	0.11	14.34	0.004
$I_p * I_p$	1	0.26	0.26	33.64	0.003
2-way interaction	6	2.95	0.49	61.70	0.000
$V_g * T_{on}$	1	0.24	0.24	30.77	0.000
$V_g * T_{off}$	1	0.63	0.63	79.63	0.000
$V_g * I_p$	1	1.36	1.36	170.26	0.000
$T_{on} * T_{off}$	1	0.28	0.28	35.88	0.000
$T_{on} * I_p$	1	0.03	0.03	4.46	0.056
$T_{off} * I_p$	1	0.39	0.39	49.18	0.000

**Fig. 10.3** Surface plot of SR versus  $T_{on}$  and  $I_p$



### 10.3.3 Optimization Using Response Surface Methodology

Response optimization is used to recognize the combination of variable setting that jointly optimizes a single output or a set of responses. This method is useful to see the effects of multiple variables on the response. It gives individual desirability for each response. However, these values are combined to evaluate the composite, or overall,

the desirability of the multi-response system. To obtain an optimal solution composite desirability should be maximum. The optimal solution is given in Table 10.7.

It is revealed that maximum value of MRR = 3.2178 and a minimum value of SR = 2.92695 can be obtained at the optimized setting parameter, though, the value of  $I_p = 2.84$  cannot work practically. These are the theoretical assumptions, the close approximation of  $I_p = 3$  can be considered for the experimentation, therefore, some error has been found out after confirmation experiment.

In Fig. 10.4, the graph is plotted between MRR and  $I_p$  while keeping the other parameter constant. It has been monitored that MRR is increasing with an increase in  $I_p$ , because peak current increases the available energy in the machining area and hence more materials are removed by spalling as well as melting and vaporization.

Figure 10.5 shows that surface roughness increases with an increase in value of peak current while keeping other parameters constant. As peak current increases the available energy in the machining area, and machining time increases, therefore, more amount of molten material is deposited on the workpiece.

It is also found that MRR firstly decreases with an increase in  $T_{on}$  and subsequently increases with a high value of  $T_{on}$  as shown in Fig. 10.6. Initially, machining stops because of a lack of deposition of carbon, therefore, MRR decreases. But at  $T_{on} =$

**Table 10.7** Optimal Solution

Solution	$V_g$	$T_{on}$	$T_{off}$	$I_p$	SR	MRR	Composite desirability
1	30	80	5	2.84	2.92	3.21	0.922

**Fig. 10.4** MRR versus  $I_p$  graph while other parameters are constant

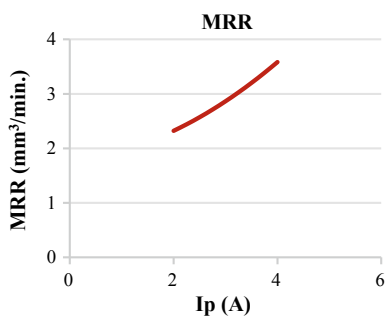


**Fig. 10.5** SR versus  $I_p$  graph while other parameters are constant

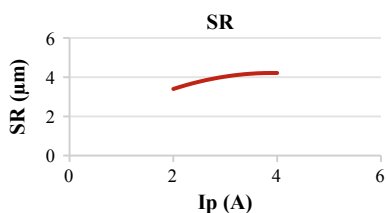
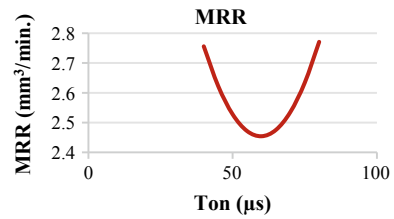




**Fig. 10.6** MRR versus  $T_{on}$  graph while other parameters are constant



60  $\mu s$ , pulse on time increases the machining time and more amounts of material are removed, hence MRR increases.

In Fig. 10.7, it is revealed that surface roughness is continuously increasing with an increase in  $T_{on}$ . Pulse on time increases the machining time, thereby, more amount of materials melt, hence a greater amount of recast layer formation has been observed.

The surface of the machined sample is examined using a Leica metallurgical microscope. The microscopic image has been taken at 50 $\times$  magnification.

It has been observed from the microscopic image (Figs. 10.8 and 10.9) that the machined surface comprises Recast layer, Spherical modules, and protruding material. The sparks produced during the machining process melt the metal's surface, which then undergoes quenching. Some molten material is not flushed away by dielectric fluid and it forms a layer on workpiece surface known as a recast layer [15] after solidification. Figure 10.8 shows the formation of recast layer is less, thereby, surface finish is good.

**Fig. 10.7** SR versus  $T_{on}$  graph while other parameters are constant

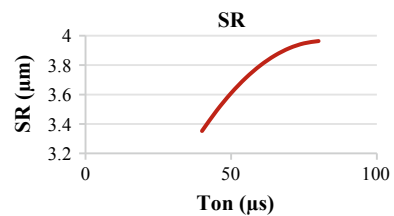


**Fig. 10.8** Microscopic image observed for minimum SR

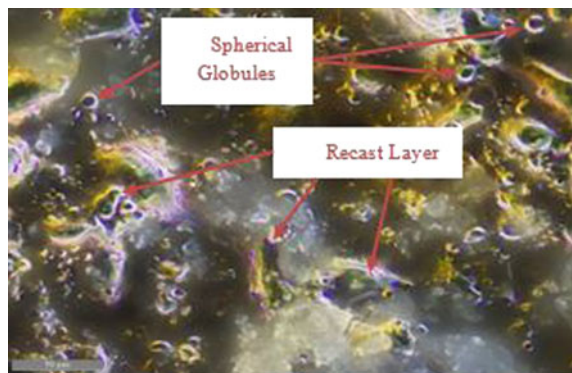


**Fig. 10.9** Microscopic image observed for maximum MRR

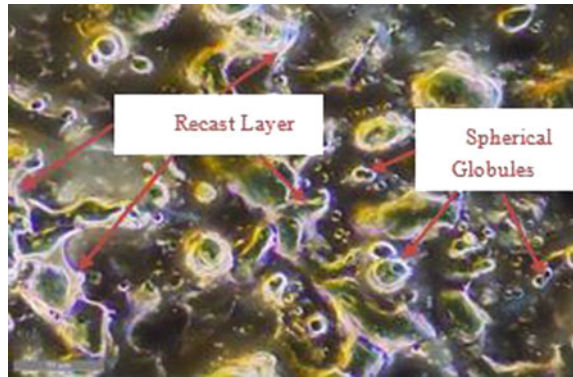


**Fig. 10.10** Machined sample



In Fig. 10.9, recast layer is more because of more machining time and less pulse off time. Machining time increases the material removal rate and therefore, MRR is high.

All 27 number of experiments have been conducted as per design of experiment with random order. The machined sample has been prepared which is shown in Fig. 10.10.

## 10.4 Conclusions

An attempt has been made here to optimize the MRR and SR in wire-cut EDM of low conductive material. This experimental work reveals the following conclusion:

- i. It is observed that significant MRR has been improved with the help of copper foil.
- ii. Copper foil can be easily removed from the workpiece after machining without any damage to the machined surface.

- iii. The optimum parameter setting obtained for best MRR and SR in WEDM of low conductive material is  $V_G = 30$ ,  $T_{ON} = 80$ ,  $T_{OFF} = 5$ , and  $I_P = 2.84848$ .
- iv. Based on ANOVA, peak current and Ton has been found the most dominating factor among all control parameters.
- v. It is revealed that MRR increases with an increase in peak current and SR increases with increase in peak current.
- vi. It is found that MRR and SR both increases with increase in  $T_{on}$ .
- vii. From the microscopic image, it is clear that MRR and SR both increases with increase in recast layer formation.

## References

1. Bobbili, R., Mahu, V., Gogia, A.K.: An experimental investigation of wire electrical discharge machining of hot-pressed boron carbide. *Def. Technol.* **11**(4), 344–349 (2015)
2. Gangil, M., Pradhan, M.K., Purohit, R.: Review on modeling and optimization of electrical discharge machining process using modern techniques. *Mater. Today Proc.* **4**, 2048–2057 (2017)
3. Schmitt-Radloff, U., Gommeringer, A., Assmuth, P., Kern, F., Klocke, F., Holsten, M., Schneider, S.: Effects of composition on mechanical and ED-machining characteristics of zirconia toughened alumina—titanium carbide (ZTA-TiC) composite ceramics. *Procedia CIRP* **68**, 17–21 (2018)
4. Pramanick, A., Sarkar, S., Dey, P.P., Das, P.K.: Optimization of wire electrical discharge machining parameters for cutting electrically conductive. *Boron Carbide, Ceramics Int.* **42**(14), 15671–15678 (2016)
5. Ho, K.H., Newman, S.T.: State of the art electrical discharge machining (EDM). *Int. J. Mach. Tools Manuf.* **43**(13), 1287–1300 (2003)
6. Kozak, J., Rajurkar, K.P., Chandarana, N.: Machining of low electrical conductive materials by wire electrical discharge machining (WEDM). *J. Mater. Process. Technol.* **149**(1–3), 266–271 (2004)
7. Mohri, N., Fukuzawa, Y., Tani, T., Saito, N., Furutani, K.: Assisting electrode method for machining insulating ceramics. *CIRP Ann. Manuf. Technol.* **45**(1), 201–204 (1996)
8. Zhao, Y., Kunieda, M., Abe, K.: Study of EDM cutting of single crystal silicon carbide. *Precis. Eng.* **38**(1), 92–99 (2014)
9. Zhao, Y., Kunieda, M., Abe, K.: Comparison on foil EDM characteristics of single crystal SiC between in deionized water and in EDM oil. *Int. J. Adv. Manuf. Technol.* **86**(9–12), 2905–2912 (2016)
10. Kluev, M., Maradia, U., Boccadoro, M., Perez, R., Stirnimann, J., Wegener, K.: Experimental study of EDM-drilling and shaping of SiSiC and SiC. *Procedia CIRP* **42**, 191–196 (2016)
11. Saleh, T., Rasheed, A.N., Muthalif, A.G.A.: Experimental study on improving  $\mu$ -WEDM and  $\mu$ -EDM of doped silicon by temporary metallic coating. *Int. J. Adv. Manuf. Technol.* **78**(9–12), 1651–1663 (2015)
12. Joshi, K., Ananya, A., Bhandarkar, U., Joshi, S.S.: Ultra-thin silicon wafer slicing using wire-EDM for solar cell application. *Mater. Des.* **124**, 158–170 (2017)
13. Mouralova, K., Kovar, J., Klakurkova, L., Bednar, J., Benes, L., Zahradnicek, R.: Analysis of surface morphology and topography of pure aluminium machined using WEDM. *Measurement* **114**, 169–176 (2018)
14. Singh, N., Routara, B.C., Das, D.: Study of machining Characteristics of Inconel 601 in EDM using RSM. *Mater. Today Proc.* **5**(2), 3438–3449 (2018)

15. Sonawane, S.A., Kulkarni, M.L.: Optimization of machining parameters of WEDM for Nimonic-75 alloy using principal component analysis integrated with Taguchi method. *J. King Saud Univ. Eng. Sci.* **30**(3), 250–258 (2018)

# Chapter 11

## Machining Performance Evaluation of Al 6061 T6 Using Abrasive Water Jet Process



Pankaj Kr. Shahu  and S. R. Maity 

**Abstract** The selection of different machining parameters of AWJM is directly related to the experience of the operator because it has a versatile operating range. In this paper, the optimal parameters of AWJM are determined by the grey-fuzzy logic based optimization technique to enhance the material removal rate and surface roughness of aluminum alloy Al 6061 T6. This investigation is formulated by using Taguchi method, the water pressure (WP), abrasive flow rate (AFR) and standoff distance (SOD) taking into account as the process parameters. The response value and input parameter for different machining process are determined by the artificial neural network using forward and reverse modeling technique, respectively. This modeling technique is very productive to determine the machining response value simultaneously process parameter setting in minimum time and with less effort otherwise experimentally trial and error method has to be used for determining it.

**Keywords** AWJM · Grey-fuzzy · MRR · SR · ANN

### 11.1 Introduction

Abrasive water jet machining (AWJM) technology is among the quickest developing nonconventional machining practice. It had received impressive consideration from the different industries, because of its gainful attributes. This procedure joins the principles of water and abrasive jet machining [1]. Abrasive water jet machining exists as a mechanical-type process that set up the intense high pressure and velocity water with abrasive thoroughly mixed together for machining a large range of material. The AWJM process has an ability to machine any material being ductile or brittle with a decrease in machining rate per unit cost.

The use of the abrasive water jet for finishing purposes is based on the principle of erosion of the material upon which the jet hits [2]. The mixing chamber has the

---

P. Kr. Shahu · S. R. Maity (✉)  
Department of Mechanical Engineering,  
National Institute of Technology Silchar, Silchar 788010, India  
e-mail: [saikat.jumtech@gmail.com](mailto:saikat.jumtech@gmail.com)

© Springer Nature Singapore Pte Ltd. 2020  
M. S. Shunmugam and M. Kanthababu (eds.), *Advances in Unconventional Machining and Composites*, Lecture Notes on Multidisciplinary Industrial Engineering, [https://doi.org/10.1007/978-981-32-9471-4\\_11](https://doi.org/10.1007/978-981-32-9471-4_11)

purpose of mixing the abrasive particles with high-pressure water jet in which both serves two purposes. Erosive force on the material is driven by the abrasive material coming out of the nozzle jet.

Due to the great number of influential parameters involved in the AWJM process, and the multitude of machining requirements, optimization of performance is important. Jai Aultrin and Dev Anand [3] develops a fuzzy logic based modeling for prediction of two response parameters namely material removal rate and surface roughness for aluminum silicon carbide material cut using AWJM process and optimization of its rule base and database using a binary-coded genetic algorithm. Vundavilli et al. [4] focus on eliminating the experimental work so as to predict the data with at most accuracy that can be used effectively in different industrial work. Venkata Rao [5] proposed a multi-objective and multi-parameter optimization technique to optimize the response parameters in abrasive water jet machining process. Cojbasic and Petkovi [6] adapted the extreme learning machine to predict the surface roughness of aluminum alloy EN AW 6060 that is cut with the help of abrasive water jet machine. Aydin et al. [7] develop a model using artificial neural network and regression analysis to predict the response parameters. The present work involves the investigation to determine the optimum combination of selected process parameters such as abrasive flow rate, water pressure, and standoff distance for achieving maximum material removal rate (MRR) and minimum surface roughness (SR) with the help of Taguchi method performing abrasive water jet machining of aluminum alloy 6061.

Recent research in the field of abrasive water jet machining process shows that the optimum selection of process parameters is the key area of interest so as to reduce the production time and accuracy in machining. So such a work was found with grey-fuzzy relation analysis in AWJM by the previous researchers. A further prediction of input data for desired output values is done using the reverse mapping in ANN technique is not done by past researchers.

The objectives of the present research work have been reduced as follows:

- (i) To analyze the machining performance based on the material removal rate and surface roughness as response parameters of abrasive water jet machining on aluminum alloy with three dominant process parameters, i.e., abrasive flow rate, water pressure, and standoff distance.
- (ii) To determine the optimal condition using multi-performance optimization of AWJM response with grey-fuzzy relation analysis. Selection of proper process parameters values is determined using the GFRG to get the desired output values.
- (iii) To study the effects of optimal parametric condition with optical images of rectangular slot machined by AWJM.
- (iv) To develop a relationship between machining performance and process parameters and predict the values with reverse and forward mapping using the neural network in abrasive water jet system carried out using a feed-forward back-propagation neural network on effective parameters.

## 11.2 Experimental Study

In the study, the operating variables and their levels were determined by considering the related studies in the relevant literature. All other machining parameters were kept constant during the experiments. In single-pass cutting, a rectangular shaped cut has been done for both material removal rate and surface finish. The image of the experimental setup is shown in Fig. 11.1.

### 11.2.1 Design of Experiment

The experimental work was planned and conducted by using Taguchi method of robust design. The following three process parameters as listed in Table 11.1 have been selected. A standard orthogonal array  $L_{27}$  has been selected for three parameters each at three levels as the total degree of freedom (DOF) is 9. Figure 11.2 depicts the cut design to be made using the machine setup. Desired dimensions for the rectangular cut is specified in the CAD file for controlled and accurate machining of aluminum alloy 6061. Each rectangular slot is of size 10 mm × 40 mm made parallel to each other sequentially. One end of the rectangular cut is kept less than 10 mm so as that the machined material can be taken out for further measurement of response parameter. A total of 12 rectangular cuts has been made on the 100 mm × 100 mm specimen.

**Fig. 11.1** Experimental setup of AWJM used

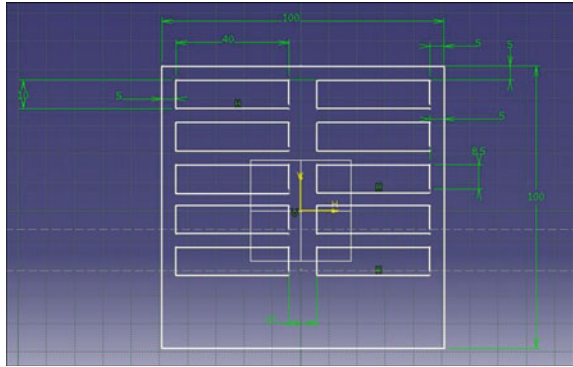


**Table 11.1** Selected process parameters

Process parameters	Different levels		
	1	2	3
Abrasive flow rate	0.44	0.54	0.64
Water pressure	280	300	320
Standoff distance	1	2	3

A = Abrasive flow rate (g/min), B = Water pressure (MPa), C = Standoff distance (mm)

**Fig. 11.2** CAD model for an array of rectangular cut



### 11.3 Results and Discussions

The rectangular slab has been cut in aluminum alloy 6061 in order to study the machinability characteristics of the material. Figure 11.3 Depict the machining of rectangular slot of aluminum alloy 6061 T6. The characteristics are evaluated by measuring MRR and SR for the machined aluminum alloy material. Practically the cut surfaces are tapered due to the inability of the flow of the abrasive particle which spreads out when it comes out of the nozzle in between workpiece and nozzle. The microscopic images of the rectangular slabs have been taken and their surfaces are observed. In total, 27 numbers of experiments have been performed on aluminum alloy sheet. In Table 11.2, MRR and SR have been estimated to compare trends with respect to water pressure (mpa), abrasive flow rate (g/min), and standoff distance (mm). The rate of machining should be higher and the surface roughness should be lower for reducing the cost of the product so that it can be used for production

**Fig. 11.3** Machining of the rectangular slot of aluminum alloy 6061 T6

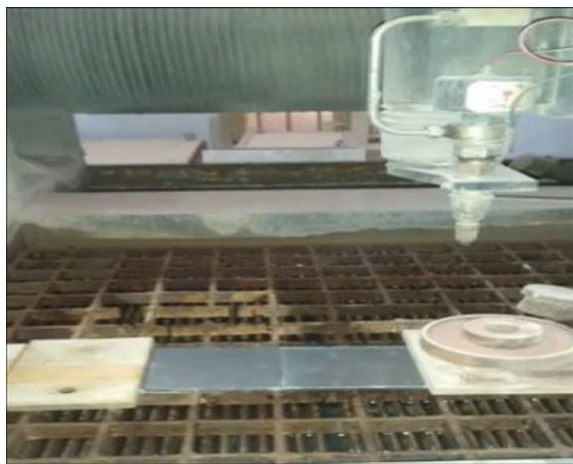




**Table 11.2** Experimental results

Exp. no.	Water pressure (MPa)	Abrasive flow rate (g/min)	Standoff distance (mm)	MRR (g/s)	SR ( $\mu\text{m}$ )
1	280	0.44	1	47.51	3.21
2	280	0.54	1	48.12	2.55
3	280	0.64	1	49.47	2.37
4	280	0.44	2	44.65	3.12
5	280	0.54	2	46.61	3.07
6	280	0.64	2	50.75	2.70
7	280	0.44	3	47.20	2.85
8	280	0.54	3	47.51	2.63
9	280	0.64	3	49.73	2.55
10	300	0.44	2	49.07	1.89
11	300	0.54	2	52.53	2.07
12	300	0.64	2	55.26	1.58
13	300	0.44	3	46.61	2.26
14	300	0.54	3	50.75	2.11
15	300	0.64	3	52.53	1.70
16	300	0.44	1	47.20	2.59
17	300	0.54	1	49.73	2.45
18	300	0.64	1	53.67	2.15
19	320	0.44	3	58.27	1.72
20	320	0.54	3	60.14	1.62
21	320	0.64	3	62.01	1.56
22	320	0.44	1	57.37	1.79
23	320	0.54	1	61.12	1.80
24	320	0.64	1	63.71	1.60
25	320	0.44	2	58.72	1.89
26	320	0.54	2	60.14	2.06
27	320	0.64	2	61.12	2.04

purpose in the industries. Surface roughness is considered as a response parameter to investigate the accuracy and precession of the rectangular cuts. These factors should be as small as possible which will help in achieving perfect rectangular slab.

### 11.3.1 Calculation of Grey Relational Coefficient (GRC)

In grey relational analysis, trial results were first normalized and then the grey relational coefficient (GRC) was calculated from the normalized experimental data to definite the relationship between the desired and actual experimental records. It is observed that the experiment number one with process parameters at 280 MPa water pressure, 0.44 g/min abrasive flow rate and 1 mm standoff distance gives the highest GRC value for surface roughness. Similarly, process parameters at 320 MPa water pressure, 0.64 g/min abrasive flow rate and 1 mm standoff distance gives the highest GRC value for material removal rate.

### 11.3.2 Grey-Fuzzy Logic System

The grey relation coefficient for two response parameters is considered as two input variables in the fuzzy logic system. In Fig. 11.4, triangular membership function is considered taking into consideration the works from past researchers. Range of linguistic variables are Low [0, 0.25, 0.5], Medium [0.25, 0.5, 0.75], and High [0.5, 0.75, 1].

In grey-fuzzy relational analysis, greater the value of grey-fuzzy relational grade of the trials confirms that the corresponding experimental solution is the optimum condition for multi-objective optimization and gives enhanced engineering material quality [6].

From Table 11.3, it is clear that experiment number 24 with process parameters as WP = 320 MPa, AFR = 0.64 kg/min, and SOD = 1 mm has the best multiple performance characteristics among 27 set of trials, because it has the highest grey-fuzzy relational grade of 0.784. The values of corresponding response parameters to the highest grey-fuzzy relational grade are MRR = 63.72 kg/min and SR = 1.60  $\mu$  mm.

**Fig. 11.4** Linguistic variables for GRC response values

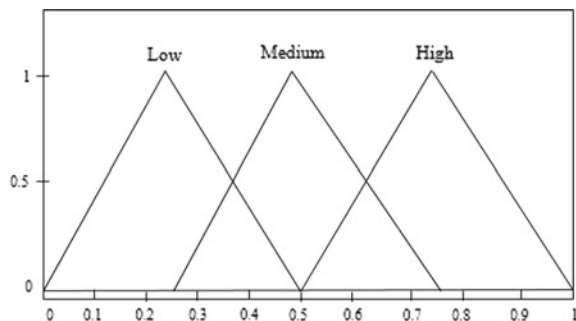


**Table 11.3** Grey-fuzzy relation grade (GFRG) with rank

Sl no.	GFRG	Rank
1	0.249	27
2	0.482	20
3	0.501	18
4	0.252	26
5	0.341	25
6	0.486	19
7	0.411	24
8	0.472	21
9	0.504	16
10	0.509	12
11	0.507	13
12	0.557	10
13	0.461	23
14	0.506	14
15	0.543	11
16	0.468	22
17	0.505	15
18	0.502	17
19	0.613	7
20	0.663	4
21	0.763	2
22	0.655	5
23	0.707	3
24	0.784	1
25	0.601	9
26	0.607	8
27	0.634	6

### 11.3.3 Analysis of MRR and SR with Process Parameters

The variations of the output parameters, i.e., material removal rate and surface roughness have been studied by plotting main effect graphs with respect to abrasive flow rate, water pressure, and standoff distance.

In Fig. 11.5, MRR has been observed to increase with the increase in water pressure. It was observed that increase in water pressure increases the MRR because on increasing the water pressure the kinetic energy of the abrasive particles increases which improves its MRR capability. When the abrasive flow rate is increased then MRR increased up to certain value after that it decreases. This happens because when abrasive flow rate increases beyond a certain value the abrasive particles start

**Fig. 11.5** Variation of MRR with **a** water pressure, **b** abrasive flow rate, **c** standoff distance

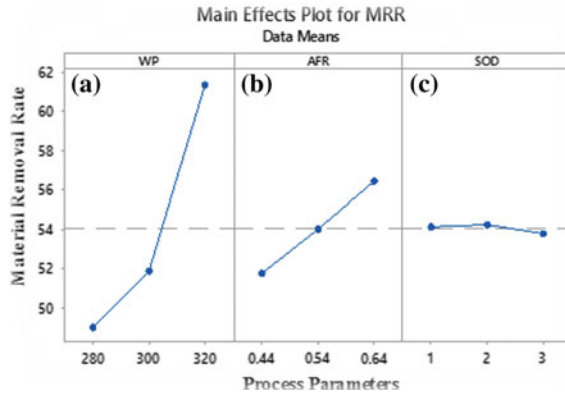
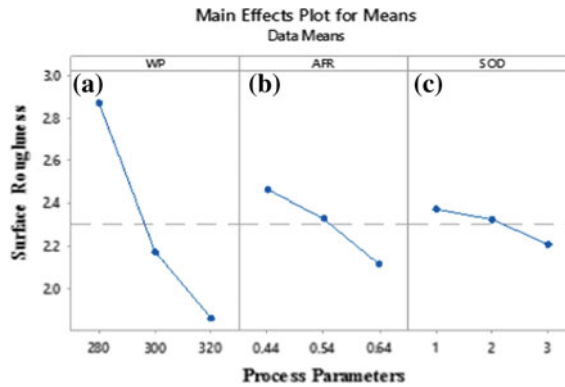


**Fig. 11.6** Variation of SR with **a** water pressure, **b** abrasive flow rate, **c** standoff distance



colliding among themselves which breaks their sharp cutting edges, consequently, MRR decreases. But when standoff distance increases then the jet is expanded before impingement and the diameter of the jet increases which reduces the kinetic energy density and also decreases the efficiency to hit at the pinpoint of the material which results in decrease of MRR.

It is also seen in Fig. 11.6 that the value of SR increases with increase in standoff distance and abrasive flow at different levels because in both the cases kinetic energy of the abrasive particles decreases because of increase in diameter of the jet and due to the collision of the particles among themselves, respectively.

### 11.3.4 Analysis of Variance

Table 11.4 clearly depicts that water pressure has the highest contribution among the three process parameters with a value of 70.8%. Standoff distance is the least influential parameter for multi-performance optimization of MRR and SR.

**Table 11.4** Analysis of variance for GFRG

Source	DF	SS	MS	F	P	A
WP	2	0.3082	0.1541	53.74	0.000	70.08
AFR	2	0.0619	0.0309	10.81	0.001	14.09
SOD	2	0.0122	0.0061	2.14	0.144	2.79
Error	20	0.0573	0.0028			13.04
Total	26	0.4398				100.0

A = % Contribution

Table 11.5 depicts the response value of grey-fuzzy relation grade for different levels of process parameters. Deviation in GFRG value is found to be maximum in case of water pressure with the variation of maximum to minimum value of 0.258778. Least deviation can be seen in the case of abrasive flow rate. The regression equation for multi-performance optimization GFRG has been stated below:

Regression equation for multi-objective optimization GFRG has been stated below:  $GFRG = 0.5290 - 0.1181 A(1) - 0.0226 A(2) + 0.1407 A(3) - 0.0602 B(1) + 0.0032 B(2) + 0.0570 B(3) + 0.0102 C(1) - 0.0297 C(2) + 0.0194 C(3)$

**Table 11.5** Response table for the Grey-fuzzy reasoning grade (GFRG)

Level	WP (MPa)	AFR (g/min)	SOD (mm)
1	0.410889	0.539222	0.408778
2	0.506444	0.499333	0.532222
3	0.669667	0.548444	0.586666
Max – Min	0.258778	0.049111	0.177888
Rank	1	3	2

**Table 11.6** Coefficient of regression equation for GFRG

Term	B	C	D	E
Constant	0.5290	0.0103	51.33	0
<i>WP</i>				
280	-0.1181	0.0146	-8.10	0
300	-0.0226	0.0146	-1.55	0.137
<i>AFR</i>				
0.44	-0.0602	0.0146	-4.13	0.001
0.54	0.0032	0.0146	0.22	0.827
<i>SOD</i>				
1	0.0102	0.0146	0.70	0.491
2	-0.0297	0.0146	-2.04	0.055

**Table 11.7** Comparison of results obtained from initial and optimal machining condition

Levels	Initial machining parameters level	Optimal machining parameters level
	WP = 280, AFR = 0.54, SOD = 1	WP = 320, AFR = 0.64, SOD = 1
MRR	49.224	64.81
SR	2.65	1.72
GFRG	0.482	0.784
Improvement in GFRG		0.302

Coefficient of the regression equation for GRFG is mentioned in Table 11.6. It is clear from the table is that the P-value of water pressure is minimum and is the most influential process parameter.

Improvement in GFRG value of 0.302 has been stated in Table 11.7 with initial machining level, i.e., WP = 280 MPa, AFR = 0.54 g/min and SOD = 1 mm and optimal machining condition, i.e., WP = 320 MPa, AFR = 0.64 g/min and SOD = 1 mm. This enhancement of GFRG value to get the desired output by performing less number of experiment.

### 11.3.5 Characteristics of Machined Surface

Leica DM 2500 M trinocular metallurgical microscope is shown in Fig. 11.7, which is used for the optical micrograph of the rectangular cut and for the measurement of the output parameters.

Figure 11.8 shows the variation of the surface profile for the optimum set of process parameters. Abrasive particles can be seen embedded in the material after the machining process which is due to the high water pressure at 320 MPa and low standoff distance at 1 mm.

All the three input parameters affect the MRR and SR but water pressure is the most significant factor for changing the MRR and SR. When all the three parameters are changed then the effect of process parameters on MRR and SR would be different because it will show the combined effect of all parameters and sometimes the effect of water pressure dominates over other. So, there are deviations in the result of the experiment which can be seen in Table 11.2.

**Fig. 11.7** Metallurgical optical microscopes



**Fig. 11.8** Optical microscopic images at WP = 320 MPa, AFR = 0.64 kg/min, and SOD = 1 mm



## 11.4 Artificial Neural Network (ANN) Prediction

Selection of the optimal ANN architecture is used for prediction which is usually decided by hit and trial method, choosing the one which gives the lowest value of mean square error (MSE). Among several ANN architectures tried, it is found that the 3-5-2 architecture provides the minimum MSE value. Further forward and reverse mapping using ANN tool is observed with five numbers of nodes for 27 sets of the experiment.

### 11.4.1 Forward Mapping

Forward mapping deals with predicting the responses/outputs of the AWJM process for known sets of input conditions. It thus fulfills the end user's requirements of achieving the desired responses for varying values of AWJM process parameters. In forward mapping, the end user may also obtain the uncertain response values for a new set of AWJM process parameters.

When comparison is made between the experimental and ANN-predicted values of MRR and SR, respectively, for the considered AWJM process, and it is interesting to observe that for all the two responses, the ANN-predicted responses closely match with those obtained experimentally. It is also observed that the average prediction errors for MRR and SR are only 2.45% and 3.24%, respectively, which confirm the developed ANN model to almost accurately predict the output responses for a given set of AWJM process parameters.

### 11.4.2 Reverse Mapping

An ANN model is also established for reverse mapping of the considered AWJM process based on a 2-5-3 ANN architecture. The reverse model is now specifically applied for a single input dataset which can be thought of as the requirement of the end user, and it successfully predicts the necessary AWJM process parameter settings to achieve those desired response values. For the response values of MRR = 63 g/min and SR = 1.7  $\mu\text{m}$ , the corresponding AWJM process parameters are to be set at WP = 320 MPa, AFR = 0.64 kg/min and SOD = 1 mm respectively.

During the comparison of simulated and ANN-predicted water jet pressure values, ANN-predicted abrasive flow rate values are studied, it is observed that the developed reverse ANN model is quite successful in predicting both water pressure and abrasive flow rate as process parameters. The developed reverse ANN model is also capable to successfully predict the standoff distance.



## 11.5 Conclusion

The present research work develops optimization system using GRA and fuzzy logic method for instantaneously optimizing multiple performance characteristics of MRR and SR in AWJM.

Based on the above experimental investigation as well as analysis, the following conclusions are presented:

- The optimal AWJM parametric combination of  $WP = 320$  MPa,  $AFR = 0.64$  g/min, and  $SOD = 1$  mm has been determined using grey-fuzzy logic with an aim to achieve minimum AWJM surface roughness and maximum material removal rate of aluminum alloy 6061.
- Analysis of variance results confirmed that the water pressure is the most significant parameter followed by abrasive flow rate, whereas standoff distances do not significantly affect the multi-performance characteristics of response parameters.
- It is seen that the error in prediction for MRR and SR are only 2.45% and 3.24% respectively which confirm the accuracy of developed ANN model for predicting the values of the response parameter of AWJM. Similarly, the errors in prediction for three process parameters, i.e., WP, AFR, and SOD were found to be 2.92%, 4.04%, and 3.52%, respectively.
- Evaluation of machining performance achieved under initial and optimal condition of machining designates and enhancement of GFRG of 0.302 for predicted values.

## References

1. Liu, S., Forrest, J.Y.-L.: Grey Systems-Theory and application. Springer (2012)
2. Parikh, P.J., Lam, S.S.: Parameter estimation for abrasive water jet machining process using neural networks. *Int. J. Adv. Manuf. Technol.* **40**, 497–502 (2009)
3. Jai Aultrin, K.S., Dev Anand, M.: Experimental framework and study of AWJM process for an aluminium 6061 alloy using RSM. In: 2014 International Conference on Control, Instrumentation, Communication and Computational Technologies (ICCCCT), 2014, pp. 1432–1440
4. Vundavilli, P.R., Parappagoudar, M.B., Kodali, S.P., Benguluri, S.: Fuzzy logic-based expert system for prediction of depth of cut in abrasive water jet machining process. *Knowl. Based Syst.* **27**, 456–464 (2012)
5. Venkata Rao, R.: Modeling and Optimization of Machining Processes. Springer Series in Advanced Manufacturing (2011)
6. Cojbasic, Z., Petkovi, D.: Surface roughness prediction by extreme learning machine constructed with abrasive water jet. *Precis. Eng.* **43**, 86–92 (2016)
7. Aydin, G., Karakurt, I., Hamzacebi, C.: Artificial neural network and regression models for performance prediction of abrasive water jet in rock cutting. *Int. J. Adv. Manuf. Technol.* **75**, 1321–1330 (2014)

# Chapter 12

## Formulating Empirical Model of MRR in Near-Dry EDM



Gurinder Singh Brar , Nimo Singh Khundrakpam   
and Dharmpal Deepak 

**Abstract** In this paper, material removal rate (*MRR*) of near dry EDM which use two-phase liquid and gas instead of single-phase liquid dielectric medium is investigated. Experiment is conducted with a Taguchi OA L<sub>9</sub> considering three input parameters viz. discharge current, duty factor and tool rotational speed with three levels each. The effect of input parameters on *MRR* is studied. The experimental results show that discharge current is the most effective input parameters on the *MRR* followed by the duty factor. Moreover, discharge current has most percentage of contribution of 91.51% and duty factor has 10.5% on *MRR*. The empirical models of *MRR* are formulated from the experimental results. Finally, the empirical models are examined and validated.

**Keywords** EDM · Near dry · MRR · Empirical model

### 12.1 Introduction

In day today scenario, improvement in the machining process is key research area in the field of manufacturing. Near-dry EDM is one of most recent research areas in EDM that use liquid-gas mixture as dielectric medium instead of liquid dielectric medium. Air and oxygen are commonly used in the ND-EDM. The air is mixed with the liquid dielectric medium and supplied in between the inter-electrode gap between the electrode. Due to absence of mechanical cutting force, EDM is used to cut complex and precise geometric shapes material components, such as heat-treated

---

G. S. Brar (✉)

Department of Mechanical Engineering, National Institute of Technology Uttarakhand, Srinagar (Garhwal) 246174, India  
e-mail: [brar.gurinder@gmail.com](mailto:brar.gurinder@gmail.com)

N. S. Khundrakpam

Department of Mechanical Engineering, National Institute of Technology Manipur, Imphal 795004, India

D. Deepak

Department of Mechanical Engineering, Punjabi University, Patiala 147002, India

© Springer Nature Singapore Pte Ltd. 2020

M. S. Shunmugam and M. Kanthababu (eds.), *Advances in Unconventional Machining and Composites*, Lecture Notes on Multidisciplinary Industrial Engineering, [https://doi.org/10.1007/978-981-32-9471-4\\_12](https://doi.org/10.1007/978-981-32-9471-4_12)

141

tool steels, composites, super alloys, ceramics, carbides, heat resistant steels etc. Now, EDM is widely used in aerospace, aeronautics, nuclear industries and die and mould making industries. EDM has also come into the new fields such as sports, medical and surgical, instruments, optical, including automotive R&D areas. In spite of its advantages, EDM has many limitations such as low MRR and surface finish due to short circuit with higher tool wear rate and also produced carcinogenic substances due to burning of dielectric medium [1]. Thus, researcher focused on another dielectric medium instead of liquid dielectric medium. As compared to conventional EDM, ND-EDM can improve the MRR at low energy levels [2]. Moreover, ND-EDM has good surface finish, lower micro-cracks and craters from the wet EDM. Use of tool rotational attachment in the ND-EDM can improved material removal rate (MRR), tool wear rate (TWR) [3]. Many researcher have carried out the experiment on the different two-phase near dry dielectric medium such as kerosene-air [4, 5], deionized water-air [6] and air-water [7–9]. Moreover, ND-EDM produces negligible toxic fumes and it also no circuit limit at lower boundary [10]. Therefore, it is essential to study the effect of input parameters on MRR of ND-EDM and also essential to formulate acceptable empirical model of MRR. The non-linear regression analysis based on power function for MRR of ND-EDM is not revealed from the literature review. Thus, this paper mainly focused on the formulation of empirical models the MRR of ND-EDM using non-linear regression analysis based on power function and also based on the power and exponential function.

## 12.2 Experimental Setup and Methodology

In conventional EDM simply wet EDM, liquid dielectric medium is used for the machining process. In ND-EDM, liquid dielectric medium is replaced by the two-phase dielectric medium. In order to fulfil the requirement, a minimum quality lubrication (MQL) system is used to produce and supply the two-phase near dry dielectric medium at the inter electrode gap between the electrodes. In this experiment, liquid dielectric medium (deionized water) is mixed with compressed air at the MQL system and then supply the two-phase near dry mist at the inter electrode gap. The flow of the dielectric medium is synchronized by an MQL flow synchronizer with a solenoid valve which works on the pulsating AC.

Schematic working diagram of ND-EDM is shown in Fig. 12.1. An electrical operated solenoid valve is used to control the supply of compressed air to the MQL device through the tool electrode. The mild steel EN-8 material (0.4% C, 0.25% Si, 0.8% Mn, 0.05% S and 0.05% P) is used as workpiece and copper as tool electrode which has 10 mm external diameter with a hole diameter of 2 mm.

Weight loss method is used to measure the MRR and given in Eq. 12.1.

$$\text{MRR} = \frac{[\Delta W]}{\rho_w t} \times 1000 \text{ mm}^3/\text{min} \quad (12.1)$$

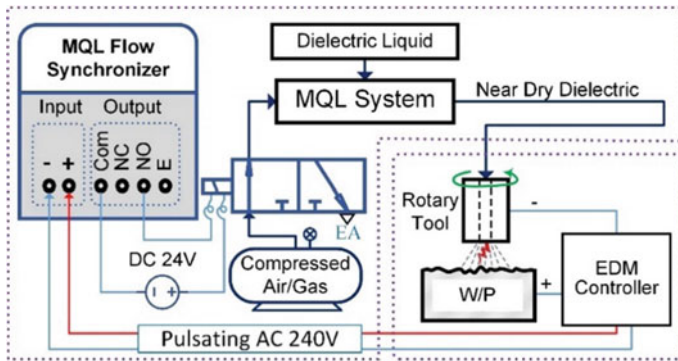


Fig. 12.1 Schematic working diagram of ND-EDM [11]

Here,  $\rho_w$  is the density of EN-8 workpiece and value is  $7.8 \text{ g/cm}^3$ ;  $\Delta W$  is the material remove from workpiece in g;  $t$  is the machining time.

ND-EDM exhibits the advantage of good machining stability and smooth surface finish at low discharge energy [12], thus experiment is focused to machine at low discharge energy. Thus, essential input parameter is revealed from the pilot test and literature review. The three input parameters namely discharge current, duty factor and tool rotational speed are chosen for the experiment. The basic parameters and input parameters are tabulated in Table 12.1 and Table 12.2 respectively. Taguchi  $L_9$  OA design is used to collect the raw values of MRR. The raw data of MRR is transferred into S/N ratio for Taguchi study. MRR has ‘larger-the-better, LB’ characteristics, thus corresponding value of S/N ratio is measured by using Eq. 12.2. Effect of each process parameters on the machining performance is determined on both raw data and S/N ratios to find the significant process parameters.

Table 12.1 Basic parameters of the experiment

Process parameter	Unit	Values
Tool polarity	–	Negative
Machining time	min	20
Tool lifting time	s	0.2
Gap voltage	V	50
Working pressure	bar	5 bar

Table 12.2 ND-EDM process parameters and levels

Process parameters	Units	Levels
A: discharge current	A	2, 5, 8
B: duty factor	–	0.7, 0.8, 0.9
C: tool rotational speed	rpm	100, 300, 500

$$S/N_{LB} = -10 \log_{10} \left[ \frac{1}{n} \sum_{i=1}^n \frac{1}{y_i^2} \right] \tag{12.2}$$

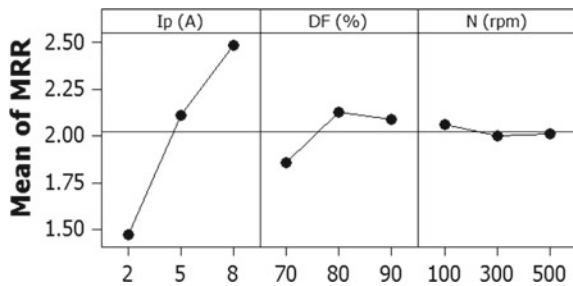
### 12.3 Results and Analysis

Using Taguchi L<sub>9</sub> OA table, three runs for each trial is carried out and measured the MRR. The raw data of MRR is transferred into corresponding S/N ratios considering ‘Higher-the-better’ characteristics. The measured raw data of MRR and corresponding S/N ratios are shown in Table 12.3.

**Table 12.3** Raw and SN data of MRR

Trial	A	B	C	MRR (mm <sup>3</sup> /min)			Average of MRR	S/N ratio of MRR
				1	2	3		
1	1	1	1	1.38	1.34	1.38	1.367	2.713
2	1	2	2	1.61	1.64	1.24	1.497	3.503
3	1	3	3	1.53	1.56	1.55	1.547	3.788
4	2	1	2	1.96	1.98	1.91	1.950	5.801
5	2	2	3	2.21	2.26	2.23	2.233	6.979
6	2	3	1	2.18	2.17	2.12	2.157	6.676
7	3	1	3	2.21	2.23	2.32	2.253	7.057
8	3	2	1	2.61	2.58	2.77	2.653	8.476
9	3	3	2	2.58	2.57	2.53	2.560	8.165

**Fig. 12.2** Mean effect plot of MRR



### 12.3.1 Analysis of MRR

The mean and corresponding mean of S/N ratio of MRR is shown in the Figs. 12.2 and 12.3 respectively. It is observed that increase of discharge current significantly increased both the mean and mean of S/N ratio of MRR. The discharge energy increases with the increase of discharge current, similar trend is also found by Pandey et al. [13]. Thus, the ionization of dielectric medium at inter electrode gap (IEG) improved that produce more thermal energy that increases melting and evaporation rate. As a result, MRR increases with the increase of discharge current. Both the mean and mean of S/N ratio of MRR initially increases then decreases with the increase of duty factor which has similar trend observed by Pandey et al. [13]. This is due to increase of duty factor increases the sparking duration thus more thermal energy is supplied at the IEG caused increase in MRR. However, further increase in the duty factor reduces the cooling effect and unwanted restriction of spark on the machined surface occur, thus reduces the MRR. While, increase in the tool rotational slightly decreases the mean and S/N ratio of mean of MRR due to disturbing of sparking at localize spot. Analysis of variance (ANOVA) is carried out on the mean of MRR and results are shown in Table 12.4. The result shows most significant process parameter is discharge current with highest percentage of contribution (% CB) of 91.51% followed by duty factor with 7.38% CB. Tool rotational speed has less percentage of contribution on MRR with a value 0.32%.

Fig. 12.3 Mean effect plot of S/N ratio of MRR

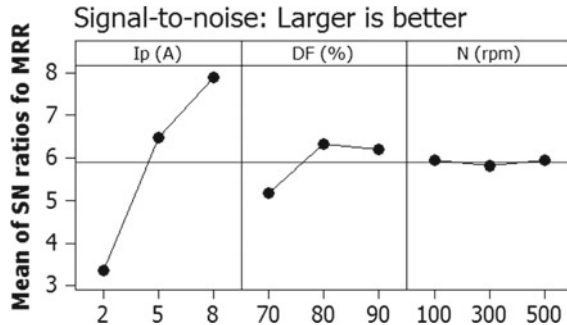


Table 12.4 ANOVA table for MRR

Source	DF	Seq SS	Adj MS	F	% CB
A: $I_p$	2	1.5930	0.7963	116.1	91.51
B: $DF$	2	0.1285	0.0642	9.37	7.38
C: $N$	2	0.0055	0.0027	0.41	0.32
Error	2	0.0137	0.0068		0.79
Total	8	1.7407			100

### Formation of empirical model of MRR

The empirical formula of *MRR* is based on nonlinear regression analysis using Minitab 16 software. Empirical formula of *MRR* is formulated with three independent variable such as discharge current, duty factor and tool rotational speed. Two empirical formula for *MRR* are formulated based on (a) power function and (b) power and exponential function.

**Empirical model of MRR based on power function.** Using power function, empirical model of *MRR* can be formulated as follows:

$$MRR = CI_p^a DF^b N^c \quad (12.3)$$

Here,  $I_p$ ,  $DF$  and  $N$  are the independent variable on dependent variable *MRR*;  $C$ ,  $a$ ,  $b$  and  $c$  are the constant to be verified.

In order to simplify in the regression analysis, natural logarithm of Eq. 12.3 is taken and converted into a linear equation (Eq. 12.4).

$$\ln MRR = \ln C + a \ln I_p + b \ln DF + c \ln N \quad (12.4)$$

**Empirical model of MRR based on power and exponential function.** Using power and exponential function, empirical model of *MRR* can be formulated as follows:

$$MRR = CI_p^a DF^b \exp\left(\frac{c}{N}\right) \quad (12.5)$$

Here,  $I_p$ ,  $DF$  and  $N$  are the independent variable of dependent variable, *MRR*;  $C$ ,  $a$ ,  $b$  and  $c$  are the constant to be verified. In order to simplify in the regression analysis, natural logarithm of Eq. 12.5 is taken and converted to a linear equation (Eq. 12.6).

$$\ln MRR = \ln C + a \ln I_p + b \ln DF + \frac{c}{N} \quad (12.6)$$

Validation of empirical model of *MRR*. Non-linear regression analysis is performed to formulate empirical model of *MRR* based on power function and also based on power and exponential function. Regression coefficient values of the *MRR* are evaluated for each model. To perform the non-linear regression analysis based on power function, the data of *MRR*,  $I_p$ ,  $DF$  and  $N$  from the Table 12.3 are converted into  $\ln MRR$ ,  $\ln I_p$ ,  $\ln DF$  and  $\ln N$ . Regression coefficient of *MRR* for power function is evaluated and tabulated in Table 12.5. From the Table 12.5, the value of  $S$  stand for the residual standard deviation of coefficient is very small, thus have higher accuracy. Moreover,  $P$  value of coefficient shows that constant term,  $I_p$  and  $DF$  are most near to zero and have more significant on the model.  $R^2$  and  $R^2$  (adj) values are found as 97.51% and 96.02% respectively. It signified the model is within the acceptable range.

**Table 12.5** Evaluated regression coefficients of MRR based on power function

Term	Coefficient	S	T	P
ln C	-1.95328	0.699092	-2.794	0.038
ln $I_p$	0.38137	0.027919	13.6599	0.000
ln DF	0.47818	0.156542	3.0547	0.028
ln N	-0.00303	0.023934	-0.1267	0.904

S = 0.0482146,  $R^2 = 97.51\%$ ,  $R^2$  (adj) = 96.02%

The empirical model of MRR based on the power function is depicted in Eqs. 12.7 and 12.8.

$$\ln MRR = -1.95328 + 0.38137 \ln(I_p) + 0.47818 \ln(DF) - 0.00303 \ln(N) \tag{12.7}$$

$$MRR = \frac{0.141808 I_p^{0.381374} DF^{0.4788183}}{N^{0.00303}} \tag{12.8}$$

To perform the non-linear regression analysis based on power and exponential function, the data of MRR,  $I_p$ , DF and N from the Table 12.3 are converted into ln MRR, ln  $I_p$ , ln DF and (1/N). Regression coefficient of MRR for power and exponential function is evaluated and tabulated in Table 12.6. It is observed that the S value of coefficient is also very small and P value of coefficient shows that constant term,  $I_p$  and DF are most near to zero, thus the terms are significant to the model.  $R^2$  and  $R^2$  (adj) values are found as 97.52% and 96.02% respectively. It signified the model is within the acceptable range. Thus, both the empirical model is validated.

The empirical model of MRR based on the power function and exponential function is depicted in Eqs. 12.9 and 12.10.

$$\ln MRR = -1.98905 + 0.38137 \ln(I_p) + 0.47818 \ln(DF) + \left(\frac{0.10337}{N}\right) \tag{12.9}$$

$$MRR = 0.136825 I_p^{0.381374} DF^{0.47818} \exp\left(\frac{0.10337}{N}\right) \tag{12.10}$$

**Table 12.6** Evaluated regression coefficients of MRR based on power and exponential function

Term	Coefficient	S	T	P
ln C	-1.98905	0.69719	-2.853	0.036
ln $I_p$	0.38137	0.027898	13.6702	0.000
ln DF	0.47818	0.156425	3.0569	0.028
ln N	0.10337	0.673348	0.1535	0.884

S = 0.0481785,  $R^2 = 97.52\%$ ,  $R^2$  (adj) = 96.02%



## 12.4 Conclusions

MRR of ND-EDM has been discussed with Taguchi  $L_9$  OA. The following valuable outcomes are found from the experimental.

1. Discharge current has highest percentage of contribution of 91.51% followed by duty factor with 7.38%.
2. Tool rotational speed has less percentage of contribution on MRR with a value 0.32%.
3. The empirical formula of MRR base on power function and combination of power and exponential function has been formulated. Both the empirical models have less value of the residual standard deviation and within the acceptable range.

**Acknowledgements** The authors acknowledge IKG Punjab Technical University, Kapurthala and National Institute of Technology Manipur, for providing the facility to conduct the experiments.

## References

1. Leão, F.N., Pashby, I.R.: A review on the use of environmentally-friendly dielectric fluids in electrical discharge machining. *J. Mater. Process. Technol.* **149**(1–3), 341–346 (2004)
2. Gholipour, A., Baseri, H., Shabgard, M.R.: Investigation of near dry EDM compared with wet and dry EDM processes. *J. Mech. Sci. Technol.* **29**(5), 2213–2218 (2015)
3. Khundrakpam, N.S., Brar, G.S., Deepak, D.: Experimental investigation on EDM processes by tool rotating speed. *Bonfring Int. J. Ind. Eng. Manag. Sci.* **6**(4), 171–173 (2016)
4. Fujiki, M., Ni, J., Shih, A.J.: Investigation of the effects of electrode orientation and fluid flow rate in near-dry EDM milling. *Int. J. Mach. Tools Manuf.* **49**(10), 749–758 (2009)
5. Tao, J., Shih, A.J., Ni, J.: Near-dry EDM milling of mirror-like surface finish. *Int. J. Electr. Mach.* **13**, 29–33 (2008)
6. Khundrakpam, N.S., Singh Brar, G., Deepak, D.: Grey-Taguchi optimization of near dry EDM process parameters on the surface roughness. *Mater. Today Proc.* **5**(2), 4445–4451 (2018)
7. Tao, J., Shih, A.J., Ni, J.: Experimental study of the dry and near-dry electrical discharge milling processes. *J. Manuf. Sci. Eng.* **130**(1), 011002 (2008)
8. Dhakar, K., Pundir, H., Dvivedi, A., Kumar, P.: Near-dry electrical discharge machining of stainless steel. *Int. J. Mach. Mach. Mater.* **17**(2), 127–138 (2015)
9. Yang, J.J., Zuo, Z.J., Yu, W.X.: Experimental investigation on air-aided water EDM. *Adv. Mater. Res.* **148–149**, 471–474 (2010)
10. Dhakar, K., Dvivedi, A.: Parametric evaluation on near-dry electric discharge machining. *Mater. Manuf. Process.* **31**(4), 413–421 (2016)
11. Khundrakpam, N.S., Brar, G.S., Deepak, D.: Genetic algorithm approach for optimizing surface roughness of near dry EDM. *IOP Conf. Ser. Mater. Sci. Eng.* **376**(1), 012130 (2018)
12. Tao, J., Shih, A.J., Ni, J.: Near-dry EDM milling of mirror-like surface finish. *Int. J. Electr. Mach.* **13**(2008), 29–33 (2008)
13. Pandey, H., Dhakar, K., Dvivedi, A., Kumar, P.: Parametric investigation and optimization of near-dry electrical discharge machining. *J. Sci. Ind. Res. (India)* **74**(9), 508–511 (2015)

# Chapter 13

## A Model for Average Surface Roughness for Abrasive Waterjet Cut Metal Matrix Composites



N. R. Prabhu Swamy and S. Srinivas

**Abstract** Abrasive waterjet is a cool cutting technology with the ability to cut most of the difficult to cut materials. Average surface roughness value is a measure of surface finish of a manufactured product. Modeling of the average roughness value of aluminium–silicon carbide metal matrix composites by dimensional method technique is carried out for both cutting and deformation mode regions. Abrasive waterjet cutting experimentation is carried out on trapezoidal-shaped aluminium–metal matrix composites by varying the process parameters. The model results are in good relation with the experimental results for the cutting wear region. The deformation wear results have slightly more percentage of error in comparison with the cutting wear region. Average surface roughness value is measured along the depth of penetration with noncontact confocal microscope. The average results of the cutting and deformation wear region are considered for modeling.

**Keywords** Abrasive waterjet · Modeling · Cutting wear · Deformation wear

### 13.1 Introduction

Abrasive water jet (AWJ) is a cool cutting technology to cut difficult to cut materials such as tool steel, titanium, brass, concrete, rock, glass, polymer matrix composites, ceramic matrix composites and metal matrix composites (MMCs) [1, 2]. The advantages of using AWJ cutting includes cutting of complicated shapes, no thermal distortion, narrow kerf width, negligible heat affected zone, and environmental friendliness [3, 4]. Surface finish is an important parameter of any manufactured product. Average surface roughness ( $R_a$ ) value is one of the measures of surface finish.  $R_a$  of AWJ cut surface is influenced by a number of parameters such as hydraulic, abrasive, cutting, and work material properties. In AWJ cutting, the material removal takes place in two modes namely cutting wear and deformation wear [5–7]. The

---

N. R. Prabhu Swamy (✉) · S. Srinivas  
B.M.S. College of Engineering, Bengaluru 560019, India  
e-mail: [prabhuswamy.mech@bmsce.ac.in](mailto:prabhuswamy.mech@bmsce.ac.in)

present research work makes an attempt to find the  $R_a$  of cutting and deformation wear mode by noncontact-type surface roughness measurement.

Guo et al. [8], has investigated the surface topography of aluminium samples cut by AWJ. The cutting wear region is dominated by microstructure roughness and the deformation wear region is dominated by macrostructure waviness. The  $R_a$  increases with increasing the size of the abrasive particles. In the cutting wear region, microchipping takes place during cutting, making the cut surface smooth. Whereas during cutting in the deformation wear region the discontinuously and three-dimensional cutting takes place. Also, the inclination and oscillation of the jet contribute to the waviness and rougher  $R_a$  value in the region. Chen et al. [9], has investigated the  $R_a$  of ceramic, perspex, aluminium and mild steel plates. A smooth surface finish was seen at the top of the cut and the rough surface finish with striations towards the bottom of the cut. The fluctuations of the AWJ, vibration of the workpiece and nozzle and oscillations of the jet are also the reasons for the striations formation. Neusen et al. [10], has investigated the effect of waterjet pressure, traverse speed and abrasive flow rates on  $R_a$  of aluminium–silicon carbide and magnesium–silicon carbide MMCs. AWJ cutting experiments are conducted on aluminium reinforced with 7, 11, and 15% SiC particles and magnesium reinforced with 26.5% SiC particles.  $R_a$  measurement is done at depth of 12.7 mm from the top of the cut on the MMC samples. A low  $R_a$  value of 5  $\mu\text{m}$  is seen for cutting with higher waterjet pressure and higher abrasive flow rates. The  $R_a$  has increased with higher jet traverse speed and low abrasive flow rates. Hashish [11], also carried out research to find the  $R_a$  of aluminium reinforced with 15 and 25% of silicon carbide MMCs. Low traverse speed and high abrasive flow rates have given better  $R_a$ . Hamatani and Ramulu [12], has carried out an experimental investigation on  $R_a$  of AWJ machined Al6061–30% SiC MMCs. The  $R_a$  measurement is carried out at 1, 2.5, and 4 mm along the direction of the cut. The upper half of the cut had a smooth surface roughness of  $R_a$  value 1.75  $\mu\text{m}$  but the lower half resulted in the rougher surface roughness with  $R_a$  value of 2.4  $\mu\text{m}$ . Shanmughasundaram [13], has investigated the  $R_a$  of AWJ cut aluminium–graphite MMCs produced by squeeze casting.  $R_a$  is measured at top, middle and bottom positions of AWJ cut samples. The regression equation for  $R_a$  is developed and the experimental results are compared with it. The waterjet pressure has the highest influence on the  $R_a$ , followed by traverse speed and standoff distance. Naresh Babu and Muthukrishnan [14], have conducted experiments of AWJ cutting on brass-360 of 3 mm thick. The  $R_a$  was measured at the top, middle and the bottom of the cut. A regression model equation for  $R_a$  is being developed. The experimental results and the model results of  $R_a$  are compared. The high waterjet pressure and low abrasive flow rate have given better  $R_a$ .  $R_a$  is investigated for Titanium 7.0, 13.2, and 20.32 mm thick AWJ cut samples.  $R_a$  is measured at top and bottom of the cut at distance of 1 mm from the top and bottom edge. The top side  $R_a$  ranges from 2 to 5  $\mu\text{m}$  at low cutting speed whereas the bottom side  $R_a$  ranges from 3 to 30  $\mu\text{m}$ . The experiments results of  $R_a$  are validated with empirical model equation of  $R_a$  developed from regression analysis. The developed model results match well with the experimental results [15]. Wang [16] has developed a depth of cut model equation for alumina ceramics using dimensional analysis and the model results are validated

with the experimental results. Shanmugam et al. [17] has developed a model equation for kerf taper angle for alumina ceramics using dimensional analysis and validated the model results with the experimental results. Xu and Wang [18] has predicted model equation for depth of cut of alumina ceramics using dimensional analysis and compared the model and experimental results.

The literature review reveals that the research has been carried by many researchers in the area of  $R_a$  measurements at top, middle, and bottom of the cut of many materials such as aluminium, ceramic, mild steel, aluminium and magnesium metal matrix composites, and many more. However, there is a need to evaluate the  $R_a$  along the DOP to understand process capabilities of AWJ and to measure the  $R_a$  by noncontact surface roughness measurement technique. In view of this, the present research work is an attempt to find the  $R_a$  along the DOP with noncontact confocal microscope. Hence this research work is carried out to investigate the  $R_a$  along the DOP in aluminium–silicon carbide composites. To access the DOP, it was planned to use 70-mm-thick trapezoidal MMC blocks. Stir casting method will be used to manufacture the MMC blocks of different compositions.

## 13.2 Experimentation

To manufacture aluminium 6061 and silicon carbide particles (Al6061-SiCp) MMCs, aluminium 6061 (Al6061) was chosen as matrix material and silicon carbide particles (SiCp) of #80 mesh size was chosen as reinforcement.

Al6061-SiCp MMCs were produced by stir cast method. Figure 13.1 shows the geometry of trapezoidal specimens [19, 20]. The specimens were prepared by adding different weight percentage of SiC particles (5, 10 and 15%) to the Al6061

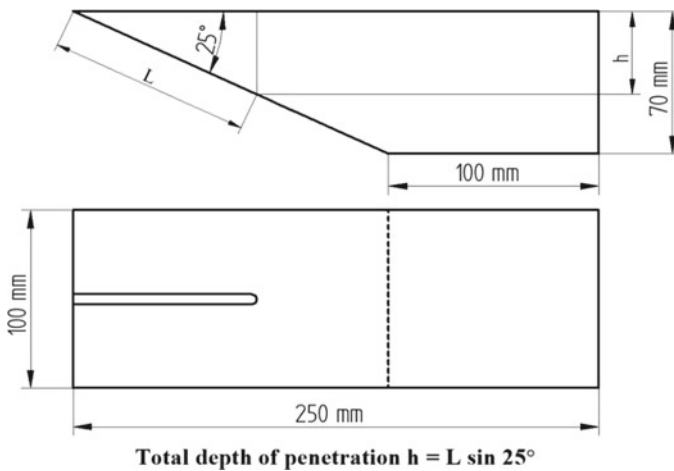


**Fig. 13.1** Geometry of trapezoidal specimens

matrix material. A custom-made split die of C-40 steel was used for the preparation of the specimen. The casting of Al6061–5%SiCp, Al6061–10%SiCp and Al6061–15%SiCp were prepared. Further, these specimens are subjected for AWJ cutting.

### 13.2.1 AWJ Cutting

To study the influence of dynamic parameters and their interactions on DOP in different MMCs, 3<sup>3</sup> full factorial experiments were considered. AWJ cutting experiments with #80 mesh size garnet abrasives were conducted on both Al6061 base alloy and Al6061–SiCp MMCs the dynamic parameters such as waterjet pressure, abrasive flow rate and jet traverse speed were varied at three different levels. Hence, 27 experiments were conducted on each specimen considered for experimentation. Table 13.1 refers to the process parameters employed for considering the full factorial experiments. Initial experiments of AWJ cutting on Al6061 base alloy were conducted to consider the process parameters levels and arrive at these values. The cutting experiments were conducted by keeping the focusing nozzle at a distance of 2 mm from the workpiece material. The jet was made to strike the material at an angle of 90° and traversed over the length of the specimen only once in order to observe the maximum penetration depth on the specimen. Jet splashed when it could not penetrate further into the specimen material. In total, 108 cutting experiments were carried out on the samples of Al6061 base alloy, Al6061–5%SiCp, Al6061–10%SiCp, and Al6061–15%SiCp MMCs.

**Table 13.1** Process parameters used in the experiments

Process parameters	Level-1	Level-2	Level-3
Water jet pressure (MPa)	100	200	300
Abrasive flow rate (kg min <sup>-1</sup> )	0.195	0.304	0.406
Traverse speed (mm min <sup>-1</sup> )	100	200	300
Abrasive-type and mesh size	Garnet, 80 mesh		
Orifice diameter (mm)	0.35		
Orifice material	Sapphire		
Focusing nozzle diameter (mm)	1.02		
Focusing nozzle material	Tungsten carbide		
Standoff distance	2 mm		

### 13.2.2 Measurement of DOP and $R_a$

The DOP measurement was carried out on all the 108 cutting experiments samples. The DOP was measured by measuring the slant length of cut ( $L$ ), the penetration of jet ( $h$ ), for each set of parameters. The DOP was determined using the relation,  $DOP = L \sin 25^\circ$  [19]. The DOP was also measured with a vernier height gauge to minimize the error.

The 108 cutting experiments samples were cut and subjected to  $R_a$  measurement. The  $R_a$  measurement is carried on a noncontact confocal microscopy at  $\times 5$  optical zoom with scan field of  $2.56 \text{ mm} \times 2.56 \text{ mm}$ . The  $R_a$  is measured along the surface of DOP from the top to bottom of the kerf insteps of  $2.56 \text{ mm}$ . The average reading of this area is taken as the  $R_a$  value.

### 13.2.3 Modeling of $R_a$

The  $R_a$  values are changing with respect to the depth along the DOP. From the top of the cut to about one-third of the depth along the DOP the region is regarded as the cutting wear region and the remaining region till the bottom of the cut is regarded as the deformation wear region. The cut surface is smooth with a good surface finish with lesser  $R_a$  values in the cutting wear region. Whereas the deformation region is marked with striations having higher  $R_a$  values. So for the purpose of the modeling, the average of the  $R_a$  values in the cutting and deformation wear region is considered.

### 13.2.4 Development of $R_a$ Model

Dimensional analysis method is followed for the development of  $R_a$  model.  $R_a$  depends on  $p$ -waterjet pressure (MPa),  $u$ -traverse speed (m/min), and  $\dot{m}$ -abrasive flow rate (N/min),

Mathematically,  $R_a = f(p, u, \dot{m})$  where  $f$  denotes function.

Solving for  $R_a$ , one dimensionless product is formed.

$$\pi_1 = R_a \text{sqrt}\left(\frac{p}{u\dot{m}}\right) \quad (1)$$

With power-law formulation, Eq. (1) can be rewritten as follows:

$$R_a = b \text{sqrt}\left(\frac{u\dot{m}}{p}\right)^a \quad (2)$$

Equation (2) is a generalized model equation for  $R_a$ , where  $a$  and  $b$  constants and can be determined from the experiments.

### 13.2.5 Model Verification

For the purpose of verification of the model, the data from the experiments are used in nonlinear regression analysis to find the values of a and b constants. The values of a and b are input in Eq. (2)

$$R_a = 10.27 \text{sqrt} \left( \frac{u\dot{m}}{p} \right)^{0.17} \quad (3)$$

Equation (3) gives the model equation for  $R_a$  for cutting wear region of Al6061 base alloy

$$R_a = 6.61 \text{sqrt} \left( \frac{u\dot{m}}{p} \right)^{-0.10} \quad (4)$$

Equation (4) gives the model equation for  $R_a$  for deformation wear region of Al6061 base alloy

$$R_a = 11.39 \text{sqrt} \left( \frac{u\dot{m}}{p} \right)^{0.20} \quad (5)$$

Equation (5) gives the model equation for  $R_a$  for cutting wear region of Al6061–5%SiC MMCs.

$$R_a = 6.21 \text{sqrt} \left( \frac{u\dot{m}}{p} \right)^{-0.14} \quad (6)$$

Equation (6) gives the model equation for  $R_a$  for deformation wear region of Al6061–5%SiC MMCs.

$$R_a = 10.90 \text{sqrt} \left( \frac{u\dot{m}}{p} \right)^{0.17} \quad (7)$$

Equation (7) gives the model equation for  $R_a$  for cutting wear region of Al6061–10%SiC MMCs.

$$R_a = 6.15 \text{sqrt} \left( \frac{u\dot{m}}{p} \right)^{-0.15} \quad (8)$$

Equation (8) gives the model equation for  $R_a$  for deformation wear region of Al6061–10%SiC MMCs.

$$R_a = 12.5 \text{sqrt} \left( \frac{u\dot{m}}{p} \right)^{0.20} \quad (9)$$

Equation (9) gives the model equation for  $R_a$  for cutting wear region of Al6061–15%SiC MMCs.

$$R_a = 7.22 \sqrt[3]{\left(\frac{u\dot{m}}{p}\right)^{-0.11}} \quad (10)$$

Equation (10) gives the model equation for  $R_a$  for deformation wear region of Al6061–15%SiC MMCs.

### 13.3 Results and Discussions

#### 13.3.1 DOP Results

Table 13.2 shows the experimental values of DOP for the Al6061 base alloy and Al6061–SiCp MMCs. From the table, it is clear that the maximum DOP are 54.62 mm, 54.44 mm, 54.40 mm, and 54.32 mm for Al6061 base alloy, Al6061–5%SiCp, Al6061–10%SiCp, and Al6061–15%SiCp MMCs, respectively, was observed at maximum waterjet pressure of 300 MPa, abrasive flow rate of  $0.406 \text{ kg min}^{-1}$  and at least traverse speed of  $100 \text{ mm min}^{-1}$ . In most of the experimental DOP values, the DOP decreases with increase in reinforcement percentages in Al6061–SiCp MMCs. This can be attributed to the fact that with the increase in the percentage of SiC particles, the hardness of the specimen is increased, thereby the cutting ability of the waterjet has decreased. In general, the DOP has increased with increase in waterjet pressure and abrasive flow rate but decreased with increase of jet traverse speed. The increase in waterjet pressure increased the cutting ability of the jet so that jet could penetrate to the larger depths. A marginal increase of DOP can be seen with increase of abrasive flow rate. With the increase in abrasive flow rate, more abrasives

**Table 13.2** Experimental values of DOP for the Al6061 base alloy and Al6061–SiC MMCs

Exp. no.	Pressure (Mpa)	Abrasive flow rate (kg/min)	Traverse speed (mm/min)	DOP (mm)			
				Al6061	Al6061–5% SiC	Al6061–10% SiC	Al6061–15% SiC
1	100	0.195	100	11.70	11.40	11.30	11.30
2	100	0.195	200	5.89	5.76	5.69	5.48
3	100	0.195	300	5.20	5.10	5.06	5.02
4	200	0.195	100	28.72	28.00	27.34	27.35
5	200	0.195	200	17.30	17.08	16.70	16.30
6	200	0.195	300	12.60	11.30	11.00	11.02
7	300	0.195	100	49.36	48.10	47.35	45.92

(continued)



**Table 13.2** (continued)

Exp. no.	Pressure (Mpa)	Abrasive flow rate (kg/min)	Traverse speed (mm/min)	DOP (mm)			
				Al6061	Al6061-5% SiC	Al6061-10% SiC	Al6061-15% SiC
8	300	0.195	200	29.88	27.76	27.86	24.84
9	300	0.195	300	19.66	19.30	19.18	18.42
10	100	0.304	100	11.84	11.44	11.40	11.38
11	100	0.304	200	6.31	6.06	5.69	5.20
12	100	0.304	300	5.72	5.62	5.48	5.42
13	200	0.304	100	29.70	29.70	29.18	28.10
14	200	0.304	200	17.50	17.30	17.25	16.36
15	200	0.304	300	12.64	12.40	12.36	12.34
16	300	0.304	100	52.62	52.42	52.36	52.30
17	300	0.304	200	30.10	29.86	29.50	29.30
18	300	0.304	300	21.60	21.40	21.11	21.00
19	100	0.406	100	11.90	11.58	11.48	11.46
20	100	0.406	200	6.46	6.18	5.78	5.40
21	100	0.406	300	6.30	6.10	6.00	5.81
22	200	0.406	100	29.71	29.70	29.50	28.91
23	200	0.406	200	17.60	17.48	17.36	16.78
24	200	0.406	300	13.38	12.58	12.54	12.36
25	300	0.406	100	54.62	54.44	54.40	54.32
26	300	0.406	200	32.86	31.60	31.08	31.06
27	300	0.406	300	21.68	21.60	21.12	21.08

are available for the interaction with the workpiece material. At the same time, more abrasive may accumulate in the mixing tube and obstruct the flow of high-velocity water also there can be improper mixing of abrasive with the waterjet. The abrasives can inter collide among themselves and damage the cutting edges of the abrasives. This reduces the cutting ability of the waterjet at very high abrasive flow rates. With the increase of traverse speed, less time was available for the cutting action, which has reduced the DOP.

### 13.3.2 $R_a$ Results

From the  $R_a$  results along the DOP, it is observed that the  $R_a$  values are changing with respect to the depth along the DOP. It is observed that the  $R_a$  values at the top of the cut are lower compared to the bottom of the cut. The same is observed for all

the experimental cutting conditions. Due to this reasons, the  $R_a$  values from the top of the cut to the about one-third of the depth along the DOP the region is regarded as the cutting wear region and the remaining region till the bottom of the cut is regarded as the deformation wear region. The cut surface is smooth with a good surface finish with lesser  $R_a$  values in the cutting wear region. The deformation region is marked with striations having higher  $R_a$  values.

### 13.3.3 Validation of the $R_a$ Model

The  $R_a$  values of both cutting and deformation wear region are used for of validation of  $R_a$  model. The experimental values of pressure (MPa), traverse speed (m/min) and abrasive flow rate (N/min) are input to the corresponding  $R_a$  model equations and their results are tabulated. Figure 13.2. Shows the  $R_a$  values predicted with the proposed model and the experimental values for Al6061 base alloy and Al6061-5%SiCp, Al6061-10%SiCp, and Al6061-15%SiCp MMCs for the cutting

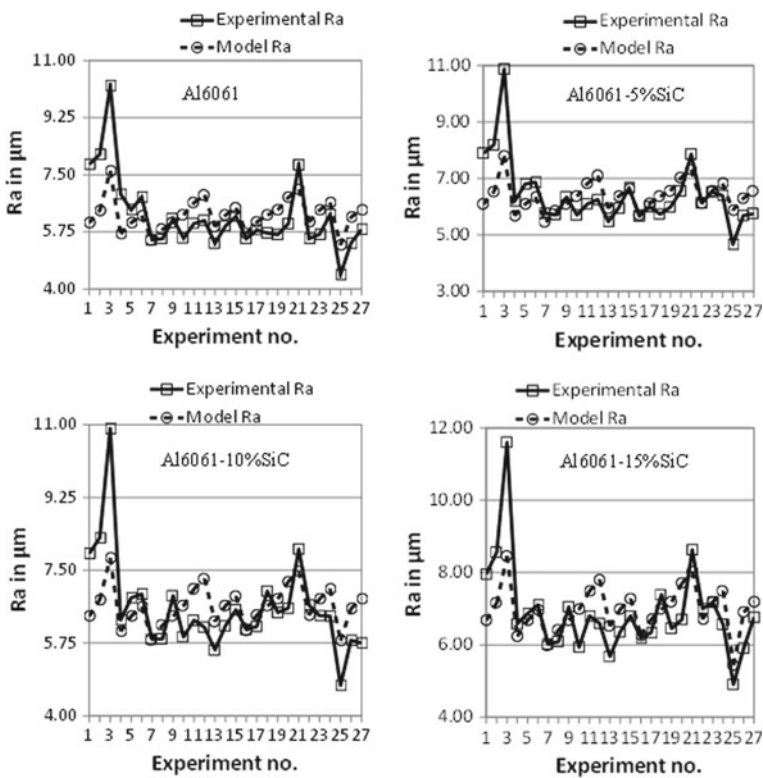


Fig. 13.2 Experimental and model  $R_a$  of cutting wear region

wear region. The percentage of error is calculated based on the equation number 11. The proposed model predicted almost 10–26%, 4–18%, and 0–20% lower or higher  $R_a$  values than the experimental  $R_a$  values for 100, 200, and 300 MPa waterjet pressures, respectively, for Al6061 base alloy. For MMCs, the proposed model predicted almost 7–28%, 5–29%, and 7–27% lower or higher  $R_a$  values than the experimental  $R_a$  values for 100 MPa waterjet pressures cutting conditions for Al6061–5%SiCp, Al6061–10%SiCp and Al6061–15%SiCp MMCs, respectively. Similarly, the proposed model predicted almost 0–9%, 4–12%, and 0–15% lower or higher  $R_a$  values than the experimental  $R_a$  values for 200 MPa waterjet pressures cutting conditions for Al6061–5%SiCp, Al6061–10%SiCp, and Al6061–15%SiCp MMCs, respectively. For 300 MPa waterjet pressures cutting conditions, the proposed model predicted almost 1–26%, 0–23%, and 1–17% lower or higher  $R_a$  values than the experimental  $R_a$  values for Al6061–5%SiCp, Al6061–10%SiCp, and Al6061–15%SiCp MMCs, respectively.

In both Al6061 base alloy and Al6061–SiCp MMCs, the percentage of variation between the experimental and model  $R_a$  values is being higher at 100 MPa waterjet pressure conditions compared to the other higher waterjet pressure conditions. This can be attributed to the fact that at 100 MPa waterjet pressure conditions, lesser kinetic energy is available. In addition, jet spreading takes place due to the less amount of kinetic energy of the waterjet. At 200 and 300 MPa waterjet pressures,  $R_a$  values show a close relation with the experimental  $R_a$  values when compared with  $R_a$  values of 100 MPa waterjet pressure. At higher waterjet pressures 200 MPa and above, the kinetic energy available with waterjet is more than that of 100 MPa waterjet pressure. Here also, jet spreading takes place but at a higher depth of the waterjet. In cutting wear mode, the material is subjected to shear at shallow angles of attack of abrasive particles and the cutting process is steady. With higher waterjet energy, the jet deflection is also very less. These factors will facilitate for more amount of time interaction of the waterjet with work piece. This contributes to achieving smooth surface finish with less  $R_a$  values in the cutting wear region. Thus, this analysis clearly indicates the suitability of proposed model for predicting  $R_a$  values of cutting wear region of Al6061 base alloy and Al6061–5%SiCp, Al6061–10%SiCp, and Al6061–15%SiCp MMCs.

Figure 13.3 shows the  $R_a$  values predicted with the proposed model and the experimental values for Al6061 base alloy and Al6061–5%SiCp, Al6061–10%SiCp, and Al6061–15%SiCp MMCs for the deformation wear region. The percentage of error is calculated based on the equation number 11. The proposed model predicted almost 4–29%, 1–18%, and 1–28% lower or higher  $R_a$  values than the experimental  $R_a$  values for 100, 200, and 300 MPa waterjet pressures, respectively, for Al6061 base alloy. The proposed model predicted almost 2–30%, 2–29%, and 0–27% lower or higher  $R_a$  values than the experimental  $R_a$  values for 100 MPa waterjet pressures cutting conditions for Al6061–5%SiCp, Al6061–10%SiCp, and Al6061–15%SiCp MMCs, respectively. Similarly, the proposed model predicted almost 0–20%, 1–17%, and 2–17% lower or higher  $R_a$  values than the experimental  $R_a$  values for 200 MPa waterjet pressures cutting conditions for Al6061–5%SiC, Al6061–10%SiC, and Al6061–15%SiC respectively.

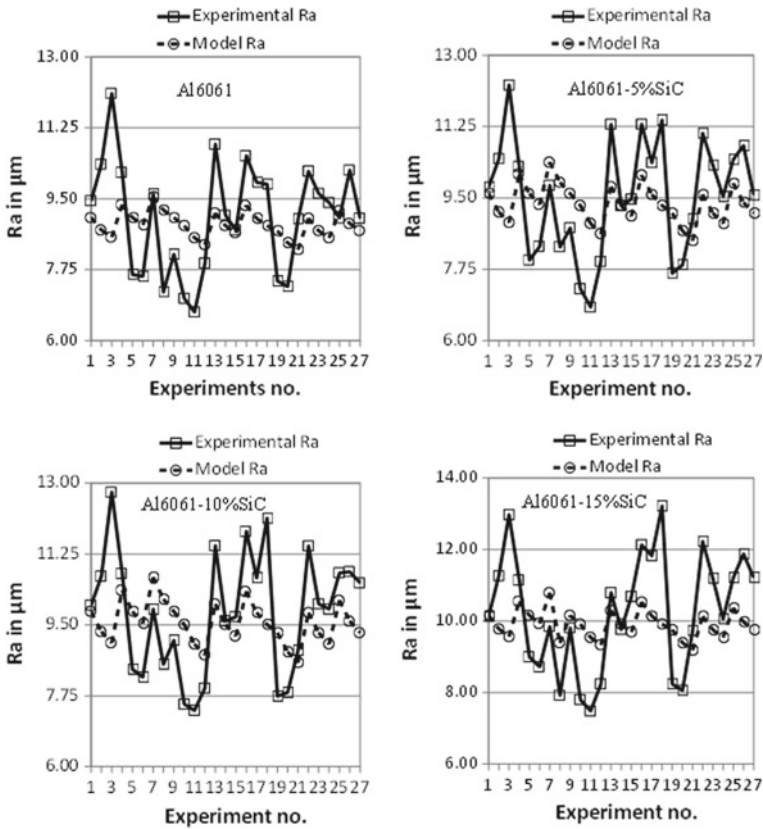


Fig. 13.3 Experimental and model  $R_a$  of deformation wear region

$$\text{Percentage of error} = \frac{\text{experimental DOP} - \text{model DOP}}{\text{experimental DOP}} \times 100 \quad (11)$$

For 300 MPa waterjet pressures cutting conditions, the proposed model predicted almost 0–19%, 8–22%, and 4–25% lower or higher  $R_a$  values than the experimental  $R_a$  values for Al6061–5%SiCp, Al6061–10%SiCp, and Al6061–15%SiCp MMCs, respectively. The percentage of variation between the experimental and model  $R_a$  values is being higher at 100 MPa waterjet pressure conditions compared to the other higher waterjet pressure conditions for both Al6061 base alloy and Al6061–SiCp MMCs. This can be attributed to the consideration that 100 MPa of waterjet pressure has lesser amount of kinetic energy. This waterjet pressure has lesser amount of kinetic energy compared to the higher waterjet pressures. In addition, waterjet pressure coupled with lesser abrasive flow rate at 0.195 kg/min and higher traverse speed of the jet will add up to give higher  $R_a$  values compared to the higher waterjet pressures conditions. In addition, jet spreading takes place due to less amount of kinetic energy of the waterjet. In deformation wear mode, the material is subjected to

plastic deformation at large angles of attack and is removed by the abrasive particles. During the deformation wear mode, the jet deflection happens which in turn generates striations on the surface cut with AWJ. This factor contribute to achieving striations on the cut surface with higher  $R_a$  values in the deformation wear region. At 200 MPa and higher waterjet pressures,  $R_a$  values show a close relation the experimental  $R_a$  values when compared with the  $R_a$  values of 100 MPa waterjet pressure. At higher waterjet pressures 200 MPa and above, the kinetic energy available with waterjet is more than that of 100 MPa waterjet pressure. Here also, jet spreading takes place but at a higher depth of the waterjet. These factors will facilitate for more amount of time interaction of the abrasive waterjet with workpiece. These factors facilities for having lesser amount of striations with  $R_a$  values lesser than the surface cut with 100 MPa AWJ. Thus, this analysis clearly indicates the suitability of proposed model for predicting  $R_a$  values in Al6061 base alloy and Al6061-SiCp MMCs.

### 13.4 Conclusions

This article attempts to show the suitability of model  $R_a$  for predicting the surface roughness of Al6061 base alloy and Al6061-SiCp MMCs. Consequently, this effort can be considered as a database that would help to choose the parameters depending on desired  $R_a$  for Al6061 base alloy and Al6061-SiCp MMCs. For a better surface finish with lower  $R_a$  values for larger depth, it is suitable to adopt, higher waterjet pressure and abrasive flow rate with low traverse speed of the jet.

**Acknowledgements** The work reported in this paper is supported by B M S College of Engineering through the Technical Education Quality Improvement Programme [TEQIP-III] of the MHRD, Government of India.

### References

1. Aydin, G., Karakurt, I., Aydiner, K.: An investigation on surface roughness of granite machined by abrasive waterjet. *Bull. Mater. Sci.* **34**, 985–992 (2011)
2. Jegaraj, J.J.R., Babu, N.R.: A strategy for the efficient and quality cutting of materials with abrasive waterjets considering the variation in orifice and focusing nozzle diameter. *Int. J. Mach. Tools Manuf.* **45**, 1443–1450 (2005)
3. Akkrut, A., Kulekci, M.K., Seker, U., Ercan, F.: Effect of feed rate on surface roughness in abrasive waterjet cutting applications. *J. Mater. Process. Technol.* **147**, 389–396 (2004)
4. Kovacevic, R., Hashish, M., Mohan, R., Ramulu, M., Kim, T.J., Geskin, E.S.: State of the art of research and development in Abrasive waterjet machining. *J. Manuf. Sci. Eng.* **119**, 776–785 (1997)
5. Kovacevic, R.: Surface texture in abrasive waterjet cutting. *J. Manuf. Syst.* **10**, 32–40 (1991)
6. Hashish, M.: A model for abrasive waterjet (AWJ) machining. *J. Eng. Mater. Technol.* **111**(2), 154–162 (1989)
7. Hashish, M.: Characteristics of surfaces machined with abrasive waterjets. *J. Eng. Mater. Technol.* **113**, 354–362 (1991)

8. Guo, N.S., Louis, H., Meier, G.: Surface structure and kerf geometry in abrasive waterjet cutting: formation and optimization. In: 7th American Water Jet Conference, pp. 1–25 (1993)
9. Chen, F.L., Siores, E.: The effect of cutting jet variation on striation formation in abrasive water jet cutting. *Int. J. Mach. Tools Manuf.* **41**, 1479–1486 (2001)
10. Neusen, K.F., Rohatgi, P.K., Vaidyanathan, C., Alberts, D.: Abrasive waterjet cutting of metal matrix composites. In: Proceedings of the 4th U S Waterjet Conference, pp. 272–283 (1987)
11. Hashish, M.: Machining of advanced composites with abrasive-waterjets. In: The Winter Annual Meeting of the ASME, pp. 1–19 (1988)
12. Hamatani, G., Ramulu, M.: Machinability of high temperature composites by Abrasive waterjet. *J. Eng. Mater. Technol.* **112**, 381–386 (1990)
13. Shanmugasundaram, P.: Influence of abrasive waterjet machining parameters on the surface roughness of eutectic Al-Si alloy - graphite composites. *Mater. Phys. Mech.* **19**, 1–8 (2014)
14. Naresh Babu, M., Muthukrishnan, N.: Investigation on surface roughness in abrasive waterjet machining by the response surface method. *Mater. Manuf. Process.* **29**, 1422–1428 (2014)
15. Zhang, S., Yugiang, W., Wang, Y.: An Investigation of surface quality cut abrasive waterjet. *Open Mech. Eng. J.* **5**, 166–177 (2011)
16. Wang, J.: A new model for predicating the depth of cut in abrasive waterjet contouring of alumina ceramics. *J. Mater. Process. Technol.* **209**, 2314–2320 (2009)
17. Shanmugam, D.K., Wang, J., Liu, H.: Minimisation of kerf tapers in abrasive waterjet machining of alumina ceramics using a compensation technique. *Int. J. Mach. tools Manuf.* 1527–1534 (2008)
18. Xu, S., Wang, J.: A study of abrasive waterjet of alumina ceramics with controlled nozzle oscillation. *Int. J. Adv. Manuf. Technol.* 693–702 (2006)
19. Srinivas, S., Ramesh Babu, N.: Role of garnet and silicon carbide abrasives in abrasive waterjet cutting of aluminium-silicon carbide particulates metal matrix composites. *Int. J. Appl. Res. Mech. Eng.* **1**, 109–122 (2011)
20. Srinivas, S., Ramesh Babu, N.: Penetration ability of abrasive waterjets in cutting of aluminum-silicon carbide particulate metal matrix composites. *Mach. Sci. Technol.* **16**, 337–354 (2012)

# Chapter 14

## Abrasive Jet Machining of Soda Lime Glass and Laminated Glass Using Silica Sand



A. Karmakar , D. Ghosh , Deb Kumar Adak , Bijoy Mandal , Santanu Das , Ahmed Mohammed  and Barun Haldar 

**Abstract** In many engineering applications, erosion is one of the frequently occurring wear phenomena, either in favor or against the desired performance. Positive aspects of abrasive wear are the focused area of this study. An abrasive jet machining (AJM) system propels irregular shaped abrasive particle with high velocity for machining of difficult-to-machine work materials. Investigation of machining rate in terms of material removal rate (MMR) is the key issue of this nontraditional machining process. In addition to this, the reusability of the abrasive particle for subsequent machining cycle is another area of interest. The investigation is carried out for the sustainability of the process on the two hard-to-machine engineering materials, soda lime glass and laminated glass. The rate of erosion is measured under various processing conditions by changing different process parameters. Effect of different process parameters on MRR is explored. The reusability of abrasive silica sand is also investigated.

**Keywords** Abrasive jet machining · Material removal rate · Reusability

---

A. Karmakar · D. Ghosh · B. Mandal · S. Das (✉)  
Department of Mechanical Engineering, Kalyani Government Engineering College, Kalyani,  
Nadia 741235, India  
e-mail: [sdas.me@gmail.com](mailto:sdas.me@gmail.com)

D. K. Adak  
Department of Mechanical Engineering, College of Engineering and Management, Kolaghat  
721171, India

A. Mohammed  
School of Mechanical Engineering, Jimma Institute of Technology, Jimma University, Jimma 378,  
Ethiopia

B. Haldar  
Department of Mechanical Engineering, Global Institute of Management and Technology,  
Krishnanagar, Nadia 741102, WB, India  
e-mail: [principal@gimt-india.com](mailto:principal@gimt-india.com)

© Springer Nature Singapore Pte Ltd. 2020  
M. S. Shunmugam and M. Kanthababu (eds.), *Advances in Unconventional Machining and Composites*, Lecture Notes on Multidisciplinary Industrial Engineering, [https://doi.org/10.1007/978-981-32-9471-4\\_14](https://doi.org/10.1007/978-981-32-9471-4_14)

## 14.1 Introduction

Industries always face problems regarding the manufacturing of different products from hard and difficult-to-machine materials [1] and also products with complex geometries with specified tolerance. Conventional machining processes often fail to fulfill these requirements. In such cases, non-conventional machining processes are being selected. In the AJM process, material removal occurs by impact erosion and due to brittle fracture of the work material [2–4]. In the present day of advanced manufacturing scenario, many experimental investigations were performed on this process. Some works focused on the characteristics of abrasive jets and observed the influence of all process parameters on the process response. Other investigations dealt with a carrier gas, nozzle shape and size, wear, jet velocity, jet pressure, stand-off-distance (SOD), etc. These papers explained the process performed in connection with material removal rate, geometrical tolerances on the surface finish of workpieces. Some research works consist of the modeling of the process. Some researchers are working on the optimization of the machining parameters for better performance in AJM.

Abhishek and Hiremath [5] presented a novel approach for machining holes in quartz, using a microabrasive jet machine to reduce the tapering effect. The nozzle was fed at a rate equal to the average rate of change of the thickness of the workpiece. It was found that the entrance diameter of the machined hole was reduced by 29% and the taper angle of the hole was reduced by approximately 58% with improved cylindricity. Recently, AJM drilling was efficiently done by Ghara et al. [6] successfully on soda lime glass and porcelain at some parametric conditions. They used an indigenously made abrasive jet system for this investigation. The diameter of the holes machined was reported to have an increasing trend with SOD for a particular pressure. Srikanth and Rao [7] conducted experiments by abrasive jet drilling on glass sheets using different values of SOD, pressure and nozzle diameter to assess its machinability using the AJM process. The effect of process parameters on MRR was analyzed, and high MRR was obtained at an air pressure of 8 kgf/cm<sup>2</sup>, 10 mm SOD and a nozzle diameter of 4 mm and less kerf were found at 6 kgf/cm<sup>2</sup> air pressure, 9 mm SOD and a nozzle diameter of 3 mm. Verma and Lal [8] performed research work with AJM on a designed setup using aluminium oxide of grain sizes 25, 30, 38, and 48 μm, taking dry air as the carrier gas with pressure  $9.81 \times 10^4$  to  $29.43 \times 10^4$  N/m<sup>2</sup> (gauge pressure) and using WC nozzle of diameter 0.712 mm. They suggested larger SOD for deburring and finishing whereas micro-drilling should be carried out at smaller SOD. Some experiments were done by Ray et al. [9] on abrasive jet drilling to observe the effect of different process parameters on MRR. They used SiC of grain size 60–120 μm and stainless steel nozzles with diameters 1.83 and 1.63 mm. It was observed that the Material Removal Factor (MRF) became maximum at a range of pressure of 2 to 3 kgf/cm<sup>2</sup>. They also found out higher SOD more preferable for higher MRR and higher pressure and lower SOD preferable for precision work.

A semi-empirical equation to find the shape of the generated surface in AJM was derived by Balasubramaniam et al. [10]. It was shown that the shape of the



abrasive jet machined surface had a reverse bell-mouthed type with an increased edge radius at the entry side of the work surface. The abrasives mixed with hot air forming abrasive hot air jet was used for machining glass to study the effect of hot abrasive air jet on MRR and surface roughness by Jagannatha et al. [11]. They found that above 100 °C, the effect of temperature was more significant on MRR and with an increase in temperature, MRR also increased. It was also noticed that the MRR was 1.4–1.7 times higher at a higher temperature than that at room temperature. The surface roughness was seen to be reduced at a higher temperature. Wakuda et al. [12] identified the material response to abrasive particle impact during AJM of alumina ceramics. They used three kinds of commercial abrasive grits for indentation in sintered alumina samples and it was observed that the material response to particle impact depended remarkably on the abrasive particle characteristics. Ghobeity et al. [13] worked on the improvement of process repeatability in AJM. They introduced a mixing device within the pressure reservoir which ensured the abrasive powder to remain loose and to flow through the small opening to the air stream. This approach improved the repeatability of the AJM process. Fan et al. [14] developed predictive mathematical models for assessing the erosion rates in the drilling of micro-holes and micro-channel cutting on glasses with an abrasive jet. They used a technique for the formulation of the models as a function of the properties of the target material impact parameters and the process parameters affecting the erosion of brittle materials. It was shown that model predictions were similar to some extent to the experimental results with a deviation of 1%.

In the present investigation, an indigenously made AJM setup is used to explore the parametric conditions to obtain max MRR in soda lime and soda lime laminated glass using common silica sand and to find out reusability of the silica sand abrasive particle used.

## 14.2 Experimental Investigation

The newly fabricated abrasive jet machining setup (shown in Fig. 14.1) is used for investigating its performance regarding MRR and other responses as discussed in the following paragraphs.

### 14.2.1 *Experimental Conditions and Process Parameters*

The whole experiment is done on soda lime glass and laminated glass by taking three levels of three parameters i.e. standoff distance, flow rate, grain size as shown in Table 14.1. The pressure is kept constant as 6 kgf/cm<sup>2</sup> during the whole experiment. The used nozzle is made from stainless steel with 10 mm inlet diameter, 3.2 mm outlet diameter and 40 mm length of circular cross section.

**Fig. 14.1** Indigenously developed AJM setup

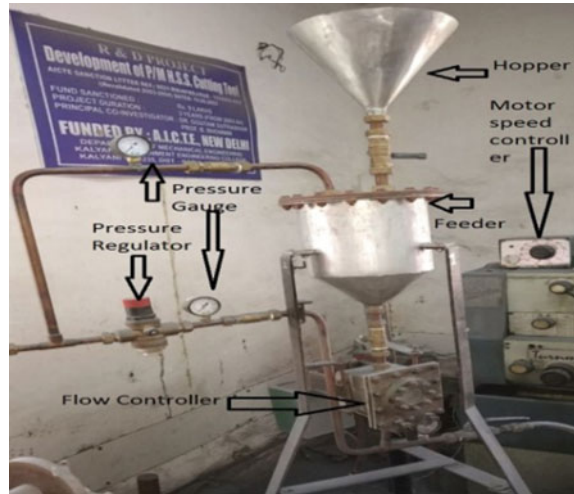


**Table 14.1** Process parameters used for the experiments

Parameter	Level 1	Level 2	Level 3
Stand-off distance (mm)	2	4	6
Flowrate (g/min)	600	800	1000
Grain size ( $\mu\text{m}$ )	225	325	425

### 14.2.2 Procedures for Experiments

For this experimental work, silica sand is used as an abrasive particle of different grain sizes of 425, 325 and 225  $\mu\text{m}$ . Throughhole is not produced and the only cavity is formed in the workpieces with 10 s of machining time. Flow rates selected are 600, 800 and 1000 g/min. The stand-off distance is selected as 2, 4, and 6 mm. The experiments carried out with the help of RSM Table. With the same condition, the whole experiment is conducted on sodalime glass and laminated glass workpieces. The pressure of 6  $\text{kgf/cm}^2$  is taken as constant for all the experimental conditions for calculating the MRR. The types of the cavity generated are observed and MRR rates are calculated. Then changes in diameter of the nozzle are measured by a microscope. Also, nozzle wear is measured by taking the weight of the nozzle after each experiment.

### 14.2.3 Flow Rate Calculation of Silica Sand

In this set of experiment, the flow rates of a constant volume (of 500  $\text{mm}^3$ ) silica sand of various grain sizes 425, 325 and 225  $\mu\text{m}$  are experimentally measured and

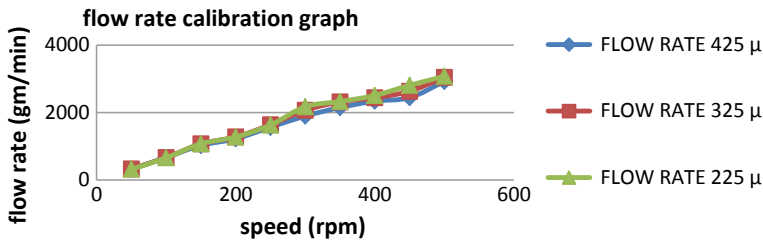


Fig. 14.2 Flow rate calibration graph of silica sand

Table 14.2 The flowrate of silica sand of grain size 425 μm

Sl. No.	Speed of flow controller (RPM)	Volume of silica sand (mm <sup>3</sup> )	Weight of silica sand (g)	Average time (s)	Flow rate (g/min)
1	500	500	742.56	15.25	2922.7
2	450	500	742.56	18.25	2422.27
3	400	500	742.56	19.05	2339.71
4	350	500	742.56	20.75	2148.02
5	300	500	742.56	23.5	1896.66
6	250	500	742.56	28.5	1563.91
7	200	500	742.56	36.5	1221.13
8	150	500	742.56	43.5	1024.63
9	100	500	742.56	67	665.24
10	50	500	742.56	138.4	322.39

presented in the graph of Fig. 14.2. The obtained results from the graph show that in different (rpm of flow controller) flow rates of abrasives, the flow rates of individual abrasives are slightly different. In case of large particle size, it will take slightly more time for emptying the abrasive than the small particles. It may due to less flowability of larger particles than the smaller particles or measurement error. The differences are not much significant. Hence, on flow rate measurement, a set of data of 425 μm particles are presented in Table 14.2.

### 14.2.4 Drilling of Soda Lime Glass Using Silica Sand (Exp. I)

In this experiment, drilling of soda lime glass is performed for calculating the MRR using silica sand with three types of grain sizes, taking three stand-off distances and three flow rates. For the sake of simplicity, experiments are designed with RSM. The results obtained from this set of experiment are tabulated in Table 14.3. The values of MRR of the workpiece are measured and tabulated in the same table (Table 14.3).

**Table 14.3** The material removal rate of soda lime glass

Sl. No.	SOD (mm)	Flow rate (g/min)	Grain size ( $\mu\text{m}$ )	Workpiece		MRR (g/min)
				Initial wt. (g)	Final wt. (g)	
1	6	1000	425	141.770	141.555	1.29
2	4	800	325	141.555	141.486	0.414
3	2	1000	425	141.486	141.439	0.282
4	4	800	325	141.439	141.313	0.435
5	2	600	425	141.200	141.127	0.438
6	4	800	325	141.127	141.052	0.45
7	6	600	425	142.788	142.600	1.128
8	4	800	325	142.600	142.530	0.42
9	6	1000	225	142.530	142.475	0.33
10	4	800	325	142.475	142.402	0.438
11	6	600	225	142.402	142.307	0.57
12	4	800	325	142.307	142.245	0.372
13	2	1000	225	142.245	142.201	0.264
14	2	600	225	142.201	142.158	0.258

### Observation of Cavity Operation on Soda Lime Glass Plate with Silica Sand for MRR Calculation.

With the help of Minitab soft tool, ANOVA is carried out and the model summary obtained is given below.

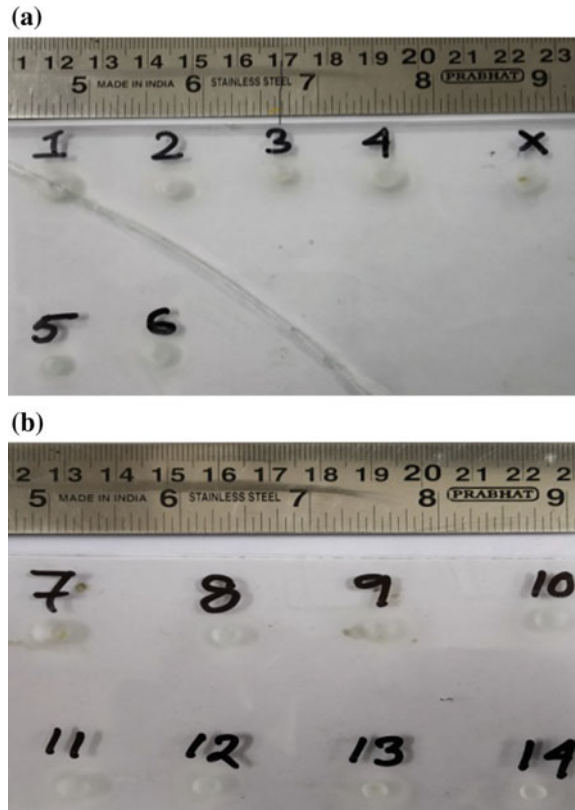
S	R-sq	R-sq (adj)	R-sq (Pred)
0.0851836	96.54%	92.50%	0.00%

Regression Equation (in uncoded unit) obtained is as follows:

$$\begin{aligned} \text{MRR} = & 1.448 - 0.453 \text{ SOD} - 0.000720 \text{ FR} - 0.00236 \text{ GS} + 0.0371 \text{ SOD} * \text{SOD} \\ & + 0.000023 \text{ SOD} * \text{FR} + 0.000825 \text{ SOD} * \text{GS} + 0.000001 \text{ FR} * \text{GS} \dots \end{aligned} \quad (14.1)$$

where FR is feed rate and GS is grain size.

**Fig. 14.3** In the images **a** and **b** the show cavities on the soda lime glass plates



### 14.2.5 Drilling of Laminated Glass Using Silica Sand (Exp. II)

Drilling experiment on the laminated glass is performed for calculating the MRR using silica sand with three types of grain sizes, taking three stand-off distances and three flow rates. For the sake of simplicity, experiments are designed with RSM. Experimental results are tabulated below in Table 14.4. Figure 14.10a, b show the cavities formed by abrasive impact in laminated glass plates. The values of MRR of the workpiece are measured and tabulated in the same table.

#### Observation of Cavity on Laminated Glass Plates with Silica Sand for MRR Calculation.

With the help of the same Minitab soft tool, Analysis of Variance (ANOVA) is carried out in this experiment set also and the model summary obtained is given below.

**Table 14.4** The material removal rate of laminated glass

Sl. No.	SOD (mm)	Flow rate (g/min)	Grain size (μm)	Workpiece		MRR (g/min)
				Initial wt.(g)	Final wt.(g)	
1	6	1000	425	160.477	160.385	1.104
2	4	800	325	160.385	160.346	0.468
3	2	1000	425	160.346	160.287	0.708
4	4	800	325	160.287	160.242	0.54
5	2	600	425	160.242	160.180	0.744
6	4	800	325	160.131	160.087	0.53
7	6	600	425	160.087	160.074	0.156
8	4	800	325	146.062	146.024	0.46
9	6	1000	225	146.024	145.968	0.672
10	4	800	325	145.955	145.908	0.438
11	6	600	225	145.908	145.846	0.744
12	4	800	325	145.838	145.790	0.572
13	2	1000	225	145.790	145.739	0.636
14	2	600	225	145.737	145.617	1.644

S	R-sq	R-sq (adj)	R-sq (Pred)
0.0585020	98.31%	96.35%	53.44%

Regression Equation (in uncoded units) obtained is given below.

$$\begin{aligned}
 \text{MRR} = & 7.080 - 1.0821 \text{ SOD} - 0.005801 \text{ FR} - 0.011161 \text{ GS} \\
 & + 0.06272 \text{ SOD} * \text{SOD} + 0.000541 \text{ SOD} * \text{FR} \\
 & + 0.000286 \text{ SOD} * \text{GS} + 0.000011 \text{FR} * \text{GS} \dots \quad (14.2)
 \end{aligned}$$

where FR is feed rate and GS is grain size

### 14.3 Result and Discussions

#### 14.3.1 Discussion on Experiment Set I

From these plots, the effect of three factors i.e. grain size, stand-off distance, and abrasive flow rate on material removal rate (MRR) is visible. Figure 14.4 and Fig. 14.5 are the contour plot and the surface plot, respectively, of MRR vs SOD and grain size. It is observed that if the grain sizes of the abrasive particle increase, then MRR will also increase. It may due to the fact that, larger grain size particle has higher kinetic energy and more sharp edges than the small grain particle. So, the large particles having a high chance to impinge into the workpiece, remove more amount of material than the smaller particle. Again from Figs. 14.4 and 14.5, it is observed that MRR increases with the increase in SOD, and decrease with the decrease in SOD within the range of experiment. Because of smaller SOD, the abrasive particles cannot accelerate properly; also collision with rebound particles takes place. So, the impact strength of the abrasive particle is less for smaller SOD. From this experiment,

**Fig. 14.4** Contour plot of MRR versus grain size (GS), SOD

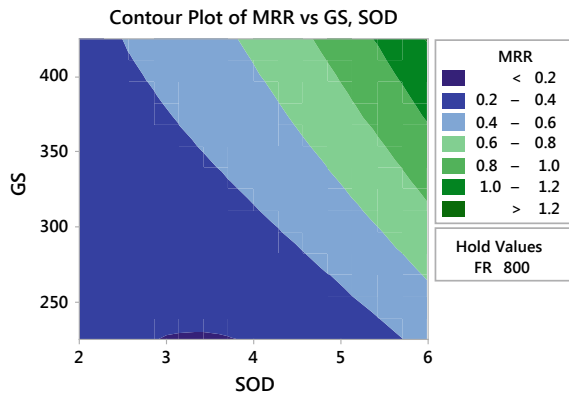


**Fig. 14.5** Surface plot of MRR versus grain size, SOD

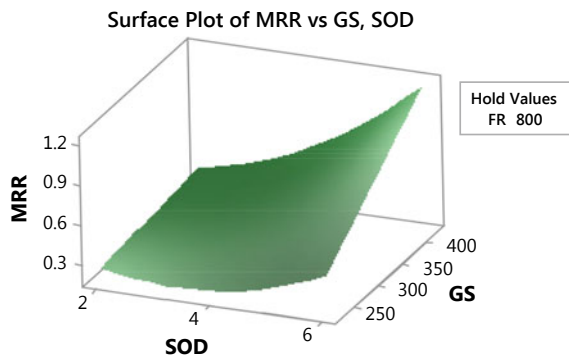


**Fig. 14.6** Contour plot of MRR versus grain size, flow rate

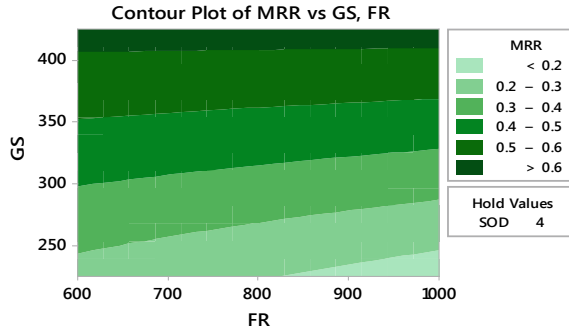
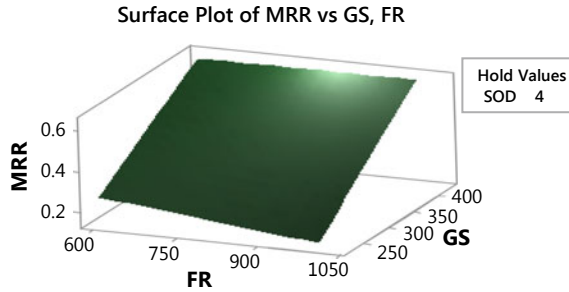


**Fig. 14.7** Surface plot of MRR versus grain size, flow rate



it is clear that MRR is higher for 425  $\mu\text{m}$  grain size Silica Sand with 6 mm SOD. From Figs. 14.6 and 14.7 (the contour plot and the surface plot of MRR with grain size and flow rate), it is clear that if particle size increases then MRR increases. As shown in Figs. 14.6 and 14.7, there is no such effect of flow rate on MRR. When particle size decreases, the effect of flow rate on MRR rises. For smaller grain size particle, the MRR decreases with an increase in flow rate. When flow rate increases gradually, more amounts of abrasive particles are coming out through the nozzle and might collide with each other and lose its strength, and may reduce the overall efficiency of the abrasive jet. So, it is clear that at a particular flow rate, MRR increases and after that it decreases. From the surface plot, it is clear that below 600 g/min flow rate is suitable for machining, because, after the 600 g/min flow rate, MRR gradually decreases. From Figs. 14.8 and 14.9 (the contour plot and the surface plot of MRR vs flow rate and SOD), it is clear that MRR increases with increase in SOD from 2 mm to 6 mm with a particular grain size of 325  $\mu\text{m}$ . Again MRR decreases with the increase in flow rate from 850 to 1000 g/min for that particular grain size.



**Fig. 14.8** Contour plot of MRR versus flow rate, SOD

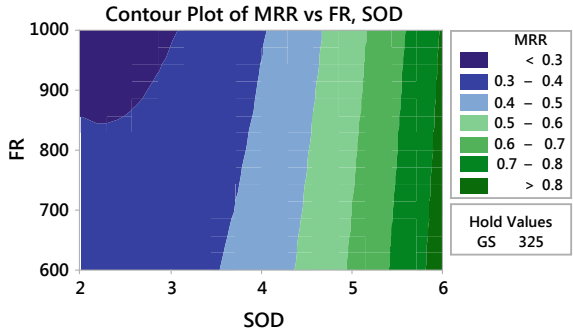


**Fig. 14.9** Contour plot of MRR versus flow rate, SOD

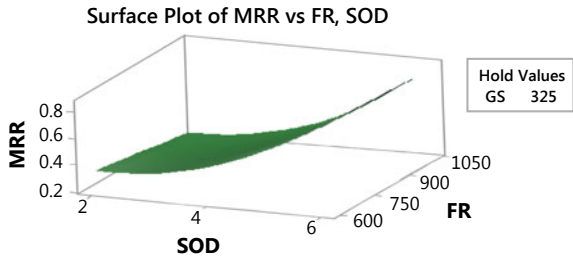
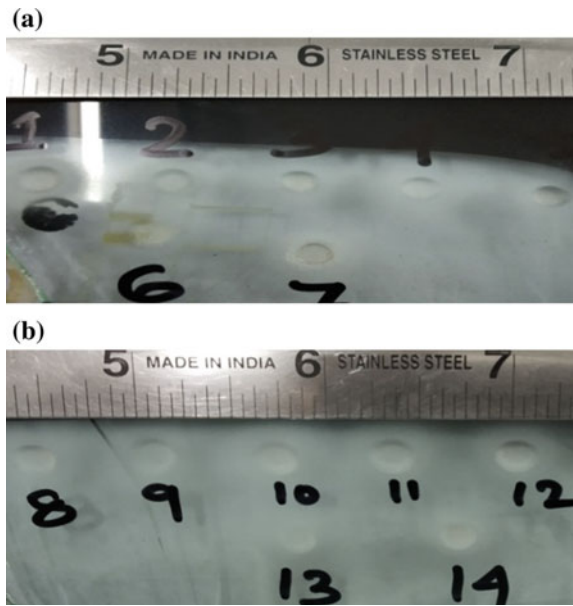


**Fig. 14.10** In the images **a** and **b** show the cavities on laminated glasses



### 14.3.2 Discussion on Experiment Set II

From the plots, the effect of three factors i.e. grain size, stand-off distance and abrasive flow rate on material removal rate (MRR) is visible. From Figs. 14.11 and 14.12 (the contour plot and the surface plot of MRR vs. SOD and grain size), it is observed that the material removal rate for laminated glass decreases with the increase in SOD. The 225  $\mu\text{m}$  grain size silica sand particles are best suitable for material removal. It may be because; laminated glass is less brittle than soda lime glass. So, the 225  $\mu\text{m}$  particle has enough strength for maximum material removal with 2 mm SOD. From Figs. 14.13 and 14.14 (the contour plot and the surface plot of MRR vs. grain size, flow rate), it is clear that both the grain size and flow rate have the same effect on MRR with a particular SOD of 4 mm. The MRR is higher with larger grain size and also low flow rate. So when the flow rate decreases, the particle less collides with each other and MRR increases. From Figs. 14.15 and 14.16 (the contour plot and the surface plot of MRR vs flow rate and SOD), it is clear that MRR is maximum at 2 mm of minimum SOD. Due to increase of SOD, abrasive velocity reduces and divergences increases thus MRR decreases. Again due to increase of flow rate MRR increase at the flow rate of 1000 gm/min due to more number of impact erosion.

**Fig. 14.11** Contour plot of MRR versus grain size, SOD

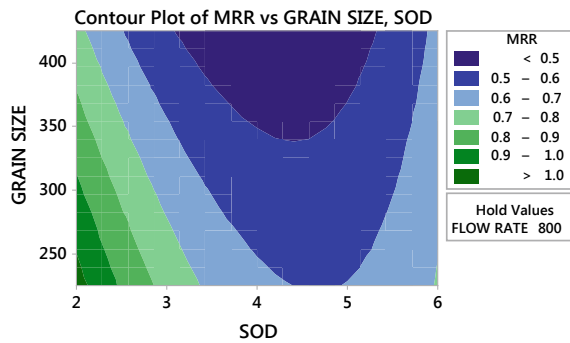


**Fig. 14.12** Surface plot of MRR versus grain Size, SOD

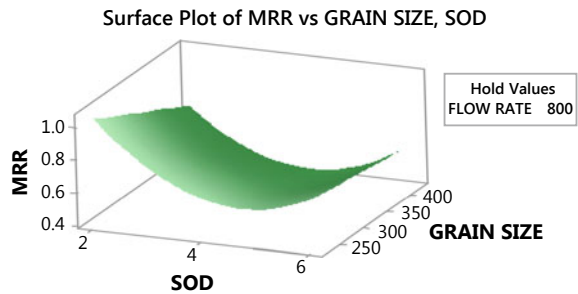


**Fig. 14.13** Contour plot of MRR versus grain size, flow rate

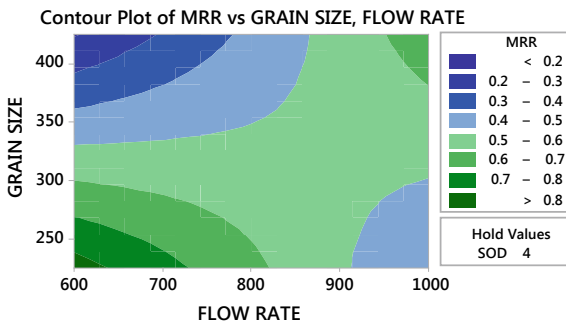


**Fig. 14.14** Surface plot of MRR versus grain size, flow rate

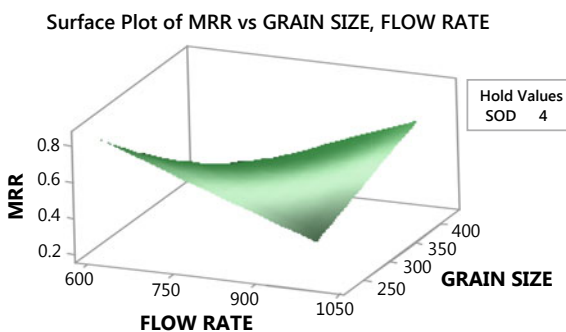


**Fig. 14.15** Contour plot of MRR versus flow rate, SOD

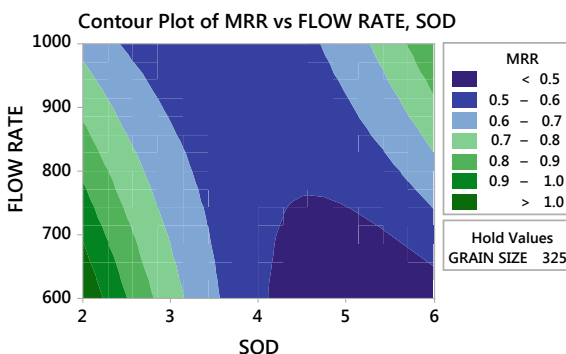
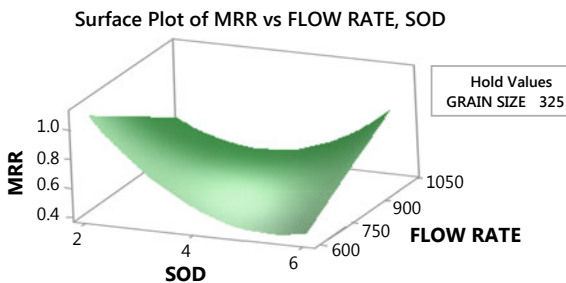


**Fig. 14.16** Surface plot of MRR versus flow rate, SOD



### 14.3.3 Observation on Reusability of Silica Sand

The silica sand is used as abrasive in three different grain sizes, 425, 325 and 225  $\mu\text{m}$ . The reasons for using silica sand are considerable cutting ability, high hardness, cheap, and readily available. Though considerable time is required to segregate the particular grains from the aggregates, still, it is economic. From Figs. 14.17, 14.18, and 14.19, following snaps, have been taken before and after the single use of silica sand for abrasive machining.



Fig. 14.17 Silica sand of 425  $\mu\text{m}$  before and after machining respectively

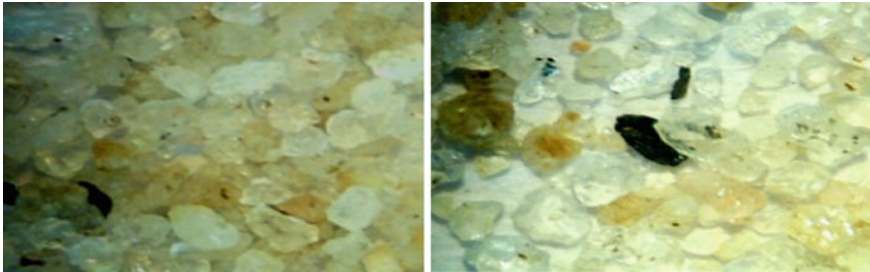


Fig. 14.18 Silica sand of 325  $\mu\text{m}$  before and after machining respectively

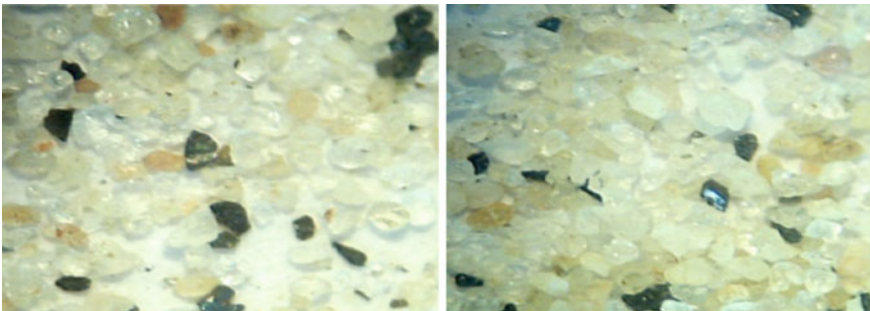


Fig. 14.19 Silica sand of 225  $\mu\text{m}$  before and after machining respectively

It has been observed from the microscopic observation that cutting edge sharpness reduces drastically even after single use for machining. The abrasive particles are getting the more regular shape. So, the chance of reusability of the silica sand abrasive is less.

## 14.4 Conclusions

In this present experimental investigation, MRR analysis of soda lime glass and laminated glass under varying abrasive jets are performed. From the experimental investigations, the following were concluded:

- The volumetric flow rates of various particles are almost the same using the abrasive flow controller.
- The MRR increases with the increasing grain size.
- The MRR increases with the increase in SOD and decreases with the decreasing SOD.
- In the case of smaller grain size particles, the MRR decreases with increasing abrasive flow rate.
- There are noticeable differences observed with respect of contour plot and surface plot between soda lime glass and laminated glass. It may due to lamination of the glass with other materials.
- Chance of reusability of silica sand is less.

## References

1. Park, D.S., Cho, M.W., Lee, H., Cho, W.S.: Micro-grooving of glass using micro-abrasive jet machining. *J. Mater. Process. Technol.* **146**(2), 234–240 (2004)
2. Belloy, E., Thurre, S., Walckiers, E., Sayah, A., Gijs, M.A.M.: The introduction of powder blasting for sensor and micro system applications. *Sens. Actuators A* **84**(3), 330–337 (2000)
3. Haldar, B., Adak, D.K., Ghosh, D., Karmakar, A., Habtamu, E., Ahmed, M., Das, S.: Present status and some critical issues of abrasive jet materials processing—a review. *Procedia Manuf.* **20**, 523–529 (2018)
4. Haldar, B., Ghara, T., Ansari, R., Das, S., Saha, P.: Abrasive jet system and its various application in abrasive jet machining, erosion testing, shot peening and fast cleaning. In: *Proceeding of the International Conference on materials, Manufacturing and Modeling*, Vellore, India (2017)
5. Abhishek, K., Hiremath, S.S.: Improvement of geometrical accuracy of micro holes machined through micro abrasive jet machining. In: *Proceedings of The CIRP Conference on High Performance Cutting*. *Procedia CIRP* **46**, 47–50 (2016)
6. Ghara, T., Ansari, R., Adak, D.K., Ahmed, M., Das, S., Haldar, B.: Abrasive jet drilling of porcelain tiles and soda lime glass under different condition. In: *Proceeding of the 1st International Conference in Mechanical Engineering*, Jadavpur University, Kolkata, pp. 534–537 (2018)
7. Srikanth, D.V., Rao, M.S.: Metal removal and kerf analysis in abrasive jet drilling of glass sheets. In: *Proceedings of the 3rd International Conference on Materials Processing and Characterization*. *Procedia Mater. Sci.* **6**, 1303–1311 (2014)

8. Verma, A.P., Lal, G.K.: An experimental study of abrasive jet machining. *Int. J. Mach. Tool Des. Res.* **24**(1), 19–29 (1984)
9. Ray, P.K., Paul, A.K.: Some studies on abrasive jet machining. *J. Inst. Eng. (India)*, **68**(Part PE 2), 27–30 (1987)
10. Balasubramaniam, R., Krishnan, J., Ramakrishnan, N.: A study on the shape of the surface generated by abrasive jet machining. *J. Mater. Process. Technol.* **121**(1), 102–106 (2002)
11. Jagannatha, N., Somashekhar, S.H., Sadashivappa, K., Arun, K.V.: Machining of soda lime glass using abrasive hot air jet: an experimental study. *Mach. Sci. Technol. Int. J.* **16**(3), 459–472 (2012)
12. Wakuda, M., Yamauchi, Y., Kanzaki, S.: Material response to particle impact during abrasive jet machining of alumina ceramics. *J. Mater. Process. Technol.* **132**(1–3), 177–183 (2003)
13. Ghobeity, A., Getu, H., Krajac, T., Spelt, J.K., Papini, M.: Process repeatability in abrasive jet micro-machining. *J. Mater. Process. Technol.* **190**(1–3), 51–60 (2007)
14. Fan, J.M., Wang, C.Y., Wang, J.: Modelling the erosion rate in micro abrasive air jet machining of glasses. *Wear* **266**(9–10), 968–974 (2009)

# Chapter 15

## A Novel Magnetorheological Grinding Process for Finishing the Internal Cylindrical Surfaces



Ankit Aggarwal and Anant Kumar Singh

**Abstract** A novel magnetorheological grinding process is introduced to finish the inner cylindrical surface of the workpiece. In this approach, magnetorheological polishing fluid is used as a medium for the finishing of the inner cylindrical surface. The magnetorheological grinding tool helps to slash away the roughness peaks present on the workpiece surface. The simulation along with experimentation is performed to validate the effectiveness of the process. The input parameters such as current, tool reciprocation speed, tool, and workpiece rotation speed are considered for experimentation. The output parameter is observed in terms of change in surface roughness value from 250 to 110 nm in 60 min of finishing time. The roughness profiles and scanning electron microscope images proved the efficacy of the developed magnetorheological grinding process. This process can finish the internal cylindrical surfaces for industrial applications such as cylindrical molds, dies, hydraulic cylinders, etc.

**Keywords** Magnetorheological fluid · Magnetorheological grinding tool · Magnetic flux density · Surface roughness

### 15.1 Introduction

The continuous development in the manufacturing industry and demand for a highly finished surface of the components has gained the attention of the researchers. Some of the areas that require very fine precision surface finish are aerospace industry, medical industry, atomic energy sector, and semiconductor components manufacturing [1]. The conventional processes were being used for so many years but with such a demand there was immense pressure on the researcher to develop new and advanced processes. Further, there were some limitations in conventional processes

---

A. Aggarwal · A. K. Singh (✉)

Department of Mechanical Engineering, Thapar Institute of Engineering and Technology, Patiala 147004, Punjab, India  
e-mail: [anantsingh@thapar.edu](mailto:anantsingh@thapar.edu)

© Springer Nature Singapore Pte Ltd. 2020

M. S. Shunmugam and M. Kanthababu (eds.), *Advances in Unconventional Machining and Composites*, Lecture Notes on Multidisciplinary Industrial Engineering, [https://doi.org/10.1007/978-981-32-9471-4\\_15](https://doi.org/10.1007/978-981-32-9471-4_15)

179

such as they cannot possess to finish complex shapes and high precision components. If this requirement is not achieved then the performance of the components that require finished surface can decrease [2, 3]. Also, the conventional grinding process causes defects such as heat-affected zone, tensile residual stresses, and micro and macrocracks, etc. Removal of these defects raises the cost of the end product [4, 5].

Beyond these limitations, there is also no control over the forces acting during the finishing of the workpiece. Thus, the finishing process becomes one of the costly and difficult tasks in the manufacturing industry which consumes a lot of time [6]. There are various applications which require finishing such as hydraulic cylinders, barrels of the injection molding machine, cylindrical molds, and dies [7]. Thus, the conventional processes are being replaced by new and advanced finishing processes that include fluid jet polishing, magnetic abrasive jet finishing, magnetorheological abrasive flow finishing, and magnetorheological honing process. The fluid jet polishing is a process for the finishing of the internal cylindrical surface. In this process, the workpiece used is a tube made up of SS 316L in which the tool is inserted that contains nozzle which jets abrasive-laden fluid on the internal cylindrical surface [8]. The limitation of the process is the need for the continuous supply of the abrasive.

Another process is magnetic abrasive jet finishing in which the internal surface of SUS 304 stainless-steel tube is finished. The magnetic abrasives are jetted into the stainless-steel tube and the externally applied magnetic field pulls the magnetic abrasive particles toward the workpiece inner surface where finishing action is performed. A minimum velocity of the jet is restricted to 13 m/s which becomes a limitation in this process [9]. The MRAFF (magnetorheological abrasive flow finishing) process which is capable of finishing the internal cylindrical workpiece. But the low rate of finishing on material surfaces and excessive time consumption is the limitation to this process so the development of the MRAFF became very important [10]. The rotational magnetorheological abrasive flow finishing is a development over the MRAFF process that utilizes the magnetic poles to rotate around the workpiece and the magnetorheological polishing fluid sticks to the surface of the workpiece under the action of the applied magnetic field, the magnetorheological polishing fluid form stiffened chains which due to the rotating action of the magnetic poles finishes the inner cylindrical surface of the workpiece [11]. The basic limitation of this process is that it cannot be used for the finishing of ferromagnetic workpieces. Besides the above-mentioned process, the magnetorheological honing process is used for the finishing of cylindrical inner surface of workpiece. This process utilizes magnetorheological polishing fluid to finish the inner cylindrical portion. Initially, an electromagnetic core is used for the magnetization of the magnetorheological polishing fluid [12]. But the tool cannot be used for different diameter of workpiece. So, to overcome this problem, the magnetorheological honing tool was developed that uses permanent magnet cores. The diameter of the tool can be varied according to the workpiece but was limited to a particular range only [13]. Thus, a novel process has been developed which could overcome the problem of finishing a ferromagnetic workpiece and changing the tool for various workpieces with different diameters.



## 15.2 Design of the Magnetorheological Grinding Tool

The design of the magnetorheological grinding tool must be in such a way that uniform and strong magnetic field is attained on its outer cylindrical surface. It offers strongly bonded chains over the tool surface. On the other hand, the rigidity of the magnetorheological polishing fluid is dependent on the intensity of the magnetic flux density which is helpful in attaining better surface finish. Thus, to finish the inner cylindrical surface of the specimen, a magnetorheological grinding process has been purposed. The schematic diagram of the magnetorheological grinding tool is shown in Fig. 15.1 which clearly indicates its functioning.

Various simulations are performed in order to obtain maximum flux density over the cylindrical surface of the MR grinding tool. The software used for the simulation and determining the magnetic flux density is Ansoft Maxwell v13. Around the core, an electromagnetic coil is then modeled. The outer cylindrical tool surface is layered by magnetorheological polishing fluid and later a workpiece of ferromagnetic material is also modeled as represented in Fig. 15.2. Further, the number of turns and the current which is allowed to flow through the copper coil is assigned as mentioned in Table 15.1. The working gap is represented in Fig. 15.2a. It is used to determine the magnetic flux density magnitude between the tool and the workpiece. The electromagnetic coil is split in two parts and then separated by a plane to which excitation is assigned. In this software, various input parameters as provided described in Table 15.1 were inserted to attain the results. After defining all the input parameters, the setup boundaries are insulated in order to block the magnetic flux leakage to the surrounding. The boundary conditions are assumed in the magnetostatics model for finite element analysis (FEA) and is set up by providing the region with value of the percentage offset as 20. The initial mesh size for the setup is selected as default in the Ansoft Maxwell software. The analysis is performed by selecting the setup in the magnetostatics analysis where the number of passes is taken to be 10 along with the

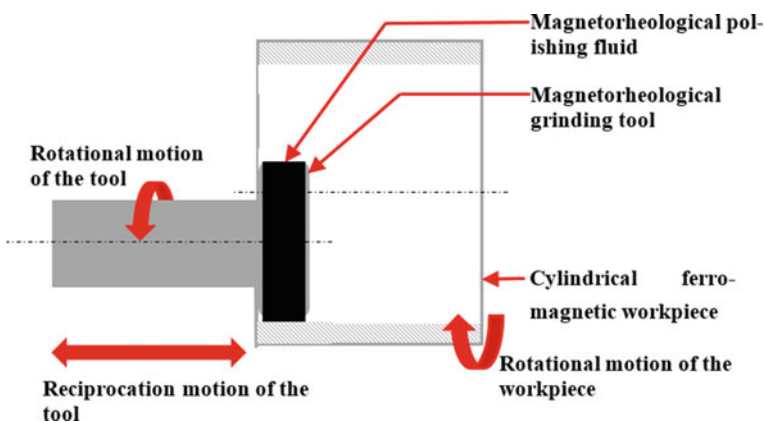
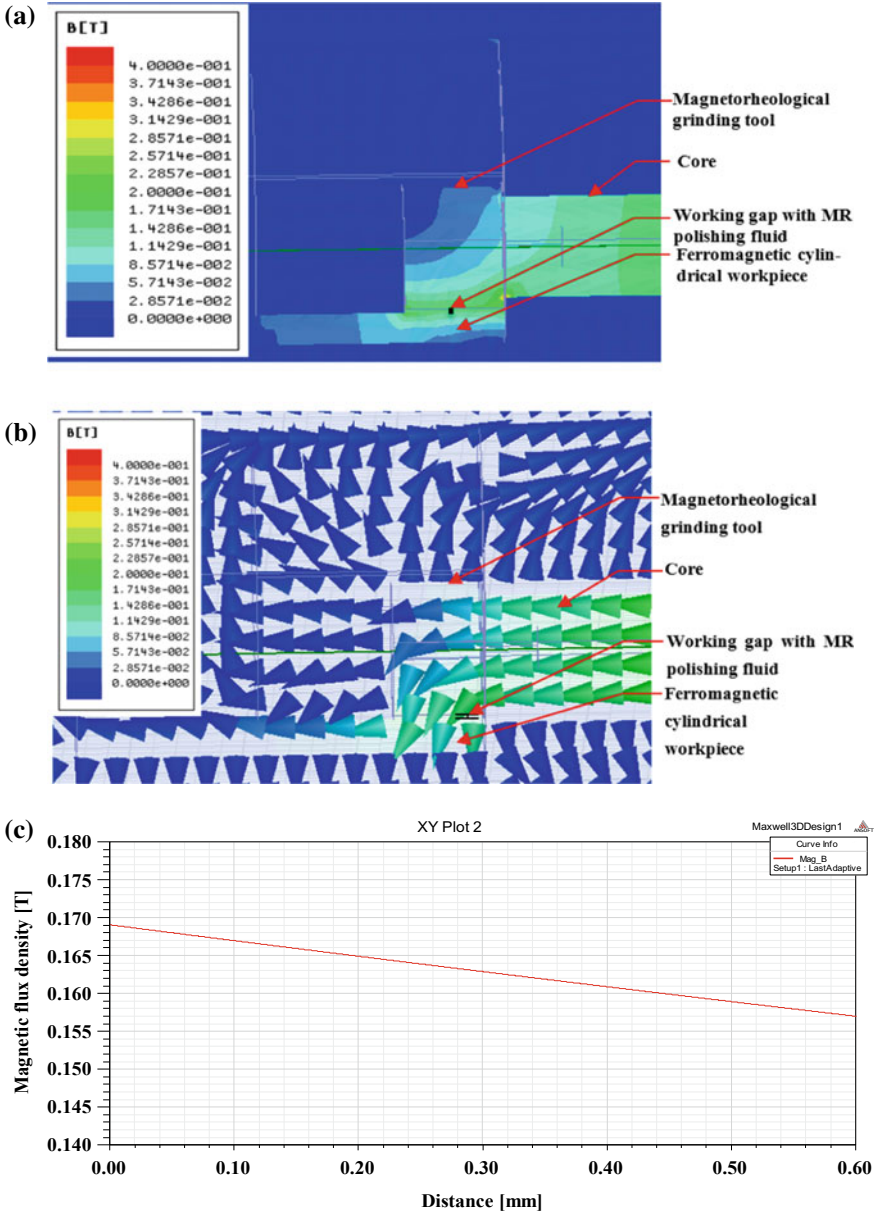


Fig. 15.1 A schematic diagram of the magnetorheological grinding tool



**Fig. 15.2** a Magnetic flux density distribution through cross-sectional area of grinding setup along with cylindrical workpiece and b the direction of flow for the magnetic flux lines from outer cylindrical surface of the tool toward the workpiece. c 2D plot of the magnitude of magnetic flux density within the working gap

**Table 15.1** Material and parameter assigned to the parts of the MR grinding model for FEA

Components	Material	Relative permeability	Other parameters
Electromagnetic coil	Copper	1	2 A and 2600 turns
Core of the MR grinding tool	Mild steel	600	–
Polishing fluid	MR polishing fluid	5	–
Workpiece (Ferromagnetic cylinder)	Mild steel	600	–

percentage error of 1. The two-dimensional plot is generated under the Maxwell 3D electromagnetic model. These plots represent magnitude of magnetic flux density.

Thus, this shape of the tool provided maximum flux density at the outer cylindrical surface of the MR grinding tool as shown in Fig. 15.2a. Also, the direction of the magnetic field lines from the core to the workpiece can be seen in Fig. 15.2b. Due to this, magnetic field gradient is greater toward the MR grinding tool and less toward the workpiece due to which the magnetorheological fluid stick to the tools outer surface and does not stick against the surface of the internal cylindrical workpiece. The 2D plot of the distribution of the magnetic flux density can be observed in Fig. 15.2c. It depicts the magnetic flux gradient between the tool peripheral surface and the internal cylindrical workpiece surface.

Thus, due to the magnetic field, the carbonyl iron particles (CIPs) in the magnetorheological polishing fluid gets stiffened and holds the abrasive particles rigidly. Owing to which the abrasion action caused material removal. So, the strongly entrapped active abrasive comes in contact with the internal workpiece surface which performs the finishing action as represented by Fig. 15.3a. It can be seen from Fig. 15.3b that how the active abrasive shears out the peaks on the cylindrical inner surface of the workpiece. During the experiment, the rotation along with reciprocation movement of the tool and the rotation of the workpiece exerts the force on the cylindrical surface of the workpiece. The magnetic forces and other forces which are being produced due to the movement of the tool and the workpiece mentioned above causes the active abrasive along with carbonyl iron particle chains to perform the finishing operation. Thus, in this manner surface peaks are sheared off.

In the present developed MR grinding process as shown in Fig. 15.4, an electromagnet is made up of the coil with a number of turns as 2600 which is wound around a bobbin which is placed in the vicinity of the aluminum casing. The aluminum casing is held tight on the aluminum structure for the tool. A tool core is passed through the aluminum casing containing the coils. The core used in the finishing process is of 25 mm diameter with a length of 270 mm which is allowed to rotate in the center of the electromagnetic coil. By considering the simulation results the tool was designed and thus the tooltip was fabricated like a wheel. The tooltip diameter is kept as 30 mm which is kept greater in diameter than rest of the core but less than inner diameter of the workpiece. This is made so that the tool can enter the workpiece without coming in contact with its surface.

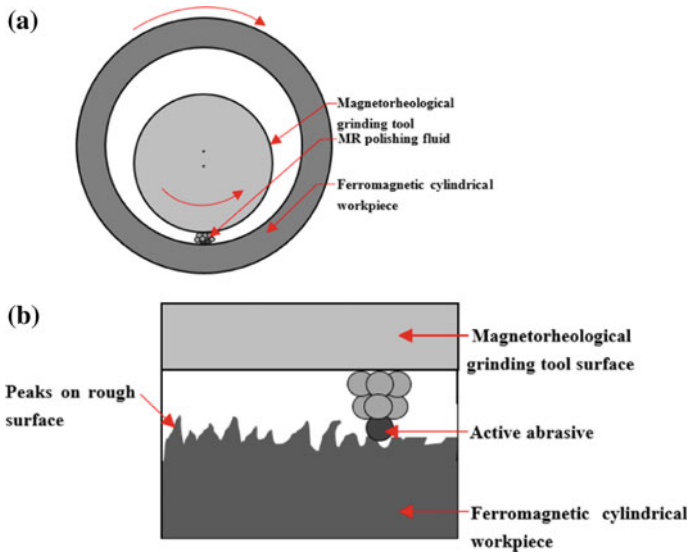


**Fig. 15.3** a Mechanism of the finishing in the magnetorheological grinding process, b interaction of the active abrasive particle of MR polishing fluid with the internal cylindrical workpiece surface

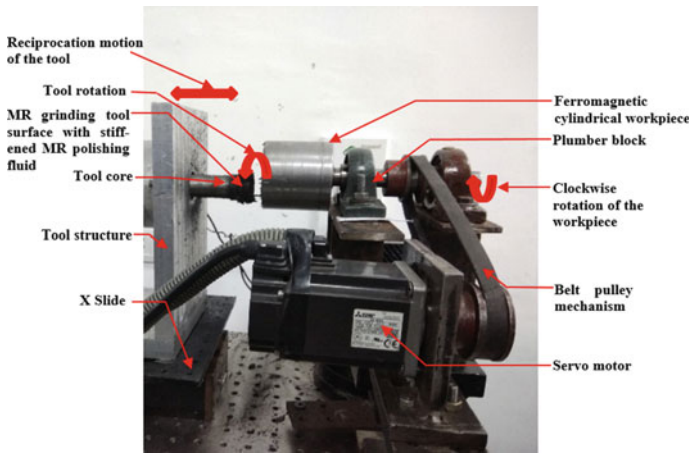


**Fig. 15.4** Setup of the magnetorheological grinding process

Figure 15.4 shows the setup for the experimentation which is used to finish the cylindrical workpiece surface. The tool structure that holds the tool was mounted on the X-slide is driven by a servo motor, which provides reciprocation motion to it. The tool is provided with rotational motion using another servo motor which is fixed to the tool structure. It is done by using a belt pulley mechanism. On the other hand, the workpiece is held on a structure for maintaining the height of the workpiece according to the height of the tool. Thus, this system helps in maintaining the working gap between the inner cylindrical surface of workpiece and the tool surface. Rest of the workpiece setup is comprising of two plumber blocks through which a shaft is allowed to pass. This shaft is driven with the help of the third servo motor that provides rotational motion to the workpiece.

### 15.3 Experimentation

The setup was prepared for analyzing the performance of the newly developed magnetorheological grinding process for the finishing of the inner cylindrical surface. The preliminary experiments were performed for the investigation of the effectiveness of the tool in the form of output parameter, i.e., change in surface roughness. The dial gauge and height gauge were used so to find any error or misalignment in the axis of the tool and the workpiece. The deflection in the system was analyzed and the results obtained were zero. Thus, we were successful in maintaining the requisite gap between the tool and the workpiece.

Before performing the experimentation, the initial surface roughness value for the cylindrical inner workpiece was recorded with the help of surf test SJ-400 (Mitutoyo, Japan) using 0.25 mm cut off length and the number of intervals as 5. The value of the surface roughness was measured at different locations within the cylindrical workpiece and an average value was considered. After the initial preparations, the direct current was passed through the coil utilizing a DC system. As the current started flowing through the coil the heat is generated which is controlled with the help of cooling system whose inflow and outflow path are present on the bobbin surrounding the coil. The digital gauss meter is used for the analysis of the magnetic flux density on the surface of the tooltip which is cylindrical in shape.

The MR polishing fluid was made in a mixer with percentage composition of carbonyl iron powder (CIP) as 20% average particle size of 18  $\mu\text{m}$ , silicon carbide powder (SiC) as 20% with an average particle size of 19  $\mu\text{m}$  and rest 60% is paraffin and AP3 grease. This composition of the MR polishing fluid is considered on the basis of the available literature for finishing of internal cylindrical surface [7]. They are allowed to mix together for a while and then they are ready to use as polishing fluid. Table 15.2 shows the parameters which are considered for the finishing process of the internal cylindrical workpiece. The experiment was performed with the magnetorheological polishing fluid which is renewed after every 20-min cycle time. The process was performed for three machine cycles before the final measurement of surface roughness was recorded after total finishing time of 60 min. Later, the

**Table 15.2** Parameters and conditions used for experimentation

Parameters	Conditions
Total finishing time (min)	60
Tool rotational speed (rpm)	500
Workpiece rotational speed (rpm)	300
Tool reciprocation speed (cm/min)	10
Gap between tool and workpiece (mm)	0.6

surface topography of the initial and final surfaces was recorded with the help of scanning electron microscope.

## 15.4 Results and Discussion

The magnetic flux density in the working gap can be seen in Fig. 15.2a. This signifies that the maximum magnetic flux density in the working gap is around 0.17 T on the cylindrical surface of the tool. As higher the induced magnetic flux density, the higher will be the finishing forces that are acting on the abrasives through the carbonyl iron particles. Therefore, the higher finishing forces and relative motion provides greater finishing on the surface of the workpiece. Due to this the magnetorheological finishing fluid will remain stick to the tool surface which further will shear out microchips from the surface of the workpiece. Thus, the capability of the newly developed magnetorheological grinding process was also analyzed after the preliminary experiment was performed on the inner cylindrical surface of the workpiece. The analysis is done on the bases of the surface roughness profile for inner cylindrical workpiece surface. This is represented in Fig. 15.5. In the initial surface roughness profile, it can be seen that the graph indicates the roughness of the initial inner cylindrical workpiece surface. But after the MR grinding process is performed, the surface roughness was reduced. Thus, this denotes that the peaks had been removed from the inner cylindrical surface and hence the outcome of the process is much smoother surface from the initial one.

In Fig. 15.5 shows the surface roughness profile prior to and post finishing process has been shown. The reduction in the surface roughness value is observed which varies from the initial value of  $R_a = 250$  nm,  $R_q = 359$  nm and  $R_z = 2300$  nm to the finally finished value of  $R_a = 110$  nm,  $R_q = 200$  nm and  $R_z = 1130$  nm in 60 min, respectively. The total percentage reduction in roughness value is calculated to be 56%. The percentage change in  $R_a$  values for each cycle with 20 min of finishing time till 60 min was found to be 28%, 22%, and 21.4%, respectively.  $R_a$  is calculated as the arithmetic mean deviation of the surface measurement of filtered roughness profile. It is determined from deviation about the centre line along the evaluation length and used for the characterization of the material for internal cylindrical applications. The  $R_a$  value in the first cycle was reduced from 250 to 180 nm, with next 20 min cycle the value was reduced to 180–140 nm and with the last cycle the reduction was obtained

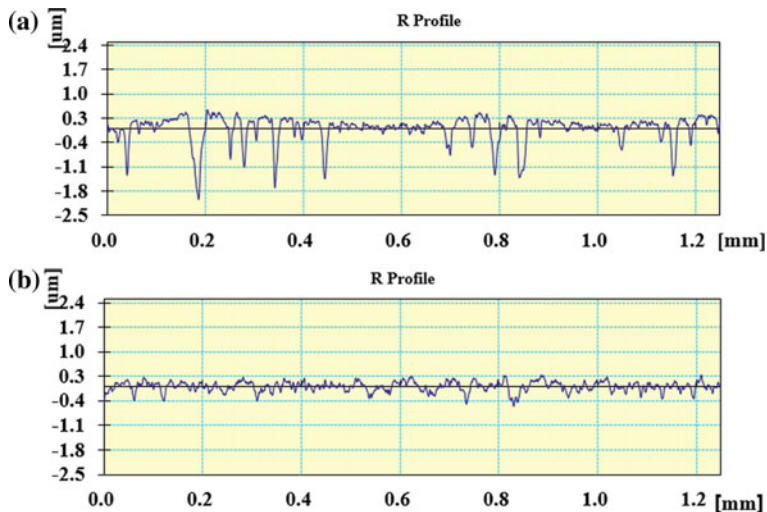


**Fig. 15.5** Surface roughness profile **a** before, and **b** after implementation of the MR grinding process

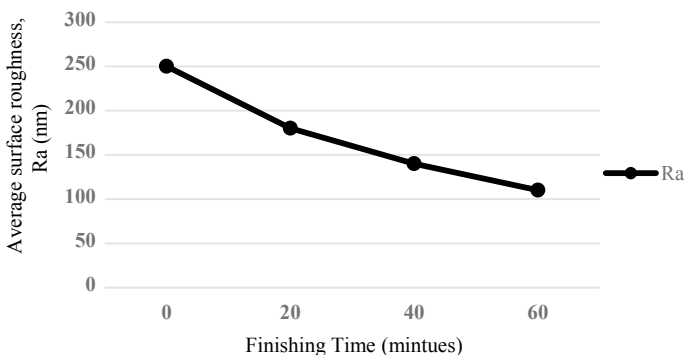
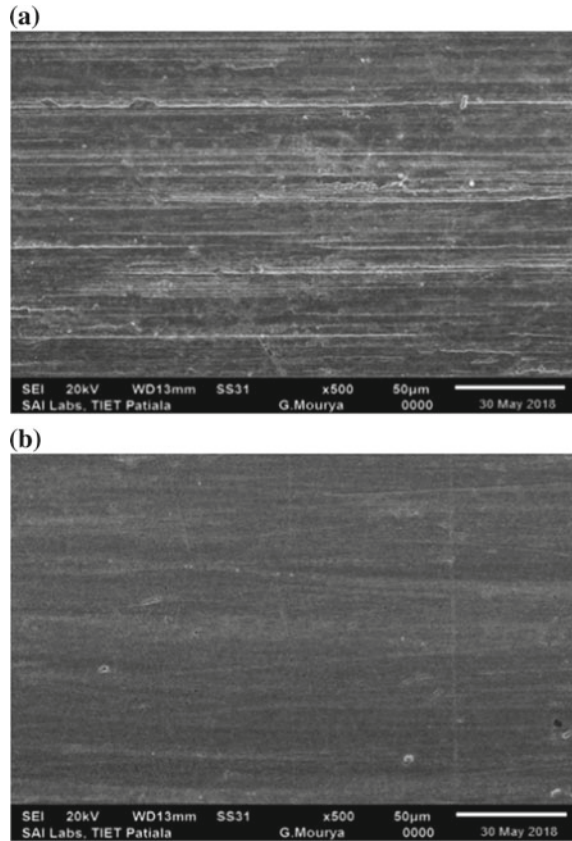


**Fig. 15.6** Change in average surface roughness (Ra) in 60 min finishing time during the MR grinding process

as 110 nm. The graph in Fig. 15.6 represent the reduction in the surface roughness value.

The surface characteristics of the workpiece were observed with the help of scanning electron microscopy (SEM) by simply differentiating the surface topography of the initial and the final image which is as shown in Fig. 15.7. Thus, with SEM images improvement can be seen in the surface characteristics of the initial and final surfaces of the internal cylindrical surfaces. The lower value of the surface roughness can be attained by further finishing the workpiece with the finer abrasives. Therefore, this magnetorheological grinding process demonstrates the finishing of the workpiece

**Fig. 15.7** Scanning electron microscope images **a** before, and **b** after the MR grinding process



without heating of the electromagnetic coil. Hence, this MR process is capable of finishing internal cylindrical workpiece of any diameter.

## 15.5 Conclusions

The following conclusions are made considering the finite element analysis and the experimentation performed. It ensures the effectiveness and performance of the magnetorheological grinding tool.

- The new designed magnetorheological grinding tool is found capable to finish the internal cylindrical parts. It can also be useful for the finishing of various parts with different diameters as the tool rotates eccentrically to the center axis of the workpiece.
- The roughness value of the internal cylindrical surface changed from the initial value of 250 nm to the final value of 110 nm in a period of 60 min.



- The surface characteristics of the MR finished surface is improved as it is revealed from the scanning electron microscopy images.
- The obtained results revealed that the newly developed magnetorheological grinding tool is useful to finish the various internal surface of workpieces such as the barrel of injection molds, dies, etc.

## References

1. Baron, Y.M.: Technology of Abrasive Finishing in the Magnetic Field. Masino-strojenje, Leningrad (1975)
2. Jain, V.K.: Magnetic field assisted abrasive based micro-nano-finishing. *J. Mater. Process. Technol.* **209**(20), 6022–6038 (2009)
3. Shinmura, T., Yamaguchi, H.: Study on a new internal finishing process by the application of magnetic abrasive machining: internal finishing of stainless-steel tube and clean gas bomb. *JSME Int. J. Ser. C Dyn. Control Robot. Des. Manuf.* **38**(4), 795–804 (1995)
4. Chang, Y.P., Hashimura, M., Dornfeld, D.A.: An investigation of material removal mechanism in lapping with grain size transition. *J. Manuf. Sci. Eng.* **122**(3), 413–419 (2000)
5. Li, C.H., Cai, G.Q., Xiu, S.C., Li, Q.: Material removal model and experimental verification for abrasive jet precision finishing with wheel as restraint. *Key Eng. Mater.* **304**, 555–559 (2006)
6. Gorana, V.K., Jain, V.K., Lal, G.K.: Experimental investigation into cutting forces and active grain density during abrasive flow machining. *Int. J. Mach. Tools Manuf.* **44**(2–3), 201–211 (2004)
7. Bedi, T.S., Singh, A.K.: A new magnetorheological finishing process for ferromagnetic cylindrical honing surfaces. *Mater. Manuf. Process.* **33**(11), 1141–1149 (2017)
8. Barletta, M., Tagliaferri, V.: Development of an abrasive jet machining system assisted by two fluidized beds for internal polishing of circular tubes. *Int. J. Mach. Tools Manuf.* **46**(3–4), 271–283 (2006)
9. Kim, J.D., Kang, Y.H., Bae, Y.H., Lee, S.W.: Development of a magnetic abrasive jet machining system precision internal precision of circular tubes. *J. Mater. Process. Technol.* **71**(3), 384–393 (1997)
10. Jha, S., Jain, V.K.: Design and development of the magnetorheological abrasive flow finishing (MRAFF) process. *Int. J. Mach. Tools Manuf.* **44**(10), 1019–1029 (2004)
11. Das, M., Jain, V.K., Ghoshdastidar, P.S.: Nanofinishing of flat workpiece using rotational magnetorheological abrasive flow finishing (R-MRAFF) process. *Int. J. Abras. Manuf. Technol.* **62**(1–4), 405–420 (2012)
12. Paswan, S.K., Bedi, T.S., Singh, A.K.: Modelling of simulation of surface roughness in magnetorheological fluid based honing process. *Wear* **376**, 1207–1221 (2017)
13. Grover, V., Singh, A.K.: Improved magnetorheological honing process for nanofinishing of various cylindrical internal surface. *Mater. Manuf. Process.* **33**(11), 1177–1187 (2018)

# Chapter 16

## A Study on Micro-tool and Micro-feature Fabrication in Micro-EDM



Biswesh Ranjan Acharya , Abhijeet Sethi , Akhil Dindigala , Partha Saha  and Dilip Kumar Pratihar 

**Abstract** In micro-EDM, micro-tool of precise shape and size is a prerequisite for successful micro-feature fabrication. Complexity in micro-tool shape increases significantly, when the tool size is reduced below 100  $\mu\text{m}$ . In this paper, a cylindrical micro-tool of average diameter 68  $\mu\text{m}$  and length 1776  $\mu\text{m}$  is successfully fabricated using the wire-EDG process in two steps, at first a rough machining, which is followed by a finish machining step. Moreover, a step-by-step procedure is discussed to determine the optimal parameter values for both rough machining and finish machining by analyzing the effects of various significant parameters, such as capacitance, voltage, duty ratio and radial feed on lateral slit overcut and number of short circuits taking place during machining of micro-slit on tungsten rod with a brass wire during wire-EDG. Both machining time and consumption of tungsten electrode are minimized by employing this methodology. Finally, micro-features like micro-hole, micro-channel and square slot are fabricated on 100  $\mu\text{m}$  thick SS304 sheet.

**Keywords** Lateral slit overcut · Micro-hole · Micro-channel · Square slot · Tungsten rod

### 16.1 Introduction

With the continuous development in technology and growing popularity of miniaturized products, manufacturers are forced to manufacture the products to meet the demand of the market. In some cases, the present fabrication processes fail to deliver the product with the required functionality, which motivated researchers either to invent some new fabrication process or to improve the current fabrication process so as to make the required product. Electrical discharge micromachining (micro-EDM) is an improvisation of widely used electrical discharge machining (EDM) process,

---

B. R. Acharya · A. Sethi · A. Dindigala · P. Saha (✉) · D. K. Pratihar  
Department of Mechanical Engineering, Indian Institute of Technology Kharagpur, Kharagpur  
721302, West Bengal, India  
e-mail: [psaha@mech.iitkgp.ernet.in](mailto:psaha@mech.iitkgp.ernet.in)

© Springer Nature Singapore Pte Ltd. 2020  
M. S. Shunmugam and M. Kanthababu (eds.), *Advances in Unconventional Machining and Composites*, Lecture Notes on Multidisciplinary Industrial Engineering, [https://doi.org/10.1007/978-981-32-9471-4\\_16](https://doi.org/10.1007/978-981-32-9471-4_16)

where comparatively less discharge energy is used for fabricating complex micro-features on any electrically conductive material irrespective of its mechanical properties [1]. Unlike EDM process, where a pre-designed tool is used according to the final shape of the desired product, in micro-EDM, a simple tool, preferably a cylindrical tool with diameter less than 500  $\mu\text{m}$ , is moved along the desired path for successful micro-feature fabrication. During the process, the higher resolution movements of sub-micron range for X, Y and Z axes are intended. As comparatively less discharge energy is used during the micro-EDM process, it minimizes major disadvantage like HAZ on final product. But, in some cases, fabrication of micro-tool is a difficult task, where micro-tool diameter is preferred to be less than 100  $\mu\text{m}$ . Rahman et al. [2] suggested for an in situ micro-tool fabrication to avoid clamping errors, which may be up to 5–10  $\mu\text{m}$  that may lead to unwanted inaccuracy in fabricated micro-feature. Jahan et al. [3] found that the use of resistance/capacitance (RC) pulse generator is the most suitable one for micro-EDM process for providing minimum pulse energy to melt very small amount of work material, which can be easily flushed away from machined zone. Masuzawa et al. [4] used micro-wire electric discharge grinding (micro-WEDG) process to fabricate tungsten micro-tools with high aspect ratio. The suggested method can fabricate very thin micro-tools with high accuracy and good repeatability. But handling of micro-wire and poor wire tension may lead to improper surface finish of generated micro-tool, as found by Lim et al. [5]. Rahman et al. [2] recommended to use block EDM process for high aspect ratio micro-tool fabrication, where the machining is subdivided into roughing and finishing processes by selecting the depth of a single pass, number of machining passes, and the amount of discharge energy supplied during the process. Acharya et al. [6] compared the micro-tools fabricated by block micro-EDM, disk micro-EDM, and wire micro-EDG in terms of generated taper and surface roughness. Mahendran et al. [7] discussed various EDM process parameters, such as discharge voltage, peak current, pulse duration, pulse interval, pulse waveform, polarity, and electrode gap. Mahdavejad and Mahdavejad [8] studied the reasons for instability in electrical discharge machining of WC-Co composites and found that prevention of short circuits is essential for stability of the process. Short circuits are harmful in EDM as it can deteriorate the quality of machined surface and causes decrease in material removal rate. Wang et al. [9] fabricated micro-hole in SUS 304 by both micro-EDM and micro-ECM process and found that later gave undesired stray corrosion. However, there is no step-by-step procedure to determine the optimal parameter values for each process. The current paper discusses the methodology for determining the necessary parameter values for both roughing process and finishing process by measuring lateral slit overcut and number of short circuits occurring at different parametric setup during fabrication of various micro-slits. This methodology not only saves time but also avoids the unnecessary consumption of tungsten material by determining the optimal process parametric values. After determining the values of different process parameters, a micro-tool was fabricated using wire-EDG process. Later micro-features like micro-hole, micro-channels, square slot were fabricated on 100  $\mu\text{m}$  thick SS304 sheet and scanning electron microscope (SEM) was used to measure the final dimensions of fabricated micro-tools and micro-features.

## 16.2 Micro-tool Fabrication and Micro-feature Fabrication in Micro-EDM

In micro-EDM, governed by the same principle as EDM, repetitive electrical discharges at the nearest local positions between anode and cathode are the sole reason for material removal from the anode by melting and vaporization, when both are immersed inside a suitable dielectric fluid and an external pulse DC power supply is applied between them. During the process, both the electrodes are separated by a very small gap, which is continuously maintained by a servo-controller mechanism. Both spark energy and spark gap are scaled down so as to effectively remove very less material from the confined position of anode.

At first, a micro-tool was fabricated by determining the values of different process parameters for both rough machining as well as finish machining. Second, the fabricated micro-tool was engaged for various micro-feature fabrication on 100  $\mu\text{m}$  thick SS304 sheet. A digital microscope was used for online monitoring of micro-tool and measuring micro-tool dimension at intermediate positions, whereas SEM was used for measuring the final dimensions of fabricated micro-tool and micro-features.

## 16.3 Experimental Procedure

### 16.3.1 *Experimental Setup*

Experiments were carried out on a micro-electrical discharge machine (model: TTECM 10, make: Synergy Nao Systems India) where both micro-electrical discharge machining and micro-electrochemical micromachining operations could be done by interchanging the dielectric with an electrolyte (Fig. 16.1). The maximum bed movements were restricted to 135 mm, 60 mm and 70 mm along X, Y, Z axes, respectively. Linear motions along the three axes were controlled by separate optical sensors with a resolution of 0.1  $\mu\text{m}$ . Resistance–capacitance type EDM circuit with constant resistance of 1000  $\Omega$  used for providing the required pulsed DC power supply. A wire-EDG module was also externally attached for in situ micro-tool fabrication.

### 16.3.2 *Experimental Scheme*

Tungsten has certain distinct properties, such as high melting point, high thermal and electrical conductivity and high corrosion resistance. Due to its unique ability to maintain rigidity at high temperature at diameter below 100  $\mu\text{m}$ , it is suitable as micro-tool material. As the selection of appropriate process parameters was vital for micro-tool fabrication, a distinctive methodology was used for determining its

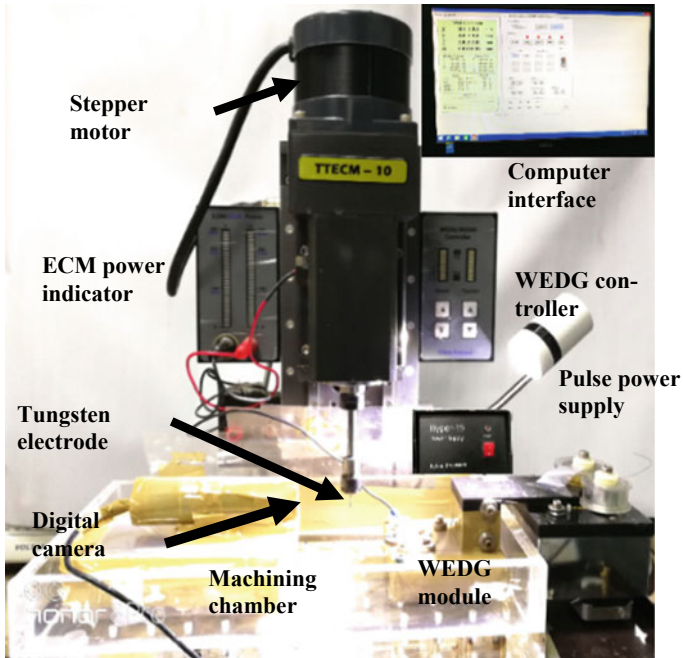


**Fig. 16.1** Micro-EDM setup

value for both roughing as well as finishing processes. During the process, micro-slits were cut on a tungsten rod of  $1000\ \mu\text{m}$  diameter, by penetrating a moving brass wire of  $250\ \mu\text{m}$  inside it and responses like lateral slit overcut and number of short circuits were measured. Both lateral slit overcut and number of short circuits were considered as the performance measures of the micro-slit cut process, which helped to select the optimal value for a specific parameter during micro-tool fabrication. Lateral slit overcut  $((D - d)/2)$  is defined as the half of the difference between lateral slit width ( $D$ ) and brass wire diameter ( $d$ ), which also signifies the machining accuracy. Figure 16.2a, b represent the schematic view of micro-slitting process and geometrical representation of micro-slit cut, respectively. During the experimentations, the effect of a single parameter was observed on lateral slit overcut and number of short circuits, and based upon their collective effect, optimal parameter values were determined for micro-tool fabrication. At first, the effect of voltage on lateral slit overcut and number of short circuits were measured at different capacitance values. Based upon the combined result, voltage and capacitance values were set for both rough machining as well as finish machining. Second, based upon the effect of duty ratio on lateral slit overcut and number of short circuits, duty ratio was also determined. Third, the optimal radial feed value was determined by noticing the variation of lateral slit overcut and number of short circuits. Wire feed was kept fixed at  $0.2\ \text{mm/s}$  to minimize consumption of brass wire during micro-slit formation. Though tool was kept stationary during micro-slit fabrication, spindle was

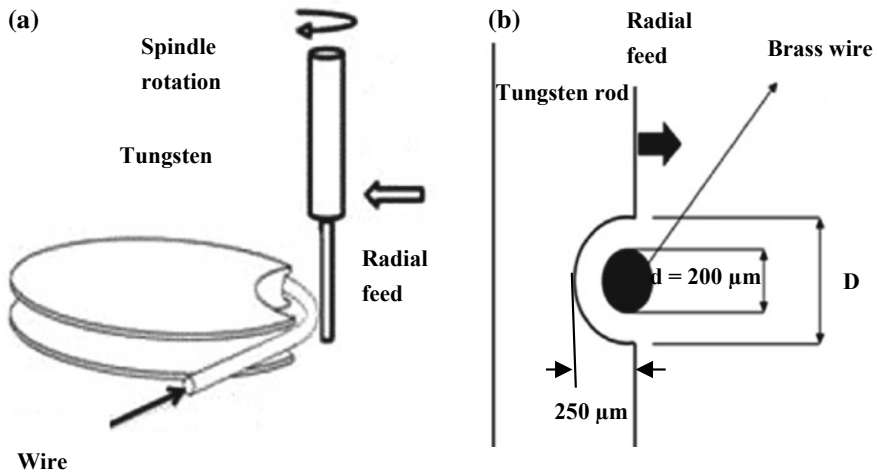


**Fig. 16.2** Micro-slit cut process. **a** Schematic view, **b** geometrical representation

kept rotating at 1500 RPM to maintain dimensional accuracy and avoid any taper [2] during micro-tool fabrication process. It is to be noted that sludge removal was accelerated by moving brass wire and rotating spindle during micro-slit formation and micro-tool fabrication, respectively. After successfully fabricating a micro-tool, it was used for generating micro-features such as micro-hole, micro-channels and a square slot on a 100 μm thick SS304 sheet. Chemical composition of tungsten tool is shown in Table 16.1. Feasible parameter ranges and experimental layout for fabricating micro-slits to determine the significant parametric values for micro-tool fabrication are shown in Table 16.2 and Table 16.3 respectively. Figure 16.3 shows the SEM images of slit cuts at different parameters' setup.

**Table 16.1** Chemical composition of tungsten material

Element	K	C	O	W
Weight %	0.01	0.01	0.03	99.95

**Table 16.2** Feasible parameter ranges

Capacitance (nF)	10, 47
Applied voltage (V)	80, 110, 140, 170, 200
Duty ratio (%)	30, 50, 70
Radial feed (μm/s)	0.1, 0.2, 0.3
Wire feed (mm/s)	0.2

**Table 16.3** Experimental layout for micro-slit formation

Sl. No.	Capacitance (nF)	Voltage (V)	Duty ratio (%)	Radial feed ( $\mu\text{m/s}$ )	Lateral slit width ( $\mu\text{m}$ )	Lateral slit overcut ( $\mu\text{m}$ )	No. of short circuits
1	10	80	50	0.1	216.8	8.4	44
2		110			227.1	13.6	9
3		140			228.6	14.3	7
4		170			230	15.0	0
5		200			232.9	16.5	2
6	47	80	50	0.1	234.4	17.2	37
7		110			235.8	17.9	26
8		140			237.3	18.7	17
9		170			241.7	20.9	7
10		200			247.6	23.8	13
11	10	170	30	0.1	228.6	14.3	5
12			70		232.9	16.5	7
13	10	170	50	0.2	224.1	12.1	6
14				0.3	227.1	13.6	11

## 16.4 Results and Discussion

Figure 16.4 shows the effects of various significant parameters such as capacitance, voltage, duty ratio, and radial feed on the responses like lateral slit overcut and number of short circuits, based upon which, the parameters for both rough machining and finish machining are to be determined.

In micro-EDM, the amount of discharge energy per pulse imparted during machining is a function of both capacitance and gap voltage and the crater size produced on the micro-tool surface can be decreased by decreasing the capacitance and gap voltage. It was also reported that when the discharge energy becomes the higher, the discharge column lasts for the longer, which increases the spark gap and ultimately reduces the accuracy of micro-electrode by forming the larger craters on tool surface [2]. But, it is practically quite difficult to measure the spark gap during micro-EDM process, which is an important index for determining the surface quality of fabricated micro-tool. As lateral slit overcut during micro-slit cut resembles with the spark gap during the micro-tool fabrication process, the effects of various process parameters on fabricated micro-tool can be understood by analyzing micro-slit cut at the same parameter settings. This methodology is capable of determining optimal process parameter values for roughing process and finishing process during micro-tool fabrication, which saves both time and unnecessary consumption of tungsten electrode. Although both lateral slit overcut and number of short circuits are to be minimized

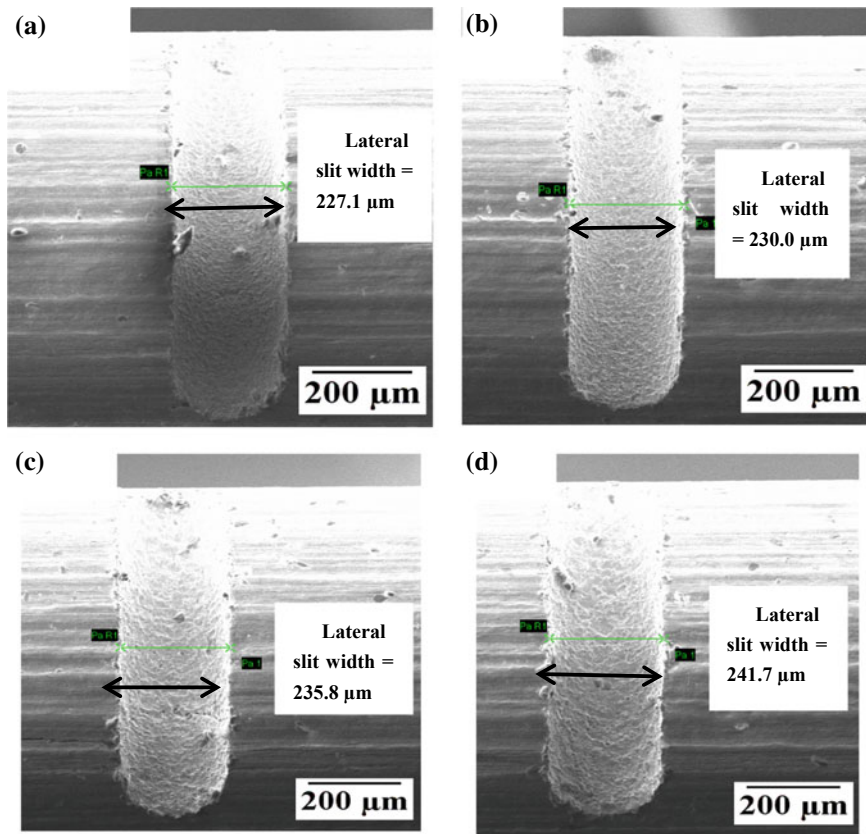


**Fig. 16.3** SEM images of lateral slit cuts obtained at **a** 110 V, 10 nF; **b** 170 V, 10 nF; **c** 110 V, 47 nF; **d** 170 V, 47 nF; with 50% duty ratio, 0.2 mm/s wire feed, and 0.1  $\mu\text{m/s}$  radial feed

during micro-slit cut, after reaching a certain minimum lateral slit overcut, the number of short circuits increases as it becomes difficult for sludge removal within very small interelectrode gap.

Figure 16.4a, b shows the effects of voltage on lateral slit overcut and number of short circuits at different capacitance values. For the same voltage, at 47 nF, the discharge energy was more than that at 10 nF and the discharge column lasted for the longer, which increased the spark gap. So, the measured lateral slit overcut was found to be more at the higher capacitance than that at the lower capacitance, for the same voltage value. As discharge energy increased with the increase in voltage, lateral slit overcut increased continuously with the increase in voltage at constant capacitance. Again, the number of short circuits decreased, attained a minimum value and then increased with the increase in voltage. It was due to the fact that at low voltage, the discharge energy was small, which resulted in short lasting of discharge column. As a result, spark gap at the lower voltage was found to be small in comparison to that



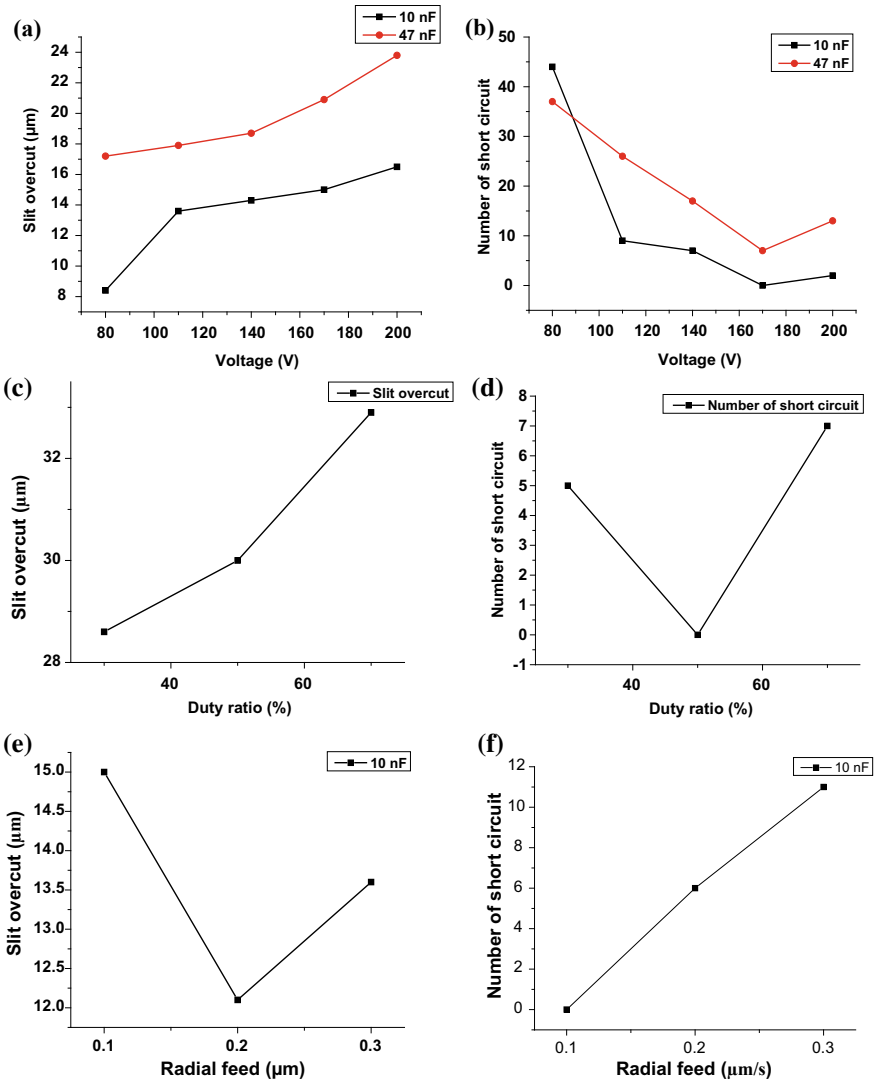


**Fig. 16.4** Effect of significant parameters on lateral slit overcut and number of short circuits. **a** Variation of voltage versus lateral slit overcut for different capacitance values, **b** variation of voltage versus number of short circuits for different capacitance values, **c** variation of duty ratio versus lateral slit overcut for 10 nF and 0.1  $\mu\text{m/s}$  radial feed, **d** variation of duty ratio versus number of short circuits for 10 nF and 0.1  $\mu\text{m/s}$  radial feed, **e** variation of radial feed versus lateral slit overcut for 10 nF and 50% duty ratio, **f** variation of radial feed versus number of short circuits for 10 nF and 50% duty ratio

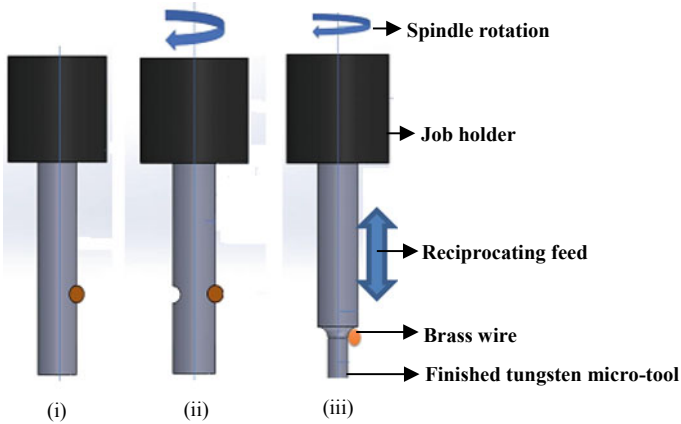
of the higher voltage value, which made sludge removal difficult, and the number of short circuits increased. So, the capacitance values of 47 nF and 10 nF were selected for rough machining and finish machining, respectively. Although for both the capacitances, machining at 170 V resulted in less number of short circuits, the lateral slit overcut increased abruptly after 140 V for the higher capacitance. So, for rough machining, 140 V was selected as optimal voltage value, whereas 170 V was chosen as optimal voltage value for finish machining during micro-tool fabrication.

Figure 16.4c, d show the effects of duty ratio on lateral slit overcut and the number of short circuits for 10 nF capacitance and 0.1  $\mu\text{m/s}$  radial speed. At 30% duty ratio, lateral slit overcut was found to be the minimum but it yielded a significant number of short circuits. At 50% duty ratio, the number of short circuits was found to be minimum with moderate increase in lateral slit overcut. But, at 70% duty ratio, both the lateral slit overcut and the number of short circuits increased abruptly, which was not desired. It might be due to the fact that pulse off time was less enough to remove the sludge effectively, which also avoided further machining. So, 50% duty ratio was selected as the optimal one for micro-tool fabrication. Pulse period was kept fixed at 10  $\mu\text{s}$  for all cases.

Figure 16.4e, f displays the variation of radial feed on lateral slit overcut and number of short circuits. During the experimentation, both capacitance and duty ratio was kept constant at 10 nF and 50%, respectively. With the increase in radial feed from 0.1 to 0.2  $\mu\text{m/s}$ , there was a sudden decrease in lateral slit overcut as the brass wire penetrated the tungsten rod at the faster rate, which decreased the amount of local machining time. But, the number of short circuits constantly increased with the increase in the radial feed. It was also observed that at 0.2  $\mu\text{m/s}$  radial feed, a few number of short circuits occurred, and it might be due to less spark gap, which was evident from less lateral slit overcut. Despite the higher spark gap, which was indicated by moderate lateral slit overcut, the larger number of short circuits were experienced at 0.3  $\mu\text{m/s}$  radial feed, which might be due to the fact that radial feed was much faster than machining speed. Finally, 0.2  $\mu\text{m/s}$  was selected as an optimal radial feed for micro-tool fabrication, as the lateral slit overcut was minimum, which ensured the minimum spark gap for maintaining accuracy during finishing process. Table 16.4 shows the various process parameter values used for both rough and finish machining processes for micro-tool fabrication. Figure 16.5 displays the sequential steps used for micro-tool fabrication using wire-EDG.

**Table 16.4** Parametric setup for micro-tool fabrication

Process parameters	Rough machining	Finish machining
Voltage (V)	140	170
Capacitance (nF)	47	10
Radial feed ( $\mu\text{m/s}$ )	0.2	0.2
Duty ratio	0.5	0.5
Wire feed (mm/s)	0.2	0.2
Spindle speed (RPM)	1500	1500



**Fig. 16.5** Sequential steps for micro-tool fabrication using wire-EDG

Figure 16.6a shows the image of micro-tool fabricated using wire-EDG process with the obtained optimal process parameters for both rough and finish machining processes. Tool diameter was reduced from 1000 to 250  $\mu\text{m}$  by rough machining

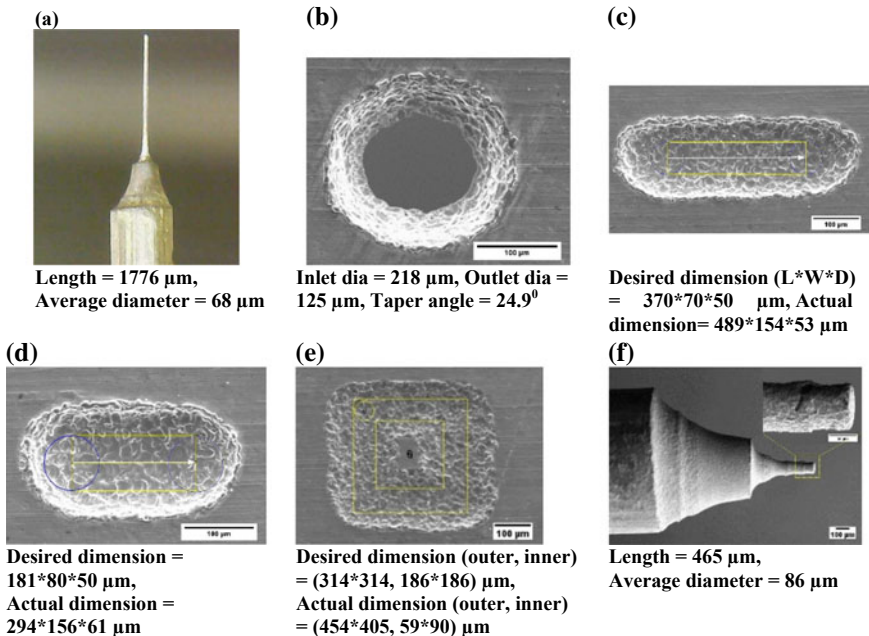


**Fig. 16.6** Image of fabricated micro-tool and various micro-features: **a** image of fabricated micro-tool, **b** SEM image of micro-hole, **c** SEM image of micro-channel 1, **d** SEM image of micro-channel 2, **e** SEM image of square slot, **f** SEM image of micro-tool after machining with an enlarged view

and it was further reduced below 100  $\mu\text{m}$  by finish machining. Length and average diameter of micro-tool were measured to be equal to 1776  $\mu\text{m}$  and 68  $\mu\text{m}$ , respectively.

After successful fabrication of micro-tool, different micro-features such as micro-hole, micro-channels, and square slot were fabricated on 100  $\mu\text{m}$  thick SS304 sheet. SEM images of fabricated micro-features with dimensions are shown in Fig. 16.6b–e. The inlet and outlet diameter of fabricated micro-hole were found to be 218  $\mu\text{m}$  and 125  $\mu\text{m}$ , respectively, and the calculated taper was found to be  $24.9^\circ$ . The actual length, width, and depth of fabricated micro-channels were found to deviate from their desired values. The dimensions of fabricated square slot were also found to deviate from their desired values. Figure 16.6f shows the SEM image of micro-tool with enlarged micro-tool tip after micro-feature fabrication. The final micro-tool diameter is also found to be increased. It may be due to the adherence of molten SS304 from workpiece material during micro-feature fabrication.

## 16.5 Conclusions

A sequential methodology was discussed to determine the necessary parameter setup for micro-tool fabrication using micro-EDM. Later, the possibility of fabricating various micro-features on 100  $\mu\text{m}$  thick SS304 sheet was also explored.

First of all, various micro-slits were cut on a tungsten rod by penetrating a moving brass wire inside it, while varying different process parameters.

Effects of various significant parameters, such as capacitance, voltage, duty ratio, and radial feed on lateral slit overcut and number of short circuits, were analyzed and according to their combined influences on lateral slit overcut and number of short circuits, optimal process parameter values for micro-tool fabrication were determined.

Lastly, a micro-tool was fabricated using wire-EDG process with the already found out optimal parameter values. Various micro-features such as micro-hole, micro-channels, and square slot were successfully produced on SS304 sheet.

## References

1. Masaki, T., Kawata, K., Masuzawa, T.: Micro electro-discharge machining and its applications. In: Proceedings of Micro Electro Mechanical Systems, 1990. An Investigation of Micro Structures, Sensors, Actuators, Machines and Robots. IEEE, pp. 21–26
2. Rahman, M., Asad, A.B.M.A., Masaki, T., Saleh, T., Wong, Y.S., Kumar, A.S.: A multiprocess machine tool for compound micromachining. *Int. J. Mach. Tools Manuf.* **50**(4), 344–356 (2010)
3. Jahan, M.P., Rahman, M., Wong, Y.S., Fuhua, L.: On-machine fabrication of high-aspect-ratio micro-electrodes and application in vibration-assisted micro-electro discharge drilling of tungsten carbide. *Proc. Inst. Mech. Eng. Part B J. Eng. Manuf.* **224**(5), 795–814 (2010)
4. Masuzawa, T., Fujino, M., Kobayashi, K., Suzuki, T., Kinoshita, N.: Wire electro-discharge grinding for micro-machining. *CIRP Ann. Manuf. Technol.* **34**(1), 431–434 (1985)

5. Lim, H.S., Wong, Y.S., Rahman, M., Lee, M.E.: A study on the machining of high-aspect ratio micro-structures using micro-EDM. *J. Mater. Process. Technol.* **140**(1–3), 318–325 (2003)
6. Acharya, B.R., Sethi, A., Saha, P., Pratihari, D.K.: A comparative study of micro-tool fabrication methods using micro-EDM. In: *Proceedings of 10th International Conference on Precision, Meso, Micro and Nano Engineering (COPEN 10)*, Indian Institute of Technology Madras, Chennai, India, pp. 210–213 (2017)
7. Mahendran, S., Devarajan, R., Nagarajan, T., Majdi, A.: A review of micro-EDM. In: *Proceedings of the International Multi Conference of Engineers and Computer Scientists*, vol. 2 (2010)
8. Mahdavinejad, R.A., Mahdavinejad, A.: ED machining of WC–Co. *J. Mater. Process. Technol.* **162**, 637–643 (2005)
9. Wang, C., He, W., Xiao, Y.: Fabrication of micro structures by ultrashort voltage pulse electrical discharge machining. *J. Miner. Mater. Charact. Eng.* **6**(02), 235–243 (2018)

# Chapter 17

## Influence of Graphite Nanopowder-Mixed Dielectric Fluid on Machining Characteristics of Micro Electric Discharge Milling



K. V. Arunpillai  and P. Hariharan 

**Abstract** There is a need for efficient micro-machining process due to increasing demand for miniaturization. In this paper, an attempt has been made to improve the machining characteristics of Micro Electric Discharge Milling by mixing graphite nanopowder in EDM oil dielectric. Titanium alloy was machined using tungsten carbide as electrode and experiments were designed based on full factorial method, three parameters such as voltage, capacitance, and concentration were varied to find optimum machining conditions. Surface characteristics and material removal rate have improved by addition of graphite nanopowder in EDM oil while machining Ti-6Al-4V. The maximum Material Removal rate is obtained at medium discharge energy levels and low levels of discharge energy yielded good surface characteristics.

**Keywords** Micro electric discharge milling · Graphite nanopowder

### 17.1 Introduction

Focus toward miniaturization to achieve compactness is raising among industries such as consumer electronics, micropower generators, robotics and healthcare, so micromachining is a sought out area for research. Miniaturization of systems and components resulted in advantages such as less space consumption, lightweight, and easy handling. Micro-EDM uses the same principle as that of Electric Discharge Machining where controlled spark occurs between tool electrode and work piece but the specific energy and inter-electrode gap is less. In micro-EDM, there is no contact between tool electrode and workpiece which enables to machine complex micro features on hard materials, micro electric discharge milling employs scanning movement of tool electrode which makes it suitable for machining 3D microcavities. Titanium alloy is being used in major applications such as aerospace, healthcare industries due to their high strength, corrosion and fatigue resistance. Machining of

---

K. V. Arunpillai (✉) · P. Hariharan  
Department of Manufacturing Engineering,  
College of Engineering Guindy, Chennai 600 025, India  
e-mail: [arunceg88@gmail.com](mailto:arunceg88@gmail.com)

© Springer Nature Singapore Pte Ltd. 2020  
M. S. Shunmugam and M. Kanthababu (eds.), *Advances in Unconventional Machining and Composites*, Lecture Notes on Multidisciplinary Industrial Engineering, [https://doi.org/10.1007/978-981-32-9471-4\\_17](https://doi.org/10.1007/978-981-32-9471-4_17)

complex 3D cavities and microchannels in titanium alloy is difficult with conventional micromachining, so nontraditional micromachining can be used to machine harder materials such as titanium alloy Ti-6Al-4V. But the problem associated with process is that low material removal rate and poor surface characteristics make it less applicable for usage. Various techniques have been experimented by researchers to improve the machining characteristics of titanium alloy, powder mixed dielectric is an advanced technique used to improve machining performance and surface quality.

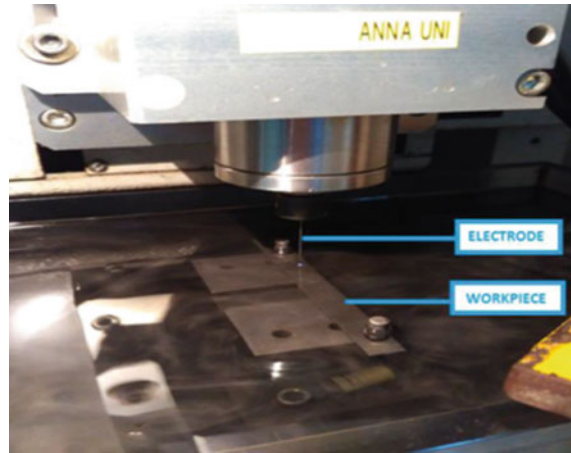
Surface characteristics and topography of tungsten carbide are improved by addition of graphite nanopowder in dielectric, high material removal rate is obtained due to increased spark gap and uniform distribution of energy. Powder mixed micro EDM provided better surface finish compared to die sinking with smoother and defect-free surface [1]. Discharge energy plays a major part in surface topography obtained in micro electric discharge milling of SKH-51 tool steel [2]. In micro electric discharge milling low concentration of silicon carbide powder and high energy level resulted in high MRR while machining Titanium alloy, also high surface roughness is observed with high energy level [3]. Recast layer thickness and material removal rate increases with concentration levels of 4–6 g/l beyond that concentration level material removal rate decreases, optimum surface roughness value is obtained at low values of discharge current [4]. Machining characteristics in micro electric discharge milling is greatly influenced by capacitance, voltage and powder concentration, low levels of powder concentration resulted in minimum tool wear rate [5]. Surface quality is improved by addition of micro molybdenum disulfide powder in dielectric with combined effect of ultrasonic vibration and a flat surface without black spots is obtained [6]. The combined effect of ultrasonic vibration and magnetic field resulted in low material removal compared to separate application of each in micro electric discharge milling [7]. Horizontal feed rate, tool rotational speed along with layer thicker affect the machining characteristic of micro electric discharge milling [8]. Generated a solid lubricating layer on Ti6Al4V using tungsten disulfide mixed dielectrics in micro-EDM process [9]. High aspect micro holes and thin white layer achieved in micro-EDM process using copper-added dielectrics [10]. Length of sparking and machining stability is augmented with powder-suspended dielectrics resulted in increase in overcut and material removal rate [11] Determined the optimum machining parameters that more influenced the material removal rate and overcut using grey relational analysis [12]. Applied ultrasonic vibration in micro-EDM process to achieve high quality of microchannels and MRR [13].

## 17.2 Experimentation Details

The experimental work was performed using DT-110 Micro Electric Discharge milling setup as shown in Fig. 17.1 it has the capability to generate the Micro and Macro components on any conductive (electrical) materials.

Average Surface Roughness ( $Ra$ ) was measured by means of Non-Contact Taly-surf CCI3000A. 3D surface roughness profiles of micro slots machined at different

**Fig. 17.1** Micro electric discharge milling setup



energy levels for EDM oil and 0.2 g/l concentration of graphite nanopowder mixed dielectric was observed. Titanium alloy Ti-6Al-4V is used as workpiece which has very high tensile strength and toughness at extreme temperature and it is widespread across the engineering field. Initially, workpiece has been prepared in form rectangular strips using an abrasive jet cutting process and then workpiece surface was cleaned by submerging into acetone in order the deposited abrasive particles on the surface. Non-hollow cylindrical shape tungsten carbide of diameter 500  $\mu\text{m}$  is used as tool electrode; it is hard and provides good resistance to deformation and deflection. Micrograph of non-hollow cylindrical tungsten carbide is shown in Fig. 17.5. Table 17.1 depicts the experimental conditions considered.

EDM oil 3 was used as the dielectric fluid for this study and graphite nanopowder of average particle size 1–2 nm (procured from nanoshell) is mixed in dielectric fluid and experiment is carried out. In order to ensure the proper mixing of nanographite powder particles with EDM oil dielectric two mechanical stirrers were employed and it placed over the tank. Before using as an EDM dielectric the nano graphite fluid was ultra-sonicated for two hours in order to avoid the agglomeration of powder particles. The speed of stirrer was kept constant for considered different spark energy. A separate dielectric system was used for nanopowder mixed dielectric without distributing the existing system. Also experiments are conducted in general factorial method considering levels as shown in Table 17.2.

**Table 17.1** Experimental condition for micro electric discharge milling

Workpiece	Titanium alloy (Ti-6Al-4V)
Electrode	Tungsten carbide
Dielectric	EDM oil 3
Powder	Graphite nanopowder
Pulse generator	RC-type pulse generator



**Table 17.2** Levels considered for design of experiments

Factor	Unit	Levels
Voltage	V	80, 90, 100, 110, 120
Capacitance	nF	0.1, 1, 10
Concentration	g/L	0, 0.2

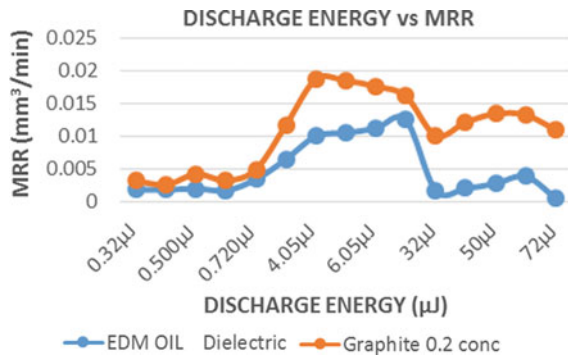
Experiments are conducted with EDM oil dielectric and graphite nanopowder mixed dielectric by machining rectangular slot of dimension 2.5 mm × 1 mm × 0.1 mm with tool spindle rotation speed of 1800 rpm and feed rate of 60 mm/min and time for machining is noted, to determine material removal rate (MRR) and tool wear rate (TWR). Also crater distribution on milled micro slots was analyzed using a lower version SEM.

From the previous studies, it is clear that no investigation has been carried using graphite nanopowder with apparent powder particles (2 nm) in micro-EDM milling of titanium alloy under three different discharge regimes. The present study discusses the benefits of added graphite nanopowder particles in micro-EDM milling of titanium alloy under different discharge energy conditions.

### 17.3 Results and Discussion

Material Removal Rate (MRR) increased with graphite nanopowder mixed dielectric compared to EDM oil dielectric, and maximum MRR is obtained at medium discharge energy levels for both EDM oil dielectric and graphite nanopowder mixed dielectric. Figure 17.2 shows the variation of material removal rate with respect to discharge energy, addition of graphite nanopowder reduces the breakdown strength of dielectric and improves the sparking frequency and thus augmentation of material removal rate (1). Moreover, due to the existence of nanopowder particles, the spark energy is distributed uniformly across the ionized gap which inturn increases MRR . As the discharge energy increases, material removal rate decreases due to

**Fig. 17.2** Variation of MRR with respect to discharge energy



increased spark gap and less distribution of energy to workpiece. In addition, due to the presence of nanopowder particles the ionized gap is enlarged due to that tool feed mechanism is unable to explore the optimum gap to discharge the spark while  $\mu$ ed milling process and this increased short-circuits occurrence, which inturn decreases MRR .

Variation of TWR with respect to discharge energy for EDM oil and nanographite powder mixed dielectric has been shown in Fig. 17.3. Tool Wear Rate (TWR) is less in the case of Powder-Mixed Dielectric as compared to EDM oil Dielectric, TWR decreased at higher energy levels due to deposition of particles on tool electrode and presence nanopowder particles the tool electrode heat is easily carried away across the ionized gap which reduced the tool wear (9). Also the availability of additives in the dielectric fluid will enhance the ionized (interelectrode) gap which reduces the debris interaction with electrode. As result of that tool wear decreased. The tool wear was low at high discharge energy because the time gap between each spark is higher due to heat energy is easily dissipated from the tool electrode which inturn decreases TWR . Maximum tool wear rate is obtained at medium discharge energy level as shown in Fig. 17.3 it is a well known fact that as the material removal rate increases the tool wear will increase vice versa.

Figure 17.4 shows the plot of 3D surface roughness value (Sa) with respect to discharge energy at 0.2 g/L graphite nanopowder concentration and EDM oil. At low discharge energy levels, good surface finish is obtained due to uniform sparking. Figure 17.5 shows the SEM image of tungsten carbide tool electrode showing deposition of graphite nanopowder after machining.

Roughness value (Sa) seemed to decrease (from the Fig. 17.4.) after addition of nano graphite powder particles for each individual level of discharge energy. This happens because of the presence of nanoparticles the thermal energy generated at the ionized gap will be widely distributed due to shallower craters created on the parental metal. As a result of that roughness decreased. Low roughness might be attributed

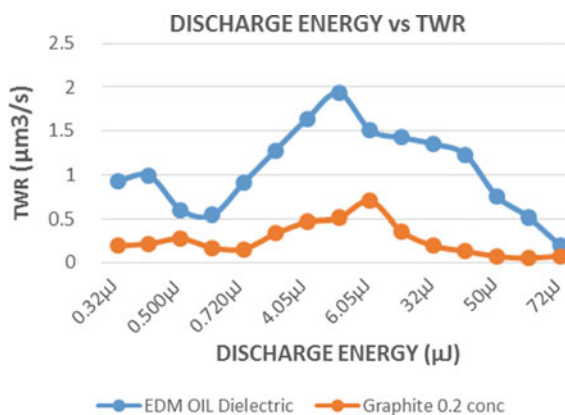
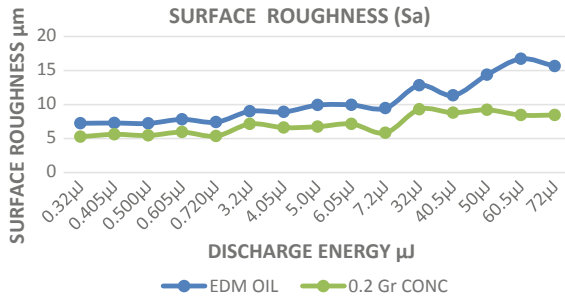
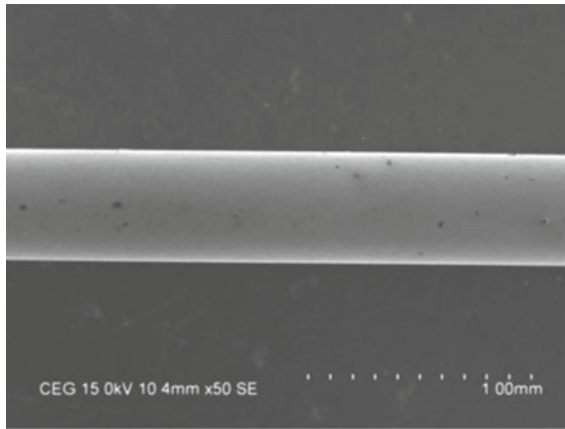


Fig. 17.3 Variation of TWR with respect to discharge energy



**Fig. 17.4** Variation of surface roughness value with respect to discharge energy



**Fig. 17.5** SEM image of tungsten carbide tool electrode after machining

in the case of nanographite powder mixed EDM oil due effective removal of chips particles from ionized gap. Uniform distribution of craters and small crater size is observed at lower discharge energy and lower surface roughness values is due to fine grain size distribution with no overlapping between craters. Crater distribution at low discharge energy levels is shown in Fig. 17.6. Overlapping of craters and nonuniform distribution of craters produced high surface roughness value at higher discharge energy compared to low energy levels. Crater distribution of micro-milled slots at higher discharge energy levels is shown in Fig. 17.7. Increment in roughness value with respect to increase in discharge energy. As the discharge energy increases, more thermal energy generated at the ionized gap due to more material removal and it makes to unable of flushing of chips particles which inturn roughness increased.

**Fig. 17.6** SEM image of crater distribution at low discharge energy levels

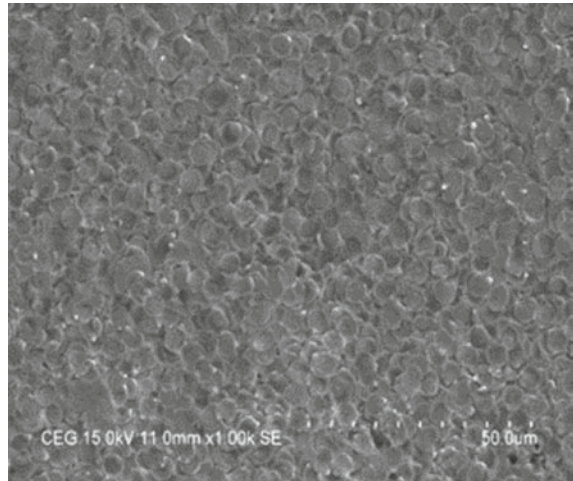
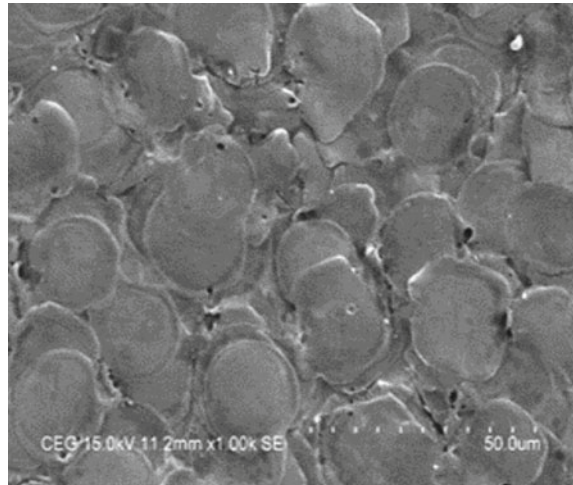


**Fig. 17.7** SEM image of crater distribution at high discharge energy levels



## 17.4 Conclusions

Machining with graphite nanopowder mixed dielectric produced high MRR and less Tool wear rate compared to EDM oil dielectric. MRR increased with graphite nanopowder mixed micro electric discharge milling due to improved machining stability with high sparking frequency and reduced breakdown strength of dielectric. Maximum MRR and TWR are obtained at medium discharge energy levels. In micro Electric Discharge Milling, powder concentration and capacitance are the predominant factors which influence the machining characteristics. At higher energy levels

there is a decrease in Material Removal rate due to large spark gap and less distribution of spark to workpiece, less tool wear rate is obtained at higher energy level due to deposition of graphite nanopowder on tool electrode. Surface Roughness decreased with graphite nanopowder mixed dielectric due to uniform distribution of energy. Low surface roughness is obtained at low discharge energy levels, as discharge energy increase surface roughness tends to be high due to overlapping of craters.

## References

1. Jahan, M.P., Rahman, M., Wong, Y.S.: Study on the nano-powder-mixed sinking and milling micro-EDM of WC-Co. *Int. J. Adv. Manuf. Technol.* **53**, 167–180 (2011)
2. Jahan, M.P., Anwar, M.M., Wong, Y.S., Rahman, M.: Nanofinishing of hard materials using micro-electrodischarge machining. *J. Eng. Manuf.* (2009)
3. Ali, M.Y., Atiqah, N., Erniyati: Silicon carbide powder mixed micro electro discharge milling of titanium alloy. *Int. J. Mech. Mater. Eng.* (2011). Kanada, T., *Modern metrology concerns*. InTech, 281–289 (1995)
4. Kolli, M., Kumar, A.: Effect of dielectric fluid with surfactant and graphite powder on Electrical Discharge Machining of titanium alloy using Taguchi method. *Eng. Sci. Technol. Int. J.* (2015)
5. Kuriachen, B., Mathew, J.: Effect of powder mixed dielectric on material removal and surface modification in micro electric discharge machining of Ti-6Al-4V. *Mater. Manuf. Process.* (2015)
6. Prihandana, G.S., Mahardika, M., Hamdi, M., Wong, Y.S., Mitsui, K.: Effect of micro-powder suspension and ultrasonic vibration of dielectric fluid in micro-EDM processes—Taguchi approach. *Int. J. Mach. Tools Manuf.* (2009)
7. Jafferson, J.M., Hariharan, P., Ram Kumar, J.: Effects of ultrasonic vibration and magnetic field in micro-EDM milling of nonmagnetic material. *Mater. Manuf. Process.* (2014)
8. Jafferson, J.M., Hariharan, P., Ram Kumar, J.: Effect of non-electrical parameters in  $\mu$ ED milling: an experimental investigation. *Int. J. Adv. Manuf. Technol.* (2015)
9. Mohanty, S., Kumar, V., Tyagi, R., Kumar, S., Bhushan, B., Das, A.K., Dixit, A.R.: Surface alloying using tungsten disulphide powder mixed in dielectric in micro-EDM on Ti6Al4V. In: *IOP Conference Series: Materials Science and Engineering*, vol. 377, no. 1, p. 012040. IOP Publishing (2018, June)
10. Cyril, J., Paravasu, A., Jerald, J., Sumit, K., Kanagaraj, G.: Experimental investigation on performance of additive mixed dielectric during micro-electric discharge drilling on 316L stainless steel. *Mater. Manuf. Process.* (2017)
11. Tiwary, A.P., Pradhan, B.B., Bhattacharyya, B.: Study on the influence of micro-EDM process parameters during machining of Ti-6Al-4V superalloy. *Int. J. Adv. Manuf. Technol.* **76**(1–4), 151–160 (2015)
12. Elsiti, N.M., Noordin, M.Y., Idris, A., Majeed, F.S.: Optimization of maghemite ( $\gamma$ -Fe<sub>2</sub>O<sub>3</sub>) nano-powder mixed micro-EDM of CoCrMo with multiple responses using gray relational analysis (GRA). In: *Journal of Physics: Conference Series*, vol. 914, no. 1, p. 012025. IOP Publishing (2017, October)
13. Unune, D.R., Mali, H.S.: Experimental investigation on low-frequency vibration-assisted  $\mu$ -ED milling of Inconel 718. *Mater. Manuf. Process.* (2018)

# Chapter 18

## Realization of Green Manufacturing Using Citric Acid Electrolyte for WC–Co Alloy Micro-tool Fabrication in Micro-WECM



Abhijeet Sethi , Biswesh Ranjan Acharya , Pranai Kumar ,  
Rajib Chakraborty and Partha Saha

**Abstract** This paper promotes green manufacturing by utilizing the environment-friendly electrolyte of citric acid for tungsten carbide alloy (WC–Co) micro-tool fabrication through micro-wire-electro chemical machining (WECM) process. The electrochemical dissolution behavior of WC–Co in different concentrations of citric acid has been investigated through open-circuit potentials and polarization curves obtained from cyclic voltammetry analysis. Response surface methodology (RSM) technique has been utilized to study the micro-WECM process characteristics and the influence of significant process parameters like electrolyte concentration, applied voltage, and reciprocating speed has been studied by analysis of variance (ANOVA). Moreover, optimization of machining parameters has been done through desirability function approach to maximize the MRR and the optimized values are found to be 0.25 M electrolyte concentration, 15 V applied voltage and 5.31  $\mu\text{m/s}$  reciprocating speed. Finally, a confirmation experiment has been conducted to fabricate a micro-tool of 111.2  $\mu\text{m}$  diameter in the citric acid electrolyte.

**Keywords** Micro-wire-electrochemical machining · Citric acid · Tungsten carbide alloy · Green manufacturing · Cyclic voltammetry

### 18.1 Introduction

Micro-tools have become the cornerstone of the micromachining industry due to their versatility in creating profiles varying from 2D structures like micro-holes, microchannels, micro-dimples, etc., to 3D structures like micro-gears, micro-nozzles, micro-grooves, etc. These micro-features are the essential parts and components of different miniaturized products in MEMS devices, fuel injectors, micro-dies, biomedical devices, sensors, and avionics industry. The use of tungsten carbide

---

A. Sethi · B. R. Acharya · P. Kumar · R. Chakraborty · P. Saha (✉)  
Department of Mechanical Engineering, Indian Institute of Technology Kharagpur, Kharagpur  
721302, West Bengal, India  
e-mail: [psaha@mech.iitkgp.ernet.in](mailto:psaha@mech.iitkgp.ernet.in)

© Springer Nature Singapore Pte Ltd. 2020  
M. S. Shunmugam and M. Kanthababu (eds.), *Advances in Unconventional Machining and Composites*, Lecture Notes on Multidisciplinary Industrial Engineering, [https://doi.org/10.1007/978-981-32-9471-4\\_18](https://doi.org/10.1007/978-981-32-9471-4_18)

alloy(WC–Co) as micro-tools is inevitable as it is one of the hardest metal widely used in industry and the properties like high toughness and high rigidity make it as an ideal material to be used as micro-tools [1–3]. Electro-discharge grinding (EDG) processes such as Wire-EDG and block-EDG are the most popular methods to fabricate WC alloy micro-tools [4, 5]. However, the abovementioned machining methods have the disadvantage of low material removal rate and high tool wear rate. On the contrary, electrochemical machining (ECM) easily dissolves hard metals with advantages like negligible tool wear, no machining force, no thermally induced stress, excellent surface quality and low roughness [6]. Micro-tool fabrication by micro-ECM process has become popular in recent times as it can generate micro-tools without any surface defects like residual stress and micro-cracks. Researchers have electrochemically machined tungsten carbide alloy through micro-ECM by using the acid and neutral electrolytes. Choi et al. fabricated WC micro-shaft of 5  $\mu\text{m}$  diameter through electrochemical etching method by using  $\text{H}_2\text{SO}_4$  [7]. Shibuya et al. made tungsten carbide alloy micro-pin through ECM using  $\text{NaNO}_3$  aqueous solution and 1% concentration solution are necessary to obtain a micro-pin with uniform diameter [8]. However, these electrolytes are not environmentally friendly and have hazardous effects such as chemical burn and permanent scarring on unprotected human being. Citric acid is a very good alternative to the present electrolytes, which is eco-friendly, and it is abundantly found in fruits and used as a preservative in food and beverages.

In this paper, an attempt has been made to fabricate tungsten carbide alloy (WC–Co) micro-tool through the micro-Wire-ECM process by using an eco-friendly citric acid electrolyte. To study the electrochemical dissolution behavior of WC–Co in citric acid, voltammetric analysis has been conducted. The influence of electrolyte concentration on material dissolution has been analyzed by measuring the open-circuit potential (OCP) and anode polarization curve. Moreover, in this paper, an RSM-based optimization process has been developed to optimize the machining parameters of micro-WECM for fabrication of WC–Co micro-tool. Additionally, the significant parameters and their respective effects have been investigated using ANOVA analysis. Finally, the model has been validated by doing confirmation test to obtain a WC–Co micro-tool by using the optimal process parameters.

## 18.2 Materials and Methods

### 18.2.1 Materials

The material used for the fabrication of micro-tool is tungsten carbide alloy (WC–Co) rod of 510  $\mu\text{m}$  diameter. It is one of the hardest metal which is widely used in industry due to properties like high toughness and high rigidity. The properties of WC–Co alloy is given in Table 18.1. In micro-WECM process brass wire of 200  $\mu\text{m}$  diameter was used as the cathode. Brass having a very good electrical conductivity is one of the most industrially accessible material and the brass wire is broadly utilized

**Table 18.1** The properties of WC–Co alloy

Cobalt (%)	Density (g/cm <sup>3</sup> )	HRA	TRS (N/mm <sup>2</sup> )	Grain size (μm)
10	14.5	92.1	3800	0.6–0.8

**Table 18.2** Parameters for cyclic voltammetry

Parameter	Values
Electrolyte (M)	C <sub>6</sub> H <sub>8</sub> O <sub>7</sub> (0.25, 0.30, 0.35)
Potential range (V)	–1 to 1
Polarization rate (V/s)	0.05
Temperature	Room temperature

for the wire cut EDM process. Citric acid is a natural organic acid in the family of carboxylic acid widely used in the food industry for flavor and preservative. It is also abundantly available in nature in the form of citrus fruits and widely used as a safe and environmentally friendly material. In the present investigation, to develop an environmentally friendly micro-ECM process 99% pure citric acid monohydrate (C<sub>6</sub>H<sub>8</sub>O<sub>7</sub>·H<sub>2</sub>O) of Loba Chemie Pvt. Ltd. is used as the electrolyte by diluting it in distilled water.

### 18.2.2 Methods

In order to study the electrochemical behavior of WC–Co in citric acid, cyclic voltammetry has been conducted. The open-circuit potentials(OCP) and polarization curves have been measured for citric acid with different concentrations. A biologic SP150 potentiostat was used for the process and a three-electrode system was implemented. The working electrode is cylindrical WC–Co alloy rod of 0.510 mm having working area (3 × 0.510) mm<sup>2</sup> which has been polished to obtain a flattened surface having a length of 3 mm and the width of 0.510 mm. The counter electrode and the reference electrode were an SS304 wire and the saturated Ag/AgCl, respectively. The parameters used for the test is given in Table 18.2.

### 18.3 Experimental Setup

In the present investigation TTECM-10 machine of Synergy Nanosystems, Mumbai has been used to fabricate WC–Co micro-tool by the micro-WECM process. The machine setup consisted of a DC pulse power supply, computer, electrolyte circulation and filtration unit, machining chamber, wire guide and feed system, and online digital camera. The machine and its component are given in Fig. 18.1a. The computer



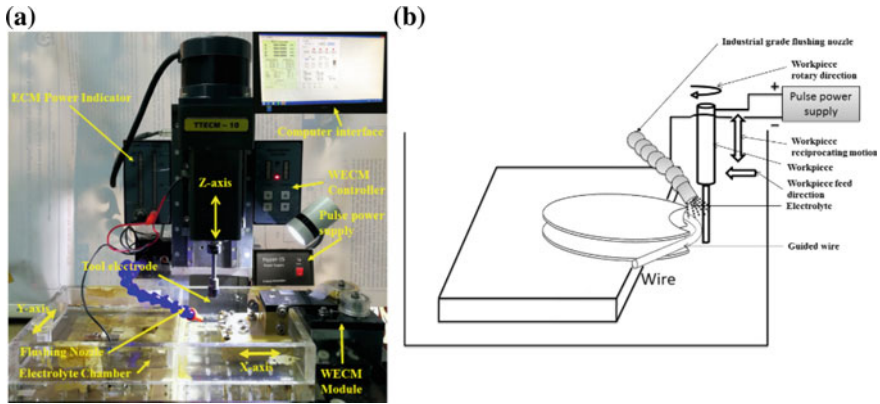


**Fig. 18.1** a Micro-electrochemical machine, TTECM-10, b a schematic illustration of micro-WECM

is fitted with Hyper 2GUI software which controls the stepper motors that subsequently control the three linear travel directions in X-, Y-, and Z-axes and the least count is  $0.1 \mu\text{m}/\text{step}$  for each linear stage. Micro-tool fabrication by micro-WECM technique follows the principle of reverse micro-ECM where the polarity between the workpiece and the tool is reversed, i.e., the tool is made anode against a cathodic wire with the electrolyte in between them and a pulsed power is supplied to increase the localization of dissolution. A schematic illustration of micro-WECM is given in Fig. 18.1b. During micro-tool fabrication by citric acid, the WC–Co cylindrical rod is given three types of motion, rotation about its own axis, reciprocating motion along z-axis and motion towards the wire cathode, i.e., depth of cut. The reciprocating motion is started at the base of WC–Co alloy rod and is moved upwards. After it completed one cycle of movement, i.e., one upward movement and then a downward movement it is given a depth of cut towards the wire cathode electrode. The process is repeated until the desired diameter is achieved and is monitored online by a digital camera attached to the system. The tool fabrication process is done under electrolyte flushing condition.

During micro-tool fabrication in micro-WECM, there are three input process parameters namely applied voltage, electrolyte concentration and reciprocating speed that can affect the MRR. Thus, to study the effect of these process parameter on MRR a design of experiment through response surface methodology (RSM) has been utilized. In the present investigation Box–Behnken design of experiments for three factors of variables was followed. The ranges of three independent factors were decided by doing numerous trial experiments and the coded form of the parameter with their respective levels are given in Table 18.3. The other parameters like pulse frequency, tool rpm, electrolyte flushing flow rate and depth of cut were kept constant whose values are given in Table 18.4. Also, the wire feed was not given as there is a negligible amount of tool wear during micro-ECM. The experimental design and ANOVA analysis of response were carried out by using Design Expert software. A

**Table 18.3** Input process parameters and their levels

Process parameters	Units	Factors in coded form	Levels		
			-1	0	1
Electrolyte concentration	Molar	A	0.25	0.30	0.35
Applied voltage	Volt	B	7	11	15
Reciprocating speed	μm/s	C	2	6	10

**Table 18.4** Machining condition

Parameter	Values
Anode electrode	WC-Co rod of 510 μm diameter
Cathode electrode	Brass wire (Φ 0.2 mm)
Electrolyte	C <sub>6</sub> H <sub>8</sub> O <sub>7</sub> (0.25, 0.30, 0.35 M)
Applied voltage	7, 11, 15 V
Pulse frequency	500 kHz
Tool RPM	500
Reciprocating speed	2, 6, 10 μm/s

total of 15 experiments were carried out by taking three levels of process parameters and are given in Table 18.5. The obtained micro-tool diameter is kept at 200 ± 50 μm for all the experiment. After conducting all the experiments as per design table, the responses were taken up for further analysis. The material removal rate was measured using the formula given below

$$MRR = (W_{initial} - W_{final}) \div t$$

where  $W_{initial}$  and  $W_{final}$  are the initial and final weights of the job in grams and  $t$  is the total machining time in minutes.

**Table 18.5** Design of experiment and response

Run sequence	Input process parameters			Response parameter
	Electrolyte concentration (M)	Applied voltage (V)	Reciprocating speed (μm/s)	MRR (g/min)
1	0.25	7	6	3.94E-05
2	0.25	11	2	0.000049
3	0.3	15	10	8.38E-05
4	0.3	7	2	0.000014
5	0.3	11	6	5.92E-05

(continued)

**Table 18.5** (continued)

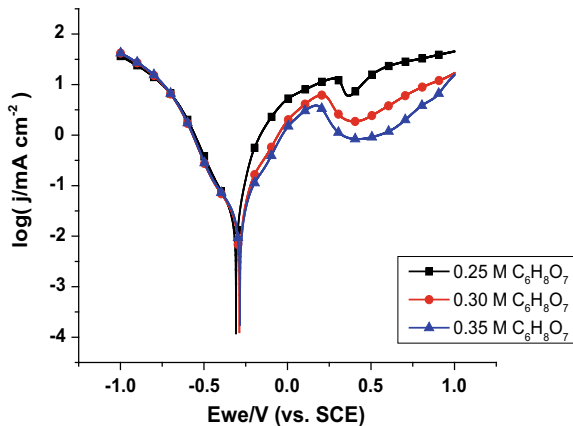
Run sequence	Input process parameters			Response parameter
	Electrolyte concentration (M)	Applied voltage (V)	Reciprocating speed ( $\mu\text{m/s}$ )	MRR (g/min)
6	0.35	11	10	0.000028
7	0.3	7	10	0.000025
8	0.3	15	2	0.000101
9	0.3	11	6	0.000079
10	0.3	11	6	5.81E-05
11	0.25	15	6	0.000166
12	0.35	7	6	0.000052
13	0.35	15	6	9.77E-05
14	0.25	11	10	4.21E-05
15	0.35	11	2	0.000026

## 18.4 Results and Discussion

### 18.4.1 Cyclic Voltammetry

Figure 18.2 shows the polarization curves obtained from cyclic voltammetry of WC-Co in citric acids with concentrations of 0.25, 0.30, and 0.35 M. The open-circuit potentials (OCPs) obtained are  $-0.267$  V,  $-0.244$  V, and  $-0.231$  V, respectively. It can be noted that the OCP defines the voltage measured when there is no current applied in the cell and it reflects the thermodynamic tendency of the electrode

**Fig. 18.2** Semi-logarithmic plot of the cyclic voltammetry of WC-Co in citric acid



material to participate in the electrochemical process with the neighboring medium or the electrolyte. So the metal having lower OCP will chemically react faster in the electrolyte than the metal having higher OCP. In this case, at 0.25 M  $C_6H_8O_7$  the OCP obtained is the lowest and with an increase in concentration, the OCP increases. In all the concentrations passivation occurs at around 0.2 V (vs. SCE) as oxide layers formed on the surface of WC-Co electrode. However, with the increase in potential beyond 0.5 V (vs. SCE) current density increases in all the cases but in case of 0.25 M concentration, it increases sharply. However, the current density decreases with increase in concentration from 0.25 to 0.35 M. This may be due to the fact that in case of weak acid like citric acid the mobility of ions decreases in higher concentration. Also, the thickness of oxide layer increases with higher concentration which decreases the electrochemical reaction subsequently reducing the current density.

### 18.4.2 Effect of Process Parameters on Material Removal Rate (MRR)

Table 18.6 represents the ANOVA of MRR. The model F-value of 28.99 implies the model is significant. Values of “Prob > F”, i.e., P-values less than 0.05 indicate model terms are significant. In this case electrolyte concentration (A), applied voltage (B), the interaction effect of electrolyte concentration and applied voltage (AB), the quadratic effect of applied voltage ( $B^2$ ) and quadratic effect of reciprocating speed ( $C^2$ ) are significant model terms. The “Pred R-Squared” of 0.8745 is in reasonable agreement with the “Adj R-Squared” of 0.9473. “Adeq Precision” measures the signal-to-noise ratio. A ratio greater than 4 is desirable. The ratio of 20.317 indicates an adequate signal. Thus, this model can be used to navigate the design space. The final equation in terms of coded factors:

$$\begin{aligned} MRR = & 6.54333E - 05 - 0.0000116 \times A + 3.97625E - 05 \\ & \times B - 0.000020225 \times A \times B + 2.15083E - 05 \\ & \times B^2 - 3.09917E - 05 \times C^2 \end{aligned}$$

Figure 18.3 shows the contour plots for various combination of process parameters. The numbers inside the contour plot are represented by MRR values. The parameter not considered in different plots are kept at their respective mid-value. From Fig. 18.3a, it can be deduced that with the increase in applied voltage the MRR increases. As higher applied voltage generates greater machining current at the inter-electrode gap thus enhancing the MRR. This outcome is in line with the fundamental principle of material removal rate in micro-ECM and thus validate the model developed here for MRR. However, the same figure shows that at a lower voltage the concentration is not a significant parameter but at a higher voltage, the MRR decreases with increase in electrolyte concentration. This result confirms the

**Table 18.6** ANOVA of MRR

Source	Sum of squares	df	Mean square	F-value	p-value Prob > F	
Model	2.1E-08	9	2.36504E-09	28.988	0.0009	Significant
A—Electrolyte concentration	1.1E-09	1	1.07648E-09	13.194	0.015	Significant
B—Applied voltage	1.3E-08	1	1.26485E-08	155.03	<0.0001	Significant
AB	1.6E-09	1	1.6362E-09	20.055	0.0065	Significant
B <sup>2</sup>	1.7E-09	1	1.70809E-09	20.936	0.0060	Significant
C <sup>2</sup>	3.5E-09	1	3.5464E-09	43.468	0.0012	Significant
<b>R-Squared</b>	0.9811		<b>Pred R-Squared</b>	0.8745		
<b>Adj R-Squared</b>	0.9473		<b>Adeq Precision</b>	20.317		

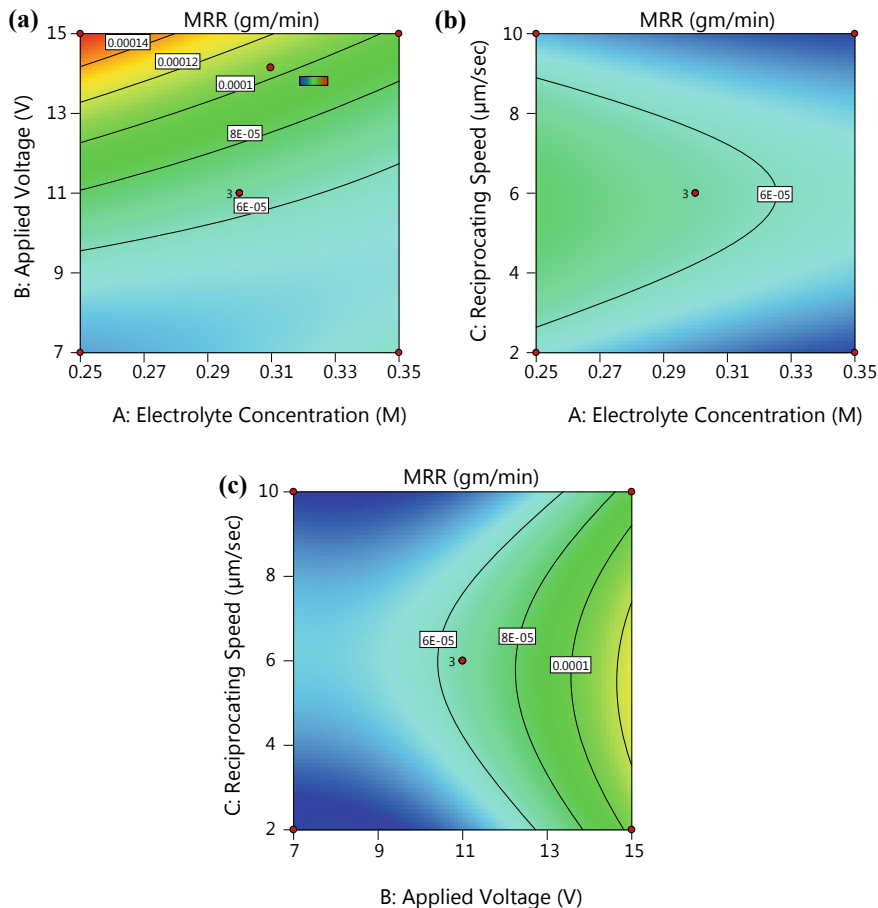


**Fig. 18.3** **a** Effect of applied voltage and concentration on MRR, **b** effect of reciprocating speed and electrolyte concentration on MRR, **c** effect of reciprocating speed and applied voltage on MRR

findings in CV analysis where the current density decreases with the increase in concentration. As in higher concentration, the passivation is more creating the tungsten or cobalt oxide on the anode surface hindering the chemical reaction to progress thus reducing the MRR. Also, the electrolyte concentration is directly related to the ion activity during the ECM process. At higher concentration, the solution becomes thick and thus limiting the ion activity due to ionic interference and less permittivity [9]. As applied voltage and concentration are the most two significant independent parameters their interaction is also found to be significant as shown in Fig. 18.3a and the highest MRR is found at 15 V applied voltage and 0.25 M electrolyte concentration.

Figure 18.3b shows the contour plot for reciprocating speed and electrolyte concentration. As ANOVA analysis showed a negative quadratic effect of reciprocating

speed on MRR it can be validated from Fig. 18.3b that with the increase in reciprocating speed the MRR increases up to a certain point and then decreases for all the electrolyte concentrations. During reciprocating motion, the ions produced at the interface of anodic WC–Co rod and the electrolyte move at the same velocity as the rod due to kinematic viscosity of the electrolyte. Thus higher reciprocating speed leads to the higher kinetic energy of the ions in the diffusion layer increasing the diffusion of dissolved ions from the anode surface [10]. As a result, the thickness of diffusion layer decreases, and the MRR increases. But with further increase in reciprocating speed, the interaction time between anodic WC–Co rod and the wire cathode decreases resulting in lower MRR. Figure 18.3c shows the contour plot for the reciprocating speed and applied voltage. From the ANOVA analysis, it was already found that their interaction does not have any significant effect on the MRR. However, at a higher voltage and intermediate reciprocating speed, the MRR is higher. SEM images of micro-tools obtained after fabrication and their surface microstructure for some experiments is given in Fig. 18.4. From Fig. 18.4d, it can be observed that for higher concentration the surface quality is greater as the material removal rate is low.

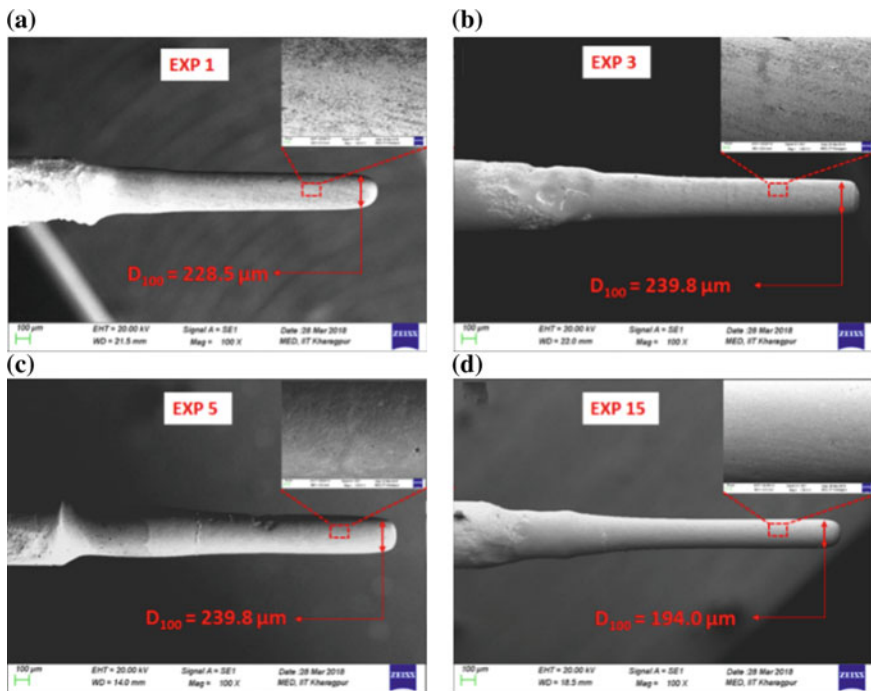


**Fig. 18.4** SEM images of micro-tool after machining obtained for **a** expt. no 1, **b** expt. no 3, **c** expt. no 5, **d** expt. no 15

### 18.4.3 Optimization of Process Parameters

The response surface optimization by desirability function is an ideal technique for obtaining the optimal process parameters of the micro-WECM process. Here the goal is to maximize the material removal rate (MRR). This method converts each process parameter to a dimensionless quantity called desirability that varies from zero to one, i.e., zero implies the least desirable and one being the most desirable. Here, with the help of Design Expert software constraints have been put on input process parameters and the desired goal was set for the response parameter which is given in Table 18.7. The optimal parameters for maximum MRR are found to be electrolyte concentration 0.25 M, applied voltage 15 V and reciprocating speed 5.31  $\mu\text{m/s}$  with the highest desirability of 0.969. The confirmation experiment has been conducted to fabricate a WC–Co alloy micro-tool of diameter 111.2  $\mu\text{m}$  with the optimized parameter in a citric acid electrolyte (Fig. 18.5).

## 18.5 Conclusions

In order to promote green manufacturing, this paper proposes the citric acid as an environment-friendly electrolyte for WC–Co micro-tool fabrication in micro-WECM process. The CV results indicated the passivation of WC–Co alloy in citric acid solutions. The resulting current density is higher at 0.25 M concentration and it decreases with the increase in concentration towards 0.35 M. During fabrication of micro-tool in micro-WECM, the significant parameters that affect the MRR are applied voltage, electrolyte concentration, and reciprocating feed. The applied voltage has a linear relationship with the MRR as it provides the machining current at the inter-electrode gap during machining. At higher voltage, the MRR decreases with the increase in concentration which is in agreement with the findings of CV analysis. Reciprocating speed exerts a negative quadratic effect on the MRR and thus with the increase in reciprocating speed MRR increases up to a certain value and then decreases with further increase in speed. The optimal solution of input process parameters is found to be electrolyte concentration 0.25 M, applied voltage 15 V and reciprocating speed of 5.31  $\mu\text{m/s}$ . By utilizing the optimal solution, a confirmation experiment was conducted by fabricating a micro-tool of 111.2  $\mu\text{m}$  diameter through the micro-WECM process in the citric acid electrolyte.



**Table 18.7** Constraints and optimal solutions

Parameters	Goal	Lower limit	Upper limit	Lower weight	Upper weight	Importance	Optimal solutions
Electrolyte concentration (M)	Is in range	0.25	0.35	1	1	3	0.25
Applied voltage (V)	Is in range	7	15	1	1	3	15
Reciprocating speed ( $\mu\text{m/s}$ )	Is in range	2	10	1	1	3	5.31
MRR (g/min)	Maximize	0.000014	0.000166	1	1	5	0.000161279

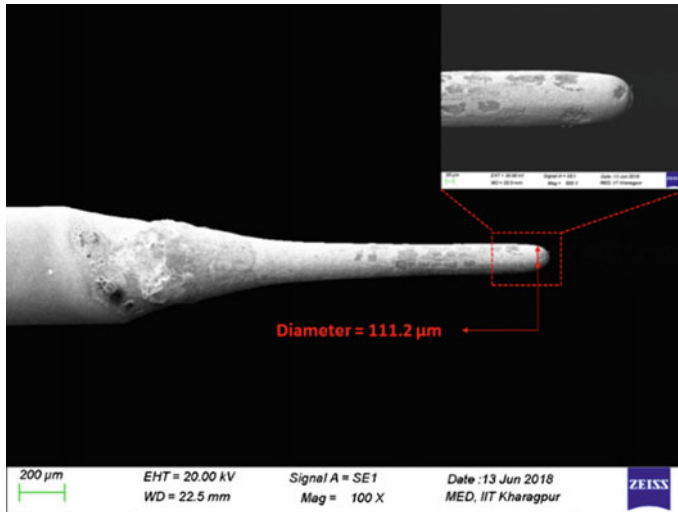


**Fig. 18.5** Fabricated WC–Co alloy micro-tool with the optimized parameter

## References

1. Mahdavinejad, R.A., Mahdavinejad, A.: ED machining of WC–Co. *J. Mater. Process. Technol.* **162**, 637–643 (2005)
2. Jahan, M.P., Rahman, M., Wong, Y.S.: A review on the conventional and micro-electrodischarge machining of tungsten carbide. *Int. J. Mach. Tools Manuf.* **51**(12), 837–858 (2011)
3. Bozzini, B., De Gaudenzi, G.P., Fanigliul, A., Mele, C.: Electrochemical oxidation of WC in acidic sulphate solution. *Corros. Sci.* **46**(2), 453–469 (2004)
4. Lim, H.S., Wong, Y.S., Rahman, M., Lee, M.E.: A study on the machining of high-aspect ratio micro-structures using micro-EDM. *J. Mater. Process. Technol.* **140**(1–3), 318–325 (2003)
5. Masuzawa, T., Fujino, M., Kobayashi, K., Suzuki, T., Kinoshita, N.: Wire electro-discharge grinding for micro-machining. *CIRP Ann.-Manuf. Technol.* **34**(1), 431–434 (1985)
6. Lohrengel, M.M., Rataj, K.P., Schubert, N., Schneider, M., Höhn, S., Michaelis, A., Schubert, A.: Electrochemical machining of hard metals–WC/Co as example. *Powder Metall.* **57**(1), 21–30 (2014)
7. Choi, S.H., Ryu, S.H., Choi, D.K., Chu, C.N.: Fabrication of WC micro-shaft by using electrochemical etching. *Int. J. Adv. Manuf. Technol.* **31**(7–8), 682–687 (2007)
8. Shibuya, N., Ito, Y., Natsu, W.: Electrochemical machining of tungsten carbide alloy micro-pin with  $\text{NaNO}_3$  solution. *Int. J. Precis. Eng. Manuf.* **13**(11), 2075–2078 (2012)
9. Bard, A.J., Faulkner, L.R.: *Electrochemical Methods*, 2nd edn, p. 669. Wiley, New York (2001)
10. El-Taweel, T.A., Gouda, S.A.: Performance analysis of wire electrochemical turning process—RSM approach. *Int. J. Adv. Manuf. Technol.* **53**(1–4), 181–190 (2011)

# Chapter 19

## Effect of Powder Mix and Ultrasonic Assistance on Pulse Train-Based Specific Energy in EDM of D3 Steel



R. Rajeswari and M. S. Shunmugam

**Abstract** In this work on electrical discharge machining (EDM), pulse characteristics and pulse types are assessed from the pulse trains using a novel thresholding approach. For the first time, discharge energy is derived from the pulses, instead of using the setting voltage, setting current and duty cycle. Specific energy is computed as the discharge energy required for removing unit volume of work material. The experiments are carried out on D3 die steel and the specific energies are determined for conventional, powder-added and ultrasonic-assisted EDM. The maximum specific energy increases from  $406.6 \text{ J/mm}^3$  in conventional EDM to  $463.1 \text{ J/mm}^3$  with powder mix, while it reaches  $486.8 \text{ J/mm}^3$  with ultrasonic assistance. However, only the powder mix increases the maximum material removal rate (*MRR*) from  $0.384$  to  $0.464 \text{ mm}^3/\text{s}$ . The ultrasonic-assisted EDM results in a marginally reduced maximum *MRR* of  $0.369 \text{ mm}^3/\text{s}$ , even though the specific energy is the highest.

**Keywords** Electrical discharge machining · Powder addition · Ultrasonic assistance · Specific energy · Material removal rate

### 19.1 Introduction

Electrical discharge machining (EDM) is one of the non-traditional machining processes used extensively in aerospace, automobile and medical devices manufacturing industry for machining of complex three-dimensional (3D) shapes and difficult-to-machine conductive materials. The discharges that occur between tool and work immersed in a dielectric medium lead to local melting and evaporation of materials from the surface. The process being highly complicated, its understanding has remained as a challenge for academic researchers as well as industrial practitioners. A comprehensive review of the state-of-the-art and future prospects of EDM process

---

R. Rajeswari (✉)  
SSN College of Engineering, Chennai 603 110, India  
e-mail: [rajeswarir@ssn.edu.in](mailto:rajeswarir@ssn.edu.in)

R. Rajeswari · M. S. Shunmugam  
Indian Institute of Technology Madras, Chennai 600 036, India

© Springer Nature Singapore Pte Ltd. 2020  
M. S. Shunmugam and M. Kanthababu (eds.), *Advances in Unconventional Machining and Composites*, Lecture Notes on Multidisciplinary Industrial Engineering, [https://doi.org/10.1007/978-981-32-9471-4\\_19](https://doi.org/10.1007/978-981-32-9471-4_19)

has been presented and discussed in the literature [1]. Attempts have also been made to explain the process and the gap phenomena to certain extent [2]. Certain variants of the EDM process such as powder-added EDM, ultrasonic-assisted EDM, dry or near dry EDM and water-assisted EDM have been investigated [3]. Different models have been developed to predict the EDM performances. Regression models have also been developed to predict the *MRR*, surface finish and electrode wear in EDM for hard to rough machine alloys [4].

Generally, EDM is carried out in two different machine settings as the industrial practitioners prefer to perform rough and finish machining under different conditions. The process is performed under powder-mixed condition to enhance the material removal rate in rough machining [5]. The improvement in surface finish in powder-mixed EDM is also a focus search in finishing operation. In both cases, the powder additives change the discharge phenomena in the gap. Also researchers have established parameter settings like voltage, current, pulse on time, pulse off time, and so on, for different powder materials and work materials such as EN 31, H11 and HCHCr in the powder-mixed EDM [6].

Literature also reveals that ultrasonic vibration, current and pulse on time enhance the process output like *MRR* by increasing normal discharges in roughing region and improving surface finish by decreasing crack density in the finishing region [7]. Attempt has also been made to synchronize ultrasonic vibrations of tool with EDM discharges, and strong influence of hydrostatic pressure in the gap on the process is established [8].

Adaptive control techniques have been applied to EDM process and it is concluded that the adaptive control systems are faster, improve *MRR* and surface finish, as well as reduce tool wear rate [9]. Researchers have also explained how the inactive pulses, like short-circuit and open-circuit pulses, affect the erosive action in EDM [10]. A software program is used to analyse pulse train for grouping of different pulses to correlate with *MRR* [11]. Also pulse train study reveals that voltage and current signals obtained out of pulse relaxation generator are different from ideal shapes and there is an appreciable deposition of tool material on the surface of the workpiece material [12].

Also, empirical approach is followed to predict the energy efficiency in EDM as it is of stochastic in nature. The empirical model is validated by conducting experiments and it can predict the EDM process with 90% accuracy [13]. Analytical model for energy density of specific material has also been developed to predict the *MRR*, electrode wear and surface roughness. The conclusion is that *MRR*, surface roughness and electrode wear are high with positive polarity for Inconel 600 [14]. Hybrid machining process like electro-discharge diamond grinding is analysed for relating specific energy, and *MRR* as specific energy is an important parameter in deciding *MRR* in any metal removal process. The conclusion is that it requires less specific energy compared to EDM with a rotating disk electrode [15].

It is seen from the literature that several variants of EDM have been studied to relate the machining parameters with the output responses, but the changes in the gap phenomena have not been given adequate attention. In the present work, the pulse trains that reflect the gap phenomena are analysed using a novel thresholding

approach. To the best of authors' knowledge, the effect of powder addition and ultrasonic assistance on the specific energy has not been reported in the literature. EDM conditions selected for rough machining of hardened D3 die steel in a previous work are used [16]. In this regime, investigations are carried out to find the effect of powder mix and ultrasonic assistance on *MRR*. The discharge energy is derived from pulse characteristics and it forms a basis to correlate the changes in *MRR*. The specific energy computed from pulse trains is found to be more useful in getting an insight into the EDM processes with and without powder addition and ultrasonic assistance. The relevant results are presented and discussed in the paper.

## 19.2 Experimental Details

The workpiece material is D3 die steel which is extensively used for moulds and dies. The chemical composition of D3 die steel is given in Table 19.1. The work material is cut into samples having dimensions of 20 mm × 20 mm × 20 mm in annealed condition. The samples are then heated in steps of 100 °C to reach a temperature of 1000 °C after 10 h. A salt water bath is used to quench the samples for 14 h duration. The final hardness of samples achieved is approximately 55–58 HRC. A surface grinder is used to fine grind all the six faces of the samples. The experiments are conducted using Electronica ZNC machine with DC pulse generator shown in Fig. 19.1.

Major specifications of the machine are given in Table 19.2. A cylindrical copper tool with diameter 10 mm is selected as electrode. EDM oil is used as the dielectric fluid. A digital storage oscilloscope (DSO) of model DSOX2002A from Agilent, USA with two channels and 1GSPS speed is used to capture the voltage and current pulses. While a voltage probe available with the DSO is used for acquiring voltage signal, a current probe based on Hall effect technology, model E3N from Chauvin Arnoux, France, is used for capturing current pulses.

Powder-mixed EDM (PMEDM) experiments are carried out in a separate container of dimension 400 mm × 200 mm × 200 mm made of mild steel sheet kept inside the main container of the EDM machine. Main pump is disconnected to prevent the main dielectric tank getting contaminated. Instead, a separate pipe line fitted with a pump of 0.75 hp and a regulator is used to circulate the dielectric at a flow rate of 8 l/min. The accessories like a pressure gauge, a T-connector and a valve are

**Table 19.1** Chemical composition of D3 steel

Chemical Analysis: CML/OES/SOP/04					
C	Si	Mn	P	S	Ni
2.058	0.387	0.534	0.028	0.023	0.105
Cr	Mo	Al	W	V	Fe
11.330	0.061	0.006	0.096	0.057	85.315

**Fig. 19.1** Experimental setup



**Table 19.2** Specification of EDM machine: Electronica, E5030

Parameters	Range	Details
Voltage, $V_s$ (Rotary switch)	0–200 V (continuously varied)	Dial graduated in 5 V
Current, $C_s$ (Setting no.: 1–40)	1–40 A (1 A step)	Dial graduated in 1 A
Pulse on time, $T_{on}$	Setting no.: 1–99	2–1050 $\mu$ s
Pulse off time, $T_{off}$	Setting no.: 1–9	Setting no. 5: 14.5–282 $\mu$ s

provided in the pipe line. The connecting pipes/hoses are so designed that a nozzle of diameter 5 mm supplies dielectric into the inter-electrode gap with a pressure of 0.7 kgf/cm<sup>2</sup>. The conductive powder graphite of size 25  $\mu$ m is added to the dielectric at a concentration of 2 g/l.

For carrying out ultrasonic-assisted EDM (UAEDM) experiments, an ultrasonic agitator tub made of stainless steel having dimensions of 300 mm  $\times$  150 mm  $\times$  100 mm supplied by LABLINE, India is used. The other specifications of the agitator tub like capacity, power, frequency and amplitude are 3.5 l, 120 W, 30 kHz and 12  $\mu$ m, respectively. The agitator tub is kept on the bed of the main container of the EDM machine. The experiments are carried out inside the tub, in which the workpiece is subjected to ultrasonic vibration along the horizontal direction. The main pump available with the EDM machine is used to supply the dielectric with a pressure of 0.7 kgf/cm<sup>2</sup> into the inter-electrode gap. The drain valve in the tub allows the dielectric

to flow into the main container of the EDM machine from where it reaches the main tank of the machine.

Three levels of three process parameters, namely voltage  $V_s$ , current  $C_s$  and pulse on time  $T_{on}$ , are selected for the EDM experiments. The tool is connected to positive terminal and the workpiece to negative terminal. Table 19.3 lists the parameter settings for all the 27 experiments. Each experiment is conducted for 5 min. In all the experiments the weight of the sample before and after machining is measured using a weighing balance having a resolution of 0.001 g. The change in weight over 5 min is used to calculate material removal rate ( $MRR$ ). The  $MRR$  values in  $\text{mm}^3/\text{s}$  are also listed in the same table.

### 19.3 Pulse Train Analyses

The pulse trains obtained in three different EDM processes reveal the gap phenomena that are quite distinct from each other. Therefore, it becomes necessary to identify pulse shapes and their characteristics [16]. Important pulse characteristics are breakdown voltage  $V_b$ , ignition delay time  $t_i$ , discharge voltage  $V_d$ , discharge current  $C_d$  and discharge duration ( $t_d'$  from voltage signal,  $t_d''$  from current signal), as shown in Fig. 19.2. The signals show two distinct phases for the sparks to occur. The build-up phase shows the voltage increase. After certain delay, referred to as ignition delay, breakdown of dielectric occurs and discharge phase starts. Depending on the ignition delay, the spark can be an effective one or weak one. In the absence of the build-up phase, arc with continuous discharge happen at the electrode gap. Short- and open-circuit pulses are ineffective pulses not contributing to the material removal.

#### 19.3.1 Pulse Characteristics

In order to arrive at the pulse characteristics, a novel approach of thresholding is used. Rise and fall of the signals happen in millisecond in real time. However, these portions of the signals are shown slightly exaggerated in Fig. 19.2 to explain the thresholding approach. To analyse the voltage signal, two threshold voltages, namely one high value and another low value, designated as  $V_{TH}$  and low  $V_{TL}$ , are used. For the build-up phase, the average maximum breakdown voltage is around 150 V. Therefore threshold  $V_{TH}$  for build-up phase is taken as 75 V. For the discharge phase, the average discharge voltage is found to be around 22 V. In this case, a lower threshold voltage  $V_{TL}$  is taken as 11 V. Time interval between two positions with the threshold 75 V in the build-up phase determines the ignition delay time,  $t_i$ . The peak reached between them gives the maximum breakdown voltage. Using the threshold value of 11 V, pulse duration  $T_p$  is determined. The difference between pulse duration  $T_p$  and ignition delay time  $t_i$  determines the discharge duration  $t_d'$ . In order to remove the effect of transition phenomena, sufficient margin is allowed at either end of the

**Table 19.3** Results for three different EDM processes

Sl. No.	$V_s$ (V)	$C_s$ (A)	$T_{on}$ ( $\mu$ s)	$f_p$ (kHz)	Duty factor	EDM		PMEDM		UAEDM	
						$E$ over second (J)	$MRR$ ( $mm^3/s$ )	$E$ over second (J)	$MRR$ ( $mm^3/s$ )	$E$ over second (J)	$MRR$ ( $mm^3/s$ )
1	40	4	170	4.09	0.697	115.4	0.094	101.5	0.161	171.0	0.081
2	40	4	270	2.81	0.758	118.7	0.114	124.3	0.173	207.5	0.084
3	40	4	370	2.10	0.777	116.1	0.118	130.3	0.135	138.8	0.100
4	40	6	170	4.09	0.697	120.0	0.196	188.1	0.308	141.3	0.187
5	40	6	270	2.81	0.758	149.6	0.262	208.0	0.331	170.3	0.244
6	40	6	370	2.10	0.777	141.4	0.267	177.1	0.318	132.0	0.250
7	40	8	170	4.09	0.697	134.0	0.298	196.0	0.411	116.3	0.306
8	40	8	270	2.81	0.758	113.7	0.384	215.0	0.464	179.8	0.369
9	40	8	370	2.10	0.777	158.1	0.389	209.4	0.418	142.9	0.368
10	60	4	170	4.09	0.697	116.6	0.055	111.0	0.119	135.0	0.059
11	60	4	270	2.81	0.758	131.4	0.072	112.6	0.135	150.2	0.065
12	60	4	370	2.10	0.777	113.5	0.077	126.9	0.122	153.9	0.069
13	60	6	170	4.09	0.697	145.8	0.146	108.5	0.231	175.0	0.142
14	60	6	270	2.81	0.758	149.3	0.170	175.2	0.243	156.7	0.166
15	60	6	370	2.10	0.777	165.6	0.180	149.2	0.186	200.9	0.177

(continued)



**Table 19.3** (continued)

Sl. No.	$V_s$ (V)	$C_s$ (A)	$T_{on}$ ( $\mu$ s)	$f_p$ (kHz)	Duty factor	EDM		PMEDM		UAEDM	
						$E$ over second (J)	$MRR$ ( $mm^3/s$ )	$E$ over second (J)	$MRR$ ( $mm^3/s$ )	$E$ over second (J)	$MRR$ ( $mm^3/s$ )
16	60	8	170	4.09	0.697	144.3	0.213	192.8	0.252	186.5	0.206
17	60	8	270	2.81	0.758	152.5	0.233	196.2	0.265	154.0	0.253
18	60	8	370	2.10	0.777	146.7	0.244	205.3	0.266	192.5	0.246
19	80	4	170	4.09	0.697	101.2	0.047	95.2	0.075	134.8	0.033
20	80	4	270	2.81	0.758	91.6	0.057	128.5	0.073	157.2	0.054
21	80	4	370	2.10	0.777	98.9	0.061	102.0	0.051	131.5	0.053
22	80	6	170	4.09	0.697	104.4	0.108	156.0	0.144	182.6	0.111
23	80	6	270	2.81	0.758	162.3	0.129	164.8	0.152	187.8	0.137
24	80	6	370	2.10	0.777	128.8	0.128	184.3	0.144	212.5	0.130
25	80	8	170	4.09	0.697	131.3	0.127	149.7	0.197	216.0	0.163
26	80	8	270	2.81	0.758	115.1	0.152	195.3	0.216	213.6	0.200
27	80	8	370	2.10	0.777	122.3	0.159	215.0	0.205	190.7	0.197

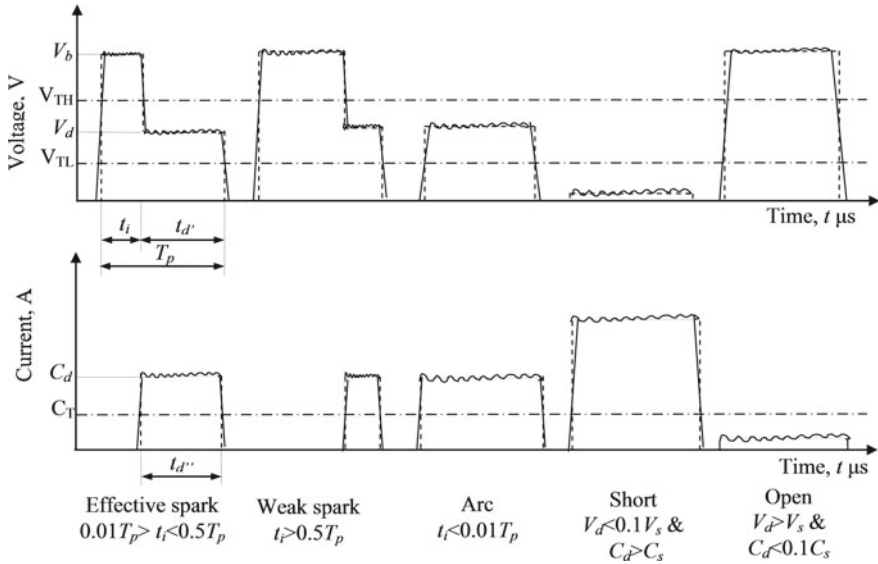


**Fig. 19.2** Determination of pulses characteristics and types

discharge duration and a horizontal line is fitted to arrive at discharge voltage  $V_d$ . To analyse the current signal, a threshold current  $C_T$  is taken as 2 A as it suits all combinations of process parameters. Time interval between two crossing points on the current signal provides the value of discharge duration  $t_d''$ . As described earlier, discharge current  $C_d$  is determined leaving sufficient margin at both ends of the current signal. Since there are two discharge durations, one derived from voltage signal and other one from current signal, the discharge duration  $t_d$  is determined by taking mean value. Based on the thresholding approach described in this section, a program is developed using MATLAB version R2010a software to automatically scan the signals and identify the pulse characteristics.

### 19.3.2 Pulse Types

The pulse type is identified from the ideal shapes shown in dashed lines in Fig. 19.2, passing through the salient points identified by the thresholding approach.

**Effective Spark (ES) Pulse:** This is a typical pulse in EDM in which sparking is more efficient. In this case, the ignition delay is very short and the discharge happens over longer duration of the pulse. If the ignition delay time ( $t_i$ ) is between 0.01 and 0.5 time of pulse duration ( $T_p$ ), the spark is considered as effective. The condition is given as  $0.01T_p > t_i < 0.5T_p$ . The spark forms a plasma channel, melts and evaporates

the work material which gets removed by the flow of dielectric medium as debris. These types of pulses are the best in removing material and generating surface with better integrity.

**Weak Spark (WS) Pulse:** If the ignition delay time ( $t_i$ ) is  $>0.5$  times of pulse duration ( $T_p$ ), that is  $t_i > 0.5T_p$ , the spark is considered as weak. It is a case, in which a spark exists, but the ignition delay occupies more of the pulse duration and the resultant shorter discharge duration does not contribute to significant material removal.

**Arc (A) Pulse:** It is a case where the ignition delay time ( $t_i$ ) is zero or negligible in comparison with pulse duration ( $T_p$ ). The build-up phase is practically absent for this condition,  $t_i < 0.01T_p$ . However, the continuous discharge leads to arcing phenomenon. Though material removal takes place, the intense arcing can lead to more local heating, thereby affecting the surface integrity adversely.

**Short (S) Circuit Pulse:** It is also undesirable in EDM as it occurs when the asperities on electrode surfaces touch each other. In this case the current rises to a very high value with the voltage reaching a very low value. The conditions for shorting are given as  $V_d < 0.1V_s$  and  $C_d > C_s$ . These pulses are not preferred at all, as they severely damage the surface of the workpiece and stop the machining process.

**Open (O) Circuit Pulse:** It is a reverse of short-circuit phenomenon. In this case, the voltage rises to a very high value with the current at its lowest value.  $V_d > V_s$  and  $C_d < 0.1C_s$  show the conditions favouring open-circuit pulse. These pulses, like short-circuit pulses, do not contribute to material removal.

MATLAB program developed in this work also identifies the pulse type based on the conditions incorporated in the program.

### 19.3.3 Specific Energy

The specific energy in machining refers to energy expended for removal of unit volume of material. Since effective spark, weak spark and arc pulses contribute to material removal, only the energy associated with these pulses are taken into account. Based on the phenomenological reasoning, the authors propose a new parameter, namely energy, expended over a second (E) as in Eq. 19.1

$$E = V_{d(avg)} C_{d(avg)} t_{d(avg)} f_p \left( \frac{N_{ES} + N_{WS} + N_A}{N_{ES} + N_{WS} + N_A + N_S + N_O} \right) \quad (19.1)$$

where  $V_{d(avg)}$ ,  $C_{d(avg)}$  and  $t_{d(avg)}$  are the average discharge voltage, average discharge current and average discharge duration, respectively, for a pulse train and  $f_p$  is the pulse frequency. Number of effective spark, weak spark, arc, short and open-circuit pulses is denoted as  $N_{ES}$ ,  $N_{WS}$ ,  $N_A$ ,  $N_S$  and  $N_O$ , respectively, in the pulse train. The values of E are included in Table 19.3 for all the experiments.

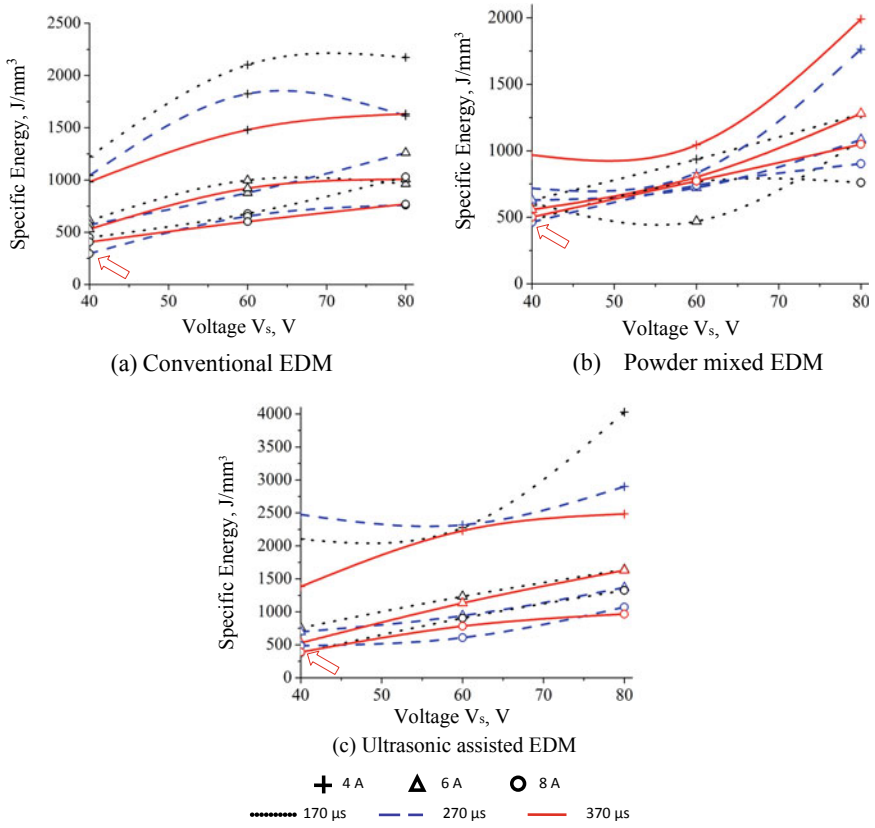


Fig. 19.3 Variation in specific energy for three different EDM processes

The specific energy is computed using the following Eq. 19.2.

$$SE = E/MRR \tag{19.2}$$

where  $MRR$  is expressed in  $mm^3/s$ . The specific energy values are plotted in Fig. 19.3.

### 19.4 Results and Discussion

The discharge energy associated with a pulse train depends on the type of pulses, and therefore average discharge voltage ( $V_{d(avg)}$ ), average discharge current ( $C_{d(avg)}$ ) and average discharge duration ( $t_{d(avg)}$ ) are computed considering only effective spark, weak spark and arc pulses in a given pulse train. The discharge energy is computed

from  $V_{d(avg)}C_{d(avg)}t_{d(avg)}$ . The energy expended over a second is obtained by multiplying discharge energy by pulse frequency  $f_p$  and ratio of sum of ES, WS and A pulses to total number of pulses. From the results in Table 19.3, it is evident that the energy derived from pulse characteristics plays an important role in deciding the *MRR* rather than the energy calculated with setting parameters,  $V_s, C_s, f_p$  and duty factor given by  $t_{on}/(t_{on} + t_{off})$ .

In the Table 19.3, for the conventional EDM the maximum *MRR* of 0.389 mm<sup>3</sup>/s is obtained for the combination of 40 V, 8 A and 370 μs (exp. no. 9) compared to the combination of 40 V, 8 A and 270 μs (exp. no. 8) giving a marginally reduced *MRR* of 0.384 mm<sup>3</sup>/s. The reason is that the discharge energy is higher (158.1 J over a second) in the case of exp. no. 9, due to longer discharge duration. This allows the spark to form relatively larger craters resulting in slightly higher *MRR*. The pulse characteristics are better for exp. no. 8 with increase of number of sparks compared to exp. no. 9 and discharge energy is slightly lower (113.7 J over a second). The experiment no. 8 also gives the least specific energy of 295.9 J/mm<sup>3</sup>. An arrow marks this condition in Fig. 19.3a which shows variation in specific energy (SE) with setting voltage  $V_s$ , setting current  $C_s$  and pulse frequency  $f_p$ . The specific energy, in general, is higher with increase of setting voltages.

It is interesting to note that discharge energy is the maximum (215 J over a second) for exp. no. 8 of PMEDM and hence it leads to higher *MRR* of 0.464 mm<sup>3</sup>/s. However, the specific energy reaches the least value of 463.1 J/mm<sup>3</sup>. In the case of exp. no. 9, the discharge energy reduces marginally and the *MRR* decreases to 0.418 mm<sup>3</sup>/s. In Fig. 19.3b, the least specific energy is marked by an arrow. In general, specific energies for all other conditions are higher. The PMEDM results in higher *MRR* compared to conventional EDM, as the discharge energies are higher with PMEDM than that in conventional EDM. This is because, the powder particles act as nucleation sites for plasma formation and hence increase the energy associated with the electrons hitting the surface of the workpiece, thereby increasing the *MRR* [5].

Figure 19.3c shows a plot of specific energy in UAEDM for different setting voltage, current and pulse frequency. From Table 19.3 and Fig. 19.3c, it is clear that in the case of ultrasonic-assisted EDM, exp. no. 8 shows a maximum *MRR* of 0.369 mm<sup>3</sup>/s with a corresponding specific energy of 486.8 J/mm<sup>3</sup>. However, the next specific energy of 388.7 J/mm<sup>3</sup> corresponds to exp. no. 9 with a corresponding *MRR* of 0.368 mm<sup>3</sup>/min. Frequency of vibration together with pulse frequency seems to have certain effect on the *MRR*. The minimum specific energy condition is shown by an arrow for a combination of 40 V, 8 A and 370 μs. Compared to conventional EDM and PMEDM, UAEDM produces lesser *MRR*. The ultrasonic vibration is known for its cleaning effect and, for this reason, it helps in flushing the debris particles and reduces the *MRR* to certain extent.

## 19.5 Conclusions

The following conclusions can be drawn for the specific tool-work material combination and the given working conditions:

Conventional EDM, PMEDM and UAEDM processes are performed on the same machine for the same setting parameters and hence the results provide a better comparison of these processes.

The specific energy is computed as energy expended per unit volume of material removed. In the present work, the discharge energy is uniquely derived from the characteristics of the pulse trains. Comparison of *MRR* obtained in all the three EDM shows that both discharge energy and specific energy play important role.

The conventional EDM results in low discharge energy of 113.7 J for voltage of 40 V, current of 8 A and pulse on time of 270  $\mu$ s. For these conditions, the *MRR* remains at 0.384 mm<sup>3</sup>/s with a specific energy of 295.9 J/mm<sup>3</sup>.

A maximum *MRR* of 0.464 mm<sup>3</sup>/s with corresponding specific energy of 463.1 J/mm<sup>3</sup> is obtained in the case of PMEDM. The discharge energy in this case is 215 J which is responsible for higher *MRR* compared to conventional EDM and UAEDM. The powder particles are responsible for higher current to flow between the electrodes and hence increase the discharge energy in the gap. This results in deeper craters on the surface of the workpiece to enhance *MRR*.

The ultrasonic-assisted EDM results in discharge energy of 179.8 J, which is a lesser value compared to powder-mixed EDM. This is because the process is more efficient in flushing the debris particles which results in reduced *MRR* even compared to the conventional EDM.

## References

1. Ho, K.H., Newman, S.T.: State of the art electrical discharge machining (EDM). *Int. J. Mach. Tools Manuf.* **43**(13), 1287–1300 (2003)
2. Kunieda, M., Lauwers, B., Rajurkar, K.P., Schumacher, B.M.: Advancing EDM through fundamental insight into the process. *CIRP Ann.* **54**(2), 64–87 (2005)
3. Abbas, N.M., Solomon, D.G., Bahari, M.F.: A review on current research trends in electrical discharge machining EDM. *Int. J. Mach. Tools Manuf.* **47**(7–8), 1214–1228 (2007)
4. Torres, A., Puertas, I., Luis, C.J.: Modelling of surface finish, electrode wear and material removal rate in electrical discharge machining of hard-to-machine alloys. *Precis. Eng.* **40**, 33–45 (2015)
5. Zhao, W.S., Meng, Q.G., Wang, Z.L.: The application of research on powder mixed EDM in rough machining. *J. Mater. Process. Technol.* **129**(1–3), 30–33 (2002)
6. Bhattacharya, A., Batish, A., Singh, G., Singla, V.K.: Optimal parameter settings for rough and finish machining of die steels in powder-mixed EDM. *Int. J. Adv. Manuf. Technol.* **61**(5–8), 537–548 (2012)
7. Shabgard, M.R., Alenabi, H.: Materials and manufacturing processes ultrasonic assisted electrical discharge machining of Ti-6Al-4V Alloy. *Mater. Manuf. Process.* **30**(8), 37–41 (2015)
8. Kremer, D.: A study of the effect of synchronizing ultrasonic vibrations with pulses in EDM. *Ann. CIRP* **40**(1), 211–214 (1991)

9. Snoeys, R., Dauw, D., Kruth, J.P.: Survey of adaptive control in electro discharge machining. *J. Manuf. Syst.* **2**(2), 147–164 (1983)
10. Crookall, J.R.: A basic analysis of pulse trains in electro-discharge machining. *Int. J. Mach. Tool Des. Res.* **13**(3), 199–213 (1973)
11. Çoğun, C.: A technique and its application for evaluation of material removal contributions of pulses in Electrical Discharge Machining (EDM). *Int. J. Mach. Tools Manuf.* **30**(1), 19–31 (1990)
12. Gangadhar, A., Shunmugam, M.S., Philip, P.K.: Pulse train studies in EDM with controlled pulse relaxation. *Int. J. Mach. Tools Manuf.* **32**(5), 651–657 (1992)
13. Li, W., Kara, S.: Characterising energy efficiency of electrical discharge machining (EDM) processes. *Procedia CIRP* **29**, 263–268 (2015)
14. Salcedo, A.T., Arbizu, I.P., Pérez, C.J.L.: Analytical modelling of energy density and optimization of the EDM machining parameters of Inconel 600. *Metals* **7**(5), 166–187 (2017)
15. Jain, V.K., Mote, R.G.: On the temperature and specific energy during electro discharge diamond grinding (EDDG). *Int. J. Adv. Manuf. Technol.* **26**(1–2), 56–67 (2005)
16. Rajeswari, R., Shunmugam, M.S.: Investigations into process mechanics of rough and finish die sinking EDM using pulse train analysis. *Int. J. Adv. Manuf. Technol.* (published online). <https://doi.org/10.1007/s00170-018-2701-7>

# Chapter 20

## Performance Evaluation of Si–Cu-Hybrid Dust as a Powder Additive of EDM Dielectrics to Machine Ti6Al4V with Copper Electrode



Shirsendu Das , Swarup Paul , Biswanath Doloi   
and Kumar Rahul Dey 

**Abstract** The wide utility of the EDM in industrial and biomedical sectors has drawn the attention of the researchers in the last few decades. In the meantime, intensive works have been performed to improve the machining performance of the EDM. Addition of powder additives in dielectric medium is one of those approaches which moderate the strength of the plasma channel by increasing the concentration of the ions. Powder dusts of copper, titanium, aluminum, tungsten, silicon/silica and carbon nanoparticles are some of the additives which have significant contributions on EDM process parameters. In this work the Si–Cu hybrid powder dust is added with kerosene oil and the comparative analysis is done based on the performance evaluations in terms of material removal rate (MRR) and surface roughness (SR). Silicon and copper are used individually earlier with other powder dust, but here both are added together with dielectric medium to evaluate their combined effects on surface characterizations. Because of the highly conductive nature of the copper, it increases the mobility of the ions and charge particles inside the ionization gap. On the other side, silicon is partially conductor and partially insulator in nature. So because of its semi-conductive properties, it can restrict the spark span and domain which possesses controlled machining. Therefore, the combined influence of these two powder additives gives some excellent features which are highlighted in this article.

**Keywords** Powder additives · Copper · Silicon · MRR · SR · Micro-structures

---

S. Das (✉) · S. Paul · K. R. Dey  
Department of Production Engineering, National Institute of Technology, Agartala 799046, India  
e-mail: [Shirsendu.sch@nita.ac.in](mailto:Shirsendu.sch@nita.ac.in)

B. Doloi  
Department of Production Engineering, Jadavpur University, Kolkata 700052, India

© Springer Nature Singapore Pte Ltd. 2020  
M. S. Shunmugam and M. Kanthababu (eds.), *Advances in Unconventional  
Machining and Composites*, Lecture Notes on Multidisciplinary  
Industrial Engineering, [https://doi.org/10.1007/978-981-32-9471-4\\_20](https://doi.org/10.1007/978-981-32-9471-4_20)



## 20.1 Introduction

Addition of powder dust in dielectric fluid develops a mass exchange mechanism because of which some new surface allotropies are found, in terms of micro-hardness and micro-particle deposition. Tahsin et al. observed that EDM process parameters like current, pulse ON and OFF time along with additive concentration (g/l) influence the exchanging process significantly. The domain of the propagation of the influence depends on the distance of the particular location from the plasma column. It is observed that the dielectric strength continuously moderates with the differences in powder concentration, which implies new surface properties when the Ti6Al4V is machined with silicon carbide (SiC) powder dust [1]. SEM and EDS analysis conveys some evidence in favor of the migration of additive particles during machining. Bhattacharya et al. conducted experiments with both kerosene and EDM oil using Si–W–C hybrid dust and observed that powder-mixed dielectrics exhibit good surface integrity because of rapid transfer of heat from the machined zone. During the ANOVA analysis, powder concentration, pulse ON time and current are found as most important factors that influence surface properties and micro-hardness, whereas the tool and workpiece materials are found insignificant [2]. Regarding the issue of tool wear it initially increases with process parameters and powder concentration but subsequently decreases after a certain limit. Chaudhury et al. observed that at 7 A current and 100  $\mu$ s pulse OFF time the machining optimum is optimum when the powder concentration is 10 g/l [3]. Microscopic defects like fractures and cracks which are extensively associated with discharge machining can be mitigated by enhancing the wettability of the surface. In this context, the addition of titanium dust with deionized water can exhibit impressive machining responses by synchronizing the thickness of the recast layer formation. Experimentally, it has been observed that addition of titanium at the rate of 3–6 g/l significantly improves the wettability of the surface by varying the recast layer thickness which imparts the chances of occurring micro-fractures [4]. Duty cycle and spark time are the two vital issues which should be considered during machining with powder additives because larger spark time influences the stability of the arc and rises the chances of occurring short circuit. For stable machining responses, certain optimum level of pulse ON time should be set; otherwise it reduces the MRR due to the increase in duty cycle. It is observed that nozzle flushing does not have remarkable influence in MRR while the experiments are carried out with silicon powder additive because of the removal of powder particles from the plasma channel due to high flushing thrust. Optimum machining responses are achieved with silicon-aided dielectrics at 10 A pulse current, 100  $\mu$ s pulse ON time and 15  $\mu$ s pulse OFF time when the powder concentration is 4 g/l [5]. EDM operation with tungsten additives causes the infiltration of micro-particles of tungsten in the presence of hydrocarbon dielectrics which exhibit different allotropic phases of iron–carbon equilibrium system. Evacuation of these particles improves the micro-hardness of the machined zone to more than 10% because of the presence of tungsten particle in dissolved/undissolved (carbide) form on die-steel workpiece [6].

Copper is highly conductive in nature, so involvement of copper can enhance the ion movement through the channel by reducing the breakdown strength of the medium, which may exhibit better material transfer than conventional dielectrics. But addition of copper (particle size 70 nm) causes excessive surface indentation, especially at high pulse current, which is not desirable. Experimentally, it is found that addition of silicon dust (particle size 80 nm) can prolong the remedial treatment against the surface indentations while machining is performed with copper dust as a powder additive. Therefore, this paper tried to highlight an extensive experimental overview of machining responses under different sets of input variables and powder concentrations using silicon–copper hybrid dust as powder additive of EDM dielectrics, which is rarely used earlier.

## 20.2 Literature Review and Motivation of the Work

Involvement of powder additives in dielectric medium generally causes two impacts in case of EDM operation. It accelerates or retards the machining rate according to the requirement of operators, and besides this, it migrates new material characteristics with better micro-hardness by moderating the recast layer thickness. Inclusion of different additives renders the evacuation of different new structural allotropy depending on the nature of the additives, concentration of the additives and range of the input variables. Addition of powders in dielectrics improves the conductivity and breakdown strength of the medium which have a significant contribution in machining responses. Different powder-aided EDM approaches have been discussed in detail in Table 20.1.

Utilization of graphite causes an appreciable reduction in surface indentations, microscopic defects and recast layer formation. Beside this, it encourages the hardenability of the surface by forming carbide layers on the machined surface. It is observed that the controlled machining can be achieved up to 6 g/l dust concentrations but when the concentration is 8 g/l or beyond this, surface roughness increases significantly due to unstable arcing and inadequate flushing. Addition of graphite dust reduces the available discharge energy on the surface and increases the span of the crater extension which possesses fine surface integrity with minimum surface indentations. It is found that the thickness of the recast layers decreases with the rise in powder concentrations. Analysis of the surface characterization of the species obtained after the electrical discharge machining with graphite additives conveys the evidences of thin layer formation in the form of carbides of Ni, Cr and Mo, which improve the micro-hardness and the fatigue strength of the surface [14]. EDM operation with Cr dust provides a coated layer of Cr on the machined surface, and maximum migration of Cr powder is obtained when the machining is performed at low pulse current with high powder concentration. Cr improved the micro-hardness and corrosive resistance of the surface [15]. On the other hand, the inclusion of powder dust of highly conductive materials like Al, shortened the breakdown capacity and moderates the spark gap of ionization channel which exhibits excellent surface

**Table 20.1** Impacts of different additives on surface characterizations

Sl. No.	Tool	Workpiece	Additive	Observations
1.	Electrolytic copper	Die-steel (H11)	Silicon carbide	Surface imperfections, like formation of craters, recast layers, globules etc., are commonly associated with thermal-assisted machining like EDM. But the comparative analysis of images obtained from SEM conveys evidence that SiC-added dielectric can impart better surface properties than conventional dielectrics [7]
2.	Copper	SKH-54	Silicon/graphite	Presence of the powder additives like Si/graphite reduces the breakdown strength and distributes the discharge energy within a wide range. So they possess fine surface finish up to 2 A range of pulse current [8]
3.	Copper	SiCp/Al composite	Al	Involvement of Al dust in dielectric fluid can improve the surface by 31%. It improves the micro-hardness of the machined surface by 40–60% because of the formation of a thicker recast layer of un-melted SiC on the top surface of Al composite [9]
4.	Copper pipe	Non-conductive ceramic	Graphite	After the initiation of the first spark, the conductive layer of ceramic materials is eroded and then the additive dust of graphite provides the required conductive channels. Out of all ceramic materials, machining of Al <sub>2</sub> O <sub>3</sub> faces hurdles like long machining duration with low removal rate, whereas machining of ZrO <sub>2</sub> was quite easier with vertical depth of 15 mm [10]

(continued)

**Table 20.1** (continued)

Sl. No.	Tool	Workpiece	Additive	Observations
6.	Copper	Ti6Al4V	CNTs	CNTs promote a stable EDM operation under control sparks while the machining is performed with large pulse ON time. Generally, inclusion of CNTs reduces the MRR but can exhibit impressive removal rate at low pulse current and long pulse gap. Involvement of CNTs reduces the TWR and size of micro-cracks [11, 12]
7.	Electrolytic copper	Steel (H13) AISI	Silicon	Silicon can check the occurrence of uncontrolled sparks up to a greater extent. So, Si mixed dielectrics can promote better surface integrity with negligible abnormal sparking [13]

properties but reduces the efficiency of the machining with considerable amount of spark losses [16]. From the literature review, it is clear that each powder additive has a specific utility depending on the materials which are selected as tool and workpiece. So, it is very tough to prescribe any one of them as a suitable additive to machine Ti6Al4V (material used in this work) with copper tool. Meanwhile, an efficient and sustainable EDM operation demands the following criteria:

- Material removal rate (MRR) should be impressive and satisfactory so that machining time can be reduced.
- Prior consideration on surface roughness (SR) also needed while encouraging the removal rate.
- Machining process will be subjected to minimum discharge losses so that maximum possible spark energy can be utilized.
- Diameter of the crater which forms after the initiation of each spark should be optimum so that both MRR and SR can come in a compromise limit.

Now, considering the issue of MRR and spark energy, powder dust of highly conductive materials like copper should get priority. So initially, machining is performed with copper dust of 70 nm as a powder additive of EDM, and the experimental outcomes, that is, responses, are compared with the outcomes of pure kerosene dielectrics. Experiments are carried out at 4–16 A range of pulse current with varying pulse ON and OFF time, and in most of the cases it is found that Cu-added dielectric encourages the material removal rate but not suitable in the point of view of surface finishing. The concentration of copper dust has been varied from 1 to 5 g/l and it is observed that it enhances the removal rate, but beyond 5 g/l surface roughness

increases successively. On the other hand, if the priority is given to the surface finishing and crater diameter, powder dust of non-metallic materials like graphite and silicon is suitable. From the literature review, it is clear that graphite as a powder additive can give better surface finishing than normal dielectrics, but at a high value of pulse current, it can cause excessive surface erosion because of its conductive nature, which will promote the poor surface integrity [14]. Besides this, involvement of graphite will increase the concentration of carbon monoxides during machining and will promote an unhygienic breathing atmosphere, which cannot be encouraged in the perception of sustainability. Silicon is a material which has a huge utility in electronic field because of its excellent semi-conductive natures. Generally, Si is insulator but when an external potential more than its breakdown voltage is applied, it polarizes and permits a limited current to pass through it. Moreover, during EDM operation of H13 steel with copper tool using Si dust as powder additive has shown some appreciable surface properties with reduced amount of operating time [13]. So, inspired from this outcome, Cu–Si hybrid dust is used as a powder additive in this article.

### 20.3 Experimental Methodology

The experiment is carried out in Sparkonix die-sinking electro-discharge machine, where a Servomax Servo stabilizer feeds the sparks during the operation. Titanium–aluminum alloy (Ti6Al4V), especially called aerospace alloy, has a huge utility in aerospace industries and in biomedical instrumentations. But because of its excessive hardenability, it possesses slow machining responses with low removal rate while EDM with conventional kerosene oil is used as dielectric. So, to improve the machining efficiency and to reduce the machining time, the powder additives are incorporated with kerosene. The selection process of powder additives is already discussed in sub-content 20.2. On the other hand, in most of the literature review, it is observed that cylindrical copper bar of different diameters have been chosen for tool. Besides this, it is highly conductive and causes less tool erosions. So, in this experimental study solid copper bar of 10 mm external diameter is used as the tool. Experiments have been conducted in a separate chamber made with fiber having the dimensions of 45 cm × 40 cm × 30 cm. A circulating rotor (vertical axis) is assembled with the fiber chamber to mix both the powder additives with the kerosene perfectly and homogeneously. An ANOVA analysis of some of the earlier researchers concluded that flushing process has negligible impacts on responses if the experiment is carried out with powder dust [5]. Therefore, in this present setup no flushing arrangement is used. Workpiece of Ti6Al4V is fixed with the help of fixture inside the fiber chamber and the copper tool (dia. 10 mm) is hold by the main tool holder of the machine. Experiments are carried out between 4 and 16 A ranges of the pulse current. The range of the other response parameters along with the pulse current has been listed in Table 20.2.

**Table 20.2** Ranges of different input parameters

Parameters	Ranges
Pulse current (I)	4, 7, 10, 13, 16
Gap voltage (V)	20, 30, 40, 50, 60
Pulse ON time ( $\mu$ s)	50, 100, 150, 200, 250
Pulse OFF time ( $\mu$ s)	10, 20, 30, 40, 50

## 20.4 Results and Discussions

### 20.4.1 Effects of Process Parameters on Material Removal Rate

Figure 20.1 shows the variation in MRR with respect to pulse current, taking different values of pulse ON time when the other variable is constant. From Fig. 20.6a, it is

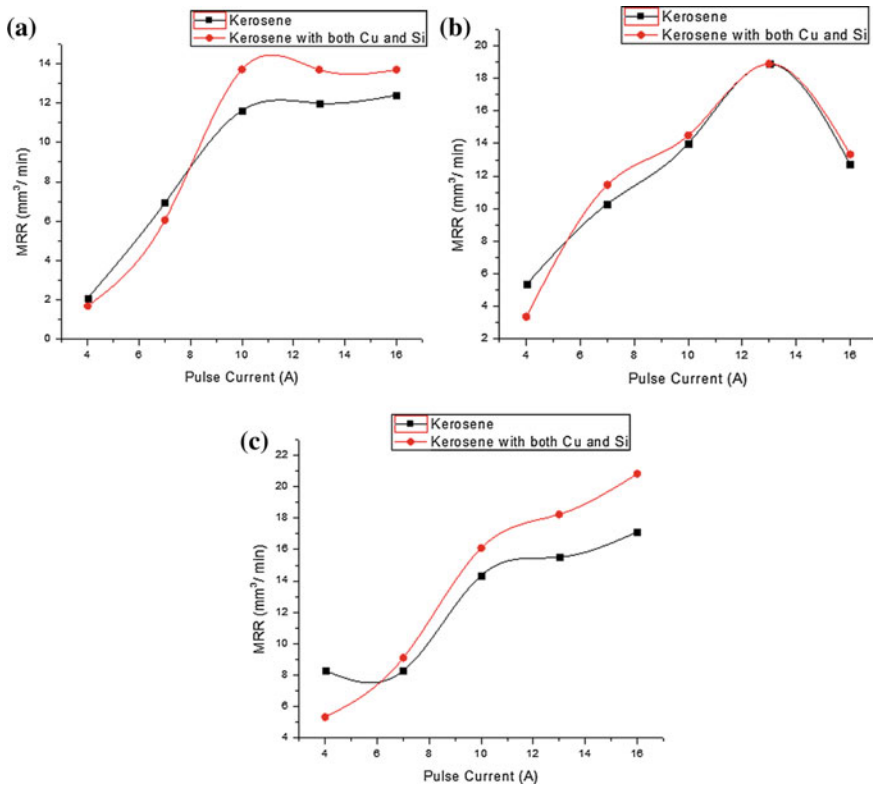


**Fig. 20.1** Variation of MRR with respect to pulse current for both powder-added and normal dielectrics when the pulse ON time is 50  $\mu$ s (a); 150  $\mu$ s (b); and 250  $\mu$ s (c)

clear that at 50  $\mu\text{s}$  of pulse ON time MRR varies proportionally with pulse current for both the dielectrics. Hybrid powder-added dielectrics initially possess less MRR than kerosene when the pulse current is below 8 A. But beyond 8 A, a significant increment is observed in MRR with pulse current.

Hybrid dust-added dielectric exhibits maximum 14  $\text{mm}^3/\text{min}$  MRR at 11 A of pulse current, whereas the kerosene possesses maximum 12  $\text{mm}^3/\text{min}$  MRR at the same value of pulse current, shown in Fig. 20.1a. But after 13 A of pulse current, MRR slightly reduces because of insufficient field strength at lower value of pulse ON time. Thus, material removal rate is directly proportional to the pulse current and pulse ON time, so at lower value of pulse time the developed field strength is insufficient to handle the higher concentration of powder additives and because of which mobility and activeness of the channel reduces. This is the only reason behind the slight reduction of MRR with pulse current, which is shown in Fig. 20.1a. EDM operation with hybrid powder dust in dielectrics does not impart much better responses than kerosene when the pulse ON time is 150  $\mu\text{s}$ . Figure 20.1b shows the variation patterns of MRR for both the dielectrics with respect to pulse current when the pulse ON time is 150  $\mu\text{s}$ . From Fig. 20.1b, it is clear that both the dielectrics are showing almost closer responses where MRR first increases up to 11 A of pulse current, then again decreases when the current is beyond this limit. Maximum MRRs are observed for both the fluids at 11 A current, which is approximately equal to 19  $\text{mm}^3/\text{min}$  for each. But significant variation in MRR is observed when the pulse ON time is 250  $\mu\text{s}$ . Figure 20.1c shows this variation where the powder-added dielectrics possess much better MRR than normal kerosene oil when the machining is conducted within 4–16 A range. Basically, the strength of the electro-static field, which develops between the workpiece and tool during machining, increases proportionally with the pulse current and pulse ON time. So, at low value these two input variables promote the stable machining performance. This is the reason behind the steady machining responses at 50  $\mu\text{s}$  of pulse ON time, as shown in Fig. 20.6a. But at 150  $\mu\text{s}$  of pulse ON time, the field strength is very high and it attains the peak value when the pulse current is 11 A or more than this. So, a large quantity of powder particles gets attracted by the field. Because of the presence of high concentration of charge particles around the field, the spark energy distributed within a wide range hampers the localized heating, and it is the only reason behind the gradual decrease in MRR beyond the 11 A of pulse current (shown in Fig. 20.1b). But, at 250  $\mu\text{s}$  value of pulse ON time, the discharge energy is so high that it causes extensive metal erosion from the workpiece surface with significant surface roughness; that is why, impressive MRR is obtained at 250  $\mu\text{s}$  pulse ON time (shown in Fig. 20.1c). The concentration of charge particles is more in case of additive-mixed dielectrics than normal kerosene. But to attain satisfactory metal erosions, the applied field strength should be capable enough to arrange as maximum as possible numbers of charge particles along the field. Otherwise, the machining process will be subjected to less removal rate. At 4 A current the field strength is less enough to be incapable to arrange high concentration of powder additives along the field. Besides this, huge concentration of uncontrolled ions offers a resistive effect on the progressive sparks. So, the initiated sparks have less erosive heat flux which causes less material removal.

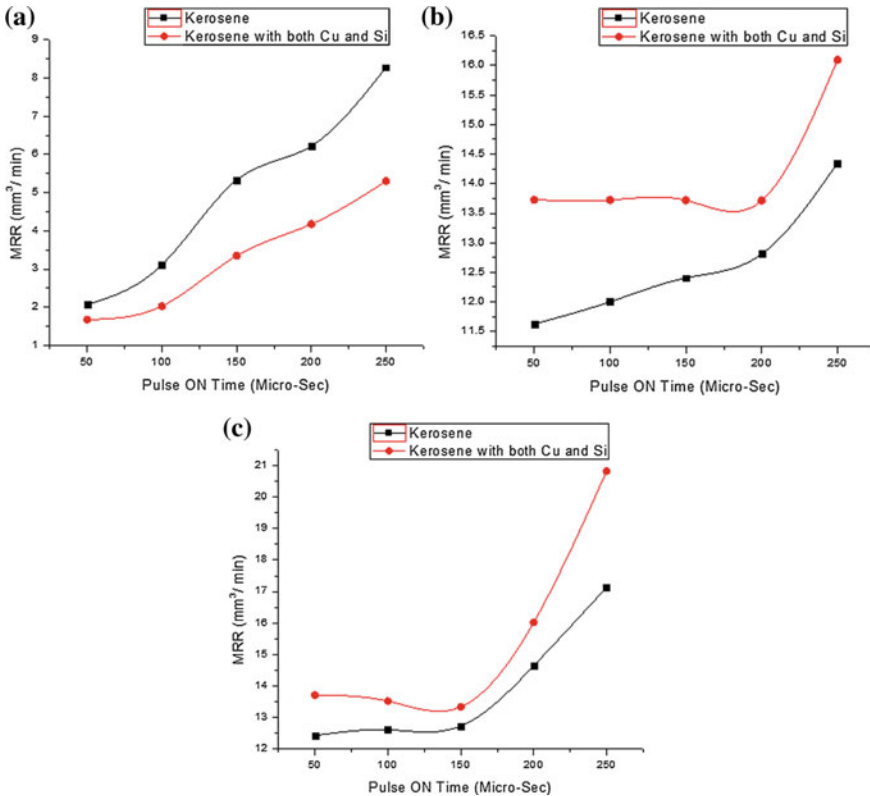


**Fig. 20.2** Variation of MRR with pulse ON time, when the pulse current is 4 A (a); 10 A (b); and 16 A (c)

This is the only reason behind getting less MRR with powder-added dielectrics than normal kerosene at 4 A value of pulse current, which is shown in Fig. 20.2a. But, machining responses improved with the increase in pulse current. Figure 20.2b, c shows the variation in MRR with pulse ON time when the currents are 10 and 16 A, respectively. So, at higher value of pulse current, field strength is capable enough to sustain the sufficient electrostatic field so that powder particle can get accelerated along the field, which causes high erosive heat flux and encourages the removal rate. This is the grounded theory behind getting better MRR with 10 and 16 A pulse current, which are shown in Fig. 20.2b, c. Gap voltage has a typical impact on machining performance. Generally, erosive energy increases with gap voltage initially but after a certain limit it reduces with further increase in voltage. This type of fluctuation is common for both kerosene and powder-added kerosene. So, this is the reason behind the fluctuation and gradual degradation in MRR with respect to gap voltage. Figure 20.3a represents the variation in MRR with gap voltage. Here, MRR initially increases slightly during 20–30 kV of gap voltage than gradually decreases up to 11.5 mm<sup>3</sup>/min (for powder-added dielectrics) and up to 10 mm<sup>3</sup>/min (for kerosene)



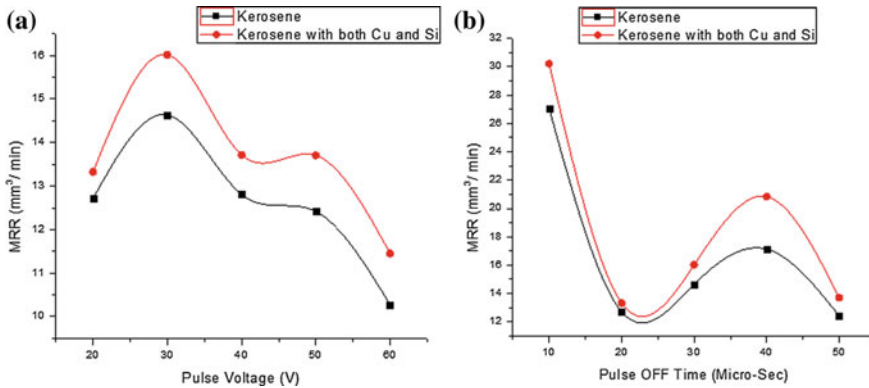


**Fig. 20.3** Variation of MRR with respect to pulse voltage (a) and pulse OFF time (b)

when the pulse voltage is 60 kV. The discharge energy always varies inversely with the pulse OFF time. So, in general, MRR decreases with the rise in pulse OFF time. In this experiment it is varied between 10 and 50  $\mu$ s and the fluctuation in MRR is observed, as shown in Fig. 20.3b. Moreover, from general analysis it is clear that hybrid powder-added dielectrics show comparatively better responses in terms of MRR than normal kerosene except when the machining is performed at lower value of current (4 A).

The machining has been conducted under restricted flushing condition to avoid the chances of unwanted washout of powder additives from the machining zone. But restricted or 'inadequate flushing' condition may cause agglomeration of powder additives on the tool material. Copper is high electronegative in nature, so at high temperature copper has a tendency of attracting negatively charged ions. But in this particular case, the copper powder dusts ionize in  $\text{Cu}^{+2}$  ions and Si dusts remain unionized because of their non-reactive and non-conductive nature and the remains are present in carbide form on the recast layer and the rest react with oxygen to form silicon oxide. Regarding the  $\text{Cu}^{+2}$  ions, the chances of copper oxide formation are also there, but due to mutual repulsive nature, there is very less chance of agglomerations on the tool because the tool is also made of same materials.

#### 20.4.2 Effects of Process Parameters on Surface Roughness

In this sub-content, the impacts of the variations of different input parameters like current, pulse ON time, pulse OFF time and gap voltage on surface roughness are examined for both powder added and normal dielectrics. Because of semi-conductive behavior of Si, it can restrict the spreading of spark energy and control the conductivity of the ionization channels during machining. Involvement of copper as a powder additive makes the channel highly conductive, which undoubtedly encourages the

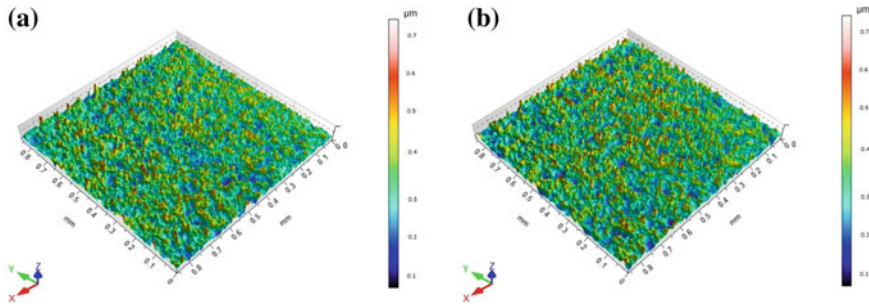


**Fig. 20.4** Roughness profile at 12 A current, 150  $\mu\text{s}$  pulse ON time and 20  $\mu\text{s}$  pulse OFF time for **a** kerosene, **b** hybrid powder-added dielectrics

removal rate but causes surface indentations in a large scale and makes the surface rough. On the other hand, silicon has just opposite types of electro-thermal nature, so the involvement of these two additives has exhibited excellent surface properties along with less dimensional inaccuracies compared to normal kerosene. Figure 20.4a, b represent the roughness profiles, whereas Fig. 20.5a–c has shown the variation in SR with the pulse current when the pulse current and other physical constrains are constant.

Generally, MRR and SR are proportional. So, MRR has to maximize in such a way so that it should not promote excessive surface roughness. In this experiment, 3 g/l Si is added with 5 g/l copper dust to restrict the erosion rate so that excessive surface roughness can be eliminated. As a result of this, appreciable surface properties have been achieved with copper–silicon hybrid dust which promotes less surface roughness for every set of pulse ON time, when the variation between SR and current are examined (Fig. 20.5). Almost similar types of machining responses (SR) are observed, while its variations are plotted against pulse ON time for different values of pulse current, keeping other physical constrains and input parameters constant. Figure 20.5a, b and c shows the variation in SR with respect to pulse ON time when pulse current is 4, 10 and 16 A, respectively. On the other hand, as MRR reduces with gap voltage (kV) and pulse OFF time ( $\mu\text{s}$ ), an appreciable reduction in SR is also observed with respect to these two parameters when others are constant.

Figure 20.6a, b has shown variation in SR with respect to these two parameters, that is, gap voltage and pulse OFF time. So, from Figs. 20.6a–c and 20.7a, b, it is clear in every respect that the hybrid powder-mixed dielectrics cause less surface roughness than normal kerosene oils as dielectrics.

### 20.4.3 Analysis of the Micro-structure

Figure 20.8 shows the microscopic views of the developed craters with copper additives (5 g/l), silicon additives (3 gm/l) and hybrid additives (5 g/l Cu + 3 g/l Si), when

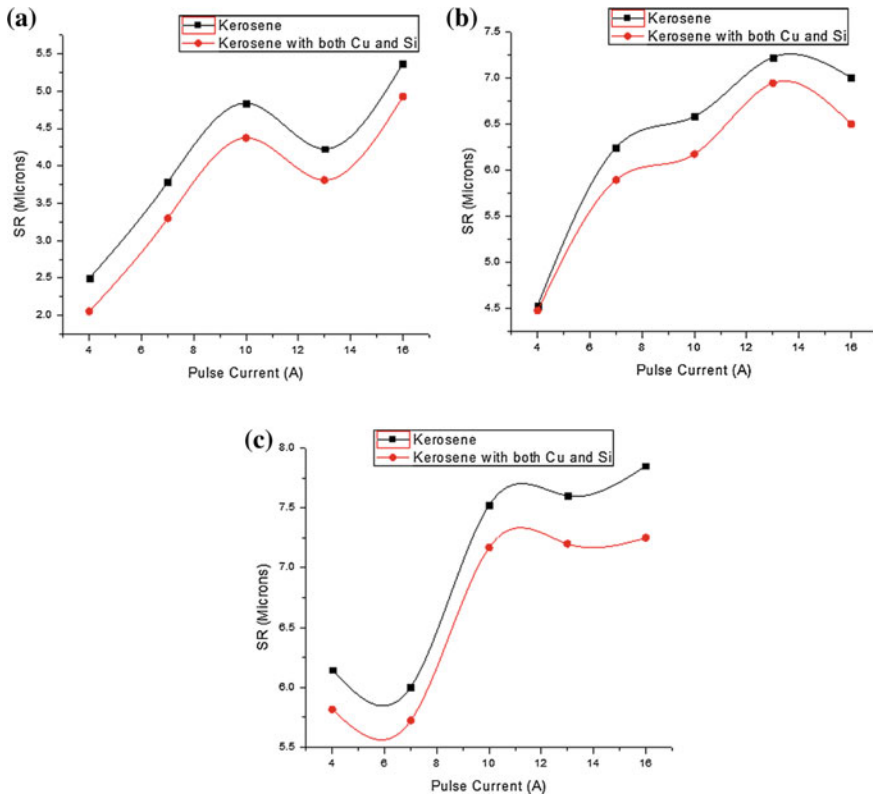


**Fig. 20.5** Variation of SR with respect to pulse current when the pulse ON time is 50 μs (a); 150 μs (b); and 250 μs (c)

machining was done at 10 A current, 30 kV gap voltage, 200 μs pulse ON time and at 20 μs pulse OFF time. Because of the presence of the copper (5 g/l concentrations) the plasma channel becomes highly conductive, which mobilized the large quantity of charge particles toward the workpiece. These large concentrations of ions develop high amount of heat while they collide with the workpiece surface and transmit huge discharge energy inside the machined zone which causes excessive removal rate with large shape of surface irregularities or roughness, as shown in Fig. 20.8a.

But, while only silicon is present as an additive dust in dielectric at a concentration of 3 g/l, it reduces the conductivity of the channel because of its semi-conductive nature or poor conductivity. Because of this, the energy which is associated with each spark suffers resistive effects in the way of progression. This causes a huge loss of spark energy and reduces the machining efficiency. But, on the other hand, due to its resistive nature it controls the spreading of spark energy and promotes a fine surface with precised dimensional accuracy, as shown in Fig. 20.8b. Silicon-added dielectrics can give better surface properties than normal kerosene dielectric medium and copper-added dielectrics, but it reduces the efficiency of the machining

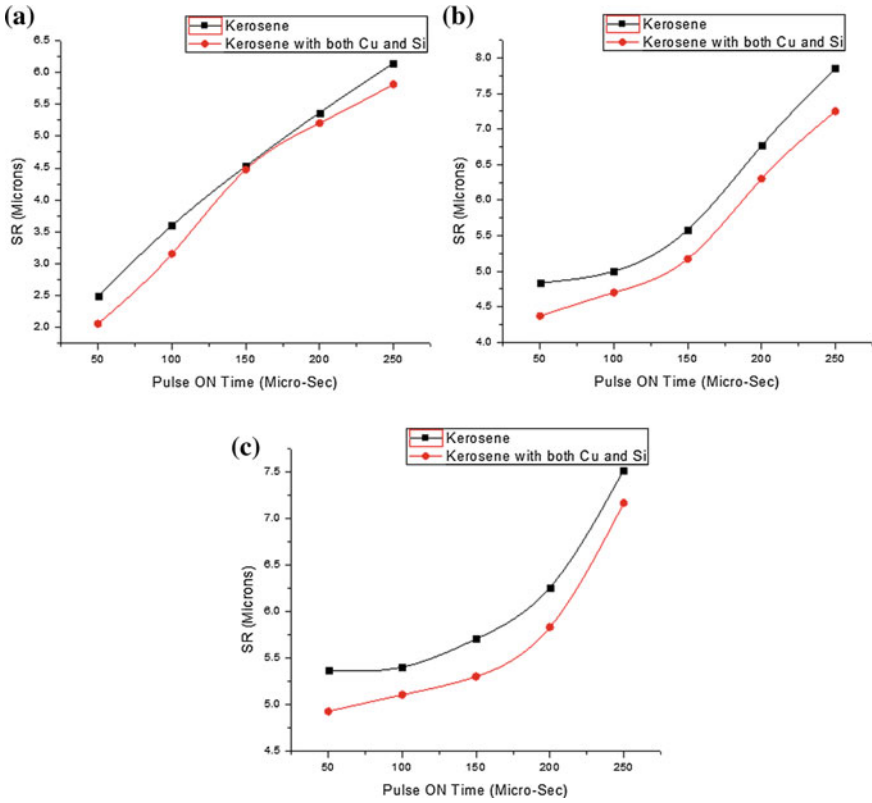


Fig. 20.6 Variation of SR with respect to pulse ON time when the pulse current is 4 A (a); 10 A (b); and 16 A (c)

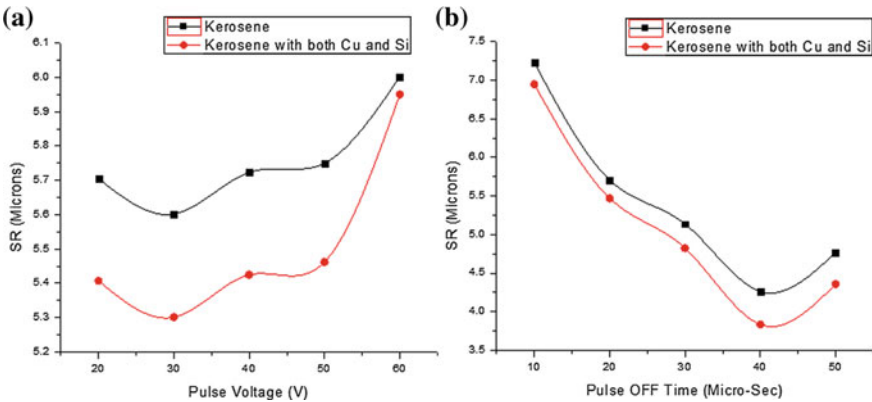
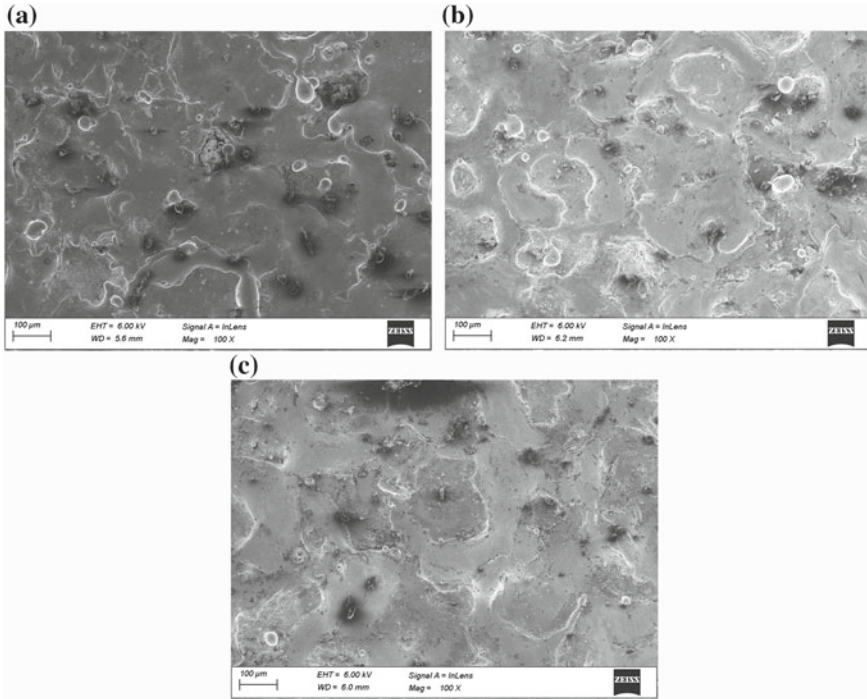


Fig. 20.7 Variation of SR with pulse voltage (a) and pulse OFF time (b)



**Fig. 20.8** Micro-structure and crater formations with copper additives (5 g/l) (a), silicon dust (3 g/l) (b) and hybrid dust (5 g/l Cu + 3 g/l Si) (c) when  $I = 10$  A,  $V = 30$  V,  $T_{ON} = 200$   $\mu$ s and  $T_{OFF} = 20$   $\mu$ s

by reducing the MRR and increasing the amount of discharge losses during every spark. Now, to overcome both of these two hurdles and to establish a compromised relation, both the dusts, that is, copper with 5 g/l concentrations and silicon with 3 g/l concentrations, are introduced in the dielectric medium. The copper dust present in the medium takes care of MRR, whereas the silicon particles control the span and domain of the spark and permit controlled spark energy to pass through the channel, which take cares of the SR. Therefore, a compromised surface finishing (more than normal kerosene) is achieved with satisfactory MRR, which is shown in Fig. 20.8c.

## 20.5 Conclusions

So, the involvement of both the copper and silicon dust with the dielectric medium incorporates some fine surface characteristics with reasonable MRR when Ti6Al4V is machined with copper tool. Comparative analysis of the machining performance using normal kerosene oil as dielectric and powder-added kerosene oil clearly

signifies that the powder-added dielectrics have far better responses than normal dielectrics. In addition to this, the article wants to draw the following conclusions:

- Because of excellent lubricating nature, graphite is widely acceptable as a suitable powder additive of near dry machining. But EDM is a thermal-assisted machining approach, so the involvement of graphite, with no doubt, not only improves the surface characterization but also raises the amount of carbon monoxide evolution because of the partial burning of this graphite at high temperature. These gases are not good for operator's health. But silicon has very high flash point and it never partially burns during machining. Moreover, the remains are present on the recast layer in silicon-carbide form. So, in this context involvement of silicon can encourage the sustainability of EDM operation with good surface integrities as a strong substitute of graphite particles.
- Hybrid powder-added dielectric (5 g/l Cu and 3 g/l Si) possesses better removal rate than normal dielectrics when the machining is performed at 50 and 250  $\mu\text{s}$  of pulse ON time for 4–16 A range of pulse current when the pulse OFF time and gap voltage is constant. This type of behavior is obtained during the machining of Ti6Al4V with copper tool. So, the ranges can be varied for other sets of tool and workpiece.
- At 4 A value of pulse current, the powder-mixed dielectrics show less removal rate than kerosene when the pulse ON time is varied between 50 and 250  $\mu\text{s}$ . But at higher value of pulse current, powder-mixed dielectrics show impressive responses.
- Powder-mixed dielectrics possess better surface properties than normal dielectrics for wide range of variations of input parameters. As evidence, microscopic views of Ti6Al4V alloy are shown in Fig. 20.7, where micro-structures and crater formation patterns are captured for 10 A current, 30 V voltage, 200  $\mu\text{s}$  pulse ON time and 20  $\mu\text{s}$  pulse OFF time. From Fig. 20.8, it is also clear that hybrid dielectrics (5 g/l Cu and 3 g/l Si) exhibit much better surface properties in terms of less surface indentations and small crater formation when Ti6Al4V is electrical discharge machined with copper tool.
- In this particular case study, machining is performed at low flushing speed ( $>0.15$  m/s) in a separate chamber to avoid the unwanted excretions of powder additives. In this context, center flushing, that is, flushing through the tool in the axial direction can give better performances than the obtained results. Moreover, this work concludes that involvement of Cu–Si hybrid dust can give better responses than normal kerosene oil as a dielectrics when Ti6Al4V is machined without flushing condition for 4–16 A of pulse current, 50–250  $\mu\text{s}$  of pulse ON time, 20–60 kV of gap voltage and 10–50  $\mu\text{s}$  of pulse OFF time using cylindrical copper rod (diameter 10 mm) as a tool.

## References

1. Opoz, T.T., Yasar, H., Ekmekci, N., Ekmekci, B.: Particle migration and surface modification on Ti6Al4V in SiC powder mixed electrical discharge machining. *J. Manuf. Process.* **31**, 744–758 (2018)
2. Bhattacharya, A., Batish, A., Kumar, N.: Surface characterization and material migration during surface modification of die steels with silicon, graphite and tungsten powder in EDM process. *J. Mech. Sci. Technol.* **27**(1), 133–140 (2013)
3. Chaudhury, P., Samantaray, S., Sahu, S.: multi response optimization of powder additive mixed electrical discharge machining by Taguchi analysis. *Mater. Today: Proc.* **4**, 2231–2241 (2017)
4. Chen, S.-L., Lin, M.-H., Huang, K.-H., Wang, C.-C.: Research of the recast layer on implant surface modified by micro-current electrical discharge machining using deionized water mixed with titanium powder as dielectric solvent. *Appl. Surf. Sci.* **311**, 47–53 (2014). <https://doi.org/10.1016/j.apsusc.2014.04.204>
5. Kansal, H.K., Singh, S., Kumar, P.: Effect of silicon powder mixed EDM on machining rate of AISI D2 die steel. *J. Manuf. Process.* **9**(2007)
6. Kumar, S., Batra, U.: Surface modification of die steel materials by EDM method using tungsten powder-mixed dielectric. *J. Manuf. Process.* **14**, 35–40 (2012)
7. Tripathy, S., Tripathy, D.K.: Surface Characterization and Multi-response optimization of EDM process parameters using powder mixed dielectric. *Mater. Today: Proc.* **4**, 2058–2067 (2017)
8. Wong, Y.S., Lim, L.C., Rahuman, I., Tee, W.M.: Near-mirror-finish phenomenon in EDM using powder-mixed dielectric. *J. Mater. Process. Technol.* **79**, 30–40 (1998)
9. Hu, F.Q., Cao, F.Y., Song, B.Y., Hou, P.J., Zhang, Y., Chen, K., Wei, J.Q.: Surface properties of SiCp/Al composite by powder-mixed EDM. *Procedia CIRP* **6**, 101–106 (2013)
10. Kucukturk, G., Cogun, C.: A new method for machining of electrically nonconductive work-pieces using electric discharge machining technique. *Eng. Sci. Technol.: Int. J.* **14**(2), 189–207. <https://doi.org/10.1080/10910344.2010.500497>
11. Mohala, S., Kumar, H.: Study on the multiwalled carbon nano tube mixed EDM of Al-SiCp metal matrix composite. *Mater. Today: Proc.* **4**, 3987–3993 (2017)
12. Shabgard, M., Khosrozadeh, B.: Investigation of carbon nanotube added dielectric on the surface characteristics and machining performance of Ti–6Al–4V alloy in EDM process. *J. Manuf. Process.* **25**, 212–219 (2017)
13. Pecas, P., Henriques, E.: Influence of silicon powder-mixed dielectric on conventional electrical discharge machining. *Int. J. Mach. Tools Manuf.* **43**, 1465–1471 (2003)
14. Talla, G., Gangopadhyay, S., Biswas, C.K.: Influence of graphite powder mixed EDM on the surface integrity characteristics of Inconel 625. *Part. Sci. Technol.* (2016). <https://doi.org/10.1080/02726351.2016.1150371>
15. Toshimitsu, R., Okada, A., Kitada, R., Okamoto, Y.: Improvement in surface characteristics by EDM with chromium powder mixed fluid. *Procedia CIRP* **42**, 231–235 (2016)
16. Zhao, W.S., Meng, Q.G., Wang, Z.L.: The application of research on powder mixed EDM in rough machining. *J. Mater. Process. Technol.* **129**, 30–33 (2002)

# Chapter 21

## Experimental Study on Material Removal Rate and Over-Cut in Electrochemical Machining of Monel 400 Alloys with Coated Tools



S. Ayyappan  and N. Vengatajalapathi 

**Abstract** Electrochemical machining (ECM) is a promising non-traditional machining process used for machining difficult-to-machine materials. It finds the applications in the field of automotive, electronics, optics, medical, petroleum, nuclear and die industries. Improving an over-cut (OC) is still a tough task in ECM, though it is benefitted with better material removal rate (MRR). Therefore, different coated tools, that is, epoxy-coated tool (ECT) and abrasive-coated tool (ACT), were used in the direction to obtain better OC. It is observed that the ECT technique performs well for reducing the OC in comparison to the other tools under similar conditions and appears more electrochemically stable. The coating on tool avoids the contact of tool surfaces with the intermittent sparks produced in the inter-electrode gap (IEG), thereby ensuring the increase of tool life.

**Keywords** Electrochemical machining · Epoxy-coated tool · Abrasive-coated tool · Material removal rate (MRR) · Over-cut (OC)

### Nomenclature

ECM : Electrochemical machining  
MRR : Material removal rate  
OC : Over-cut  
PT : Plain tool  
ECT : Epoxy-coated tool  
ACT : Abrasive-coated tool  
EC : Electrolyte concentration  
IEG : Inter-electrode gap

---

S. Ayyappan · N. Vengatajalapathi (✉)  
Department of Mechanical Engineering, Government College of Technology, 641013  
Coimbatore, India  
e-mail: [vengat92vengat@gmail.com](mailto:vengat92vengat@gmail.com)

© Springer Nature Singapore Pte Ltd. 2020  
M. S. Shunmugam and M. Kanthababu (eds.), *Advances in Unconventional Machining and Composites*, Lecture Notes on Multidisciplinary Industrial Engineering, [https://doi.org/10.1007/978-981-32-9471-4\\_21](https://doi.org/10.1007/978-981-32-9471-4_21)



## 21.1 Introduction

Dimensional accuracy plays an important role in product quality of high-precision fit applications. Several non-traditional machining techniques have been developed in the last two decades for improving the machining performance, which ensures high-quality products. Electrochemical machining (ECM) is one such technique that finds applications in various industries, such as nuclear, aircraft, medical, petroleum, die, and so on. ECM has been promised in the modern manufacturing world for than one decade. It works under the principle of Faraday's law of electrolysis and it is exactly the reverse of electroplating process. In ECM, the workpiece (anode) is connected to the positive terminal and the tool (cathode) is connected to the negative terminal of low voltage and high current DC power supply. The schematic diagram of ECM is shown in Fig. 21.1.

The strong ionic bond salts such as sodium chloride (NaCl), sodium nitrate (NaNO<sub>3</sub>), potassium chloride (KCl), and so on, are used as an electrolyte, which is the medium for ionization process in ECM. The electrolytes are pumped through the gap between workpiece and the tool to flush out the sludge (metal hydroxides) accumulated during the electrolysis. But it is very difficult to remove the passive film (metal oxides) as they are sticky in nature on the workpiece. This oxide film on the workpiece affects the dimensional accuracy [1]. The presence of oxide film in turn decreases the current efficiency [2]. The use of abrasives in the electrolyte reduces the anodic dissolution and increases the material removal rate [3]. The increase in machining voltage and gap enhances ion's mobility and conductivity, which in turn increases the MRR and over-cut [4]. The SiO<sub>2</sub> chemical vapor deposition on the tool increases the shape accuracy and surface quality of workpiece [5]. The side wall insulated tool plays a dominant role in achieving a larger MRR in one cycle compared to the other bottom-coated insulated tool [6]. Cathode-insulating layer could

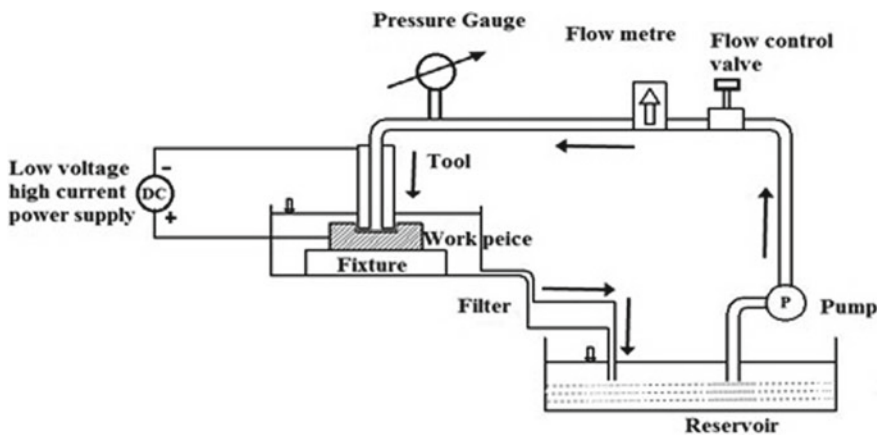


Fig. 21.1 Layout of electrochemical machining

be easily damaged during machining, and thereby, the machining accuracy could also be reduced. To avoid these problems, a metal-reinforced double-insulating layer cathode was used in ECM [7]. It is understood from the previous research works that the coating on tool improves the OC and surface quality of work specimen. Many researchers have tried to solve the dimensional inaccuracy issues in ECM. Therefore, in this work, using of different-coated materials on the sides of electrode tool is experimented for the better machining performance, especially maximizing the dimensional accuracy by reducing OC. This research paper presents the experimental investigation on the enhancement of dimensional accuracy using epoxy-coated tool (ECT) and another abrasive-coated tool (ACT). In ECT, the side surface of the tool is coated by using the epoxy (Araldite-AW4859) adhesive, while the bottom surface remains uncoated. The epoxy coating inhibits the conduction of side surfaces and makes them insulated when the electrolyte comes in contact with the side surfaces. By this method, the conduction occurs only between the uncoated bottom surfaces of the tool and the workpiece. In ACT, the side surfaces of the tool are coated by using silicon carbide (SiC) abrasives with the grain size 500. The coating of SiC insulates the side surface of the tool [6]. Additionally, the SiC coating on the tool removes the oxide film layer formed on the edges of workpiece, resulting in better dimensional accuracy. There is an improvement in the MRR also. The micro-tool coating preparation is used as a better technique to increase the MRR and reduce the OC. In this work, use of different tools, that is, plain tool (PT) without coating, ECT and ACT, is experimented for obtaining better machining accuracy.

## 21.2 Preparation of Insulated and Abrasive Tools

Copper is one of the best-conducting electrodes used in ECM. The C11-grade copper (99.9% purity) rod of 8 mm diameter was used as a tool. It possesses an excellent thermal conductivity also. The properties of C11-grade copper (Active Standard ASTM B694) are shown in Table 21.1.

At the start of the machining, excess materials are removed due to the good electrical conductive nature of copper. But over a period of time, the copper tools can be easily oxidized in the electrochemical environment by forming oxidation layer on its surfaces. As a result, copper tools have a shorter life expectancy. The uneven coating of oxide layer on the tools produces poor dimensions of the workpiece and

**Table 21.1** Properties of copper (C11)

Boiling point	2835 K
Density	8.96 g/cm <sup>3</sup>
Thermal conductivity	401 W/(mK)
Heat of fusion	13.26 kJ/mol
Heat of vaporization	300.4 kJ/mol
Electrical resistivity	0.0171 × 10 <sup>6</sup> (Ωm)

poor MRR. To avoid the abnormal removal of metal around the sides of tool, tool electrode is coated with some insulation materials on its side faces. The coating also acts as a good heat resistant and improves the dimensional accuracy of work specimen. The desired properties of the insulating and abrasive coating are the absence of defects such as pores and the stable coating composition under corrosive environments. The abrasive tools possess high strength, high melting point, low conductivity and the rigid bonding of abrasive grains. Therefore, the abrasive tools are used in the high-hardened material cutting applications. But the use of abrasive tools in the ECM applications is limited. Moreover, the abrasive tools could be used for obtaining better dimensional accuracy. The tool material was machined to a diameter of 8 mm. The burr was removed by rinsing the tool into the nitric acid solution and then with distilled water. The adhesive agent epoxy (Araldite-AW4859) was applied all over the side surfaces of the tool leaving the bottom surface uncoated. The araldite-coated tool was allowed to dry in air for 12 h. There was a negligible change in the dimension of the tool after epoxy coating. The epoxy-coated tool (ECT) is shown in Fig. 21.2. The same procedure was used for the preparation of the abrasive-coated tool (ACT). The silicon carbide (SiC) abrasives with the grain size of 82  $\mu\text{m}$  were used in this work. The SiC abrasives were coated over the tool surfaces with the Araldite-AW4859 as binding material. The fixed grain size and the uniform distribution of grains over the surfaces of the tool were ensured. The diameter of the tool is measured to be increased from 8 to 8.2 mm as a diameter. The ACT is shown in Fig. 21.3.

**Fig. 21.2** Epoxy-coated tool (ECT)





**Fig. 21.3** Abrasive-coated tool (ACT)

### 21.3 Equipment and Experimentation

The micro-ECM is an in-house method developed as shown in Fig. 21.4. ECM consists of DC power supply (0–20 V, 0–100 A), electrolyte supply system, tool feed system and work holding device. The voltage can be adjusted in the DC rectifier and the current during machining can be noted. The tool is fixed on the servomotor with separate DC power supply of 12 V. The servomotor produces the speed of 10 RPM. In ECM, factors such as applied voltage and electrolyte concentration greatly influence the machining accuracy.

The selected factors and its levels are shown in Table 21.2. The tool is attached to a chuck which is fixed in a DC motor (12 V, 10 RPM). Monel 400 alloy is used as a workpiece and aqueous sodium chloride (NaCl) is used for the ECM experiments in this work. MRR is directly proportionate to tool feed rate. Hence, the constant feed rate is considered in this work. But tool feed rate has a significant impact on the surface quality of the workpiece. At lower feed rate, OC will be more because of larger machining time. Therefore, poor surface quality is formed. If feed rate is high, micro sparks and short circuiting occur in the working area, which leads to larger over-cut. Tool damage is also observed at the larger feed rates. Therefore, small feed rate of 0.1 mm/min is adopted. The inter-electrode gap between tool and workpiece is maintained as 0.1 mm. The chemical composition of Monel 400 alloys is shown in Table 21.3.

The experiments were conducted by varying the voltage and electrolyte concentration for each tool, that is, PT, ECT and ACT according to the design matrix shown in Table 21.4. All the tools are rotated with the speed of 10 RPM. In this work, MRR

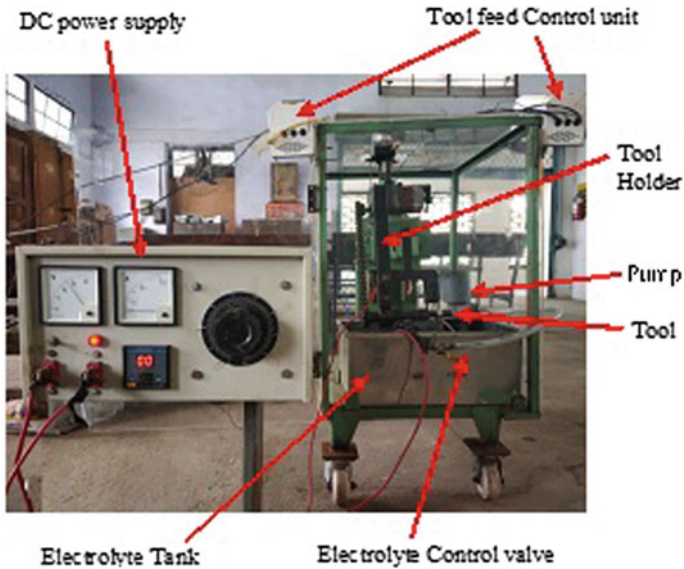


Fig. 21.4 Micro-ECM equipment setup

Table 21.2 Factors and levels of ECM experiments

Factors	Type	Levels
Workpiece	Monel 400	Hardened material
Electrolyte concentration (EC)	Sodium chloride	150, 175, 200 g/L
Tool	Copper (C11)	PT, ECT, ACT
Voltage (V)	DC	11, 13, 15 V

was measured based on rate of weight loss during machining as in Eq. (21.1).

$$\text{Material removal rate (MRR)} = \frac{\text{Loss of Weight}}{\text{Machining Time } (t)} \tag{21.1}$$

Weights were measured from weighing machine with the least count of 1 mg and maximum weight up to 1 kg. Over-cut (OC) is defined as the gap produced on both sides of the tool while machining. OC is measured as half the variance in the diameter of the tool as in Eq. (21.2).

$$OC = \frac{D_2 - D_1}{2} \tag{21.2}$$

where

D1: Diameter of the tool (mm)

D2: Diameter of the machined profile (mm)

**Table 21.3** Chemical composition of Monel 400 alloys [8]

Material	Monel 400 alloys										
	C	Si	Mn	P	S	Cr	Mo	Fe	V	W	Ni
Composition and weight (%)	0.047	0.172	1.03	0.012	0.01	0.1	0.1	1.66	0.029		
		Cu	Al	Co	Nb	Ti	Mg	Ni			
	0.1	29.24	0.01	0.103	0.1	0.047	0.031	67.4			

**Table 21.4** Experimental observation for various tools

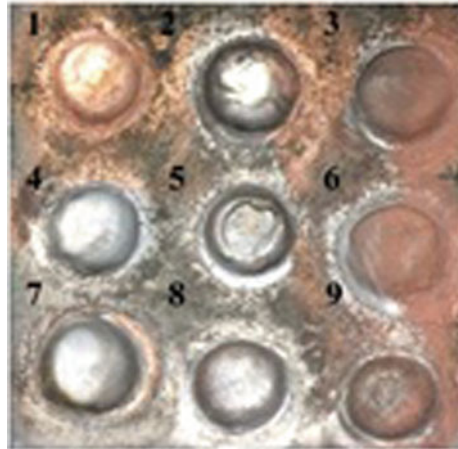
No.	Process parameters		Performance measures					
	Voltage (V)	EC (g/L)	MRR (g/min)			Over-cut (mm)		
			PT	ECT	ACT	PT	ECT	ACT
1	11	150	0.90	0.20	0.18	09.57	8.20	8.37
2	11	175	1.20	0.24	0.16	09.85	8.58	8.71
3	11	200	1.35	0.38	0.30	10.05	9.20	8.97
4	13	150	1.20	0.20	0.18	09.65	8.70	9.06
5	13	175	1.19	0.26	0.32	10.51	8.55	9.06
6	13	200	1.34	0.34	0.32	10.72	9.35	9.59
7	15	150	1.70	0.22	0.31	10.70	9.04	8.89
8	15	175	1.80	0.24	0.32	10.95	9.26	9.44
9	15	200	1.96	0.32	0.34	12.06	9.40	9.77

The diameters of the machined surface were measured with the help of profile projector. The experimental results were tabulated in Table 21.4. The performance measures such as MRR and OC for PT were compared with ECT and ACT.

## 21.4 Results and Discussions

### 21.4.1 Material Removal Rate

As per the Faraday's law, the MRR increases with the increase in current density. An increase in supply voltage leads to an increase in electrical conductivity of electrolyte, which results in high current density [2]. When the power supply increases, more amounts of electrons are produced, which raise the density of ions, and consequently, the MRR. It was studied in all the three types of tools, that is, PT, ECT and ACT. However, MRR of the ACT was noticed to be higher at almost all voltages. As the insulation coating in ECT acts as insulation between the tool and the workpiece on the side surfaces, the current is allowed to avail at the bottom surface of the tool only. The unwanted removal of excess material over the tool side surface was reduced. The abrasive surface acts as a honing surface which removes the unwanted burrs and the oxide film layer produced on the surfaces. Therefore, fresh surface is always exposed for further machining. MRR is increased because of this cumulative effect. The machined surfaces by ECT and ACT are shown in Figs. 21.5 and 21.6, respectively. Rotating tool improves the MRR as the continuous rotation avoids the formation of the gas film layer. The surfaces machined by the non-insulated and uncoated tool, that is, PT are shown in Fig. 21.7.

**Fig. 21.5** Surfaces by ECT**Fig. 21.6** Surfaces by ACT

### 21.4.2 Over-Cut

In ECM, minimizing the over-cut is a tough task. This work was aimed at reducing the OC using coated tools. OC increases with an increase in applied voltage and its increase leads to poor machining. The variations in OC with the effects of process of parameters, that is, V and EC for various tools are shown in Figs. 21.8, 21.11 and 21.13. The micro-image pictures of machined surfaces generated by the different tools are shown in Figs. 21.9, 21.10 and 21.12.

Figure 21.8 depicts the influence of process variables on the OC for plain tool with the aqueous NaCl electrolyte. Increase in voltage and electrolyte concentration



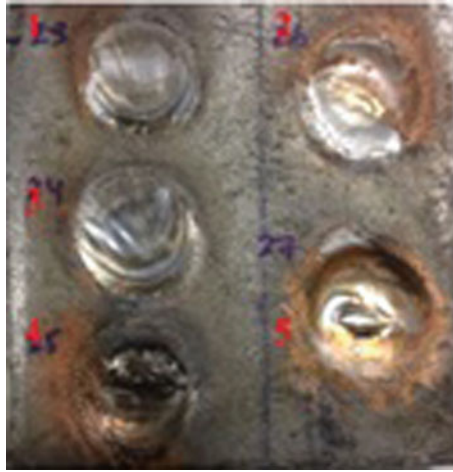


Fig. 21.7 Surfaces by PT

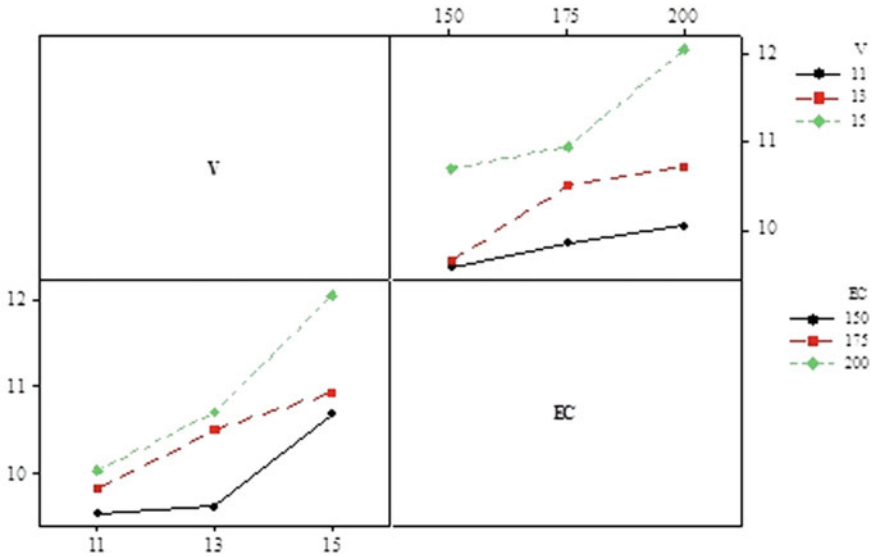
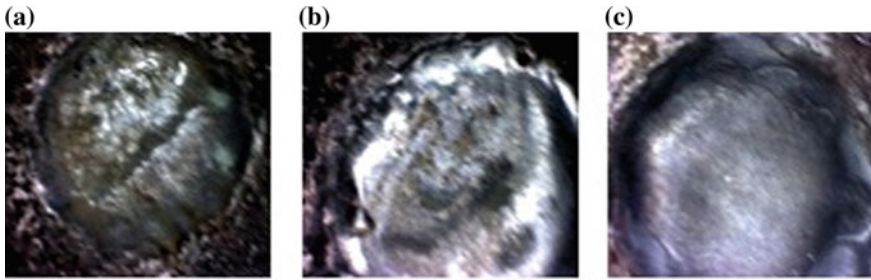
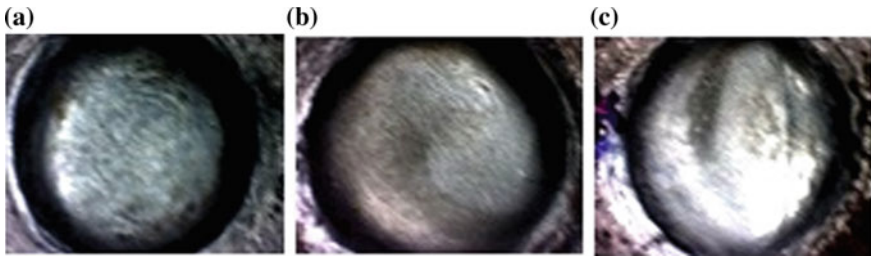


Fig. 21.8 Interaction plot of OC with plain tool (PT)



**Fig. 21.9** Machined surfaces by PT at **a** 11 V, **b** 13 V and **c** 15 V



**Fig. 21.10** Machined surfaces using ECT at **a** 11 V, **b** 13 V and **c** 15 V

increases the machining current in the inter-electrode gap, thereby increasing more material removal [9]. This conforms to the fundamental machining principle of ECM.

More material removal on the sides of the tool surfaces increases the OC. In the smaller IEG of 0.1 mm, the high current density and higher concentration allow more ions for ionization, which increases the OC significantly. The epoxy-coated tool prevents the ions interaction on the sides of tool surfaces with workpiece, thereby avoiding the material removal laterally. This phenomenon produces better dimensional accuracy by reducing the over-cut. The better images are obtained in Fig. 21.10 in comparison to Fig. 21.9. Figure 21.11 shows the interaction plot of OC with the epoxy-coated tool.

The abrasives on the sides of the tool erode the surface of the workpiece, though it prevents the electrochemical reaction. Therefore, slight increase in OC in abrasive coated tool is observed in comparison to epoxy-coated tool. But abrasive-coated tools perform better than uncoated tools (Fig. 21.12).

Figure 21.13 explicates the interaction effect of voltage and electrolyte concentration on the OC with abrasive-coated tool. The uncoated copper tool (PT) generated a surface with lower roughness than the abrasive tool at the beginning of the machining process. But after a couple of experiments, the surface quality of workpiece starts decreasing with the uncoated tool.

Initially, because of the good surface quality of the uncoated copper tool, the surface generated is good. But after some experiments, some deposition (oxides of

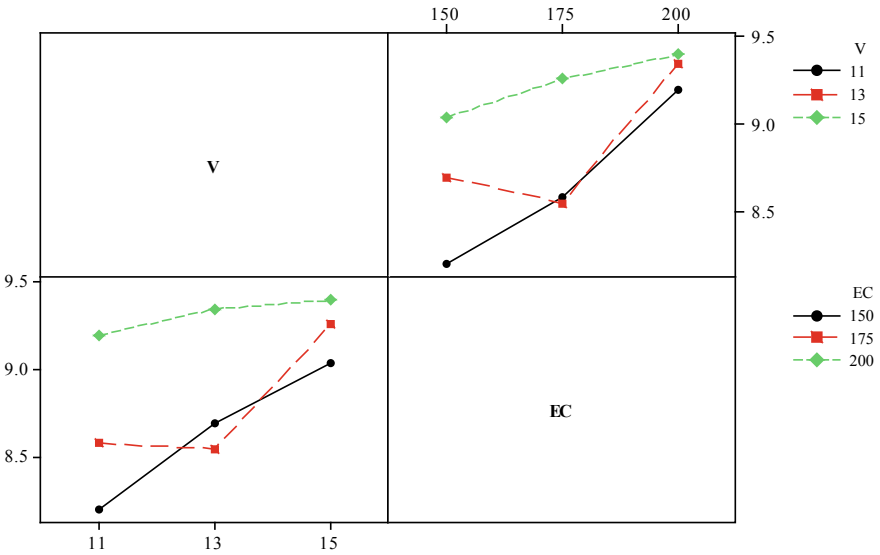


Fig. 21.11 Interaction plot of OC for epoxy-coated tool (ECT)

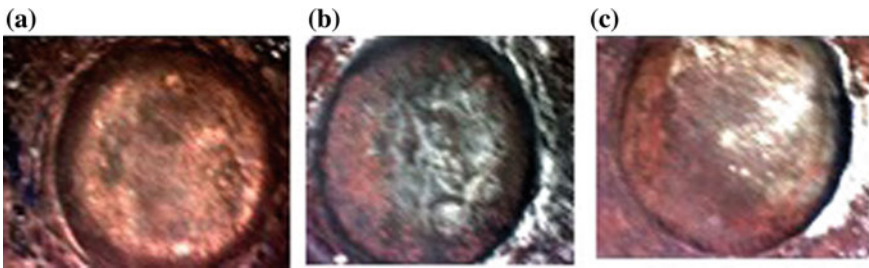


Fig. 21.12 Machined surfaces by ACT at a 11 V, b 13 V and c 15 V

copper) takes place on the uncoated tool surface, thus making the tool surface rougher. These rough surfaces produce poor machined surface quality. But the damages on the ECT and ACT are relatively less. Though some minor damages are noticed on the surfaces of ECT and ACT, the over-cut is reduced because of the absence of electrochemical reaction between the side surfaces and workpiece. The surfaces of tools before and machining are shown in Figs. 21.14, 21.15 and 21.16.

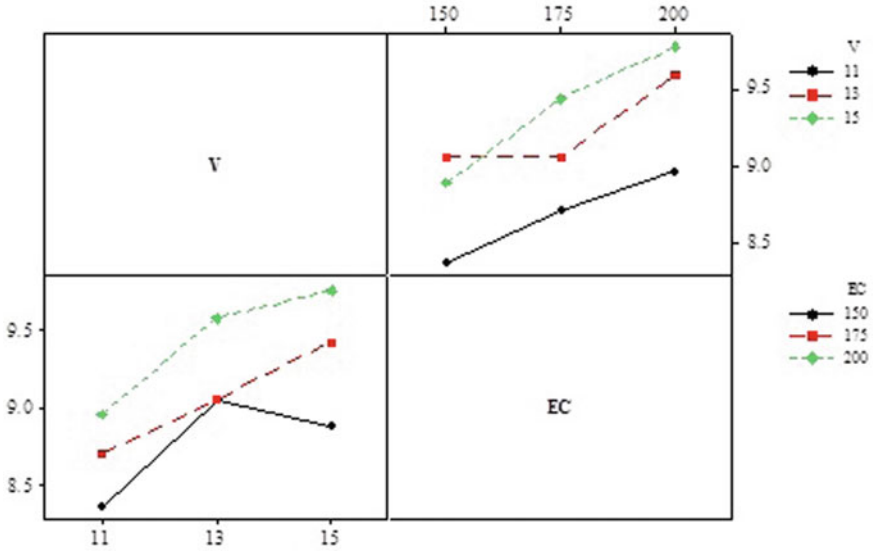


Fig. 21.13 Interaction plot of OC for abrasive-coated tool (ACT)

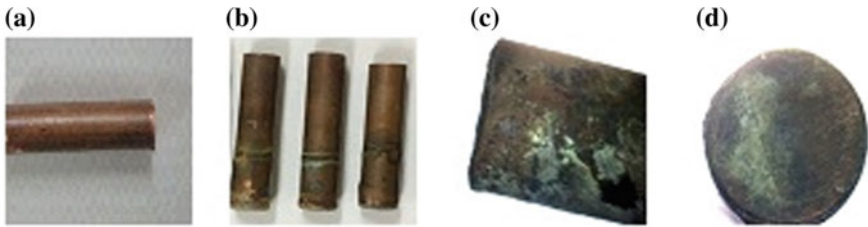


Fig. 21.14 Surface of the PT before machining (a) and after machining (b, c, d)

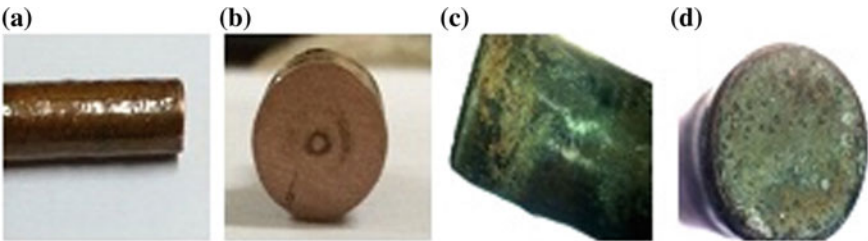


Fig. 21.15 Surface of the ECT before machining (a, b) and after machining (c, d)

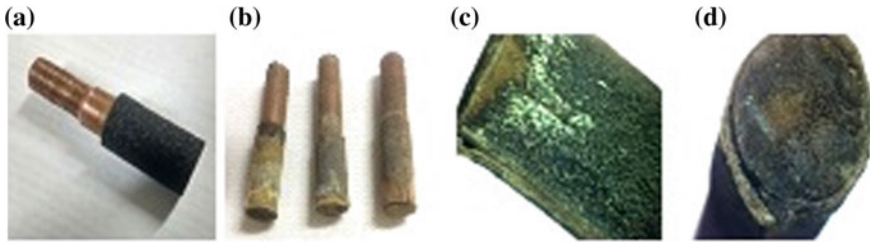


Fig. 21.16 Surface of the ACT before machining (a) and after machining (b, c, d)

## 21.5 Conclusions

The following conclusions are arrived at in ECM experimentation. Epoxy and abrasive copper tools produce better machining accuracy than uncoated tools. The epoxy coating acts as a good insulation because of its higher bonding strength and produces good surface quality and reduces overcut in an ECM process. Abrasive-coated copper tool produces higher material removal rate due to the continuous removal of oxide film layer formed between the side surfaces of tool and workpiece. The overcut is considerably reduced in comparison to uncoated tools. The current distribution on the sides of tool surfaces is reduced due to these coatings. These results confirm the reduction in tool cost by increasing tool life and improvement in the reliability of the ECM system and process outputs.

## References

1. Chin, D.T.: Anodic films and ECM dimensional control: a study of steel electrodes in solutions containing Na<sub>2</sub>SO<sub>4</sub> and NaClO<sub>4</sub>. *J. Electrochem. Soc.* **119**(8), 1043–1048 (1972)
2. Chin, D.T., Wallace Jr., A.J.: Anodic current efficiency and dimensional control in electrochemical machining. *J. Electrochem. Soc.* **120**(11), 1487–1493 (1973)
3. Liu, Z.: Machining of microchannel in SS316 surface using abrasive-assisted electrochemical jet machining. *Int. J. Adv. Manuf. Technol.* **95**(1–4), 1143–1152 (2017)
4. Sudarisman, A.W.N.: Overcut and material removal rate on electrochemical machining of aluminum and stainless steel using isolated brass electrode. In: 2nd International Conference of Industrial, Mechanical, Electrical, and Chemical Engineering (ICIMECE), pp. 69–72 (2016)
5. Liu, W.: The multi-physics analysis for a novel tool structure to improve the accuracy in electrochemical micro-machining. *Int. J. Adv. Manuf. Technol.* **94**(5–8), 1991–2001 (2018)
6. Niu, S., Qu, N., Li, H.: Investigation of electrochemical mill-grinding using abrasive tools with bottom insulation. *Int. J. Adv. Manuf. Technol.* **97**(1–4), 1371–1382 (2018)
7. Yao, J., Chen, Z.T., Nie, V., Li, Q.: Investigation on the electrochemical machining by using metal reinforced double insulating layer cathode. *Int. J. Adv. Manuf. Technol.* **89**(5–8), 2031–2040 (2017)
8. Kalaimathi, M., Venkatachalam, G., Sivakumar, M., Ayyappan, S.: Experimental investigation on the suitability of ozonated electrolyte in travelling-wire electrochemical machining. *Braz. Soc. Mech. Sci. Eng.* **39**(11), 4589–4599 (2017)
9. Ayyappan, S., Sivakumar, K.: Enhancing the performance of electrochemical machining of 20MnCr5 alloy steel and optimization of process parameters by PSO-DF optimizer. *Int. J. Adv. Manuf. Technol.* **82**(9–12), 2053–2064 (2016)

# Chapter 22

## Experimental Investigations into Ultrasonic-Assisted Magnetic Abrasive Finishing of Freeform Surface



Akshay Kumar Singh, Girish Chandra Verma, Vipin Chandra Shukla  
and Pulak Mohan Pandey

**Abstract** Ultrasonic-assisted magnetic abrasive finishing (UAMAF) is a hybrid finishing process that integrates the effect of ultrasonic vibrations in the magnetic abrasive finishing (MAF) process. This paper evaluates the finishing performance of freeform surface by UAMAF process with bonded abrasives. The bonded magnetic abrasive particles (MAPs) were prepared by sintering iron powder with SiC particles. Furthermore, in order to evaluate the effect of process parameters, experiments were designed using surface response methodology technique. Parameters, namely rotational speed of tool (N), working gap (D), abrasive weight percentage (%wt SiC), and surface angle, were considered as process variables and percentage change in surface roughness ( $\% \Delta R_a$ ) was taken as process response. A quadratic model has been developed by performing analysis of variance for the obtained results. The results show that working gap is the most significant parameter followed by surface angle, RPM, and %wt SiC, respectively. The optimum  $\% \Delta R_a$  is found out to be 77.25%.

**Keywords** Ultrasonic-assisted magnetic abrasive finishing process · Freeform surface · Surface angle

### 22.1 Introduction

In the present scenario, the industry requires nano finishing of freeform surfaces, like dies, semiconductors, metallic mirrors, and so on. The conventional finishing processes, like lapping, grinding, honing, and so on, are less controllable for finishing complex geometries [1]. These processes use a rigid tool causing application of substantial normal stress on finishing surface [2–4]. This produces micro-cracks, resulting in reduced strength of finished parts [1]. Thus, any process that can nano finish a freeform surface under gentle condition may overcome these limitations. Requirement of nano-level finish with minimal surface defects led to the development of new finishing technology, namely magnetic abrasive finishing (MAF).

---

A. K. Singh · G. C. Verma · V. C. Shukla · P. M. Pandey (✉)  
Department of Mechanical Engineering, Indian Institute of Technology Delhi, Delhi, India  
e-mail: [pmpandey@mech.iitd.ac.in](mailto:pmpandey@mech.iitd.ac.in)

MAF is a new finishing process in which the magnetic abrasive particles (MAPs) remove the material from workpiece in the form of microchips. MAPs are the mixture of iron and abrasive particles, in bonded or unbonded form. In the presence of magnetic field, these MAPs get aligned and form a flexible magnetic abrasive brush (FMAB). When this FMAB is rotated against any surface, it performs the finishing operation. Owing to the self-adaptability of the brush, MAF is considered as an efficient finishing technique and used to finish flat, cylindrical, and curved surfaces [5].

Many researchers [6–10] have examined the MAF process on different types of surfaces, which yielded very good results. Du Kim and Choi [6] finished Cr-coated roller using a hybrid process, namely magnetic electrolytic abrasive polishing (MEAP). Their experimental results showed that the combination of MAF and electrolytic polishing resulted in effective finishing. Singh et al. [7] analyzed the surface morphology (using SEM and AFM image) of the finished surface to study the behavior of abrasive particles in the finishing process. They concluded that scratching and micro-cutting were the mechanisms of material removal in MAF process.

Mulik and Pandey [8] developed an ultrasonic-assisted magnetic abrasive finishing (UAMAF) for efficient finishing of planar surfaces. In this process ultrasonic vibrations were provided to the workpiece during magnetic abrasive finishing (MAF) process. They have reported that application of ultrasonic vibrations resulted in shortening of finishing time. They studied the effect of process parameters (rotation of magnet, supply voltage, abrasive mesh number, %wt SiC, and pulse on time of ultrasonic vibration) on  $\% \Delta Ra$  in finishing of AISI 52100 steel sheets. They obtained a best surface finish of 22 nm with optimized finishing parameters in 80 s. Kala et al. [9] performed experimental investigations on a novel setup to finish flat workpiece (copper alloy) efficiently using UAMAF. Effects of electromagnet voltage, mesh number, rotational speed, and pulse on time of ultrasonic vibration on  $\% \Delta Ra$  were studied. The study showed that voltage was the most effective parameter. Kim and Choi [6] studied the behavior of sintered MAPs in inner surface finishing and analyzed that large-sized MAPs were most suitable for efficient machining. It was also found that the supplied amount of MAPs was one of the most important parameter in the finishing process.

Shinmura et al. [10] analyzed the effect of iron particle and abrasive particle size on material removal and surface roughness. The results showed that the stock removal and surface roughness increased with increase in iron and abrasive particle size. They also concluded that iron particle size had more dominating effect on material removal and surface roughness than abrasive particle size. They finished ceramic bars ( $Si_3N_4$ ) with diamond magnetic abrasive, composed of diamond micron size powder and iron particles. The results showed that samples with surface roughness of 0.45  $\mu m$  Ra were efficiently reduced to 0.04  $\mu m$  Ra when iron particle of 100  $\mu m$  and diamond particle of 0.5  $\mu m$  were used.

From the literature review presented above, it can be seen that most of the previous attempts have been made on flat or cylindrical surfaces using mostly unbonded abrasives. It was also observed that UAMAF process which has better efficiency as compared to MAF process had never been tried on freeform surfaces. Therefore, the

present study intends to study the effect of UAMAF process on freeform surface using bonded abrasive and permanent magnet tool. In freeform surface the surface angle (angle between the tool axis and surface normal at point of contact) keeps changing with the tool movement. Singh et al. have reported that  $\Delta Ra$  varies on changing the values of surface angle. Thus, in order to evaluate the effect of UAMAF process, surface angle was considered as one of the process parameter.

The objective of the present study was to evaluate the effect of UAMAF process parameters on the finishing performance of freeform surface. AISI 1017 steel workpiece was chosen as workpiece material for finishing freeform surfaces along with bonded abrasives of iron and SiC particles in the present study. Central composite design methodology was chosen for designing the experiments. RPM, gap, surface angle, and %wt SiC with the specified range based on trial experiments and literature review were taken as effective process variables. Subsequently, ANOVA was performed to establish a statistical relation (regression model) between effective process parameters and process response ( $\% \Delta R_a$ ). Genetic algorithm method was further used to obtain the optimized finishing parameters. Further to evaluate the finishing process, morphology of the finished and unfinished surfaces was captured from optical profilometer and USB microscope.

## 22.2 Experimental Design and Setup

### 22.2.1 Preparation of Bonded Abrasive

Many researchers have [11, 12] suggested that using sintered MAPs in MAF process improves the efficacy of the process. It is due to higher bonding strength between iron and abrasive particle (compared to unbonded) which allows it to sustain higher rotational speed [12]. Bonded MAPs are generally prepared by sintering of iron and SiC particles. Good finishing performance and improved surface quality can be achieved by sintered MAPs [13].

In order to prepare bonded MAPs mixture, Fe (mesh no. 300) and SiC (mesh no. 600) particles were mixed in ball mill. The mixture was then compacted in the form of pallets by using die punch assembly and compaction machine. These pallets were then sintered in high temperature tube furnace (MT-11-14P, make: Metrex Scientific Instruments Pvt. Ltd) as per the given sintering cycle (Fig. 22.1). The pallets were crushed and screened to obtain bonded MAPs of 100–120  $\mu\text{m}$  size. The following parameters (Table 22.1) based on literature survey and trials were considered during the preparation of sintered MAPs [12, 14].

**Characterization of sintered magnetic abrasive.** SEM images (of unbonded and bonded MAPs) were obtained to ensure adequate sintering between iron particles and SiC particles. It was found that Fe and SiC particles got adequately bonded after sintering. SEM images of simply mixed MAPs and sintered MAPs are shown in Fig. 22.2. It can be seen that after sintering (Fig. 22.2b) all the SiC particles were



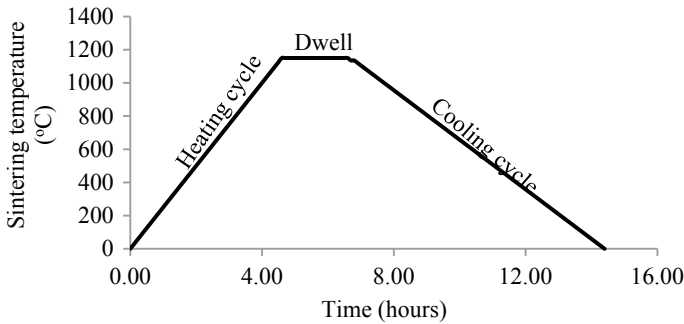


**Fig. 22.1** Sintering cycle for bonded MAPs

**Table 22.1** Parameters and process variable for preparation of sintered MAPs

Compacting load	80 kN
Compaction time	5 min
Sintering temperature	1150 °C
Heating rate	250 °C/h
Soaking time	2 h
Cooling rate	150 °C/h
Atmosphere	Inert (argon gas)

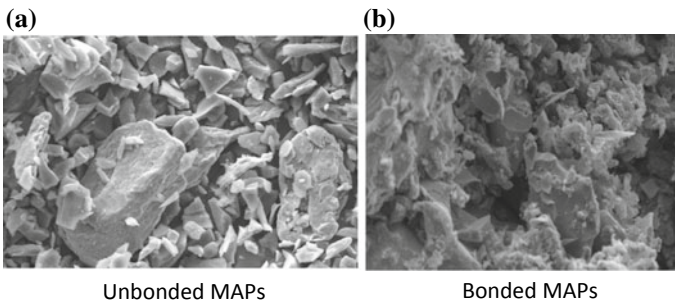
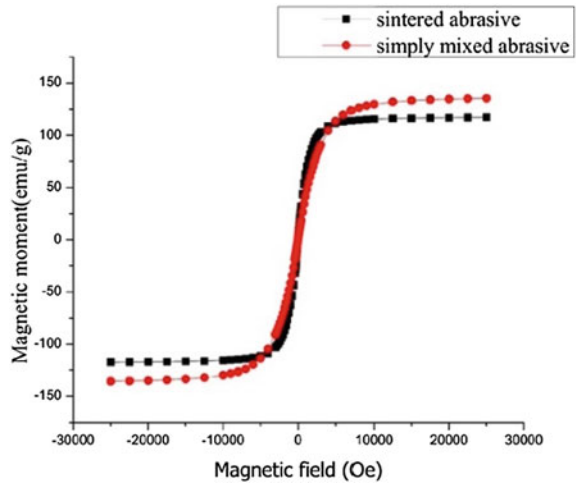


**Fig. 22.2** SEM image of MAPs

adhered to the Fe particle forming bonded MAPs.

**Electromagnetic property of sintered MAPs.** Magnetic moment–magnetic field intensity ( $M$ – $H$ ) curve was plotted with the help of physical property measurement system vibrating sampling magnetometer (PPMS-VSM) test facility for unbonded and bonded MAPs within  $-20$  KOe to  $+20$  KOe magnetic field range at room temperature. It was observed from the results (Fig. 22.3) that magnetic moment of bonded MAPs was less than that of magnetic moment of unbonded MAPs. This could be due to the formation of different iron silicides during the high temperature

**Fig. 22.3** M–H curve for bonded (sintered) and unbonded (simply mixed) MAPs for 25% weight of abrasive

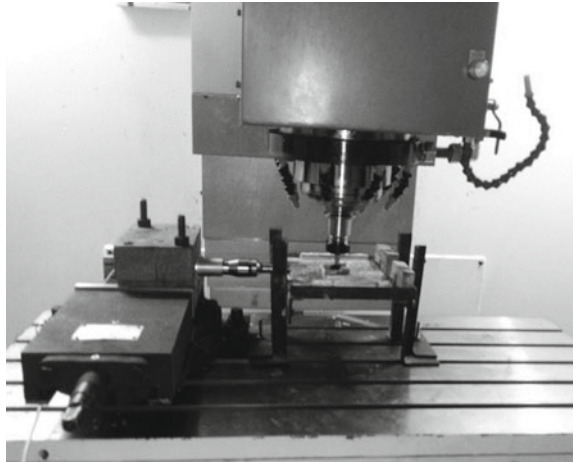


solid reactions between iron and silicon carbide [15]. However, bonded MAPs are more effective than unbonded MAPs because they provide higher bonding strength between iron and abrasive particles which allows the FMAB chains to sustain at higher RPM.

### 22.2.2 Experimental Setup

Figure 22.4 shows the experimental setup used for performing UAMAF on freeform surface. The experimental setup comprised a permanent magnet tool, ultrasonic vibration generator unit, and workpiece holding fixture. This designed fixture consisted of adjustable table for holding the workpiece. The spring and slotted guide ways were also provided on the fixture to accomplish sliding motion of the plate. Furthermore, an ultrasonic vibration of 20 kHz frequency was supplied to the workpiece holding plate through the horn. The ultrasonic vibration generator unit contained a piezoelectric transducer, horn, and power supply. The permanent magnet tool was fabricated by placing six NdBF<sub>e</sub> cylindrical magnets ( $\Phi$  8 mm  $\times$  10 mm thick) inside a steel tube ( $\Phi$  8.1 mm  $\times$  1 mm thick). The magnetic flux density of the developed tool was 0.46 T and was kept constant during the experiments. The entire setup was mounted on the table of the CNC vertical mill machine and the tool was held in the spindle. Then bonded MAPs were filled in the gap between the workpiece and tool for FMAB formation at the tool tip.

**Fig. 22.4** Experimental setup



**22.2.3 Design of Experiment and Selection of Process Parameters**

In the present study the central composite design was used for designing the experiments as it yields second-order model for the response (Eq. 22.1) [16].

$$y = a_o + \sum_{i=1}^n a_i x_i + \sum_{i=1}^n a_{ii} x_i^2 + \sum_{i=1}^n \sum_{j>i}^n a_{ij} x_i x_j \tag{22.1}$$

where  $y$  is the response variable,  $n$  represents the number of process variables and  $a_o$ ,  $a_i$ ,  $a_{ii}$ , and  $a_j$  are the tuning parameter.  $x_i$ ,  $x_i^2$  and  $x_i x_j$  represent first-order, second-order, and interaction term of the process variable, respectively. Equation 22.1 represents the response surface. The proposed methodology establishes relation between response surface and process parameter. The process parameters and their respective levels selected (Table 22.2) in the present study were based on the literature survey, trial experiments and setup constraints. The initial surface roughness of all the milled

**Table 22.2** Selected process parameter for respective ranges

Factor representation	Description	Levels				
		-2	-1	0	1	2
X <sub>1</sub>	Rotational speed (RPM)	100	200	300	400	500
X <sub>2</sub>	Working gap (mm)	1.6	1.8	2	2.2	2.4
X <sub>3</sub>	Abrasive weight percentage (%)	15	20	25	30	35
X <sub>4</sub>	Surface angle (°)	0	5	10	15	20

samples was not the same. Therefore, in order to compensate this variance, percentage change in surface roughness ( $\% \Delta R_a$ ) was considered as the process response which is given as (Eq. 22.2).

$$\% \Delta R_a = \frac{\text{initial surface roughness} - \text{final surface roughness}}{\text{initial surface roughness}} \times 100 \quad (22.2)$$

Several researchers reported that magnetic field, gap, rotational speed, % wt SiC, and abrasive size were the most effective parameters for MAF process [11, 17, 18]. However, for finishing freeform surface the surface angle played a significant role in MAF [19]. Surface angle at any point (Fig. 22.5) was defined as the angle between the tool rotational axis and normal vector at that point [19]. It was suggested that the normal finishing force varied with the change in surface angle which subsequently changed the efficacy of the process [19]. The results of the pilot experimentation also showed that finishing at higher angle resulted in ineffective finishing. Therefore, the surface angle was chosen as one of the process parameter. Therefore, to evaluate the effect of surface angle on  $\% \Delta R_a$ , an effective range of surface angle [ $0^\circ$ – $20^\circ$ ] was considered for experimentation (Fig. 22.5).

For the present study RPM, working gap, and abrasive weight percentage in MAPs (%wt SiC) were also considered as the process variables. It was observed from the results of pilot experiments that finishing mild steel workpiece with high gap resulted in ineffective finishing. However, finishing with working gap  $< 1.5$  (points with highest surface angle) resulted in gauging. Finishing with MAPs having very low or very high abrasive concentration had resulted in ineffective finishing. It may be due to the fact that at lower abrasive concentration the number of cutting edges available for finishing was very less, however, at higher concentration the stiffness of the FMAB decreased [11]. RPM was considered as process parameter as it affects the  $\% \Delta R_a$ . Pilot experimentation also showed that at lower RPM finishing rate was very low and at higher RPM the chains of FMAB started disintegrating and resulted in ineffective finishing.

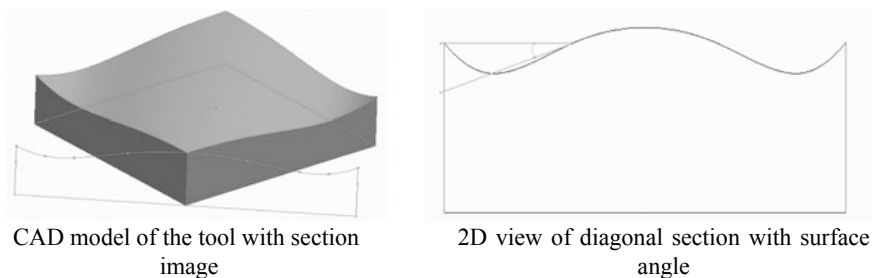


**Fig. 22.5** CAD image of the tool with surface angle

**Table 22.3** Weight of sintered MAPs used for different working gap

Working gap (mm)	Total weight of sintered abrasive (g)
1.6	1.0
1.8	1.2
2	1.4
2.2	1.6
2.4	1.8

### 22.2.4 Experimentation

Freeform surface were machined on AISI 1017 steel with 120 vickers hardness using 3D CNC milling machine. In order to maintain uniformity in workpieces, all samples were prepared under same machining conditions. The measurements for surface roughness were taken at the same locations (points) before and after UAMAF using templates. The surface roughness measurement was carried out on Talysurf 6 machine (Taylor Hobson, U.K., resolution in Z-direction = 16 nm). The surface angle at different locations on the freeform surface was determined by Creo parametric 1.0 software. Based on the surface angle given in DoE, the spots were chosen and marked for performing the experiments.

For evaluating the effect of %wt SiC, different sintered MAPs with different %wt SiC were prepared. At different gaps different weight of sintered MAPs were used for the formation of FMAB (Table 22.3). The amount of sintered MAPs for different working gap varied for experimentation (Table 22.3). Pulsed (pulse with on time of 3 s and pulse off time of 2 s) ultrasonic vibration of constant amplitude  $\sim 20 \mu\text{m}$  was provided to the workpiece as it yields better result [8, 9]. Based on the trial experiment, the finishing time was fixed to be 30 min. Further details of all the experiments performed with the obtained result are given in Table 22.4.

### 22.2.5 Statistical Modeling of $\% \Delta R_a$

In order to evaluate the effect of process parameters on  $\% \Delta R_a$ , analysis of variance (ANOVA) was performed for experimental results (Table 22.4). Adequacy of the developed model was checked at 95% confidence interval. The F (Fisher's value) value of the predictive model was compared with the standard F-value (for 95% confidence level). The ANOVA results confirmed the adequacy of the model as it qualified for the F test and lack of fit was also insignificant. However, this predictive model contained too many terms, thus it was simplified by removing insignificant terms ( $p$  values  $< 0.05$ ). The ANOVA result for predictive model with significant terms has been shown in Table 22.5. The ANOVA results (Table 22.5) showed that the  $F_{0.05, 9, 21}$  (32.28) was more than the standard F value (2.366) at 95% confidence interval for the response.

**Table 22.4** Details of experiments performed with the response variable

Exp. No.	X <sub>1</sub> (RPM)	X <sub>2</sub> (mm)	X <sub>3</sub> (%)	X <sub>4</sub> (°)	Initial R <sub>a</sub> (μm)	Final R <sub>a</sub> (μm)	%ΔR <sub>a</sub> (%)
1.	200	1.8	30	5	0.2014	0.1012	49.75
2.	300	2.0	25	10	0.2173	0.1068	50.85
3.	200	2.2	20	5	0.2418	0.1468	39.29
4.	400	1.8	30	15	0.3158	0.1640	48.07
5.	200	2.2	30	15	0.2316	0.1653	28.63
6.	400	2.2	30	5	0.3415	0.2052	39.91
7.	200	1.8	30	15	0.2813	0.1754	37.65
8.	400	1.8	20	15	0.3529	0.1987	43.70
9.	400	2.2	30	15	0.2937	0.1862	36.60
10.	200	2.2	20	15	0.3974	0.2934	26.17
11.	300	2.0	25	10	0.2383	0.1373	42.38
12.	300	2.0	25	10	0.2937	0.1741	40.72
13.	200	1.8	20	5	0.4219	0.2061	51.15
14.	300	2.0	25	0	0.3386	0.1454	57.06
15.	100	2.0	25	10	0.3107	0.2181	29.8
16.	300	2.0	25	10	0.2758	0.1436	47.93
17.	300	2.0	25	10	0.3759	0.1873	50.17
18.	300	2.0	15	10	0.2431	0.1678	30.97
19.	400	2.2	20	5	0.1974	0.1253	36.52
20.	300	1.6	25	10	0.2573	0.0868	66.27
21.	300	2.0	25	10	0.2593	0.1565	39.64
22.	500	2.0	25	10	0.3288	0.1982	39.72
23.	200	1.8	20	15	0.3571	0.2426	32.06
24.	300	2.0	35	10	0.3068	0.1909	37.78
25.	400	1.8	30	5	0.2356	0.0957	59.38
26.	300	2.0	25	20	0.4135	0.2743	33.66
27.	400	2.2	20	15	0.2837	0.1944	31.47
28.	400	1.8	20	5	0.3284	0.1440	56.15
29.	300	2.0	25	10	0.2354	0.1298	44.86
30.	300	2.4	25	10	0.4279	0.2754	35.64
31.	200	2.2	30	10	0.1938	0.1052	45.72

**Table 22.5** Analysis of variance (ANOVA) % $\Delta R_a$  with significant terms

Source	DF	Seq SS	MS	F	P	R <sup>2</sup> (adj)	Remarks
Regression	9	2655.77	295.09	32.28	0.000	90.40%	F <sub>0.05, 9,21</sub> = 2.366 F > F <sub>0.05, 9,21</sub> Model is adequate and lack of fit is insignificant
Linear	4	2042.16					
Square	3	496.02					
Interaction	2	117.58					
Residual error	21	191.98	9.14				
Lack of fit	15	68.85	4.59	0.22	0.980		
Pure error	6	123.13					
Total	30	2847.74					

The following regression equation was developed after carrying out ANOVA of the obtained results (Table 22.4)

$$\begin{aligned}
 \% \Delta R_a = & 110 + 0.351 \times X_1 - 147 \times X_2 + 5.74 \times X_3 - 2.27 \times X_4 \\
 & - 0.108 \times X_3^2 - 0.000272 \times X_1^2 + 0.00366 \times X_1 X_4 \\
 & - 0.100 \times X_1 X_2 + 36.3 \times X_2^2
 \end{aligned}
 \tag{22.3}$$

The value of R2 (adj) has been obtained as 90.40%, which shows high accuracy of the developed model. Therefore, Eq. 22.3 was considered as the predictive model for % $\Delta R_a$  in UAMAF process.

**Precision of the developed models.**

The actual % $\Delta R_a$  obtained from the experiments may vary from the predicted % $\Delta R_a$  (from Eq. 22.3) due to the presence of experimental error. However, by considering the variance in the result, the range for % $\Delta R_a$  can be predicted using Eq. 22.4 (in which the experimental % $\Delta R_a$  will lie).

$$\% \Delta R_{a\_range} = \% \Delta R_{a\_predicted} \pm t_{\alpha/2, DF} \times \sqrt{V_e}
 \tag{22.4}$$

where % $\Delta R_{a\_range}$  is the predicted range of % $\Delta R_a$ , % $\Delta R_{a\_predicted}$  is the % $\Delta R_a$  calculated using Eq. 22.3,  $t_{\alpha/2, DF}$  is the statistical t-value at a specified level of significance ( $\alpha/2$ ) and degree of freedom (DF), and  $V_e$  is the variance of the error of the predicted model. Using Eqs. 22.3 and 22.4, the range for the predictive models for % $\Delta R_a$ , at a 95% level of significance, has been calculated as:

$$\% \Delta R_{a\_range} = \% \Delta R_{a\_predicted} \pm 5.05
 \tag{22.5}$$

In order to validate the predictive model, few confirmation experiments were conducted at random set of variables. Results of confirmation experiments (Table 22.6)

**Table 22.6** Experimental table for validation experiment performed

Exp. No.	RPM	Working gap (mm)	%wt SiC (%)	Surface angle (θ)	%Δ R <sub>a</sub> -predicted (%)	Confidence interval at 95% confidence interval	Experimental results		Exp. % change in R <sub>a</sub> (%)
							Initial R <sub>a</sub> (μm)	Final R <sub>a</sub> (μm)	
1.	350	1.6	25	0	76.50	71.45–81.55	0.4536	0.1221	72.94
2.	350	1.6	25	0	76.50	71.45–81.55	0.4524	0.0923	79.59
3.	310	1.8	30	12	50.45	45.40–55.50	0.4001	0.2101	47.52



verified the precision of the developed model as the experimental  $\% \Delta R_a$  was found to be well within the predicted range.

## 22.3 Results and Discussion

### 22.3.1 Effect of Process Parameters

The main effect plot (Fig. 22.6) and the percentage contribution (Fig. 22.7) of significant parameters were further evaluated to study the effect of process parameters.

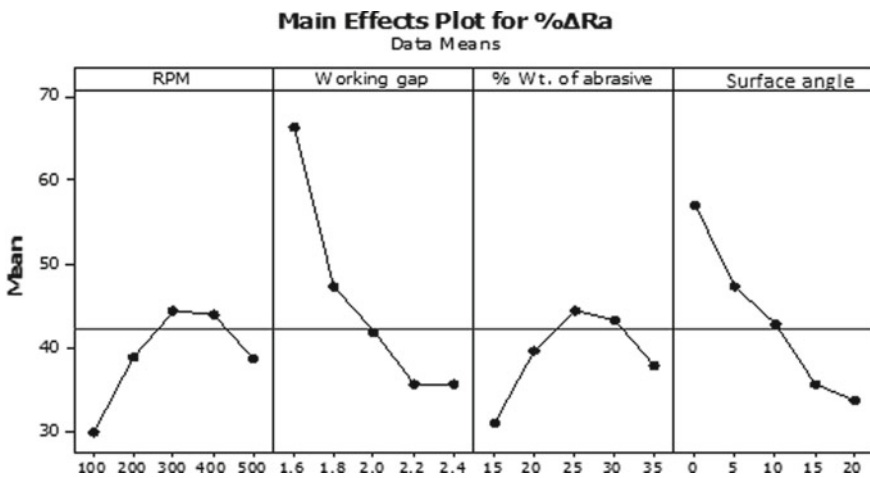


Fig. 22.6 Main effect plots for  $\% \Delta R_a$  with respect to all parameters

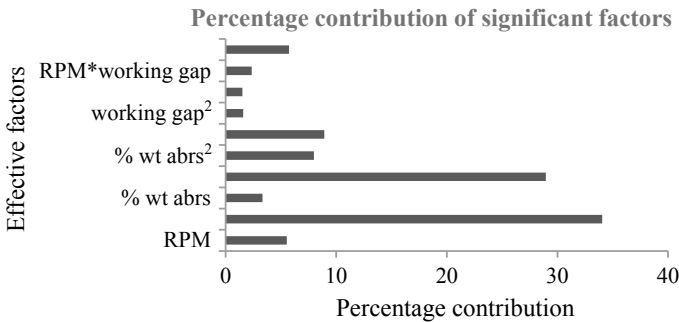


Fig. 22.7 Percentage contributions of significant factors

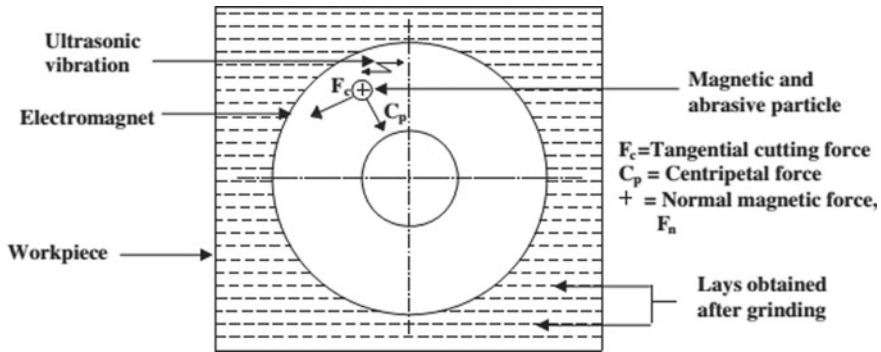


Fig. 22.8 Schematic diagram showing forces in UAMAF process [5]

**Effect of RPM.** The effect of varying rotational speed on  $\% \Delta R_a$  is shown in Fig. 22.6a. It can be seen from the main effect plot that on increasing the RPM,  $\% \Delta R_a$  increased initially; however, after a value of 300 RPM, it decreases. The reason for such a trend may be understood by the behavior of forces acting on MAPs during UAMAF. Figure 22.8 shows the schematic view of the forces acting on MAPs. The net force acting on MAPs can be divided into three main forces: normal indentation force ( $F_n$ ), tangential cutting force ( $F_c$ ), and centripetal force ( $C_p$ ). The initial increase in  $\% \Delta R_a$  may be because of increase in total number of collisions per unit time [9, 17]. However, further increase in the rotational speed (above 300 RPM) resulted in disintegration of FMAB chains due to insufficient centripetal force [9, 17] causing decrease in  $\% \Delta R_a$ . Additionally, at higher rotational speed there was more likelihood of toppling of MAPs which led to less indentation [11].

**Effect of working gap.** The effect of working gap on  $\% \Delta R_a$  can be seen in Fig. 22.6b. Figure 22.6b shows that with the increase in working gap  $\% \Delta R_a$  decreases. This was due to the decrease in polishing pressure which was directly proportional to applied magnetic flux density (Eq. 22.6) and inversely proportional to working gap (Eq. 22.7) [20, 21].

$$P = \frac{B_z^2}{\mu_o} \left( 1 - \frac{1}{\mu_{am}} \right) \text{ N/m}^2 \tag{22.6}$$

where  $P$  is the polishing pressure,  $B_z$  is the magnetic flux density,  $\mu_o$  is the permeability of air, and  $\mu_{am}$  is the permeability of abrasive material.

$$B_z \propto \frac{1}{z} \tag{22.7}$$

where  $z$  is the working gap. As the polishing pressure varied inversely with working gap, a high indentation force could be obtained at lower working gap. Owing to

this as the working gap increased, the polishing pressure decreases, causing drop in  $\% \Delta R_a$ .

**Effect of percentage weight of abrasive.** It is evident from the Fig. 22.6c that as the  $\%wt$  SiC increased, the finishing was improved. This may be due to the presence of more number of cutting edges in MAPs with higher  $\%wt$  SiC [17, 22]. Presence of more cutting edges improved the finishing. However, further increase in  $\%wt$  SiC, the permeability of the MAPs reduces, which led to the reduction in the strength of FMAB which further results in reduction in  $\% \Delta R_a$  [11, 23].

4.1.4 Effect of surface angle: Fig. 22.6d shows that with increase in surface angle there was a decrease in  $\% \Delta R_a$ . This may be because of the fact that as the surface angle increased, the normal component finishing force decreases, which in turn results in lower  $\% \Delta R_a$  [19].

### 22.3.2 Interaction Effects

The ANOVA result showed that there were some interactions between process parameters which also had significant effect on  $\% \Delta R_a$ .

**Interaction effect of RPM and working gap:** The simultaneous effect of working gap and rotational speed on  $\% \Delta R_a$  is shown in Fig. 22.9. From Fig. 22.9b, it can be seen that at lower working gap, the drop in  $\% \Delta R_a$  was observed at higher rotational speed, however, at higher working gap, the drop in  $\% \Delta R_a$  was observed at relatively lower rotational speed. It is because at lower working gap, the stiffness of FMAB was high which allowed it to sustain at higher RPM. However, at higher working gap the stiffness of FMAB was very low which caused it to disintegrate at lower

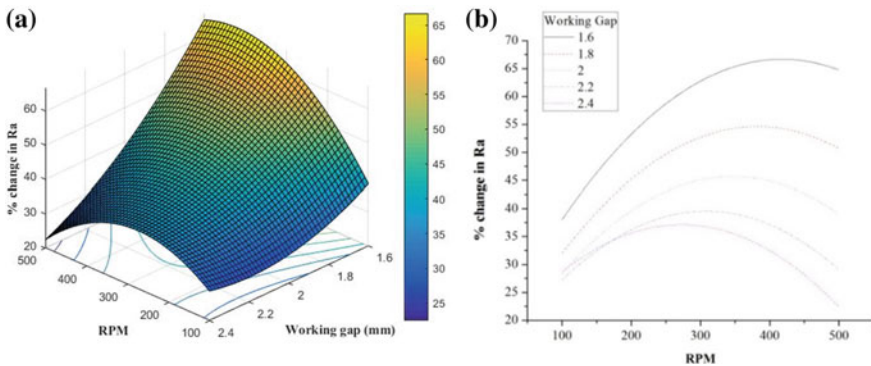


**Fig. 22.9** Interaction effect between RPM and working gap. **a** Response surface for  $\% \Delta R_a$  ( $\%wt$  of abrasive-25%, surface angle-10). **b** Variation in  $\% \Delta R_a$  with RPM and working gap ( $\%wt$  of abrasive-25%, surface angle-10)

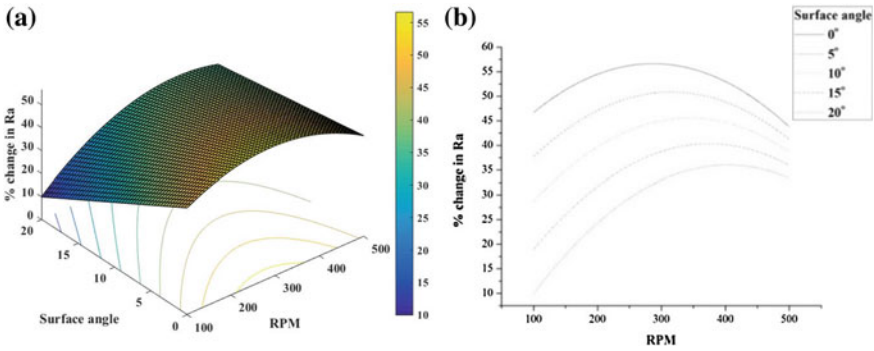


**Fig. 22.10** Interaction effect between RPM and surface angle. **a** Response surface for  $\% \Delta R_a$  (%wt of abrasive-25%, working gap-2 mm). **b** Variation of  $\% \Delta R_a$  with RPM and surface angle (%wt of abrasive-25%, working gap-2 mm)

RPM [23, 24]. Thus, at higher working gaps the drop in  $\% \Delta R_a$  was observed at a relatively lower RPM.

**Interaction effect of rpm and surface angle:** The combined effect of surface angle and rotational speed on  $\% \Delta R_a$  is shown in Fig. 22.10. It can be seen that at lower surface angle the  $\% \Delta R_a$  dropped at lower RPM while for higher surface angle  $\% \Delta R_a$  dropped at higher RPM. This may be because at higher angle, a component of tangential cutting force acts in the surface normal direction and aids finishing. Furthermore, at lower surface angle the magnitude of this tangential cutting force decrease resulting in drop in  $\% \Delta R_a$ .

## 22.4 Surface Generation in UAMAF of Freeform Surface

In order to illustrate the effect of UAMAF process, surface roughness profiles of unfinished and finished workpiece are shown in Fig. 22.11. It is evident that maximum peak to valley height was considerably reduced after finishing. The surface roughness profiles alone do not reflect the morphology of the finished surface. Hence images from the optical profilometer (Fig. 22.12) and optical microscope (Fig. 22.13) have also been taken before and after finishing. Figure 22.12 shows 3D optical profilometer images of the unfinished and finished surfaces. The images from optical profilometer and optical microscope also shows that the milled marks have been replaced by finishing marks, which elucidates the material removal mechanism involved in UAMAF process.

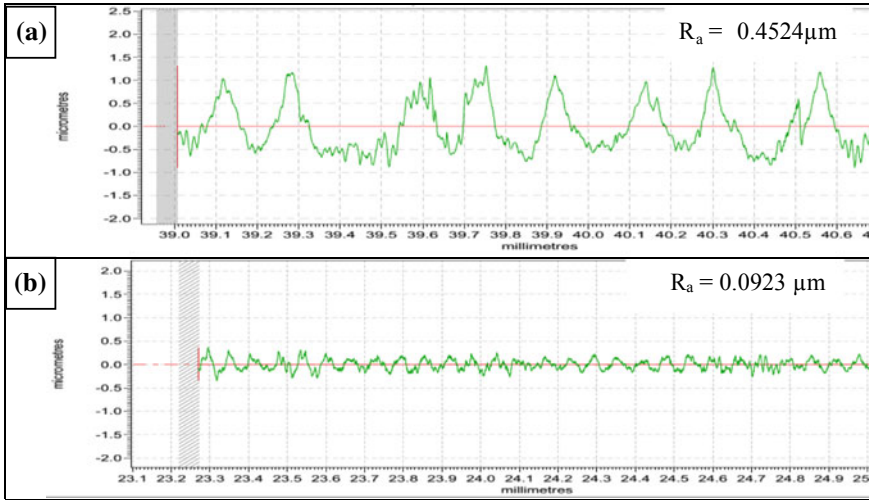


Fig. 22.11 a Unfinished workpiece, b finished workpiece (RPM 350, working gap-1.6, %wt of abrasive-25, surface angle-0)

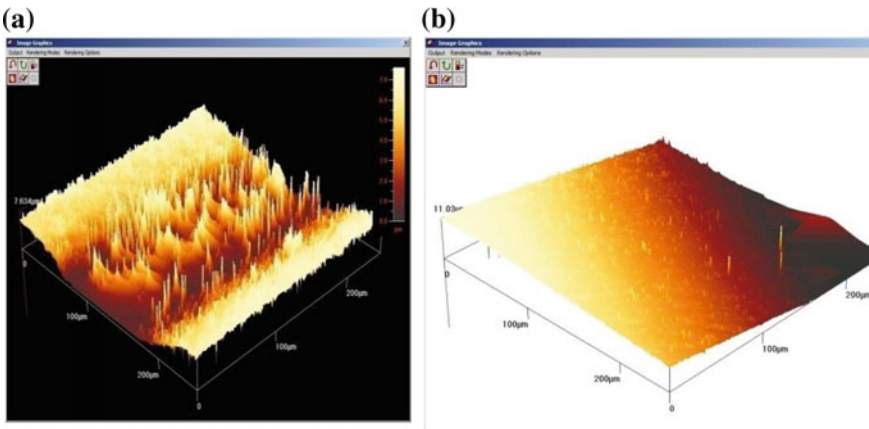
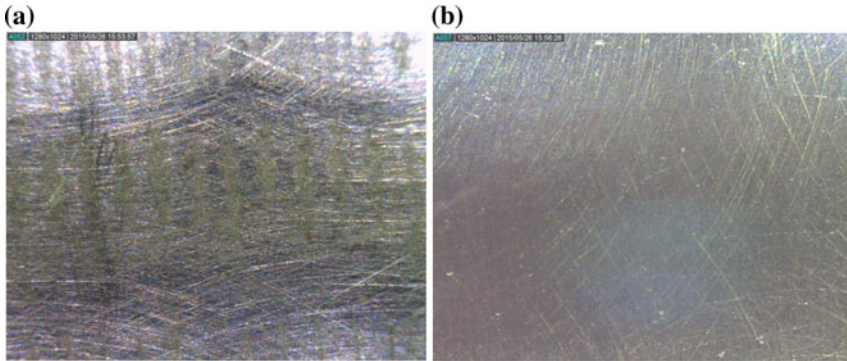


Fig. 22.12 3D image obtained from optical profilometer (500 $\times$ ), a milled surface, b finished surface (RPM 350, working gap-1.6 mm, %wt of abrasive-25, surface angle-10)

## 22.5 Conclusions

Sintered MAPs were developed and used for finishing freeform surfaces in the present study. Further, a regression model constituting all effective parameters was developed for the  $\% \Delta R_a$ . SEM and optical profilometer images also verified the effectiveness of the UAMAF process. The conclusions made from the study are as follows:



**Fig. 22.13** **a** Images of milled surface. **b** Image of finished surface (magnification 200 $\times$ )

1. SiC particles are diffused around iron particles making a sufficient bonding in the sintered MAPs.
2. Magnetization moment of sintered MAPs has been found lesser than unbonded MAPs.
3. The developed model shows that working gap is the most effective parameter contributing 35% followed by surface angle in the given range of variables.
4. The optimized result of 77.250% change is achieved with RPM = 350, working gap = 1.6 mm, %wt of abrasive = 25, and surface angle = 0 $^{\circ}$ .

## References

1. Singh, A.K., Jha, S., Pandey, P.M.: Design and development of nanofinishing process for 3D surfaces using ball end MR finishing tool. *Int. J. Mach. Tools Manuf.* **51**(2), 142–151 (2011)
2. Givi, M., Fadaei Tehrani, A., Mohammadi, A.: Polishing of the aluminum sheets with magnetic abrasive finishing method. *Int. J. Adv. Manuf. Technol.* **61**(9–12), 989–998 (2012)
3. Hoshino, T., Kurata, Y., Terasaki, Y., Susa, K.: Mechanism of polishing of SiO<sub>2</sub> films by CeO<sub>2</sub> particles. *J. Non-Cryst. Solids* **283**, 129–136 (2001)
4. Shukla, V.C., Pandey, P.M., Dixit, U.S., Roy, A., Silberschmidt, V.: Modeling of normal force and finishing torque considering shearing and ploughing effects in ultrasonic assisted magnetic abrasive finishing process with sintered magnetic abrasive powder. *Wear* **390–391**, 11–22 (2017)
5. Kim, J.D., Choi, M.S.: Study on magnetic polishing of free-form surfaces. *Int. J. Mach. Tools Manuf.* **37**(8), 1179–1187 (1997)
6. Kim, J.D., Choi, M.S.: Development of the magneto-electrolytic-abrasive polishing system (MEAPS) and finishing characteristics of a Cr-coated roller. *Int. J. Mach. Tools Manuf.* **37**(7), 997–1006 (1997)
7. Singh, D.K., Jain, V.K., Raghuram, V.: Experimental investigations into forces acting during a magnetic abrasive finishing process. *Int. J. Adv. Manuf. Technol.* **30**(7–8), 652–662 (2006)
8. Mulik, R.S., Pandey, P.M.: Ultrasonic assisted magnetic abrasive finishing of hardened AISI 52100 steel using unbonded SiC abrasives. *Int. J. Refract. Met. Hard Mater.* **29**(1), 68–77 (2011)

9. Kala, P., Kumar, S., Pandey, P.M.: Polishing of copper alloy using double disk ultrasonic assisted magnetic abrasive polishing. *Mater. Manuf. Process.* **28**(2), 200–206 (2013)
10. Shinmura, T., Hatano, E., Matsunaga, M.: Study on magnetic abrasive finishing. *CIRP Ann. Manuf. Technol.* **39**(1), 325–328 (1990)
11. Mulik, R.S., Pandey, P.M.: Magnetic abrasive finishing of hardened AISI 52100 steel. *Int. J. Adv. Manuf. Technol.* **55**(5–8), 501–515 (2010)
12. Liu, Z.Q., Chen, Y., Li, Y.J., Zhang, X.: Comprehensive performance evaluation of the magnetic abrasive particles. *Int. J. Adv. Manuf. Technol.* **68**(1), 631–640 (2013)
13. Chen, H.L., Li, W.H., Yang, S.Q., Yang, S.C.: Research of magnetic abrasive prepared by hot pressing sintering process. In: *Proceedings of the 5th IEEE Conference on Industrial Electronics Application*, pp. 776–778 (2010)
14. Yodkaew, T., Morakotjinda, M., Tosangthum, N., Coovattanachai, O., Krataitong, R., Siriphol, P., Vetayanugul, B., Chakthrin, S., Poolthong, N.: Sintered Fe-Al<sub>2</sub>O<sub>3</sub> and Fe-SiC Composites. *J. Met. Mater. Miner.* **18**(1), 57–61 (2008)
15. Shukla, V.C., Pandey, P.M.: Experimental investigations into sintering of magnetic abrasive powder for ultrasonic assisted magnetic abrasive finishing process. *Mater. Manuf. Process.* **32**(1), 108–114 (2017)
16. Myres, R., Montgomery, D., Anderson, C.: *Process and Product Optimization Using Designed Experiments*, vol. 3, pp. 1–25. Wiley, New York (2009)
17. Verma, G.C., Kala, P., Pandey, P.M.: Experimental investigations into internal magnetic abrasive finishing of pipes. *Int. J. Adv. Manuf. Technol.* **88**(5–8), 1–12 (2016)
18. Kala, P., Pandey, P.M.: Experimental study on finishing forces in double disk magnetic abrasive finishing process while finishing paramagnetic workpiece. *Procedia Mater. Sci.* **5**, 1677–1684 (2014)
19. Singh, A.K., Jha, S., Pandey, P.M.: Nanofinishing of a typical 3D ferromagnetic workpiece using ball end magnetorheological finishing process. *Int. J. Mach. Tools Manuf.* **63**, 21–31 (2012)
20. Singh, A.K., Jha, S., Pandey, P.M.: Mechanism of material removal in ball end magnetorheological finishing process. *Wear* **302**(1–2), 1180–1191 (2012)
21. Yin, S., Shinmura, T.: A comparative study: Polishing characteristics and its mechanisms of three vibration modes in vibration-assisted magnetic abrasive polishing. *Int. J. Mach. Tools Manuf.* **44**(4), 383–390 (2004)
22. Mulik, R.S., Pandey, P.M.: Experimental investigations and optimization of ultrasonic assisted magnetic abrasive finishing process. *Proc. Inst. Mech. Eng. Part B J. Eng. Manuf.* **225**(8), 1347–1362 (2011)
23. Kala, P., Pandey, P.M.: Experimental investigations into ultrasonic-assisted double-disk magnetic abrasive finishing of two paramagnetic materials. *Proc. Inst. Mech. Eng. Part B J. Eng. Manuf.* **231**(6), 1021–1038 (2017)
24. Sihag, N., Kala, P., Pandey, P.M.: Chemo assisted magnetic abrasive finishing: experimental investigations. *Procedia CIRP* **26**, 539–543 (2015)

# Chapter 23

## Fiber Laser Cutting of Nimonic C263 Alloy and Investigation of Surface Integrity



Mukul Anand , Niladri Mandal , Vikas Kumar , Shakti Kumar ,  
A. K. Sharma  and Alok Kumar Das 

**Abstract** Nimonic C263 is a super alloy which contains more than 50% nickel, and is mainly used in gas turbines and internal combustion engines. The present study deals with the fiber laser cutting of Nimonic C263 super alloy using nitrogen as assisting gas. Several experiments were performed by varying the process parameters, such as cutting speed, laser power, gas pressure, position of focus point with respect to the top surface of the workpiece and duty cycle, to observe their influences on the cut-surface integrity. The prepared samples were characterized by FESEM examination, microhardness test, optical microscopy and XRD technique. The average kerf width, heat-affected zone and surface roughness values varied from 201 to 261  $\mu\text{m}$ , 7.96 to 9.30  $\mu\text{m}$  and 2.02 to 3.42  $\mu\text{m}$ .

**Keywords** Fiber laser · Cutting · Surface integrity · Striation

### 23.1 Introduction

High-power laser can cut many types of materials, like metals and its alloys, ceramics, super alloys, composites, rubber, wood, stone, and so on. It has several advantages, which include smooth cut surface, narrow kerf width, no tool wear, small metal deformation, small heat-affected zone, perpendicular and sharp cut sides, low thickness of oxide layer, absence of cutting forces, and so on [1]. In addition, this process is flex-

---

M. Anand · V. Kumar · S. Kumar · A. K. Sharma · A. K. Das (✉)  
Department of Mechanical Engineering, Indian Institute of Technology (ISM) Dhanbad, Dhanbad  
826004, Jharkhand, India  
e-mail: [eralok@yahoo.co.in](mailto:eralok@yahoo.co.in)

N. Mandal  
Defence Research and Development Laboratory, Kanchanbagh, Hyderabad, India

© Springer Nature Singapore Pte Ltd. 2020  
M. S. Shunmugam and M. Kanthababu (eds.), *Advances in Unconventional Machining and Composites*, Lecture Notes on Multidisciplinary Industrial Engineering, [https://doi.org/10.1007/978-981-32-9471-4\\_23](https://doi.org/10.1007/978-981-32-9471-4_23)



ible, takes less processing time and minimum wastage of material. The laser process can also be combined with other cutting/machining process to utilize the benefits of both, to process different materials. Few of the prominent researches in this area are described in the following paragraphs; for instance, [2] conducted experiments to cut Ni-based super alloy using Nd:YAG laser. They carried out optimization of the process parameters using gray-based Taguchi approach and reported that cutting was done successfully and the optimization technique was helpful in finding the parameter setting for getting better cut-surface quality. Proposed a FES model to examine the influence of power, gas pressure and standoff distance on kerf width during the machining of 3 mm thick PMMA sheet using CO<sub>2</sub> laser. They observed wider kerf width with the increment in laser power and standoff distance, but when speed increases the kerf width decreases [3].

Laser cutting is a non-contact operation, so no special jigs or fixtures are required for the work. This process eliminates the use of expensive tools and reduces the chance of damage to work because of less thickness. Assistant gas (oxygen, nitrogen, argon, helium, etc.) generally acts as a source of mechanical energy which blows the molten material from the cutting spot and forms the kerf. When oxygen is used as assistant gas, an exothermic reaction takes place, increasing the supplied energy for the cutting process. Argon or helium prevents the exothermic reaction, hence avoids the sideways burnings and excessive removal [4].

Nowadays, types of laser used for cutting operations are: Nd:YAG laser (1.06 μm wavelength), CO<sub>2</sub> laser (10.6 μm wavelength) and fiber laser (wavelength 1.07 μm). Fiber laser can be used for several purposes such as material processing (marking, engraving, cutting, welding and heat treatment), telecommunication, energy weapons, spectroscopy, and so on. Cutting of sheets (up to 4 mm) with higher speed can be done by fiber laser [5]. Generally, for cutting of very thin metal sheet and non-metal sheet, laser sublimation process is adopted, and for thick metal sheet laser fusion cutting is preferred. In case of laser cutting process, a focused laser beam of high intensity is made to fall onto the work with the help of a mirror, focusing lens arrangement. The focused beam acts as a source of heating and the work material starts melting quickly and gets evaporated. Assistant gas such as oxygen, nitrogen is used to blow away the molten and evaporated material. Laser cutting is hardly affected by work material properties, such as hardness, brittleness, wear resistance, and so on [6].

Striation marks (also called periodic line) generally develop on all surfaces cut by lasers, which decide the cut-surface quality. In most of the cases three zones are found from the top to the bottom of the cut section. All the zones are having the different patterns, such as horizontal striation zone (HSZ), vertical striation zone (VSZ) and oblique striation zone (OSZ) [7].

Till now very few researches are reported on the surface integrity of Nimonic C263 alloy cut with fiber laser. This paper deals with the influence of process parameters (cutting speed, laser power, gas flow rate, focus position, duty cycle) on the cut-surface quality, such as kerf width, heat-affected zone, surface roughness, micro-hardness and microstructure. The different issues and advantages related to the laser cutting of Nimonic C263 alloy have been discussed in-depth in this article.

## 23.2 Materials and Methods

### 23.2.1 Workpiece Preparation

Nimonic C263 alloy sheet with dimension 300 mm × 110 mm × 3 mm was chosen as the workpiece. The work sample of the said size was cut from the parent sheet through the abrasive water jet machining process. Then the sample was cleaned in acetone bath which is subjected to the ultrasonic vibration, to remove the dirt and the oil from the surface.

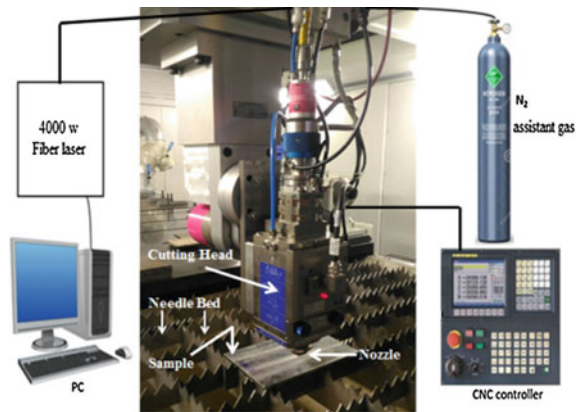
### 23.2.2 Experimental Setup

Figure 23.1 shows the setup arrangement for conducting the experiments. Fiber laser was used for cutting purpose in this study. The laser beam from the laser source was transmitted to a cutting head through an optical fiber of diameter 0.3 mm. Nitrogen gas was used as an assistant gas to obtain narrow kerf width, smooth cut surface and to prevent oxidation of the material on the cut surface. The whole experiment was performed on a needle bed.

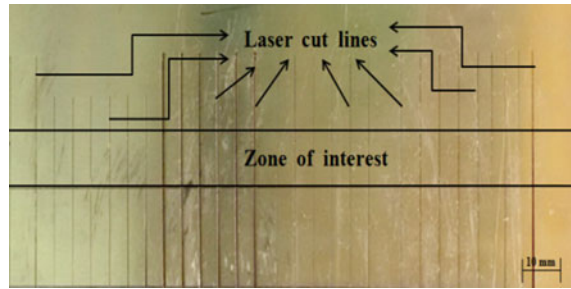
### 23.2.3 Experimentation

At the beginning, a number of trial experiments were conducted to select the working range of different experimental parameter. Specimen (Nimonic C263) was mounted rigidly on a needle bed in order to reduce the vibration produced during the process. A total of final 20 experiments were conducted. Some parameters were kept constant

**Fig. 23.1** Schematic diagram of experimental setup



**Fig. 23.2** Nimonic C263 alloy after the laser cutting operation



throughout the experiment, which are focal length of focusing lens: 125 mm, nozzle tip diameter: 1.5 mm, nozzle stand-off distance: 1.0 mm, frequency: 700 Hz and piercing pressure: 5 bar. A length of 50 mm was cut in each experiment, and for the evaluation of the surface integrity, the middle part of the cut surfaces was selected. Each experiment was repeated three times for getting consistent results. Figure 23.2 represents the Nimonic C263 workpiece after laser cutting operation. The analysis for the surface integrity was performed in the zone of interest (Fig. 23.2).

### 23.2.4 Characterization Procedure

After cutting, the sample was again cut into several test samples (zone of interest in Fig. 23.2) by wire electro-discharge machining (WEDM) for cross-sectional examination. Diamond abrasive papers of mesh size 400, 800, 1200 and 1800 were used for polishing the cross-sectional and cut surface of the test samples. Then diamond paste was used to get smooth and mirror finish surface. Acetone was used to clean the polished test samples and then etched with a solution of hydrochloric acid (45 parts), nitric acid (15 parts) and glycerol (40 parts) for 90 s. Surface morphology and heat-affected zone were investigated using field emission scanning electron microscope (FESEM; Model: Supra 55, Make: Zeiss, Germany) equipped with an energy-dispersive X-ray spectroscopy (EDS). EDS was performed to observe the change in chemical composition on the cut surface. Surface profilometer (Make: Mitutoyo) was used to measure the surface roughness (Ra) of cut surfaces and kerf width was measured using Olympus metallurgical microscope (model-BH2-UMA).

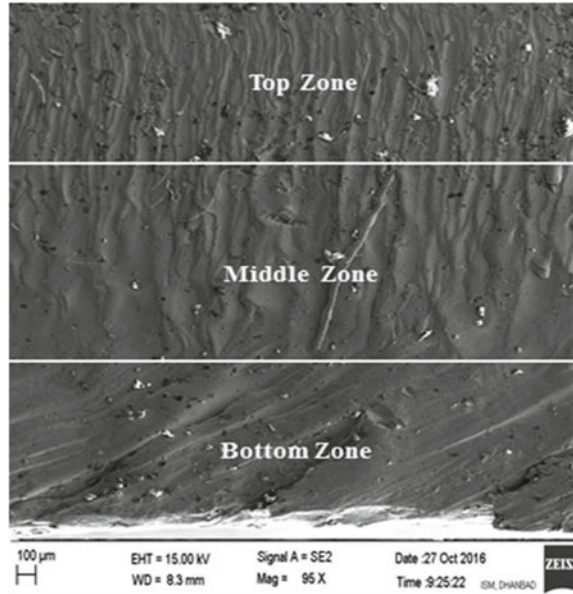
## 23.3 Results and Discussions

The testing operations were carried out on all the prepared samples and the results were recorded for analysis. The values of kerf width, surface roughness, heat-affected zone, microhardness with respect to the corresponding input process parameter settings are illustrated in Table 23.1. For each experiment, ten measurements were taken,

**Table 23.1** Effect of process parameters on kerf width, heat-affected zone, surface roughness and microhardness

Experiment no.	Laser power (kW)	Cutting speed (m/min)	Gas pressure (bar)	Focus offset position (mm)	Duty factor (%)	Kerf-width (μm)	HAZ (μm)	R <sub>a</sub> (μm)	Microhardness (HV)
01	2.9	1.0	15	02	80	239	8.10	2.77	214.84
02	3.2					243	8.44	2.53	217.54
03	3.5					249	8.93	2.43	225.88
04	3.8					261	9.30	2.39	234.43
05	3.5	0.5				249	9.04	2.35	221.20
06		1.0				243	8.54	2.35	209.84
07		1.5				237	8.12	2.40	237.08
08		2.0				231	7.96	2.51	235.20
09		1.0	05			201	9.27	2.02	207.38
10			10			209	9.03	2.07	211.07
11			15			224	8.52	2.30	216.09
12			20			234	8.328	2.544	218.89
13			15	00		245	8.514	2.34	214.05
14				01		241	8.718	2.778	237.38
15				02		230	8.928	3.225	241.86
16				03		221	9.192	3.422	246.87
17				02	75	202	8.206	2.679	231.10
18					80	206	8.556	2.671	235.10
19					85	210	8.923	2.625	238.84
20					90	221	9.256	2.671	242.74

**Fig. 23.3** FESEM image of Nimonic C263 showing different striation zones on the cut surface



and the average of all was noted for further analysis. The influence of different process parameters on the surface integrity is discussed in the succeeding sections.

### 23.3.1 Microstructure and EDS Analysis

The polished and etched surface was examined through FESEM and the images were captured. Figure 23.3 shows the image of cut surface of the Nimonic C263 alloy.

From the FESEM image it is clear that cut surface has three zones, namely upper zone, middle zone, bottom zone or washout zone. It is to be carried out experiments on fiber laser cutting of AA2219 aluminum alloy. They classified the cut surface into three zones, namely top zone or HSZ, middle zone or VSZ, bottom zone or washout zone or OSZ. Horizontal striation patterns were found in the top zone; hence this zone is also known as horizontal striation zone (HSZ). Vertical patterns were found in the middle zone and this zone is known by vertical striation zone (VSZ). Oblique striation pattern was found in the bottom zone and this zone is also known as oblique striation zone (OSZ). The levels of gas pressure used during the above experiments were 5, 7, 9 and 11 bars [8].

The elements present in the cut surface (either in elemental state or in the form of compounds) were detected by EDS analysis. Figure 23.4 shows the EDS plots of the cut surface of test samples. EDS images confirm that significant amount of carbon (C), oxygen (O), titanium (Ti), aluminum (Al), iron (Fe), chromium (Cr), nickel (Ni) and cobalt (Co) are present in the cut surface.

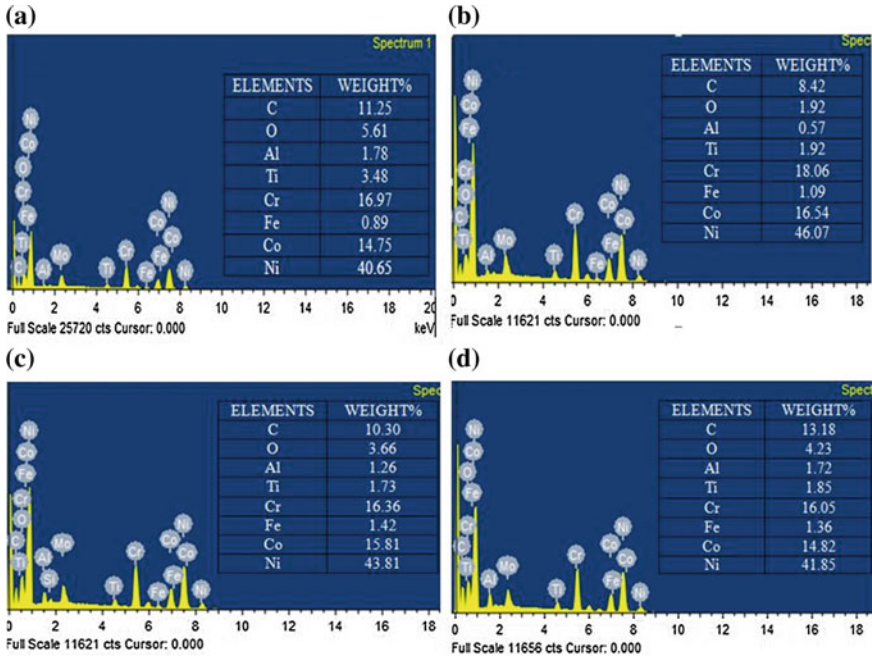


**Fig. 23.4** EDS plots showing compositions of various elements present in cut surface of sample at laser power of **a** 2.9 kW, **b** 3.2 kW, **c** 3.5 kW and **d** 3.8 kW

**Analysis of kerf width and heat-affected zone.**

Figure 23.5 represents the optical images of the kerf width with respect to the laser power, while other experimental parameters are kept constant. Figure 23.6 represents the plot for variation in kerf width with respect to the different experimental parameter settings. With the increase of laser power more amount of material are melted, which leads to wider kerf width. At higher cutting speed, the interaction time between the work material and the laser beam is less, which leads to the melting of low amount of work material and hence the narrow kerf width. The values of kerf width for different parameters are shown in Table 23.1. Also, the average values of HAZ for different experimental parameters setting are shown in Table 23.1 (Fig. 23.7).

Figure 23.8 represents the plot for variation in HAZ with respect to the different experimental parameter settings. Higher laser power causes more heat input into the work sample which leads to wider heat-affected zone (Fig. 23.8a). From Fig. 23.8b, it is seen that higher cutting speed yields small heat-affected zone because of less time of interaction between the material and the beam. Width of HAZ reduces with increase in assisting gas pressure due to efficient cooling and efficient removal of the molten material from the cutting zone (Fig. 23.8c) [9]. With the increase in duty cycle, the width of HAZ increases due to more amount of heat input to the cutting zone (Fig. 23.8d).

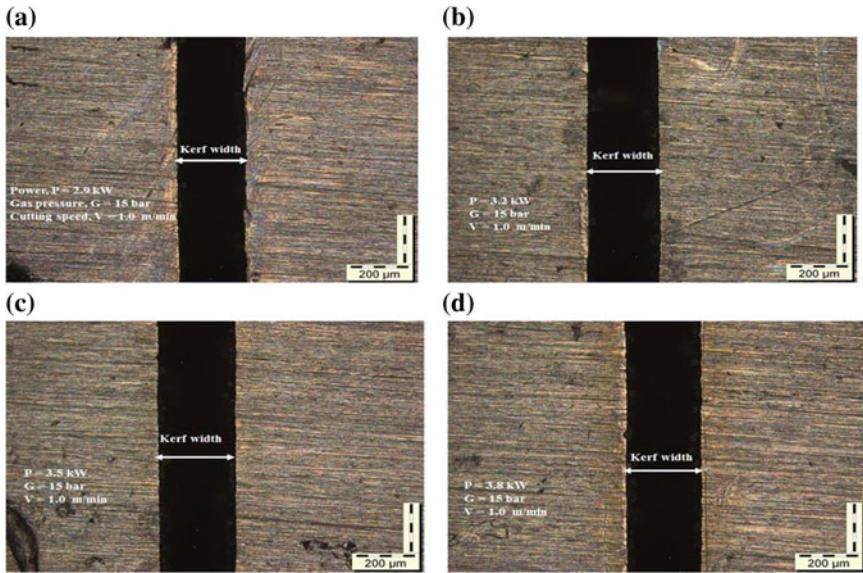
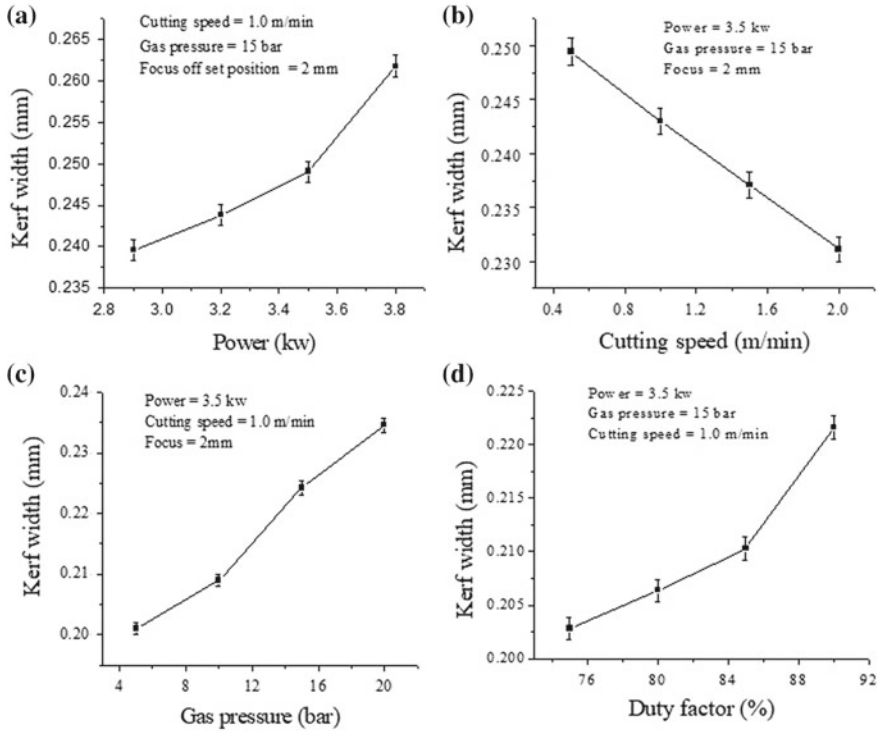


Fig. 23.5 Optical images showing the variation in cut kerf width with laser power

### Surface roughness analysis.

Average surface roughness ( $R_a$ ) of cut surface was measured using a surface profilometer (Mitutoyo). Values of surface roughness for different parameters are shown in Table 23.1. Figure 23.9 represents the plot for variation in  $R_a$  with respect to the different experimental parameter settings. From Fig. 23.9a, it is clear that at higher laser power the molten metal in the cutting zone would have low viscosity by which it is flushed out easily by the pressure of the assisting gas and hence the surface roughness reduces. From Fig. 23.9b, it is clear that due to less interaction time between beam and material, less conduction of heat into work material occurs and hence time for the dross formation is less, resulting in a better surface finish. Figure 23.9c indicates that by increasing the gas pressure surface roughness of the cut surface is reduced because at higher assisting gas pressure, high blow force is experienced by the molten material, hence more amount of molten material would be blown away, resulting in better surface finish [10]. With the increase in duty cycle, the  $R_a$  value decreases due to increase in laser power.



**Fig. 23.6** Plots for kerf width versus **a** laser power, **b** cutting speed, **c** gas pressure and **d** duty factor

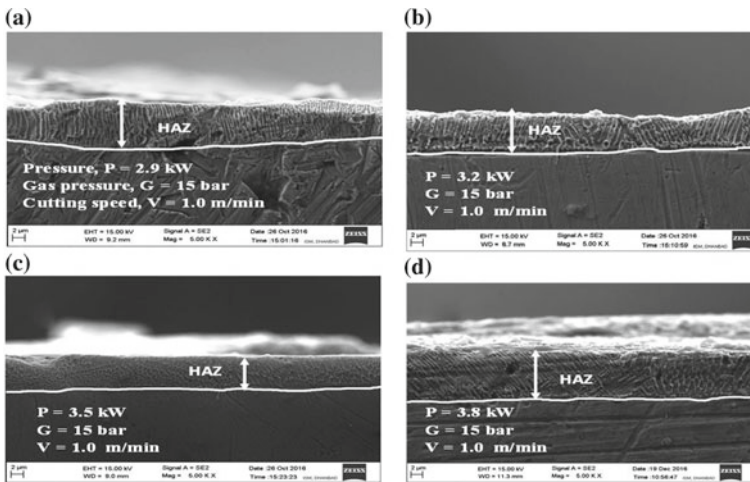


**Fig. 23.7** FESEM images showing the variation in HAZ of cut surfaces with respect to laser power



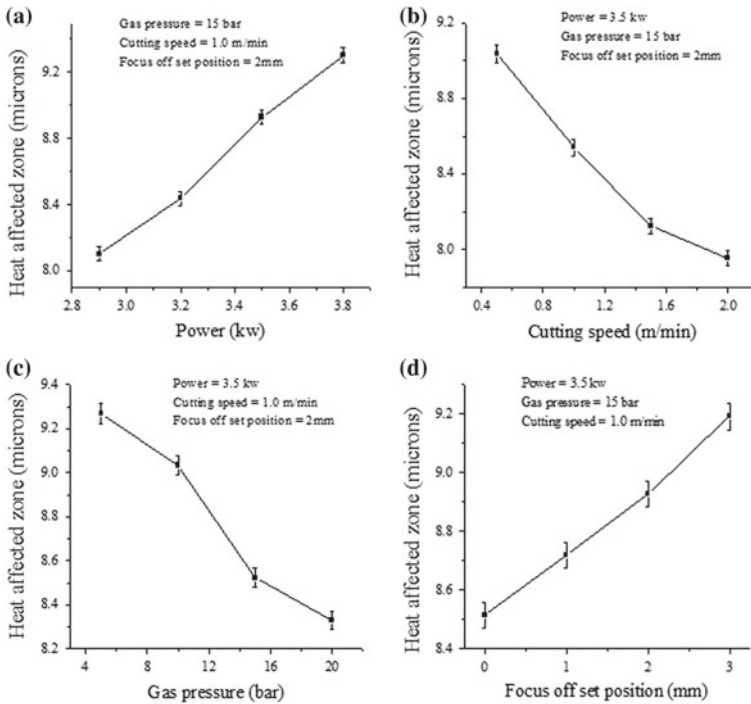


**Fig. 23.8** Plots for heat-affected zone versus **a** power, **b** cutting speed, **c** gas pressure and **d** duty cycle

### 23.4 Conclusions

Laser cutting operation was carried out on Nimonic C263 alloy (3 mm thickness) by varying the process parameters, such as gas pressure, cutting speed, laser power, duty cycle and focus offset position, to observe the effects of process parameters on the cut-surface integrity. From the experimental observation and obtained results, the following conclusions can be drawn.

The microstructure analysis of cut surface revealed that cutting surface comprises three zones, namely initial penetration zone, middle zone (VSZ) and washout zone (OSZ). EDS analysis predicted the presence of oxygen and carbon in the cut surface.

Higher laser power produces wider kerf width, and high cutting speed results in narrow kerf width. Higher assisting gas pressure leads to a slight increase in the kerf width. Higher laser power produces a deeper heat-affected zone (HAZ) and higher cutting speed produces smaller heat-affected zone depth. The higher gas pressure resulted in smaller heat-affected zone. Minimum value of width of HAZ (7.96 μm) is achieved when laser power is 3.5 kW, gas pressure is 15 bar, cutting speed is 2.0 m/min, focus offset position is 2 mm and duty factor is 80%.

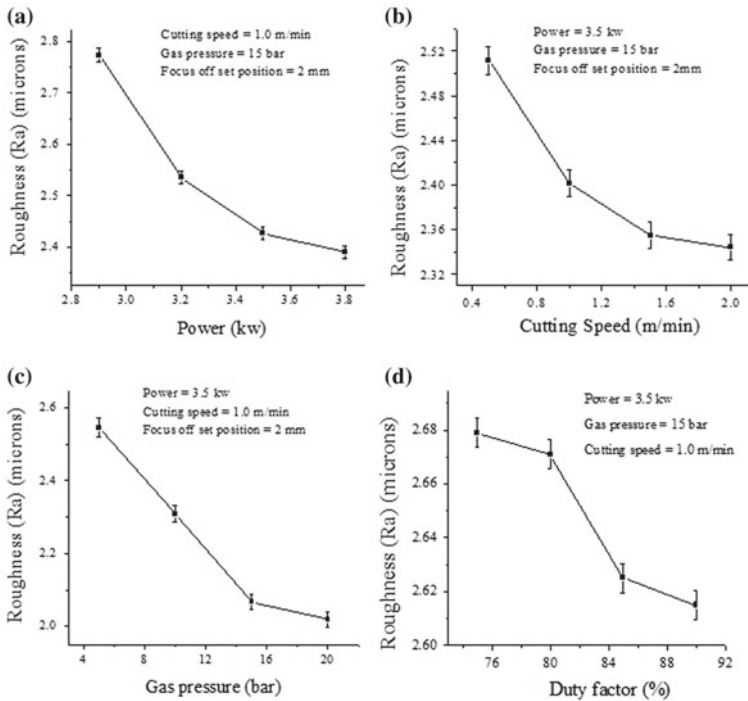


**Fig. 23.9** Plots for roughness versus **a** power, **b** cutting speed, **c** gas pressure and **d** duty factor

Surface roughness would be improved by decreasing the laser power and gas pressure. It can be improved by raising cutting speed. Better surface finish ( $2.02 \mu\text{m}$ ) is achieved when laser power is 3.5 kW, gas pressure is 5 bar, cutting speed is 1.0 m/min, focus offset position is 2 mm, and duty factor is 80%. However, fine tuning of experiments are required for the industrial applications of this laser cutting process of Nimonic C263.

## References

1. Jarosz, K., Löschner, P., Niesłony, P.: Effect of cutting speed on surface quality and heat-affected zone in laser cutting of 316L stainless steel. *Procedia Eng.* **149**, 155–162 (2016). <https://doi.org/10.1016/j.proeng.2016.06.650>
2. Venkatesan, K., Ramanujam, R.: Improvement of machinability using laser-aided hybrid machining for Inconel 718 alloy. *Mater. Manuf. Processes* **31**(14), 1825–1835 (2016). <https://doi.org/10.1080/10426914.2015.1117626>
3. Al-Ahmari, A.M., Rasheed, M.S., Mohammed M.K., Saleh, T.: A hybrid machining process combining Micro-EDM and laser beam machining of Nickel–Titanium–Based shape memory alloy. *Mater. Manuf. Processes* **31**(4), 447–455 (2016). <https://doi.org/10.1080/10426914.2015.1019102>

4. Xiaohong, Z., Cuo, Y., Genyu, C., Weike, A., Zhaohui, D.: Experimental investigations of microcracks in laser-induced cracking turning alumina ceramic. *Mater. Manuf. Processes* **29**(10), 1277–1283 (2014). <https://doi.org/10.1080/10426914.2014.930884>
5. Alavi, S.H., Cowell, C., Harimkar, S.P.: Experimental and finite element analysis of ultrasonic vibration—assisted continuous-wave laser surface drilling. *Mater. Manuf. Processes* **32**(2), 216–225 (2017). <https://doi.org/10.1080/10426914.2016.1176193>
6. Sharma, A., Yadava, V.: Optimization of cut quality characteristics during Nd: YAG laser straight cutting of Ni-based superalloy thin sheet using grey relational analysis with entropy measurement. *Mater. Manuf. Processes* **26**(12), 1522–1529 (2011). <https://doi.org/10.1080/10426914.2011.551910>
7. Daurelio, G., Giorleo, G.: Experimental techniques to cut and weld copper by laser—a review. *Mater. Manuf. Processes* **6**(4), 577–603 (1991). <https://doi.org/10.1080/10426919108934791>
8. Yilbas, B.S., Akhtar, S.S.: Laser cutting of alloy steel: three-dimensional modeling of temperature and stress fields. *Mater. Manuf. Processes* **26**(1), 104–112 (2011). <https://doi.org/10.1080/10426914.2010.501092>
9. Ghany, K.A., Newishy, M.: Cutting of 1.2 mm thick austenitic stainless steel sheet using pulsed and CW Nd: YAG laser. *J. Mater. Process. Tech.* **168**(3), 438–447 (2005). <https://doi.org/10.1016/j.jmatprotec.2005.02.251>
10. Pocorni, J., Powell, J., Deichsel, E., Frostevarg, J., Kaplan, A.F.: Fibre laser cutting stainless steel: Fluid dynamics and cut front morphology. *Opt. Laser Tech.* **87**, 87–93 (2017). <https://doi.org/10.1016/j.optlastec.2016.08.002>

# Chapter 24

## Generation of Three-Dimensional Features on Ti6Al4V by EC Milling



K. Mishra , S. Sinha, B. R. Sarkar and B. Bhattacharyya

**Abstract** Titanium and nickel alloys are the most popular high-strength temperature-resistant (HSTR) alloys which have different applications for their outstanding material properties. The process of electrochemical milling (EC milling) is similar to conventional electrochemical machining where the material is removed by simple geometric tool following a predefined path in a layer-by-layer fashion and has great application in machining of any HSTR alloys. With the indigenously developed setup, the present research work investigates the influence of process parameters, like feed rate and milling layer depth, on various performance criteria, such as, overcut, machining depth, perpendicularity and radius of curvature of the side wall, by EC milling process on Ti6Al4V. It was observed that EC milling with NaCl(1 M) + NaNO<sub>3</sub>(1 M) mixed electrolyte generates different complex and three-dimensional features on Ti6Al4V with desired accuracy. Internal flushing with tool rotation improves the accuracy of the machined profile due to better removal of sludge from the machining zone.

**Keywords** EC milling · Feed rate · Milling layer depth · Tool rotation · Internal flushing · Mixed electrolyte · 3D complex features

### 24.1 Introduction

Development of new manufacturing process leads to increment of the productivity, product variety and invention of different kinds of materials—like different alloys, ceramics and composites. Specific demands in different sectors, for example, in aerospace industry, space applications, defense, biomedical, have brought huge challenges for manufacturing industry. High-strength temperature-resistant (HSTR) alloys are one of the most difficult-to-machine materials. Titanium and nickel alloys are the most popular HSTR alloys which have different applications in those industries due to its outstanding material properties like, high strength to weight ratio,

---

K. Mishra · S. Sinha (✉) · B. R. Sarkar · B. Bhattacharyya  
Production Engineering Department, Jadavpur University, Kolkata 700032, India  
e-mail: [sourabhsinha.sourabh@gmail.com](mailto:sourabhsinha.sourabh@gmail.com)

© Springer Nature Singapore Pte Ltd. 2020  
M. S. Shunmugam and M. Kanthababu (eds.), *Advances in Unconventional Machining and Composites*, Lecture Notes on Multidisciplinary Industrial Engineering, [https://doi.org/10.1007/978-981-32-9471-4\\_24](https://doi.org/10.1007/978-981-32-9471-4_24)

corrosion resistance and biocompatibility. The conventional machining processes are completely based on machine tool; however, HSTR alloys are not really suitable for conventional machining processes because the cutting tool should be harder, stronger and more wear-resistant than the job. The issue with cutting tool can be overcome by using non-traditional machining processes very effectively and economically. Generally, there is no direct contact between tool and workpiece and energy is used in its direct form to machine those difficult-to-machine materials in non-traditional processes.

In modern days of manufacturing, improvement in non-traditional machining has occurred through advancement in already existing processes or by combining two or more processes to take advantages of the constitute process simultaneously. EC milling is a modified form of traditional ECM process which can generate three-dimensional surface profiles with the help of simple-shaped tools. In comparison with conventional ECM process, EC milling eliminates the complexity of tool design to achieve complex three-dimensional profiles. In this method simple geometrical tool follows a predefined path in a layer-by-layer fashion with multiple downward steps. Any kind of 3D feature, contour profile with great precision can be obtained by a simple geometrical tool, which is the main advantage of EC milling. Similar to the conventional end milling process, EC milling also removes material in the same layer-by-layer fashion. The used electrolyte should be highly conductive inorganic salt solution, for example, sodium chloride, sodium bromide and sodium nitrate [1]. Machining of titanium is relatively difficult for electrochemical machining of commonly used material because titanium has a huge tendency of forming passive oxide layer. The tenacious passive oxide layer film which makes titanium very useful as a corrosion-resistant material renders the electrochemical machining of this material. With simple chloride and nitrate electrolytes, high applied potential differences are often required to achieve machining condition although the passive films are then broken only at weak points, causing deep attacks at grain boundaries [2]. Researchers have reported two methods for blind slot or channel generation with EC milling, one is scanning method and another is the sinking and milling method [3]. In the case of sinking and milling method, one slot is produced in a single pass and there is a chance of end deviation at the initial point. This limitation leads to scanning method to be more effective for macro EC milling process.

Till date, researchers have successfully conducted the conventional ECM process with the aid of internal flushing. However, in this research work an advanced machining technique named EC milling has been tried with the incorporation of internal flushing and tool rotation simultaneously. The aim of this paper is to study the influence of EC milling process parameters on various performance criteria through generation of simple slots on Ti6Al4V workpiece with the help of indigenously developed EC milling setup. Finally, the experimental results have been analyzed for finding out the best process parameters setting for generation of different complex three-dimensional features.

### 24.2 Experimental Setup

An indigenously developed EC milling setup has been used for this experimentation. Incorporation of internal flushing with rotating tool is one of the most remarkable challenges in EC milling. The developed setup mainly consists of mechanical machine unit, power supply unit, electrolyte supply unit and control unit. Electrolyte supply unit and control unit are the most important among the other units. EC milling completely depends on the movement of the tool and the accuracy of tool motion directly influences the accuracy of machined profile. Tool rotation with internal flushing makes the design of electrolyte flow system more stringent and complex. To evaluate the quality of the machined surface and profile accuracy, Telesurf surface roughness measuring machine (SJ-410, Mitutoyo, Japan) and a contour scope (CONTRACER-CV-3200, Mitutoyo, Japan) has been adapted respectively. Considering all the constraints of EC milling, an EC milling setup has been developed, as shown in Fig. 24.1. The mechanical machine unit consists of XYZ CNC stage and a bipolar stepper motor drive with lead screws. A CNC controller is interfaced with desktop computer which permits to move the tool on desired path with desired feed by synchronizing the stepper motors.

In the machining chamber, a work-holding arrangement has been fabricated for holding the workpiece and to facilitate the experimentation on it. During experimentation, to control the rotational speed of the tool and its direction, a separate controller has been used. For generating the required nature of pulse power during machining operation, a pulsed DC power supply (DOSF 20-60, Mastusada Inc., Japan) has been used. For online monitoring of pulse nature, digital storage oscilloscope (TETRONIX 2000 SERIES) has been used, and for measurement of current values, multimeter has been connected in series to the circuit. Electrolyte flow rate and pressure has been controlled and visualized through rotameter and analog pressure gauge attached to the electrolyte supply unit, as shown in Fig. 24.1. Lieca DM-2500

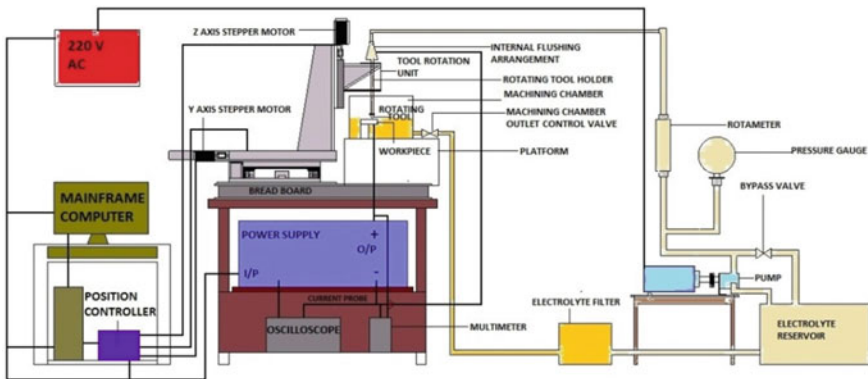


Fig. 24.1 Schematic of EC milling setup

optical measuring microscope has been used for imaging and measuring different feature of the machined profiles.

### 24.3 Experimental Planning

The main drawbacks of EC milling with solid tool are unavailability of electrolyte in the machining zone and improper removal of sludge from the machined surface and these can be overcome only by hollow tool with internal flushing. So, in this experimentation, a flat head cylindrical hollow tool made of copper with 10 mm of outer diameter and 4 mm of inner diameter has been used. For achieving sharp edge of the machined profile as well as to minimize the stray current effect during machining, cylindrical with flat head tools are preferred instead of square or curved head shape and to get better dimensional accuracy [4]. A titanium-based super alloy of grade -V with 50 mm in length, 30 mm in width and 5 mm thickness has been used as work-piece. In electrochemical milling, sodium chloride (NaCl), sodium bromide (NaBr) and sodium nitrate ( $\text{NaNO}_3$ ) are the only choice as electrolyte for better machining of Ti6Al4V by electrochemical machining [5]. In this study, NaCl and  $\text{NaNO}_3$  mixed electrolyte has been used. The reason behind the use of  $\text{NaNO}_3$  in the mixed electrolyte is to overcome the shortcomings of NaCl electrolyte. Use of NaCl in the mixed electrolyte has increased the generation of hydrogen bubbles at anode surface, results in complete removal of passive layer from the premachined anode surface. Some pilot experiments have been conducted with same aqueous solution of mixed electrolyte having the concentration of 0.5, 1 and 1.5 M. In the case of EC milling, out of various electrical and non-electrical process parameters, feed rate, milling layer thickness and tool rotation are the most influencing process parameters as reported by the researchers [6, 7].

Therefore, in this study these process parameters have been varied to study the influence on various responses of EC milling, for example, overcut, average machining depth, side angle, radius of curvature, while other process parameters have been kept constant. In the preliminary experimentation, milling layer depth has been varied from 0.1 to 0.35 mm with the increment of 0.05 mm and feed rate has been varied from 1.4 to 5.4 mm/min with the increment of 1 mm/min. In EC milling, tool rotation has great impact on the EC milling performance characteristics. Rotation improves various responses of EC milling by effective sludge removal and supply of fresh electrolyte at every instantaneous machining zone. When machining depth increases, proper removal of sludge is possible due to high radial outward force of electrolyte gained from tool rotation. High rotational speed cannot be used with high milling layer depth as it deteriorates the surface finish with some unwanted impressions of the electrolyte flow lines at the machined surface.

### 24.4 Experimental Methodology

In this study, initially simple slots have been machined to find out the suitable range of most influential process parameters and to study their impact on various responses of EC milling. Machining of a simple slot of length 20 mm with depth of 1.25 mm has been fabricated on the Ti6Al4V workpiece. Slots have been machined by means of electrochemical milling process in a layer-by-layer fashion. In each layer, the electrode has been controlled to move along a predefined path, as shown in Fig. 24.2. To study the effect of rotation on the responses, experiments have been repeated by the same set of value of milling layer depth (MLD) and feed rate with incorporation of moderate value of rotation, that is, 300 rpm at the tool.

Proper balance of feed rate and MLD is required; otherwise it will directly leads to short circuit in the subsequent passes. From the trial experiments, it has been observed that the machined zone has not been deteriorated as far as surface finish and overcut are concerned. Material removal rate increases with the increment of concentration without compromising the accuracy of the machined zone with 1 M of mixed electrolyte; therefore, finally 1 M concentration of NaCl and NaNO<sub>3</sub> has been chosen for further study.

Tables 24.1 and 24.2 show the different values of variable and fixed process parameters, respectively. In Fig. 24.2, cross-sectional view and various measured responses have been shown. Width overcut, side angle and radius of curvature clearly state the deviation of various geometrical features, whereas, machining depth accounts for the accuracy and amount of material removal. Width overcut has been calculated by Eq. 24.1 as follows:

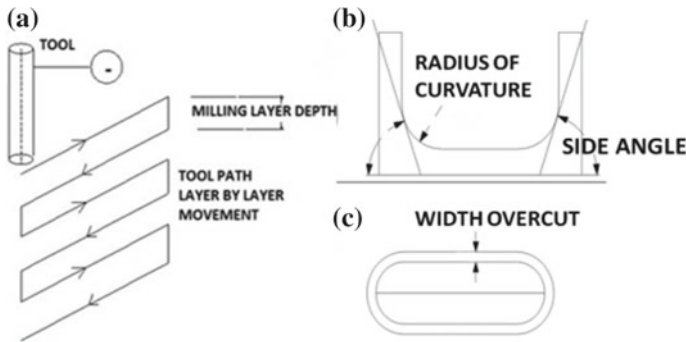


Fig. 24.2 Schematic of tool path and various responses

Table 24.1 Variable process parameters

Feed rate (mm/min)	2.4, 3.4, 4.4, 5.4
Milling layer depth (mm)	0.15, 0.2, 0.25, 0.3
Tool rotation	With and without rotation



**Table 24.2** Fixed process parameters

Input voltage (V)	20 (pulse DC)
Input current (A)	20
Pulse type	Square pulse
Pulse frequency (kHz)	5
Duty ratio	0.9
Electrolyte type	NaCl + NaNO <sub>3</sub>
Electrolyte concentration	1 M
Initial inter electrode gap (mm)	0.3
Feed along Z direction (mm/min)	1.2
Electrolyte flow pressure (kgf/cm <sup>2</sup> )	0.2
Electrolyte flow rate (lpm)	4
Tool rotational speed (rpm)	300

$$W_{oc} = \frac{W_{ob} - D}{2} \quad (24.1)$$

Where,  $W_{oc}$  is the measured overcut value,  $W_{ob}$  is the obtained width of machining zone and  $D$  is the diameter of the tool. Side angle and radius of curvature are the other responses those have been taken. Side angle value describes the deterioration of perpendicularity of the wall and radius of curvature shows the deterioration of edges in-between base and side wall of the machined zone. Both side angle and radius of curvature values have also been calculated by the contour scope.

## 24.5 Results and Discussion

Experiments have been conducted to find out the best set of process parameter which results in lower value of overcut, higher value of side angle, lower average radius of curvature of the side wall and machining depth closer to desired depth.

### 24.5.1 Influence of Feed Rate and MLD on Overcut

In ECM process, stray current effect is an uncontrollable phenomenon that leads to removal of material from the undesired portion of the workpiece which results in inaccuracy at the machined profile. It has been clearly observed from Figs. 24.3 and 24.4 that width overcut decreases with increasing feed rate and milling layer depth. The same trend has also been followed in case of rotating tool. During tool rotation, short-lived reaction compound can be hydrolyzed very easily and results in higher amount of material removal and overcut.

**Fig. 24.3** Effect of feed rate on width overcut

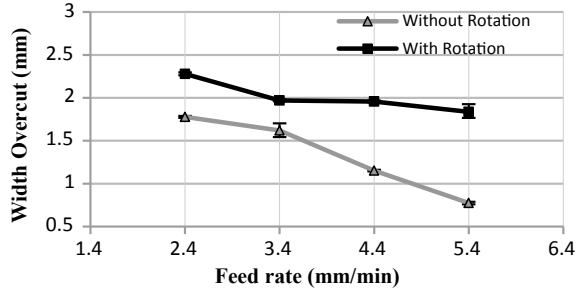
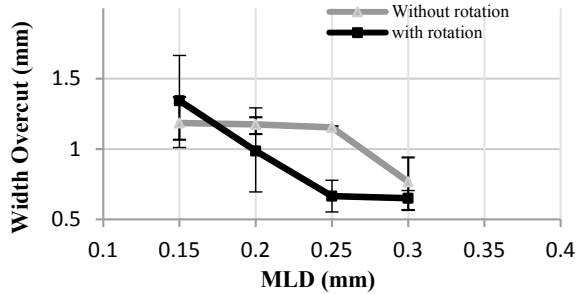


**Fig. 24.4** Effect of milling layer depth on width overcut



The difference between final slot width in case of rotation and without rotation clearly justifies the situation. Alternatively, at higher value of MLD, the value of width overcut is more compared to without rotation. Higher amount of milling layer depth enables tool to sink in higher machining depth at a faster rate, thus the chances of interaction between bare tool tip and neighboring machining zone are less. During rotation at a higher value of MLD, after completing initial pass the instantaneous gap between both electrodes reduce which results in lower gap voltage and higher gap current.

### 24.5.2 Influence of Feed Rate and MLD on Average Machining Depth

The depth of the machined zone has been decreased with the increment of feed rate, and it has been clearly observed from the Figs. 24.5 and 24.6 that slight decrement of depth has been occurred with increasing feed rate in the case of EC milling without tool rotation. However, in the case of tool rotation, depth has been decreased significantly with the increment of feed rate and at the higher feed rate machining with tool rotation reaches nearer to the desired depth value. In the case of EC milling, flushing is very important phenomenon and a little reduction in amount of material removal occurs due to unstable machining, which is possible at the dynamic flow pattern of ECM in the case of higher feed rate.

**Fig. 24.5** Effect of feed rate on average machining depth

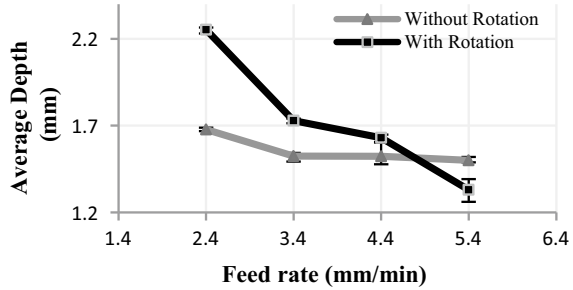
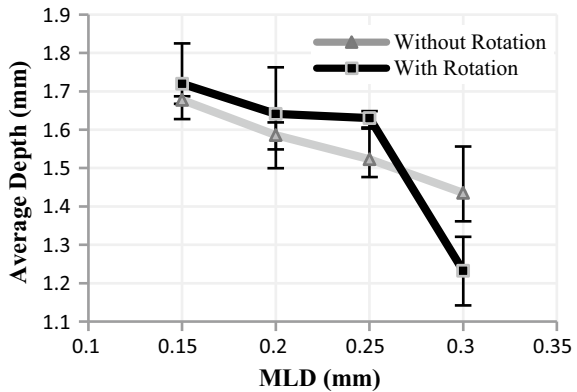


**Fig. 24.6** Effect of milling layer depth on average machining depth



It can also be observed from Fig. 24.6 that in the case of without rotation, the variation in depth is very less compared to rotating tool, and the velocity of electrolyte flow and machining current are the main contributing factors for this. On the other side, rotational movement of tool causing change in flushing pattern and material removal leads to higher variation in depth and the obtained depth is higher with rotating condition of the tool.

### 24.5.3 Influence of Feed Rate and MLD on Side Angle

From Figs. 24.7 and 24.8, the trend in variation of side angle values is the same with variable feed rate and milling layer depth. Side angle also depends on the overcut and depth value of the machining zone. Only at the maximum milling layer depth, the value of side angles is increased again with high value in the case of without rotation as increment of milling layer depth and which directly results in decrement of machining depth. A higher value for side angle is obtained in the case of with rotation.

**Fig. 24.7** Effect of feed rate on side angle

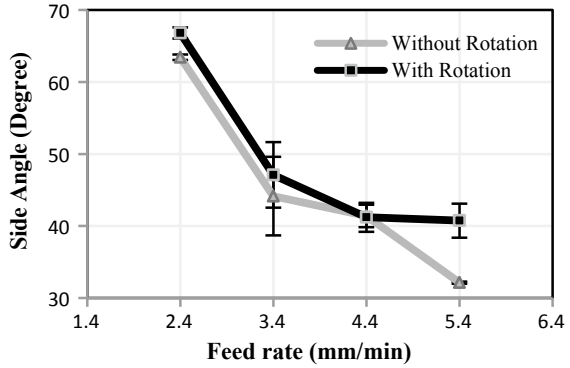
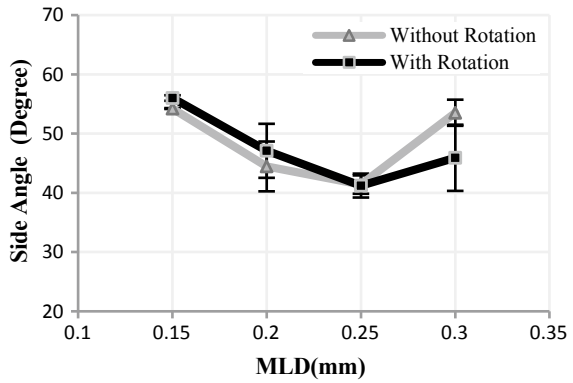


**Fig. 24.8** Effect of milling layer depth on side angle



### 24.5.4 Influence of Feed Rate and MLD on Radius of Curvature

It can be clearly observed from Figs. 24.9 and 24.10 that average radius of curvature

**Fig. 24.9** Effect of feed rate on average radius of curvature

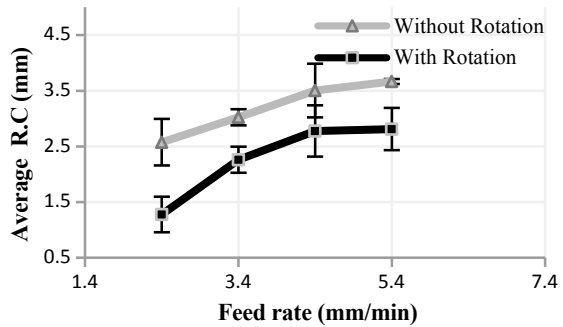
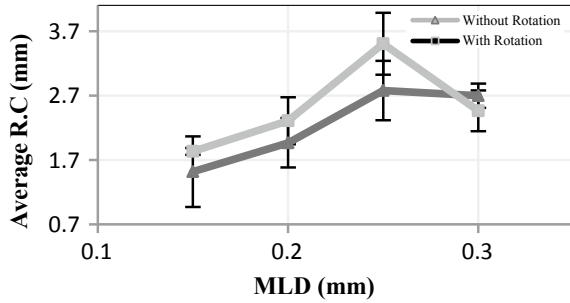


**Fig. 24.10** Effect of milling layer depth on average radius of curvature



of the side wall increases drastically in both the cases. Radius of curvature determines the deviation of the edge between sidewall and machined surface. Again at the maximum value of milling layer depth, the radius of curvature value is less in case of without rotation.

**24.5.5 Influence of Tool Rotation on Machining Quality**

Considering all the responses at a time, it can be seen that with tool rotation is more effective than without rotation as far as accuracy and surface quality of the machined profiles are concerned.

Figure 24.11 depicts the photographic image of best quality EC milled slots and the comparison with the tool rotation has been observed. After all the experimentation, it has been seen that with feed rate of 4.4 mm/min and 0.25 mm of milling layer depth, better homogeneity of the slot, least overcut and desired depth have been achieved. However, with the comparison of Fig. 24.11 a, b, it can be seen that after incorporation of tool rotation, the surface quality of the EC milled profile has been greatly improved, which justifies the advantage of tool rotation in EC milling.

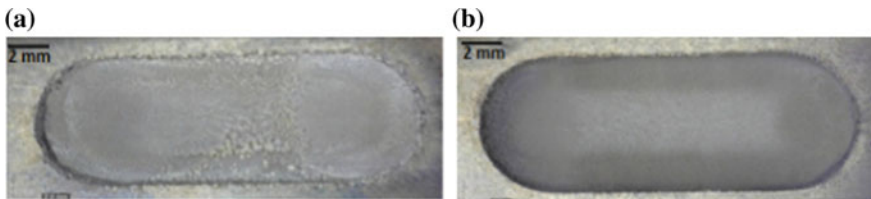


**Fig. 24.11** EC-milled slots at feed rate of 4.4 mm/min and 0.25 of milling layer depth. **a** without tool rotation and **b** with tool rotation

### 24.6 Selection of Best Parametric Combination by Analyzing Experimental Results

From the obtained response values at every parametric combination, the choice of best set of parametric combination has been made. Results have been obtained from the produced milled slots from both feed rate and milling layer depth with stationary tool as well as with tool rotation. Furthermore, these best parametric settings have been utilized for producing complex three-dimensional features. Simple slot features have been generated on Ti6Al4V by these set of combinations, as shown in Table 24.3. Considering the most influencing process parameters, that is, feed rate, milling layer depth and tool rotation, best set of process parametric combination has been found out, which is responsible for lower width overcut, lower radius of curvature of wall, surface roughness of the machined surface and desired value of machining depth and side angle.

Multicriteria decision-making (MCDM) problem involves several objective functions within a predetermined set of constraints. Another important factor is to assign weight to the specific criteria. In this study, all the five criteria are directly related to the dimensional and profile accuracy of the machining profile. Therefore, for all operations performed, similar weight is given to all the criteria. Five responses, for

**Table 24.3** Decision matrix for MADM analysis

Higher the better						Lower the better		
Sl. No.	Rotation/without rotation	Feed	M.L.D	Side angle (°)	Depth (mm)	Radius of curvature (mm)	Overcut (mm)	Surface roughness (µm)
1	Rotation	2.4	0.25	66.812	2.252	1.278	2.277	1.941
2	Rotation	3.4	0.25	47.101	1.729	2.261	1.969	1.565
3	Rotation	5.4	0.25	40.745	1.329	2.812	1.837	1.406
4	Rotation	4.4	0.15	56.013	1.719	1.518	1.343	1.413
5	Rotation	4.4	0.2	47.101	1.641	1.963	0.986	1.44
6	Rotation	4.4	0.25	47.001	1.538	2.091	0.666	1.462
7	Rotation	4.4	0.3	45.918	1.232	2.695	0.65	1.591
8	Without rotation	2.4	0.25	63.444	1.677	2.576	1.777	2.047
9	Without rotation	3.4	0.25	44.145	1.523	3.024	1.619	1.781
10	Without rotation	4.4	0.25	41.395	1.523	3.504	1.152	1.71
11	Without rotation	5.4	0.25	32.134	1.499	3.667	0.775	1.706
12	Without rotation	4.4	0.15	54.227	1.677	1.833	1.184	1.47
13	Without rotation	4.4	0.2	44.457	1.585	2.308	1.128	1.664
14	Without rotation	4.4	0.3	53.519	1.435	2.461	0.762	1.71

example, width overcut, machining depth, side angle of the side wall, radius of curvature of the side wall and surface roughness, have been considered as five conflicting criteria. Out of this five criteria, side angle and machining depth has been selected as beneficial criteria because their higher values are desirable and surface roughness, width overcut and radius of curvature of the side wall has been considered as non-beneficial criteria. In this study, simple additive weightage (SAW), technique for order preference by similarity to ideal solution (TOPSIS) and multiobjective optimization ratio analysis (MOORA) methods have been used for finding best alternative. Decision matrix has been formed after measuring all the values of responses as obtained after conducting EC milling experiments, as shown in Table 24.3.

From Tables 24.4, 24.5 and 24.6, it has been clearly observed that feed rate of 4.4 mm/min and milling layer depth of 0.25 mm with tool rotation are the best set of experimental parametric combination, which perfectly matches with the settings obtained from basic experimentation. Further, this particular set of best parametric combination has been used for generation of different 3D linear as well as nonlinear complex-shaped features.

**Table 24.4** Best parametric combinations based on TOPSIS

Exp. No.	Feed (mm/min)	MLD (mm)	Tool rotation	Closeness coefficient	Rank
6	4.4	0.25	With	0.65796	1
13	4.4	0.2	Without	0.65756	2
14	4.4	0.3	Without	0.65405	3

**Table 24.5** Best parametric combinations based on MOORA

Exp. No.	Feed (mm/min)	MLD (mm)	Tool rotation	Closeness coefficient	Rank
6	4.4	0.25	With	-0.01244	1
4	4.4	0.15	With	-0.01591	2
12	4.4	0.15	Without	-0.01823	3

**Table 24.6** Best parametric combinations based on SAW

Exp. No.	Feed (mm/min)	MLD (mm)	Tool rotation	Closeness coefficient	Rank
1	2.4	0.25	With	0.81980	1
6	4.4	0.25	With	0.78706	2
4	4.4	0.15	Without	0.78452	3

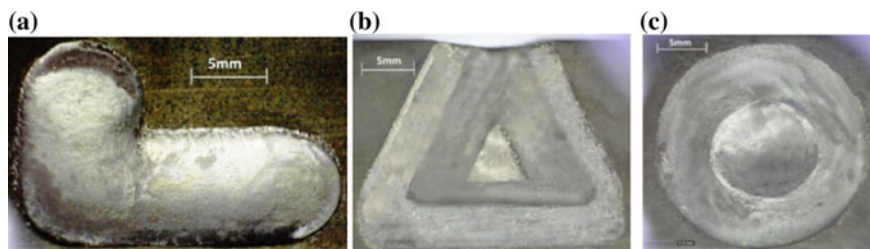


**Fig. 24.12** Photographic image of various complex-shaped features. **a** ‘L’ shaped feature. **b** Trapezoidal stepped profile. **c** Circular stepped groove

## 24.7 Generation of Various Three-Dimensional Features

With the help of common best parametric combination, some 3D complex features have been generated, like ‘L’ shape feature, trapezoidal stepped profile and circular stepped groove, as shown in Fig. 24.12a–c. After EC milling operation, different performance characteristics and features of these complex geometrical profiles have been calculated. During these experiments, the fixed process parameters have been kept constant, same as pilot experimentation as depicted in Table 24.2. For generation of different complex feature, tool path should have to be designed properly and the accuracy of the generated profile completely depends upon the tool movement path and the accuracy of the motion.

Therefore, it is too difficult to produce complex 3D profiles on Ti6Al4V as the controlled dissolution is very tough for Ti6Al4V. After analyzing all the produced 3D features, it can be seen that all the responses are within the accuracy limit.

## 24.8 Conclusions

From all the experimental analysis and the obtained responses, it can be concluded that the developed EC milling setup is capable of performing EC milling operation successfully on any difficult-to-cut materials. It is also capable of producing any kind of linear, nonlinear and complex 3D features. Using 1 M NaNO<sub>3</sub> and NaCl mixed electrolyte, at 5.4 mm/min of feed rate with 0.3 mm of MLD, lower overcut has been achieved. Best surface finish has been attained with feed rate of 5.4 mm/min and 0.25 mm of MLD. However, considering all the responses at a time, 4.4 mm/min of feed rate and MLD of 0.25 mm with tool rotation are the best parametric combination during EC milling of Ti6Al4V. Internal flushing with tool rotation improves the accuracy of the machined profile due to better removal of sludge from the instantaneous machining zone. Analysis based on this study will definitely help manufacturing industry to utilize EC milling successfully for the fabrication of any complex 3D shape with great precision and cost effectiveness.



**Acknowledgements** The authors acknowledge special thanks to AR&DB, DRDO, New Delhi, for the financial assistantship.

## References

1. Anasane, S.S., Bhattacharyya, B.: Experimental investigation on suitability of electrolytes for electrochemical micromachining of titanium. *Int. J. Adv. Manuf. Technol.* **86**, 2147–2160 (2016)
2. Bhattacharyya, B.: *Electrochemical Micromachining for Nanofabrication, MEMS and Nanotechnology*. William Andrew App. Science, U.S.A. (2015)
3. Ghosal, B., Bhattacharyya, B.: Investigation on profile of micro-channel generated by electrochemical micromachining. *J. Mater. Process. Technol.* **222**, 410–421 (2015)
4. Hindujaa, S., Pattavanitch, J.: Experimental and numerical investigations in electro-chemical milling. *CIRP J. Manuf. Sci. Technol.* **12**, 79–89 (2016)
5. Mishra, K., Dey, D., Sarkar, B.R., Bhattacharyya, B.: Experimental Investigation into electrochemical milling of Ti6Al4V. *J. Manuf. Process.* **29**, 113–123 (2017)
6. Mishra, K., Dey, D., Sarkar, B.R., Bhattacharyya, B.: Modeling on volumetric material removal for fabrication of complex shapes by EC milling of Ti6Al4V. *J. Electrochem. Soc.* **165**, 388–396 (2018)
7. Vanderauweraa, W., Vanloffelta, M., Perezb, R., Lauwersa, B.: Investigation on the performance of macro electrochemical milling. *Procedia CIRP* **6**, 356–361 (2013)

# Chapter 25

## Enhancement in Machining Efficiency and Accuracy of ECDM Process Using Hollow Tool Electrode



Rajendra Kumar Arya and Akshay Dvivedi

**Abstract** Electrochemical discharge machining process (ECDM) can perform drilling operation on conductive or non-conductive materials. However, the accuracy and efficiency of the process is still limited. Different methods were reported to improve the ECDM process. Tool modification is one of the reported methods for ECDM process. Although fabrication of the reported tools is complicated, they also require additional processing. This article reports the competitive study on ECDM process using solid and hollow tool electrodes. The mechanism of material removal using solid and hollow tool electrodes is discussed. The results show that the use of hollow tool electrode enhanced the performance of ECDM process by increasing the numbers of discharges at inner edge. Through holes were drilled using solid and hollow tool electrodes. The use of hollow tool electrode reduced the drilling time by 34.66%. Also, hollow tool resulted in lesser entrance and exit diameter as compared to solid tool electrode.

**Keywords** ECDM · Solid tool · Hollow tool · Micro hole

### 25.1 Introduction

ECDM process has been widely used to machine all kinds of materials, irrespective of their mechanical and electrical properties. In the last few decades, the process is a prior choice for machining of non-conductive materials, especially in micro domain. The main advantages to use the ECDM facility are: it requires low space and low initial cost for development.

The ECDM process facility includes an electrolyte bath, DC power source and two electrodes (i.e. cathode and anode). Both the electrodes are immersed (tool electrode 1–2 mm in length and auxiliary electrode fully immersed) in an electrolyte bath and both are connected to the DC power source. The mechanism of material removal in

---

R. K. Arya (✉) · A. Dvivedi  
Department of Mechanical and Industrial Engineering,  
Indian Institute of Technology Roorkee, Roorkee 247667, India  
e-mail: [aryarajendra10iitr@gmail.com](mailto:aryarajendra10iitr@gmail.com)

© Springer Nature Singapore Pte Ltd. 2020  
M. S. Shunmugam and M. Kanthababu (eds.), *Advances in Unconventional Machining and Composites*, Lecture Notes on Multidisciplinary Industrial Engineering, [https://doi.org/10.1007/978-981-32-9471-4\\_25](https://doi.org/10.1007/978-981-32-9471-4_25)

ECDM process was explained by several researchers [1–3]. They reported two main phenomena of ECDM process (i.e. electrochemical action and electro-discharge) [3]. The electrochemical action starts when DC power source is provided to the electrodes (i.e. anode as an auxiliary electrode and cathode as a tool electrode). The H<sub>2</sub> bubbles form around the immersed or dipped surface of tool electrode and O<sub>2</sub> bubbles around the anode surface [4]. Surface area of the auxiliary electrode is approximately 100 times larger as compared to tool electrode. Hence, the H<sub>2</sub> bubbles easily coalesce with each other and form an insulating gas film around the dipped surface of tool electrode [4]. The insulating gas film ceases the flowing current in the circuit. This generates high electric field between electrolyte and tool electrode. The high electric field breaks down the gas film and starts electro-discharge action around the tool electrode edges. The electro-discharge action produces thermal energy for removal of work material by melting and vaporization [3]. Also, the thermal energy accelerates the high temperature chemical etching under the presence of electrolyte. Hence, chemical etching also contributes in material removal [5].

The ECDM process has been frequently accepted for fabrication of micro holes on a glass and ceramic substrates for micro fluidic and MEMS applications. The drilling operation on glass work material was performed first time by Kurafuji and Suda in 1968 [6]. After that, numerous investigations have been conducted to improve the efficiency and accuracy of drilled micro holes. Still, a low-cost and less-challenging solution is hardly reported in the existing literature. Tool electrode modification is the frequently accepted choice of the researchers in previous works done in ECDM process, because tool modification does not require any additional attachment with ECDM facility. However, the other reported choices such as tool or electrolyte vibration, tool rotation and magnetic field-assisted ECDM require additional apparatus with ECDM facility. Zheng et al. [7] used a flat side-walled tool electrode instead of conventional cylindrical tool electrode. They reduced the hole entrance diameter from 436 to 330  $\mu\text{m}$  by decreasing the discharges around the tool side wall. However, the additional cost of fabricating side wall tool electrode increased the overall machining cost. Spherical end tool electrode was used by Yang et al. [8] for fabrication of micro hole. The enhancement on machining efficiency and accuracy by improving the localized electrolyte flow inside the machining zone was reported. However, an additional operation is needed to fabricate special geometry tool electrode in micro domain like spherical end micro tool electrode. Micro-drilling-assisted ECDM was reported by Jiang et al. [9]. They observed that the use of drill-bit as a tool electrode improved the machining performance by adding mechanical action with electrochemical discharge action. However, additional tool rotation unit was used, which requires additional apparatus in ECDM facility. Singh and Dvivedi [10] used an abrasive-coated tool electrode; the micro cavities on abrasive-coated tool electrode improved the localized electrolyte flow into the machining zone. Also, they achieved near to zero working gap between tool electrode and material under pressurized feeding approach [10]. Thus, the machining performance was improved even at high drilling depth. However, the coated tool electrode increased the cost of tool electrode and the abrasive on tool electrode requires special pressurized feeding system to reduce the working gap. Therefore, in the present work a simple hollow

tool electrode was used with ECDM process. The hollow tool electrode does not require any special processing for tool fabrication or any additional apparatus with ECDM facility. The comparison of solid tool and hollow tool electrode is reported in subsequent sections. At the end, the through holes on borosilicate glass substrate are fabricated using solid and hollow tool electrodes.

## 25.2 Material and Method

### 25.2.1 Experimental Setup

The facility of ECDM process used in experiments was designed and fabricated in the advanced manufacturing processes laboratory of MIED, IIT Roorkee, Uttarakhand, India. The schematic view of the facility is shown in Fig. 25.1. The facility consists of an electrical power source, tool feeding and positioning system, electrolytic cell, X–Y axes for holes drilling position system and a process monitoring system. The electrical power source used in ECDM facility was a programmable pulsed DC power supply, which was connected to the tool electrode (as a cathode) and auxiliary electrode (as an anode). Hence, the electrolytic cell was formed by immersing both the electrodes (which are already connected to the power source +ve and –ve terminals) in an electrolyte tank (typically aqueous solution of NaOH). The tool electrode of stainless steel (SS-304 hollow and solid) was partially immersed (i.e. 1–2 mm) and a relatively larger size (i.e. >100 times) auxiliary electrode of graphite ring was

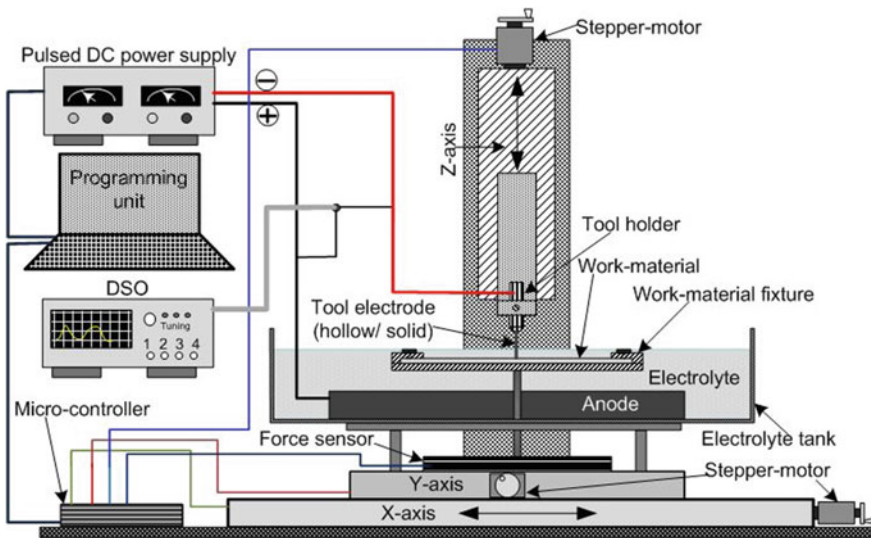


Fig. 25.1 Schematic view of developed ECDM facility

submerged in the electrolyte tank. The work material of borosilicate glass was also submerged in electrolyte tank and placed at the beneath of tool electrode tip with the help of work material fixture. The positioning and feeding of tool electrode (with the drilling progress) was achieved by a separate system, which consists of a force sensor (mechanically connected to the work material fixture), a micro controller and Z-axis. The force sensor operates electrically while connecting to the micro controller. The force sensor generated the force signals while the tool electrode makes mechanical contact with work material during the tool electrode feeding toward the work material. The micro controller was also connected to the stepper motor of Z-axis. Hence, the stepper motor was controlled by a prescribed program in micro controller to position the tool electrode. As per the program, if the force signal was less than the predefined load (i.e. 0.5 N) the tool moves toward the work material and if the force signal exceeds the predefined load the tool retrieves back to form a predefined working gap (i.e. 4–5  $\mu\text{m}$ ) between tool electrode and work material. The electrolyte tank was mounted on X–Y axis, thus the positioning of drilling point on the work material was controlled by moving the X–Y axis. The real-time monitoring of the ECDM process was accomplished by using a digital storage oscilloscope (Model: DSOX3034A, Agilent, New Delhi, India).

Two tool electrode shapes (i.e. hollow and solid) were selected for drilling of micro holes on borosilicate glass. Both the tool electrodes had an outer diameter of 550  $\mu\text{m}$ , and the internal diameter of hollow tool was 300  $\mu\text{m}$ . The microscopic images of both the electrodes are shown in Fig. 25.2.

The performances of both the tool electrodes (i.e. hollow and solid) were evaluated by measuring the depth of hole (DOH), hole overcut (HOC) and surface damage (SD) of the drilled holes. A stereo zoom microscope (Make: Nikon, Model: SMZ745T) was used to capture the image of machined hole and for necessary measurements like HOC and SD. The DOH was measured using a dial gauge (Make: Mitutoyo), and the least count of dial gauge was 1  $\mu\text{m}$ . The representation of measuring method for measurement of DOH, HOC and SD is shown in Fig. 25.3.

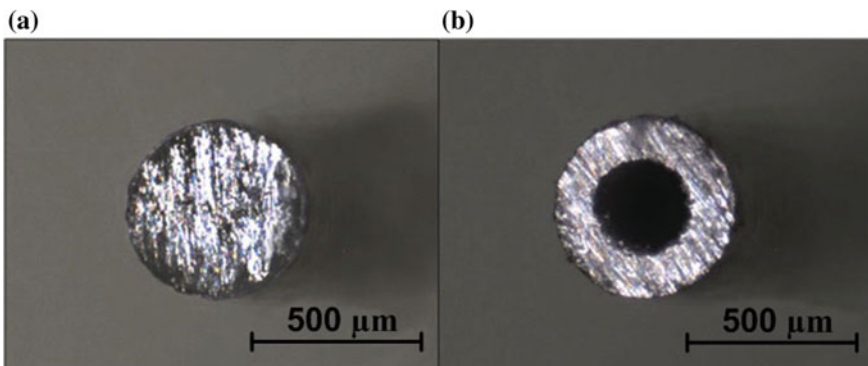


Fig. 25.2 Microscopic images of both **a** solid and **b** hollow tool

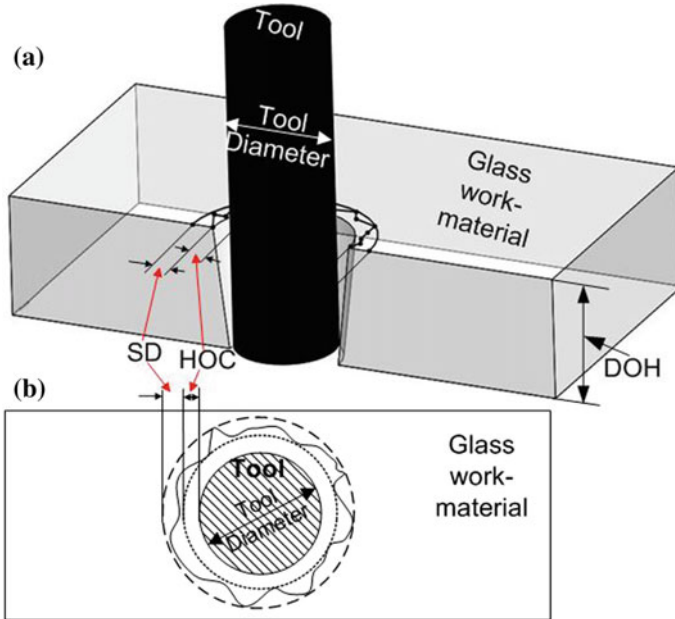


Fig. 25.3 Schematic view of drilled micro hole with terminology

### 25.2.2 Mechanism of Material Removal Using Solid and Hollow Tool Electrode

Figure 25.4 shows simulation of electric field intensity performed on Comsol Multiphysics 4.2, schematic of material removal mechanism and received DSO voltage signal images during ECDM with solid and hollow tool electrodes. The parametric condition for both the tool electrodes was similar during the ECDM process. As can be seen in simulated images, the hollow tool electrode provides additional high electric field intensity region, which increases the number of discharges at tool tip. This is illustrated in schematic view. The increased number of discharges at tool tip increased the frequency of discharges, as can be observed from DSO images. Also, the uniform distribution of discharges reduced the intensity of discharges (i.e.  $P_k - P_k$  in DSO images) using hollow tool electrode. The unique behavior of discharges using hollow tool electrode resulted in more DOH and less HOC and SD.

### 25.2.3 Experimental Procedure

In the existing literatures the applied voltage and pulse on time were found to be the most influencing process parameters of the ECDM process, which directly control

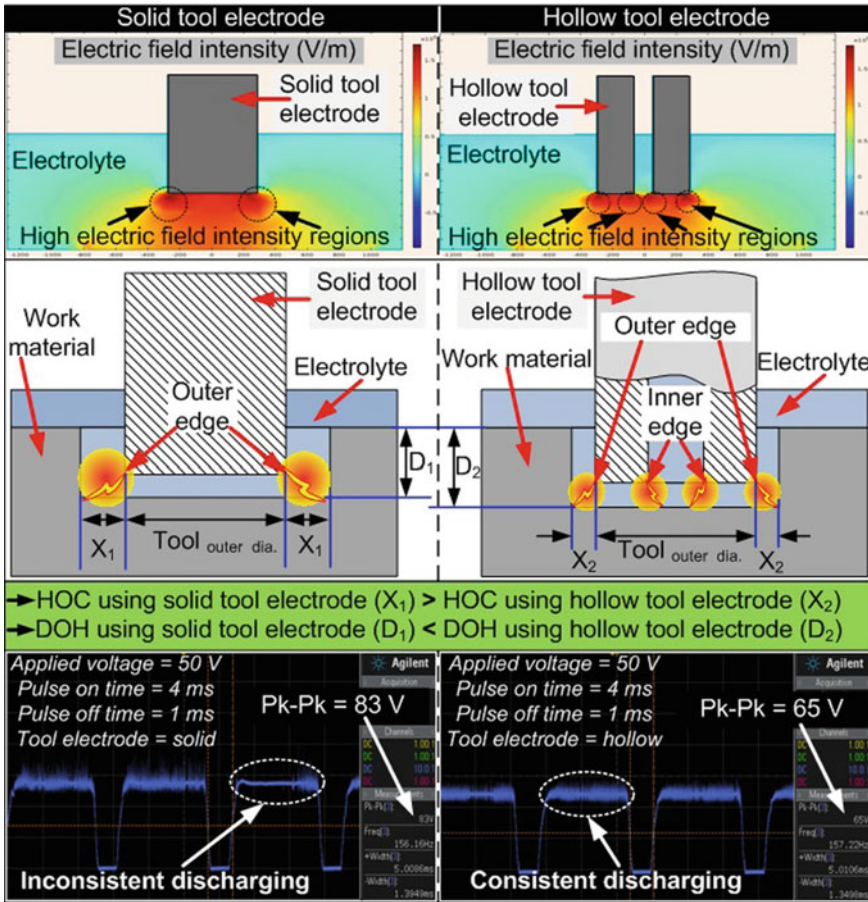


Fig. 25.4 Mechanism of material removal using solid and hollow tool electrode

the input thermal energy into the machining zone [7–11]. Thus, both the process parameters (i.e. applied voltage and pulse on time) were selected to obtain the process performance of ECDM process with hollow and solid tool electrodes. Pilot experiments were performed to select the range of variable parameters and other fixed parameters. All the selected process parameters (constant and variable) are tabled in Table 25.1. One-factor-at-a-time (OFAT) approach was acquired to perform the experiments. OFAT was widely adopted in previous experimental work [10, 12]. The comparison of hollow and solid tool electrodes was made using suitable graphs. Finally, a through hole was machined on the 1350  $\mu\text{m}$  thick borosilicate glass work material using hollow and solid tool electrodes. The experiments were repeated three times at the same parametric conditions, and the mean value of three experimental results was noted as a final result. The experiments were conducted at room temperature (i.e. 30  $^{\circ}\text{C}$ ).

**Table 25.1** Parameters selected for experimentations

Constant parameter	Specification
Electrolyte type/concentration (% wt./vol.)	NaOH/20
Tool electrode (solid and hollow) material	SS-304
Tool electrode size ( $\mu\text{m}$ )	Solid (OD 550) and hollow (OD 550/ID 300)
Anode (auxiliary electrode)	Graphite
Work material/size	Borosilicate glass slide/(75 * 25 * 1.35) mm <sup>3</sup>
Pulse off time (ms)	1
Drilling time (s)	120
Variable parameter	Range
Applied voltage (V)	40, 45, 50, 55
Pulse on time (ms)	2, 3, 4, 5

## 25.3 Results and Discussion

### a. Performance Evaluation of Hollow and Solid Tool Electrodes at Different Applied Voltage

In ECDM process the applied voltage controls the produced energy inside the machining zone, thus controls the material removal [10]. In this section the effect of applied voltage on DOH, HOC and SD is discussed using solid and hollow tool electrodes. This is illustrated in Fig. 25.5a–c for DOH, HOC and SD, respectively. As can be observed, the DOH, HOC and SD increased with increase in applied voltage. The reason thereof was more H<sub>2</sub> bubbles were produced with increased applied voltage, hence more thermal energy was produced [10, 11]. However, after 50 V applied voltage, the HOC and SD abruptly increased. This was because at 55 V excessive H<sub>2</sub> bubbles are produced around the dipped surface of tool electrode, thus thick gas film formed and high intensity discharges produced. This resulted in unavailability of electrolyte inside the machining zone, which also produced more discharges at the hole entrance.

The comparison of use of solid and hollow tool electrodes in Fig. 25.5a–c shows that the hollow tool enhanced the performance of ECDM process. The hollow tool electrode provides additional high current density regions on active tool electrode tip due to additional inner edge. Also, in hollow tool electrode the electric field intensity uniformly distributed over the tip of tool electrode, as can be observed from Fig. 25.4. Thus, this increased the discharges from both the edges (i.e. outer and inner edge). However, in solid tool only outer edge can provide the discharges. These additional



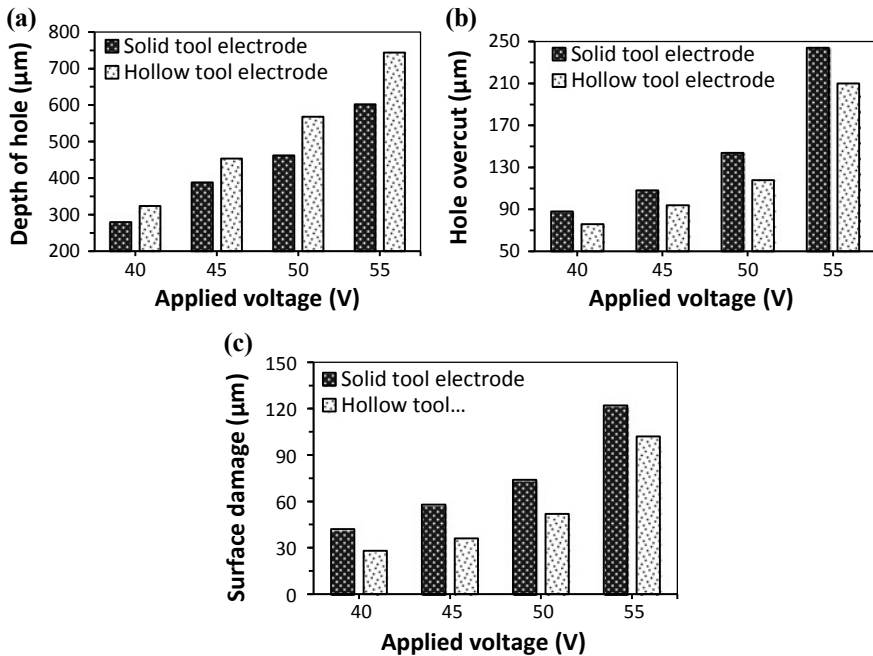


**Fig. 25.5** Effect of applied voltage on **a** DOH, **b** HOC and **c** SD using solid and hollow tool electrodes

discharges resulted in more DOH and less HOC and SD as compared to solid tool electrode.

### **b. Performance Evaluation of Hollow Solid Tool Electrode at Different Pulse On Time**

The accuracy of the ECDM process increases by using pulse power supply [10, 11, 13], hence the pulse power supply has been used during ECDM process. The effect of pulse on time with constant pulse off time (i.e. 1 ms) on DOH, HOC and SD was obtained using solid and hollow tool electrodes and the results are shown in Fig. 25.6 a, b and c. The results show that as the pulse on time increased from 2 to 5 ms with 1 ms pulse off time the DOH, HOC and SD increased. The reason behind this phenomenon is that as the pulse on time increases the thermal energy is produced for longer time inside the machining zone [13, 14]. Also, the DOH was increased rapidly till 4 ms pulse on time, after that increased slowly. But, beyond 4 ms pulse on time the HOC and SD rapidly increased. It is because at higher pulse on time (beyond 4 ms) the larger duration of discharging results in lack of electrolyte present in the machining zone. Hence, the discharges produced at near the hole entrance, eventually resulted in more HOC and SD. Additionally, Fig. 25.6a, b and c shows that the hollow tool performed better than the solid tool electrode. This is already discussed in Sect. 25.2.2. The additional inner edge of hollow tool

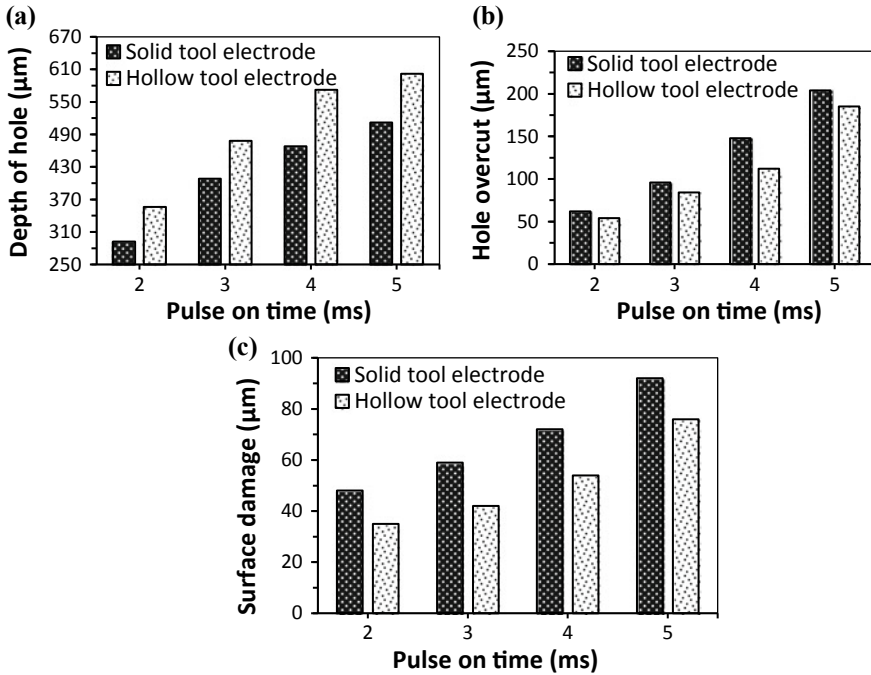


Fig. 25.6 Effect of pulse on time on a DOH, b HOC and c SD using solid and hollow tool electrodes

electrode produced more numbers of discharges at tool tip as compared to the solid tool electrode. Eventually, the DOH increased and HOC and SD decreased using hollow tool electrode.

**c. Fabrication of Through Holes Using Solid and Hollow Tool Electrodes**

Through holes were drilled on 1350 µm thick borosilicate glass work material using solid and hollow tool electrodes. The process parameters selected for through holes drilling are applied voltage 50 V, pulse on time 4 ms, pulse off time 1 ms and electrolyte NaOH 20%, wt./vol. The above-mentioned parametric setting was selected because it provided higher DOH with lesser HOC and SD. Figure 25.7a, b shows the microscopic images of drilled holes using solid and hollow tool electrodes, respectively. The drilling time during through holes fabrication was recorded using stopwatch. The recorded drilling time for solid tool electrode was 528 s and for hollow tool electrode was 345 s. As a result, the hollow tool electrode reduced the drilling time by 34.66%. Also, the entrance diameter was reduced from 1097 to 912 µm and diameter from 698 to 616 µm using hollow tool electrode.

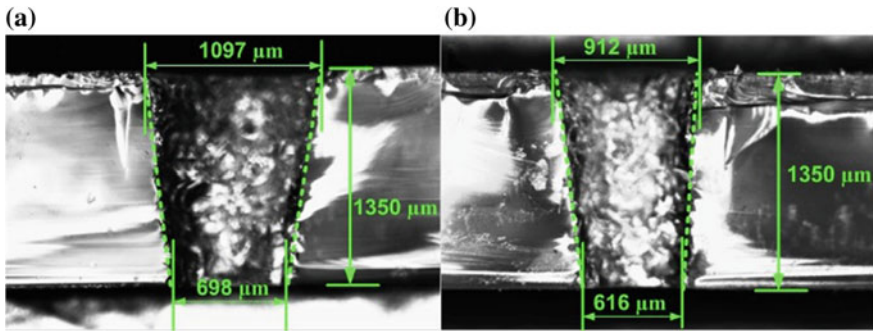


Fig. 25.7 Cross-sectional view of through holes drilled using **a** solid and **b** hollow tool electrode

## 25.4 Conclusions

The present study was performed to use the solid and hollow tool electrodes during ECDM process. The process performance was investigated on DOH, HOC and SD of drilled holes on borosilicate glass. The main conclusions drawn from the present work are as follows:

1. ECDM is effectively used to drill through holes on borosilicate glass using solid and hollow tool electrodes.
2. Use of hollow tool electrode enhanced the efficiency and accuracy of the ECDM process.
3. The drilling time is reduced by 34.66% using hollow tool electrode during drilling of through hole.
4. Entrance diameter of drilled hole is reduced from 1097 to 912  $\mu\text{m}$  and exit diameter from 698 to 616  $\mu\text{m}$  using hollow tool electrode.

## References

1. Jain, V.K., Dixit, P.M., Pandey, P.M.: On the analysis of the electrochemical spark machining process. *Int. J. Mach. Tools Manuf.* **39**(1), 165–186 (1999)
2. Basak, I., Ghosh, A.: Mechanism of spark generation during electrochemical discharge machining: a theoretical model and experimental verification. *J. Mater. Process. Technol.* **62**(1–3), 46–53 (1996)
3. Bhattacharyya, B., Doloi, B.N., Sorkhel, S.K.: Experimental investigations into electrochemical discharge machining (ECDM) of non-conductive ceramic materials. *J. Mater. Process. Technol.* **95**(1–3), 145–154 (1999)
4. Wüthrich, R., Hof, L.A.: The gas film in spark assisted chemical engraving (SACE)—a key element for micro-machining applications. *Int. J. Mach. Tools Manuf.* **46**(7–8), 828–835 (2006)
5. Singh, T., Dvivedi, A.: Developments in electrochemical discharge machining: a review on electrochemical discharge machining, process variants and their hybrid methods. *Int. J. Mach. Tools Manuf.* **105**, 1–13 (2016)

6. Kurafuji, H., Suda, K.: Electrical discharge drilling of glass. *Ann. CIRP* **16**(1), 415–419 (1968)
7. Zheng, Z.P., Su, H.C., Huang, F.Y., Yan, B.H.: The tool geometrical shape and pulse-off time of pulse voltage effects in a Pyrex glass electrochemical discharge microdrilling process. *J. Micromech. Microeng.* **17**(2), 265 (2007)
8. Yang, C.K., Wu, K.L., Hung, J.C., Lee, S.M., Lin, J.C., Yan, B.H.: Enhancement of ECDM efficiency and accuracy by spherical tool electrode. *Int. J. Mach. Tools Manuf.* **51**(6), 528–535 (2011)
9. Jiang, B., Lan, S., Ni, J.: Investigation of micro-drilling assisted electro chemical discharge machining. In: *Proceedings of 9th International Workshop on Microfactories*, Honolulu, USA, pp. 96–100 (2014)
10. Singh, T., Dvivedi, A.: On pressurized feeding approach for effective control on working gap in ECDM. *Mater. Manuf. Process.* **33**(4), 462–473 (2018)
11. Singh, T., Dvivedi, A.: On performance evaluation of textured tools during micro-channeling with ECDM. *J. Manuf. Process.* **32**, 699–713 (2018)
12. Kumar, S., Dvivedi, A.: Fabrication of microchannels using rotary tool micro-USM: an experimental investigation on tool wear reduction and form accuracy improvement. *J. Manuf. Process.* **32**, 802–815 (2018)
13. Gupta, P.K., Dvivedi, A., Kumar, P.: Effect of pulse duration on quality characteristics of blind hole drilled in glass by ECDM. *Mater. Manuf. Process.* **31**(13), 1740–1748 (2016)
14. Bhuyan, B.K., Yadava, V.: Experimental study of traveling wire electrochemical spark machining of borosilicate glass. *Mater. Manuf. Process.* **29**(3), 298–304 (2014)

# Chapter 26

## Evaluation of Cutting Force and Surface Roughness of Inconel 718 Using a Hybrid Ultrasonic Vibration-Assisted Turning and Minimum Quantity Lubrication (MQL)



Habtamu Alemayehu , Sudarsan Ghosh and P. V. Rao

**Abstract** Inconel 718 is the most widely used nickel-based superalloy in aerospace, automobile and nuclear energy industries for its superior chemical, mechanical and thermal properties. However, the aforesaid properties by themselves offer poor machining characteristics. To overcome machining difficulties, hybrid machining processes have been introduced. A hybrid of an ultrasonic vibration-assisted turning and lubri-cooling technique is considered as one of the similar strategies. In the present study, a hybrid setup combining indigenously developed ultrasonic vibration-assisted turning (UVAT) and minimum quantity lubrication (MQL) has been used. UVAT changes the conventional cutting (CT) process into vibro-impact process whereas MQL makes the cutting process able to minimize the heat from the machining and ultrasonic system as well. MQL is eco-friendly as it answers some of the problems associated with the cutting fluids. Lower cutting force ( $F_y$ ) and feed force ( $F_z$ ), and average surface roughness have been obtained with MQL + UVAT compared to CT + MQL.

**Keywords** Inconel 718 · Ultrasonic vibration-assisted turning · MQL · Cutting force · Surface roughness

### 26.1 Introduction

In the area of aerospace, petroleum engineering, nuclear energy and automobile industries, materials which have superior chemical, mechanical and thermal properties are highly recommended. Aircraft engines and gas turbine are some of the vital aerospace components which are manufactured from Inconel 718 [1]. Also, these

---

H. Alemayehu (✉) · S. Ghosh · P. V. Rao  
Department of Mechanical Engineering, Indian Institute of Technology Delhi,  
New Delhi 110016, India  
e-mail: [ameyahabtam@gmail.com](mailto:ameyahabtam@gmail.com)

© Springer Nature Singapore Pte Ltd. 2020  
M. S. Shunmugam and M. Kanthababu (eds.), *Advances in Unconventional Machining and Composites*, Lecture Notes on Multidisciplinary Industrial Engineering, [https://doi.org/10.1007/978-981-32-9471-4\\_26](https://doi.org/10.1007/978-981-32-9471-4_26)

components are mostly operating at extreme temperature conditions for a long duration. Therefore, Inconel 718 is one of the most widely used nickel-based superalloys that consist of the aforesaid properties. Elemental compositions which are found in Inconel 718 have been playing a crucial role associated with its excellent properties. For example, the presence of (i) nickel, aluminum, chromium and tantalum, (ii) nickel, chromium, iron, molybdenum, tungsten and tantalum leads to excellent oxidation resistance and high strength behaviors, respectively. Similarly, combinations of other elements also provide other properties which make Inconel 718 more preferable over other nickel-based superalloys [2].

In contrary to the above, Inconel 718 is considered as one of the difficult-to-cut materials. This is due to low thermal conductivity, high strength and high hardness it has gained from its elemental compositions. Accordingly, the difficulties in machining of Inconel 718 are characterized by:

(a) Built-up-edge (BUE) formation at the tip of cutting tool due to high heat generated between tool and workpiece interface during machining; in this case poor thermal conductivity behavior of this alloy exacerbates the situation; (b) High power consumption due to high strength and hardness behavior; and (c) Diffusion and oxidation tool wear due to a high chemical affinity behavior of Inconel 718 [3].

To advance the machining performance of Inconel 718, several enhancement techniques have been attempted. Application of different cooling (MQL, NanoMQL, Cryogenic cooling), softening (laser-assisted machining, induction heating), vibration-assisted machining, and the combination (hybrid) of these techniques are some of the ongoing strategies to enhance machinability of Inconel 718. Recently, hybrid machining processes are considered as a primary solution method associated with machining of difficult-to-machine materials. Hybrid machining process can be defined as a combination of two or more machining processes, which are simultaneously implemented during machining operations. It has been giving an extra merit over a standalone machining process. For instance, the combined implementation of softening and cooling techniques can offer a reduction of strength and hardness of work materials, and reduction of heat which is generated during the machining process, respectively [4]. In the present study, a hybrid of an ultrasonic vibration-assisted turning (UVAT) and minimum quantity lubrication (MQL) during machining of Inconel 718 is investigated and the results are discussed.

UVAT is one of the active-assisted machining processes, and it is working by integrating conventional and non-conventional machining process. Here, the vibration which is coming out from the ultrasonic transducer through acoustic horn is imposed at the tip of the cutting tool. It can be imposed in the three different directions, namely cutting, feed and radial directions, simultaneously or separately. Subsequently, due to the vibro-impact phenomena at the tool-workpiece interface, the conventional cutting process is switched to the intermittent cutting process. Therefore, this intermittent cutting process can offer a lower average cutting force, good surface finish and minimize chatter that has been formed due to machine vibration [5, 6]. However, the ultrasonic vibration turning process will be effective only if the cutting speed is less than the critical speed. The critical speed can be determined using a function of

vibration parameters ( $2\pi af$ ), where  $a$  is the amplitude of the vibration and  $f$  the working frequency of the ultrasonic system [5]. Even though there is a positive response from UVAT, there is still high-temperature accumulation in the cutting zone. This is due to deformation, friction and shearing during machining and additional heat which is coming from the ultrasonic system. Therefore, it is recommended to use a suitable lubri-coolant strategy to eliminate or minimize the heat from the cutting zone and acoustic horn as well.

Minimum quantity lubrication (MQL) is a promising strategy that can reduce the heat developed during the machining process. It is mixed with compressed air inside the commercially available nozzle and can form a mist. The amount of cutting fluid which has been using in MQL is nearly 10,000 times lesser than that of common cutting fluids. The mist which has been formed inside the nozzle gets sprayed into the cutting zone with a flow rate of 50–500 ml/h [7]. Generally, the MQL can be applied to the working area either externally spray system or through-tool system [8]. Accordingly, the machining process under MQL environments can offer lower cutting forces, lower power consumption, better surface quality and lower tool wear as compared to dry process [9]. Additionally, when MQL method uses vegetable oil-based lubricant, it is considered as an eco-friendly process. As a result, it is addressing the environmental problems, health issues and high cost associated with the application of lubricants during the machining processes [10].

Wang et al. [1] have studied machinability of Inconel 718 using cryogenically and plasma-enhanced hybrid machining process. They reported that a hybrid process is surface roughness; the cutting force gets reduced; and the tool life gets extended by 250%, 30–50% and up to 170%, respectively, compared to CT. In another study, Feyzi and Safavi [11] presented a new hybrid strategy which included plasma and cryogenic enhanced machining, with ultrasonic vibration-assisted machining. They have suggested that the hybrid system was suitable to obtain a high surface quality for Inconel 718. Hsu et al. [12] investigated the machinability characteristics of Inconel 718 using a hybrid ultrasonic-assisted vibration and oxyacetylene source high temperature-aided machining process. To address environmental issues, CryoMQL hybrid machining technique has been introduced by Pereira et al. [13] during machining of AISI 304. In addition to this, they highlighted that the CryoMQL has been offering both cooling and lubrication characteristics. As a result, tool life has been improved by 50% when compared to CT.

Generally, from the previous research work, it can be inferred that hybrid machining processes are promising techniques that can offer environmental, economic and technical benefits as compared to standalone processes. This paper attempts to evaluate the cutting force and surface roughness of Inconel 718 using indigenously developed hybrid ultrasonic vibration-assisted turning and minimum quantity lubrication. Also, comparable results of surface roughness and cutting force with and without UAVT under MQL condition will be discussed.

## 26.2 Materials and Methods

For experimentation purpose, a round bar of Inconel 718 with a diameter of 70 mm and length of 300 mm has been selected. Ni-52.26%, Cr-18.63%, Fe-18.32% and Nb-4.98% are the major elemental compositions of Inconel 718. A plain carbide insert (WIDIA: K Grade-CNMA 120408-THMF) has been used for the cutting process. Experiments were conducted using an indigenously developed hybrid ultrasonic vibration-assisted turning (UVAT) according to our previous study [14] and minimum quantity lubrication (MQL) which is given in Fig. 26.1. After separately fabricated and sub-assembled, the hybrid system coupled to Leadwell T6 CNC Lathe machine. During machining, the UVAT provides vibration at the tip of the cutting tool which is transmitted from a high-frequency ultrasonic generator via a transducer. The transducer converts the high-frequency electrical energy which is coming out of the generator into longitudinal vibration in the form of amplitude. However, the amplitude which is coming out from the transducer is not sufficient for the ultrasonic application. As a result, the acoustic horn has been designed to amplify the amplitude, and later it uses to hold the cutting tool.

Likewise, the MQL system provides lubri-coolant to the tool–workpiece interface. For this study, sunflower oil has been selected. The MQL is prepared by proper mixing of sunflower oil and water in the ratio 1:10 [15] using magnetic stirring. Compressed air coming from the compressor (Model-LG 02 100 TP) and a small amount of liquid coming from oil container mixed inside the nozzle chamber and forms a mist. The MQL jet is sprayed through a nozzle over the tool surface and gets spread over the secondary contact zone.

Machining responses, such as the three components of cutting forces and surface roughness were measured by Kastler's piezoelectric dynamometer (model-9257B)

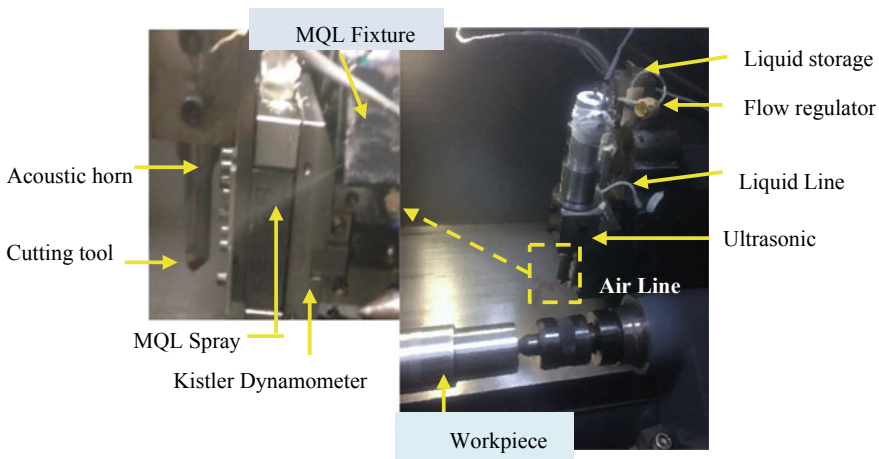


**Fig. 26.1** Ultrasonic vibration-assisted turning (UVAT) and minimum quantity lubrication (MQL) setup



**Table 26.1** Summary of cutting conditions

Items	Items parameter
Workpiece	Inconel 718 (70 mm diameter and 300 mm length)
Cutting tool	Plain carbide insert, CNMA 120408 THM-F
Cutting speed (m/min)	15, 20 and 25
Feed rate (mm/rev)	0.07 and 0.13
Depth of cut	0.5 mm
Frequency	22.3 kHz
Amplitude	12 $\mu$ m
MQL flow rate	250 ml/h
Sunflower to water ratio	1:10
Air pressure	3 bar
Nozzle diameter	2 mm

and Zeiss roughness tester (Handy Surf), respectively. Vibration parameters, such as frequency and vibration, were measured by laser vibrometer (Polytech OVF 303 SENSOR HEAD) and micrometer dial gauge, respectively. The summary of machining parameters and vibration parameters is given in Table 26.1.

## 26.3 Results and Discussion

### 26.3.1 Cutting Forces

The three components ( $F_x$ ,  $F_y$  and  $F_z$ ) of cutting forces have been measured during experimentations. The experiment has been conducted according to machining and vibration parameters which are given in Table 26.1. For each case, three replicates have been performed.

According to the data recorded during experimentations, the average main cutting force ( $F_y$ ) is lesser in UVAT + MQL compared to CT + MQL for lower machining parameters. As it has been illustrated in Fig. 26.2, the main cutting force ( $F_y$ ) is reduced at the given cutting speeds and lower feed rate (0.07 mm/rev). Accordingly, at a feed rate of 0.07 mm/rev, the main cutting force ( $F_y$ ) is decreased by 11.3, 10 and 12% at cutting speed of 15, 20, and 25 m/min, respectively in the hybrid process compared to CT + MQL.

However, at a higher feed rate (0.13 mm/rev) a significant change in the main cutting force is not shown. Eventually, at the cutting speed of 25 m/min and feed rate 0.13 mm/rev,  $F_y$  value is increased for UVAT + MQL than CT + MQL. This may

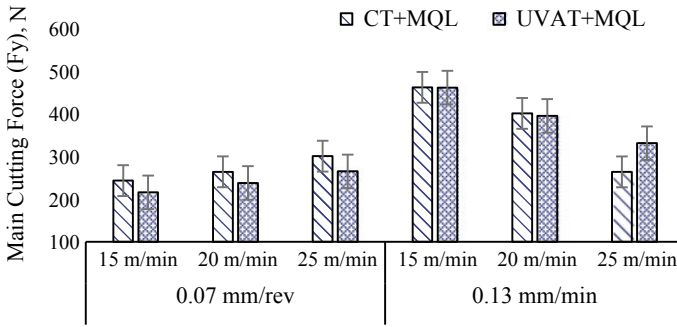


Fig. 26.2 Main cutting force ( $F_y$ ) for UVAT + MQL and CT + MQL

be due to the increased tool wear, as a result of high feed rate. Also, as it has been inferred from Fig. 26.3 that the feed force ( $F_z$ ) has shown a significant change except for one condition (25 m/min and 0.13 mm/rev). Hence, at a feed rate of 0.07 mm/rev the feed force ( $F_z$ ) is decreased by 25, 9 and 14% for a cutting speed of 15, 20 and 25 m/min, respectively, in UVAT + MQL compared to CT + MQL. As shown in Fig. 26.4, unlike feed force ( $F_z$ ) and main cutting force ( $F_y$ ), the radial force ( $F_x$ ) has not shown a significant change in both UVAT + MQL and CT + MQL.

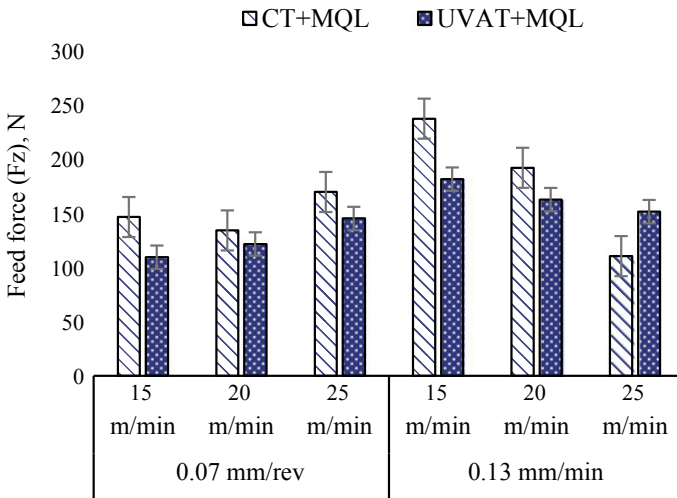


Fig. 26.3 Feed force ( $F_z$ ) for UVAT + MQL and CT + MQL

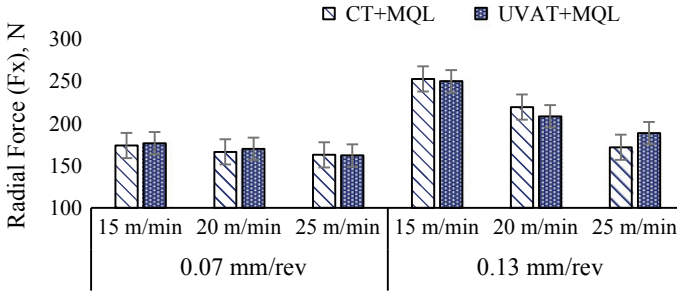


Fig. 26.4 Radial force (Fx) for UVAT + MQL and CT + MQL

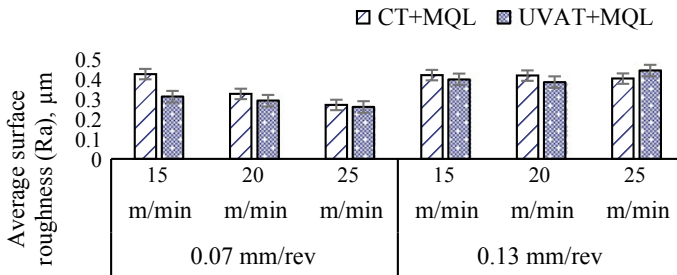


Fig. 26.5 Average surface roughness for UVAT + MQL and CT + MQL

### 26.3.2 Average Surface Roughness

As it has been inferred from Fig. 26.5, at lower cutting speed (15 and 20 m/min) and feed rate (0.07 mm/rev), the average surface roughness (Ra) has shown an improvement in the case of UVAT + MQL. Accordingly, at a feed rate of 0.07 mm/rev average surface roughness (Ra) is reduced by 27 and 10% at cutting speed of 15 and 20 m/min, respectively, in UVAT + MQL compared to CT + MQL. Also, at higher feed rate (0.13 mm/rev) for a cutting speed of 15 and 20 m/min, a slight improvement has shown in the case of UVAT + MQL. However, at a feed rate of 0.13 and 25 m/min, higher surface roughness has been observed in UVAT + MQL.

This might be related to the increased tool-work contact ratio (TWCR) at higher cutting speed and increased tool wear. Also, the glossy and matte finish for hybrid and MQL + CT surfaces were observed, respectively.

## 26.4 Conclusions

To assess the machinability of Inconel 718, a customized (UVAT + MQL) hybrid setup has been developed and experiments were conducted on various machining and vibration parameters. In addition to lubri-cooling purpose, to address environmental and health issues sunflower oil has been used for MQL application. Experimental results have revealed that at a feed rate of 0.07 mm/rev, the main cutting force ( $F_y$ ) is reduced by 11.3%, 10% and 12% at cutting speed of 15, 20 and 25 m/min, respectively, in UVAT + MQL compared to CT + MQL. Similarly, at a feed rate of 0.07 mm/rev the feed force ( $F_z$ ) is decreased by 25%, 9% and 14% for a cutting speed of 15, 20, and 25 m/min, respectively, in the case of UVAT + MQL compared to CT + MQL. However, a significant change in the radial force ( $F_x$ ) between UVAT + MQL and CT + MQL processes has not been observed. The surface quality improved for lower cutting parameters. At a feed rate of 0.07 mm/rev average surface roughness ( $R_a$ ) is decreased by 27 and 10% at cutting speed of 15 and 20 m/min, respectively, in a hybrid compared to CT + MQL. Therefore, for lower machining parameters (UVAT + MQL), the hybrid process can be considered as a promising technique for the machining of nickel-based superalloys.

## References

1. Wang, Z.Y., Rajurkar, K.P., Fan, J., Lei, S., Shin, Y.C., Petrescu, G.: Hybrid machining of Inconel 718. *Int. J. Mach. Tools Manuf.* **43**, 1391–1396 (2003). [https://doi.org/10.1016/S0890-6955\(03\)00134-2](https://doi.org/10.1016/S0890-6955(03)00134-2)
2. Ezugwu, E.O.: Key improvements in the machining of difficult-to-cut aerospace superalloys. *Int. J. Mach. Tools Manuf.* **45**, 1353–1367 (2005). <https://doi.org/10.1016/j.ijmachtools.2005.02.003>
3. Dudzinski, D., Devillez, A., Moufki, A., Larrouquère, D., Zerrouki, V., Vigneau, J.: A review of developments towards dry and high-speed machining of Inconel 718 alloy. *Int. J. Mach. Tools Manuf.* **44**, 439–456 (2004). [https://doi.org/10.1016/S0890-6955\(03\)00159-7](https://doi.org/10.1016/S0890-6955(03)00159-7)
4. Kramar, D.: *Hybrid Machining Processes*. Springer International Publishing (2018)
5. Nath, C., Rahman, M.: Effect of machining parameters in ultrasonic vibration cutting. *Int. J. Mach. Tools Manuf.* **48**, 965–974 (2008)
6. Xiao, M., Karube, S., Soutome, T., Sato, K.: Analysis of Chatter Suppression in Vibration Cutting, vol. 42, pp. 1677–1685 (2002). [https://doi.org/10.1016/s0890-6955\(02\)00077-9](https://doi.org/10.1016/s0890-6955(02)00077-9)
7. Chetan, S., Ghosh, Rao, P.V.: Application of sustainable techniques in metal cutting for enhanced machinability: a review. *J. Clean. Prod.* **100**, 17–34 (2015)
8. Filipovic, A., Stephenson, D.A.: Minimum quantity lubrication (Mql) applications in automotive power-train machining. *Mach. Sci. Technol.* **102**, 3–22 (2006). <https://doi.org/10.1080/10910340500534258>
9. Ekinovi, E., Begovic, E., Prcanovi, H.: Mql Machining of Difficult to Cut Materials, pp. 10–11 (2013)
10. Lawal, S.A., Choudhury, I.A., Nukman, Y.: A critical assessment of lubrication techniques in machining processes: a case for minimum quantity lubrication using vegetable oil-based lubricant. *J. Clean. Prod.* **41**, 210–221 (2013). <https://doi.org/10.1016/j.jclepro.2012.10.016>
11. Feyzi, T., Safavi, S.M.: Improving machinability of Inconel 718 with a new hybrid machining technique. *Int. J. Adv. Manuf. Technol.* **66**, 1025–1030 (2013). <https://doi.org/10.1007/s00170-012-4386-7>

12. Hsu, C.Y., Lin, Y.Y., Lee, W.S., Lo, S.P.: Machining characteristics of Inconel 718 using ultrasonic and high temperature-aided cutting. *J. Mater. Process. Technol.* **198**, 359–365 (2008). <https://doi.org/10.1016/j.jmatprotec.2007.07.015>
13. Pereira, O., Rodríguez, A., Fernández-Abia, A.I., Barreiro, J., López de Lacalle, L.N.: Cryogenic and minimum quantity lubrication for an eco-efficiency turning of AISI 304. *J. Clean. Prod.* **139**, 440–449 (2016). <https://doi.org/10.1016/j.jclepro.2016.08.030>
14. Habtamu, A., Ghosh, S., Rao, P.V.: Experimental study on machinability of Inconel 718 using ultrasonic vibration assisted turning. In: *Proceeding of the 10th International Conference on Precision, Meso, Micro and Nanoengineering (COPEN 10)*, Chennai, India, pp. 583–586 (2017)
15. Chetan, Behera, B.C., Ghosh, S., Rao, P.V.: Wear behavior of PVD TiN coated carbide inserts during machining of Nimonic 90 and Ti6Al4V superalloys under dry and MQL conditions. *Ceram. Int.* **42**, 14873–14885 (2016). [https://doi.org/10.1016/s0890-6955\(03\)00134-2](https://doi.org/10.1016/s0890-6955(03)00134-2)

# Chapter 27

## On Performance Evaluation of Helical Grooved Tool During Rotary Tool Micro-ultrasonic Machining



Sandeep Kumar and Akshay Divedi

**Abstract** The present investigation reports on reduction of width overcut (WOC) and edge chipping in micro-channels developed by rotary tool micro-ultrasonic machining using helical grooved tool. The experiments were conducted to evaluate the effectiveness of the helical grooved tool in terms of WOC and edge chipping. The tool rotation speed, work feed rate, power rating and abrasive size were selected as variable parameters. The results showed that the tool with helical grooved tool assisted the abrasives to replenish from machining zone, thereby reducing the WOC and edge chipping. Both very low and very high tool rotation speed, work feed rate, abrasive mesh size and low power rating resulted in lower WOC and edge chipping. The parametric combination of tool rotation speed 300 rpm, workpiece feed rate 20 mm/min, power rating 40% and abrasive mesh size #1200 resulted in lowest WOC and edge chipping and hence better form accuracy.

**Keywords** Micro-USM · Tool rotation · Micro-channel · WOC · Edge chipping

### 27.1 Introduction

Micro-channels are widely used in micro-fluidic devices and bio micro-electromechanical systems (MEMS) for mixing and analyzing the properties of fluid at micro scale [1]. The micro-fluidic devices are generally made from brittle materials such as glass and ceramic quartz. However, machining of these materials is either very difficult, time-consuming or very costly, specifically in micro-domain. The reason behind this is the superior properties of these materials such as high hardness, high strength and resistance to high temperature. In the past few years, several traditional and non-traditional manufacturing techniques have been used to develop micro-channels on these materials. These techniques include dry and wet etching, LIGA, electrochemical discharge machining, laser, micro-ultrasonic

---

S. Kumar (✉) · A. Divedi  
Department of Mechanical and Industrial Engineering, Indian Institute of Technology Roorkee,  
Roorkee 247667, India  
e-mail: [sandeepkumar71@gmail.com](mailto:sandeepkumar71@gmail.com)

© Springer Nature Singapore Pte Ltd. 2020  
M. S. Shunmugam and M. Kanthababu (eds.), *Advances in Unconventional Machining and Composites*, Lecture Notes on Multidisciplinary Industrial Engineering, [https://doi.org/10.1007/978-981-32-9471-4\\_27](https://doi.org/10.1007/978-981-32-9471-4_27)

335

machining (micro-USM), and so on. But all of these techniques have some limitations. Etching technique is limited to low aspect ratio micro-feature only [2]. LIGA requires an extremely clean environment and costly as well. ECDM and laser caused thermal damage to the work material [3]. Micro-ultrasonic machining (USM) is one of the mechanical-type non-traditional material removal process. It is used for the fabrication of micro-hole, micro-channels and other complex micro-features on hard and brittle materials, such as glass, quartz and ceramics [4]. Micro-USM does not modify the properties of the work material. Both conductive and non-conductive material can be easily machined by this process. In micro-USM, the material removal takes place from the work surface predominantly by the impact and hammering action of the abrasives in the form of tiny chips [5]. Some of the material is removed due to the erosion caused by the cavitation action and chemical reaction between abrasive slurry and the work material [6–8]. The limitations of this process are the low machining rate and high tool wear which hampered its use in many other applications. The literature revealed that the main cause of low machining rate and high tool wear in micro-USM is the debris accumulation in machining gap. In this process, the shape of the machined feature is decided by the tool shape. As the abrasive particle hits the tool, tool wear is inevitable in USM, which affects the dimensional accuracy of final machined cavity. Tool wear depends upon the tool material, shape and size of tool. Pei et al. in their investigation on micro-USM reported that the debris accumulation blocks the abrasive particles movement in the machining zone, which deteriorated the bottom surface of micro-hole [9]. Jain et al. [10] reported that in micro-USM, the relative contact between tool surface and machined cavity was responsible for the excessive tool wear. This deteriorates the form accuracy of machined feature. Cheema et al. [11] reported that higher power rating and higher slurry concentration deteriorated the surface finish and increased the tool wear also. Improper slurry circulation also leads to dimensional inaccuracy (in terms of overcut and edge chipping) of the machined micro-channels. Edge chipping becomes a serious issue where leakage is critical. Therefore, these issues also need to be addressed. In order to overcome the problem of debris accumulation and high tool wear, tool rotation was provided in the existing micro-USM process. This variant is known as rotary tool micro-USM (RTMUSM). The feasibility of RTMUSM to generate micro-features on glass was verified by Kumar and Dvivedi [12, 13]. They reported that the rotary motion of the tool assists the abrasives slurry to replenish from the machining gap. Tool wear also was reduced by providing the rotary motion to the tool. In another investigation, Kumar and Dvivedi [14] reported that desired dimensional accuracy of micro-channels can be obtained by providing tool wear compensation. In order to further enhance the dimensional accuracy of rotary tool micro-USM, tool modification may be applied. Also, tool modification does not require any additional attachment on the existing setup. Therefore, in the present investigation, a helical grooved tool was selected for RTMUSM, and micro-channels were machined on borosilicate glass workpiece. The effect of RTMUSM parameters on the width overcut and edge chipping of micro-channels was analyzed. Further, the quality (in terms of form accuracy) of machined micro-channels was analyzed with the help of scanning electron microscope (SEM) images.

## 27.2 Materials and Methods

### a. Experimental Setup

In this investigation self-developed facility of RTMUSM process, shown in Fig. 27.1, was used to fabricate micro-channels. The main components of RTMUSM setup are ultrasonic generator, rotary transducer, micro-tool, work feeding system and slurry feeding unit. The frequency of ultrasonic generator and maximum amplitude of vibration of the tool are  $21 \pm 1$  kHz and  $20 \mu\text{m}$ , respectively. The maximum tool rotation speed of 2500 rpm can be provided to the tool. The linear motion to the work material was provided with the help of X- and Y-axis table (resolution of  $0.1 \mu\text{m}$ ). The axes were controlled with the help of NC programming unit attached with the facility. Borosilicate glass, silicon carbide and high speed steel (HSS) were selected as work, abrasive and tool material, respectively. The tool along with machined micro-channel is shown in Fig. 27.2. The properties and chemical composition of work material is given in Table 27.1 [15, 16]. Tap water was used as liquid medium for slurry. The slurry was fed at a constant rate throughout the experimentation (Table 27.2).

### b. Process Parameters

The experimentation was carried out by adopting one-factor-at-a-time approach taking tool rotation speed, power rating, feed rate and abrasive size as variable parameters. The WOC and edge chipping were selected as responses in this investigation. The values of variable and constant parameters are given in Table 27.3. The range of process parameters were selected on the basis of literature and successive experiments. Each experiment was conducted thrice and their average was taken as final response value. The WOC and edge chipping are schematically shown in Fig. 27.3.

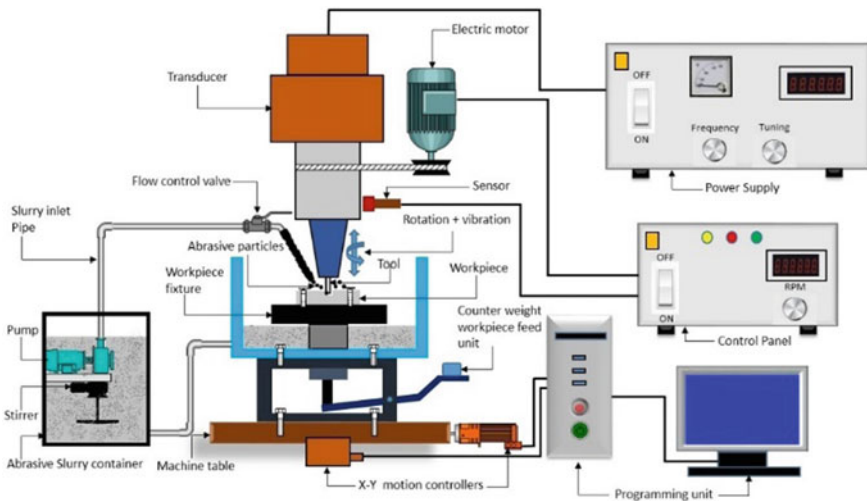
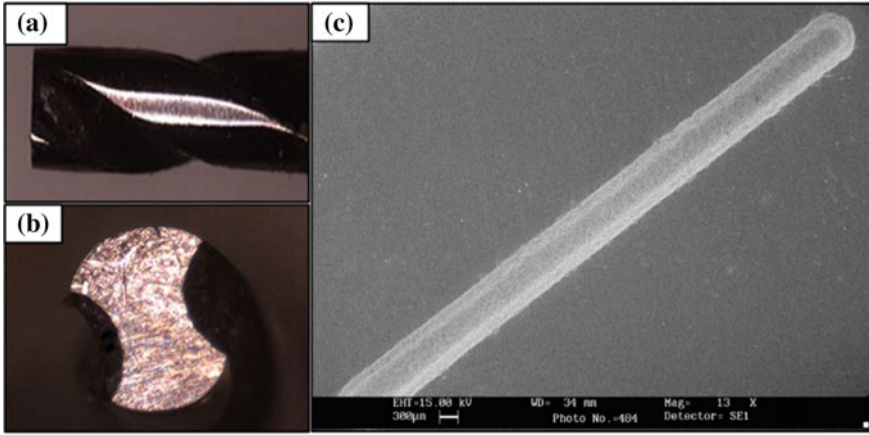


Fig. 27.1 Schematic of rotary tool micro-USM setup





**Fig. 27.2** a, b Front and top view of tool, c SEM image of machined micro-channel

**Table 27.1** Chemical composition of borosilicate glass workpiece

Contents	SiO <sub>2</sub>	B <sub>2</sub> O <sub>3</sub>	Na <sub>2</sub> O + K <sub>2</sub> O	Al <sub>2</sub> O <sub>3</sub>	Mixed
% weight	80.6	13	4	2.4	0.1

**Table 27.2** Properties of borosilicate glass workpiece material

Properties	Value
Coefficient of thermal expansion	$32.5 \times 10^{-7} \text{ cm/cm}^\circ\text{C}$
Density	$2.23 \text{ g/cm}^3$
Melting point	821 °C
Glass transition temperature	525 °C
Poisson’s ratio	0.2
Young’s modulus	$6.4 \times 10^3 \text{ kg/mm}^2$

The WOC was measured using stereo zoom microscope (Make: NIKON, Model: SMZ-746T). The WOC was calculated using the formula given in Eq. 27.1. Edge chipping is the unwanted damage around the edges of the machined micro-channels (as shown in Fig. 27.3). Edge chipping was expressed in percentage and it was calculated using the formula given in Eq. 27.2.

$$WOC (\mu\text{m}) = (W_a - D_t) \tag{27.1}$$

where  $W_a$  and  $D_t$  are the actual width of micro-channel and tool diameter, respectively.

**Table 27.3** Process parameters and their values

S. no.	Parameter	Value
1	Rotational speed (rpm)	100–700
2	Work feed rate (mm/min)	10–25
3	Power rating (%)	10–60
4	Abrasive size (mesh)	#800–#1800
5	Frequency (kHz)	21 ± 1
6	Slurry concentration (%)	20
7	Liquid medium	Water
8	Tool diameter (μm)	850
9	Static load (g)	45
10	Tool material	HSS
11	Workpiece material	Borosilicate glass
12	Abrasive material	Silicon carbide

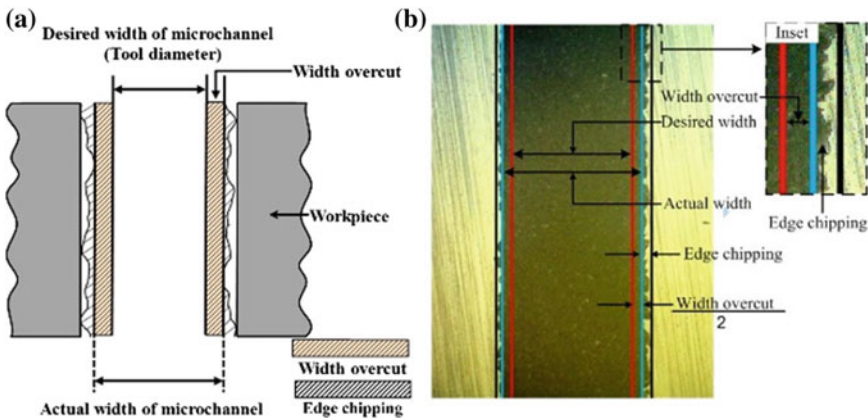


**Fig. 27.3** a Schematic of WOC, b top view of machined micro-channel

$$Edge\ chipping\ (\%) = \frac{(V_t - V_d)}{V_d} \times 100 \tag{27.2}$$

where  $V_t$  and  $V_d$  are the total volume and desired volume of material removed, respectively.

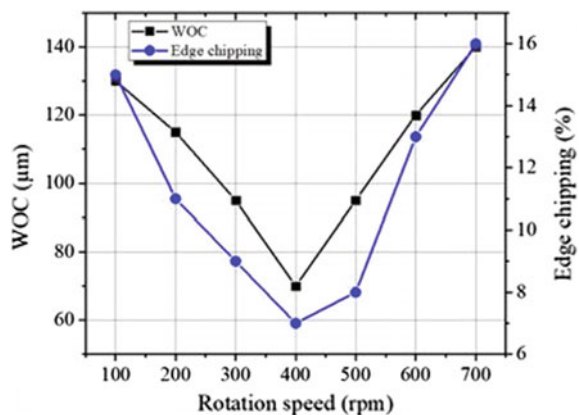
## 27.3 Discussion of Experimental Results

### 27.3.1 Process Parameters Effect on WOC and Edge Chipping

The effect of tool rotation speed on WOC is presented in Fig. 27.4. From Fig. 27.4, it can be clearly seen that as the rotation speed increased from 100 to 400 rpm, both the WOC and edge chipping reduced. Beyond 400 rpm an increasing trend was observed in both WOC and edge chipping. The reason attributed to the observed trend was that rotary motion of tool exerted centrifugal force on abrasive slurry. The centrifugal force eases the circulation of abrasives in the machining zone. On increasing the tool rotation speed, centrifugal force on abrasive slurry was increased, leading to faster slurry replenishment. In addition, the helical groove provided extra space to the abrasives slurry to enter and exit from machining zone (as shown in Fig. 27.5). As a result of that, WOC and edge chipping reduced. The minimum WOC and edge chipping were achieved at 400 rpm. Also, the tool rotation speed of 400 rpm resulted in maximum depth and better form accuracy of micro-channel (Fig. 27.6a). This implies that tool rotation speed of 400 rpm was sufficient for effective circulation of slurry. Beyond 400 rpm, excessive centrifugal force applied on the slurry due to which the abrasives present in the slurry stroked on the edges and side wall of the machined micro-channel. Consequently, WOC and edge chipping increased.

The effect of feed rate on WOC and edge chipping is presented in Fig. 27.7. It was observed that the WOC and edge chipping initially decreased up to 20 mm/min of feed rate and after that both started to increase (Fig. 27.7). It is believed that the feed rate governs the time of interaction between abrasive, tool and work material. At lower feed rate, interaction time was more due to which abrasives contributed to machining for longer period of time and higher WOC and edge chipping were obtained. On the other hand, at very high feed rate (i.e. beyond 20 mm/min), interaction time between tool, abrasives and work material significantly reduced due to which lesser

**Fig. 27.4** Rotation speed effect on WOC and edge chipping



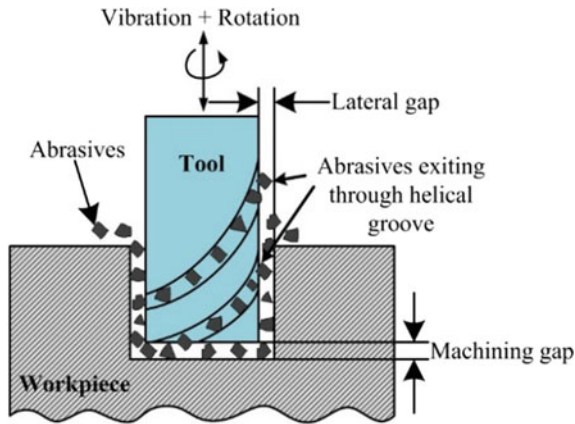
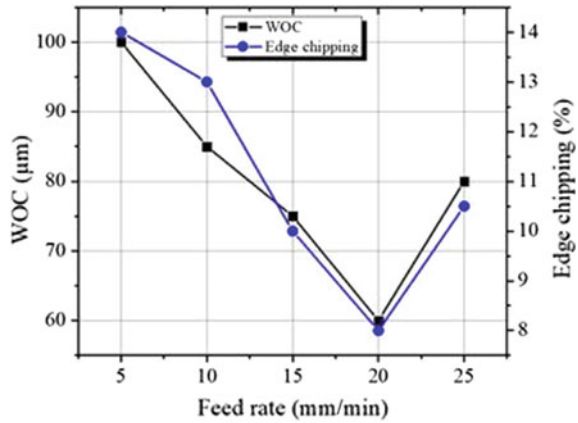


Fig. 27.5 Schematic representation showing abrasive replenishment through helical grooves

Process parameters	Cross-sectional front view	Top view	Dimensional accuracy
(a) Tool rotation speed (400 rpm)			Depth = 740 μm WOC = 70 μm Edge chipping = 7%
(b) Feed rate (20 mm/min)			Depth = 700 μm WOC = 60 μm Edge chipping = 8%
(c) Power rating (20%)			Depth = 750 μm WOC = 75 μm Edge chipping = 8%
(d) Abrasive size (#1200mesh)			Depth = 690 μm WOC = 65 μm Edge chipping = 9%

Fig. 27.6 Cross-sectional and top view of machined micro-channels

**Fig. 27.7** Feed rate effect on WOC and edge chipping



quantity of abrasives took part in machining. Moreover, there might be a direct contact between tool and work material causing damage to sidewall of micro-channel. Consequently, higher WOC and edge chipping were observed. The feed rate of 20 mm/min was found to be sufficient for tool abrasive and workpiece interaction. The maximum depth of micro-channel and good form accuracy were obtained at 20 mm/min (Fig. 27.6b).

The power rating is directly related to the impact energy imparted by the tool to the work surface via abrasive particles. Power rating has a linear relation with the amplitude of vibration. Figure 27.8 illustrates the effect of power rating on WOC and edge chipping. From Fig. 27.8, it can be observed that on increasing power rating, the WOC and edge chipping were found to be increased. At power rating of 20%, both the WOC and edge chipping were low due to lesser impact energy transfer to abrasive particles on work surface. On increasing the power rating from 20 to 70%, the impact energy significantly increased and deep crater was created by the

**Fig. 27.8** Power rating effect on WOC and edge chipping

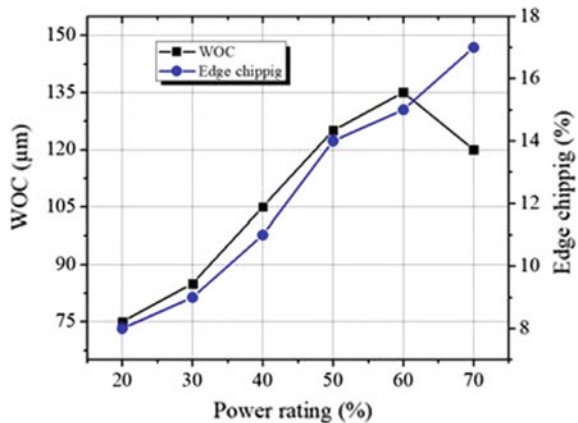
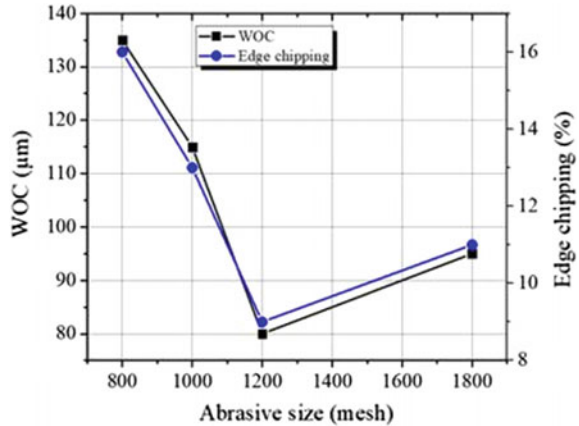


**Fig. 27.9** Abrasive size effect on WOC and edge chipping



impact of abrasives. Thus, WOC and edge chipping increased. The form accuracy of micro-channel at 20% of power rating was found to be better (Fig. 27.6c).

The size of abrasive particle greatly affects the performance of micro-USM because in USM, the width of the machined cavity is defined as the sum of tool diameter and twice of the abrasive particle size [4]. The abrasive mesh size has inverse relation with average grain diameter of abrasive particle. The effect of abrasive mesh size on the WOC and edge chipping is presented in Fig. 27.9. From Fig. 27.9, it can be seen that on increasing the abrasive size from #800 mesh to #1200 mesh, both the WOC and edge chipping decreased. The average grain diameter of abrasive particles reduced by increasing the mesh size, due to which the lateral gap (the gap between the side wall of cavity and tool surface) decreased. Thus, low WOC was obtained. The damage at the edges of the micro-channels was also reduced due to the smaller grain diameter of abrasives. On further increasing the abrasive mesh size from #1200 mesh to #1800 mesh, the average grain diameter significantly reduced. This caused the formation of multiple abrasives layers in machining gap. The multiple layers of abrasives when exited through the lateral gap increased the WOC and edge chipping. The form accuracy of the micro-channels was better when #1200 mesh size abrasive particles were used (Fig. 27.6d). This implies that a uniform layer of abrasive particles circulated while using #1200 mesh size abrasives.

## 27.4 Conclusions

In the current investigation, the effectiveness of tool with helical groove in rotary tool micro-USM was evaluated. Experiments were conducted on borosilicate glass work material as per OFAT approach. The RTMUSM parameters, namely tool rotation speed, feed rate, power rating and abrasive size, varied and the performance was

evaluated in terms of WOC and edge chipping. The conclusions drawn from this investigation are summarized as follows:

- The helical grooved tool was found to be an effective solution for abrasive replenishment in RTMUSM.
- Micro-channels were developed on glass using helical grooved tool in RTMUSM.
- For an increase in tool rotation speed, feed rate and abrasive size, the WOC and edge chipping initially decreased and after that both increased.
- By increasing power rating, the WOC and edge chipping were found to increase.
- The lowest WOC and edge chipping were observed at rotation speed = 400 rpm, work feed rate = 20 mm/min, power rating = 20% and abrasive size = 1200 mesh, respectively.
- Further, there is a need to optimize the process parameters of rotary tool micro-USM using helical grooved tool to achieve the minimum WOC and edge chipping simultaneously.

## References

1. Yao, P., Garrett, J.S., Prather, D.W.: Three-dimensional lithographical fabrication of microchannels. *J. Micro-Electro-Mech. Syst.* **14**, 799–805 (2005)
2. Jáuregui, A.L., Siller, H.R., Rodríguez, C.A., Elías-Zúñiga, A.: Evaluation of micromechanical manufacturing processes for microfluidic devices. *Int. J. Adv. Manuf. Technol.* **48**, 963–972 (2010)
3. Liu, X., DeVor, R.V., Kapoor, S.G., Ehmann, K.F.: The mechanics of machining at the micro-scale: assessment of the current state of the science. *J. Manuf. Sci. Eng.* **126**, 666–678 (2004)
4. Pandey, P.C., Shan, H.S.: *Modern Machining Processes*, pp. 7–38. Tata McGraw-Hill Education Pvt. Ltd. (1980)
5. Thoe, T.B., Aspinwall, D.K., Wise, M.L.H.: Review on ultrasonic machining. *Int. J. Mach. Tools Manuf.* **38**(4), 239–255 (1998)
6. Shaw, M.C.: Ultrasonic grinding. *Microtechnic* **10**(6), 257–265 (1956)
7. Cook, N.H.: *Manufacturing Analysis*, pp. 133–138. Addison-Wesley, New York (1996)
8. Miller, G.E.: Special theory of ultrasonic machining. *J. Appl. Phys.* **28**(2), 149–156 (1957)
9. Pei, W., Yu, Z., Li, J., Ma, C., Xu, W., Wang, X., Natsu, W.: Influence of abrasive particle movement in micro USM. *Procedia CIRP* **6**, 551–555 (2013)
10. Jain, V., Sharma, A.K., Kumar, P.: Fabrication of microchannels using layer-by-layer machining in micro USM. In: *Proceedings of the All India Manufacturing Technology Design and Research Conference, Jadhavpur, India* (2012)
11. Cheema, M.S., Dvivedi, A., Sharma, A.K., Acharya, S.: Experimental investigations in development of 3D microchannels through ultrasonic micromachining. In: *Proceedings of the 9th International Workshop on Microfactories, Honolulu, USA*, pp. 92–95 (2014)
12. Kumar, S., Dvivedi, A.: Investigations on fabrication of microchannels using rotary tool micro-ultrasonic machining. In: *Proceedings of the All India Manufacturing Technology Design and Research Conference, Pune, India*, pp. 444–447 (2016)
13. Kumar, S., Dvivedi, A.: Experimental investigation on drilling of borosilicate glass using micro-USM with and without tool rotation: a comparative study. *Int. J. Addit. Subtract. Mater. Manuf.* **1**(3–4), 213–222 (2017)

14. Kumar, S., Dvivedi, A.: Fabrication of microchannels using rotary tool micro-USM: an experimental investigation on tool wear reduction and form accuracy improvement. *J. Manuf. Process.* **32**, 802–815 (2017)
15. Chemical composition of borosilicate glass. 05 May 2018. <http://www.udel.edu/chem/GlassShop/PhysicalProperties.htm>
16. Properties of borosilicate glass. 05 May 2018. <http://www.technosklo.com/userdata/properties-of-manufactured-glasses>



# Chapter 28

## Experimental Investigation on Surface Topography of the Natural Ceramics in Abrasive Water Jet Cutting and Its Optimization Validation by Formulated Model



Vijay Mandal , Amandeep Singh , Ganesh Singh Yadav ,  
J. Ramkumar  and S. Agrawal 

**Abstract** In the recent past, many researchers have examined the striation and taper angle emergence on the machined surface of several kinds of materials, machined through Abrasive Water Jet (AWJ). There are a few investigations that focused on the undesirable striation and taper angle formation on the machined surface of natural ceramics. In this work, machining of three different natural ceramic materials such as granite, white marble, and gray marble, is carried out through the AWJ process. The influence of the machining process parameters on zone thickness, kerf striation angle and kerf taper angle were investigated. In order to understand the surface morphology, the machined surface is divided into three different zones such as smooth (Zone 1,  $0^{\circ}$ – $5^{\circ}$ ), transition (Zone 2,  $5^{\circ}$ – $10^{\circ}$ ), and rough (Zone 3,  $>10^{\circ}$ ) respectively. The entire result shows good agreement between the formulated model (using Buckingham's  $\pi$ -theorem) and Response Surface Methodology (RSM).

**Keywords** Striation angle · Kerf taper angle · AWJ

---

V. Mandal (✉) · J. Ramkumar

Department of Mechanical Engineering, Indian Institute of Technology Kanpur, Kanpur 208016, India

e-mail: [vijaym@iitk.ac.in](mailto:vijaym@iitk.ac.in)

A. Singh

Department of Industrial and Production Engineering, NIT, Jalandhar 144011, India

G. S. Yadav · S. Agrawal

Department of Mechanical Engineering, BIET, Jhansi 284128, India

© Springer Nature Singapore Pte Ltd. 2020

M. S. Shunmugam and M. Kanthababu (eds.), *Advances in Unconventional Machining and Composites*, Lecture Notes on Multidisciplinary Industrial Engineering, [https://doi.org/10.1007/978-981-32-9471-4\\_28](https://doi.org/10.1007/978-981-32-9471-4_28)

## 28.1 Introduction

Natural ceramics have excellent mechanical and physical properties, owing to their strong chemical bonds. The remarkable properties of ceramics are high hardness, electrical insulation, lightweight, and high wear, heat, pressure and chemical resistance. Abrasive Water Jet (AWJ) machine is generally utilized for the cutting and processing of hard materials. This process offers advantages such as the absence of heat affected zone and ability to machine both conducting as well as non-conducting materials [1]. Numerous research articles were published on the topography and most of these suggested minimizing the striation and kerf taper angle formation in the AWJ machined surface components, and it has been found that the quality of surface significantly depends on material properties and operating process parameters. The material properties such as hardness and density of the stone and working parameters such as pump pressure and traverse speed are found as influencing factors which affect the topography of the stones [2, 3]. Undesirable striation formation in the machined surface is directly associated with machining inaccuracy. Due to inaccuracy, micromechanism of step striation formation was studied at different times and working traverse speeds [4, 5]. Moreover, the machined surface is divided into different zones for the better evolution of surface morphology [6, 7], an experiment was conducted to perform machining using different jet impact angles and investigated the surface quality. It was found that the value of parameters such as Sq (Root Mean Square), Sz (Maximum height), and SA (Average Roughness) decreases when the jet angle is  $70^\circ$  while only Sa value decreases if the jet angle is  $90^\circ$ . Researchers have reported various material removal mechanisms, of which erosion process is the most prominent mechanism [8]. The machining of ceramic materials such as marble and glass is also done through AWJ. From the experiments, it was observed that poor surface finish prevails with an increase in traverse speed and standoff distance [9, 10]. Also, tried multi-mode operations such as cutting, milling, and counter sinking associated with abrasive water jet to investigate the influence of surface quality and geometrical accuracy. Also, multi-mode operations such as cutting, milling, and counter sinking associated with abrasive water jet machining were performed and the dependence of process parameters on the machined surface quality and geometric accuracy was investigated [11]. Furthermore, many researchers examined the kerf taper angle with various machining process parameters by statistical analysis. It was reported that the nozzle traverse speed as the most considerable process parameter [12].

The present study deals with the machining of three different natural ceramics through abrasive water jet and validate the formulated model (by using dimensional analysis) and RSM. Initially, the machined surface quality is good, however, due to an abrupt change in material removal rate; it leads the step formation at the bottom of the machined surface. Hence, to overcome all these problems, cut depth divided into three different zones to examine the better morphology of the surface.

### 28.2 Materials and Methods

The experiments were carried out using a CNC controlled AWJ machine, OMAX 2652. The complete setup consisted of a controller, cutting head, nozzle, high-pressure intensifier pump, abrasive delivery system, and catcher tank. The experimental setup is shown in Fig. 28.1. The CNC code is written that gives the cutting path to the nozzle. The specimens were machined in a rectangular prism of dimensions (50 × 50 × 20) mm. The cutting conditions, taken were: abrasive size (80 mesh, U.S. STD), abrasive flow rate (0.300 kg/min), mixing tube diameter (0.7620 mm), and pressure (1500 bar) respectively.

The nomenclature and properties of the ceramics, i.e., granite, white marble, and gray marble listed in Table 28.1. The values of properties of materials are sequenced in the order of granite, white marble, and gray marble respectively.

Trial experiments were performed to obtain the optimum range of working parameters such as traverse speed and standoff distance. Machining at the lower traverse speed resulted in high energy consumption, and at the higher traverse speed, the abrasive particles were not successfully able to machine through the entire thickness

**Fig. 28.1** Experimental setup of abrasive water jet machine (OMAX 2652)

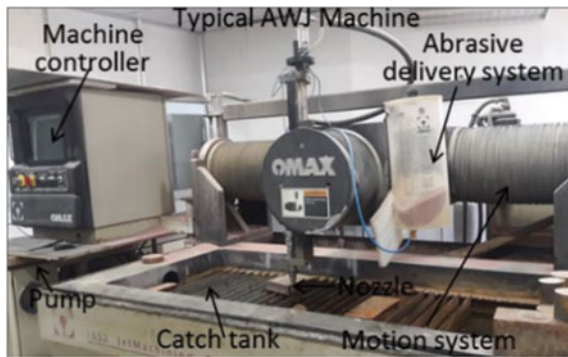


**Table 28.1** Nomenclatures and properties of natural ceramic materials [13]

TS = Traverse speed (mm/min)	Wb = Bottom kerf width (mm)
SoD = Standoff distance (mm)	Wt = Top kerf width (mm)
Z = Zone thickness (mm)	T = Thickness of workpiece (mm)
P = Jet pressure (1500 bar)	$\sigma_c$ = Compressive strength (150, 55.85, 87.6 MPa)
$m_a$ = Mass flow rates (0.3 kg/min)	$\lambda_f$ = Fracture toughness (1.83, 0.87, 1.56 MPa m <sup>0.5</sup> )
$d_n$ = Nozzle diameter (0.762 mm)	H = Vickers's hardness (1107.6, 498, 235 HV)
$\theta$ = kerf taper angle (degree)	Density (2720, 2727, 2705 kg/m <sup>3</sup> )
$\rho_p$ = Particle density (4000 kg/m <sup>3</sup> )	Young's modulus (91.12, 58.57, 72.94 GPa)
$d_p$ = Particle diameter (0.177 mm)	Tensile strength (4.89, 8.65, 7.52 MPa)
$\rho_w$ = Water density (1000 kg/m <sup>3</sup> )	Coefficient of friction (0.9–1, 0.6–0.8, 0.6–0.8)

**Table 28.2** Input process parameters

Parameters	Level				
	1	2	3	4	5
Standoff distance (SOD) (mm)	1	1.5	2	2.5	3
Traverse speed (TS) (mm/min)	48	62	87	138	162

of the sample. Design of experiments was conducted using RSM to obtain the values of the variables, as shown in Table 28.2.

After cutting, the machined surface of the samples was polished by emery papers for five hours for each sample. The emery papers grit size was from 500 to 2000 g/in. The specimens were then dried with the help of an air dryer, followed by cloth polishing. Vickers hardness was determined using the microhardness testing machine with a load of 100 g and indentation time of 10 s. Each specimen was indented at ten separate points on the surface, and the values were averaged. The average microhardness value of the ceramic granite, white marble, and gray marble was found to be 1107.6 HV<sub>0.05</sub>, 498.4 HV<sub>0.05</sub>, and 235.6 HV<sub>0.05</sub> respectively.

The 13 combinations of experiments were obtained for each material by central composite design (CCD) using Design-Expert software (DoE). After machining, the images of machined surfaces were captured by a microscope. The microscopic images are shown in Fig. 28.2. It was found that the surface roughness of the samples

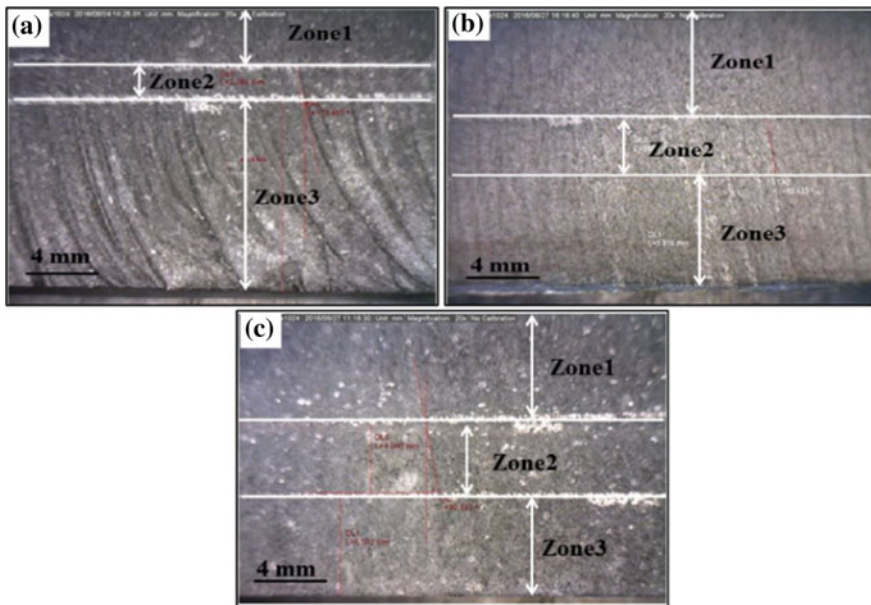


**Fig. 28.2** Optical microscope images of the machined surface at a standoff distance of 2 mm and traverse rate of 162 mm/min of work material **a** granite, **b** white marble, and **c** gray marble

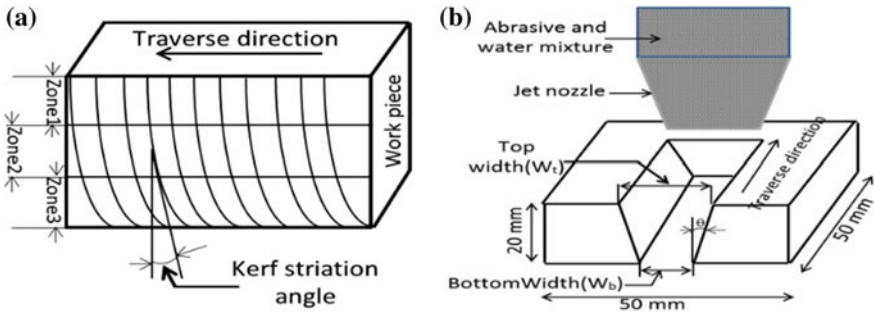


Fig. 28.3 Schematic diagram of **a** zone thickness or kerf striation angle, **b** kerf taper angle ( $\theta$ )

was not uniform throughout the machined surface. Also, from the captured images, the kerf striation was observed on the machined surfaces. Present images show that the surface finishes on the machined surface, in the direction of the abrasive jet is better at the initial stage, and kerf deviation is less in comparison to the later stages. The stages here start from the top of the images and proceed towards the bottom.

In order to examine the surface morphology of the machined surface, it is divided into three different zones: Zone 1, Zone 2, and Zone 3 as shown in Fig. 28.3a. The machined surface was divided into different zones. These zones are categorized according to a surface finish of the machined work samples [6]. In the present study, the machined surface divided into three different zones based on the angle of deviation (kerf striation angle) with the vertical axis. An optical microscope was used to determine the kerf striation angle. Kerf striation angles  $0^{\circ}$ – $5^{\circ}$ ,  $5^{\circ}$ – $10^{\circ}$  and beyond  $10^{\circ}$  were considered as a smooth zone, transition zone, and rough zone respectively.

Kerf taper angle (or taper angle) is one of the fundamental issues that determine the exactness of the machining accuracy. In the AWJ machining, the formation of kerf walls is not equally inclined, because of the “jet tail back affect” [12] as shown in Fig. 28.3b. The kerf taper angle for each sample was measured using a microscope. Four replications for the top and bottom width of the kerf taper angle zone were taken, and the values were averaged. The taper angle is calculated using the Eq. (28.1).

$$\theta = \tan^{-1} \frac{(W_t - W_b)}{2T} \tag{28.1}$$

where  $\theta$  = kerf taper angle,  $W_b$  = bottom kerf width,  $W_t$  = top kerf width,  $T$  = thickness of workpiece. This value of the  $\theta$  was used as a response parameter.

## 28.3 Results and Discussion

### 28.3.1 Model Fitting and Statistical Analysis

After conducting the experiments, the data obtained was to be analyzed. The process variables such as A (SoD mm), B (TS mm/min), and C (Materials, i.e., granite (Gr), white marble (Wm), and gray marble (Gm)), and responses such as Zone 1, Zone 3, and  $\theta$  were taken. It is evident from Fig. 28.2 that Zone 1 needs to be maximized; Zone 3, and  $\theta$  are minimized for the best results. Zone 2, which is a transition zone, was avoided as it does not influence the process when the other two zones are taken.

#### 28.3.1.1 Analysis of Zone Thickness

ANOVA was used to determine the variables influencing the process. Tables 28.3 and 28.4 summarize the ANOVA results for Zone 1 and Zone 3. Table 28.3 suggested that transverse speed, standoff distance, and material significantly influence the kerf striation angles for Zone 1. However, Zone 3 is influenced by only the transverse speed and the material, as depicted from the Table 28.4 at 95% significant level (Prob. < 0.05). Regression models were obtained for Zone 1 and Zone 3, with the material as a categorical variable. The resulting model consisted of three equations for the three types of material. Equations for Zone 1 and Zone 3 were:

$$G_r(\text{Zone 1}) = +35.86382 - 9.26804 * SoD - 0.56002 * TS$$

**Table 28.3** ANOVA for Zone 1

Source	Sum of squares (SS)	df	Mean square (MS)	F-value	p-value (Prob > F)
Model	99.35	13	7.64	32.86	<0.0001
A-SoD	1.11	1	1.11	4.77	0.0385
B-TS	59.85	1	59.85	257.39	<0.0001
C-Material	19.58	2	9.79	42.09	<0.0001
AB	0.049	1	0.049	0.21	0.6488
AC	0.015	2	7.368E-003	0.032	0.9689
BC	0.69	2	0.35	1.49	0.2450
A <sup>2</sup>	0.040	1	0.040	0.17	0.6813
B <sup>2</sup>	8.40	1	8.40	36.11	<0.0001
A <sup>3</sup>	0.65	1	0.65	2.78	0.1080
B <sup>3</sup>	9.04	1	9.04	38.87	<0.0001
Residual		5.81	25	0.23	
Cor Total		105.16	38		

**Table 28.4** ANOVA for Zone 3

Source	SS	df	MS	F-value	p-value
Model	214.74	13	16.52	25.76	<0.0001
A-SoD	0.28	1	0.28	0.43	0.5157
B-TS	38.87	1	38.87	60.63	<0.0001
C-Material	158.77	2	79.39	123.81	<0.0001
AB	0.13	1	0.13	0.20	0.6597
AC	2.71	2	1.35	2.11	0.1423
BC	1.40	2	0.70	1.09	0.3519
A <sup>2</sup>	1.75	1	1.75	2.73	0.1110
B <sup>2</sup>	1.25	1	1.25	1.95	0.1746
A <sup>3</sup>	0.29	1	0.29	0.45	0.5100
B <sup>3</sup>	10.62	1	10.62	16.57	0.0004
Residual		16.03	25	0.64	
Cor Total		230.77	38		

$$\begin{aligned}
 & - 3.37719E-003 * SoD * TS + 4.81809 * SoD^2 + 5.00818E-003 * TS^2 \\
 & - 0.78698 * SoD^3 - 1.50100E-005 * TS^3 \tag{28.2}
 \end{aligned}$$

$$\begin{aligned}
 W_m(Zone 1) &= 35.90433 - 9.23938 * SoD - 0.55043 * TS \\
 & - 3.37719E-003 * SoD * TS + 4.81809 * SoD^2 + 5.00818E-003 * TS^2 \\
 & - 0.78698 * SoD^3 - 1.50100E-005 * TS^3 \tag{28.3}
 \end{aligned}$$

$$\begin{aligned}
 G_m(Zone 1) &= 36.96959 - 9.33588 * SoD - 0.55193 * TS \\
 & - 3.37719E-003 * SoD * TS + 4.81809 * SoD^2 + 5.00818E-003 * TS^2 \\
 & - 0.78698 * SoD^3 - 1.50100E-005 * TS^3 \tag{28.4}
 \end{aligned}$$

$$\begin{aligned}
 G_r(Zone 3) &= -6.99693 + 2.38901 * SoD + 0.45225 * TS \\
 & + 5.42105E-003 * SoD * TS - 2.50884 * SoD^2 - 4.75959E-003 * TS^2 \\
 & + 0.52396 * SoD^3 + 1.62736E-005 * TS^3 \tag{28.5}
 \end{aligned}$$

$$\begin{aligned}
 W_m(Zone 3) &= -12.71918 + 3.72951 * SoD + 0.44164 * TS \\
 & + 5.42105E-003 * SoD * TS - 2.50884 * SoD^2 - 4.75959E-003 * TS^2 \\
 & + 0.52396 * SoD^3 + 1.62736E-005 * TS^3 \tag{28.6}
 \end{aligned}$$

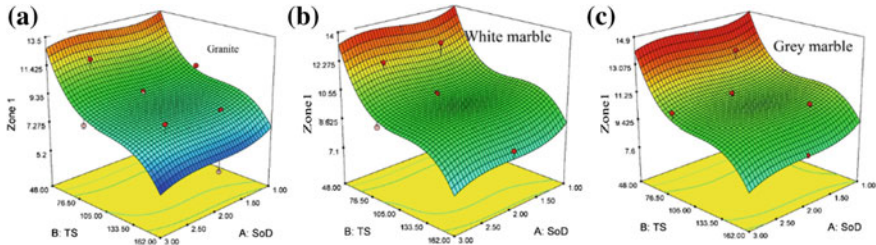


**Fig. 28.4** Influence of the interaction between transverse speed and standoff distance on zone 1 for **a** granite, **b** white marble, and **c** gray marble

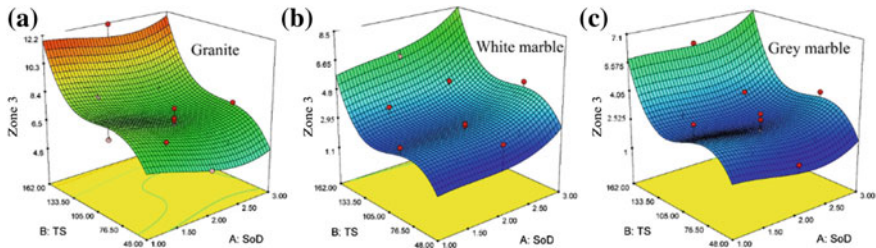


**Fig. 28.5** Influence of the interaction between transverse speed and standoff distance on zone 3 for **a** granite, **b** white marble, and **c** gray marble

$$\begin{aligned}
 G_m(\text{Zone } 3) = & -11.36554 + 2.98851 * SoD + 0.43819 * TS \\
 & + 5.42105E-003 * SoD * TS - 2.50884 * SoD^2 - 4.75959E-003 * TS^2 \\
 & + 0.52396 * SoD^3 + 1.62736E-005 * TS^3 \tag{28.7}
 \end{aligned}$$

Coefficient of determination (R2(adj.)) values for the models for Zone 1 and Zone 3 were 95.59 and 94.47 respectively. Also, it can be seen from the equations that the models for Zone 1 were quadratic and for Zone 3 were cubic. These models were found to be the best fit. Also, cubic models for Zone 1 were also obtained. The difference between the coefficients of the quadratic models and cubic models was not significant. Additionally, the quadratic model and the cubic model exhibited significant differences in coefficients from the linear model. For all the comparisons, the level of significance was taken at 5%. In all the models, it was observed that the influence of TS was much higher in comparison to SoD, which is also evident from Figs. 28.4 and 28.5.

**28.3.1.2 Analysis of Kerf Taper Angle ( $\theta$ )**

Measurement procedure and calculations for  $\theta$  are already discussed in the foregoing sections. Also, we discussed kerf striation and zone thickness of the machined



**Table 28.5** ANOVA for  $\theta$

Source	SS	df	MS	F-value	p-value
Model	9.39	11	0.85	53.19	<0.0001
A-SoD	0.20	1	0.20	12.37	0.0016
B-TS	0.76	1	0.76	47.19	<0.0001
C-Material	8.30	2	4.15	258.61	<0.0001
AB	2.137E-003	1	2.137E-003	0.13	0.7180
AC	0.014	2	7.228E-003	0.45	0.6420
BC	0.068	2	0.034	2.13	0.1381
A <sup>2</sup>	5.436E-003	1	5.436E-003	0.34	0.5653
B <sup>2</sup>	0.041	1	0.041	2.58	0.1197
Residual	0.43	27	0.016		
Cor total		9.82	38		

surface. In this section, the effect of the taper angle with respect to different input process parameters is presented.

Here also, ANOVA was used to determine the variable influencing the process. Table 28.5 summarizes the ANOVA results for  $\theta$ . Regression models were obtained  $\theta$ , with material as a categorical variable. The resulting model consisted of three equations for the three types of material. The obtained models were:

$$G_r(\theta) = +1.26372 - 0.067779 * SoD + 8.18436E-003 * TS + 6.76392E-004 * SoD * TS + 0.035386 * SoD^2 - 3.20195E-005 * TS^2 \tag{28.8}$$

$$G_m(\theta) = +7.21943E-003 - 6.12622E-004 * SoD + 0.011423 * TS + 6.76392E-004 * SoD * TS + 0.035386 * SoD^2 - 3.20195E-005 * TS^2 \tag{28.9}$$

$$G_m(\theta) = +0.069715 - 0.096196 * SoD + 9.96684E-003 * TS + 6.76392E-004 * SoD * TS + 0.035386 * SoD^2 - 3.20195E-005 * TS^2 \tag{28.10}$$

Coefficient of determination (R2(adj.)) values for the models for  $\theta$  was 93.05. For all the comparisons, the level of significance was taken at 5%. In all the models, it was observed that the influence of transverse speed was much higher in comparison of standoff distance, which is also evident from Fig. 28.6. However, the material has the maximum influence (largest F-value in Table 28.5), which can be attributed to the significant difference in the hardness of granite, white marble, and gray marble.

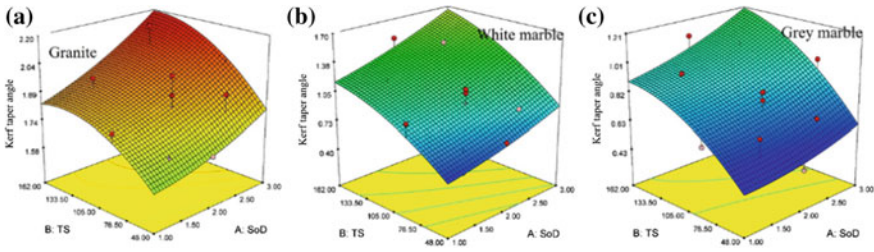


Fig. 28.6 Influence of the interaction between transverse speed and standoff distance on  $\theta$  for **a** granite, **b** white marble, and **c** grey marble

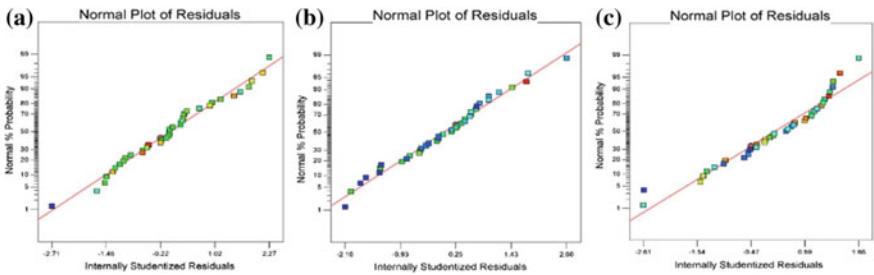


Fig. 28.7 Normal probability plot for **a** zone 1, **b** zone 3, and **c**  $\theta$

The normal probability residual plot of Zone 1, Zone 3, and  $\theta$  is shown in Fig. 28.7a–c, respectively. The present figure shows that most of the points are scattered to the fitted straight line. It makes great acceptability of the current model for these responses.

### 28.3.1.3 Influence of $\theta$ and Zone Thickness on TS and SoD

The kerf striation angle usually increases with an increase in traverse speed because of the exposure time for the complete material removal in a particular section is not sufficient. Alternatively, by increasing the traverse speed, the interaction time between abrasives and the workpiece decreases which leads to its incomplete erosion [14].

The influence of zone thickness (Zone 1 and Zone 3) with respect to input process parameters can be depicted in Figs. 28.4, 28.5, and 28.8a, b, d, e. From the above figures, it was observed that with an increase in traverse speed, Zone 1 thickness decreases nevertheless Zone 3 thickness increases. Also, with an increase in SoD within the selected range, inferior changes occur in Zone 1 the Zone 3 in comparison to those the traverse speed. Moreover, the hardness of gray marble, white marble, and granite are in increasing order. Through the cutting performance of gray marble, a particle of work material removes easily as compared to granite and white marble

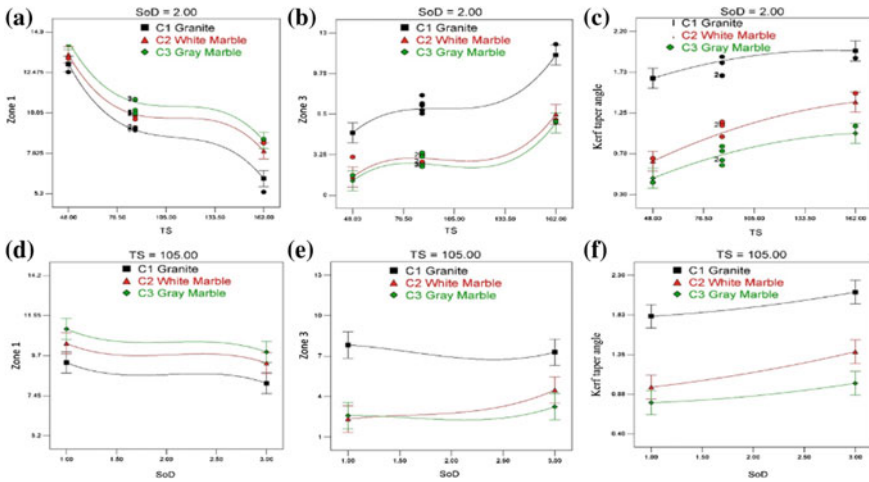


**Fig. 28.8** Influence of the interaction between zone thickness and  $\theta$  on TS **a, b, c** at constant SoD=2 mm and SoD **d, e, f** at constant TS=105 mm/min

because of lower bonding strength. From the above results, it can be concluded that lower the hardness of work material, Zone 1 thickness is larger. Alternatively, among these three work samples, it can be seen that at lower hardness values the surface is better. Figures 28.6a–c and 28.8c, f, represents the variation of  $\theta$  with TS and SoD for three different hardness natural ceramic samples. In this case, also, it was observed that the kerf taper angle increases with an increase in TS and SoD, because of similar process mechanics.

### 28.3.1.4 Optimal Solution

The optimization was carried out using Design-Expert® Software. In this design, to obtain the optimum value of output results, multi-objective optimization was carried out viz., maximize Zone 1, and minimize both Zone 3 and  $\theta$ . It is found that the optimum values of Zone 1, Zone 3, and  $\theta$  are 14.3325 mm, 1.16048, and 0.49 respectively, under the optimum variable setting as SoD = 1.99 mm and TS = 48 mm for gray marble work sample. For the above optimal solution, the desirability of the model is 0.991. From the regression models, gray marble was selected as the best material as it exhibited best results viz. maximum intercept value for Zone 1 (Eq. 28.4) and low intercept value for Zone 3 (Eq. 28.7) and minimum intercept value  $\theta$  (Eq. 28.10). However, for Zone 3, white marble and gray marble showed close intercept values, but gray marble was selected due to its dominance in other variables. This is also evident from Fig. 28.8.

### 28.3.2 Mathematical Model Formulation

After determining the influential process parameters, a mathematical model was formulated using dimensional analysis, to quantify the efficacy of the process. Buckingham’s  $\pi$ -theorem was chosen for this purpose. In AWJ, modeling for kerf taper angle and striation angle involves many variables as shown in Eq. (28.11). Some of the noise variables such as particle interference and particle fragmentation may also influence the kerf taper and striation phenomenon. However, mathematically modeling for these variables is not feasible in the current stage. Also, this makes the theoretical models very less reliable [14]. On the other hand, Buckingham’s  $\pi$ -theorem uses dimensional analysis and thereby offers a technique to simplify such problems.

$$Z \text{ or } \theta = f(TS, SoD, P, m_a, d_n, d_p, \rho_p, \rho_w, H, \sigma_c, \lambda_f) \tag{28.11}$$

All the variables present in the Eq. (28.11), assembled into small nondimensional groups. It has been found that there are three fundamental variables: length, mass, and time out of 12 variables. In this formulation, TS, SoD, and ma are taken as repeating variables, such that the combination of these three always forms nondimensional groups. Sequentially, there are nine independent, nondimensional groups were found form these variables for both the cases, i.e., Z and  $\theta$  by using power law methods as shown in Eqs. (28.12) and (28.13).

$$Z = K \left( \frac{P(SoD)^3}{(TS)m_a} \right)^a (d_n)^b (d_p)^c \left( \frac{(TS)\rho_w(SoD)^3}{m_a} \right)^d \left( \frac{(TS)\rho_p(SoD)^3}{m_a} \right)^e \left( \frac{H(SoD)^3}{(TS)m_a} \right)^f \left( \frac{\sigma_c(SoD)^3}{(TS)m_a} \right)^g \left( \frac{\lambda_f(SoD)^{2.5}}{(TS)m_a} \right)^h \tag{28.12}$$

$$\theta = K \left( \frac{P(SoD)^2}{(TS)m_a} \right)^a \left( \frac{d_n}{SoD} \right)^b \left( \frac{d_p}{SoD} \right)^c \left( \frac{(TS)\rho_w(SoD)^2}{m_a} \right)^d \left( \frac{(TS)\rho_p(SoD)^2}{m_a} \right)^e \left( \frac{H(SoD)^2}{(TS)m_a} \right)^f \left( \frac{\sigma_c(SoD)^2}{(TS)m_a} \right)^g \left( \frac{\lambda_f(SoD)^{1.5}}{(TS)m_a} \right)^h \tag{28.13}$$

The constants a, b, c, d, e, f, g, and h are the degrees of the non-dimensional  $\pi$ -groups, and k is the proportionality factor that can be determined from experiments that are mentioned in the earlier sections of this paper. Multivariate regression analysis is conducted to obtain these values separately for granite, white marble, and gray marble. The corresponding values of fracture toughness ( $\lambda_f$ ), Vickers’s hardness (HV), and Compressive strength (MPa) were used for the three materials. The models for Zone1 and  $\theta$  for granite, white marble, and gray marble are given in Eqs. (28.14)–(28.19), where TS is in mm/min, SoD is in mm,  $\rho_w$  is in  $\text{kg/m}^3$ , ma is in  $\text{kg/min}$ , P is in bar and  $d_n$  is in mm.

$$\text{Zone 1(granite)} = 2.083 \frac{(TS)^{0.5131} (SoD)^{0.0843} \rho_w^{0.2706}}{m_a^{0.2181} P^{0.2425}} \quad (28.14)$$

$$\text{Zone 1(white marble)} = 1.734 \frac{(TS)^{0.354} (SoD)^{0.0324} \rho_w^{0.1847}}{m_a^{0.0124} P^{0.1693}} \quad (28.15)$$

$$\text{Zone 1(grey marble)} = 1.786 \frac{(TS)^{0.345} (SoD)^{0.0708} \rho_w^{0.1847}}{m_a^{0.0236} P^{0.1607}} \quad (28.16)$$

$$\theta(\text{Granite}) = 0.4467 \frac{(TS)^{0.1486} (SoD)^{0.1128} m_a^{0.1486}}{P^{0.1486} d_n^{0.41}} \quad (28.17)$$

$$\theta(\text{White marble}) = 0.781 \frac{(TS)^{0.623} (SoD)^{0.397} m_a^{0.623}}{P^{0.623} d_n^{1.643}} \quad (28.18)$$

$$\theta(\text{Grey marble}) = 0.682 \frac{(TS)^{0.592} (SoD)^{0.227} m_a^{0.592}}{P^{0.592} d_n^{1.411}} \quad (28.19)$$

From the above-formulated equations, it can be seen that the Zone 1 and  $\theta$  primarily depends on parameters TS, SoD,  $\rho_w$ ,  $m_a$ , P and  $d_n$  respectively. It is noted that, in these Eqs. (28.14)–(28.19) a higher degree of a variable represents the more influencing parameters and vice versa. Equations (28.14)–(28.16), and Eqs. (28.17)–(28.19) respectively represent the variation of Zone 1 thickness and  $\theta$  for the different work materials. Also, it has been found from the above equations TS and SoD are proportional to Zone 1 and  $\theta$ . In this equation, the degree of TS is higher as compared to SoD, which indicates that traverse speed is the more influencing parameter. The exponents in the equations give the individual factors influencing similar results as were obtained in the ANOVA models in the previous section of this paper.

## 28.4 Conclusions

The experimental result shows the striation angle (or zone thickness), and the  $\theta$  are influenced by TS, SoD, and hardness of the materials. From the ANOVA and formulated model, it was concluded that the effect of traverse speed is more influencing parameters as compared to SoD in both the cases, i.e., striation and  $\theta$ . The hardness of the work material is also found to be an important characteristic of the surface morphology. Experimental results show that the Zone 1 thickness is comparatively lesser in granite. A higher value of Zone 1 thickness indicates better surface finishing. Therefore, it can state that ceramic work materials with high hardness value, exhibit bad surface finish. The kerf striation and  $\theta$  are reduced by decreasing TS and SoD for each of the work materials (i.e., Granite, White marble, and Gray marble) in the experimental ranges. The model assessment shows optimum values of Zone 1, Zone 3, and  $\theta$  are 14.3325 mm, 1.16048, and 0.49 respectively, under optimum condition of SoD 1.99 mm and TS 48 mm for gray marble work sample.

## References

1. Jurisevic, B., Brissaud, D., Junkar, M.: Monitoring of abrasive water jet (AWJ) cutting using sound detection. *Int. J. Adv. Manuf. Technol.* **24**(9–10), 733–737 (2004)
2. Engin, I.C.: A correlation for predicting the abrasive water jet cutting depth for natural stones. *S. Afr. J. Sci.* **108**(9–10), 1–11 (2012)
3. Momber, A.W., Eusch, I., Kovacevic, R.: Machining refractory ceramics with abrasive water jets. *J. Mater. Sci.* **31**(24), 6485–6493 (1996)
4. Hashish, M., Steele, D.E., Bothell, D.H.: Machining with super-pressure (690 MPa) waterjets. *Int. J. Mach. Tools Manuf.* **37**(4), 465–479 (1997)
5. Orbanic, H., Junkar, M.: Analysis of striation formation mechanism in abrasive water jet cutting. *Wear* **265**(5–6), 821–830 (2008)
6. Valíček, J., Hloch, S., Kozak, D.: Surface geometric parameters proposal for the advanced control of abrasive waterjet technology. *Int. J. Adv. Manuf. Technol.* **41**(3–4), 323 (2009)
7. Yuvaraj, N., Kumar, M.P.: Surface integrity studies on abrasive water jet cutting of AISI D2 steel. *Mater. Manuf. Processes* **32**(2), 162–170 (2017)
8. Matsumura, T., Muramatsu, T., Fueki, S.: Abrasive water jet machining of glass with stagnation effect. *CIRP Ann. Manuf. Technol.* **60**(1), 355–358 (2011)
9. Abdullah, R., Mahrous, A., Barakat, A.: Surface quality of marble machined by abrasive water jet. *Cogent Eng.* **3**(1), 1178626 (2016)
10. Zhong, Z.W., Han, Z.Z.: Turning of glass with abrasive waterjet. *Mater. Manuf. Process.* **17**(3), 339–349 (2002)
11. Kong, M.C., Srinivasu, D., Axinte, D., Voice, W., McGourlay, J., Hon, B.: On geometrical accuracy and integrity of surfaces in multi-mode abrasive waterjet machining of NiTi shape memory alloys. *CIRP Ann. Manuf. Technol.* **62**(1), 555–558 (2013)
12. Gupta, V., Garg, M.P., Batra, N.K., Khanna, R.: Analysis of kerf taper angle in abrasive water jet cutting of Makrana white marble. *Asian J. Eng. Appl. Technol.* 35–39 (2013)
13. Wong, T.F., Wong, R.H., Chau, K.T., Tang, C.A.: Microcrack statistics, Weibull distribution and micromechanical modeling of compressive failure in rock. *Mech. Mater.* **38**(7), 664–681 (2006)
14. Shanmugam, D.K., Wang, J., Liu, H.: Minimisation of kerf tapers in abrasive waterjet machining of alumina ceramics using a compensation technique. *Int. J. Mach. Tools Manuf.* **48**(14), 1527–1534 (2008)

# Chapter 29

## Prediction and Comparison of Vision Parameter of Surface Roughness in WEDM of Al-6%Si<sub>3</sub>N<sub>4</sub> and Al-10%Si<sub>3</sub>N<sub>4</sub> Using ANN



H. R. Gurupavan, H. V. Ravindra and T. M. Devegowda

**Abstract** The need for composite material has increased in various sectors due to the technological developments and requirement of complex shapes in the manufacturing sectors. Metal matrix composites are the most widely used composite materials. Due to the presence of abrasive reinforcing particles, conventional machining of these causes severe tool wear and hence reduces the life of the cutting tool. This difficulty can be overcome by using an advanced machining technique. One such advanced machining technique is Wire Electrical Discharge Machining (WEDM). WEDM is a thermal machining method used for cutting any conductive materials and capable of precisely cutting parts of hard materials with complex shapes. This paper focuses on the prediction and comparison of vision parameter of surface roughness during wire electrical discharge machining of Al-6%Si<sub>3</sub>N<sub>4</sub> and Al-10%Si<sub>3</sub>N<sub>4</sub> composite materials. Stylus instruments are widely used for measuring surface roughness of machined components, which have limited flexibility in handling various machined parts. Due to high resolution, reliability, and ease of automatic processing of data, vision systems are recently being exploited for various measurements. Using the machine vision system, the surface images of machined specimens were acquired. Based on the analysis of the distribution of light intensity of a rough surface, the surface roughness (Ga) of a machined component is measured. Surface roughness prediction was carried out successfully for the two composite materials using Artificial Neural Networks (ANN). From the results, it was observed that, measured and predicted vision parameters of surface roughness (Ga) values correlated well with ANN.

**Keywords** WEDM · Surface roughness · Machine vision and ANN

---

H. R. Gurupavan (✉) · H. V. Ravindra · T. M. Devegowda  
Department of Mechanical Engineering, P.E.S. College of Engineering, Mandya, Karnataka  
571401, India  
e-mail: [gpavan1989@gmail.com](mailto:gpavan1989@gmail.com)

© Springer Nature Singapore Pte Ltd. 2020  
M. S. Shunmugam and M. Kanthababu (eds.), *Advances in Unconventional Machining and Composites*, Lecture Notes on Multidisciplinary Industrial Engineering, [https://doi.org/10.1007/978-981-32-9471-4\\_29](https://doi.org/10.1007/978-981-32-9471-4_29)

361

## 29.1 Introduction

Wire Electrical Discharge Machining (WEDM) is an advanced machining process used to cut a component to obtain the desired shape by a series of electrical discharges (sparks). WEDM serves as the best alternative for making tools, microscale parts and dies with a good surface finish and dimensional accuracy. The effect of WEDM process parameters on the surface roughness is to be investigated experimentally. Analyzing the effectiveness of all the parameters is a very tedious task. Hence, various techniques are being used to analyze the parameters for better results. Many researchers have investigated the process parameter effects on the surface roughness of the machined component. For process control and product quality control, evaluation of surface texture is essential. Mechanical surfcomflex, a widely used instrument is used to evaluate the surface texture, which has limited flexibility in handling various machined parts.

Due to high resolution, reliability, and ease of automatic processing of data, vision systems are recently being exploited for various measurements. The First step in the Machine Vision system is to capture the images using cameras and lighting, which are designed to provide a better variation required by subsequent processing. Various image processing techniques in MV software packages are used to extract the required information.

The texture of the machined surface is dramatically affected by the state of the Worn electrode in WEDM. By applying image enhancement techniques and image segmentation, Problems of image noise and nonuniform illumination can be reduced. In recent years, the surface roughness of a workpiece is inspected using computer vision techniques. Using a digital camera the surface image of the machined component is first captured and then surface image features are extracted. In order to construct the relationships between the feature of the surface image and the actual surface roughness, a polynomial network using a self-organizing adaptive modeling method is applied [1]. A machine vision system has been used to acquire the images and then regression analysis is applied for the quantification of the surface roughness of machined components. Using Cubic Convolution interpolation technique original images have been magnified. Using regression analysis, surface image parameter ( $G_a$ ) has been estimated [2]. Image analysis is easier and more flexible due to the development of high-speed digital computers and vision systems. These systems have the advantages of analyzing an area from the surface of the image rather than a single line, unlike the stylus instruments [3]. The traditional light section microscope in machine vision was designed to measure the surface roughness of the machined component. Various surface roughness parameters can be automatically measured using a specially designed vision system and it was proved that the designed vision system has a satisfying measurement precision [4]. To predict the surface roughness in WEDM of WP7V steel, Artificial Neural Network (ANN) model is developed. Experiments are conducted based on the  $L_{16}$  orthogonal array and experimental results are used to train the neural network model. The mathematical relation between WEDM cutting parameters and the workpiece surface roughness is also established by MRA.



Estimated values of roughness by ANN and MRA are compared with measured values. Good correlation can be obtained between experimental results and predicted values in the neural network with two hidden layers [5].

The present work analyzes images of workpiece surface roughness in Wire EDM, and Prediction and comparison of surface roughness of two composite materials using the artificial neural network.

## 29.2 Experimental Work

CONCORD DK7720C CNC Wire EDM was used to conduct the experiments. Wire EDM machine consists of servo control system, wire electrode, dielectric supply system, a power supply, and work table. According to the material and height of the component the input parameters of the Concord WEDM machine can be selected. Reusable wire technology is a special feature in Wire EDM., i.e., wire can be reused by adopting the re-looping wire technology, instead of throwing out after its first use. Figure 29.1 shows the WEDM experimental setup. Generally Wire EDM process has many stages like rough cut, rough cut phase with finishing, and finishing phase. But only one pass is used in this Wire EDM.

Using a computer controlled positioning system, a gap of 0.02 mm is constantly maintained between wire and workpiece. Molybdenum wire electrode of 0.18 mm diameter was used in WEDM. The selected process parameters in WEDM are as listed in Table 29.1. Based on experts and review of literature, the process parameters were selected.

**Fig. 29.1** WEDM experimental setup



**Table 29.1** WEDM parameters and their levels used in experiments

Process parameters	Levels		
	I	II	III
Pulse-on time ( $\mu\text{s}$ )	20	24	28
Pulse-off time ( $\mu\text{s}$ )	5	6	7
Current (A)	4	5	6
Bed speed ( $\mu\text{m/s}$ )	30	35	40

### 29.2.1 Surface Roughness Measurement

In the present work, surface roughness ( $G_a$ ) is measured on the basis of the analysis of the distribution of light intensity on a rough surface of workpiece.

Experiments were carried out to investigate the feasibility of vision-based parameters for the measurement of surface roughness generated by machining processes. For getting different roughness values experiments were performed on CNC Wire EDM. The stylus parameter average surface roughness ( $R_a$ ) of these specimens was measured using stylus-instrument. The image acquired by the machine vision system is shown in Fig. 29.2.

Figure 29.3 shows the surface image of the machined workpiece and Fig. 29.4 is the histogram equalized image of the same. In order to illuminate the rough surface of the workpiece a good fluorescent light source was used in machine vision system. Nikon D-90 high resolution digital camera was used to capture an image of the reflected light. Analysis of the captured image was done by a program written in Matlab software using image processing toolbox. Using this program average surface roughness vision parameter of stored image was computed.

In order to identify whether the optical parameters are sufficient to characterize a surface of the workpiece, average surface roughness ( $R_a$ ) was compared with the

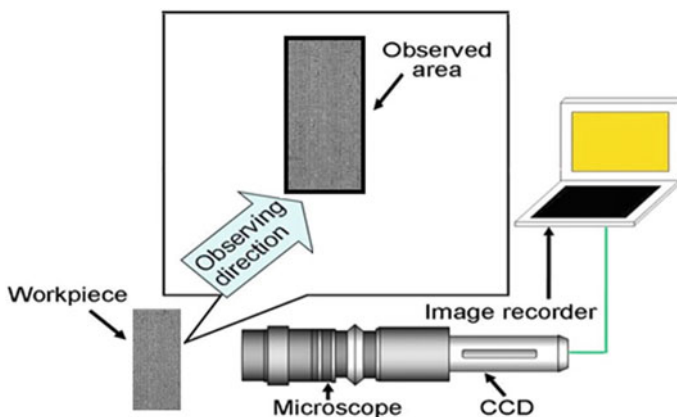
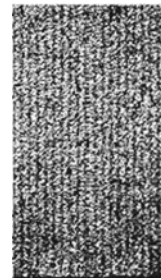


**Fig. 29.2** Machine vision system for measuring surface roughness

**Fig. 29.3** Machined surface image



**Fig. 29.4** Histogram equalized image



Vision roughness parameter ( $G_a$ ). Vision parameter of surface roughness is calculated based on the distribution of the peaks on the surface, i.e., It was assumed that more light will reflect from the peaks on any surface than its surroundings. The binary image is converted from gray image by assigning “1” for pixel having more light intensity values than its surrounding pixels in the cell and remaining all into “0”.

***Vision-Based Parameter Computed***

The arithmetic average value of the gray level intensity was calculated by the relation

$$G_a = \frac{1}{N} \sum_{x=0}^{255} (F_i X_i) \tag{29.1}$$

where  $N$  is the total number of pixels in the distribution,  $X_i$  are the gray levels ( $i = 0, 1, 2, 3, 4, \dots, 255$ ),  $F_i$  is the number of pixels at gray-level  $X_i$ .

**29.3 Introduction to Artificial Neural Network (ANN)**

ANN is an artificial representation of the human brain, which is made by interconnecting neurons. For processing information, ANN uses a mathematical model or computational models. As the machining process is nonlinear and time-dependent, it is quite tedious for conventional identification techniques to provide an accurate

model. ANNs are global and robust when compared with traditional computing techniques. Procedure in the biological nervous system inspires neural network, which is an information processing model. ANN gives an inherent relationship between the input and output by learning from a dataset that represents the behavior of a system. Neural networks consist of simple processors called neurons which are linked by weighed connections.

By the interconnections, the output signal of a neuron is given to other neurons as input signals. Figure 29.5. Shows simple neural network architecture. To obtain the net input ‘n’ the weighted inputs are summed with bias ‘b’.

$$n = w_{1.1}p_1 + w_{1.2}p_1 + \dots + w_{1.R}p_R + b \tag{29.2}$$

‘ $X_n$ ’ represents various inputs to the neurons. ‘ $W_n$ ’ represents weights. ‘ $\varphi$ ’ represents bias, which is used to compute activation function ‘ $a_n$ ’. Then by using transfer function, activation is converted into the output ‘ $O_n$ ’.

$$a_n = w_n X_n^T + \varphi \tag{29.3}$$

$$O_n = f(a_n) \tag{29.4}$$

Complex problems can be solved by layers of neuron network which is formed by connecting many single neurons. An input layer, hidden layer, and output layer are the three layers of artificial neural network. The input layer is connected to hidden layer, which is connected to the output layer. Through the input layer the patterns are presented to the networks, and then input layer communicates with hidden layers

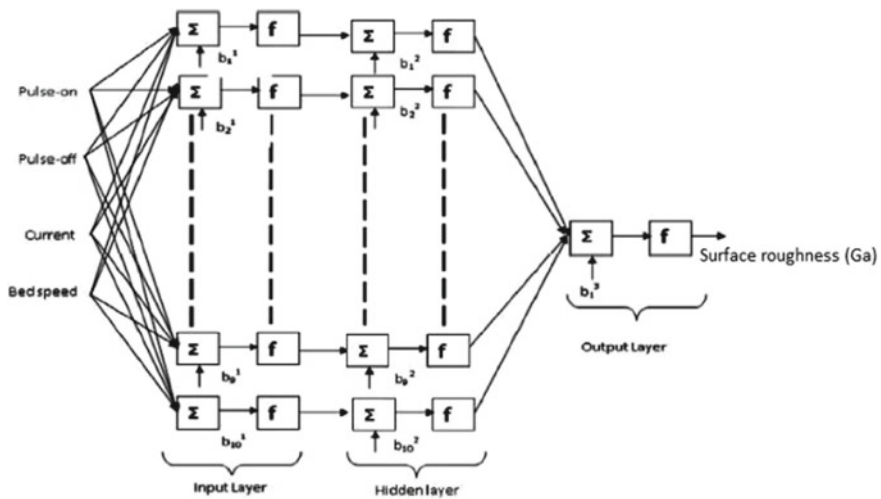


Fig. 29.5 Artificial neural network (ANN) architecture

where the actual processing is carried out. The hidden layers are then linked to an output layer.

The neural network has to train in such a way that the error between actual output and desired output is minimum and regression co-efficient (R value) between actual output and desired output is close to one.

The Levenberg–Marquardt algorithm in mathematics and computing gives solution to the problem of minimizing a function, generally nonlinear, over a space of parameters of the function. Especially in nonlinear programming and least squares curve fitting these minimization problems arises.

## 29.4 Results and Discussion

Experiments were conducted on machining of Al-6%Si<sub>3</sub>N<sub>4</sub> and Al-10%Si<sub>3</sub>N<sub>4</sub> composite materials. CONCORD DK7720C CNC Wire EDM machine was used to conduct the experiment. Current, Bed speed, Pulse-on time, and pulse-off time, were used as input parameters. Surface roughness was the response variable. Surface roughness was measured using machine vision system and then it is compared with the surfcom flex 50-A; which is conventional measuring instruments for measuring surface roughness. Surface roughness prediction was carried out by neural network fitting tool. It is necessary to check the performance of the network and to identify the change needs to be made to the training process, the datasets or network architecture.

Validation performance reached a minimum at 11th iteration. Before the training was stopped, the training continued for seven more iterations. Similar Test curves and validation can be observed. Some overfitting might occur if the test curve is increased significantly before the validation curve.

Figures 29.6, 29.7, 29.8, 29.9, 29.10 and 29.11 shows the comparison of measured surface roughness and predicted surface roughness for Al-6% Si<sub>3</sub>N<sub>4</sub> and Al-10% Si<sub>3</sub>N<sub>4</sub> materials at P-off = 5 μs and P-off = 7 μs. It was observed from Fig. 29.6, 29.7, 29.8, 29.9, 29.10 and 29.11 that the predicted surface roughness of the dataset exhibits good correlation with the measured surface roughness.

The surface roughness was better, during machining of both the materials at pulse-off time 7 μs when compared with the pulse-off time 5 μs. This is because at pulse-off time 7 μs more flushing takes place, which carries the debris from the cutting zone quickly, thereby avoiding the recast of debris on the machined area which leads to good surface roughness.

The surface roughness was higher during machining of Al-10% Si<sub>3</sub>N<sub>4</sub> material when compared with the Al-6%Si<sub>3</sub>N<sub>4</sub> material. This is because the reinforcement of the Al-10% Si<sub>3</sub>N<sub>4</sub> material is much higher than that of other material. During machining of composite materials, surface roughness is directly proportional to the percentage of reinforcement of composite material.

**Fig. 29.6** ANN prediction of surface roughness of Al-6% Si<sub>3</sub>N<sub>4</sub> at P-off = 5 μs, P-on = 20 μs and current = 4 mA

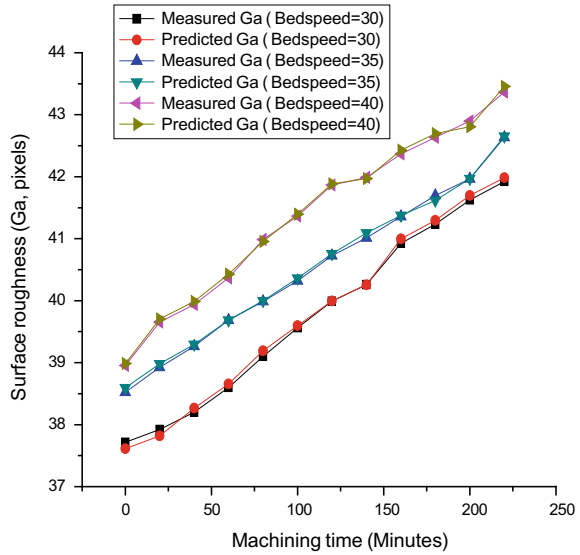
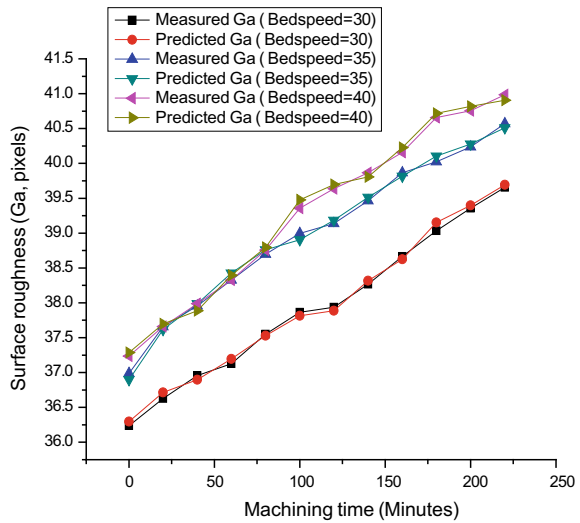


**Fig. 29.7** ANN prediction of surface roughness of Al-6% Si<sub>3</sub>N<sub>4</sub> at P-off = 7 μs, P-on = 20 μs and current = 4 mA



### 29.5 Conclusion

In this present work, a machine vision system has been implemented to measure the surface finish of the workpiece, cut by Wire EDM. The developed vision system has been well constructed to measure the surface finish of the workpiece.

**Fig. 29.8** ANN prediction of surface roughness of Al-10% Si<sub>3</sub>N<sub>4</sub> at P-off = 5 μs, P-on = 20 μs and current = 4 mA

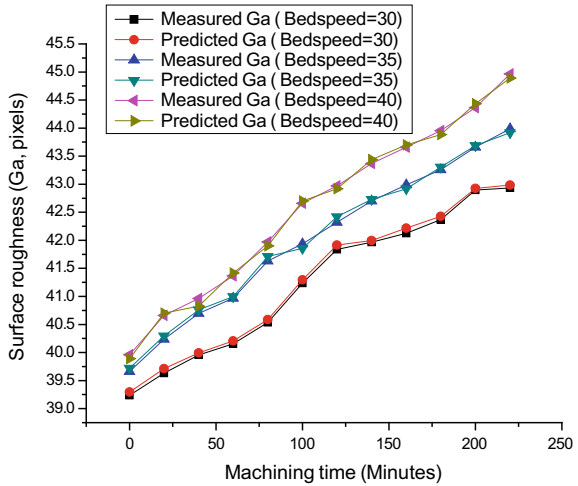


**Fig. 29.9** ANN prediction of surface roughness of Al-10%Si<sub>3</sub>N<sub>4</sub> at P-off = 7 μs, P-on = 20 μs and current = 4 mA

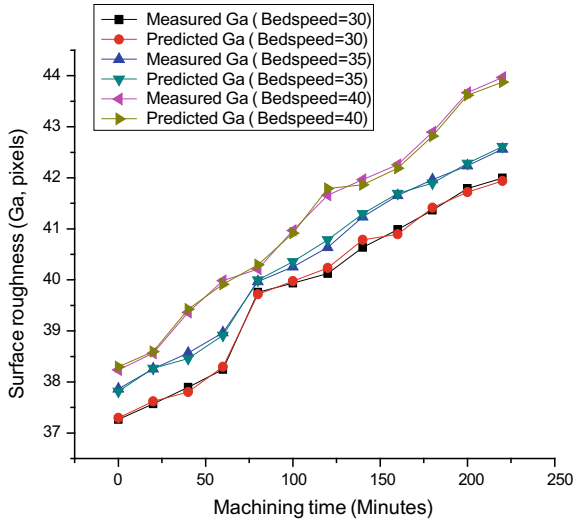
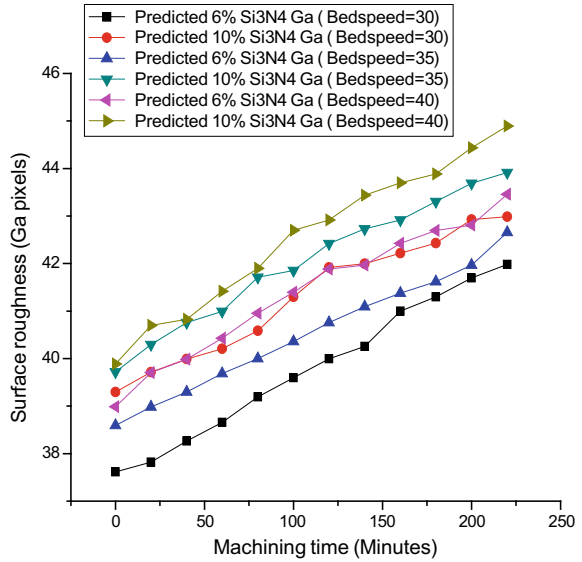


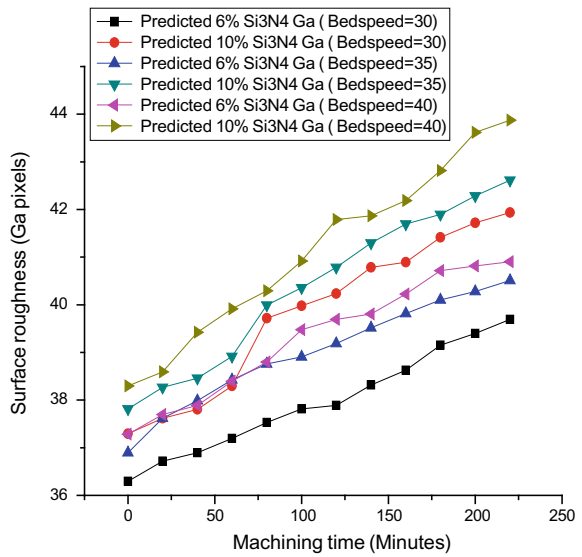
Image processing algorithms can be used for real time surface texture condition monitoring with noncontact techniques. Prediction of surface roughness could be done successfully by an artificial neural network.

Good prediction results can be obtained by a neural network trained with 70% of the data in training set. 90% of the estimated values are within the 90–95% of measured values, in both the materials studied. Hence, predicted surface roughness of 70% training set well correlates with the measured surface roughness.

**Fig. 29.10** Comparison of Al-6% Si<sub>3</sub>N<sub>4</sub> and Al-10% Si<sub>3</sub>N<sub>4</sub> predicted wear and measured wear at P-off = 5 μs, P-on = 20 μs and current = 4 mA



**Fig. 29.11** Comparison of Al-6%Si<sub>3</sub>N<sub>4</sub> and Al-10% Si<sub>3</sub>N<sub>4</sub> predicted wear and measured wear at P-off = 7 μs, P-on = 20 μs and current = 4 mA





## References

1. Lee, B.Y., Tarn, Y.S.: Surface roughness inspection by computer vision in turning operations. *Int. J. Mach. Tools Manuf.* **41**, 1251–1263 (2001)
2. Kumar, R., Kulashekar, P., Dhanasekar, B., Ramamoorthy, B.: Application of digital image magnification for surface roughness evaluation using machine vision. *Int. J. Mach. Tools Manuf.* **45**, 228–234 (2005)
3. Shivanna, D.M., Kiran, M.B., Kavitha, S.D.: Evaluation of 3D surface roughness parameters of EDM components using vision system. *Procedia Mater. Sci.* **5**, 2132–2141 (2014)
4. Songli, Y., Jiahao, J., Yuxuan, W.: Design of surface roughness measuring system based on machine vision. *Int. J. Innov. Res. Eng. Manag. (IJIREM)* **3**(4) (2016). ISSN: 2350-0557
5. Rajaram Narayanan, M., Gowri, S., Murali Krishna, M.: On line surface roughness measurement using image processing and machine vision. In: *Proceedings of the World Congress on Engineering*, London, UK, vol. 1 (2007). ISBN: 978-988-98671-5-7

# Chapter 30

## Performance Study of Electrical Discharge Drilling of Metal Matrix Composite



Anjani Kumar Singh and Vinod Yadava

**Abstract** In the present investigation Al/20Al<sub>2</sub>O<sub>3</sub>p composite has been fabricated by stir casting method. Al<sub>2</sub>O<sub>3</sub> particles containing weight fraction 20 wt% and mesh size 400 are used as reinforcement. Though Al/Al<sub>2</sub>O<sub>3</sub> MMCs possess superior mechanical properties, its high abrasiveness hinders the machining process and thereby limiting its effective applications in several areas. In the present work, One Parameter at a Time (OPAT) approach has been used to analyze the process behavior of Electrical Discharge Drilling during the fabrication of hole in aluminum alloy based MMC using copper tool electrode of 6 mm diameter. The effect of input process parameters namely discharge current (C), pulse duration (T<sub>on</sub>), pulse interval (T<sub>off</sub>), flushing pressure (P), and tool rotation (RPM) were analyzed on output performance characteristics of Material Removal Rate (MRR), Kerf Taper (T), and Radial Overcut (ROC). Brief detail about the fabrication of Al<sub>2</sub>O<sub>3</sub>/6061Al MMC has also been discussed.

**Keywords** Composites · Electrical discharge drilling · Flushing pressure · Kerf taper · Radial overcut

### 30.1 Introduction

The recent development in the area of science and technology especially in the field of transportation, aerospace, and military engineering necessitate the developments in advanced engineering materials [1, 2]. These fields demand high strength lightweight materials with good tribological properties. Aluminum-based Metal Matrix Composites (MMC) offers a promising solution for the above requirements.

MMCs possess lightweight, high wear resistance, low thermal expansion coefficient, and good specific strength [3]. They are used at large scale in industrial

---

A. K. Singh (✉)

Madan Mohan Malaviya University of Technology, Gorakhpur 273010, India  
e-mail: aksws@mmmut.ac.in

V. Yadava

National Institute of Technology Hamirpur, Hamirpur 177005, India

© Springer Nature Singapore Pte Ltd. 2020

M. S. Shunmugam and M. Kanthababu (eds.), *Advances in Unconventional Machining and Composites*, Lecture Notes on Multidisciplinary Industrial Engineering, [https://doi.org/10.1007/978-981-32-9471-4\\_30](https://doi.org/10.1007/978-981-32-9471-4_30)

applications requiring reinforcement strength and greater hardness. It is difficult to machine these materials with traditional techniques. Electrical Discharge Machining (EDM) is the most widely used advanced machining processes but it lacks the ability for axial rotation during machining [3, 4]. BiingHwa Yan et al. confirmed that EDM-drilling with a rotating hollow tube electrode have a lower surface roughness (SR) and a higher material removal rate (MRR) than that found in the use of a stationary hollow tube electrode [1]. P. Narendra Singh et al. explored the effect of pulse on time ( $T_{on}$ ), current (C), and flushing pressure (P) on tool wear rate (TWR), metal removal rate (MRR), surface roughness (SR), taper (T), and radial overcut (ROC) with brass tool electrode of 2.7 mm dia on Al/10SiCp MMC using Taguchi design of experiment [2]. Riaz Ahmad et al. reports EDM hole sinking on hybrid Al–SiCp–Glass<sub>p</sub> and Al–SiCp–B4Cp MMCs by copper electrode of  $\Phi$  4 mm and investigates the influence of pulse on time (ON), pulse off time (OFF), current (C), and flushing pressure (P) on material removal rate (MRR) and surface roughness (SR) [5]. Therefore in this study, a developed attachment has been used for rotary EDM with a cylindrical copper electrode to machine holes in Al<sub>2</sub>O<sub>3</sub>/6061Al composite. Further, to analyze the effect of process input parameters namely discharge current (C), pulse duration ( $T_{on}$ ), pulse interval ( $T_{off}$ ), flushing pressure (P), and tool rotation (RPM) on the output performance characteristics of Material Removal Rate (MRR), Kerf Taper (T), and Radial Overcut (ROC) one parameter at a time approach is used. A fabrication detail of the Al<sub>2</sub>O<sub>3</sub>/6061Al composite has also been discussed.

## 30.2 Experimental Procedure

The experiments were conducted on the fabricated composite specimen using the EDD attachment on an EDM machine. The specimens were prepared by stir casting method and holes were machined in the specimen using copper tool electrode of diameter 6 mm.

### 30.2.1 Fabrication of MMC

In the present work, Al<sub>2</sub>O<sub>3</sub> particulates having a size of 400 mesh number with 20 wt% is reinforced in the Aluminum alloy (AA6061) matrix. Ingots of AA6061 were melted in a graphite crucible of an oil-fired tilting furnace at a temperature of about 800 °C. Diesel was used as the fuel. The melting of the Al-alloy was carried for 2 h and to prevent oxidation of the molten metal a controlled atmosphere was maintained inside the furnace. Before adding Al<sub>2</sub>O<sub>3</sub> into the Al-alloy, particulates were preheated in a separate heating chamber for about 50 min in order to remove surface impurities. The ceramic particles were then poured slowly and continuously onto the molten metal followed by continuous manual stirring with a steel rod stirrer for about 20 min. Utmost care was taken in order to ensure homogenous mixing of



Fig. 30.1 Specimens prepared via stir casting method

the particulates. The composite mixture was then poured onto a sand mold and left for one hour. The casted solid MMC was then machined to obtain the cuboid shape workpiece specimen (20 mm × 20 mm × 5 mm) for experimentation (Fig. 30.1).

### 30.2.2 Experimental Setup for EDD

On the ram of the EDM machine (ECOLINE ZNC 320) the EDD setup has been installed and the actual EDM machine tool holder has been replaced. The EDD set up consist of perpendicularly mounted (butt Joint) at one side of Al-alloy plate of thickness 16 mm, Rotomag (India) make electrical PMDC motor of 0.25 hp of 1500 RPM, electrically conductive tool electrode, rotating spindle cum tool electrode holder mechanism, mounted on the ram of EDM machine (Fig. 30.2).

The housing assembly of rotating spindle has an attachment for pulley at one side and an arrangement for holding the tool electrode at another side. The rotating spindle

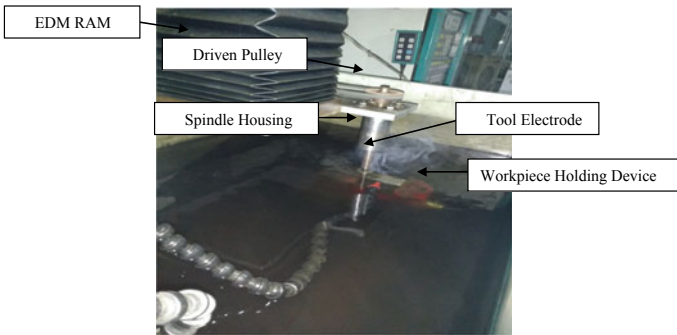


Fig. 30.2 Photograph of EDD setup mounted on RAM of ZNC EDM machine

housing is mounted on the lower side of the horizontal plate. The horizontal plate has a hole through which spindle of rotating assembly passes. The driven pulley is fitted on the rotating spindle top. The driven pulley of rotating spindle is connected to the driver pulley, mounted on rotor of electrical motor through 'V' belt of trapezoidal section. Dimensional specification of 'V' belt is Poly Belt M7X500. A certain tension is provided to the V belt to avoid slippage. The motor is mounted on vertical Al-alloy plate butted on horizontal Al-alloy plate. Mounting bolts for the DC motor are provided with insulated glass sleeves so that DC current does not pass through from Al-alloy plate to electric DC motor [6].

A speed variac controller is joined with the motor input circuit for controlling the speed of the electric motor up to maximum of 1500 rpm. At input terminal connection of DC motor, 0.5 A diode is connected against the safety for the motor. Rotating spindle is manufactured of mild steel. The lower side of the rotating spindle has provision for tool holding and fixing of tool by two screws. In this EDD, smooth running of the spindle and tool electrode is desired for better accuracy. Non-smooth rotation of spindle will affect the spark quality and may cause trouble in output parameters of machining during prolonged operation. The working of setup is tested at different rpm levels and found satisfactorily working.

### 30.2.3 Selection of Tool Electrode

Copper tool electrode of 6 mm dia is fabricated for electrical discharge drilling tests. Drawing and image of fabricated tool electrodes are shown in Fig. 30.3.

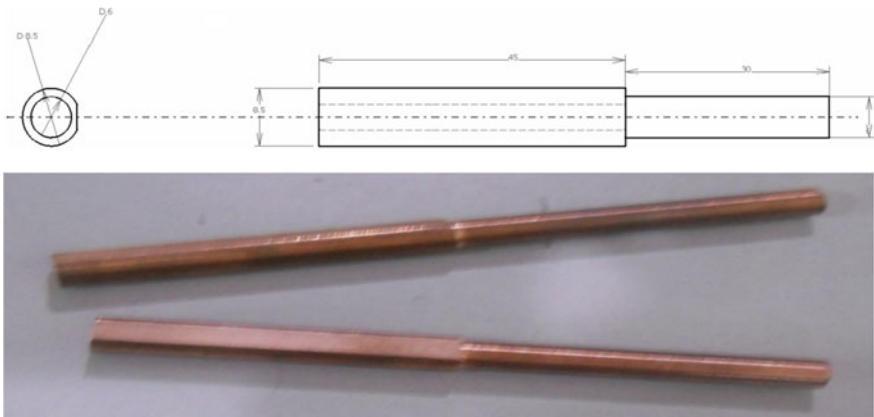


**Fig. 30.3** Copper tool electrode prepared for EDD tests

### 30.3 Experimental Conditions

The acceptable range of input process parameters and polarity of EDM, were determined by an extensive series of pilot experimentations. EDD tests were performed on the fabricated specimens to study the effect of electrical parameters like discharge current, pulse duration, pulse interval, and nonelectrical parameters such as tool electrode rotation (RPM), radial overcut (ROC) and flushing pressure on MRR, kerf taper (T). Three levels of each input parameters were studied by varying one input parameter at a time (OPAT). Levels of parameters are shown Table 30.1.

#### 30.3.1 Evaluation of Response Variables

MRR is calculated as the difference of weights of the workpiece before and after machining per unit machining time, i.e.,:

$$MRR = (w_f - w_j)/t \tag{30.1}$$

Where  $w_f$  and  $w_j$  are the weights of the workpiece before machining and after machining, and  $t$  is the time of machining.

Taper is calculated by using the expression:

$$T = (d_t - d_b)/2h \tag{30.2}$$

where  $d_t$  and  $d_b$  are the diameters of the machined hole at the top and diameter of the machined hole at the bottom of the workpiece, and  $h$  is the workpiece height.

ROC is calculated as half of the difference of diameters of the machined hole and tool diameter, i.e.,:

$$ROC = (d_t - d_{tool})/2 \tag{30.3}$$

where  $d_{tool}$  is the tool diameter.

**Table 30.1** Selected levels of parameters

Parameters	Level 1	Level 2	Level 3
Current (A)	15	20	25
Pulse duration (μs)	40	60	80
Pulse interval (μs)	30	40	50
Tool rotation (RPM)	300	450	600
Flushing pressure (kg/cm <sup>2</sup> )	0	0.5	1.0

## 30.4 Results and Discussion

The  $\text{Al}_2\text{O}_3/6061\text{Al}$  MMC workpiece specimens were machined using EDD experimental setup to study the effect of input process parameters on the performance parameters. Analysis of experimental results was performed by taking the average response value of three replications of each set of input process parameters.

### 30.4.1 Effect of Discharge Current

The influence of input current is investigated on three levels of current values 15, 20, and 25 A keeping other process parameters constant ( $T_{\text{on}}$  60  $\mu\text{s}$ ,  $T_{\text{off}}$  40  $\mu\text{s}$ , electrode RPM 300, and flushing pressure 0.5  $\text{kg}/\text{cm}^2$ ). Figure 30.4a indicates that initially MRR increases with the increase of discharge current. Rate of heat generation also increases with the increase of current. Moreover, with the increase in current, intensity of plasma zone increases that enhances the melting of material due to which the ejection and vaporization of molten material take place perfectly. This simultaneously decreases the radial overcut and kerf taper because the reinforcement particles do not get entrapped in machining region (Fig. 30.4b, c). Figure 30.4a shows that after 2.0 A the MRR starts decreasing with the increase of discharge current due to excessive melting and partial ejection thereby causing molten metal entrapment

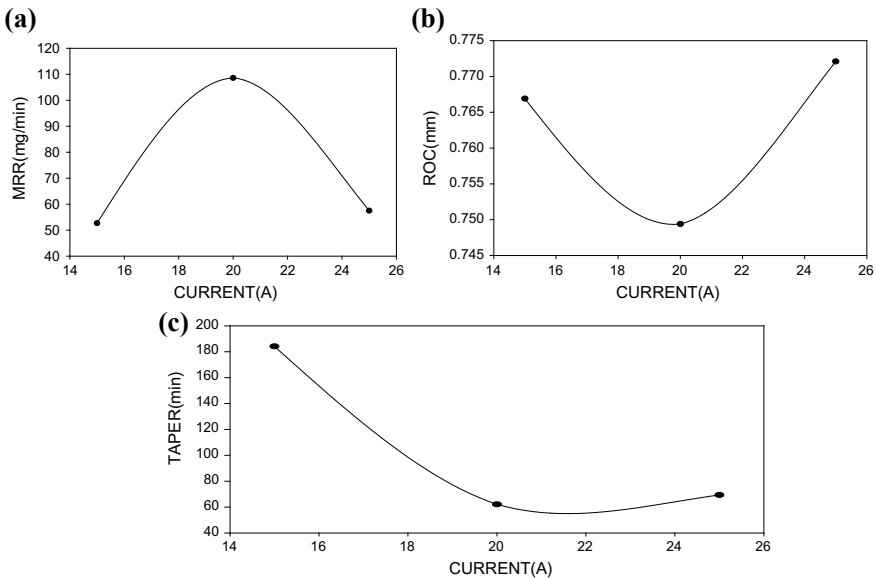


**Fig. 30.4** Influence of discharge current on **a** MRR, **b** ROC and **c** Taper at  $T_{\text{on}} = 60 \mu\text{s}$ ,  $T_{\text{off}} = 40 \mu\text{s}$ , RPM = 300,  $F = 0.5 \text{ kg}/\text{cm}^2$

and recast layer formation. This affects the accuracy in terms of higher ROC, kerf taper (Fig. 30.4b, c). At larger value of current complete amount molten material could not be ejected at same pulse interval.

### 30.4.2 Effect of Pulse Duration

Pulse duration is generally known as pulse on time and expressed in units of microseconds. The effect of pulse duration is investigated on three levels of pulse duration values 40, 60, and 80  $\mu\text{s}$  keeping other process parameters constant (Current = 20 A,  $T_{\text{off}} = 40 \mu\text{s}$ , RPM = 300,  $F = 0.5 \text{ kg/cm}^2$ ). MRR depends on the amount of energy used during the pulse on time. Increase in pulse duration cause more heat produced into the workpiece and working area, which affects the heat-affected zone will be deeper and the recast layer will be larger. And, hence, material removal rate tends to decrease after an optimal value of pulse duration (Fig. 30.5a). Simultaneously ROC and kerf taper increases due to machined surface imperfections caused irregular material removal (Fig. 30.5b, c).

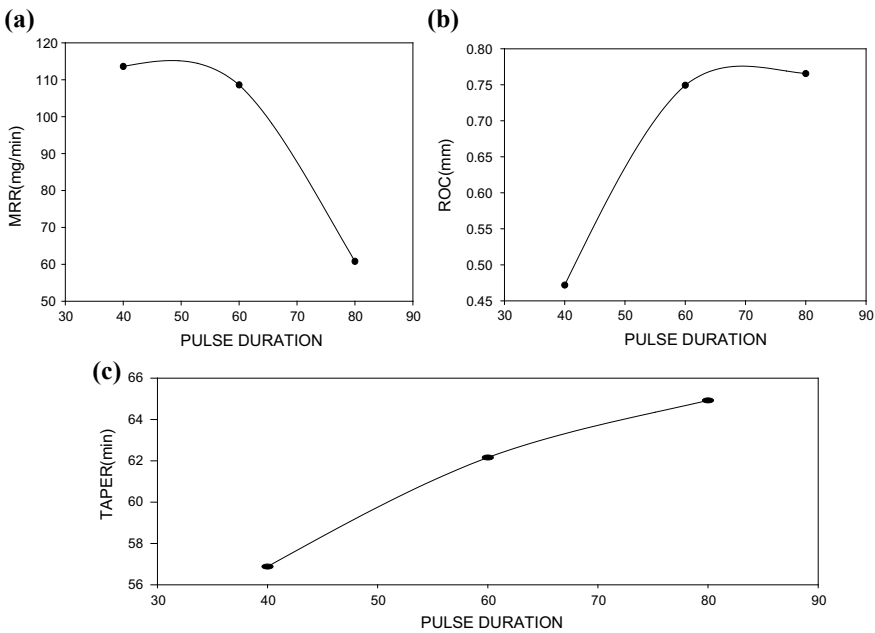


**Fig. 30.5** Influence of pulse duration on **a** MRR, **b** ROC, and **c** Taper at Current = 20 A,  $T_{\text{off}} = 40 \mu\text{s}$ , RPM = 300,  $F = 0.5 \text{ kg/cm}^2$



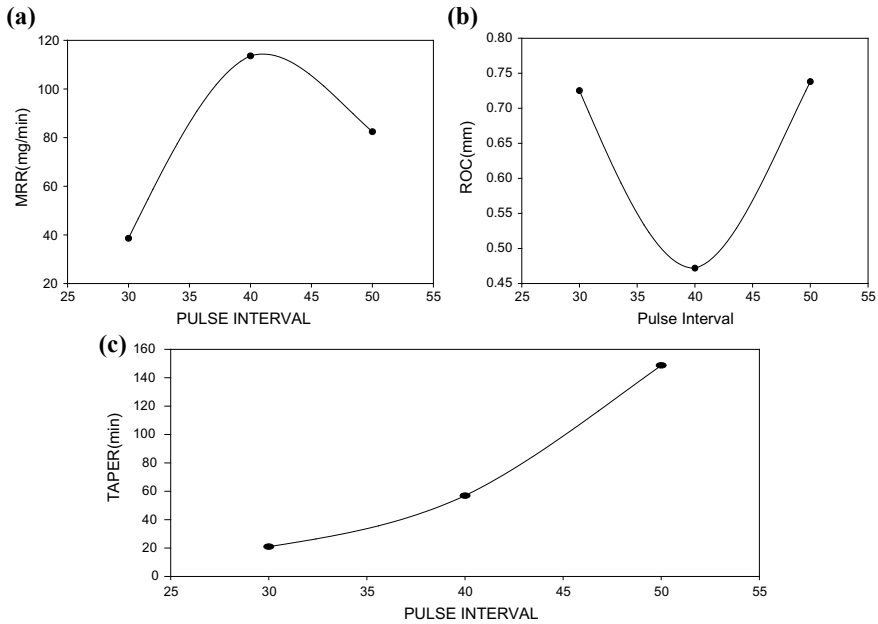


**Fig. 30.6** Influence of pulse interval on **a** MRR, **b** ROC, **c** Taper at  $T_{on} = 40 \mu s$ , Current = 20 A, RPM = 300,  $F = 0.5 \text{ kg/cm}^2$

### 30.4.3 Effect of Pulse Interval

The Influence of pulse Interval is investigated on three levels of pulse duration values 30, 40, and 50  $\mu s$  keeping other process parameters constant ( $T_{on} = 40 \mu s$  Current = 20 A, RPM = 300,  $F = 0.5 \text{ kg/cm}^2$ ). Pulse interval mainly influences machining stability and rate. Machining operation is higher at shorter interval. However, the ejected workpiece material will not be flushed away with the flow of the dielectric fluid if the pulse interval is too short and the dielectric fluid will not be deionized properly. And instability of the next spark occurs. This results enlarged machining time due to unstable spark (Fig. 30.6a). At the same time, to prevent continued sparking at one point pulse interval must be greater than the deionization time causing large value of kerf taper. With increase in pulse interval there is proper flushing and debris removal (Fig. 30.6b, c).

### 30.4.4 Effect of Tool Rotation

Better flushing action and sparking efficiency is found because of electrode rotation, causing improvement in MRR (Fig. 30.7a). At lower rotational speed the kerf taper increases (Fig. 30.7b) and at higher rpm level better accuracy is found in terms of

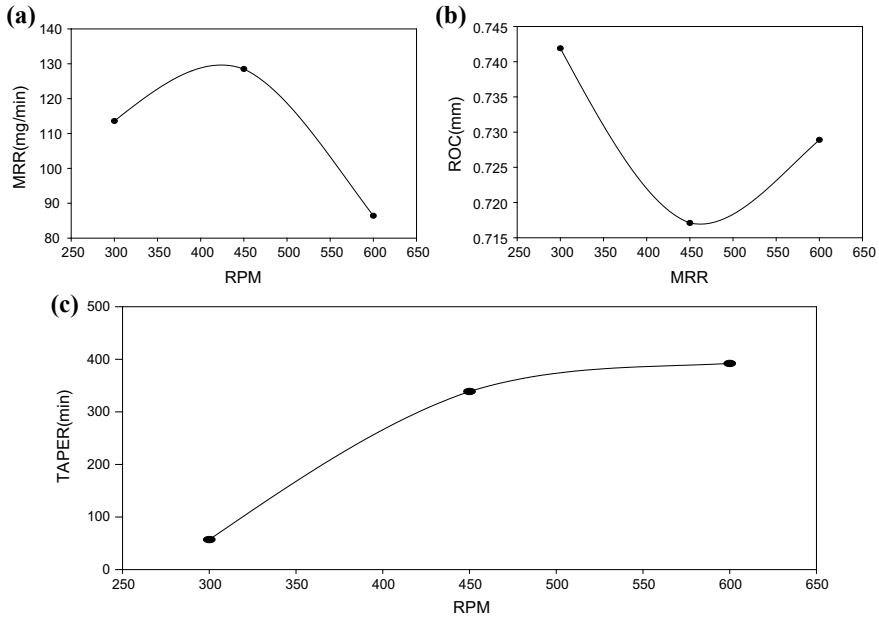


**Fig. 30.7** Influence of tool rotation on **a** MRR, **b** ROC, and **c** Taper at  $T_{on} = 40 \mu s$ ,  $T_{off} = 40 \mu s$ , Current = 20 A,  $F = 0.5 \text{ kg/cm}^2$

radial over cut and kerf taper due to proper flushing of machined alumina abrasive particles and debris from machining area (Fig. 30.7b, c).

### 30.4.5 Effect of Flushing Pressure

Flushing pressure acts as a coolant affecting the kerf taper and play an important role in flushing away the debris from the machining gap. Flushing pressure during the drilling operation affects the MRR. MRR increases with the increase of flushing pressure (Fig. 30.8a). The flushing pressure also affects the recast layer and crack density, which may be reduced by finding an optimal flushing rate.

## 30.5 Conclusions

The effect of discharge current (C), pulse interval (Toff), pulse duration (Ton), flushing pressure (P), and tool rotation (RPM) were investigated on the output performance characteristics ,e.g., Material Removal Rate (MRR), Kerf Taper (T), and Radial Overcut (ROC) during EDD of  $Al_2O_3/6061Al$  MMC. The experiments were conducted

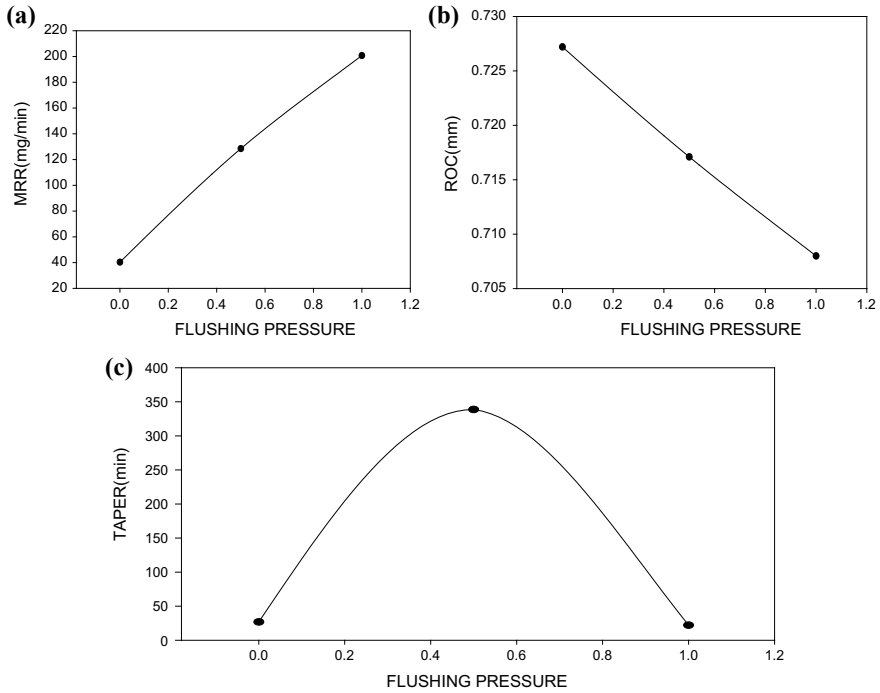


**Fig. 30.8** Effect of flushing pressure on **a** MRR, **b** ROC and **c** Taper at  $T_{on} = 40 \mu s$ ,  $T_{off} = 40 \mu s$ , Current = 20 A, RPM = 300

using self-fabricated EDD attachment on diesinking EDM machine. To analyze the effect of process behavior with the change of input process parameters one parameter at a Time approach (OPAT) was used and following conclusions were drawn:

- The feasibility of EDD of  $Al_2O_3/6061Al$  MMC by Electrical Discharge Drilling has been tested and found feasible.
- The effect of EDD with the rotating cylindrical copper electrode is studied from the observed results for getting a higher MRR.
- With the increase in discharge current MRR increases at a lower level. This decreases radial overcut, and kerf taper. At higher value of discharge current MRR starts decreasing with the increase in discharge current due to more melting and partial ejection causing molten metal entrapment and recast layer formation. This affects the accuracy in terms of higher ROC, kerf taper.
- MRR decreases after an optimal value of pulse duration. Simultaneously ROC and kerf taper increases due to machined surface imperfections caused irregular material removal. Large heat evolution and proper melting of alumina abrasive particles give better roundness.

- Better flushing action and sparking efficiency due to electrode rotation results in improvement of MRR. At lower rotational speed kerf taper has been increased and at higher rpm level better accuracy is found in terms of radial overcut, and kerf taper.
- Flushing pressure directly affects MRR. The flushing pressure also affects the recast layer and crack density, which may be reduced by finding an optimal value of flushing rate.

## References

1. Yan, B., Chung Wang, C.: The machining characteristics of  $Al_2O_3/6061Al$  composite using rotary electro-discharge machining with a tube electrode. *J. Mater. Process. Technol.* **95**, 222–231 (1999)
2. Narender Singh, P., Raghukandan, K., Rathinasabapathi, M., Pai, B.C.: Electric discharge machining of Al–10%SiCp as-cast metal matrix composites. *J. Mater. Process. Technol.* **155–156**, 1653–1657 (2004)
3. Allison, J.E., Cole, G.S.: Metal matrix composites in the automotive industry; opportunities and challenges. *JOM*
4. Ho, K.H., Newman, S.T.: State of the art electrical discharge machining (EDM). *Int. J. Mach. Tools Manuf.* **43**, 1287–1300 (2003)
5. Riaz Ahamed, A., Asokan, P., Aravindan, S.: EDM of hybrid Al–SiCp–B4Cp and Al–SiCp–Glassp MMCs. *Int. J. Adv. Manuf. Technol.* **44**, 520–528 (2009)
6. Yadav, U.S., Yadava, V.: Experimental investigation on electrical discharge drilling of Ti-6Al-4V alloy. *Mach. Sci. Technol.* **4**(19), 515–535

# Chapter 31

## Multi-objective Optimisation of Electro Jet Drilling Process Parameters for Machining of Crater in High-Speed Steel Using Grey Relational Analysis



Kalinga Simant Bal , Amal Madhavan Nair , Dipanjan Dey ,  
Anitesh Kumar Singh  and Asimava Roy Choudhury 

**Abstract** In the present investigation, electro jet drilling has been implemented to machine crater in the high-speed steel sheet. Input parameters (applied voltage, electrolyte concentration, and standoff distance) were varied to study the change in output characteristics of the crater (mass removal rate (MRR), roundness error (RE) and mean diameter-to-height ratio (DHR)). MRR was found to increase with the increase in applied voltage and electrolyte concentration, while an increase in standoff distance was found to cause a decrease in MRR. RE was found to increase with applied voltage and standoff distance, while the increase in electrolyte concentration was found to cause a reduction in RE. DHR was increased with the increase in electrolyte concentration and standoff distance, while an increase in applied voltage resulted in the decrease of mean DHR. Optimization of input parameters was carried out to (a) maximize MRR and mean DHR and (b) minimize RE, of the machined crater, using Taguchi grey relation analysis.

**Keywords** Electro jet drilling · High-speed steel · Optimisation · Electrochemical machining · Crater

### 31.1 Introduction

Machining of micro- and macro-holes in hard-to-machine materials have gained prominence for use in aerospace, medical, electronic, computer, and optics industry. The need for machining accurate holes has led researchers looking into new nontraditional techniques. Electro jet drilling (EJD) is one such process that has the potential to meet the stringent demands of the industry offering significant advantages in accuracy, ease of material removal and micro-hole cutting ability. This process utilizes a

---

K. S. Bal · A. M. Nair · D. Dey · A. K. Singh · A. Roy Choudhury (✉)  
Laser Material Processing Laboratory, Mechanical Engineering Department, Indian Institute of  
Technology Kharagpur, Kharagpur 721302, West Bengal, India  
e-mail: [archie@mech.iitkgp.ac.in](mailto:archie@mech.iitkgp.ac.in)

© Springer Nature Singapore Pte Ltd. 2020  
M. S. Shunmugam and M. Kanthababu (eds.), *Advances in Unconventional  
Machining and Composites*, Lecture Notes on Multidisciplinary  
Industrial Engineering, [https://doi.org/10.1007/978-981-32-9471-4\\_31](https://doi.org/10.1007/978-981-32-9471-4_31)

385

negatively charged stream of electrolyte which is allowed to impinge on the workpiece, and the material is removed via electrolytic dissolution. This eliminates the need for fabrication of micro-tools and tools that are harder than the material to be worked upon. Mohan and Shan [1, 2] generated small holes by electrochemical jet drilling process and studied the effects of different process parameters on the quality of the holes. Response surface methodology was applied to optimize the input process parameters and to enhance the output quality [1, 2]. Mohan and Shan [3, 4] used hybrid neural network, desirability function and genetic algorithm to optimize the process parameters of electrochemical drilling process. With the help of these multi-object optimization techniques, material removal rate and surface quality were enhanced significantly [3, 4]. Conductive mask electrochemical machining [5] was applied to reduce undercutting of micro-dimple and improve the machining localization. With the help of simulation, etch factor was improved significantly [5]. Liu et al. [6] carried out electrochemical jet machining on TB6 titanium alloy and studied the feasibility of the process. Optimum process parameters were found out to improve the output characteristics such as material removal rate and surface quality [6]. Hua and Xu [7] incorporated hybrid technology, i.e., laser drilling with electrochemical jet drilling, to remove the recast layer and spatter generated during the laser drilling. The output was improved significantly but the efficiency was reduced to 30%. Goel and Pandey [8] developed electrochemical jet drilling experimental setup and studied the effects of several inputs on different output characteristics like hole taper and material removal rate. They [8] successfully fabricated 140-micron diameter micro-hole with the help of their setup. Kozak et al. [9] developed a mathematical model on electrochemical jet machining process relating the machining rate with the working condition. The mathematical model was used to determine the maximum material removal rate and electrolyte flow for a fixed set of input process parameters. Ming et al. [10] studied kerosene submerged electrochemical jet drilling process and reported that the localization of the machining was possible by submerging both the workpiece and the nozzle. Endo et al. [11] machined small hole by electrochemical jet drilling process, and applied Fourier analysis to estimate the accuracy of the drilled hole. Natsu et al. [12] proposed a method to develop 3D surfaces with the help of micro electrolyte jet machining and discussed the possible way to find effective nozzle path and scan speed.

## 31.2 Problem Definition

Machining of crater using electrochemical drilling requires insulation of electrode tip at sides to prevent overcut caused due to the stray machining effect. Also, it is required for electrochemical drilling to immerse the sample completely in the electrolyte solution. This causes the development of electrode potential between the sample and the electrolyte, and could result in corrosion of the sample. Hence, electro jet drilling could be alternative to machine crater of suitable dimension, because (a) the crater dimension does not depend on the tool diameter, and at the same time (b)

sample is not completely immersed in the electrolyte solution. So, in the present study, machining of the crater has been carried out using electro jet drilling technique. For this purpose, nozzle diameter through which electrolyte jet impinges on the sample has been increased to facilitate the machining of the crater.

### 31.3 Experimental Details

High-speed steel sheet of dimension 30 mm × 10 mm × 1 mm was sectioned and polished in SiC abrasive paper to remove the surface contaminants. Table 31.1 shows the chemical composition of the high-speed steel sheet. After ultrasonic cleaning in 2-Propanol solution, the sample was clamped in the sample holder in the electro jet drilling machine. Figure 31.1 shows the electro jet drilling setup. A platinum wire having diameter of 0.5 was used as a tool. The platinum wire was recessed within the glass nozzle of outlet diameter of 0.75 mm. DC power supply was used in this experimentation. The tool was connected with the negative terminal of the power supply, and the high-speed steel substrate was connected with the positive terminal of the power supply. Electrolyte flow was supplied concentrically with the tool.

**Table 31.1** Composition of the high-speed steel sheet used in the present study

Element	Fe	Cr	Mo	W	C	V
wt. %	82.15	3.98	5.01	6.11	0.77	1.98

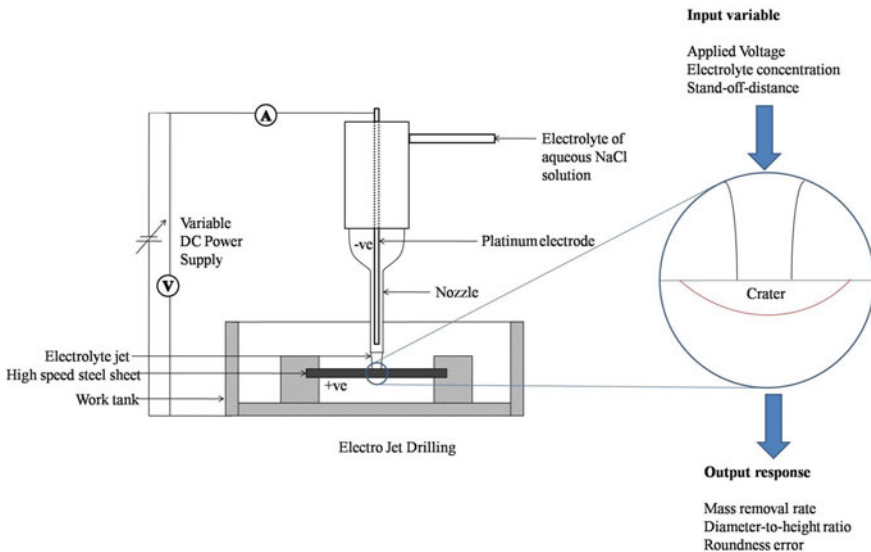


**Fig. 31.1** Electro jet drilling setup

**Table 31.2** Input process parameters

Applied voltage (V)	Electrolyte concentration (N)	Standoff distance (mm)
20, 40, 60	0.1, 0.3, 0.5	0.5, 1.0, 1.5

750 W reciprocating type three-phase pump was used to supply the metered quantity of electrolyte solution into the required machining zone. NaCl aqueous solution with variable concentration was used as the electrolyte for machining.

Applied voltage, electrolyte concentration, and standoff distance were chosen as the input parameters. Table 31.2 shows the input process parameters along with their levels used in the experiment. Taguchi L9 orthogonal array was used to design the experimental run. Machining time for each run was 1 min. Output responses chosen for the present study include mass removal rate from the crater, roundness error and mean diameter-to-height ratio of the crater. The mass removal rate is defined as the weight loss of the sample per unit time after the machining. The roundness error of the crater is defined as the difference between the maximum crater diameter and the minimum crater diameter. The mean diameter-to-height ratio of the crater is defined as the ratio of the average diameter of the crater and the depth of the crater. In the present study, it is desired to increase the mass removal rate from the crater as well as increase the mean diameter-to-height ratio of the crater that would decrease the specific cutting energy (i.e., power required to remove a unit volume of material). Simultaneously, it is desired to reduce the roundness error of the crater to improve the circularity of the machined zone. Hence, grey relation analysis is used in the present study to solve the multi-objective optimization problem to obtain crater of the desired dimension.

## 31.4 Result and Discussion

Table 31.3 shows the output responses corresponding to the combination of input parameters designed according to Taguchi L9 run. The effect of input process parameters on output responses has been discussed in details below.

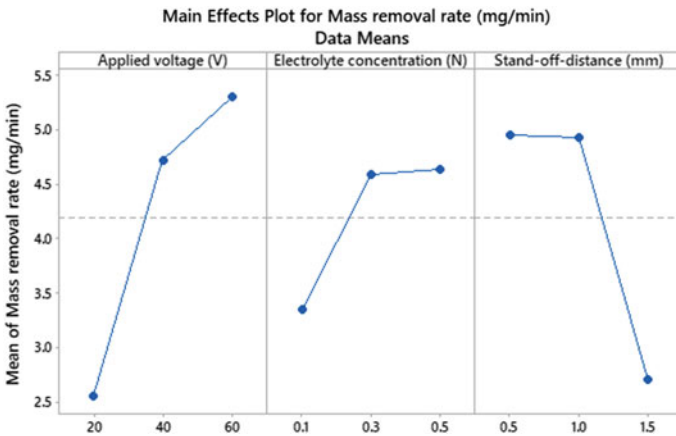
### 31.4.1 Effect of Process Parameters on Mass Removal Rate

Figure 31.2 shows the effect of process parameters on the mass removal rate of the high-speed steel sheet. It could be observed that the mass removal rate was found to increase with the increase in the applied voltage and the electrolyte concentration, while an increase in the standoff distance was found to cause a decrease in the mass removal rate. An increase in the applied voltage causes an increase in the current, and results in the increase in the mass removal rate. Figure 31.3 shows the increase in



**Table 31.3** Output responses corresponding to the combination of input parameters according to Taguchi L9 run

Run	Input parameter			Output response		
	Applied voltage (V)	Electrolyte concentration (N)	Standoff distance (mm)	Avg. mass removal rate (mg/min)	Avg. roundness error (mm)	Avg. mean diameter-to-height ratio
1	20	0.1	0.5	3.81	0.246	20.3593
2	20	0.3	1.0	2.96	0.533	73.4251
3	20	0.5	1.5	1.23	0.2455	108.1178
4	40	0.1	1.0	4.34	0.346	36.4649
5	40	0.3	1.5	5.01	0.283	74.5380
6	40	0.5	0.5	5.22	0.3715	18.8301
7	60	0.1	1.5	2.25	0.857	56.9229
8	60	0.3	0.5	6.19	0.4295	18.0141
9	60	0.5	1.0	7.86	0.507	40.9559



**Fig. 31.2** Effect of process parameters on mass removal rate

the crater dimension with the applied voltage. The increase in NaCl concentration of the electrolyte solution causes an increase in the number of ions ( $\text{Na}^+$  and  $\text{Cl}^-$ ), and hence, the conductivity of the electrolyte solution increases. This result in the increase in the mass removal rate due to the increase in current flow in the solution. The increase in the standoff distance causes an increase in the flaring of the electrolyte jet. This causes a decrease in the effectiveness of the electrolyte jet column for carrying out machining, and hence, the mass removal rate decreases.

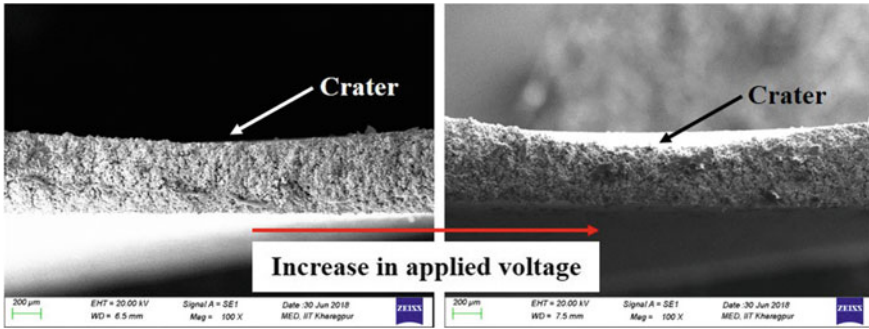


Fig. 31.3 Increase in crater dimension with applied voltage

### 31.4.2 Effect of Process Parameters on Roundness Error of Top of the Crater

Figure 31.4 shows the effect of process parameters on the roundness error of the top of the crater. It could be observed that the roundness error was found to increase with the increase in the applied voltage and the standoff distance, while an increase in electrolyte concentration was found to cause a decrease in the roundness error. Higher electrolyte concentration increases the ion availability in the solution, and might lead to homogeneous electrochemical dissolution. Consequently, higher electrolyte concentration could have lowered the roundness error. The conductivity of the electrolytic cell is inversely proportional to the standoff distance, and thus, inhomogeneous electrolytic dissolution could have occurred at high standoff distance. If the applied voltage exceeds the threshold voltage, then the spark may occur. Thus, at

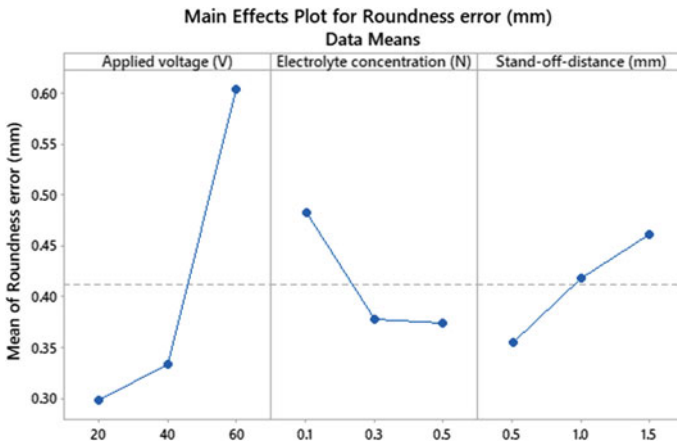


Fig. 31.4 Effect of process parameters on roundness error of top of the crater

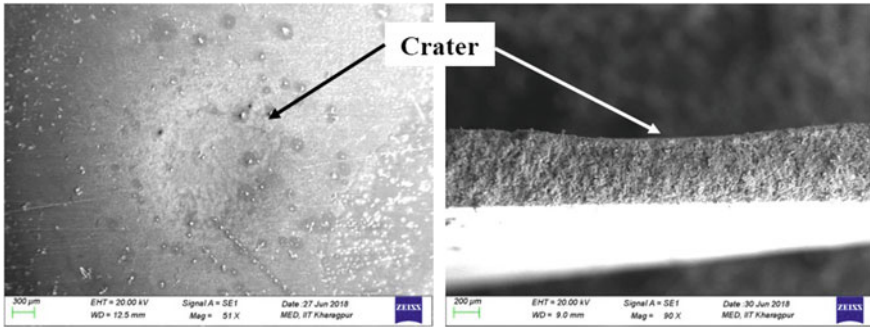


Fig. 31.5 Crater formation due to electro jet drilling

high applied voltage, spark occurring at the tool-workpiece interface might lead to higher roundness error. Figure 31.5 shows the crater formation due to the electro jet drilling.

### 31.4.3 Effect of Process Parameters on Mean Diameter-to-Height Ratio of the Crater

Figure 31.6 shows the effect of process parameters on the mean diameter-to-height ratio of the crater. It could be observed that the mean diameter-to-height ratio of the crater was found to increase with the increase in the electrolyte concentration and the standoff distance, while the increase in applied voltage was found to

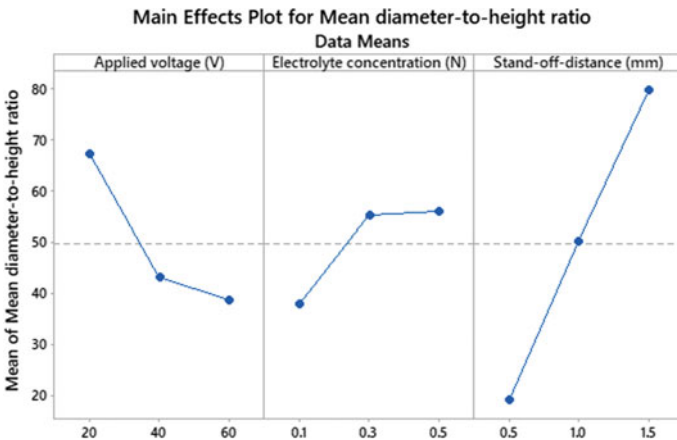


Fig. 31.6 Effect of process parameters on mean diameter-to-height ratio of the crater

cause a decrease in the mean diameter-to-height ratio. With the increase in stand-off distance, material dissolution becomes less, and height of the crater obtained is lower, and thus, the mean diameter-to-height ratio increases. Less material dissolution occurred at lower applied voltage, thus height of the crater is reduced. Consequently, diameter-to-height ratio is increased on decreasing the applied voltage. As NaCl is non-passivating electrolyte, thus increase in the concentration causes more dissolution because no oxide film formation occurs on the workpiece at the time of electrochemical reaction. So, with the increase in the electrolyte concentration, the diameter as well as the height of the crater increases. However, after the reaction, sludge ( $\text{FeCl}_3$ ) produced is precipitated in the machining zone, and thus, it is difficult to replace the sludge completely by the fresh electrolyte in that intricate zone. So, machining along the depth became difficult, and thereby, on increasing the electrolyte concentration, the diameter of the crater is increased more as compare to the increment of the height of the crater. Hence, with the increase in electrolyte concentration, the mean diameter-to-height ratio is increased. The probable reaction [1] for the formation of  $\text{FeCl}_3$  is as shown below:

Electrolytic reaction	Anodic reaction	Cathodic reaction
$\text{NaCl} \leftrightarrow \text{Na}^+ + \text{Cl}^-$ $\text{H}_2\text{O} \leftrightarrow \text{H}^+ + \text{OH}^-$ $\text{Na}^+ + \text{OH}^- \leftrightarrow \text{NaOH}$	$\text{Fe} \rightarrow \text{Fe}^{2+} + 2\text{e}^-$ $\text{Fe}^{2+} + 2\text{Cl}^- \rightarrow \text{FeCl}_2$ $\text{FeCl}_2 + \text{Cl}^- \rightarrow \text{FeCl}_3 \downarrow$	$2\text{H}^+ + 2\text{e}^- \rightarrow \text{H}_2 \uparrow$

### 31.4.4 Optimization of Process Parameters Using Grey Relational Analysis

In Fig. 31.7 grey relational grade for each experimental run has been shown. It is desired to maximize the mass removal rate and mean diameter-to-height ratio, and minimize the roundness error of the machined crater. So, considering the desired aspects for all the outputs, higher grey relational grade value results in better performance characteristics. Thus experiment number 9 has the highest value of grey relational grade among all the nine experimental runs as shown in Fig. 31.7. However, upon combining the input process parameters, there could be another set of input parameters that might show better performance than these nine runs. The average grey relational grade is determined to determine the best optimum process parameters.

In Fig. 31.8, the average grey relational grade for each level of process parameters has been shown. Among all the three level of each process parameters, the level that shows the highest average grey relational grade would be chosen as the best level for that process parameter. Thus, from the Fig. 31.8 it can be observed that the best combination of optimal set of input process parameters are: (a) applied voltage: level 3 (=60 V); (b) electrolyte concentration: level 3 (=0.5 N); and (c) standoff distance:

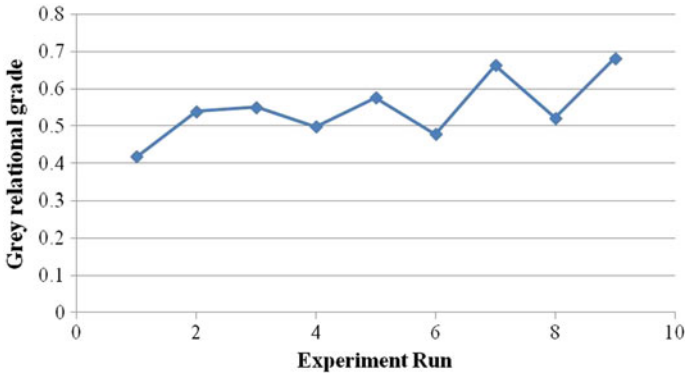


Fig. 31.7 Variation of grey relational grade with experimental run

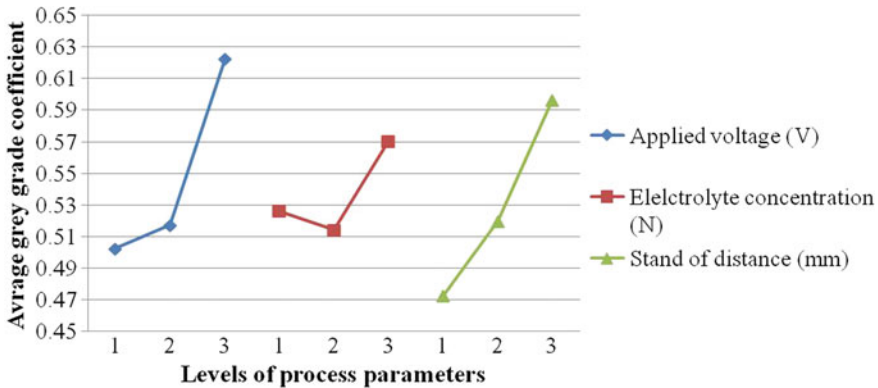


Fig. 31.8 Variation of average grey relational grade with the level of process parameter

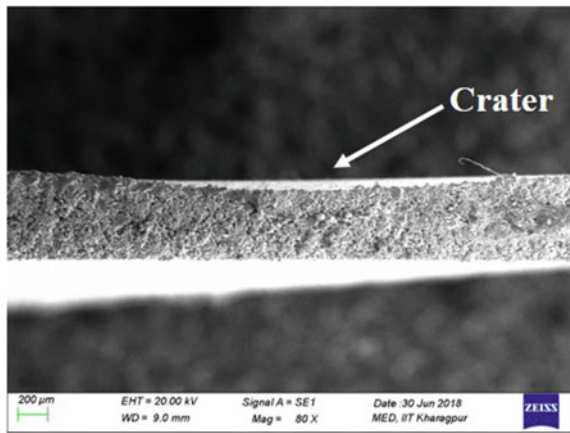
level 3 (=1.5 mm). Hence, the analysis of the average value of grey relational grade shows that keeping the applied voltage (=60 V) and electrolyte concentration (=0.5 N) constant, an increase in standoff distance from 1.0 to 1.5 mm would result in a desired crater dimension. A confirmation experiment was performed using the optimal set of input process parameters obtained through the analysis of grey relational grade. Table 31.4 shows the comparison of output responses obtained using “experimental run 9” and “optimum combination of process parameters obtained through grey relational grade analysis”. It was observed that the increase in the standoff distance from 1.0 mm to 1.5 mm resulted in the improvement of the average values of mass removal rate, roundness error and mean diameter-to-height ratio of the machined crater. Figure 31.9 shows the crater formed at the optimal combination of process parameters obtained through grey relational grade analysis.

In addition, the highest difference of average grey relational grade between the levels of each process parameters indicates the influence of that process parameters

**Table 31.4** Output responses obtained using “experimental run 9” and “optimum combination of process parameters obtained through grey relational grade analysis”

Run	Input parameter			Output response		
	Applied voltage (V)	Electrolyte concentration (N)	Standoff distance (mm)	Avg. mass removal rate (mg/min)	Avg. roundness error (mm)	Avg. mean diameter-to-height ratio
Run 9	60	0.5	1.0	7.86	0.50	40.95
Optimized	60	0.5	1.5	8.69	0.45	74.98

**Fig. 31.9** Crater formed at the optimal combination of process parameters



on the output. Thus, higher difference implies a significant influence on the output response. From Fig. 31.8. it can be stated that the order of significant effect on the output is as follows: standoff distance > applied voltage > electrolyte concentration. This is possible because an increase in standoff distance above the threshold value causes the jet to flare out. Flaring of jet increases the effective area of machining, and hence, increases the overall dimension of the machined crater.

### 31.5 Conclusions

In the present study, electro jet drilling has been successfully used to machine crater of the desired dimension. Applied voltage, concentration of NaCl in the electrolyte and standoff distance was varied to study the change in mass removal rate, roundness error and mean diameter-to-height ratio of the machined crater. The mass removal rate was found to increase with an increase in applied voltage and electrolyte concentration, while the increase in standoff distance was found to cause a decrease in the mass removal rate. The roundness error of the top of the crater was found to increase

with the applied voltage and the standoff distance, while the increase in electrolyte concentration was found to cause a decrease in the roundness error. The mean diameter-to-height ratio of the crater was found to increase with the increase in the electrolyte concentration and the standoff distance, while the increase in applied voltage was found to cause a decrease in the mean diameter-to-height ratio. A confirmation test was performed to obtain the desired crater dimension. It was observed that the optimal combination of process parameters (i.e., applied voltage = 60 V, electrolyte concentration = 0.5 N and standoff distance = 1.5 mm), obtained through grey relational grade analysis, resulted in (a) maximum value of mass removal rate as well as mean diameter-to-height ratio and (b) minimum value of the roundness error of the machined crater. Analysis of average grey relation grade showed that standoff distance has a significant effect on the machining of crater followed by applied voltage and electrolyte concentration.

## References

1. Mohan, S., Shan, H.S.: Analysis of hole quality characteristics in the electro jet drilling process. *Int. J. Mach. Tools Manuf.* **45**, 1706–1716 (2005). <https://doi.org/10.1016/j.ijmactools.2005.03.005>
2. Mohan, S., Shan, H.S.: Response surface analysis of electro jet drilled holes. *Int. J. Adv. Manuf. Technol.* **31**, 520–527 (2006). <https://doi.org/10.1007/s00170-005-0196-5>
3. Mohan, S., Shan, H.S.: Electro jet drilling using hybrid NNGA approach. *Robot. Comput. Integr. Manuf.* **23**, 17–24 (2007). <https://doi.org/10.1016/j.rcim.2005.08.004>
4. Mohan, S., Shan, H.S.: Optimal selection of machining conditions in the electrojet drilling process using hybrid NN-DF-GA approach. *Mater. Manuf. Process.* **21**, 349–356 (2006). <https://doi.org/10.1080/10426910500411561>
5. Chen, X.L., Dong, B.Y., Zhang, C.Y., Wu, M., Guo, Z.N.: Jet electrochemical machining of micro dimples with conductive mask. *J. Mater. Process. Technol.* **257**, 101–111 (2018). <https://doi.org/10.1016/j.jmatprotec.2018.02.035>
6. Liu, W., Ao, S., Li, Y., LiuZ, Wang Z., Luo, Z., Wang, Z., Song, R.: Jet electrochemical machining of TB6 titanium alloy. *Int. J. Adv. Manuf. Technol.* **90**, 2397–2409 (2017). <https://doi.org/10.1007/s00170-016-9500-9>
7. Hua, Zhang, Jiawen, Xu: Modeling and experimental investigation of laser drilling with jet electrochemical machining. *Chin. J. Aeronaut.* **23**(4), 454–460 (2010)
8. Goel, H., Pandey, P.M.: Performance evaluation of different variants of jet electrochemical micro-drilling process. *Proceed. Inst. Mech. Eng. Part B J. Eng. Manuf.* **232**, 451–464 (2018). <https://doi.org/10.1177/0954405416646689>
9. Kozak, J., Rajurkar, K.P., Balkrishna, R.: Study of electrochemical jet machining process. *J. Manuf. Sci. Eng.* **118**, 490–498 (1996). <https://doi.org/10.1115/1.2831058>
10. Ming, P., Li, X., Zhang, X., Song, X., Cai, J., Qin, G., Yan, L., Zheng, X.: Study on Kerosene submerged jet electrolytic micromachining. *Procedia CIRP* **68**, 432–437 (2018). <https://doi.org/10.1016/j.procir.2017.12.091>
11. Endo, H., Murahashi, T., Marui, E.: Accuracy estimation of drilled holes with small diameter and influence of drill parameter on the machining accuracy when drilling in mild steel sheet. *Int. J. Mach. Tools Manuf* **47**, 175–181 (2007). <https://doi.org/10.1016/j.ijmactools.2006.02.001>
12. Natsu, W., Ooshiro, S., Kunieda, M.: Research on generation of three-dimensional surface with micro-electrolyte jet machining. *CIRP J. Manuf. Sci. Technol.* **1**, 27–34 (2008). <https://doi.org/10.1016/j.cirpj.2008.06.006>

# Chapter 32

## Machining of Bio-Implant Materials Using WEDM and Optimization of Process Parameters



P. Hema , J. Mallikarjuna Rao  and C. Eswara Reddy 

**Abstract** Nonconventional machining is one of the revolutions in present manufacturing scenario. Among various machining techniques, Wire Electrical Discharge Machining (WEDM) is being used to machine biomaterials applied in medical field to machine suitable implant limbs in human body. An attempt is made in the present work to machine Mg AZ31b and SS304 biomaterials on WEDM, with an objective to optimize process parameters. Machining uses brass electrode wire and distilled water as dielectric fluid. Machining consists of linear cut and circular cut by considering Taguchi design of experiments. Input parameters are pulse-on time, pulse-off time, and wire feed. The output consists of Material Removal Rate (MRR), Surface Roughness (SR), and Kerf. Experimental results are validated with antlion optimization technique for optimization of process parameters. Regression analysis is used for validation.

**Keywords** WEDM · Taguchi design of experiments · Antlion optimization · Biomaterials · MRR · SR · Kerf

### 32.1 Introduction

Several machining techniques are being evolved in the present modern manufacturing industries. Wire Electrical Discharge Machining (WEDM) is also one of them and it is an unconventional specialized machining process. It has capability of machining hard materials which are difficult to machine sharp edges with complex shapes quite accurately. Such materials also can be easily machined by WEDM process. Nonconventional machining is one of the revolutions in manufacturing today. In the present work, optimization of parameters of biomaterials (Mg AZ31b and 316L SS) while machining on Wire EDM is considered. Unconventional machining process especially WEDM is a more appropriate technique for machining of hard materials.

---

P. Hema (✉) · J. M. Rao · C. E. Reddy  
Department of Mechanical Engineering, SV University, Tirupati 517502, India  
e-mail: [hemasvumech@gmail.com](mailto:hemasvumech@gmail.com)

© Springer Nature Singapore Pte Ltd. 2020  
M. S. Shunmugam and M. Kanthababu (eds.), *Advances in Unconventional Machining and Composites*, Lecture Notes on Multidisciplinary Industrial Engineering, [https://doi.org/10.1007/978-981-32-9471-4\\_32](https://doi.org/10.1007/978-981-32-9471-4_32)



Magnesium alloy is highly a potential material for biodegradable implant application. It has good biocompatibility and thus potential for medical implants. The use of Mg alloys as biodegradable implants has been promising. The outstanding characteristics of Mg AZ31b and 316L SS due to their compatibility and noticeable physical, mechanical, and biological performance have led to increased application in medical implants.

## **32.2 Literature Review and Objective**

A brief literature review on biomaterials is presented in the following. To start with, the metallic and metallurgical properties of materials for biomedical applications have been studied [1]. Machining capabilities of EDM to machine Mg WE43 for medical applications have been proved by experimentation [2]. Process chain for machining of bio-implant materials has been investigated and analyzed at macro and micro surface properties and then compared with biocompatibility testing for cell viability and toxicity [3]. It is followed by microstructural study and wear performance of arc-deposited Ti-N-O coatings on 304 SS [4]. Based on the need of implant materials, machining of biodegradable AZ31 Mg, alloys on EDM is proved by experimentation [5]. Many mathematical models are introduced for optimization of WEDM process parameters for surface roughness on 316L SS using full factorial design and analyzed the output results [6]. The invention of Antlion Optimizer (ALO) algorithm is a breakthrough in research [7] for modeling of EDM process parameters followed by Grey Relation Analysis in machining of Al HE30 Alloy [8]. Taguchi method is used for process parameters in machining of SS304 Steels [9]; SS316 [10] and AZ31 Biodegradable Mg Alloy [11]. Experimental results of machining of SS 316 on WEDM are analyzed by a combination of Taguchi, ANOVA, and Grey Relation Analysis [12]. Though a reasonable research is carried out, a lacuna is found on investigation of Mg- and SS-based alloys. Therefore, the present work is carried out.

### **32.2.1 Objectives**

An initial and solemn attempt is made in the present work for the first time to conduct experimentation on WEDM to machine bio-implant materials consisting of Mg AZ31b and SS 316L and then validation of optimization of process parameters by implementation of Antlion Optimization (ALO) algorithm.

### 32.3 Work Materials

Bio-implant Materials used in the present work are explained in the following:

#### 32.3.1 Mg AZ31b

Biodegradable (Mg AZ31b) implants possess good biocompatibility, nontoxicity, biodegradable, absorbable in human body, and good mechanical properties, and therefore used for repairing the damaged bone tissues.

#### 32.3.2 SS 316L

It has been widely used in various industries and domestic applications, because of their good mechanical properties. Medical grade 316L SS is presently used extensively in orthopedic, dental implants, and cardiovascular stents in the present medical field.

### 32.4 Experimental Work

Experimental work is carried out based on Taguchi Design of Experiment (DOE). The L9 orthogonal array is selected from Table 32.1 for machining of Mg AZ31b and SS 316L on WEDM. Trial and error method is adopted to select the parameters. The input parameters are varied simultaneously during machining to check the wire break condition. Ranges of parameters with equal intervals are then selected for machining and input parameters are shown in Table 32.2.

**Table 32.1** Design of experiments

S. no.	Ton	Toff	Wire feed
1	1	1	1
2	1	2	2
3	1	3	3
4	2	1	3
5	2	2	1
6	2	3	2
7	3	1	2
8	3	2	3
9	3	3	1

**Table 32.2** Input parameters for WEDM

Material	Type of cut	Pulse-time (T) ( $\mu$ s)		Wire feed (m/min)
		On	Off	
Mg Z31b	Linear	90–103	40–45	25–30
	Circular	100–106	40–45	25–30
SS 316L	Linear	100–140	40–45	25–30
	Circular	100–140	40–45	25–30

**Table 32.3** Levels of process parameters in linear cuts for Mg AZ31b

Parameters	Level 1	Level 2	Level 3
T <sub>on</sub>	90	99	103
T <sub>off</sub>	40	43	45
WF	25	28	30

**Table 32.4** Levels of process parameters circular cuts for Mg MgAZ31b

Parameters	Level 1	Level 2	Level 3
T <sub>on</sub>	100	103	106
T <sub>off</sub>	40	43	45
WF	25	28	30

**Table 32.5** Levels of process parameters linear and circular cuts for SS 316

Parameters	Level 1	Level 2	Level 3
T <sub>on</sub>	100	120	140
T <sub>off</sub>	40	43	45
WF	25	28	30

### 32.4.1 Design of Experiments

Process parameters chosen at three levels are shown in Table 32.3 for Mg Alloy for linear and circular in Table 32.4 followed by SS Alloy in Table 32.5 for linear and circular cuts.

### 32.4.2 Experimental Methodology

Experimental work carried out in machining is explained in the following. The wire EDM machine considered in the present work is shown in Fig. 32.1 followed by the experimental setup in Fig. 32.2. Experiments are conducted by running the wire EDM with input parameters for machining of Mg Alloy and SS Alloy. Brass wire of diameter 0.25 mm and water as dielectric fluid are used.



**Fig. 32.1** WEDM machine



**Fig. 32.2** Clamping of SS 316L on WEDM

### **Input Data and Parameters.**

Linear shape cut: Volume = Area  $\times$  Length, Area =  $\pi dt$ .

Circular shape cut: Volume = Area  $\times$  thickness, A = Area =  $\pi(D^2 - d^2)/4$ .

L = Length = Total path length (mm), d = diameter of the wire (0.25 mm).

tc = difference in thickness of workpiece (mm) and t = thickness of workpiece (mm).

**Output Results.** The workpiece after machining with a linear cut of Mg is shown in Fig. 32.3a and circular cut in Fig. 32.3b followed by linear and circular cuts of SS in Fig. 32.4.

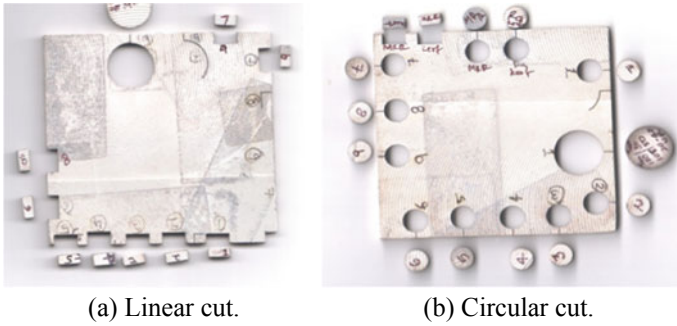
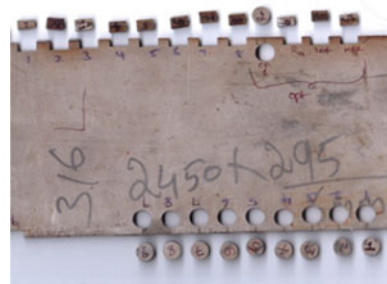


Fig. 32.3 Workpiece after machining of Mg

Fig. 32.4 Workpiece after machining of SS



Linear and Circular cuts

**Material Removal Rate (MRR).** The Material Removal Rate (MRR) of the workpiece is the amount of the material removed per minute in 3 mm/min.

**Kerf.** It is the amount of wobble created during cutting and amount of material pulled out of the sides of the cut. It is measured using Digital Vernier Calipers.

**Surface Roughness.** It is the surface condition obtained on the workpiece after machining.

The results obtained during the machining of linear Mg AZ31 are shown in Table 32.6 and circular in Table 32.7 followed by SS 316L linear in Table 32.8, and circular in Table 32.9.

### 32.5 Antlion Optimization (ALO)

A new metaheuristic called Antlion Optimization (ALO) technique inspired by antlions (doodlebugs) has been proposed [7]. The ALO algorithm mimics the leadership hierarchy and hunting mechanism of antlions in nature. But, it is limited as theoretical algorithm. Such algorithm is implemented for the first time in machining

**Table 32.6** Experimental results for Mg AZ31 b linear cut

Input parameters			Output results		
T <sub>on</sub>	T <sub>off</sub>	WF	SR	Kerf	MRR
95	40	25	0.57	0.41	9.91
95	43	28	0.55	0.53	13.5
95	45	30	0.62	0.69	17.7
99	40	28	0.43	0.57	15.13
99	43	30	0.51	0.34	8.72
99	45	25	0.47	0.55	12.92
103	40	30	0.32	0.52	14.52
103	43	25	0.56	0.65	16.31
103	45	28	0.46	0.35	9.46

**Table 32.7** Experimental results for Mg AZ31b circular cut

Input parameters			Output results		
T <sub>on</sub>	T <sub>off</sub>	WF	SR	Kerf	MRR
100	40	25	0.44	0.57	7.01
100	45	28	0.55	0.54	5.37
100	50	30	0.63	0.53	4.87
103	40	28	0.73	0.56	6.81
103	45	30	0.57	0.51	6.26
103	50	25	0.49	0.48	5.46
106	40	30	0.64	0.54	7.17
106	45	25	0.59	0.59	6.53
106	50	28	0.53	0.66	8.10

**Table 32.8** Experimental results for SS316L linear cut

Input parameters			Output results		
T <sub>on</sub>	T <sub>off</sub>	WF	SR	Kerf	MRR
100	40	25	0.493	0.72	3.56
100	50	28	0.513	0.67	2.77
100	60	30	0.6	0.72	2.51
120	40	25	0.667	0.72	7.95
120	50	28	0.65	0.66	7.30
120	60	30	0.647	0.59	5.59
140	40	28	0.61	0.64	6.03
140	50	30	0.656	0.68	7.79
140	60	25	0.77	0.682	5.80

**Table 32.9** Experimental results for SS316L circular cut

Input parameters			Output results		
T <sub>on</sub>	T <sub>off</sub>	WF	SR	Kerf	MRR
100	40	25	0.4	0.59	1.60
100	50	28	0.56	0.625	1.08
100	60	30	0.61	0.6	1.17
120	40	28	0.76	0.37	1.50
120	50	30	0.5	0.52	2.05
120	60	25	0.51	0.47	1.84
140	40	30	0.55	0.395	1.82
140	50	25	0.62	0.58	2.51
140	60	28	0.67	0.465	1.88

of implant machining of Mg- and SS-based materials in the present wok. The ALO is explained briefly in the following:

### 32.5.1 ALO Algorithm

ALO algorithm mimics the interaction between antlions and ants in the trap. To model such interactions, ants are required to move over the search space and antlions are allowed to hunt them and become fitter using traps. Since ants move stochastically in nature when searching for food, a random walk is chosen for modeling.

$$x(t) = \left[ 0, \sum (2r(t_1) - 1), \sum (2r(t_2) - 1), \dots, \sum (2r(t_n) - 1) \right] \quad (32.1)$$

where  $n$  is the maximum number of iteration,  $t$  shows the step of random walk (iteration in this study), and  $r(t)$  is a stochastic function defined as follows:

$$r(t) = \begin{cases} 1 & \text{if } rand > 0.5 \\ 0 & \text{if } rand \leq 0.5 \end{cases}$$

- Ants move around the search space using different random walks.
- Random walks are applied to all the dimension of ants.
- Random walks are affected by the traps of antlions.
- Antlions can build pits proportional to their fitness (the higher fitness, the larger pit).
- Antlions with larger pits have a higher probability to catch ants.
- Each ant can be caught by an antlion in each iteration fittest antlion.
- The range of random walk is decreased adaptively to simulate sliding ants toward antlions.

### 32.5.2 Random Walks of Ants

Random walks are all based on the Eq. (32.1). Ants update their positions with a random walk at every step of optimization. Since every search space has a boundary (range of variable); however, Eq. (32.1) cannot be directly used for updating the position of ants. In order to keep the random walks inside the search space, they are normalized using the following equation (min-max normalization):

$$X_i^t = \frac{(b_i^t - a_i) \times (d_i - c_i)}{(d_i^t - a_i)} \quad (32.2)$$

where  $a_i$  is the minimum of random walk of  $i$ -th variable,  $b_i$  is the maximum of random walk in  $i$ -th variable,  $c_i^t$  is the minimum of  $i$ -th variable at  $t$ -th iteration, and  $d_i^t$  indicates the maximum of  $i$ -th variable at  $t$ -th iteration.

### 32.5.3 Trapping Antlion Pits

As discussed above, random walks of ants are “affected by antlions” traps. In order to mathematically model this assumption, the following equations are proposed:

$$c_i^t = Antlion_j^t + c^t \quad (32.3)$$

$$d_i^t = Antlion_j^t + d^t \quad (32.4)$$

where

- $c_i$  is the minimum of all variables at  $t$ -th iteration,
- $d_i$  indicates the vector including the maximum of all variables at  $t$ -th iteration,
- $c_j^t$  is the minimum of all variables for  $i$ -th ant,
- $d_j^t$  is the maximum of all variables for  $i$ -th ant, and antlion
- $t_j$  shows the position of the selected  $j$ -th antlion at  $t$ -th iteration.

Equations 32.3 and 32.4 show that ants randomly walk in a hypersphere defined by the vectors  $c$  and  $d$  around a selected antlion.

### 32.5.4 Proposed Algorithm

Based on the parameters 5.0–5.1, the antlions, the behavior of the antlion optimization is implemented to find the optimal process parameters in machining of Mg- and SS-based bio-implant materials in the present paper and analyze the experimental results obtained from WEDM. The following Eq. (32.5) are proposed in this regard:



$$c^t = \frac{c^t}{I}, d^t = \frac{d^t}{I} \quad (32.5)$$

where  $I$  is a ratio,  $c_t$  is the minimum of all variables at  $t$ -th iteration, and  $d_t$  indicates the vector including the maximum of all variables at  $t$ -th iteration.

### 32.5.5 Proposed Path

The proposed ALO optimization algorithm is defined as a three-tuple function that approximates the global optimum for optimization problems as follows:

ALO (A, B, and C), where A is a function that generates the random initial solutions, B manipulates the initial population provided by the function A, and C returns true when the end criterion is satisfied. The functions A, B, and C are defined as follows:

$$\emptyset \rightarrow \{M_{Ant}, M_{OA}, M_{Antlion}, M_{OAL}\}, \{M_{Ant}, M_{Antlion}\} \rightarrow \{M_{Ant}, M_{Antlion}\} \text{ and} \\ \{M_{Ant}, M_{Antlion}\} \rightarrow \{\text{true}, \text{false}\}$$

where  $M_{Ant}$  is the matrix of the position of ants,  $M_{Antlion}$  includes position of antlions,  $M_{OA}$  contains the corresponding fitness of ants, and  $M_{OAL}$  has fitness of antlions.

## 32.6 Results and Discussions

Experimental results obtained are presented in the form of graphs as shown in the following:

### 32.6.1 Material Removal Rate

Characteristic curves for input parameters versus output results for MRR are drawn for Mg and SS materials. From the graph, Fig. 32.5, it can be seen that the MRR, in the linear case of machining Mg, gradually increases and reaches a maximum at Experiment (Expt.) 3 and falls to minimum at 5. Again it reaches a maximum at Expt. 8 and then falls to minimum at Expt. 9. Further, the MRR is almost uniform without much variation in circular machining of Mg. Similar trend is found in machining of SS, Fig. 32.6, that the MRR is uniform in case of circular cut. In contrast, the MRR in linear cut starts from minimum and reaches maximum at Expt. 4 and then slowly reaches minimum at Expt. 9. That shows to obtain maximum MRR, one can follow linear cut for Mg and in case of SS, for uniform MRR, follow the circular machining.

**Fig. 32.5** Output results of MRR cut of Mg

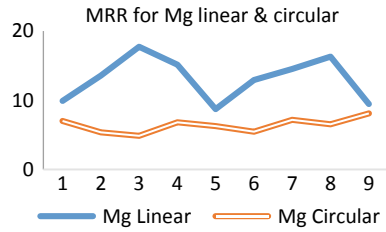
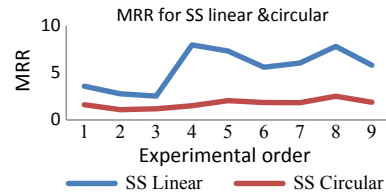


**Fig. 32.6** Output results of MRR cut of SS



### 32.6.2 Surface Roughness

The SR performance curves are drawn in Fig. 32.7. It is found that waviness is a uniform form for Mg linear cut and circular machining without much variation of profile of the machined surfaces. In case of machining of SS, Fig. 32.8, the SR is gradually increasing in circular cut in Expt. 4 and falls in Expt. 5, resulting in very much waviness. The SR is almost showing uniformity with linear cut. Thus, indicating the Expt. 4 and Expt. 5 require modification.

**Fig. 32.7** Output results of SR cut of Mg

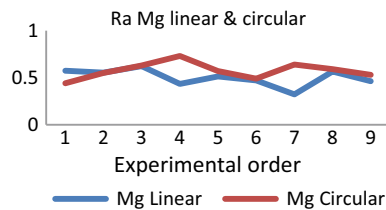
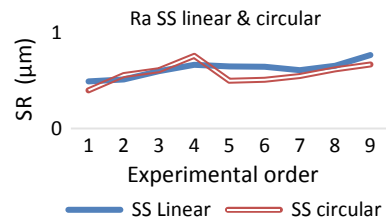


**Fig. 32.8** Output results of SR cut of SS



### 32.6.3 Kerf

Performance curves for circular machining of Kerf of Mg are shown in Fig. 32.9. The SR is found to be uniform in comparison to linear machining. SR is found uniform in case of linear machining of SS, Fig. 32.10. It is varying from level to level in circular machining. Both linear and circular machining performance curves are drawn and shown in Figs. 32.11 and 32.12. The same conditions for Mg linear machining conditions are suggested whereas any one of the methods either linear or circular can be followed in machining of SS. Further, the levels versus Kerf

**Fig. 32.9** Output results Kerf for cut of Mg

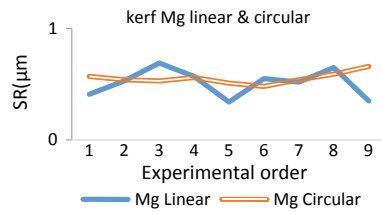


**Fig. 32.10** Output results of Kerf cut of SS

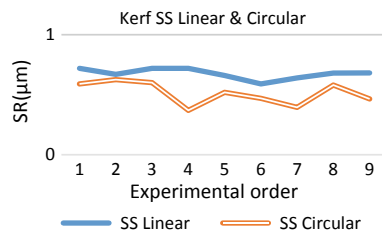


**Fig. 32.11** Output results of SR of Mg and SS

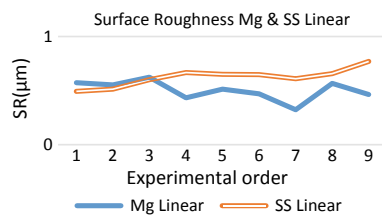


**Fig. 32.12** Output results of SR of Mg and SS

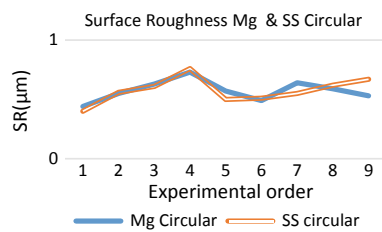


**Fig. 32.13** Output results of Kerf of Mg and SS

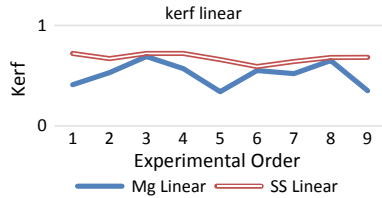
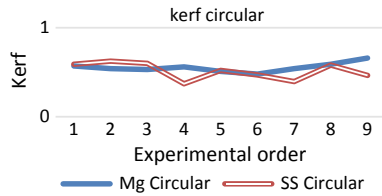


**Fig. 32.14** Output results of Kerf of Mg and SS



performance curves are shown in Fig. 32.13. It can be observed from the graph that the linear machining of Mg, the Kerf obtained is almost uniform, but in case of SS linear against non-uniformity in machining of Mg. Accordingly, taking the case of Kerf, linear cut, as shown in Fig. 32.14, Mg circular is found to be uniform whereas varying in case of SS. Therefore, it is suggested that it is better to consider linear Kerf of SS whereas circular Kerf is preferred for Mg.

### 32.7 Regression Analysis

The parameters are optimized using Antlion technique and the optimum. Further, the regression relation between the input and output values are carried out by using Minitab Software. The analyses generated are given as Regression Equations and shown in the following and the optimum values of ALO Results are shown in Table 32.10.

**Mg AZ31b linear.**

$$\begin{aligned} \text{Kerf} &= 2.52 - 0.005 \text{ Ton} - 0.012 \text{ Toff} - 0.035 \text{ WF} \\ \text{SR} &= 1.71 - 0.017\text{F12} \text{ Ton} + 0.014 \text{ Toff} - 0.0045 \text{ WF} \\ \text{MRR} &= 53.9 - 0.038 \text{ Ton} - 0.362 \text{ Toff} - 0.778 \text{ WF} \end{aligned}$$

**SS 316L linear.**

$$\begin{aligned} \text{Kerf} &= 1.044 - 0.0009 \text{ Ton} - 0.00047 \text{ Toff} - 0.0068 \text{ WF} \\ \text{SR} &= 0.282 + 0.00358 \text{ Ton} + 0.00569 \text{ Toff} - 0.0135 \text{ WF} \\ \text{MRR} &= -0.44 + 0.01497 \text{ Ton} - 0.011 \text{ Toff} + 0.003 \text{ WF} \end{aligned}$$

**Mg AZ31b circular.**

$$\text{Kerf} = -0.395 + 0.0083 \text{ Ton} + 0.0005 \text{ Toff} + 0.0023 \text{ WF}$$

**Table 32.10** Optimum values of ALO results

Responses	Input parameter			Optimal value
	T <sub>on</sub>	T <sub>off</sub>	WF	
<i>Linear Mg</i>				
Kerf	103	45	30	0.380
SR	103	40	30	0.387
MRR	95	40	25	16.454
<i>Circular Mg</i>				
Kerf	100	40	25	0.517
SR	100	50	30	0.518
MRR	106	40	25	7.806
<i>Linear SS</i>				
Kerf	140	60	30	0.632
SR	100	40	30	0.432
MRR	140	40	30	6.223
<i>Circular SS</i>				
Kerf	140	40	25	0.410
SR	100	60	30	0.504
MRR	140	40	25	0.829

$$SR = 0.08 + 0.0078 T_{on} - 0.0058 T_{off} - 0.0018 WF$$

$$MRR = -22.2 + 0.253 T_{on} - 0.046 T_{off} + 0.168 WF$$

**SS 316L circular.**

$$Kerf = 1.037 - 0.0031 T_{on} + 0.00196 T_{off} - 0.009 WF$$

$$SR = 0.632 + 0.0023 T_{on} - 0.00004 T_{off} - 0.0117 WF$$

$$MRR = -0.33 + 0.0197 T_{on} - 0.0015 T_{off} - 0.008 WF$$

### 32.8 Conclusions

In the present work, machining of Mg- and SS-based biomaterials considering two different profiles—linear and circular cuts by WEDM are presented. The process parameters are optimized using ALO technique and confirmation tests have also been conducted using Regression Analysis. Based on the results and discussions, the following conclusions are drawn:

- The average deviation between ALO and experimental results is found to be 6.5% among the biodegradable and nondegradable materials.
- The maximum deviation of 9.9% is obtained from Mg-based degradable material for linear cut in terms of MRR.

- Such optimum values can be used in the machining of Mg- and SS-based medical implants to suit the patient requirements.
- Further, the experiments are recommended to obtain output characteristics, MRR, SR, and Kerf considering the suggested optimal range of input parameters.

## References

1. Niinomi, M.: Recent metallic materials for biomedical applications. *Metall. Mater. Trans.* **33A**, 477–485 (2002)
2. Klocke, F.M., Schwade, M., Klink, A., Kopp, A.: EDM machining capabilities of Magnesium (Mg) alloy WE43 for medical applications. *Procedia Eng.* **19**, 190–195 (2011)
3. Klocke, F., Schwade, M., Klink, A., Veselovac, D.: Influence of electro discharge machining of biodegradable magnesium on the biocompatibility. In: *The First CIRP Conference on Bio-manufacturing, Procedia CIRP-5*, pp. 88–93 (2013)
4. Hsu, C.H., Huang, K.H., Lin, Y.H.: Microstructure and wear performance of Arc-deposited Ti-N-O coatings on AISI 304 Stainless Steel. *Wear* **306**(1–2), 97–102 (2013)
5. Abdul Rani, M.A., Razak, M.A., Littlefair, G.: Improving EDM process on AZ31Mg Alloy towards sustainable biodegradable implant manufacturing. *Procedia Manuf.* **19**, 190–195 (2017)
6. Raju, P., Sarcar, M.M.M., Satyanarayana, B.: Optimization of wire electrical discharge machining parameters for surface roughness on 316 L stainless steel using full factorial experimental design. *Procedia Mater. Sci.* **5**, 1670–1676 (2014)
7. Seyedal, M.: The ant Lion optimizer. *Adv. Eng. Softw.* **83**, 80–98 (2015)
8. Chengal Reddy, V., Deepthi, N., Jayakrishna, N.: Multiple response optimization of wire EDM on Aluminum HE30 by using grey relational analysis. *Mater. Today Proc.* **2**, 2548–2554 (2015)
9. Bharathi, P., Tummalapenta, G.L.P., Srinivasa Rao, G., Nageswara Rao B.G.: Optimum WEDM process parameters of SS304 using Taguchi method. *Int. J. Ind. Manuf. Syst. Eng.* **1**(3), 69–72 (2016)
10. Rajesh Kanna, S.K., Sethuramalingam, P.: Stainless steel 316 wire EDM process parameters optimization by using Taguchi method. *Int. J. Emerg. Res. Manag. Technol.* **6**(2), 69–73 (2017)
11. Razak, M.A., Abdul Rani, A.M., Rao, T.V.V.L.N., Pedapati, S.R., Kamal, S.: Electrical discharge machining on biodegradable AZ31 magnesium alloy using Taguchi method. In: *4th International Conference on Process Engineering and Advanced Materials, Procedia Eng.* **148**, 916–922 (2016)
12. Manish, S., Rahul, S., Abhinav, Gurupreet, S., Prabhat, M., Amit, S.: Optimizations of machining parameter in wire EDM for 316L Stainless Steel by using Taguchi method, Anova, and grey analysis. *Int. J. Mech. Eng. Technol.* **7**, 307–320 (2016)

# Chapter 33

## Experimental Investigations of Abrasive Waterjet Machining Parameters on Titanium Alloy Ti-6Al-4V Using RSM and Evolutionary Computational Techniques



A. Gnanavelbabu and P. Saravanan

**Abstract** In this research, an experimental investigation has been carried out on the Abrasive Water Jet Machining (AWJM) process for the machining of Grade 5 Titanium alloy (Ti-6Al-4V) using the Response Surface Methodology (RSM). Process parameters such as Mesh size (M), Abrasive Flow Rate (AFR), Water Pressure (WP) and Traverse Speed (TS) have been considered. Their influence on the kerf taper angle ( $\theta$ ) and surface roughness (Ra) has been obtained. An L29 Box-Behnken experimental design has been used in this experiment. Regression models have been developed for correlating the data generated using experimental results. Evolutionary optimization techniques like Particle Swarm Optimization (PSO), Cuckoo Search Algorithm (CSA) and Simulated Annealing (SA) are attempted for the considered AWJM process. CSA outperformed all other algorithms by its optimal solution. The confirmatory experiments have been carried out to validate the predicted parameters from the CSA which effectively produced minimized experimental response.

**Keywords** Waterjet · Ti-6Al-4V · Roughness · Kerf · RSM · Optimization

### 33.1 Introduction

Titanium is a very strong metal having excellent durability, corrosion resistance, fatigue resistance and a high strength-to-weight ratio which is maintained at increased temperatures. It finds application in the aerospace industry [1], automotive industry and medical industry [2]. Since Ti-6Al-4V has very high hardness, machining such a material with intricate shapes using conventional methods is very difficult. To overcome these difficulties, unconventional machining techniques must be utilized to machine titanium and its alloys.

---

A. Gnanavelbabu (✉) · P. Saravanan  
Department of Industrial Engineering, CEG Campus, Anna University, Chennai 600025, India  
e-mail: [agbabu@annauniv.edu](mailto:agbabu@annauniv.edu)

© Springer Nature Singapore Pte Ltd. 2020  
M. S. Shunmugam and M. Kanthababu (eds.), *Advances in Unconventional Machining and Composites*, Lecture Notes on Multidisciplinary Industrial Engineering, [https://doi.org/10.1007/978-981-32-9471-4\\_33](https://doi.org/10.1007/978-981-32-9471-4_33)

Some of the unconventional machining processes include Electrochemical Machining (ECM), Electrical Discharge Machining (EDM), Laser Beam Machining (LBM), Ultrasonic Machining (USM) and Abrasive Water Jet Machining (AWJM). ECM is not suited for all types of materials because of the high specific energy consumption, machining of only electrically conductive materials and the saline (or acidic) electrolyte which poses the risk of corrosion to the tool, work piece and equipment [3]. EDM provided a very low rate of material removal, high specific power consumption and excessive tool wear [4]. LBM is unsuitable due to high energy consumption and converging/diverging shape of the beam profile [5]. USM is detrimental because of the low material removal rate and quick wearing of the sonotrode tip [6].

AWJM is most suitable for titanium and its alloys because the process involves no heat affected zone, higher material removal rate (MRR) and no tool wear. High quality cutting by AWJM process assists in achieving a better surface finish than conventional processes [7]. AWJM utilizes a multitude of fine abrasives in the form of a high-pressure jet for machining materials.

In past literature, process parameters such as mesh size (#), stand-off distance (mm), pressure of water-jet (MPa), transverse rate (mm/min) and abrasive flow rate (g/min) were considered as the most important input variables in AWJM process [8]. Babu and Chetty [9] observed the effects of abrasive flow rate, water pressure and traverse speed on different performance parameters using recycled local garnet abrasives during machining of aluminium. Shanmugam and Masood [10] also reported that as the abrasive flow rate increased, the kerf taper angle seemed to decrease insignificantly. Wang [11] reported that kerf taper angle increases with an increase in the nozzle's traverse speed. They also suggested that by increasing the water pressure, the kerf top width slightly increased.

Hascalik et al. [12] has shown that increased traverse speed had decreased the smooth cutting region about 25% of the total cutting region of the material and shows a significant increase in kerf taper ratio for cutting narrower widths. Çaydaş and Hascalik [13] used artificial neural networks to optimize process parameters proved that surface roughness is maximum at the highest pressure and thus pressure of water-jet is a significant factor. Azmir and Ahsan [14] showed that a better machining performance with respect to surface roughness and kerf taper ratio was obtained by increasing the abrasive mass flow rate and hydraulic pressure. Gnanavelbabu et al. [15] revealed that high abrasive flow rate and low water pressure produced maximum material removal on the AWJM machining process.

In this paper, AWJM process parameters were optimized using RSM and evolutionary optimization algorithms, such as PSO, CSA and SA for the effective implementation of process parameters with respect to optimal response.



### 33.2 Experimental Setup and Material

In this experiment, commercial grade 5 titanium alloy Ti-6Al-4V with a thickness of 5 mm was machined using Precision Abrasive Water Jet Machining Center manufactured by OMAX Corporation (Model: 2626). The detailed description of the experimental setup and constant parameters are listed in Table 33.1.

By using each level of process parameters, 29 cuts were executed in the titanium alloy under the appropriate environmental circumstances which is shown individually in Fig. 33.1.

After the machining process, the kerf width was measured using Video Measurement System (VMS) for calculating kerf taper angle ( $\theta$ ). Later surface roughness (Ra) was measured using portable stylus-type contact roughness meter. The L29 Box-Behnken design of the selected parameters and experimental results is shown in Table 33.2.

The parameter kerf taper angle is calculated using Eq. (33.1):

$$\theta = \tan^{-1} \frac{k_t - k_b}{2t} \quad (33.1)$$

where

- $k_t$  Kerf top width;
- $k_b$  Kerf bottom width;
- $t$  Thickness of the work-piece

**Table 33.1** Parameters and its range of operation

Parameters	Range of operation
Orifice diameter (constant)	0.25 mm
Nozzle diameter (constant)	0.75 mm
Focusing tube length (constant)	75 mm
Focusing tube diameter (constant)	1 mm
Impact angle (constant)	90°
Abrasive type (constant)	Garnet
Standoff distance (constant)	1.5 mm
Abrasive mesh size (M)	80,100,120 #
Abrasive flow rate (AFR)	240, 340, 440 g/min
Water pressure (WP)	125, 200, 275 MPa
Traverse speed (TS)	60, 90, 120 mm/min

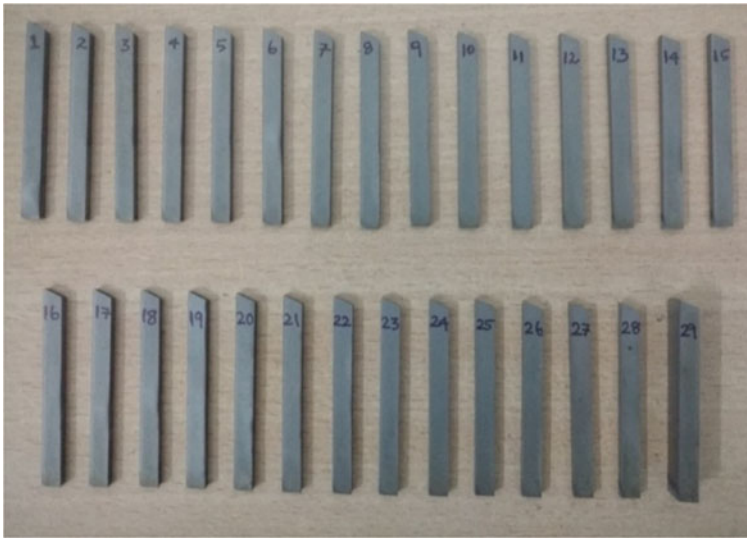


**Fig. 33.1** Typical AWJM of Ti-6Al-4V alloy

**Table 33.2** Experimental results using L29 Box-Behnken design

Exp. No.	M (#)	AFR (g/min)	WP (MPa)	TS (mm/min)	Ra ( $\mu\text{m}$ )	$\theta$ ( $^\circ$ )
1	100	440	200	120	2.4020	0.746
2	80	340	125	90	2.3460	0.742
3	100	340	275	120	2.3660	0.762
4	100	340	200	90	2.2920	0.752
5	100	340	200	90	2.2926	0.756
6	120	340	275	90	2.2460	0.776
7	100	340	200	90	2.2922	0.759
8	100	440	200	60	2.1660	0.778
9	80	240	200	90	2.2860	0.744
10	80	340	200	60	2.1589	0.766
11	100	240	275	90	2.2360	0.776
12	120	340	200	120	2.4213	0.732
13	120	240	200	90	2.3126	0.762
14	100	440	275	90	2.2386	0.784
15	120	340	200	60	2.1890	0.769
16	100	440	125	90	2.3622	0.756
17	100	340	200	90	2.2939	0.762
18	80	340	275	90	2.2326	0.78

(continued)

**Table 33.2** (continued)

Exp. No.	M (#)	AFR (g/min)	WP (MPa)	TS (mm/min)	Ra ( $\mu\text{m}$ )	$\theta$ ( $^\circ$ )
19	100	340	275	60	2.1320	0.786
20	120	340	125	90	2.3622	0.753
21	100	340	200	90	2.3061	0.766
22	80	440	200	90	2.2756	0.764
23	100	240	200	60	2.1810	0.758
24	100	340	125	120	2.4880	0.726
25	100	340	125	60	2.2120	0.754
26	100	240	200	120	2.4210	0.728
27	120	440	200	90	2.3006	0.766
28	80	340	200	120	2.3966	0.731
29	100	240	125	90	2.3460	0.739

### 33.3 Response Surface Methodology (RSM)

RSM is a collection of statistical and mathematical techniques used for analysis of problems in which the output variable(s) is influenced by several input variables. In this experiment, the Box-Behnken design is used to optimize the number of experiments needed to be carried out in order to determine the possible interactions between the parameters studied and their effects. A statistical analysis of the output obtained using Analysis of Variance (ANOVA) is used for ascertaining the contribution of each process parameter on the quality of cutting.

#### 33.3.1 Analysis of Surface Roughness

The ANOVA result for surface roughness is given in Table 33.3. It is observed that the P-Value for the abrasive flow rate is greater than 0.05 and is, therefore, an insignificant contributor to the surface roughness. Hence, at the confidence level of 95%, the remaining factors have a great influence on the surface roughness. The interaction effect between water pressure and traverse speed is also significant.

The percentage contribution of the process parameters and the interaction effect of water pressure and traverse speed on the surface roughness is shown in Table 33.4. It is clear that traverse speed is the most significant contributor at 81.456%.

#### 33.3.2 Analysis of Kerf Taper Angle

The ANOVA result for kerf taper angle is given in Table 33.5. It is observed that the P-Value for the mesh size is greater than or equal to 0.05 and is, therefore, an

**Table 33.3** ANOVA for surface roughness

Source	DF	Adj SS	Adj MS	F-value	P-value
Model	5	0.215636	0.043127	797.61	0.000
<b>Linear</b>	4	0.215195	0.053799	994.97	0.000
A: Mesh	1	0.001541	0.001541	28.51	0.000
B: Abrasive flow rate	1	0.000118	0.000118	2.18	0.153
C: Water pressure	1	0.036874	0.036874	681.96	0.000
D: Traverse speed	1	0.176661	0.176661	3267.23	0.000
<b>2-way interaction</b>	1	0.000441	0.000441	8.16	0.009
CD: Water pressure * Traverse speed	1	0.000441	0.000441	8.16	0.009
<b>Error</b>	23	0.001244	0.000054		
Lack-of-fit	19	0.001097	0.000058	1.58	0.355
Pure error	4	0.000146	0.000037		
<b>Total</b>	28	0.216879			

**Table 33.4** Percentage contribution to surface roughness

Source	% contribution
A: Mesh	0.7105
B: Abrasive flow rate	0.0544
C: Water pressure	17.0021
D: Traverse speed	81.4560
CD: Water pressure * Traverse speed	0.2033

**Table 33.5** ANOVA for kerf taper angle

Source	DF	Adj SS	Adj MS	F-value	P-value
Model	6	0.007348	0.001225	65.66	0.000
<b>Linear</b>	4	0.006730	0.001683	90.21	0.000
A: Mesh	1	0.000080	0.000080	4.29	0.050
B: Abrasive flow rate	1	0.000631	0.000631	33.82	0.000
C: Water pressure	1	0.003136	0.003136	168.15	0.000
D: Traverse speed	1	0.002883	0.002883	154.57	0.000
<b>Square</b>	2	0.000618	0.000309	16.56	0.000
C <sup>2</sup> : Water pressure * Water pressure	1	0.000167	0.000167	8.98	0.007
D <sup>2</sup> : Traverse speed * Traverse speed	1	0.000370	0.000370	19.85	0.000
<b>Error</b>	22	0.000410	0.000019		
Lack-of-fit	18	0.000294	0.000016	0.56	0.822
Pure error	4	0.000116	0.000029		
<b>Total</b>	28	0.007758			

**Table 33.6** Percentage contribution to kerf taper angle

Source	% contribution
A: Mesh	1.0312
B: Abrasive flow rate	8.1335
C: Water pressure	40.4228
D: Traverse speed	37.1616
C <sup>2</sup> : Water pressure * Water pressure	2.1526
D <sup>2</sup> : Traverse speed * Traverse speed	4.7693

insignificant contributor to the kerf taper angle. Hence, at the confidence level of 95%, the remaining factors have a great influence on the kerf taper angle. The interaction effect between water pressure and water pressure, and traverse speed and traverse speed is also significant.

The percentage contribution of the process parameters and the interaction effect of water pressure with water pressure and traverse speed with traverse speed is shown in Table 33.6. Water pressure is the most significant contributor at 40.4228%.

### 33.3.3 Single Objective Optimization Using RSM

Regression equations are obtained from the MINITAB software by analyzing the experimental data and are incorporated in the previously described optimization techniques. The predicted regression equation for the response variable surface roughness and kerf taper angle are given in Eqs. (33.2) and (33.3) respectively.

$$\begin{aligned} \text{Surface roughness} = & 1.9488 + 0.000567 * x(1) - 0.000031 * x(2) - 0.000319 * x(3) \\ & + 0.004978 * x(4) - 0.000005 * x(3) * x(4) \end{aligned} \tag{33.2}$$

$$\begin{aligned} \text{Kerf taper angle} = & 0.6936 + 0.000129 * x(1) + 0.000073 * x(2) - 0.000135 * x(3) \\ & + 0.000948 * x(4) + 0.000001 * x(3) * x(3) - 0.000008 * x(4) * x(4) \end{aligned} \tag{33.3}$$

where

- x(1) Mesh;
- x(2) Abrasive flow rate;
- x(3) Water pressure;
- x(4) Traverse speed

Figure 33.2a, b show the single objective optimization of the performance parameters i.e. surface roughness and kerf taper angle respectively. For the L29 Box-Behnken

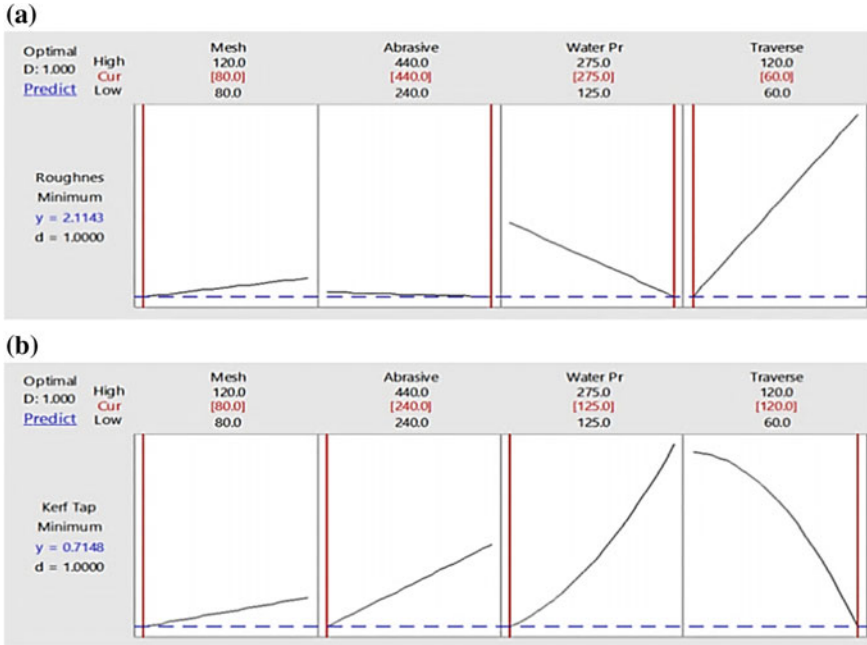
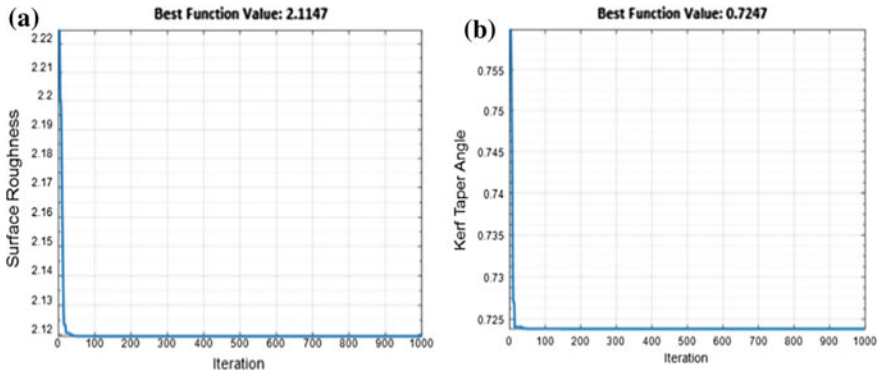


Fig. 33.2 Single objective optimization using RSM **a** surface roughness and **b** kerf taper angle

experimental data, the current settings are mesh size = 80# (low), abrasive flow rate = 440 g/min (high), water pressure = 275 MPa (high) and traverse speed = 60 mm/min (low) produced surface roughness of 2.1143  $\mu\text{m}$  at the optimal desirability of 1.000. For the L29 Box-Behnken experimental data, the current settings are mesh size = 80# (low), abrasive flow rate = 240 g/min (low), water pressure = 125 MPa (low) and traverse speed = 120 mm/min (high the kerf taper angle of 0.7148° at the optimal desirability of 1.000.

### 33.4 Evolutionary Optimization Techniques

The use of evolutionary optimization techniques is adopted by researchers because these techniques have been used in a variety of applications and can also determine a solution for complex optimization problems effectively. Single objective optimization techniques are run in MATLAB for 1000 iterations (for uniformity in comparative analysis) to measure effectiveness of each algorithm using the regression Eqs. (33.2) and (33.3) from the experimental analysis using MINITAB software.



**Fig. 33.3** Convergence of PSO for the AWJM process **a** surface roughness and **b** kerf taper angle

### 33.4.1 Particle Swarm Optimization (PSO)

James Kennedy and Russell C. Eberhart developed the PSO algorithm in 1995. According to this algorithm, each individual (candidate solution) is considered as a particle of the population (swarm). The steps of PSO are given as follows,

1. Given the problem dimension, initialize the random position and velocities of the particles.
2. Evaluate the fitness function value of each particle present in the swarm.
3. Compare the various fitness function values to obtain the local and global best.
4. Update the velocity of each individual particle.
5. Update the position of each individual particle.
6. Based on the updated position of the individual evaluate the fitness function and determine the local and global best particle.
7. Update the result; if the iteration number exceeds the maximum generation limit go to step 8, else, go to step 4.
8. Save and store the result; terminate the process.
9. Export the convergence plot of each fitness function (i.e.) surface roughness and kerf taper angle as shown in Fig. 33.3a, b.

### 33.4.2 Cuckoo Search Algorithm (CSA)

The CSA was developed by Xin-She Yang and Suash Deb in 2009. It is inspired by the behavior of cuckoo species which laid their eggs in the nests of other bird's species.

The three idealized rules on which the CSA principle is based on are (1) Each cuckoo lays only one egg and dumps its egg in the nest of a host bird randomly, (2) The nests having the best quality of eggs will be considered for succeeding

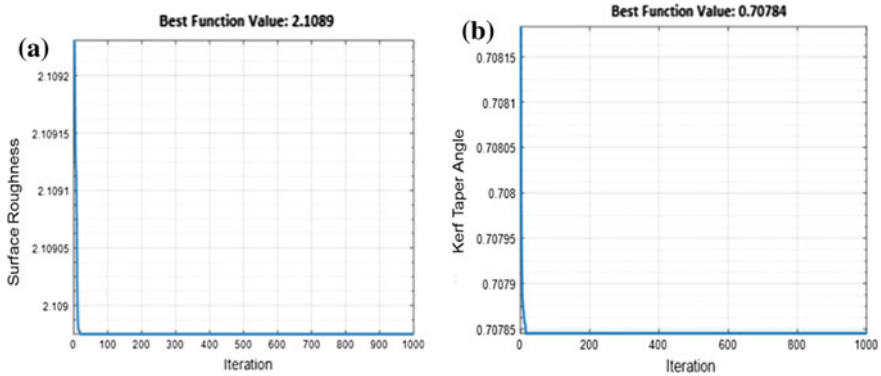


**Fig. 33.4** Convergence of CSA for the AWJM process **a** surface roughness, **b** kerf taper angle

generations, and (3) The number of host's nests that are available is fixed. A Levy flight is executed to obtain the new nest position for each cuckoo. The parameter values (i.e.) probability to alienate egg ( $P_a$ ) and step size ( $\alpha$ ), varies in accordance to the generation in order to perform a global and local search within the domain range. The algorithm's convergence rate depends on the fine tuning of the parameters to locate the optimal solution. It must be noted that the  $P_a$  and  $\alpha$  values should be reduced in final generations to achieve a better solution vectors.

1. Initialization of the random host nest position.
2. Evaluate the host nest's position fitness function.
3. Identify the best egg in that nest having the highest fitness function value.
4. By using levy flights generate new cuckoos by using the factors  $P_a$  and  $\alpha$ .
5. If the alien egg is discovered, replace the host nest position with the new host nest position randomly.
6. Evaluate the fitness function values for the new host positions.
7. Inspect the stopping criteria; if the criteria are satisfied, go to step 8, else, go to step 4.
8. Save and store the result; terminate the process.
9. Export the convergence plot of each fitness function (i.e.) surface roughness and kerf taper angle as shown in Fig. 33.4a, b.

### 33.4.3 Simulated Annealing (SA)

SA is a metaheuristic developed by Kirkpatrick in 1983 for approximating the global optimum of a given function in a large search space. The concept of slow cooling in annealing can be interpreted as slow fall in the probability of accepting bad solutions as the solution space is searched out. The Boltzmann probability distribution is used to control the temperature parameter. During the search for the optimum value, the



temperature is progressively decreased till it reaches zero. The energy difference between two points (initial point and the next point generated in the vicinity of the initial point) is calculated. Acceptance or rejection of the point is done using the metropolis algorithm based on the energy difference. In the succeeding cycles, a new point is generated in the vicinity of the updated point and the energy difference is computed again. The process continues till the temperature reaches a minimum value or the required target value is achieved in the fitness function value. Initialize the start point ( $x_1$ ) in a random fashion, the initial temperature ( $T$ ), and termination criteria.

1. Evaluate the energy  $E_1$ , i.e., the fitness value, for the generated point.
2. Compute a neighborhood point ( $x_2$ ) and evaluate the fitness  $E_2$  at this point.
3. Calculate the energy difference between the two points  $\Delta E$ .
4. (i) Accept the point if  $\Delta E < 0$  and go to step 6.  
 (ii) If  $\Delta E \geq 0$ , create a random number ( $r$ ) between 0 and 1 and verify if  $r \leq e^{-\frac{\Delta E}{T}}$ ; if yes, accept the point with some probability and go to step 6; else generate a new initial point and go to step 3.
5. Decrease the temperature and inspect the criteria for termination; if satisfied go to step 7, else, go to step 3.
6. Save and store the result; terminate the process.
7. Export the convergence plot of each fitness function (i.e.) surface roughness and kerf taper angle as shown in Fig. 33.5a, b.

Table 33.7 shows the optimized results of each algorithm for single objectives of AWJM process.

The best optimum value for surface roughness and kerf taper angle is obtained for CSA algorithm as  $2.1089 \mu\text{m}$  and  $0.70784^\circ$  respectively. Then, all the optimized parameter values obtained from CSA are rounded-off and a confirmatory test run is carried out as shown in Table 33.8.

It is found that the percentage of error for the performance parameters is within 3%. Moreover, the obtained results are in accordance with the results of RSM. The

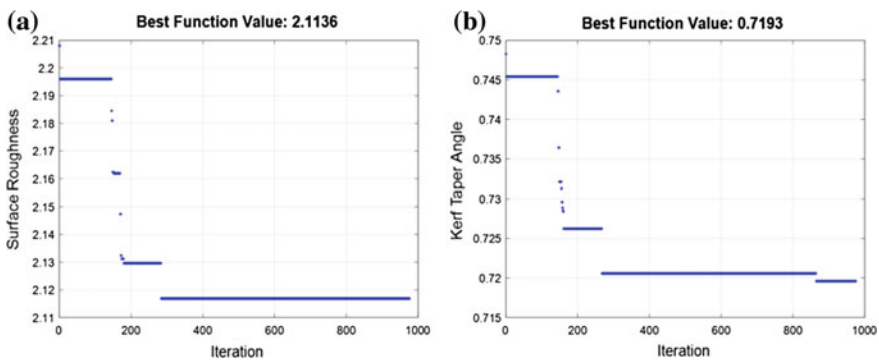


Fig. 33.5 Convergence of SA for the AWJM process **a** surface roughness, **b** kerf taper angle

**Table 33.7** Single objective optimization results of AWJM process

Algorithm	Response	Optimal solution	M (#)	AFR (g/min)	WP (MPa)	TR (mm/min)
PSO	Ra ( $\mu\text{m}$ )	2.1147	108.134	296.860	187.080	60.000
	$\theta$ ( $^\circ$ )	0.7247	112.929	264.019	125.000	119.999
CSA	Ra ( $\mu\text{m}$ )	<b>2.1089</b>	<b>80.001</b>	<b>439.973</b>	<b>275.000</b>	<b>60.000</b>
	$\theta$ ( $^\circ$ )	<b>0.70784</b>	<b>80.013</b>	<b>240.007</b>	<b>125.015</b>	<b>120.000</b>
SA	Ra ( $\mu\text{m}$ )	2.1136	80.456	331.632	272.938	60.026
	$\theta$ ( $^\circ$ )	0.7193	80.018	245.135	126.619	119.983

**Table 33.8** Confirmatory test results for surface roughness and kerf taper angle

Performance parameter	M (#)	AFR (g/min)	WP (MPa)	TS (mm/min)	Optimized result	Experimental result
Ra ( $\mu\text{m}$ )	80	440	275	60	2.1089	2.15107
$\theta$ ( $^\circ$ )	80	240	125	120	0.70784	0.72554

values of process parameters can be easily adjusted on the AWJM machine to obtain the optimum performance characteristic for the considered titanium alloy Ti-6Al-4V to have better and an improved cutting quality.

### 33.5 Conclusions

In this research, the AWJM process parameters for Ti-6Al-4V titanium alloy have been optimized by using three evolutionary optimization techniques and RSM. From ANOVA, it is revealed that traverse speed is the most significant contributor to surface roughness with a contribution of 81.456% and water pressure being the most significant contributor to kerf taper angle with a contribution of 40.4228%. Regression models were also developed for the given process parameters. Evolutionary optimization techniques such as PSO, CSA, and SA have been applied to the data set for obtaining the optimal parameter setting. From the results obtained, it was revealed that CSA was the best evolutionary optimization technique. The confirmatory test results validated that the error was less than 3% between the experimentally obtained values and the optimized values by CSA.

**Acknowledgements** The authors acknowledge the financial support for Research Consumables rendered by DST PURSE Phase II.

## References

1. Ali, M.H., Ansari, M.N.M., Khidhir, B.A., Mohamed, B., Oshkour, A.A.: Simulation machining of titanium alloy (Ti-6Al-4V) based on the finite element modeling. *J. Braz. Soc. Mech. Sci. Eng.* **36**(2), 315–324 (2014)
2. Elias, C.N., Lima, J.H.C., Valiev, R., Meyers, M.A.: Biomedical applications of titanium and its alloys. *JOM* **60**(3), 46–49 (2008)
3. Rajurkar, K.P., Zhu, D., McGeough, J.A., Kozak, J., De Silva, A.: New developments in electrochemical machining. *CIRP Ann.* **48**(2), 567–579 (1999)
4. Ho, K.H., Newman, S.T.: State of the art electrical discharge machining (EDM). *Int. J. Mach. Tools Manuf.* **43**(13), 1287–1300 (2003)
5. Dubey, A.K., Yadava, V.: Laser beam machining—a review. *Int. J. Mach. Tools Manuf.* **48**(6), 609–628 (2008)
6. Thoe, T.B., Aspinwall, D.K., Wise, M.L.H.: Review on ultrasonic machining. *Int. J. Mach. Tools Manuf.* **38**(4), 239–255 (1998)
7. Gnanavelbabu, A., Saravanan, P., Rajkumar, K., Karthikeyan, S., Baskaran, R.: Effect of abrasive waterjet machining parameters on hybrid AA6061-B4C-CNT composites. *Mater. Today: Proc.* **5**(5), 13438–13450 (2018)
8. Gnanavelbabu, A., Rajkumar, K., Saravanan, P.: Investigation on the cutting quality characteristics of abrasive water jet machining of AA6061-B4C-hBN hybrid metal matrix composites. *Mater. Manuf. Processes.* **33**(12), 1313–1323 (2018)
9. Babu, M.K., Chetty, O.K.: A study on recycling of abrasives in abrasive water jet machining. *Wear* **254**(7–8), 763–773 (2003)
10. Shanmugam, D.K., Masood, S.H.: An investigation on kerf characteristics in abrasive waterjet cutting of layered composites. *J. Mater. Process. Technol.* **209**(8), 3887–3893 (2009)
11. Wang, J.: Abrasive waterjet machining of polymer matrix composites—cutting performance, erosive process and predictive models. *Int. J. Adv. Manuf. Technol.* **15**(10), 757–768 (1999)
12. Hascalik, A., Çaydaş, U., Gürün, H.: Effect of traverse speed on abrasive waterjet machining of Ti–6Al–4V alloy. *Mater. Des.* **28**(6), 1953–1957 (2007)
13. Çaydaş, U., Hascalik, A.: A study on surface roughness in abrasive waterjet machining process using artificial neural networks and regression analysis method. *J. Mater. Process. Technol.* **202**(1–3), 574–582 (2008)
14. Azmir, M.A., Ahsan, A.K.: A study of abrasive water jet machining process on glass/epoxy composite laminate. *J. Mater. Process. Technol.* **209**(20), 6168–6173 (2009)
15. Gnanavelbabu, A., Saravanan, P., Rajkumar, K., Karthikeyan, S.: Experimental investigations on multiple responses in abrasive waterjet machining of Ti-6Al-4V alloy. *Mater. Today: Proc.* **5**(5), 13413–13421 (2018)

# Chapter 34

## Design of Fixture for Trimming of a Composite Material Shim by Abrasive Water Jet Machining



Kushal Singh , Ch. Venkateswarlu , B. Hari Prasad  and A. P. Dash 

**Abstract** The fixtures required in manufacturing must correctly locate workpiece in a given orientation with respect to cutting tool. The present work aims at design of fixture for trimming of a component called shim which is made of composite material. The trimming is done by abrasive water jet machine. Machining by conventional methods compromise the strength of the composite materials and/or cause delamination, making it less suitable for aerospace applications, thus Abrasive Water Jet (AWJ) technology is used for machining composite materials. In present work, the shim made of composite material is required to be cut at specified orientation at given location in a circular path. Since the shim is a thin-walled structure, excess clamping force may deform it and it may not get cut at required positions, although sufficient support and clamping is required to hold the component during trimming operation by water jet machining. The fixture needs to be designed for an abrasive water jet machine in which the water jet nozzle head is stationary and automation, e.g., rotary table is not available for maintaining circular cut at specified location and orientation. A fixture is designed to meet the above requirements. The suitable rotational speed to cut the shim is found experimentally and the shim is cut in circular path at desired location on the fixture.

**Keywords** Fixture design · Abrasive water jet machining · Composite material

### 34.1 Introduction

The composite structure delivers higher strength to weight ratio requirement in aerospace systems. In present work, the shim made of composite material is required to be cut at specified orientation at a given location for an aerospace application. Since composites are not homogenous materials and are reinforced for greater strength, cutting composites require a different approach than ceramic cutting or metal cutting.

---

K. Singh (✉) · Ch. Venkateswarlu · B. Hari Prasad · A. P. Dash  
Defence Research and Development Laboratory (DRDL),  
Kanchanbagh, Hyderabad 500058, India  
e-mail: [kushalsingh2000@gmail.com](mailto:kushalsingh2000@gmail.com)

© Springer Nature Singapore Pte Ltd. 2020  
M. S. Shunmugam and M. Kanthababu (eds.), *Advances in Unconventional Machining and Composites*, Lecture Notes on Multidisciplinary Industrial Engineering, [https://doi.org/10.1007/978-981-32-9471-4\\_34](https://doi.org/10.1007/978-981-32-9471-4_34)

Using conventional cutters and machining techniques will quickly cause parts to wear out and require replacement. As an alternative, cutting with a water jet offers a number of benefits for composite machining. Abrasive water jet machining does not produce heat-affected zones (HAZ) or leave rough edges/burrs that require the material to undergo secondary finishing with other composite machines. In other words, the load imposed by the machine on the workpiece is almost zero as pressure acts only at the required points. However, the positioning of the workpiece on specific location is an important aspect to manufacture the components without any discrepancies. Hence, the fixture design is important. Additionally, very little waste is created with water jet technology to protect material investment. Speed and accuracy of the technology make it well suited to high production requirements [1]. A typical abrasive water jet cutting machine setup is shown in Fig. 34.1.

Proper tooling is the key factor in water jet machine for machining for thin-wall composite material, Rex and Ravindran [2] have developed a procedure to find the optimal position for the locators and clamps in order to reduce the elastic deformation of the workpiece during machining with respect to the deterministic location. Improper tooling and cutting parameters may also lead to delamination of composite materials. Delamination is influenced by abrasive flow rate, traverse rate, and hydraulic pressure and minimum delamination damage can be achieved by increasing the kinetic energy of abrasive water jet [3]. It is also important to choose the correct abrasive grit. For example, most composites will have a better surface finish if they are cut with 120-grit abrasive [4].

The above machining parameters are adapted for trimming of composite material; however, when machining composites, it is important to support the material properly to avoid any material failure, e.g., delamination by the undesired deflected water jet



**Fig. 34.1** Abrasive water jet cutting machine setup

on the surface of workpiece. It is necessary to develop a methodology to adapt the process parameters for composite material trimming, along with design of suitable fixture which will allow AWJ trimming operations to be carried out in the desired manner, to meet the component design requirements.

In present work, a thin-walled component of composite material is required to be cut at specified orientation at given location in a circular path. The fixture needs to be designed for an abrasive water jet machine in which the water jet nozzle head is stationary and automated, e.g., rotary table is not available for maintaining circular cut at specified location and orientation.

## 34.2 Fixture Design Requirements

The shim made of composite material is a thin-walled structure with height ( $H$ ) and diameter  $5H$ . The shim is required to be cut in a circular path, at specified orientation at given locations, i.e.,  $\alpha^\circ$  from horizontal position (or  $\beta^\circ$  from vertical position) at lower side at distance  $D$  from bottom face of shim and  $\gamma^\circ$  from horizontal position (or  $\delta^\circ$  from vertical position) at upper side at distance  $5D$  from top face of the shim, as shown in Fig. 34.2.

In water jet cutting of composites precise location of abrasive water jet nozzle with respect to component is required to be maintained, otherwise jet shooting out of the intended cut might perform an unintended cut on some other surface of the part.

Due to thin wall, excessive clamping force may distort the shim, geometry. Thus to make a desired circular cut at specified location a fixture is to be designed to hold the shim with sufficient clamping force during water jet machining while rotating about the shim axis.

The fixture is required to rotate the shim while trimming by water jet machine. The rotation speed should be optimized to perform effective cut by water jet. The prime role of the fixture is to hold the job at the location without any deflection during the machining.

## 34.3 Design of Composite Shim Cutting Fixture

The water jet machine used in present work, for shim cutting it has only two-axis movements, i.e., X axis and Y axis in a plane. The nozzle moves in these two axes over the job during the operation. If the shim is to be cut in circular path with a cut normal to flat surface it can be achieved by moving the nozzle in circular path by combined X, Y movements of nozzle. But if the cut is required to be made at specific angle, as in present case, i.e.,  $\delta^\circ$  and  $\gamma^\circ$  from horizontal plane, the nozzle has to tilt continuously while maintaining circular path and the trimming angle. The

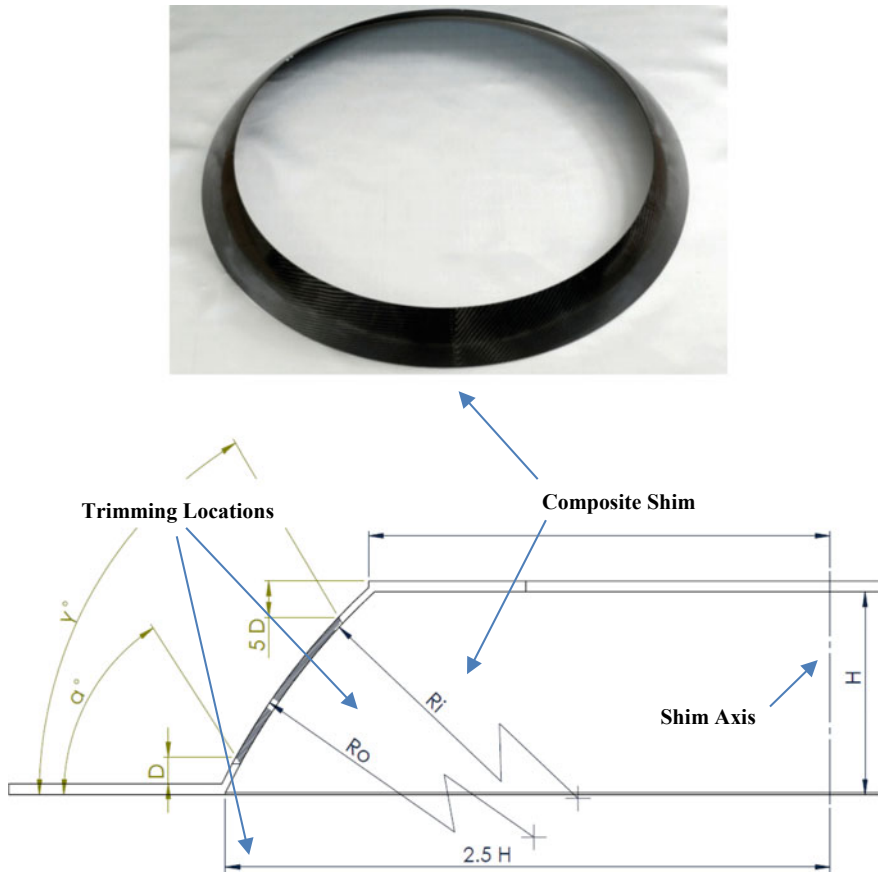


Fig. 34.2 Composite shim geometry and trimming locations

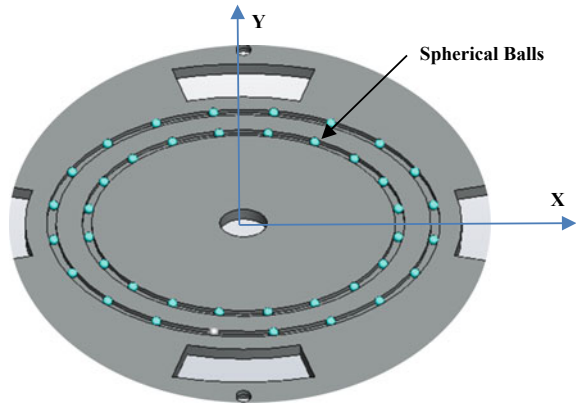
present abrasive water jet machine has a stationary water jet nozzle and it cannot tilt continuously as desired. However, the nozzle can be tilted and fixed at an angle.

Other solution is to tilt and fix the nozzle at required angle and rotate the shim. Since the water jet machine does not have the rotary table, nozzle head of the water jet machine is kept steady at desired angle and a rotary table is designed to rotate the shim, to cut it in a circular path.

The rotary table is consists of two halves. The bottom plate is stationary and the top plate is rotated. Hardened spherical stainless steel balls are placed between the top and bottom plates, along the grooves provided in each plate to enable the rotation of top plate over the bottom plate through spherical balls. Two such tracks of rectangular cross section are made for better stability of plates during rotation (Fig. 34.3).

The plates and spherical balls undergo through the condition of rolling friction during the operation, while the top plate is rotating and the bottom plate is stationary.

**Fig. 34.3** Hardened spherical stainless steel balls along the grooves



Spherical balls and bearings are designed as per ANSI/ABMA 24.1 standard for “Thrust Bearings of Ball, Cylindrical Roller and Spherical Roller Types—Metric Design.” Bearing life is another important consideration while designing fixture which is defined as the total number of revolutions (or hours at a constant speed) of bearing operation until the failure criterion is developed. Four Bearings are provided, each at 90° angle apart to prevent lateral movement during cutting and enable the smooth rotation of the upper plate (Fig. 34.4).

Since the composite shims are made of thin walls, clamping is designed to apply a balanced clamping force by external support pins and internal support pins as shown in Fig. 34.5. Two external support threaded pins are provided on top support blocks with tapped holes to control the clamping pressure externally and one fix pin support is provided internally.

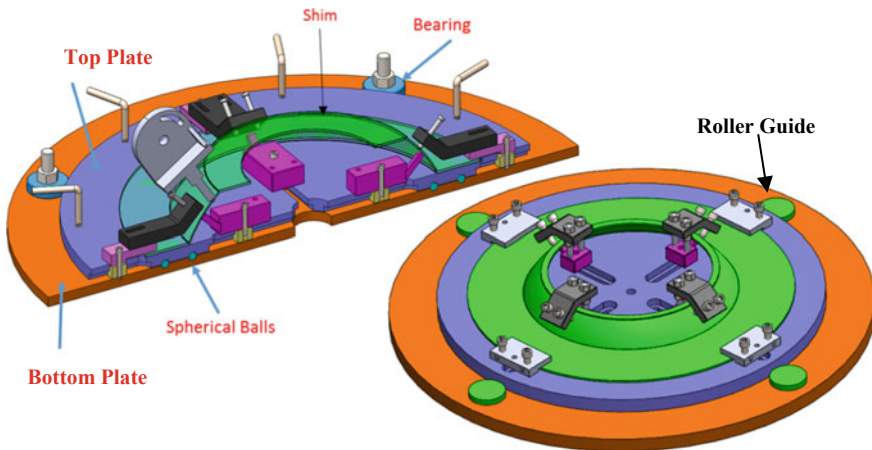


**Fig. 34.4** Shim cutting fixture design



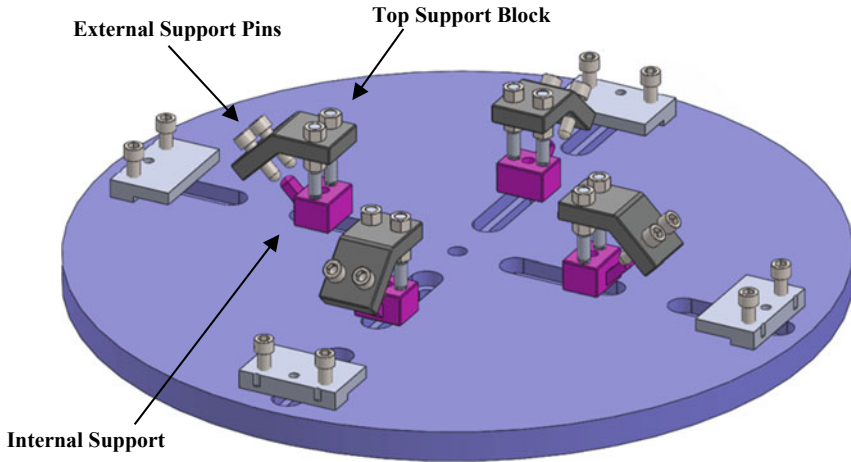


Fig. 34.5 External and internal support

As per design requirement, the shim is required to be cut at an angle of  $\alpha^\circ$  from horizontal position (or  $\beta^\circ$  from vertical position) at lower side, and  $\gamma^\circ$  from horizontal position (or  $\delta^\circ$  from vertical position) at upper side of shim. The normal orientation of the abrasive water jet head is vertically downward. To get the specified angle of cut, i.e.,  $\alpha^\circ$  and  $\gamma^\circ$ , the head of the water jet nozzle is tilted manually and fixed at these angles as per requirements as shown in Fig. 34.6. After fixing the nozzle, top plate is rotated manually using handles provided on top plates. The speed of rotation is found with experimental trails for effective cut on shims.

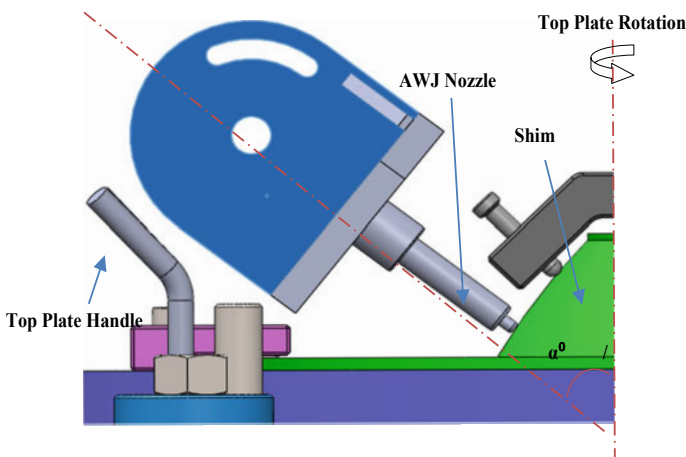
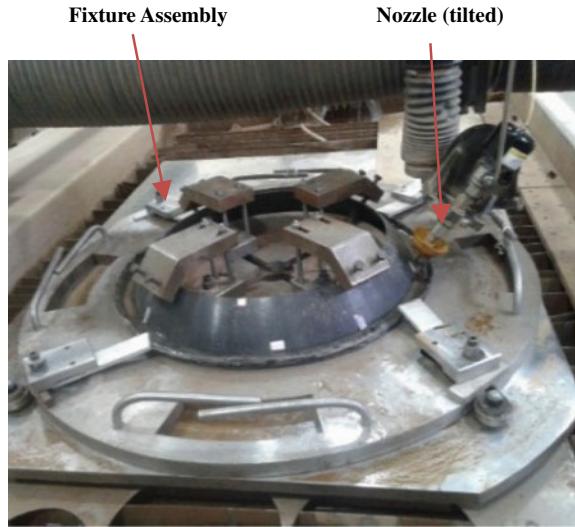


Fig. 34.6 Tilted water jet machine head for angular cut

Fixture assembly with all the fixture elements and shim is shown in Fig. 34.7 and the cutting process carried out on shims in abrasive water jet machine is shown in Fig. 34.8.

**Fig. 34.7** Fixture assembly



**Fig. 34.8** AWJ cutting of shim



### 34.4 Design Analysis

The total weight of the fixture with component (composite shim) is calculated as below:

$$\text{clamping setup} + \text{shim} + \text{upper plate} = 295 \text{ kgs} = 2.95 \text{ kN}$$

Structural analysis of design is carried out with the following material properties:

Component	Material	Young's modulus (GPa)	Density	Poisson's ratio
Upper plate	Structural steel	200	7850	0.3
Balls (30)	AISI 52100 Chrome steel (Bearing steel) (Ø 20 mm)	210	7800	0.3
Lower plate	Structural steel	200	7850	0.3

When ball bearing works, it is usually that more than one rolling ball bears the load. The condition is complex between rollers and rings. When the load is 0, the contact area is a point, i.e., point contact. When the load increases in running, the bearing inner ring, outer ring, and rolling elements bring forth plastic deformation in the contact area, so the point contact becomes face contact [5]. Furthermore, the contact area gradually becomes ellipse and generates residual stress [6]. The contact parameters, such as the place, size, shape of contact area, as well as the contact pressure, and friction force distribution, will be variable with load changes. These are typical boundary nonlinear problems. On the base of Hertzian theory, ball bearing's contact stress is

$$P_m = \frac{1}{\pi e_a e_b} \times \sqrt[3]{\left(\sum \rho\right)^2 \times \frac{5F_r}{Z \cos \alpha}}$$

In the formula,  $e_a$ ,  $e_b$  is, respectively, Hertzian contact coefficient;  $\sum \rho$  is the sum of main curvature;  $F_r$  is the radial load;  $Z$  is the number of rolling elements; and  $\alpha$  is contact angle under loads. The corresponding equations can be found in the appendix A3.

Hertzian contact pressure is used to derive the value for stress. Standard empirical relation is used to determine the load  $P$  on the topmost ball that bears the largest portion of the load.

#### *Load and Boundary Conditions*

- The bottom face of the lower plate is defined as fixed support.
- The balls are given a body to ground joint constraint.
- Load is defined on the upper face of the upper plate acting downward.

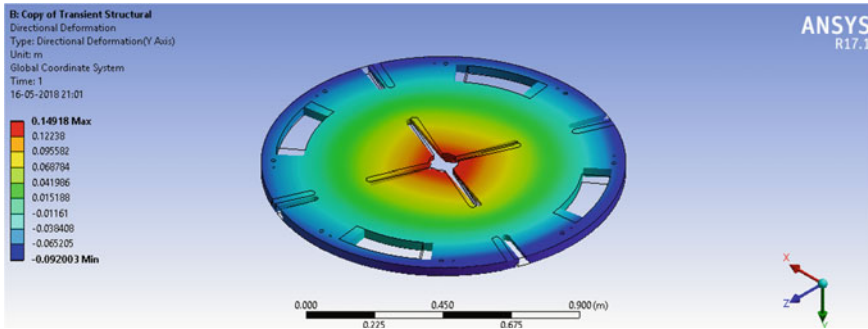


**Fig. 34.9** Deformation distribution

- The given RPM for the upper plate is 1 rpm. So the rotational velocity for all the balls in each raceway is defined accordingly.

In the model discussed in this report, four-point contact bearings are employed. They have ball-raceway contact at four points rather than over a full-contact radius. This arrangement maximizes load capacity and minimizes ball skidding under heavy load. However, the Hertzian contact ellipses are at four points and there is substantial slip as contact is made at different diameters with respect to the ball’s axis of rotation. To compensate this, a contact angle between ball and race, measured from the radial (horizontal) center line of the ball which ranges from 35 to 60° is used, depending on the application and its particular combination of loads.

### 34.5 Results

Deformation along Y axis is observed in center as the pressure acts on the face vertically downwards due to the weight of the shim and clamping setup. The deformation is shown in Fig. 34.9.

### 34.6 Conclusions

A fixture is designed and developed for augmentation of existing abrasive water jet machine capability for trimming of the composite material shim. The fixture is designed and fabricated to meet the requirements of trimming the shim at specified locations and orientations. Since the geometry of the shim includes thin-walled structure, appropriate clamping scheme is made to apply sufficient clamping force without deforming the shape of the shim. Instead of complex solution of continuous tilting of nozzle to maintain cutting requirements, a simple solution is given by tilting

the nozzle and rotating the shim by a fixture. The fixture can be further improved by incorporating automation for rotating the top plate.

**Acknowledgements** The authors thank Shri MSR Prasad (Distinguished Scientist and Director DRDL) for his encouragement and active support in conducting this task. We would like to sincerely thank the project team and personnel of work centers for their support and guidance for the design and development activity.

## References

1. Venkateswarlu, C., Poddar, B., Sai Kumar, S., Lahari, S.G.: Optimization of process parameters in abrasive water jet cutting of aluminum AA 2014 and Titanium Ti6Al4. In: International Conference on Advances in Materials & Manufacturing (ICAMM—2016), Hyderabad (2016)
2. Rex, F.M.T., Ravindran, D.: An integrated approach for optimal fixture layout design. *J. Eng. Manuf.* **231**(7), 1217–1228 (2017)
3. Irina Wong, M.M., Azmi, A.I., Lee, C.C., Mansor, A.F.: Kerf taper and delamination damage minimization of FRP hybrid composites under abrasive water-jet machining. *Int. J. Adv. Manuf. Technol.* (2016)
4. Product information on machining composites with abrasive water jet by Omax Corporation
5. Kashyap, S., DeVries, W.R.: Finite element analysis and optimization in fixture design. *Struct. Optim.* **18**, 193–201 (1999)
6. Renold Elsen, S.: Design of composite fixture for machining ceramic materials using abrasive water jet machining (awjm). *ARPN J. Eng. Appl. Sci.* (2014)

# Chapter 35

## Fabrication and Characterization of Helical Grooved Cylindrical Electrodes Generated by WED Turning Process



Jacob Serah Krupa and G. L. Samuel

**Abstract** Electric discharge drilling (EDD) process has got worldwide attention in the manufacturing industries owing to its unique electro–thermo-erosion mechanism capable of creating precise microholes on any conductive materials, irrespective of its hardness. The thrust of the research activities in this area is to address the challenges and explore the possibilities of EDD in the machining of high aspect ratio holes in turbine blades, fuel injectors, nozzles of inkjet printers, microchemical reactors, and biomedical devices. The motivation of the present work is to develop a new machining strategy by altering the electrode surface in order to enhance the flushing rate, which will eventually result in the accomplishment of better quality and high aspect ratio holes. Hence in the present work, the electrodes used for the EDD process are modified by creating a helical groove using wire electric discharge turning process (WEDT). Further analysis of the geometry of micro helical grooves machined on cylindrical electrodes has been carried out for the first time. The best geometry of helical groove was obtained at a pulse on time of 30  $\mu\text{s}$ , pulse off time 186  $\mu\text{s}$ , and depth of cut of 150  $\mu\text{m}$  with a helix angle of 34.12° and pitch of 2.22 mm. Extracting the surface characteristics of the micro helical grooves is very difficult, an attempt has been made to quantify the surface roughness, the best surface is obtained has 12.27  $\mu\text{m Ra}$ . The proposed electrode has the potential to replace the existing EDM electrodes as it is superior in terms of flushing and hence machining of good quality microholes.

**Keywords** EDM electrode geometry · Geometrical deviation · Helical grooves

### 35.1 Introduction

Wire electric discharge machining (WEDM) is widely used in many industries and has gained high popularity over the past decades, due to the easiness in creating intricate geometries on any conductive materials in a cost-effective way. Of late,

---

J. S. Krupa · G. L. Samuel (✉)  
Manufacturing Engineering Section, Department of Mechanical Engineering,  
Indian Institute of Technology Madras, Chennai 600036, India  
e-mail: [samuelgl@iitm.ac.in](mailto:samuelgl@iitm.ac.in)

© Springer Nature Singapore Pte Ltd. 2020  
M. S. Shunmugam and M. Kanthababu (eds.), *Advances in Unconventional Machining and Composites*, Lecture Notes on Multidisciplinary Industrial Engineering, [https://doi.org/10.1007/978-981-32-9471-4\\_35](https://doi.org/10.1007/978-981-32-9471-4_35)

researchers have been making modification in the tool geometry of EDM electrodes for attaining better and efficient flushing so that machining of high aspect ratio features is possible. The demand for high aspect ratio holes is increasing with the popularization of micromachining in industries like aerospace, biomedical, automobile, and electronics industry. For example, they are seen in microchemical reactors, micro heat exchangers, integrated circuit packages, fuel injection nozzles, spinneret holes, cooling vents for gas turbine, micromolds, and biomedical filters [1]. Electric discharge drilling (EDD) has become a widely accepted fabrication method for these features since the hardness of the material does not matter and investment and maintenance costs are economic [2].

Machining of high aspect ratio features in the microscale is very difficult or nearly impractical with conventional machining methods as the problems like tool breaking and thermal damage of machined area arises. To tackle this problem, researchers started discovering methods to modify the EDD process to make it suitable for deep hole drilling by facilitating efficient debris removal out of which modification of tool geometry has become very favored [3]. Low-speed wire electric discharge turning (LSWEDT) was used to fabricate helical slots on cylindrical and conical microtools with fast and slow helix by Sun and Gong [4]. An improvised tool electrode with slots at particular angles was successfully developed to show that the inclined microslot was able to prevent the accumulation of debris by Kumar and Singh [5]. Out of all methods used to modify the electrode geometry, wire electric discharge turning (WEDT) is the most advantageous. Helical profiles and axisymmetric shapes were machined on cylindrical workpieces having diameters as low as 1 mm using WEDT by Dhake and Samuel [6]. It was stated that EDM drilling is promising to drill high aspect ratio holes compared to conventional methods through a comparative study conducted by Hasan et al. [7].

Research activities focusing on improvement of the flushing and debris removal during EDD by various methods have been carried out by the scientific community. Experimental investigation of flushing efficiency was conducted using a bunched electrode as a substitute for the single-hole conventional electrode and a reduction of debris concentration to 1% due to the improved flushing which was reported by Li et al. [8]. Ultrasonic vibration has been incorporated into the EDM process and an improved MRR due to the increased flushing efficiency which was reported by Mohammadi et al. [9]. Further planetary motion was given to the tool electrode by giving it a preset value of offset from the spindle axis and increased flushing and debris recirculation was reported by John et al. [10]. It can be noted that EDM with improved flushing produces better machined parts.

From the literature survey, it is observed that few successful attempts have been made to modify the tool geometry of an EDM electrode and it has improved the machining characteristics while performing EDD. The research activities conducted up to now were centered on the surface characteristics of the machined electrodes like foreign material accumulation and microvoids, study of adjusting parameters to get different shapes of electrode, economics of machining, and machining time of electrode. However, not many attempts have been made to study the factors which influence the dielectric flow and flushing characteristics. Hence in the current work,

the authors have made an effort to fabricate helical grooves on cylindrical rods and study the geometry and surface roughness (Ra). The main contribution of the paper is an understanding of the influence of the process on surface roughness and helical geometry.

## 35.2 Material Removal Mechanism in WEDT

In the current work, the machining of micro helical grooves on cylindrical rods are done by the process of WEDT. In WEDT material erosion happens due to the erosion of material by a sparking phenomenon between the workpiece and the wire separated by a large potential difference and in relative motion. The mechanism is based on an electro-thermal process which depends on the discharge of electrons through a dielectric creating a channel of partially ionized gas. Around 2–10% of the total discharge energy is dissipated into this plasma channel. A small gap of 30–100  $\mu\text{m}$  is required to be maintained between the electrodes to prevent arcing, short circuits, and open circuits. Since the discharge frequencies range between 103 and 106 Hz, the pulse duration is extremely small and tiny craters are formed on the workpiece surface. Once the spark duration is over, the molten material solidifies in the dielectric as tiny spherical debris which needs to be carried away from the sparking area by dielectric flushing [11]. The WEDM is a modification of the EDM, a numerically controlled traveling wire is made as one electrode and it is used to machine parts with complex profiles by the same spark erosion process. Turning with WEDM was introduced to generate cylindrical form and axisymmetric features, mainly on difficult to machine materials in microscale. WEDT is implemented in a conventional WEDM machine by adding a rotary axis. The MRR of WEDT is higher than that of WEDM [12].

In Fig. 35.1 the material removal mechanism when the WEDT is used to create micro helical grooves on a cylindrical electrode is shown. For removing material in a helical path, the rpm given to the workpiece is considerably less than that used

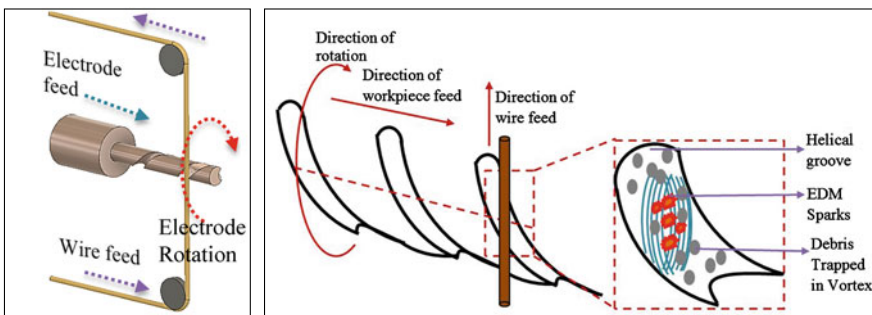


Fig. 35.1 Representation of the mechanism of machining helical grooves by WEDT



for turning rods. During WEDM, the vibrations on the wire can reach up to 10  $\mu\text{m}$  in amplitude which can cause geometrical errors when performing micro-WEDT. To prevent this a wire guide is provided. The wire is kept in position as it slips over the wire guide at the sparking point and the process is termed as wire electric discharge grinding (WEDG) by Masuzawa et al. [13]. The modified electrodes can be fabricated by WEDT by controlling the ratio of wire feed to the rpm of the workpiece. By changing the ratio, helical profiles with different helix angles may be obtained on the workpiece.

### 35.3 Machining of Electrodes

The experimental investigations are conducted on Electronica Ecocut CNC Wire EDM machine by adding an additional spindle (Fig. 35.2) developed by Janardhan and Samuel [12]. The workpiece used for the EDM electrode is an electrolytic copper rod of diameters 1 and 0.7 mm for a length of 8 mm. The electrodes have a stepped portion of 3 mm for proper work holding using an ER11-3 mm collet. The electrode wire is 0.25 mm in diameter and made of brass material. Copper electrodes are

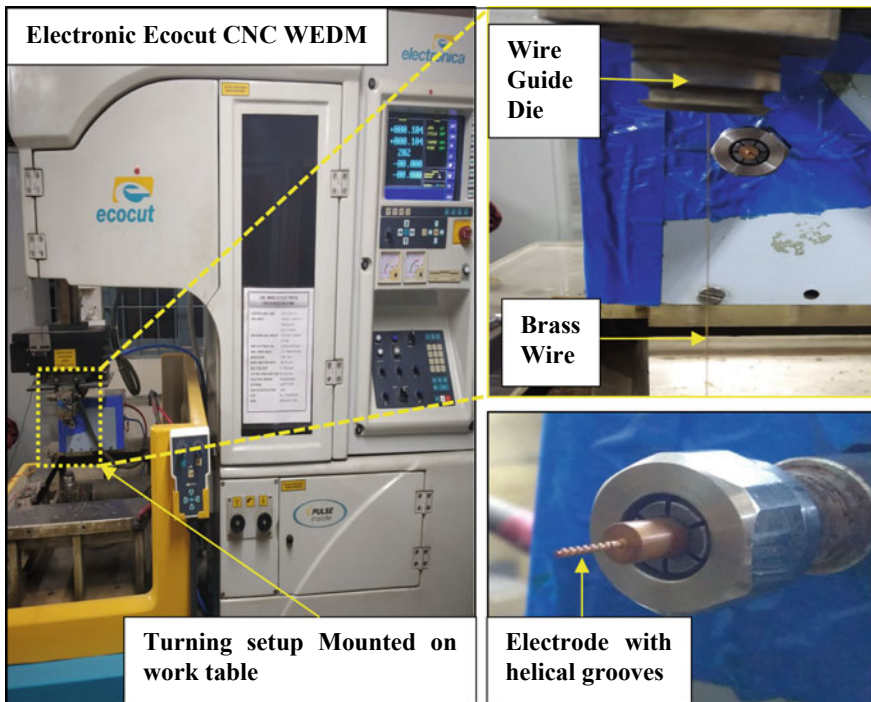


Fig. 35.2 Turning setup mounted on wire EDM along with cylindrical workpiece

chosen as the workpiece since the focus of the study is on the machinability of the helical pattern by WEDM and copper is favorable for EDM tools owing to its good conductivity.

The experiments were carried out by setting the depth of cut values to 75, 100, and 150  $\mu\text{m}$ . The depth of cut was not set above 150  $\mu\text{m}$  as it could lead to bending of the rod during the process of machining. The settings of pulse on time are 3, 4, and 5 values of the knob settings which is approximately 30, 40, and 50  $\mu\text{s}$  [14]. The pulse off time is set to 7, 8, and 9 knob setting values and the corresponding pulse off times are found to be 174, 184, and 186  $\mu\text{s}$ . The required pulse trains were captured using an oscilloscope (Keysight technologies, model no: DSOX 2024A) with a sampling rate of 2 Giga samples per second. The feed and rpm are set to constant values of the 5th value of knob setting and 3 rpm since it was found from preliminary experiments that this combination gives a value of the helix angle about 30–50° which is a desirable value for flushing grooves. The feed rate is set such that the fluctuation of gap current is within the permissible range indicated on the machine.

### 35.4 Results and Discussions

Machining of eight electrodes was successfully carried out and it was observed that the selection of cylindrical rods with minimal run out is crucial for obtaining a helical pattern. It was also observed that the helix angle was affected by machining parameters apart from the feed and the rpm of the spindle, different angles were obtained on each workpiece. A rod of electrolytic copper was machined to 5 mm and partially stepped down to 1 mm and 0.7 mm by CNC turning and machining of the desired geometry was carried out by WEDM as shown in Fig. 35.3. It can be noted that uniform depth of grooves can be obtained if the electrode is turned to lesser

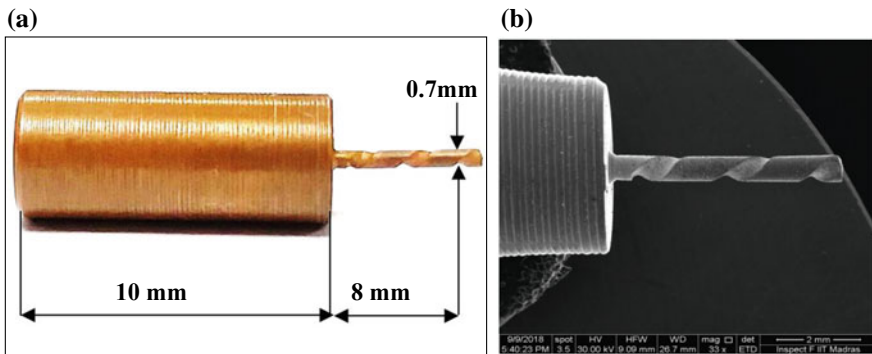


**Fig. 35.3** Electrode with helical grooves **a** photograph. **b** SEM image

diameter on the WEDT setup before machining of helical grooves. This eliminates all possible eccentricity and bent caused by CNC tuning.

### 35.4.1 Evaluation of Helical Geometry Machined on the Electrode

According to Lancet’s theorem, a necessary and sufficient condition that a curve be a general helix is that the ratio of curvature to torsion be constant [15]. The equation of helix was expressed in the vector form by using the measured values of radius and pitch and a Matlab program was made to calculate the curvature and torsion of the helix at all three angles for all workpieces. Then the ratio of curvature to torsion was calculated and the standard deviation was computed. Figure 35.4 shows the deviation of the tool geometry from actual helix, where  $\alpha_{ideal}$  is the angle of exact helix and  $\alpha$  is the obtained angle,  $P_{ideal}$  is the pitch of exact helix and  $P$  is the obtained pitch. The deviation of the helical geometry was estimated by checking the conformance to Lancet’s theorem. The machined electrode was first fixed rigidly to an ER11 collect with slots at angles of every  $60^\circ$  inserted on a nylon roller with an SKF 608 bearing and further mounted on a V block as shown in Fig. 35.5. The electrode was precisely rotated between  $0^\circ$ ,  $120^\circ$ , and  $240^\circ$  with the help of this arrangement and a height gauge. At each angle, the measurement of pitch and radius was measured by using a Zeiss Stemi 2000 CS stereo microscope. Three sets of readings were taken at each angle for all electrodes and the average value was considered.

The vector representation of helix is

$$r(\varphi) = R \cos(\varphi)i - R \sin(\varphi)j + C \varphi k \tag{35.1}$$

where  $R$  is the radius of the helix and  $C\varphi$  is the  $z$  coordinate value. The unit tangent vector is estimated by taking the first derivative of the helix equation with respect to  $\varphi$  and dividing it by its modulus.

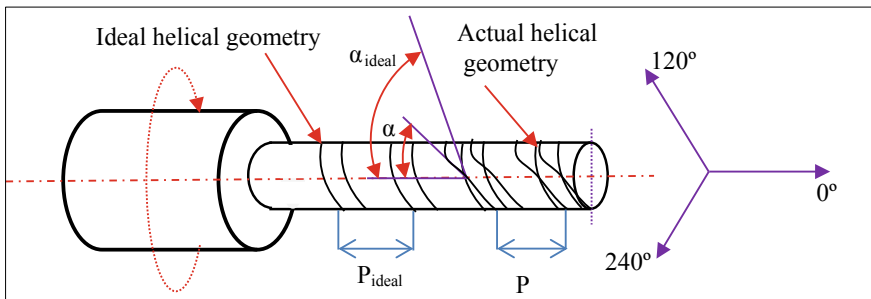


Fig. 35.4 Representation of variation of the helical profile from actual helix

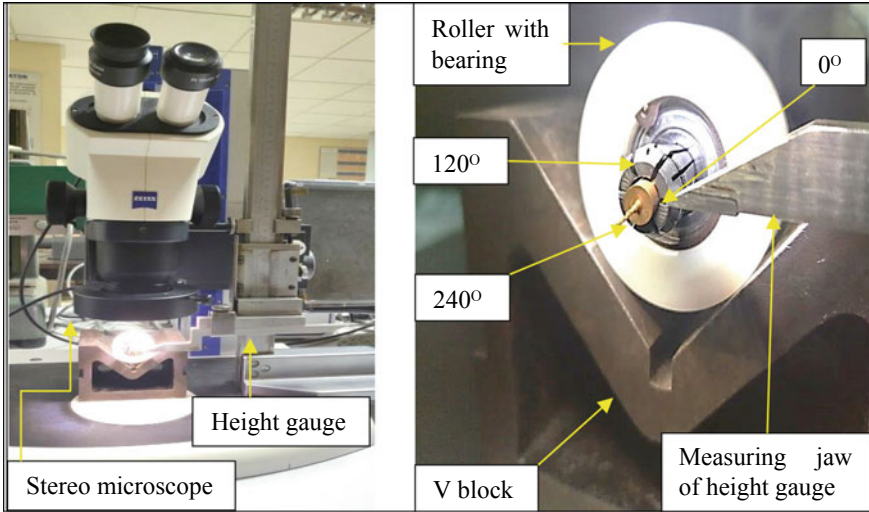


Fig. 35.5 Arrangement to view the electrode at different angles

$$t = \frac{dr/d\phi}{|dr/d\phi|} \tag{35.2}$$

The curvature or first curvature of a helix is the partial derivative of the tangent with respect to the arc length and it can be expressed as

$$\text{Curvature}(\kappa) = \frac{|dt/d\phi|}{|dr/d\phi|} \tag{35.3}$$

For calculation of the torsion, the normal and binormal vectors are calculated as

$$\text{Normal Vector} = \frac{dt/d\phi}{|dt/d\phi|} \tag{35.4}$$

$$\text{Binormal Vector (B)} = t \times N \tag{35.5}$$

The osculating plane of a curve is spanned by the tangent vector and the normal vector. Binormal vector is perpendicular to the osculating plane and its rate of change with respect to the arc length is given by the vector

$$\frac{dB}{ds} = \frac{dB/d\phi}{|dr/d\phi|} \tag{35.6}$$

The torsion of a space helix is also called as the second curvature and it is the rate of change of the curve's osculating plane and is expressed as.

$$\text{Torsion } (\tau) = -N \frac{dB}{dS} \tag{35.7}$$

Finally, the ratio of curvature to torsion is taken and this should be constant for a perfect helix.

$$\text{Ratio of curvature to torsion} = \frac{\kappa}{\tau} \tag{35.8}$$

Standard deviation of ratio of curvature to torsion at each angle is expressed as

$$\text{Standard deviation of } \frac{\kappa}{\tau} = \sqrt{\frac{\sum \left( \left( \frac{\kappa}{\tau} \right)_{\text{mean}} - \left( \frac{\kappa}{\tau} \right) \right)^2}{3}} \tag{35.9}$$

The measured values shown in Table 35.1 are used to compute the ratio of curvature to torsion by substituting in a Matlab program. It is observed that the ratio is not constant from which it is inferred that there is error of the machined geometry from the perfect helix profile. The standard deviation of the ratio of  $\kappa/\tau$  of each electrode is calculated using Eq. (35.9). Plots of the standard deviation of ratio with respect to influential factors are made to study the trend of the deviation of profile.

From Fig. 35.6a, b it is observable that the least deviation of the profile from the exact helix occurs at a depth of cut of 150  $\mu\text{m}$  and a pulse on time of 30  $\mu\text{s}$ . This can be explained by the fact that when machining of micro helical grooves is done at a lower depth of cut, a major portion of the energy released from the spark is concentrated at the surface and subsurface of the cylindrical rod, hence most of the material removal happens at the surface. However, at higher depths of cuts, the energy gets dissipated to the bulk of the electrode and material is removed both from the surface and the bulk of the electrode. As the pulse on time increases, duration of the live spark increases and material erosion happens for a longer time, hence greater

**Table 35.1** Calculated values of average helix angle and standard deviation of  $\kappa/\tau$

Sl. No.	Depth of cut ( $\mu\text{m}$ )	Pulse on time ( $\mu\text{s}$ )	Pulse off time ( $\mu\text{s}$ )	Helix angle ( $^\circ$ )	$\kappa/\tau$			Standard deviation of $\kappa/\tau$
					$\varphi = 0$	$\varphi = 120$	$\varphi = 240$	
1	75	30	174	49.96	-1.9	-0.79	0.37	0.95
2	75	40	184	56.08	-1.8	-0.77	0.41	0.94
3	75	50	186	62.87	-1.5	-1.31	0.73	1.03
4	100	30	184	44.7	-1.5	-0.61	0.55	0.85
5	100	40	186	56.21	-1.5	-1.19	0.77	1.02
6	100	50	174	54.17	-1.5	-1.19	0.65	0.98
7	150	30	184	34.12	-1.4	-0.31	0.45	0.77
8	150	40	174	45.23	-1.8	-0.48	0.34	0.93

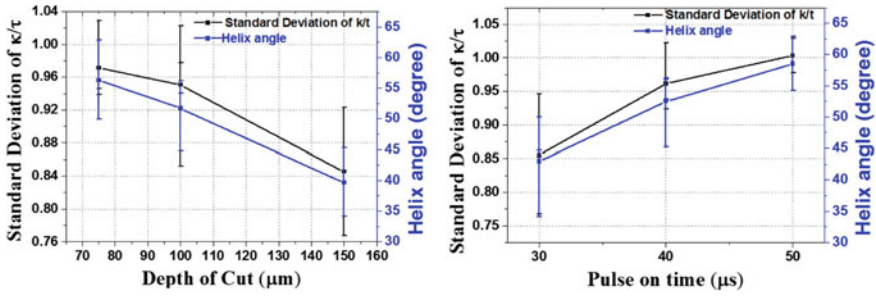


**Fig. 35.6** Variation of standard deviation of  $\kappa/\tau$  and average helix angle with **a** depth of cut. **b** Pulse on time

amount of material is removed per cycle causing localized deviation from expected geometry. The pulse off time has negligible effect on the geometry.

The average helix angle shows a decreasing trend with increase in depth of cut (Fig. 35.6a), a helix angle of  $34.12^\circ$  is obtained at a depth of cut of  $150 \mu\text{m}$  which is closest to the standard helix angle of commercial drill. The increasing trend of average helix angle (Fig. 35.6b) with pulse on time is due to the fact that a higher material removal rate in localized areas along the direction of motion of workpiece causes decrease in the pitch of the helix leading to an increased helix angle. Similar to the trend of geometrical deviation with respect to pulse off time, the variation of average helix angle is also independent of pulse off time. For obtaining a helix angle near to  $30^\circ$  it is noticed that a setting of depth of cut of  $150 \mu\text{m}$ , pulse on time of  $30 \mu\text{s}$ , and pulse off time of  $186 \mu\text{s}$  is desirable.

It is expected that these electrodes can be used for providing better flushing during EDD process compared to conventional cylindrical electrodes. Apart from calculating the  $\kappa/\tau$  ratio, the average helix angle was also considered since the dielectric movement through the grooves will be affected highly by the angle of the helix.

### 35.4.2 The Surface Roughness of the Helical Grooves

The surface roughness was measured by using a Veeco 3D optical surface profiler and Ra values were recorded as three sets for each workpiece. A  $465 \times 612 \mu\text{m}^2$  area of the workpiece is scanned, three subsections of approximately  $200 \times 200 \mu\text{m}^2$  are taken at random along the helical groove surface as shown in Fig. 35.7. Horizontal and vertical sections are taken along a subsection to demonstrate the calculation of surface roughness Fig. 35.8.

The surfaces are made flat by removing the cylindrical curvature, tilt, and high pass filtering then the values obtained are averaged as shown in Table 35.2. This is done to avoid the contribution of the curvature in the Ra calculation. The surface roughness increases with the increase in depth of cut since a larger amount of material is removed

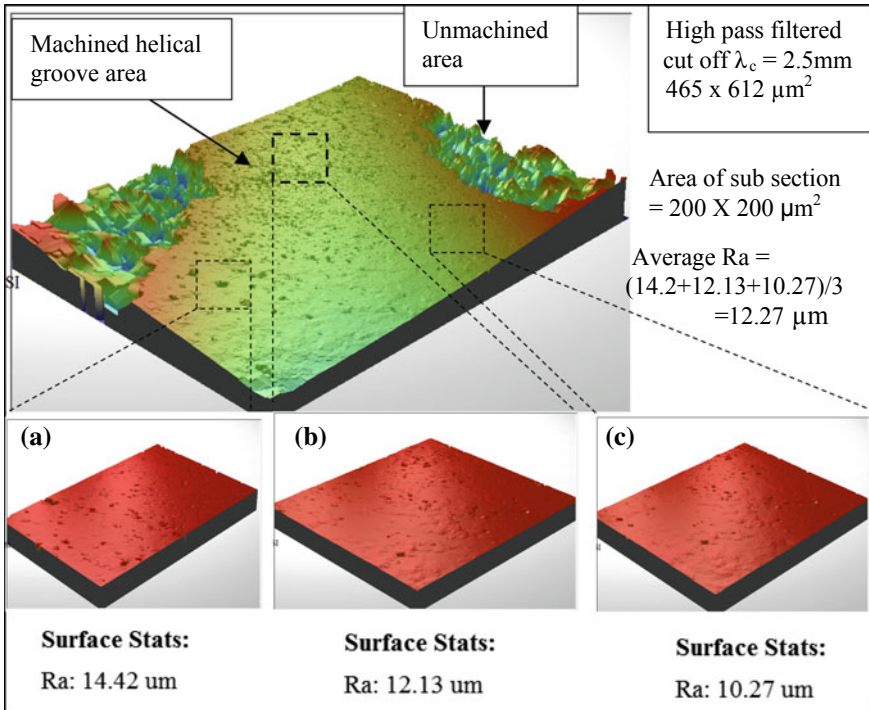
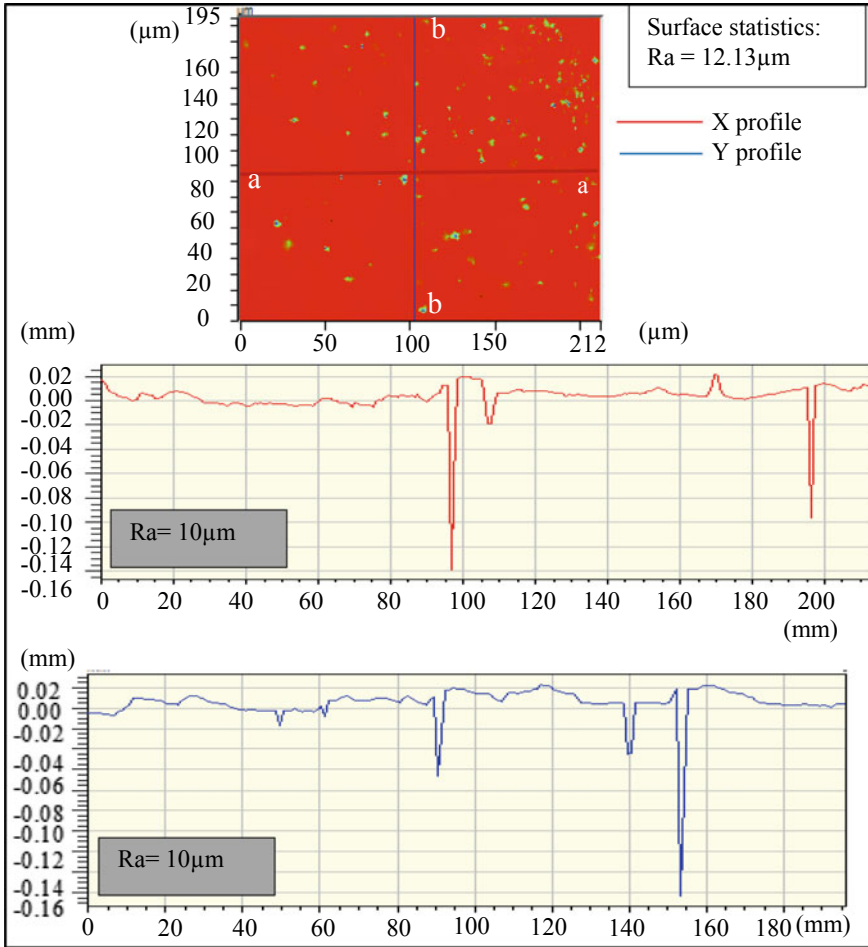


Fig. 35.7 Sample surface scan from optical profiler showing three subsections

as the wire electrode is in close proximity with a larger area of the cylindrical rod. This is in agreement with the proportionality of the surface roughness and depth of cut seen in conventional EDM process and also many unconventional machining processes. Even though from Fig. 35.9b it is seen that the surface roughness shows a decreasing trend with the increase in pulse on time, the least and maximum surface roughness are both obtained at the same setting of the pulse on time of 30  $\mu\text{s}$ . So it can be concluded that the effect of the pulse on time on surface roughness is rather overshadowed by the effect of the depth of cut factor. The best surface finish obtained is 12.27  $\mu\text{m}$  (Ra) and it is obtained at a setting of 75  $\mu\text{m}$  depth of cut, 50  $\mu\text{s}$  pulse on time, and a pulse off time of 186  $\mu\text{s}$ . To further reduce the value of surface roughness it is required to conduct the machining in two steps, a rough cut and finish cut in which the depth of cut can be considerably reduced.

### 35.5 Conclusions

The experimental study of helical geometry and surface roughness of helical grooves machined on mesoscale cylindrical rods by WEDT was carried out for the first time.



**Fig. 35.8** Sample 2D plot of surface roughness at section a-a and b-b

Investigation of the geometrical deviation of helical form and surface roughness were carried out. It was observed that the pulse on and off times and depth of cut influences the helix angle apart from the ratio of the feed to the rotational speed. The most relevant finding of the investigation is that the best geometrical characteristics are obtained at the least value of pulse on time which is 30  $\mu$ s and highest pulse off time which is 186  $\mu$ s. The geometrical deviation shows an increasing trend with the increase in pulse on time and decrease in depth of cut. The smallest helix angle obtained is 34.12° and highest pitch is 2.22 mm which are both obtained with a standard deviation of the ratio of the helix curvature to torsion as 0.77. This is obtained at the highest value of the depth of cut of 150  $\mu$ m and pulse off time of 186  $\mu$ s and a pulse on time of 30  $\mu$ s. The best average surface roughness obtained is 12.27  $\mu$ m Ra and it shows an increasing trend with the increase in depth of cut.



**Table 35.2** Average values of Ra

Sl. no.	Depth of cut ( $\mu\text{m}$ )	Pulse on time ( $\mu\text{s}$ )	Pulse off time ( $\mu\text{s}$ )	Ra ( $\mu\text{m}$ )			Average Ra value ( $\mu\text{m}$ )	Standard deviation of Ra
				Trial 1	Trial 2	Trial 3		
1	75	30	174	13.98	14.52	13.06	13.85	0.60
2	75	40	184	13.52	21.24	14.62	16.46	3.40
3	75	50	186	14.42	12.13	10.27	12.27	1.69
4	100	30	184	16.72	31.17	8.49	18.79	9.37
5	100	40	186	23.96	30	28.14	27.36	2.52
6	100	50	174	19.09	13.74	11.01	14.61	3.36
7	150	30	184	57.64	38.63	19.53	38.60	15.56
8	150	40	174	27.24	26.63	25.67	26.51	0.65

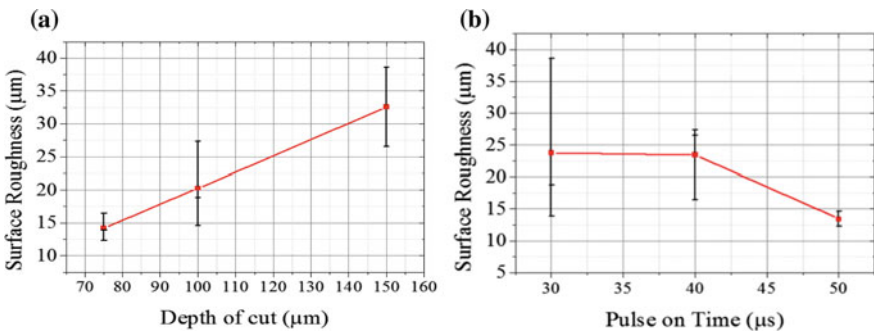


**Fig. 35.9** Variation of surface roughness with **a** depth of cut and **b** pulse on time

The geometry of the cylindrical electrode with helical grooves is greatly influenced by the pulse on time as well as the depth of cut. The surface roughness is highly influenced only by the depth of cut.

It is also observed that the initial run out of the rod used for machining has a significant effect on the form and if not eliminated, can cause undesired geometries on the workpiece. The work carried out in the present paper demonstrates that helical grooves can be manufactured on mesoscale cylindrical rods by WEDT. The feasibility of extending the same process to machine helical grooves on microrods can also be explored. Moreover, further studies can be carried out to investigate the machinability of high aspect ratio holes in difficult to machine materials using the electrodes fabricated in the present work.

**Other Related Information** The authors have provisionally filed a part of this research idea for an Indian patent under the application number “201841047112”.

## References

1. Barman, S., Hanumaiah, N., Puri, A.B.: Investigation on shape, size, surface quality and elemental characterization of high-aspect-ratio blind micro holes in die sinking micro EDM. *Int. J. Adv. Manuf. Technol.* **76**(1–4), 115–126 (2013)
2. Yu, Z., Zhang, Y., Li, Y., Lua, J., Zhao, F., Guo, D.: High aspect ratio micro-hole drilling aided with ultrasonic vibration and planetary movement of electrode by micro-EDM. *CIRP Ann.—Manuf. Technol.* **58**(1), 213–216 (2009)
3. Plaza, S., Sanchez, J.A., Perez, E., Gil, R., Izquierdo, B., Ortega, N., Pombo, I.: Experimental study on micro EDM-drilling of Ti6Al4V using helical electrode. *Precis. Eng.* **38**(4), 821–827 (2014)
4. Sun, Y., Gong, Y.: Experimental study on fabricating spirals microelectrode and micro-cutting tools by low speed wire electrical discharge turning. *J. Mater. Process. Tech.* **258**, 271–285 (2018)
5. Kumar, R., Singh, I.: Productivity improvement of micro EDM process by improvised tool. *Precis. Eng.* **51**, 529–535 (2018)
6. Dhake, H.G., Samuel, G.L.: Machining of axisymmetric forms and helical profiles on cylindrical workpiece using wire cut EDM. *Int. J. Mach. Mach. Mater.* **12**(3), 252–265 (2012)
7. Hasan, M., Zhao, J., Jiang, Z.: A review of modern advancements in micro drilling techniques. *J. Manuf. Process.* **29**, 343–375 (2017)
8. Li, L., Gu, L., Xi, X., Zhao, W.: Influence of flushing on performance of EDM with bunched electrode. *Int. J. Adv. Manuf. Technol.* **58**(1–4), 187–194 (2012)
9. Mohammadi, A., Tehrani, A.F., Abdullah, A.: Investigation on the effects of ultrasonic vibration on material removal rate and surface roughness in wire electrical discharge turning. *Int. J. Adv. Manuf. Technol.* **70**(5–8), 1235–1246 (2014)
10. John, V., Harshit, M., Keyur, K.D.: Experimental investigations on EDM of Ti6Al4V with planetary tool actuation. *J. Braz. Soc. Mech. Sci. Eng.* **39**(9), 3467–3490 (2017)
11. Mahendran, S., Devarajan, R., Nagarajan, T., Majdi, A.: A review of micro-EDM. *Proc. Int. Multi Conf. Eng. Comput. Sci.* **2**, 21–26 (2010)
12. Janardhan, V., Samuel, G.L.: Pulse train data analysis to investigate the effect of machining parameters on the performance of wire electro discharge turning (WEDT) process. *Int. J. Mach. Tools Manuf.* **50**(9), 775–788 (2010)
13. Masuzawa, T., Fujino, M., Kobayashi, K., Suzuki, T., Kinoshita: Wire electro-discharge grinding for micro-machining. *CIRP Ann.—Manuf. Technol.* **34**(1), 431–434 (1985)
14. Janardhan, V., Samuel, G.L.: Investigations on material removal rate in wire electrical discharge turning (WEDT) using pulse train data analysis. *J. Mechatron. Intell. Manuf.* **2**, 17–39 (2011)
15. Barros, M.: General helices and a theorem of Lancret. *Proc. Am. Math. Soc.* **125**(5), 1503–1509 (1997)

# Chapter 36

## A Study of Wire Electrical Discharge Machining of Carbon Fibre Reinforced Plastic



Hrishikesh Dutta , Kishore Debnath  and Deba Kumar Sarma 

**Abstract** The need for nonconventional machining of carbon fibre reinforced plastics (CFRPs) has emerged due to several problems encountered during their conventional machining. Wire electrical discharge machining (WEDM) is a potential nonconventional machining process having the ability to produce delamination and damage-free features in CFRP laminate. But machining of CFRPs by means of WEDM is a challenging task due to their low electrical conductivity characteristic. The present work focuses on the feasibility study of machining of CFRP laminate by WEDM process. Sandwich assisting electrode method was applied to improve the machining performance of the chosen material. The influence of three input factors, namely, (i) pulse on time, (ii) pulse off time, and (iii) current on machining time has been investigated. The experiments were performed according to full factorial design by taking three levels of each input factor. It was found from the experimental results that the machining time increases marginally with an increase in the pulse on time at a lower level of current (current level of 2). However, the machining time is almost constant for a higher level of current (current level of 4 and 6). The results also showed that the machining time increases with pulse off time and decreases with the current.

**Keywords** Wire electrical discharge machining · Carbon fibre reinforced plastic · Sandwich assisting electrode

### 36.1 Introduction

CFRP composites possess some superior properties, viz., (i) high strength, (ii) high stiffness, (iii) good toughness, (iv) good fatigue, creep, wear, and corrosion resistance, (v) low friction coefficient, and (vi) good dimensional stability [1]. Due to these properties, CFRPs are being extensively used in various applications like aerospace,

---

H. Dutta (✉) · K. Debnath · D. K. Sarma  
Department of Mechanical Engineering, National Institute  
of Technology Meghalaya, Shillong 793003, India  
e-mail: [hrishi\\_aipl@rediffmail.com](mailto:hrishi_aipl@rediffmail.com)

© Springer Nature Singapore Pte Ltd. 2020  
M. S. Shunmugam and M. Kanthababu (eds.), *Advances in Unconventional Machining and Composites*, Lecture Notes on Multidisciplinary Industrial Engineering, [https://doi.org/10.1007/978-981-32-9471-4\\_36](https://doi.org/10.1007/978-981-32-9471-4_36)

commercial aircraft, sports items, automobile parts, robotic arms, bridges, chemical storage containers, tripods, golf clubs, fishing rods, etc. [2]. Recently, manufacturers have used CFRP up to 25% and 53% in two aircrafts, namely, (a) Airbus 380 and (b) A350 XWB, respectively. CFRP is extensively used to manufacture fuselage, wing, and empennage assemblies in these aircrafts. It is possible to achieve a stronger and stiffer structure with the application of CFRP in these aircrafts. Also, the overall weight of the aircraft is reduced due to the use of CFRP. This led to more efficiency in terms of fuel consumption [3]. While manufacturing different components from CFRP, it is necessary to perform machining operations in order to get the product with the required dimension and tolerances. Cutting is an important operation among all the machining operations to get the required size and shape of CFRP laminate. Damages like delamination, fibre breakage, fibre pull out, etc., frequently occur during conventional cutting of CFRP laminate by hack saw, power saw, milling, etc. These damages can be avoided by adopting nonconventional machining processes during cutting or trimming of CFRP laminate. WEDM is such a nonconventional machining process by which electrically conductive material can be cut with minimal surface damage. Another advantage of WEDM is that any intricate shapes which are difficult to achieve by conventional machining processes can be easily obtained by this process. CFRP consists of electrically conductive carbon fibre and nonconductive epoxy matrix. Therefore, it is quite challenging to machine CFRP by WEDM. A comparative study between laser cutting and WEDM process presented while cutting CFRP [4]. The important factors under consideration were cutting rate, edge quality, and damage to the workpiece. It was observed that the WEDM resulted in better cutting edge profile and better control of the process parameters for lesser damage to the workpiece. But it was not discussed how the spark is initiated during WEDM of CFRP laminate which has low electrical conductivity. Also, the material removal mechanism was not discussed thoroughly.

In the present work, sandwich assisting electrode is used to initiate the spark while performing WEDM on CFRP laminate. Also, the mechanism of material removal is discussed comprehensively. The cutting length is kept constant to 4 mm under each experimental trial to study the effects of input factors such as pulse on time, pulse off time, and current on the machining time.

## **36.2 Materials and Methods**

### ***36.2.1 Fabrication of CFRP Laminate***

CFRP laminate was prepared using hand layup process. 3k plain weave carbon fibre mats were used as reinforcement and epoxy resin was used as matrix. A steel mould with a nut and bolt fastening mechanism was used to prepare the laminates. The fibre mat was placed over the lower mould plate after cutting to the required size. Epoxy (Lapox L12) in liquid form was then mixed properly with the recommended

hardener (K6) in a weight ratio of 10:01. The mixture was uniformly distributed over the fibre mat. Then the second layer of fibre mat was placed over it. This process was repeated until the required number of fibre mats was incorporated. A hand roller was used to remove the trapped gas bubbles between the fibre mats and excess resin as well. Finally, the top mould plate was placed over the layup stack and pressure was applied. The whole setup was kept at room temperature for 24 h for curing. The thickness of 1 mm of the composite plate was achieved by maintaining a distance between the upper and lower mould with the help of nuts and bolts used for fastening the mould plates.

### 36.2.2 Experimental Work

A WEDM (Model: DK7732C and Make: Concord Limited, Bangalore, India) setup was used to machine the CFRP laminates, as shown in Fig. 36.1. The schematic of machining operation is shown in Fig. 36.2.

Based on the literature survey, three input factors, namely, (i) pulse on time, (ii) pulse off time, and (iii) input current were considered for the experimentation. For each factor, three levels were considered. The full factorial experimental design was carried out as shown in Table 36.1. A total of 27 experimental runs were carried out. The values of input parameters that were fixed during the experiments are listed in Table 36.2. CFRP laminate of 1 mm thickness was held between two metallic plates of the same thickness (2 mm) and then this arrangement was clamped in the WEDM table for cutting, as shown in Fig. 36.3. Figure 36.4 shows the CFRP specimen after machining by WEDM.

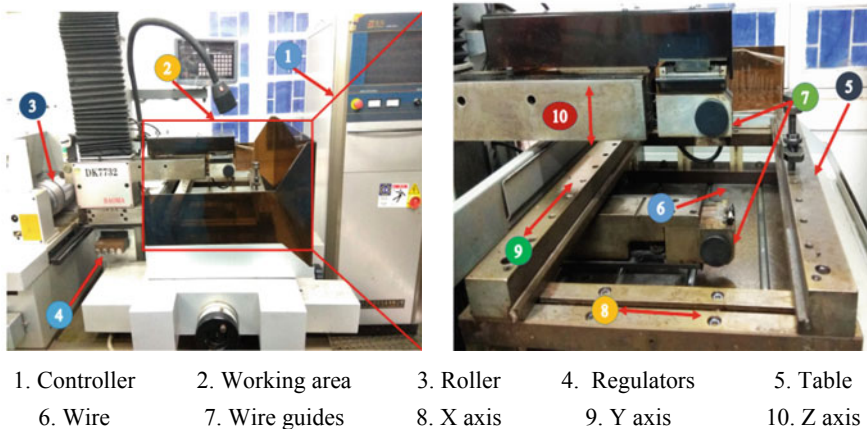


**Fig. 36.1** Experimental setup

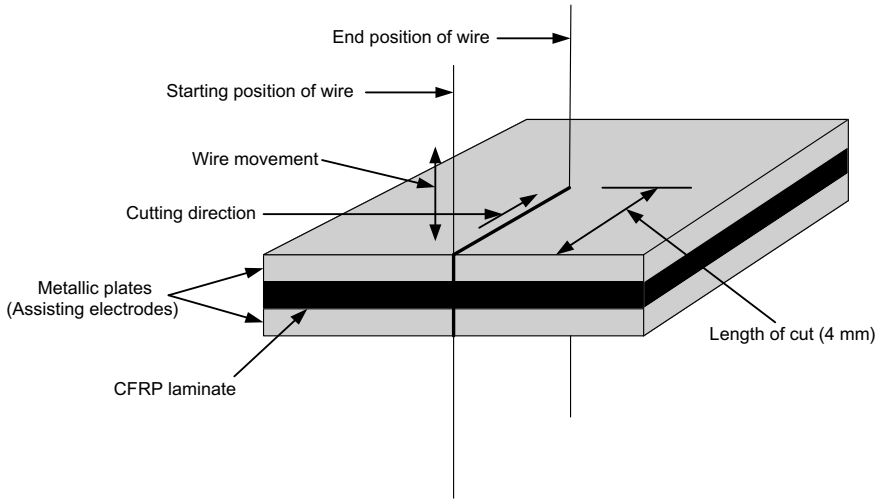


**Fig. 36.2** Schematic of cutting of CFRP laminate by means of WEDM

**Table 36.1** Input parameters and their levels

Input factors	Level 1	Level 2	Level 3	Unit
Pulse on time	30	40	50	$\mu s$
Pulse off time	15	25	35	$\mu s$
Input current	2	4	6	–

**Table 36.2** Values of fixed machine parameters

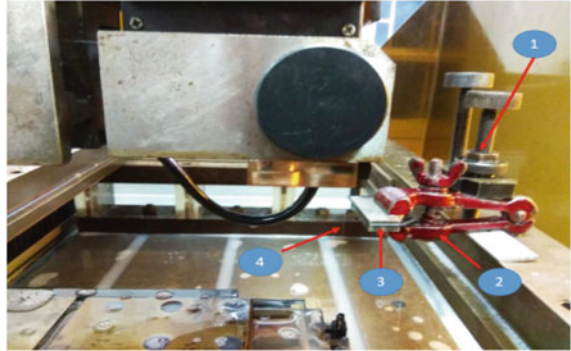
Parameters	Values
Voltage	70 V
Wire speed	2 (level)
Wire material	Molybdenum
Wire diameter	0.18 mm
Polarity	Straight
Conductivity of the dielectric	0.70 $\mu S/cm$

### 36.3 Results and Discussion

#### 36.3.1 Mechanisms of Material Removal

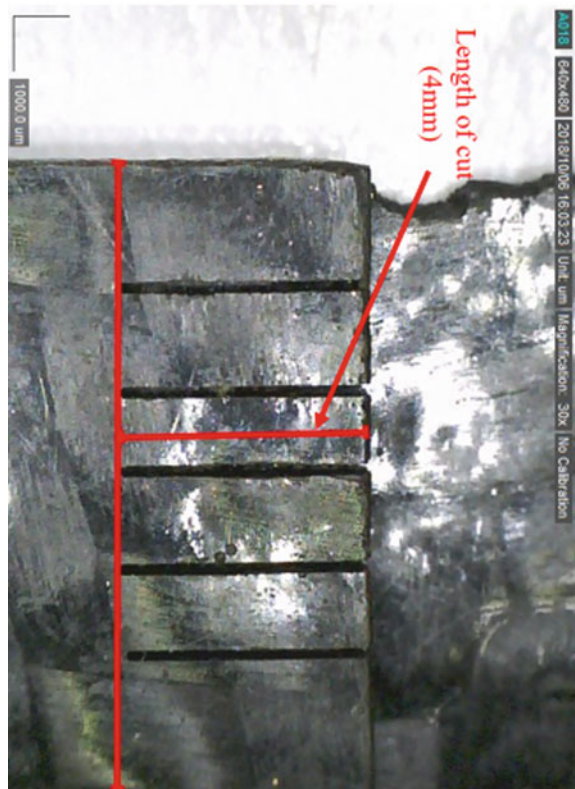
In the present study, sandwich assisting electrode method was adopted in order to machine CFRP laminate by WEDM. The CFRP laminate was placed between two metallic plates while performing WEDM. CFRP consists of electrically conductive

**Fig. 36.3** Experimental setup with the workpiece held by clamp for machining



1. Clamp 2. Additional clamp 3. Workpiece 4. Wire

**Fig. 36.4** CFRP specimen showing the length of cut



carbon fibre and nonconductive epoxy resin which makes it a heterogeneous material. It is quite difficult to initiate the spark generation during WEDM of CFRP laminate because of the presence of nonconductive epoxy resin over the surface of the composite laminate. Therefore, the approach of using metallic plates as sandwich assisting electrode was adopted so that the spark could be initiated efficiently in spite of the partial conductive nature of the CFRP laminate. The length of cut achieved after machining is shown in Fig. 36.4. The length of cut is kept constant to 4 mm during the experimentation at all parametric settings. The schematic of heat generation and material removal during WEDM of CFRP laminate is shown in Fig. 36.5. Initially, the spark is generated on the surface of the metallic plates due to their superior electrical conductivity. The initial sparking zone on the surface of the metallic plates (zone 1 and 2) where intense heat is generated is shown in Fig. 36.5. This heat then propagates throughout the thickness of the CFRP laminate. Finally, a sparking zone is developed on the surfaces of both metallic plates and laminate (zone 3), as shown in Fig. 36.5. Thus melting and evaporation of both the composite constituents and metallic plates take place which eventually removes some amount of material from the metallic plates and composite laminate. This process is continued until the required length of cut is achieved. The heat-affected zone (HAZ) is detected over the surface of the workpiece during machining, as shown in Fig. 36.5. The HAZ may be controlled by optimizing the amount of heat produced through proper selection of the level of input parameters. Also, the cooling effect produced by the dielectric during machining should be maximized in order to control the HAZ.

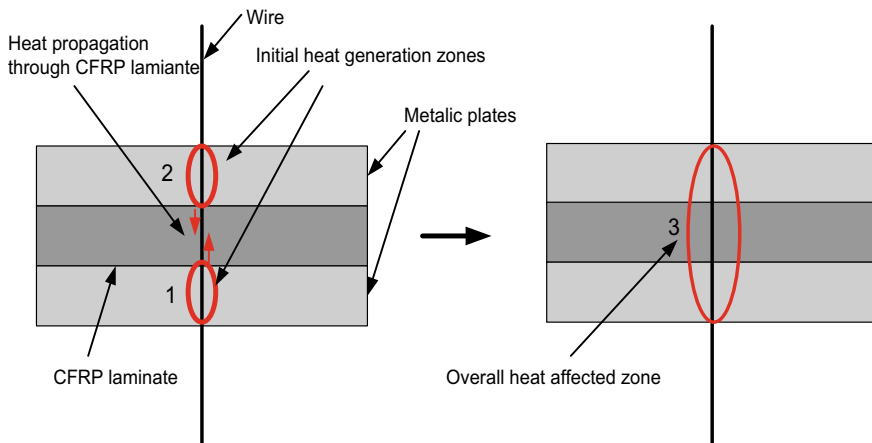


**Fig. 36.5** Mechanism of material removal in WEDM of CFRP



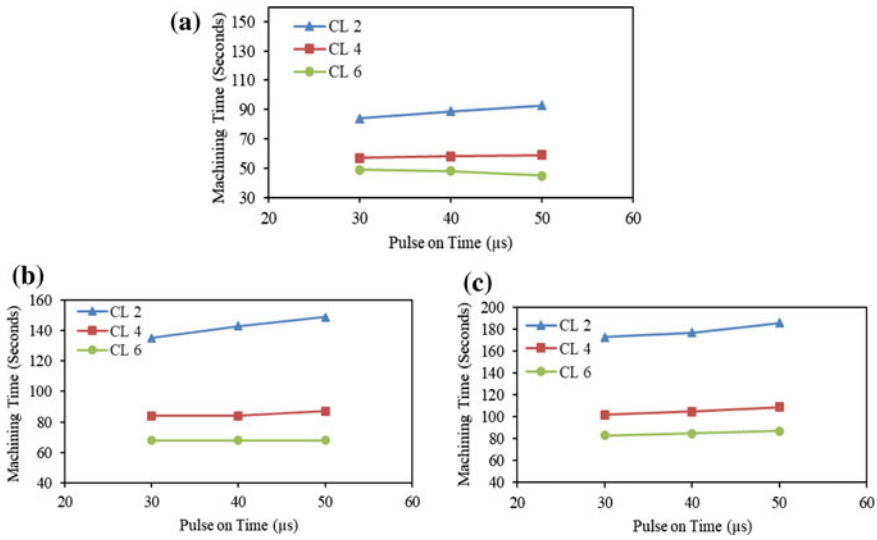


**Fig. 36.6** Variation in machining time with pulse on time at pulse off time of **a** 15  $\mu\text{s}$ , **b** 25  $\mu\text{s}$ , and **c** 35  $\mu\text{s}$

### 36.3.2 Effect of Input Factors on Machining Time

The machining performance of the CFRP laminates has been studied considering machining time as the output response. The variation of machining time with various input factors are represented graphically and comprehensively discussed. From the experimental analysis, it was observed that the machining time does not follow any specific trend with an increase in the pulse on time, as shown in Fig. 36.6. Generally, the net heat flux is increased when the pulse on time is increased due to longer spark duration. This eventually leads to a higher amount of material removal from the workpiece. In the present study, it can be observed that the machining time increases marginally with an increase in the pulse on time for current level of 2 in each level of pulse off time (15, 25, and 35  $\mu\text{s}$ ), as shown in Fig. 36.6. However, the machining time is almost constant for the current level of 4 and 6. Therefore, the influence of pulse on time on the material removal rate is not clearly understood at a higher level of current during WEDM of CFRP laminate. The variation in machining time with pulse off time is shown in Fig. 36.7. It can be observed from the figure that the machining time tends to increase with an increase in the pulse off time. The pulse off time is the time required for re-establishing the insulation in the working gap (gap between the wire electrode and workpiece) at the end of each discharge cycle [5]. There is no sparking during this period. Hence, machining will not occur during this period. Therefore, the machining time will increase when the level of pulse off time is increased. Thus the material removal rate will decrease with the higher level of pulse off time. It can be seen that the machining time is increased by 105.95% for the

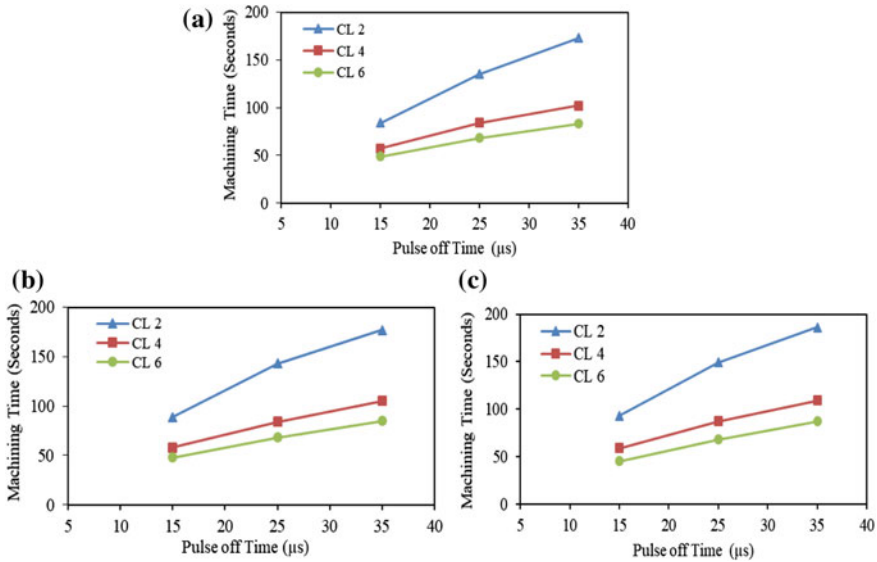


**Fig. 36.7** Variation in machining time with pulse off time at pulse on time of **a** 30  $\mu\text{s}$ , **b** 40  $\mu\text{s}$ , and **c** 50  $\mu\text{s}$

pulse off time of 35  $\mu\text{s}$  as compared to pulse off time of 15  $\mu\text{s}$  at the constant current level of 2 and pulse on time of 30  $\mu\text{s}$ . The corresponding values at the current level of 4 and 6 are 78.94 and 69.38% at pulse on time of 30  $\mu\text{s}$ . It can be observed in Fig. 36.8 that the machining time tends to decrease with the increase in current level in all instances. The total heat flux is increased with the increase in input current. The more amount of material is melted and removed due to this intense heat generation at a higher level of current making the machining process faster for a required length of cut. Therefore, machining time will decrease with increase in the current level while machining CFRP. The machining time is seen to be decreased by 52.02% for a current level of 6 as compared to current level 2 at a pulse off time of 35  $\mu\text{s}$  and pulse on time of 30  $\mu\text{s}$ . For pulse off time of 25 and 15  $\mu\text{s}$ , the corresponding values are 49.63 and 41.66% at a pulse on time of 30  $\mu\text{s}$ .

### 36.4 Conclusions

It can be concluded from the present study that it is feasible to machine CFRP laminate by WEDM process. While performing WEDM of CFRP, metallic plates should be used as assisting electrodes to initiate the spark. Initially, intense heat is generated on the metallic plates and then this heat propagates to the CFRP laminate. This eventually creates an overall heat-affected zone and causes removal of material from the workpiece. It was observed that the machining time increases with the pulse

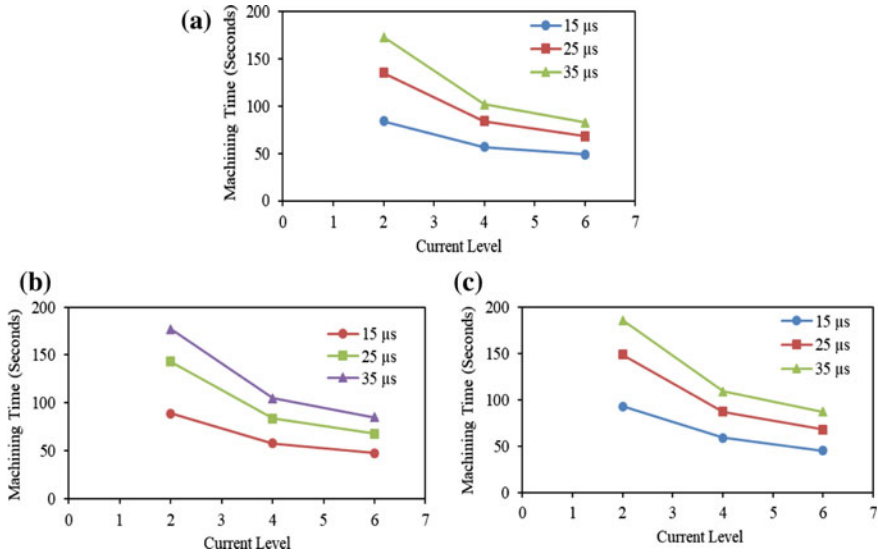


**Fig. 36.8** Variation in machining time with current level at pulse on time of **a** 30  $\mu$ s, **b** 40  $\mu$ s, and **c** 50  $\mu$ s

on time for current level of 2 (lowest) in each level of pulse off time. But machining time is almost constant for other levels of current (level 4 and 6). Therefore, it can be concluded that the machining time does not follow any specific trend with an increase in the pulse on time at a higher level of current. It can also be concluded from the study that the machining time increases with an increase in the pulse off time. Whereas machining time was found to be decreased with input current. The machining time is decreased by 52.02, 49.63, and 41.66% for a current level of 6 as compared to the current level of 2 at pulse off time of 35, 25, and 15  $\mu$ s for a constant pulse on time of 30  $\mu$ s. However, further study is needed to optimize the different parameters affecting the machining performance while cutting CFRP laminate by WEDM.

## References

- Uhlmann, E., Sammler, F., Richarz, S., Heitmuller, F., Bilz, M.: Machining of carbon fibre reinforced plastics. *Procedia CIRP* **24**, 19–24 (2014)
- Habib, S., Okada, A., Ichii, S.: Effect of cutting direction on machining of carbon fibre reinforced plastic by electrical discharge machining process. *Int. J. Mach. Mach. Mater.* **13**(4), 414–427 (2013)
- El-Hofy, M.H., Soo, S.L., Aspinwall, D.K., Sim, W.M., Pearson, D., Harden, P.: Factors affecting workpiece surface integrity in slotting of CFRP. *Procedia CIRP* **19**, 94–99 (2011)

4. Lau, W.S., Lee, W.B.: A comparison between EDM wire-cut and laser cutting of carbon fibre composite materials. *Mater. Manuf. Processes*. **6**(2), 331–342 (1991)
5. Kumar, S., Choudhury, S.K.: Prediction of wear and surface roughness in electro-discharge diamond grinding. *J. Mater. Process. Technol.* **191**(1–3), 206–209 (2007)

# Chapter 37

## Development of a Bore Using Jet Electrochemical Machining (JECM) in SS316 Alloy



J. Deepak , N. Vivek , B. MouliPrasanth  and P. Hariharan 

**Abstract** Jet Electrochemical Machining (JECM) has established itself as one of the major alternatives of machining conductive materials that are difficult to machine and to generate complex contours. Some of the components used in aerospace and gas turbine blades are to be machined without any defects, residual stress, and tool wear which is not possible or is difficult to achieve using conventional machining processes. In electrochemical machining, the workpiece and tool are submerged in electrolyte, it is observed that while machining, metal oxide is formed in between the electrode and workpiece, that negatively affects the geometrical features of the hole produced. In this paper, the effect of producing a jet of electrolyte using a hollow electrode and their effect on material removal rate, circularity, and conicity (geometrical quality of holes) is studied. Experiments were conducted in two different modes, one set of experiments were conducted with flushing and the other set is done without flushing. Experiments were performed by varying the following input parameters—voltage, electrolyte concentration, duty ratio, and the output parameters considered is material removal rate, circularity, and conicity. The flushing experiments were conducted at a constant velocity. From the results, it is observed that experiments conducted using flushing operation showed higher MRR, lower circularity, and lower conicity. Experiments are analyzed and optimized by Taguchi optimization Technique.

**Keywords** Jet electrode flushing technique (JEFT) · Passivation layer · Material removal rate (MRR) · Circularity · Conicity

---

J. Deepak (✉) · N. Vivek · B. MouliPrasanth · P. Hariharan  
Department of Manufacturing Engineering, College of Engineering  
Guindy, Anna University, Chennai 600025, India  
e-mail: [deepakjs123@gmail.com](mailto:deepakjs123@gmail.com)

© Springer Nature Singapore Pte Ltd. 2020  
M. S. Shunmugam and M. Kanthababu (eds.), *Advances in Unconventional Machining and Composites*, Lecture Notes on Multidisciplinary Industrial Engineering, [https://doi.org/10.1007/978-981-32-9471-4\\_37](https://doi.org/10.1007/978-981-32-9471-4_37)

## 37.1 Introduction

Over the years, Electrochemical machining (ECM) has gained importance as one of the important unconventional machining processes. It works on the principle of anodic electrochemical dissolution of the workpiece (i.e., principle based on Faraday's law of electrolysis but not electroplating). It is one of the best technologies and an economical process for the fabrication of complex shapes and counters on difficult to cut materials. Some basic advantages are better process efficiency and superior surface integrity primarily due to the absence of detrimental thermal residual stress [1–4]. Electrochemical machining has found wide applications in automobile industries, ordinance, aerospace, and general engineering industry [5]. Factors affecting the quality of machined surface in electrochemical machining process is dependent on the type of machining process involved and selection of optimal parameter setting [6]. It is observed that with increase in material removal rate the surface quality decreases. So, optimum parameters are required in getting good surface finish and a good amount of material removal rate. Feed rate, electrolyte concentration, voltage, and interelectrode gap are the input parameters that have major influence on MRR and surface roughness [7–9]. In electrochemical machining process, the workpiece is connected to anode and tool is connected to cathode. The reaction that occurs within the solution depends mainly on the selection of electrolytes. The most commonly used electrolyte is sodium nitrate or sodium chloride. Material removal rate is mainly affected by the formation of passive layer. Different electrolyte types such as passivating and non-passivating electrolyte are used in ECM process [10]. Different flushing flow rates of electrolyte were taken as input parameters to machine copper and Inconel and the effect of oxide layers formed in and around the tool–workpiece interface are studied [11]. Taguchi method is carried as an optimization to find the optimal parametrical combinations in the chosen input parameters and also ANOVA is carried out to find the percentage contributions of the chosen input parameters [12]. Various methods are available for providing flushing that is used to remove the metal oxide layer formed between the workpiece and tool during the machining process so as to improve the machined features.

## 37.2 Experimental Procedure

### 37.2.1 *Experimental Setup*

The experimental setup consists of an electrolyte supply tank, PLC controller, and power supply as shown in Fig. 37.1. In addition, separate electrolyte storage tank, pump, and flushing tube are used to provide flushing. The flushing tube of 2 mm is used to circulate electrolyte to provide flushing. The electrolyte is made to flow through a hollow copper tube. The tool is connected to the cathode and the workpiece is connected to the anode of the power supply. In this work, a set of experiments

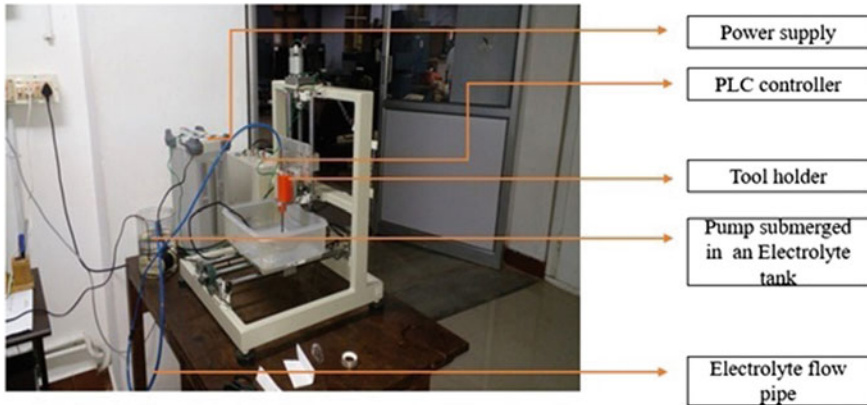


Fig. 37.1 Experimental setup

with flushing and another set of experiments without flushing is carried out. The experiments are conducted using flushing mode of operation, the electrolyte is made to flow at a constant velocity. Both the effect of with and without jet flushing is taken into account for the study.

### 37.2.2 Selection of Tool, Workpiece, and Electrolyte

Hollow copper rod is used to provide jet electrode flushing. The hollow copper tube with an outer diameter of 3 mm and an inner diameter of 2 mm is used. The length of the copper tube used is 150 mm. SS316 alloy material of 0.4 mm thickness is used as an anodic workpiece. In this study, an electrolytic solution of sodium nitrate at different concentrations is used. Sodium nitrate is a passivating electrolyte and is made to flow at a velocity of 0.1327 m/sec.

### 37.2.3 Design of Experiments

The selection of orthogonal array (OA) is an important factor in the design of experiments, Taguchi method is used to conduct experiments. Three input process parameters—voltage, electrolyte concentration, and duty ratio as shown in Table 37.1 has been chosen for conducting experiments with and without flushing. The number of levels is equal to three and L9 orthogonal array has been selected as per Taguchi's design of experiments theory. With these input parameters, the output parameters such as MRR, circularity, and conicity have been observed. The machining parameters for with and without flushing experiments are listed in Table 37.1.

**Table 37.1** Input parameters

Parameters	Level-1	Level-2	Level-3
Voltage (V)	30	35	40
Electrolyte concentration (g/l)	15	20	25
Duty ratio (%)	0.6	0.7	0.8

### 37.3 Results and Discussion

#### 37.3.1 Without Flushing Experiment

For experiments without flushing operation, MRR, circularity, and conicity are obtained and analyzed to find the most influencing input parameters. Response graphs for MRR, circularity, and conicity are also shown in Fig. 37.2. From Table 37.2, the most influencing input parameters over output parameters are observed. The most influencing parameter for MRR is voltage followed by electrolyte concentration and duty ratio. However, the most influencing parameter for circularity is electrolyte concentration, followed by duty ratio and voltage. Moreover, the most influencing parameter for conicity is duty ratio followed by voltage and electrolyte concentration.

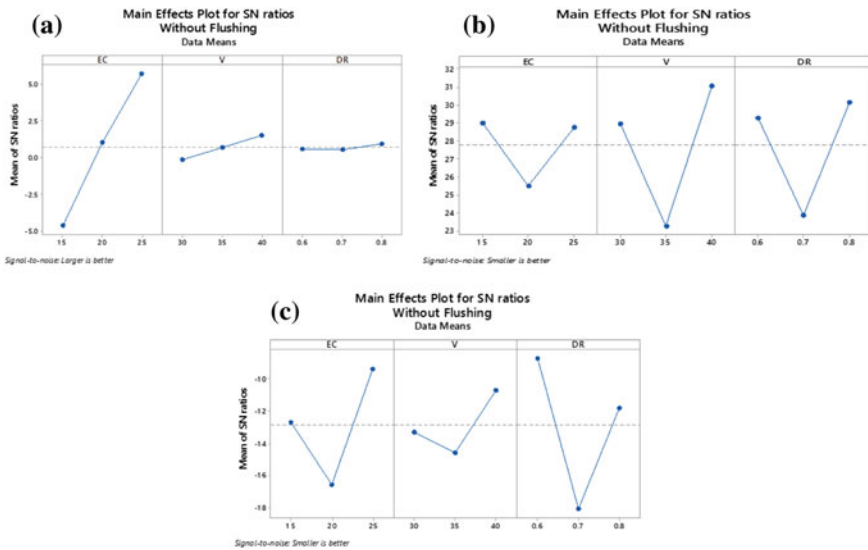


**Fig. 37.2** Response graphs of without flushing for **a** MRR, **b** circularity, and **c** conicity



**Table 37.2** Response table for MRR, circularity, and concity

Response Levels	MRR			Circularity			Concity		
	V	EC	Duty ratio.	V	EC	Duty ratio	V	EC	Duty ratio
1	-4.639	-0.156	0.563	29.01	28.94	29.28	-12.68	-13.33	-8.76
2	0.986	0.680	0.530	25.51	23.26	23.85	-16.56	-14.61	-18.08
3	5.655	1.479	0.909	28.77	31.08	30.16	-9.41	-10.72	-11.81
Delta	10.29	1.63	0.378	3.50	7.82	6.31	7.15	3.887	9.32
Rank	1	2	3	3	1	2	2	3	1

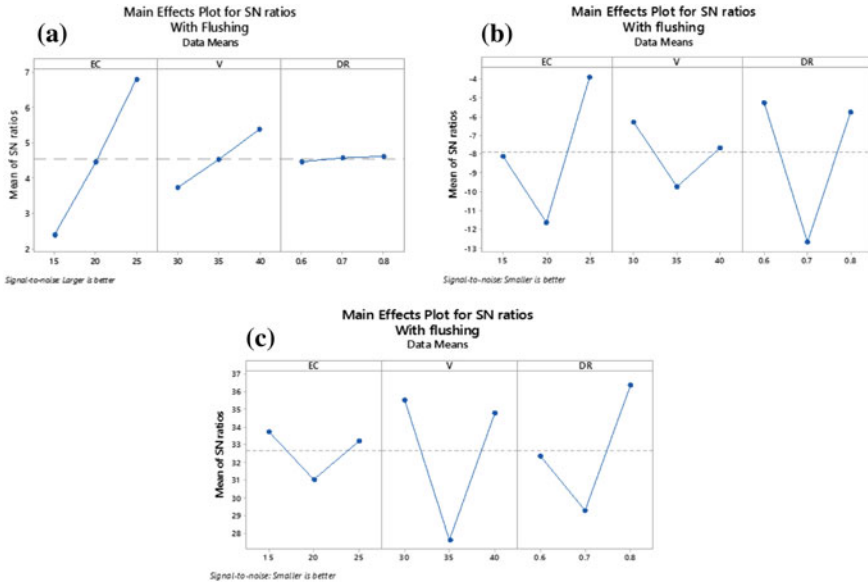


Fig. 37.3 Response graphs of with flushing for a MRR, b circularity, and c conicity

### 37.3.2 Flushing Experiment

For experiments conducted using flushing operation, MRR, circularity, and conicity are obtained and analyzed to find the most influencing input parameters. Response graphs for MRR, circularity, and conicity are also shown in Fig. 37.3. From Table 37.3, the most influencing input parameters over output parameters are observed. The most influencing parameter for MRR with flushing condition is voltage followed by electrolyte concentration and duty ratio. The most influencing parameter for circularity is electrolyte concentration followed by duty ratio and voltage. The most influencing parameter for conicity is duty ratio followed by voltage and electrolyte concentration.

## 37.4 Comparison of with and Without Flushing Experiment

### 37.4.1 Effect of Flushing on MRR

The material removal rate for experiments without and with flushing is compared and is shown in Fig. 37.4. In experiments conducted without flushing operation, insoluble by-products (metal hydroxides) is formed between the workpiece and tool

**Table 37.3** Response table for MRR, circularity, and conicity

Response Levels	MRR			Circularity			Conicity		
	V	EC	Duty ratio	V	EC	D.R.	V	EC	Duty ratio
1	-2.40	3.737	4.456	-2.406	28.94	29.28	3.108	2.843	1.973
2	4.46	4.534	4.585	4.463	23.26	23.85	3.882	3.733	4.500
3	6.800	5.399	4.29	6.800	31.08	30.16	1.733	2.507	2.250
Delta	4.39	1.663	0.172	4.394	7.82	6.31	2.148	1.250	2.527
Rank	1	2	3	3	1	2	2	3	1

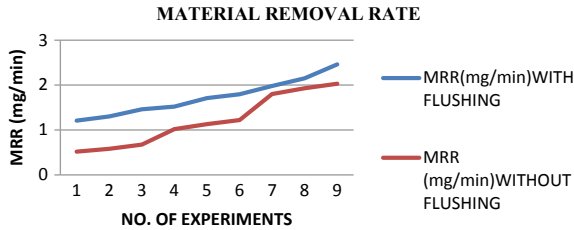


Fig. 37.4 Comparison of MRR for the holes machined with and without flushing operation

Experiment	With flushing	Without flushing
Top view (mm)		
Bottom view (mm)		
MRR (mg/min)	2.46	2.03

Fig. 37.5 VMS images of machined hole with highest MRR for experiments with and without flushing operation

which act as a barrier in machining, thus reducing material removal rate compared to flushing condition. In case of experiments conducted using internal flushing operation the flow of electrolyte did not allow the formation of passive layer, thus the unstable passive layer becomes transpassive. Hence, MRR is higher in experiments performed with flushing operation compared with experiments conducted without internal flushing operation. In addition, more ionic displacement occurs as the electrolyte is made to flow continuously. Increase in applied voltage leads to an increased current density in the interelectrode gap with the consequent rapid anodic dissolution, thereby increasing material removal rate. At the parameter setting of 40 V, 25 g/l, and 70% duty ratio, the highest MRR of 2.46 mg/min is obtained for flushing experiments and at the same parameter setting highest MRR of 2.03 mg/min is obtained for experiments conducted without internal flushing operation. Figure 37.5 shows the machined holes at 40 V, 25 g/l, and 70% duty ratio for experiments with and without flushing operation.

### 37.4.2 Effect of Flushing on Circularity

Figure 37.6 shows the effect of circularity on experiments conducted without and with flushing operation. In experiment conducted without flushing operation, because

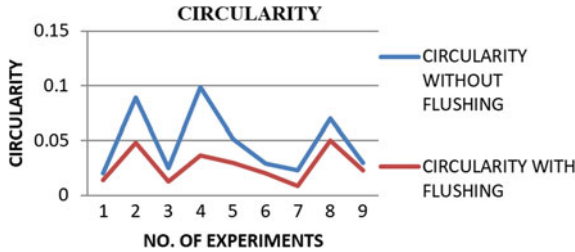


Fig. 37.6 Comparison of circularity for experiments with and without flushing

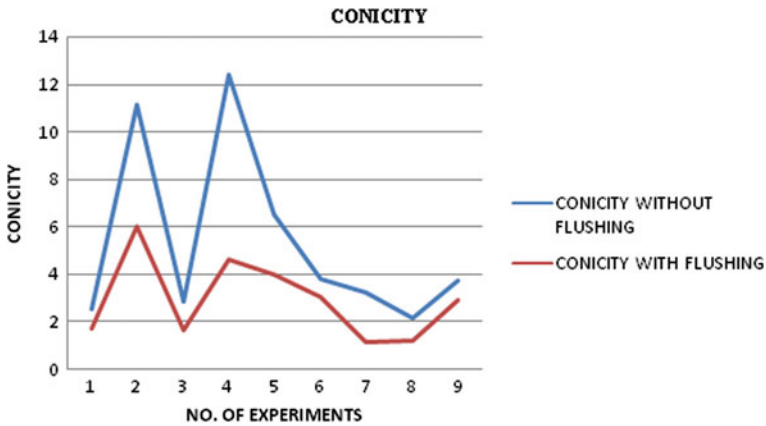
Experiment	With flushing	Without flushing
Top view (mm)		
Bottom view (mm)		
Circularity	0.01	0.02

Fig. 37.7 VMS images of machined hole with lowest circularity for experiments with and without flushing operation

of the stagnation of electrolyte, the metal oxide formed were not removed from the machining zone, which resulted in higher circularity compared to experiments conducted with flushing operation. In the experiment done using flushing operation, the metal oxides formed are removed by the continuous flow of electrolyte between the tool and workpiece and hence decrease in circularity is observed. At the parameter setting of 30 V, 15 g/l, and 60% duty ratio lowest circularity of 0.01 mm was observed for experiments without flushing operation and at the parameter setting of 30 V, 25 g/l, and 80% duty ratio lowest circularity of 0.02 mm was observed for experiments conducted without flushing operation. Figure 37.7 shows the images of the machined holes with lower circularity for experiments conducted with and without flushing operation. It can be observed from Fig. 37.6 that the samples machined with flushing operation has decreased circularity compared to experiments done without flushing operation for the same conditions.

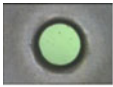
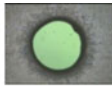


### 37.4.3 Effect of Flushing Experiment in Conicity

The results of experiments conducted without and with flushing operation are compared and are shown in Fig. 37.8. In the experiment without flushing operation, hydrogen bubbles that are generated helped in improving removal of the metal oxides



**Fig. 37.8** Comparison of conicity for experiments with and without flushing

formed as they cause disturbances that aided in the removal of metal oxides formed. In the experiments conducted with the flushing operation, the bubbles did not have a major effect and the flowing electrolyte caused the electrode to reach the exit of hole, thereby decreasing conicity in experiment with flushing. Moreover, in the experiments done using flushing operation, the metal oxide layers formed are pushed out from the machining zone thereby reducing conicity. At the parameter setting of 35 V, 25 g/l, and 60% duty ratio lowest conicity of 1.13 is observed for experiments conducted using flushing operation and lowest conicity of 2.15 is observed obtained for experiments conducted without flushing operation. Figure 37.9 depicts the machined holes at 35 V, 25 g/l, and 60% duty ratio for experiments with and without flushing.

Experiment	With flushing	Without flushing
Top view (mm)		
Bottom view (mm)		
Conicity	1.13	2.15

**Fig. 37.9** VMS images of machined hole with lowest conicity for experiments with and without flushing operation

## 37.5 Conclusions

The output parameters MRR, circularity, and conicity are obtained and analyzed. The optimum parameter for MRR in with and without flushing is 40 V, 25 g/l, and 80% duty ratio. The most influencing parameter for increase in MRR is voltage. The optimum parameter for circularity in without and with flushing is 35 V, 20 g/l, and 70% duty ratio. Electrolyte concentration is the cause for decrease in circularity. The optimum parameter for conicity in without and with flushing is 35 V, 20 g/l, and 70% of duty ratio. Duty ratio is the influencing parameter for improved conicity in without and with flushing experiment. In experiment with flushing, provides an increase of 41.87% in MRR, decrease of 50% in circularity, and decrease of 44.19% in conicity when compared to the experiment without flushing.

## References

1. Mount, A.R., Clifton, D., Howarth, P., Sherlock, H.: An integrated strategy for process characterisation and simulation in electrochemical machining. *J. Mater. Process. Technol.* **138**, 449–454 (2003)
2. Klocke, F., Zeis, M., Harst, S., Klink, A., Veselovac, D., Baumgärtner, M.: Modelling and simulation of the electrochemical machining (ECM) material removal process for the manufacture of aero engine components. *Proc. CIRP* **8**, 265–270 (2013)
3. Rajurkar, K.P., Zhu, D., McGeough, J.A., Kozak, J., De Silva, A.: New developments in electrochemical machining. *CIRP Ann. Manuf. Technol.* **48**(2), 567–579 (1999)
4. Mount, A.R., Howarth, P.S., Clifton, D.: The electrochemical machining characteristics of stainless steels. *J. Electro-chem. Soc.* **150**(3), 63–69 (2003)
5. Mc Geough, J.A.: *Advanced Methods of Machining*. Chapman and Hall, London (1988)
6. Ross, P.J.: *Taguchi Techniques for Quality Engineering*, international edn. McGraw Hill Book Company, New York (1985)
7. Bhattacharya, B., Munda, J.: Experimental investigation on the influence of electrochemical machining parameters on machining rate and accuracy in micromachining domain. *Int. J. Mach. Tool Manuf.* **43**(13), 1301–1310 (2003)
8. Neto, J., Da Silva, E., Da Silva, M.: Intervening variables in electrochemical machining. *J. Mater. Process. Technol.* **179**, 92–96 (2006)
9. Singh, A., Anandita, S., Gangopadhyay, S.: Micro structural analysis and multi response optimization during ECM of Inconel 825 using hybrid approach. *Mater. Manuf. Process.*, 1–10 (2015)
10. Datta, M.: Anodic dissolution of metals at high rates. *IBM J. Res. Dev.* **37**, 207–226 (1993)
11. Pooranachandran, K., Deepak, J., Hariharan, P., Mouliprasanth, B.: Effect of Flushing on Electrochemical Micromachining of Copper and Inconel 718 Alloy. *Advances in Manufacturing Processes. Lecture Notes in Mechanical Engineering*. Springer, Singapore (2019)
12. Sadagopan, P., Mouliprasanth, B.: Investigation on the influence of different types of dielectrics in electrical discharge machining. *Int. J. Adv. Manuf. Technol.* **92**, 277 (2017). <https://doi.org/10.1007/s00170-017-0039-1>

# Chapter 38

## Machining and Characterization of Channels on Quartz Glass using Hybrid Non-conventional Machining Process $\mu$ -ECDM



J. Bindu Madhavi and Somashekhar S. Hiremath 

**Abstract** Electrochemical Machining (ECM) and Electro Discharge Machining (EDM) are commercialized non-conventional machining processes due to its high accuracy of machining advance engineering conductive materials which are otherwise difficult with conventional processes. On combining ECM: etching and EDM: erosion, a hybrid technique called Electro Chemical Discharge Machining (ECDM) is used to machine non-conductive engineering materials like soda-lime, borosilicate, pyrex glasses, etc. Quartz glass is one of the hardest glass materials to process features on it and it widens the scope of its application in the field of microfluidic devices. Hence, machining of channels was carried out with 350  $\mu\text{m}$  diameter tungsten carbide (WC) tool on 4000  $\mu\text{m}$  thickness quartz glass for a length of 10,000  $\mu\text{m}$  using developed micro-ECDM ( $\mu$ -ECDM) experimental setup. The machining condition chosen was Voltage (V) of 60 V, Duty Factor (DF) of 60%, 20 wt% Sodium Hydroxide (NaOH) Electrolyte Concentration (C), and 0.01 mm/s feed rate (FR). Investigation was carried out to know the effect of varying number of machining passes for 200  $\mu\text{m}$  depth on responses like material removed (MR), surface roughness ( $R_a$ ), tool wear (TW), depth and width of the channel. Channel machined with 2 machining passes (100  $\mu\text{m}$ /pass) showed better responses of a higher depth of 290  $\mu\text{m}$ , MR of 2.77 mg, and lower  $R_a$  of 1.786  $\mu\text{m}$  with a width of 480  $\mu\text{m}$  and tool wear (TW) of 1.36 mg as compared to channels machined with 1 machining pass (200  $\mu\text{m}$ ) and 4 machining pass (50  $\mu\text{m}$ /pass). Further machining of channels with 2 pass was carried out to engrave letters and square wave channels formed on quartz glass may be used as microfluidic channels.

**Keywords** Micro-Electro Chemical Discharge Machining · Voltage · Duty Factor · Electrolyte Concentration

---

J. Bindu Madhavi · S. S. Hiremath (✉)

Precision Engineering & Instrumentation Laboratory, Department of Mechanical Engineering,  
Indian Institute of Technology Madras, Chennai 600036, Tamil Nadu, India  
e-mail: [somashekhar@iitm.ac.in](mailto:somashekhar@iitm.ac.in)

© Springer Nature Singapore Pte Ltd. 2020

M. S. Shunmugam and M. Kanthababu (eds.), *Advances in Unconventional Machining and Composites*, Lecture Notes on Multidisciplinary Industrial Engineering, [https://doi.org/10.1007/978-981-32-9471-4\\_38](https://doi.org/10.1007/978-981-32-9471-4_38)



### 38.1 Introduction

Non-conventional manufacturing processes are developed to machine very hard to fragile materials like nitralloy, carbides, waspaloy, nimonics, glass, etc. which are otherwise difficult to machine by conventional machining. Commercialized EDM: erosion and ECM: etching, are utilized to process such advance conductive engineering materials. Both these processes fail to machine non-conducting material. To address this issue EDM and ECM are combined to form a hybrid process called ECDM.

Figure 38.1 shows the schematic diagram of  $\mu$ -ECDM cell. It mainly consists of a tool and counter electrodes connected to a DC power supply and a non-conductive workpiece kept just below the tool electrode where sparking occurs. All immersed in an electrolyte solution in a chemical resistant beaker. An anode with a larger surface area than the cathode approximately of ratio 100:1 is used to limit the anodic dissolution and ensures high current density at the cathode. As the voltage increased from 0 to 10 V, the electrolysis process begins. From 10 to 26 V, electrolysis process accelerates and isolates the tool from the surrounding electrolyte. On further increasing the voltage above 30 V, spark discharge occurs between the tooltip and the surrounding electrolyte [1]. The discharge energy and chemical energy is utilized to melt, vaporize, and etch the material to be removed [2]. Melting and vaporization process predominates for material removal than chemical effect.

Researchers have investigated on process parameters like spark duration, electrode material, electrolyte, voltage, duty factor, workpiece material, feed rate on machining performances such as material removal rate (MRR), tool wear rate (TWR), width,  $R_a$ , depth, and quality of features machined.

According to Crichton and McGeough [3], on applying shorter spark duration with a maximum frequency of sparking results in maximizing MRR. Wuthrich et al. [4] have reported on platinum, aluminum, copper, silver, gold, tungsten, tungsten carbide, and nickel in use as cathode tool electrode materials and platinum foil, graphite plate as auxiliary anode electrode materials. Bhattacharyya et al. [5] found that NaOH as electrolyte solution yields higher MRR. They reported that this was

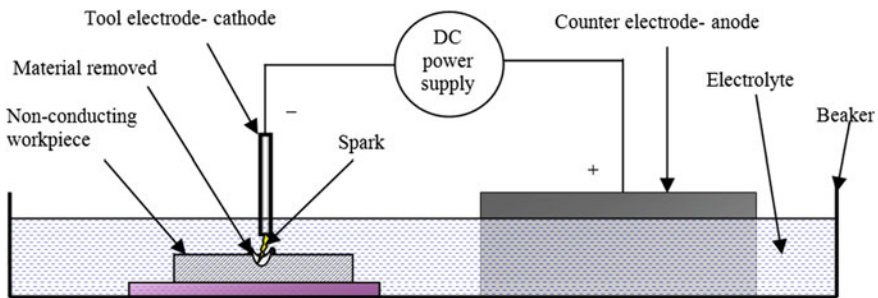


Fig. 38.1 Schematic diagram of  $\mu$ -ECDM cell

due to higher conductivity of NaOH which causes chemical reactions and gas bubble generation at a faster rate. Madhavi and Hiremath [6], machined channels on borosilicate and soda-lime glasses with 60 V, 25 wt% C NaOH, 70% DF, 300  $\mu\text{m}$  diameter tungsten alloy tool and found the machining performance to be different. They found for borosilicate glass: MRR was 0.359 mg/min, TWR was 0.42 mg/min, and width was 340  $\mu\text{m}$  and for soda-lime glass: MRR was 0.215 mg/min, TWR was 0.155 mg/min, and width was 630  $\mu\text{m}$ . Lijo and Hiremath [7] performed experiments to machine channels on soda-lime glass with tungsten carbide tool of 300  $\mu\text{m}$  diameter and results were modeled with response surface methodology. MRR and  $R_a$  were found to be increased from 1.08 mg/hr to 2.11 mg/hr and 0.614  $\mu\text{m}$  to 1.512  $\mu\text{m}$ , respectively, with an increase in voltage of 35 to 45 V. Wuthrich et al. [4] machined channel at 30 V on 1000  $\mu\text{m}$  thick borosilicate glass. They found that the machined channel width of 1000  $\mu\text{m}$  was more than the tool diameter, i.e., 700  $\mu\text{m}$ . They also observed that the obtained depth of the channel of 72  $\mu\text{m}$  was more than the given depth of cut (DOC) of 50  $\mu\text{m}$ . Didar et al. [8] machined channels with 30 wt% NaOH, 500  $\mu\text{m}$  diameter 316 L stainless steel (SS) tool, optical glass as a workpiece of 1000  $\mu\text{m}$  thickness for a machining length of 15,000  $\mu\text{m}$ . They found that with an increase in machining time and voltage resulted in increased depth of the channel. Increase in feed rate and standoff distance (SOD) resulted in a decreased depth of the channel.

From literature, it can be observed that in-depth investigated has been carried out on  $\mu$ -ECDM of soda-lime, borosilicate, and pyrex glasses. Besides, quartz glass, which poses considerable processing challenge as it composes pure  $\text{SiO}_2$  and is one of the hardest glass materials. Machining features like holes and channels would widen the scope of its application in the field of microfluidic devices. Microfluidic devices are sets of microchannels which are used for channelizing, delivering, separating, blending, stirring, and processing the working fluids. Hence, an attempt is made to machine channels on quartz glass using  $\mu$ -ECDM process. Most of the researchers have focused on the effects of parameters like V, DF, C, FR, and SOD on enhancing performances like MRR, TWR, width, and DOC. However, lacks study on performances of the machining channel as a result of varying number of passes. Considering this fact into account, the present paper reports on the investigation carried out on channels machined on quartz glass for MRR, TWR, width, depth,  $R_a$ , and shape of the channel concerning with the number of machining passes.

## 38.2 Experimentation

Figure 38.2 shows the schematic diagram of developed  $\mu$ -ECDM experimental setup. In present work, the beaker used was made up of a chemical resistant acrylic material of 100 mm diameter and 50 mm height. NaOH aqueous solution of 20 wt% C is used as an electrolyte. The workpiece used to machine channels having dimension of (20 mm  $\times$  20 mm  $\times$  4 mm) and was immersed in the electrolyte solution. The auxiliary electrode graphite material having dimension of (50 mm  $\times$  50 mm  $\times$  5 mm) was also immersed in the electrolyte solution.

Tungsten carbide (WC) tool of diameter 350  $\mu$ m is used as cathode. The inter-electrode gap was kept fixed at 30 mm throughout the experiments. A voltage of 60 V with 60% DF was applied across the electrodes. A linear motorized actuator obtained z-direction movement of the tool and X, Y directions movements of the workpiece were achieved by XY scanning stage with 0.01 mm/s feed rate. Channels were machined for 10,000  $\mu$ m length with an objective to know the effect of varying number of machining passes.

The machining performances of interest were MR, TW, width, depth,  $R_a$ , and shape of the channels. The amount of MR and TW are obtained from measuring weights of workpiece and tool before and after each machining by Mettler Toledo electronic balance. BRUKER Contour GT profilometer was used to obtain the width, depth,  $R_a$ , and shape of the channel. Confocal microscope images analyzed the machined surfaces of the channels and tool profiles before and after machining were analyzed using optical microscope images.

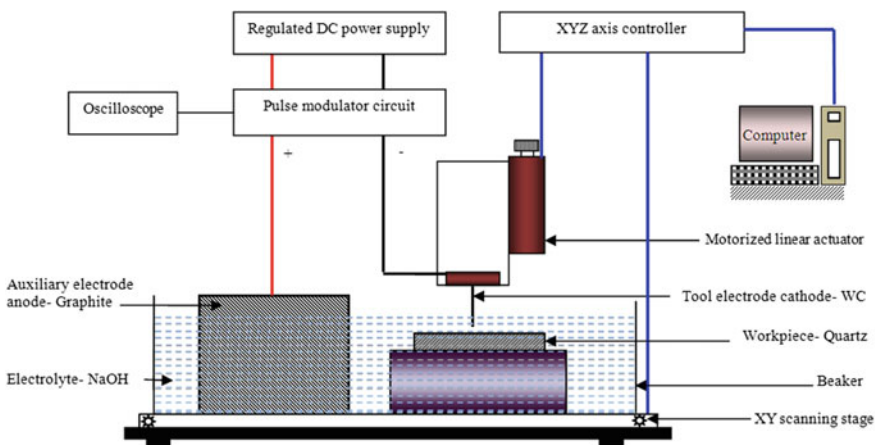


Fig. 38.2 Schematic diagram of developed  $\mu$ -ECDM experimental setup

### 38.3 Results and Discussion

Figure 38.3(a), (b), (c) shows the machined channel width, depth,  $R_a$ , surface, and edges of 1 pass, 2 pass, and 4 pass. Channel was machined in one pass as shown in Fig. 38.3(a). The obtained material removal from the workpiece was 2.62 mg, the tool wear was 0.55 mg. The machined channel width was 400  $\mu\text{m}$ , depth was 220  $\mu\text{m}$ , and  $R_a$  was 3.733  $\mu\text{m}$ . The obtained shape of the channel was tapered walls with a “V shape” at the bottom surface of the channel. This obtained shape can be due to eroding of the tool resulted from the high discharge of 60 V for a longer duration of 60% DF. Which in turn increases the temperature and conductivity of electrolyte at the tooltip accelerating the etching process and wearing the tool to lose its cylindrical surface and flat tip as shown in Fig. 38.4(a) and attaining tapered surface with a pointed tip as shown in Fig. 38.4(b). Thus, the material removed from the workpiece takes the replica shape of the continuously wearing out tool during the channel machining. The edges of the channel are found to be linear.

Channel machined with 2 pass is as shown in Fig. 38.3(b). The obtained material removal from the workpiece was 2.77 mg and the tool wear was 1.36 mg. The machined channel width was 480  $\mu\text{m}$ , depth was 290  $\mu\text{m}$ , and  $R_a$  was 1.786  $\mu\text{m}$ . The obtained shape of the channel was tapered walls with a “U shape” at the bottom surface of the channel. The material removed from the workpiece and the tool wear was higher than the one-pass machining. This can be due to the exposure of the material to high-intensity discharge [9] which erodes and etches the material for the longer duration for every pass. The obtain shape of channel depicts that the tool wears out to become tapered but attains a curved tip and hence the bottom surface of the channel attains the shape of “U” and a reduced  $R_a$  value. The availability of electrolyte around the tool during the second pass of machining increases the depth of the channel as well as the widths at the top and bottom of the channel [4]. The edges of the channel are found to be linear and jaggy.

Channel machined with 4 pass is a shown in Fig. 38.3(c). The obtained material removal from the workpiece was 2.31 mg and the tool wear was 2.48 mg. The machined channel width was 500  $\mu\text{m}$ , depth was 202  $\mu\text{m}$ , and  $R_a$  was 1.94  $\mu\text{m}$ . The tapered shape of a channel was obtained with an “irregular flat shape” at the bottom surface of the channel. Compared to one and two passes, the material removed from the workpiece was lower and tool wear was higher in 4 pass. Increase in tool wear can be due to high-intensity discharge for the longer duration with the increased number of machining passes. Which results in reduced length of the tool, increasing the gap between the tool and workpiece. Thus, the amount of sparking effect on the workpiece is comparatively less than that of 1 pass and 2 pass machining. This resulted in the decreased material removal of the workpiece and lower depth of the channel per pass. The obtained shape of channel depicts that the tool does get tapered but retains some flatness at the tip resulting in a channel with tapered walls and an “irregular flat shape” bottom surface. However, the irregular surface of the channel increases the  $R_a$  value as compared to the 2 pass channel. As described earlier, the availability of electrolyte around the tool during each successive passes of machining

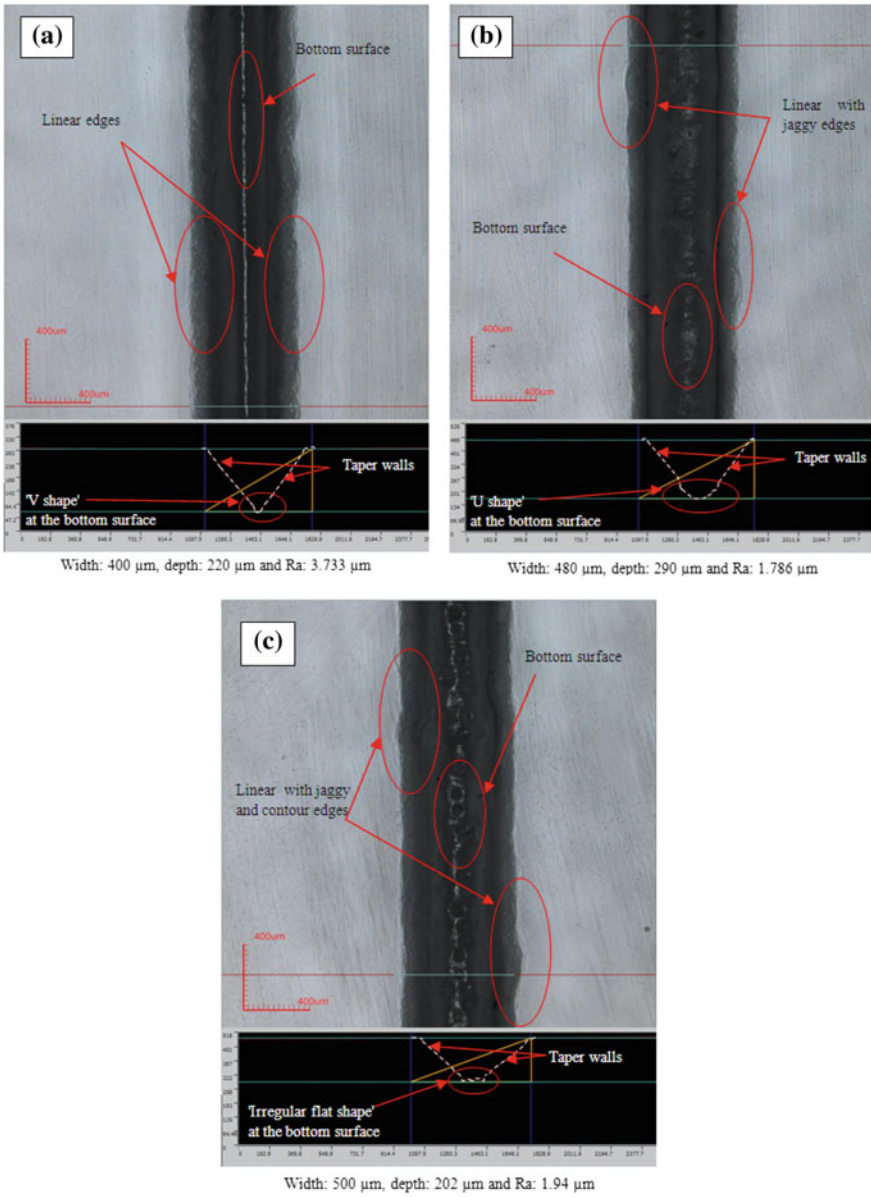


**Fig. 38.3** Machined channel width, depth,  $R_a$ , surface, and edges of (a) 1 pass, (b) 2 pass, (c) 4 pass

results in an increase in the top and bottom width of the channel. At the bottom surface this channel, dints with the formation of rims around it can be observed. During the duration of sparking, the melted lump of the material gets pileup around the tool forming a rim and during the duration of no spark, this lump cools and solidifies, resulting in trapping of the tool. As the machining feed continuous, this trapped tool is forced to jump over the rim, leaving its impression in the form of a dint [10]. Throughout the length of the machined channel, such dints with the formation of rims around occurs. The machined channel was found to be linear with jaggy and contour edges.

From the above discussions, it is clear that the channel machined with 2 pass showed a higher depth of  $290\ \mu\text{m}$ , higher MR of  $2.77\ \text{mg}$ , and lower  $R_a$  of  $1.786\ \mu\text{m}$  with a width of  $480\ \mu\text{m}$  and TW of  $1.36\ \text{mg}$  as compared to channels machined with 1 pass and 4 pass.

Hence, considering 2 pass, sets of channels were machined on quartz glass to engrave letters of “FPSI” and square wave microfluidic channel as shown in Fig. 38.5(a) and (b), respectively.

### 38.4 Conclusion

Channel on quartz glass was machined using  $\mu$ -ECDM process. Following observation was made during machining:

Two passes of machining channel showed the higher depth of  $290\ \mu\text{m}$ , higher MR of  $2.77\ \text{mg}$ , lower  $R_a$  of  $1.786\ \mu\text{m}$  with a width of  $480\ \mu\text{m}$  and TW of  $1.36\ \text{mg}$  as compared to channels machined with 1 pass and 4 pass.

Taper and over cut are inherent properties of this machining process.

Reduced DOC with an increase in the number of machining passes resulted in the flat bottom surfaced channel.

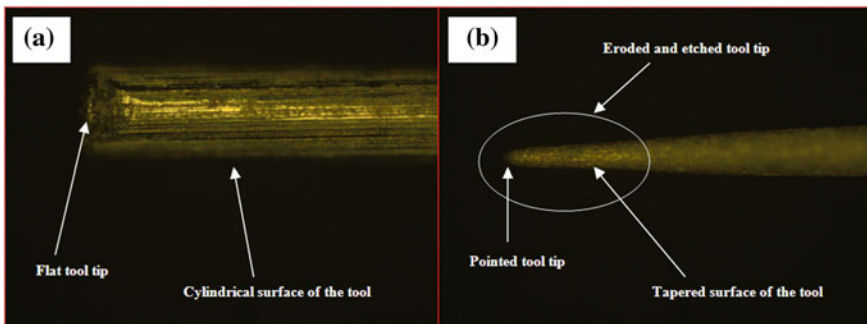


**Fig. 38.4** Optical microscopic image of tool with 1 machining pass (a) before machining, (b) after machining

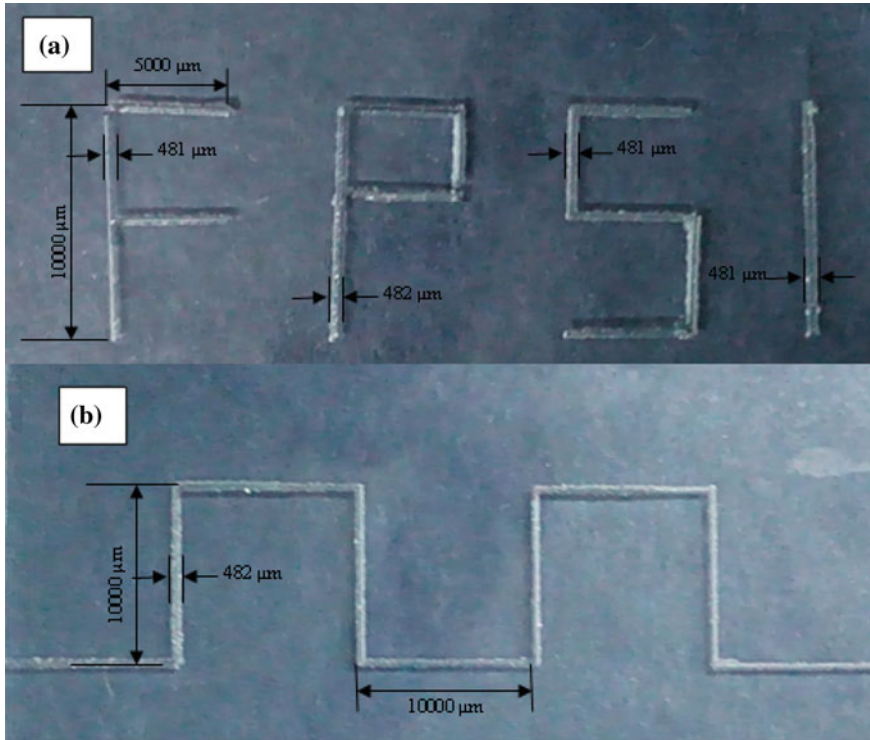


**Fig. 38.5** Photographic image of (a) letter engraving, (b) square wave microfluidic channel

Successful machining of channels with two pass was carried out to engrave letters and fabricate square wave microfluidic channel.

## References

1. Sabahi, N., Hajian, M., Razfar, M.R.: Experimental study on the heat-affected zone of glass substrate machined by electrochemical discharge machining (ECDM) process. *Int. J. Adv. Manuf. Technol.*, 1–8 (2018)
2. Paul, L., Hiremath, S.S.: Evaluation of process parameters of ECDM using grey relational analysis. *Procedia Mater. Sci.* **5**, 2273–2282 (2014)
3. Crichton, I.M., McGeough, J.A.: Studies of the discharge mechanisms in electrochemical arc machining. *J. Appl. Electrochem.* **15**(1), 113–119 (1985)
4. Wuthrich, R., Fascio, V., Viquerat, D., Langen, H.: In situ measurement and micromachining of glass. In: *Proceedings of 1999 International Symposium on Micromechatronics and Human Science, 1999, MHS '99*, pp. 185–191. IEEE (1999)
5. Bhattacharyya, B., Doloi, B.N., Sorkhel, S.K.: Experimental investigations into electrochemical discharge machining (ECDM) of non-conductive ceramic materials. *J. Mater. Process. Technol.* **95**(1–3), 145–154 (1999)

6. Madhavi, J.B., Hiremath, S.S.: Investigation on machining of holes and channels on borosilicate and sodalime glass using  $\mu$ -ECDM setup. *Procedia Technol.* **25**, 1257–1264 (2016)
7. Lijo, P., Hiremath, S.S.: Characterisation of micro channels in electrochemical discharge machining process. In: *Applied Mechanics and Materials*, vol. 490, pp. 238–242. Trans Tech Publications (2014)
8. Didar, T.F., Dolatabadi, A., Wüthrich, R.: Characterization and modeling of 2D-glass micro-machining by spark-assisted chemical engraving (SACE) with constant velocity. *J. Micromech. Microeng.* **18**(6), 065016 (2008)
9. Goud, M., Sharma, A.K.: On performance studies during micromachining of quartz glass using electrochemical discharge machining. *J. Mech. Sci. Technol.* **31**(3), 1365–1372 (2017)
10. Saranya, S., Nair, A., Sankar, A.R.: Experimental investigations on the electrical and 2D-machining characteristics of an electrochemical discharge machining (ECDM) process. *Microsyst. Technol.* **23**(5), 1453–1461 (2017)



# Chapter 39

## Parametric Study of a Newly Developed Magnetorheological Honing Process



Talwinder Singh Bedi and Anant Kumar Singh

**Abstract** A new magnetorheological honing process is developed to fulfill the requirement for finishing the internal surface of ferromagnetic workpieces. In this process, the electromagnetic tool with retained MR polishing fluid moved inside the ferromagnetic cylindrical-type workpiece as similar to traditional honing tool for precise surface finishing. Response surface methodology is carried out to plan and evaluate the effect of different process parameters for determining the percentage change in surface roughness ( $R_a$ ) values. The experimental analysis revealed that the higher percentage change in  $R_a$  values is determined by magnetizing currents followed by tool linear speeds, mesh sizes of CIPs, tool rotational speeds, and mesh sizes of SiC abrasive particles. The surface roughness ( $R_a$ ) value is found as 96 nm from initial 401 nm after 90 min of finishing with the optimum process parameters. The application of present magnetorheological honing process is found in internal surface finishing of injection barrel, bearings, etc.

**Keywords** Magnetorheological fluid · Honing · Response surface methodology

### 39.1 Introduction

At present, the various cylindrical mold cavities made of EN-24 die steel are of greater demand in today's industry. The traditional finishing operations such as internal surface grinding and honing are commonly used to finish the internal cylindrical surface of such components [1]. The larger surface roughness ( $R_a$ ) values produced on the internal cylindrical surface after traditional finishing operations results into decrease in the functional and operational capability of the machine. This is because, during finishing, the solid abrasive stones of finishing tool which is in touch with the internal cylindrical surface produce various surface defects, such as deeper grooves and sharp edges, on the workpiece surface [2, 3]. The prime examples such as various

---

T. S. Bedi (✉) · A. K. Singh  
Thapar Institute of Engineering & Technology, Patiala 147004, Punjab, India  
e-mail: [talwindersinghbedi@gmail.com](mailto:talwindersinghbedi@gmail.com)

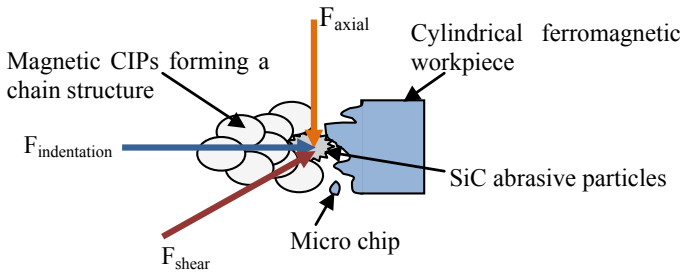


**Fig. 39.1** Surface finishing mechanism using present MR honing process

final-made parts like plastics caps, oil seals, etc. produced by injection barrel through injection molding machine result in the lesser surface quality and appearance of products which ultimately results in rejection of these parts [4]. The challenge to finish the internal cylindrical surface has been overcome by the different finishing processes such as magnetic abrasive finishing (MAF) [5], magnetorheological abrasive flow finishing (MRAFF) [6], and rotational–magnetorheological abrasive flow finishing (R-MRAFF) [7]. These processes utilize magnetorheological (MR) fluid for precise surface finishing under the magnetic field effect [8]. The MR polishing contains a mixer of nonmagnetic abrasive particles, magnetic iron particles, and base fluid. The base fluid consists of grease, mineral oil, silicon oil, water, etc. [9]. The finishing process such as MAF [5] is developed for internal finishing of non-ferromagnetic cylindrical workpiece like SUS-304 steel. MRAFF [6] and R-MRAFF [7] are developed and mainly found useful for internal finishing of non-ferromagnetic cylindrical workpiece such as stainless steel and brass materials. Above-said finishing processes based on MR fluid are likely less efficient to finish the internal ferromagnetic surface. This is because of their tool design structure. Later, a magnetorheological honing process has been developed [10] for internal cylindrical surface finishing of ferromagnetic materials. The mechanism of surface finishing using present MR honing process is shown in Fig. 39.1. The axial force ( $F_{axial}$ ) is developed by the tool vertical reciprocation movement. The indentation force ( $F_{indentation}$ ) is developed along the magnetic force. The active abrasives indent into the cylindrical ferromagnetic workpiece through a CIPs chains structure. The shear force ( $F_{shear}$ ) is developed by the continuous rotation of active abrasives on the internal workpiece surface. During finishing, the peaks of roughness cutoff to microchips due to combined effect of  $F_{axial}$ ,  $F_{indentation}$ , and  $F_{shear}$  as shown in Fig. 39.1.

## 39.2 MR Honing Process Variables

Magnetorheological (MR) honing process [10] is useful for fine finishing of internal cylindrical surface made of ferromagnetic material. On the basis of experimentations, the controlled variables are selected such as mesh sizes of SiC abrasive particles

(S), mesh sizes of carbonyl iron particles (CIPs) (C), magnetizing currents (I), tool rotational speeds (R), and tool linear speeds (L).

### 39.3 Design of Experiments

To examine the influence of different process parameters on the percentage change in surface roughness ( $\% \Delta R_a$ ) values, the design of experiments was used. The experiments were conducted on the newly developed magnetorheological (MR) honing process [10]. The material used for finishing the cylindrical internal surface was EN-24 die steel (ferromagnetic in nature) which is mainly used in injection barrels. The initial surface roughness ( $R_a$ ) values of the key-type workpieces were found in the range of 669–692 nm which were measured by SJ-210 surftest. The value of 0.25 mm was taken as cutoff length during surface roughness measurements. The response surface methodology (RSM) is the combination of both numerical and statistical data which is helpful for analyzing the engineering models. RSM determines the relation between the independent controlled variables and the final response surfaces. At present, five factors and five levels with six central and axial runs were selected for experimentations. The regression analysis was carried using central composite design (CCD). Further, from the analysis of variance (ANOVA), the F-test was performed to determine the consequence of regression equation. The regression equation helps to evaluate the relationship among independent controllable variables and the improvement in surface finish. The effect of five process variables was examined on the  $\% \Delta R_a$  values by the full factorial design. The process parameters represented by its coded levels and along with its actual values used for finishing of internal ferromagnetic surface using MR honing setup is given in Table 39.1. The MR polishing fluid composition was taken by vol. i.e. 20% of SiC abrasive particles, 20% of carbonyl iron particles (CIPs), 60% of base fluid (80% paraffin oil + 20% AP3 grease by weight). The total 50 experiments were conducted using design of experiments.

**Table 39.1** MR honing process variables

Parameter along with units	Coded levels				
	-2	-1	0	1	2
SiC abrasives (S) in mesh size	400	600	800	1000	1200
CIPs (C) in mesh size	200	300	400	500	600
Magnetizing current (I) in Amp	0.4	0.8	1.2	1.6	2.0
Tool rotational speeds (R) in rpm	200	300	400	500	600
Tool linear speeds (L) in cm/min	10	20	30	40	50

### 39.4 Response Surface Regression Analysis

The responses in terms of %  $\Delta R_a$  values were analyzed using Eq. (39.1).

$$\% \Delta R_a = \frac{(Initial R_a \text{ value} - Final R_a \text{ value})}{(Initial R_a \text{ value})} \times 100 \tag{39.1}$$

The sequential sum of squares was evaluated to choose the elevated order of polynomial. The extra terms are regarded as significant and the model is not aliased. At present, the significant level, i.e.,  $\alpha = 0.05$ , was taken for the given hypothesis for which a p-value which is  $\leq 0.05$  is considered as significant. The ANOVA after eliminating the insignificant terms is given in Table 39.2. The model F-value is 59.84 suggests that the model is significant, i.e., the value of Prob > F is less than 0.05 which clearly indicates that the model terms are considered as significant. The  $R^2$  for the given model is 0.9599. A ratio of 36.968 (i.e., greater than 4), is considered as desirable. The following Eq. (39.2) represents the quadratic equations which define the empirical relations between the process parameters. The final equation as per the

**Table 39.2** ANOVA for %  $\Delta R_a$  values after eliminating the insignificant terms

Source	Sum of squares	df	Mean square	F-value	P-value Prob > F	Remarks
Model	2008.12	14	143.44	59.84	<0.0001	Significant
S	28.90	1	28.90	12.06	<0.0001	
C	62.50	1	62.50	26.07	<0.0001	
I	372.10	1	372.50	155.23	<0.0001	
R	57.60	1	57.60	24.03	<0.0001	
L	72.90	1	72.90	30.41	<0.0001	
S <sup>2</sup>	182.41	1	182.41	76.09	<0.0001	
C <sup>2</sup>	61.61	1	61.61	25.70	<0.0001	
I <sup>2</sup>	1017.01	1	1017.01	424.26	<0.0001	
R <sup>2</sup>	61.61	1	61.61	25.70	<0.0001	
SC	15.13	1	15.13	6.31	0.0168	
SI	15.13	1	15.13	6.31	0.0168	
SR	18.00	1	18.00	7.51	0.0096	
SL	28.13	1	28.13	11.73	0.0016	
IL	15.13	1	15.13	6.31	0.0168	
Residual	83.90	35	2.40			
Lack of fit	73.90	28	2.64	1.85	0.2042	Not significant
Pure error	10.00	7	1.43			
Cor total	2092.02	49				

actual factors is represented in Eq. (39.2)

$$\begin{aligned}
 \% \Delta R_a = & -111.62500 + 0.096250S + 0.09600 + 90.46875I \\
 & + 0.15300R + 0.71625L - 0.0000596875S^2 - 0.000138750C^2 \\
 & - 35.23438I^2 - 0.000138750R^2 + 0.0000343750SC + 0.00859375SI \\
 & - 0.0000375000SR - 0.000468750SL - 0.17187I \tag{39.2}
 \end{aligned}$$

The contribution of each process parameters on  $\% \Delta R_a$  values was S as 1.43, C as 3.09, I as 18.34, R as 2.85, L as 3.61, S2 as 9.03, C2 as 3.05, I2 as 50.39, R2 as 3.05, SC as 0.74, SI as 0.74, SR as 0.89, SL as 1.39 and IL as 0.74.

### 39.5 Results and Discussion

#### 39.5.1 Effect of Mesh Sizes of SiC Abrasive Particles

The effect of mesh sizes of SiC abrasive particles on  $\% \Delta R_a$  values is shown in Fig. 39.2. At 800 mesh size of abrasive particles, the  $\% \Delta R_a$  values increases. The abrasive particles have an optimum size which finally gripped strongly by the CIPs chains structure. This gripped abrasive particle helps to remove the roughness peaks from the internal ferromagnetic surface.

#### 39.5.2 Effect of Mesh Sizes of CIPs

The effect of mesh size carbonyl iron particles (CIPs) on  $\% \Delta R_a$  values is shown in Fig. 39.3. With 400 mesh size of CIPs, the SiC abrasive particles gripped by these CIPs chains structure provided a feasible or gentle indentation of gripped SiC

**Fig. 39.2** Effect of mesh size of SiC abrasive particles on %age change in surface roughness ( $R_a$ ) value

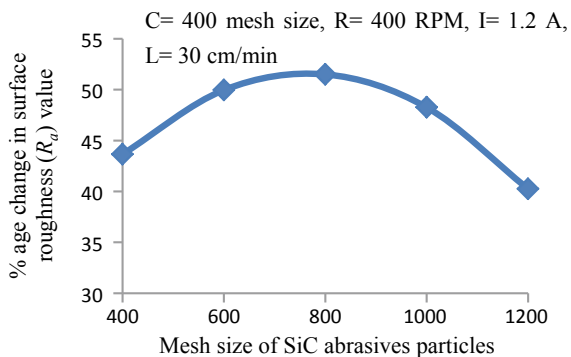
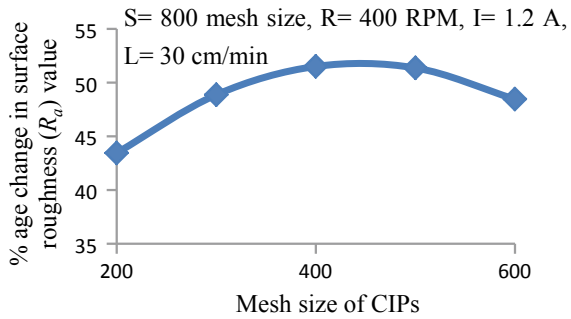


**Fig. 39.3** Effect of mesh size of CIPs on %age change in surface roughness ( $R_a$ ) value



abrasive particles onto the internal ferromagnetic cylindrical surface. This results in higher  $\% \Delta R_a$  from the internal ferromagnetic cylindrical surface.

### 39.5.3 Effect of Magnetizing Currents

The effect of magnetizing currents on  $\% \Delta R_a$  values is shown in Fig. 39.4. At 1.2 A of magnetizing current, the CIPs provided a strong bonding chains strength. This further helps to grip the SiC abrasive particles more strongly by the strong bonding strength of CIPs chains structure. As a result, the  $\% \Delta R_a$  values increase.

### 39.5.4 Effect of Tool Rotational Speeds

The effect of tool rotational speeds on  $\% \Delta R_a$  values is shown in Fig. 39.5. At lower tool rotational speed, i.e., 200 rpm, the tangential shearing force provided by the SiC abrasive particles was lower which resulted in a smaller  $\% \Delta R_a$  values. The tangential shearing force increased with the higher tool rotational speed. The  $\% \Delta R_a$  value increased gradually up to the tool rotational speed of 400 rpm. At 500 rpm, the

**Fig. 39.4** Effect of magnetizing currents on %age change in surface roughness ( $R_a$ ) value

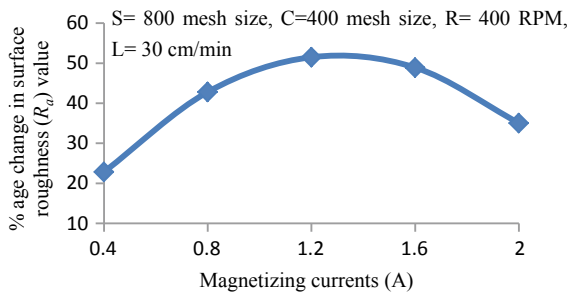


**Fig. 39.5** Effect of tool rotational speeds on %age change in surface roughness ( $R_a$ ) value

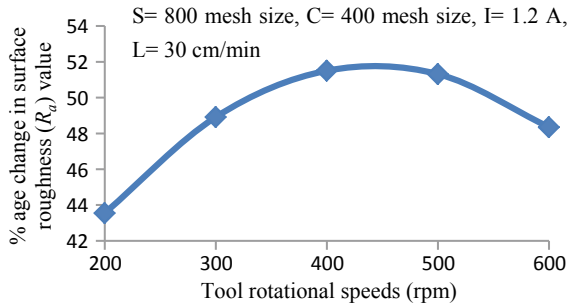
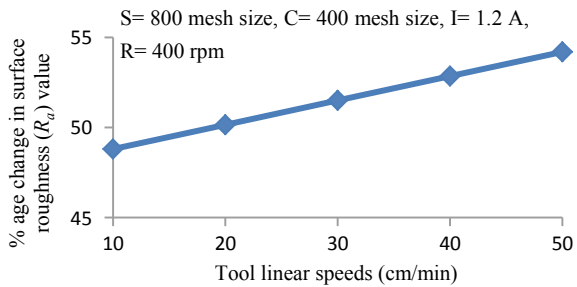


**Fig. 39.6** Effect of tool linear speeds on %age change in surface roughness ( $R_a$ ) value



$\% \Delta R_a$  values were likely almost constant. This is because the effect of centrifugal force was withstood by the strongly bonded CIPs chains up to 500 rpm of tool rotational speed.

### 39.5.5 Effect of Tool Linear Speeds

The effect of tool linear speeds on  $\% \Delta R_a$  values is shown in Fig. 39.6. As the tool linear speed increased, the  $\% \Delta R_a$  values also increased. Therefore, the SiC abrasive particles provided a sufficient axial shearing strength at higher tool linear speed, i.e., at 50 cm/min. As a result, the higher  $\% \Delta R_a$  values were found.

## 39.6 Confirmatory Experiments for Validating Results

The five different experiments were conducted in order to confirm the validity of regression model as obtained in Eq. (39.2). From this analysis, percentage among the experimental and predicted data was from  $-5.71$  to  $5.40\%$ .

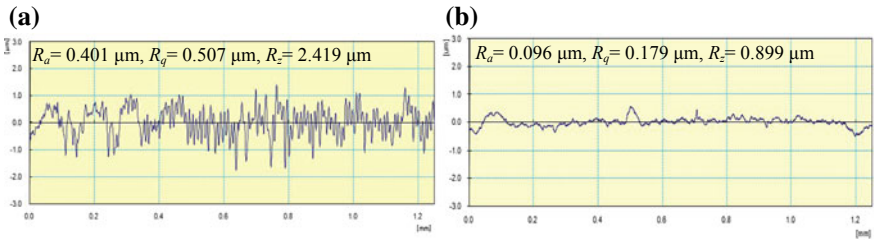


**Fig. 39.7** Surface roughness profiles of **a** initial ground surface and **b** final finished surface after 90 min of finishing

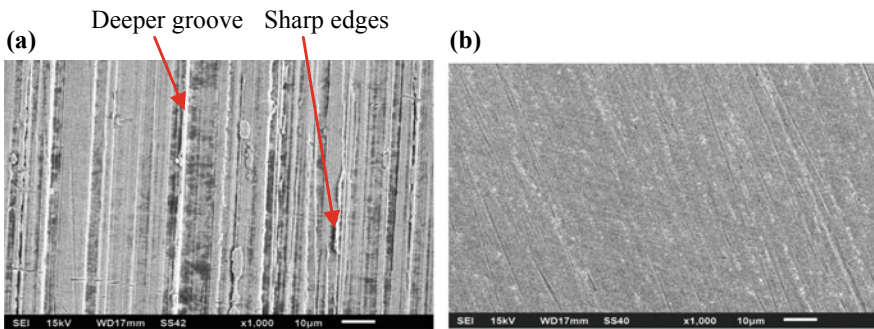


**Fig. 39.8** Scanning electron microscopy images at 1000× of **a** initial ground surface and **b** final finished surface after 90 min of finishing

### 39.7 Optimization of Process Parameters

After analyzing, the optimum process parameters were found as  $S = 800$  mesh size,  $C = 400$  mesh size,  $I = 1.2$  A,  $R = 400$  rpm, and  $L = 50$  cm/min. The initial ground and final surface roughness profiles followed by SEM images are shown in Figs. 39.7 and 39.8.

### 39.8 Conclusions

In the present work, the magnetorheological (MR) honing process was used for internal finishing of EN-24 cylindrical ferromagnetic workpiece. Using response surface methodology, the effects of mesh sizes of SiC abrasive particles, mesh sizes of CIPs, magnetizing currents, tool rotational speeds, and tool linear speeds on  $\% \Delta R_a$  values were analyzed. From the response surface regression analysis, the maximum contribution was made with magnetizing currents followed by tool linear speeds, mesh sizes of CIPs, tool rotational speeds, and mesh sizes of SiC abrasive particles.



The lowest surface roughness ( $R_a$ ) value was found as 96 nm from 401 nm after 90 min of finishing with optimum parameters as 800 mesh size of SiC abrasive particles, 400 mesh size of CIPs, 1.2 A of magnetizing current, 500 RPM of tool rotational speed, and 50 cm/min of tool linear speed. The surface defects like deeper grooves and sharp edges left out on the internal surface by grinding operation were completely removed by the present MR honing process and can be clearly correlated by the scanning electron microscopy images at  $1000\times$ .

The present developed magnetorheological (MR) honing process is useful in significant finishing of the internal ferromagnetic cylindrical surface after the traditional finishing operations in order to improve its functional applications in today's manufacturing industries. The fine finishing of different internal ferromagnetic cylindrical surfaces is required even after traditional honing or grinding operations of various mechanical components such as molds and dies of cylindrical types, connecting rods, and bearings. which can only be possible by using the present MR honing process.

**Acknowledgements** The authors acknowledged SERB-DST, India, for providing a financial support for the project work (Project No. EMR/2015/000330).

## References

1. Jain, V.K.: Magnetic field assisted abrasive based micro-/nano-finishing. *J. Mater. Process. Technol.* **209**(11), 6022–6038 (2009)
2. Dimkovski, Z., Anderberg, C., Ohlsson, R., Rosen, B.G.: Characterisation of worn cylinder liner surface by segmentation of honing and wear scratches. *Wear* **271**(3–4), 548–552 (2011)
3. Gupte, P.S., Wang, Y., Miller, W., Barber, G.C., Yao, C., Zhou, B., Zou, Q.: A study of torn and folded metal (TFM) on honed cylinder bore surfaces. *Tribol. Trans.* **51**(6), 784–789 (2008)
4. Maan, S., Singh, G., Singh, A.K.: Nano-surface-finishing of permanent mould punch using magnetorheological fluid based finishing process. *Mater. Manuf. Process.* **32**(9), 1004–1010 (2016)
5. Yamaguchi, H., Shinmura, T.: Study of the surface modification resulting from an internal magnetic abrasive finishing process. *Wear* **225–229**(1), 246–255 (1999)
6. Jha, S., Jain, V.K.: Design and development of the magnetorheological abrasive flow finishing (MRAFF) process. *Int. J. Mach. Tools Manuf.* **44**(11), 1019–1029 (2004)
7. Das, M., Jain, V.K., Ghoshdastidar, P.S.: Nanofinishing of flat workpiece using rotational-magnetorheological abrasive flow finishing (R-MRAFF) process. *Int. J. Adv. Manuf. Technol.* **62**(1–4), 405–420 (2012)
8. Bedi, T.S., Singh, A.K.: Magnetorheological methods for nanofinishing—a review. *Part. Sci. Technol.* **34**(4), 412–422 (2016)
9. Sadiq, A., Shunmugam, M.S.: Investigation into magnetorheological abrasive honing (MRAH). *Int. J. Mach. Tools Manuf.* **49**(7–8), 554–560 (2009)
10. Bedi, T.S., Singh, A.K.: Development of magnetorheological fluid-based process for finishing of ferromagnetic cylindrical workpiece. *Mach. Sci. Technol.* **22**(1), 120–146 (2018)

# Chapter 40

## Investigation on Surface Roughness During Finishing of Al-6061 Hybrid Composites Tube with Traces of Rare Earth Metals Using Magnetic Abrasive Flow Machining



V. K. Sharma , V. Kumar  and R. S. Joshi 

**Abstract** This paper studies the effect of magnetic abrasive flow machining process on internal finishing of the Al-6061-based hybrid composites tubes reinforced with SiC, Al<sub>2</sub>O<sub>3</sub>, and rare earth particulates. The characteristics of internal finishing for getting a mirror-like surface are influenced by the nature of magnetic abrasive particles. A novel systematic methodology to identify the optimal MAF process parameters is presented in present work. Moreover, effects of process parameters, namely, extrusion pressure and number of cycles on surface roughness, have also been investigated. An experimental study was carried out on Al-6061 hybrid composites containing wt% of SiC and Al<sub>2</sub>O<sub>3</sub> from 5 to 15% and CeO<sub>2</sub> from 0.5 to 2.0%. The results obtained from the roughness profile curve shows that at extrusion pressure of 20.68 bar least percentage improvement in surface roughness occurred whereas, at 48.26 bar, maximum improvement in surface roughness occurred with the use of magnetic field intensity.

**Keywords** Magnetic · Abrasive flow · Machining · Box–Behnken · Design · Finishing

---

V. K. Sharma (✉) · V. Kumar · R. S. Joshi  
Department of Mechanical Engineering, Thapar Institute  
of Engineering & Technology, Patiala 147004, India  
e-mail: [vipin2871985@gmail.com](mailto:vipin2871985@gmail.com)

V. K. Sharma  
Department of Mechanical Engineering, Faculty of Meerut  
Institute of Engineering & Technology, Meerut 250005, India

© Springer Nature Singapore Pte Ltd. 2020  
M. S. Shunmugam and M. Kanthababu (eds.), *Advances in Unconventional Machining and Composites*, Lecture Notes on Multidisciplinary Industrial Engineering, [https://doi.org/10.1007/978-981-32-9471-4\\_40](https://doi.org/10.1007/978-981-32-9471-4_40)

## 40.1 Introduction

The mechanism of magnetic abrasive finishing process is entirely different from the conventional abrasive finishing process. The magnetic field-assisted finishing process depends on the utilization of slurry comprising of ferrous particles blended with fine rough particles (Diamond, Aluminum Oxide ( $Al_2O_3$ ), Silicon Carbide (SiC), Cubic Boron Nitride (CBN), and so on. These nonmetallic abrasives have hard sharp edges with unpredictable shapes. This blended mixture consolidates along the lines of the magnetic field (created by poles connected to magnets) and forms flexible magnetic abrasive brush. The brush performs like a multipoint cutting apparatus for completing procedure since it can adjust itself as indicated by surface forms. The magnetic field is sufficiently solid to beat the inalienable erosion between the abrasive and an objective surface; the movements of the rough brush complete the surface. In this procedure, ferromagnetic particles sintered with previously mentioned non-metallic abrasives (diamond,  $Al_2O_3$ , SiC, or CBN); what's more, such particles are called magnetic abrasives. The principle goals of AFM process are to accomplish high dimensional accuracy, great surface characteristics, and MRR. Surface complete of an item is a vital angle as it can influence the item life. The innovative move from large scale to small scale and nanolevels has additionally expanded the pushed on different completing procedures. Also, the improvement in materials has made certain interest in new propelled completing procedures. Among the different propelled completing procedures, magnetic-based completing procedures are picking up significance in view of their ability to deliver great surface finish with slightest surface harm. Another reason that magnetic abrasive-based finishing procedures are getting consideration by the scientists has been that the completing powers in these procedures can be controlled effectively amid wrapping up. They have revealed an astounding change in surface unpleasantness over the traditional approach in which a static direct current was provided to the electromagnet. In another approach subjected a SUS 304 example to three methods of vibrations [1]. It was watched that the vibration along the course of feed brought about a smoother surface while the vibrations at opposite heading of feed brought about a superior cleaning adequacy. They likewise detailed that the blend of both the vibrations yielded a superior cleaning viability and in addition a smoother surface. In an ongoing endeavor subjected a diligent workpiece AISI 52100 to ultrasonic vibrations while performing MAF [2]. It brought about a critical change in cleaning viability as a result of expansion of ultrasonic vibrations. Likewise, it estimated the machining powers if there should arise an occurrence of MAF and UAMAF and called attention to that the utilization of ultrasonic vibrations brought about an expansion in distracting cutting power, which yields in creating better surface wrap up [3]. Magneto Abrasive Flow Machining (MAFM) procedure enhances the material removal rate and diminishes surface harshness by applying a magnetic field around the workpiece [4]. Enhanced surface roughness and MRR are seen in MAFM over AFM. It was investigated double disc magnetic finishing (DDMAF) process for finishing of the two paramagnetic materials is used and finally compare their finishing components [5, 6]. It was proposed that

Magnetic Abrasive Finishing Technique (MAF) utilized for the burrs evacuation on the surface of little parts produced using ferromagnetic or non-attractive materials [7, 8].

In this experiment, two process parameters including extrusion pressure and number of cycles were considered that affects magnetic abrasive finishing process on the surface finish of aluminum hybrid composites reinforced with cerium oxide ( $\text{CeO}_2$ ) rare earth particulate. Based on literature review, it was analyzed that very less work has been conducted on the MAFM for the finishing of hybrid composites reinforced with rare earth particulate. Generally, MAFM was used for the finishing of metals, nonmetals, alloys, and metal matrix composites. So, an approach will be planned to finish the hybrid composites based on rare earth particulates.

## 40.2 Experimental Details

### 40.2.1 Material Selection

The test set of connections was planned and created in the lab. Process variables can be altered in the setup (e.g., extrusion pressure may differ up to 48.26 bars). The material utilized for the pressure-driven barrels of double-acting hydraulic cylinders was EN8. Inside barrel measurement was 90 mm and stroke length was 250 mm and water-driven oil no. 68 was utilized. A nylon fixture with openings was utilized to hold the workpiece. This was used due to easy machinability so that the slots could easily be cut to match the shape of the work piece. Entry cross area was progressively lessened in the apparatus permitting the smooth section of medium with least pulsation. Subsequent to the coveted number of cycles, the workpiece and installation were evacuated and another workpiece put in the openings. Two vertically flexible plates were joined so the installation may possibly be held firmly with no spillage of medium. Workpiece materials are taken as Al-6061 hybrid composites with 5, 10, and 15 wt% of SiC and  $\text{Al}_2\text{O}_3$  each as a reinforced material. Little measure of cerium oxide as rare earth metal (with average particle size 5  $\mu\text{m}$ ) normally 0.5–2 wt% likewise utilized with the mixture of reinforcement.

### 40.2.2 Stir Casting

RE-based hybrid composites were fabricated with the help of bottom pouring stir casting route. The mixture of measured amount of reinforced particles was preheated into the furnace at temperature of 350 °C in order to remove the moisture content in it. Now, the mixture was slowly poured into the Al-6061 melt to 900 °C with the help of conical hopper by utilized stirrer speed which was kept constant of 300 rpm. The different compositional solid bars of SiC and  $\text{Al}_2\text{O}_3$  reinforced particles with

5, 10, and 15% by weight were fabricated. Small amount of cerium oxide rare earth particulate with wt% 0.5–2 was also used as reinforcement materials. The fabricated specimens had dimension of 150 × 15 mm and 5 mm in thickness. Finally, the surface finish of all fabricated specimens was evaluated with the help of talysurf instrument called Mitutoyo Surftest SJ201P (made in Japan).

### 40.3 Finishing Mechanism of Magnetic Abrasive Finishing Process

The finishing mechanism of magnetic abrasive finishing process depends upon the amount of force created by the magnetic field. Figure 40.1 a, b demonstrates the two-dimensional circulation of magnetic field and its sum on the ferromagnetic particles. It is clear from Fig. 40.1 a that the force “F” is the value of magnetic force intensity on the ferromagnetic particles (A) due to magnetic field. The value of magnetic force intensity can be further resolved into two parts say  $F_x$  and  $F_y$ . The power intensity of magnetic force (F) which follows up on the single volume of magnetic abrasive molecule at the position “j” which is for the most part arranged at the outside of the working zone can be composed as

$$F = V_0 B \nabla B / \mu \tag{40.1}$$

where  $B =$  Magnetic Induction.

$\nabla B =$  Gradient of magnetic induction at the “j” position of the abrasive particles. It was found that the magnetic permeability of the magnetic particles used in the MAF process has larger value as compared to the permeability of free space, i.e., ( $\mu > \mu_0$ ). Subsequently, the estimation of magnetic force in condition (40.1) can

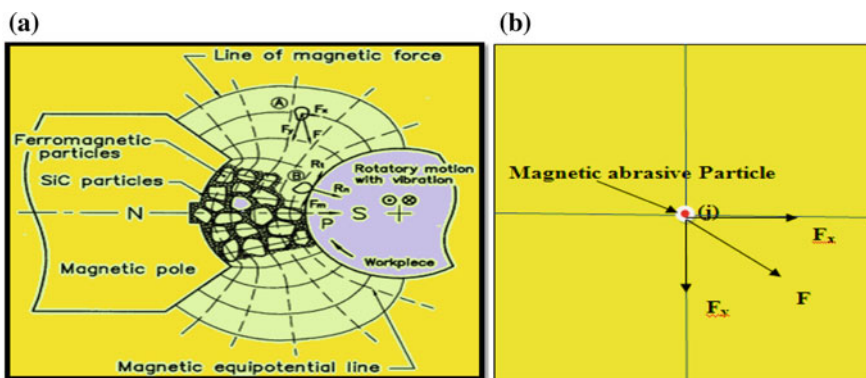


Fig. 40.1 Mechanism of MAF process, a distribution of magnetic field, b magnetic force acting on ferromagnetic particle [9]

be settled into two-dimensional magnetic field dispersion conditions as composed beneath:

$$F_x = V_0 X_m \mu_o H \frac{\partial H}{\partial x} \quad (40.2)$$

$$F_y = V_0 X_m \mu_o H \frac{\partial H}{\partial y} \quad (40.3)$$

Component of magnetic force in x-direction is  $F_x$  and in y-direction is  $F_y$ . Volume of the magnetic particle is denoted by  $V_0$ .  $X_m$  is the magnetic susceptibility of the magnetic particles and permeability of free space is  $\mu_o$ . Magnetic field strength at point “j” is given by H. The values of magnetic gradient in x- and y-directions are indicated by  $\frac{\partial H}{\partial x}$  and  $\frac{\partial H}{\partial y}$ . It is especially obvious from the condition 40.2 and 40.3 that the magnetic forces in x- and y-directions are corresponded to the volume of the rough abrasive particles, magnetic susceptibility, strength of magnetic field, and magnetic gradients in x- and y-directions also. The estimations of magnetic force in x and y courses keep the sprinkling of attractive particles in the finishing process of the parts which are generally caused by the value of high speed of rotation of magnetic poles. The rotational speed of poles is used from 200 to 300 rpm. In the completing procedure of MAF strategy, substantial number of a magnetic abrasive rough particles toward magnetic lines of force shaping an adaptable magnetic abrasive brush inside the working zone, which at last causes the pressure “P” on the free frame surface and this pressure will follow up on the work surface to evacuate the burr or scratch on it. The estimation of pressure “P” is given by

$$P = \left[ \mu_o H^2 \left( 1 - \frac{1}{\mu_m} \right) \right] / 2 \quad (40.4)$$

In Eq. (40.4),  $\mu_m$  represents the relative magnetic permeability of the magnetic abrasive particles.

## 40.4 Results and Discussions

Percentage improvements in surface finish (PISF %) and material removal per cycle (MRC) are taken as the measure of execution of MAFM process. The principle purpose of this experiment was to investigate the significant effect of extrusion pressure and number of cycles on surface finish of an Al-6061 hybrid composite tube reinforced with rare earth particulate. The preliminary experiments were done thrice on each pressure value on different specimens on MAFM setup. The readings of the preliminary experiments are recorded on micrograph Fig. 40.2a–e. As it is clearly illustrated from the plotted graph that there has been a steep increase when the pressure value switched from 20.68 bar to 34.47 bar is slightly greater in case where

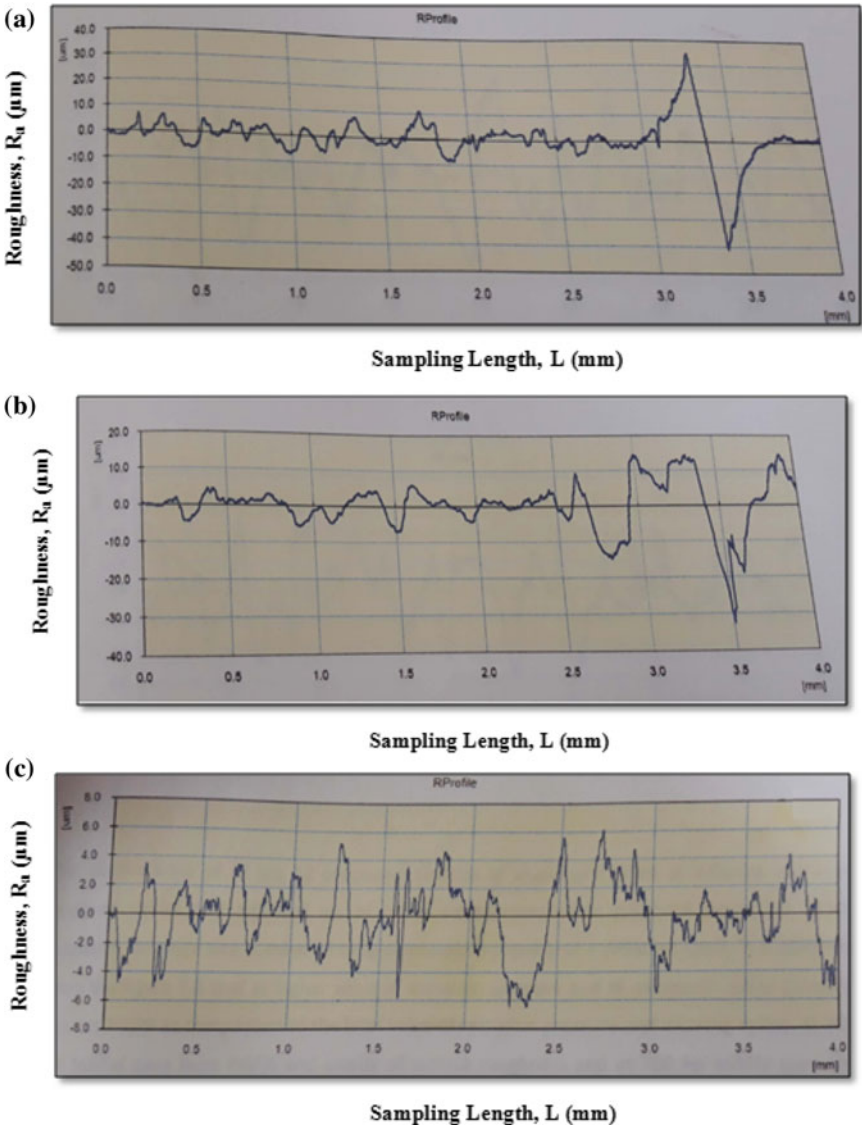


**Fig. 40.2** R-Profile of Al-6061 Tube at different cycles and extrusion pressure on MAFM, **a** after 10 cycles at 20.68 bar, **b** after 20 cycles on 20.68 bar, **c** after 15 cycles at 34.47 bar, **d** after 15 cycles at 48.26 bar, **e** after 20 cycles at 48.26 bar

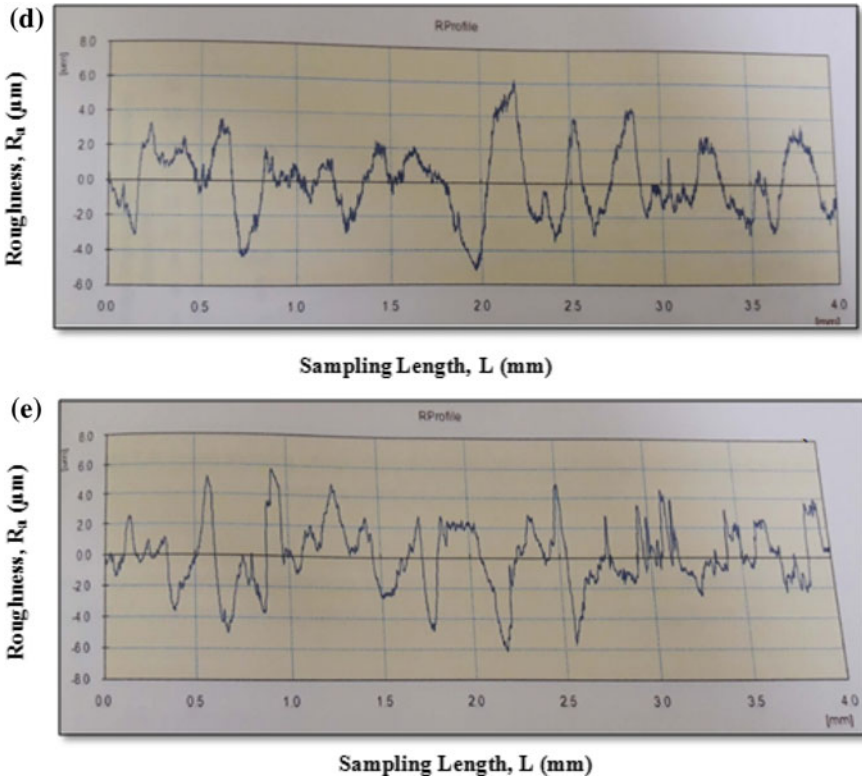


Fig. 40.2 (continued)

magnetic field is applied. The improvement beyond the 34.47 bar appeared to be of much significance as compared to before and on 48.26 bar value. One factor has to be constant for finding the range of the other parameter. It is further observed that after 48.26 bar pressure value there has been little rise in the value of surface finish. Moreover, after the 48.26 bar value there have been insignificant surface finish results as it appeared to attain stagnant value but in case of MAFM value is increasing even at 48.26 bar. So the selected range of the extrusion pressure from these 12 experiments was from 20.68 bar to 48.26 bar.

### 40.4.1 Results from Optical Micrograph

The microstructure of the Al-6061 rare earth-based hybrid composite aluminum tube samples before and after MAFM finishing to differentiate the surface roughness was observed using the optical micrograph. In Fig. 40.3, inner surface micrograph of aluminum tube is shown, which clearly indicates scratches, pullouts, and irregularities



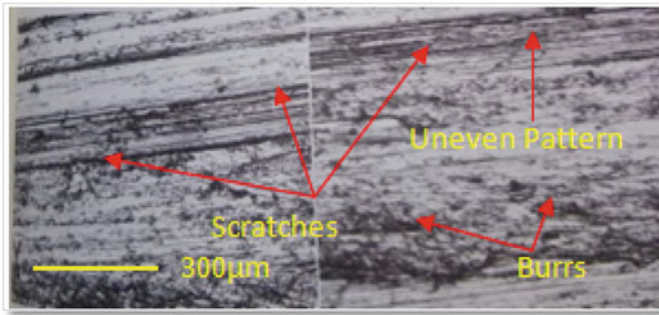


**Fig. 40.3** Optical micrograph of Al-6061 hybrid composite tube before MAFM

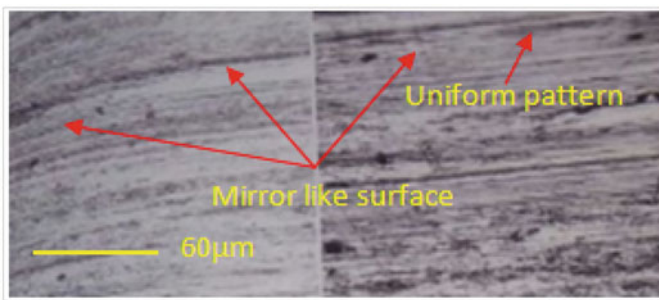


**Fig. 40.4** Optical micrograph of Al-6061 hybrid composite tube after MAFM

in the surface, i.e., surface roughness was more. On the other side in Fig. 40.4, with the use of optical micrograph, MAFM finished surfaces are shown, having characteristics like homogenous structure, continuous line patterns, mirror-like shine and least scratches. Hence, MAFM helps to reduce tool marks and increase surface finish which leads to plain visible surface.

## 40.5 Conclusions

This paper presents the finishing characteristics of MAF applied to an internal surface of Al-6061 hybrid composite tubes reinforced with cerium oxide as rare earth particulate using diamond powder magnetic abrasive in special prepared media. MAF process was successfully applied to remove the burrs from the internal surface of RE-based hybrid composites tubes without damage of its original surface. It was observed that percent improvement in surface roughness mostly influenced by the interaction effects of abrasive mesh size and rotational speed of the poles. Better

surface characteristics were achieved with the increase in the percentage of the magnetic abrasive particles as well as with the rotational speed of the poles. But, the most dominant polishing factor which helps significantly in the percent improvement of the surface roughness was found to be magnetic flux density produced by the magnets. On observed percentage improvement in surface roughness, extrusion pressure has the optical impact at higher rate as compared to lower value of pressure with varying number of cycles. The ploughing and rubbing marks are seen amid traditional machining, i.e., boring and reaming of RE-based hybrid composites tubes and these have been effectively evacuated by the MAF procedure. Fewer deeper marks visible even after magnetic abrasive finishing, it may be due to micro level cutting by up and down movement of magnetic abrasive particles. The proposed mechanism of material removal at higher values of pressure and magnetic flux density lucratively justifies the actions of process parameters during MAF of RE-based hybrid composites tubes and energized mechanically bounded diamond abrasive particles are capable to clean the surface irregularities of the hybrid composites.

## References

1. Jain, V.K., Singh, D.K., Raghuram, V.: Analysis of performance of pulsating flexible magnetic abrasive brush (P-Fmab). *Mach. Sci. Technol.* **12**(1), 53–76 (2008)
2. Yin, S., Shinmura, T.: A comparative study: polishing characteristics and its mechanisms of three vibration modes in vibration-assisted magnetic abrasive polishing. *Int. J. Mach. Tools Manuf.* **44**(4), 383–390 (2004)
3. Mulik, R.S., Pandey, P.M.: Ultrasonic assisted magnetic abrasive finishing of hardened AISI 52100 steel using unbonded SiC abrasives. *Int. J. Refract. Met. Hard Mater.* **29**(1), 68–77 (2011)
4. Mulik, R.S., Pandey, P.M.: Experimental investigations and modeling of finishing force and torque in ultrasonic assisted magnetic abrasive finishing. *J. Manuf. Sci. Engm. ASME* **5**(134), 1–12 (2012)
5. Singh, S., Shan, H.S., Kumar, P.: Wear behavior of materials in magnetically assisted abrasive flow machining. *J. Mater. Process. Technol.* **128**, 155–161 (2002)
6. Kala, P., Pandey, P.: Comparison of finishing characteristics of two paramagnetic materials using double disc magnetic abrasive finishing. *J. Manuf. Process.* **17**, 63–77 (2015)
7. Ko, S.L., Baron, Y.U., Park, J.I.: Micro Deburring for precision parts using magnetic abrasive finishing method. *J. Mater. Process. Technol.* **187**, 19–25 (2007)
8. Zou, Y.H., Jiao, A.Y., Aizawa, T.: Study on plane magnetic abrasive finishing process-experimental and theoretical analysis on polishing trajectory. *Adv. Mater. Res.* **126**, 1023–1028 (2010)
9. Yamaguchi, H., Shinmura, T., Ikeda, R.: Study of internal finishing of austenitic stainless steel capillary tubes by magnetic abrasive finishing. *J. Manuf. Sci. Eng.* **129**(5), 885–892 (2007)

# Chapter 41

## Part Program-Based Process Control of Ball-End Magnetorheological Finishing



F. Iqbal , Z. Alam , D. A. Khan and S. Jha

**Abstract** Ball-end magnetorheological finishing (BEMRF) process is an advanced finishing process which produces roughness up to nanometers. The BEMRF process also involves complicated process parameters along with other subprocesses (work-piece cleaning and roughness measurement) which make the automation of this process difficult. This paper presents automatic process control of BEMRF based on CNC part programming, i.e., each parameter and subprocess control of BEMRF is mapped on to standard CNC codes (G and M) and newly defined codes wherever necessary. Integrated part program is developed and tested for control of BEMRF. Results show good and proper functioning of BEMRF parameters and subsystems.

**Keywords** Automation · CNC · Part program · Process control

### 41.1 Introduction

Automation of machining processes came to existence many years ago and changed production processes; similar was the case with conventional finishing processes. With the advent of advanced finishing processes, final quality of products increased but at the cost of time due to the involvement of many process parameters which were difficult to control automatically and their manipulation required time and human intervention. BEMRF process is developed as an ultra-advanced process for nanofinishing in recent times. Over the years during the development of this process various research works were carried out for analytical and qualitative behavior of this process. Primarily, the research on BEMRF process has focused on its finishing capabilities on different materials such as mild steel, silicon, copper and aluminum [1], glass, polycarbonate [2], etc. Other than the materials researchers have focused on studying the effect of varying constituents of magnetorheological polishing (MRP) fluid [3] while some other experimental attempts are on studying the parameters in BEMRF process [4]. Some attempts have been made to mathematically model the

---

F. Iqbal · Z. Alam · D. A. Khan · S. Jha (✉)

Department of Mechanical Engineering, Indian Institute of Technology Delhi, Delhi 110016, India  
e-mail: [suniljha@mech.iitd.ac.in](mailto:suniljha@mech.iitd.ac.in)

© Springer Nature Singapore Pte Ltd. 2020

M. S. Shunmugam and M. Kanthababu (eds.), *Advances in Unconventional Machining and Composites*, Lecture Notes on Multidisciplinary Industrial Engineering, [https://doi.org/10.1007/978-981-32-9471-4\\_41](https://doi.org/10.1007/978-981-32-9471-4_41)

503

BEMRF process [5], while a very few attempts were also made to automate the BEMRF process [6, 7].

## 41.2 i5-B CNC BEMRF Machine Tool

This process was first developed at IIT Delhi. The setup developed was a three-axis system which could finish flat and inclined surfaces but had limited applications in finishing of freeform surfaces, irregular curves, intricate geometries, etc. Apart from the limited applications to difficult geometries, the automation of the three-axis setup was limited and only the manual control of motion and process parameters was available. To deal with the existing limitations of automatic solutions to BEMRF motion and process parameters and also to address the finishing of complex geometries which was difficult to obtain until now, a five-axis CNC BEMRF system is designed and developed [8].

The system is termed as i5-B CNC BEMRF and is a thorough solution to all automation needs of the BEMRF process. The five-motion axes of the machine tool thus developed are X-Y-Z (linear movement) and B-C (rotary movement); these are controlled in coordinated interpolation through CNC part programs. Other than the motion parameters, the machining parameters, viz., electromagnet current, work gap, and spindle speed, are controlled in the same way. To make the developed machine tool an advanced automatic system, a workpiece cleaning system is integrated which cleans the remaining polishing fluid from the work surface at the end of finishing cycle. A roughness metrology system is also integrated with the BEMRF system. This provides the in situ feedback of roughness parameters which is then used for closed-loop controlling of the process. The developed five-axis system governs the functioning of all three cycles, viz., finishing, workpiece cleaning, and measurement by a single part program. The operation of BEMRF machine tool is divided into functioning cycles as follows.

### 41.2.1 *The Surface Finishing Cycle*

The surface finishing cycle governs the control of motion control hardware for the five-axis arrangement, the BEMRF tool head for magnetizing current control, the MRP fluid delivery system, and the refrigerated water bath for coolant to the electromagnet.

### ***41.2.2 Work Piece Cleaning Cycle***

In the automation of the BEMRF process, it is required to eliminate the need of removing the workpiece every time the finishing cycle is completed and measurement of roughness parameters is to be carried out, this ensured that the complete finishing process is carried out till the desired finish is achieved with the workpiece being fixed in its place throughout the process. To carry out measurement of surface finish within the BEMRF setup the workpiece must be cleaned automatically. Manual removal of MR fluid cannot be done in an automatic system. To achieve this, workpiece cleaning system was developed which had certain controls that are also to be controlled through part programming.

### ***41.2.3 Roughness Measurement Cycle***

The measurement of surface roughness in BEMRF process can only be conducted in situ. For in situ surface roughness measurement, the chromatic confocal sensor being light in weight and compact in size is used with the BEMRF tool head. The controls for roughness measurement cycle are also mapped with CNC part program codes for better control.

## **41.3 Manual Controls of the Developed System**

In all the automatic CNC machine tools that are developed and used in the industry, a certain degree of manual operations is always in use. For the BEMRF process, also manual controls are available which are as follows:

- JOG mode: The motion axes are required to be moved manually for applications such as setting the zero for different workpieces and to have precise incremental stepwise movement of the required axis. The jog movements of the axes are linked with the F-keys of the keypad which are inbuilt into the industrial panel PC.
- Manual button controls: Push buttons and selector switches are used for the following manual operations:
  - Key switch: For main machine access to authorized users.
  - Machine ON: To power on the machine.
  - PC on: ON/OFF control of the panel PC.
  - Drives ON: To power on the servo drives.
  - FDS ON: Manual push button to deliver the MRP fluid to the tooltip manually.
  - Stirrer ON: To switch on the stirrer at a fixed speed.
  - Emergency stop: NC push button for emergency purposes.

- Cleaning system controls: Similar manual push buttons and selector switches are used for manual operation of the workpiece cleaning system.

## 41.4 CNC Part Program Control of Each Cycle

The BEMRF process automated through the combined use of finishing cycle, workpiece cleaning cycle, and roughness measurement cycle is governed by the motion and process parameters of each cycle. These parameters are all controlled by the CNC part programs by carefully using the conventionally available CNC codes (G and M codes) and associating the new and BEMRF specific parameters with newly defined M codes and H codes.

### 41.4.1 Part Program Codes for Finishing Cycle

The finishing cycle is the main central operation of the BEMRF process. It consists of the motion control of all five axes, spindle control, and the feed table control using conventional CNC codes. Apart from the conventional operations, the in-process control of the magnetizing current has also been developed. Table 41.1 gives a listed overview of the parameters of finishing cycle and the CNC codes associated with them.

The finishing cycle thus developed will govern primarily the motion part which relates to the geometry of the workpiece, the basic process controls and the magnetizing current controls to the electromagnet. Following is an example of a standalone part program for finishing cycle.

```

%Main
N05 G00 X0 Y0      ; Move to workpiece zero position
N07 M12            ; Enable stirrer and deliver MRP fluid to tool tip
N08 G04 X05       ; Delay of 5 seconds for fluid delivery
N09 M13           ; Disable MRP fluid delivery system and stirrer
N10 M03 S300     ; Start spindle at 300RPM
N15 M10 H45      ; Electromagnet enabled with 4.5A current
N20 G01 Z0.8 F10 ; Move to the defined working gap
N25 G90 G01 X10  ; Move x-axis to 10 units
N30 X0           ; Move x-axis back to 0
N35 M05 M11 H0   ; Spindle stop, electromagnet disable, current 0
N40 G01 Z35      ; Move tool upwards after finishing
N45 M30          ; program end

```

\*The above program is a simple example of finishing cycle and not a fully fledged finishing CNC code.

**Table 41.1** Finishing cycle parameters and CNC codes

Parameter	CNC code syntax	Function
X-axis motion	X	The x-axis coordinates are taken from the number that follows the X in the CNC part program
Y-axis motion	Y	The y-axis coordinates are taken from the number that follows the Y in the CNC part program
Z-axis motion	Z	The z-axis coordinates are taken from the number that follows the Z in the CNC part program
B-axis motion	B	The b-axis coordinates are taken from the number that follows the B in the CNC part program
C-axis motion	C	The c-axis coordinates are taken from the number that follows the C in the CNC part program
Spindle speed	S	Defines the magnitude of spindle speed in RPM
Feed rate	F	Defines the work table feed rate
Magnetizing current	H	Controls the magnitude of magnetizing current ( $\times 100$ mA), i.e., H5 means 500 mA. For a considerable change in magnetic field, the resolution of magnetizing current is kept at 500 mA which means the H codes are defined at a minimum interval of 5. E.g., H5, H10, H15. .. H150. The maximum limit of current to the electromagnet is 15 A
Standard M codes	M02, M03, M05, etc.	Spindle rotation direction, spindle start/stop, etc.
Defined M codes	M10, M11	Electromagnet current enable/disable
	M12, M13	MRP Fluid delivery enable/disable

#### 41.4.2 Part Program Codes for Work Piece Cleaning Cycle

The workpiece cleaning cycle requires movements of the enclosure box and the jet nozzles along with the air and kerosene jet pump controls. Motion of worktable which moves the workpiece along with it is also required at the beginning and end of the cleaning cycle. As soon as the workpiece cleaning cycle is called the worktable after ensuring safety from BEMRF tool, is moved to the cleaning station. At cleaning station, enclosure box moves to enclose the workpiece, kerosene jet is started and nozzle to and fro motion begins for a fixed period of time. After cleaning from kerosene the air jet is started and nozzle again moves to and fro to clean the residual kerosene droplets. The workpiece is moved away from cleaning station after completion of cleaning process. Automated cleaning process using part programming is achieved here by especially associating the movements of enclosure box, jet nozzles,

and jet pump; air pressure controls with the M codes. New M codes are defined for each action required in cleaning process. Table 41.2 gives a list of M codes specially defined for workpiece cleaning system.

The newly defined M codes specific to workpiece cleaning system are used in the part program for workpiece cleaning cycle. An example CNC code for the workpiece cleaning cycle is shown below.

```

%Main
N05 G90 G01 X70 Y-70 F100      ; Move worktable to cleaning station
N10 M15                          ; Enclose workpiece
N15 M17 M21                      ; Start kerosene jet, nozzle forward
N20 G04 X5                        ; Delay
N25 M18                          ; nozzle backward
N30 M22                          ; Stop kerosene jet
N35 M17 M26                      ; Start air jet, nozzle forward
N40 G04 X5                        ; Delay
N45 M18                          ; nozzle backward
N50 M27                          ; Stop air jet
N55 X0 Y0                        ; Move worktable to finishing station
N60 M30                          ; Program end
    
```

In the above example, only single stroke of nozzle each for kerosene jet as well as the air jet is shown for indicative purposes; however, in actual practice this is multiple strokes and the CNC code is written accordingly.

**Table 41.2** Cleaning system parameters and associated M codes

Cleaning parameter	Associated CNC code	Function
Enclosure box	M15	Moves the enclosure box down
	M16	Moves the enclosure box up
Jet nozzle	M17	Moves the jet nozzles forward
	M18	Moves the jet nozzles backward
Kerosene jet	M21	Starts the kerosene jet
	M22	Stops the kerosene jet
Air jet	M26	Starts the air jet
	M27	Stops the air jet



### 41.4.3 Part Program Codes for Roughness Measurement Cycle

The roughness measurement cycle requires movement of the confocal axis and the ON/OFF triggering of data acquisition by confocal sensor. Once the workpiece cleaning cycle is completed immediately the measurement of surface roughness is required. For this purpose, the roughness measurement cycle is called soon after the workpiece cleaning cycle. First at the start of roughness measurement cycle, the worktable is moved to the roughness measurement station, i.e., the area on the workpiece under consideration for finishing and measurement is moved underneath the confocal sensor. The confocal sensor controlled by a stepper axis is moved toward the workpiece and reaches the measuring range.

The measuring range (6 mm approx.) once reached stops the confocal axis movement. At this point, data acquisition is switched on and movement of the worktable is also started for the sampling length on which roughness is to be measured. As the end of sampling length is reached, the data acquisition is also stopped. The data acquired is saved in an MS Excel file which is used by the roughness measurement software for calculation of surface roughness parameters. Similar to the workpiece cleaning cycle, the roughness measurement cycle also required defining of new M codes for roughness measurement cycle-specific tasks such as movement of confocal axis and triggering of data acquisition, etc. (Table 41.3).

An example CNC code for the roughness measurement cycle is shown below.

```

%Main
N05 G90 G01 X-50 Y0 F100           ; Move worktable to measuring station
N10 M24                             ; Move sensor in range
N15 M32                             ; Start data acquisition
N20 G01 X-54                       ; Sampling length movement
N25 M33                             ; Stop data acquisition
N30 M25                             ; Move sensor up
N35 X0 Y0                           ; Move worktable to finishing station
N40 M30                             ; Program end
    
```

**Table 41.3** List of M codes for roughness measurement cycle

Measurement cycle parameter	Associated CNC code	Function
Confocal axis	M24	Moves the confocal axis to bring sensor in range
	M25	Moves the confocal axis up to idle position
Measurement	M32	Starts the data acquisition
	M33	Stops the data acquisition

#### 41.4.4 *Integrated CNC Part Program for All Three Cycles*

Individual control of each cycle as explained earlier is used when any of these actions are required separately. However, the automated performance of BEMRF process requires these cycles to operate in tandem and therefore it is required to have an integrated CNC code which can have all these tasks performed in a single program. A program can be written which will contain all these codes in the sequence required to get the required automated sequence of the BEMRF process. But such a program will become too long and prone to errors. Thus, automation of BEMRF process is obtained using certain subroutine calling functions which are explained as follows.

The CNC code files are used with an extension.nc (read as dot NC), the cycles are called as a subroutine by their file names. The sequence call subroutine function termed as “L SEQUENCE” is used in the main program from which the subroutines are called. The main program file is uploaded to the CNC program reader and the program is then started. The CNC code of the main file is executed line by line and whenever it encounters the following line:

```
L SEQUENCE [NAME = "filename.nc", REPEAT = 06, N05, N25]
```

The program then jumps to the subroutine file name of which is given in the L SEQUENCE call and the subroutine is repeated the number of times specified in the call line, also a specific section of the subroutine file can be called by specifying the serial number of the start and stop lines of subroutine file. For example in the L SEQUENCE line mentioned above the filename.nc file will be called as a subroutine and lines N05–N25 all will be executed six times as specified. For an automated BEMRF cycle, individual cycles of finishing, cleaning, and measurement are to be called in a similar manner. An example of the integrated CNC code for automated BEMRF cycle is given below.

```
N10 G00 X0 Y0 Z0      ; Rapid positioning
N20 M10 H30           ; Enable magnet, set current to 3A
N40 G01 Z0.8 F10      ; Move to machining zone
N50 M03 S300          ; Start spindle, set spindle speed
N60 L SEQUENCE [NAME="Finishing.nc", REPEAT = 20, N01, N02]
                    ; Finishing cycle,
N70 L SEQUENCE [NAME="Cleaning.nc", REPEAT = 1, N01, N12]
                    ; Cleaning cycle
N80 L SEQUENCE [NAME="Measurement.nc", REPEAT = 1, N01, N08]
                    ; Measurement cycle
N90 G01 X0 Y0 Z0 F200 ; Return to zero
N100 M11              ; Magnet disable
N110 M30              ; Program end
```

The above is an example of the integrated CNC code for automated BEMRF cycle; in this, the finishing cycle named as finishing.nc will only have the movement of five axes according to the geometry of workpiece. The cleaning.nc and measurement.nc files are same as examples given in Sects. 4.2 and 4.3, respectively. Thus, the

integrated CNC code executes all three cycles in tandem to achieve the automated BEMRF process.

### 41.5 Testing and Results

A freeform knee prosthetic shown in Fig. 41.1a is finished along the path shown in Fig. 41.1b for testing of the integrated part program.

The positional coordinates of three linear axes (X-Y-Z) and one rotary axis (B) are altered to finish the work surface. It must be noted that during the finishing of the knee prosthetic the position of rotary C-axis is unchanged while X-Y-Z and B vary as shown in Fig. 41.2.

The position data of X-Y-Z and B axes are continuously logged and is plotted at selected points along the paths 1–4 as shown in Figs. 41.3, 41.4, 41.5 and 41.6, respectively.

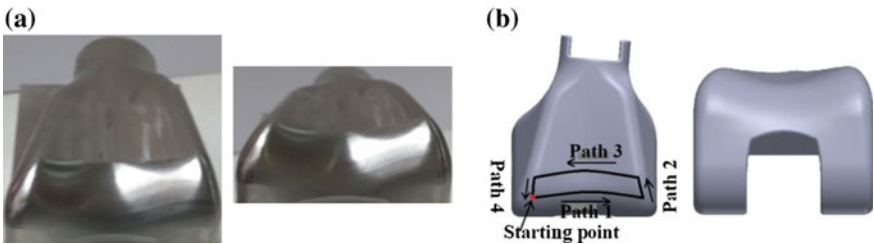


Fig. 41.1 a Knee prosthetic, b CAD model of knee prosthetic

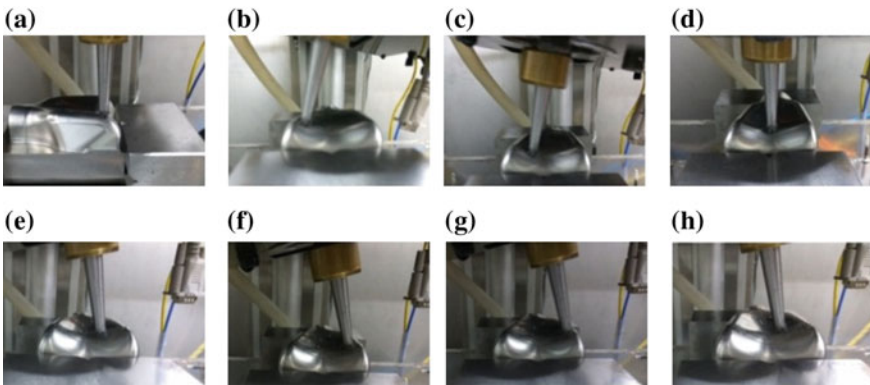
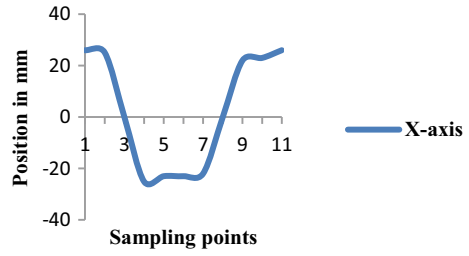
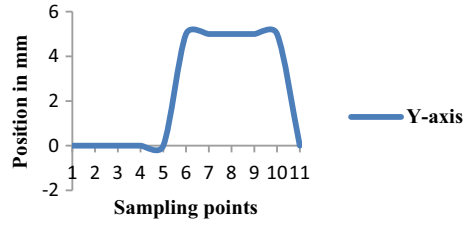


Fig. 41.2 Different positions of BEMRF tooltip during BEMR finishing of knee prosthetic work-piece: a C-axis: 90°, b first sampling point, c second sampling point, d workpiece zero, e fifth sampling point, f sixth sampling point—end of path 1, g path 2: after movement of Y-axis and h eighth sampling point on path 3

**Fig. 41.3** Position of X-axis along paths 1–4



**Fig. 41.4** Position of Y-axis along paths 1–4



**Fig. 41.5** Position of Z-axis along paths 1–4

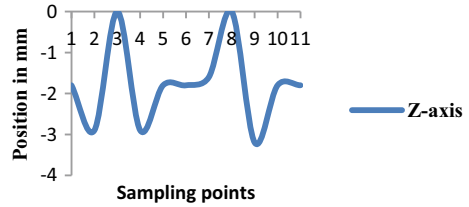


**Fig. 41.6** Position of B-axis along paths 1–4

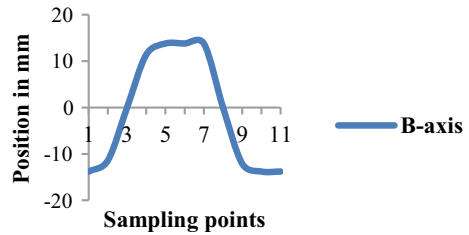


Figure 41.7 shows actual photographs of the i5-B CNC BEMRF system at different stages of the integrated part program.

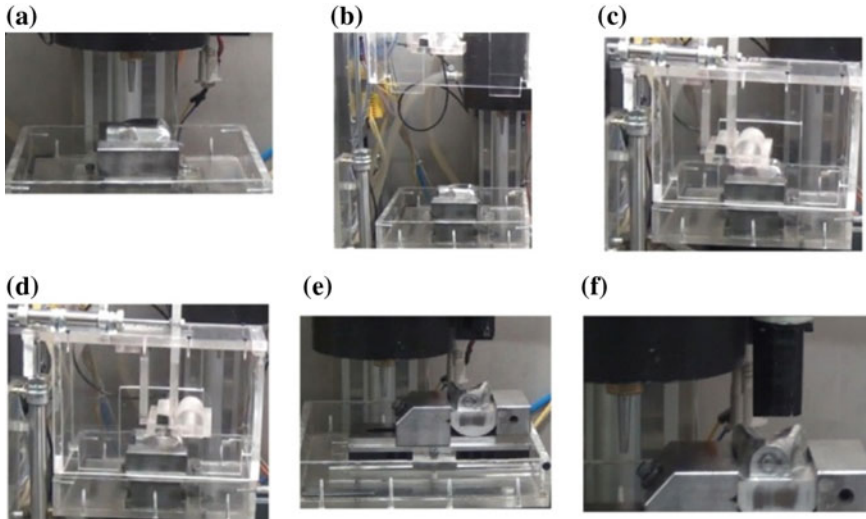


Fig. 41.7 Different stages of integrated part program of i5-B CNC BEMRF system

## 41.6 Conclusions

A part program-based BEMRF process control is achieved which includes control of surface finishing cycle (governing the motion aspects of the process), workpiece cleaning cycle (governing the process controls of workpiece cleaning system), and the surface roughness measurement cycle (governing movements of the confocal axis and data acquisition from the confocal sensor). Such control allows the user to control the motion axes through an NC part program in coordinated five-axis motion along with the process parameters which are all linked to newly defined H codes and M codes wherever necessary.

## References

1. Khan, D.A., Alam, Z., Jha, S.: Nanofinishing of copper using ball end magnetorheological finishing (BEMRF) process. In: ASME 2016 International Mechanical Engineering Congress and Exposition, 11 November 2016, pp. V002T02A002–V002T02A002. American Society of Mechanical Engineers
2. Khan, D.A., Kumar, J., Jha, S.: Magneto-rheological nano-finishing of polycarbonate. *Int. J. Precis. Technol.* **6**, 89–100 (2016)
3. Alam, Z., Khan, D.A., Jha, S.: A study on the effect of polishing fluid volume in ball end magnetorheological finishing process. *Mater. Manuf. Process.* **33**(11), 1197–1204 (2018)
4. Iqbal, F., Jha, S.: Experimental investigations into transient roughness reduction in ball-end magneto-rheological finishing process. *Mater. Manuf. Process.* **34**(2), 224–231 (2019)
5. Alam, Z., Jha, S.: Modeling of surface roughness in ball end magnetorheological finishing (BEMRF) process. *Wear* **374–375C**, 54–62 (2017)

6. Alam, Z., Iqbal, F., Jha, S.: Automated control of three axis CNC ball end magneto-rheological finishing machine using PLC. *Int. J. Autom. Control.* **9**, 201–210 (2015)
7. Iqbal, F., Jha, S.: Closed loop ball end magnetorheological finishing using in-situ roughness metrology. *Exp. Tech.* **42**(6), 659–669 (2018)
8. Alam, Z., Iqbal, F., Ganesan, S., Jha, S.: Nanofinishing of 3D surfaces by automated five-axis CNC ball end magnetorheological finishing machine using customized controller. *Int. J. Adv. Manuf. Technol.* 1–2 (2018)

# Chapter 42

## Modelling and Analysis of Change in Shape of sintered Cu–TiC tool tip during Electrical Discharge Machining process



Arminder Singh Walia , Vineet Srivastava , Vivek Jain   
and Mayank Garg 

**Abstract** Electrode wear is a major problem in electrical discharge machining process. Due to electrode wear during machining, the required geometrical dimensions and form of the electrode are not reproduced on the workpiece. In the present study, change in shape of the copper–titanium carbide tooltip during the electrical discharge machining of hardened EN31 steel workpiece has been carried out at different processing conditions. The process parameters selected for the study are peak current, pulse on time, pulse off time, gap voltage and dielectric flushing pressure. Buckingham’s dimensional analysis has been used to model the change in shape, and the required coefficients are calculated based on the experimental data. The physical and electrical properties chosen for the study are density of the material, thermal conductivity, hardness, electrical resistivity and linear thermal expansion coefficient. The developed empirical model based on dimensional analysis has been validated and was found to be in good agreement with experimental findings.

**Keywords** Electrical discharge machining · Dimensional analysis · Buckingham’s  $\pi$ -theorem · Tool shape · Out of roundness

---

A. S. Walia · V. Srivastava (✉) · V. Jain · M. Garg  
Department of Mechanical Engineering, Thapar Institute  
of Engineering & Technology, Patiala 147004, India  
e-mail: [vineet.srivastava@thapar.edu](mailto:vineet.srivastava@thapar.edu)

A. S. Walia  
e-mail: [arminderwalia@gmail.com](mailto:arminderwalia@gmail.com)

V. Jain  
e-mail: [vivek.jain@thapar.edu](mailto:vivek.jain@thapar.edu)

M. Garg  
e-mail: [mgarg\\_me16@thapar.edu](mailto:mgarg_me16@thapar.edu)

© Springer Nature Singapore Pte Ltd. 2020  
M. S. Shunmugam and M. Kanthababu (eds.), *Advances in Unconventional Machining and Composites*, Lecture Notes on Multidisciplinary Industrial Engineering, [https://doi.org/10.1007/978-981-32-9471-4\\_42](https://doi.org/10.1007/978-981-32-9471-4_42)

## 42.1 Introduction

There are many modern machining processes in which metal removal is based on thermal principles and Electrical Discharge Machining (EDM) is one of them. In EDM, consecutive series of electrical sparks of very small duration, between the workpiece and the tool electrode, are used to remove material. The electrical discharges generated in the liquid dielectric gap create a plasma channel and the temperature reaches up to 8000–20,000°C, thus removing the material from the electrodes by heating, melting and evaporation [1]. The plasma channel breaks down as the supply of pulsating direct current supply is stopped, thus allowing the circulating dielectric fluid to implore the plasma channel and flush the molten material from the electrode surfaces in the form of microscopic debris. The performance of EDM process is influenced by many input parameters such as discharge current, gap voltage, breakdown voltage, pulse on time, pulse off time, duty cycle, polarity, and dielectric flushing pressure. Various techniques like dimensional analysis, Artificial Neural Network (ANN), Finite Element Method (FEM) and thermal modelling have been used to analyse the effects of these process parameters and predict the output of the process in terms of Material Removal Rate (MRR), Electrode Wear Rate (EWR) and surface finish. From these models, it is quite evidence that no single property of the tool or workpiece material can predict its eroded volume and change in the shape. Thus, it is required to consider both the thermal and physical properties to assess precisely the volume of material removed and change in the shape of electrodes. Dimensional analysis has been used by many researchers to determine material removal rate, tool wear rate and surface finish for the EDM process.

Jeswani [2] applied dimensional analysis to analyse the erosion in EDM process. An empirical equation was generated which related the eroded material volume from the tool electrode with the thermal conductivity, latent heat of vaporization, pulse, density and specific heat of tool material. Using dimensional analysis a semi-empirical model was developed by Tsai and Wang [3] to study the surface finish during EDM process. The average error for the surface finish for the experimental results and predicted results was found less than 10%. Gu et al. [4] used semi-empirical model and predicted MRR with 12.7% error, EWR with 6.8% error and surface finish with an average error of 9.6%. The model predicted the response with more than 99% accuracy. Talla et al. [5] developed semi-empirical model for the powder mixed EDM of aluminium and alumina metal matrix composite. Principal component analysis-based grey technique was used for the optimization. Bobbili et al. [6] applied the Buckingham  $\pi$ -theorem to study the effect of input variables on MRR and surface roughness during wire EDM of aluminium alloy 7017 and rolled homogeneous armour.

From the literature review, it has been found that various techniques have been applied for the prediction of MRR, EWR and SR. However, there is no model available to predict the change in shape of tool during EDM. In view of the above research gap, the objective of this paper is to present a model for the change in shape of the copper–titanium carbide tooltip during the EDM of hardened EN31 steel workpiece.



The change in the roundness of the tool has been selected as a response. Dimensional analysis has been used to correlate the analytical results with experimental data. The process parameters for this study are peak current, pulse on time, pulse off time, gap voltage and dielectric flushing pressure. The physical and electrical properties chosen are density of the material, thermal conductivity, hardness, electrical resistivity and linear thermal expansion coefficient. The results estimated by the model were compared with the experimental results.

## 42.2 Experimental Procedure

Hardened EN31 workpieces were spark eroded using die-sinking EDM (Reliable, 55,300) machine with copper–titanium carbide tooltip. The machining was performed for 30 min for all the experiments. Central Composite Rotatable Design (CCRD) was used for the design of experiments. In this work, five controllable variables, namely, discharge current, gap voltage, pulse on time, pulse off time and flushing pressure, have been examined. By keeping each independent variable at five different levels, 52 experiments were performed. The discharge current ( $I_p$ ) was kept in a range from 3 to 11 A (step size 2 A), the pulse off time ( $T_{off}$ ) was kept between 10 and 50  $\mu\text{s}$  (step size 10  $\mu\text{s}$ ), the pulse on time ( $T_{on}$ ) was selected in the range of 100–500  $\mu\text{s}$  (step size 100  $\mu\text{s}$ ), gap voltage ( $V_g$ ) was varied from 40 to 80 V (step size 10 V) and flushing pressure ( $P$ ) ranged from 12 to 20  $\text{kgf/cm}^2$  (step size 2  $\text{kgf/cm}^2$ ).

High electrical and thermal conductivity makes copper (Cu) one of the most desirable materials for the tool in EDM. However, low melting point of copper leads to a higher amount of tool wear during the machining of hard metals. This problem raises the requirement of such a reinforcement material which can enhance the copper's melting temperature, hardness and wear resistance. Titanium carbide (TiC) has high melting temperature, high hardness, excellent thermal shock and wear resistance, thus making it a very good choice for the hybrid tooltip [7]. The cermet tooltip was fabricated by the mixture of copper powder (75%, 99.9 wt% purity, and particle size 44  $\mu\text{m}$ ) and titanium carbide powder (25%, 99 wt% purity, and particle size 44  $\mu\text{m}$ ). The pellets were fabricated by the cold compaction of the powder mixture uniaxially in a hydraulic press at a load of 12 tonnes in a die followed by sintering. The polished pellets were brazed to the copper rods as shown in Fig. 42.1a. Measurement of the out of roundness of the tool has been performed, both before and after machining. The difference between the two observations has been taken as the response in this study. Coordinate measuring machine (Accurate, model Spectra 564) was used for the measurement of the out of roundness. The roundness of each tool was measured at 12 points before and after machining with coordinate measuring machine. The measured values of out of roundness for all the conducted experiments are shown in Fig. 42.1b.

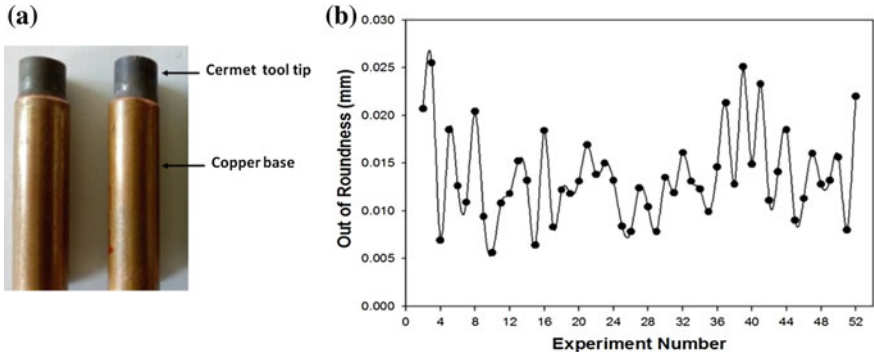


Fig. 42.1 a Cermet tooltip electrode. b Measured out of roundness

### 42.3 Dimensional Analysis for Electrode Shape Using Buckingham’s $\pi$ -Theorem

#### 42.3.1 Buckingham’s $\pi$ -Theorem

The Buckingham  $\pi$ -theorem is a very important theorem in dimensional analysis. According to the theorem, if there is a physically meaningful equation involving a certain number,  $n$ , of physical variables, and these variables are expressible in terms of  $r$  independent fundamental physical quantities, then the original expression is equivalent to an equation involving a set of  $p = n - r$  dimensionless variables constructed from the original variables: it is a scheme for non-dimensionalization [8]. The required relations connecting the individual variables are determined as the algebraic expressions relating the  $\pi_s$ . Hence,

$$f(\pi_1, \pi_2, \pi_3, \dots, \pi_{n-k}) = 0 \tag{42.1}$$

#### 42.3.2 Modelling for Electrode Shape Using Buckingham’s $\pi$ -Theorem

The change in the shape of the tool is expressed in terms of out of roundness (OOR) and is dependent upon discharge current ( $I_p$ ), pulse on time ( $T_{on}$ ), pulse off time ( $T_{off}$ ), gap voltage ( $V_G$ ), dielectric flushing pressure  $P$ , density  $\rho$ , thermal conductivity  $\kappa$ , hardness  $HV$ , linear thermal expansion coefficient  $\alpha$  and electrical resistivity  $\rho_e$  of the material. So the equation may be written as

$$OOR = f(I_p, T_{on}, T_{off}, V_G, P, \rho, k, HV, \alpha, \rho_e) \tag{42.2}$$

In EDM, the material is removed primarily by melting and evaporation and a small amount of molten metal remains in the crater. Part of it may be ejected owing to the various forces operating in the spark region. Therefore, the effect of the latent heat of melting and the melting temperature has been neglected in this study [2]. The density and thermal expansion coefficient of tool material is very important property because it affects the shape factor of tool. The wear characteristic of a material is directly related to its hardness. Therefore, hardness has been considered as a factor in this study. Thermal conductivity of the tool plays an important role in the material removal. The dimensions of the quantities given in Eq. (42.2) are expressed in the most widely used Mass (M), Length (L), Time (T), Temperature ( $\theta$ ) and Charge (Q) systems given in Table 42.1.

$$[L]^{k1}[T^{-1}Q]^{k2}[T]^{k3}[T]^{k4}[ML^2T^{-2}Q^{-1}]^{k5}[ML^{-1}T^{-2}]^{k6}[\theta^{-1}]^{k7}[ML^{-3}]^{k8} \\ [MLT^{-3}\theta^{-1}]^{k9}[ML^{-1}T^{-2}]^{k10}[ML^3T^{-1}Q^{-2}]^{k11} = [M^0L^0T^0\theta^0Q^0] \quad (42.3)$$

Powers of the fundamental units on both sides of Eq. (42.3) were compared and a set of simultaneous linear equations was obtained which was later solved to obtain the magnitudes of the constants. The values of the power indexes on the dimensional parameter are listed in Table 42.2. The rank of the dimensional matrix was determined by solving the determinant formed from the square matrix of last five columns. Since this is a fifth-order determinant and is not equal to zero, the rank of the dimensional matrix is five. It has been shown that the number of dimensionless products in a complete set is equal to the difference between the total number of variables and the rank of their dimensional matrix. Therefore, in the present case, since there are 11 variables and the matrix is of rank 5, there will only be 6 dimensionless products in the complete set of equations.

**Table 42.1** Physical quantities, symbols and dimensions

Characteristic	Factor	Symbol	Dimensions	Units
Quality	Out of roundness	<i>OOR</i>	L	M
Parameter	Discharge current	<i>I<sub>p</sub></i>	$T^{-1}Q$	A
	Pulse on time	<i>T<sub>on</sub></i>	<i>T</i>	μs
	Pulse off time	<i>T<sub>off</sub></i>	<i>T</i>	μs
	Gap voltage	<i>V<sub>G</sub></i>	$ML^2T^{-2}Q^{-1}$	V
	Dielectric flushing pressure	<i>P</i>	$ML^{-1}T^{-2}$	kg/ms <sup>2</sup>
Material	Linear coefficient of expansion	$\alpha$	$\theta$	1/k
	Density of the material	$\rho$	$ML^{-3}$	kg/m <sup>3</sup>
	Thermal conductivity	<i>K</i>	$MLT^{-3}\theta^{-1}$	W/mk
	Hardness	HV	$ML^{-1}T^{-2}$	MPa
	Electrical resistivity	$\rho_e$	$ML^3T^{-1}Q^{-2}$	Ωm

**Table 42.2** Dimensions of the parameters

Dimension	Index (Factor)										
	k <sub>1</sub> (OOR)	k <sub>2</sub> (Ip)	k <sub>3</sub> (T <sub>on</sub> )	k <sub>4</sub> (T <sub>off</sub> )	k <sub>5</sub> (V <sub>g</sub> )	k <sub>6</sub> (P)	k <sub>7</sub> ( $\alpha$ )	k <sub>8</sub> ( $\rho$ )	k <sub>9</sub> ( $\kappa$ )	k <sub>10</sub> (HV)	k <sub>11</sub> (R)
M	0	0	0	0	1	1	0	1	1	1	1
L	1	0	0	0	2	-1	0	-3	1	-1	3
T	0	-1	1	1	-2	-2	0	0	-3	-2	-1
$\theta$	0	0	0	0	0	0	-1	0	-1	0	0
$\mathcal{Q}$	0	1	0	0	-1	0	0	0	0	0	-2

### 42.3.3 Dimensionless Products

Based on the homogenous linear algebraic equations for the dimensions, the coefficients are the numbers in the rows of the dimensional matrix as simultaneous equations. After solving those simultaneous equations [9], the solutions are arranged in the form of a matrix as shown in Table 42.3. Since the matrix of solutions contains  $n - r$  row where  $n = 11$  is the number of variables and  $r = 5$  is the rank of the matrix, it constitutes a fundamental system of solutions. Each row in the matrix of solutions is a dimensionless product. Therefore, in the present study the following complete set of dimensionless products is obtained

$$\begin{aligned} \pi_1 &= \frac{OOR \times \alpha \times HV^{\frac{3}{2}}}{\rho^{\frac{1}{2}} \times K}, & \pi_2 &= \frac{I_p \times \alpha^{\frac{3}{2}} \times HV^{\frac{5}{2}} \times R^{\frac{1}{2}}}{\rho^{\frac{1}{2}} \times K^{\frac{3}{2}}}, \\ \pi_3 &= \frac{T_{on} \times \alpha \times HV^2}{\rho \times K}, & \pi_4 &= \frac{T_{off} \times \alpha \times HV^2}{\rho \times K}, & \pi_5 &= \frac{V_G \times \alpha^{\frac{1}{2}}}{K^{\frac{1}{2}} \times R^{\frac{1}{2}}}, \\ \pi_6 &= \frac{P}{HV} \end{aligned}$$

The relation between the dimensionless products can be written as

$$f(\pi_1, \pi_2, \pi_3, \pi_4, \pi_5, \pi_6) = 0$$

Or

$$\pi_1 = f(\pi_2, \pi_3, \pi_4, \pi_5, \pi_6) \tag{42.4}$$

$$\begin{aligned} OOR &= Z \times \left( \frac{\rho^{\frac{1}{2}} \times \kappa}{\alpha \times HV^{\frac{3}{2}}} \right) \times \left( \frac{I_p \times \alpha^{\frac{3}{2}} \times HV^{\frac{5}{2}} \times R^{\frac{1}{2}}}{\rho^{\frac{1}{2}} \times \kappa^{\frac{3}{2}}} \right)^a \times \left( \frac{T_{on} \times \alpha \times HV^2}{\rho \times \kappa} \right)^b \\ &\times \left( \frac{T_{off} \times \alpha \times HV^2}{\rho \times \kappa} \right)^c \times \left( \frac{V_G \times \alpha^{1/2}}{\kappa^{1/2} \times R^{1/2}} \right)^d \times \left( \frac{P}{HV} \right)^e \end{aligned} \tag{42.5}$$

## 42.4 Results

The calculated values of thermal, physical and electrical properties of the electrode material have been given in Table 42.4. The dimensionless constant Z and exponents a, b, c, d and e have been determined by nonlinear estimation of experimental data and found to be 0.3867, 1.2381, -0.2898, -0.1441, -0.1604 and -0.230, respectively. Therefore, Eq. (42.5) is simplified and rewritten as Eq. (42.6) and the results for out of roundness are predicted. In Fig. 42.2, the comparison of experimental

**Table 42.3** Results of dimensional analysis

	$k_1$ (OOR)	$k_2$ (Ip)	$k_3$ ( $T_{on}$ )	$k_4$ ( $T_{off}$ )	$k_5$ ( $V_g$ )	$k_6$ (P)	$k_7$ ( $\alpha$ )	$k_8$ ( $\rho$ )	$k_9$ ( $\kappa$ )	$k_{10}$ (HV)	$k_{11}$ (R)
$\pi_1$	1	0	0	0	0	0	1	-1/2	-1	3/2	0
$\pi_2$	0	1	0	0	0	0	3/2	-1/2	-3/2	5/2	1/2
$\pi_3$	0	0	1	0	0	0	1	-1	-1	2	0
$\pi_4$	0	0	0	1	0	0	1	-1	-1	2	0
$\pi_5$	0	0	0	0	1	0	1/2	0	-1/2	0	-1/2
$\pi_6$	0	0	0	0	0	1	0	0	0	-1	0

**Table 42.4** Thermal, physical and electrical properties of tooltip

Factor	Symbol	Value	Units
Density of the material	$\rho$	7439.6	kg/m <sup>3</sup>
Thermal conductivity	$K$	75.96	W/mk
Hardness	HV	116	MPa
Electrical resistivity	$\rho_e$	$9.45 * 10^{-8}$	$\Omega$ m
Linear thermal expansion coefficient	$\alpha$	$13.41 * 10^{-6}$	1/k

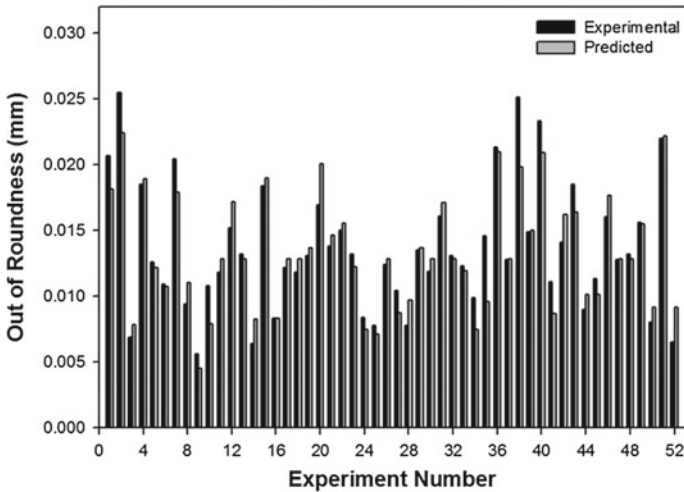


**Fig. 42.2** Comparison of experimental and predicted values of the out of roundness

results and predicted values for out of roundness is shown. The predicted results are showing good agreement with the experimental observations. The error recorded for the prediction of out of roundness varied from +5.89% in trial 21 to -6.91% in trial 9. The developed model has been validated by conducting experiment at different processing conditions and it can be concluded from Table 42.5 that the developed model is able to predict the out of roundness with good accuracy.

**Table 42.5** Validation of the developed model

Ip (A)	Vg (V)	T <sub>on</sub> (μs)	T <sub>off</sub> (μs)	P (kgf/cm <sup>2</sup> )	Experimental out of roundness (mm)	Predicted out of roundness (mm)	Error (%)
4	45	150	15	13	0.0065	0.0068	4.62
10	65	350	45	17	0.0177	0.0183	3.38

$$\begin{aligned}
 OOR = & 0.3867 \times \left( \frac{\rho^{\frac{1}{2}} \times \kappa}{\alpha \times HV^{\frac{3}{2}}} \right) \times \left( \frac{I_p \times \alpha^{\frac{3}{2}} \times HV^{\frac{5}{2}} \times R^{\frac{1}{2}}}{\rho^{\frac{1}{2}} \times \kappa^{\frac{3}{2}}} \right)^{1.2381} \\
 & \times \left( \frac{T_{on} \times \alpha \times HV^2}{\rho \times \kappa} \right)^{-0.2898} \times \left( \frac{T_{off} \times \alpha \times HV^2}{\rho \times \kappa} \right)^{-0.1441} \\
 & \times \left( \frac{V_G \times \alpha^{1/2}}{\kappa^{1/2} \times R^{1/2}} \right)^{-0.1604} \times \left( \frac{P}{HV} \right)^{0.23} \tag{42.6}
 \end{aligned}$$

The out of roundness continuously increased with the increase in discharge current as shown in Fig. 42.3a. With the rise in the discharge current, results in the formation of more energy in the gap between the electrodes. This results in removal of material from both electrodes causing distortion of tool electrode along with material removal [10]. The effect of change in pulse on time on out of roundness is shown in Fig. 42.3b. Large pulse on time results in increased diameter of plasma channel thus reducing the available energy at the discharge spot. There is more deposition of carbon on the surface of electrode due to the decomposition of hydrocarbon-based dielectric. The deposited layer enhances the wear resistance of electrode and reduces the shape distortion. The effect of pulse off time on out of roundness is shown in Fig. 42.3c. The change in roundness of tool decreased with the increase in pulse off time. At lower pulse off time, more frequent discharges are generated leading to more discharge

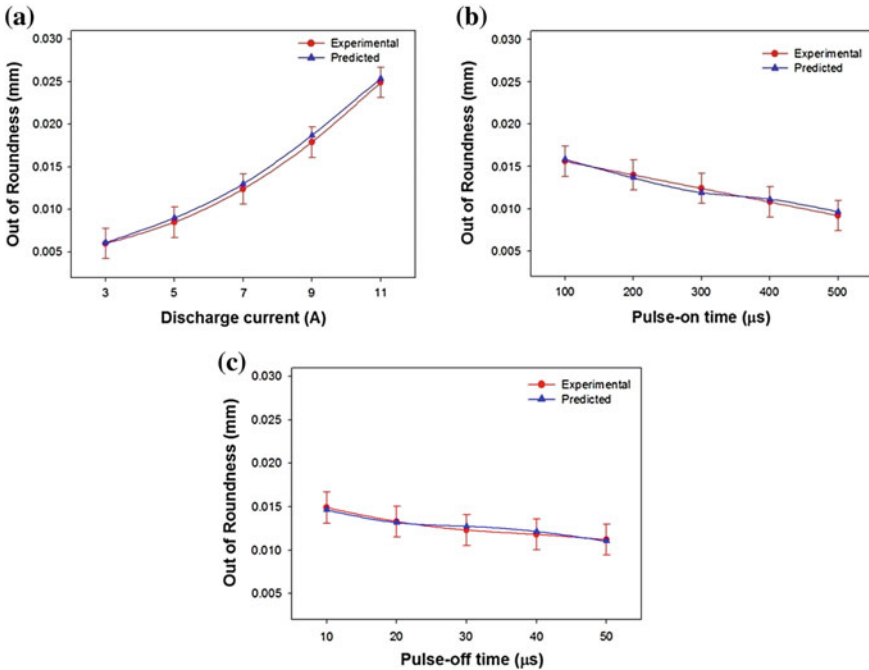


Fig. 42.3 Variation of out of roundness with a discharge current b pulse on time c pulse off time



energy in the discharge column. Due to this there is greater tool wear resulting in more distortion of tool shape. As the pulse off time increases, the spark contact time decreases resulting in reduction in out of roundness of the tool.

## 42.5 Conclusions

In this work, a model of the tool shape has been formulated using dimensional analysis by correlating the input parameters, namely, discharge current, pulse on time, pulse off time, gap voltage and flushing pressure. It is found that the changes in the shape of tool during EDM are proportional to the discharge current  $I_p$ , flushing pressure  $P$ , density  $\rho$ , linear thermal expansion coefficient  $\alpha$ , hardness  $HV$ , electrical resistivity  $\rho_e$  and inversely proportional to thermal conductivity  $K$ , pulse on time  $T_{on}$ , pulse on time  $T_{off}$  and Gap Voltage  $V_G$ . The individual influences of all significant process parameters on the shape of tool were analysed based on the developed mathematical models. Results from the model show good agreement when compared to the experimental findings. The model can thus be used to predict the change in shape of tool for a die-sinking electrical discharge machining process.

## References

1. Ho, K.H., Newman, S.T.: State of the art electrical discharge machining (EDM). *Int. J. Mach. Tools Manuf.* **43**(13), 1287–1300 (2003). [https://doi.org/10.1016/S0890-6955\(03\)00162-7](https://doi.org/10.1016/S0890-6955(03)00162-7)
2. Jeswani, M.L.: Dimensional analysis of tool wear in electrical discharge machining. *Wear* **55**(1), 153–161 (1979). [https://doi.org/10.1016/0043-1648\(79\)90187-X](https://doi.org/10.1016/0043-1648(79)90187-X)
3. Tsai, K.M., Wang, P.J.: Predictions on surface finish in electrical discharge machining based upon neural network models. *Int. J. Mach. Tools Manuf.* **41**(10), 1385–1403 (2001). [https://doi.org/10.1016/S0890-6955\(01\)00028-1](https://doi.org/10.1016/S0890-6955(01)00028-1)
4. Guu, Y.H., Chou, C.Y., Chiou, S.T.: Study of the effect of machining parameters on the machining characteristics in electrical discharge machining of Fe-Mn-Al alloy. *Mater. Manuf. Process.* **20**(6), 905–916 (2005)
5. Talla, G., Sahoo, D.K., Gangopadhyay, S., et al.: Modeling and multi-objective optimization of powder mixed electric discharge machining process of aluminum/alumina metal matrix composite. *Eng. Sci. Technol. Int. J.* **18**(3), 369–373 (2015). <https://doi.org/10.1016/j.jestch.2015.01.007>
6. Bobbili, R., Madhu, V., Gogia, A.K.: Modelling and analysis of material removal rate and surface roughness in wire-cut EDM of armour materials. *Eng. Sci. Technol. Int. J.* **18**(4), 664–668 (2015). <https://doi.org/10.1016/j.jestch.2015.03.014>
7. Li, L., Wong, Y.S., Fuh, J.Y.H., Lu, L.: EDM performance of TiC/copper-based sintered electrodes. *Mater. Des.* **22**(8), 669–678 (2001). [https://doi.org/10.1016/S0261-3069\(01\)00010-3](https://doi.org/10.1016/S0261-3069(01)00010-3)
8. Buckingham, E.: On physically similar systems; illustrations of the use of dimensional equations. *Phys. Rev.* **4**(4), 345–376 (1914). <https://doi.org/10.1103/PhysRev.4.345>
9. Mulik, R.S., Srivastava, V., Pandey, P.M.: Experimental investigations and modeling of temperature in the work-brush interface during ultrasonic assisted magnetic abrasive finishing process. *Mater. Manuf. Processes* **27**(1), 1–9 (2012)
10. Rahman, M.M., Khan, M.A.R., Kadirgama, K., Noor, M.M., Bakar, R.A.: Experimental investigation into electrical discharge machining of stainless steel 304. *J. Appl. Sci.* **11**(3), 549–554 (2011)

# Chapter 43

## Experimental Investigations on C-263 Alloy by Electrochemical Milling



K. Mishra , S. Sinha, B. R. Sarkar and B. Bhattacharyya

**Abstract** Electrochemical machining has great potential of machining of any HSTR metals due to its various advantages like free of tool wear, thermal, and residual stresses. The process of electrochemical milling is similar to conventional electrochemical machining (ECM). Here, a simple shaped tool follows a pre-identified tool path and material is removed by electrochemical reactions in a layer-by-layer approach. Electrochemical milling (EC milling) is extensively used for the fabrication of complex shaped features on various HSTR alloys so far due to its process simplicity and many superior advantages than conventional ECM process. Present research work looks into the influence of EC milling characteristics, e.g., tool feed rate and milling layer depth on various responses, e.g., overcut, surface roughness, and quality of machined profile by EC milling process. It was observed that EC milling with one molar solution of sodium chloride and sodium nitrate along with tool rotation generates accurate machined profiles with excellent surface finish on Nimonic-263 alloy.

**Keywords** Electrochemical milling · Feed rate · Milling layer depth · Tool rotation · Overcut · Surface roughness · Nimonic-263

### 43.1 Introduction

Due to the excellent material properties, e.g., resistant to corrosion, retaining higher strength at elevated temperature and excellent machinability, Nickel and its different alloys are more suitable materials for the different modern manufacturing applications. The mechanism of material removal of electrochemical milling is alike to the conventional ECM process which can produce any types of three dimensional shaped features, free form surface profiles with precision. This can machine any electrically conducting materials without depending on their mechanical properties

---

K. Mishra (✉) · S. Sinha · B. R. Sarkar · B. Bhattacharyya  
Production Engineering Department, Jadavpur University, Kolkata 700032, India  
e-mail: [mishra.koushik050@gmail.com](mailto:mishra.koushik050@gmail.com)

© Springer Nature Singapore Pte Ltd. 2020  
M. S. Shunmugam and M. Kanthababu (eds.), *Advances in Unconventional Machining and Composites*, Lecture Notes on Multidisciplinary Industrial Engineering, [https://doi.org/10.1007/978-981-32-9471-4\\_43](https://doi.org/10.1007/978-981-32-9471-4_43)

527

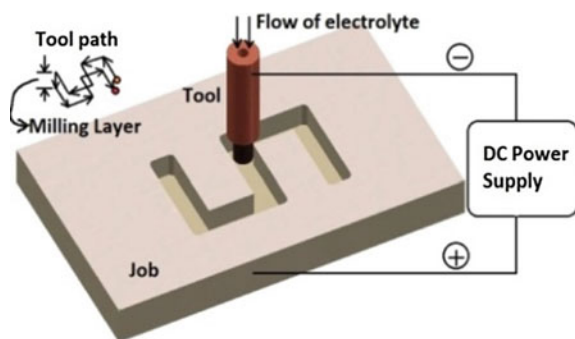
by simple shaped tool. Using sodium nitrate based electrolyte and DC power supply, researchers had produced an intricate shaped products by EC milling process in macro domain [1]. During fabrication of microgroove features by EMM, researchers had reported the influence of various process parameters, e.g., voltage, on time, and electrolyte flow, etc. on different performance characteristics, e.g., MRR and accuracy of the machined features [2]. For the fabrication of blind microchannel, two methods had been reported by the researchers, one is the scanning machining mode in a layer-by-layer approach and another is the sinking and milling mode [3]. A mathematical model had been developed by the researchers to predict the volumetric material removal for various complex shapes generation on Ti6Al4V during EC milling and after experimental verification researchers had successfully revealed a good correlation with the theoretical predictions [4].

So, from the literature survey, it can be stated that till date very few studies have been done in the area of EC milling, no literature has been found especially on Nickel and its different alloys. So, it is the time when in-depth study is necessary for EC milling technique not only to understand the rising trend of EC milling but also to fabricate any three dimensional free form surfaces on HSTR Nickel and its different alloys. Thus, present research work looks into the influence of EC milling characteristics, e.g., tool feed rate and milling layer depth on various responses, e.g., overcut, surface roughness, and quality of machined profile by EC milling process followed by comparing these effects with the tool rotation on Nimonic-263 alloy. Finally, more accurate shaped features have been produced on Nimonic-263 alloy to study the capability and acceptability of the EC milling at macro domain in modern manufacturing industries.

### 43.1.1 Scheme of EC Milling

Strategy of EC milling with a pre-identified tool path is shown in Fig. 43.1. Here, the desired shape can be fabricated by simple shaped tool which follows that tool path by controlling the tool as well as the job in a CNC controlled system. In EC milling,

**Fig. 43.1** Strategy of EC milling



electrolyte is supplied through a hollow tool with the high pressure to the machining gap for better removal of debris as well as for achieving optimal machining condition instead of crossed flow. Any profiles can be generated on the job by controlling the simultaneous movement of three axis of the CNC stage.

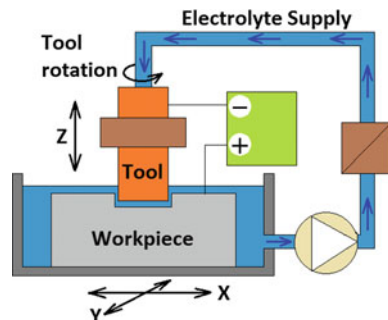
The complications of tool fabrication prior to ECM operation can be overcome if machining can be done using a simple geometric tool. Desired shaped profile over the workpiece can be achieved only by controlling the simultaneous movement of three axis of the CNC stage. By EC milling, with the help of simple shaped smaller dimensional tool relatively bigger area can be milled which is one of the major advantages. For this, in EC milling the same amount of current density can be achieved with relatively lesser amount of current than sinking ECM due to the smaller electrode surface area.

## 43.2 Experimental Details

### 43.2.1 Experimental Setup

For carrying out this research activity as well as to achieve desired shape on various HSTR alloys by EC milling process, an indigenous EC milling setup needs to be developed which is shown in Fig. 43.2. The main units of the setup are X-Y-Z nonlinear CNC stage, a constant DC power supply, rotary union, pump, and a filter. Pulse DC power supply is basically used where effective sludge removal is not possible, e.g., in case of micro-ECM. In this research work effective sludge removal is possible by means of internal flushing as well as by tool rotation thus; continuous DC supply has been used instead of pulse DC power supply. A rotary union has also been designed and developed indigenously to facilitate not only to supply the electrolyte but also current at the rotating condition of the tool. The developed setup makes EC milling process capable to vary the process parameters such as voltage, tool feed rate, rotational speed, and flow of electrolyte during experimentation.

Fig. 43.2 EC milling setup



### 43.2.2 Scheme of Experiments

As no literature have been found in EC milling of Nimonic-263 alloy, several pilot experimentations need to be carried out to select the best types of electrolyte with their most favorable concentrations for high accuracy machining of Nimonic-263 alloy. Experiments have been carried out with a pure copper cylindrical tool with 10 mm OD and 4 mm ID on 5 mm thick C-263 alloy plate. After several pilot experiments, all ranges of process parameters have been selected. It has been observed that EC milling of Nimonic-263 alloy is suitable for using one molar sodium chloride and sodium nitrate mixed electrolyte as far as accuracy and the quality of the profiles are concerned [5].

In this research work, the two most significant process parameters of EC milling have been chosen. One is feed rate and another is milling layer depth. In EC milling, feed is defined as the velocity of the tool at which it moves over the workpiece, expressed in mm/min. Milling layer depth is the depth which is given to the tool after completing each pass to achieve the desired depth, expressed in mm. Experiments have been conducted at different feed rate and milling layer depth to produce a groove on the workpiece as depicted in Table 43.1. Entire experimentation has been performed on the basis of one-factor-at-a-time method to investigate the influence of one factor on the responses of EC milling. In this study feed rates have been varied from 5 to 8 mm/min with the increment of 1 mm/min and milling layer depth has differed from 0.15 to 0.3 mm with the increment of 0.05 mm and total machining depth has been kept constant at 1.2 mm. During entire experimentation, feed rate has been fixed at 8 mm/min while tool milling layer depth has been varied and similarly, tool milling layer depth has been kept constant at 0.3 mm while tool feed rate has been varied. Other process parameters have been kept constant during entire EC milling operation as depicted in Table 43.2.

**Table 43.1** Varied process parameters

Parameters	Ranges
Tool feed rate (mm/min)	5, 6, 7, 8
Milling layer depth (mm)	0.15, 0.2, 0.25, 0.3

**Table 43.2** Other considered fixed process parameters

Parameters	Ranges
Input DC voltage (V)	20
Initial machining gap (mm)	0.3
Type of power supply	Constant DC
Types of electrolyte	NaCl(1M)+NaNO <sub>3</sub> (1M)
Type of flushing	Through tool
Tool rotational speed (R.P.M)	500

### 43.2.3 Evaluation of Response Variables

In this research work two most significant responses of EC milling have been chosen which mostly affects the quality of the machined profile, one is width overcut and another is surface roughness. Width Overcut (WO) is measured with the help of Contourscope made by Mitutoyo, Japan by the following equation:

$$WO = \frac{\text{Width of the groove} - \text{Diameter of the tool}}{2} \text{ (mm)}. \tag{1}$$

R<sub>a</sub> value of surface roughness of the grooves has been calculated by Telysurf also manufactured by Mitutoyo, Japan. All the responses values have been taken from the average of five samples on the same machining condition and the error graph has also been plotted accordingly.

### 43.3 Experimental Investigations

Experiments have been conducted to find out the influence of feed rate and milling layer depth with tool rotation (WR) on various responses like overcut, surface roughness, and quality of the surface of the profile. Subsequently, experimentations have been done by altering tool feed rate as well as milling layer depth and after that the consequent outcomes of tool rotation on different responses have been studied.

#### 43.3.1 Influence of Tool Feed Rate and Milling Layer Depth with Tool Rotation on Width Overcut

In ECM, due to the stray current effect for the bare portion of the tooltip, overcut occurs. At a constant milling layer depth of 0.3 mm, it can be observed from the Fig. 43.3 that overcut gradually decreases with the increment of tool feed rate. The reason behind this is with the increment of tool feed rate, reaction time in between

**Fig. 43.3** Effect of tool feed rate on width overcut

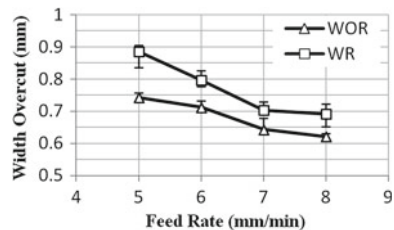
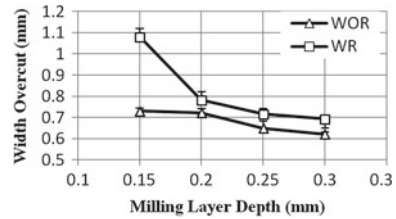


**Fig. 43.4** Effect of milling layer depth on width overcut



workpiece and the tool shortens. As a result, decrement of total amount metal removed from the job which leads to decrement of width overcut.

Figure 43.4 shows that when feed rate has been fixed at 8 mm/min, width overcut is varied considerably for differing milling layer depth. The almost same trend has been followed as in case of feed rate. The reason behind that is, with the increment of milling layer depth, more material gets removed in a single pass, which leads to decrement of total machining time. As the milling layer depth increases, total number of passes to achieve the desired depth decreases which result in decrement of total machining time as well as total interaction time in-between tool and the workpiece.

From the Fig. 43.3 and 43.4 it has also been observed that the value of width overcut is less in case of without tool rotation compared to tool rotation. The electrolyte present in the neighbor of the machining zone and current flux concentration is mainly responsible for stray current effect which leads to machining in the undesired zone. Availability of excess amount of electrolyte at the surrounding of the machining zone and higher current flux associated with always results in higher overcut than stationary tool. The lowest value of width overcut, i.e., 0.62128 mm has been achieved at 8 mm/min feed and milling layer depth of 0.3 mm without any rotation at the tool.

### 43.3.2 Influence of Feed Rate and Milling Layer Depth with Tool Rotation on Surface Roughness

Unlike the previous response, from the Fig. 43.5 and 43.6, it has been observed that surface roughness has been increased with the increment of tool feed rate and milling layer depth. With the increment of feed, the time required to complete a pass reduces and due to lesser tool workpiece interaction time, inhomogeneous electrochemical

**Fig. 43.5** Effect of feed rate on surface roughness

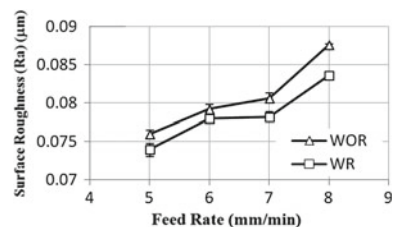
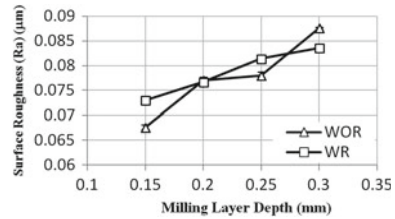


**Fig. 43.6** Effect of milling layer depth on surface roughness



dissolution may occur. As total machining time is lower, higher amount of material removal rate gives lower surface finish. So, surface irregularities have been increased with the increment of tool feed rate. These graphs have been plotted from the data which is average of  $R_a$  values and have been taken from ten different positions of the machined profile and accordingly error graph has been incorporated. The surface roughness of the machined surface also depends on various factors, e.g., rate of material removal, material removal mechanism (homogeneous or inhomogeneous), quality of the sludge produced (sticky or nonsticky, soluble or insoluble), etc. The sludge produced by  $\text{NaCl} + \text{NaNO}_3$  mixed electrolyte is insoluble and light but little sticky in nature. A thin sticky sludge layer has been observed during machining which is the main reason for higher value of roughness in case of without tool rotation. With high rotational speed, the outward radial force of electrolyte removes that layer of sludge and makes dissolution homogeneous and generates better surface finish.

From the Fig. 43.6, it can also be stated that the value of surface irregularities are less with the tool rotation up to 0.25 mm of milling layer depth but, as the milling layer value increases, further the value of roughness of the machining zone is rougher than the without tool rotation. The reason behind it is the material removal rate. It is well known that surface roughness is the inverse to the MRR. It has been observed that at 0.3 mm of milling layer depth, the value of MRR has been increased with compare to no tool rotation which results in a higher value of surface roughness.

During the experimentation, with a variety of tool feed rate, milling layer depth has been kept constant at 0.3 mm and that is the reason behind the value of surface roughness which gets higher with the tool rotation in all the value of tool feed rate as shown in the Fig. 43.5. In this experiment, excellent surface finish with  $R_a$  value of  $0.0676 \mu\text{m}$  has been achieved at 8 mm/min feed rate with 0.15 mm milling layer depth.

### 43.3.3 Influence of Tool Rotation on Quality of the Machined Surface

Apart from the various quantifiable responses like overcut and surface roughness of the machined profile, tool rotation has also influenced the quality of the machined



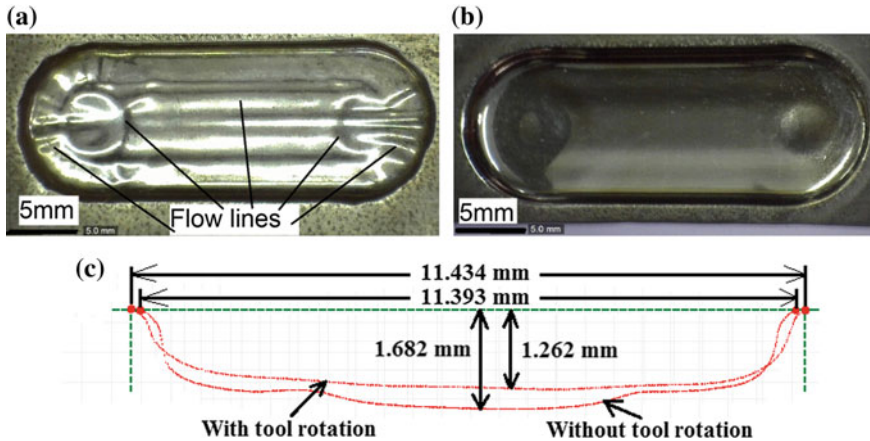


**Fig. 43.7** Photographic view of the EC milled profile using  $\text{NaCl}(1\text{M})+\text{NaNO}_3(1\text{M})$  electrolyte at a tool feed rate of 8 mm/min with 0.15 milling layer depth. **a** Without tool rotation. **b** With tool rotation. **c** Contourscopic profile

surface which cannot be measured but identifiable only by the observations. Photographic view of the machined profile at different experimental condition and contourscopic image using  $\text{NaCl}(1\text{M})+\text{NaNO}_3(1\text{M})$  electrolyte at feed rate of 8 mm/min with 0.15 milling layer depth has been depicted in Fig. 43.7. Figure 43.7a represents the photographic view of the EC milled profile without any tool rotation and photographic view of the machined profile with tool rotation has been shown in Fig. 43.7b.

During EC milling on Nimonic-263 with the tool having an internal hole at the flat end, some undesirable flow lines are clearly visible which has been shown in Fig. 43.7a. During experimentation, the initial gap between tool and the workpiece has been kept at 0.3 mm and amount of electrolyte flow and flow pressure has been kept at 4 LPM and  $0.2 \text{ kgf/cm}^2$  respectively. At this high pressure and narrow gap, electrolyte produces some flow lines and make a similar impression on the machined surface which is clearly shown in Fig. 43.7a. This phenomenon definitely hampers the quality of the machined surface profile and should be overcome. The edge of the machined profile has also been deteriorated when machining without giving any tool rotation. The phenomena can be overcome by introducing the rotation at the tool which is clearly observed from the Fig. 43.7b. As the distribution of the electrolyte is homogeneous with the rotation of the tool and the previously stated flow lines are always moving for the rotation of the tool thus, no unwanted impression of the flow lines and excess depth slot at the vicinity of the internal hole of the tool has been observed. A contourscopic profile of the combination of with and without tool rotation machined profile has been shown in the Fig. 43.7c. From this figure it has been observed that machined surface generated by the tool rotation gives most nearer to the desired depth, more flat, and even surface with compared to without tool rotation.

## 43.4 Conclusions

In this study, lowest value of width overcut, i.e., 0.62128 mm has been achieved at 8 mm/min feed and milling layer depth of 0.3 mm whereas, best surface finish with  $R_a$  value of 0.0676  $\mu\text{m}$  has been achieved at 8 mm/min feed rate with 0.15 mm milling layer depth without any rotation of the tool. From the contoursopic image, it can be concluded that EC milling of Nimonic-263 with tool rotation is more preferable as far as accuracy and the surface qualities of the machined profiles are concerned. Finally, authors feel that this study could help for the effective utilization of EC milling at various modern manufacturing industries like defense, power, and aerospace, etc.

**Acknowledgements** Financial assistantship of AR & DB, DRDO, New Delhi for carrying out this research activity is highly acknowledgeable.

## References

1. Hindujaa, S., Pattavanitch, J.: Experimental and numerical investigations in electro-chemical milling. *CIRP J. Manuf. Sci. Technol.* **12**, 79–89 (2016)
2. Vanderauweraa, W., Vanloffelta, M., Perezb, R., Lauwersa, B.: Investigation on the performance of macro electrochemical milling. *Procedia CIRP* **6**, 356–361 (2013)
3. Ghoshal, B., Bhattacharyya, B.: Investigation on profile of micro channel generated by electro-chemical micromachining. *J. Mater. Process. Technol.* **222**, 410–421 (2015)
4. Mishra, K., Dey, D., Sarkar, B.R., Bhattacharyya, B.: Modeling on volumetric material removal for fabrication of complex shapes by EC milling of Ti6Al4 V. *J. Electrochem. Soc.* **165**, 388–396 (2018)
5. Mishra, K., Dey, D., Sarkar, B.R., Bhattacharyya, B.: Experimental investigation into electro-chemical milling of Ti6Al4V. *J. Manuf. Process.* **29**, 113–123 (2017)

# Chapter 44

## Influence of Discharge Energy on Electrical Discharge Machining of Ti-Foam Material



S. Avinash, Karthick Chetti, M. Haribaskar, S. Jeyanthi, Abimannan Giridharan and R. Krishnamurthy

**Abstract** Titanium foams are most widely used in aircraft filters and in biomedical application as an implant material. Electro discharge machining (EDM) is an electrothermal non-traditional machining process used to generate intricate profiles on difficult to machine material including Titanium alloys. In this paper an attempt has been made to study the influence of EDM process parameters such as pulse ON time, peak current and gap voltage on discharge energy and hole dimensions which are taken as output parameter. Among these input parameters, peak current is having dominant effect on discharge energy. The effect of discharge energy on hole dimension viz. overcut and depth of hole is also analysed. Increasing the discharge energy overcut is mostly maintained between 0.035 and 0.104 mm. A mathematical model is proposed using regression analysis to identify the significant parameter that affects discharge energy and effective machining time. The proposed model predicts discharge energy and effective machining time with an error of 12.73% and 14.98% respectively.

**Keywords** Electro discharge machining · Titanium foam · Discharge energy · Hole overcut · Regression analysis

### 44.1 Introduction

Materials with unique metallurgical properties such as high strength, thermal resistance, reactivity, corrosion and wear resistance has become important in various industries such as aerospace, automotive, marine, etc. Titanium and its alloys are most commonly used in aircraft, marine and biomedical application for its high corrosion resistance and strength. Titanium alloys have proven to be difficult to machine

---

S. Avinash · K. Chetti · M. Haribaskar · S. Jeyanthi · A. Giridharan (✉)  
School of Mechanical and Building Sciences, Vellore Institute  
of Technology, Chennai 600127, India  
e-mail: [giridharan.abimannan@vit.ac.in](mailto:giridharan.abimannan@vit.ac.in)

R. Krishnamurthy  
Indian Institute of Technology Madras, Chennai 600036, India

© Springer Nature Singapore Pte Ltd. 2020  
M. S. Shunmugam and M. Kanthababu (eds.), *Advances in Unconventional Machining and Composites*, Lecture Notes on Multidisciplinary Industrial Engineering, [https://doi.org/10.1007/978-981-32-9471-4\\_44](https://doi.org/10.1007/978-981-32-9471-4_44)

material by conventional methods owing to high temperature involved and rapid tool wear. Electrical discharge machining (EDM) is most widely used for machining of difficult to machine material such as titanium alloys. EDM works on the principle of electrothermal erosion. A high potential difference is applied between the tool and electrode immersed in a dielectric medium (most commonly hydrocarbon oil) separated by a small gap (spark gap). The ignition of the discharge is initiated by the applied potential difference, by overcoming the dielectric breakdown strength of the small gap filled with dielectric medium. Incidence of discharge starts melting and vaporizing of both electrode (tool and workpiece) and dielectric medium. As the discharge continues, a vapour bubble is formed. As the discharge ceases, the rapid burst of vapour bubble ejects the molten material from the surface. The ejected molten material (called as debris) present in the gap is flushed away by the dielectric medium [1].

Many researchers have attempted to study the machining characteristics of EDM on titanium alloys. Furutani et al. proposed a surface modification method by EDM with a green compact electrode to generate thick TiC layer using titanium alloy powder in kerosene-like dielectric medium [2]. Chow et al. attempted to study the effect of SiC and aluminium powder mixed in kerosene dielectric medium for machining micro-slit in titanium alloy and stated that higher material removal rate is achieved while using dielectric mixed with SiC compared to that of aluminium powder [3]. Authors studied the effect of grain size and concentration of SiC abrasive powder mixed in kerosene dielectric medium during EDM finish machining of titanium alloys [4]. Yan et al. attempted to study the surface characteristics of titanium machined using urea solution in water as a dielectric medium during EDM process. Authors proposed that the nitrogen element decomposed from urea dielectric and migrated into workpiece material forming TiN hard layer possesses improved wear resistance on EDM machined surface [5].

Authors studied the effect of EDM process parameters such as pulse on time, gap voltage, discharge current and duty factor on machining characteristics of Inconel 718 material. Antar et al. attempted to study the influence of discharge current on recast layer thickness (RCLT) during EDM drilling of Inconel 718 material. Authors stated increasing discharge current RCLT increases and decreases by increasing discharge current. Authors attempted to study the influence of different tool electrode material such as copper, brass and zinc on machining characteristics of Ti-5Al-2.5Sn material. Authors proposed that varying the process parameters, copper tool electrodes produces better machining characteristics compared to brass and zinc [6–9]. Chen et al. studied the influence of EDM process parameters such as pulse on time, pulse off time and discharge current on machining of TiNiCr and TiNiZr shape memory alloys. Authors stated that during machining the formation of oxide and carbides on the machined surface exhibit higher hardness compared to that of parent material [10]. Kliuev et al. used EDM process for creating cooling hole on Inconel 718 turbine blades [11]. Authors proposed a hypothesis using CFD simulation for the effect of dielectric flow velocity on high aspect ratio hole drilled using EDM process [12].

From literature, it is observed that researchers have attempted to study the influence of EDM process parameters on titanium materials and not much work is carried out in studying the influence of EDM process parameters on discharge energy and hole dimension during machining of pure Titanium foam material. In this paper, an attempt has been made to analyze the influence of EDM process parameters on discharge energy and hole dimension of pure titanium foam machined surface. A model is proposed using regression analysis to predict discharge energy during EDM process.

### 44.2 Experimentation

Experiments were conducted on ELECTRONICA Smart ZNC die-sinking EDM machine with three controllable axes (X, Y and Z). The pulses are generated from MOSFET pulse generator circuit (Technology manual, M/s. Electronica India Limited). A solid Brass of 8 mm diameter is used as the tool electrode and hydrocarbon oil (named ELEKTROL supplied by M/s. Electronica India Limited) is used as the dielectric medium. Pure titanium (Ti) foam sheet of pore size 100 μm with dimension 100 × 100 × 2 mm is taken as the workpiece material. Among the various EDM process variables, parameters such as pulse on time, peak current and gap voltage are having significant influence on machining characteristics. The process parameters such as pulse on time can be varied from 0 to 2000 μs, peak current from 0 to 100 A and gap voltage from 0 to 250 V. Preliminary experiments were conducted to study the effect of EDM process parameters on machining characteristics of Ti-foam material. It is observed from preliminary experiments, by increasing pulse on time beyond 200μs and peak current beyond 12A tool electrode undergo rapid wear. Therefore, the process parameters are varied at four levels and L16 is used for conduct of experiment as given in Table 44.1. Parameters such as retraction distance, sensitivity, anti-arc sensitivity, duty factor and depth of cut are maintained constant at 2.5, 3, 3, 6 and 1 mm respectively.

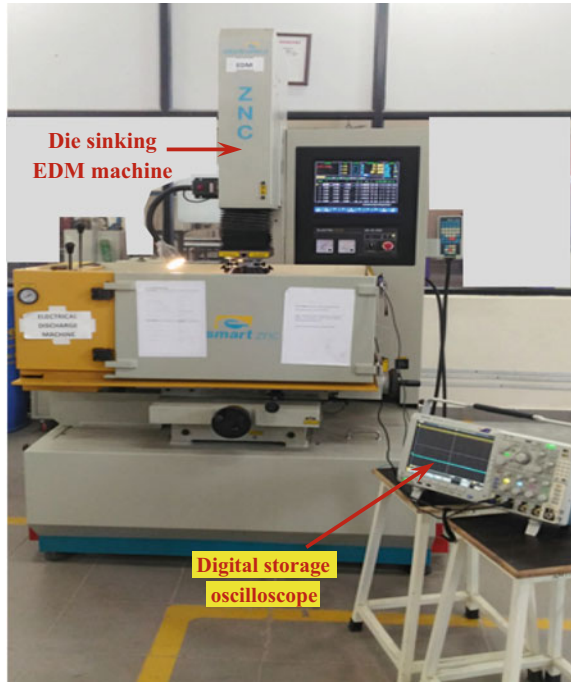
The effect of these input process variables on discharge energy and hole dimension is analysed. The discharge energy is calculated using Eq. (44.1).

$$\text{Energy} = \int_0^{t_c} u(t)i(t)dt \tag{44.1}$$

**Table 44.1** Machine setting parameters

Parameters	Level 1	Level 2	Level 3	Level 4
Pulse on time (μs)	50	100	150	200
Peak current (A)	6	8	10	12
Gap voltage (V)	30	45	60	75

**Fig. 44.1** Complete view of experimental setup



where

$u(t)$  instantaneous voltage (V)

$i(t)$  instantaneous current (A)

$t_e$  effective machining time (s).

The input to Eq. (44.1) is obtained from the voltage and current pulse train data acquired during machining using digital storage oscilloscope for a time duration of 1 s. The hole dimensions such as overcut and depth are measured using optical microscope. The machined samples are cut using wire cut EDM process for analysis of overcut and depth. The experimental setup used for conduct of experiment and the micrograph of Ti-foam workpiece (before and after machining) is given in Fig. 44.1 and Fig. 44.2 respectively.

## 44.3 Results and Discussion

### 44.3.1 Effect of Process Parameters on Discharge Energy

The discharge energy is calculated using Eq. (44.1) and the effect of process parameters on discharge energy is given in Table 44.2. Varying gap voltage and peak current,

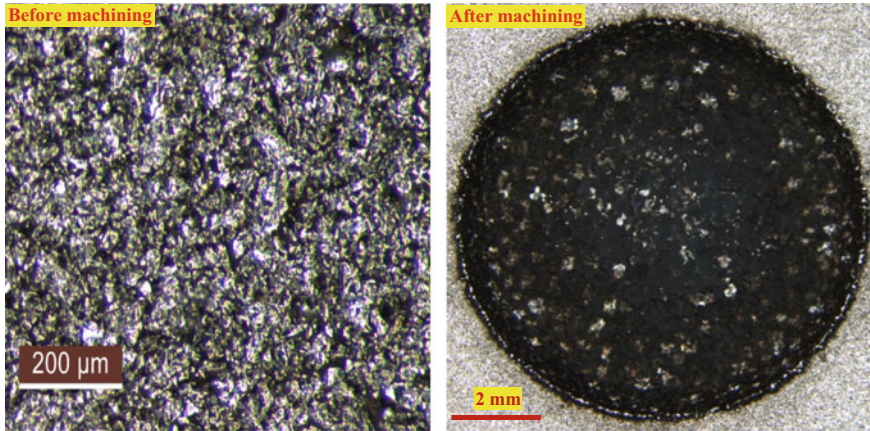


**Fig. 44.2** Micrograph of Ti-foam material

discharge energy show an increasing trend for a pulse on time of 50, 100 and 150  $\mu\text{s}$ . A pulse on time of 200  $\mu\text{s}$ , discharge energy reduces and then increases. For all pulse on time, increasing the gap voltage discharge energy increases. As the peak current is increased from 6 to 12 A, there is no significant change in current magnitude is observed. Figure 44.3 shows the typical pulse train acquired for pulse on time of 200  $\mu\text{s}$  at different peak current. It is seen from the pulse train for same pulse on time at 6 A of peak current input, the discharge current magnitude is  $\sim 2$  A and for 12 A of peak current input the discharge current magnitude is  $\sim 2.2$  A. It is observed that the occurrence of low magnitude of discharge current at high peak current input is due to the resistance offered by the tool material. Titanium is one of the highly reactive and difficult to machine material. During EDM, Titanium reacts with dielectric medium resulting in deposition of the Ti compound on tool electrode. The deposited Ti compounds on the tool electrode offer electrical resistance to the tool during discharge and consequent reduction in erosion. The deposition of work-piece material on the tool electrode can be seen from snapshot taken at magnification of 2X as shown in Fig. 44.4. This resulted in reduced current magnitude for higher peak current input that leads to have insignificant effect on discharge energy. It is observed from Table 44.2, for given peak current and gap voltage increasing the pulse on time number of pulses acquired per second decreases. At smaller values of pulse on time the number of pulses is large but the average effective machine time per pulse is small that resulted in reduced discharge energy. For larger values of pulse on time the average effective machining for each pulse is large that resulted in high discharge energy with less number of pulses. Metal erosion phenomena in EDM process are highly transient, stochastic and complex in nature. A model is proposed using regression analysis for better understanding of the influence of process parameters on discharge energy and effective machining time. In conducting regression analysis it is assumed that factors and the response are linearly related to each other. The regression Eq. (44.2) as follows

**Table 44.2** Effect of process parameters on discharge energy

S. no	TON (μs)	IP (A)	Vg (V)	Np	E (J)	TE (μs)	Hole dimension (mm)				DA
							Øm	Overcut	Depth		
							Left	Middle	Right		
1	50	6	30	83,700	6.06	6.12	0.96	0.62	0.96	0.847	
2	50	8	45	82,270	6.22	5.94	0.89	0.45	0.82	0.720	
3	50	10	60	77,100	7.39	6.30	0.89	0.45	0.83	0.723	
4	50	12	75	75,200	9.42	6.12	0.83	0.69	0.69	0.737	
5	100	6	45	51,750	5.95	10.26	0.89	0.76	0.89	0.847	
6	100	8	30	32,800	6.11	7.92	1.03	0.69	1.03	0.917	
7	100	10	75	45,205	9.37	8.28	0.76	0.76	0.83	0.783	
8	100	12	60	44,800	9.07	10.44	0.89	0.59	0.93	0.803	
9	150	6	60	32,250	7.20	12.60	0.76	0.62	0.69	0.690	
10	150	8	75	21,665	9.22	14.94	0.62	0.76	0.55	0.643	
11	150	10	30	33,180	7.51	11.88	0.93	0.76	0.93	0.873	
12	150	12	45	30,700	8.90	12.60	0.97	0.69	0.97	0.877	
13	200	6	75	24,250	9.26	15.30	0.55	0.93	0.69	0.723	
14	200	8	60	18,350	7.75	23.04	0.69	0.76	0.76	0.737	
15	200	10	45	23,250	7.94	24.48	0.89	0.76	0.89	0.847	
16	200	12	30	21,250	8.82	20.16	1.03	0.76	1.03	0.940	

TON—Pulse on time, IP—Peak current, Vg—Gap Voltage, Np—Number of pulses, E—Discharge energy, TE—Average effective machining time, Øm—Measured hole diameter, DA—Average hole depth



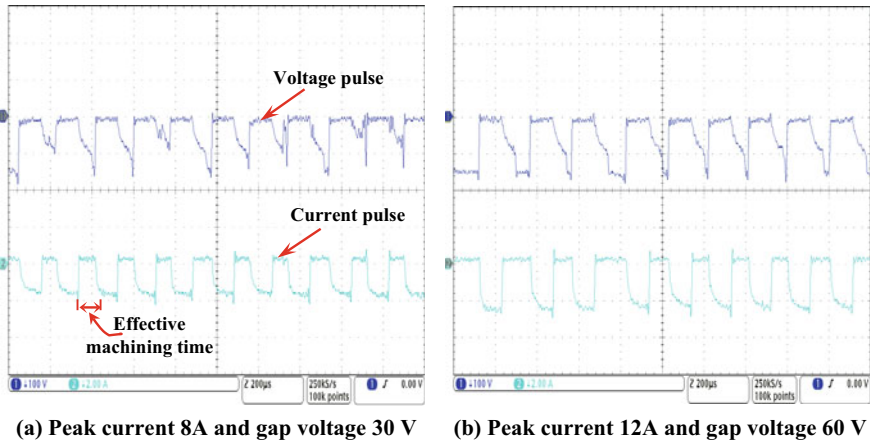
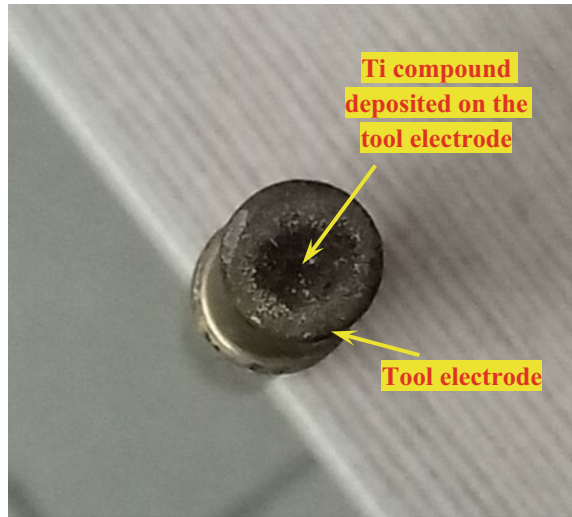


Fig. 44.3 Voltage and current pulse trains acquired for pulse on time 200 μs

Fig. 44.4 Snapshot of machined tool electrode



$$Y = \beta_0 + \beta_1x_1 + \beta_2x_2 + \dots + \beta_nx_n + C \tag{44.2}$$

In which Y is the response and ‘βi’ is the regresses of i-th factor and denotes residual. A mathematical model using regression analysis is proposed for discharge energy and effective machining time. The discharge energy and effective machining time is a function of input process variables. However, during EDM nearly one-third of the total discharge energy is dissipated into workpiece material. The remaining energy is conducted by the tool electrode and dissipated in the machining gap. The effective machining time (EMT) is the time for which spark exists in the gap [1]. It

is also important to know the parameter that influences EMT. Therefore, regression analysis is performed to identify the process variable significantly affects discharge energy and effective machining time. The derived regression equation for discharge energy and effective machining time is given in Eqs. (44.3) and (44.4) respectively.

$$\text{Discharge energy} = 1.413 + 0.00818T_{ON} + 0.3266I_P + 0.04784V_g \quad (44.3)$$

$$\text{Effective machining time} = -0.78 + 0.0953T_{ON} + 0.178I_P - 0.0087V_g \quad (44.4)$$

It is observed from the regression equation that discharge energy is mostly influenced by peak current compared to that of pulse on time and gap voltage. The regression model predicts the discharge energy and effective machining time at 87.27% and 85.02% respectively.

### 44.3.2 Effect of Discharge Energy on Hole Dimension

The influence of discharge energy on hole dimension such as overcut and depth is given in Table 44.2 and Fig. 44.5. The overcut in this paper is defined as the difference between the hole entry diameter and the tool electrode diameter. The data in Table 44.2 shows that over cut is maintained around 0.05–0.07 mm with low order discharge energy and tends to cloud around 0.06 mm with higher energy (around 9 J). As the discharge energy increases more amount of material is removed from the

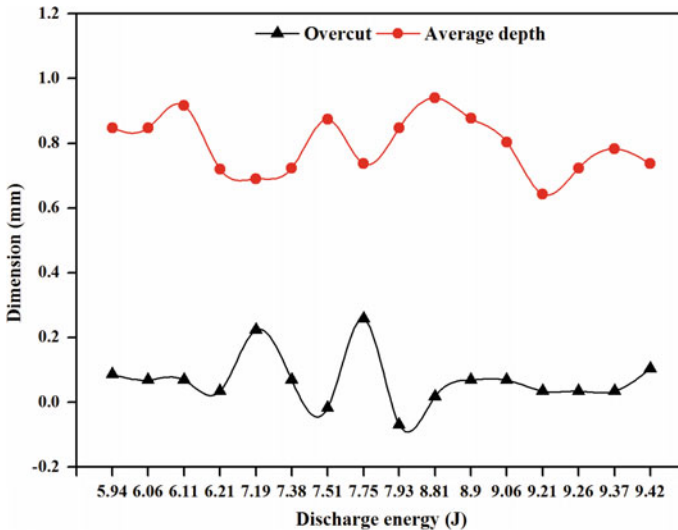
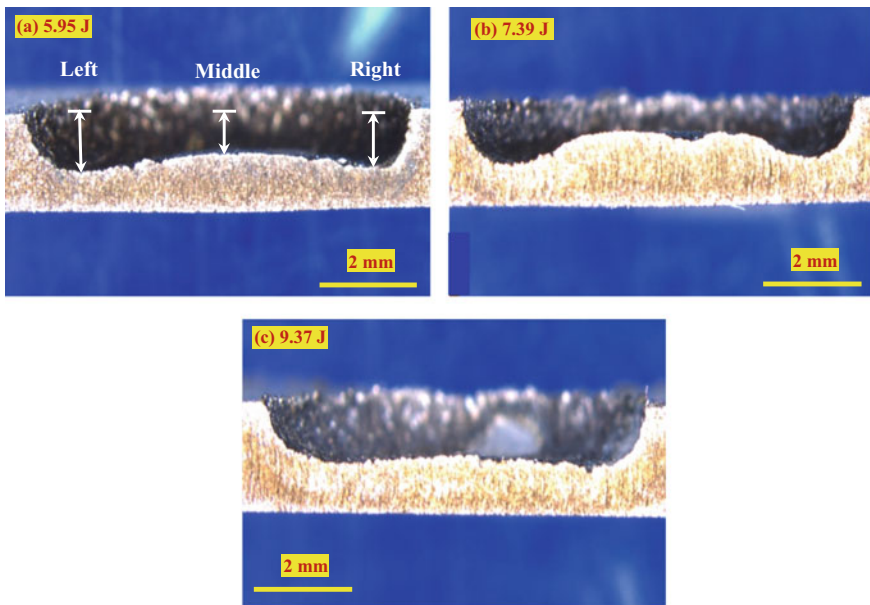


Fig. 44.5 Effect of discharge energy on overcut and depth of hole

machined surface that resulted in increased overcut. The increase in overcut may be due to the flow velocity of dielectric fluid at the workpiece surface. At discharge energy of 7.19 J and 7.75 J the measured overcut values are at 0.224 mm and 0.254 mm respectively. This is due to the increase in effective machining time for these two discharge energies as given in Table 44.2. Effective machining time is the time during which current pulse exists in the gap, which is responsible for erosion as shown in Fig. 44.4. Higher the effective machining time more material is eroded from the machined surface that resulted in increased overcut of the machined hole diameter. At discharge energy of 7.5 and 7.93 J, undercut is observed on the hole diameter, i.e., the hole diameter is smaller than the tool electrode diameter. This may be caused due to the wear of tool electrode. As the spark begins, the generated debris particle (harder than the soft brass tool electrode) carried away by dielectric fluid erodes the tool electrode at outer periphery. As the machining continues, tool electrode wears rapidly which resulted in reduced tool diameter at entry that leads to undersized hole diameter. It is observed from Table 44.2 and Fig. 44.5 as the discharge energy increases the depth is varied between 0.69 and 0.94 mm. Figure 44.6 shows the micrograph of machined hole on Ti-foam workpiece at different discharge energy. It is observed from Fig. 44.6, discharge energy of 5.95 and 9.37 J the hole bottom is almost straight, whereas at 7.39 J of discharge energy there is a bulge observed at the bottom of hole. This may be due to improper flushing of the debris from the machining gap by dielectric medium. As the workpiece material is having pore size



**Fig. 44.6** Micrograph of machined hole cross section for different discharge energy (a–c)

of 100  $\mu\text{m}$  the machined debris particle gets accumulated due to poor flushing of the dielectric medium. This resulted in bulged edge at bottom of hole.

## 44.4 Conclusions

Experiments were conducted on Ti-foam material of average pore size of 100  $\mu\text{m}$  by varying input process variables such as pulse on time, peak current and gap voltage. The effect of these parameters on discharge energy and hole dimensions was analysed. The following are the important conclusions arrived

1. Discharge energy increases with increase in pulse on time, peak current and gap voltage. Among the input parameters, the effect of pulse on time and peak current shows a dominant effect. As the pulse on time increases the number of pulse decrease and the average effective machining time increases that resulted in increased discharge energy.
2. Varying the input peak current from 6 to 12 A, the magnitude of discharge current acquired from the machining gap is between 2 and 2.2 A. The deposition of titanium oxide and titanium carbide on the tool electrode offers electrical resistance that resulted in reduced discharge current magnitude.
3. Overcut of the hole increases with increase in discharge energy. Undercut in hole diameter is observed due to rapid erosion of tool electrode caused by debris present in dielectric fluid. Due to improper flushing of dielectric medium a bulge is observed at the bottom of hole.
4. A mathematical model is developed for predicting discharge energy and effective machining time. The proposed model predicts discharge energy and effective machining time with 87.27% and 85.02% respectively.

Erosion of Titanium foam with medium discharge energy could facilitate with a progressive rise in overcut with discharge energy, constrained depth and effective machining time. The work can be extended in performing detailed experiments and perform ANOVA analysis for understanding the effect of EDM process variables on discharge energy and machining characteristics of Ti-foam material.

## References

1. Kunieda, M., Lauwers, B., Rajurkar, K.P., Schumacher, B.M.: Advancing EDM through Fundamental Insight into the Process. *CIPR Annals* **54**(2), 64–87 (2005). [https://doi.org/10.1016/S0007-8506\(07\)60020-1](https://doi.org/10.1016/S0007-8506(07)60020-1)
2. Furutani, K., Hideki Takezawa, A.S., Mohri, N., Miyake, H.: Accretion of titanium carbide by electrical discharge machining with powder suspended in working fluid. *J. Int. Soc. Precis. Eng. Nanotechnol.* **25**(2), 138–144 (2001). [https://doi.org/10.1016/s0141-6359\(00\)00068-4](https://doi.org/10.1016/s0141-6359(00)00068-4)
3. Chow, H.M., Yan, B.H., Huang, F.Y., Hung, H.C.: Study of added powder in kerosene for the micro-slit machining of titanium alloy using electro-discharge machining. *J. Mater. Process. Technol.* **101**(1–3), 95–103 (2000). [https://doi.org/10.1016/s0924-0136\(99\)00458-6](https://doi.org/10.1016/s0924-0136(99)00458-6)

4. Lin, Y.C., Chow, H.M., Yan, B.H., Tzeng, H.J.: Effects of finishing in abrasive fluid machining on microholes fabricated by EDM. *Int. J. Adv. Manuf. Technol.* **33**(5–6), 489–497 (2007). <https://doi.org/10.1007/s00170-006-0485-7>
5. Yan, B.H., Tsai, H.C., Huang, F.Y.: The effect in EDM of a dielectric of a urea solution in water on modifying the surface of titanium. *Int. J. Mach. Tools Manuf.* **45**(2), 194–200 (2005). <https://doi.org/10.1016/j.ijmachtools.2004.07.006>
6. Antar, M., Chantzis, D., Marimuthu, S., Hayward, P.: High speed EDM and laser drilling of aerospace alloys. *Procedia CIRP* **42**, 526–531 (2016). <https://doi.org/10.1016/j.procir.2016.02.245>
7. Bhaumik, M., Maity, K.: Effect of different tool materials during EDM performance of titanium grade 6 alloy. *Eng. Sci. Technol. Int. J.* **21**(3), 507–516 (2018). <https://doi.org/10.1016/j.jestch.2018.04.018>
8. Kuppan, P., Rajadurai, A., Narayanan, S.: Influence of EDM process parameters in deep hole drilling of Inconel 718. *Int. J. Adv. Manuf. Technol.* **38**(1–20), 74–84 (2008). <https://doi.org/10.1007/s00170-007-1084-y>
9. Kao, J.Y., Tsao, C.C., Wang, S.S., Hsu, C.Y.: Optimization of the EDM parameters on machining Ti–6Al–4V with multiple quality characteristics. *Int. J. Adv. Manuf. Technol.* **47**(1–4), 395–402 (2010). <https://doi.org/10.1007/s00170-009-2208-3>
10. Chen, S.L., Hsieh, S.F., Lin, H.C., Lin, M.H., Huang, J.S.: Electrical discharge machining of TiNiCr and TiNiZr ternary shape memory alloys. *Mater. Sci. Eng. A* **445–446**, 486–492 (2007). <https://doi.org/10.1016/j.msea.2006.09.109>
11. Kluiev, M., Boccadoro, M., Perez, R., Dal Bo, W., Stirnimann, J., Kuster, F.: EDM drilling and shaping of cooling holes in Inconel 718 turbine blades. *Procedia CIRP* **42**, 322–327 (2016). <https://doi.org/10.1016/j.procir.2016.02.293>
12. Kluiev, M., Baumgart, C., Wegener, K.: Fluid dynamics in electrode flushing channel and electrode-workpiece gap during EDM drilling. *Procedia CIRP* **68**, 254–259 (2018). <https://doi.org/10.1016/j.procir.2017.12.058>

# Chapter 45

## Gang Drilling of Square Micro-Holes on Glass Using USM



T. Debnath , K. K. Patra  and P. K. Patowari 

**Abstract** The industry needs to develop faster and efficient production for the increase in demands of the society, without compromising the cost. Sometimes, gang operations are performed to generate multiple profiles on a workpiece at once to fulfill the demand. On the other hand, ultrasonic machining (USM) is one of the advanced machining processes used to machine brittle materials or ceramics like glass. This paper focuses on the drilling of multiple square micro-holes at a time on glass using USM. Initially, arrays of square micro-rods have been prepared using wire electrical discharge machining (Wire EDM) method. Using these micro-tools/micro-rods, arrays of square micro-holes have been drilled on the glass slides. In addition, the effect of the control parameters on the performance measures has also been observed.

**Keywords** USM · Micro-hole · Array · Micro-rods · Wire EDM

### 45.1 Introduction

Ultrasonic machining (USM) is one of the mechanical type advanced machining processes that does not change the physical and chemical properties of the workpiece while machining. Here, a slurry (abrasive particles mixed with water) is used to machine the workpiece and the machining phenomenon takes place because of the brittle failure of the workpiece material. The abrasive particles are propelled by the tool and strikes on to the workpiece, creating micro-indentations resulting in precision machining and finer chip formation. This machining process is suitable than other machining processes for the reason of minimal effect on the workpiece. On the other hand, glass is being used in many day-to-day applications. Also, glass is highly brittle, so to machine glass, USM is highly preferable.

Researches have been conducted on the machining accuracy of the holes generated using USM. Parameters such as, static load, machining time, type of abrasives,

---

T. Debnath (✉) · K. K. Patra · P. K. Patowari  
Advanced Manufacturing Laboratory, Department of Mechanical Engineering,  
National Institute of Technology Silchar, Silchar 788010, Assam, India  
e-mail: [nit.tapas11@gmail.com](mailto:nit.tapas11@gmail.com)

© Springer Nature Singapore Pte Ltd. 2020  
M. S. Shunmugam and M. Kanthababu (eds.), *Advances in Unconventional Machining and Composites*, Lecture Notes on Multidisciplinary Industrial Engineering, [https://doi.org/10.1007/978-981-32-9471-4\\_45](https://doi.org/10.1007/978-981-32-9471-4_45)

and grit size have been considered for the dimensional accuracy of holes. It has been reported that fine abrasives increased the hole's accuracy [1]. The material removal rate (MRR) and tool wear rate (TWR) are the most important performance measures which describe the machining efficiency and accuracy. The removal of material from workpiece takes place by abrasive hammering caused by the tool and the impact of high velocity of abrasives on work material [2]. It has been observed that abrasive hammering has more significance for material removal as compared to the impact mechanism; also the glass has higher MRR. On the contrary, tool material also gets affected due to the abrasive hammering, resulting in deformation of the tool shape. Types of tool material also influence machining accuracy. It has been reported that stainless steel and high carbon steel can retain its shape than other materials while machining using USM [1, 3]. Several experiments have been conducted on a variety of work materials like glass, ferrite, and alumina. It has been reported that workpiece materials which are highly brittle in nature have high MRR and are also associated with higher surface roughness [4]. Other than traditional glass, the investigation has been carried out on  $Zr_{60}Cu_{30}Ti_{10}$  metallic glass by drilling micro-holes using micro-USM [5]. Performance parameters like overcut, edge deviation, taper angle, MRR, and TWR have been analyzed by varying input parameters such as feed, abrasive grit size, and concentration of abrasive slurry. It has been reported that the amorphous structure of metallic glass remained the same even after drilling micro-holes. The abrasive tool materials and its type along with the slurry concentration can also influence the ultrasonic machining. Three types of abrasives have been considered, viz., aluminum oxide, silicon carbide, and boron carbide for machining of Satellite 6 [6]. The tool materials that have been used are Titan12, Titan15, and Titan31 for the experimentation. The effectiveness of the USM process has been determined in terms of MRR and surface finish and at optimum conditions, the MRR and surface roughness have been found as  $0.198 \text{ mm}^3/\text{min}$  and  $0.582 \text{ }\mu\text{m}$ , respectively. The ultrasonic machining is not limited to the traditional circular drilling only; 3-D microstructures having high aspect ratios have been fabricated using micro-ultrasonic machining [7]. The micro-tool (tungsten carbide) for USM has been formed using a combination of wire electrical discharge grinding (WEDG) and electrical discharge machining (EDM). An attempt has been made to drill multiple holes on a glass slide [8], but the intermediate hole wall fails due to inefficient spacing in between the tools.

From the literature, it has been observed that a lot of work has already been found on the drilling on glass using USM. Most of the drilling operations have been observed to be a circular hole and very minimal work is found on the drilling of square micro-holes on the glass. Moreover, the gang operations/multiple operations at a time have not been observed in USM. In this paper, arrays of square micro-holes have been drilled on glass (microscopic slides) slides by preparing an array of tools using Wire EDM.

### 45.2 Methodology and Experimentation

Initially, the glass slide of thickness 0.33 mm has been chosen as workpiece material and square stainless steel (3 mm × 3 mm) as the tool material. To drill multiple holes on the glass, multiple tools need to be fabricated. Arrays of square micro-rods have been fabricated on the stainless-steel tool material using wire electrical discharge machining (Wire EDM). A computer numerical control (CNC) code has been generated for monitoring the wire path using RR-CAD software, to fabricate square micro-rods in Wire EDM. The fabrication of arrays of micro-tools has been accomplished by two runs/cuts and both the cuts follow the same wire path (CNC code). After the first cut, the workpiece has to rotate 90° (in any direction) to perform the second cut. Debnath et al. [9] fabricated an array of 625 (25 × 25) square micro pin fins/rods on stainless steel and copper rods using Wire EDM. The similar wire path has been followed to fabricate these micro-tools for ultrasonic machining. As the generated features are in microscale, the minimum possible spark energy is applied while fabrication to reduce the surface roughness and corner roundness.

Arrays of 9 (3 × 3) square micro-rods/extruded pins have been fabricated. The generated cross section of the micro-rods is around 200 μm × 200 μm. Figure 45.1a depicts the desirable dimensions taken for the micro-tool fabrication and the designed tool is shown in Fig. 45.1b. Based on these dimensions, the USM tool has been fabricated using Wire EDM. Figure 45.1c visualizes the fabricated micro-tool which is soldered onto a tool holder as shown in Fig. 45.1d. The optical image of the fabricated micro-tool is shown in Fig. 45.1e. The soldered micro-tool is then attached to the ultrasonic horn for the experimentations. Figure 45.2 shows the ultrasonic

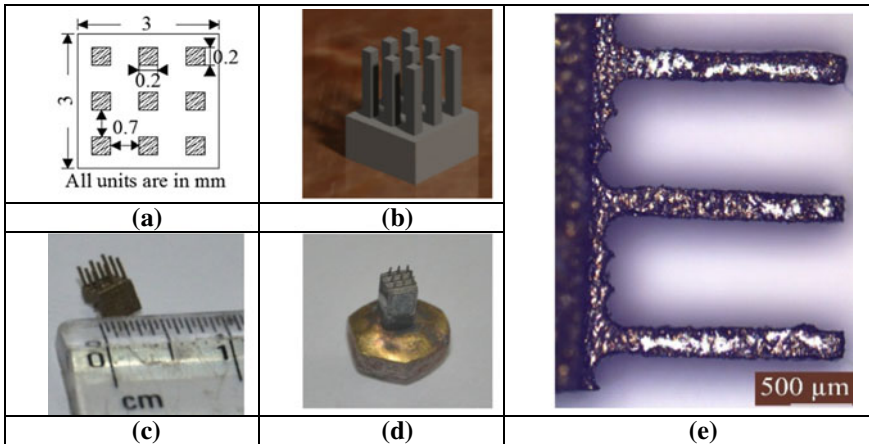


**Fig. 45.1** a Desired dimensions of the micro-tool; b Designed array of square micro-rods; c Actual micro-tool after fabrication using Wire EDM; d Attached micro-tool on the tool holder; e Magnified image of the micro-tool



**Fig. 45.2** Ultrasonic machining setup: 1. Cutting tool, 2. Horn, 3. Transducer, 4. Acoustic head, 5. Abrasive flow pipe, 6. Magnetic plate, 7. Control unit

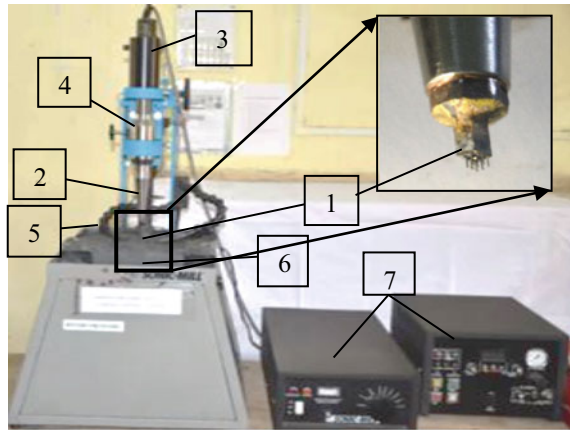


**Table 45.1** Chosen variables and their corresponding levels

Sym.	Parameters	Levels	Values
GS	Grit size (Mesh number)	3	600, 400, 220
SF	Slurry flow rate (cm <sup>3</sup> /s)	3	125, 100, 75
FR	Feed rate (μm/s)	3	75, 50, 25

machine and its different parts. The inset image in Fig. 45.2 shows the attached micro-tool to the horn and ready for ultrasonic machining.

Initially, the glass slide is fixed on the heat plate using heat glue and this heat plate is then attached to the workbench with the help of a magnetic medium. After each experimentation, the workpiece samples are removed from the heat plate by applying heat. Then the samples are cleaned using acetone and observed under a microscope for measuring desired dimensions. For machining, a mixture of water and B<sub>4</sub>C abrasive particles is used as a slurry, which is kept constant at 50%. While machining, the effect of control parameters are observed on the performance measures. The control parameters which have been varied are abrasive grit size (mesh number), feed rate (μm/s), and slurry flow rate (cm<sup>3</sup>/s), and the other parameters are kept constant. The chosen variables along with their levels are shown in Table 45.1.

Taguchi L<sub>9</sub> orthogonal array has been chosen to conduct the experiments. Table 45.2 shows the chosen parametric combinations for the experimentation. The effect of the control parameters on material removal rate (MRR), tool shortening rate (TSR), and the overcut (OC) has been observed while machining. Equations (45.1)–(45.3) represent the calculations for the performance measures. Based on the measured parameters and using Eqs. (45.1)–(45.3), the performance measures have been calculated for each experimentation.

**Table 45.2** Experimental combinations based on Taguchi L9 orthogonal array

Exp. No.	GS (Mesh number)	SF (cm <sup>3</sup> /s)	FR (μm/s)
1	220	75	25
2	220	100	50
3	220	125	75
4	400	75	50
5	400	100	75
6	400	125	25
7	600	75	75
8	600	100	25
9	600	125	50

Material removal rate:

$$MRR \text{ (mm}^3\text{/min)} = \frac{\text{Total volume of the drilled holes}}{\text{Machining time}} \tag{45.1}$$

Tool shortening rate:

$$TSR \text{ (}\mu\text{m/min)} = \frac{\text{Initial height} - \text{final height of tool}}{\text{machining time}} \tag{45.2}$$

Overcut:

$$OC \text{ (}\mu\text{m)} = \frac{\text{Average width of hole} - \text{average edge of tool}}{2} \tag{45.3}$$

### 45.3 Results and Discussion

Based on the microscopic images and the experimental results, the performance measures have been calculated. The images of the drilled array of square micro-holes are shown in Fig. 45.3. Figure 45.4 represents the drilled image under an optical microscope. Table 45.3 shows the obtained performance measures after the experimentations.

The variation of response measure with the control parameters is shown in Figs. 45.5, 45.6, 45.7. With the increase in mesh number actual grit size decreases, resulting in smaller indentation by the abrasive particles on the workpiece. For this reason, the material removal rate (MRR) decreases. Figure 45.5 shows the variation of MRR with the control parameters. On the other hand, with an increase in slurry flow rate, the total number of active particle increases in the slurry, which results in higher MRR due to a higher number of indentations. Also, with the increase in feed



**Fig. 45.3** The drilled glass samples after experimentations

**Fig. 45.4** Drilled micro-hole under an optical microscope

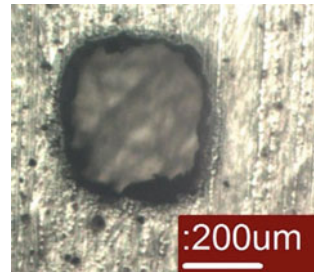


**Table 45.3** Average performance measures after experimentation

Exp. No.	MRR (mm <sup>3</sup> /min)	TSR (μm/min)	OC (μm)
1	0.39	96	92
2	0.41	79	85
3	0.53	60	84
4	0.37	63	69
5	0.39	69	66
6	0.33	72	74
7	0.32	66	41
8	0.33	54	61
9	0.39	59	58

**Fig. 45.5** Variation of material removal rate with control parameters

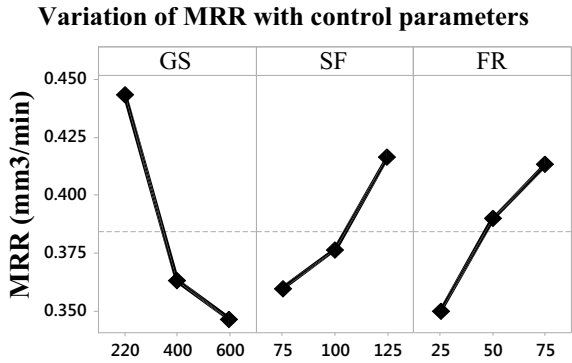


**Fig. 45.6** Variation of tool shortening rate with control parameters

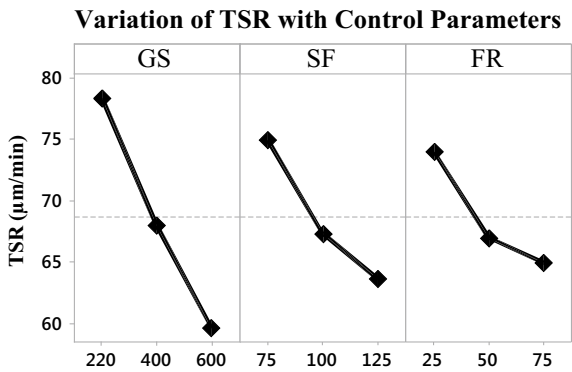
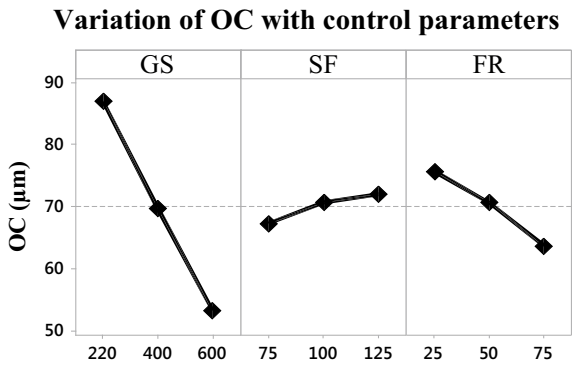


**Fig. 45.7** Variation of overcut with control parameters



rate, the tool progresses toward the workpiece at a faster rate, minimizing the total machining time consequences in higher MRR.

From Fig. 45.6, it is clear that, with the increase in mesh number, slurry flow rate, and feed rate, the tool shortening rate (TSR) decreases. With the increase in mesh number, the smaller abrasive particles create a smaller indentation to the workpiece as well as micro-rods, hence reducing the tool wear consequences lower TSR. But with the increase in slurry flow rate and feed rate, faster material removal takes place resulting in the lower machining time consequences minimum TSR.

Figure 45.7 shows the variation of overcut with the control parameters. The overall overcut (OC) decreases with the increase in mesh number and the feed rate but increases with the increase in slurry flow rate. With the increase in mesh number, the overall size of the abrasive particle decreases, creating a smaller indentation resulting in lower OC. With the increase in feed rate, faster machining takes place, resulting in minimum abrasion and striking to the work surface by the abrasive particles. On the other hand, the number of striking particles increases with an increase in slurry flow rate; also, overlapping of particles takes place, creating a bigger hole size, which results in higher OC.

## 45.4 Conclusions

Initially, arrays of micro-tools were fabricated using Wire EDM and these micro-tools have been used for drilling multiple square holes using USM on glass slides. From the results and discussions, the following conclusions have been drawn.

- Finer abrasive particles produce lower MRR, TSR, and OC.
- With the increase in slurry flow rate, MRR and OC increase providing minimum TSR.
- Higher feed rate is suitable for better MRR, TSR, and OC.
- The drilled hole quality is precise and accurate. Although corner roundness has been observed on the holes, these are very minimum. The overall quality of the drilled square micro-hole is very much acceptable.

## References


1. Adithan, M., Venkatesh, V.C.: Production accuracy of holes in ultrasonic drilling. *Wear* **40**, 309–318 (1976)
2. Soundararajan, V., Radhakrishnan, V.: An experimental investigation on the basic mechanisms involved in ultrasonic machining. *Int. J. Mach. Tool Des. Res.* **26**(3), 307–321 (1986)
3. Jadoun, R.S., Kumar, P., Mishra, B.K., Mehta, R.C.S.: Optimisation of MRR in ultrasonic drilling (USD) based on Taguchi's robust design methodology. *Int. J. Mach. Mach. Mater.* **1**(4), 445 (2006)

4. Komaraiah, M., Manan, M.A., Reddy, P.N., Victor, S.: Investigation of surface roughness and accuracy in ultrasonic machining. *Precis. Eng.* **10**(2), 59–65 (1988)
5. Kuriakose, S., Patowari, P.K., Bhatt, J.: Machinability study of Zr–Cu–Ti metallic glass by micro hole drilling using micro—USM. *J. Mater. Process. Technol.* **240**, 42–51 (2017)
6. Vinod, K., Khamba, J.S.: An investigation into the ultrasonic machining of co-based super alloy using the Taguchi approach. *Int. J. Mach. Mach. Mater.* **7**(3–4), 230–243 (2010)
7. Sun, X.Q., Masuzawa, T., Fujino, M.: Micro ultrasonic machining and self—aligned multi-layer/machining/assembly technologies for 3D micromachines. In: *Proceedings of Ninth International Workshop on Micro Electromechanical Systems*, pp. 312–317 (1996)
8. Patra, K.K., Debnath, T., Patowari, P.K.: Fabrication of an array of square micro—Holes on glass using ultrasonic machining. In: *AIP Conference Proceedings*, vol. 1998(1) (2018). <https://doi.org/10.1063/1.5049109>
9. Debnath, T., Patowari, P.K.: Fabrication of an array of micro-fins using Wire—EDM and its parametric analysis. *Mater. Manuf. Process.* **34**(5), 580–589 (2019). <https://doi.org/10.1080/10426914.2019.1566959>

# Chapter 46

## Parametric Optimization of Micro Ultrasonic Drilling of Quartz Based on RSM



S. Kumar , B. Doloi and B. Bhattacharyya

**Abstract** Micro ultrasonic machining is the process for micro hole drilling on hard and brittle materials like ceramic, glass, quartz, silicon, etc. Quartz has wide applications in microelectromechanical systems (MEMS), lenses, pressure and flow sensors, and micro-optical systems. In the present research work, optimization of the process parameters for responses such as material removal rate, overcut, and taper angle during micro ultrasonic drilling has been performed utilizing the developed empirical relationship between the responses and process parameters. Three different process parameters— power rating, abrasive slurry concentration, and tool feed rate were considered for this experimental investigation. The parametric studies have also been made based on response surface plot. Based on multi-objective optimization, optimal parametric setting for maximum material removal rate, minimum overcut and minimum taper angle have been obtained.

**Keywords** Micro ultrasonic machining · Quartz · Material removal rate · Overcut · Taper angle · Optimization

### 46.1 Introduction

The employment of hard and brittle materials has been increased largely in industrialized fields such as the optical component, aeronautic, automotive, and semiconductor sector, for uniqueness. The uniqueness of hard and brittle materials, including their high hardness, high strength at superior temperatures, high heat resistance, low wear rate, and lightweight in comparison to metals [1], are precious in the making of meticulousness mechanical equipment. Yet, the machining of these materials left-overs pose a big for this superior uniqueness. For these materials, it is not easier to make tools that can machine with no compromise in profile accuracy.

---

S. Kumar (✉) · B. Doloi · B. Bhattacharyya  
Production Engineering Department, Jadavpur University, Kolkata 700032, India  
e-mail: [santosh14fiem@gmail.com](mailto:santosh14fiem@gmail.com)

© Springer Nature Singapore Pte Ltd. 2020  
M. S. Shunmugam and M. Kanthababu (eds.), *Advances in Unconventional Machining and Composites*, Lecture Notes on Multidisciplinary Industrial Engineering, [https://doi.org/10.1007/978-981-32-9471-4\\_46](https://doi.org/10.1007/978-981-32-9471-4_46)

Micro ultrasonic machining (micro USM) is the emerging and effective machining technology among all the mechanical energy-based micromachining techniques to generate  $\mu$  features with high aspect ratio in hard and brittle materials such as quartz, silicon, glass, and ceramics [2, 3]. In micro USM, the material is removed by the repetitive shock through abrasives particles into the workpiece with ultrasonic vibration. Micro USM has been applied to make micro holes in micro products and components of quartz. Demand for micro apparatus from different engineering sectors such as electronics, optics, medical, biotechnology, automotive, communications, and avionics industries where micro USM can be applied for micromachining.

Generally, material removal rate in micro USM raise with the rise in the size of abrasive particle for both water-based abrasive slurry and oil-based abrasive slurry, but material removal rate is higher using water as a slurry medium [4]. Micro drills produce on borosilicate glass utilizing micro USM. The MRR is more affected by static load and at the same time, tool wear rate (TWR) affects by abrasive size [5]. Ultrasonic micromachining is much affected by abrasive slurry concentration which judges against the power rating and tool feed rate during the generation of micro hole on quartz [6].

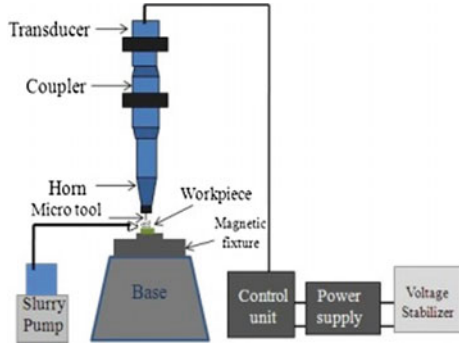
It has been analyzed from the previously published works that the performance of micro USM has to be optimized to enhance the ability of micromachining of quartz. The present research work is to establish the empirical model between machining performance and convenient machining parameters such as power rating, abrasive slurry concentration, and tool feed rate using response surface methodology (RSM). Multi-objective optimization of micro USM process has also been performed utilizing the developed empirical models.

## 46.2 Fundamentals of Micro USM

Micro USM process initiates the conversion of low-frequency electrical energy to high mechanical frequency, which is then fed to acoustic system. For this, tool vibrates along its longitudinal axis at high frequency. In micro ultrasonic machining, tool of desired shape pulsates at ultrasonic frequency (20–40 kHz) and with less than 25  $\mu\text{m}$  amplitude over work piece. Machining region is recirculated with abrasive particles mixed in a liquid medium. In micro USM, the abrasive particles are vibrated between the tool and workpiece by a high-frequency vibratory system. The vibrated abrasive particles hit the workpiece and material removal takes place due to microcrack. Figure 46.1 shows the schematic diagram of micro USM system.



**Fig. 46.1** Schematic diagram of micro USM system



### 46.3 Experimental Planning and Methods

Experiments have been done in micro ultrasonic machine system made by Sonic Mill. The frequency of vibration of the ultrasonic machine was set at 20 kHz. The quartz material was set on the fixture made of magnetic material. Tool feed rate was given along longitudinal axis. B<sub>4</sub>C fine particles (24 μm) were flooded around workpiece surface after being mixed with liquid medium. Stainless steel (SS304) cylindrical tools of 20 mm long with tip diameter 350 μm were chosen for micro tool and fixed to the hexagonal head. The microscopic view of micro tool tip is shown in Fig. 46.2.

Design of experiments (DOE) is used to conduct the experiments. The design of experiments (DOE) is a proficient technique for setting up conduct test so that the data can be able to be analyzed to yield value. The picking of an experimental design depends on the goal of the experiment and the number of issues to be investigated.

With 20 runs, central composite half design (CCD) was chosen with an alpha value of 1.68. CCD is an extremely proficient technique to fit a second-order form. Three factors and five levels were taken for investigational goal. After carrying out some pilot experiments, the range of each factor was decided. The actual and coded values are given in Table 46.1. The real values of process parameters as per experimental design and corresponding values of responses of micro USM are given in Table 46.2.

**Fig. 46.2** Micro tool tip used in USM

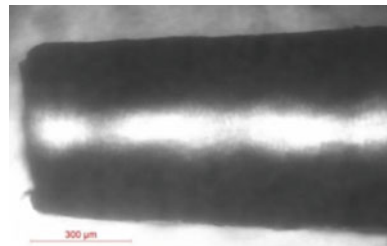


**Table 46.1** Real and coded values of ultrasonic micromachining

Factor	Unit	Symbol	Level				
			-1.68	-1	0	1	1.68
Abrasive slurry concentration	g/l	X <sub>1</sub>	20	25	30	35	40
Power rating	W	X <sub>2</sub>	200	250	300	350	400
Tool feed rate	mm/min	X <sub>3</sub>	0.8	0.9	1	1.1	1.2

**Table 46.2** Values of parameters with corresponding outcomes

Exp No.	Abrasive slurry concentration (g/l)	Power rating (W)	Tool feed rate (mm/min)	MRR (mm <sup>3</sup> /min)	Overcut (μm)	Half taper angle (deg.)
1	25	250	1.1	0.3661	62.30	1.2864
2	35	250	1.1	0.3673	63.01	1.3000
3	20	300	1.0	0.4931	66.91	2.5200
4	30	300	1.0	0.1912	54.00	0.7540
5	30	300	1.0	0.2111	58.00	1.0100
6	30	300	1.0	0.3156	54.00	1.2070
7	30	300	0.8	0.4543	64.09	2.0400
8	30	300	1.0	0.3661	62.00	1.3020
9	30	200	1.0	0.6436	66.19	2.8190
10	25	250	0.9	0.1977	55.00	0.7540
11	35	350	1.1	0.2127	52.00	1.0000
12	30	400	1.0	0.3881	62.00	1.2200
13	35	350	0.9	0.3690	62.00	0.9000
14	35	250	0.9	0.1511	51.00	0.6640
15	30	300	1.2	0.4739	66.00	2.6909
16	25	350	1.1	0.3673	62.78	0.9200
17	30	300	1.0	0.3661	62.98	1.2520
18	25	350	0.9	0.3432	66.03	1.3200
19	30	300	1	0.3002	64.16	1.1890
20	40	300	1	0.3517	67.99	1.8862

### 46.3.1 Empirical Model

Response surface modeling has been done to create the practical model between the responses and the different machining parameters. The second-order polynomial equation, that is used to analyze the different response criterion, is given below

$$Y_u = \beta_o + \sum_{i=1}^n \beta_i x_{iu} + \sum_{i=1}^n \beta_{ii} x_{iu}^2 + \sum_{i < j=2}^n \sum_{j=2}^n \beta_{ij} x_i x_j + \epsilon_u \quad (46.1)$$

In the above Eq. (46.1),  $Y_u$ : corresponding response.  $X_{iu}$ : coded values of the  $i_{th}$  machining process parameters. The terms  $\beta_o$ ,  $\beta_i$ ,  $\beta_{ii}$ , and  $\beta_{ij}$ : the regression coefficients and the residual,  $\epsilon_u$  measures the experimental error of the  $u_{th}$  observations. The process limitations have been chosen from the proposed analysis. The range of each process parameter has been chosen from the outcome of preliminary experiments. In this experimentation, three factors with five levels were considered. The mathematical relationship has been established to follow Eq. 46.1. Hence, the corresponding empirical equation for the responses is represented as material removal rate ( $Y_{MRR}$ ), overcut ( $Y_{OC}$ ), and taper angle ( $Y_{TA}$ ). Based on RSM, an empirical relationship have been established and given as follows:

The equation corresponding to material removal rate ( $Y_{MRR}$ ) is given as

$$\begin{aligned} Y_{MRR} = & 0.359999 + 0.040065 X_1 + 0.092684 X_2 + 0.058961 X_3 \\ & - 0.011284 X_1^2 + 0.004091 X_2^2 - 0.009714 X_3^2 + 0.007618 X_1 X_2 \\ & + 0.009332 X_1 X_3 - 0.005557 X_2 X_3 \end{aligned} \quad (46.2)$$

The equation corresponding to overcut ( $Y_{OC}$ ) is given as

$$\begin{aligned} Y_{OC} = & 62.6051 + 1.3681 X_1 + 3.8956 X_2 + 1.6281 X_3 - 0.4556 X_1^2 \\ & - 0.9319 X_2^2 - 0.4669 X_3^2 + 1.0260 X_1 X_2 - 2.0035 X_1 X_3 - 2.0110 X_2 X_3 \end{aligned} \quad (46.3)$$

The equation corresponding to taper angle ( $Y_{TA}$ ) is given as

$$\begin{aligned} Y_{TA} = & 1.12257 + 0.33050 X_1 + 0.39814 X_2 + 0.24824 X_3 \\ & + 0.12185 X_1^2 + 0.12661 X_2^2 + 0.10048 X_3^2 + 0.16977 X_1 X_2 \\ & + 0.03273 X_1 X_3 - 0.04152 X_2 X_3 \end{aligned} \quad (46.4)$$

#### 46.4 Parametric Analysis Found on Response Surface Plots

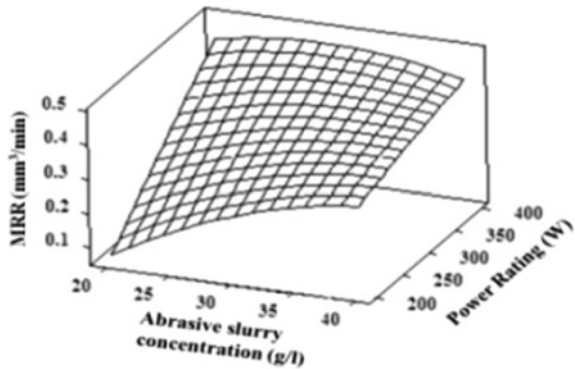
The effects of different process parameters of micro USM like abrasive slurry concentration, power rating, and tool feed rate on responses like material removal rate, overcut, and taper angle during micro hole drilling of quartz plate have been analyzed based on the response surface plots.

### 46.4.1 Parametric Effects on Material Removal Rate (MRR)

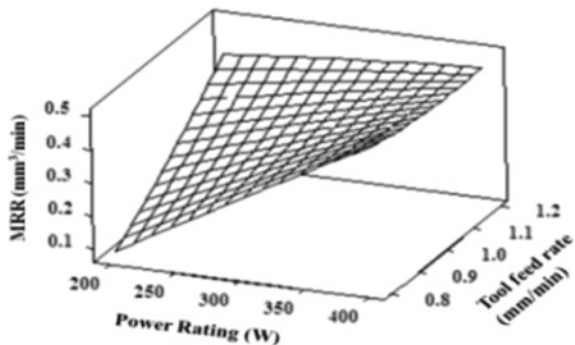
Abrasive slurry concentration is one of the important parameters which influences the machining characteristics. The response surface graph as shown in Fig. 46.3 illustrates the influence of abrasive slurry concentration and power rating on material removal rate at the same preset values of tool feed rate. Higher MRR can be obtained with higher value of abrasive slurry concentration and power rating because more material is removed with higher abrasive slurry concentration in micro ultrasonic machining. As power rating is higher, the abrasive particles strike on the workpiece with high applied force and as a result, material removal rate becomes higher at higher abrasive slurry concentration and higher power rating.

Figure 46.4 shows the influence of power rating and tool feed rate on MRR at the same preset value of abrasive slurry concentration. From the figure, it is clear that MRR increases with an increase in power rating and also with an increase in tool feed rate. As tool feed rate increases, the momentum of the abrasive particles increases, and as a result, MRR increases.

**Fig. 46.3** Effects of abrasive slurry concentration and power rating on MRR



**Fig. 46.4** Effects of power rating and tool feed rate on MRR

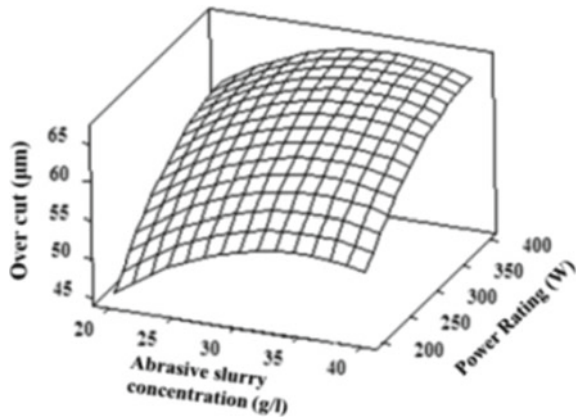


### 46.4.2 Parametric Effects on Overcut of Micro Hole

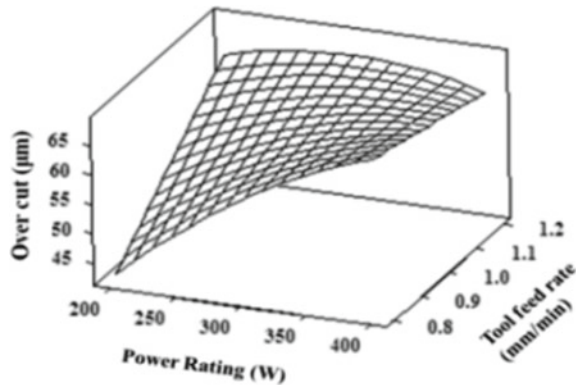
Figure 46.5 illustrates the influence of abrasive slurry concentration and power rating on overcut of hole at the same preset values of tool feed rate. From the graph, it is clear that lower value of overcut of hole have been observed at the lower value of abrasive slurry concentration and power rating. Overcut gradually increases from lower value to higher value of abrasive slurry concentration while the rate of increase of overcut is more with power rating during micro USM drilling operation.

Figure 46.6 shows the influence of power rating and tool feed rate on overcut of hole at the same preset value of abrasive slurry concentration. From response graph, it is observed that lower value of overcut of micro hole has been observed at the lower value tool feed rate and lower value of power rating. Overcut increases rapidly with an increase in tool feed rate at low power rating but overcut slowly increases with tool feed rate at a high power rating.

**Fig. 46.5** Effects of abrasive slurry concentration and power rating on overcut



**Fig. 46.6** Effects of power rating and tool feed rate on overcut

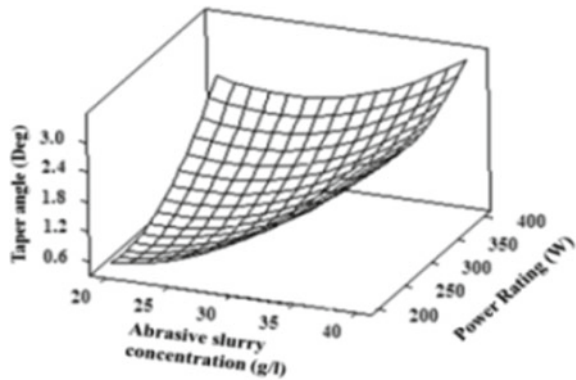


### 46.4.3 Parametric Effects on Taper Angle of Micro Hole

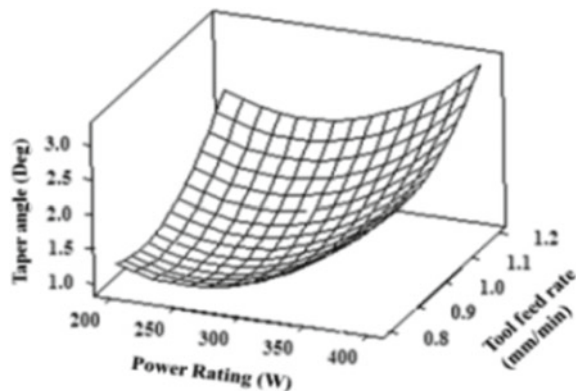
Figure 46.7 illustrates the effects of abrasive slurry concentration and power rating on taper angle at the same preset values of tool feed rate. The lower value of taper angle can be obtained with lower abrasive slurry concentration and power rating. At low abrasive slurry concentration, machining rate is also less. The cause of taper angle is that the time taken during machining at the entrance surface is more and accessibility of abrasive at the entrance of the micro hole is also more. Hence, entrance width of the micro hole is more. The presence of abrasive slurry is not as much at the bottom surface of the workpiece, so exit diameter of micro hole is less.

Figure 46.8 illustrates the influence of power rating and tool feed rate on taper angle of generated hole at the same preset values of abrasive slurry concentration. From response graph, it is clear that lower value of taper angle of generated hole has been observed at the lower value of tool feed rate and lower value of power rating. The taper angle of generated hole sharply increases with an increase in tool feed rate while power rating is high.

**Fig. 46.7** Effects of abrasive slurry concentration and power rating on taper angle



**Fig. 46.8** Effects of power rating and tool feed rate on taper angle



### 46.5 Multi Objective Optimization of Micro Ultrasonic Machining of Quartz

Multi-objective optimization of micro ultrasonic machining process parameters for generating micro hole on quartz plate has been performed based on desirability function analysis using MINITAB software. Multi-objective optimization has been done to obtain the best possible combination of process parameters for maximum material removal rate, minimum overcut, and minimum taper angle. Figure 46.9 demonstrates the result of multi-objective optimization of material removal rate, overcut, and taper angle. The optimal values of process parameters are obtained as abrasive slurry concentration of 23.43 g/l, power rating of 290.84 W, and tool feed rate of 0.80 mm/min. The maximum value of MRR, i.e., 0.2008 mm<sup>3</sup>/min, minimum value of overcut, i.e., 50.29 μm, and minimum value of half taper angle, i.e., 0.7880° were achieved. The value of overall composite desirability (d) is obtained as 1.

The experiments have been performed at optimal parametric combination and the actual responses were observed. Figure 46.10 shows the micro hole on quartz.

**Fig. 46.9** Multi objective optimization of material removal rate, overcut, and taper angle during micro ultrasonic machining of quartz

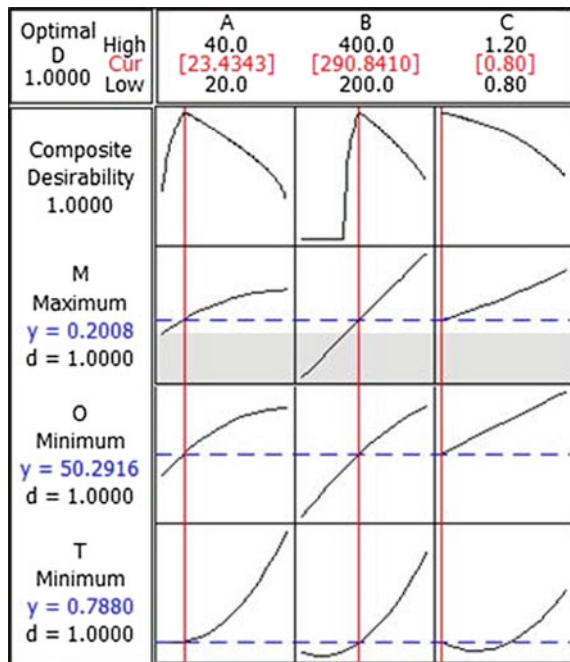
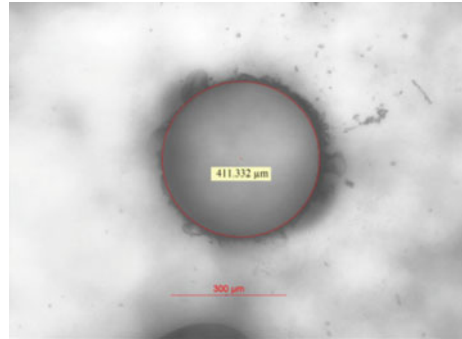


**Fig. 46.10** Micro hole on quartz



## 46.6 Conclusions

The investigational results emphasize that the micro USM characteristics like material removal rate, overcut, and taper angle for generating micro hole on quartz are influenced by the various major machining parameters such as abrasive slurry concentration, power rating, and tool feed rate. Based on the response surface plot and optimization analysis in the present investigation, the following conclusions have been drawn:

- (i) Micro USM process can be effectively used to generate micro hole on quartz.
- (ii) The developed empirical models on MRR, overcut, and taper angle are found as adequate to examine the effects of process parameters on response characteristics of micro hole on quartz by micro ultrasonic machining process.
- (iii) The multi-objective optimization was performed to obtain the optimal parametric setting for achieving maximum material removal rate, minimum overcut, and minimum taper angle. The optimal values of abrasive slurry concentration, power rating, and tool feed rate are obtained as 23.43 g/l, 290 W, and 0.8 mm/min, respectively. The maximum value of MRR has been obtained as 0.2008 mm<sup>3</sup>/min. The minimum value of overcut and taper angle has been achieved as 50.29 μm and 0.78800 respectively.

Few research works are reported on micro hole drilling on quartz by micro USM process. But, further research has to be carried out in the area of generation of microchannel and array of micro hole on quartz. Investigation of tool wear rate and surface roughness, etc., during micromachining of quartz by micro USM is also the area of research interest for wider application in modern micro-manufacturing industry.



## References

1. Zeng, W.M., Li, Z.C., Pei, Z.J., Treadwell, C.: Experimental observation of tool wear in rotary ultrasonic machining of advanced ceramics. *Int. J. Mach. Tools Manuf.* **45**, 1468–1473 (2005)
2. Sun, X.Q., Masuzawa, T., Fujino, M.: Micro ultrasonic machining and its applications in MEMS. *Sensor Actuat. A* **57**(2), 159–164 (1996)
3. Masuzawa, T.: State of the art of micromachining. *Ann. CIRP* **49**(2), 473–488 (2000)
4. Sundaram, M.M., et al.: Micro ultrasonic machining using oil based abrasive slurry. In: *Proceedings of the ASME International Manufacturing Science and Engineering Conference*, Evanston, pp. 221–226 (2008)
5. Jain, V.: Application of Taguchi approach in the optimization of cutting parameters in micro-ultrasonic drilling process. *Int. J. Eng. Res. Appl. (IJERA)* (2014). ISSN: 2248-9622
6. Kumar, S., Hansda, B., Das, S., Doloi, B., Bhattacharyya, B.: Micro hole fabrication on quartz using ultrasonic micromachining process. *Int. J. Precis. Technol.* **7**, 222–236 (2017)

# Chapter 47

## Investigations into the Effect of Varying Electrode Diameter on Cutting Rate and Kerf Width in WEDM of Varying Thickness Inconel718



Susheel Ramchandra Dhale  and Bhagyesh B. Deshmukh

**Abstract** Wire electrical discharge machining of varying thickness Inconel718 plate of 8, 10, and 12 mm, which is widely used as aircraft turbine material having extremely good high-temperature characteristics, is done to investigate the effect of zinc-coated wire electrode diameter of 0.15, 0.20, and 0.25 mm on the cutting rate which is the most important economic considerations in the manufacturing and kerf width is known to be dimensional accuracy of the WEDM. The commonly used large diameter of wire we end with larger kerf width is not desirable in precision jobs. In the ocean of research on WEDM parametric effects, light is focused on the effect of using small diameter wire on cutting rate, checking its feasibility with high thickness plates and accuracy it gives. Taguchi L27 array has been used for experimental design. And further to that, ANOVA is done to find the most influencing factor. It is found that small wire diameter gives good cutting rate along with promisingly small kerf width.

**Keywords** WEDM · Cutting rate · Kerf · Inconel

### 47.1 Introduction

Nickel-based superalloys are widely utilized in high-temperature applications like gas turbines in aerospace [1]. It is calculated that nickel-based superalloys compose over half the materials that are utilized in the aircraft market, particularly for red-hot segment parts like rotary engine disk, blades, and combustors. WDEM is the most suitable machine for machining such superalloys. Wire electrical discharge machining is a nontraditional, noncontact, material removal process that uses a discontinuously sparking wire in dielectric media (Fig. 47.1). WEDM attracts the researchers all over the world because of its fascinating features and continuously increasing the spectrum of being able to machine almost anything with little modifications. Anything challenging is also at the same time proactive for research fraternity. The

---

S. R. Dhale (✉) · B. B. Deshmukh  
Walchand Institute of Technology, Ashok Chowk, Solapur 413006, India  
e-mail: [srdhale@dbatu.ac.in](mailto:srdhale@dbatu.ac.in)

© Springer Nature Singapore Pte Ltd. 2020  
M. S. Shunmugam and M. Kanthababu (eds.), *Advances in Unconventional Machining and Composites*, Lecture Notes on Multidisciplinary Industrial Engineering, [https://doi.org/10.1007/978-981-32-9471-4\\_47](https://doi.org/10.1007/978-981-32-9471-4_47)

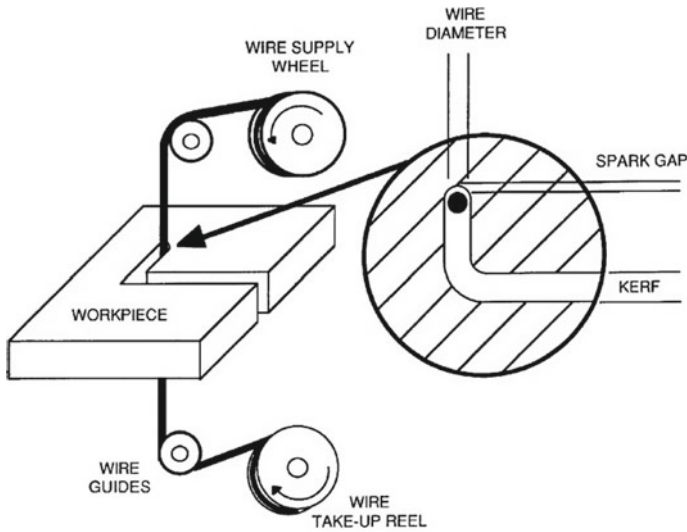


**Fig. 47.1** WEDM process and kerf width [3]

challenges ahead are the machining at faster cutting speed with higher accuracy. Widely accepted theories for material removal rate are an electromechanical theory, thermomechanical theory, and thermoelectrical theory [2]. But selecting the proper combination of all electrical parameters for a particular type of workpiece is still a challenging task and here a lot of research is witnessing today. The researchers have tried to optimize the process parameters in the recent past.

The parameters such as pulse on time, pulse off time, servo voltage, wire feed, flushing pressure, and wire tension were studied while cutting of high-strength armor steel by Bobbili [4]. The impact of WEDM input parameters on cutting speed during machining of titanium was evaluated. The study concluded that pulse on time, pulse off time, and servo voltage were the most contributing factors for cutting speed [5]. Voltage and current are dominant factors to determine kerf width along with feed rate reported by Sulaiman [6]. But for the simultaneous responses such as cutting rate and kerf width, not only electrical parameters and their setting are important rather one should look into the insight cause of cutting rate and kerf width. Wire electrode-related parameters such as material, coating effect, wire feed, and wire tension play a vital role reported in research work. Wire diameter among all other wire related parameters is the deciding factor for high cutting rate and kerf width. Pramanik [7] investigated the degradation of wire electrode by varying the on time and tension to uncover the interaction between machining parameters. The electric sparks not only remove the workpiece material but also affect the dimensions of the electrode. Further, the original circular-shaped became oval after machining regardless of the workpiece material-type indicating permanent deformation of the wire due to high temperature and possible interaction with electrolyte and melted workpiece material. Antar [8] studied the material effect of the wire electrode, and brass has turned into

the most usually used electrode material. He explored the impact on the productivity, workpiece surface, surface roughness, and other surface integrity by comparing coated with brass wire. Increase in productivity of 40% was recorded with coated wire, under the same operating conditions. Unune [9] conjointly thought of the result of assorted conductor materials like copper, copper–tungsten, and metallic element on material removal rate and conductor wear rate in the micro-EDM drilling of Inconel718. It absolutely was found that copper electrodes end up in highest MRR the least bit values of gap voltage and capacitance followed by copper–tungsten and tungsten electrodes. Prohaszka [10] unconcealed that machinability throughout WEDM was improved significantly with the correct combination of mechanical, physical, and geometrical properties of the conductor. Electrode materials ought to have high melting and evaporation temperature. The coating could increase the cutting potency considerably. Rajurkar [11] used Taguchi technique to analyze the result high-speed brass wire and zinc-coated wire. The influence of zinc-coated brass wire on the performance of WEDM was compared with high-speed brass. Compared with high-speed brass wire, zinc-coated brass wire ends up in higher cutting speed and smoother surface finish. Also, SEM images revealed that uncoated wire produces a surface finish with more cracks, craters, and liquefied drops. Also, high-speed brass wire resistance against wire rupture in tough conditions, high pulse width and low time between two pulses, was rather more than zinc-coated wire since the durability of zinc-coated wire was less than the high-speed brass durability. Chalisgaonkar [5] studied the result of brass and zinc-coated along with other parameters. The microstructure analysis indicated that zinc-coated wire produced an overlapping thick layer of debris while uncoated wire made an additional number of craters underneath similar higher pulse discharge energy conditions. Yadav et al. [12] created a comparative study of zinc-coated and bare electrode in EDM. It was concluded that the coated tool electrode has a significant effect on the material removal rate, tool wear, and surface finish. The copper tool without coating gives poor performance in machining. It gives high surface roughness value and maximum tool wear rate as compared to coated tool with the same machining parameters. The coated tool takes less machining time as compared to the naked copper tool at the constant machining parameters. Priyaranjan [13] has studied the effect of brass wire diameter on the surface integrity. It was observed that with smaller diameter wire the cutting speed is 20% higher compared to larger diameter wire under similar experimental conditions. The surface roughness of larger diameter wire is found to be 8% higher compared to smaller diameter wire under similar experimental conditions. Smaller diameter wire is well suited for cutting for the delicate specimen. However, research with varying diameter is restricted with plain brass wire only. So in this paper, proven zinc-coated wires of 0.15, 0.20, and 0.25 micron were specifically manufactured to study the impact of small diameter wire with large wire diameter under the similar operating conditions. The present research is mainly focused on small zinc wire diameter analysis for improving the cutting rate and improving the accuracy of WEDM in terms of kerf width and understanding its feasibility with various thickness jobs.

## 47.2 Materials and Methods

### 1. Workpiece Material

A peculiar profile cutting of Inconel-718 blocks of (25 × 25) mm of varying thickness 8, 10, and 12 mm is carried out in this research. The chemical composition of Inconel-718 tested with a spectrometer from a reputed lab is given in Table 47.1.

### 2. Electrode Material

The specifically manufactured zinc-coated wire of 0.15, 0.20, and 0.25 mm diameter are used.

### 3. Machine Tool

Electronica manufactured Ecocut model is employed to carry out this research.

### 4. Experimental Design

Taguchi L27 orthogonal array is utilized. Five process parameters, namely, wire diameter, pulse on time (Ton), pulse off time (Toff), wire feed (Wf), and work material thickness were selected as input variables during peculiar profile cutting of Inconel-718. Four two-way interactions of Wire dia × Pulse on, Wire Dia × pulse off, Wire dia × wire feed, and Wire dia × work material thickness were selected (Table 47.2).

### 5. Measurement of Performance Measures

Two machining outcomes, namely, the cutting rate and kerf width, were taken for the investigation (Fig. 47.2).

**Cutting rate** is directly recorded from the machine display unit, and also it is found by total cutting length divided by the time recorded for the cut in mm/min.

**Table 47.1** The chemical composition of Inconel718

Element	wt%	Element	wt%
Ni	54.132	Ti	0.89
Fe	19.6	Co	0.26
Cr	16.5	Si	0.2
Nb	5.13	Mn	0.11
Mo	3.14	C	0.038

**Table 47.2** Wire EDM process parameters and their level values

Process parameter (Unit)	Parameter designation	Level-1	Level-2	Level-3
Wire diameter (mm)	A	0.15	0.20	0.25
Pulse on time (μs)	B	114	117	120
Pulse off time (μS)	C	58	55	52
Wire feed (m/min)	D	6	8	10
Work material thickness (mm)	E	8	10	12



Fig. 47.2 Cutting rate and kerf width measurement

**kerf width** is measured by Mitutoyo toolmakers TM500 microscope. It is a summation of the wire diameter to two-wire workpiece gap distance [3]. Additionally, the camera is used for capturing images with Tsview 7 software. Kerf width is directly recorded in excel to lessen the manual observation error.

### 47.3 Results and Discussions

To assess the impact of machining parameters on performance measures (cutting rate and kerf width), a powerful Taguchi’s experimental technique has been utilized for the plan of the experiment [14]. Taguchi technique helps to find the variability and at the same time with less no experiment [15]. The L27 orthogonal array has been used. All the analysis is carried with Minitab17, statistical software. The experiments were conducted in random order, and each experiment was repeated twice and some few of them thrice to reduce the experimental error and to confirm respectively. Further to that, ANOVA is done to find out the most affecting parameters. The experimental results obtained as per Taguchi’s L27 orthogonal array are tabulated in Table 47.3.

1. **Taguchi signal-to-noise ratio (S/N Ratio)** is the ratio of signal-to-noise where signal represents the desired value and noise represents the undesirable value. Therefore, S/N ratio is the mean to square deviation ratio [3]. The characteristic that higher observed value speaks to better performance accordingly cutting rate is taken as higher the better and where lower observed value represents better performance kerf width is selected as smaller the better.

From the main effects plots as per Fig. 47.3, for S/N ratio of curring rate, it is observed that small wire diameter of 0.20 mm gives the highest cutting rate than large wire diameter wire of 0.25 mm. Also, cutting rate is increased with the increase in pulse on and decrease in pulse off time [5]. Cutting rate increases with an increase in wire feed and decreases with an increase in work material thickness from 8 to 12 mm.

**Table 47.3** Experimental results according to Taguchi's L27 array

Expt. No.	Wire dia	Ton	Toff	W feed	Block thick	Cutting rate 1	Cutting rate 2	Kerf width 1	Kerf width 2
1	0.150	114	58	6	8	0.82	0.81	0.2155	0.189
2	0.150	114	55	8	10	0.73	0.71	0.1995	0.2045
3	0.150	114	52	10	12	0.59	0.62	0.209	0.19
4	0.150	117	58	8	12	0.51	0.5	0.2125	0.1935
5	0.150	117	55	10	8	1.07	1.09	0.208	0.1945
6	0.150	117	52	6	10	1.06	1.07	0.216	0.192
7	0.150	120	58	10	10	0.88	0.9	0.2205	0.2005
8	0.150	120	55	6	12	0.71	0.69	0.2205	0.2145
9	0.150	120	52	8	8	1.55	1.49	0.215	0.199
10	0.200	114	58	6	8	0.97	1.06	0.2775	0.2625
11	0.200	114	55	8	10	0.92	0.95	0.263	0.258
12	0.200	114	52	10	12	0.74	0.85	0.2465	0.251
13	0.200	117	58	8	12	0.65	0.74	0.257	0.2565
14	0.200	117	55	10	8	1.41	1.43	0.2495	0.247
15	0.200	117	52	6	10	1.29	1.34	0.27	0.264
16	0.200	120	58	10	10	1.13	1.18	0.2655	0.257
17	0.200	120	55	6	12	0.88	1	0.2665	0.2705
18	0.200	120	52	8	8	1.97	1.96	0.2665	0.264

(continued)

Table 47.3 (continued)

Expt. No.	Wire dia	Ton	Toff	W feed	Block thick	Cutting rate 1	Cutting rate 2	Kerf width 1	Kerf width 2
19	0.250	114	58	6	8	0.77	0.81	0.308	0.309
20	0.250	114	55	8	10	0.7	0.72	0.308	0.305
21	0.250	114	52	10	12	0.65	0.66	0.316	0.3005
22	0.250	117	58	8	12	0.55	0.58	0.321	0.2909
23	0.250	117	55	10	8	1.1	0.98	0.326	0.3105
24	0.250	117	52	6	10	1.03	0.93	0.32	0.3015
25	0.250	120	58	10	10	0.92	0.83	0.282	0.2985
26	0.250	120	55	6	12	0.69	0.7	0.29	0.3095
27	0.250	120	52	8	8	1.48	1.48	0.283	0.306



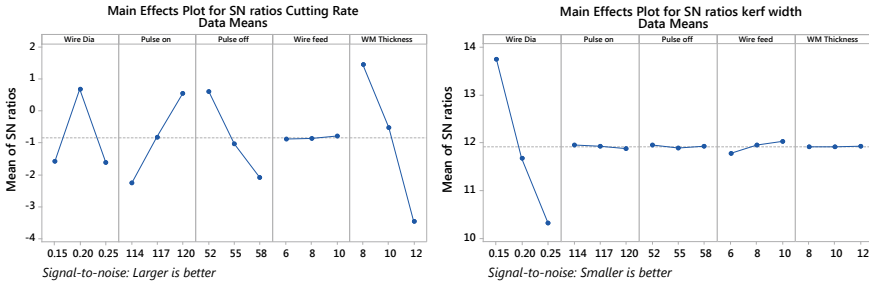


Fig. 47.3 Main effects’ plot for SN ratio

From the main effects plots of kerf width, it is clear that as wire diameter increases, kerf width increases and there is no effect of work material thickness on the kerf width. A negligible effect of the pulse on, pulse off on kerf width is noticed here.

2. **ANOVA:** ANOVA (analysis of variance) is a factually based, objective decision-making tool for identifying any differences in the response that might be attributed to the variation in the control parameters considered in the study. The most important statistic in the analysis of variance table is the p-value. There is a p-value for each term in the model (except for the error term). The p-value for a term tells you whether the effect for that term is significant. In this research, the confidence interval was set at 95% ( $\alpha = 0.05$ ). Any factor having a p-value less than set  $\alpha$  value is to be considered a significant factor. S, R, adjusted R, and predicted R are measures of how well the model fits the data. These values can help you select the model with the best fit. S is measured in the units of the response variable and represents the standard distance that data values fall from the regression line. R ( $R^2$ ) describes the amount of variation in the observed response values that is explained by the predictor(s). Adjusted R is a modified R that has been adjusted for the number of terms in the model.  $R^2$  (pred) is a measure of how well the model predicts the response for new observations. The results of ANOVA for cutting rate and kerf width are tabulated in Tables 47.4 and 47.5.

From the ANOVA of cutting rate work, material thickness is proved to be the main factor deciding cutting rate. Nevertheless to note, wire diameter is the fourth parameter affecting the cutting rate. Pulse on and pulse off are the major factor for deciding cutting rate. Among the interactions, Figs. 47.4 and 47.5, wire diameter and work material thickness interaction is the most influencing interaction and after that wire diameter and pulse on time interaction is important interaction.

From the ANOVA of kerf width, it is revealed that wire diameter is the most influencing parameter. Next important parameter is wire feed. Among the interactions, wire diameter and pulse on is the most important interaction.

**Discussion on the Experimental Results:**

It is found that the smaller diameter wire efficiently cuts the material at the higher cutting rate [13, 15]. This could be due to the rapid movement of wire into the material

**Table 47.4** ANOVA for cutting rate

Factor	DF	Adj SS	Adj MS	F-value	P-value
Wire dia	2	0.84758	0.42379	251.20	0.000
Pulse on	2	1.12378	0.56189	333.06	0.000
Pulse Off	2	1.10440	0.55220	327.32	0.000
Wire feed	2	0.07295	0.03647	21.62	0.000
WM thickness	2	2.74455	1.37227	813.42	0.000
Wire dia * Pulse on	4	0.03402	0.00850	5.04	0.004
Wire dia * Pulse off	4	0.01923	0.00481	2.85	0.043
Wire dia * Wire feed	4	0.00522	0.00130	0.77	0.552
Wire dia * WM thickness	4	0.05922	0.01480	8.78	0.000
Error	27	0.04555	0.00169		
Total	53	6.05650			
Model summary	S 0.0410736		R <sup>2</sup> 99.25%	R <sup>2</sup> (adj) 98.52%	R <sup>2</sup> (pred) 96.99%

**Table 47.5** ANOVA for kerf width

Factor	DF	Adj SS	Adj MS	F-value	P-value
Wire dia	2	0.089533	0.044767	388.21	0.000
Pulse on	2	0.000011	0.000006	0.05	0.953
Pulse off	2	0.000038	0.000019	0.17	0.848
Wire feed	2	0.000464	0.000232	2.01	0.153
WM thickness	2	0.000006	0.000003	0.03	0.974
Wire dia *Pulse on	4	0.001484	0.000371	3.22	0.028
Wire dia *Pulse off	4	0.000168	0.000042	0.36	0.832
Wire dia *Wire Feed	4	0.000401	0.000100	0.87	0.496
Wire dia *WM thickness	4	0.000162	0.000041	0.35	0.840
Error	27	0.003114	0.000115		
Total	53	0.095381			
Model summary	S 0.0107385		R <sup>2</sup> 96.74%	R <sup>2</sup> (adj) 93.59%	R <sup>2</sup> (pred) 86.94%



Fig. 47.4 Interaction plot for SN ratio cutting rate

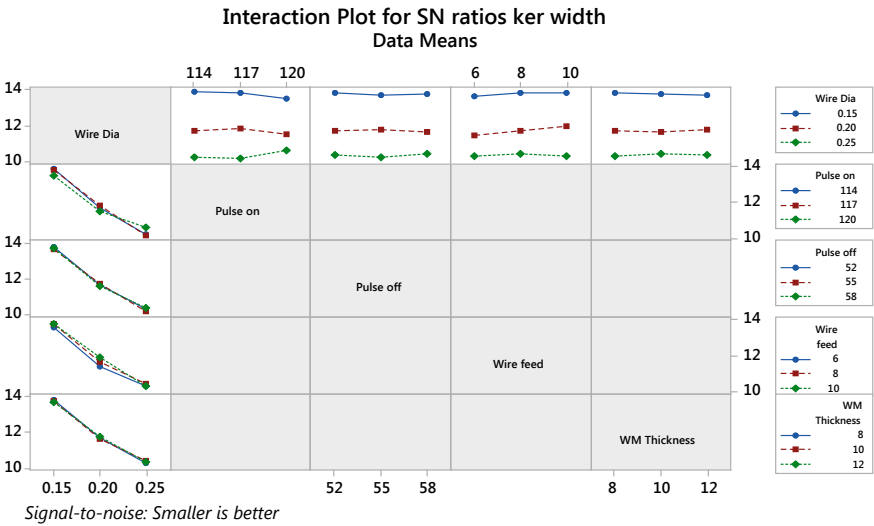


Fig. 47.5 Interaction plot for SN ratio kerf width

owing to its smaller cross-sectional area. [13]. However, in case of larger diameter wire, the cutting rate reduces due to the more cross-sectional area of the wire. Further, the small diameter wire has more resistance and hence more heat generation leading to larger cutting rate. The surface area that needs to be vaporized is also a deciding factor.

From the ANOVA of kerf width, also it is confirmed that wire diameter is the most influencing parameter for kerf width. As 0.15 mm diameter gives maximum kerf width of 0.22 mm, 0.25 diameter wire gives the kerf width of 0.3105 mm. The difference in their diameter is almost 0.10 mm, and so accordingly kerf width increases as an increase in the cross-sectional area of the electrode. Also, there is a significant effect of the interaction of wire diameter and pulse on. The amount of current supplied for the moment and the diameter of the wire are crucial factors in deciding the performance of the WEDM.

## 47.4 Conclusions

1. The small wire diameter of 0.20 mm gives the highest cutting rate of 1.97 mm/min at the same operating conditions. Work material thickness is the deciding factor in cutting rate.
2. WEDM accuracy given in manufacturer catalogue is one micron. Small wire diameter gives the maximum kerf width of 0.22 mm, and hence can be used for high-precision jobs requiring accuracy of one micron.
3. The 0.15-mm-diameter wire can be easily used to cut Inconel718, 12 mm thick which is very appreciable.

## 47.5 Future Scope

Small wire diameter is the future of WEDM. All the parametric effects need to be explored so as to get maximum cutting speed and minimum kerf width.

**Acknowledgements** The author wishes to acknowledge the TEQIP-II, Dr. Babasaheb Ambedkar Technological University, Lonere for the availability of funds for carrying experimentation work.

## References

1. Li, L., Guo, Y.B., Wei, X.T., Li, W.: Surface integrity characteristics in wire-EDM of inconel718 at different discharge energy. *Procedia CIRP* **6**, 220–225 (2013)
2. Han, F., Jiang, J., Yu, D., Tosun, N., Cogun, C., Tosun, G.: Influence of machining parameters on surface roughness in finish cut of WEDM. *J. Mater. Process. Technol.* **34**(5–6), 538–546 (2007)
3. Tosun, N., Cogun, C., Tosun, G.: A study on kerf and material removal rate in wire electrical discharge machining based on Taguchi method. *J. Mater. Process. Technol.* **152**(3), 316–322 (2004)
4. Bobbili, R., Madhu, V., Gogia, A.K.: Effect of wire-EDM machining parameters on surface roughness and material removal rate of high strength armor steel. *Mater. Manuf. Process.* **28**(4), 364–368 (2013)
5. Chalisingaonkar, R., Kumar, J.: Parametric optimization and modelling of rough cut WEDM operation of pure titanium using grey-fuzzy logic and dimensional analysis parametric optimization and modelling of rough cut WEDM operation of pure titanium using grey-fuzzy logic and dimensional analysis, pp. 1–28 (2014)
6. Kasim, M.S., Mohamad, E., Sulaiman, M.A.: Study on cutting parameter on kerf width using wire electrical discharge machining of Inconel718 (2014)
7. Pramanik, A., Basak, A.K.: Degradation of wire electrode during electrical discharge machining of metal matrix composites. *Wear* **346–347**, 124–131 (2016)
8. Antar, M.T., Soo, S.L., Aspinwall, D.K., Jones, D., Perez, R.: *Procedia engineering productivity and workpiece surface integrity when WEDM aerospace alloys using coated wires.* *Procedia Eng.* **19**, 3–8 (2012)
9. Unune, D.R.: Performance investigations of different electrode materials in micro-EDM drilling of inconel-718
10. Prohaszka, J., Mamalis, A.G., Vaxevanidis, N.M.: The effect of electrode material on machinability in wire electro-discharge machining. **69**, 233–237 (1997)
11. Nourbakhsh, F., Rajurkar, K.P., Malshe, A.P., Cao, J.: Wire electro-discharge machining of titanium alloy. *Procedia Soc. Behav. Sci.* **5**, 13–18 (2013)
12. Yadav, A.K., Yadav, S.K.S.: Experimental study of Zinc coated and bare electrode machining of Ni-alloy for EDM-A comparative study
13. Sharma, P., Chakradhar, D., Narendranath, S.: Effect of wire diameter on surface integrity of wire electrical discharge machined Inconel 706 for gas turbine application. *J. Manuf. Process.* **24**, 170–178 (2016)
14. Mahapatra, S.S., Patnaik, A.: Optimization of wire electrical discharge machining (WEDM) process parameters using Taguchi method. *Int. J. Adv. Manuf. Technol.* **34**, 911–925 (2007)
15. Ishfaq, K., Mufti, N.A., Mughal, M.P., Saleem, M.Q., Ahmed, N.: Investigation of wire electric discharge machining of stainless-clad steel for optimization of cutting speed. *Int. J. Adv. Manuf. Technol.* **96**(1–4), 1429–1443 (2018)

# Chapter 48

## Comparative Evaluation of Drilling on GFRP Made by Different Fabrication Techniques



R. Raja and Sabitha Jannet

**Abstract** Glass-fiber-reinforced plastics (GFRP) are used in engineering applications such as automotive, aerospace, and industrial applications due to their significant advantages over other materials. The optimization is done using Taguchi method and the influence of process parameters is analyzed using ANOVA analysis and the corresponding regression equations and graphs are plotted. Fabrication of GFRP is done by manual layup method and compression molding using glass fiber and epoxy resin. Acquire tools, drill bits (twisted carbide drill bit). Perform high-speed drilling on GFRP by varying spindle speed, feed, and drill bit diameter. Find thrust force and torque associated with drilling using kistler dynamometer. Analyze and compare delamination at the entry and exit for GFRP made by Manual Layup and compression molding. Analyze tool wear and matrix composition through SEM analysis. Optimize thrust force, torque, and delamination at the exit and entry using Taguchi design of experiment. Find optimal machining parameters for best quality drilled holes.

**Keywords** Manual layup · Compression molding · ANOVA · Optimization

### 48.1 Introduction

Due to the inhomogeneous and anisotropic nature of the GFRP composite, machining of GFRP is comparatively tricky than metals. GFRP is fabricated using two different production methods, and high-speed drilling is done on the fabricated specimen. Glass-fiber-reinforced plastic refers to a composite plastic which has been reinforced with glass fibers. It consists of a plastic matrix that may be of thermosetting plastic reinforced by fine fibers of glass [1]. The fiberglass is a lightweight, stable, and robust material which has broad applications. Its bulk strength and weight properties are favorable when compared to metals. A lot of research has been conducted to

---

R. Raja · S. Jannet (✉)

Mechanical Engineering Department, Karunya Institute of Technology and Sciences, Coimbatore 641114, Tamil Nadu, India

e-mail: [sabithajannet@gmail.com](mailto:sabithajannet@gmail.com)

© Springer Nature Singapore Pte Ltd. 2020

M. S. Shunmugam and M. Kanthababu (eds.), *Advances in Unconventional Machining and Composites*, Lecture Notes on Multidisciplinary Industrial Engineering, [https://doi.org/10.1007/978-981-32-9471-4\\_48](https://doi.org/10.1007/978-981-32-9471-4_48)

583

achieve efficient drilling of composite materials. Experimental results suggested that feed rate is seen to make the most substantial contribution to delamination, thrust force, and tool wear during drilling of composite laminates [2]. The results obtained showed that twist drill bit produces less cutting pressure and thrust force than jobber length type drill bit for the same set of cutting parameters. The twist drill delivers less damage on GFRP than the jobber length type drill and has better efficiency. Lesser delamination was observed after drilling with the carbide tools with comparison to cemented tungsten carbide drills. In a twist drill, lower delamination factor was observed compared to the four flute drill [3]. An increase in spindle speed did not result in significant elevation of the damage. For HSM, delamination is dictated by the parameter cutting temperature, i.e., with the softening of the matrix, delamination will not be affected by feed and speed [4]. Minimum amount of delamination on both entry and exit of the drilling was observed with a better surface finish and tool life with high cutting speed and low feed [5]. The increase in the fiber orientation angle increases the delamination factor in the drilling of GFR–polyester composites [6]. The increase in thrust force increases the delamination factor [4]. Two advanced drilling methods such as vibration-assisted twist drilling and high-speed drilling were used to decrease drilling-induced delamination [7]. The peel-up and push-out delamination of woven/epoxy composite has an inverse relationship with cutting speed. The delamination enjoys a direct relationship with thrust force and feed. The delamination associated with push-out is more severe than that of peel-up [8, 9]. It then describes the principal characteristics of the epoxy resins and how it is possible to enhance them by adding several fillers to the epoxy system. Production methods play an important role in the delamination of GFRP, spindle speed is a significant factor in high-speed drilling, and feed rate is the most influential parameter.

## 48.2 Materials and Methods

The high-speed vertical milling machine is modified to measure the thrust force and torque, and for this Syscon dynamometer is attached to the drilling machine. It was fixed in such a way that the axis of the drill bit passes through the center of the dynamometer. Based on the literature, spindle speed (rpm), feed (mm/rev), and drill bit diameter (mm) were identified as significant process parameters which influence the geometrical and dimensional integrity of the holes. Levels of these parameters were selected based on the trial runs, which shows the process parameters and their levels (Table 48.1).

We use the above three sets of spindle speed, feed, and drill bit diameter to perform nine run experiments on the specimen. The spindle speed, feed rate, and drill bit diameters are selected based on the references.

### 48.2.1 Manual Layup Process

Hand layup is a simple and widely used process. It is treated with vinyl ester resin for preventing sticking. The mixing is done in 10:1 ratio, i.e., for 100 ml of resin 10 ml hardener is used. The mixture is in gel form. Gel coat layers are placed on the mold to give a decorative and protective surface. The reinforcement (woven rovings or chopped strand mat) is placed in a mould and coated with thermosetting resin.

After curing, the part was disassembled from the mold. The equipment used is simple since pressure and temperature are not employed. Figure 48.1 shows the laminates which were prepared by hand layup method.

### 48.2.2 Compression Molding

Compression molding machine is used to mold materials like rubber, plastic, composites, etc. They can be used for wide variety of functions as bounding, laminating, assembling, etc. The compression molding machine consists of two heated plates (molds), one at the top and the other at the bottom, which are used for pressing. Uniform and constant curing pressure, is an essential requisite for accurate molding, was achieved by the presses and modern energy-efficient hydraulic system is employed.

**Table 48.1** Drilling process parameters

Spindle speed (rpm)	Feed (mm/rev)	Drill bit diameter (mm)
4000	0.005	3
5000	0.015	5
6000	0.025	8

**Fig. 48.1** GFRP made of manual layup method





**Fig. 48.2** Laminated compression molding



The temperature of the plates can be adjusted. Compression molded laminate is as shown in Fig. 48.2.

Wax is applied to the polythene sheet, which will help in easy removal of the molded material from the polythene sheet. An aluminum casing is kept on the polythene sheet. The reinforcement material is placed inside the aluminum casing. Epoxy resin mixed with hardener in 10:1 ratio is poured over the reinforcement material and spread using a roller. The reinforcement material is kept layer by layer on top until the desired thickness is obtained. Another polythene sheet is kept on the top. The above materials are then held inside the compression molding machine between the heated pressing plates. Plates are maintained at a temperature of 80 °C. Curing is done at high temperature and high pressure for 2 h.

### **48.2.3 Vertical Machining Center**

The V33 vertical machining focuses on rapid machining with great exactness, proficient chip expulsion, and simple operation. The shaft includes Makino's remarkable center cooling and under-race lubricating framework, limiting heat distortion at high axle speeds. Coordinated development of the shaft and drive engine rotor diminishes vibration amid rapid task

Figure 48.3 shows a quick drilling setup with the dynamometer. Very high cutting speeds, extended tool life, and various materials can be machined with carbide tools. Long periods of drilling can be achieved with these tools. Figure 48.4 shows the different drill bits used which are made of carbide and their diameters are 3, 5, and 8 mm in this study.

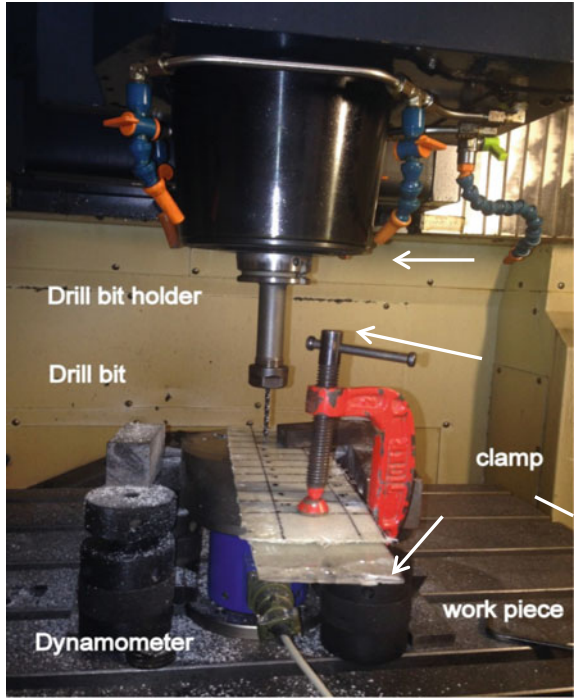
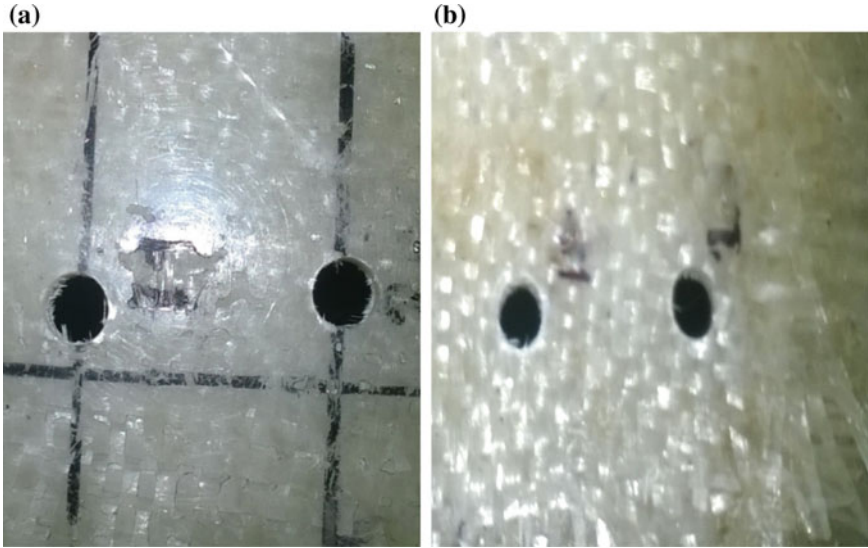


Fig. 48.3 High-speed drilling setup



Fig. 48.4 Carbide drill bits used



**Fig. 48.5** Delamination. **a** Entry. **b** Exit

#### **48.2.4 Delamination Factor**

Delamination is a mode of failure for composite materials. It is caused due to the weak bonding of constituents. Delamination causes layers of glass fibers to separate after repeated cyclic stress. This makes the material to lose the mechanical toughness. The ratio of the maximum diameter ( $D_{max}$ ) of delamination to the diameter of the hole ( $D$ ) determines the delamination factor.

$$F_d = D_{max}/D$$

Figure 48.5a, b shows the delamination at entry and exit, respectively.

#### **48.2.5 Design of Experiment**

For the same set of operating parameters, drilling experiments were performed on the laminates prepared by manual layup method and compression molding method. Table 48.2 shows results of laminate made by compression molding method and Table 48.3 shows the results of laminate made by manual layup method.

For the same set of trial conditions, laminate prepared by compression molding gave desirable results. That is, lesser thrust force, lesser torque, and lesser delamination (both at entry and exit) are achieved in the laminate prepared by compression molding.

**Table 48.2** Compression molding L9 orthogonal array

Run (rpm)	Feed (mm/rev)	Drill bit dia (mm)	Thrust force (n)	Torque (nm)	Delamination factor at entry	Delamination factor at exit
4000	0.005	3	24	0.03	1.05	1.04
4000	0.015	5	28	0.06	1.12	1.09
4000	0.025	8	44	0.15	1.17	1.11
5000	0.005	5	20	0.02	1.05	1.03
5000	0.015	8	32	0.08	1.08	1.06
5000	0.025	3	35	0.1	1.11	1.09
6000	0.005	8	18	0.02	1.04	1.02
6000	0.015	3	20	0.04	1.09	1.06
6000	0.025	5	26	0.06	1.16	1.12

**Table 48.3** Manual layup L9 orthogonal array

	Run (rpm)	Feed (mm/rev)	Drill bit dia (mm)	Thrust force (n)	Torque (nm)	Delamination factor at entry	Delamination factor at exit
1	4000	0.005	3	20	0.02	1.08	1.12
	4000	0.015	5	24	0.04	1.11	1.15
	4000	0.025	8	42.5	0.15	1.19	1.22
	5000	0.005	5	18	0.01	1.04	1.06
	5000	0.015	8	28	0.06	1.09	1.12
	5000	0.025	3	30	0.08	1.15	1.17
	6000	0.005	8	16	0.01	1.11	1.15
	6000	0.015	3	18	0.02	1.13	1.17
	6000	0.025	5	24	0.04	1.16	1.20

Tables 48.4 and 48.5 show the significance of each input parameter on the response delamination factor at the entry. In both cases, feed is the most significant parameter which is followed by spindle speed and drill bit diameter.

Tables 48.6 and 48.7 show the significance of each input parameter on the response delamination factor at the exit. In both cases, feed is the most significant parameter which is followed by spindle speed and drill bit diameter.

Tables 48.8 and 48.9 show the significance of each input parameter on the response torque. In both cases, feed is the most significant parameter which is followed by spindle speed and drill bit diameter.

Tables 48.10 and 48.11 show the significance of each input parameter on the response thrust force. In both cases, feed is the most significant parameter which is followed by spindle speed and drill bit diameter. Regression analysis is used when you want to predict a continuous dependent variable from some independent variables.

**Table 48.4** ANOVA analysis delamination factor at the entry (compression molding)

Col#/factor	DOF (f)	Sum of sqrs. (S)	Variance (V)	F-ratio (F)	Pure sum (S')	Percent P(%)
Spindle speed	2	0	0	6.219	0	5.167
Feed	2	0.008	0.004	88.227	0.008	86.357
Drill bit diameter	2	0	0	5.56	0	4.515
Other errors	2	-0.001	-0.001			3.961
Total	8	0.01				100.00

**Table 48.5** Delamination factor at the entry (manual layout)

Col#/factor	DOF (f)	Sum of sqrs. (S)	Variance (V)	F-Ratio (F)	Pure sum (S')	Percent P(%)
Spindle speed	2	0.002	-0.001	9.564	0.002	14.903
Feed	2	0.012	-0.006	43.115	0.012	73.293
Drill bit diameter	2	0.001	0	3.782	0	4.841
Other errors	2	-0.001	-0.001			6.963
Total	8	0.016				100.00

**Table 48.6** Delamination factor at the exit (compression molding)

Col#/factor	DOF (f)	Sum of sqrs. (S)	Variance (V)	F-ratio (F)	Pure sum (S')	Percent P(%)
Spindle speed	2	0.001	0	6.289	0.001	7.79
Feed	2	0.015	0.007	56.583	0.014	81.86
Drill bit diameter	2	0.001	0	4.026	0	4.457
Other error	2	0	0			5.893
Total	8	0.018				100.00

Independent variables with more than two levels can also be used in regression analyses, but they first must be converted into variables that have only two levels. Usually, regression analysis is adopted for naturally occurring variables.

**Table 48.7** Delamination factor at the exit (manual layup)

Col#/factor	DOF (f)	Sum of sqrs (S)	Variance (V)	F-ratio (F)	Pure sum (S')	Percent P(%)
Spindle speed	2	0.005	0.002	35.274	0.005	29.482
Feed	2	0.011	0.005	72.978	0.011	61.914
Drill bit diameter	2	0.001	0	7.001	0	5.162
Other errors	2	0	0			3.442
Total	8	0.018				100.00

**Table 48.8** ANOVA analysis on torque (compression molding)

Col#/factor	DOF (f)	Sum of sqrs. (S)	Variance (V)	F-ratio (F)	Pure sum (S')	Percent P(%)
Spindle speed	2	0.002	0.001	8.615	0.002	15.114
Feed	2	0.009	0.004	33.307	0.009	64.122
Drill bit diameter	2	0.002	0.001	7.461	0.001	12.824
Other errors	2	-0.001	-0.001			7.94
Total	8	0.014				100.00

**Table 48.9** ANOVA analysis on torque (manual layup)

Factor	DOF (f)	Sum of sqrs. (S)	Variance (V)	F-ratio (F)	Pure sum (S')	Percent P(%)
Spindle speed	2	0.003	0.001	4.774	0.002	16.093
Feed	2	0.009	0.004	13.193	0.008	51.994
Drill bit diameter	2	0.003	0.001	4.483	0.002	14.855
Other errors	2	0	0			17.058
Total	8	0.016				100.00

**Table 48.10** ANOVA analysis on thrust force (compression molding)

Factor	DOF (f)	Sum of sqrs. (S)	Variance (V)	F-ratio (F)	Pure sum (S')	Percent P(%)
Spindle speed	2	181.555	90.777	116.716	180	31.789
Feed	2	310.888	155.444	199.86	309.333	54.631
Drill bit diameter	2	72.222	36.111	46.429	70.666	12.48
Other errors	2	1.555	0.777			1.1
Total	8	566.222				100.00

**Table 48.11** ANOVA analysis on thrust force (manual layup)

Factor	DOF (f)	Sum of sqrs. (S)	Variance (V)	F-ratio (F)	Pure sum (S')	Percent P(%)
Spindle speed	2	138.5	69.25	10.519	125.334	23.039
Feed	2	307.167	153.583	23.33	294	54.044
Drill bit diameter	2	85.166	42.583	6.468	72	13.235
Other errors	2	13.166	6.583			9.682
Total	8	544				100.00

**48.2.6 Manual Layup Method**

THRUST FORCE

$$C4 = 30.61 - 0.00475C1 + 708C2 + 1.316C3$$

$$TORQUE = 0.0681 - 0.000023C1 + 3.833C2 + 0.00728C3$$

$$DELAMINATION ENTRY = 1.0200 + 0.000003C1 + 64.502C2 + 0.00254C3$$

$$DELAMINATION EXIT = 1.0475 + 0.000005C1 + 4.33C2 + 0.00254C3$$

**48.2.7 Compression Molding Method**

$$THRUST FORCE = 37.51 - 0.00533C1 + 717C2 + 1.096C3$$

$$TORQUE = 0.0709 - 0.000020C1 + 4C2 + 0.00588C3$$

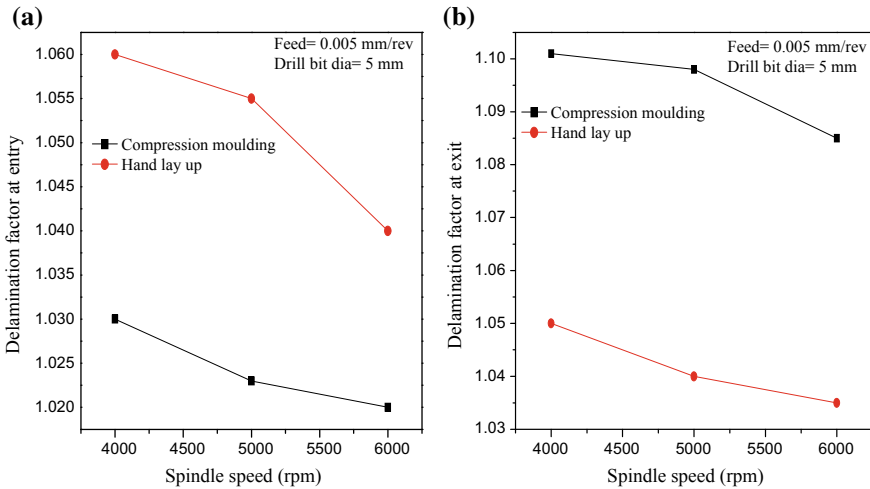


Fig. 48.6 Spindle speed versus delamination factor (manual layup). a Entry. b Exit

$$\text{DELAMINATION ENTRY} = 1.0471 - 0.000007C1 + 3.833C2 - 0.00044C3$$

$$\text{DELAMINATION EXIT} = 1.0521 - 0.000008C1 + 5C2 + 0.00211C3$$

These equations give the mathematical relations between the various parameters and their responses and help to find the unknown parameters from the known values. These mathematical models also help to predict the responses even without conducting the experiments. The effect of spindle speed on the delamination entry and delamination exit is as shown in Fig. 48.6.

### 48.3 Results and Discussion

Figure 48.7 shows the effect of spindle speed on the delamination entry and exit both for the laminates prepared by manual layup method and compression molding. In both entry and exit, delamination is high for manual layup method.

Figure 48.8 shows the effect of spindle speed on torque. Spindle speed has an inverse relationship with torque. Laminate prepared by compression molding gave better result

Figure 48.9 shows the effect of feed on the delamination entry and exit both for the laminates prepared by manual layup method and compression molding. Feed has a positive correlation with delamination. Here, also compression molding gave better result. It is due to the fact that compression molding produces relatively better homogenous laminate and a similar trend experienced for delamination exit also. Feed has direct relation with thrust force and torque. Higher feed causes higher thrust force and torque.



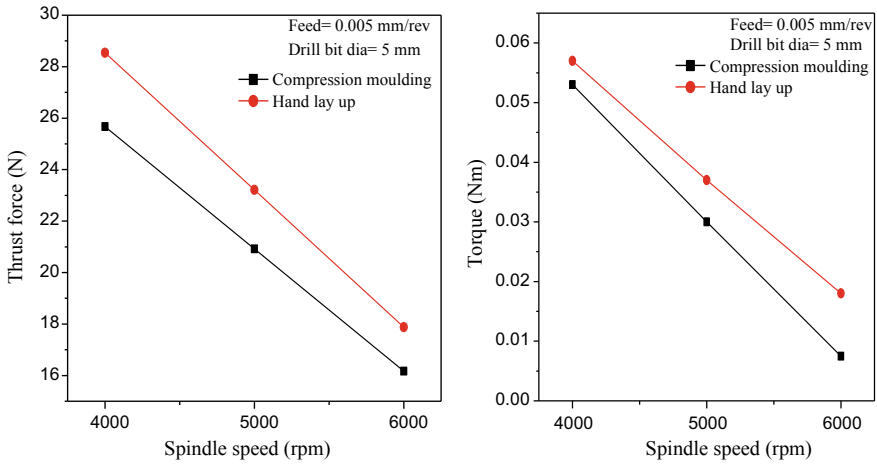


Fig. 48.7 Spindle speed versus thrust, torque

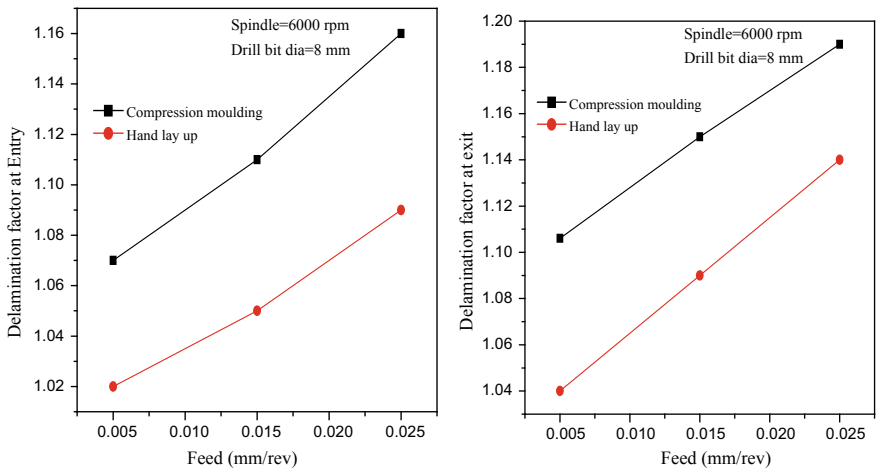


Fig. 48.8 Feed versus del-entry (compression moulding)

Figure 48.10 presents the response of drill bit diameter on the delamination entry. Drill bit diameter is directly proportional to the delamination at entry and exit.

### 48.3.1 SEM Images

It is found from the SEM images in Figs. 48.10 and 48.11 that the glass fibers and the matrix maintain wall surface roughness to the minimum in GFRP made

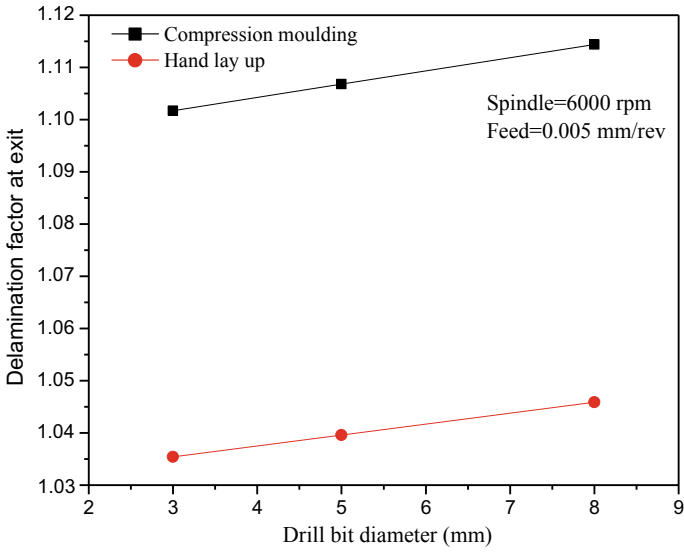


Fig. 48.9 Drill bit dia versus del-entry (manual layup)

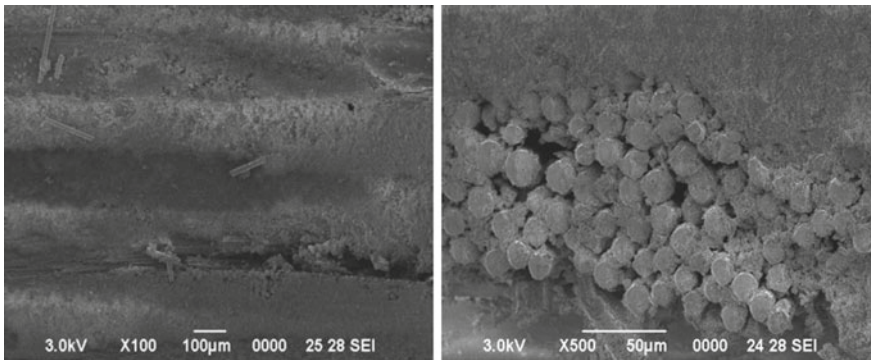
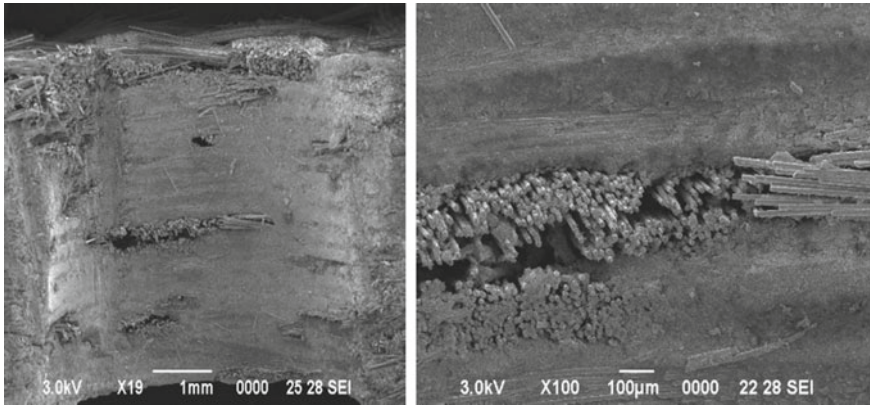


Fig. 48.10 SEM image of compression molding

by compression molding. And hence, hole wall integrity is comparatively better in GFRP made by compression molding than by manual layup method.



**Fig. 48.11** SEM image of manual layup method

## 48.4 Conclusions

From the data received after optimizing the output parameters by adjusting the input parameters, we come to the following conclusions.

When feed rate is kept at lower value minimum delamination can be achieved in higher cutting speed range. Here, we absorb delamination is highly sensitive to cutting feed rate. The feed rate is the cutting parameter which has a greater influence on cutting force, torque, and delamination. In twist drill list, cutting action takes place at the center of the hole. Due to this, the cut fibers are pushed toward the walls.

When spindle speed increases the machining takes place at an elevated temperature. Due to the elevated temperature, softening of the matrix takes place. It enables a smooth drilling operation. Even though the manual glass fibers and soft matrix are encountered in the alternate layers, the above-softening attribute of the matrix guides the drilling process and also at higher spindle speed eventually the cutting speed increases. It is due to this higher cutting speed the chips are pushed toward the wall of the hole at a faster rate. Hence, chips are removed within a short span of time. It is also a reason for better holes at higher spindle speed.

From the experimental observations, it has been found that the delamination defect was found to be minimum for the specimen prepared by compression molding technique. This is because during compression molding the fibers are tightly packed together than that in manual layup process due to the high pressure applied. During drilling the fibers do not get entangled with each other and thus delamination is minimized. And hence, compression molding is a better fabrication technique than manual layup for minimum delamination.

## References

1. Ramachandra, A.: Delamination analysis in drilling process of glass fiber reinforced plastic (GFRP) composite materials. *J. Mater. Process. Technol.* **186**, 265 (2007)
2. Kumar, D., Singh, K.K., Zitoune, R.: Experimental investigation of delamination and surface roughness in the drilling of GFRP composite material with different drills. *Adv. Manuf. Polym. Compos. Sci.* **2**, 47–56 (2016). <https://doi.org/10.1080/20550340.2016.1187434>
3. Kavialagan, R.: Experimental investigation and optimization in drilling GFRP polymeric composites using Taguchi and ANOVA. *Int. J. Mech. Prod. Eng.* **2**, 52 (2013)
4. Khan, M.A., Kumar, A.S.: Machinability of glass fibre reinforced plastic (GFRP) composite using alumina-based ceramic cutting tools. *J. Manuf. Process.* **13**, 67–73 (2011). <https://doi.org/10.1016/j.jmapro.2010.10.002>
5. Raja, R., Chandramohan, G., Jannet, S., Alexander, D.: Delamination analysis in drilling of glass fiber reinforced plastics (GFRP) by special drill bits. *Eur. J. Sci. Res.* **83** (2012)
6. Sureshkumar, M.S., Lakshmanan, D., Murugarajan, A.: Experimental investigation and mathematical modelling of drilling on GFRP composites. *Mater. Res. Innov.* **18**, S1-94-S1-97 (2014). <https://doi.org/10.1179/1432891713z.000000000361>
7. Mardi, N.A.: Applying ultrasonic vibration to decrease drilling-induced delamination in GFRP laminates. Seventeenth CIRP Conference on Electro Physical and Chemical Machining (ISEM). *Procedia CIRP*. vol. 6, p. 577 (2013)
8. Raja, R., Jannet, S.: Experimental investigation of high speed drilling of glass fiber reinforced plastic (GFRP) composite laminates made up of different polymer matrices, *Int. J. Mech. Prod. Eng. Res. Dev.* **7** (2017). <https://doi.org/10.24247/ijmperddcc201739>
9. Antonio, C.C.: Experimental study of drilling glass fiber reinforced plastics (GFRP) manufactured by manual lay-up. *Compos. Sci. Technol.* **64**, 289 (2004)

# Chapter 49

## An Experimental Analysis of Square Stepped Hole Fabrication on Zirconia Bio-Ceramics



S. Das , S. Kumar , B. Doloi and B. Bhattacharyya

**Abstract** Hard, brittle, and easily broken materials, such as quartz, ceramics, bio-ceramics, and inorganic glasses can simply be machined by ultrasonic machining process. In biomedical engineering application, Zirconia ( $ZrO_2$ ) is used for high-quality fracture strength property. Stepped hole shape production on zirconia bio-ceramic with square shape is immensely complicated. The main objective of this research work is to produce square-type stepped hole on bio-ceramic material, i.e., zirconia using USM and also conduct a successful research analysis. The effects of USM process parameters such as grain diameter of abrasive, power rating, slurry concentration, and feed rate of the tool have also been studied on responses, i.e., material removal rate (MRR), flat to flat overcut (FFOC), circularity error of top diameter (CETD), and circularity error of bottom diameter (CEBD) of stepped hole with square shape bio-ceramic material such as zirconia. The effects of USM process parameters on responses have been shown and explained with the help of some graphical representation.

**Keywords** Ultrasonic machining · Bio-ceramic · Circularity error of top diameter · Flat to flat overcut · Circularity error of bottom diameter

### 49.1 Introduction

The importance in the use of any brittle and hard materials such as ceramics, glass, quartz, crystal, etc. grows up rapidly in the recent years owing to their greater properties like high hardness, corrosion resistance, and strength [1–4]. These nonconductive, brittle, and hard materials are machined only by USM process. USM is also be used for machining electrical nonconductive materials (which are not machined by EDM, ECM, etc.) [5, 6]. Zirconia ( $ZrO_2$ ) is extensively used bio-ceramic material. It has enough mechanical properties for developing some medical devices. The

---

S. Das (✉) · S. Kumar · B. Doloi · B. Bhattacharyya  
Production Engineering Department, Jadavpur University, Kolkata 700032, India  
e-mail: [somnath96@gmail.com](mailto:somnath96@gmail.com)

whiteness of zirconia material is useful in clinical situations. White color of tooth implant materials improves the aesthetic look and at the same time being extremely biocompatible. It also withstands the forces present in the oral cavity which might be a solution [7, 8].

The intent of the research work is to develop square stepped tool and produce stepped hole with square shape on the top and cylindrical circular through hole on the bottom on zirconia bio-ceramics by ultrasonic machining. In this research paper, it also includes the influences of USM process parameters such as grain size of abrasive, feed rate of tool, slurry concentration, power rating on MRR, circularity error of top diameter (CETD) and bottom diameter (CEBD), and flat to flat overcut (FFOC) of square stepped hole.

## 49.2 Details of Experimental Setup of USM

AP-1000 Sonic-Mill ultrasonic machine has been used in this research investigation with the 20 kHz frequency of vibration and 25  $\mu\text{m}$  amplitude of vibration. The thinner mixtures are used to promote efficient flow when drilling deep holes and also for forming complex cavities. Previously, abrasive slurry is prepared with required concentration and slurry is pumped to tool-workpiece boundary by recirculating pumps with flow rates up to 26.5 lit/min. The water-based abrasive granules are hammered on the workpiece top surface by the tool, and consequently abrade the small particle from workpiece top surface into a conjugate replica of tool form. Figure 49.1 exhibits the USM setup.

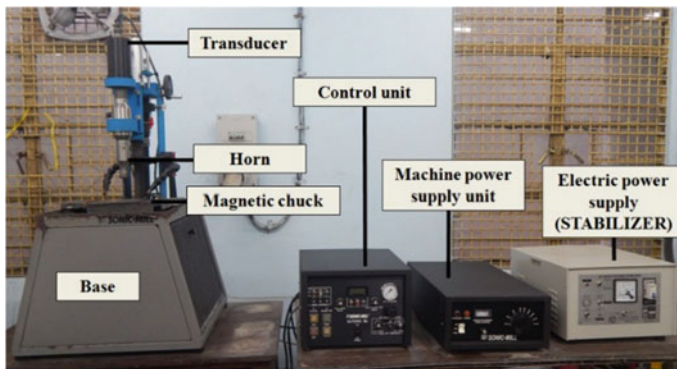


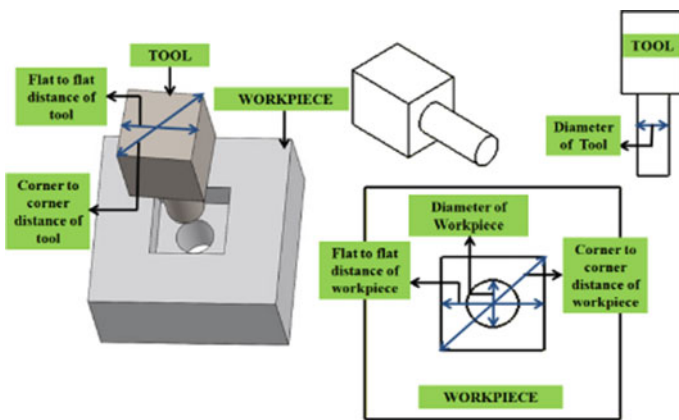
**Fig. 49.1** Ultrasonic machining setup

### 49.3 Experimentation

For the period of ultrasonic machining, workpiece of zirconia bio-ceramic material with 57.5 mm length, 57.5 mm width, and 5.2 mm thick has been used. The shape of the tool is cylindrical and material is stainless steel rod (SS304 grade). This SS rod is selected for developing the square-shaped stepped and cylindrical circular end tip of the tool. Then, the tool has been silver-brazed with top of the hexagonal bolt. Table 49.1 represents the experimental conditions of USM on zirconia. The square-shaped stepped tool and the machined workpiece later than machining is shown in Fig. 49.2. The experimental setting of USM process parameters and responses are listed in Table 49.2. The photographic view of the developed tool is shown in Fig. 49.3. After machining, the square-shaped stepped holes are also shown on

**Table 49.1** Experimental conditions of ultrasonic machining

Machining condition	Description
(1) Frequency of vibration (kHz)	20
(2) Amplitude of vibration ( $\mu\text{m}$ )	25
(3) Static load (kg)	0.9
(4) Workpiece thickness (mm)	5.5
(5) Depth of cut (mm)	5.7
(6) Abrasive type	Boron carbide
(7) Abrasive grain diameter ( $\mu\text{m}$ )	14–64
(8) Abrasive slurry concentration (%)	30–50
(9) Slurry medium	Water
(10) Power rating (W)	300–500
(11) Tool feed rate (mm/min)	0.9–1.3

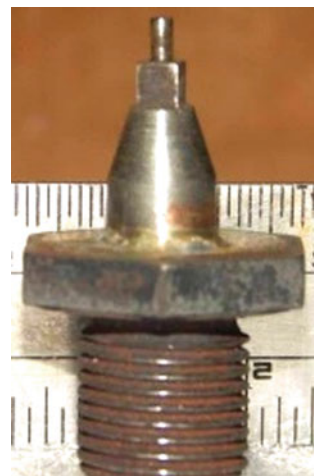


**Fig. 49.2** Schematic diagrams of square shape

**Table 49.2** Values of USM process parameters and observed responses for square-shaped stepped hole generation on zirconia

Exp. no	A	B	C	D	MRR (g/min)	FFOC (mm)	CETD ( $\mu\text{m}$ )	CEBD ( $\mu\text{m}$ )
1	14	40	400	1.1	0.017	0.113	29	19
2	24	40	400	1.1	0.026	0.132	38	31
3	34	40	400	1.1	0.038	0.193	58	45
4	44	40	400	1.1	0.052	0.302	69	58
5	64	40	400	1.1	0.069	0.412	75	72
6	34	30	400	1.1	0.029	0.143	49	44
7	34	35	400	1.1	0.033	0.175	52	50
8	34	40	400	1.1	0.038	0.198	60	55
9	34	45	400	1.1	0.042	0.224	63	61
10	34	50	400	1.1	0.049	0.257	72	70
11	34	40	300	1.1	0.019	0.132	53	48
12	34	40	350	1.1	0.028	0.157	60	53
13	34	40	400	1.1	0.038	0.196	64	59
14	34	40	450	1.1	0.042	0.254	69	63
15	34	40	500	1.1	0.051	0.312	77	71
16	34	40	400	0.9	0.027	0.108	40	36
17	34	40	400	1	0.036	0.134	49	42
18	34	40	400	1.1	0.038	0.197	55	51
19	34	40	400	1.2	0.046	0.266	61	59
20	34	40	400	1.3	0.051	0.321	68	65

where A = grain diameter of abrasive, B = slurry concentration of abrasive, C = power rating, and D = feed rate of tool

**Fig. 49.3** Developed square stepped tool and workpiece after machining tool for USM



zirconia workpiece in Fig. 49.4. MRR, circularity error of top diameter (CETD), and circularity error of bottom diameter (CEBD) of square-shaped stepped hole and flat to flat overcut (FFOC) are chosen as responses for USM. The procedure of measurement is explained here.

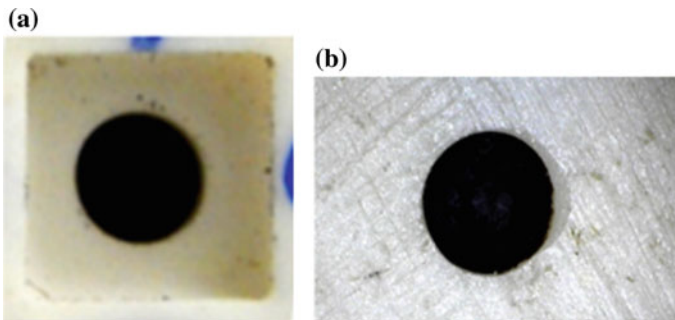
### ***49.3.1 Basic Influences of USM Process Parameters on Responses of Square-Shaped Stepped Hole Production on Zirconia***

Table 49.2 shows the values of USM process parameters and experimental responses for producing square-shaped stepped hole on zirconia bio-ceramics. The effects of major process variables such that grain diameter of abrasive, power rating, slurry concentration of abrasive and tool feed rate on the responses have been discussed here. The influences of USM process parameters on a variety of responses have been studied and explained using different plotted graphs.

### ***49.3.2 Influences of USM Process Parameters on MRR***

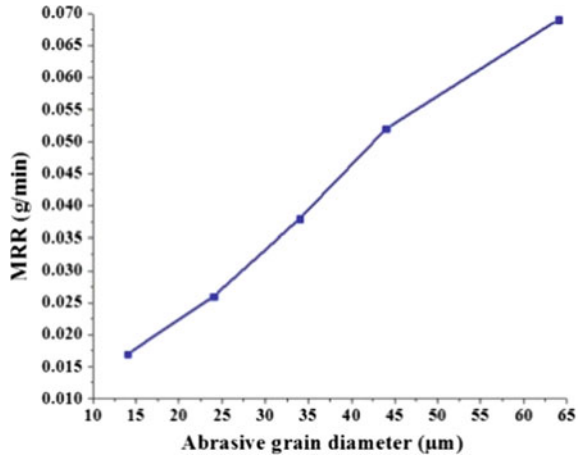
One of the most important parameters in the ultrasonic machining process is abrasive grain diameter. The experiments have been carried out with changing grain diameter of abrasive.

Figure 49.5 shows the outcome of average diameter of abrasive grain on MRR. From the graph, it is achieved that fine abrasive grain diameter, i.e., 14  $\mu\text{m}$  grain diameter results in low MRR but the coarser abrasive grain, i.e., 54  $\mu\text{m}$  grain diameter causes high MRR. Coarser abrasive grain has sharp corner in every grain particle, and therefore MRR is more. The material of machined surface is removed by abrasive



**Fig. 49.4** Square-shaped stepped hole on zirconia workpiece after machining (a) Top view (b) Bottom view

**Fig. 49.5** Effect of abrasive grain diameter on MRR

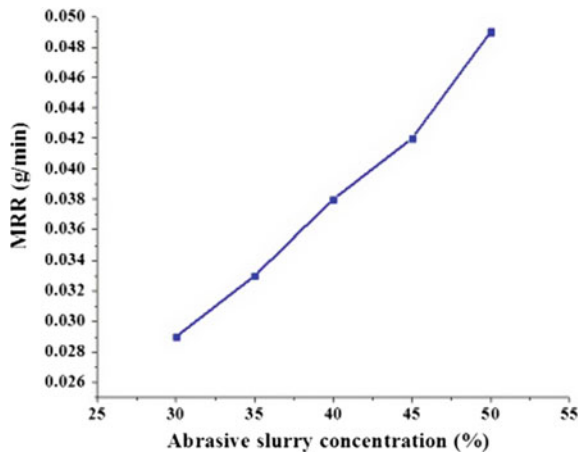


particles which are striking with kinetic energy. When the coarser abrasive grain sizes are used, the kinetic energy of abrasive particles is high due to their weight. So, those coarser abrasive grains penetrate the workpiece material very fast.

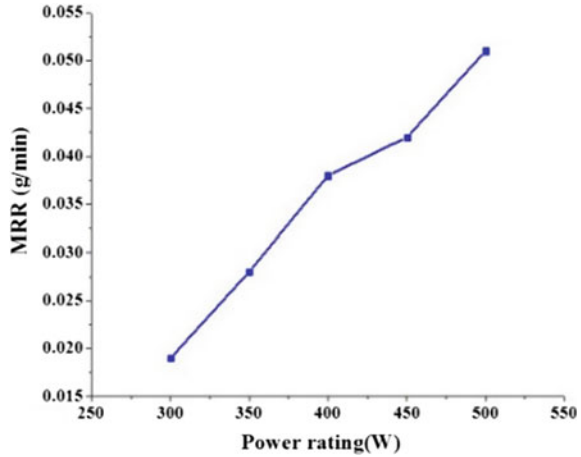
Figure 49.6 presents the effect of slurry concentration of abrasive on MRR of square-shaped stepped hole on zirconia bio-ceramics. Hence, the material removal rate depends on the effective particles of abrasive grains. If abrasive slurry concentration is high that means the density of the slurry is high. So, the more effective particles of abrasive grains come to the working gap. So that the more MRR is achieved using high percentage of slurry concentration of abrasive.

Figure 49.7 presents the effect of power rating on MRR. From the graph, it is undoubtedly shown that with enhancement in power rating MRR increases. When

**Fig. 49.6** Effect of abrasive slurry concentration on MRR



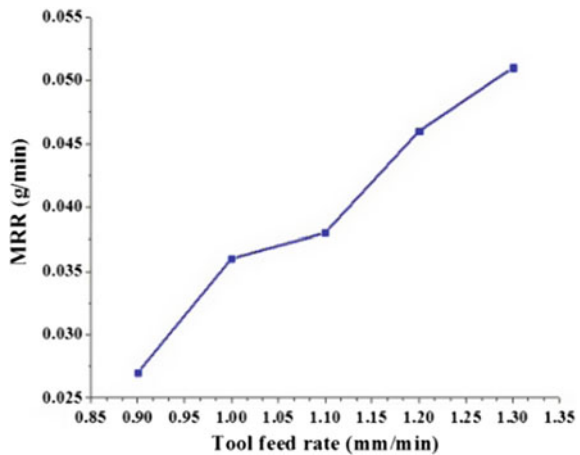
**Fig. 49.7** Effect of power rating on MRR



power rating is supplied more, then the abrasive particle strikes on the workpiece surface with higher value of force. When the particles are striking with more momentum, it causes rapid fracturing of the work surface due to faster propagation of cracks. For this reason, the material is removed from the workpiece at faster rate thus promoting MRR.

It is observed from Fig. 49.8 that the tool feed rate affects the material removal rate during the square-shaped stepped hole generation by USM on zirconia workpiece very significantly. The tool is stirred downward direction at high value of feed rate of tool. So that the crack propagation rate from the workpiece is effectively more. Material is removed from the workpiece at faster rate. For this reason, high value of tool feed rate gives maximum MRR.

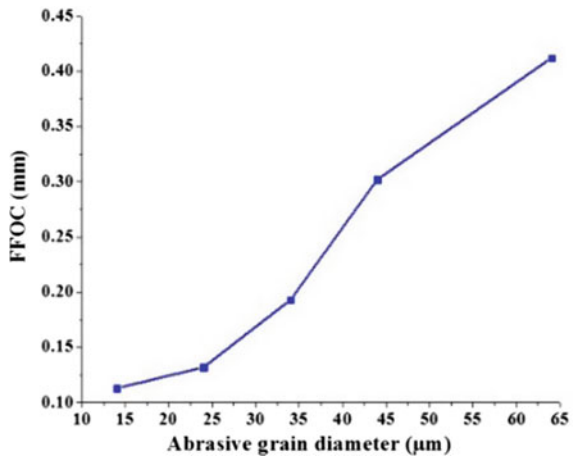
**Fig. 49.8** Effect of tool feed rate on MRR



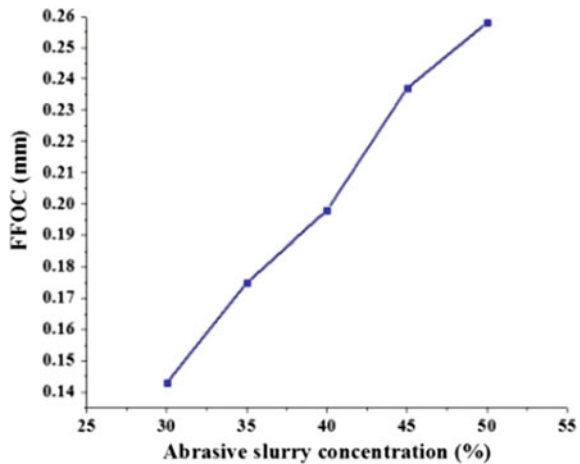
Influences of USM process parameters on FFOC of square-shaped stepped hole Fig. 49.9 shows the outcome of grain diameter of abrasive on FFOC of square-shaped stepped hole, respectively. From the graph, it is observed that fine abrasive grain manufactures hole with low value of flat to flat overcut (FFOC) but the coarser abrasive grain generates hole with high overcut. Average larger grain diameter is 64 micron and average smaller grain diameter is 14 micron. So that the area of average larger grain diameter is very high compared to the average smaller grain diameter. The surface contact area is less when the fine or smaller abrasive grain diameter is utilized. So that flat to flat overcut (FFOC) production by USM is less.

Figure 49.10 exhibits the slurry concentration of abrasive on flat to flat overcut (FFOC). If slurry concentration is low, then profile accuracy value is good. When slurry concentration is very small, then total accumulation of abrasive grain in the

**Fig. 49.9** Effect of grain diameter of abrasive on FFOC for square stepped hole generation



**Fig. 49.10** Effect of slurry concentration of abrasive on FFOC for square stepped hole generation

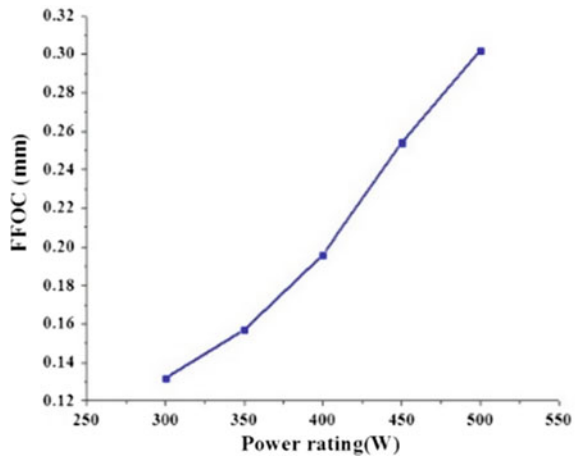


working zone is low. So that hammering force is very small. For this reason, flat to flat overcut (FFOC) value is low due to the usage of low slurry concentration of abrasive.

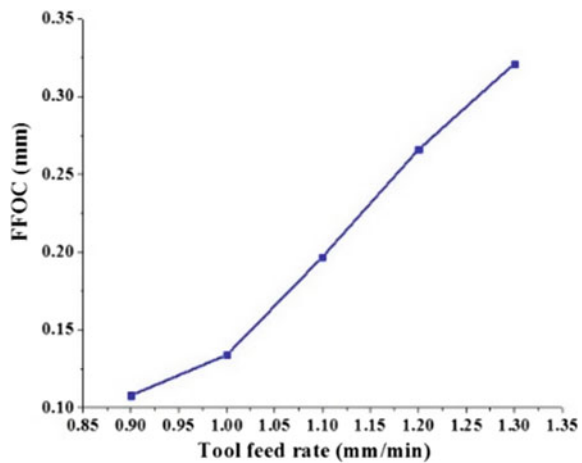
Figure 49.11 shows the effect of power rating on flat to flat overcut (FFOC). From the graph, it is evidently observed that with the increase in power rating, the flat to flat overcut (FFOC) increases. Actually, high value of power rating means the tool vibrates with high power and particle of abrasive strikes on the surface of the workpiece with high energy. So, the overcut is increased. From the graph, it is undoubtedly shown that if the power rating is increasing, the overcut increases. So that for attaining low overcut, lower value of power rating is favored.

Figure 49.12 shows the effect on flat to flat overcut (FFOC) with varying tool feed rate, respectively. From this graph, it is observed that higher value of tool feed

**Fig. 49.11** Effect of power rating FFOC for square-shaped stepped hole generation



**Fig. 49.12** Effect of feed rate of tool FFOC for square-shaped stepped hole production

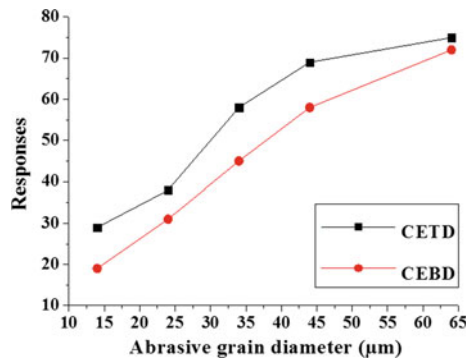


rate gives maximum overcut. With high value of applied feed rate of tool, additional material is removed by the action of the abrasive grains just below tool tip. Therefore, overcut is enlarging with increase in applied tool feed rate. Low value of feed rate of tool is preferred to achieve low flat to flat overcut (FFOC) of stepped hole.

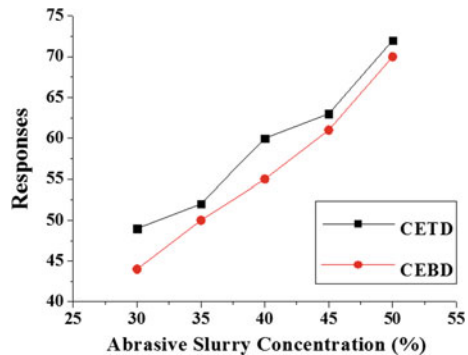
### 49.3.3 Influences of USM Process Parameters on Circularity Error

Figure 49.13 illustrates the effect of grain diameter of abrasive on circularity error of top diameter (CETD) and circularity error of bottom diameter (CEBD) of stepped hole. From the graph, it is found that fine grain diameter provides the low value of circularity error but the coarser grain diameter gives high value of circularity error. Average lesser grain diameter is 14  $\mu\text{m}$ . So that impacting area of smaller abrasive grain diameter is extremely small compared to the higher grain diameter. So that circularity error of top diameter (CETD) and bottom diameter (CEBD) of stepped shape hole generation by USM is less. Figure 49.14 exhibits the influence of slurry

**Fig. 49.13** Effect of grain diameter of abrasive on CETD and CEBD for square-shaped stepped hole generation



**Fig. 49.14** Effect of slurry concentration on CETD and CEBD for square-shaped stepped hole production

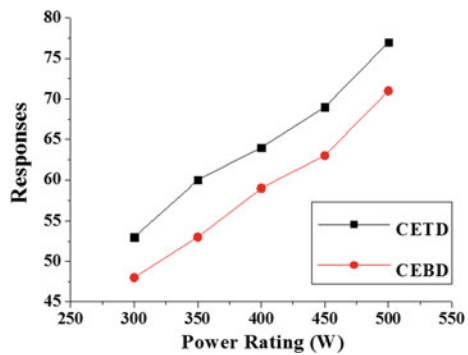


concentration of abrasive on diametrical overcut, i.e., CETD and CEBD. When slurry concentration is extremely low, then whole mass of active abrasive grain is small, so hitting force is minuscule. Therefore, CETD and CEBD values are low due to the usage of low slurry concentration.

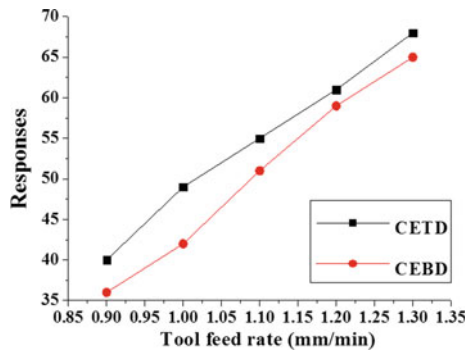
Figure 49.15 illustrates that outcome of power rating on diametrical circularity error, i.e., CETD and CEBD. From the graph, it is evidently shown that if the power rating is increasing the circularity error, i.e., CETD and CEBD are increasing. Actually, when high value of power rating is provided, the abrasive grains strike with high kinetic energy on the top surface of the workpiece. The particles are striking with more momentum causing rapid fracturing of the workpiece face due to faster propagation of cracks. So, the circularity error is increased. So that for attaining low circularity error lower value of power rating is favored.

Figure 49.16 explains the effect on circularity error, i.e., CETD and CEBD with changeable tool feed rate, respectively. From the diagram, it is acquired that high value of tool feed rate provides higher circularity error. With high value of applied tool feed rate, material is removed with more quantity by the action of the abrasive grain particles just below the tool tip. At that time, more fractures are produced due to side cutting. Therefore, circularity error is raised with enhancement of the

**Fig. 49.15** Effect of power rating on CETD and CEBD for square-shaped stepped hole production



**Fig. 49.16** Effect of feed rate of tool on CETD and CEBD for square-shaped stepped hole production



applied tool feed rate. For attaining lower circularity error of top diameter (CETD) and bottom diameter (CEBD) of stepped hole, low value of tool feed rate is chosen.

## 49.4 Conclusions

It is concluded that the ultrasonic machining process can be effectively utilized for fabricating stepped hole in square shape with higher accuracy on zirconia. The experimental study highlights that the USM characteristics like MRR, FFOC, CETD, and CEBD of stepped hole are influenced by the variety of machining process parameters such as grain diameter of abrasive, slurry concentration, feed rate of tool, and power rating for production of stepped hole with square shape on zirconia bio-ceramics.

At higher grain diameter of abrasive, slurry concentration of abrasive, tool feed rate, power rating, and the high value of MRR can be achieved. The influence of various USM process parameters on machining performance criteria is exhibited through graphical representation. For obtaining the better machining accuracy such as flat to flat overcut (FFOC), circularity error of top diameter (CETD), and circularity error of bottom diameter (CEBD) of stepped hole, the lower value of grain diameter, tool feed rate, slurry concentration, and power rating is preferred.

**Acknowledgements** The financial support provided by UGC Delhi under Centre of Advanced Study Program (Phase-IV) of Production Engineering Department of Jadavpur University.

## References




1. Singh, R.P., Singhal, S.: Investigation of machining characteristics in rotary ultrasonic machining of alumina ceramic. *Mater. Manuf. Process.* **32**(3), 309–326 (2017)
2. Kumar, J., Khamba, J.S.: Modeling the material removal rate in ultrasonic machining of titanium using dimensional analysis. *Int. J. Adv. Manuf. Technol.* **48**, 103–119 (2010)
3. Lee, T.C., Zhang, J.H., Lau, W.S.: Machining of engineering ceramics by ultrasonic vibration assisted EDM method. *Mater. Manuf. Process.* **13**(1), 133–146 (1998)
4. Lin, Y.C., Wang, A.C., Wang, D.A., Chen, C.C.: Machining performance and optimizing machining parameters of  $Al_2O_3$ -TiC ceramics using EDM based on the Taguchi method. *Mater. Manuf. Process.* **24**, 667–674 (2009)
5. Jain, A.K., Pandey, P.M.: Experimental investigations of ceramic machining using  $\mu$ -grinding and  $\mu$ -rotary ultrasonic machining processes: a comparative study. *Mater. Manuf. Process.* **32**(6), 598–607 (2017)
6. Rao, R.V., Pawar, P.J., Davim, J.P.: Parameter optimization of ultrasonic machining process using nontraditional optimization algorithms. *Mater. Manuf. Process.* **25**, 1120–1130 (2010)
7. Dvivedi, A., Kumar, P.: Surface quality evaluation in ultrasonic drilling through the Taguchi technique. *Int. J. Adv. Manuf. Technol.* **34**, 131–140 (2007)
8. Singh, J., Gill, S.S.: Fuzzy modeling and simulation of ultrasonic drilling of porcelain ceramic with hollow stainless steel tools. *Mater. Manuf. Process.* **24**(4), 468–475 (2009)



# Chapter 50

## Pulse and Work Revolution Parameters of Wire Electrical Discharge Turning on Ti-6Al-4V Alloy



S. Ram Prakash , K. Rajkumar  and G. Selvakumar 

**Abstract** The present study investigates the effect of process parameters on Wire Electrical Discharge Turning (WEDT) of Ti-6Al-4V alloy. WEDT is the promising technique, which is capable of producing precise cylindrical form component for all electrically conductive materials regardless of its hardness and toughness. This work discusses the effect of various machining parameters over the responses like Material Removal Rate (MRR) and surface roughness (Ra). Response Surface Methodology (RSM) method is adopted to conduct the experiment and ANOVA technique has been employed to identify the significant parameters. From the experimental results, the maximum MRR obtained is 1.3449 mm<sup>3</sup>/min and the minimum surface roughness value is 1.627 μm. Moreover, the ANOVA results indicated that the pulse off current has significant impact on MRR. In the case of Ra, Ton and Toff played predominant role on deciding the surface quality.

**Keywords** Wire electrical discharge turning · Response surface methodology · Surface roughness · Material removal rate

### 50.1 Introduction

Wire Electrical Discharge Machining (WEDM) process is an emerging technology in the global market for producing intricate components with high precision. It escalates the growth of tool- and die-making industries to the next level by fulfilling the demands with its state-of-the-art facilities. Of late, it extends its applications on processing micro-tools, micro-electrodes, small diameter pins, and micro-ejectors [1, 2]. Machining of all conducting materials irrespective of its mechanical properties without burrs and chatters is the advantage of WEDM process. The material removal in WEDM is due to the synergized energy of electrical and thermal processes. The continuous spark between the tool (i.e., the wire) and workpiece melts and vaporizes

---

S. Ram Prakash · K. Rajkumar · G. Selvakumar (✉)  
Department of Mechanical Engineering, SSN College of Engineering, Kalavakkam, Chennai  
603110, India  
e-mail: [selvakumaratju@gmail.com](mailto:selvakumaratju@gmail.com)

© Springer Nature Singapore Pte Ltd. 2020  
M. S. Shunmugam and M. Kanthababu (eds.), *Advances in Unconventional Machining and Composites*, Lecture Notes on Multidisciplinary Industrial Engineering, [https://doi.org/10.1007/978-981-32-9471-4\\_50](https://doi.org/10.1007/978-981-32-9471-4_50)

the material. The flushing dielectric medium passed around the wire takes off the molten materials and further cools the work material [3]. Wire Electrical Discharge Turning (WEDT) is the derivative of WEDM process by appending an additional rotary axis with the existing machine to produce axisymmetric cylindrical components [4, 5]. The metal removal mechanism of WEDT is very much identical with the WEDM.

A new hybrid technology has been introduced on combining wire electrical discharge turning assisted with ultrasonic vibration for evaluating MRR of the cylindrical component. The results stated that the ultrasonic-vibration-assisted WEDT produces significant improvement on MRR [5]. Sun et al. [6] studied the effects of fabrication of micro-electrodes in Low-Speed-Wire Electrical Discharge Turning (LS-WEDT) by employing multi-cut process and compared the surface characteristics of LS-WEDT with the results of Low-Speed-Wire Electrical Discharge Machining (LS-WEDM). It is interesting to note that there is a phenomenal improvement in surface texture of LS-WEDT compared with LS-WEDM. Qu et al. [7] studied the roundness and surface integrity of the cylindrical parts processed by wire EDM turning process for carbide and brass work materials. Surface and subsurface characteristics of the machined surface are demonstrated with Scanning Electron Microscope (SEM) images. An investigation on the metal removal rate of cemented steel cylindrical workpiece on WEDM by turning operation using Taguchi methodology and optimal condition has been obtained by analyzing the signal-to-noise (S/N) ratio [8].

Like WEDT, Electrical Discharge Turning (EDT) is potential candidate for precise turning of cylindrical workpiece. Many researchers have investigated the effect of machining parameters on performance characteristics like MRR, Tool Wear Ratio (TWR), and Ra on EDT [9–11].

Many researchers have made an attempt on investigating the effect of machining parameters of performance characteristics of WEDT. Very few research works have been reported on the machining of Ti-6Al-4V alloy on WEDT. Machining of Ti-6Al-4V by conventional process is difficult due to its high hardness and toughness. Ti alloy has numerous applications in medical implants, surgical instruments, automotive, and marine and aerospace industry. From the literature, it is found that the pulse on time (Ton), pulse off time (Toff), peak current (Ip), and chuck speed are the significant parameters on deciding the machining performance like machining rate and surface quality. In this present study, the effect of main controlling parameters on machining Ti-6Al-4V alloy was studied for the responses of MRR and surface roughness.

## 50.2 Materials and Methods

The experimentation is carried out in Ratna Parki CNC WEDM, model: smart cut 2530. It consists of a machine tool, a control panel unit, and dielectric supply unit. An auxiliary device is attached with machine tool to render rotary motion to the workpiece. A microcontroller-based stepper motor driving unit is used to control

the rotation of the spindle. Figure 50.1a and b shows the image of the spark erosion condition. The process parameters chosen for the experiments are based on the trial experiments and also from the literature. Ti alloy is selected as the work material. Table 50.1 shows the main controlling parameters used in this study. The other constant parameters—wire: brass, wire diameter: 0.25 mm, wire feed: 2 m/min, servo voltage: 40 V, dielectric: deionized water, wire tension: 20 N, water pressure: 99 bar—were used.

The computation of MRR [5] is done by the following expression:

$$MRR = \pi(R^2 - r^2)V_f \tag{50.1}$$

where

R and r—radius before and after machining (mm),

$V_f$ —cutting speed which is calculated by  $V_f = L/t$ , where L—cutting length, t—machining time (m/s).

Ra value is measured by Mitutoyo SJ 210 surface roughness tester with aid of V-block to hold the workpiece.

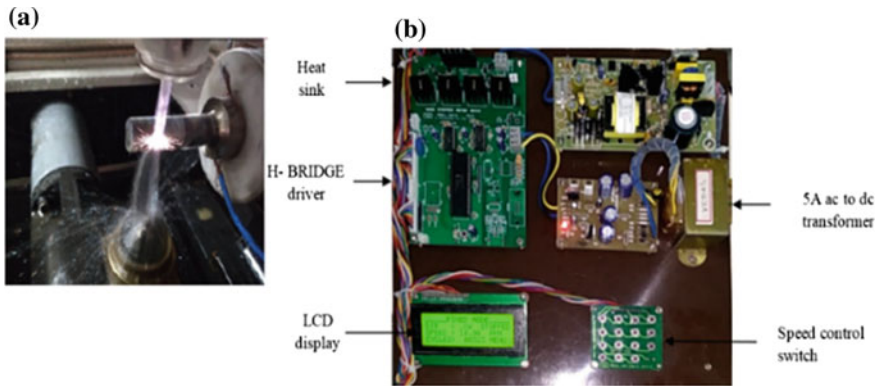


**Fig. 50.1** a Spark erosion condition, b Driving unit

**Table 50.1** Process parameters with its levels

S. No.	Parameter	Min. value	Max. value
1	A: Ton (μs)	102	106
2	B: Toff (μs)	40	50
3	C: I (A)	1	3
4	D: Chuck speed (rpm)	5	15

## 50.3 Experimental Results and Discussion

### 50.3.1 Effect of Process Parameters on MRR

The experimental results for all the 28 experiments are shown in Table 50.2. Further, the response factors were analyzed in ANOVA to identify the influence of individual parameters. It is perceived that the optimum MRR ( $1.345 \text{ mm}^3/\text{min}$ ) was achieved at Ton 104 ( $\mu\text{s}$ ), Toff 40 ( $\mu\text{s}$ ), current 2A, and chuck speed 15 RPM. Table 50.3 presents the ANOVA of MRR. It is observed that the effect of interaction between pulse off and chuck speed is the predominant factor for yielding higher material removal rate. It is due to the fact that if the values of pulse off time and chuck speed are lesser, it produces more sparks which tends to increase the MRR. Followed by this, current plays the significant role on the machining rate where the increase in current, increases the energy level of the spark which enables the material to sudden melting and vaporization. Next to current, Ton has meager effect on the MRR. It shows a reverse proportionality to the MRR. All the other parameters have almost null significance on the MRR. From Table 50.2, the optimum parameter setting for acquiring maximum surface quality ( $1.63 \mu\text{m}$ ) is identified as Ton 104 ( $\mu\text{s}$ ), Toff 45 ( $\mu\text{s}$ ), current 2A, and chuck speed at 10 rpm. Table 50.3 presents the ANOVA analysis for surface roughness.

### 50.3.2 Effect of Process Parameters on Ra

Surface roughness determines the surface quality of the material. Minimum the surface roughness value the higher the surface quality of the material. Table 50.3 shows that the pulse off time is the major influence on surface roughness. Followed by pulse off time, pulse on time plays a significant role on deciding the surface quality of the machined surface. Increase in Toff enables the dielectric medium to transport the micro molten metal chip particles produced during the sparking process which in turn produces smoother surface on the machined region. Increase in Ton generates more electrical discharges during this interim period, and gas bubbles were formed and entrapped in the dielectric medium. These gas bubbles form small pockmarks on the surface on the machined region.

### 50.3.3 3D Surface Analysis Plots for MRR

These plots are the graphical representation of the potential variables which influence the machining processes.

Figure 50.2a represents the estimated response surface for MRR by varying the parameter's chuck speed and the peak current. It is revealed that the MRR increases

**Table 50.2** Experimental results

Run	A	B	C	D	MRR	Ra	Run	A	B	C	D	MRR	Ra
Order/unit	$\mu\text{s}$	$\mu\text{s}$	A	RPM	$\text{mm}^3/\text{min}$	$\mu\text{m}$	Order/unit	$\mu\text{s}$	$\mu\text{s}$	A	RPM	$\text{mm}^3/\text{min}$	$\mu\text{m}$
1	106	45	2	5	0.998	2.44	15	104	45	2	10	0.723	1.91
2	106	45	1	10	0.800	1.98	16	102	45	2	15	1.084	2.00
3	104	45	1	15	0.793	2.49	17	104	40	1	10	0.883	3.74
4	102	45	2	5	1.066	1.80	18	104	40	2	5	0.845	2.60
5	104	50	2	15	0.580	1.94	19	104	50	2	5	1.148	1.89
6	104	45	2	10	0.901	2.01	20	104	50	3	10	0.962	1.80
7	104	40	2	15	1.345	2.76	21	104	45	2	10	0.861	1.63
8	102	50	2	10	1.005	1.71	22	106	50	2	10	0.751	1.71
9	104	45	3	15	1.056	2.40	23	106	40	2	10	0.845	3.22
10	102	45	3	10	1.033	1.93	24	106	45	2	15	0.976	2.53
11	104	50	1	10	0.535	1.74	25	104	45	1	5	1.131	2.46
12	104	45	3	5	0.979	1.96	26	102	40	2	10	1.195	2.47
13	102	45	1	10	0.833	2.07	27	106	45	3	10	1.094	3.02
14	104	45	2	10	0.582	1.92	28	104	40	3	10	1.108	2.39

**Table 50.3** ANOVA table for MRR and Ra

Source	MRR					Ra				
	Sum of squares	DF	Mean square	f-value	p-VALUE	Sum of squares	DF	Mean square	f-value	p-value
Model	0.844	14	0.0603	4.6	0.005 <sup>a</sup>	6.03	14	0.4309	6.3	0.001 <sup>a</sup>
A	0.047	1	0.047	3.59	0.081	0.7004	1	0.7004	10.23	0.007
B	0.128	1	0.128	9.76	0.008	3.42	1	3.42	49.95	0.000
C	0.1314	1	0.1314	10.02	0.007	0.0787	1	0.0787	1.15	0.303
D	0.0091	1	0.0091	0.696	0.419	0.0767	1	0.0767	1.12	0.309
AC	0.0022	1	0.0022	0.168	0.689	0.3452	1	0.3452	5.04	0.043
BC	0.0102	1	0.0102	0.777	0.394	0.4966	1	0.4966	7.25	0.018
B <sup>2</sup>	0.0191	1	0.0191	1.46	0.249	0.4280	1	0.4280	6.25	0.027
C <sup>2</sup>	0.0197	1	0.0197	1.5	0.242	0.4381	1	0.4381	6.4	0.025
Residual	0.1705	13	0.0131			0.8898	13	0.0684		
Lack of fit	0.1074	10	0.0107	0.511	0.816	0.8082	10	0.0808	2.97	0.201
Error	0.0631	3	0.021			0.0817	3	0.0272		
Cor total	1.01	27				6.92	27			

<sup>a</sup>Significant

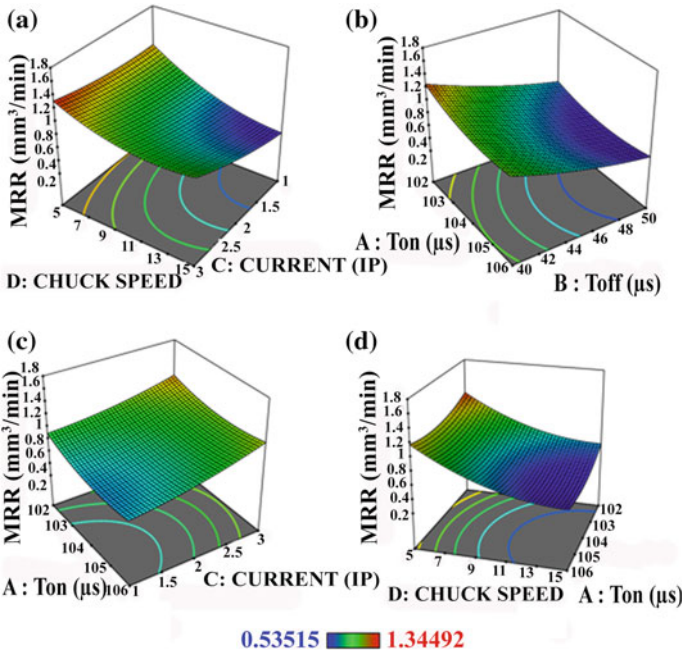


Fig. 50.2 3D surface plot for MRR

with the increase in current and decrease in chuck speed. Figure 50.2b shows the estimated response surface of MRR by considering the parameters Ton and Toff. It is indicated that lowering the value of Ton and Toff is preferred for attaining higher MRR. Figure 50.2c represents the surface plot for MRR with the factors Ton and current. It can be understood that decreasing the value of Ton and increasing the value of current maximize the MRR. Figure 50.2d shows the surface plot for MRR by considering the factors Ton and chuck speed. MRR is increased by decreasing the chuck speed and increasing the Ton value.

### 50.3.4 3D Surface Analysis Plots for Ra

Minimum surface roughness value indicates the surface is so smooth. The estimated surface plot of surface roughness for various parameters is shown in Fig. 50.3. From Fig. 50.3a, it is evident that the increase in current and chuck speed increases the surface roughness which leads to poor surface quality. As can be seen from Fig. 50.3b, increase in Ton and decrease in Toff produce irregular surface on the machining region. Increase in Toff provides an appropriate time for flushing the debris and possible reduction of recast layer. The surface plot for Ton and current from Fig. 50.3c indicates that decreasing the values of both Ton and current minimizes the surface

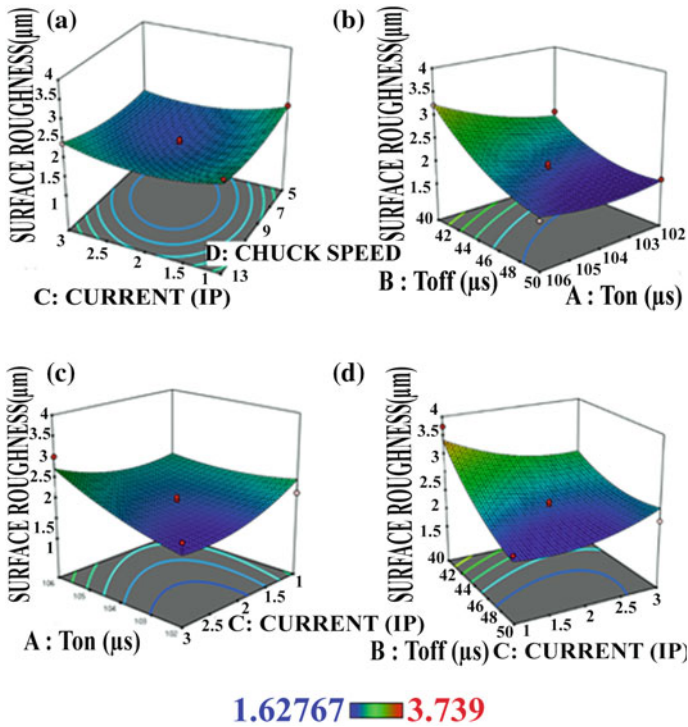


Fig. 50.3 3D scatter plot for Ra

roughness. Figure 50.3d shows the surface plot for variables Toff and current. It points out that increasing the value of current and Toff increases the value of surface quality.

### 50.3.5 Regression Analysis of MRR and Ra

Linear regression analysis was used to determine the relationship between dependent variables to independent variables. The predicted values for MRR and Ra were obtained using Eqs. 50.2 and 50.3.

#### Regression analysis for MRR.

The predicted value for MRR was derived using Eq. (50.1)

$$\begin{aligned}
 &= 333.829 - 6.199A - 0.387B - 2.007C + 0.412D + 0.002AB + 0.012AC \\
 &\quad - 0.00099AD + 0.01009BC - 0.01067BD + 0.0206CD + 0.029A^2 + 0.00226B^2 \\
 &\quad + 0.0244C^2 + 0.0666D^2 \tag{50.2}
 \end{aligned}$$



**Table 50.4** Confirmatory test validation

S. No.	A	B	C	D	Actual value		Predicted value		Confirmatory test	
	μs	μs	A	RPM	MRR (mm <sup>3</sup> /min)	Ra (μm)	MRR (mm <sup>3</sup> /min)	Ra (μm)	MRR (mm <sup>3</sup> /min)	Ra (μm)
1	104	40	2	15	1.345	2.76	1.32	2.96	1.326	2.92
2	104	45	2	10	0.861	1.63	0.767	1.74	0.782	1.68

The correlation coefficient ( $R^2$ ) describes the relationship between actual and predicted values. For MRR and Ra, the  $R^2$  was calculated as 83.20% and 87.75%, respectively. Regression analysis is used to develop the predictive equation.

**Regression analysis for surface roughness.**

The predicted value for Ra was derived using Eq. (50.2)

$$\begin{aligned}
 &= 1.82 + 0.2325A - 0.6498B - 0.0940C + 0.0644D - 0.1648AB + 0.2465AC \\
 &\quad - 0.0218AD + 0.2985BC - 0.0182BD + 0.1156CD + 0.1662A^2 + 0.1968B^2 \\
 &\quad + 0.2208C^2 + 0.1205D^2 \tag{50.3}
 \end{aligned}$$

From Table 50.4, it is evident that the predicted value from regression is in good agreement with the confirmatory test results. Hence, it can be deduced that the proposed regression model fits with minimal deviations.

**50.4 Conclusion**

The experimental work reports that the WEDT is a viable technique to process cylindrical components used in dental implants and surgical instruments. Following conclusions were drawn from the investigation:

1. All the factors investigated in the study are statistically significant for their impact on the MRR with major contributions from current and Toff.
2. In case of surface roughness, pulse off time and pulse on time play a major role, and increase in pulse off time enables proper flushing which removes the molten material completely from the surface and reduces the occurrence of recast layer.
3. The 3D surface plots for MRR revealed that current >2 A and pulse off >40 μs produce optimum value of MRR >1.345 mm<sup>3</sup>/min in optimization domain. For surface roughness, to improve the quality of the cut surface, the value of surface roughness should always be minimum, when chuck speed <10 rpm and current <2 A achieves the optimum surface quality <1.63 μm.

## References

1. Sun, Y., Gong, Y.: Experimental study on fabricating spirals microelectrode and micro-cutting tools by low speed wire electrical discharge turning. *J. Mater. Process. Technol.* **258**, 271–285 (2018)
2. Zhu, Y., Liang, T., Gu, L., Zhao, W.: Machining of micro rotational parts with wire EDM machine. In: 44th Proceedings of the North American Manufacturing Research Institution of SME, vol. 5, pp. 849–856 (2016)
3. Selvakumar, G., Kuttalingam, K.G.T., Ram Prakash, S.: Investigation on machining and surface characteristics of AA5083 for cryogenic applications by adopting trim cut in WEDM. *J. Braz. Soc. Mech. Sci. Eng.* **40**, 267–274 (2018)
4. Giridharan, A., Samuel, G.L.: Investigation into erosion rate of AISI 4340 steel during wire electrical discharge turning process. *Mach. Sci. Technol.* **22**, 287–298 (2017)
5. Mohammadia, A., Tehrania, A.F., Abdullahb, A.: Introducing a new technique in wire electrical discharge turning and evaluating ultrasonic vibration on material removal rate. In: The Seventeenth CIRP Conference on Electro Physical and Chemical Machining (ISEM), vol. 6, pp. 583–588 (2013)
6. Sun, Y., Gong, Y., Liu, Y., Li, Q., Zhou, Y.: Experimental study on surface characteristics and improvement of microelectrode machined by low speed wire electrical discharge turning. *Arch. Civil Mech. Eng.* **17**, 964–977 (2017)
7. Jun, Qu, Shih, J., Scattergood, O.: Development of the cylindrical wire electrical discharge machining process, Part 2: surface integrity and roundness. *J. Manuf. Sci. Eng. Trans. ASME* **124**, 708–714 (2002)
8. Mohammadi, M., Tehrani, A.F., Emanian, E., Karimi, D.: Statistical analysis of wire electrical discharge turning on material removal rate. *J. Mater. Process. Technol.* **205**, 283–289 (2008)
9. Gohila, V., Puri, Y.M.: Optimization of electrical discharge turning process using Taguchi-Grey relational approach. In: 19th CIRP Conference on Electro Physical and Chemical Machining, 23–27 April 2017, Bilbao, Spain, *Procedia CIRP*, vol. 68, pp. 70–75 (2018)
10. Matorian, P., Sulaiman, S., Ahmad, M.M.H.M.: An experimental study for optimization of electrical discharge turning (EDT) process. *J. Mater. Process. Technol.* **204**, 350–356 (2008)
11. Song, K.Y., Chung, D.K., Park, M.S., Chu, C.N.: EDM turning using a strip electrode. *J. Mater. Process. Technol.* **213**, 1495–1500 (2013)

# Chapter 51

## Modeling of Areal Surface Roughness Using Soft-Computing-Based ANN and GA to Estimate Optimal Process Parameters During Wire Electrical Discharge Turning of Inconel 825



Jees George , G. Ravi Chandan , R. Manu  and Jose Mathew 

**Abstract** Wire electrical discharge turning (WEDT) is a nontraditional machining process, which is used to generate accurate cylindrical components from difficult-to-cut materials. A model was developed to predict these parameters from the experimental data. In the present work, cylindrical workpieces of Inconel 825 are used as work material. The process parameters, viz., spark gap, rotational speed, pulse on time, and pulse off time were considered while conducting the experiments. The areal surface roughness was measured as the output response for quality improvement. Soft-computing-based artificial neural network (ANN) model was developed to predict the areal surface roughness value with the given data. The model prediction was compared with the experimental results for verifying the model and present good agreement with them. Genetic algorithm (GA) is used to estimate the optimal process parameters. The results of this study show that the computational approach, viz., GA, managed to estimate the optimal process parameters, leading to the minimum value of machining performance when compared to the result of experimental data.

**Keywords** WEDM · WEDT · ANN · Inconel 85 · Areal surface roughness

### 51.1 Introduction

Wire electric discharge machining (WEDM) is a well-renowned nonconventional manufacturing process widely used in industries nowadays. It has a distinct attrition technique of material removal in which the erosion of the material is caused by repetitive electric sparks between the wire and the workpiece. The removed material is then washed away by the dielectric (normally de-ionized water or kerosene). The wire is

---

J. George (✉) · G. Ravi Chandan · R. Manu · J. Mathew  
Department of Mechanical Engineering, National Institute of Technology Calicut, Calicut  
673601, India  
e-mail: [jeesgeorge@gmail.com](mailto:jeesgeorge@gmail.com)

© Springer Nature Singapore Pte Ltd. 2020  
M. S. Shunmugam and M. Kanthababu (eds.), *Advances in Unconventional Machining and Composites*, Lecture Notes on Multidisciplinary Industrial Engineering, [https://doi.org/10.1007/978-981-32-9471-4\\_51](https://doi.org/10.1007/978-981-32-9471-4_51)

mostly made of brass, zinc-coated brass, and tungsten carbide whose diameter ranges from 0.05 to 0.25 mm. Wire electrode discharge turning (WEDT) is an innovative alteration of WEDM in which a rotating platform is fabricated to make it feasible for turning. Inconel 825 is a nickel-based alloy having high strain-hardening tendency, high dynamic shear strength, and poor thermal diffusivity making it difficult to machine using conventional machining processes.

Researchers have led their pursuit of developing the WEDM and WEDT processes. Sun et al. [1] have analyzed the surface damage in low-speed-wire electric discharge machining (LS-WEDM) by introducing a multiple cutting strategy into LS-WEDT to improve surface quality and minimizing the surface defects. Aspinwall et al. [2] have employed multiple trim cut strategies for roughing and finishing operations using pulse generators to minimize surface integrity damage. Das and Pradhan [3] have attempted to bring forth three different classes of artificial neural network (ANN) models, given by backpropagation network (BPN), radial basis function network (RBFN), and recurrent neural network (RNN) for the prediction of the surface roughness values ( $R_a$ ) in EDM. RBFN model has shown a better case of accurate prediction compared to other two models used. Assarzadeh and Ghorishi [4] developed a new integrated neural network approach for the optimization of the parameters and prediction in die-sinking EDM. In the present work, a back-propagation neural network is used with inputs as input current (I), period of pulses (T), source voltage (V) and material removal rate (MRR), surface roughness ( $R_a$ ) as output parameters of the model.

Sun and Gong [5] worked on the fabrication of microelectrode and spiral micro-cutting tools with the help of LS-WEDT. In their work, the effects of parameters like rotating speed on surface roughness, surface microstructure, elemental changes, and material removal rate in LS-WEDT are analyzed in great detail. Janardhan and Samuel [6] have provided an insight into the WEDT process by evaluating the effects of machining parameters on material removal rate (MRR), surface roughness ( $R_a$ ), and roundness error with the use of pulse train data obtained at the spark gap. The authors found that the rotation of the workpiece significantly influences the nature of discharges occurring at the spark gap. It has been perceived from the results that the surface roughness and roundness error of WEDT components are influenced by the arc regions, width of arc, and average ignition delay time. Krishnan and Samuel [7] in their work proposed that the WEDT process modeling is done using an artificial neural network (ANN) with feedforward backpropagation algorithm using adaptive neuro-fuzzy inference system. A non-dominated sorting genetic algorithm-II, a multi-objective optimization method is used to optimize the process. The output parameters are material removal rate (MRR) and surface roughness which are conflicting in nature. Kuriakose and Shunmugam [8] have developed a multiple regression model to represent the relationship between surface finish and cutting speed. They have also considered a multi-objective optimization method based on non-dominated sorting genetic algorithm (NSGA) to optimize the WEDM process. Liao et al. [9] employed a feedforward neural network to obtain the height of the workpiece and distinguish the machining conditions in WEDM. A rule-based strategy is being used to adjust correctly the servo voltage and power settings to suit

the workpiece profile to get optimal results. Newton et al. [10] have investigated the main parameters that contribute to the recast layer on the workpiece surface. Energy per spark, peak discharge current, and current pulse duration are the parameters considered in this work.

WEDT is an emerging technology by which cylindrical parts with high accuracy can be produced. Analyzing the parameters and investigating the significant factors take major priority. WEDT being a noncontact machining process is independent to the mechanical properties of the workpiece material making it viable to machine the superalloys and difficult-to-cut materials. Inconel 825 being one such material has got many applications like micro-shafts in radial motors, corrosion-resistant parts, sensors, and microelectrodes in aerospace industries, neurosurgical implants, and so on. From the literature, it has been found that most of the researchers have worked on Ra value of surface roughness. Study of areal surface roughness is an area yet not explored while machining with WEDT. Areal surface roughness ( $S_a$ ) gives a better picture of topography of the machined surface making the judgment of surface quality easier and more relevant for us. In the current work, a soft-computing-based model is developed using ANN to predict the areal surface roughness ( $S_a$ ) accurately. Consequently, optimization of process parameters was carried out using GA which is a novel attempt in the machining of Inconel 825 using WEDT process.

## 51.2 Experimental Details

### 51.2.1 Experimental Setup

In the ecocut CNC WEDM machine, an additional platform is fabricated by which the rotation of the cylindrical workpiece is achieved as shown in Fig. 51.1. WEDT setup was developed using precise base and high-quality bearings. An ER-16 straight shank adapter is used as the spindle for the turning setup. A DC-g geared motor is used to drive the spindle with the help of a toothed flat belt. Inconel 825, an aerospace alloy, is chosen as the workpiece material for conducting the experiments.

10 mm diameter workpieces are taken to conduct the experiments and machining of 10 mm length was carried out in each experimental run as shown in Fig. 51.2. The areal surface roughness  $S_a$  is measured using Alicona 3D optical profilometer for each section having a cutoff wavelength of 500  $\mu\text{m}$ .

### 51.2.2 Design of Experiments

Spark gap, rotational speed, pulse on time, and pulse off time are considered as the input parameters. The factors and their levels are selected as shown in Table 51.1.

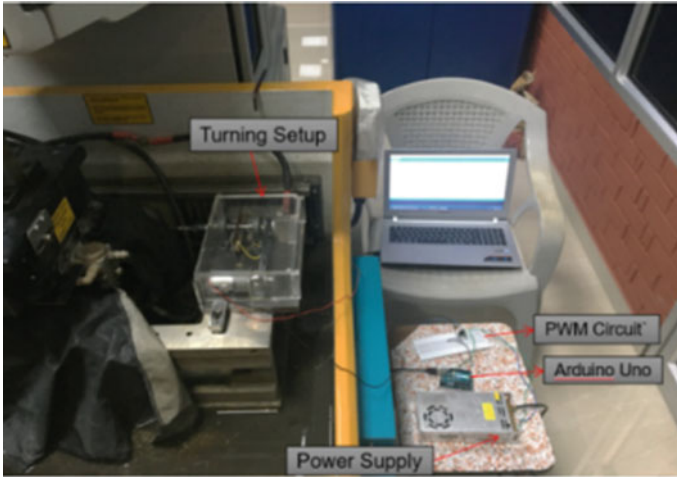


**Fig. 51.1** Experimental setup

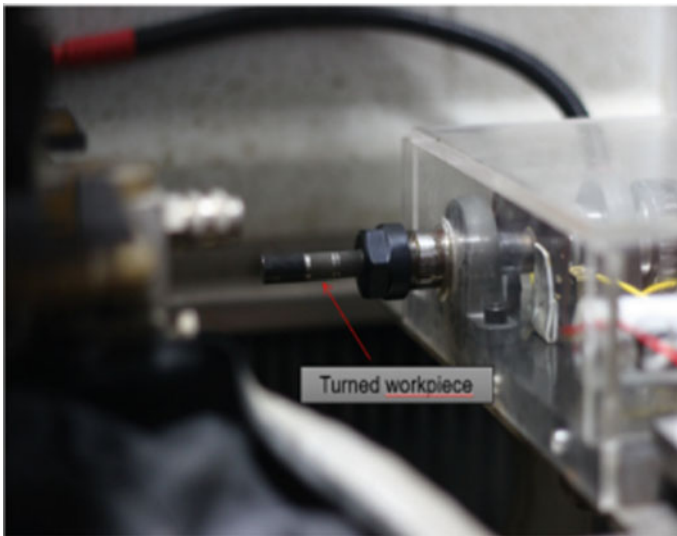


**Fig. 51.2** Specimen turned

In the current research, Box–Behnken design of experiments was chosen, containing 27 experimental runs. Table 51.2 shows L27 Box–Behnken design along with the obtained data for areal surface roughness.

**Table 51.1** Factors and levels

Factor	Levels		
	-1	0	1
Pulse ON time ( $\mu\text{s}$ )	10	15	20
Pulse OFF time ( $\mu\text{s}$ )	25	30	35
Spark gap ( $\mu\text{m}$ )	40	50	60
Rotational speed (rpm)	30	60	90

**Table 51.2** L27 Box–Behnken design with the experimental data obtained

Run order	Pulse ON ( $\mu\text{s}$ )	Pulse OFF ( $\mu\text{s}$ )	Spark gap ( $\mu\text{m}$ )	Rotational speed (rpm)	Areal surface roughness ( $\mu\text{m}$ )
1	10	25	50	60	2.319
2	20	25	50	60	2.932
3	10	35	50	60	2.04
4	20	35	50	60	4.286
5	15	30	40	30	3.862
6	15	30	60	30	3.544
7	15	30	40	90	3.459
8	15	30	60	90	3.521
9	10	30	50	30	3.077
10	20	30	50	30	3.271
11	10	30	50	90	2.358
12	20	30	50	90	4.419
13	15	25	40	60	3.313
14	15	35	40	60	2.433
15	15	25	60	60	2.88
16	15	35	60	60	4.208
17	10	30	40	60	2.492
18	20	30	40	60	3.917
19	10	30	60	60	2.889
20	20	30	60	60	4.56
21	15	25	50	30	2.506
22	15	35	50	30	3.354
23	15	25	50	90	3.393
24	15	35	50	90	3.529
25	15	30	50	60	3.521
26	15	30	50	60	3.614
27	15	30	50	60	3.49

### 51.2.3 ANN Modeling

For accurate predictions, the ANN should be trained using the obtained experimental data. In the present model, a single hidden layer and 12 neurons are taken to run the training exercise using the TRAINGDX training function and LEARNGDM adaptation module in MATLAB. So, out of the 27 data entries, we take 22 entries to train the ANN network using LOGSIG transfer function up to 1000 iterations each time. The training of the network was continued until the fitting curve converges with the training and testing datasets.

## 51.3 Results and Discussion

The ANN model is validated by feeding the network with experimented inputs and comparing the predicted values to the original values. As discussed in the previous section, only 22 entries were taken randomly for training and the other 5 entries are used as samples for prediction using the trained network. The optimal neural network architecture details including its weights and biases are given in Table 51.3.

This sample matrix is fed to the network and the predicted values are found. The corresponding entry numbers (order taken), actual values, predicted values, and error in prediction are tabulated in Table 51.4. The average accuracy of the model is

**Table 51.3** Weights and bias obtained

Hidden layer weights and bias (HL) Transfer function: LOGSIG Number of neurons: 12				Output layer (OL) Transfer function: TRANSIG Number of neurons: 1		
Weights				Bias	Weights	Bias
<i>iw1j</i>	<i>iw2j</i>	<i>iw3j</i>	<i>iw4j</i>	<i>lb1j</i>	<i>iw2j</i>	<i>lb2j</i>
-2.786	-3.683	-0.862	2.494	5.090	0.275	0.346
-3.849	-2.275	-1.581	-2.647	3.930	-1.523	
-1.767	-2.597	2.414	-3.157	3.457	-0.357	
-3.650	-0.611	3.554	-1.241	2.253	0.823	
1.709	-3.361	1.000	-2.815	-2.126	-0.464	
-3.548	0.686	-1.841	3.411	-0.202	-0.825	
-3.193	-0.097	-3.407	2.550	-0.160	1.101	
-4.744	-1.017	1.941	-0.588	-1.258	-1.794	
-2.898	2.208	-1.755	-3.273	-2.272	-0.135	
-4.175	3.018	-1.495	-0.586	-3.196	0.966	
2.332	-4.187	1.435	-1.309	4.561	2.569	
-0.166	0.273	-4.882	3.186	4.462	-1.612	



95.54% as calculated from Table 51.4.

Areal surface roughness ( $S_a$ ) can be accurately predicted using the present ANN model which can be useful in predicting the surface quality with the given input parameters before machining. With further training of the network with additional data, we can increase the accuracy. This can be used for quick inspection based on the input parameters without actually measuring the roughness of the workpiece, which would save a lot of time.

### 51.4 GA Optimization Solution

The genetic algorithm is a search heuristic for solutions of both constrained and non-constrained optimization problems. This is inspired by Charles Darwin’s theory of Natural Evolution, which displays the natural selection process. At each step, genetic algorithm selects an individual randomly from the population and makes some changes in it to produce another set of results. Over the successive iterations, the population “evolves” toward an optimal solution.

Target in the current work is to find the optimal combination of input parameters to get minimal  $S_a$  (areal surface roughness) value. The regression equation is developed using MINITAB software, which is fed to the GA toolbox as objective function in MATLAB. The regression equation is given as follows:

$$\begin{aligned}
 \text{Minimize } S_a = & 8.76 - 0.246 \text{ Pulse on} + 0.243 \text{ Pulse off} - 0.3135 \text{ Spark Gap} \\
 & - 0.0437 \text{ Rpm} - 0.00980 \text{ Pulse on} * \text{ Pulse on} \\
 & - 0.01663 \text{ Pulse off} * \text{ Pulse off} \\
 & + 0.01633 \text{ Pulse on} * \text{ Pulse off} + 0.003112 \text{ Pulse on} * \text{ Rpm} \\
 & + 0.01104 \text{ Pulse off} * \text{ Spark Gap} \qquad (51.1)
 \end{aligned}$$

Table 51.5 shows the GA parameter rates taken for running the GA program.

The optimal process parameters that lead to minimum  $S_a$  value from MATLAB solver are 10.001  $\mu$ s for pulse on time, 35  $\mu$ s for pulse off time, 40.001  $\mu$ m for spark gap, and 90 rpm for rotational speed. The optimal value for  $S_a$  is found to be

**Table 51.4** Result validation

Entry no.	Predicted value	Actual value	% Error
6	3.591	3.544	+1.350
11	2.325	2.358	+1.374
15	2.881	2.880	+0.010
22	3.717	3.354	+10.828
21	2.682	2.506	+7.043
Avg: +4.46			

1.853  $\mu\text{m}$  at the 54th iteration. Validation experiment is conducted using the optimal process parameters obtained from GA technique. Figure 12 shows the best fitness value of GA as 1.853  $\mu\text{m}$  with the mean fitness value being 1.8595  $\mu\text{m}$ .

Table 51.6 presents the results obtained from GA approach along with the validation experiment. It shows a close agreement with the predicted value of  $S_a$ .

## 51.5 Conclusions

This study proposed soft-computing-based ANN modeling to predict the areal surface roughness of the workpiece, viz., Inconel 825. From the literature, it has been shown that areal surface roughness ( $S_a$ ) is more relevant to describe the surface quality and topology of a product. From the results, the predicted values of areal surface roughness ( $S_a$ ) give an accuracy of 96% using this model. Genetic algorithm is found to be fairly useful method for obtaining process parameters in order to attain the required surface quality. From the results of validation experiments, it has been observed that the predicted optimized value for  $S_a$  is in good agreement with the experimental result. The application of the GA approach to obtain optimal machining conditions will be useful at the computer-aided process planning (CAPP) stages in the machining of high-quality products using WEDT process.

**Table 51.5** GA parameter rates

Parameters	Value/function type
Population size	100
Scaling function	Rank
Selection function	Roulette
Crossover function	Scattered
Crossover rate	0.8
Mutation function	Adaptive feasible

**Table 51.6** Results of validation experiment

Optimization for	Optimal parametric combination				Fitness value
	Pulse on time ( $\mu\text{s}$ )	Pulse off time ( $\mu\text{s}$ )	Spark gap ( $\mu\text{m}$ )	Rotational speed (rpm)	
Minimization of areal roughness ( $S_a$ ) using GA	10.001	35	40.001	90	1.853
Validation experiment	10	35	40	90	2.010

**Acknowledgements** Authors would like to sincerely thank Department of Science & Technology (DST), Govt. of India and Centre for precision measurements and Nano-mechanical Testing, Department of Mechanical Engineering, National Institute of Technology Calicut, for providing support to carry out this work under the scheme “Fund for improvement of Science & Technology” (No. SR/FST/ETI-388/2015).

## References

1. Sun, Yao, Gong, Yadong, Yin, Guoqiang, Cai, Ming, Li, Pengfei: Experimental study on surface quality and machinability of Ti-6Al-4V rotated parts fabricated by low-speed wire electrical discharge turning. *Int. J. Adv. Manuf. Technol.* **4**, 13–24 (2017)
2. Aspinwall, D.K., Soo, S.L., Berrisford, A.E., Walder, G.: Workpiece surface roughness and integrity after WEDM of Ti-6Al-4V and Inconel 718 using minimum damage generator technology. *CIRP Ann. Manuf. Technol.* **57**(1), 187–190 (2008)
3. Das, R., Pradhan, M.K.: ANN modelling for surface roughness in electrical discharge machining: a comparative study. *Int. J. Serv. Comput. Orient. Manuf.* **1**, 124–140 (2013)
4. Assarzadeh, S., Ghoreishi, M.: Neural-network-based modelling and optimization of the electro-discharge machining process. *Int. J. Adv. Manuf. Technol.* **39**, 488–500 (2007)
5. Sun, Y., Gong, Y.: Experimental study on fabricating spirals microelectrode and micro-cutting tools by low speed wire electrical discharge turning. *J. Mater. Process. Technol.* **16**, 17–24 (2010)
6. Janardhan, V., Samuel, G.L.: Pulse train data analysis to investigate the effect of machining parameters on the performance of wire electro discharge turning (WEDT) process. *Int. J. Mach. Tools Manuf.* **50**, 775–788 (2010)
7. Aravind Krishnan, S., Samuel, G.L.: Multi-objective optimization of material removal rate and surface roughness in wire electrical discharge turning. *Int. J. Adv. Manuf. Technol.* **67**, 2021–2032 (2013)
8. Kuriakose, S., Shunmugam, M.S.: Multi-objective optimization of wire-electro discharge machining process by non-dominated sorting genetic algorithm. *J. Mater. Process. Technol.* **170**, 133–141 (2005)
9. Liao, Y.S., Yan, M.T., Chang, C.C.: A neural network approach for the on-line estimation of workpiece height in WEDM. *J. Mater. Process. Technol.* **121**, 252–258 (2002)
10. Newton, Thomas R., Melkote, Shreyes N., Watkins, Thomas R., Trejo, Rosa M., Reister, Laura: Investigation of the effect of process parameters on the formation and characteristics of recast layer in wire-EDM of Inconel 718. *Mater. Sci. Eng.* **56**, 208–215 (2009)

# Chapter 52

## Investigation on the Influence of Process Parameters on Surface Roughness and Kerf Properties in Abrasive Water Jet Machining of Carbon Fibre Vinyl Ester Composite



Bhavik Tank and Shailendra Kumar

**Abstract** Abrasive water jet machining is one of the most developed nontraditional machining process. It is generally used to cut difficult-to-cut materials like composites. The present work is focused on machining of carbon fibre vinyl ester composite with abrasive water jet machining. The influence of process parameters, namely, water pressure, traverse rate and standoff distance on surface roughness and kerf taper is studied. Design of experiments is done using Taguchi's L16 orthogonal array. It is found that water pressure is the most influencing parameter followed by traverse rate. It is found that surface roughness and kerf taper decrease with increase in water pressure and decrease in traverse rate.

**Keywords** Abrasive water jet machining · Carbon fibre vinyl ester composite · Process parameters · Surface roughness · Kerf taper

### 52.1 Introduction

Abrasive Water Jet Machining (AWJM) is one of the most developed nontraditional machining process. It is generally used to machine difficult-to-cut materials. It is widely used in industries due to its advantages such as high material removal rate, no thermal effect, minimal stresses, no chatter and high flexibility. Heat-sensitive materials like composites can be machined by AWJM due to no heat generation as well as minimal development of stresses [1]. Carbon fibre vinyl ester composite is made by embedding carbon fibres in vinyl ester resins. It is extensively used in aerospace industries, automotive industries, sport goods, marine vehicle and pressure

---

B. Tank · S. Kumar (✉)

Department of Mechanical Engineering, S.V. National Institute of Technology, Surat 395007, India

e-mail: [skbudhwar@med.svnit.ac.in](mailto:skbudhwar@med.svnit.ac.in)

B. Tank

e-mail: [bhaviktank007@gmail.com](mailto:bhaviktank007@gmail.com)

© Springer Nature Singapore Pte Ltd. 2020

M. S. Shunmugam and M. Kanthababu (eds.), *Advances in Unconventional Machining and Composites*, Lecture Notes on Multidisciplinary Industrial Engineering, [https://doi.org/10.1007/978-981-32-9471-4\\_52](https://doi.org/10.1007/978-981-32-9471-4_52)

631

vessel parts due to its high strength-to-weight ratio, durability and good mechanical properties. Vinyl ester provides very high chemical/environmental resistance and higher mechanical properties than polyesters. Considering the same fibre content, burst pressure of the pressure vessel by the carbon fibre vinyl ester composite is 20% higher as comparison with pressure vessel made with carbon fibres and epoxy matrix [2].

Some researchers have studied the effect of process parameters of AWJM on composites like glass epoxy composites [3], graphite epoxy composites [4], carbon epoxy composites [1], aramid epoxy composites [5] and ceramic composites [6] to study surface roughness and kerf taper.

In the present experimental work, the influence of process parameters on surface roughness and kerf properties in AWJM of carbon fibre vinyl ester composite is studied. Three process parameters, namely, water pressure (WP), traverse rate (TR) and standoff distance (SOD) are considered for present study.

## 52.2 Experimental Setup

The machine used to cut carbon fibre vinyl ester composite is flying arm AWJM (Model—DARDI, DWJ1525-FA). Specifications of the machine are given in Table 52.1. The AWJM machine is equipped with intensifier to pressurise water up to 240 MPa. Attachment used to feed abrasive particles is gravity based.

Mechanical properties of the work material are given in Table 52.2. Thickness of the material used is 20 mm. Machining of carbon fibre vinyl ester composite by AWJM is shown in Fig. 52.1.

**Table 52.1** Specifications of AWJM setup

Structure		Flying arm
Cutting table size	X-axis	1600 mm
	Y-axis	2600 mm
Travel	X-axis	1500 mm
	Y-axis	2500 mm
	Z-axis	150 mm
Max. traverse speed		3 m/min
Cutting head		3 axis
Accuracy	Cutting accuracy	±0.10 mm
	Linear accuracy	±0.10 mm
	Repeatability accuracy	±0.05 mm
Drive system	Drive motor	AC stepper
	Drive mode	Ball screw and guider rail

**Table 52.2** Properties of work material [7]

Properties	Value
Volume fraction	40%
Density	1.56
Tensile strength (MPa)	938 ± 11.4%
Compression strength (MPa)	328 ± 11.5%
Traverse tensile strength (MPa)	17.8 ± 5.7%



**Fig. 52.1** Machining of carbon fibre vinyl ester composite by AWJM

### 52.3 Experimental Design

In present experiment, three process parameters are selected, namely, water pressure, traverse rate and standoff distance to measure their effect on kerf taper and surface roughness. The level of process parameters is selected based on the literature review and capacity of available machine. Trial experiments are also conducted to select levels of process parameters. Based on trial experiments and available literature, four levels of process parameters are selected as given in Table 52.3. Different levels of process parameters for surface roughness and kerf taper angle are chosen because at lower pressure, through cut is possible but it is difficult to separate material properly

**Table 52.3** Levels of process parameters

Process parameters	Level 1	Level 2	Level 3	Level 4
<i>Surface roughness</i>				
Water pressure (MPa)	180	200	220	240
Traverse rate (mm/min)	50	100	150	200
Standoff distance (mm)	2	2.5	3	3.5
<i>Kerf taper angle</i>				
Water pressure (MPa)	150	175	200	225
Traverse rate (mm/min)	70	125	175	225
Standoff distance (mm)	2	2.5	3	3.5

at the end of cut in lead-out region. Thus, to study the wide range of kerf taper angle and surface roughness, two different levels of process parameters are selected. Water pressure can be varied by pressure-regulating knob provided in the machine. Traverse rate can be changed from control panel. Standoff distance can be adjusted by inserting slip gauges between workpiece material and nozzle and then slightly motion is given to nozzle until it touches slip gauges.

In full factorial design, 64 experiments are required for each response parameters, i.e., 64 experiments to study the effect on surface roughness and another 64 experiments to study the effect on kerf taper angle. Therefore, total 128 experiments are required which is neither practical nor economical. Thus, experiments are designed based on Taguchi's L16 orthogonal array and total 32 experiments are carried out, i.e., 16 for surface roughness and 16 for kerf taper angle. Machined samples of surface roughness are measured at three regions, i.e., top, middle, and bottom and average roughness is taken into consideration. Surface roughness is measured by using surface roughness tester (Model—Mitutoyo SJ-310).

Kerf taper angle is calculated by measuring top kerf width and bottom kerf width by keeping 0.5 mm margin from top and bottom edges to nullify the effect of jet entry and jet exit. Kerf widths are measured with the help of vision measurement system (Model—Sipcon SDM-TRZ 5300). The experimental design along with measured value of surface roughness and kerf taper angle is shown in Table 52.4. Machined samples of surface roughness and kerf taper angle are shown in Figs. 52.2 and 52.3, respectively.

## 52.4 Results and Discussion

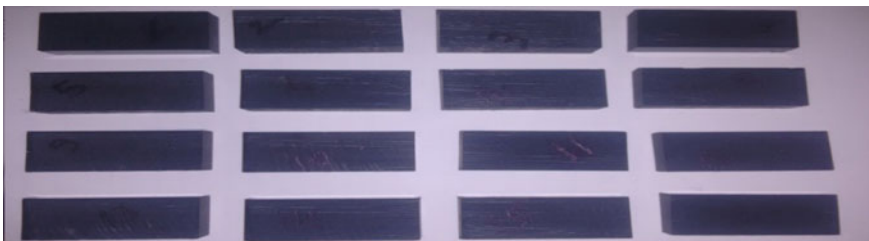
Influence of process parameters, namely, water pressure (WP), traverse rate (TR) and standoff distance (SOD) on response characteristics, namely, surface roughness and kerf taper angle is examined using Analysis of Variance (ANOVA) with the help of MINITAB 16 software. ANOVA is widely used statistical technique to measure the influence and percentage contribution of process parameters on response characteristics. Analysis is carried out at 95% confidence level. ANOVA for surface roughness and kerf taper is given in Table 52.5.

It is found that percentage contribution of water pressure is highest for both response characteristics while percentage contribution of standoff distance is least among three process parameters. Effect of traverse rate lies between the effect of water pressure and standoff distance. Contributions of water pressure, traverse rate and standoff distance for surface roughness are 47.49%, 35.67% and 9.73%, respectively and for kerf taper angle 46.79%, 33.13% and 9.24%, respectively. Figure 52.4 shows percentage contribution of each parameter on surface roughness and kerf taper angle.

**Table 52.4** Experimental design with response values

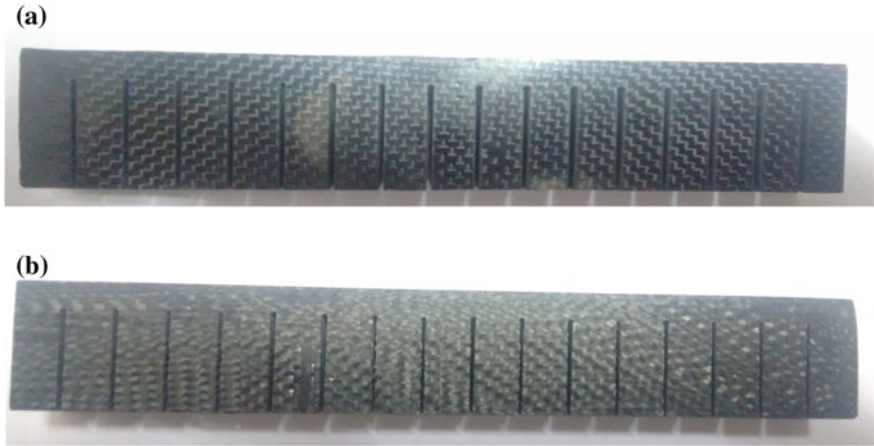
Serial No.	Control factors for roughness			Average surface roughness	Control factors for kerf taper angle			Kerf taper angle
	SOD	WP	TR		SOD	WP	TR	
1	2	180	50	5.182	2	150	70	0.3430
2	2	200	100	5.032	2	175	125	0.3240
3	2	220	150	4.835	2	200	175	0.3200
4	2	240	200	4.753	2	225	225	0.3178
5	2.5	180	100	5.287	2.5	150	125	0.3840
6	2.5	200	50	4.590	2.5	175	70	0.3150
7	2.5	220	200	5.339	2.5	200	225	0.3296
8	2.5	240	150	4.850	2.5	225	175	0.3112
9	3	180	150	5.825	3	150	175	0.4270
10	3	200	200	6.037	3	175	225	0.4620
11	3	220	50	4.677	3	200	70	0.2960
12	3	240	100	4.203	3	225	125	0.2760
13	3.5	180	200	6.670	3.5	150	225	0.6385
14	3.5	200	150	5.756	3.5	175	175	0.3980
15	3.5	220	100	5.621	3.5	200	125	0.2950
16	3.5	240	50	3.926	3.5	225	70	0.2533

Figure 52.5 depicts main effect plots for surface roughness and kerf taper angle. With increase in water pressure, kinetic energy of the jet at exit of nozzle increases, and thus increased kinetic energy of abrasive particles results in increased cutting ability and it cuts material effectively and produces smooth surfaces. With increase in traverse rate, abrasive water jet has lesser amount of exposure time with material and as a result lesser number of abrasive particles took part in cutting action. As a result, the finishing cut done by abrasive particles reduces and it produces rough surface. Standoff distance has low impact on surface roughness but it is found that with increase in standoff distance, surface roughness increases. It is because with increase in standoff distance, flaring action of jet increases and it loses part of its



**Fig. 52.2** Machined samples for surface roughness





**Fig. 52.3** Machined samples for kerf taper angle (a) top view (b) bottom view

**Table 52.5** ANOVA table for surface roughness and kerf taper angle

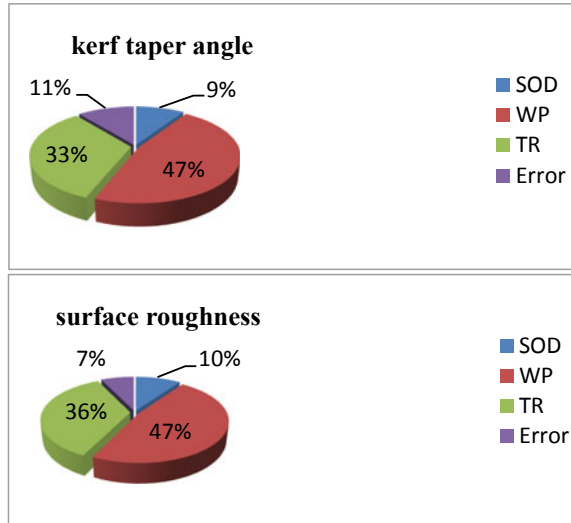
Parameters	DoF	Surface roughness			Kerf taper angle		
		F	P	%P	F	P	%P
SOD	3	2.74	0.135	9.73	1.71	0.264	9.24
WP	3	13.40	0.005	47.49	8.64	0.013	46.79
TR	3	10.06	0.009	35.67	6.12	0.030	33.13
Error	6			7.09			10.83
Total	15						

DOF—degree of freedom, F—F value, P—P value, %P—percentage contribution of respective parameters

available energy as it is exposed longer distance to environment, and thus as jet strikes the material with lesser amount of energy, abrasive particles cannot cut material with its full potential resulting in generation rougher surface. Thus, surface finish improves with increase in water pressure and reduction in traverse rate and standoff distance. Thus, surface finish can be improved by increasing water pressure and decreasing traverse rate and standoff distance.

Kerf taper angle is the angle formed due to difference in top kerf width and bottom kerf width. Generally, lower kerf taper angle is desirable. In AWJM, as abrasive water jet cuts the material from top to bottom, it uses its part of energy to cut the material. Due to this, energy available in the jet reduces as it moves from top to bottom which results in ineffective cutting at the bottom part of cut, resulting in narrower cut at bottom. With rise in water pressure, abrasive water jet contains higher amount of energy, as jet moves from top to bottom it reduces certain part of its energy to cut the material, but as jet has already higher amount of energy, it still possess sufficient amount of energy to cut the material at bottom part of the material. Thus, it reduces

**Fig. 52.4** Percentage contribution of process parameters on kerf taper angle and surface roughness



difference between top and bottom kerf widths which resulted in reduced kerf taper angle. If traverse rate is low, fresh abrasive particles are available at bottom of cut resulting in efficient cutting at bottom part also. With increase in traverse rate, ratio of cut surface area to the number of abrasive particles exposed to cut surface area decreases. As a result, lesser amount of abrasive particles is available to cut material which results in ineffective cut at bottom. Further, lack of availability of fresh particles to cut the material at bottom resulted in narrower bottom cut and difference between top kerf width and bottom kerf width is more resulting in increased kerf taper angle. Standoff distance has negligible effect on kerf taper angle but the increase in standoff distance resulted in narrower bottom kerf width due to reduced energy of jet because of flaring action. Thus, kerf taper angle can be reduced by increase in water pressure and decrease in traverse rate and standoff distance.

## 52.5 Conclusion

In the present work, experimental investigation has been done to study the influence of process parameters, namely, standoff distance, water pressure and traverse rate in AWJM of carbon fibre vinyl ester composite. On the basis of experimental results, the following conclusions are drawn:

1. Water pressure is the most influencing process parameters for surface roughness and kerf taper angle followed by traverse rate.
2. Surface roughness and kerf taper angle decrease with increase in water pressure.
3. Surface roughness and kerf taper angle increase with increase in traverse rate.

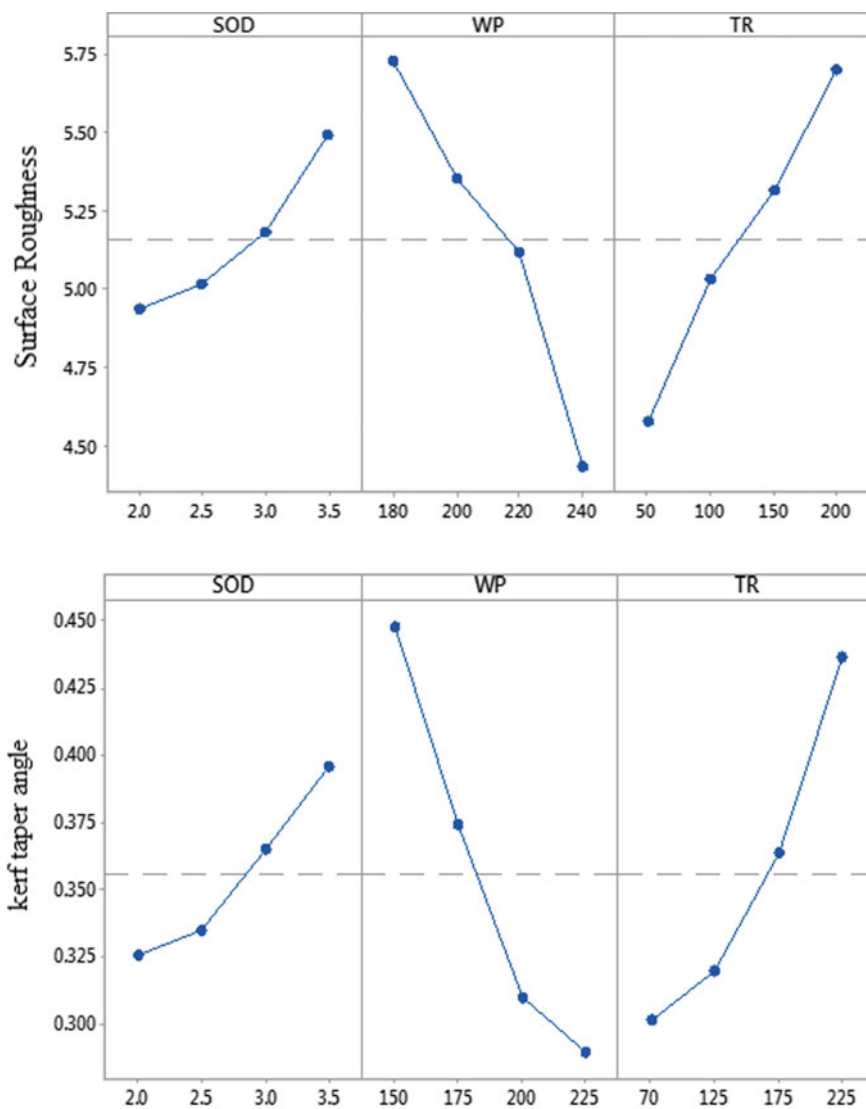


Fig. 52.5 Main effects plot for surface roughness and kerf taper angle

4. Standoff distance has negligible effect on response characteristics, namely, surface roughness and kerf taper angle.
5. Surface roughness and kerf taper angle increase with increase in standoff distance.

## References

1. Dhanawade, A., Kumar, S., Kalmekar, R.V.: Abrasive water jet machining of carbon epoxy composite. *Def. Sci. J.* **66**(5), 522 (2016)
2. Shao, Y., Betti, A., Carvelli, V., Fujii, T., Okubo, K., Shibata, O., Fujita, Y.: High pressure strength of carbon fibre reinforced vinylester and epoxy vessels. *Compos. Struct.* **140**, 147–156 (2016)
3. Azmir, M.A., Ahsan, A.K.: Investigation on glass/epoxy composite surfaces machined by abrasive water jet machining. *J. Mater. Process. Technol.* **198**(1), 122–128 (2008)
4. Ramulu, M., Arola, D.: Water jet and abrasive water jet cutting of unidirectional graphite/epoxy composite. *Composites* **24**(4), 299–308 (1993)
5. Azmir, M.A., Ahsan, A.K., Rahmah, A.: Effect of abrasive water jet machining parameters on aramid fibre reinforced plastics composite. *Int. J. Mater. Form.* **2**(1), 37–44 (2009)
6. Hamatani, G., Ramulu, M.: Machinability of high temperature composites by abrasive waterjet. *J. Eng. Mater. Technol.* **112**(4), 381–386 (1990)
7. Wonderly, C., Grenestedt, J., Fernlund, G., Čepus, E.: Comparison of mechanical properties of glass fiber/vinyl ester and carbon fiber/vinyl ester composites. *Compos. Part B Eng.* **36**(5), 417–426 (2005)

# Chapter 53

## Fluidized Bed Hot Abrasive Jet Machining (FB-HAJM) of K-60 Alumina Ceramic



B. K. Nanda, A. Mishra, Sudhansu Ranjan Das and D. Dhupal

**Abstract** This paper is focused on machining of hard and brittle K-60 alumina ceramic composite material which is widely used as an important insulator in electrical components. The combined effect of hot silicon carbide abrasive particles with compressed air is investigated on technological response parameters after passing the mixture through the fluidized bed abrasive jet machining (FB-AJM) setup. The effect of different machining parameters on material removal rate (MRR), depth of cut (DOC), and surface roughness (Ra) is studied and analyzed. Experiments are conducted according to Box–Behnken design of experiment of response surface methodology to develop quadratic regression models for responses and the model adequacies are confirmed by analysis of variance (ANOVA). The SEM micrograph analysis of the machined composite surface is performed to reveal the plastic deformations. The methodology described here is expected to be highly beneficial to manufacturing industries.

**Keywords** Alumina ceramic · FB-HAJM · Response surface · SEM

### 53.1 Introduction

Alumina ceramic (K-60) is a versatile material for its use in domestic and engineering applications, but difficulties arise in its economic machining operation with proper dimensional accuracy. Abrasive jet machining (AJM) is the most effective technique that can precisely perform the different machining processes like material removal, surface finishing, etching, deburring, and polishing operations on hard and brittle

---

B. K. Nanda (✉)

School of Mechanical Engineering, KIIT University, Bhubaneswar 751024, India  
e-mail: [basantananda\\_2005@yahoo.co.in](mailto:basantananda_2005@yahoo.co.in)

A. Mishra

Department of Mechanical Engineering, IIT, Guwahati 781039, India

S. R. Das · D. Dhupal

Department of Production Engineering, VSS University of Technology, Burla 768018, India

© Springer Nature Singapore Pte Ltd. 2020

M. S. Shunmugam and M. Kanthababu (eds.), *Advances in Unconventional Machining and Composites*, Lecture Notes on Multidisciplinary Industrial Engineering, [https://doi.org/10.1007/978-981-32-9471-4\\_53](https://doi.org/10.1007/978-981-32-9471-4_53)

641

materials like alumina ceramics, glass, quartz, sapphire, and semiconductor materials. The mechanism in AJM is associated with the high-speed abrasive grits in the stream of compressed air to impinge on the work surface to create tiny brittle fractures and the following jet takes away the dislodged particles. Machinability in AJM is associated with the bed pressure, fluid pressure, nozzle tip distance, nature and size of the grain, hardness of the workpiece, temperature, etc. The uniform, high-speed, and homogeneous mixture of the hot abrasives and carrier gas is prepared inside a developed hot mixing chamber of AJM setup known as fluidized bed abrasive jet machining (FB-AJM).

Many researchers reported about the performance of AJM, design of experiments, development of empirical models and different techniques of optimization of process parameters, numerical and experimental analysis, and necessary modifications in the different components of the AJM process so that the effectiveness of AJM can be improved. The names and works of some scientists, researchers, and their contribution to AJM are summarized and briefly discussed below.

Jafar et al. [1] investigated the roughness reduction of unmasked channel in borosilicate glass and observed that post-blasting at shallower angles was more efficient and smaller particles resulted in smoother surfaces, and a relatively large particle significantly increased channel depth. The unwanted consequence of embedding of erodent particles of aluminum oxide abrasive particles into acrylonitrile butadiene styrene, polytetrafluoroethylene, polydimethylsiloxane, and polymethyl methacrylate under cryogenic and room temperature conditions was experimentally studied by Getu et al. [2] found the significant reduction in fractional area coverage by embedded  $\text{Al}_2\text{O}_3$  particles under cryogenic conditions. The surface evolution models for abrasive jet micromachining (AJMM) of metallic substrates like aluminum alloy and stainless steel using alumina abrasive powder with an average velocity were investigated [3] to obtain that the peak erosion rate occurred with jet inclined between 20 and 35°. Using abrasive slurry jet, the mechanism of V-shaped micro-channeling on glasses was performed [4] to study the surface morphology features with two types of major and minor wave patterns. Abrasive water jet cutting technology was used by Ibraheem et al. [5] for production of bolt holes in the assembly of structural frames of glass-fiber-reinforced plastic (GFRP) and statistically approached the influence of abrasive water jet machining parameters to find the optimum values of the process parameters. Li et al. [6] discussed the radial-mode abrasive water jet turning process to understand the mechanism of material removal process and the effect of process variables on depth of cut, material removal rate, and surface roughness. Cárach et al. [7] dealt with tangential abrasive water jet (AWJ) turning of Incoloy alloy 925 to analyze the impact of AWJ traverse speed on the surface quality in terms of microstructure formed on the created surface using Australian garnet as abrasive. Some papers of AJM give importance to the numerical models or statistical approaches for optimizing the process parameters for proper optimum combinations of the variables by suitably considering design of experiment (DOE) and applying the optimization processes like gray-based Taguchi analysis, response surface method, evolutionary algorithms, etc. Routara et al. [8] performed the machining of glass workpieces in AJM to obtain the optimal combination of the process parameters for

the multi-responses, namely, material removal rate and surface roughness by applying Taguchi-based gray relational analysis. Nanda et al. [9] performed experiments on fluidized bed abrasive jet machining (FB-AJM) of alumina ceramic and GFRP using SiC abrasives at normal temperature to analyze the influence of process parameters on different responses and finally applied the particle swarm optimization technique for predicting the optimal values.

The hot air chamber is the latest extension to the abrasive jet machine which replaces the feeder so that the abrasive particles can be heated to the required temperature. Jagannatha et al. [10] carried out the experiments on abrasive hot air jet machining and studied the effect of air temperature on the material removal rate of glass etching and grooving along with the roughness to reveal that roughness was reduced by increasing the temperature of carrier media. The present work represents the use of hot abrasive mixing chamber in the fluidized bed abrasive jet machining setup for K-60 alumina ceramic with three different grades of silicon carbide at various abrasive temperatures with the RSM design of experiment.

## 53.2 Experimental Setup and Procedure

The experiments are performed on the hot abrasive jet machining (HAJM) setup where the abrasive feeder is modified to heat the abrasive grits. Jagannatha et al. [10] performed experiments by mixing of hot air to the abrasive particles, but the use of hot SiC abrasives are considered in this paper. The pressurized air coming from the multistage air compressor acts as the carrier medium after passing through the filter–regulator–lubricator (FRL) unit that produces clean and dry air so as to prevent blocking of abrasives at the nozzle exit. The high carbon and high chromium alloyed AISI D<sub>2</sub> steel is used as the nozzle material. The experiments are conducted inside the properly designed airtight machining chamber of glass fiber materials for preventing the pollution due to the leakage of fine abrasive particles to the atmosphere.

The hard and brittle rectangular pieces of K-60 alumina ceramic material with dimension of 25 mm × 25 mm × 4 mm are used as workpiece materials and black-colored silicon carbide abrasives (SiC) with three different grits sizes 260, 525, and 745 μm are used as abrasives for this experiment. Alumina ceramic composite (K-60) is a dense castable metal which has low iron content and can resist carbon monoxide attack for which it is generally used in foundries, boiler industries, furnaces, etc. Silicon carbide is selected as the suitable abrasive for this alumina ceramic material for obtaining the desired surface finish and material removal rate.

The selection and combination of proper input parameters are important to achieve the best performance of the experimental setup. Here, the bed pressure (P), nozzle tip distance (NTD), abrasive size (S), and temperature (T) are taken as input parameters, each with three different levels as shown in Table 53.1 to measure the output factors such as material removal rate (MRR), surface roughness ( $R_a$ ), and depth of cut (DoC). The range of process parameters setting has been selected after performing some pilot experiments by inspecting the workpiece for a through-hole of acceptable

**Table 53.1** Parameters and levels

Parameters	Levels		
	1	2	3
Pressure, P (bar)	4	6	8
Temperature, T (°C)	60	70	80
Abrasive size, S (μm)	260	525	745
Nozzle tip distance, NTD (mm)	3	5	7

quality. Material removal rate is calculated on mass (g/s) basis as  $MRR = (m_1 - m_2)/\Delta t$ , where  $m_1$  and  $m_2$  (in gram) are the weights of the specimen before and after machining for a time span of  $\Delta t$  seconds. MITUTOYO 400 roughness tester is used to measure the surface roughness of the secondary etched surfaces at different positions of each workpiece and the average is taken as the final surface roughness ( $R_a$ ). The machined hole in AJM resembles a truncated cone in which the depth of cut (DoC) is generated on the surface, which is measured with the help of coordinate measuring machine (CMM 876, Zeiss MC850 with stylus and a probe attachment) (Fig. 53.1).

## 53.3 Results and Discussion

### 53.3.1 Design of Experiment (DOE)

Experimental design of experiment (DOE) is the quality assurance technique which explains the conduct of the experiment and analysis of data. Here, Box–Behnken design (BBD) of response surface methodology (RSM) is implemented to perform the experiments with four input parameters such as pressure (P), nozzle tip distance (NTD), grain size (S), and temperature (T), and each with three levels for developing the required design of experiment to measure the three important responses, viz., material removal rate (MRR), surface roughness ( $R_a$ ), and depth of cut (DoC). The design matrix, statistical calculations, and surface plots are obtained with the help of Design-Expert software. All the experiments are conducted on the indigenously fabricated hot abrasive jet machining setup according to the design matrix as shown in Table 53.2. These results along with the three levels of process parameters are put in the Design-Expert software for detailed analysis.

### 53.3.2 Regression Analysis

The regression analysis for each response is performed by considering quadratic models, as given in Eqs. (53.1)–(53.3).



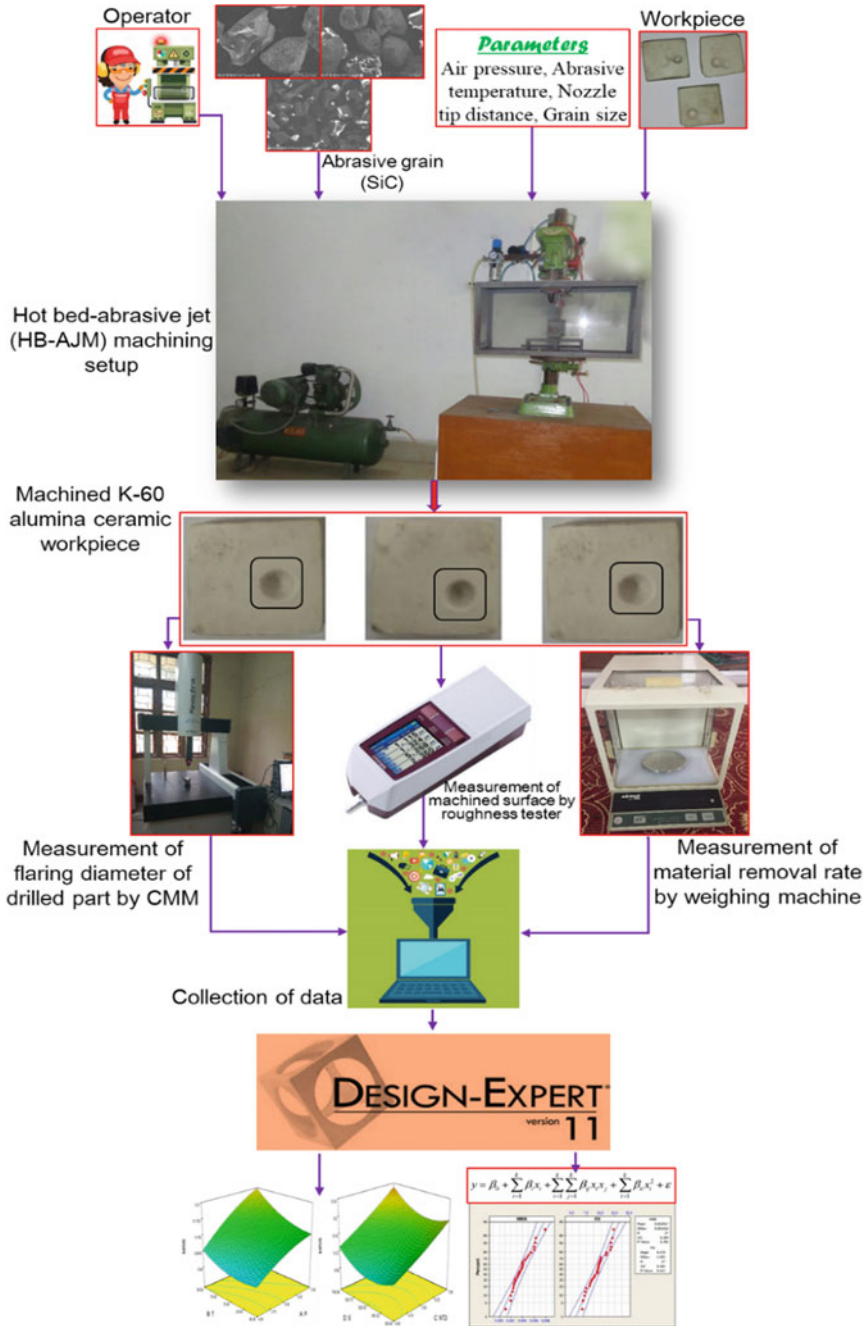


Fig. 53.1 Schematic of experimental setup and methodology presented

**Table 53.2** Experimental design and results

Run no.	P (bar)	T (°C)	NTD (mm)	S (μm)	MRR (gm/min)	DOC (mm)	Ra (μm)
1	6	60	7	525	0.161475	3.4125	0.074
2	8	70	3	525	0.1485	5.2204	0.071
3	6	80	3	525	0.08235	3.8922	0.0657
4	6	60	5	745	0.13725	3.4351	0.0756
5	4	60	5	525	0.07665	2.4606	0.0887
6	8	70	5	260	0.150375	3.19	0.074
7	8	70	5	745	0.170175	5.118	0.0716
8	6	60	3	525	0.03615	2.2364	0.071
9	6	70	5	525	0.1326	3.2866	0.7016
10	8	60	5	525	0.13665	5.5244	0.027
11	6	80	5	745	0.184125	5.182	0.0676
12	6	70	3	745	0.110625	4.1596	0.069
13	6	60	5	260	0.13605	3.4266	0.0746
14	6	80	7	525	0.26595	3.41	0.851
15	4	80	5	525	0.09165	4.6852	0.074
16	6	70	7	745	0.204	4.3138	0.943
17	6	70	5	525	0.0939	2.3931	0.0753
18	4	70	5	745	0.08415	2.1268	0.0743
19	8	70	7	525	0.16815	4.5408	0.074
20	8	80	5	525	0.209475	6.017	0.071
21	4	70	7	525	0.0369	1.084	0.0713
22	4	70	5	260	0.086325	2.6252	0.073
23	6	70	7	260	0.21375	3.04	0.0743
24	6	80	5	260	0.1296	2.9866	0.723
25	4	70	3	525	0.0132	3.1461	0.0703
26	6	70	5	525	0.12045	3.2533	0.0723
27	6	70	3	260	0.13909	2.0672	0.923

$$\begin{aligned}
MRR = & 1.30692 - 0.023903P - 0.031008T - 0.051640 * NTD \\
& + 1.0264 \times 10^{-3}S + 7.22812 \times 10^{-4}PT + 2.5312 \times 10^{-4}P * NTD \\
& + 1.355 \times 10^{-5}PS - 7.284 \times 10^{-4}T * NTD + 5.966 \times 10^{-6}T * S \\
& + 9.84810^{-6}NTD * S - 0.623 \times 10^{-3}P^2 + 1.5904 \times 10^{-4}T^2 \\
& + 1.875 \times 10^{-3}NTD^2 + 4.8788 \times 10^{-7}S^2
\end{aligned} \tag{53.1}$$

**Table 53.3** Results of ANOVA for response model

Responses	p-value	Lack of fit	R-squared	Adj R-squared
MRR	0.0169	0.2074	0.8056	0.5788
DoC	0.0076	0.3491	0.8348	0.6421
Ra	0.0461	0.9525	0.7591	0.4780

$$\begin{aligned}
 DoC = & 32.7102 - 0.79427P - 0.82814T + 1.29906NTD - 0.02132S \\
 & - 0.02165PT + 0.0864P * NTD + 1.2882 \times 10^{-3}PS \\
 & - 0.02073T * NTD + 2.2973 \times 10^{-4}T * S + 9.848 \times 10^{-6}NTD * S \\
 & + 0.1477P^2 + 7.0722 \times 10^{-3}T^2 - 0.01524NTD^2 + 2.23356 \times 10^{-3}S^2
 \end{aligned}
 \tag{53.2}$$

$$\begin{aligned}
 Ra = & -1.45556 + 0.66287P - 0.07944T - 1.3042NTD - 8.38135 \times 10^{-4}S \\
 & + 7.3375 \times 10^{-4}PT + 1.25 \times 10^{-4}P * NTD - 2.8141 \times 10^{-6}PS \\
 & + 9.77875 \times 10^{-3}T * NTD - 6.880 \times 10^{-5}T * S \\
 & + 8.9468 \times 10^{-4}NTD * S - 0.05967P^2 - 6.08 \times 10^{-4}T^2 - 0.019NTD^2 \\
 & + 9.729 \times 10^{-7}S^2
 \end{aligned}
 \tag{53.3}$$

The results obtained from Table 53.2 are used in Design-Expert software to find the most significant variable, statistical parameters values (p-value, Lack of fit, R<sup>2</sup>, and Adj-R<sup>2</sup>) of the response models from the analysis of variance (ANOVA), as shown in Table 53.3. It is observed that the p-values of all three responses are less than 0.05 which implies that models are significant. Again, lack of fit value is nonsignificant, more value of R<sup>2</sup> and the Model-F value is significant for each response which ensures satisfactory validation of the designed models.

### 53.3.3 Analysis of Surface Plots

The surface plots of material removal rate (MRR) versus input parameters are given in Fig. 53.2a which depict that MRR increases with increase in pressure (P). MRR remains almost constant at lower temperatures, but it increases at higher temperatures as the impinging grains achieve higher kinetic energy. Also, it increases with increase of standoff distance (SOD) and grain size (GS). From the surface plots of depth of cut (DOC) in Fig. 53.2b, it is clear that DoC first decreases with pressure and then increases, but it increases at higher temperatures. DoC slightly decreases with increase of NTD but gradually increases with increase of grit size. The surface plot of Ra in Fig. 53.2c shows that Ra increases with increase in NTD, but it first decreases

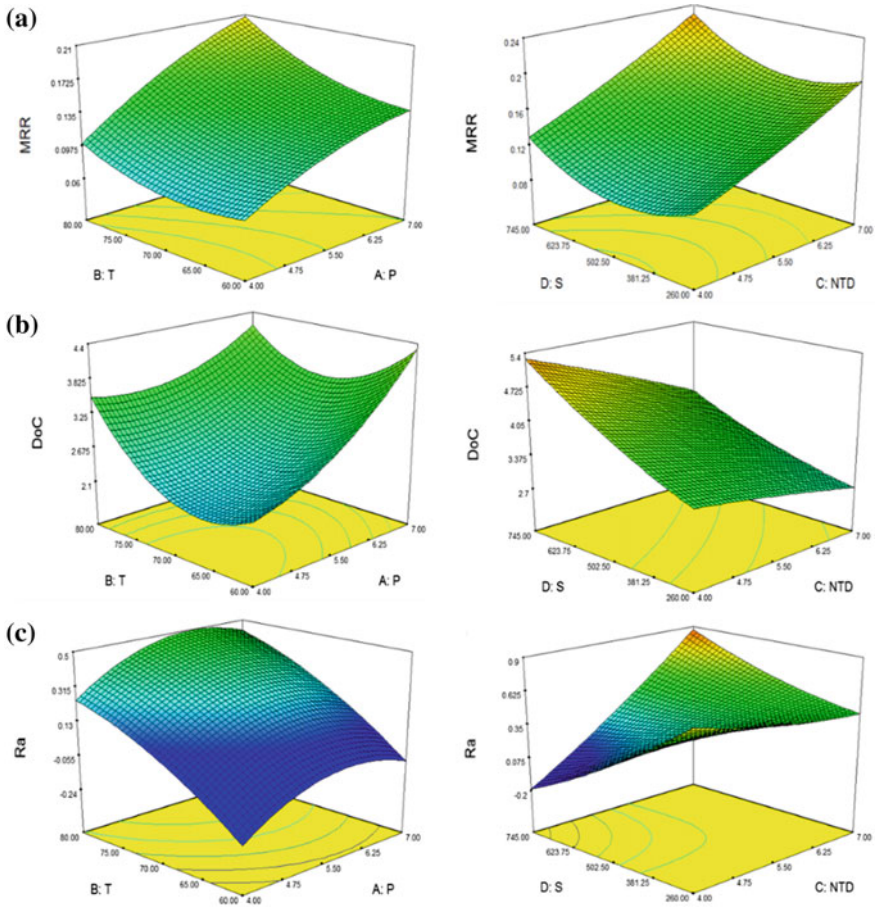
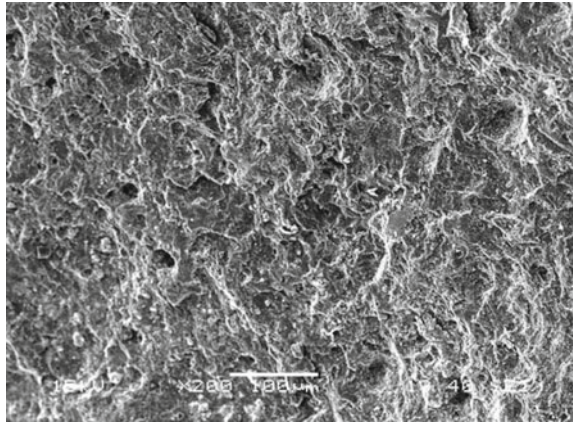


Fig. 53.2 Surface plots for material removal rate (a); depth of cut (b); surface roughness (c)

with grain size and then increases. Surface roughness gradually increases with the increase of temperature and pressure.

The SEM micrograph analysis of the machined ceramic surface is given in Fig. 53.3. The eroded surface is very rough and nonuniformity of material removal is visible giving that the erodent particles are not in uniform size and shape as shown in Fig. 53.3. The plastic deformations are clearly visible by the white lines. Some abrasive particles are embedded to the machined surface, but the percentage of embedment is less at higher temperatures. The SEM micrograph also indicates that maximum erosion occurs at the center.

**Fig. 53.3** SEM micrograph of machined workpiece



## 53.4 Conclusions

From the various investigations during fluidized bed hot abrasive jet machining (FB-HAJM) of K-60 alumina ceramic materials with the three grades of SiC abrasives, the outcomes of the study present that (1) better material removal rate (MRR) is achieved at parametric combinations of high pressure, higher standoff distance, higher grain sizes, and temperature; (2) surface plots of depth of cut (DOC) for this experimental work shows that DOC increases after mid-values of pressure, increases with temperature, and gradually increases with increase of particle size but DOC slightly decreases with increase of NTD; and (3) surface roughness, Ra gradually increases with the increase of temperature and pressure, whereas Ra first decreases with increasing NTD and then increases with grain size.

## References

1. Jafar, R.H.M., Spelt, J.K., Papini, M.: Numerical simulation of surface roughness and erosion rate of abrasive jet micro-machined channels. *Wear* **303**, 302–312 (2013)
2. Getu, H., Spelt, J.K., Papini, M.: Conditions leading to the embedding of angular and spherical particles during the solid particle erosion of polymers. *Wear* **292**, 159–168 (2012)
3. Ally, S., Spelt, J.K., Papini, M.: Prediction of machined surface evolution in the abrasive jet micro-machining of metals. *Wear* **292**, 89–99 (2012)
4. Pang, K.L., Nguyen, T., Fan, J., Wang, J.: A study of micro-channeling on glasses using an abrasive slurry jet. *Mach. Sci. Technol.* **16**, 547–563 (2012)
5. Ibraheem, H.M.A., Iqbal, A., Hashemipour, M.: Numerical optimization of hole making in GFRP composite using abrasive water jet machining process. *J. Chin. Inst. Eng.* **38**, 66–76 (2015)
6. Li, W., Zhu, H., Wang, J., Ali, Y.M., Huang, C.: An investigation into the radial-mode abrasive waterjet turning process on high tensile steels. *Int. J. Mech. Sci.* **77**, 365–376 (2013)

7. Cárach, J., Hloch, S., Hlaváček, P., Ščučka, J., Martinec, P., Petrů, J., Zlámal, T., Zeleňák, M., Monka, P., Lehocká, D.: Tangential turning of Incoloy alloy 925 using abrasive water jet technology. *Int. J. Adv. Manuf. Technol.* **82**, 1747–1752 (2016)
8. Routara, B.C., Nanda, B.K., Sahoo, A.K., Thatoi, D.N., Nayak, B.B.: Optimisation of multiple performance characteristics in abrasive jet machining using grey relational analysis. *Int. J. Manuf. Technol. Manage.* **24**, 4–22 (2011)
9. Nanda, B.K., Mishra, A., Dhupal, D.: Fluidized bed abrasive jet machining (FB-AJM) of K-99 alumina ceramic using SiC abrasives. *Int. J. Adv. Manuf. Technol.* **90**, 3655–3672 (2017)
10. Jagannatha, N., Somashekhar, S.H., Sadashivappa, K., Arun, K.V.: Machining of soda lime glass using abrasive Hot Air Jet: An experimental Study. *Mach. Sci. Technol.* **16**, 459–472 (2012)

# Chapter 54

## Performance Evaluation of Abrasive Water Jet Machining on AA6061-B<sub>4</sub>C-HBN Hybrid Composites Using Taguchi Methodology



A. Gnanavelbabu , K. T. Sunu Surendran  and K. Rajkumar 

**Abstract** Aluminum Metal Matrix Composites (AMMCs) have received considerable attention due to their high strength-to-weight ratio, low cost, and high wear resistance that are appropriate for automotive and aerospace applications. Stir casting technique has been attempted to fabricate AMMC using boron carbide (B<sub>4</sub>C) as hard reinforcement and hexagonal boron nitride (hBN) as the solid lubricant by varying volume (5, 10, and 15%) method. Experimental investigation on machining of hybrid composites to study the effect of Abrasive Water Jet Machining (AWJM) parameters such as mesh size, abrasive flow rate, pressure, traverse speed, and % of reinforcement on Kerf Taper Angle (KTA) and Surface Roughness (R<sub>a</sub>) was carried out. Taguchi's L<sub>27</sub> Orthogonal Array (OA) and Analysis of Variance (ANOVA) have been used to determine the significant parameters affecting the responses and results were validated using Pareto analysis.

**Keywords** Aluminum hybrid composites · AWJM · Taguchi method

### 54.1 Introduction

The fundamental challenge faced by the manufacturing industries today is to achieve economic goals by increasing the production rate, improving the quality of a product, lowering the production cost, and making simultaneous reduction in environmental impact through energy conservation. Optimization techniques can be used for choosing optimum process parameters for economic, effective, and efficient utilization of these processes. Optimization is the process of estimating the potential minimum value of machining performance at the optimal point of process parameters [1]. Modeling and optimization of modern machining parameters through advanced

---

A. Gnanavelbabu (✉) · K. T. Sunu Surendran  
Department of Industrial Engineering, College of Engineering Guindy, Anna University,  
Chennai 600025, India  
e-mail: [agbabu@annauniv.edu](mailto:agbabu@annauniv.edu)

K. Rajkumar  
Department of Mechanical Engineering, SSN College of Engineering, Chennai 603 110, India

© Springer Nature Singapore Pte Ltd. 2020  
M. S. Shunmugam and M. Kanthababu (eds.), *Advances in Unconventional Machining and Composites*, Lecture Notes on Multidisciplinary Industrial Engineering, [https://doi.org/10.1007/978-981-32-9471-4\\_54](https://doi.org/10.1007/978-981-32-9471-4_54)

optimization techniques are now proving as a milestone for manufacturing industries and hence focus has been made on various advanced optimization techniques [2].

AMMCs have properties like lightweight, high strength, and ease of machinability, and boron carbide ( $B_4C$ ) being a prominent ceramic material can be added as reinforcement due to its properties like high strength, low density, extremely high hardness, good chemical stability, and neutron absorption capability. Hexagonal Boron Nitride (hBN) can be used as solid lubricant additives. Further, hBN solid lubricant at various concentrations on mixing with water reduces the cutting zone temperature and enhances the efficiency of machining process. Also, it has been experimentally proved that addition of 10% hBN ensures the optimal condition [3]. Since the traditional machining of reinforced MMCs is very complex, nontraditional machining techniques such as electro-discharge (EDM), Abrasive Water Jet Machining (AWJM), Electrochemical Machining (ECM), Electrochemical Discharge Machining (ECDM), etc. are widely used for machining MMCs [4]. Abrasive Water Jet Machining (AWJM) does not induce high temperatures and as a consequence there is no thermally affected zone and AWJM can be considered to be a very fast machining process for MMCs as very high feed rates are possible in this process [5].

Mugendiran et al. [6] applied Design of Experiment (DOE) to study the effect of  $R_a$  and wall thickness on AA5052 alloy. The optimal results were predicted using Response Surface Methodology (RSM) and ANOVA. Caydas and Hascalik [7] developed Artificial Neural Network (ANN) and the regression model to predict the roughness of surface using Taguchi's DOE. Azmir et al. [8] studied the characteristics of abrasive jet machines surface of glass/epoxy composites laminate. Hence, with these references, Taguchi's DOE and ANOVA are used to determine the effect of machining parameters on  $R_a$  and  $T_r$ . The most significant control factor influencing  $R_a$  and  $T_r$  are hydraulic pressure and type of abrasive materials, respectively. Ghodsiyeh et al. [9] applied RSM to create the optimum situation for verifying the region of factor space where the operation needs are fulfilled. Gupta et al. [10] investigated the kerf characteristics in abrasive water jet machining of marble. Experiments were conducted using Taguchi's design of experiment and ANOVA, and data were evaluated to determine the process that was significantly affecting the kerf properties. It was concluded that nozzle transverse speed was the most significant factor affecting the top kerf width and the kerf taper angle.

Several authors have worked on AMMCs reinforced by  $SiC$ ,  $B_4C$ ,  $Al_2O_3$ ,  $TiO_2$ , and  $ZrO_2$  which have been successfully fabricated and optimized using various optimization techniques. There is no detailed study concerning  $B_4C$ -hBN-based particulate aluminum matrix composites. This article focuses on optimization of process parameters of AWJM over hybrid AA6061 MMCs with various compositions of  $B_4C$  and hBN. The parameters and responses are explored using Taguchi's DOE and ANOVA.



**Table 54.1** Composition of fabricated composites

Composites	AA6061 (vol.%)	B <sub>4</sub> C (vol.%)	hBN (vol.%)
Comp 1	85	5	10
Comp 2	80	10	10
Comp 3	75	15	10

## 54.2 Materials and Methods

### 54.2.1 Materials

In the present investigation, hybrid AMMC has been developed by reinforcing AA6061 with 5–15 vol.% B<sub>4</sub>C and 10 vol.% hBN. Table 54.1 indicates the composition of B<sub>4</sub>C and hBN in fabricated composite. The size of reinforcement particles ranges from 10 to 25  $\mu\text{m}$  for B<sub>4</sub>C and 5  $\mu\text{m}$  for hBN. Aluminum hybrid composites were fabricated using stir casting method. Presence and uniform distribution of reinforced particles in aluminum matrix were confirmed by Scanning Electron Microscopy (SEM).

### 54.2.2 Experimental Setup

To machine the fabricated AMMC, abrasive water jet machining was deployed with various compositions of B<sub>4</sub>C and hBN being reinforced with AA6061 composite. Fabricated composites were subjected to a T6 heat treatment process to increase the grain boundary strengths. The constant values of process parameters kept during the process of machining are given in Table 54.2. Effective process parameters selected for machining are mesh size, abrasive flow rate, pressure, and traverse speed. The standoff distance and jet impingement angle were maintained at 1.5 mm and 90°, respectively, for all cutting conditions.

**Table 54.2** Constant values of process parameters

S.No.	Process parameters	Values
1.	Orifice diameter	0.25 mm
2.	Nozzle diameter	0.75 mm
3.	Focusing tube length	75 mm
4.	Focusing tube diameter	1 mm
5.	Impact angle	90 <sup>θ</sup>
6.	Abrasive type	Garnet
7.	Standoff distance	1.5 mm

### 54.2.3 Measurement of Kerf Taper Angle and Roughness

To identify the inclination formed in the kerf wall during AWJM, the kerf taper angle is calculated. The kerf width is measured using a rational Video Measurement System (VMS). Kerf taper angle was calculated using top kerf and bottom kerf of each pass as in Eq. (54.1).

$$\text{Kerf Taper Angle, } \theta = \frac{\arctan[w_t - w_b]}{2t} \quad (54.1)$$

( $t$  = thickness of material = 10 mm,  $w_t$  = top kerf in mm, and  $w_b$  = bottom kerf in mm).

The kerf taper is calculated to determine the inclination formed in kerf wall during machining of a fabricated composite. The development of kerf taper is not desirable in AWJ cut surfaces since it disturbs the precision of the cut. At lowest pressure and traverse speed, the jet is able to perform smooth cutting across the whole thickness, but later increase in pressure and traverse speed reduces the smooth cutting and there is increase in the rough cutting region throughout the cut. Thus, there is much difference between a top and bottom kerf due to the change in pressure and traverse speed. The aim of the present work is to minimize Ra. The measurements are repeated three times and the average of these values is taken as the Ra.

### 54.2.4 Taguchi Methodology

Taguchi defined an experimental design as “off-line quality control” since it is a method of confirming good performance of a process. While designing experiments using Taguchi’s DOE, selection of OA is an important factor. To measure the quality characteristics, Taguchi converts objective function values into S/N ratio, which is the ratio of mean to standard deviation. The performance characteristics in S/N ratio is categorized in three main divisions such as “Smaller-the-better”, “Nominal-the-best,” and “Larger-the-better.” Having 5 factors, each varied at 3 levels, one needs to conduct 35 experiments using full factorial experimental design. The full factorial design if considered is costly since it has many runs. So, lesser number of experiments saves time and material cost involved in experimentation. An  $L_{27}$  OA was found to be appropriate and hence it is chosen.

**Table 54.3** Levels and values of factors

Factors	Levels		
	1	2	3
Mesh size	80	100	120
Abrasive flow rate (g/min)	240	340	440
Pressure (MPa)	125	200	275
Traverse speed (mm/min)	60	90	120
Reinforcement (vol.%)	5	10	15

### 54.3 Results and Discussion

#### 54.3.1 Experimental Results and Data Analysis

Table 54.3 gives the factors and levels used in the analysis. The experimental results of kerf taper angle and Ra with their computed S/N ratio using  $L_{27}$  orthogonal array are presented in Table 54.4. After conducting the trials for various levels of inputs, namely, mesh size, abrasive flow rate, pressure, traverse speed, and reinforcement, the responses, Kerf taper, and roughness are plotted as per Taguchi’s design of experiments.

#### 54.3.2 Analysis of Variance (ANOVA)

The effect of control factors is investigated through ANOVA. It is a statistical technique used to determine the influence of various parameters on the response and to observe the degree of sensitivity of response to different factors that affect the quality characteristics. The analysis has been carried out at 95% confidence level on S/N ratio of kerf taper angle. The ANOVA results of S/N for kerf taper angle is given in Table 54.5a and from percent contribution, it can be seen that maximum contribution (23.86, 17.36) % is observed at interactions AFR\*Reinforcement and Traverse Speed, respectively. Thus, it can be concluded that reinforcement along with AFR plays an important role in influencing the kerf taper angle.

The ANOVA results of S/N for Ra are given in Table 54.5b and from percent contribution, it can be seen that maximum contribution (32.12, 13.43) % is observed at Traverse Speed and interactions Mesh Size \* Water Pressure, respectively. Thus, it can be concluded that traverse speed is the most influential factor in the quality of the surface.

For prioritizing problem-solving, a simple technique—Pareto analysis—can be used. The Pareto chart provides a graphic illustration of the Pareto principle, a theory upholding that 80% of the output in a given condition or system is produced by 20% of the input. It is commonly called as 80/20 rule. A Pareto chart is combined to confirm the results obtained by ANOVA for S/N parameters. For better comparison, the effect

**Table 54.4** Experimental results using  $L_{27}$  orthogonal array

Ex. No.	Mesh size	AFR	Water pressure	Traverse speed	vol. %	Kerf taper angle (°)	S/N (Kerf taper angle)	$R_a$ ( $\mu\text{m}$ )	S/N ( $R_a$ )
1	80	240	125	60	5	0.399600	7.9675	3.3210	-10.4254
2	80	240	125	60	10	0.378200	8.4456	3.3365	-10.4658
3	80	240	125	60	15	0.357920	8.9243	3.3428	-10.4822
4	80	340	200	90	5	0.387200	8.2413	3.3369	-10.4669
5	80	340	200	90	10	0.372100	8.5868	3.3468	-10.4926
6	80	340	200	90	15	0.369288	8.6527	3.3572	-10.5195
7	80	440	275	120	5	0.499416	6.0308	3.3479	-10.4954
8	80	440	275	120	10	0.435440	7.2214	3.3568	-10.5185
9	80	440	275	120	15	0.307484	10.2435	3.3687	-10.5492
10	100	240	200	120	5	0.604448	4.3728	3.3533	-10.5094
11	100	240	200	120	10	0.467905	6.5968	3.3628	-10.5340
12	100	240	200	120	15	0.396980	8.0246	3.3712	-10.5557
13	100	340	275	60	5	0.450718	6.9219	3.3128	-10.4039
14	100	340	275	60	10	0.442124	7.0891	3.3265	-10.4398
15	100	340	275	60	15	0.408703	7.7718	3.3365	-10.4658
16	100	440	125	90	5	0.635300	3.9404	3.3475	-10.4944
17	100	440	125	90	10	0.462176	6.7039	3.3512	-10.5040
18	100	440	125	90	15	0.312903	10.0918	3.3588	-10.5237

(continued)

Table 54.4 (continued)

Ex. No.	Mesh size	AFR	Water pressure	Traverse speed	vol. %	Kerf taper angle (°)	S/N (Kerf taper angle)	R <sub>a</sub> (μm)	S/N (R <sub>a</sub> )
19	120	240	275	90	5	0.657918	3.6366	3.3368	-10.4666
20	120	240	275	90	10	0.624499	4.0894	3.3421	-10.4804
21	120	240	275	90	15	0.582835	4.6891	3.3512	-10.5040
22	120	340	125	120	5	0.616160	4.2061	3.3468	-10.4926
23	120	340	125	120	10	0.432575	7.2788	3.3533	-10.5094
24	120	340	125	120	15	0.395335	8.0607	3.3588	-10.5237
25	120	440	200	60	5	0.544294	5.2833	3.3421	-10.4804
26	120	440	200	60	10	0.468860	6.5791	3.3482	-10.4962
27	120	440	200	60	15	0.367988	8.6833	3.3563	-10.5172

**Table 54.5** (a) ANOVA for S/N (kerf taper angle). (b) ANOVA for S/N ( $R_a$ )

Source	DF	Adj. SS	Adj. MS	F-value	% Cont.	S/I
<i>(a)</i>						
x1	1	0.0172	0.0172	0.04	0.08	I
x2	1	1.5102	1.5102	3.32	6.59	I
x3	1	1.6104	1.6104	3.54	7.02	I
x4	1	3.9840	3.9840	8.75	17.36	S
x5	1	1.5435	1.5435	3.39	6.72	I
x1 * x2	1	0.4840	0.4840	1.06	2.10	I
x1 * x3	1	2.2031	2.2031	4.84	9.61	S
x1 * x5	1	0.6193	0.6193	1.36	2.69	I
x2 * x3	1	0.0017	0.0017	0.00	0	I
x2 * x5	1	5.4716	5.4716	12.02	23.86	S
x3 * x5	1	1.9582	1.9582	4.30	8.54	I
x4 * x5	1	3.5343	3.5343	7.76	15.40	S
Error	14	6.3754	0.4553			
Total	26	92.835				
<i>(b)</i>						
x1	1	0.0047	0.0026	229.82	19.16	S
x2	1	0.0028	0.0047	140.40	11.78	S
x3	1	0.0016	0.0016	81.69	6.86	S
x4	1	0.0078	0.0078	382.61	32.12	S
x5	1	0.0005	0.0005	28.05	2.35	S
x1 * x2	1	0.0031	0.0031	153.72	12.90	S
x1 * x3	1	0.0032	0.0032	159.94	13.43	S
x1 * x5	1	0.0002	0.0002	13.60	1.14	S
x2 * x3	1	0.00003	0.00003	0.13	0.01	I
x2 * x5	1	0.00003	0.00003	1.71	0.14	I
x3 * x5	1	0.0001	0.00010	5.22	0.44	S
x4 * x5	1	0.00005	0.00005	2.42	0.20	I
Error	14	0.0002	0.00002			
Total	26	0.0320				

S = 0.674824,  $R^2 = 93.13\%$ , Adj.  $R^2 = 87.25\%$ , Pred.  $R^2 = 73.28\%$

Here, x1—mesh size, x2—abrasive flow rate, x3—pressure, x4—traverse speed, x5—% of reinforcement, S—significant, I—insignificant

S = 0.0045388,  $R^2 = 99.1\%$ , Adj.  $R^2 = 98.33\%$ , Pred.  $R^2 = 95.41\%$

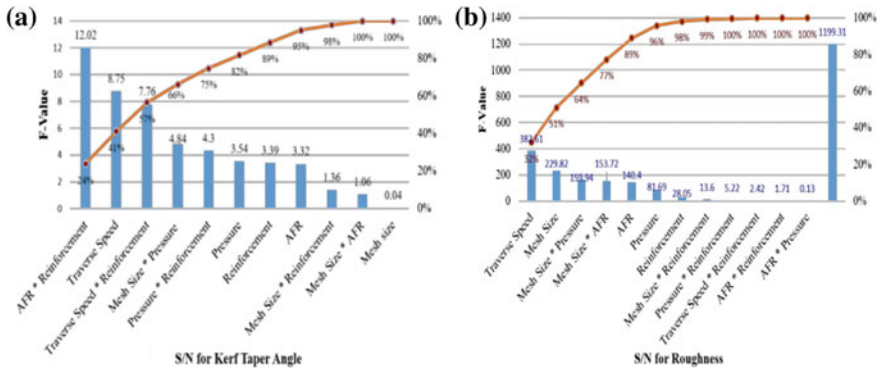


Fig. 54.1 Pareto charts for effect of cutting parameters on a KTA. b Ra

of factors and the interaction on the responses are standardized. The chart aims to rank the interactions in mesh size, AFR, pressure, traverse speed, and reinforcement in descending order. The Pareto chart for effect of cutting parameters is represented in Fig. 54.1a, b.

### 54.4 Conclusions

The AA6061-B<sub>4</sub>C-hBN composites were successfully fabricated using stir casting process and machined using AWJM process. To check the influence of various parameters on responses, ANOVA for S/N ratio is used and it has been found that reinforcement along with AFR having the percentage contribution of 23.86 has the most significant effect on kerf taper angle, while traverse speed along with AFR with the percentage contribution of 32.12 has the most significant effect on Ra. The results attained by ANOVA of technological parameters have been confirmed using Pareto chart.

**Acknowledgements** The authors acknowledge the financial support for the research consumables rendered by DST PURSE Phase II.

### References

1. Azlan, M.Z., Habibollah, H., Safian, S.: Optimization of process parameters in the abrasive water jet machining using integrated SA-GA. *J. Appl. Soft Comput.* **11**(8), 5350–5359 (2011). <https://doi.org/10.1016/j.asoc.2011.05.024>
2. Rao, R.V., Kalyankar, V.D.: Optimization of modern machining processes using advanced optimization techniques : a review. *Int. J. Adv. Manuf. Tech* **73**(5–8), 1159–1188 (2014). <https://doi.org/10.1007/s00170-014-5894-4>

3. Santosh, S., Rajkumar, K., Gnanavelbabu, A.: Effect of hBN solid lubricant concentration on machinability of Titanium (Ti-6Al-4 V) alloy. *Mater. Sci. Forum* **830–831**, 87–90 (2015). <https://doi.org/10.4028/www.scientific.net/MSF.830-831.87>
4. Sankar, M., Gnanavelbabu, A., Rajkumar, K., Thushal, N.A.: Electrolytic concentration effect on the abrasive assisted-electrochemical machining of an aluminum–boron carbide composite. *Mater. Manuf. Process.* **32**(6), 687–692 (2017). <https://doi.org/10.1080/10426914.2016.1244840>
5. Gnanavelbabu, A., Rajkumar, K., Saravanan, P.: Investigation on the cutting quality characteristics of abrasive water jet machining on AA6061-B<sub>4</sub>C-hBN hybrid metal matrix composites. *Mater. Manuf. Process.* **33**(12), 1313–1323 (2018). <https://doi.org/10.1080/10426914.2018.1453146>
6. Mugendiran, V., Gnanavelbabu, A., Ramadoss, R.: Parameter optimization for surface roughness and wall thickness on AA5052 aluminium alloy by incremental forming using response surface methodology. *Procedia Eng.* **97**, 1991–2000 (2014). <https://doi.org/10.1016/j.proeng.2014.12.442>
7. Caydas, U., Hasçalık, A.: A study on surface roughness in abrasive water jet machining process using artificial neural networks and regression analysis method. *J. Mater. Process. Technol.* **202**(1–3), 574–582 (2008). <https://doi.org/10.1016/j.jmatprotec.2007.10.024>
8. Azmir, M.A., Ahsan, A.K.: A study of abrasive water jet machining process on glass/epoxy composite laminate. *J. Mater. Process Tech.* **209**(20), 6168–6173 (2009). <https://doi.org/10.1016/j.jmatprotec.2009.08.011>
9. Ghodsiyeh, Danial, Golshan, A., Izman, S.: Multi-objective process optimization of wire electrical discharge machining based on response surface methodology. *J. Brazilian Soc. Mech. Sci. Eng.* **36**(2), 301–313 (2014). <https://doi.org/10.1007/s40430-013-0079>
10. Gupta, V., Pulak, M.P., Mohinder, P.G., Khanna, Rajesh, Neel, K.B.: Minimization of kerf taper angle and kerf width using Taguchi’s method in abrasive water jet machining of marble. *Procedia. Mater. Sci.* **6**, 140–149 (2014). <https://doi.org/10.1016/j.mspro.2014.07.017>



# Chapter 55

## Empirical Modelling and Optimisation of Bio-Micromachining on Antimicrobial Copper to Fabricate Micromixing System



Abhishek Singh , Arul Manikandan , M. Ravi Sankar ,  
K. Pakshirajan  and L. Roy 

**Abstract** Bio-micromachining is upcoming future unconventional manufacturing process. It has many benefits over other conventional as well as non-conventional process, some of them are no heat-affected zone, no recast layer, no formation of the white layer, and many others. In the present paper, bio-micromachining on copper has been demonstrated. Fabrication of microchannel, as well as optimisation of the process, is done by using central composite run design (CCRD) in combination with response surface methodology (RSM). ANOVA analysis shows that the machining time is the main influencing parameter followed by inoculum size. The maximum material removal obtained was 0.571 grams, when machining time was 32 h and inoculum size was 7.5% (v/v). It is suggested to use the inoculum age of microorganism after 5 days of culture and best before 12 days, in order to get the maximum amount of material removal.

**Keywords** Bio-micromachining · ANOVA · Machining time · Material removal

---

A. Singh

Centre for the Environment, Indian Institute of Technology Guwahati, Guwahati 781039, Assam, India

A. Manikandan

Department of Chemical Engineering, Indian Institute of Technology Guwahati, Guwahati 781039, Assam, India

M. R. Sankar (✉)

Department of Mechanical Engineering, Indian Institute of Technology Guwahati, Guwahati 781039, Assam, India

e-mail: [evms@iitg.ac.in](mailto:evms@iitg.ac.in)

K. Pakshirajan

Department of Bioscience and Bioengineering, Indian Institute of Technology Guwahati, Guwahati 781039, Assam, India

L. Roy

Department of Mechanical Engineering, National Institute of Technology Silchar, Silchar 788810, Assam, India

© Springer Nature Singapore Pte Ltd. 2020

M. S. Shunmugam and M. Kanthababu (eds.), *Advances in Unconventional Machining and Composites*, Lecture Notes on Multidisciplinary Industrial Engineering, [https://doi.org/10.1007/978-981-32-9471-4\\_55](https://doi.org/10.1007/978-981-32-9471-4_55)

661

## 55.1 Introduction

As with the growing population, we require more sustainable and more economical manufacturing technique with the least wastage of parent material. Although we have non-conventional manufacturing processes, still these techniques have some disadvantages like the change of surface morphology, recast layer, porosity, undercut, and many others, as well as their machining and setup cost is too high. The solution to all the above-said disadvantages is bio-micromachining. This process involves microorganism, which acts as the tool for machining the workpiece surface. Uno et al. [1] executed pioneer work by using *Acidithiobacillus ferrooxidans*. They executed experiments by changing some parameters like pH, temperature, and many other parameters. They also suggested a method to fast-track the process by application of the electric field. Zhang and Li [2] experiment result mainly focused on the pure iron and copper machining. They also generated micro-gear and grooves on copper by using the bio-machining technique. Zhang and Li [3] suggest the thermodynamics and kinetic of bio-machining of copper by *Thiobacillus ferrooxidans*. They also proposed the microorganism kinetic effect on the ion-cycle between  $Fe^{2+}$  and  $Fe^{3+}$  as well as thermodynamic effort. Yasuyuki et al. [4] show the practicability of micro-scale levels of material removal in bio-machining on low carbon steels using *Acidithiobacillus ferrooxidans*. Johnson et al. [5] performed experiments to illustrate the surface roughness and quantified the material removal in bio-machining, but they did not clarify the relationship between machining time and surface roughness. Istiyanto et al. [6] inspected the material removal and surface roughness rate features in the bio-machining of copper for many machining periods. They concluded that the metal removal is inversely proportional to the machining time during bio-micromachining of copper. Hocheng et al. [7] observed that the indirect mechanism is answerable for the oxidation of elements and they concluded that copper demonstrates advanced MRR followed by Jadhav et al. [8] demonstrated that the concentration of  $FeSO_4$ , volume, and shaking speed of culture supernatant presented the apparent result on surface roughness and specific metal removal rate (SMRR).

In this paper, the bio-micromachining of copper has been demonstrated. By using bio-micromachining, microchannels are created. Also, optimisation of all the input parameters is done by using response surface methodology (RSM) in combination with central composite rotatable design (CCRD).

## 55.2 Experimental Details

### 55.2.1 Culturing of Microorganism

*Acidithiobacillus ferrooxidans* was procured from Microbial Type Culture Collection (MTCC) and Gene Bank, Chandigarh, India. The microorganism was cultured in the natural atmosphere with low pH and iron to assist as the electrons source

for their development. About 5 ml of microorganism is placed and incubated at 35 °C until microorganism development became light yellow. The 9 K + media is consisting of  $MgSO_4 \cdot 7H_2O$ –0.5 g/l,  $KH_2PO_4$ –0.5 g/l,  $HCl$ –0.1 g/l,  $FeSO_4$ –44.2 g/l,  $(NH_4)_2SO_4$ –3 g/l, and pH is adjusted to 2.5 with 1 N  $H_2SO_4$ . Afterwards, 100 ml of recently developed 9 K + media with 0.5 ml of the culture was nurtured at 35 °C with 180 rpm, until the media became red. Subsequently, the cultured microorganism was sub-cultured for further use (Fig. 55.1). The bacterial hood with positive flow high-efficiency particular air (HEPA) filter was used for complete operation in order to prevent contamination. Then inoculated flasks were incubated at 35 °C with pH = 2.5 at 180 rpm shaking speed using cultured protocol population which were cultivated from 5 to 12 days. At last the workpiece was removed and cleaned with distilled water.

### 55.2.2 Sample Preparation

The copper workpiece of dimension 10 × 10 × 2 mm was used for experimental work. One face of the workpiece was selected. The surface roughness of that face ground to the desired level. Polishing of the selected side carried out by SiC of 320, 600 and 1200 grit sizes each used an array until the preferred level of surface roughness attained. Afterwards, each sample had been put into the sealed plastic bag to avoid surface corrosion. By using AutoCAD, micromixer design was prepared.

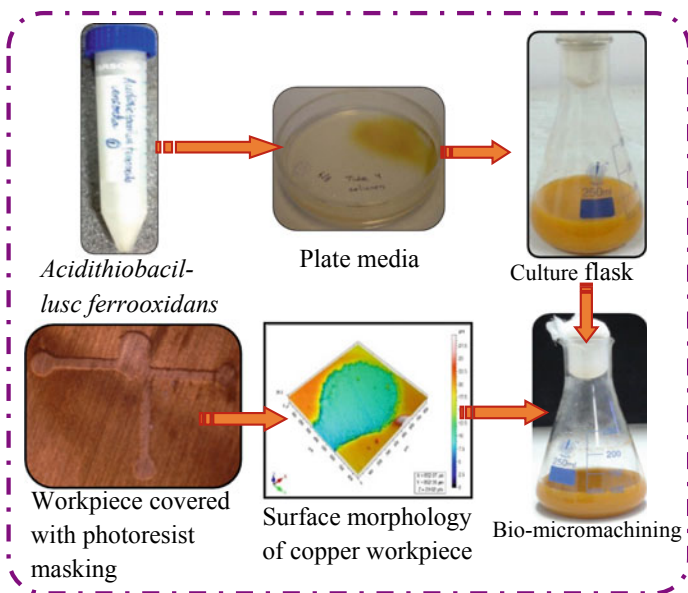


Fig. 55.1 Overview of bio-micromachining of copper

Afterwards, LPR E-1020 masking agent was used to coat the copper workpiece. The workpiece was dipped into photoresist for 10 seconds and dried in the hot air chamber. After this, workpiece was exposed to ultraviolet (UV) light. Afterwards, the workpiece was immersed in the developer and dehydrated in an open atmosphere. Finally, a carbon copy of micromixer was developed on the copper workpiece surface and corresponding surface roughness of uncovered region was measured using non-contact-type profilometer as well as the optical microscope (Fig. 55.2). The uncovered area was exposed to the microorganism during the bio-micromachining process and as a result machining will take place in the uncovered area.

### 55.3 Experimental Plan

Experiments organized in a manner that beneficial information could be determined by carrying out the lowest amount of experiments to maximise material removal. Total sum of experiments in a central composite rotatable design (CCRD) method =  $2k + \text{rotatable} + \text{central runs}$ .

Hence, for this study, experiments were to be arranged for different variables ( $k = 3$ ), i.e., inoculum size, inoculum age and machining time. The entire amount of experiments to be done for these parameters is 20 ( $2^3 + 6 + 6$ ). The rest of the parameters like pH = 2.5, temperature 35 °C and shaking speed = 180 rpm are kept constant. The influence of input parameters on output response, i.e., the material removal rate has been examined. The CCRD-coded input values have been presented in Table 55.1.

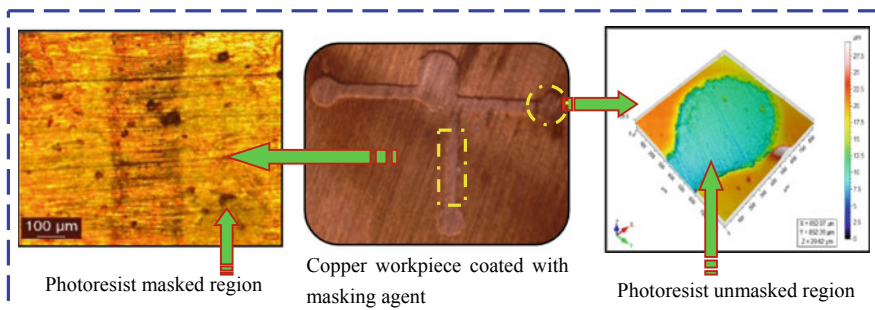


**Fig. 55.2** Photoresist-masked and photoresist-unmasked regions of micromixer on copper workpiece surface

**Table 55.1** Coded levels and resultant absolute values of process parameters

Parameters	Units	Coded variable level				
		-1.682	-1.000	0.000	1.000	1.682
<i>IV</i>	% (v/v)	3.3	5	7.5	10	11.7
<i>IA</i>	Days	3.3	5	7.5	10	11.7
<i>MT</i>	Hours	5	16	32	48	59

## 55.4 Result and Discussion

### 55.4.1 Material Removal

The experiments had been performed according to the CCRD and RSM examined the outcomes. Inlet parameters (machining time, inoculum size and inoculum age) and output response (material removal) for bio-micromachining of copper are given below (Eq. (55.1)):

$$\begin{aligned}
 MR = & -2.84576 + 0.35621IV + 0.34588IA + 0.046874MT + 1.62160^{-003}IV * \\
 & IA + 3.22937^{-004}IV * MT - 4.71875^{-005}IA * MT - 0.025796IV^2 - \\
 & 0.023037IA^2 - 7.43500^{-004}MT^2
 \end{aligned}
 \tag{55.1}$$

where *IV*, *IA* and *MT* represent the inoculum size % (v/v), inoculum age (days) and machining time (hours), respectively, and MR (grams) is material removal.

In the analysis of variance (ANOVA) for material removal using bio-micromachining process, machining time is found to have the maximum influence (43.7%), surveyed by inoculum size (31%) and rest is inoculum age (25.2%). The coefficient of determination ( $R^2$ ) is found to be 0.96 for output response. This results in excellent agreement between input parameters and output response.

In order to check the validity of the process, few verification experiments had been conducted (Table 55.2); one at the optimum parametric condition as well as other three at different conditions within the limit of the parameter (Table 55.1). Designed for 96% assurance interval the confidence band: lower limit for material removal is

**Table 55.2** Validation results of response surface methodology

Experimental condition				Experimental results	
S. No.	<i>IV</i>	<i>IA</i>	<i>MT</i>	<i>MR</i>	Desirability
1	7.29	7.64	32.54	0.5711	1.0000
2	7.37	7.61	34.01	0.5703	0.9810
3	7.50	7.81	33.35	0.5707	1.0000
4	7.48	7.79	33.23	0.5709	0.9981

95% and the higher limit is 96% and Number 1 and 2 drops within the confidence band for material removal. Therefore, the efficiency of the RSM is comforted.

Figure 55.3 shows the effect of inoculum size on the material removal of copper for various inoculum ages. The observation shows that the material removal increases as the inoculum age and inoculum size increase. It is because as the inoculum age increases the microorganism growth also increases and the microorganism growth helps in the material removal, but inoculum plays a vital role. It is because the population of *Acidithiobacillus ferrooxidans* microorganism increases and higher the population more significant will be material removal rate. It appears that very higher population of microorganism sometimes may create a problem of hindrance and this may result in the generation of the random profile as shown in Fig. 55.3.

Figure 55.4 shows the relationship between inoculum size and material removal for various machining time. The observation shows that an increase in machining time gives high material removal. Machining time of 32 h at the inoculum size of 7.5% (v/v) is the best outcome for this process because as we increase the machining time randomness of profile or distortion of the profile is observed as shown in Fig. 55.4. The randomness in profile generation is due to higher exposition to the microorganism that will leach out more material sidewise and this will cause more randomness of profile and will result in the undercut. Also, after 32 h of machining, the microorganism reaches in stationary phase (Fig. 55.6). Therefore, material removal almost becomes constant.

The effect of inoculum age for various inoculum sizes on material removal is shown in Fig. 55.5. Therefore, by varying inoculum size, the population density of

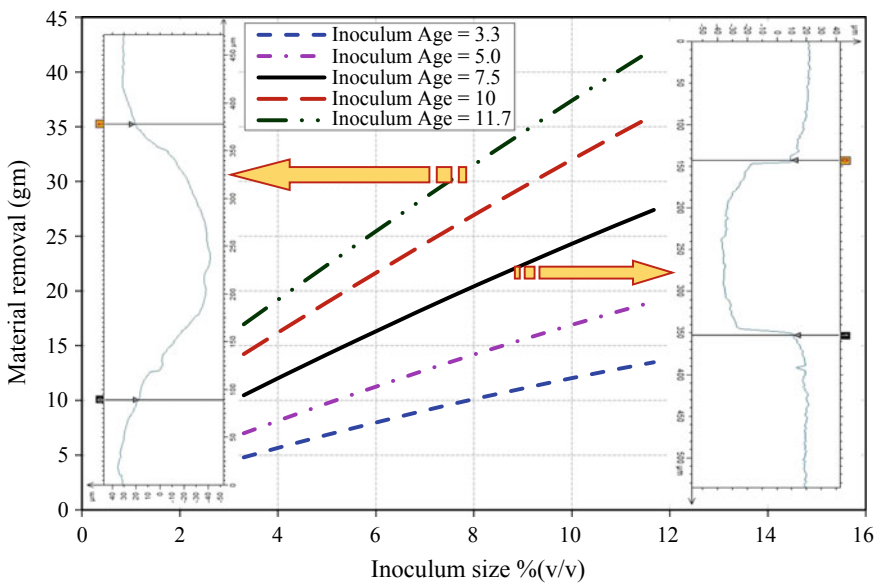


Fig. 55.3 Relationship of inoculum size with material removal for different inoculum ages

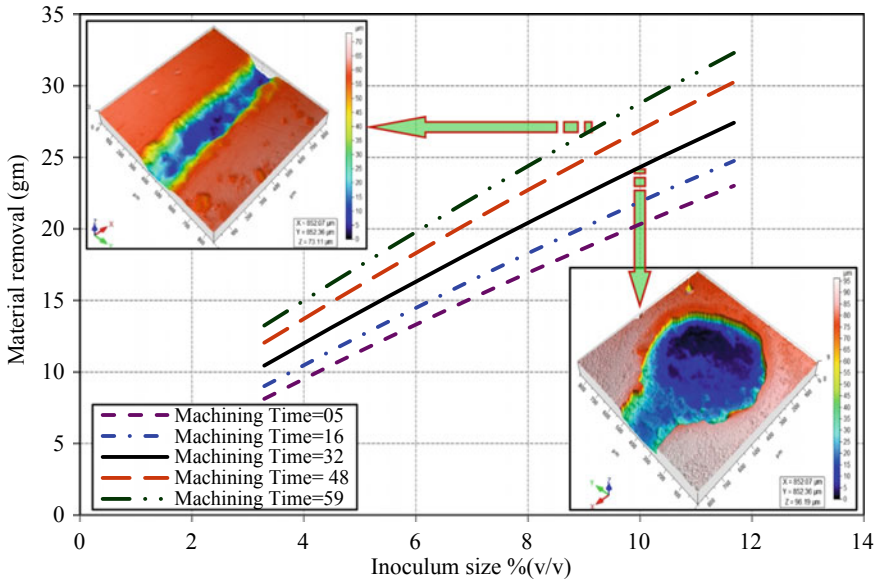


Fig. 55.4 Effect of inoculum size on material removal for different machining time

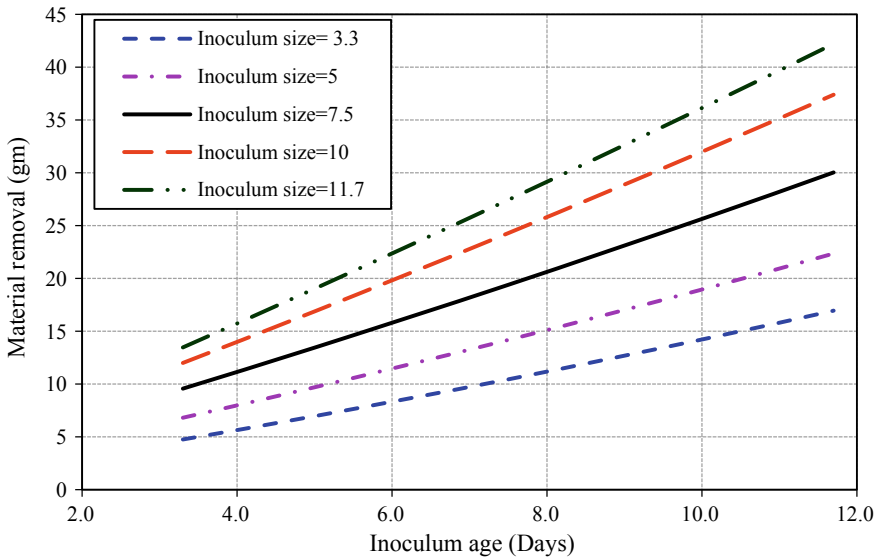
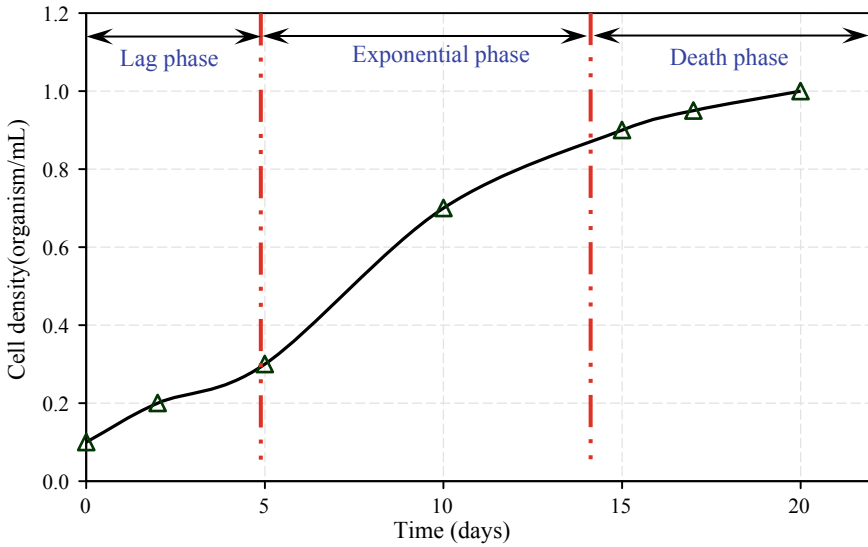


Fig. 55.5 Relationship between inoculum age and material removal for different inoculum sizes



**Fig. 55.6** *Acidithiobacillus ferrooxidans* microorganism growth curve w.r.t. cell density and time

microorganism also varies. This high population density results in a high material removal of the copper workpiece at 7.5 days of inoculum age. Therefore, Fig. 55.6 shows the full growth graph of *Acidithiobacillus ferrooxidans* which is done by growing the microorganism from zero day to their death phase, i.e., 20 days. First, there is a small increase in the growth of microorganisms, i.e., microorganism is in lag phase up to 5 days. Afterwards, there is an exponential increase in the growth of microorganism because they enter into the exponential phase, i.e., from 5 days to 13 days. The microorganism exponentially increases because the generation of new daughter cells takes place. Then, after 13 days of the exponential phase, the growth rate becomes stationary and microorganism starts to die because of lag of nutrition in media as shown in Fig. 55.6. This life cycle of microorganism affects the material removal of the workpiece and it is suggested that for the high amount of material removal the growth of microorganism should be in exponential phase, i.e., between 5 and 15 days in order to achieve the higher amount of material removal by this process.

Figure 55.7 shows the effect of varying inoculum age for various machining time on material removal. The material removal increases when the inoculum age increases. The experimental results show that the best suitable machining time is 32 h and best suitable inoculum age is between 5 and 12 days.



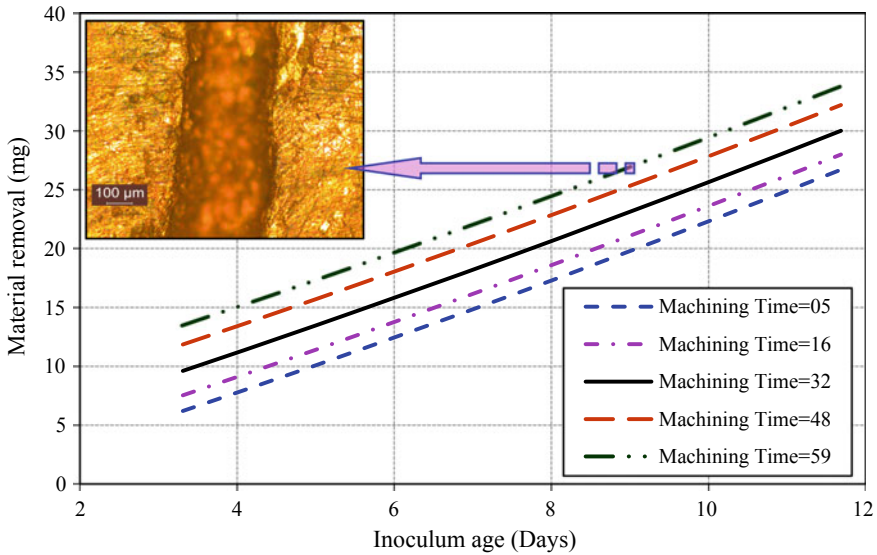


**Fig. 55.7** Effect of inoculum age on material removal for varying machining time

## 55.5 Conclusion

At inoculum size of 7.5% (v/v), highest material removal of 0.56 g is achieved. Followed by inoculum age of 7 days and 12 h and machining time was 32 h. The machining time is the most influencing parameter among all input parameters because as the machining time increases, the material removal will also increase but after 32 h, the increase in machining time will influence profile of the workpiece and undercut will occur. The inoculum size is another important parameter because as the inoculum size increases, the material removal also increases but after 7.5%(v/v) material removal is not much high because the higher concentration of microorganism creates hindrance effect and that is why the material removal is not much higher. The least influencing factor is inoculum age and it is suggested to use microorganism when the age of microorganism is 5 days.

The new future technology is bio-micromachining. There is still more development in this process is required and this technique has broad scope in metal extraction and waste management field.

## References

1. Uno, Y., Kaneeda, T., Yokomizo, S.: Fundamental study on biomachining: machining of metals by *Thiobacillus ferrooxidans*. *JSME Int. J. Ser. C Dyn. Control, Robot. Des. Manuf.* **39**(4), 837–42 (1996)
2. Zhang, D., Li, Y.: Possibility of biological micromachining used for metal removal. *Sci. China, Ser. C Life Sci.* **41**(2), 151–156 (1998)
3. Zhang, D., Li, Y.: Studies on kinetics and thermodynamics of biomachining pure copper. *Sci. China, Ser. C Life Sci.* **42**(1), 57–62 (1999)
4. Miyano, Y., Kamiya, O., Chouanine, L., Kikuchi, Y.: Fundamental studies on biomachining of carbon steel by iron oxidizing bacteria (Materials, Metallurgy & Weldability, International Symposium of JWRI 30th Anniversary). *Trans. JWRI* **32**(1), 239–242 (2003)
5. Johnson, D., Warner, R., Shih, A.J.: Surface roughness and material removal rate in machining using microorganisms. *J. Manuf. Sci. Eng.* **129**(1), 223–227 (2007)
6. Istiyanto, J., Ko, T.J., Yoon, I.C.: A study on copper micromachining using microorganisms. *Int. J. Precision Eng. Manuf.* **11**(5), 659–664 (2010)
7. Hocheng, H., Chang, J.H., Jadhav, U.U.: Micromachining of various metals by using *Acidithiobacillus ferrooxidans* 13820 culture supernatant experiments. *J. Cleaner Prod.* **20**(1), 180–185 (2012)
8. Jadhav, U.U., Hocheng, H., Weng, W.H.: Innovative use of biologically produced ferric sulfate for machining of copper metal and study of specific metal removal rate and surface roughness during the process. *J. Mater. Proc. Technol.* **213**(9), 1509–1515 (2013)

# Chapter 56

## Investigation on Magnetic Field-assisted Near-dry Electrical Discharge Machining of Inconel 600



G. Mannoj Rajkumar, Abimannan Giridharan, R. Oyyaravelu  
and A. S. S. Balan

**Abstract** This paper presents the experimental investigation of magnetic field-assisted near-dry electrical discharge machining (EDM) process. Experiments were conducted by varying pulse on time and discharge current. Material removal rate, surface integrity, and tool wear rate were taken as the performance measures. Results of magnetic field-assisted near-dry EDM are compared with near-dry and wet EDM. Magnetic field-assisted near-dry EDM process produces MRR equivalent to that of wet EDM and 73% compared to that of near-dry EDM process. Better surface finish and less debris reattachment are observed compared to that of wet EDM and near-dry EDM process. Among the three process variants, magnetic field-assisted near-dry EDM possess higher tool wear rate. Scanning electron microscopy images of the machined surfaces obtained through magnetic field-assisted near-dry EDM is found to have lesser debris deposition and 9% surface finish enhancement when compared with other EDM processes.

**Keywords** Magnetic field-assisted near-dry EDM · Near-dry EDM · Wet EDM · Material removal rate · Surface roughness · Tool wear rate · Surface morphology

### 56.1 Introduction

Materials such as titanium alloys, nickel-based alloys, and ferrous alloys used in aerospace, nuclear, medical, and automotive industries are referred to as difficult to machine materials. Machining these materials using conventional methods produce

---

G. M. Rajkumar

School of Mechanical Engineering, Vellore Institute of Technology, Vellore 632014, India

A. Giridharan

School of Mechanical Engineering, Vellore Institute of Technology, Chennai 632014, India

R. Oyyaravelu · A. S. S. Balan (✉)

Centre for Innovative Manufacturing Research, Vellore Institute of Technology, Vellore 632014, India

e-mail: [balan.sheytra@vit.ac.in](mailto:balan.sheytra@vit.ac.in)

© Springer Nature Singapore Pte Ltd. 2020

M. S. Shunmugam and M. Kanthababu (eds.), *Advances in Unconventional Machining and Composites*, Lecture Notes on Multidisciplinary Industrial Engineering, [https://doi.org/10.1007/978-981-32-9471-4\\_56](https://doi.org/10.1007/978-981-32-9471-4_56)

671

excessive tool wear, heat generation, and higher cutting force that results in low productivity and poor surface finish. Electrical discharge machining (EDM) is one of the nonconventional machining processes used to machine difficult to machine materials with intricate shapes. The mechanism of material removal in EDM is by means of rapid repetitive spark occurring in between the tool and workpiece immersed in a dielectric medium. Tool and workpiece are maintained at constant gap known as a spark gap. When a high potential difference is applied between the tool and workpiece separated by a distance of spark gap, dielectric breaks down and sparks discharge in the gap. As the discharge begins, melting and vaporization of the tool, workpiece, and dielectric medium take place. The servo control maintains the constant gap between the tool and workpiece. As the discharge ceases, the dielectric medium cools the electrode (both tool and workpiece) and flushes out the molten material, vaporized, and condensed debris particles from the spark gap [1]. The energy contained in each spark is transferred to tool and workpiece through the dielectric fluid. The properties such as dielectric strength, thermal conductivity, heat capacity, and viscosity of the dielectric fluid affect the machining performance of EDM process. Deionized water and kerosene/hydrocarbon oil are the most commonly used dielectric fluid in conventional wet EDM process. Dry EDM, near-dry EDM, and magnetic field-assisted near-dry EDM are the emerging areas of EDM process which uses gaseous, mist (liquid–gas mixture), and application of external magnetic field, respectively, as dielectric fluids.

Several researchers attempted to study the influence of process parameters on machining characteristics, viz., material removal rate (MRR) and surface integrity of dry EDM process. In dry EDM process, a high velocity of gas jet (dielectric fluid) is supplied to the spark gap through a rotating or planetary motion pipe tool electrode [2]. Authors have attempted to compare the MRR of dry EDM milling and conventional milling of quenched steel and proposed a hypothesis of achieving equivalent MRR and better machining accuracy using dry EDM milling [3]. Machining of cemented carbide using dry EDM milling exhibits high machining speed and lower electrode wear compared to that of oil EDM milling and oil die-sinking EDM process [4]. Saha and Choudhury [5] attempted to study the parametric influence of dry EDM on MRR of mild steel and stainless steel [6] materials. Authors stated that the effect of discharge current, duty factor, and air pressure on MRR is dominant. Govindan and Joshi analyzed the dry EDM machining of SS 304 steel material on MRR, tool wear rate, and oversize using different shapes of tool electrode [7, 8]. Fattahi and Baseri proposed a hypothesis on the effect of process parameters such as discharge current, pulse on time, gas pressure, and electrode rotation speed on MRR and tool electrode wear rate [9]. Authors stated that MRR increases with increase in pulse duration and tool electrode wear reduces by increasing gas pressure [10, 11]. Researchers have attempted to improve the performance of dry EDM by applying external magnetic field intensity into the machining zone. Joshi et al. [12] proposed a hybrid dry EDM process using pulsating magnetic field intensity and studied the performance and mechanism of material removal using single spark analysis [13]. Teimouri and Baseri studied the influence of magnetic field intensity on rotating tool

electrode in die-sinking process and stated that the applied external magnetic field enhances the better flushing of the gap [14].

Near-dry EDM is one of the emerging areas of EDM process that uses mist (liquid–gas mixture) as the dielectric medium. Researchers have attempted to study the influence of process parameters on MRR and surface finish on different materials during near-dry EDM process. Kao et al. studied the influence of process parameters such as pulse on time and pulse off time on the material removal rate of aluminum 6061 material [15]. Authors proposed that near-dry EDM produces higher material removal rate, sharp cutting edge, and less debris deposition on the machined surface compared to that of wet and dry EDM process. The process parameters such as current, pulse on time, and pulse off time are varied to compare the surface finish of machined components during dry and near-dry EDM process. Authors stated that for lower values of pulse on time and discharge current, near-dry EDM produces the better surface finish on machined component than that of dry EDM process [16]. Increasing the dielectric flow rate in near-dry EDM increases the material removal rate [17]. From the literature, it is observed that a lot of work has been published in analyzing the performance of dry EDM process using different gaseous dielectric fluids. Limited work is been published in studying the effect of process parameters on MRR and surface integrity of components machined using near-dry EDM and magnetic field-assisted near-dry EDM process.

In this research work, the effect of the pulse on time and discharge current on machining characteristics, viz., material removal rate, surface finish, and surface topography of the machined component, is analyzed during near-dry EDM and magnetic field-assisted near-dry EDM (MFAND EDM) process. The results obtained are compared with the results from normal EDM process. The surface of the machined components is analyzed using 2D roughness profile and using scanning electron microscope (SEM) images. The following section presents the experimental procedure and results obtained in detail.

## 56.2 Experimental Details

Experiments were conducted on Electronica C425 EDM machine. Copper (99.9% Cu) of 8 mm diameter is used as an electrode material. Inconel 600 plate of 100 mm length, width 50 mm, and depth of 4 mm is used as workpiece material. The chemical composition of Inconel 600 is given in Table 56.1. The commercial EDM oil, IPOL spark erosion 450 is used as a liquid dielectric in normal or wet EDM process.

**Table 56.1** Chemical composition of Inconel 600

Ni	Cr	Fe	Mn	Cu	Si	C	S
72.0	14.0–17.0	6.0–10.0	1.0	0.5	0.5	0.15	0.015

In near-dry EDM, the dielectric fluid (oil–air mixture) is sprayed through Accu-Lube precision pump used for minimum quantity lubrication (MQL) in conventional machining that is adopted. Compressed air at 6 bar pressure is given to MQL setup to generate oil–air mixture dielectric at a flow rate of 300 ml/h. In magnetic field-assisted near-dry EDM process, pulsating magnetic fields are produced by three electromagnets arranged in triangular configuration [13] so as to get the resultant magnetic field tangential to the plasma column. The magnetic field intensity is maintained constant at 0.3 T [12]. The experimental setup used for conducting experiments is given in Fig. 56.1. In this work, the pulse on time and discharge current were taken as the input parameters. The input parameters are varied at three levels, viz., pulse on time 100  $\mu$ s, 200  $\mu$ s, 300  $\mu$ s and discharge current as 12, 16, 20 A. The effects of these input parameters on material removal rate, the surface roughness of the machined components, and tool wear rate of the electrode were analyzed. The parameters such as voltage, duty factor, air pressure, dielectric flow rate (for near-dry and MFAND EDM), and magnetic field intensity were maintained constant at 40 V, 80%, 6 bar, 300 ml/h, and 0.3 T, respectively. The material removal rate (g/min) and tool wear rate are calculated using the formulae given in Eqs. (56.1) and (56.2), respectively

$$MRR = \frac{w_i - w_f}{t_m} \quad (56.1)$$

$$TWR = \frac{w_i - w_f}{t_m} \quad (56.2)$$

where

$w_i$  and  $w_f$  Initial and final mass of workpiece (g)

$t_m$  Machining time (min).

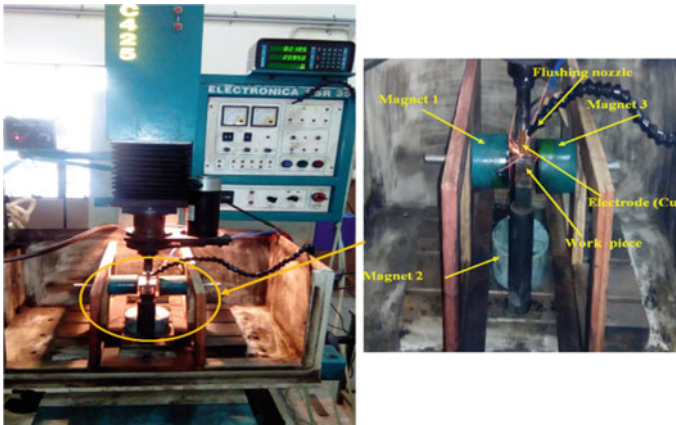


**Fig. 56.1** Experimental setup used for conducting experiments

The mass of the component before and after machining and loss in mass of tool electrode is measured by using the weighing balance of 0.1 mg accuracy. The surface roughness of the machined component is measured using Marsurf XR20. For each process parameter combination, three experiments were conducted and their average value is given in Table 56.2.

## 56.3 Results and Discussion

The input parameters such as pulse on time and discharge current and output parameters such as MRR and surface roughness are given in Table 56.2.

### 56.3.1 *Effect of Process Parameters on Material Removal Rate*

The effect of pulse on time and discharge current on the material removal rate of wet, near-dry, and MFAND EDM are given in Fig. 56.2. Varying pulse on time and discharge current, MRR is higher for wet EDM process compared to that of near-dry and MFAND EDM. The dielectric oil used in wet EDM is having a higher viscosity than oil–gas mixture dielectric used in near-dry and MFAND EDM. The higher the viscosity of dielectric fluid, the more the material removed from the surface. In wet EDM process, as pulse on time increases MRR decreases. At low pulse on time, the discharge energy of the pulse is used effectively that resulted in increased MRR. As the pulse on time increases, the discharge energy per pulse increases. During pulse on time, dielectric breaks down and discharge begins in the gap that starts melting and vaporization the material on the surface. As the discharge proceeds, large portion of heat is utilized to melt the material. At the end of pulse on time, the discharge ceases and the molten material gets re-solidified back on to the machined surface, possibly due to insufficient flushing of the dielectric medium [18, 19]. As the pulse on time increases, discharge energy per pulse resulted in increased debris concentration in the gap. Increase in concentration of debris leads to the formation of the arc and short-circuit pulse. Short-circuit pulses are an inactive pulse which does not contribute to material removal [20].

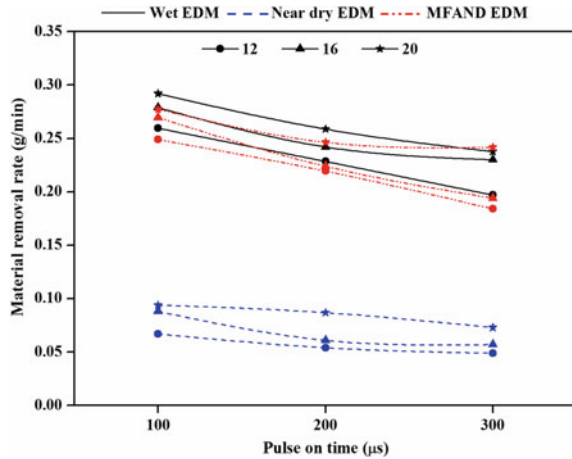
In near-dry EDM, the dielectric medium used is an oil–gas mixture. Due to the low viscosity of the oil–gas mixture, the explosive force generated inside the plasma channel reduces. This resulted in reduced MRR. For all pulse on time and discharge current values, the MRR obtained using MFAND EDM is almost equivalent to that obtained using wet EDM process. In MFAND EDM process, the applied magnetic field acts tangentially to the plasma that tries to prevents its further expansion. As the growth of plasma channel is constrained, that increases the pressure inside the plasma. Increase in pressure of plasma erodes more amount of material from the

**Table 56.2** Effect of process parameters on MRR, surface roughness, and tool wear rate

TON	I	Measured MRR (g/min)			Surface roughness ( $R_a$ ) ( $\mu\text{m}$ )			Tool wear rate (g/min)		
		Wet EDM	Near-dry EDM	MFAND EDM	Wet EDM	Near-dry EDM	MFAND EDM	Wet EDM	Near-dry EDM	MFAND EDM
100	12	0.2595	0.067	0.2489	2.5411	2.5025	2.3025	0.0046	0.0048	0.0056
200	12	0.2285	0.054	0.2194	3.6593	3.5965	3.3965	0.0043	0.0045	0.0053
300	12	0.1970	0.049	0.1840	4.6327	3.7824	3.5824	0.0040	0.0042	0.0050
100	16	0.2789	0.088	0.2695	2.9189	2.7863	2.5863	0.0053	0.0055	0.0063
200	16	0.2420	0.061	0.2240	3.7340	3.6390	3.4390	0.0046	0.0048	0.0053
300	16	0.2300	0.057	0.1940	4.8777	4.6323	4.4323	0.0042	0.0044	0.0053
100	20	0.2919	0.094	0.2774	3.1361	3.1078	2.9078	0.0067	0.0069	0.0076
200	20	0.2588	0.087	0.2464	4.3407	4.2323	4.0323	0.0052	0.0054	0.0065
300	20	0.2378	0.073	0.2417	4.9040	4.8770	4.6770	0.0046	0.0048	0.0056



**Fig. 56.2** Influence of process parameters on MRR



surface. As the pulse on time increases, more debris particle generated in the gap resulted in reduced MRR as explained earlier. Figure 56.3 shows the SEM micrograph of component machined under wet EDM, near-dry EDM, and MFAND EDM taken at a magnification of 300X.

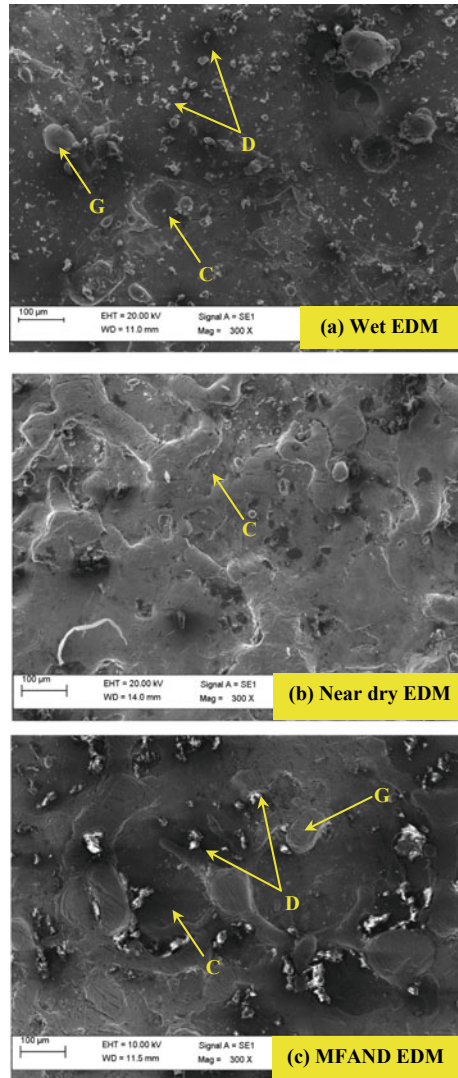
From SEM micrograph, the reattachment of debris particle generated due to arcing can be seen in both wet EDM and MFAND EDM machined surfaces. The surface generated by near-dry EDM composed of shallow craters due to less material removal and clean surface due to the better flushing of oil–air mixture dielectric fluid.

### 56.3.2 Effect of Process Parameters on Surface Roughness

Typically, influence of process parameters on surface roughness is given in Fig. 56.4.

As the pulse on time and discharge current magnitude increases, surface roughness increases. Among the three EDM processes, wet EDM produces a surface with more irregularities. This is due to higher inertia and viscosity of liquid dielectric compared to that of oil–gas mixture dielectric. High dielectric fluid viscosity prevents the expansion of plasma channel which builds up more pressure inside plasma and generates larger explosive force to remove material [15]. As the pulse on time increases, more debris is generated in the gap. Increasing the concentration of debris in the gap, the material is removed from the surface at random location. This resulted in the poor surface finish on surface generated using wet EDM. As the current increases, the intensity of the spark produced is more which leads to larger and deeper crater on the work material which increases the surface roughness [21]. The surface roughness obtained in near-dry EDM and MFAND EDM is low compared to that obtained using wet EDM. The lower viscosity of oil–gas mixture resulted in a shallow crater in the region of spark that leads to the better surface finish [16]. Due to lesser entrapment of

**Fig. 56.3** SEM micrograph of components machined at 300  $\mu$ s pulse on time and 20 A discharge current (C—Crater, D—Debris, G—Spherical globules)



debris on the work material because of the magnetic force which flushes the debris from the machined surface and protects the surface from remelting and sticking. The flushed debris will also ground the rough edge of discharge craters and make the little surface smooth which further reduces the surface roughness [22]. Figure 56.5 shows the typical 2D roughness profiles of the component machined under wet EDM, near-dry EDM, and MFAND EDM.

**Fig. 56.4** Influence of process parameters on surface roughness

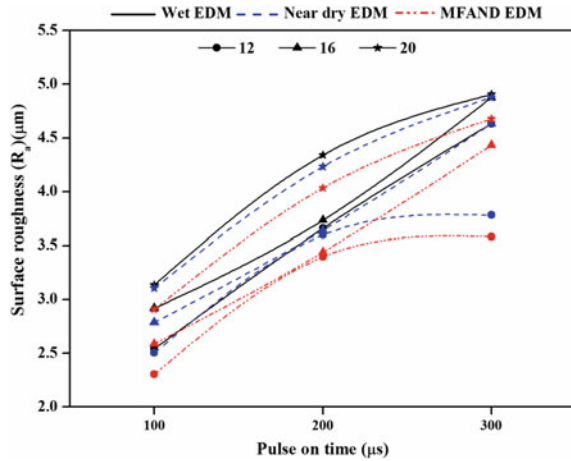
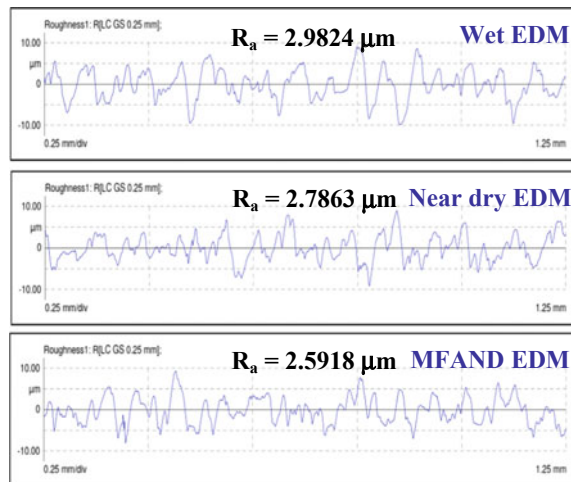


**Fig. 56.5** Roughness profile of component machined at 100 μs pulse on time and 16 A discharge current



### 56.3.3 Effect of Process Parameters on Surface Morphology

The surface morphology of the work material machined under different dielectric environments for the condition 300 μs pulse on time and 20 A discharge current taken at a magnification of 400X is investigated using scanning electron microscope (SEM) as shown in Figs. 56.6, 56.7, and 56.8 for wet EDM, near-dry, and MFAND EDM, respectively.

Higher entrapment of debris was seen in Wet EDM when compared to that of near-dry EDM and MFAND EDM machined surface. SEM micrograph of the surface is obtained using near-dry EDM process with less number of debris. In ND EDM process, the dielectric used is the combination of liquid and pressurized air. The

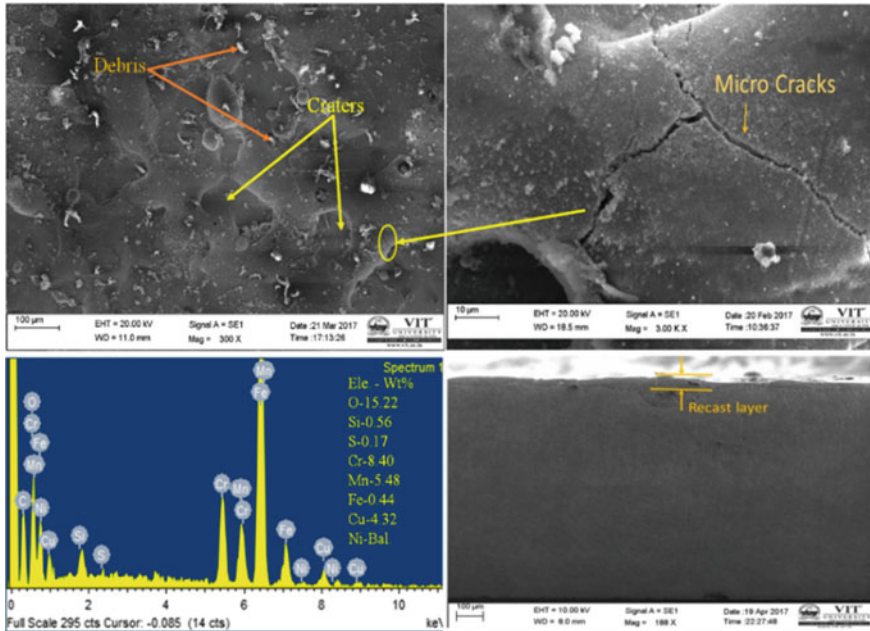


**Fig. 56.6** Surface morphology of Inconel 600 under wet EDM

dielectric is in the form of mist which flushes the debris away from the machining gap. Finer surface with lesser debris accumulation was obtained by MAND EDM process (Fig. 56.8a). In MAND EDM process, the debris is flushed away by both the pressurized dielectric and magnetic fields. The magnetic force flushes away the debris from the machined surface and protects the surface from debris reattachment. Figures 56.6b, 56.7b, and 56.8b show the variation of recast layer under various EDM processes. The higher order thickness of recast layer was seen in wet EDM process, due to more amount of re-solidified material adhered onto the surface when compared with near-dry EDM and MFAND EDM process. Microcracks were observed on the surface obtained by wet EDM and near-dry EDM processes intersecting each other, which are shown in Figs. 56.6 and 56.7c. The formation of these microcracks is mainly due to the abnormal discharges caused by the accumulation of debris in the machining zone. These regions are subjected to severe residual stress, and hence more prone to cracking [23]. No such microcracks were found on the surfaces obtained by MAND EDM process as shown in Fig. 56.8(c).

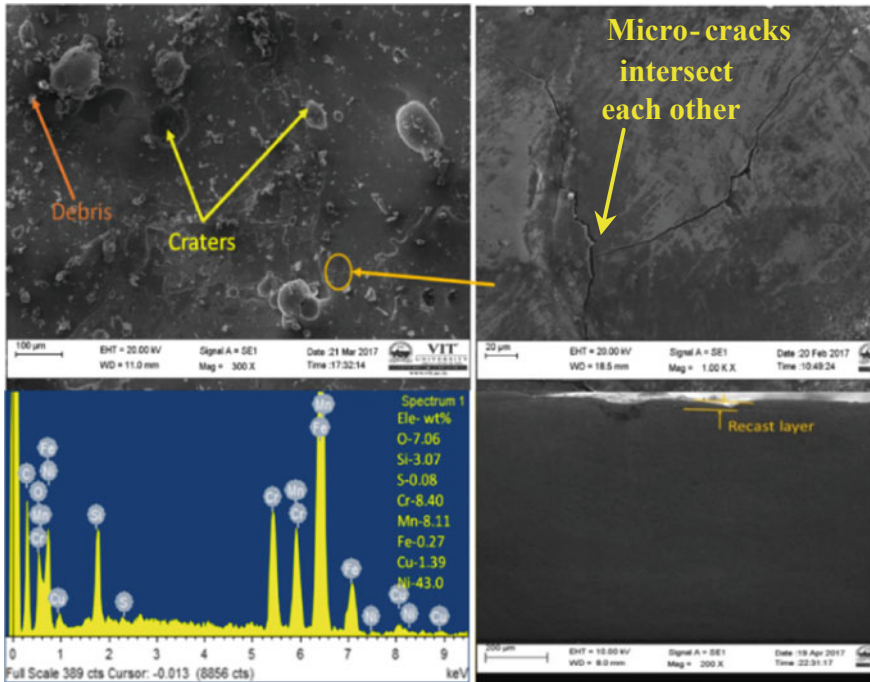


Fig. 56.7 Surface morphology of Inconel 600 under near-dry EDM

### 56.3.4 Tool Wear Rate

The effect of process parameters on tool wear rate is given in Fig. 56.9. As the current increases, there is an increase in TWR; this is due to the spark produced in the gap which will be higher which removes more material from the tool as well as work material. As the pulse duration increases, there is a decrease in TWR; this is mainly attributed due to higher temperatures prevail in the machining zone to facilitate the carbon particles present in the dielectric medium to adhere on the tool surface which protects from erosion [21].

The tool wear rate in MFAND EDM is higher compared to that of other two processes. Due to rapid ionization and increased explosion force in the plasma created by external magnetic field, more material is melted on the tool electrode. Also, oil–air mixture dielectric has lower thermal conductivity and heat capacity compared to that of oil dielectric which resulted in increased tool electrode wear rate. Lower thermal conductivity and heat capacity of oil–air dielectric resulted in increased tool wear rate than liquid dielectric used in wet EDM process. Less tool wear in wet EDM, when compared with MFAND EDM process, is observed. Thermal conductivity and heat capacity are the important properties of the dielectric medium that controls the solidification of molten materials and cooling of tool and workpiece surface. The

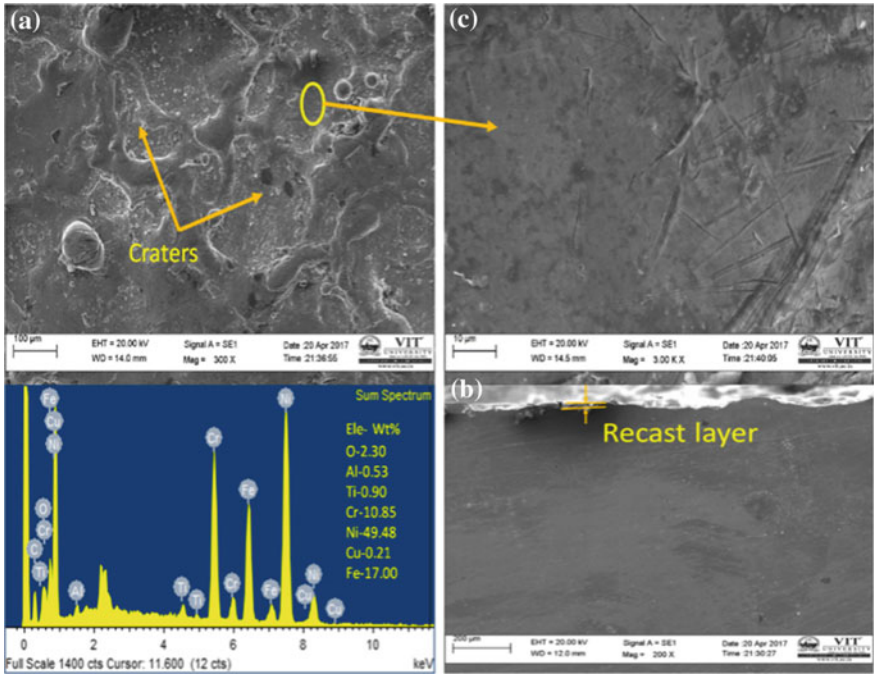
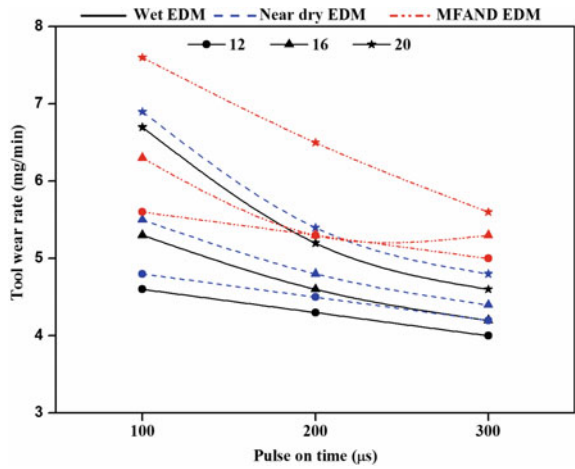


Fig. 56.8 Surface morphology of Inconel 600 under MFAND EDM

Fig. 56.9 Variation of tool wear rate at different machining conditions



thermal conductivity and heat capacity liquid dielectric are at least 10 times and twice that of gas dielectrics [16] which resulted in reduced tool wear in wet EDM process.

## 56.4 Conclusion

Electrical discharge machining of Inconel 600 is performed under wet, near-dry, and magnetic field-assisted near-dry EDM (MFAND EDM) process. Also the effect of process parameters such as pulse on time and discharge current on MRR, surface integrity, and tool wear rate is analyzed. The following are the important conclusions drawn from the work:

- Higher MRR is obtained in wet EDM due to higher dielectric fluid viscosity of the liquid dielectric. Least MRR is obtained in near-dry EDM process due to lower viscosity of oil–air mixture dielectric. Magnetic field-assisted near-dry EDM produces MRR equivalent to that of wet EDM and 73% higher MRR compared to that of near-dry EDM. The external magnetic field applied during machining aids in rapid ionization of gap and more material removal.
- Magnetic field-assisted near-dry EDM to produce the better surface finish and less debris reattachment on the machined surface compared to that of wet and near-dry EDM process.
- Higher tool wear is observed in magnetic field-assisted near-dry EDM process due to higher thermal loads generated by spark and lower thermal conductivity and heat capacity of oil–air mixture dielectric. Least tool wear is observed in wet EDM due to higher thermal conductivity and heat capacity of liquid dielectric which cools the tool electrode rapidly.

Using the proposed work, different dielectric mediums can be used to enhance the material removal mechanism of EDM process. The proposed work can be extended in online monitoring of EDM process while using different dielectric environments.

## References

1. Rebelo, J.C., Morao Dias, A., Kremer, D., Lebrun, J.L.: Influence of EDM pulse energy on the surface integrity of martensitic steels. *J. Mater. Process. Technol.* (1998). [https://doi.org/10.1016/S0924-0136\(98\)00082-X](https://doi.org/10.1016/S0924-0136(98)00082-X)
2. Kunieda, M., Yoshida, M., Taniguchi, N.: Electrical discharge machining in gas. *CIRP Ann. Manuf. Technol.* (1997). [https://doi.org/10.1016/S0007-8506\(07\)60794-X](https://doi.org/10.1016/S0007-8506(07)60794-X)
3. Kunieda, M., Miyoshi, Y., Takaya, T., et al.: High speed 3D milling by dry EDM. *CIRP Ann. Manuf. Technol.* (2003). [https://doi.org/10.1016/S0007-8506\(07\)60552-6](https://doi.org/10.1016/S0007-8506(07)60552-6)
4. Yu, Z.B., Jun, T., Masanori, K.: Dry electrical discharge machining of cemented carbide. *J. Mater. Process. Technol.* (2004). <https://doi.org/10.1016/j.jmatprotec.2003.10.044>

5. Saha, S.K., Choudhury, S.K.: Experimental investigation and empirical modeling of the dry electric discharge machining process. *Int. J. Mach. Tools Manuf.* (2009). <https://doi.org/10.1016/j.ijmactools.2008.10.012>
6. Beşliu, I., Schulze, HP., Coteață, M., Amarandei, D.: Study on the dry electrical discharge machining. *Int. J. Mater. Form.* (2010). <https://doi.org/10.1007/s12289-010-0965-z>
7. Govindan, P., Joshi, S.S.: Experimental characterization of material removal in dry electrical discharge drilling. *Int. J. Mach. Tools Manuf.* (2010). <https://doi.org/10.1016/j.ijmactools.2010.02.004>
8. Puthumana, G., Joshi, S.S.: Investigations into performance of dry EDM using slotted electrodes. *Int. J. Precis. Eng. Manuf.* (2011). <https://doi.org/10.1007/s12541-011-0128-2>
9. Fattahi, S., Baseri, H.: Analysis of dry electrical discharge machining in different dielectric mediums. *Proc. Inst. Mech. Eng. Part E J. Process. Mech. Eng.* (2017). <https://doi.org/10.1177/0954408915611540>
10. Shen, Y., Liu, Y., Zhang, Y., et al.: High-speed dry electrical discharge machining. *Int. J. Mach. Tools Manuf.* (2015). <https://doi.org/10.1016/j.ijmactools.2015.03.004>
11. Shen, Y., Liu, Y., Sun, W., et al.: High-speed dry compound machining of Ti6Al4 V. *J. Mater. Process. Technol.* (2015). <https://doi.org/10.1016/j.jmatprotec.2015.05.012>
12. Joshi, S., Govindan, P., Malshe, A., Rajurkar, K.: Experimental characterization of dry EDM performed in a pulsating magnetic field. *CIRP Ann. Manuf. Technol.* (2011). <https://doi.org/10.1016/j.cirp.2011.03.114>
13. Govindan, P., Joshi, S.S.: Analysis of micro-cracks on machined surfaces in dry electrical discharge machining. *J. Manuf. Process.* (2012). <https://doi.org/10.1016/j.jmapro.2012.05.003>
14. Teimouri, R., Baseri, H.: Effects of magnetic field and rotary tool on EDM performance. *J. Manuf. Process.* (2012). <https://doi.org/10.1016/j.jmapro.2012.04.002>
15. Kao, C.C., Tao, J., Shih, A.J.: Near dry electrical discharge machining. *Int. J. Mach. Tools Manuf.* (2007). <https://doi.org/10.1016/j.ijmactools.2007.06.001>
16. Tao, J., Shih, A.J., Ni, J.: Experimental study of the dry and near-dry electrical discharge milling processes. *J. Manuf. Sci. Eng.* (2008). <https://doi.org/10.1115/1.2784276>
17. Fujiki, M., Ni, J., Shih, A.J.: Investigation of the effects of electrode orientation and fluid flow rate in near-dry EDM milling. *Int. J. Mach. Tools Manuf.* (2009). <https://doi.org/10.1016/j.ijmactools.2009.05.003>
18. Williams, R.E., Rajurkar, K.P.: Study of wire electrical discharge machined surface characteristics. *J. Mater. Process. Tech.* (1991). [https://doi.org/10.1016/0924-0136\(91\)90212-W](https://doi.org/10.1016/0924-0136(91)90212-W)
19. Lee, H.T., Tai, T.Y.: Relationship between EDM parameters and surface crack formation. *J. Mater. Process Technol.* (2003). [https://doi.org/10.1016/S0924-0136\(03\)00688-5](https://doi.org/10.1016/S0924-0136(03)00688-5)
20. Çoğun, C.: A technique and its application for evaluation of material removal contributions of pulses in electric discharge machining (EDM). *Int. J. Mach. Tools Manuf.* (1990). [https://doi.org/10.1016/0890-6955\(90\)90038-K](https://doi.org/10.1016/0890-6955(90)90038-K)
21. Ahmad, S., Lajis, M.A.: Electrical discharge machining (EDM) of Inconel 718 by using copper electrode at higher peak current and pulse duration. In: *IOP Conference Series: materials Science and Engineering* (2013). <https://doi.org/10.1088/1757-899X/50/1/012062>
22. Gholipour, A., Baseri, H., Shakeri, M., Shabgard, M.: Investigation of the effects of magnetic field on near-dry electrical discharge machining performance. *Proc. Inst. Mech. Eng. Part B J. Eng. Manuf.* (2016). <https://doi.org/10.1177/0954405414558737>
23. Lee, L.C., Lim, L.C., Wong, Y.S., Lu, H.H.: Towards a better understanding of the surface features of electro-discharge machined tool steels. *J. Mater. Process. Tech.* (1990). [https://doi.org/10.1016/0924-0136\(90\)90212-D](https://doi.org/10.1016/0924-0136(90)90212-D)



# **Part II**

## **Composites**

# Chapter 57

## Selection of Aluminum Hybrid Metal Matrix Composite Material Using Additive Ratio Assessment Approach and Comparing with the Experimental Results Varying Different Weight Percentage of the Reinforcements



Soutrik Bose  and Titas Nandi 

**Abstract** Proper material selection is essential in manufacturing arena with superior product and cost-effectivity. This paper focuses on the multi-criteria approach namely additive ratio assessment (ARAS) for best material selection of a hybrid composite using aluminum (Al) and silicon carbide (SiC) with varying reinforcements like waste carbonized eggshells (WCE), cow dung ash (CDA), snail shell ash (SSA), and boron carbide ( $B_4C$ ) varying different reinforcement weights by stir casting. There is an increment in hardness, tensile, fatigue strength while decrement in fracture toughness, ductility and corrosion rate which gets improved by heat treatment. The optimum values obtained are 7.5 wt% of WCE and SiC + SSA, preheat temperature of WCE and SiC as 300 °C and 500 °C, respectively. WCE is obtained to be the best reinforcement both by ARAS and after experiments at the lowest cost than the other reinforcements.

**Keywords** ARAS · Hybrid composite · Corrosion rate · Wettability · Porosity

### Nomenclature

CR	Corrosion Rate
A	Exposed Area ( $cm^2$ )
t	Exposure Time (hours)
K	Constant
W	Weight Loss (g)

---

S. Bose (✉)

MCKV Institute of Engineering, 243 G.T. Road (N), Liluah, Howrah 711204, West Bengal, India  
e-mail: [soutrikboseju@gmail.com](mailto:soutrikboseju@gmail.com)

S. Bose · T. Nandi

Jadavpur University, Kolkata 700032, West Bengal, India

© Springer Nature Singapore Pte Ltd. 2020

M. S. Shunmugam and M. Kanthababu (eds.), *Advances in Unconventional Machining and Composites*, Lecture Notes on Multidisciplinary Industrial Engineering, [https://doi.org/10.1007/978-981-32-9471-4\\_57](https://doi.org/10.1007/978-981-32-9471-4_57)

$\rho$	Alloy Density ( $\text{g}/\text{cm}^3$ )
P	Percent Porosity
$\rho_{\text{exp}}$	Experimental Density
$\rho_{\text{theo}}$	Theoretical Density
BHN	Brinell Hardness Number

## 57.1 Introduction

Different public sectors use AMC for their improved physical and mechanical properties. Recent improvement includes stir casting by using the ceramic reinforcements but in this manuscript, uncarbonized eggshells (ES), waste carbonized eggshells (WCE), snail shell ash (SSA), silicon carbide (SiC), and boron carbide ( $\text{B}_4\text{C}$ ) are used with different weight fractions by stir casting at squeezed pressure at optimum controlled conditions. Selection of the best material in an adept material selection approach depends on the manufacturing scope and to minimize cost while meeting the product performance objectives. Inappropriate material selection leads to immature product failure with high cost. So proper identification and selection of appropriate materials with definite functionalities to acquire the best product with least cost and high performance are the most important criteria. The mechanical properties like hardness, tensile strength, fatigue strength, porosity, corrosion rate, and ductility are the prime concern. Therefore, a competent and organized approach like ARAS [1], based on some strong mathematical establishment, is hence proposed for the integration of design and manufacturing objectives but the actual performance of the material under different conditions may vary from the expected results which need to be optimized. Strong interfacial bonds are the main criteria for improved wettability. Better tribomechanical characteristics can be obtained with higher percentage of WCE than ES by Deep et al. [2] analyzed aluminum-silicon carbide of different weight percentages and concluded that mechanical properties increased with increased weight fractions to an optimum level. Solidification of AMC was characterized by Kayal et al. [3] by stir casting. Jyothi et al. [4] concluded better performance of cow dung ash than rice husk ash with Al-5% Si alloy. Emenike [5], obtained dissimilar corrosion characteristics of Al-MgA535 + fly ash and found enhanced corrosion rate with the increase of fly ash content. Al-based composites are vulnerable to erosion–corrosion [6, 7] for automobile cooling sectors, so hybrid reinforcements are introduced. The main research gap is to compare the physio-mechanical properties of the best hybrid green composite and to scrutinize the viability of producing this novel Al/WCE composite material using stir casting process by recycling these hazardous wastes. The mechanical and physical properties of these hybrid green composites can be compared and the best result can be optimized.

## 57.2 Additive Ratio Assessment Method

The ARAS method is the perceptible measurements and utility theory where a utility function value designates the relative efficiency of various alternatives. It is directly proportional to the relative outcome of the criteria values and weightage parameters of the criteria. The steps of ARAS [1] method is as follows:

Step 1: A definite normalization process is proposed for the beneficial attributes and reciprocal of all the criteria is considered for non-beneficial attributes and hence, the normalized decision matrix is determined with respect to all the alternatives:

$$X_{ij}' = \frac{1}{X_{ij}} \quad (57.1)$$

Step 2: The normalized values are calculated:

$$R = [r_{ij}]_{m \times n} = \frac{X_{ij}'}{\sum_{i=1}^m X_{ij}'} \quad (57.2)$$

Then the weighted normalized decision matrix, D is determined:

$$D = [Y_{ij}]_{m \times n} = r_{ij} \times w_j (i = 1, 2, 3, \dots, m; \quad j = 1, 2, 3, \dots, n) \quad (57.3)$$

Step 3: The optimality function ( $S_i$ ) for  $i$ th alternative is hence determined:

$$S_i = \sum_{j=1}^n Y_{ij} \quad (57.4)$$

Greater the  $S_i$  value, superior is the alternative, which is directly proportional to the decision matrix values and criteria weights.

Step 4: The degree of utility ( $U_i$ ) is computed for each alternative and compared with the maximum efficient alternative ( $S_0$ ). The equation for calculating utility degree ( $U_i$ ) is given below

$$U_i = \frac{S_i}{S_0} \quad (57.5)$$

The degree of utility of the alternatives varies from 0 to 100% and the one with the highest utility value ( $U_{\max}$ ) is the best choice (Rank 1) among all the alternatives.

By following the above steps, the best hybrid composite material is obtained by ranking and material number A30 is found to be rank 1 which is Al + Al<sub>2</sub>O<sub>3</sub> at 12.5 wt% addition and material number A24 is found to be rank 2 (Fig. 57.1) which is heat-treated 12.5 wt% WCE. From this approach, 25 samples were fabricated as shown in Table 57.1 and experiments were done and best result was obtained to be A24 experimentally.

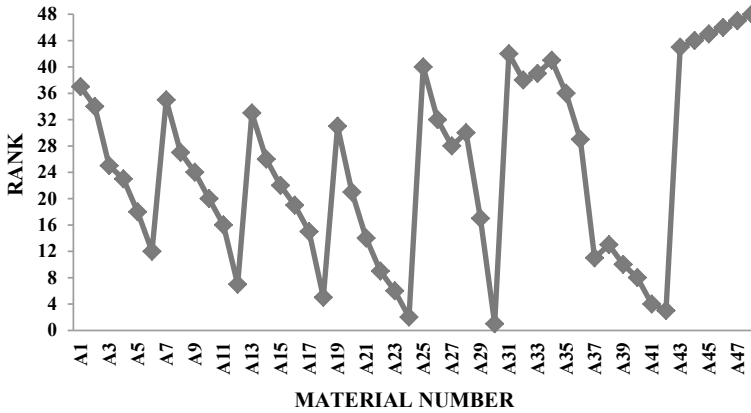


**Fig. 57.1** Rank of composite materials by ARAS approach

**Table 57.1** Different samples fabricated by varying the weight percentage of the reinforcements

Sample no.	SiC (wt%)	Eggshells (wt%)	Sample no.	SiC (wt%)	Eggshells (wt%)	Sample no.	SiC (wt%)	Eggshells (wt%)
S1	2.5	2.5	S10	5	12.5	S19	10	10
S2	2.5	5	S11	7.5	2.5	S20	10	12.5
S3	2.5	7.5	S12	7.5	5	S21	12.5	2.5
S4	2.5	10	S13	7.5	7.5	S22	12.5	5
S5	2.5	12.5	S14	7.5	10	S23	12.5	7.5
S6	5	2.5	S15	7.5	12.5	S24	12.5	10
S7	5	5	S16	10	2.5	S25	12.5	12.5
S8	5	7.5	S17	10	5			
S9	5	10	S18	10	7.5			

### 57.3 Experimental Setup

#### 57.3.1 Material Library

The chemical composition is Si (0.6), Fe (0.5), Cu (4.2), Mn (0.7), Mg (0.6), Zn (0.25), Ti (0.2), Ni (0.1), and Cr (0.1) with balanced Al in percentage and 25 different samples varying the weight percentage of the reinforcements are taken as shown in Table 57.1.

### 57.3.2 Composite Development

Figures 57.2 and 57.3 depicts the schematic experimental setup diagram and squeeze casting in Universal Testing Machine (UTM). Al was heated to 750 °C in a graphite crucible furnace and cooled approximately at 600 °C. The reinforcements were pre-heated to 300 °C for 30 min to improve wettability by removing dampness and stirred manually for 5 min. The mixture varying the wt% (0, 2.5, 5, 7.5, 10, 12.5, and 15) of reinforcements before and after heat treatment was then solidified into the mold.

Where, (1) represents Motor, (2) represents Stirrer, (3) represents Furnace, (4) signifies Graphite Crucible, (5) stands for Molten Metal, and (6) symbolizes Thermocouple.

Fig. 57.2 Stir casting experimental setup

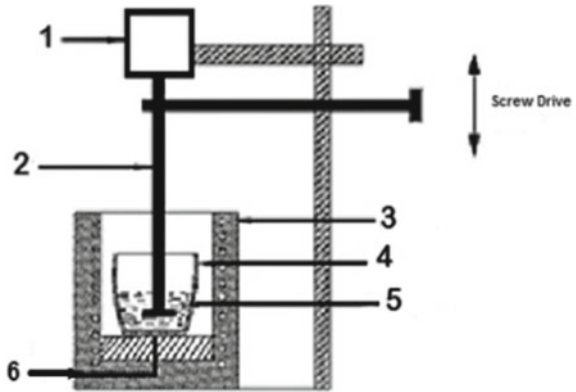
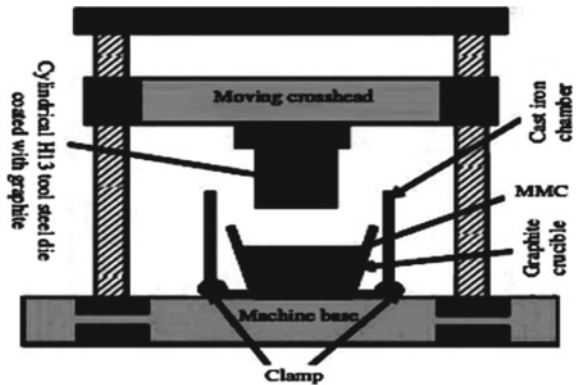


Fig. 57.3 Squeeze casting on UTM



### 57.3.3 Porosity Analysis

Porosity, as obtained by Dwivedi et al. [8], is the incremental ratio of theoretical and experimental density of the composites. The equation is

$$P = 1 - \frac{\rho_{\text{exp}}}{\rho_{\text{theo}}} \times 100\% \quad (57.6)$$

### 57.3.4 Corrosion Test

The corrosion tests of all fabricated composites were immersed in 4% NaCl solution for approximately 5 days at room temperature. Corrosion rate formula as provided by Dwivedi et al. [8], where,  $K = 8.75 \times 10^4$ ,  $A = 9 \text{ cm}^2$ ,  $t = 5 \text{ days (120 h)}$ :

$$CR = \frac{W \times K}{\rho \times A \times t} \quad (57.7)$$

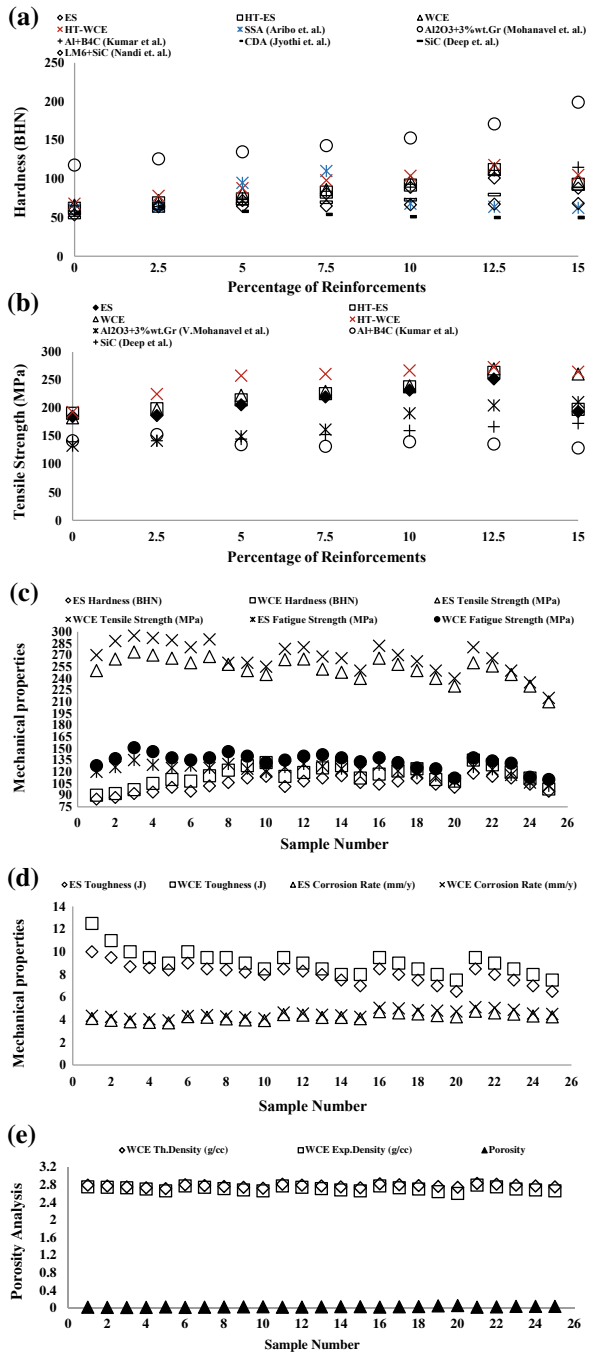
## 57.4 Results and Discussion

### 57.4.1 Evaluation of Mechanical Properties

The hardness values augment from 60 BHN (0 wt%) to 101 BHN (12.5 wt%) for ES and 113 BHN (12.5 wt%) for WCE. It deviates from 61 BHN (0 wt%) to 110 BHN (7.5 wt%) of SiC + SSA according to Aribo et al. [7] and then it decreases to a constant factor. When it is correlated with Mohanavel et al. [10] hardness increases to 200 BHN with  $\text{Al}_2\text{O}_3 + \text{Gr}$ , reaches to 115 BHN when reinforced by  $\text{B}_4\text{C}$  by Kumar et al. [9], but decreases to 87.1 BHN when reinforced by SiC by Deep et al. [2] and to 68.2 BHN when reinforced with LM6/SiC by Nandi et al. [3]. Figure 57.4a represents decrease of hardness beyond 12.5 wt% of reinforcements, which may be due to the air entrapment indicating larger pore formation resulting in decrease in mechanical properties. However, when compared with Jyoti and Bharath [4], hardness reaches to a maximum about 64 BHN at 2.5 wt% addition of CDA with the Al matrix and then decreases gradually. Hardness of WCE and ES improve to 118 BHN and 112 BHN, respectively, after heat treatment.

Figure 57.4b shows the improvement of the tensile strength up to 12.5 wt% which progresses from 185 MPa (0 wt%) to 252 MPa and 270 MPa for ES and WCE, respectively, because uniform eggshells particles are distributed in the Al alloy matrix and then decreases due to weak particle–matrix interaction, and again it is further

**Fig. 57.4** Mechanical properties: **a** Hardness, **b** tensile strength, **c** comparative analysis of hardness, tensile strength and fatigue strength, **d** toughness and corrosion rate, **e** porosity analysis





improved to 264 MPa (for ES) and 273 MPa (for WCE) after heat treatment because of strengthening characteristics of particle–matrix interface. Mohanavel et al. [10] obtained increase in the tensile strength up to 205 MPa with increased wt% of Alumina ( $\text{Al}_2\text{O}_3$ ) and Graphite (Gr) which then decreases. But with the increase of reinforcements it gets decreased to 167 MPa by Deep et al. [2] but with the addition of Al with  $\text{B}_4\text{C}$  by Kumar et al. [9] tensile strength increases a maximum value to 153 MPa at 2.5 wt% and then decreases resulting in less ductility than with eggshells reinforcements. The toughness decreases with increase in eggshell particles addition. S3 proves to be the best sample (2.5 wt% of SiC + 7.5 wt% of ES/WCE) after comparing all the 25 samples where the optimum conditions are satisfied. The optimum values of tensile strength of ES is 274 MPa, of WCE is 295 MPa, fatigue strength of ES is 135 MPa and WCE is 151 MPa, corrosion rate, and porosity is the least.

### 57.4.2 Porosity Analysis and Corrosion Rate

Figure 57.4e shows the porosity analysis graph where the best result obtained is  $(1 - 2.69/2.70) \times 100 = 0.37\%$ . Corrosion rate and loss of weight of Al alloy continuously show a decrement after addition of ES and WCE powder as shown in Fig. 57.4d and improves after the heat treatment process.

## 57.5 Conclusion

Recycling of industrial waste is the prime focus of this present investigation for the fabrication of green hybrid composite as these waste cause serious environmental hazards. In this paper, ARAS method is used which is a two-step linear normalization technique of both qualitative and quantitative criteria to select the best material (A30), and it is compared with the results obtained after experiments. Eggshell particles are much better reinforcements than SiC + SSA at higher weights but  $\text{B}_4\text{C}$  shows brittle failure at much higher reinforcements wt%, while when compared with cow dung ash it is favorable at much lower wt%. All the mechanical properties improve at 12.5 wt% for WCE reinforcement and further improves after heat treatment, but decreases on further addition of WCE. Minimum porosity is 0.37% for Al/WCE at 12.5 wt% which proves that reinforcing with WCE with Al results in a better composite material. Corrosion rate continuously decreases with the increase of WCE addition and improves after the heat treatment process owing to the best result as 4.28 mm/year.

## References

1. Chatterjee, P., Chakraborty, S.: Gear material selection using complex proportional assessment and additive ratio assessment-based approaches: A comparative study. *Int. J. Mater. Sci. Eng.* **1**, 104–111 (2013)
2. Deep, G., Idrisi, A.H., Siddiqui, T.U.: A new bio-filler for polypropylene composites. *Int. J. Innov. Res. Sci., Eng. Technol.* **5**, 16720–16725 (2016)
3. Kayal, S., Behera, R., Nandi, T., Sutradhar, G.: Solidification behavior of stir-cast Al alloy metal matrix composites. *Int. J. Appl. Eng. Res., Dindigul* **2**, 350–359 (2011)
4. Jyothi, P.N., Bharath, B.S.K.: Comparison of mechanical properties of Al-5%Si alloy reinforced with cow dung ash and rice husk ash. *Int. J. Latest Res. Eng. Technol.* **1**, 55–58 (2015)
5. Emenike, R.O.: Corrosion behaviour of fly ash reinforced aluminium magnesium alloy A535 composite. MSc. Thesis (2008). University of Saskatchewan, Canada
6. Prasad, S.D., Krishna, R.A.: Tribological properties of A356.2/RHA composite. *J. Mater. Sci. Technol.* **33**, 51–58 (2011)
7. Aribo, S., Barker, R., Hu, X., Neville, A.: Erosion-corrosion behavior of lean duplex stainless steels in 3.5% NaCl solution. *Wear* **302**, 1602–1608 (2013)
8. Dwivedi, S.P., Sharma, S., Mishra, R.K.: Characterization of waste eggshells and CaCO<sub>3</sub> reinforced AA2014 green metal matrix composites: a green approach in the synthesis of composites. *Int. J. Precis. Eng. Manuf.* **17**, 1383–1393 (2016)
9. Kumar, K.C.K., Raju, T.N., Laxmi, Y.N.: Studies on Al6061-B<sub>4</sub>C metal matrix composites fabricated by stir casting process. *SSRG Int. J. Mech. Eng.* **4**, 296–299 (2017)
10. Mohanavel, V., Rajan, K., Senthil, P.V., Arul, S.: Mechanical behaviour of hybrid composite (AA6351 + Al<sub>2</sub>O<sub>3</sub> + Gr) fabricated by stir casting method. *Mater. Today: Proc.* **4**, 3093–3101 (2017)

# Chapter 58

## The Role of HBN Solid Lubricant Reducing Cutting Forces of Dry Machined Al-B<sub>4</sub>C Composite



M. Rajesh , K. Rajkumar , A. Gnanavelbabu  and K. M. Nambiraj 

**Abstract** The Aluminum metal matrix composites are known as advanced engineering materials due to their mechanical and thermal characteristics. The machining of these materials, as extremely hard, required an intrinsic lubrication to reduce the cutting forces. The present study focuses on the machining of Aluminum–Boron carbide composites with the effect of solid lubricant hexagonal boron nitride (hBN). The machining of composites was done with constant B<sub>4</sub>C-5% and hBN varied from 5 to 15%. The machining performance is characterized by cutting force and tool wear with the effect of feed, speed, and depth of cut. Polycrystalline diamond (PCD) inserts were used to perform the machining. The composite microstructure shows that fairly distribution of hBN and boron carbide particles. The increase in the boron carbide increases hardness obviously. The depth of cut, feed and cutting speed was correlated to the cutting forces and tool wear. The rate of flank wear was significantly reduced with hBN particle concentration due to the smearing of these particles in the cutting zone. The machining forces were also reduced to an extent with increasing in hBN particles due to covered soft film over the cutting zone.

**Keywords** hBN · PCD · Tool wear · Cutting force

---

M. Rajesh

Department of Mechanical Engineering, Prathyusha Engineering College, Thiruvallur 602 025, India

K. Rajkumar (✉)

Department of Mechanical Engineering, SSN College of Engineering, Kalavakkam 603 110, India  
e-mail: [rajkumark@ssn.edu.in](mailto:rajkumark@ssn.edu.in)

A. Gnanavelbabu

Department of Industrial Engineering, College of Engineering – Guindy, Anna University, Chennai 600025, India

K. M. Nambiraj

Department of Mechanical Engineering, Jeppiaar SRR Engineering College, Padur, Chennai 603 103, India

© Springer Nature Singapore Pte Ltd. 2020

M. S. Shunmugam and M. Kanthababu (eds.), *Advances in Unconventional Machining and Composites*, Lecture Notes on Multidisciplinary Industrial Engineering, [https://doi.org/10.1007/978-981-32-9471-4\\_58](https://doi.org/10.1007/978-981-32-9471-4_58)

697

## 58.1 Introduction

The demands made on materials for better overall performance are so great and diverse that no one material can satisfy them. That naturally leads to a resurgence of the ancient concept of combining different materials in an integral composite material system that result in a better performance. Particle reinforced aluminum matrix composites are widely used to engineer several parts of automobiles and many other mechanical and electrical products. This is because of MMC's extensive engineering properties such as wear resistance, fracture toughness, good strength, and stability. The yield strength and modulus are higher for the metal matrix composites [1]. In complexity lead by High Speed Steel (HSS) and carbide tools when an encounter with machining MMC composites, due to higher hardness reinforcing particles and its abrasive nature, which in many cases, MMC composites are slightly harder than the commonly used tools [2]. Composite material consists of Al-6061 is the matrix since its lighter and corrosion resistance and easily workable.  $B_4C$  as the reinforcement added to the matrix since it has extreme hardness, resistance to chemicals, excellent nuclear properties. Aluminum 6061- $B_4C$  composite system dispersed with solid lubricant particles like hexagonal boron nitride (hBN) has been established as potential engineering materials for a number of antifriction applications [3]. The role of hBN in such applications is to reduce the friction, wear and cutting force of materials by forming a tribo-induced layer of hBN on the interacting surfaces. There is a significant reduction in direct metal-to-metal contact with the presence of hBN particles [4]. During machining, the hBN particles are smearing between a cutting tool and work surface due to weak intermolecular force between the hBN layers. The concentration of hBN influenced the topography of machined surfaces [5].

The major issue preventing wider use of MMCs is their poor machinability. Since the soft matrix holding together with very hard particulates, however, it possible to reduce a tendency of abrasive action to cutting tool by an introduction of softly layered films between them. Polycrystalline diamond tools (PCD) insert is normally used for machining MMC composites under dry machining conditions [6]. Many research studies were undertaken for the machining of aluminum composite the important observation of BUE formation significantly affects the tool wear at low speeds whereas thermal softening plays important role at higher speeds and feed rates [7]. The decrease in the amount of hexagonal boron nitride also affects the formation of built-up edge thus leading to tool wear. The rate of flank wear and cutting force are high when machining with a higher depth of cut. Increase the feed rate increases the flank wear and cutting force [8].

In this present study has been carried out to investigate of high speed turning parameters like cutting speed, feed rate and depth of cut to thrust force of Al- $B_4C$ -hBN metal matrix composites. Tool selection is very important for machining of metal matrix composites. Gallab and Sklad [9] showed that the employability of PCD tools over composite  $Al_2O_3/TiC$  tools due to higher hardness and thermal conductivity. It is found that PCD and PCBN tools were much better than WC tools for the MMC machining. Tomac and Tonnessen [10] experimented that softening of MMC at a

higher temperature; causes reinforced particles to plow into the workpiece prevents rapid tool wear. However, no work addresses the machinability of Al-B<sub>4</sub>C-hBN as hybrid composite produced by stir casting. Hence, the main objective of the present work is to study the role of hBN and machining parameters.

## 58.2 Experimental Procedure

### 58.2.1 Composite Fabrication

The MMC consists of Al 6061 was the base matrix material. Initially, it was subjected to melting for 90 min in an electric furnace to a temperature of about 740 °C. Then the reinforcement material B<sub>4</sub>C (16–20 μm) and the solid lubricant hexa boron nitride (<10 μm) mixture were preheated to 250 °C in a muffle furnace and added to the base matrix. The three-step addition of reinforcement process is carried out to avoid agglomeration and better distribution of microparticles. This mixture is then subjected to stirring at the rate of 90 rpm for 20 min. This is done so that there is sufficient dispersion of the B<sub>4</sub>C and hBN. The molten slurry was poured into the mold; the mold was preheated so that fast cooling of the melt can be avoided. The mold's dimensions are 22 mm inner diameter and 110 mm length. After the solidification of the MMC, T6 heat treatment process was done. The concentration of reinforcement's particles in a matrix is shown in Table 58.1.

### 58.2.2 Machining

The fabricated composites were turned on a medium-duty lathe with a drive motor power of 1.5 kW. The cutting parameters such as cutting speed, feed and depth of cut are taken as the control factors and are listed in Table 58.2. The cutting force was measured using an IEICOS lathe tool dynamometer with a digital force indicator. The PCD cutting tool was used to perform machining.

The cutting forces generated during machining are noted. The one factor at a time-based experimentation work helps to understand the mechanics of cutting force produced in response to the input process parameter. SEM image analysis is done to understand the cutting surfaces of composites and tool wear.

**Table 58.1** Concentration of Al/B<sub>4</sub>C/hBN composite in (vol.%)

Composition	Al	B <sub>4</sub> C	hBN
C1	80	15	5
C2	75	15	10
C3	70	15	15

**Table 58.2** Machining parameters

Cutting parameter	Units	Levels
Cutting speed	m/min	25, 85
Feed rate	mm/rev	0.15, 0.3
Depth of cut	Mm	0.2, 0.6
Dry machining		

### 58.3 Results and Discussion

#### 58.3.1 Microstructure of Composite

The uniform distribution of microparticles investigation on fabricated MMC is carried out by SEM image analysis. There is no agglomeration of the reinforcement particles, any micro cracks, and voids in the MMC, as observed from SEM image of composites, as depicted in Fig. 58.1. The relative size of boron carbide and hBN particles are clearly seen from this figure. These reinforcement’s particles were intact with an aluminum matrix. EDX spectrum shows peaks of aluminum, boron carbide, hBN particle, and alloying elements thus confirm chemical composition of the composite.

#### 58.3.2 Effect of Cutting Force to Cutting Speed in Minimum and Maximum Feed and Depth of Cut

Cutting force measurements are quite complex due to composition, size and uniform distribution of reinforced particles. Anyway measurement of cutting force makes understanding the concepts of composite machining. Cutting force analysis with varying cutting speed, feed, and depth of cut are taken for discussion. For every

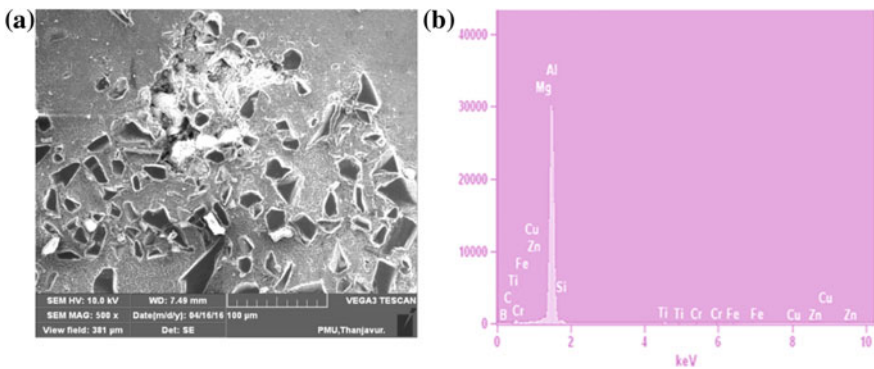


**Fig. 58.1** Typical SEM image with EDX of Al/B<sub>4</sub>C/hBN composite microstructure

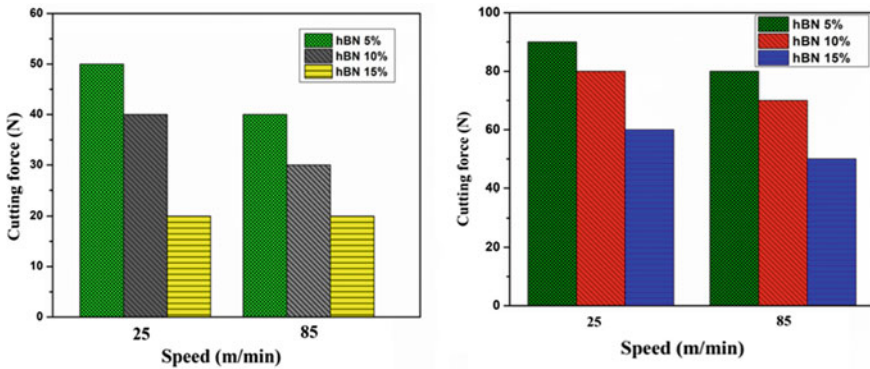


Fig. 58.2 Cutting force versus speed (minimum and maximum feed and depth of cut)

cutting condition, three trails were availed and mean value is taken for better accuracy. Figure 58.2 shows a variation cutting force with speeds at conditions of feed rate 0.15 mm/rev, depth of cut 0.2 mm and maximum feed rate 0.3 mm/rev and depth of cut 0.6 mm are constant. The cutting speed is much influenced at low concentration hBN particles due to scarcity solid lubricant particles. The boron carbide particle raises the cutting forces when interacting with a cutting tool. The cutting force is stabilized with speed at higher concentration of hBN particles. The general observation is that the cutting force decrease with increasing cutting speed. A similar observation is made from the machining experiment. The thrust force decrease as a result of low shear hBN thin-film covered in the machining area. Moreover, to increase the hBN particle to decrease the magnitude of cutting force. From the graph it is also observed that with increase in cutting speed, thermal softening of the aluminum MMC makes the easier flow of chip and results lower cutting force consumption.

### 58.3.3 *Effect of Cutting Force to Feed Rate in Minimum and Maximum Speed and Depth of Cut*

Figure 58.3 shows a variation cutting force with feed rate at conditions of minimum speed 25 m/min and depth of cut 0.2 mm and maximum speed 85 m/min and depth of cut 0.6 mm are constant. From the plot shows is increasing the feed rate to increase the magnitude of cutting force. This affects the cutting force increases with an increase in feed rate. The heat generated is also more which increase in feed rate and the generated heat is mostly carried away by chip and remaining is present in the material. This may cause micro dimensional changes in the material. Moreover, considering all the processing parameters the cutting forces decreased with increasing hBN particles in the matrix. From the graph, it is also plotted that with increase in feed rate cutting force is also increased. At higher feed rate, cutting temperature is very high due to

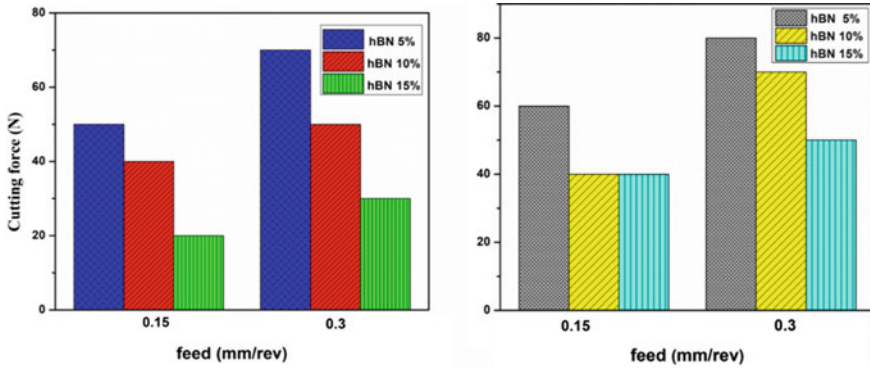


Fig. 58.3 Cutting force versus feed (minimum and maximum speed and depth of cut)

short period of machining the same length and developed cutting temperature cannot be taken away completely by the chip.

### 58.3.4 Effect of Cutting Force to Depth of Cut in Minimum and Maximum Cutting Speed and Feed

Figure 58.4 shows the cutting force to a depth of cut at conditions of minimum cutting speed 25 m/min and feed rate 0.15 mm and maximum cutting speed 85 m/min and feed rate 0.3 mm are constant. From the plot, it shows a depth of increase in magnitude force. This is a cause of more materials removed at the same time. The number of layers to be removed in a single pass is high with increased depth of cut and relatively high inclusion of abrasive particles (B<sub>4</sub>C) in chip removal also very high. This requires

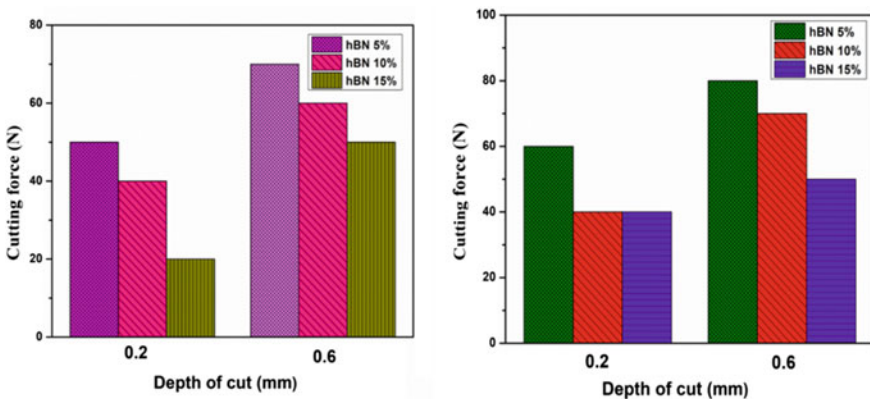
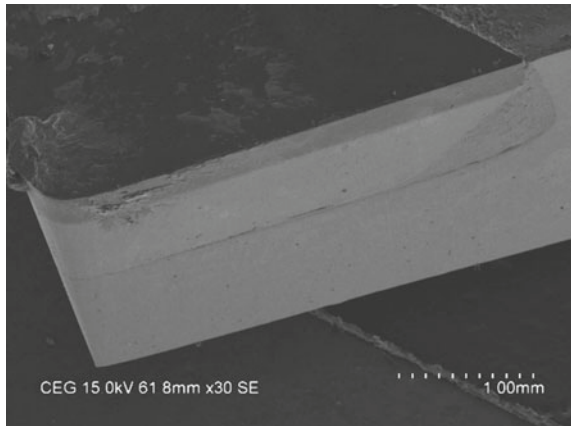


Fig. 58.4 Cutting force versus depth of cut (minimum and maximum speed and feed rate)



**Fig. 58.5** SEM image of flank wear for 5% hBN composite



higher cutting force to remove excess layers of materials. The magnitude of cutting force is higher when considering the depth of cut with other parameters.

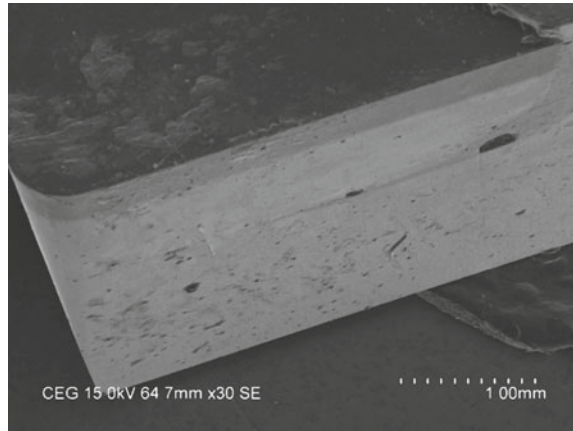
### 58.3.5 Flank Wear Analysis

Aluminum composite machining is difficult due to the presence of hard particles inclusion. Though, it is made easier by the addition of self-lubricating powders (hBN). The tool wear for the turning of the composite was characterized by flank wear and built-up edge formation. The cutting tool undergoes high stress, cutting temperature and rubbing action and micro-welding during machining. Both abrasive and adhesive wear mechanism stimulates the rapid tool wear at higher cutting temperature. The SEM image of the worn out PCD insert (at various cutting speed), is shown in Figs. 58.5 and 58.6. This SEM image shows that occurrence of flank wear and formation of a built-up edge as in the case of C1 composite. Considering the built-up edge, hBN reduces the welding of work material over the tool rake surface. Increasing the hBN particles in composite decrease the tool wear as shown in Fig. 58.6, there is a mild tool wear observed. So, it is evident that hBN reduces the tool wear.

## 58.4 Conclusions

The results of turning operation on hybrid metal matrix Al-B<sub>4</sub>C-hBN composites using PCD tool by varying machining parameters were presented. From the results obtained, the following conclusions can be drawn:

**Fig. 58.6** SEM image of flank wear for 15% hBN composite



1. Higher depth of cut and feed rate produces more cutting force.
2. Higher cutting speed with lower depth of cut and lower feed rates develop low cutting forces.
3. Cutting force reduced by adding hBN due to the formation of low shear strength thin film on the cutting surface. This is possibly reduced friction between tool and work during machining.
4. Flank wear of cutting tool reduces with increasing hBN addition which confirmed by SEM observation.

## References

1. Chawla, K.K.: Composite Materials Science and Engineering. Springer-Verlag (1998)
2. Kennedy, A.R.: The microstructure and mechanical properties of Al-Si-B<sub>4</sub>C metal matrix composites. *J. Mater. Sci.* **37**, 317–323 (2002)
3. Pawlak, Z., Kaldonski, T., Pai, R.: A comparative study on the tribological behaviour of hexagonal boron nitride (h-BN) as lubricating micro-particles—An additive in porous sliding bearings for a car clutch. *Wear* **267**(5–8), 1192–1208 (2009)
4. Chen, B., Bi, Q., Yang, J., Xia, Y., Hao, J.: Tribological properties of solid lubricants (graphite, h-BN) for Cu-based P/M friction composition. *Tribol. Int.* **41**, 1145–1152 (2008)
5. Gnanavelbabu, A., Rajkumar, K., Saravanan, P.: Investigation on the cutting quality characteristics of abrasive water jet machining of AA6061-B<sub>4</sub>C-hBN hybrid metal matrix composites. *Mater. Manuf. process.* **33**(12), 1313–1323 (2018)
6. Rajkumar, K., Nambiraj, K.M., Gnanavelbabu, A., Sabarinathan, P.: Machining characteristics evaluation of aluminium composites based on cBN and PCD inserts. *Mat. Today: Proc.* **5**, 8424–8430 (2018)
7. Hooper, R.M., Henshall, J.L., Klopfer, A.: The wear of polycrystalline diamond tools used in the cutting of metal matrix composites. *Int. J. Refract. Met. Hard Mater.* **17**, 103–109 (1999)

8. Rajkumar, K., Thushal, N.A., Gnanavelbabu, A., Sabarinathan, P.: Experimental investigations on the Wire Electrochemical Micro Machining (WECM) integrity of AA6061-TiB<sub>2</sub> composite. *Mat. Today Proc.* **5**, 6990–6998 (2018)
9. El-Gallab, M., Sklad, M.: Machining of Al/SiC particulate metal–matrix composites, Part I: tool performance. *J. Mater. Process. Technol.* **83**, 151–158 (1998)
10. Tomac, N., Tonnessen, K.: Machinability of particulate aluminum matrix composites. *Ann CIRP* **41**, 55–58 (1992)

## Chapter 59

# Experimental Investigation on Influence of Process Parameters of Abrasive Water Jet Machining on Kerf Taper of Glass Fiber-Reinforced Polymer Composites



H. J. Prajapati , Puneet Kumar , Shailendra Kumar  and Ravi Kant 

**Abstract** The present paper describes an experimental investigation on the influence of process parameters namely water pressure, stand-off distance and traverse speed of abrasive water jet machine (AWJM) on kerf taper of glass fiber-reinforced polymer composite (GFRP) composite. Design of Experiment is done with the help of Taguchi methodology and Taguchi's  $L_{25}$  orthogonal array is selected for experiments. By using vision measuring system kerf top width and bottom width are measured and then kerf taper angle is calculated. Analysis of variance is used to determine the effect of machining parameters on kerf taper of machined GFRP. It is found that hydraulic pressure and traverse rate are the most significant parameters to control kerf taper. A set of optimum process parameters is determined on the basis of analysis of experimental data.

**Keywords** Abrasive water jet machining · Glass fiber-reinforced polymer composite · Kerf taper angle

### 59.1 Introduction

Abrasive water jet machining (AWJM) process is generally used to machine difficult to cut materials. It is widely used in industries due to its advantages such as high material removal rate, no thermal effect, minimal stresses, no chatter, and high flexibility. AWJM process is suitable for heat-sensitive materials, especially, composites because it produces almost no heat and chatter with low stresses. In today's technological applications, composite material is very widely used. Glass fiber-reinforced polymer (GFRP) composite is high mechanical strength and a preferred alternative once it involves corrosion resistance. Also, GFRP has unique characteristic such as lightweight, superb temperature resistant properties and offers thermal insulation [1]. It is used in several technological applications including marine, aerospace, sports

---

H. J. Prajapati (✉) · P. Kumar · S. Kumar · R. Kant  
Department of Mechanical Engineering, Sardar Vallabhbhai National Institute of Technology,  
Surat 395 007, India  
e-mail: [harshprp@gmail.com](mailto:harshprp@gmail.com)

© Springer Nature Singapore Pte Ltd. 2020  
M. S. Shunmugam and M. Kanthababu (eds.), *Advances in Unconventional Machining and Composites*, Lecture Notes on Multidisciplinary Industrial Engineering, [https://doi.org/10.1007/978-981-32-9471-4\\_59](https://doi.org/10.1007/978-981-32-9471-4_59)

goods, transportation, infrastructure, etc. Even though machining of GFRP composite is possible by conventional method using diamond edge cutter, but it ends up in extreme tool wear, high temperature and stresses, fiber pull outs, delamination, impermissible kerf properties, etc. [2]. In AWJM (Fig. 59.1), abrasive particles are mixed with a stream of water and forced through the small nozzle at high pressure so that the abrasive slurry impinges on the work surface at high velocity causing erosion. There is no heat-affected zone (HAZ) or thermal distortion occur in AWJM, which can arise in electrodischarge machine (EDM) and laser beam machine (LBM) [3]. Also, AWJM is nontoxic, can be cut any contour including sharp corner, cheap and readily available.

Researchers have studied AWJM of various composite materials including graphite epoxy, kevlar epoxy, ceramic matrix, and natural fiber composite materials to improve kerf properties and surface quality. For example, Siddiqui and Shukla [4] studied experimentally and optimize kerf characteristic in abrasive water jet trepanning of thick Kevlar-epoxy composites. It was found that when increasing water pressure of abrasive water jet machine then its provide high surface finish with low kerf taper, fine garnet abrasive, and medium value of abrasive flow rate are desirable for good surface finish. Arora and Ramulu [5] studied the kerf characteristics of abrasive water jet (AWJ) machined graphite epoxy composite. It was found that entry kerf width was more affected by stand-off distance as compared to exit kerf width. Dhanawade et al. [6] investigated abrasive water jet machining of carbon epoxy composite. It was found that hydraulic pressure and traverse rate are most major parameters to control surface roughness and kerf taper. When decreasing traverse rate, surface finish and kerf taper improve. By using scanning electron microscope (SEM), microscopic features of the machined surfaces are evaluated and compared

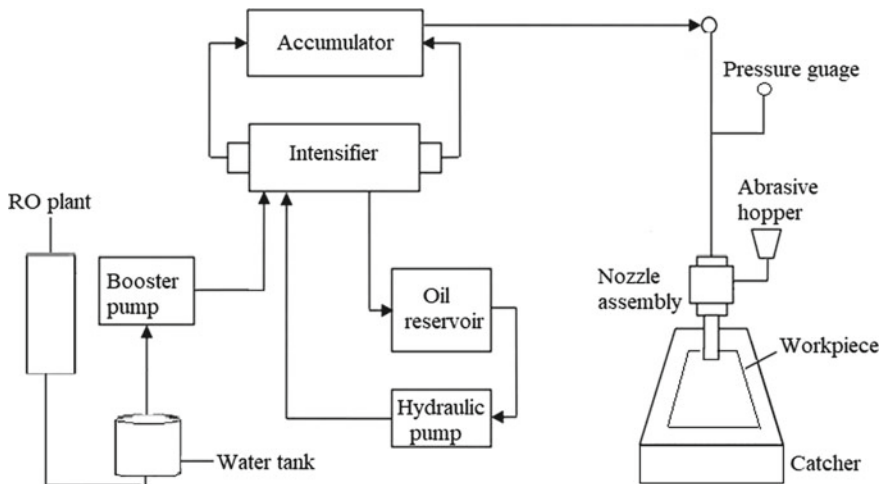


Fig. 59.1 Schematic of abrasive water jet machining setup

with sample surfaces machined by conventional method using diamond edge cutter. Kumaran et al. [7] studied relation between input process parameters of AWJM on surface roughness ( $R_a$ ) for unidirectional carbon fiber-reinforced polymer and a unidirectional with fabric surface CFRP composites was evaluated using regression analysis. It was observed that higher pressure resulted in better peeling of carbon fibers from the matrix, forming a uniform top and bottom kerf width. Good finish observed on both composites while machining at minimum traverse speed.

Review of the available literature in the area of AWJM of composites reveals that this process is widely used to machine composites. Most of the researchers have investigated the cutting performance of AWJM of composites measuring response parameter including kerf properties, surface roughness, material removal rate (MRR), etc. some researchers have investigated the effect of various process parameters such as pressure, traverse rate, stand-off distance, abrasive mass flow rate, grit size on delamination, depth of cut, etc. and develop mathematical models to predict kerf characteristics, surface roughness, material removal rate, etc. Very less work is reported on AWJM of GFRP composites. In the present experimental work, influence of process parameters of AWJM on kerf taper of GFRP composite is studied. Three process parameters namely stand-off distance, water pressure, and traverse rate are considered to study their influence on kerf taper of machined parts.

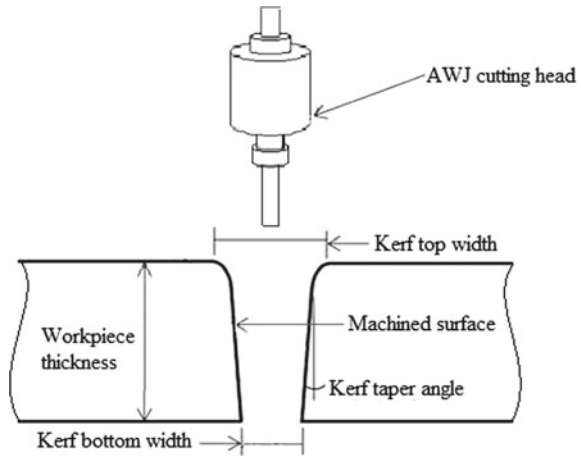
## 59.2 Experimental Work

In the present work, experiments are performed on a computer-controlled flying arm AWJ machine. This machine is equipped with hydraulic pump having maximum pressure of 240 MPa. Abrasives are supplied through gravity feed abrasive hopper system. Garnet abrasives with mesh size of #80 are used. The positional and repeat accuracy of the machine is  $\pm 0.05$  mm. Mechanical properties of GFRP composite material are given in Table 59.1. The thickness of workpiece material used in this work is 16 mm. In AWJM, kerf geometry is significant characteristic. In a through cut, a taper is generated with top width wider than the bottom. Kerf is a machining term that refers to the material removal during cutting. Figure 59.2 shows that schematic of kerf geometry. Kerf taper angle is calculated by using the following equation [8]:

**Table 59.1** Mechanical properties of GFRP composite

Property	Value
Volume Fraction	70%
Density ( $\text{gm/cm}^3$ )	1.9
Ultimate tensile strength (MPa)	1000
Ultimate compressive strength (MPa)	600
Young's modulus (GPa)	40
Hardness (MPa)	3000–6000

**Fig. 59.2** Schematic of kerf geometry



$$\theta = \tan^{-1} \frac{W_t - W_b}{2t}$$

where

- $W_t$  Top kerf width (mm)
- $W_b$  Bottom kerf width (mm)
- $t$  Work piece thickness (mm)

The levels of process parameters namely stand-off distance, water pressure and traverse rate are selected on the basis of literature review and available setup range. Table 59.2 gives the levels of process parameters. In this present work, process parameters, namely nozzle diameter, orifice diameter, and impact angle were kept constant as 0.8 mm, 0.25 mm, and 90°, respectively, during experimentation. A scientific approach is required to plan experiments in order to conduct and analyze data efficiently. Design of experiments is generally used to get more information with few runs. With full factorial design, number of experiments to be carried out for present study in 125 (i.e.  $5^3 = 125$ ), which is time consuming and uneconomical. Also it may result in high experimental error. So in this study, Taguchi’s L25 orthogonal array (OA) is selected for experiments.

**Table 59.2** Levels of process parameters

Process Parameters	Units	Levels				
		1	2	3	4	5
Stand-off Distance (SOD)	mm	2.0	2.5	3.0	3.5	4.0
Water Pressure (WP)	MPa	160	180	200	220	240
Traverse Rate (TR)	mm/min	100	125	150	175	200

In this work, a total of 25 experiments were carried out using AWJM setup. After machining with AWJM, by using vision measuring system (Model-Sipcon SDM-TRZ 5300), kerf top width and bottom width are measured. In this measurement process, video edge detection with pointer is used for selecting point on cut edge with active crosshair. Then kerf taper angle is calculated by using equation. L25 orthogonal array along with measured values of kerf taper is depicted in Table 59.3.

**Table 59.3** L25 orthogonal array with response measurements

Sr. No.	Stand-off distance (mm)	Water pressure (MPa)	Traverse rate (mm/min)	Kerf taper angle (Degree)
1	2	160	100	0.2454
2	2	180	125	0.3551
3	2	200	150	0.3284
4	2	220	175	0.2365
5	2	240	200	0.2845
6	2.5	160	125	0.4225
7	2.5	180	150	0.3112
8	2.5	200	175	0.3682
9	2.5	220	200	0.3425
10	2.5	240	100	0.1125
11	3	160	150	0.5062
12	3	180	175	0.3885
13	3	200	200	0.4574
14	3	220	100	0.2456
15	3	240	125	0.2345
16	3.5	160	175	0.5088
17	3.5	180	200	0.6099
18	3.5	200	100	0.2145
19	3.5	220	125	0.3075
20	3.5	240	150	0.2012
21	4	160	200	0.6245
22	4	180	100	0.4189
23	4	200	125	0.3251
24	4	220	150	0.3921
25	4	240	175	0.3557



### 59.3 Results and Discussion

Influence of process parameters on the kerf taper is investigated through analysis of variance (ANOVA) using Minitab 14 software. It is a computational technique to learn about the influence of various factors on response parameters. Table 59.4 depicts the ANOVA for kerf taper. The analysis is carried out at 95% confidence level. F-ratio value is used to test whether the effect due to the factors are significantly changing or not. Larger F-ratio value indicates that there is a big change in the performance characteristics. The P-values test the statistical significance of each of the parameters. The factor that passes the test of significance or having a P-value less than the significance level (i.e. 0.05) is considered statistically significant.

As depicted in Table 59.4, the P-value of stand-off distance (SOD), water pressure (WP) and traverse rate (TR) is less than significance level i.e. 0.05. Hence all parameters have passed the test of significance for kerf taper. The P-value of water pressure and traverse rate is smallest. Therefore, it can be concluded that the water pressure and traverse rate are the most significant parameter influencing kerf taper angle of GFRP. The percent contribution of each of the control factor is calculated by the ratio of the individual parametric sum of square to the total sum of square of all the parameters. Percentage contribution for water pressure is highest of 42.7% followed by traverse rate with 32.8% and stand-off distance 14.8%. Residual error in the process is 9.7%.

Figure 59.3 depicts the main effects plot of process parameters on kerf taper. With the increase in stand-off distance, kerf taper angle increases. As stand-off distance increases, it allows the water jet to expand before impingement on the workpiece which increases susceptibility to external drag from the surrounding environment [9]. Therefore, water jet loses its kinetic energy as it penetrates into the work material, and diverged jet does not cut effectively in the bottom of kerf. Thus, increases in stand-off distance results in wider kerf top width than bottom width. Because of at the same time, the energy of jet decreases at lead exit region.

Water pressure plays a very important role in kerf taper angle of glass fiber-reinforced polymer by machining of abrasive water jet. Increase in water pressure results in decrease in kerf taper angle. As water pressure increases, the kinetic energy of the jet increases and it leads to increased momentum of abrasives. Therefore, the

**Table 59.4** Analysis of variance for means

Process parameter	DOF	F-value	P-value	%P
Stand-off distance	4	4.60	0.017	14.8
Water pressure	4	13.18	0.000	42.7
Traverse rate	4	10.15	0.001	32.8
Error	12	–	–	9.7
Total	24	–	–	

DOF- degree of freedom; F- F ratio; P- P value; %P- percentage contribution

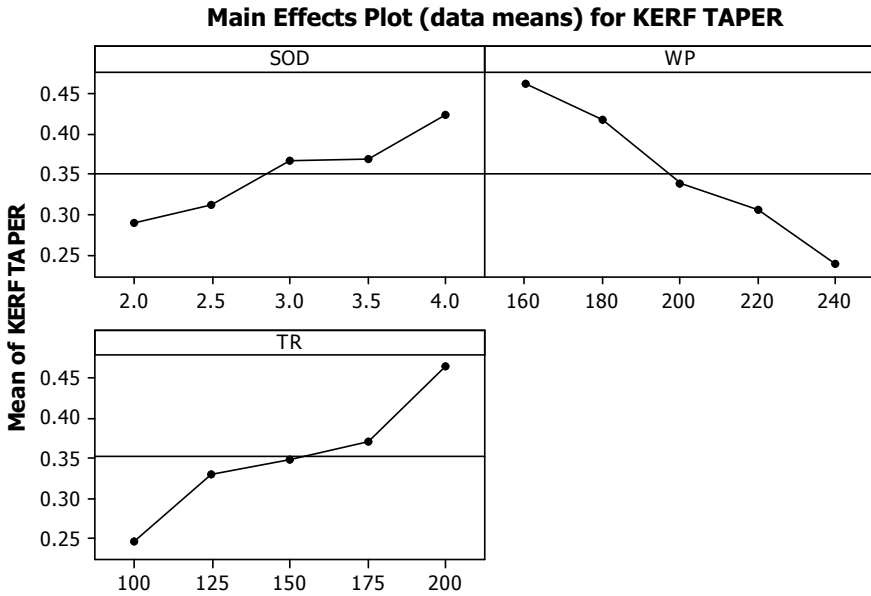


Fig. 59.3 Main effects plot for kerf taper

jet is able to retain its energy at the lead exit region and material removal in this region is effective with increase in water pressure [6]. As a result kerf top width of work material will be larger and bottom width also may have relatively bigger due to this obtain lower kerf taper.

With increase in traverse rate, kerf taper angle increases. The minimum value of kerf taper angle is observed at 100 mm/min of traverse rate as shown in Fig. 59.3. This is due to the fact that as abrasive water jet passes on work piece surface with faster moving rate means exposure time decreases and it results in impingement of less number of abrasive particles on the workpiece material. It causes wider kerf top width as compared to bottom width [9].

For minimizing kerf taper, an optimal set of machining process parameter as determined by ANOVA is given as under -Stand-off distance- 2.0 mm, Water pressure-240 MPa, Traverse rate- 100 mm/min.

### 59.4 Conclusions

In the present work, an experimental investigation has been done to study the influence of process parameters namely stand-off distance, water pressure and traverse rate on kerf taper in AWJM of glass fiber-reinforced polymer composite. On the basis of experimental results, the following conclusions are drawn:

- i. Water pressure and traverse rate are the most significant parameters influencing kerf taper angle of AWJM of GFRP. Whereas stand-off distance is least significant parameter.
- ii. It has been found that kerf taper angle varies inversely to water pressure.
- iii. Kerf taper angle decreases with decreasing traverse rate and stand-off distance.

The above findings are certainly helpful in effective machining of GFRP composite by AWJM.


## References

1. Chawla, K.K.: *Composite Materials: Science and Engineering*. Springer Science & Business Media (2012)
2. Teti, R.: Machining of composite materials. *CIRP Ann.-Manuf. Technol.* **51**(2), 611–634 (2002)
3. Komanduri, R.: Machining of fiber-reinforced composites. *Mach. Sci. Technol.* **1**(1), 113–152 (1997)
4. Siddiqui, T.U., Shukla, M.: Abrasive water jet hole trepanning of thick Kevlar-epoxy composites for ballistic applications—experimental investigations and analysis using design of experiments methodology. *Int. J. Mach. Mach. Mater.* **10**(3), 172–186 (2011)
5. Arora, D., Ramulu, M.: The kerf characteristic of abrasive water jet machining on graphite/epoxy composite. *J. Eng. Mater. Technol.* **118**, 256–265 (1996)
6. Dhanawade, A., Kumar, S., Kalmekar, R.V.: Abrasive water jet machining of carbon epoxy composite. *Def. Sci. J.* **66**(5), 522 (2016)
7. Kumaran, S.T., Ko, T.J., Uthayakumar, M., Islam, M.M.: Prediction of surface roughness in abrasive water jet machining of CFRP composites using regression analysis. *J. Alloy. Compd.* **724**, 1037–1045 (2017)
8. Shukla, R., Singh, D.: Experimentation investigation of abrasive water jet machining parameters using Taguchi and Evolutionary optimization techniques. *Swarm and Evol. Comput.* **32**, 167–183 (2017)
9. Wang, J.: A machinability study of polymer matrix composites using abrasive waterjet cutting technology. *J. Mater. Process. Technol.* **94**, 30–35 (1999)

# Chapter 60

## WEDM Studies on TiB<sub>2</sub>-15% SiC Ceramic Composite Processed Through SPS Process



K. Jayakumar 

**Abstract** Ceramic matrix composites (CMCs) are also known as the advanced ceramics or synthetic ceramics, because the major constituent of CMC is basically synthetically produced ceramic material such as oxide, carbides, titanates. In the present study, TiB<sub>2</sub> microparticle was chosen as a matrix and SiC as reinforcement. The method selected for the consolidation and fabrication of CMC in this work is Spark Plasma Sintering (SPS) furnace at IIT, Madras. Synthesis and characteristics study on TiB<sub>2</sub> matrix and SiC reinforcement with varying volume% of 0, 5, 10, and 15 vol.% produced using the SPS furnace at 1100 °C, 40 MPa, and 10 min hold of time as the initial study. Among four processed CMCs, the CMC with 15% SiC gave good fracture toughness of 6.3 MPa√m and hardness of 22.1 GPa. Due to difficulty in machining of CMCs from conventional machining processes, Wire Electric Discharge Machining (Wire EDM) studies study was carried out on TiB<sub>2</sub>-15% SiC CMC by varying Current (2, 3, and 4 A), Pulse ON (30, 60, and 90 μs) and Pulse OFF time (5, 10, and 15 μs). Results showed that at 4A current, 60 μs Ton, and 5 μs Toff gave maximum MRR of 0.621 mm<sup>3</sup>/sec. To reduce material wastage during machining, kerf is considered for which 3A current, 90 μs Ton, and 5 μs Toff gave least kerf of 0.28 mm for the initial wire diameter of 0.25 mm.

**Keywords** TiB<sub>2</sub>-SiC CMC · Spark plasma sintering · WEDM study · MRR · Kerf

### 60.1 Introduction

Normally ceramic material is rigid, strong, high hardness, good corrosion, and erosion resistance [1]. At the same time, its fracture toughness must be enhanced in order to achieve its full potential possibilities. This problem can be resolved by developing CMCs by adding reinforcements such as aluminum, copper, titanium, ceramics,

---

K. Jayakumar (✉)

Department of Mechanical Engineering, SSN College of Engineering, Kalavakkam, Chennai 603110, India

e-mail: [kjayakumar@ssn.edu.in](mailto:kjayakumar@ssn.edu.in)

© Springer Nature Singapore Pte Ltd. 2020

M. S. Shunmugam and M. Kanthababu (eds.), *Advances in Unconventional Machining and Composites*, Lecture Notes on Multidisciplinary Industrial Engineering, [https://doi.org/10.1007/978-981-32-9471-4\\_60](https://doi.org/10.1007/978-981-32-9471-4_60)

715

and nickel to the monolithic ceramics. A composite is called CMC when the reinforcement is ceramics and is embedded in ceramic matrix. Since ceramic matrices often present brittle behaviour, CMCs have been developed to achieve quasi-ductile fracture behaviour and maintain other advantages of monolithic ceramics at high temperature.

CMCs can process several methods, which include Hot Pressing, Inductive Heating, Indirect Resistance Heating, Field-Assisted Sintering Technique, Spark Plasma Sintering, Hot Isostatic Pressing, Reactive Hot Pressing, etc. Each method has its own positives and negatives. SPS technique is used in the present study in which uniaxial force and a pulsed (on-off) direct electrical current (DC) under vacuum atmosphere is used to perform high-speed consolidation of the powder. This direct way of heating allows the application of very high heating and cooling rates, enhancing densification over grain growth-promoting diffusion mechanisms, allowing maintaining the intrinsic properties of micro/nanopowders in their fully dense products.  $\text{TiB}_2$  ceramic particle was selected as matrix since its high hardness, melting point, elastic modulus, and electrical conductivity, relatively lower coefficient of thermal expansion than common ceramics [2]. SiC was selected as reinforcement due to closeness of melting point of with  $\text{TiB}_2$ .  $\text{TiB}_2$  with varying volume% of SiC (0, 5, 10 and 15%) were prepared using SPS process.  $\text{TiB}_2$ -SiC-based CMCs are mainly used in automotive breaks, Vehicle armor, Automotive clutch, cutting tools, crucibles, Propulsion Engine Exhaust, etc. [3]. Recently, SPS has been popular in processing of ceramic-based composites. Huang and Nayak [4] in 2018 used SPS to synthesize  $\text{Al}_2\text{O}_3$ - $\text{Cr}_2\text{O}_3$ / $\text{Cr}_3\text{C}_2$  nano ceramic composites and demonstrated an increase in hardness and fracture toughness of  $\text{Al}_2\text{O}_3$  ceramic with  $\text{Cr}_2\text{O}_3$ / $\text{Cr}_3\text{C}_2$  s phase addition. Mechanical and Tribological Properties of  $\text{Al}_2\text{O}_3$ -TiC composite fabricated through SPS was analyzed by Kumar et al. [5]. and showed that wear resistance, hardness, and density were increased with the addition of binders (Ni/Nb). Murty et al. [6] extensively used SPS for CMCs and high entropy alloys. Densification mechanisms during reactive spark plasma sintering of Titanium diboride and Zirconium diboride was carried by his team in 2017 and claimed that Dense ultra-fine-grained high-temperature  $\text{ZrB}_2$  and  $\text{TiB}_2$  CMC. Electrical Discharge Machining (EDM)/Wire EDM (WEDM) techniques are the suitable machining processes for machining ceramics. In 2014, Saha et al. [7] tried to use WEDM for machining  $\text{ZrB}_2$ -SiC CMC and explained that the addition of SiC in  $\text{ZrB}_2$  increased the surface finish and decreased the MRR. Modeling and analysis of machinability evaluation in WEDM process of  $\text{Al}_2\text{O}_3$  + TiC based ceramic were attempted by Kung et al. [8]. Effect of WEDM parameters on surface roughness and MRR was analyzed and predicted. From the literature, it was observed that machining of high-density CMCs processed by SPS is in the beginning stage and especially machining of  $\text{TiB}_2$ -based composites needs detailed investigation to increase its potential application and it was undertaken in the present study.

## 60.2 Experimental Details

### 60.2.1 Synthesis of Composite

Initially, graphite die with ID of 25 mm and suitable punches were fabricated for powder compaction. TiB<sub>2</sub> ceramic particles of average size 14 μm were used as matrix and SiC powders (average size of 1 μm) were used as reinforcement with four different volume percentages (0, 5, 10, and 15%). The composite powder in four said combinations were weighed and poured separately into the die and compressed with punch using hands so that the height of the initial specimen is around 10 mm and the excess powder is removed. The inner layer of die and outer layer of punches were laced with MoS<sub>2</sub> lubricant. The punch and die set were placed inside the SPS furnace for hot pressure-assisted sintering and sintering conditions were used are given below.

Max. applied Load: 40 MPa: Max. Temperature: 1450 °C: Hold time: 10 min  
Heating Rate: 100 °C/min

The sintering operation is set such that there is gradual increase in loading from 0 to 40 MPa till the specimen reaches 400 °C and after attaining 400 °C, 40 MPa load was kept as constant till the end of sintering.

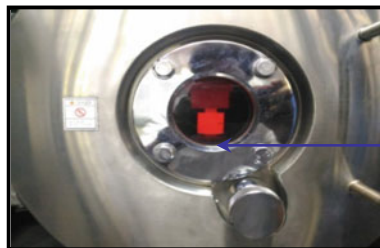
Major specifications of the SPS furnace available at IIT Madras are

Current-10,000 A: Voltage-600 V: T –1500 °C. Complete sintering of 4 CMCs was carried out in vacuum atmosphere and Fig. 60.1 shows closer view of the SPS furnace with punch and die. Processed CMCs are shown in Fig. 60.4.

### 60.2.2 Wire EDM Study

Because of the toughness and the brittle nature of CMCs, conventional machining cannot be done. So, for this reason, the CMCs to be machined using any of the nonconventional machining methods. For this, wire electric discharge machining (WEDM) was selected to machine the TiB<sub>2</sub>-SiC CMC. The WEDM parameters

**Fig. 60.1** Die and punch assembly inside the SPS furnace used from IIT Madras



Punch and die

were selected through the study of literature and the parameters for the machining experiment is sequenced using Taguchi's 3 factors-3 levels  $L_9$  orthogonal array.

The minimum number of experiments were conducted due to the limitation in final specimen size ( $\varnothing = 25$  and  $h = 5$  mm) and holding in WEDM machine. Wire feed and voltage values were kept as constant. Current, pulse on time and pulse off time were selected as variables and these major factors affect the machinability of the given material in WEDM and also commonly considered in the literature. Other major WEDM parameters are Wire feed: 60 mm/min, Wire diameter: 0.25 mm (Brass). Table 60.1 shows the experimental condition in  $L_9$  orthogonal array form.

Specifications of WEDM Machine used in this study are given below.

Make: Ratnaparki Electronics Ind. Pvt. Ltd, Chennai, Model: EZEECUT PLUS X, Y, Z Axis Travel:  $300 \times 400 \times 360$  mm, Best Surface Finish: 1–15  $\mu\text{m}$ .

Material Removal Rate (MRR) and Kerf were considered as output measures in this study. MRR of the CMC is determined by the volume removed by machining and the time taken for it. WEDM cut was carried for 3 mm depth.

Kerf includes the wire diameter and overcut. For a better machining outcome the kerf should be minimal. Tool maker's microscope was used to measure kerf and there is a cross-hair that can be moved using a micrometer gauge to measure kerf and Fig. 60.2 shows the kerf of a specimen. Taking the reading of the micrometer gauge from the start to end of the gap gives the kerf which is listed in Table 60.2. Figure 60.3a shows the close view of WEDM with workpiece and 3b shows machined CMC with 9 slots. For each experiment, kerf is measured at three different locations and average is considered.

**Table 60.1** WEDM process parameters and experimental conditions

Exp. No	Current (A)	T on ( $\mu\text{s}$ )	T off ( $\mu\text{s}$ )
1	2	30	5
2	2	60	10
3	2	90	15
4	3	30	10
5	3	60	15
6	3	90	5
7	4	30	15
8	4	60	5
9	4	90	10

**Fig. 60.2** Cross hair traveling between the kerf of a single cut. and Kerf

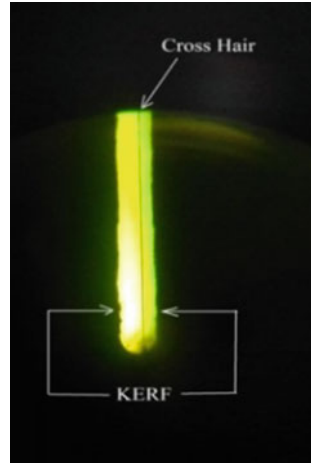


**Table 60.2** WEDM experimental results

Exp.No	MRR (mm <sup>3</sup> /sec)	Kerf (mm)	Exp.No	MRR (mm <sup>3</sup> /sec)	Kerf (mm)
1	0.081	0.31	<b>6</b>	<b>0.371</b>	<b>0.28</b>
2	0.128	0.32			
3	0.009	0.3	7	0.294	0.37
4	0.125	0.33	<b>8</b>	<b>0.621</b>	0.38
5	0.264	0.31	9	0.170	0.39

**(a)**



**(b)**

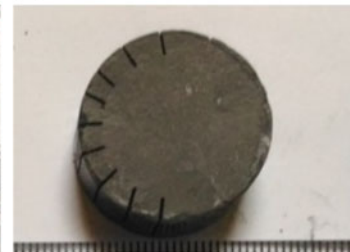


**Fig. 60.3** a. WEDM setup with CMC b. WEDM cut (9 cuts) on specimen



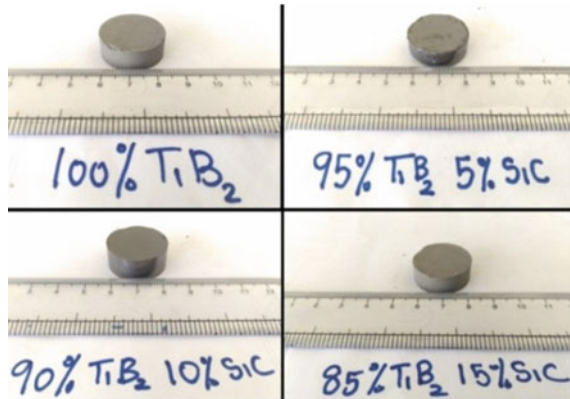
### 60.3 Results and Discussions

#### 60.3.1 Microstructure Analysis

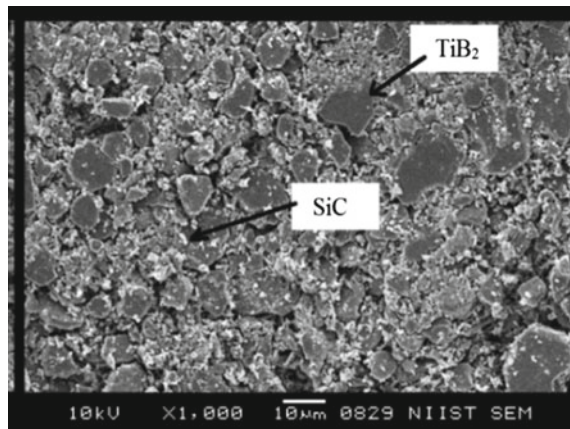
Processed CMCs are shown in Fig. 60.4 and relative densities were measured using Archimedes principle and maximum value obtained as 90% for CMC with 15% SiC.

Fracture toughness values were measured based on the measurement of Vicker's hardness test, measurement of diagonal length and standard formula. Maximum fracture toughness of 6.3 MPa $\sqrt{m}$  was observed for the same CMC with 15% SiC and hence further WEDM studies were carried out on CMC of TiB<sub>2</sub> + 15% SiC. Figure 60.5 shows the SEM image of the CMC with 15% SiC in which black colored bigger size particles are TiB<sub>2</sub> and smaller sized white particles are SiC. From the image it was observed that the reinforcements (SiC) were well distributed over the matrix surface to give uniform and good properties.

**Fig. 60.4** CMC specimens prepared from SPS ( $\phi$  = 25 mm and t = 5 mm)



**Fig. 60.5** SEM image of CMC (85% TiB<sub>2</sub> 15%SiC) at 1000X magnification



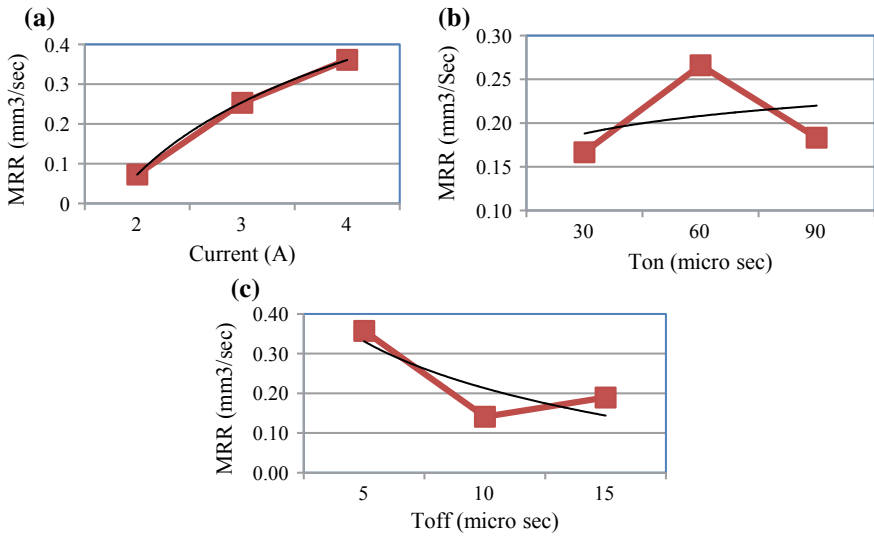


Fig. 60.6 a–c. MRR versus experiment parameters

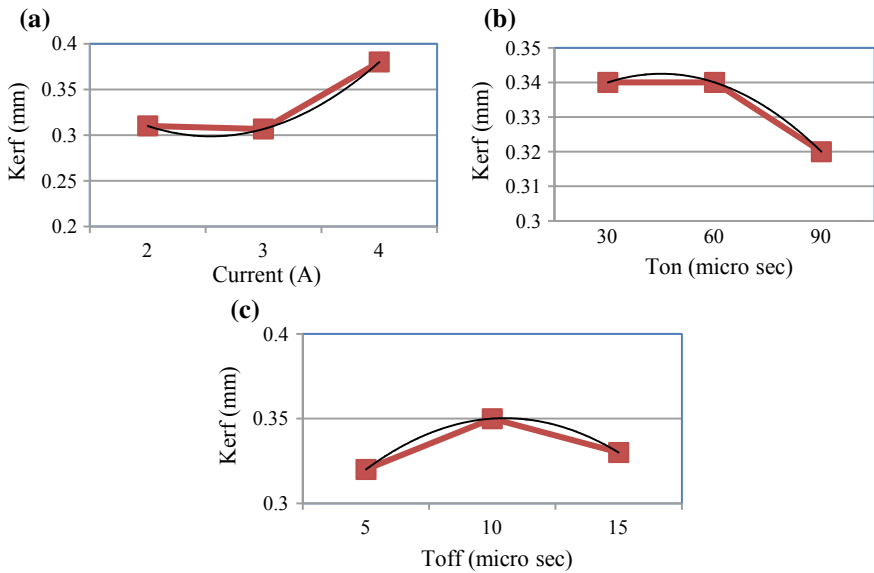


Fig. 60.7 a–c. Kerf versus experiment parameters

### 60.3.2 Effect of Input Variables on MRR

Table 60.2 lists the experimental results and Figs. 60.6 and 60.7 shows the effect of input variables on responses. In each graph, best-fit line is shown to explain the clear

trend of responses versus input parameters. In Fig. 60.6a. MRR versus Current, it is observed that there is an increase in the MRR when current is increased. This is due to when the current is at low value, small amount of thermal energy is absorbed by the surrounding, this keeps the available energy less. Thus, increased power generates an intense discharge, which impacts the surface of the workpiece and caused more molten material to be out of the crater [9]. Figure 60.6b (MRR vs. Ton) shows that there is a rise in MRR as the Ton increased. The increase in Ton time resulted in the formation of larger craters on the machined surface. The longer period of spark duration, the number of discharge increases, resulting in increased MRR [9].

In Fig. 60.6c, MRR versus Toff, it can be observed that the MRR is reduced as the Toff time is increased, this is because Toff time reduced the amount of continuous discharge of sparks resulting in molten metal cooling down and reduced the additional metal to be removed [9].

### 60.3.3 Effects of Input Variables on Kerf

In Fig. 60.7a. Kerf versus Current, it can be seen that there is an increase in the kerf as the current is increased. The main reason behind this is the higher the peak current, higher will be the spark energy. This high spark energy produces larger amount of debris. This causes the kerf to increase as there is an increase in current and amount of spark discharged by the increased current [10].

In Fig. 60.7b (kerf Vs Ton), it is observed that the kerf decreased when the Ton time increased. It may be that with an increase of pulse on time, discharge energy increases, causing evenly distribute the spark which decreases the kerf [10]. From Fig. 60.7c (kerf vs. Toff), there is also a dip in the kerf and this may be due to the fact that the increase in Toff time gave time for molten metal to solidify again reducing the MRR there by reducing the Kerf [10].

## 60.4 Conclusions

- $\text{TiB}_2 + \text{SiC}$  CMCs were synthesized using  $\text{TiB}_2$  as the matrix and SiC as the reinforcement with varying volume% of 0, 5, 10, and 15 using SPS method.
- Giving more importance to fracture toughness, the specimen with 15% SiC gave high fracture toughness of  $6.3 \text{ MPa}\sqrt{\text{m}}$  among 4 CMCs with maximum hardness of 22.1 GPa and further machined effectively through WEDM.
- In wire EDM the best parameter is determined by considering the least kerf and the maximum MRR. From 9 experiments, the experiment number 6, with parameters 3A current,  $90 \mu\text{s}$  Ton, and  $5 \mu\text{s}$  Toff is the second highest in MRR. The same experiment gave the least kerf of 0.28 mm.

## References

1. Cheloui, H., Zhang, Z., Shen, X., Wang, F., Lee, S.: Microstructure and mechanical properties of TiB-TiB<sub>2</sub> ceramic matrix composites fabricated by spark plasma sintering. *Mater. Sci. Eng. A* **528**(10-11), 3849-3853 (2011)
2. Bhaumik, S.K., Divakar, C., Singh, A.K., Upadhyaya, G.S.: Synthesis and sintering of TiB<sub>2</sub> and TiB<sub>2</sub>-TiC composite under high pressure. *Mater. Sci. Eng. A* **279**(1-2), 275-281 (2000)
3. Zhao, G., Huang, C., Liu, H., Zou, B., Zhu, H., Wang, J.: Microstructure and mechanical properties of TiB<sub>2</sub>-SiC ceramic composites by reactive hot pressing. *Int. J. Refract. Met. Hard Mater.* **42**, 36-41 (2014)
4. Huang, J.-L., Nayak, P.K.: Strengthening alumina ceramic matrix nanocomposites using spark plasma sintering. In: Woodhead Publishing Series in Composites Science and Engineering, pp. 231-247 (2018)
5. Kumar, R., Chaubey, A.K. Maity, T., Prashanth, K.G.: Mechanical and tribological properties of Al<sub>2</sub>O<sub>3</sub>-TiC composite fabricated by spark plasma sintering process with metallic (Ni, Nb) binders. *Met. Open Access Metall. J.* **8**(50), 1-12 (2018)
6. Karthiselva, N.S., Kashyap, S., Yadav, D., Murty, B.S., Bakshi, S.R.: Densification mechanisms during reactive spark plasma sintering of Titanium diboride and Zirconium diboride. *Philos. Mag.* **97**(19), 1588-1609 (2017)
7. Saha, N., Chakraborty, S., Dey, P.P., Das, P.K.: Machining of ZrB<sub>2</sub>-SiC composites by Wire-EDM technique. *Trans. Indian Ceram. Soc.* **73**(2), 94-97 (2014)
8. Kung, K.-Y., Chiang, K.-T.: Modeling and analysis of machinability evaluation in the wire electrical discharge machining (WEDM) process of aluminum oxide-based ceramic. *Mater. Manuf. Process.* **23**(3), 241-250 (2008)
9. Bobbili, R., Madhu, V., Gogia, A.K.: An experimental investigation of wire electrical discharge machining of hot-pressed boron carbide. *Defence Technol.* **11**(4), 344-349 (2015)
10. Gupta, P., Khanna, R., Gupta, R.D., Sharma, N.: Effect of process parameters on kerf width in WEDM for HSLA using response surface methodology. *J. Eng. Technol.* **2**(1), 1-6 (2012)

# Chapter 61

## Study of Mechanical Properties and Thermal Conductivity of Carbon and Basalt Fibre-Reinforced Hybrid Polymer Composites



V. Durga Prasada Rao , N. V. N. Sarabhayya  and A. Balakrishna 

**Abstract** The objective of the present work is to investigate the mechanical properties, viz., tensile strength and hardness, and thermal conductivity properties of eight varieties of carbon–basalt hybrid composites, and analyse the microstructure of the hybrid composite with highest tensile strength using Scanning Electron Microscopy (SEM). In this work, carbon and basalt fibre-reinforced hybrid composites are produced through vacuum bagging technique using epoxy resin as the matrix. The hybrid composites are prepared in different fibre stacking sequences satisfying the predetermined volume percentages of carbon and basalt. In each sequence, 90/45 quasi-isotropic fibre orientations are used. The eight volume percentage combinations of Carbon (C) and Basalt (B) considered in the study are (0:100), (20:80), (40:60), and (50:50) with carbon fibres in 450 orientation, (50:50) with basalt fibres in 450 orientation, (60:40), (80:20), and (100:0). The stacking sequences of the aforesaid eight hybrid composites, respectively, are (B-B-B-B-B-B-B-B-B), (B-B-B-C-B-B-B), (B-B-C-C-B-B-C-C-B-B), (C-B-C-B-C-B-C-B-C-B), (B-C-B-C-B-C-B-C-B-C), (C-C-B-B-C-C-B-B-C-C), (C-C-C-B-C-C-B-C-C-C), and (C-C-C-C-C-C-C-C-C-C). It is observed from the results that the average values of tensile strength, hardness, and thermal conductivity are high, respectively, for (50:50) carbon–basalt hybrid composite with basalt fibres in 450 orientation and stacking sequence (C-B-C-B-C-B-C-B-C-B), (80:20) hybrid composite with stacking sequence (C-C-C-B-C-C-B-C-C-C), and (40:60) hybrid composite with stacking sequence (B-B-C-C-B-B-C-C-B-B). Finally, the SEM analysis of fractured tensile specimen of (50:50) hybrid composite with the stacking sequence (C-B-C-B-C-B-C-B-C-B) reveals that the matrix cracking, fibre breakage, de-bonding, and delamination between fibres and matrix plays an important role, and they are dominant fracture mechanisms.

**Keywords** Carbon · Basalt · Hybrid composite · Microscopy · Delamination

---

V. Durga Prasada Rao (✉) · N. V. N. Sarabhayya · A. Balakrishna  
Department of Mechanical Engineering, S.R.K.R. Engineering College, Bhimavaram 534204,  
India  
e-mail: [vdp009@gmail.com](mailto:vdp009@gmail.com)

© Springer Nature Singapore Pte Ltd. 2020  
M. S. Shunmugam and M. Kanthababu (eds.), *Advances in Unconventional Machining and Composites*, Lecture Notes on Multidisciplinary Industrial Engineering, [https://doi.org/10.1007/978-981-32-9471-4\\_61](https://doi.org/10.1007/978-981-32-9471-4_61)

725

## 61.1 Introduction

In present-day research, relatively new fibre-reinforced composite is the hybrid, which is obtained by using two or more different kinds of fibre in a single matrix. Carbon fibres are a type of high-performance fibre available for engineering application and have high elastic modulus and fatigue strength than those of glass fibres. On the other hand, basalt fibre has a similar chemical composition as glass fibre but has better strength characteristics (tensile strengths of glass, carbon and basalt are 1.72, 1.79 and 3.0 GPa, respectively) and unlike most glass fibres is highly resistant to alkaline, acidic and salt attack. Glass and carbon fibres have their common application in the construction industry, and a wide range of applications of basalt and its products include its uses in civil engineering, automotive, boat building, wind turbine blades and sporting goods. Taking into consideration these fibres, a brief review of literature on their composites is presented in the next paragraphs.

Richard Parnas et al. [1] investigated mechanical properties and durability of basalt fibre-reinforced polymer composites. To determine the quality of the basalt composites and glass composites, fibre volume fraction and void content were determined through the density measurements of polymer matrix and composites. It is found in tensile test that the modulus of basalt fibre is higher than the glass. Zhishen Wu et al. [2] presented the fatigue behaviour of various fibre-reinforced polymer composites, namely, carbon, glass, polyparaphenylene benzobisoxazole (PBO) and basalt fibres, including the effect of hybrid applications such as carbon/glass and carbon/basalt composites. Yihe Zhang et al. [3] fabricated the basalt fibre-reinforced composites with different fibre components by injection moulding method and explained about tensile, flexural, impact properties and thermal stability. Scanning Electron Microscopy (SEM) conducted on the fracture structures of the composite reveals superior linkage between the basalt fibres and PBS matrix. ArySubagia and Yonjig Kim [4] investigated the effect of incorporation of basalt fibres on the tensile properties of carbon fibre-reinforced epoxy laminates manufactured by vacuum-assisted resin transfer moulding. The tensile strength and stiffness of hybrid laminates linearly decrease with increase in basalt fibre content, but the fractured strain gradually increased with the increase in basalt fibre content. Ban Bakir and Haithem Hashem [5] have evaluated the effect of glass fibre orientation of reinforced composite material on mechanical properties: tensile strength, toughness and microstructure were tested. They used to compare the effect of direction of fibres in order to improve strength and toughness. Doringato and Pegoretti [6] in their work combined basalt and E-glass fibre fabrics with carbon fibre fabrics according to the rule of mixture. Charpy impact tests evidenced that the strength increases as basalt and glass content increased. ArySubagia et al. [7] fabricated carbon and basalt fibre hybrid composites by vacuum-assisted resin transfer moulding process, and studied the effect of stacking sequences of carbon and basalt fabrics on the flexural properties of composite laminates. Jae Lim et al. [8] prepared two types of carbon/basalt/epoxy hybrid composites in a sandwich form using hand layup method, conducted flexural and mode-I inter-laminar fracture tests, and studied the effect of stacking sequence on

the flexural and fracture properties. Later, Scanning Electron Microscopy (SEM) is done on the fractured surfaces.

Prabakaran et al. [9] determined tensile strength, flexural strength and impact strength of basalt fibre-reinforced vinyl ester composite experimentally. The composite laminates were prepared by mixing chopped strand basalt fibre and vinyl ester with proper coring agents. It is concluded that shortest fibres have good adhesion with the vinyl ester resin for tensile properties. Zhongyu Lu et al. [10] have investigated the effect of elevated temperatures on tensile properties of basalt fibre roving and pultruded basalt fibre-reinforced (BFRP) epoxy plates and compared the results with that of E-glass fibre roving and pultruded glass fibre-reinforced (GFRP) plates. The results show that BFRP plates have got better tensile properties and temperature resistance. Vivekdhand et al. [11] in their work found that the basalt fibre is the best reinforcement for composites and is as good as carbon fibre. They also asserted that it has got superior physical, thermal and chemical properties. Irina [12] employed vacuum-assisted resin transfer moulding method to fabricate the hybrid composite panels of glass fibre and plain-woven carbon fibre in three different arrangements, and investigated their mechanical properties. Soares et al. [13] have produced basalt fibre composite in an unsaturated polyester matrix by Resin Transfer Moulding (RTM) method, and studied the mechanical properties, viz., tensile, compression, shear and flexural properties. They observed that the first ply failure of the outermost layer is the cause for sudden failure in tensile, compression and flexural tests. Aswanikumar et al. [14] have manufactured thermoplastic composites reinforced with two-dimensional plain-woven homogeneous and hybrid fabrics of kevlar/basalt yarns by compression moulding technique with polypropylene as the resin, and studied their mechanical behaviour. They observed that kevlar and basalt yarns present better tensile and compression behaviour as compared to their base composites due to hybridization.

ArySubagia et al. [15] investigated the thermal conductivity of carbon/basalt fibre-reinforced hybrid composite structure based on stacking sequences. They also investigated thermal impedance of Carbon Fibre-Reinforced Polymer (CFRP) and Basalt Fibre-Reinforced Polymer (BFRP) with increasing thickness. Research involved processing hybrid composites by using injection moulding. Palavan and Sivagamasundari [16] have researched a work which is focused on the tensile properties of Basalt Fibre-Reinforced Polymer (BFRP) bars of 8 and 10 mm diameters. The properties were determined according to ASTM D7205/D7205M-06. In this test, each end of BFRP bar specimen was embedded in steel tube filled with 1:1 mixture of epoxy resin and hardener. The ultimate tensile strength of BFRP bars was 2.5 times higher than the conventional steel bars and modulus of elasticity is 4 times lesser than conventional steel bars. Nisini et al. [17] have prepared carbon, basalt and flax fibres in an epoxy matrix by hand layup method. They were later subjected to tensile, flexural, inter-laminar shear strength test, and to falling weight impact. From impact hysteresis curves, they suggest the possibility to tailor the mode of fracture of these hybrids under impact by modifying their stacking sequence, while leaving basically unchanged the overall impact performance. Vikas and Sudheer [18] investigated mechanical properties of basalt fibre under static and dynamic loading. They also investigated tribological and thermal properties. Basalt fibre has been found to be

a potential candidate to be used as reinforcement material with different polymer matrices.

Owing to the growing worldwide application of carbon and basalt composites over automotive, aerospace, construction, defence and sport industries, and due to the fact that the replacement of glass fibre with basalt fibre can reduce the risk of environment pollution, focus has been made in this work on hybrid composites containing both carbon and basalt fibres. Also, it is observed that, though considerable volume of research has been carried out on carbon and basalt fibre composites, there is less emphasis on the study of effect of stacking sequences on the properties of their composites. Thus, in the present work, the carbon and basalt fibre hybrid composites are prepared in different stacking sequences satisfying certain volume fraction ratios to study the effect on mechanical properties, viz., tensile strength, hardness and thermal properties, viz., thermal conductivity.

## 61.2 Preparation of Carbon–Basalt Hybrid Composites

In the present work, the hybrid fibre-reinforced composite specimens or samples are fabricated from carbon fibre, basalt fibre, and resin matrix. The carbon and basalt fibres used are of 0.2 mm thickness each, and the resin used is epoxy resin. The total number of plies used in each hybrid composite is ten, and the final thickness of each of the composites is set to be 2 mm. Eight varieties of hybrid composites in different (symmetric) fibre stacking sequences satisfying the predetermined volume percentages of carbon–basalt are prepared by vacuum bagging technique. The eight volume percentage combinations of carbon and basalt considered in the study are (0:100), (20:80), (40:60), (50:50) with carbon as the first layer, (50:50) with basalt as the first layer, (60:40), (80:20), and (100:0). In each sequence, 90/45 quasi-isotropic fibre orientations are used. The hybrid composites under consideration with their stacking sequences are

- C:B = 0:100/B-B-B-B-B-B-B-B-B, C:B = 20:80/B-B-B-C-B-B-C-B-B-B
- C:B = 40:60/B-B-C-C-B-B-C-C-B-B, C:B = 50:50/C-B-C-B-C-B-C-B-C-B
- C:B = 50:50/B-C-B-C-B-C-B-C-B-C, C:B = 60:40/C-C-B-B-C-C-B-B-C-C
- C:B = 80:20/C-C-C-B-C-C-B-C-C-C, C:B = 100:0/C-C-C-C-C-C-C-C-C

where C—Carbon fibre, and B—Basalt fibre.

### 61.2.1 Vacuum Bagging Process

Vacuum bagging or vacuum bag laminating is a clamping method and is one of the common methods used for preparing fibre-reinforced composites. It uses atmospheric pressure to hold the adhesive or resin-coated components of a lamination in place until the adhesive cures. The vacuum bagging system consists of the airtight



clamping envelope and a method for removing air from the envelope until the epoxy adhesive cures. A variety of materials are needed to complete the vacuum system and assist in the laminating process. They include release peel ply, release film, breather material, vacuum bagging film, mastic sealant, the plumbing system, mylar film, epoxy resin and fast hardener. The components used in vacuum bagging process are shown in Fig. 61.1. The vacuum pump used in the process is a two-stage pump of 370 W capacity, has a speed of 1425 RPM and works with a minimum (vacuum) pressure of 0.3 bar. Figure 61.2 shows the setup of vacuum bagging process used in

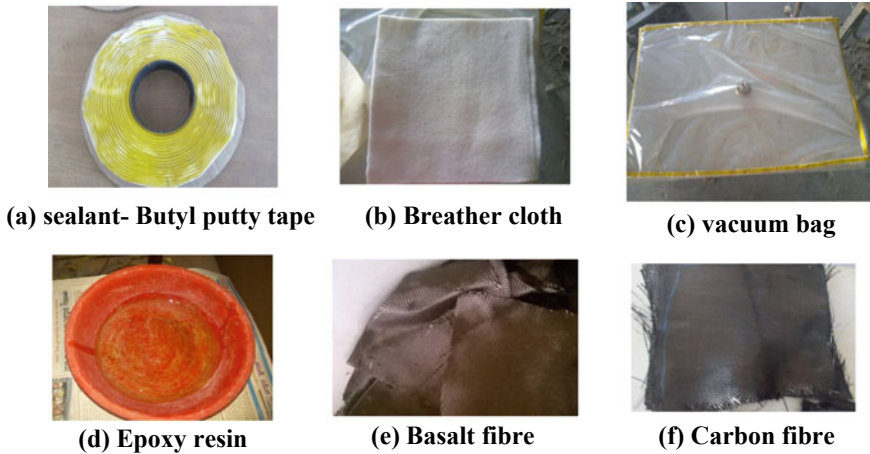


**Fig. 61.1** Components used in vacuum bagging process



**Fig. 61.2** Experimental setup of vacuum bagging

the preparation of the eight varieties of composite sheets. In the present study, while preparing all the eight varieties of composites, smooth roving interlaced fabrics (bidirectional) of carbon and basalt are used in 90/45 quasi-isotropic fibre orientations. The final thickness of each of the composites is set to be 2 mm.

## 61.3 Experimentation

The experimental work involves the tensile testing, hardness testing and thermal conductivity testing of eight varieties of composites under consideration.

### 61.3.1 Tensile Test

After the hybrid composite sheets are fabricated, cutting of required number of specimens of each composite is done in the desired shape and size to test the tensile properties of the composites. The tensile testing of the samples is done by using Universal Testing Machine (UTM). Then scanning electron microscopy of the best composite is to be done to analyse the microstructure. The tensile strength of a material is the maximum amount of tensile stress that it can take before failure. During the test, a uniaxial load with a load cell capacity of 50 kN is applied through both the ends of the specimen. The dimensions of each specimen as per ASTM D638 standards are 200 mm × 20 mm × 2 mm. Five samples of each composite are tested for obtaining better results.

The results produced by tensometer instruments provide load as a function of extension. From this data, along with the cross-sectional area of the test piece, a stress–strain curve can be plotted. The fractured samples of each composite after performing tensile test are shown in Fig. 61.3.

### 61.3.2 Hardness Test

After the hybrid composite sheets are fabricated, cutting of one sample of each composite is done in the desired shape and size to test the hardness of the composites. The hardness testing of the samples is done using Shore Durometer (SHORED) which conforms to ASTM D2240 standards. The fabricated composites were sheared according to standards in order to perform tensile test for determining the hardness of the composites prepared under this study. The samples used for hardness testing are shown in Fig. 61.4. One sample of each composite is tested at four different positions for obtaining better results.

Durometer hardness is used to determine the relative hardness of soft materials, usually plastic or rubber. The test measures the penetration of a specified indenter

**Fig. 61.3** Fractured samples after tensile test



**Fig. 61.4** Hardness test samples



into the material under specified conditions of force and time. The dimensions of each specimen are 40 mm × 40 mm × 2 mm. The hardness test is done using Shore Durometer (Shore D).

### 61.3.3 Thermal Conductivity Test

After the hybrid composites are fabricated, cutting of one sample of each composite is done in the desired shape and size to test the thermal conductivity of the composites. The thermal conductivity testing of the samples is done by using TCi thermal conductivity analyzer (C-Therm) which conforms to ASTM D7984 standards. One sample of each composite is tested in four different positions for obtaining better results.

The thermal conductivity is a measure of the ability of a material to transfer heat. During the test, a known current is applied to the sensor's spiral heating element, providing a small amount of heat to the specimen. The dimensions of each specimen are 40 mm × 40 mm × 2 mm. The thermal conductivity test is done using thermal conductivity analyzer (C-Therm). C-Therm TCi Thermal Conductivity Analyzer employs the Modified Transient Plane Source (MTPS) technique in characterizing the thermal conductivity and effusivity of materials.

## 61.4 Results and Discussion

The results of tensile tests, hardness tests and thermal conductivity tests performed on pure carbon composite, six varieties of carbon–basalt composites under consideration and pure basalt composite are furnished in Table 61.1. The comparison of tensile strengths of all the eight varieties of composites prepared in different stacking sequences is shown in Fig. 61.5. It is observed from the bar chart that the average tensile strength of (50:50) carbon–basalt hybrid composite with basalt fibres in 45° orientation and stacking sequence (C-B-C-B-C-B-C-B) is high (372.72 MPa), whereas the average tensile strength of (50:50) carbon–basalt hybrid composite with carbon fibres in 45° orientation and stacking sequence (B-C-B-C-B-C-B-C) is low (218.60 MPa). It is to be noticed that the average tensile strength of (50:50) carbon–basalt hybrid composite with basalt fibres in 45° orientation is near to that of pure carbon composite, i.e. (100:0) composite (442.21 MPa). On the other hand, the average tensile strength of (50:50) carbon–basalt hybrid composite with carbon fibres in 45° orientation is near to that of pure basalt composite, i.e. (0:100) composite (237.37 MPa).

The comparison of hardness of all the eight varieties of composites prepared in different stacking sequences is shown in Fig. 61.6. It is observed from the bar chart that the average hardness of (80:20) carbon–basalt hybrid composite with stacking sequence (C-C-C-B-C-C-B-C-C) is high (97.27), whereas the average hardness

**Table 61.1** Tensile, hardness and thermal conductivity test results of carbon–basalt hybrid composites

Sl. No.	Composite constituents volume %	Stacking sequence	Average tensile strength (MPa)	Average hardness	Average thermal conductivity (W/m-K)
1	C:B = 0:100 (Pure basalt)	B-B-B-B-B-B-B-B-B-B	237.37	96.075	0.465
2	C:B = 20:80	B-B-B-C-B-B-B-C-B-B-B	234.60	96.72	0.460
3	C:B = 40:60	B-B-C-C-B-B-B-C-C-B-B	278.64	96.65	0.532
4	C:B = 50:50	B-C-B-C-B-C-B-C-B-C-B-C	218.60	96.35	0.462
5	B:C = 50:50	C-B-C-B-C-B-C-B-C-B-C-B	372.72	96.45	0.482
6	C:B = 60:40	C-C-B-B-C-C-B-B-C-C	280.78	96.97	0.490
7	C:B = 80:20	C-C-C-B-C-C-B-C-C-C	342.39	97.27	0.487
8	C:B = 100:0 (Pure carbon)	C-C-C-C-C-C-C-C-C-C	442.21	97.07	0.525

C: Carbon B: Basalt

1: C:B= 0:100 (B-B-B-B-B-B-B-B-B-B)    5: C:B=50:50 (C-B-C-B-C-B-C-B-C-B)

2: C:B= 20:80 (B-B-B-C-B-B-C-B-B-B)    6: C:B= 60:40 (C-C-B-B-C-C-B-B-C-C)

3: C:B= 40:60 (B-B-C-C-B-B-C-C-B-B)    7: C:B= 80:20 (C-C-C-B-C-C-B-C-C-C)

4: C:B= 50:50 (B-C-B-C-B-C-B-C-B-C)    8: C:B= 100:0 (C-C-C-C-C-C-C-C-C-C)

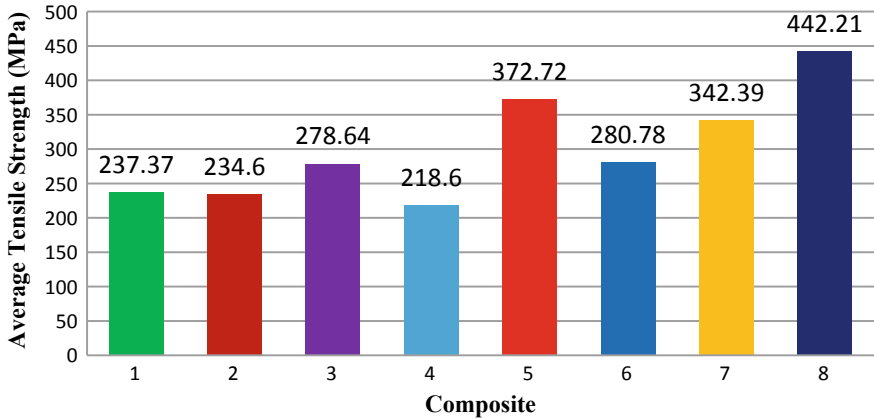


**Fig. 61.5** Comparison of tensile strengths of all the eight varieties of composites



observed from the bar chart that the average thermal conductivity of (40:60) carbon–basalt hybrid composite with stacking sequence (B-B-C-C-B-B-C-C-B-B) is high (0.532 W/m-k), whereas thermal conductivity of (20:80) carbon–basalt hybrid composite with stacking sequence (B-B-B-C-B-B-C-B-B-B) is low (0.460 W/m-k). It is to be noticed that the average thermal conductivity of (40:60) carbon–basalt hybrid composite is nearer to that of pure carbon composite, i.e. (100:0) composite (0.525 W/m-k).

#### ***61.4.1 SEM Analysis of Fractured Specimen of Tensile Test***

The tensile testing of the samples of eight composites is done by using UTM, the scanning electron microscopy of the best composite with highest tensile strength, i.e. (50:50) carbon–basalt composite with the stacking sequence (C-B-C-B-C-B-C-B-C-B) is done to analyse its microstructure. The SEM images are presented in Fig. 61.8.

### **61.5 Conclusions**

In the present work, investigation was carried out on the carbon and basalt fibre-reinforced hybrid composites. The major contributions drawn from the investigation are summarized as below:

- Except the (50:50) carbon–basalt hybrid composite with carbon fibres in 45° orientation and stacking sequence (C-B-C-B-C-B-C-B-C-B), the average tensile strengths of composites having four or more number of carbon fibres are better than the remaining composites. That is, the decrease in the number of basalt fibre layers stacked in between carbon fibre layers led to an increase in tensile strength. Also, the tensile properties of carbon basalt/epoxy hybrid composites are dependent on the basalt fibre position.
- Though the average tensile strength of (50:50) carbon–basalt hybrid composite with basalt fibres in 45° orientation and stacking sequence (C-B-C-B-C-B-C-B-C-B) is lower than that of pure carbon composite, it can be a better candidate for engineering applications because it incorporates the features of basalt like wider temperature range (–269 °C to +650 °C), higher oxidation resistance, higher radiation resistance, and higher resistance to alkaline, acidic and salt attacks.
- Disregarding the pure carbon and pure basalt composites, as the basalt volume percentage decreases the hardness of the hybrid composites has got a decreasing trend up to 50% of basalt and latter an increasing trend is observed for further decrease in the percentage of basalt.
- The stacking sequence and orientation of carbon and/or basalt fibres has no effect on hardness and thermal conductivity of hybrid composites.

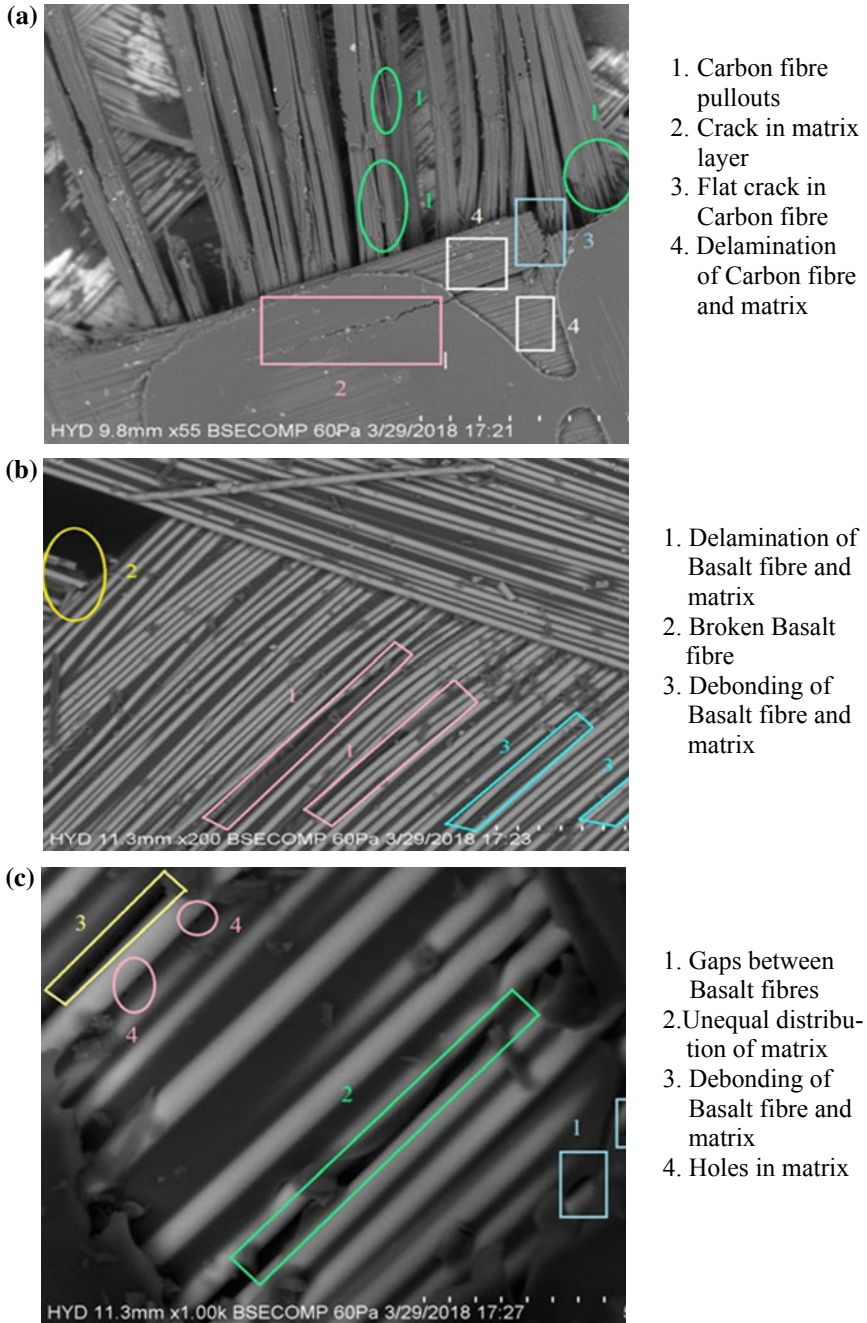


Fig. 61.8 SEM images of 50:50 carbon–basalt hybrid composite specimen



- As far as the two carbon–basalt composites with (50:50) volume percentages are considered, it has been observed that the three properties are better for the (50:50) carbon–basalt hybrid composite with basalt fibres in 45° orientation with stacking sequence (C-B-C-B-C-B-C-B-C-B) when compared to the (50:50) carbon–basalt hybrid composite with carbon fibres in 45° orientation with stacking sequence (B-C-B-C-B-C-B-C-B-C). That is to say that when carbon fibres are in 90° orientation, the properties are better than that when they are in 45° orientation.

## References

1. Parnas, R.: Montgomery Shaw and Qiang Liu., Basalt Fiber Reinforced Polymer Composites, Report no: NETCR63 (2007)
2. Wu, Z., Wang, X., Iwashita, K., Sasaki, T., Hamaguchi, Y.: Tensile fatigue behavior of FRP and hybrid FRP sheets. *Elsevier Compos.* **41**(5), 396–402 (2010)
3. Zhang, Y., Yu, C., Chu, P.K., Lv, F., Zhang, C., Ji, J., Zhang, R., Wang, H.: Mechanical and thermal properties of basalt fiber reinforced poly butylene succinate composites. *Mater. Chem. Phys.* **1**(133), 845–849 (2012)
4. ArySubagia, I.D.G., Kim, Y.: Tensile behavior of hybrid epoxy composite laminate containing carbon and basalt fibers. *Sci. Eng. Compos. Mater.* **21**(2), 211–217 (2014)
5. Bakir, B., Hashem, H.: Effect of fiber orientation for fiber glass reinforced composite material on mechanical properties. *Int. J. Min. Metall. Mech. Eng.* **1**(5), 2320–4052; 2320–4060 (2013)
6. Dorigato, A., Pegoretti, A.: Flexural and impact behaviour of carbon/basalt fibers hybrid laminates. *J. Compos. Mater.* **1**, 1–10 (2013)
7. ArySubagia, I.D.G., Kim, Y., Tijjing, L.D., Kim, C.S., Shon, H.K.: Effect of stacking sequence on the flexural properties of hybrid composites reinforced with carbon and basalt fibers. *Composites* **2**(58), 251–258 (2014)
8. Lim, J.I., Rhee, K.Y., Kim, H.J., Jung, D.H.: Effect of stacking sequence on the flexural and fracture properties of carbon/basalt/epoxy hybrid composites. *Carbon Lett.* **15**(2), 125–128 (2014)
9. Prabakaram, J., Kannan, K., Gopal, S., Palanisamy, S.: Experimental investigation of the mechanical properties of basalt fiber reinforced vinyl ester composites. *JJSETR* **3** (2014)
10. Lu, Z., Xian, G., Li, H.: Effects of elevated temperatures on the mechanical properties of basalt fibers and BFRP plates. *Constr. Build. Mater.* **127**, 1029–1036 (2016)
11. Dhand, V., Mittal, G., Rhee, K.Y., Park, S.-J., Hui, D.: A short review on basalt fiber reinforced polymer composites. *Composites* **2**(73), 166–180 (2015)
12. Irina, M.M.W.: Evaluation of mechanical properties of hybrid fiber reinforced polymer composites and their architecture. In: 2nd International Materials, Industrial, and Manufacturing Engineering Conference, MIMEC, Bail Indonesia, Procedia Manufacturing, vol. 2, pp. 236–240 (2015)
13. Soares, B., Preto, R., Sousa, L., Reis, L.: Mechanical behavior of basalt fibers in a basalt-UP composite. In: IDMEC XV Portuguese Conference on Fracture, vol. 1, pp. 82–89. Paco de Arcos (2016)
14. Bandaru, A.K., Patel, S., Sachan, Y., Ahmad, S., Alagirusamy, R., Bhatnagar, N.: Mechanical behavior of kelvar/basalt reinforced polypropylene composites. *Elsevier Compos.* **90**, 642–652 (2016)
15. Ary Subagia, I.D.G., Ketut Gede Sugita, I., Ketut Gede Wirawan, I., Dwidiani, N.M., Yuwono, A.H.: Thermal conductivity of carbon/basalt fiber reinforced epoxy hybrid composites. *Int. J. Technol.* **8**(8), 2086–9614 (2017)

16. Palavan, V., Sivagamasundari, R.: An experimental contribution on tensile performance of basalt fibre reinforced polymer bars. *IJCIET* **8**, 550–558 (2017)
17. Nisini, E., Santulli, C., Liverani, A.: Mechanical and impact characterization of hybrid composite laminates with carbon, basalt and flax fibers. *Elsevier Compos.* **2**(127), 92–99 (2017)
18. Vikas, G., Sudheer, M.: A review on properties of basalt fibre reinforced polymer composites. *Am. J. Mater. Sci.* **7**(5), 156–165 (2017)

# Chapter 62

## Design and Fabrication of Aluminium/Alumina Ultra-fine Composite and Functionally Graded Material Using Powder Metallurgy Route



Aravind Tripathy , Rajat Gupta , Saroj Kumar Sarangi   
and Anil Kumar Chaubey 

**Abstract** Composites with light metals as the matrix and ceramic particles as the reinforcements are being acknowledged widely during the past decade for their superior mechanical properties, the most successful among them have been Aluminium/Alumina (Al/Al<sub>2</sub>O<sub>3</sub>) composite where Alumina particulates are reinforced in Aluminium matrix. Present work deals with fabrication and characterization of Al/Al<sub>2</sub>O<sub>3</sub> ultra-fine composites with 10, 20, 30 and 40% Al<sub>2</sub>O<sub>3</sub>. These ultrafine composites are fabricated using uniaxial hot press under 10<sup>-5</sup> mbar vacuum pressure at 400 °C sintering temperature and 3-tonne load for 2 h experimental condition. Effect of Al<sub>2</sub>O<sub>3</sub> volume fraction on microstructural and mechanical properties of the composite are studied through optical microscopy. Phase analysis and microstructure investigations revealed that the consolidated material consists of Al as a matrix phase and Al<sub>2</sub>O<sub>3</sub> phases with size below 1 μm homogeneously dispersed in a continuous matrix. Taking into consideration the results of above experiment, Al/Al<sub>2</sub>O<sub>3</sub> system Functionally Graded (FG) Material is successfully hot pressed using powder metallurgy (PM) route under similar experimental conditions. It is found that relative density of the Al/Al<sub>2</sub>O<sub>3</sub> FG Material increased with the rise in sintering temperature and its density range changed quasi-continuously from 2.67 × 10<sup>3</sup> kg/m<sup>3</sup> to 2.71 × 10<sup>3</sup> kg/m<sup>3</sup>, while the microhardness value obtained at the top surface was 35.2 HV which gradually increased across its thickness to 74.81 HV at the other surface with the increase in reinforced Al<sub>2</sub>O<sub>3</sub>. This FGM is intended to be a good substitute

---

A. Tripathy

Mechanical Department, ITER, SOA Deemed to Be University, Bhubaneswar, India

R. Gupta

Metallurgy Department, Indian Institute of Technology (BHU), Varanasi, India

S. K. Sarangi (✉)

Mechanical Engineering Department, National Institute of Technology, Patna, Bihar, India

e-mail: [sarojksarangi@yahoo.com](mailto:sarojksarangi@yahoo.com)

A. K. Chaubey

Advanced Materials Technology Department, CSIR-IMMT, Bhubaneswar, India

© Springer Nature Singapore Pte Ltd. 2020

M. S. Shunmugam and M. Kanthababu (eds.), *Advances in Unconventional Machining and Composites*, Lecture Notes on Multidisciplinary Industrial Engineering, [https://doi.org/10.1007/978-981-32-9471-4\\_62](https://doi.org/10.1007/978-981-32-9471-4_62)

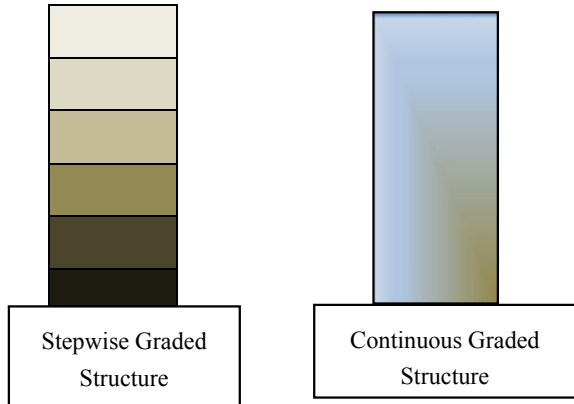
'low weight high strength material' with better wear resistance properties at elevated temperatures.

**Keywords** Ultrafine composites · Powder metallurgy · Layered structures · Hot pressing · Functionally graded materials

## 62.1 Introduction

The need for new materials in automotive and aerospace sector with superior characteristics such as low specific weight, higher strength, Young's modulus, better resistance to temperature, corrosion, wear and thermal shock, better recyclability, environmentally friendly are the areas of focus for researchers worldwide. Such composites have received widespread attention during the past decades and among them, Aluminium/Alumina (Al/Al<sub>2</sub>O<sub>3</sub>) composites are the most successful type Metal Matrix Composites [1]. The need for advanced materials is to meet the demands of extreme environments and complex thermomechanical loadings. Materials like steels, lightweight alloys (Al, Ti and Mg), copper alloys, or cast iron were tried unsuccessfully for such severe requirements. Metal-ceramic bulk composites which offer a lot of technological superiority can be the answer to the above challenge [2]. Al/Al<sub>2</sub>O<sub>3</sub> are a class of composites which exhibit characteristics like high strength-to-weight ratio, good castability and better tribological properties in comparison to unreinforced alloys [3]. MMCs comprise of lightweight metals like Al or Mg reinforced with ceramic materials like Al<sub>2</sub>O<sub>3</sub> or SiC in the form of particulates or fibres [4]. Higher specific strength and stiffness, higher operating temperature and greater wear resistance, are the hallmark of MMCs. Also, the opportunities to tailor these properties for a particular application give them the added advantage over unreinforced metals [5]. Nanostructured composites assure high strength, resistance to wear, hardness and exceptional microstructural stability at high temperatures [6]. Despite the improved properties, some issues in nanocomposite fabrication have been detected [7]. Ultra-fine composites (UFC) might be the answer to such issues. Functionally Graded (FG) Material have compositional and microstructural gradient along its thickness direction and was developed as an answer to delaminating failures in laminated composites. FG Materials exhibit flexibility regarding the functional behaviour of a single material as on one side it may exhibit metal-like properties while on the other side it will exhibit high temperature withstanding characteristics. Scholars have applied the best methods or combination of several methods depending on the characteristics of the constituent materials to fabricate these FG Materials successfully [8]. Figure-62.1 below depicts the FG Material concept in a very clear manner. These days, researchers acknowledge the importance of innovative materials in use for economic and environmental reasons [4]. These engineered materials are designed for an intended function, and the material properties are tailored by a spatial gradation in structure and/or composition. FGMs exist in nature too. Like many other human made materials, FGMs occurring in nature such as bamboo have

**Fig. 62.1** Representation of Functionally Graded Material (FGM)

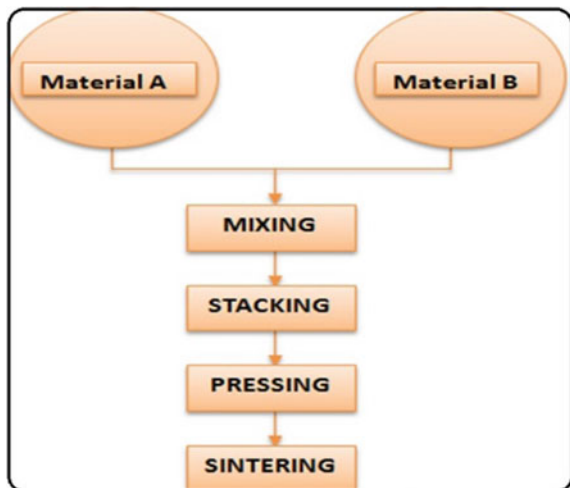


been in use for thousands of years for decoration and construction works [9]. The scientific term ‘functionally graded material’ was first introduced in the year 1984 by the Japanese researchers while developing thermal barrier materials [10].

There has been a lot of research and publications in this area in the last three decades. A great deal of detailed study of different fabrication processes, a huge amount of research investments and support by different industries and large-scale production of FGMs lead to a rise in popularity as well as the application of these engineered materials in comparison to conventional materials. Powder Metallurgy process is one such most popular process in the field of FGM fabrication.

**Powder metallurgy.** In powder metallurgy, four basic steps are followed which are mixing, stacking, pressing and sintering as explained in the flow chart (Fig. 62.2). Mixing is powder preparation, (precise weighing and blending the powder and ensure proper dispersion of each of them in the mixture which will significantly affect the

**Fig. 62.2** Powder metallurgy process



structural properties), stacking is putting the powder in the die, pressing is applying the load through the punch to give shape to the material and in order to provide strength and integrity to the powder compact, controlled heating of the powder compact is facilitated and is known as sintering. The sintering temperature is usually below the melting point of the major constituent of the powder mix [8, 11]. PM is an appropriate technology for both ultra-fine composite as well as FGM fabrication and is widely being used too [6].

## 62.2 Methodology

### 62.2.1 Raw Material

The starting materials were Alumina ( $\text{Al}_2\text{O}_3$ ) powder, (Alfa-Aesar,  $< 1 \mu\text{m}$ , purity 99.99%, density: 3.965 g/cc) and Al metal powder, (High-media,  $< 40 \mu\text{m}$ , with impurities such as Iron (Fe):0.5%, Heavy Metals (As Pb):0.03%).

### 62.2.2 Mechanical Milling

Powders of Aluminium and Alumina were weighed as per the volume fraction constituting each individual sample or layer (for FGM) and were then homogeneously mixed by using planetary ball mill (Retsch PM 400). Primarily the techniques are about proper volume fractions of the matrix and reinforcement materials that were taken for mechanical milling in order to homogenise the mixture. Phase analysis of the milled powders was done using powder diffraction technique with the help of X'Pert PRO PAN Analytical's materials research Diffractometer ( $\lambda = 1.54184\text{\AA}$ ). The ball mill system consists of one turn disc (turn table) and two or four bowls. The turn disc rotates in one direction while the bowls rotate in the opposite direction. The centrifugal forces, created by the rotation of the bowl around its own axis together with the rotation of the turn disc, are applied to the powder mixture and the balls inside the milling bowl. The powder mixture is fractured and cold-welded under high energy impact.

## 62.3 Experimental Method

First, the hot press machine chamber was thoroughly cleaned manually followed by portable vacuum cleaner. Next the frame for die holder was fitted using set of screws. On this frame the graphite die was fitted. Bottom and top graphite punches were mounted on to the hydraulically operated bottom and top actuators of the hot press

machine. First the bottom punch was inserted into the die in such a manner that a cavity of 55 mm was available for stacking the powder mix. Now measured quantity of the powder mix was taken in the die. Consolidation of powder to produce samples was done using Hot Uniaxial Vacuum Press at 400 °C for ultra-fine composite while at 400 °C as well as 450 °C for FGM samples, respectively and in all cases a dwell time of 5 min was applied after hot consolidation at respective temperatures mentioned above. After putting the powder mixture into the graphite die and adjusting the punches appropriately the hot press chamber is cleaned of all dust particles using portable vacuum cleaner. Then the front door is duly closed and tightened to prevent any air ingress. Then the hot press is switched on to create a vacuum pressure of  $10^{-5}$  mbar. Once the vacuum pressure is reached the sintering mode is switched on to reach the desired temperatures of 400 °C or 450 °C, respectively at a heating rate of 25 °C/min. Once the sintering temperatures are achieved the consolidation load of 3 tonnes are applied followed by a dwell period of 5 min at that load and temperature. Then the machine is allowed to cool and reach room temperature on its own after switching off the heaters around the graphite die. Then the vacuum pressure is released and samples are now ready to be taken out for characterization processes. After preparing the test samples in the above manner, the samples were tested for density, hardness and microstructure to find an optimum balance between matrix and reinforcement with the best characteristic for a low weight high strength composite with many other added characteristics. The figure below shows the raw samples after being taken out of the die. After fabrication of pellet samples (Fig. 62.3) and density measurements, samples were ground and polished (mirror finished), followed by cloth polishing up to 0.1  $\mu\text{m}$  with diamond paste and mounted for characterization studies as shown in Fig. 62.4. For FGM samples the pellets were cut from the middle

**Fig. 62.3** After compaction:  
**a** FGM sample and  
**b** Ultra-fine composite sample

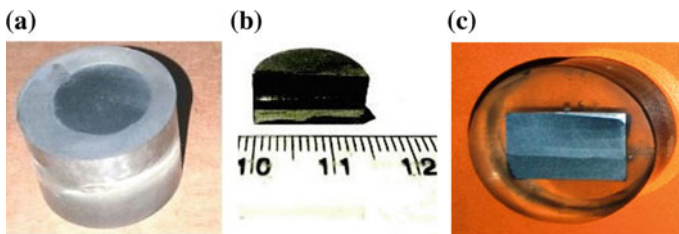
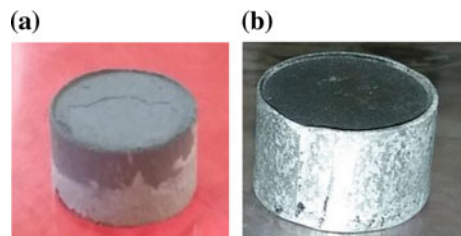


**Fig. 62.4** **a** Ultra-fine composite and **b** and **c** FGM Samples for hardness measurement

using diamond cutter and the cut surface was ground and polished up to mirror finish state and were mounted. The mounted samples were cloth polished up to 0.1  $\mu\text{m}$  with diamond paste for subsequent tests.

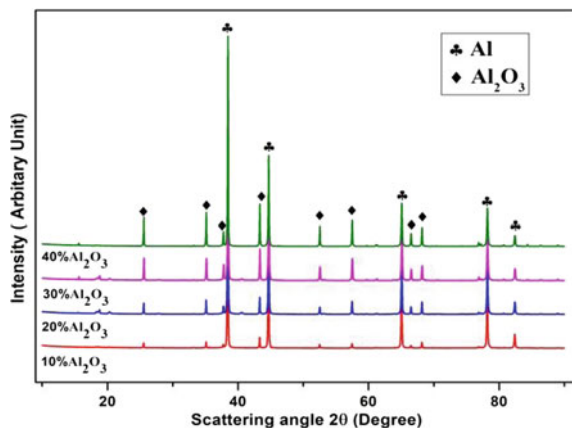
### 62.3.1 Testing

All necessary tests are carried out sequentially to ascertain the characteristics of the prepared sample before necessary trial is carried out for proving the material manufactured for a particular cause.

## 62.4 Results and Discussion

- (a) **XRD Analysis:** XRD patterns of the selected layers are shown (Fig. 62.5) in different colours to distinguish the pattern of each layer. The pattern shows only Al and  $\text{Al}_2\text{O}_3$  peaks which indicate that there is no new phase formation during the milling process. All the patterns look identical, the only difference in the intensity is observed as expected due to difference in the composition of the layers. The patterns also show a little broadening of the peaks due to fine size of the particles.
- (b) **Density Measurement:** At different volume fractions of the reinforcing material, the density was measured using Archimedes' principle in distilled water setup. The theoretical and actual density of the samples and the corresponding densification percentage for the Al/ $\text{Al}_2\text{O}_3$  ultra-fine composite specimen is shown (Fig. 62.6). Similarly, for the FGM, the data is shown in Table-62.1 for

**Fig. 62.5** XRD analysis of powders after milling





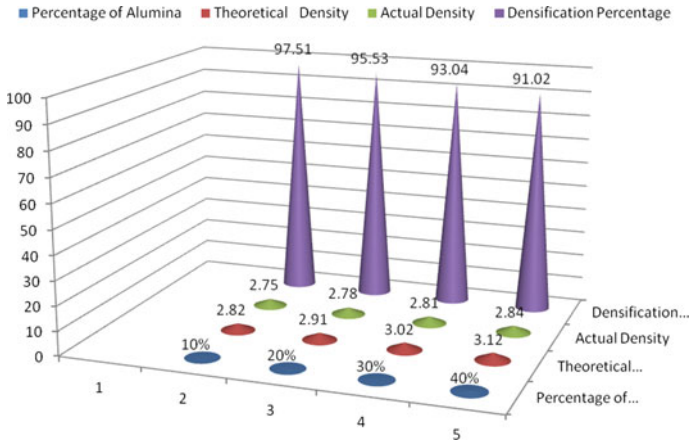


Fig. 62.6 Densification plot for ultra-fine composite samples sintered at 400 °C

Table 62.1 Density and densification data obtained for different FGM samples sintered at 400 and 450 °C

Sintering temperature (°C)	Theoretical density (Kg/m <sup>3</sup> )	Actual density (Kg/m <sup>3</sup> )	Densification percentage (%)
400	2960	2674	90.3
450	2960	2699	91.2

comparison which shows as the sintering temperature was raised, there was a rise in percentage of densification.

- (c) **Hardness measurements:** The effect of Al<sub>2</sub>O<sub>3</sub> particulate reinforcement on the hardness variations of the different ultra-fine composite samples and different layers of the FGM sample is shown in Figs. 62.7 and 62.8, respectively. For the FGM samples it was found that a sudden rise in hardness by nearly 33% in the second layer with respect to that of the first layer (pure Al). Subsequently thereafter the average hardness increased by 11% with respect to previous layer. This increase in hardness was the result of strong interfacial bonding between Al matrix and Al<sub>2</sub>O<sub>3</sub> particulates.

### 62.5 Conclusions

Ultra-fine composite samples with more than 95% density were fabricated with desired composition ratios. The hardness of each sample shows different values and it increases with the increase in the percentage of Al<sub>2</sub>O<sub>3</sub> in the sample. FGM samples with more than 90% density were also successfully fabricated at different sintering temperatures with desired composition ratios. Layers sintered are well stacked and

**Fig. 62.7** Hardness of ultra-fine composite samples

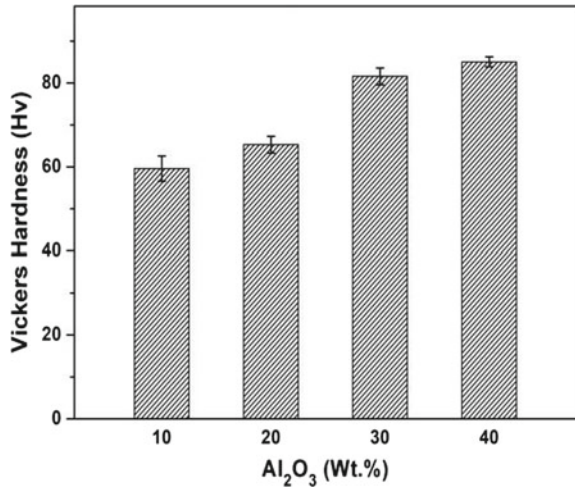
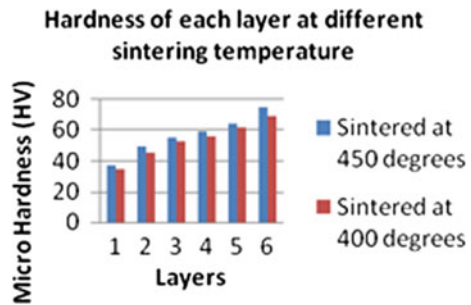


**Fig. 62.8** Hardness of FGM sample at each layer



distinct that confirms uniform gradation. The hardness at each individual layers of each sample shows different values and it increases with increase in Al<sub>2</sub>O<sub>3</sub> reinforcement.

## References

1. Koli, D.K., Agnihotri, G., Purohit, R.: Properties and characterization of Al-Al<sub>2</sub>O<sub>3</sub> composites processed by casting and powder metallurgy routes (Review). *IJLTET* **2**(4), 486–496 (2013)
2. Kaczmar, J.W., Pietrzak, K., Włosinski, W.: The production and application of metal matrix composite materials. *J. Mater. Process. Technol.* **106**, 58–67 (2000)
3. Hunt, Jr W.H., Miracle, D.B.: Automotive applications of metal matrix composites. In: Miracle, D.B., Donaldson, S.L., (eds.) *ASM Handbook: Composites*, ASM International, vol. 21. pp. 1029–32 (2001)
4. Lannutti, J.J.: Functionally graded materials: properties, potential and design guidelines. *Compos. Eng.* **1**(4), 81–94 (1994)

5. Chawla, K.K.: Composites Materials, 3rd edn. Springer, New York (2012). [Chapter 4 Metal Matrix Composites <https://www.princeton.edu/~ota/disk2/1988/8801/880107.PDF>]
6. Chaubey, A., et al.: Fabrication and characterization of W-Cu functionally graded material by spark plasma sintering process. *Fusion Eng. Des.* **135 A**, 24–30 (2018). <https://doi.org/10.1016/j.fusengdes.2018.07.010>
7. Balog, M., et al.: Novel Ultrafine-Grained Aluminium Metal Matrix Composites Prepared from Fine Atomized Al Powders. *Light Metals*, TMS (2014)
8. Tripathy, A., Sarangi, S.K., Panda, R.K.: Fabrication of functionally graded composite material using powder metallurgy route: an overview. *IJMPERD* **7**(6), 135–146 (2017)
9. Silva, E.C.N., Walters, M.C., Paulino, G.H.: Modeling bamboo as a functionally graded material: lessons for the analysis of affordable materials. *J. Mater. Sci.* **41**, 6991–7004 (2006)
10. Yamanoushi, M., Koizumi, M., Hiraii, T., Shiota, I. (eds.) *Proceedings of the 1st International Symposium on Functionally Gradient Materials*. Sendai, Japan (1990)
11. Gupta, R., Kumar, R., Chaubey, A.K., Kanpara, S., Khirwadkar, S.S.: Mechanical and microstructural characterization of W-Cu FGM fabricated by one-step sintering method through PM route. In: *IOP Conference Series: Materials Science and Engineering*, vol. 338, p. 012042 (2018). <https://doi.org/10.1088/1757-899x/338/1/012042>

# Chapter 63

## Mechanical and Crystallization Behaviour of Sisal Fiber and Talc Reinforced Polylactic Acid Composites



A. Suresh Babu , M. Jaivignesh  and D. Poovarasam 

**Abstract** Polylactic acid (PLA) is one of the widely studied renewable resource based bioplastic material which has huge potential to be on par with the commercial synthetic plastics. Commercial grades of neat PLA is yet to gain a strong commercial standpoint in applications other than packing and drug delivery system. The major barrier in the commercialization of PLA based products is its poor toughness and low heat resistance. This work focuses on the preparation of sisal fiber and talc reinforced PLA composites and investigates the effect of talc on the natural fiber reinforced biodegradable PLA composites on mechanical and thermal characteristics. The results indicate that the mechanical and thermal characteristics of the PLA composites are improved when compared to that of neat PLA. Tensile Strength has been increased by 16.7% when compared to neat PLA and maximum impact strength of about 32 J/m is achieved. Crystallinity of composites has also been improved up to 5.74%.

**Keywords** Crystallinity · Composites · Polylactic acid · Sisal fiber · Talc

### 63.1 Introduction

Plastics derived from petroleum are a challenge due to their harmful effects towards the environmental issues like greenhouse gas emissions which cause adverse effects on climate change and disposal of those synthetic plastics cause damage to the ecosystem. Bioplastics emerge as a new field, focusing on renewability and sustainability. Replacing the fossil carbon present in plastic products with renewable carbon allows to reduce the carbon footprint and greenhouse gas emissions. In recent years, natural fiber reinforced plastics have witnessed an exponential growth in automotive and aerospace applications. Natural fibers have been considered as an alternative to synthetic fibers in polymer composites due to their distinct advantages over the synthetic fibers. The traditional fiber-reinforced composites being non-renewable and

---

A. Suresh Babu · M. Jaivignesh (✉) · D. Poovarasam  
Department of Manufacturing Engineering, Anna University, Chennai, India  
e-mail: [jaivignesh.murali@gmail.com](mailto:jaivignesh.murali@gmail.com)

© Springer Nature Singapore Pte Ltd. 2020  
M. S. Shunmugam and M. Kanthababu (eds.), *Advances in Unconventional Machining and Composites*, Lecture Notes on Multidisciplinary Industrial Engineering, [https://doi.org/10.1007/978-981-32-9471-4\\_63](https://doi.org/10.1007/978-981-32-9471-4_63)

non-biodegradable, pose serious environmental problem and damage the environment and marine ecosystem after the end of their useful life as they use petroleum-based polymers as matrix material. The development of bio-based composites has been of enormous interest in materials science for both ecological and environmental perspectives. Various efforts have been made to replace the petroleum derived polymers with renewable source derived from fully degradable biopolymers. Polylactic acid is derived from resources such as corn starch, tapioca roots, chips or starch, or sugarcane and has the potential to replace the petroleum derived polymer material. It is biodegradable, thermoplastic, aliphatic and polyester possessing good mechanical properties. The major barriers of commercialization of polylactic acid are its high-cost, low toughness and less glass transition temperature [1]. Thermoplastic biodegradable polymers are widely used in various applications today such as disposable products and biomedical materials. Nowadays, applications of biodegradable PLA have been broadened into food packaging, disposable plastic products and textiles. The poor mechanical properties of the PLA polymer in bulk form restrict its use as high-performance material [2]. The way to improve the mechanical and thermal properties of PLA is the addition of fiber or filler materials since PLA is a heat-sensitive material and its property has been improved with increase in the rate of nucleation [3]. For many applications, natural fibers have the ability to provide reinforcement properties at lower cost, lower density, higher strength and stiffness [4]. Talc is a magnesium silicate material and it has an ability to improve the rate of crystallization and also acts as a nucleating agent [5]. Melt compounding followed by injection moulding is preferred to prepare the composites (it is also one of the widely used methods to develop the polymer matrix composites) [6]. Short fibers are preferred when compared to the long fibers for melt compounding process, as the short fibers are uniformly distributed in the matrix material compared to long fibers [7]. In the past research work, very less effort has been made to study the effect of talc in hybrid composites. In previous work less percentage of talc is used as reinforcement (up to 5%). In this work, the effect of talc in hybrid composites is studied and talc is used up to 15%. Sisal fiber and talc reinforced PLA composites were prepared by melt compounding technique with sisal fiber and Talc as reinforcements and PLA as the matrix. The mechanical and thermal properties and morphology of the composites were studied.

## 63.2 Experimental Work

### 63.2.1 Materials

Polylactic acid (Ingeo biopolymer 3052D) in the pellet form with a specific gravity of  $1.24 \text{ g/cm}^3$ , Sisal fibers with density of  $1.5 \text{ g/cm}^3$  and average length of 3 cm and micro talc powder of 10 to 40 microns particle size are used to prepare the composites.

**Table 63.1** Composition of composites

Composite	PLA (%)	Sisal fiber (%)	Talc (%)
A	80	15	5
B	75	15	10
C	70	15	15

### 63.2.2 Fabrication of Composites

The chopped sisal fibers were washed with distilled water to remove dust and other impurities present over the surface of the fiber. The Chopped fibers were dipped into 5% concentrated NaOH Solution for 4 h. Then the fiber was washed thoroughly in the running water to remove the final traces of alkali content present in the fiber. Fibers were dried until the moisture content was completely removed.

Prior to processing, Polylactic Acid, Sisal fiber and Talc were dried at 50 °C in order to remove the moisture from the sample. A twin-screw extruder was used to fabricate the composites with PLA, Sisal fiber and Talc by melt compounding method. Blending was carried out at a temperature range of 170, 175 and 180 °C, screw speed was maintained at 150 rpm for all composites. Composite samples which were extruded from the mould were in the form of strands, which were further chopped into small pellets with the help of pelletizing unit. Test samples according to ASTM standard were prepared by using injection moulding technique. The compositions of the prepared composites are tabulated in Table 63.1.

### 63.2.3 Tensile Test

Tensile test was done according to ASTM-D638 standard. All these tests were conducted at ambient temperature and an average value of three repeated tests were taken for each composition.

### 63.2.4 Impact Test

The Izod impact strength of each sample was tested as per ASTM-D 256–88 standard. Specimens having a thickness of about 3.2 mm with 10 mm cross section and 64 mm long were clamped in the base of the pendulum testing machine so that they were cantilevered upward. The pendulum was released and the force consumed in breaking the sample was calculated. All the samples were tested as unnotched so that they would be more sensitive towards the transition between ductility and brittleness.

### 63.2.5 Water Absorption Test

Water absorption behaviour of the composites was determined by swelling the samples in distilled water at room temperature. The specimens were prepared according to ASTM-D 750 standard. The weights of the samples were taken before being subjected to water environments. During the first 10 h, the specimens were taken out from the moisture environment for every 2 h and before weighing the samples, moisture present in the sample was removed with a dry cloth and tissue paper. The specimens were reweighed to the nearest 0.001 mg within 1 min of removing them from the moisture environment. The specimens were weighed regularly till they attain equilibrium moisture content for 24 h once. The moisture absorption was calculated by the weight difference in the specimen. The percentage weight gain of the samples was measured at different time intervals by using the Eq. (63.1);

$$\%Mt = \frac{(Wt - Wo) \times 100}{Wo} \quad (63.1)$$

where 'W0' and 'Wt' denote the dry weight and weight after time 't', respectively. Equilibrium Moisture Content of the sample is the moisture content when the periodic change in the weight of the sample is less than 0.1% and thus the state of equilibrium is assumed to be reached. The thickness swelling (TS) was calculated by using Eq. (63.2);

$$TS(t) = \frac{(Ht - Ho) \times 100}{Ho} \quad (63.2)$$

where 'Ht' and 'H0' are the composite thickness after and before the water immersion, respectively.

### 63.2.6 Differential Scanning Calorimetry

The DSC was performed on a TA DSC-200 differential scanning calorimeter to study the thermal and crystallization behaviour of PLA composites. Measurements were performed under a continuous flow of nitrogen (60 ml/min). All samples (about 10 mg in weight) were heated from ambient to 400 °C and the thermograms were recorded at a heating rate of 20 °C/min. The crystallinity of PLA and composites was evaluated using Eq. (63.3).

$$X = \frac{\Delta H}{\Delta H^{\circ}m. \left(1 - \frac{\%wt \ filler}{100}\right)} \times 100 \quad (63.3)$$

**Table 63.2** Tensile properties of composites

Sample	Tensile strength (MPa)	Elongation at break (%)	Tensile modulus (MPa)
PLA	62	6.00	1033.33
Composite A	76.36	5.55	1385.34
Composite B	66.09	4.72	1398.13
Composite C	54.22	4.16	1303.18

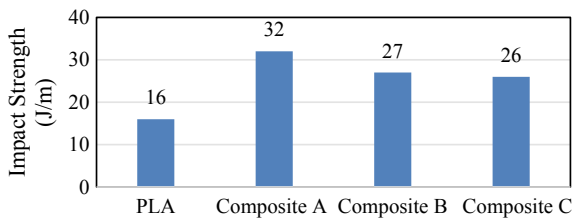
## 63.3 Results and Discussions

### 63.3.1 Tensile Properties of Composites

Three specimens were tested for each composition and the results are tabulated in Table 63.2. Thus increase in filler content initially increases the tensile strength and then it decreases the tensile strength. The general observation for any natural filler containing thermoplastic composites is decrease in the tensile strength. Low aspect ratio and its inability to transfer stress from matrix are the possible reasons for decrease in tensile strength with increase in filler content.

### 63.3.2 Impact Strength of Composites

Effect of talc on the impact strength of the PLA composites is shown in Fig. 63.1. The impact strength had been increased with increase in filler content, the increase in impact resistance was due to the presence of sisal fiber and nucleating effect of talc on the matrix material. Further increase in the concentration of filler material decreases the impact strength.

**Fig. 63.1** Impact strength of the composites



**Fig. 63.2** Immersion time versus weight gain

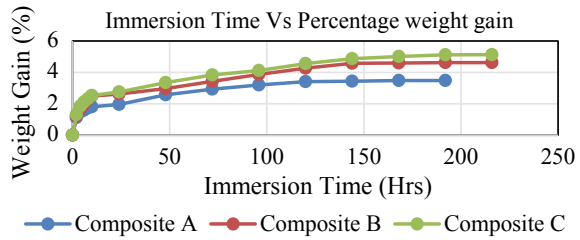
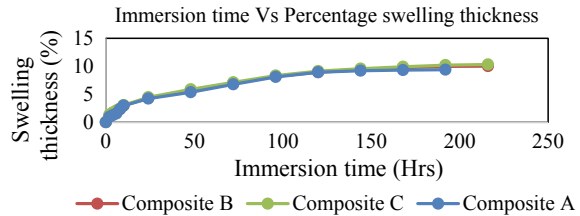


**Fig. 63.3** Immersion time versus swelling thickness



### 63.3.3 Water Absorption Behaviour of Composites

The moisture absorption of the composites increased with immersion time, and got saturated after a period of time. The time required to attain saturation varied across different composition. The saturation time was approximately 215 h. Figures 63.2 and 63.3, show the percentage of moisture absorption and the percentage of swelling thickness of the composites. From the observation, it is noted that the initial rate of moisture absorption is maximum for all different composition and moisture absorption increases with increase in filler content. Moisture absorption is maximum for composites made with 15% talc content. The factors like porosity content and fiber matrix adhesion play a vital role in the moisture absorption behaviour of natural fiber composites.

### 63.3.4 Crystallization Behaviour of Composites

The DSC was performed on a TA DSC-200 under a continuous flow of nitrogen (60 ml/min). All Samples (about 10 mg in weight) were heated from ambient to 400 °C and the thermograms were recorded at a heating rate of 20 °C/min. DSC thermograms of composites are shown in Fig. 63.4.

Influence of talc on the crystallization behaviour of composites is tabulated in Table 63.3. Presence of talc in the polymer matrix increases the rate of crystallization which is due to the nucleating effect of the talc which makes the crystallization to occur at a higher rate.

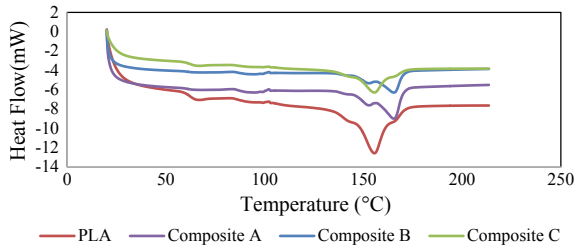


**Fig. 63.4** DSC thermogram of PLA composites

**Table 63.3** Thermal characteristics of PLA composites

Specimen	Glass transition temperature (°C)	Melting temperature (°C)	Crystallinity of composites (%)
PLA	59.89	143.6	0.93
Composite A	63.12	145.3	2.77
Composite B	62.97	145.2	5.08
Composite C	63.21	146.6	5.74

## 63.4 Conclusions

In this work, the major aim was to prepare and characterize cost-effective and biodegradable polylactic acid composites with sisal fiber and talc as reinforcements to fulfil new ecological needs in connection with environmental issues caused by the use of synthetic plastics.

Increase in talc content initially increases the tensile strength and impact strength up to 10%, further increase in filler percentage decreases the tensile strength of the material, a similar type of results has been obtained in the literature [8]. The decrease in tensile strength as the filler content increases is due to low aspect ratio of the composite. Low aspect ratio makes the material hard to transfer stress from matrix which makes the material brittle and correspondingly the tensile strength decreases.

Moisture absorption increases with the increase in filler content but there is no significant change in swelling thickness of the material. Factors like porosity and fiber matrix adhesion makes the material hydrophilic.

From the results of differential scanning calorimetry, it is clear that the crystallization rate has increased, which is due to the nucleation effect of talc which makes crystallization to occur at high rate (as PLA is a heat-sensitive material, higher nucleation rate makes the material to withstand its property in the polymer matrix but there is no significant change in the melting temperature of the material). A similar result has been found in the literature [2].

Proposed applications of PLA composites are associated with structures which have low-temperature operating conditions like automobile interior structures, since

PLA Composites have less glass transition temperature and good mechanical properties. This is a promising research field with numerous industrial applications [9] as the natural fibers are considered to be the alternatives to synthetic fibers [10].

## References

1. Murariu, M., Dubois, P.: PLA composites: from production to properties. *Adv. Drug Deliv. Rev.* **107**, 17–46 (2016)
2. Jain, S., Misra, M., Amar K.: Mechanical and rheological behaviour of poly(lactic acid)/Talc composites. *J. Polym. Environ.* **20**, 1027–1037 (2012)
3. Olivieri, R., Di Maio, L., Scarfato, P., Incarnato, L.: Preparation and characterization of biodegradable PLA/organosilylated clay nanocomposites. In: *AIP Conference Proceedings*, pp. 1736 (2016)
4. Awal, A., Rana, M., Sain, M.: Thermorheological and mechanical properties of cellulose reinforced PLA bio-composites. *Mech. Mater.* **80**, 87–95 (2015)
5. Sanchez-Olivares, G., Sanchez-Solis, A., Calderas, F., Alongi, J.: Keratin fibers derived from tannery industry wastes for flame retarded PLA composites. *Polym. Degrad. Stab.* **140**, 42–54 (2017)
6. Bulota, M., Budtova, T.: PLA/algae composites: morphology and mechanical properties. *Composites: Part A* **73**, 109–15 (2015)
7. Couture, A., Lebrun, G., Laperrière, L.: Mechanical properties of polylactic acid (PLA) composites reinforced with unidirectional flax and flax-paper layers. *Compos. Struct.* **154**, 286–295 (2016)
8. Chaitanya, S., Singh, I.: Processing of PLA/sisal fiber biocomposites using direct- and extrusion-injection moulding. *Mater. Manuf. Process.* **32**, 468–474(2017)
9. Rubio-Lopez, A., Artero-Guerrero, J., Pernas-Sánchez, J., Santiuste, C.: Compression after impact of flax/PLA biodegradable composites. *Polym. Test.* **59**, 127–135 (2017)
10. Ramesh, M., Palanikumar, K., Hemachandra Reddy, K.: Plant fiber based bio-composites: Sustainable and renewable green materials. *Renew. Sustain. Energy Rev.* **79**, 558–584 (2017)

# Chapter 64

## Assessment on Hole Quality During Drilling of Al/CFRP Stack



Tarakeswar Barik , Swगतिका Sarangi  and Kamal Pal 

**Abstract** Carbon fiber reinforced plastics (CFRP) along with metallic stacks highly used in avionics and other industries. However, assembling of such ancillaries needs holes for which primarily drilling is necessary. Drilling of such dissimilar material combinations having different mechanical properties results numerous defects. The reduction of such defects with acceptable hole quality needs a study on the effect of variations of the cutting parameters. This paper presents an experimental study on the interaction effect of different cutting parameters, like spindle speed and feed rate on delamination, circularity, and surface roughness, which was considered as hole quality characteristics. Aluminum alloy (7075) was used as the stacking metal with fabricated CFRP at fiber orientation of  $0^\circ/90^\circ$  and  $45^\circ/-45^\circ$ . Drilling is carried out using Tungsten–Carbide Twist Drill of point angle  $1100^\circ$ ,  $1180^\circ$ , and  $1250^\circ$ . Drilling defects were found to be minimum for the least point angle, higher spindle speed, and lower feed rate.

**Keywords** Drilling · Al/CFRP stack · Delamination · Circularity · Surface roughness

### 64.1 Introduction

Fibrous composite like Carbon fiber reinforced plastic (CFRP) has many advantageous applications in aerospace, automobile, defense, and sports goods industries, due to its various outstanding properties like very high strength to weight ratio high stiffness to weight ratio as well as resistance to corrosion. Also, dissimilar metallic CFRP stack-ups like Al/CFRP, Al/CFRP/Ti are used in wings and tail of plane structures. These types of structures need holes for assembly assimilation. Drilling becomes a complex machining process due to the change in cutting parameters that varies along the cutting edge. The diametric tolerance lower than or equal to  $30\ \mu\text{m}$  is mandatory for most of the recent applications [1]. There are a lot of problems

---

T. Barik · S. Sarangi · K. Pal (✉)  
Department of Production Engineering, VSSUT, Burla 768018, India  
e-mail: [kpals5676@gmail.com](mailto:kpals5676@gmail.com)

© Springer Nature Singapore Pte Ltd. 2020  
M. S. Shunmugam and M. Kanthababu (eds.), *Advances in Unconventional Machining and Composites*, Lecture Notes on Multidisciplinary Industrial Engineering, [https://doi.org/10.1007/978-981-32-9471-4\\_64](https://doi.org/10.1007/978-981-32-9471-4_64)

to maintain uniform machined surface during drilling such stack-ups of dissimilar material. The previous experimental investigation concluded that the parametric factors such as spindle speed of the drill and machining feed rate play a major role in the drilling of these metallic stacks. These parametric effects can also be studied by the monitoring parameters like thrust force and torque [2, 3].

At higher temperature which is generally generated due to the friction between the drill and the CFRP decreases the epoxy cutting resistance which eventually reduces the thrust force. Whereas, when drilling of aluminum plates takes place, if there is an increase in spindle speed it will lead to higher thrust force. The major problem faced while drilling aluminum is build up edge formation at the drill principle edge and chisel edge, and this can be decreased by increasing the spindle speed [4]. It was also established that regardless of drill diameter, there is a very negligible effect of spindle speed on surface roughness and chip breakability [5]. With the increase in temperature at elevated cutting speed which leads to the diffusion of aluminum, and it sticks to the cutting edge of the tool. During drilling as the temperature of the flank surface increases, there is a possibility of edge breaking which leads to the wear on that flank surface. As the flank surface got wearied, the thrust force got a rise, and eventually, the delamination factor, i.e., indication of drilled hole accuracy also increases. Thus, it may be concluded that with the increase in cutting velocity, composite damage also increases [4].

Similarly, machining feed rate has a major role in the drilling of these Al/CFRP stacks. When lower feed rate is employed to drill CFRP/Al stack, there is an increase in torque and thrust force during drilling aluminum as compared to fibrous composite. On the other hand, thrust force is one-third at higher feed rates of 0.1 and 0.15 mm/rev. Nevertheless, with the increase in feed rate; there is an increase in circularity error as well surface roughness [5, 6]. There is a rise in the delamination factor at higher feed rate. The area of delamination decreases with a reduction in feed rate, and there will be a sudden rise in delamination when the feed rate reaches a critical value [3, 7].

While drilling the metallic and fibrous composite stack, the drill tool geometry also has an important role to play. It greatly influences the surface integrity of the hole drilled. Tool geometry with a higher point angle leads to higher torque (the tangential force), as it is eventually the orthogonal rake angle of the tool. Therefore, to reduce the thrust force during drilling of Al/CFRP composite, the point angle should be kept smaller [2]. Similarly, when aluminum alloy (AA2024) is drilled due to high temperature and pressure at the contact zone resulted in diffusion, so some material gets moved from the workpiece and deposited on the tool rake face. It may be reduced by choosing optimal tool geometry [4]. While drilling CFRP/Al stack, with the rise in drill diameter there is a rise in thrust force and torque. This is due to an increase in cross-sectional area of the chip as well as larger chisel edge length at a larger diameter. Drill diameter also held responsible for the chip breakability which is nothing but the result of the cross-sectional area of chip [5].

Likewise, while drilling CFRPs with different Carbide drills from his experimental illustrations, the author [7] confirmed the effect of selecting tool geometry and operating condition on drilling induced damages. From his exploration he recommends

smaller drill diameter, lower point angle [8] and lower feed rate for delamination free holes. Where [9, 10] clarifies, with smaller point angle the thrust force found to be reduced and that is the reason behind the lesser hole damage. Different types of drill tool were used for the drilling of composites like twist drill, step drill, cone drills, step core drills, candlestick drill, PCD drill, spur drill, etc. The effect of cutting force and cutting velocity changes with the change in tool material but it remains unchanged for the same tool material [2]. The carbide drill is found to be the best option for drilling CFRP than that of HSS drill which produces less delamination. The flank wear is found to be negligible using carbide drill than HSS drill where drill wear value equals to one-fourth the drill diameter [2, 8]. Coatings prevent tool wear and result in better hole quality. The tool wears reduced significantly using tool coatings of TiB<sub>2</sub> or diamond [1].

Though various works on drilling of aluminum alloy and CFRP composite or its stack, there is hardly any work of drilled surface quality assessment analysis influenced by drilling parameters, especially in case of quasi-isotropic CFRP at fiber orientation of 0°/90° and 45°/-45°. The present work mainly addresses the drill parametric interaction effect in detail on the drilled hole surface integrity characterized by circularity error, delamination as well as surface roughness. The drilling experiments have been carried out with the full-factorial design of experiments, considering one geometrical parameter, i.e., point angle along with above stated cutting speed and feed rate during drilling.

## 64.2 Experimental Procedure

### 64.2.1 Machine, Workpiece, and Cutting Tool Details

The drilling of Al/CFRP stack was carried out on MTAB three-axis milling center (Fig. 64.1) with three rotational spindle speed (1650 rpm, 2250 rpm, and 2850 rpm) and three longitudinal feed rates (0.05, 0.1, and 0.15 mm/rev). The specimen is composed of aluminum (7075) and CFRP prepared by hand lay-up technique having fiber orientation in the manner of 0°/90° and 45°/-45° (quasi-isotropic) and the fiber volume fraction was 50% [11]. To prepare Al/CFRP stack, first the aluminum and CFRP laminates were cut into similar dimension (25 × 10 mm) using electrical gauge cutter. The adhesive was prepared using epoxy LY-556 (bisphenol-A-diglycidyl-ether) and hardener HY-951 (Aliphatic amine) in the ratio of 10:1. This adhesive used to attach the aluminum and CFRP such that CFRP kept as the bottom-layer CFRP and aluminum as the top layer. Mechanical fastening was done to avoid the displacement of the stack while machining. Here, dry cutting conditions were used for the machining of the specimen using tungsten carbide twist drill of diameter 10 mm and point angle of 110°, 118°, and 125°. The effect of cutting parameter on the hole quality during drilled of Al/CFRP stack was investigated separately using three drills with different point angles (110°, 118°, and 125°). For experimentation, the

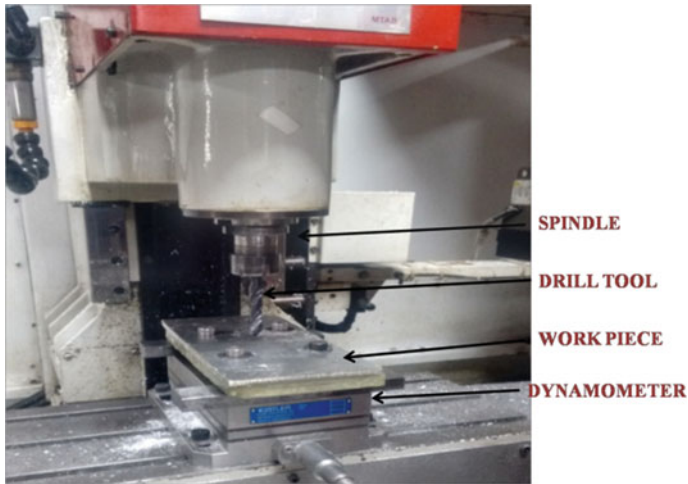


**Fig. 64.1** Experimental setup (MTAB 3 axis milling)

**Table 64.1** Machining parameters with levels

Factors	Parameters	Level 1	Level 2	Level 3
A	Point angle (°)	110	118	125
B	Spindle speed (rpm)	1650	2250	2850
C	Feed rate (mm/rev)	0.05	0.1	0.15

design of experiments has been considered using the full-factorial method in which the effect of the interaction of the factors has been studied in three-factor three-level experiments, i.e., a total of 27 drilling experiments was carried out. The process variable and its limits are presented in Table 64.1. The experimental sequences with subsequent results are summarized in Table 64.2.

## 64.2.2 Parameters for Performance Evaluation

### 64.2.2.1 Thrust Force and Torque Measurement

The significant monitoring parameters thrust force and torques during drilling have been acquired using digital drilling tool dynamometer attached with a data acquisition system. The signal-related data was stored in the computer for further analyze.

**Table 64.2** Experimental parametric design

	Point angle (°)	Spindle speed (rpm)	Feed rate (mm/rev)
1	110	1650	0.05
2	110	1650	0.1
3	110	1650	0.15
4	110	2250	0.05
5	110	2250	0.1
6	110	2250	0.15
7	110	2850	0.05
8	110	2850	0.1
9	110	2850	0.15
10	118	1650	0.05
11	118	1650	0.1
12	118	1650	0.15
13	118	2250	0.05
14	118	2250	0.1
15	118	2250	0.15
16	118	2850	0.05
17	118	2850	0.1
18	118	2850	0.15
19	125	1650	0.05
20	125	1650	0.1
21	125	1650	0.15
22	125	2250	0.05
23	125	2250	0.1
24	125	2250	0.15
25	125	2850	0.05
26	125	2850	0.1
27	125	2850	0.15

#### 64.2.2.2 Circularity Measurement

The circularity error of the drilled holes was calculated with CMM machine (SPECTRA ACCURA). In this process, first the workpiece was placed on the table of the machine which is procured with a ruby probe of 2 mm diameter. It circulates all over the hole internal wall continuously at a speed of 1 mm/s to capture the points. In order to have high accuracy results, the measurements were performed at six locations. The value of circularity obtained directly from CMM.



### 64.2.2.3 Surface Roughness Measurement

Surftest SJ-210- Series 178 is the portable surface roughness tester using a portable stylus-type profilometer has been used for surface roughness measurement. The roughness Ra was plotted by having the average value of roughness at six different locations of the machined component.

### 64.2.2.4 Measurement of Delamination

In this present work, the delamination factor of the hole was calculated by an image processing technique using IMAGE J software, in which image analysis procedure was carried out to extract the diameter from the images of the drilled holes. This process comprises various steps; first, the RGB (red, green, and blue) image shown in Fig. 64.1a was converted to the HSV (hue, saturation, and value) and in the second level, the saturation level was only found to be useful. To convert the second level (saturation. 0.3) to binary black and white (BW) picture, a mask was applied. This procedure was done to identify the drilled hole borders, as this task can be easily performed on BW pictures. After this, a smoothing process was carried out on this image to eliminate the uncut fibers. The diameter measurement was carried out using Fig. 64.2b. Hereafter, the border of the hole was located and that separates the black and white area in the given picture. Laterally, the border also recognized as the boundary pixels; then mean squared algorithm method was used to calculate the circumference that best fits the identified boundary pixels and hole diameter was obtained.

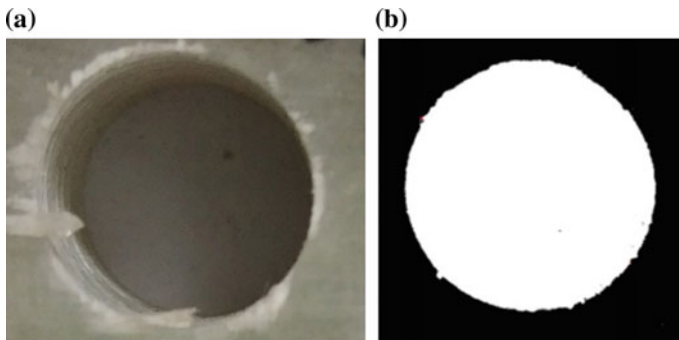


**Fig. 64.2** a RGB image b Black and white image

### 64.3 Result and Discussions

In the present research work, the interaction effects of two machining parameters, feed rate, and spindle speed at three different point angles have been studied on the drilled hole quality of Al/CFRP stack in detail.

#### 64.3.1 Delamination

##### 64.3.1.1 Effect of Spindle Speed

From Fig. 64.3a, b, and c, it was observed that if the feed rate kept constant and the spindle speed is increased, the delamination in hole decreases. The reason possibly due to preferential removal of workpiece takes place at high spindle speeds; nevertheless, it produces smoother surface; whereas, on the other hand, if the spindle speed is kept low due, the surface got rougher producing more delamination. It is because of the slow penetration of the tool in the workpiece [12].

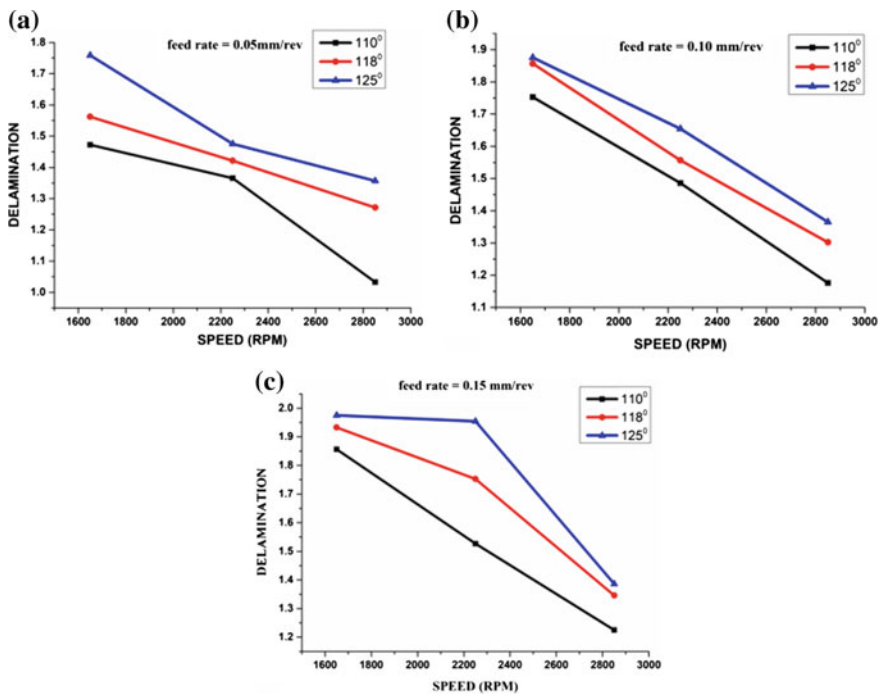


Fig. 64.3 Variation of delamination with speed at feed rate a 0.05 mm/rev b 0.10 mm/rev c 0.15 mm/rev

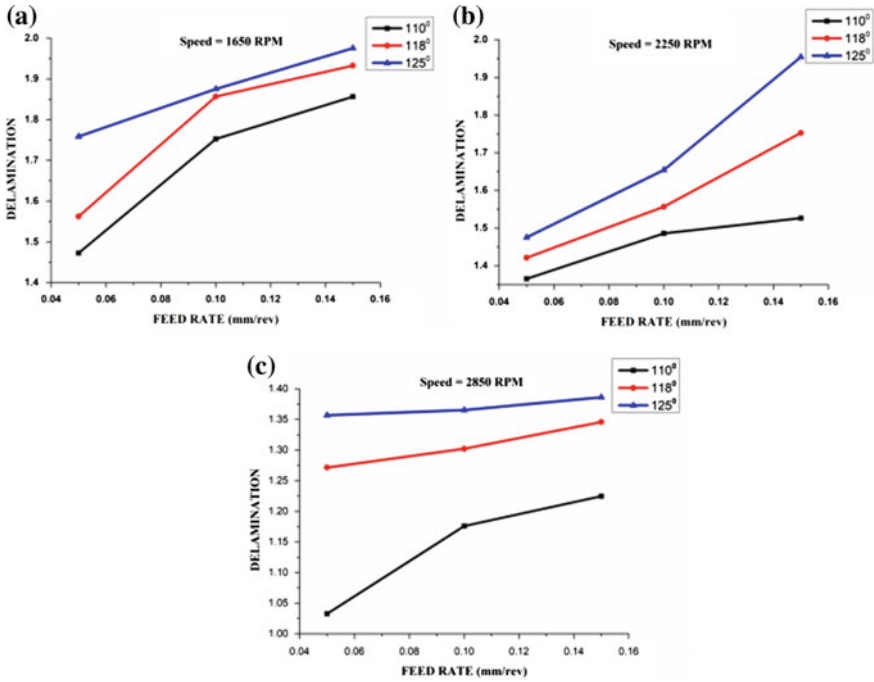


Fig. 64.4 Variation of delamination with feed rate at spindle speed a 1650 b 2250 c 2850

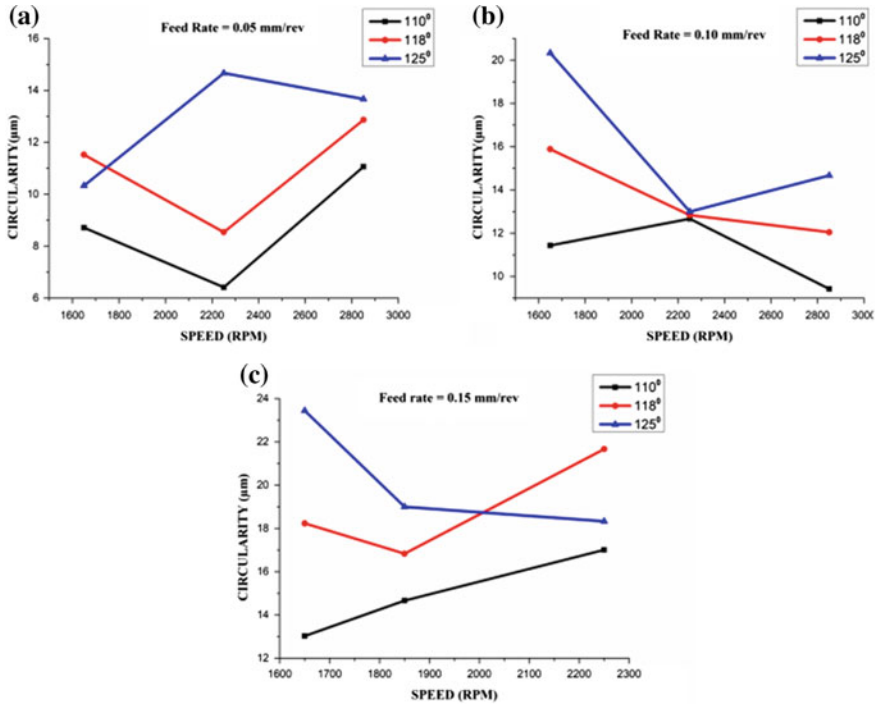
### 64.3.1.2 Effect of Feed Rate

Figure 64.4a, b, and c suggests that if there is an increase in feed rate, the delamination factor produced in the hole will reduced. It can be understood as the feed rate increases which in turn increase the thrust force as well the temperature, which results in softening of the matrix. Therefore, it reduces the delamination.

## 64.3.2 Circularity

### 64.3.2.1 Effect of Spindle Speed

During drilling at higher spindle speed, the drill tool’s rotational stability is found to be more in comparison to that of lower speed. It can be because of plowing and frictional heating. Proving the above statement right Fig. 64.5a, b, and c suggests that there is a decrease in the circularity error with increase in the spindle speed.



**Fig. 64.5** Variation of circularity with spindle speed at feed rate **a** 0.05 mm/rev **b** 0.10 mm/rev **c** 0.15 mm/rev

**64.3.2.2 Effect of Feed Rate**

At low feed rates, the circularity error of hole in the CFRP region was found to be minimal around 6–8 µm, which increased up to a maximum of 23 µm, when the feed was increased from 0.05 mm/rev to 0.15 mm/rev. It can be shown from the graph (Fig. 64.6). From this diametric analysis of the hole in the CFRP part, it was found that there is an easing of elastic stresses during machining as because there is a difference in elastics stresses between epoxy and carbon fiber which results in 10–20% diametric tolerance. As the hole diameter decreases, there is a rise in friction between drill and the surface of the hole in case of drilling aluminum.

Similarly, From Figs. 64.5 and 64.6, it was seen that out of the three drill bits used in the operation, the circularity error was found to be lowest in drill tool with least point angle, i.e., 110°. It can be explained as with the increase in point angle, there is an increase in thrust force. Which in turn increases the circularity error. Therefore, it can be concluded that in order to reduce the circularity error higher spindle speed, lower feed rate, and small point angle should be taken as machining parameters while performing drilling operation [13, 14].

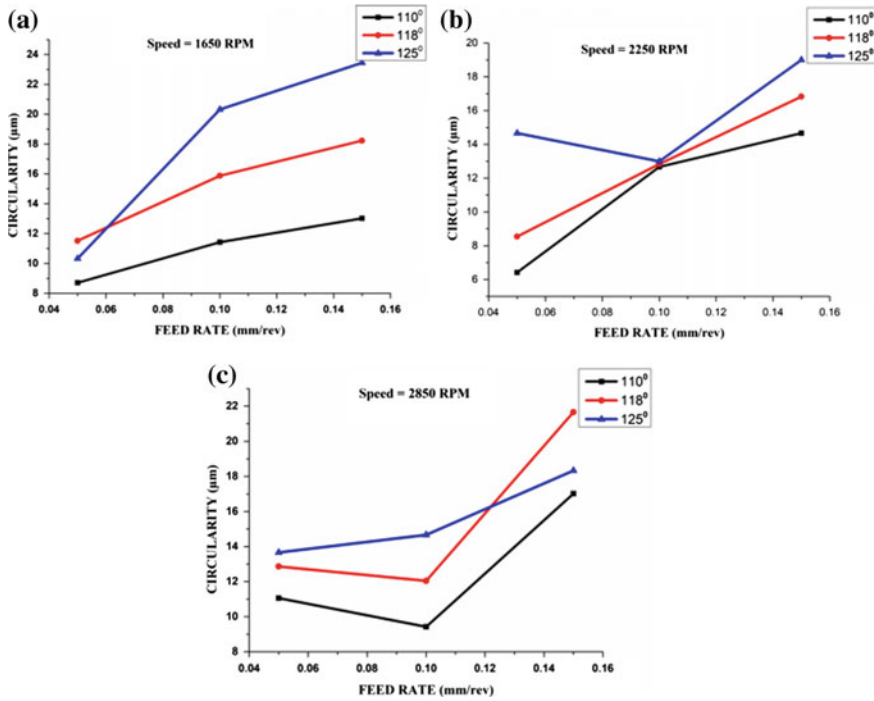


Fig. 64.6 Variation of circularity with feed rate at spindle speed a 1650 b 2250 c 2850

### 64.3.3 Surface Roughness

#### 64.3.3.1 Effect of Spindle Speed

The variation of the surface roughness value is found to be nonuniform with the variation of drilling parameters. It can be understood as; the nonhomogeneous structural composition of the composites shows a nonuniform surface throughout the hole from the entrance to exit. Figure demonstrates the surface roughness ( $R_a$ ) against feed rate as well as surface roughness against spindle speed for the three geometrically distinctive drill tools. The outcomes were further used in details study. Intended for CFRP, the surface roughness values found out to be of about 3–4 µm at low feed rates of,  $f = 0.05$  mm/rev, which increased up to 6–7 µm against constant speed (Fig. 64.7).

#### 64.3.3.2 Effect of Feed Rate

Although the surface roughness increases with increase in point angle of the tool, the feed rate remains constant and with an increase in spindle speed. However, the effect of the spindle speed on surface roughness was found to be negligible.

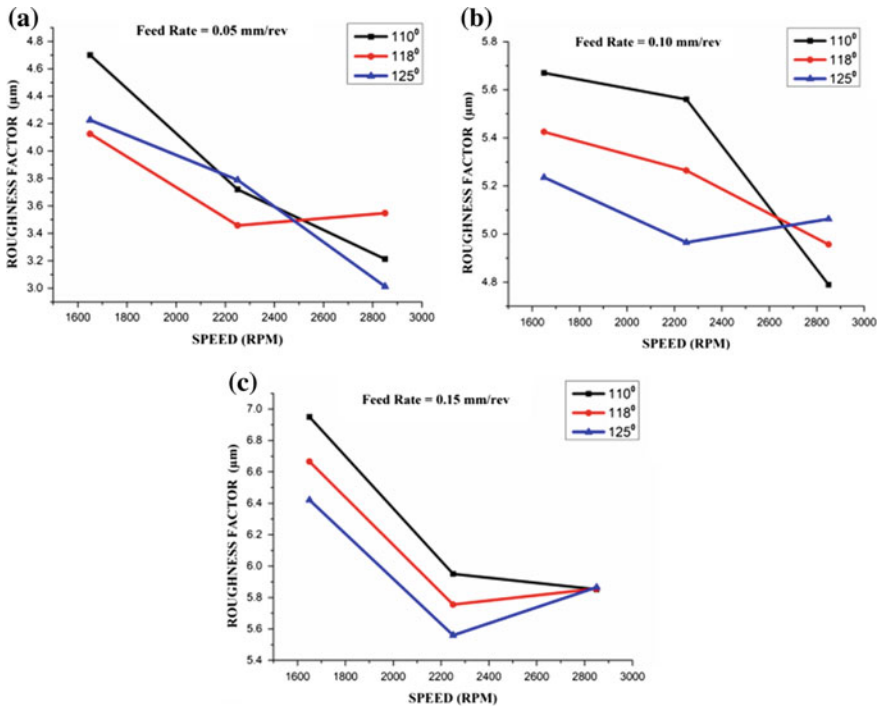


**Fig. 64.7** Variation of surface roughness with spindle speed at feed rate **a** 0.05 mm/rev **b** 0.10 mm/rev **c** 0.15 mm/rev

In this experimental study, it was found that there was less surface roughness in aluminum compared to CFRP. It was primarily due to the isotropic nature of the material. However, the hole surface finish of CFRP fibrous wall may be deteriorate during passing of hot machined aluminum particles through drill flutes just after drilling. The outcomes of the experimentation also suggest that there is less effect of machining parameters on aluminum in compare to CFRP (Fig. 64.8).

From the Figs. 64.5a–c and 64.8a–c, it can be observed that there is a decrease in drill induced damages such as delamination, roughness as well as circularity in the form of delamination, for the smaller point angle tool (i.e. 110°). The possible reason here can be established that in smaller point angle tool the thrust force is found to be less in compare to the tool with higher point angle (i.e. 118°, 125°) [12–16]. The drilled hole top views for the Expt #7 and the Expt #21 hole as an indication of defect-free and defected hole, respectively, are shown in Fig. 64.9a, b. There was metal burr as well as fiber pullout that have been noticed for the defected hole in 21st hole, whereas it was absent in 7th hole as shown.

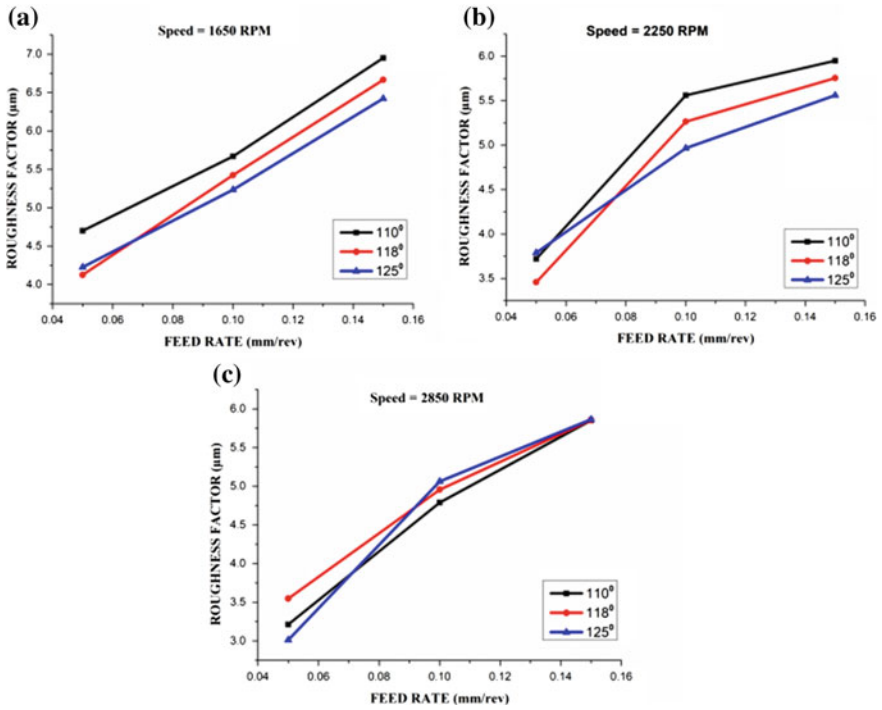


Fig. 64.8 Variation of surface roughness with feed rate at spindle speed a 1650 b 2250 c 2850 rpm

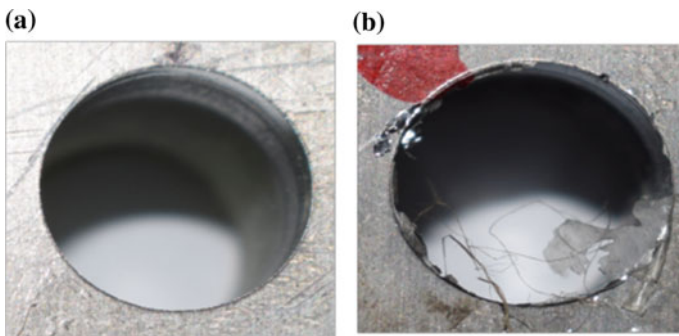


Fig. 64.9 Drilled hole top view Expt #7 and the Expt #21

## 64.4 Conclusion

The present work on drilled hole assessment, some of the remarks regarding the work are concluded below.

The hole quality is found to be best at higher spindle speed and lower feed rate at lower point angle. According to the experimental result, the hole condition of the seventh hole was found to be best which is obtained at the spindle speed of 2850 rpm and feed rate 0.05 mm/rev at point angle 110°. The worst hole quality was observed for the 21st hole with machining condition 1650 rpm spindle speed and 0.15 mm/rev feed rate at 125° point angle. It is also studied that the drilling of aluminum side was better at lower spindle speed because, at higher spindle speed, the temperature generated results into the formation of adhering on the cutting edge of the tool which creates a problem in drilling CFRP which resulted in poor hole quality. But for drilling CFRP, higher spindle speed found to be better, because as CFRP composites were known for their higher strength, so with higher spindle speed the material removal becomes easier. However, there was no such discrimination in the range of feed rate and point angle for CFRP and aluminum.

**Acknowledgements** The authors wish to acknowledge the assistance and support provided by the Metal Cutting Laboratory, Mechanical Engineering Department, IIT Patna.

## References

1. Brinksmeierl (I), E., Janssen, R.: Drilling of Multi-Layer Composite Materials Consisting of Carbon Fiber Reinforced Plastics (CFRP). Titanium and Aluminum Alloys
2. Wen-Chou, C.H.E.N.: Some experimental investigations in the drilling of carbon fiber-reinforced plastic (CFRP) composite laminates. *Int. J. Mach. Tools Mmufacet.* **37**(8), 1097–1108 (1997)
3. Davim, J.P., Reis, P.: study of delamination in drilling carbon fiber reinforced plastics (CFRP) using design experiment. *Compos. Struct.* **59**(4), 481–487 (2003)
4. Nouari, M.: Effect of machining parameters and coating on wear mechanisms in dry drilling of aluminium alloys. *Int. J. Mach. Tools Manuf.* **45**, 1436–1442 (2005)
5. Zitoune, R.: Study of drilling of composite material and aluminium stack. *Compos. Struct.* **92**, 1246–1255 (2010)
6. Shyha, I.: Drilling of carbon fibre reinforced plastic composites. School of Manufacturing and Mechanical Engineering, Ph.D. (2010)
7. Shyha, I.: Hole quality assessment following drilling of metallic-composite stacks. *Int. J. Mach. Tools Manuf.* **51**, 569–578 (2011)
8. Shunmugesh, K., Panneerselvam, K.: Machinability study of carbon fiber reinforced polymer in the longitudinal and transverse direction and optimization of process parameters using PSO-GSA. *Eng. Sci. Technol. Int. J.* **19**(3), 1552–1563 (2016)
9. Krishnaraj, V., Prabukarthi, A., Ramanathan, A., Elanghovan, N., Kumar, M.S., Zitoune, R., Davim, J.P.: Optimization of machining parameters at high speed drilling of carbon fiber reinforced plastic (CFRP) laminates. *Compos. B Eng.* **43**(4), 1791–1799 (2012)
10. Poutorda, Antoine: Local approach of wear in drilling Ti6Al4 V/CFRP for stack modelling. *Procedia CIRP* **8**, 316–321 (2013)



11. Nayak, N.V.: Composite materials in Aerospace applications. *Int. J. Sci. Res. Publ.* **4**(9) (2014). [www.ijsrp.org](http://www.ijsrp.org). ISSN 2250-3153
12. Herbert, M.A., Shetty, D., Vijay, G.S., Shetty, R.: Evaluation of drilling induced delamination of carbon fiber reinforced polymer composite using solid carbide drills. *Eur. Sci. J.* **10**(15), 279–292 (2014)
13. Samuel Raj, D., Karunamoorthy, L.: Study of the effect of tool wear on hole quality in drilling CFRP to select a suitable drill for multi-criteria hole quality. *Mater. Manuf. Process.* 1532–2475 (2015). ISSN: 1042-6914 (Print)
14. Raj, D.S., Karunamoorthy, L.: Study of the effect of tool wear on hole quality in drilling cfrp to select a suitable drill for multi-criteria hole quality. *Mater. Manuf. Process.* **31**(5), 587–592 (2016)
15. Amir, A.N., Ye, L., Chang, L.: Drilling conditions on hole quality for CFRP laminates. In: American Society for Composites Thirty-First Technical Conference (2016)
16. Zitoune, R., Krishnaraj, V., Collombet, F., Le Roux, S.: Experimental and numerical analysis on drilling of carbon fibre reinforced plastic and aluminium stacks. *Compos. Struct.* **146**, 148–158 (2016)

# Chapter 65

## Experimental and Analytical Outcomes of Carbon Fiber Orientation in Epoxy Resin Composite Laminate Under Tensile Loading



A. Rajesh, S. Deva Prasad , B. Singaravel , T. Niranjana and T. Shravan Kumar

**Abstract** A composite material is obtained by combining two or more different materials to achieve a superior quality of characteristics than its constituents. Composite materials are widely accepted and are in use across different engineering applications, viz., aerospace, marine, defense, and automobiles. Fiber-reinforced materials are widely used in engineering industries because of their superior performance and tailor-made properties. The carbon fiber orientation plays a significant role in the mechanical properties of the obtained composite, particularly in tensile properties. In this paper, the orientation of carbon fiber in the composite (prepared using epoxy resin) is investigated under tensile loading. The analysis reveals that the experimental studies characterize the type of failure occurs under tensile loading, which is directly influenced by fiber orientation in a composite laminate.

**Keywords** Composite laminate · Carbon fiber orientation · Tensile loading · Failure types

### 65.1 Introduction

Composites having two or more reinforced/bonded materials, which can be artificially made to acquire desired properties as designer wishes for his component/structure, without going into any chemical reaction. Laminate composite, a fiber-reinforced composite, comes under the classification based on reinforcing material structure while producing composite. Laminate represents stack of lamina, may be flat or curved/oriented for achieving targeted property/characteristic in the composite that is fabricated. Individual laminas of the composite are bonded by a curing

---

A. Rajesh  
Advanced Systems Laboratory, Hyderabad, India

S. Deva Prasad (✉) · B. Singaravel · T. Niranjana · T. Shravan Kumar  
Department of Mechanical Engineering, Vignana Institute of Technology and Science,  
Hyderabad, India  
e-mail: [devaprasad@vignanits.ac.in](mailto:devaprasad@vignanits.ac.in); [sdevaprasad@gmail.com](mailto:sdevaprasad@gmail.com)

© Springer Nature Singapore Pte Ltd. 2020  
M. S. Shunmugam and M. Kanthababu (eds.), *Advances in Unconventional Machining and Composites*, Lecture Notes on Multidisciplinary Industrial Engineering, [https://doi.org/10.1007/978-981-32-9471-4\\_65](https://doi.org/10.1007/978-981-32-9471-4_65)

mechanism based on the laminar preferred in preparing the composite. Multilayer (angle-ply) composite represents several layers of material structure with different fiber orientations in the laminate composite, making it to respond (mechanical response) differently from that of the individual lamina that is used in preparation of laminate composite. The laminate characteristic is directly influenced by the properties of each lamina and the stacking order of laminas [1].

Designer materials, with specific properties, are in requirement due to the emergence of technologies and ever-expanding product/component in the world of manufacturing. The conventional materials are failing in these special properties/requirements such as high in strength and low in density (low packing factor) to meet the needs of aircraft parts. The research and development behind the development of composite materials is to produce a component material, that weighs lesser than their competitors such as a pure material, an alloy, and any other that provides the desired strength and stiffness. The glass fiber-reinforced plastic (GFRP) components will weigh only one-fourth of steel component if a component is to be manufactured for addressing a load-bearing capacity. The imperfections happened during preparation of the composite or inherent flaws, as a crack that lies perpendicular to the applied load direction weakens the material, may lead to discrepancy in strength values, i.e., deviation from measured value to theoretical value of most materials that formed as a composite laminate. The orientation of the molecular structure is responsible for higher strength and stiffness values in polymeric materials.

Fibers, having smaller in cross-section dimensions, are omitted to use in directly various applications thus embedded in matrix materials to form fibrous composites. Properties of some common types of reinforcements such as fibers and nano additions as well as some conventional materials are important in achieving higher mechanical properties [2].

Graphite fibers (more than 99% Carbon) or carbon fibers (Carbon in the range 80–95%) are predominant high-strength, high-modulus reinforcement used in the fabrication of high-performance polymer-matrix composites. Carbon fibers, with superior mechanical properties and high-temperature tolerance, an important structural and functional material, have an irreplaceable role as reinforcement in producing lightweight structures. Carbon fiber reinforced using epoxy resin composites, used as a structural material in applications such as construction, automotive, aerospace, and sports industries, have outstanding properties (high specific strength and stiffness, high corrosion, and fatigue resistance) as well as easy to handle and fabricate.

## **65.2 Fabrication of Laminate Composite and Specimen Preparation**

The filament winding manufacturing (FWM-Computer Numerical Controlled with one spool and temperature can go up to 200 °C) hand lay-up method is used to prepare composite laminate, followed curing and finally cutting is completed using diamond

wheel composite cutting machine. Different test specimens, laminate composite, for tensile test are made as per ASTM D3039. The materials (Carbon fiber, Epoxy Resin, Epoxy 5200 Hardener) used for preparation of laminates are procured. Fabrication of composite laminate and specimen preparation is as follows.

**Preparation of mold**, involve cleaning the mold using emery paper (Fine Grain Size) to remove spots and using acetone to remove any dirt followed by applying wax thoroughly on all parts of the mold including spacers (shown in Fig. 65.1), nuts, bolts, and threading, for easy release of laminate from mold. Thickness of spacer used is 14.8 mm, so that the gap is maintained for tensile specimen standard.

**Filament winding machine** is used for making the laminate. The process in brief involves following stages:

- First, the carbon fiber rove one wound by an FWM through a rectangular mold.
- Epoxy Resin (heated up to 50 °C to reduce its viscosity) and hardener are mixed in the ratio 100:27 (weight ratio), and the mixture is poured into the hot bath of FWM such that the carbon roving should pass through the mixture.
- Using computer numerical code to the machine, the roving gets wined to the mold, after completion of the winding the excess resin is squeezed using the squeezer.
- The mold is removed from the spindle and fix the top and bottom plates to it using nuts and bolts, a torque of 4 N-m is applied for the uniform load as well as the closure of the mold.



**Fig. 65.1** Mold and spacers

Mold (**Curing Process**), with the prepared laminate composite, is subjected to curing cycle for 7 h in a closed oven (Heat equipments make having size  $-1\text{ m} \times 1\text{ m}$ , Maximum temperature  $-220\text{ }^\circ\text{C}$ , Material  $-V9$  fabric with Thermocouple  $-J$  type), which is shown in Fig. 65.2. During curing cycle, shown in Fig. 65.3, in an oven by raising the temperature to  $120\text{ }^\circ\text{C}$  over a period of 30 min (hold for 3 h), then



Fig. 65.2 Oven used for curing

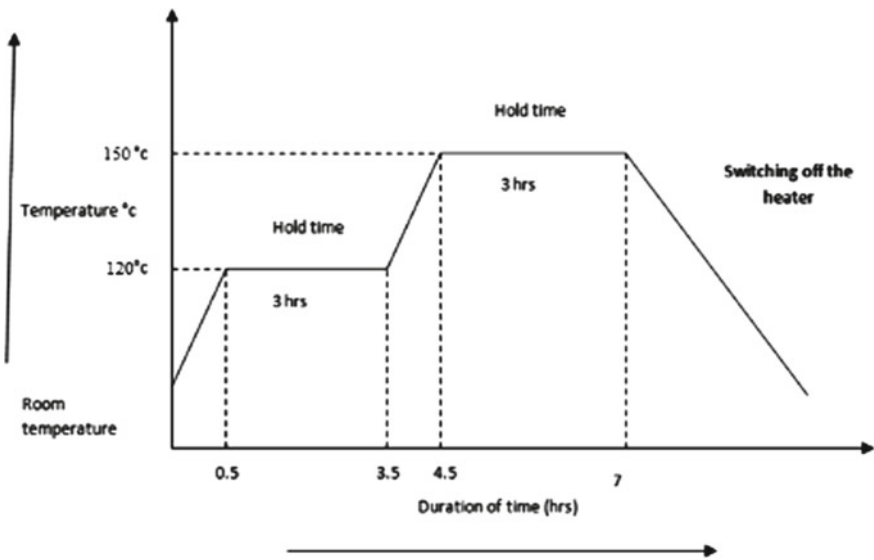


Fig. 65.3 Curing cycle graph

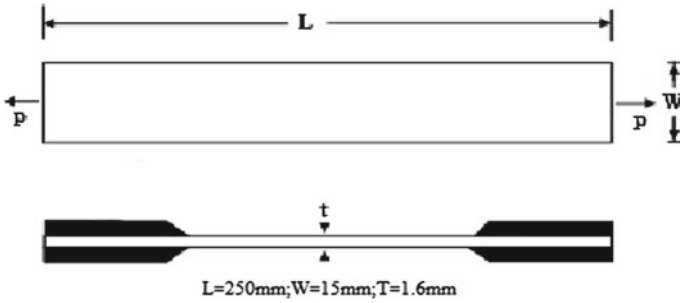
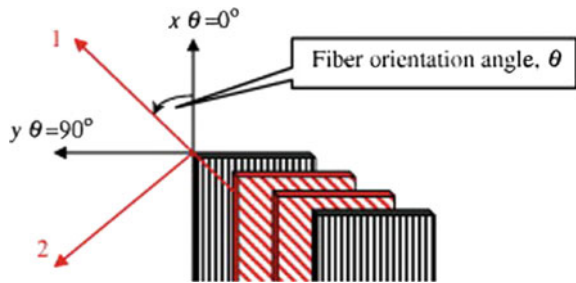


Fig. 65.4 Specifications of composite tensile test specimen (ASTM D3039)

Fig. 65.5 Fiber orientation angle [3]



increase the temperature to 150 °C and hold the same for 3 h. The mold allowed to reach normal temperature naturally after completing switch off the heaters. The mold has taken out from oven and trim the sides of the laminate to separate the top and bottom laminates. Remove the top mold by unscrewing the nuts carefully such that laminate should not be disturbed.

**Test specimens**, as per ASTM D3039 for the tensile test, are shown in Fig. 65.4—a constant rectangular cross section, of size 15 mm wide × 1.6 mm thickness, is cut from the laminate (250 mm × 250 mm cut using laminate cutting machine after removing from mold). Optional tabs to the ends of the specimen are bonded that prevents damage due to gripping. The specimens are prepared for fiber orientations, refer Fig. 65.5, having 0°, 2°, 4°, 6°, 8°, 10° to the x-axis.

### 65.3 Experiments and Modeling

ASTM D3039 defines the crosshead speed, typical value for a standard test is 3.5 mm/min, based on the material specification or time to failure (1 to 10 min). The specimens, composite laminate, prepared and tested on Universal Test Machine (UTM – 100 kN) at a specified grip separation, and tensile load are applied until

failure. An extensometer or strain gauge is used to determine elongation and tensile modulus. Depending upon the reinforcement and type, testing in more than one orientation may be necessary [4].

### 65.3.1 Experimental Outcomes from Tensile Loading Experiments

The experiments to study the characteristics of the composite under tensile loading are considered in this work. Three specimens under each orientation of fiber are tested to understand the behavior of fiber orientation in component thereby normalizing any bias to a small extent. Tensile load test, shown in Fig. 65.6 (test sample 1 with fiber orientation 0°) and in Fig. 65.7 (test sample 1 with fiber orientation 10°), the load variation during the tensile test, and extension of test sample 1 before failure are collected and represented. The plotted graphs give the information about maximum load and maximum displacement of the test specimen for the composite before its failure. The investigation results are studied, from the data collected, and the failure or load-bearing capacity of composite is lower as the fiber orientation is increased.

The experiments present clear indication, as fiber has large orientation, that the composite specimen elongation is lower, i.e., the component is failing with short elongation at lower load-bearing capacity. The experiments reveal that the broken specimen has shown three different types of fiber fracture, namely, broom (shown in Fig. 65.8), explosion and splitting (shown in Fig. 65.9). The outcomes from these experiments of composite test specimens having fiber orientations, viz., 0°, 2°, 4°, 6°, 8°, and 10° are tabulated in Table 65.1.

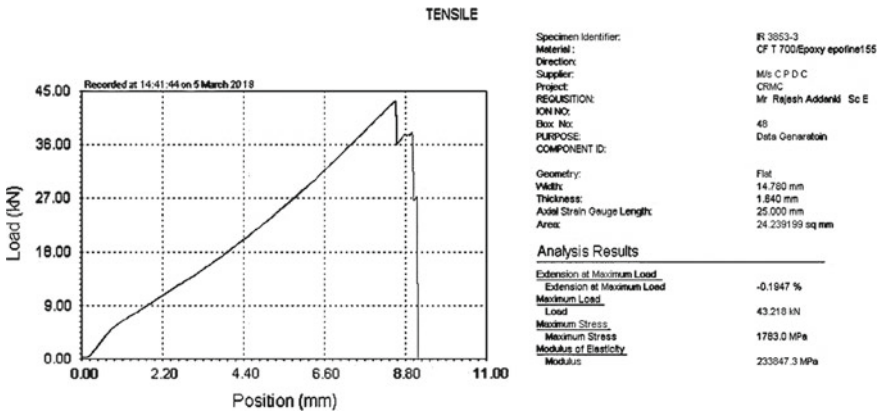


Fig. 65.6 Tensile load and extension diagram for test sample 1

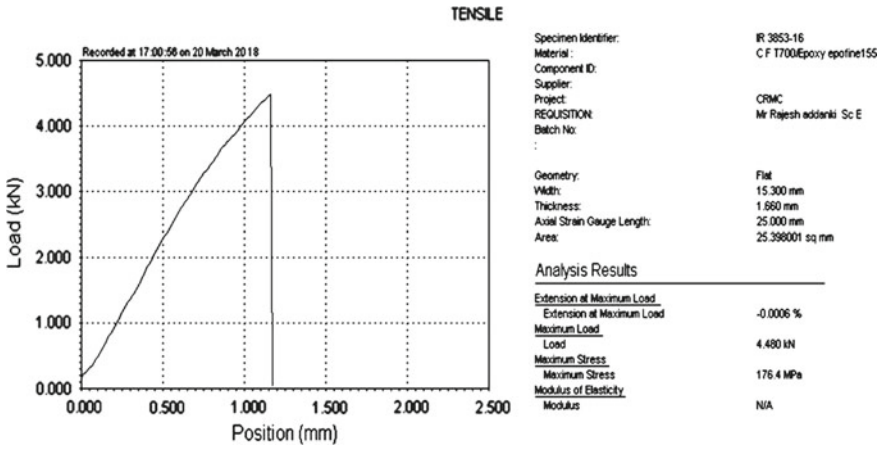


Fig. 65.7 Tensile loading of 10° laminate orientation sample 1

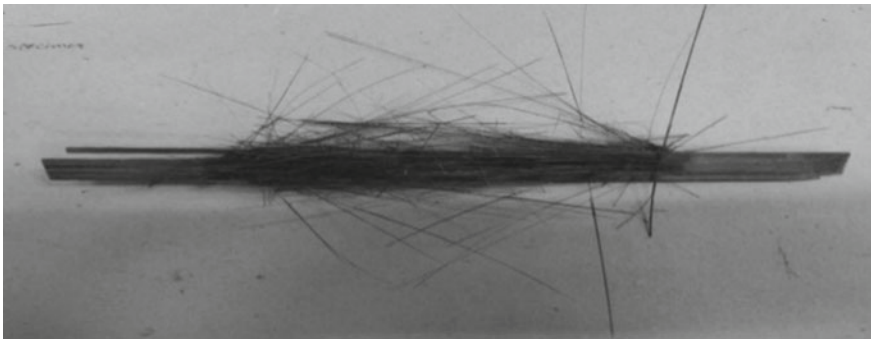


Fig. 65.8 Broom failure of the specimen

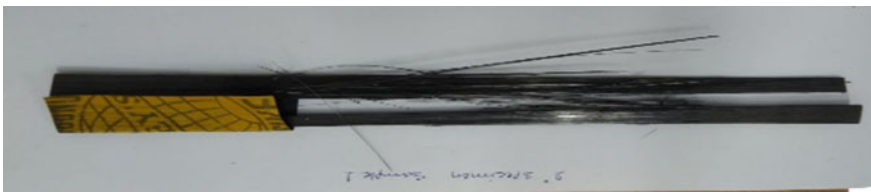


Fig. 65.9 Splitting failure of the specimen



**Table 65.1** Tensile test results of composite differing laminate orientation in test specimen

Laminate Orientation	Maximum displacement (mm)	Maximum load (kN)	Tensile strength (MPa)	Failure mode
0°	9.146	43.218	1783	Broom
	8.937	36.337	1456	Explosion
	7.990	42.937	1764	
2°	5.654	30.024	1124	Splitting
	4.876	29.426	1094	
	3.886	24.743	866	
4°	2.429	18.206	782	
	2.768	20.238	826	
	2.523	18.329	798	
6°	1.607	9.084	362	
	1.736	8.498	367	
	1.92	9.64	381	
8°	1.508	6.550	308	
	1.421	5.226	298	
	1.498	6.096	301	
10°	1.175	4.480	175	
	1.328	4.708	185	
	1.152	4.141	161	

**65.3.2 Analytical Observations from Finite Element (FE) Model Using ANSYS—Academic Version**

Finite element model is prepared using ANSYS Software (academic version) for different fiber orientations for further investigation and static analysis has been carried out as per the loading of the specimen in UTM. Static analysis is used to determine the displacements, stresses, strains, and forces in structures or components due to loads that do not induce significant inertia and damping effects. Steady loading in response conditions is assumed. The static analysis is done to understand the displacement, longitudinal stress, and traverse stress generated across the composite specimen structure, thus revealing the respective parameter distribution.

Figure 65.10 showing displacement for a specimen having 0° fiber laminate for the composite (specimen 1), showing the maximum displacement in X-direction as 7.3614 mm, and maximum stress along X-axis as 7.36133 MPa when the maximum load applied is 43.2 kN and the corresponding tensile strength as 1173 MPa.

It is observed from Fig. 65.11, longitudinal stress for the same specimen, showing the maximum displacement in X-direction as 7.3614 mm and maximum stress along normal as 1046.11 MPa, and the maximum stress recorded as 4209.24 MPa.

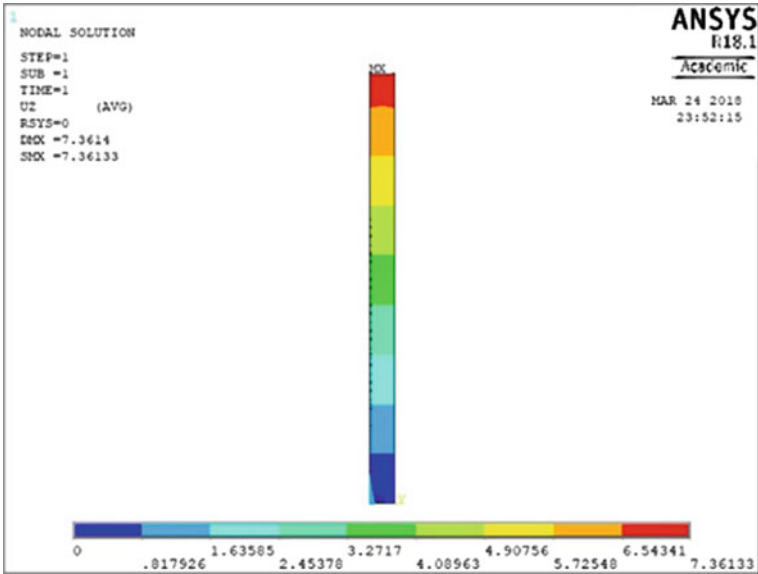


Fig. 65.10 Displacement—0° laminate orientation (specimen 1)

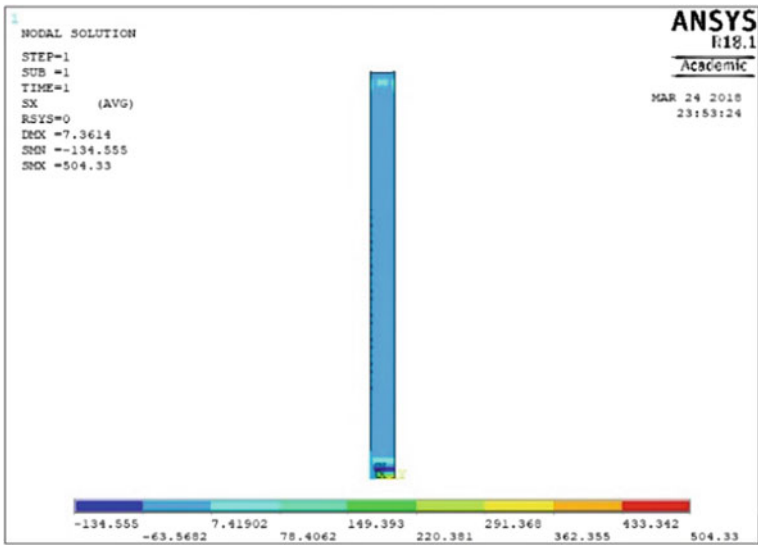
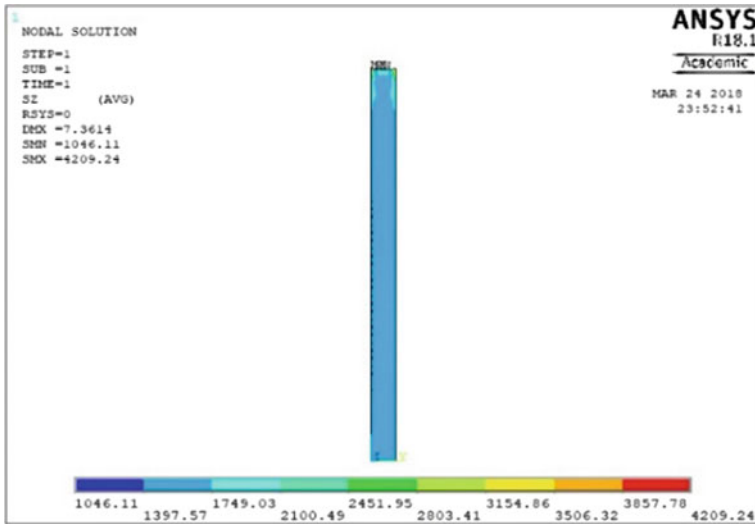


Fig. 65.11 Longitudinal stress—0° laminate orientation (specimen 1)



**Fig. 65.12** Transverse stress— $0^\circ$  laminate orientation (specimen 1)

Distribution of transverse stress, shown in Fig. 65.12, for the composite specimen prepared with  $0^\circ$  laminate orientation is shown in Fig. 65.10, for 43.2 kN applied tensile load, the maximum displacement/elongation in X-direction is 7.3614 mm having maximum stress along normal is  $-134.555$  MPa and corresponding maximum stress along X-axis is 504.33 MPa.

ANSYS result of specimen 1 having  $10^\circ$  fiber orientations shown in Figs. 65.13, 65.14, and 65.15. Figure 65.13 showing the maximum displacement values in X-direction as 2.53546 mm and maximum stress developed along X-axis as 1.21769 MPa. Longitudinal stress and traverse stress distribution in the specimen are shown in Figs. 65.14 and 65.15. Figure 65.14 shows the maximum displacement in X-direction = 2.53546 mm generating maximum longitudinal stress along normal as 121.97 MPa and corresponding maximum stress along X-axis as 442.541 MPa. For the value of displacement resulted and given above, the maximum generated along normal is  $-17.8363$  MPa and maximum transverse stress, Fig. 65.15, along X-axis is 66.6783 MPa. The variation in result of modeling and subsequent analysis for the composite structure, under static loading in ANSYS, is due to loads that do not induce significant inertia and damping effects. Steady loading and response conditions are assumed; that is, the loads and the structure's response are assumed to vary slowly with respect to time.

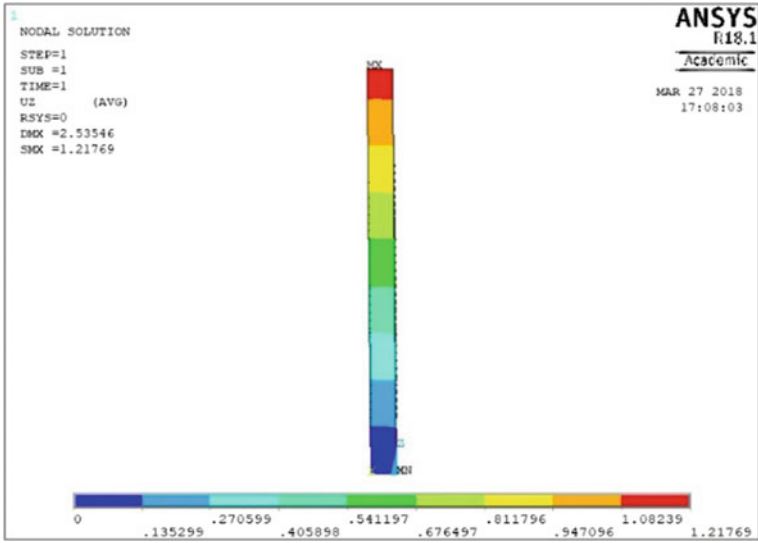


Fig. 65.13 Displacement—10° laminate orientation (specimen 1)

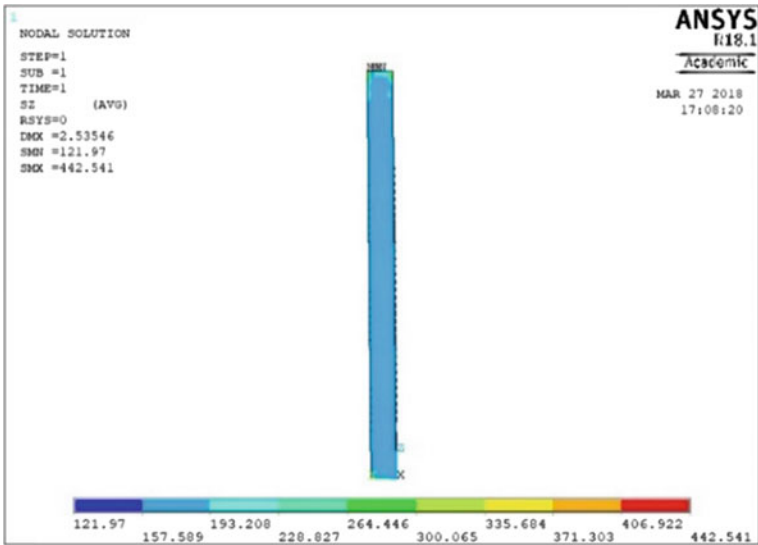


Fig. 65.14 Longitudinal stress—10° laminate orientation (specimen 1)

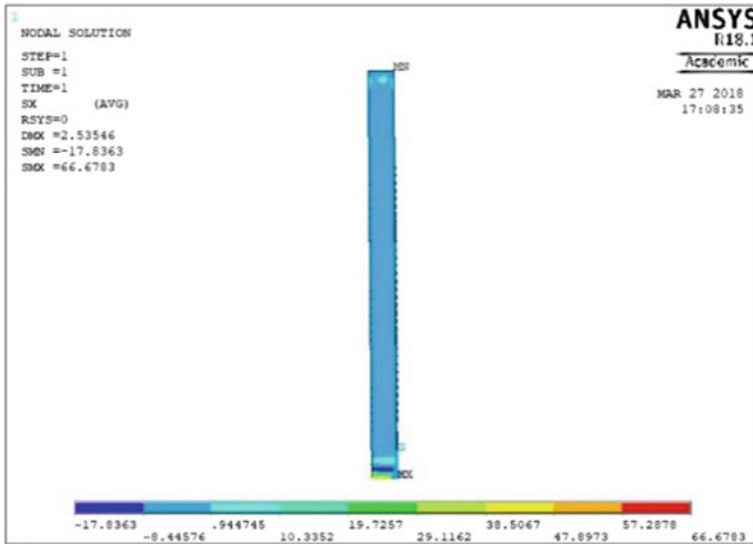


Fig. 65.15 Transverse stress— $10^\circ$  laminate orientation (specimen 1)

## 65.4 Results and Discussion

Test specimens of epoxy resin composite having carbon fiber with its orientation having  $0^\circ$ ,  $2^\circ$ ,  $4^\circ$ ,  $6^\circ$ ,  $8^\circ$ , and  $10^\circ$  to the x-axis (Fig. 65.5) are prepared and tested for tensile strength. The composite is investigated for its load-bearing capacity with respect to influence of fiber orientation is studied using experiments and analytically using ANSYS—Academic Version. The variation in its strength exists differ and it is confirming with analysis for the specimen failures. The result can be summarized as

- It is evident from the graph (load and elongation) that for axial loading, both the tensile stress and displacement values are decreased by the increase in orientation of fiber from  $0^\circ$  to  $10^\circ$ . The FE analysis results confirm the same as the experimental data.
- The results obtained can infer as changing the fiber orientation from the axial direction to transverse direction, the tensile strength of the structure is decreasing.
- The experiments conducted show that the splitting of fiber happens when fiber orientation is other than  $0^\circ$  and it may be due to gripping length. The other failures of specimen are broom and explosion of fiber at the end of the experiment.
- There is a scope to study the variation of fiber orientation further wherein the specimen can be prepared to allow the angle variation of fibers and the length adjustment to hold the sample fiber ranging in between the two grips.

## References

1. <http://www.fibre-reinforced-plastic.com/2010/12/lamina-and-laminate-what-is-that.html>. Last Accessed 25 May 2018
2. Chandra Shekar, K., Anjaneya Prasad, B., Eswara Prasad, N.: Strengthening in and fracture behavior of CNT and Carbon fiber reinforced, epoxy matrix hybrid composites. *Sadhana* **41**(12), 1443–1461 (2016)
3. Kaman, M.O.: Effect of fiber orientation on fracture toughness of laminated composite plates  $[0^\circ/\theta^\circ]_s$ . *Eng. Fract. Mech.* **78**(13), 2521–2534 (2011)
4. <http://www.ptli.com/testlopedia/tests/Thermosetting-Tensile-ASTM.asp> last accessed 29/05/2018